ELEVENTH SYMPOSIUM ON

turbulent shear flows

Grenoble, France
September 8-10, 1997

DISTRIBUTION STATEMENT A
Approved for public release
Distribution Unlimited

19971209 090

VOLUME 3
SESSIONS 23-34
POSTER SESSION 3

INSTITUT NATIONAL POLYTECHNIQUE DE GRENOBLE
INPG

CNRS CENTRE NATIONAL DE LA RECHERCHE SCIENTIFIQUE

GRENOBLE 1 UNIVERSITE JOSEPH FOURIER SCIENCES. TECHNOLOGIE. MEDECINE

DTIC QUALITY INSPECTED 4

ELEVENTH SYMPOSIUM ON

turbulent shear flows

Grenoble, France
September 8-10, 1997

VOLUME 3
SESSIONS 23-34
POSTER SESSION 3

INSTITUT NATIONAL POLYTECHNIQUE DE GRENOBLE
INPG

CNRS CENTRE NATIONAL DE LA RECHERCHE SCIENTIFIQUE

UNIVERSITE JOSEPH FOURIER SCIENCES. TECHNOLOGIE. MEDECINE

ELEVENTH SYMPOSIUM ON TURBULENT SHEAR FLOWS
Institut National Polytechnique
Université Joseph Fourier
Grenoble, September 8-10, 1997

CONTENTS OF VOLUME 3
SESSSIONS 23 - 34
POSTER SESSION 3

SESSION 23 - BUOYANT FLOWS 23-1

The influence of shear number in stably stratified turbulent shear flow 23-1
F. G. Jacobitz, S. Sarkar

DNS of natural convection between two vertical, differentially heated walls 23-7
F. T. M. Nieuwstadt, T. A. M. Versteegh

Turbulent energy transport in non-neutral shear flows 23-13
S. Heinz, A. Cadiou, K. Hanjalic

Turbulent convection at low Prandtl number 23-19
S. Cioni, J. Sommeria, S. Ciliberto

LES of buoyant cavity: subgrid scale models for inhomogeneous flows 23-24
X. Huang, D.J. Bergstrom

SESSION 24 - TWO PHASE FLOWS I 24-1

Sedimentation of small particles through the two-dimensional plane mixing layer 24-1
T. M. Dreier, M. Virant, W. Kinselbach

Dispersion of small, heavy, spherical particles in a three-dimensional, temporally developing mixing layer 24-5
B. Marcu, E. Meiburg

Lagrangian statistics of fluid/particle correlated motion in channel flow 24-11
Y. Sato, I. Hayashi, K. Hishida

Simulation and Reynolds stress modeling of particle-laden turbulent shear flows 24-17
D. B. Taulbee, F. Mashayek, P. Givi, C. Barré

Numerical study of particle motion in a turbulent mixing layer using the discrete vortex method 24-23
E. Ory, R. J. Perkins

SESSION 25 - JETS II 25-1

Investigation of mixing in a coaxial jet configuration 25-1
M. V. Salvetti, G. Lombardi, A. Talamelli

Flow regimes and mixing in the near field of large velocity ratio coaxial jets 25-7
H. Rehab, E. Villermaux, E. J. Hopfinger

On similarity of a plane turbulent jet in a co-flowing stream 25-11
J. C. LaRue, H. Rahai, T. Ly, P. Y. Jan

The influence of inlet conditions on a large eddy simulation of a turbulent plane jet 25-17
C. Weinberger, J. Rewerts, J. Janicka

Large eddy simulations of three-dimensional spatially evolving round jets 25-23
G. Urbin, C. Brun, O. Metais

SESSION 26 - SEPARATED FLOWS I 26-1

Large eddy simulation: A dynamic one-equation subgrid model for three-dimensional recirculating flow 26-1
L. Davidson

Numerical and modelling influences on large eddy simulations for the flow past a circular cylinder 26-7
M. Breuer

Response of separated flows over a backward-facing step to local forcing 26-13
K. B. Chun, H. J. Sung

An experimental investigation of the flow around a two-dimensional square prism in the proximity of a solid wall: Effect of the gap size 26-18
R. J. Martinuzzi, K. C. Q. Wu

Topology of coherent vortices in the reattachment region of a backward-facing step 26-24
F. Delcayre

SESSION 27 - TWO PHASE FLOWS II 27-1

Primary instability in liquid-gas shear layers 27-1
L. Raynal, E. Villermaux, J. Lasheras, E. J. Hopfinger

On the analysis of shear-driven liquid break-up processes 27-6
I. S. Carvalho, M.V. Heitor, D. Santos

Dispersion of bubbles in a shear flow 27-12
C. Martinez, J.C. Lasheras

Large eddy simulation of turbulent gas-solid flows in a vertical channel and evaluation of second-order models 27-18
Q. Wang, K. D. Squires, O. Simonin

Numerical investigation of turbulent heat transfer mechanisms at a gas-liquid interface ... 27-24
V. De Angelis, P. Lombardi, S. Banerjee

SESSION 28 - DNS AND LARGE EDDY SIMULATION - II 28-1

Large-eddy simulations of compressible flows on hybrid meshes 28-1
F. Ducros, F. Nicoud, T. Schönfeld

Spectral-dynamic model for LES of free and wall shear flows 28-7
E. Lamballais, M. Lesieur, J. H. Silvestrini

Large eddy simulation of turbulent channel flows 28-13
C. Fureby, A. D. Gosman, G. Tabor, H. G. Weller, N. Sandham, M. Wolfshtein

A numerical simulation on the interaction between tangled polymers and turbulent structures 28-19
Y. Hagiwara, Y. Takashina, M. Tanaka, H. Hana

Identification of vortical structures by a non-local criterion: Application to PIV measurements and DNS-LES results of turbulent rotating flows 28-25
M. Michard, L-Graftieaux, L. Lollini

SESSION 29 - COMPRESSIBLE FLOWS I 29-1

Mixing enhancement in supersonic rectangular jets 29-1
M. Samimy, J.-H.Kim, P. Clancy

Amplification/attenuation of turbulence in a heated jet/shock wave interaction 29-7
L. Jacquin, P. Geffroy

Localization and analysis of large scale structures by a wavelet transform technique in a supersonic turbulent mixing layer 29-8
P. Dupont, P. Muscat, J. P. Dussauge

Validation of a pseudo-sound theory for the pressure-dilatation in DNS of compressible turbulence 29-14
J. R. Ristorcelli, G. A. Blaisdell

Prediction of 3D supersonic flows including crossflow separation using low Reynolds number turbulence models 29-19
H. Deniau, F. Thivet, J. M. Moschetta

SESSION 30 - SEPARATED FLOWS II 30-1

Measurements in an unsteady separated flow using hot wire rakes 30-1
S. Aubrun, P. Carles, H. Ha Minh, J. Coulomb, H. Boisson

An investigation on the fluctuations of the reattachment point downstream a backward facing step using particle tracking velocimetry 30-7
G. P. Romano, S. Pomponio, G. Querzoli

Direct and Reynolds-averaged numerical simulations of a transitional separation bubble . 30-13
Ph. R. Spalart, M. Kh. Strelets

Computations of separating and reattaching flows using a low-Reynolds-number second-moment closure 30-19
T. J. Craft

Large eddy simulation of perturbed turbulent wall flows 30-25
A. Dejoan, E. Vedy, R. Schiestel

SESSION 31 - ROTATION AND CURVATURE FLOWS I 31-1

Modeling of turbulent swirling flows 31-1
T.-H. Shih, J. Zhu, W. W. Liou, K. H. Chen, N.-S. Liu, J. L. Lumley

EDQNM and DNS predictions of rotation effects in strained axisymmetric turbulence 31-7
O. Leuchter, C. Cambon

Experiments for the effects of curvature and pressure-gradient on the turbulent wake of a flat plate 31-13
A. R. Starke, R. A. W. M. Henkes, M. J. Tummers

Calculations of the flow through a U-bend 31-19
M. M. Gibson, R. D. Harper

The dissipation rate transport equation and subgri-scale models in rotating turbulence ... 31-25
R. Rubinstein, Y. Zhou, B. A. Younis

SESSION 32 - COMPRESSIBLE FLOWS II 32-1

Computations of compressible turbulent shear flows with multiple-time-scale models 32-1
A. Hadjadj, D. Vandromme, L. De Chanterac

Modeling of inhomogeneous compressible turbulence using a two-scale statistical theory 32-7
F. Hamba

An improved two-point closure for weakly compressible turbulence and comparisons with large-eddy simulation 32-13
G. Fauchet, L. Shao, R. Wunenburger, J. P. Bertoglio

Validation of linear and non-linear low-Re turbulence models in shock/boundary layer interaction 32-19
G. Barakos, D. Drikakis

Computation of turbulent shock waves using second-moment closures 32-25
G. Brun, J. M. Herard, D. Jeandel, M. Uhlmann

SESSION 33 - WALL FLOWS III 33-1

Direct numerical simulation of decelerated wall-bounded shear flows 33-1
G.N. Coleman, J. Kim, P. R. Spalart

Structure of turbulent boundary layer subjected to adverse pressure gradient 33-7
Y. Nagano, T. Tsuji, T. Houra

Application of turbulence models to equilibrium boundary layers under adverse pressure gradient 33-13
R. A. W. M. Henkes, M. Skote, D. S. Henningson

On the turbulence structure in solid and permeable pipes 33-19
C. Wagner, R. Friedrich

On the large scale organization of a turbulent boundary layer disturbed by a circular cylinder 33-25
F. de Souza, J. Delville, J. Lewalle, J.-P. Bonnet

SESSION 34 - ROTATION AND CURVATURE II 34-1

Performance of the subgrid-scale algebraic stress model for turbulent flows in a rotating frame 34-1
Y. Shimomura

Statistics of rapidly rotating turbulent plane couette flow 34-6
H. I. Andersson, K. H. Bech

Modelling near-wall effects in axially rotating pipe flow by elliptic relaxation 34-12
B. A. Pettersson, H. I. Andersson, A. S. Brunvoll

Importance of a local Rossby number for turbulence in a wake submitted to rotation 34-18
L. Tarbouriech, D. Renouard

Transition to 3-D vortex breakdown in a closed cylinder with a rotating endwall 34-24
F. Sotiropoulos, Y. Ventikos

POSTER SESSION 3 P3-1

Blowing with gas or water P3-1
J. Bellettre, F. Bataille, A. Lallemand,

Numerical study of bubble and particle motion in wall turbulence P3-6
I. A. Joia, T. Ushijima, R. J. Perkins

Turbulence modeling and first numerical simulations in turbulent two-phase flows P3-10
C. Morel

Statistical description of the bubble motion in a turbulent boundary layer P3-16
S. Tran-Cong, J. L. Marie, R. J. Perkins

Large eddy simulation and modelling of inter-particle collision influence in gas-solid turbulent shear flows P3-22
E. Deutsch, J. Lavieville, M. Sakiz, O. Simonin

The effect of turbulence modelling on turbulence modification in two-phase flows using the Euler-Lagrange approach P3-23
G. Kohnen, M. Sommerfeld

Extended algebraic stress models for prediction of three-dimensional and separating turbulent flow P3-29
R. J. A. Howard, N. D. Sandham

Computation of unsteady flows by using a semi-deterministic approach with nonlinear turbulence model P3-35
A. Kourta

Swirl flow simulation by means of Reynolds stress turbulent modelling P3-41
M. Sijercic, S. Nemoda

Modeling turbulent flow in curved duct of square cross section P3-47
Y. D. Choi, J. K. Shin, K. H. Chun, J. A. C. Humphrey

Coherence of vortices in a rotating fluid P3-53
S. Leblanc, F. S. Godeferd

Computations of strongly swirling flows with quadratic pressure-strain model P3-59
J. C. Chen, C. A. Lin

Repartition of the energy in compressible turbulence P3-65
F. Bataille, Y. Zhou, J. P. Bertoglio

Modelling of extra-compressibility terms in high speed turbulent flows P3-71
C. Lejeune, A. Kourta

Assessment of an implicit, parallel, multigrid diven algorithm for large eddy simulation P3-77
E. Arad, L. Martinelli

Numerical methods for DNS of flow past a square cylinder P3-83
R. W. C. P. Verstappen, A. E. P. Veldman

Generation of initial and boundary conditions for large-eddy simulations of wall-bounded flows P3-89
D. C. Weatherly, J. M. McDonough

On optimum filter size and efficient numerical viscosity for large eddy simulation of complex flows around a square cylinder P3-95
K. Nozawa, T. Tamura

Wavelet velocity correlation analysis in a plane turbulent jet P3-101
H. Li

Turbulence characteristics of a three-dimensional turbulent boundary layer on a rotating disk with an impinging jet P3-107
H. S. Kang, J. Y. Yoo, H. Choi

An axisymmetric wall jet with its axis removed from the wall and the effect of the wall on the evolution of coherent structures P3-113
A. Benaissa, D. Ewing, A. Pollard

Velocity structure functions in a turbulent plane jet P3-117
B. R. Pearson, R. A. Antonia

Numerical study of the detaching flow aerodynamical sound P3-122
S. Huang, C. Beguier

AUTHOR INDEX

VOLUME 1: SESSIONS 1 - 10
POSTER SESSION 1 (P1)

VOLUME 2 : SESSIONS 11 - 22
POSTER SESSION 2 (P2)

VOLUME 3 : SESSIONS 23 - 34
POSTER SESSION 3 (P3)

Abart B. , P2.1
Abdel Gawad A. F., P1.1
Abdel Latif O. E., P1.1
AbdulNour B., 15.25
AbdulNour R., 15.25
Acanski A. A., P2.25
Acton J. S., 19.13
Alboussiere T., 5.7
Alekseenko S. V., 22.18
Alvelius K., P2.107
Amano R. S., P1.18
Amielh M., 12.18
An P., P1.83
Andersson H. I., 34.6, 34.12
Anselmet F., 4.7, 12.18
Antonia R. A., 2.1, 4.7, 10.16, P3.117
Apsley D. D., 6.25
Arad E., P3.77
Arroyo G., 5.1
Asakura K., P1.61, P2.7
Aubrun S. , 30.1
Aupoix B., 6.1, 13.24
Ayrault M., P1.67
Bakic V. V., P2.25
Banerjee S., 27.24
Barakos G., 32.19
Barré C., 24.17
Bataille F., P3.1, P3.65
Bazile R., 15.1
Bech K. H., 34.6
Beguier C., P3.122
Beharelle S., 2.25
Bellettre J., P3.1
Benaissa A., P3.113
Bergstrom D. J., 14.18, 23.24
Bertoglio J. P., 32.13, P3.65
Bezard H., 13.24
Bilger R. W., 07.24
Bilski A. V., 22.18
Blaisdell G. A., 29.14
Boguslawski A., 17.18
Boiko A. V., P2.61
Boisson H.-C, 22.7, 30.1
Boniforti M. A., P1.106
Bonnet J.-P., 2.25, 5.1, 33.25, P1.55
Boree J., 15.1, 15.13
Borghi R., 7.18, 21.19, P2.30
Bouhadji A., P1.31
Bourguignon E., P2.43
Branley N., 21.1
Brasseur J. G., 16.25
Braza M., P1.31
Breard C., P1.25
Bremhorst K., 22.1
Breuer M., 26.7
Brun C., 25.23, P1.89
Brun G., 32.25
Brunet L., P2.114
Brunvoll A. S., 34.12
Cadiou A., 23.13
Cai G., P2.42
Calmet I., 8.24
Camano E. B., P2.120
Cambon C., 31.7
Carles P., 30.1
Carvalho I. S., 27.6
Castaldi S., 12.24
Cazalbou J. B., P2.114
Chaouat B., P2.71
Charnay G., 15.1
Chassaing P. , 12.24, P2.114
Chen J. C., P3.59
Chen K. H., 31.1
Chen W., 19.13
Chen W. L., 1.13
Choi H., P1.37, P3.107
Choi Y. D., P3.47
Chollet J. P., 16.19
Chun K. B., 26.13
Chun K. H., P3.47
Chung Y. M., P2.61
Ciliberto S., 23.19
Cioni S., 23.19
Citriniti J. H., 5.12, 5.18
Clancy P., 29.1
Coleman G. N., 33.1
Comte P., 1.1
Cook A. W., 16.13
Cordier L., P1.101
Corjon A., 15.13
Cotton M. A., 14.6
Coulomb J., 30.1
Cousteix J., 6.1, 13.24
Craft T.J., 20.13, 30.19
Daisaka H., P1.49
Davidson L., 26.1
De Angelis V., 27.24
De Chanterac L., 32.1
de Souza F., 33.25, P1.55
deBruynKops S. M., 16.13
deGraaff D. B., 1.19
Dejoan A., 30.25
Delcayre F., 26.24
Delville J., 2.25, 5.1, 33.25, P1.55, P1.101
Deng G. B., P2.101
Deniau H., 29.19
Deutsch E., P3.22
Doussinault M., 6.1
Dreier T. M., 24.1
Drikakis D., 32.19
Drobniak S., 17.18
Duarte D., 18.13

Dubief Y., 1.1
Ducros F., 21.13, 28.1
Dumont T., 10.11
Dupont P., 29.8
Durbin P. A., 6.19
Durst F., 2.13
Dussauge J. P., 29.8
Eaton J. K., 1.19, 8.13
Eifert C., 3.1
Elkins C. J., 8.13
Engel K., P1.11
Eulitz F., P1.11
Ewing D., 5.12, P3.113
Faghani D., 22.7
Fauchet G., 32.13
Favre Marinet M., 12.1, P2.120
Ferrao P., 18.13
Ferre J. A., 2.7, P1.95
Ferziger J. H., 16.1
Foss J. F., 15.25
Founti M., 19.7
Friedrich R., 33.19
Fu D., P2.42
Fu S., 6.7
Fu S. R., 13.1
Fujisawa N., 9.13
Fukushima C., P2.55
Fureby C., 28.13
Galzin F., 21.19, P2.30
Garem J.-H., 5.1
Gatski T. B., 13.7
Geffroy P., 29.7
Gehrke P., 22.1
Gerasimov A. V., P2.113
Gibson M. M., 31.19
Giralt F., P1.95
Girimaji S. S., P1.118
Givi P., 24.17
Gleyzes C., 6.1
Godeferd F. S., P3.53
Gokalp I., 12.6, 12.12, P2.43
Gonzalez M., 7.18
Gooden J. H. M., 6.1
Gosman A. D., 28.13
Graftieaux L., 28.25
Guy A. W., 14.6
Ha Minh H. , 30.1, P2.126
Hadjadj A. , 32.1
Hagiwara Y., 28.19
Hahn S., P1.37
Haidous Y., 12.12
Hallback M., 8.1, P2.107
Hamba F., 32.7
Hana H., 28.19
Hanjalic K., 11.16, 15.19, 23.13
Hanratty T. J., 9.25, 11.7
Harion J. L., 12.1
Harper R. D., 31.19
Harran G., 12.24
Hartmann M., 14.1
Hassel E. P., 18.1
Hauville F., P1.25
Hayashi I., 24.11
He S., 22.1, P1.83
Heinz S., 23.13
Heitor M. V., 18.13, 27.6
Heitz D., 5.1
Henkes R. A. W. M. , 31.13, 33.13
Henningson D. S., 33.13
Herard J. M., 32.25
Herbert V., 10.7
Higashio A., 19.13
Hishida K., 24.11, P1.49
Hopfinger E. J., 25.7, 27.1
Horiuti K., 16.7
Hosoda T., 19.1
Houra T., 33.7
Howard R. J. A., P3.29
Huang P. G., P2.83
Huang S., P3.122
Huang X., 23.24
Huang Z., 19.25
Huberson S., P1.25
Humphrey J. A. C., P3.47
Hwang C. B., P2.95
Iacovides H., 3.19
Ichikawa Y., 20.7, P1.61, P2.7
Iida O., 20.1
Ikeda J., 4.17, P1.77
Ilyushin B. B., 20.19
Jackson J. D., P1.83
Jacobitz F. G., 23.1
Jacquin L., 29.7
Jakirlic S., 15.19
Jan P. Y., 25.11
Janicka J., 3.1, 18.1, 25.17
Jeandel D., 32.25
Jervase L., P2.114
Johansson A. V., 8.1, 13.13, P2.107
Joia I. A., P3.6
Joly L., 12.24
Jonas P., P2.77
Jones W. P., 3.25, 21.1
Jongen T., 13.7
Jovanovic J., 2.13
Juneja A., 16.25
Kang H. S., P3.107
Kanzaki T., 20.7
Kasagi N., 9.7, 9.18, 20.1, P1.43
Kassinos S. C., 7.1

Kawaguchi Y., P1.49
Kawahara G., 1.7
Kawamura H., 8.7
Keffer J. F., P1.95
Keicher M., P2.13
Kent J. H., 7.24
Khris S., P1.19
Kida S., 1.7
Kidger J., 20.13
Kim D. S., P1.71
Kim J., 33.1
Kim J. H., 29.1
Kimura I., 19.1
Kinselbach W., 24.1
Kitamura O., P2.19
Kitoh O., 11.10
Klipfel A., 19.7
Kobayashi T., 22.24
Koch R., P1.7
Kohnen G., P3.23
Komori S., 21.25
Kopp G. A., P1.95
Kourta A., P2.126, P3.35, P3.71
Kremer A., 18.1
Kronenburg A., 7.24
Kubo T., 18.19
Kuhn D. C. S., 19.25
Kurbatskii A. F., 20.19
Lakehal D., 3.13
Lallemand A., P3.1
Lamballais E., 28.7
Landenfeld T., 18.1
Larcheveque M., 10.7
LaRue J. C., 25.11
Lasheras J. C., 22.12, 27.1, 27.12
Launder B. E, 14.6, 20.13
Lavieville J., P3.22
Le Penven L., 15.7
Le Roy O., 15.7
Leblanc S., P3.53
Lee D. H., P1.71
Lejeune C., P3.71
Leontiev A. I., P2.113
Leschziner M. A., 1.13, 6.25
Lesieur M., 28.7
Leuchter O., 31.7
Lewalle J., 33.25
Leweke T., 17.1, 17.12
Li H., P3.101
Li J., P1.83
Lien F. S., 1.13, 6.19
Lin B., P1.18
Lin C. A., P2.95, P3.59
Lindstedt R. P., P2.36
Liou W. W., 31.1
Liu N.-S., 31.1
Lollini L., 28.25
Lombardi G., 25.1, 27.24
Lucas J. F., 12.18
Lumley J. L., 31.1
Ly T., 25.11
Machiels L., 4.23, 13.7
Maeda M., P1.49
Magnaudet J., 8.24
Mantel T., 21.19, P2.30
Marc D., 15.1, 15.13
Marchal P., 5.1
Marcillat J., P1.19
Marcu B., 24.5
Marie J. L., P3.16
Markovich D. M., 22.18
Marquis A. J., 3.7
Martin J. P., 19.7
Martinelli L., P3.77
Martinez C., 27.12
Martinuzzi R. J., 11.16, 26.18
Mashayek F., 24.17
Massah H., 9.24
Mathey F., 16.19
Mazur O., P2.77
McComb W. D., 4.23
McDonough J. M., P3.89
McGrath J. J., 15.25
Meiburg E., 24.5
Meinders E. R., 11.16
Menzies K. R., 3.25
Messing R., 13.24
Metais O., 25.23
Michard M., 28.25
Michelot C., P1.67
Michou Y., P2.43
Minier J. P., P1.112
Mito Y., 9.7
Miyake Y., 11.1
Miyata M., 14.12
Miyauchi T., 4.17
Miyazaki T., P1.102
Möller S. V., P2.49
Moreau R., 5.7
Morel C., P3.10
Morganti M., P1.106
Morikawa T., 11.1
Moschetta J. M., 29.19
Motohashi T., 17.24
Muramoto Y., 19.1
Muscat P., 29.8
Nagano Y., 20.1, 33.7
Nagata K., 21.25
Nakabayashi T., 9.13, 11.10
Nakabe K., 19.13

Nakagawa S., 2.19
Nakamura I., 18.19
Nakayama A., 19.19
Namiki N., P2.19
Nedelcu G., P2.55
Nemoda S., P3.41
Nguyen P. N., 5.24
Nicolleau F., 4.13
Nicoud F., 28.1
Nieuwstadt F. T. M., 23.7
Nishimura F., 11.10
Nitta K., 2.19
Noda H., 19.19
Nozawa K., P3.95
Oberlack M., 10.21
Ohsaka K., 8.7
Oka S. N., P2.25
Ong L. Y., 3.7
Ono K., 17.24
Orlandi P., 14.22
Ormieres D., 17.7
Ory E., 24.23
Osaka H., P2.55
Oshinowo T., 19.25
Ould-Rouis M., 4.7
Page J., 12.12
Papavassiliou D. V., 11.7
Park J., P1.37
Parneix S., 6.19
Pearson B. R., P3.117
Perkins R. J., 24.23, P3.6, P3.16
Petit J. P., 19.7
Pettersson B. A., 34.12
Pfuderer D. G., 3.1
Piana J., 21.13
Picut M., P1.89
Pietri L., 12.18
Pinheiro J., 7.18
Pollard A., 11.22, P3.113
Pomponio S., 30.7
Pons M. D., 2.7
Pozorski J., P1.112
Prestridge K. P., 22.12
Prinos P., P2.89
Priymak V.G., P1.102
Protas B., 10.1
Provansal M., 17.7
Queiros-Conde D., 18.25
Querzoli G., 30.7
Ragab S. A., P1.1
Rahai H., 25.11
Raynal L., 27.1
Rehab H., 25.7
Renouard D., 34.18
Rewerts J., 25.17
Rexroth C. H., P1.7
Reynier P., P2.126
Reynolds W. C., 7.1
Riley J. J., 16.13
Ristorcelli J.R., 7.7, 29.14
Robert R., 10.11
Rodi W., 3.13
Romano G. P., 30.7
Ronneberger D., 14.1
Rubinstein R., 31.25
Rung T., 6.7, 13.1
Sabelnikov V., P1.67
Sada K., P1.61, P2.7
Saint Martin V., 13.24
Sakai Y., 18.19
Sakiz M. , P3.22
Salvetti M. V., 25.1
Samimy M., 29.1
Sanders J. P. H., 12.6
Sandham N., 28.13
Sandham N. D., P3.29
Santos D., 27.6
Sarboch J., P2.120
Sardi K., 8.19
Sarh B., 12.12
Sarkar S., 23.1
Satake S., P1.43
Sato Y., 24.11
Schiestel R., 30.25
Schönfeld T., 28.1
Sciortino G., P1.106
Semenov V. I., 22.18
Senda M., 2.19
Sevrain A., 22.7
Shaalan M. R., P1.1
Shah K. B., 16.1
Shao L., 32.13
Shih T.-H., 31.1
Shima N., 7.12
Shimomura Y., 34.1
Shin J. K., P3.47
Shishov E. V., P2.113
Sijercic M., P3.41
Silvestrini J. H., 28.7
Simoens S., P1.67
Simonin O., 27.18, P3.22
Sini J. F., P2.1
Sirovich L., 4.1
Skote M., 33.13
Smart G. M., P2.67
Sofialidis D., P2.89
Sommerfeld M., P3.23
Sommeria J., 10.11, 23.19
Song H. B., P1.71
Sotiropoulos F., 34.24

Spalart Ph. R., 30.13, 33.1
Squires K. D., 6.13, 27.18
Staquet C., 10.7, 20.25
Starke A. R., 31.13
Stefanovic M. M., P2.25
Strelets M. Kh., 30.13
Suga K., 13.18
Sullivan P., 19.25
Sung H. J., 26.13, P2.61
Suzuki Y., 9.18, 19.13
Tabor G., 28.13
Takashina Y., 28.19
Talamelli A. , 25.1
Tamura T., P3.95
Tanahashi M., 4.17
Tanaka M., 1.7, 28.19
Taniguchi N., 22.24
Tarbouriech L., 34.18
Tardu S., 9.1, 12.1
Tarman I. H., 4.1
Tatschl R., 18.7
Taulbee D. B., 24.17
Taylor A. M. K. P., 8.19, P2.13
Tenaud C., P1.101
Theodoridis G. S., 3.13
Thiele F., 6.7, 13.1
Thivet F., 29.19
Tran-Cong S., P3.16
Tropea C., 15.19
Tsang W. K., 2.1
Tsubokura M., 22.24
Tsuji T., 33.7
Tsujimoto K., 11.1
Tummers M. J., 31.13
Uhlmann M., 32.25
Urbin G., 25.23
Uruba V., P2.77
Ushijima T., P3.6
Uspenski V., 5.7
Van Kalmthout E., 21.7
Vandromme D., 32.1
Vaos E. M., P2.36
Vassilicos J. C., 4.13
Vedy E., 30.25
Veldman A. E. P., P3.83
Ventikos Y., 34.24
Verstappen R. W. C. P, P3.83
Versteegh T. A. M., 23.7
Veynante D., 21.7, 21.13
Vicari K. F. F., P2.49
Villermaux E., 25.7, 27.1
Virant M., 24.1
Visonneau M., P2.101
Volkert J., 15.19
Völtz C., 14.1
Voutsinas S. G., P1.25
Wagner C., 33.19
Wallin S., 13.13
Wang Q., 27.18
Warholic M., 9.24
Weatherly D. C., P3.89
Webster D. R., 1.19
Weinberger C., 25.17
Weller H. G., 28.13
Wesfreid J. E., 10.1
Wikstrom P. M., 8.1
Willenborg K., 15.25
Williamson C. H. K., 17.1, 17.12
Winters K. B., 20.25
Wittig S., P1.7
Wolfshtein M., 28.13
Wu K. C. Q., 26.18
Wu X., 6.13
Wunenburger R., 32.13
Xu H., 11.22
Yabe A., P1.49
Yamagami K., 2.19
Yamamoto K., 8.7
Yamamoto M., P2.19
Yanase S., 1.7
Yang T. J., 4.23
Yasuda R., P1.77
Ye Q. Y., 2.13
Yoo J. Y., P3.107
Yoon S. H., P1.71
Yoshikawa T., 11.1
Young A., 4.23
Young S., 14.18
Younis B. A., 31.25
Zahringer K., 19.7
Zhai Z., 6.7
Zhou T., 10.16
Zhou Y., 2.1, 31.25, P3.65
Zhu J., 31.1
Zhu Y., 4.7, 10.16
Zhuang F., P2.42

SESSION 23 - BUOYANT FLOWS

THE INFLUENCE OF SHEAR NUMBER IN STABLY STRATIFIED TURBULENT SHEAR FLOW

Frank G. Jacobitz & Sutanu Sarkar
Department of Applied Mechanics and Engineering Sciences
University of California, San Diego
9500 Gilman Drive
La Jolla, CA 92093-0411
USA

INTRODUCTION

An ambient stratification such that density decreases in the vertically up direction is known to have a potentially large effect in decreasing turbulence levels and associated transport in oceanic and atmospheric flows. A prototypical example which involves the competing effects of shear-induced production of turbulence and gravity-induced stabilization is the case with uniform mean shear $S = \partial\overline{U}_1/\partial x_3$ and uniform stable stratification $S_\rho = \partial\overline{\rho}/\partial x_3$. The gradient Richardson number $Ri = N^2/S^2$, where $N = (-gS_\rho/\rho_0)^{(1/2)}$ is the Brunt-Väisälä frequency, has been previously thought to be the primary stratification-related nondimensional parameter of relevance and other important parameters that have been identified include the Taylor microscale Reynolds number and the Prandtl number. Although the effect of these parameters has been the subject of previous experimental studies (Rohr, Itsweire, Helland & Van Atta 1988), and direct numerical simulations (Gerz, Schumann & Elghobashi 1989; Holt, Koseff & Ferziger 1992), the importance of the shear number has been recognized only recently. The shear number SK/ϵ is the ratio of a turbulence evolution time scale K/ϵ to the time scale $1/S$ imposed by the mean velocity gradient. The shear number effect was discovered during the DNS (direct numerical simulation) study of Jacobitz, Sarkar & Van Atta (1997) and an experimental study of Piccirillo & Van Atta (1997). In the DNS study, the gradient Richardson number Ri, the Taylor microscale Reynolds number Re_λ, and the shear number SK/ϵ were varied independently and the effects on the evolution of the turbulence stresses and the buoyancy flux were obtained.

Turbulent motion is ubiquitous in atmospheric and oceanographic flow (Caldwell & Moum 1995) and large shear number turbulence can occur in the geophysical environment. An example is the equatorial undercurrent that is believed to be controlled by turbulent effects (Crawford & Osborn 1981). While some measurements show highly turbulent spots with strong turbulent dissipation (Williams & Gibson 1974), others indicate only low turbulent dissipation rates (Caldwell 1987), which could contribute, together with the high vertical shear rates in the equatorial undercurrent, to large shear number flow. Also nonequilibrium situations near solid boundaries or at boundaries of ocean currents where the mean shear changes suddenly can lead to large shear number flow. Near-wall turbulence in the buffer region is known to have large values of the shear number in excess of $SK/\epsilon = 15$.

Recent second-order and algebraic stress models intended for nonequilibrium turbulent flows incorporate an explicit dependence on the shear number. This contribution supplements the discussion of the shear number effect in Jacobitz *et al.* (1997) by presenting additional results from simulations conducted at higher Reynolds numbers as well as by presenting new results regarding the effect of shear number on spectral dynamics and turbulence transport coefficients for momentum and mass. A parameterization of the transport coefficients can lead to an improvement of general circulation models (e.g. Gargett, Cummins & Holloway 1989). A detailed description of the effect of the Richardson number and the Reynolds number on the turbulence evolution and a discussion of the critical Richardson number is available in Jacobitz *et al.* (1997).

MATHEMATICAL PRELIMINARIES

This study is based on the direct numerical simulation of the continuity equation of an incompressible fluid, the unsteady three-dimensional Navier-Stokes equations in the Boussinesq approximation, and a transport equation for the density. No turbulence models are used and all dynamically important scales of motion are resolved.

The evolution of turbulent fluctuations can be studied by consideration of the following transport equation for the turbulent kinetic energy $K = \overline{u_i u_i}/2$ of the velocity fluctuations:

$$\frac{dK}{dt} = P - B - \epsilon \tag{1}$$

Here $P = -S\overline{u_1 u_3}$ is the production term, $B = g\overline{u_3\rho}/\rho_0$ is the buoyancy flux, and $\epsilon = \nu\overline{(\partial u_i/\partial x_k)(\partial u_i/\partial x_k)}$ is the

viscous disspation, g is the gravity coefficient, ρ_0 is the mean density, and ν is the kinematic viscosity. A scaling analysis of equation (1) leads to three nondimensional parameters governing the evolution of the turbulent kinetic energy: The gradient Richardson number Ri, the Taylor microscale Reynolds number Re_λ, and the shear number SK/ϵ.

We report here results from a study in which the shear number is varied and all other nondimensional parameters are fixed. Note that a variation of the shear number SK/ϵ also changes the turbulent Froude number $NK/\epsilon = \sqrt{Ri}SK/\epsilon$, if the Richardson number Ri is kept constant. Since both S and N are increased proportionally to increase SK/ϵ while keeping Ri constant, the shear number variation in stratified shear flow can be attributed to a change of the shear rate S as well as a change of the Brunt-Väisälä frequency N. However, the shear number effect cannot be explained as a purely stratification related effect, since it persists in unstratified shear flow.

Equation (1) can be rewritten in order to define the nondimensional growth rate γ:

$$\gamma = \frac{1}{SK}\frac{dK}{dt} = -2b_{13}(1 - \frac{\epsilon}{P} - \frac{B}{P}) \qquad (2)$$

Here b_{13} is the 1-3 component of the Reynolds stress anisotropy tensor $b_{ij} = \overline{u_i u_j}/\overline{u_k u_k} - \delta_{ij}/3$. Under the assumption (borne out by DNS and physical experiments) that each term on the right-hand-side of equation (2) becomes asymptotically constant, the equation can be integrated:

$$K = K_0 \exp(\gamma St) \qquad (3)$$

Therefore exponential growth or decay of the turbulent kinetic energy K can be expected with an asymptotically constant growth rate γ.

In order to further understand the shear number effect, the evolution in spectral space is also considered here. A transport equation for the radial spectrum of the turbulent kinetic energy $E(k)$ can be derived as follows: First, the Navier-Stokes equation is transformed into Fourier space. Second, the pressure gradient term is eliminated by ensuring the divergence-free constraint on the velocity, that is, the velocity Fourier modes which are parallel to the wave number vector are set to zero. Third, the transformed equation is multiplied with the complex conjugate of the Fourier transform of the velocity. Finally, the terms of the resulting equation are averaged over spherical shells of constant magnitude of the wavenumber vector k (eg. Lesieur 1993):

$$\frac{dE(k)}{dt} = T(k) + P(k) - B(k) - \epsilon(k) \qquad (4)$$

Here $T(k)$ is the spectral transfer term which arises from the nonlinear term $u_j \partial u_i/\partial x_j$ in the momentum equation, $P(k)$ the production term, $B(k)$ the buoyancy term, and $\epsilon(k)$ the dissipation term. The terms $P(k)$, $B(k)$, and $\epsilon(k)$ are analogs of the terms on the right-hand-side of equation (1).

The numerical algorithm used in this study is based on a spectral collocation method for the spatial discretization and a third order Runge-Kutta scheme to advance the solution in time. The initial conditions are a realization of well-established isotropic turbulence which is obtained from a simulation that is allowed to develop for approximately an eddy turnover time. The Prandtl number is $Pr = 0.72$.

INFLUENCE ON THE TURBULENT KINETIC ENERGY EVOLUTION

In this section the influence of the shear number on the evolution of the turbulent kinetic energy is addressed. Two series of simulations were performed. A low Reynolds number series with $Ri = 0.06$ and initial $Re_\lambda = 22.36$ and a high Reynolds number series with $Ri = 0.15$ and initial $Re_\lambda = 44.72$. The results of the low Reynolds number series were presented in detail by Jacobitz *et al.* (1997). The primary purpose of the high Reynolds number series is to show that the shear number influence on the turbulence evolution persists at higher Reynolds numbers and is not just a low Reynolds number effect. The final values of the Reynolds number are $Re_\lambda = 70$ for the high Reynolds number series. A computational grid overlaying a cube of length 2π was used with either 96^3 or 128^3 points in the low Re series. The streamwise extent was doubled to 4π in the high Re series to ensure that the integral length scale in the streamwise direction remains small compared to the box size. *A posteriori* checks of velocity and density autocorrelations showed that they decayed sufficiently rapidly with increasing streamwise separation. 244 points were used in the streamwise direction with 144 points in the other two directions leading to increased small-scale resolution with respect to the low Re series.

Figure 1 shows the evolution of the turbulent kinetic energy K as a function of normalized time St for a series of simulations where the initial shear number was varied while the gradient Richardson number $Ri = 0.06$ and the initial value of the Reynolds number $Re_\lambda = 22.36$ are fixed. After an initial decay, the turbulent kinetic energy K follows an approximately exponential law and the asymptotic value of the growth rate $\gamma = (1/SK)dK/dt$ is plotted as a function of initial SK/ϵ in figure 2. For small shear numbers, the growth rate γ increases sharply with increasing SK/ϵ and the turbulent kinetic energy evolution changes from decay to growth. However, the growth rate γ decreases with a further increase of SK/ϵ and the turbulent kinetic energy decays for large shear numbers.

These simulations were performed with a relatively low initial value $Re_\lambda = 22.36$. It is therefore possible that the observed influence on the turbulent kinetic energy evolution is due to low Reynolds number effects. Therefore a second series of simulations was performed with the higher initial value $Re_\lambda = 44.72$. The evolution of the turbulent kinetic energy is shown in figure 3. The evolution of K changes from decay to growth as the initial value of the shear number is increased from $SK/\epsilon = 2.0$ to $SK/\epsilon = 6.0$. An additional simulation with initial $SK/\epsilon = 14.0$ clearly shows decay of the turbulent kinetic energy. Therefore the stabilizing effect found at large shear numbers persists at higher Reynolds numbers and is not a low Reynolds number effect.

The simulations were performed to a long nondimensional time of up to $St = 30$ for the low Reynolds number series and $St = 20$ for the high Reynolds number series to ensure that shear and stratification effects are well developed. The simulations of an unstratified shear flow of Lee, Kim & Moin (1990) have shown that the Reynolds shear stress reaches its asymptotic value for $St < 10$. On the other hand, the nondimensional time $St = 30$ for the low Re_λ simulation with $Ri = 0.06$ and the nondimensional time $St = 20$ for the high Re_λ simulation with $Ri = 0.15$ both correspond approximately to a nondimensional time $Nt = 7.5$ thus giving the buoyancy effects sufficient time to develop.

In the unstratified case, there is some experimental evidence (Souza, Nguyen & Tavoularis 1995) and DNS evidence (Lee *et al.* 1990) that the growth rate and the magnitude of the Reynolds stress anisotropy $b_{13} = \overline{u_1 u_3}/2K$

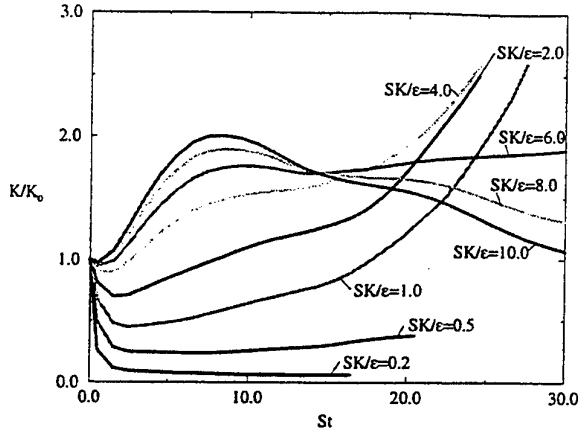


Figure 1: Evolution of the turbulent kinetic energy K for $Ri = 0.06$ and initial $Re_\lambda = 22.36$.

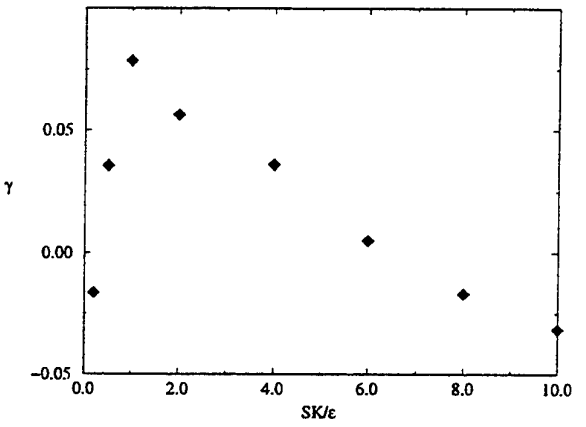


Figure 2: Dependence of the growth rate γ on the initial value of SK/ϵ for $Ri = 0.06$ and initial $Re_\lambda = 22.36$.

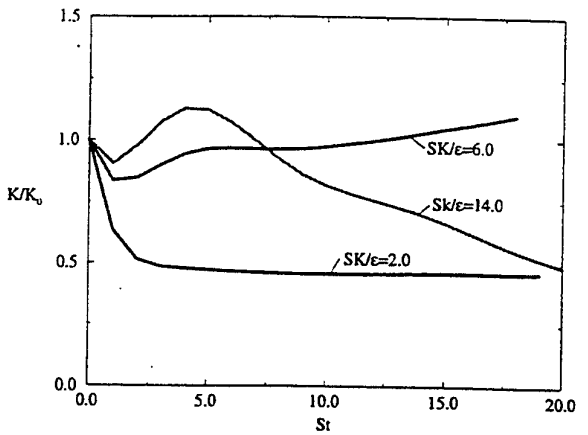


Figure 3: Evolution of the turbulent kinetic energy K for $Ri = 0.15$ and initial $Re_\lambda = 44.72$.

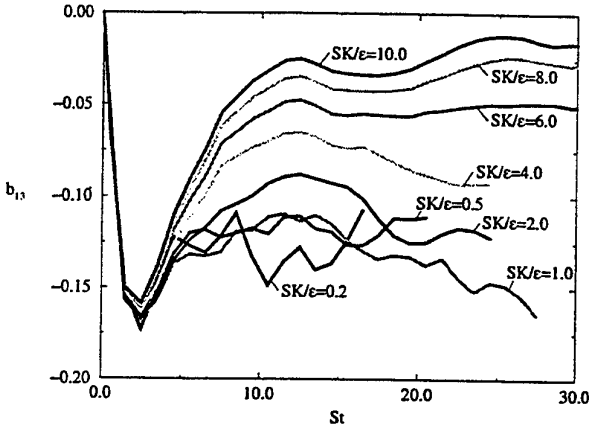


Figure 4: Evolution of b_{13} for $Ri = 0.06$ and initial $Re_\lambda = 22.36$.

decrease in the large shear number regime. It should be noted that the magnitude of b_{13} decreases with increasing shear number in our simulations as shown in figure 4. The decrease of the magnitude of b_{13} as well as the decrease of the ratio ϵ/P (not shown here) with increasing shear number are responsible for the decrease of the growth rate γ as is evident from equation (2).

In the stably stratified case, recent experimental observations of Piccirillo & Van Atta (1997) at low initial shear numbers ($SK/\epsilon < 1$) suggest that the growth rate of K increases with the shear number consistent with the behavior for $0 < SK/\epsilon < 1.0$ shown in figure 2.

The increase of γ with SK/ϵ in the low shear number regime is an expected transition from unforced, decaying turbulence to the case of shear-induced forcing. However, why does the growth rate decrease with increasing SK/ϵ in the large shear number regime? It is known that linear viscous rapid distortion theory (RDT) (eg. Rogers 1991) predicts asymptotic decay of the turbulent kinetic energy. RDT neglects the nonlinear term with respect to the mean gradient term in the velocity fluctuation equation and is strictly valid for $SK/\epsilon >> 1$ and short time $St = O(1)$, $Nt = O(1)$. However, the stabilizing trend at large shear numbers in the DNS is observed with the full governing equations and at large values of St and Nt.

In order to evaluate the extent of linear effects, the linearized viscous RDT equations were simulated for two cases with $SK/\epsilon = 2.0$ and $SK/\epsilon = 10.0$. Figures 5 and 6 compare their results with those of the full nonlinear equations. The linear and nonlinear evolution are initially very close in both cases for approximately 0.8 eddy turnover times which corresponds to $St = 1.6$ in figure 5 and $St = 8$ in figure 6. With respect to the long-time evolution, it is clear that, first, the linearized simulations predict asymptotic decay for both cases consistent with the analytical result, and second, the linear simulation is qualitatively similar at long time to the nonlinear simulation for the large shear number number case in figure 6 and *not so* for the moderate shear case in figure 5. Thus, a possible explanation for the stabilizing trend at large shear numbers is that, during the full nonlinear evolution, linear effects are progressively more *persistent* for large initial SK/ϵ.

INFLUENCE ON THE SPECTRAL TRANSPORT

In this section the influence of the shear number on the terms of the spectral transport equation (4) is discussed. The results are taken from the high Reynolds number series of simulations with $Ri = 0.15$ and initial $Re_\lambda = 44.72$.

Figure 7 shows the nonlinear transport term $T(k)$ normalized by q^3 at the nondimensional time $St = 15$. Note

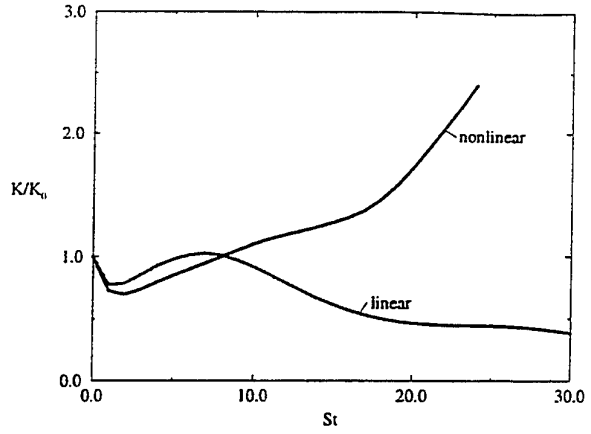


Figure 5: Linear and nonlinear evolution of K for $Ri = 0.06$, initial $Re_\lambda = 22.36$, and low initial $SK/\epsilon = 2.0$.

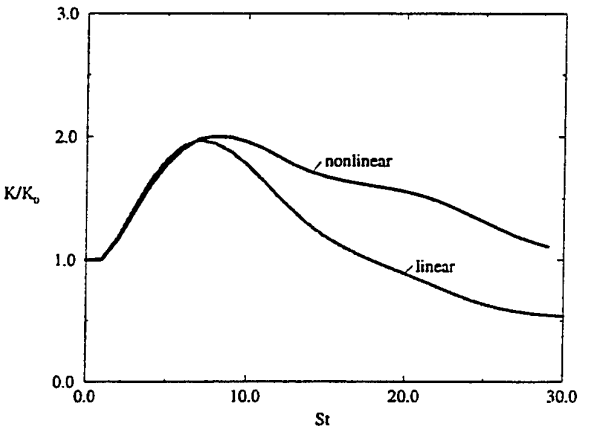


Figure 6: Linear and nonlinear evolution of K for $Ri = 0.06$, initial $Re_\lambda = 22.36$, and high initial $SK/\epsilon = 10.0$.

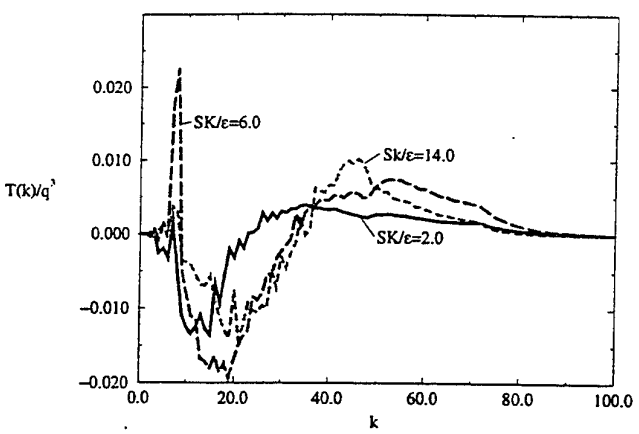


Figure 7: Spectral transfer of K at $St = 15$ for $Ri = 0.15$ and initial $Re_\lambda = 44.72$.

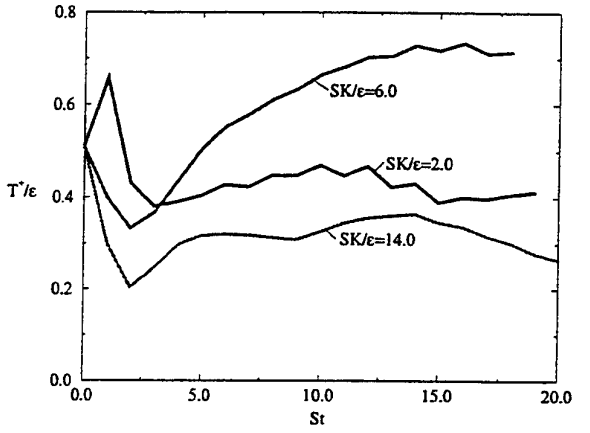


Figure 8: Ratio of T^+ to ϵ for $Ri = 0.15$ and initial $Re_\lambda = 44.72$.

that $q^2 = 2K$. The low wave number modes in the range, $1 < k < 10$, generally gain energy with localized peaks of large positive $T(k)$. This 'reverse' energy transfer results in the observed shift of energy spectra maxima to large length scales with time. The intermediate wave number range, $10 < k < 30$, is associated with negative $T(k)$ and loses energy while the high wave number modes gain energy as a result of the nonlinear transfer. The most significant difference in $T(k)$ between the asymptotically decaying $SK/\epsilon = 14$ case relative to the asymptotically growing $SK/\epsilon = 6$ case is perhaps the large reduction in the low wave number, positive peak of $T(k)$. Also, the magnitude of energy redistribution due to nonlinearity as measured by $\int T^+(k)\,dk$ is smaller in the $SK/\epsilon = 14$ case. Here $T^+ = (|T| + T)/2$. The relative importance of T^+ to ϵ during the time evolution is shown in figure 8. It shows that the strongly growing $SK/\epsilon = 6$ case has the strongest nonlinear transport and that the nonlinear transport is reduced for the $SK/\epsilon = 14$ case.

Figure 9 shows the normalized spectral production term $P(k)$ at the nondimensional time $St = 15$. The production term adds significant energy to a compact range, $1 < k < 35$, of low wavenumber modes. For the high $SK/\epsilon = 14.0$ case, the magnitude of the production term is reduced and the location of peak production is shifted to a lower wave number relative to the other cases. Furthermore, there is some countergradient momentum transport at high wave numbers in this case as indicated by negative values of $P(k)$.

Figure 10 shows the normalized spectral buoyancy term $B(k)$ at the nondimensional time $St = 15$. In the cases with initial $SK/\epsilon = 2$ and 6, there is generally cogradient buoyancy flux which spans the compact range of wave numbers associated with positive production $P(k)$. The behavior of $B(k)$ appears to be qualitatively different in the $SK/\epsilon = 14$ case. The extent of cogradient transport is limited to a narrow range, $1 < k < 8$ of very low wavenumber modes and a small countergradient buoyancy flux is observed at high wavenumber modes in the range $30 < k < 50$. In between these ranges, the buoyancy term oscillates around $B(k) = 0$.

INFLUENCE ON TRANSPORT COEFFICIENTS

In this section the influence of the shear number on momentum and mass transport is investigated. The results are taken from the series of simulations with $Ri = 0.06$ and initial $Re_\lambda = 22.36$.

Figure 11 shows the evolution of the flux Richardson number $Ri_f = B/P$ which is the ratio of the buoyancy term

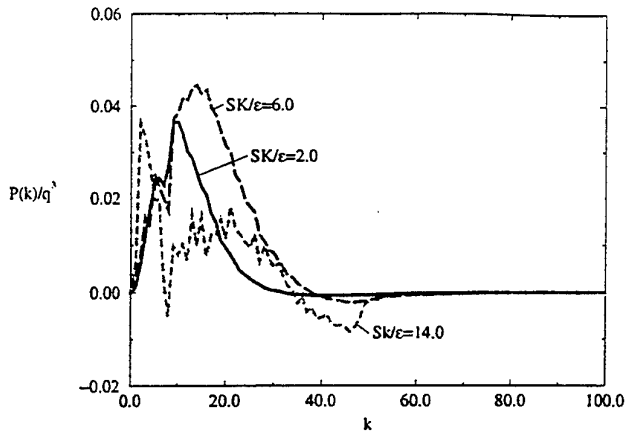


Figure 9: Spectral production of K at $St = 15$ for $Ri = 0.15$ and initial $Re_\lambda = 44.72$.

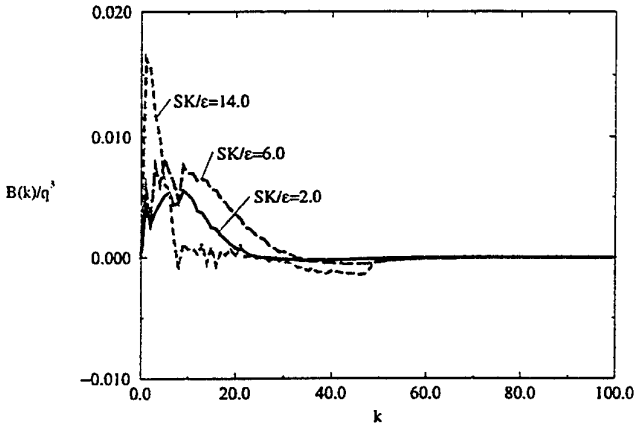


Figure 10: Spectral buoyancy flux at $St = 15$ for $Ri = 0.15$ and initial $Re_\lambda = 44.72$.

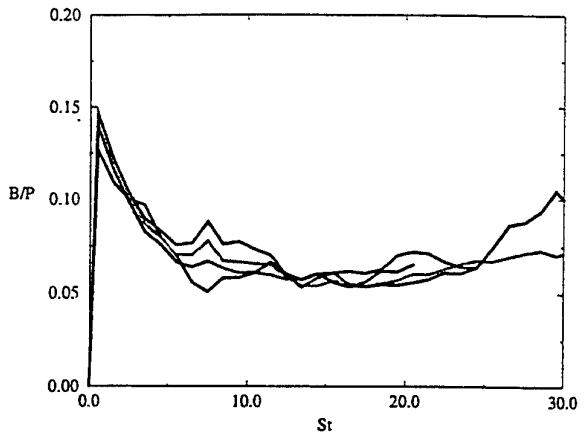


Figure 11: Evolution of the flux Richardson number $Ri_f = B/P$ for $Ri = 0.06$ and initial $Re_\lambda = 22.36$.

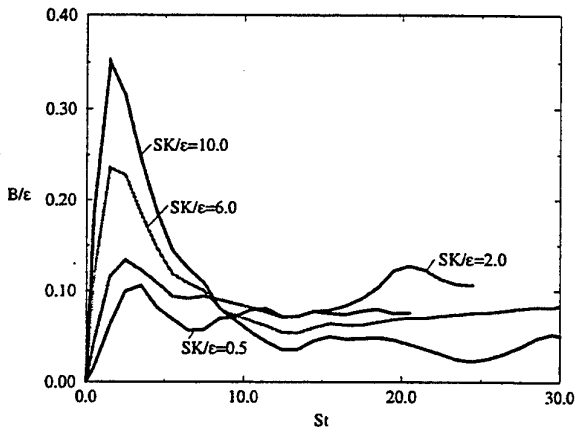


Figure 12: Evolution of the mixing efficiency B/ϵ for $Ri = 0.06$ and initial $Re_\lambda = 22.36$.

B to the production term P in the transport equation for the turbulent kinetic energy K. The asymptotic values of the flux Richardson number are not sensitive to the initial value of the shear number and Ri_f is not a determinant of the growth or decay of the velocity fluctuations in this case. An analysis of our other simulations shows that the asymptotic value of Ri_f is within 15% of Ri for the range $0 < Ri < 0.2$ that is spanned by our DNS.

Figure 12 shows the mixing efficiency B/ϵ which is used in some simple oceanographic models to obtain the vertical buoyancy flux B with measured estimates of ϵ. It appears that the asymptotic values of B/ϵ decrease with the initial value of the shear number.

The solid lines in figure 13 show the evolution of the turbulent momentum diffusion coefficient $K_u = -\overline{u_1 u_3}/S$ and the dashed lines show the evolution of the turbulent mass diffusion coefficient $K_\rho = -\overline{\rho u_3}/S_\rho$. The strong decrease of the diffusion coefficients at the large shear numbers $SK/\epsilon = 6$ and $SK/\epsilon = 10$ is apparent. The turbulent Prandtl number $Pr_t = K_u/K_\rho$ varies between 0.8 and 1.0 (not shown here). This indicates that the shear number has the same effect on both mass and momentum transport.

Turbulence closures such as the $K-\epsilon$ model will require additional modeling to account for the effect of shear and stratification. For example, the $K-\epsilon$ model assumes that $K_u = C_\mu K^2/\epsilon$ and the variation of C_μ is required. Figure 14 shows that the asymptotic value of C_μ decreases dramatically with increasing shear number.

SUMMARY

Direct numerical simulations of the turbulence evolution in stably stratified shear flow have been performed in order to study the influence of the shear number SK/ϵ. The initial value of the shear number SK/ϵ was varied, while the Richardson number Ri and the initial value of the Reynolds number Re_λ were fixed. An exponential evolution of the turbulent kinetic energy K was found with a strong dependence of the growth rate γ on the initial value of SK/ϵ. For small shear numbers, the growth rate γ increases with SK/ϵ and the evolution of K changes from decay to growth. However, for large shear numbers, the growth rate γ decreases with increasing SK/ϵ. The decrease of γ at large shear numbers is associated with a decrease of the magnitude of the shear stress anisotropy b_{13} and a decrease of ϵ/P.

A series of simulations was performed at a higher initial Reynolds number to determine the validity of the shear number effect. The asymptotic decay at high SK/ϵ was again observed. Thus, our conclusion does not appear to be an artifact of low Reynolds number effects. The reduction of the growth rate occurs at higher values of SK/ϵ in the

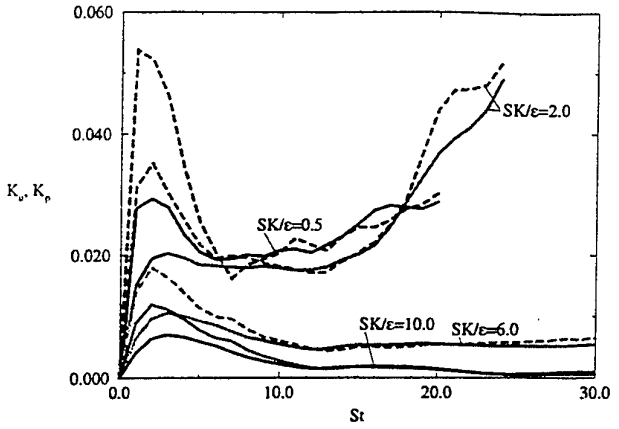


Figure 13: Evolution of the turbulent momentum diffusion coefficient $K_u = -\overline{u_1 u_3}/S$ (solid lines) and the turbulent mass diffusion coefficient $K_\rho = -\overline{\rho u_3}/S_\rho$ (dashed lines) for $Ri = 0.06$ and initial $Re_\lambda = 22.36$.

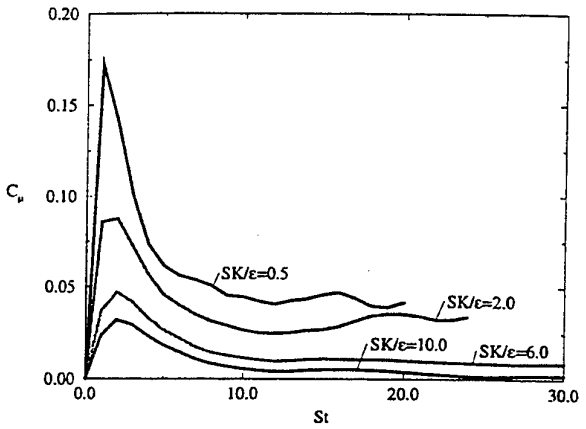


Figure 14: Evolution of the model coefficient C_μ for $Ri = 0.06$ and initial $Re_\lambda = 22.36$.

high Reynolds number series compared to the low Reynolds number simulations.

It is known that viscous rapid distortion theory (RDT) which could be applicable for large SK/ϵ predicts asymptotic decay of turbulence consistent with the observation of asymptotic decay in the DNS cases with high SK/ϵ. This motivated a comparison of simulations of the linearized Navier-Stokes equations with the full nonlinear equations. It was found that the linear and nonlinear evolution of K are qualitatively similar for high shear number simulations but different for low shear number simulations. Therefore, the reduced asymptotic growth of turbulence at large SK/ϵ may be related to the persistence of linear effects during the flow evolution at sufficiently high shear number.

An analysis of the terms in the spectral transport equation confirms the importance of linear effects in the high shear number simulation. While a strong energy redistribution to the smallest wavenumber modes was observed for the case with moderate initial $SK/\epsilon = 6$ which shows the strongest growth of turbulence, this redistribution was diminished for the asymptotically decaying case with high initial $SK/\epsilon = 14$. Also the energy redistribution to the high wavenumber modes was reduced for the high shear number case. The production of energy was found to be reduced for the $SK/\epsilon = 14$ case and a countergradient momentum flux was observed that was not present in the lower $SK/\epsilon = 6$ simulation. The cogradient buoyancy flux in the high shear number simulation was confined to the smallest wavenumber modes and again a small countergradient buoyancy flux was found at high wavenumbers.

The shear number was also found to influence the transport coefficients for momentum and mass causing a large reduction in their values at high shear numbers. Both coefficients were influenced leaving the turbulent Prandtl number close to unity. The coefficient C_μ in the eddy viscosity relation used in the $K - \epsilon$ model was found to decrease significantly with increasing shear number.

ACKNOWLEDGEMENTS

The authors acknowledge the support of the Office of Naval Research under the Physical Oceanography program (ONR N00014-94-1-0223) and useful discussions with Prof. Charles Van Atta at UCSD. Computing time was provided by the San Diego Supercomputer Center and the US Army Corps of Engineers Waterways Experiment Station.

REFERENCES

Caldwell, D.R., 1987, "Small-scale physics of the ocean", *Rev. Geophys.*, Vol. 25, pp. 183–192.

Caldwell, D.R. and Moum, J.N., 1995, "Turbulence and mixing in the ocean", *Rev. Geophys.*, Vol. 33, pp. 1385–1394.

Crawford, W.R. and Osborn, T.R., 1981, "The control of equatorial ocean currents by turbulent dissipation", *Science*, Vol. 212, pp. 539–540.

Gargett, A.E., Cummins, P, and Holloway, G., 1989, "Effects of variable diffusivity in the GFDL model", *Proceedings, Hawaiian Winter Workshop*, pp. 11–20.

Gerz, T., Schumann, U., and Elghobashi, S.E., 1989, "Direct numerical simulation of stratified homogeneous turbulent shear flows", *J. Fluid Mech.*, Vol. 200, pp. 563–594.

Holt, S.E., Koseff, J.R., and Ferziger, J.H., 1992, "A numerical study of the evolution and structure of homogeneous stably stratified sheared turbulence", *J. Fluid Mech.*, Vol. 237, pp. 499–539.

Itsweire, E.C., Helland, K.N., and Van Atta, C.W., 1988, "Growth and decay of turbulence in a stably stratified shear flow", *J. Fluid Mech.*, Vol. 195, pp. 77–111.

Jacobitz, F.G., Sarkar, S., and Van Atta, C. W., 1997, "Direct numerical simulations of the turbulence evolution in a uniformly sheared and stably stratified flow", *J. Fluid Mech.*, in press.

Lee, M.J., Kim, J., and Moin, P., 1990, "Structure of turbulence at high shear rate", *J. Fluid Mech.*, Vol. 216, pp. 561–583.

Lesieur, M., 1993, *Turbulence in Fluids*, Kluver Academic Publishers.

Piccirillo, P.S. and Van Atta, C.W., 1997, "The evolution of a uniformly sheared thermally stratified turbulent flow", *J. Fluid Mech.*, Vol. 334, pp. 61–86.

Rogers, M.M., 1991, "The structure of a passive scalar field with a uniform mean gradient in rapidly sheared homogeneous turbulent flow", *Phys. Fluids A*, Vol. 3, pp. 144–154.

Souza, F.A. de, Nguyen, V.D., and Tavoularis, S., 1995, "The structure of highly sheared turbulence", *J. Fluid Mech.*, Vol. 303, pp. 155–167.

Williams, R.B. and Gibson, C.H., 1974, "Direct measurements of turbulence in the Pacific Equatorial Undercurrent", *J. Phys. Oceanogr.*, Vol. 4, pp. 104–108.

DNS OF NATURAL CONVECTION BETWEEN TWO VERTICAL, DIFFERENTIALLY HEATED WALLS

F.T.M. Nieuwstadt and T.A.M. Versteegh
J.M. Burgers Centre, Lab. Aero and Hydrodynamics,
Rotterdamseweg 145, 2628 AL Delft, the Netherlands

ABSTRACT

A Direct Numerical Simulation (DNS) has been carried out of the turbulent flow between two vertical, differentially heated, infinite walls. Results are presented for four values of the characteristic Rayleigh number, Ra. The computational results support a relation between the Nusselt number Nu and Ra according to: $Nu \simeq Ra^{1/3}$. It has been also investigated whether the simulation results are self-similar when scaled following the scaling hypothesis proposed by George and Capp (1979). It has been found that this scaling approach leads to self-similarity for the mean temperature profile. The result is a separate similarity expression for the inner and outer layer. Matching between both expressions leads to a temperature profile which depends on the distance between the two walls according to $x^{-1/3}$. It has been also found that this inner/outer scaling fails for the mean velocity profile and another scaling approach must be used here.

INTRODUCTION

Natural convection flow is caused by density variations, usually related to temperature differences, in combination with the acceleration of gravity. One of the most well-known cases of natural convection is Rayleigh-Bénard convection. Its geometry in the most ideal case consists of a fluid between two infinite horizontal walls and where the lower wall has a higher temperature than the upper wall. When the temperature difference is below a critical value the velocity of the fluid is zero and there is only molecular heat transfer between both walls. Above the critical value a flow sets in in the form of convection cells. Due to this flow the heat transfer is increased. At still higher temperature differences the flow becomes turbulent which leads to a even larger heat transfer.

The source of turbulence in Rayleigh-Bénard convection is directly connected to the vertical heat flux between the two walls. This heat flux can therefore be considered as the main parameter which determines all further flow characteristics. Together with some additional parameters describing the geometry and the fluid, the heat flux can be used to define a characteristic velocity, length and temperature scale. With help of these scales all variables can then be expressed in terms of so-called similarity relationships. The validity of these similarity relationships for the case of Rayleigh-Bénard convection has been confirmed by means of various experiments and numerical simulations. For some results and additional discussion on the scaling of Rayleigh-Bénard convection we refer to Castaing et al. (1989) and Kerr (1996)

A less well-known case of natural convection is the flow between two infinite vertical walls where both walls have a different temperature. The main difference with Rayleigh-Bénard convection is that the temperature gradient and therefore the heat transfer between the walls is now perpendicular to the direction of gravity. Furthermore, in contrast to Rayleigh-Bénard convection one finds in this geometry always a mean flow even in the case when the value of the temperature difference is small. At such small temperature differences the flow is laminar and the velocity profile can be computed exactly (see. e.g. Bird et al. 1960). When a critical value of the temperature difference is exceeded the flow becomes unstable and in this case also convection cells appear. At still higher temperature differences a transition to turbulent flow occurs.

The dynamics of turbulence is in this case more complicated than for Rayleigh-Bénard convection. The reason is that the main heat transfer between the two walls is horizontal and such a heat flux can not directly produce turbulence. Only a vertical heat flux can be a source of turbulence. Another potential source of turbulence is the mean velocity shear. Both sources of turbulence are of course coupled through the dynamics of turbulence to the horizontal heat flux which

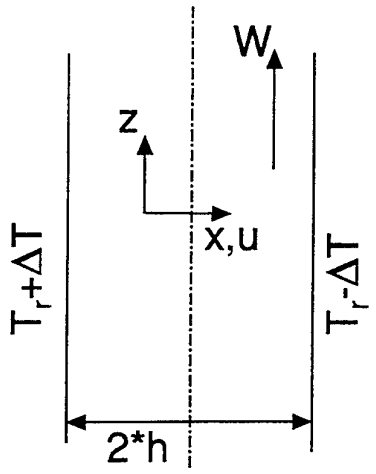


Figure 1: Flow geometry and definition of the coordinate system.

remains the "driving force" of this flow. In view of this more complex dynamics one must also expect that the scaling of this flow will be more complicated than for the Rayleigh-Bénard case.

In this paper we study the natural convection flow between two vertical walls by means Direct Numerical Simulation (DNS). The main objective is to investigate the scaling behaviour of this flow. For this we will make use of the scaling hypothesis proposed by George and Capp (1979) for a single vertical heated wall. We investigate here the validity of this scaling hypothesis with help of our DNS results.

The outline of the paper is as follows: first we will define our flow geometry and discuss the characteristics of our DNS. Next we will present the results of the DNS performed at four values of the characteristic Rayleigh number and investigate the scaling behaviour of the mean temperature and velocity profile. In the last section some conclusions are formulated.

FLOW GEOMETRY AND BASIC EQUATIONS

A schematic illustration of the flow geometry is given in Fig. 1. The distance between the two walls is $2h$ and the temperature difference $2\Delta T$. The kinematic viscosity ν, the heat conduction coefficient κ and the coefficient of volumetric expansion β are fluid properties. As mentioned before, the flow is driven by the temperature difference ΔT in combination with the acceleration of gravity g. Based on these parameters we can introduce a dimensionless parameter which characterizes the flow and which is generally known as the Rayleigh number

$$Ra = \frac{g\beta\,\Delta T\,h^3}{\nu\kappa}. \tag{1}$$

It will turn out that a more convenient parameter in our study is the "modified" Rayleigh number, H, which is defined as

$$H = PrRa = \frac{g\beta\,\Delta T\,h^3}{\kappa^2} \tag{2}$$

where the Prandtl number Pr is defined as

$$Pr = \frac{\nu}{\kappa}. \tag{3}$$

We introduce also the Nusselt number which can be interpreted as the non-dimensional temperature flux. Its definition reads

$$Nu = \frac{f_t\,h}{\Delta T\,\kappa} \tag{4}$$

where f_t is the temperature flux defined as

$$f_t = \kappa \left.\frac{\partial \overline{T}}{\partial x}\right|_0 \tag{5}$$

where $\overline{T}$ is the mean temperature and the x the horizontal coordinate between the two walls (see Fig. 1). The differential $\partial\overline{T}/\partial x$ is evaluated at the wall as indicated by the index 0.

The governing equations for this flow are

$$\begin{aligned} \frac{\partial u_i}{\partial x_i} &= 0 \\ \frac{Du_i}{Dt} &= H\,(T - T_r)\,\delta_{i3} + Pr\,\frac{\partial^2 u_i}{\partial x_j^2} \\ \frac{DT}{Dt} &= \frac{\partial^2 T}{\partial x_j^2} \end{aligned} \tag{6}$$

where all variables have been expressed in non-dimensional form with help of κ, h and ΔT. The δ_{i3} is the Kronecker delta which implies that the temperature difference, $T - T_r$, only contributes to the equation for the vertical velocity component. Furthermore, we have used the Boussinesq approximation, i.e. the flow can be considered as incompressible and the temperature difference plays only a role in combination with the acceleration of gravity. The T_r is a constant reference temperature which is defined such that the vertical flow averaged over the distance between the two walls is zero.

DNS

The set of equations (6) is numerically solved in a rectangular domain. On this domain a cartesian grid is formulated with a variable grid size in the horizontal x direction. Further details are given in Table 1.

The numerical technique that we have used, is a finite volume scheme with a second-order discretization method for both the non-linear advection and the linear diffusion terms. The time-stepping method is the explicit second-order Adams-Bashford method. The constraint of continuity is imposed by means of the pressure correction method. This method leads to a Poisson equation for the pressure which is solved by a mixed Fast-Fourier and finite difference method. Apart from the computation on the grid mentioned in Table 1, we have also performed a DNS on a coarser grid with $180 \times 90 \times 48$ grid points. By combination of the results from both grids with help of Richardson extrapolation, we can obtain a 4^{th}-order accurate numerical solution.

For the boundary conditions we employ no-slip conditions on the two vertical walls and periodic conditions in the y and z direction. The simulation has been performed at four values of the Rayleigh number given in Table 1 and with a Prandtl number equal to $Pr = 0.71$.

Table 1: Computational details of the DNS-simulations of the free convection flow between two infinite, differentially heated, vertical walls.

Computational domain	$L_z \times L_y \times L_x = 24h \times 12h \times 2h$
Number of grid points	$N_z \times N_y \times N_x = 432 \times 216 \times 96$
Resolution	$\Delta x_{min} = 0.00044h$ and $\Delta x_{max} = 0.0131h$
Rayleigh numbers computed	$Ra = 3.38\,10^4$, $5.13\,10^4$, $1.3\,10^5$, and $3.13\,10^5$
modified Rayleigh number	$H = 2.39\,10^4$, $3.63\,10^4$, $8.86\,10^4$, and $2.22\,10^5$

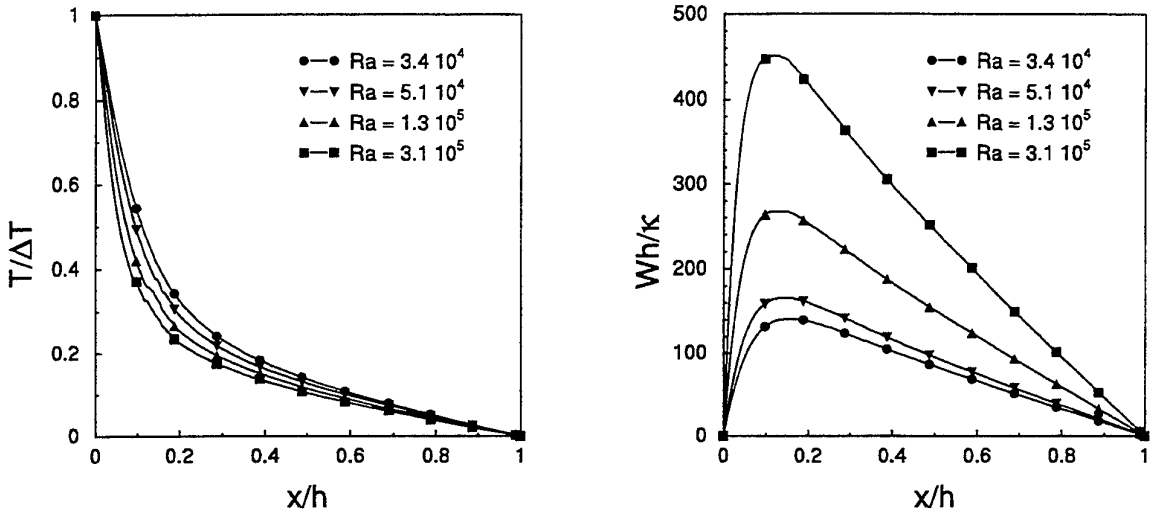


Figure 2: Profiles of the mean temperature (left) and velocity (right) for the four values of the Rayleigh numbers that have been computed by DNS.

RESULTS

Mean Profiles and Scaling Parameters

In Fig. 2 we show the profiles of the mean temperature and velocity for the four values of the Rayleigh number that we have computed. The profiles are clearly a function of the Rayleigh number.

The objective now is to formulate appropriate scaling relationships for these profiles so that the profiles collapse onto a single similarity curve. We shall follow here George and Capp (1979). These authors argue that the fundamental parameter which determines the flow characteristics throughout the whole flow region, is the horizontal temperature flux f_t which, by the way, is in our case constant, i.e. independent of the coordinate x. The other scaling parameters are the buoyancy parameter $g\beta$, the heat conduction coefficient κ and the distance between the walls h. We have omitted the Prandtl number Pr from the list of characteristic parameters because all our computations have been performed at the same value of the Prandtl number.

Based on these scaling parameters we shall consider in the following sections the scaling of the temperature and velocity profile.

Scaling of the Temperature Profile

For the scaling of the temperature profile we distinguish two regions: the inner and outer layer.

Inner layer

As inner layer we take the region close to the wall. The assumption is that in this region the size of the flow domain plays no role for the scaling behaviour. Therefore, the h can be omitted from the list of scaling parameters. Based on the remaining parameters we can now define a characteristic velocity (w_i), length (ℓ_i) and temperature (T_i) scale according to

$$\begin{aligned} w_i &= (g\beta f_t \kappa)^{\frac{1}{4}} = (HNu)^{\frac{1}{4}} \frac{\kappa}{h} \\ \ell_i &= \frac{\kappa}{w_i} = (HNu)^{-\frac{1}{4}} h \\ T_i &= \frac{f_t}{w_i} = Nu\,(HNu)^{-\frac{1}{4}} \Delta T. \end{aligned} \tag{7}$$

With help of these scales we can now formulate the following similarity expression for the mean temperature profile in the inner layer

$$\frac{T_w - \overline{T}}{T_i} = \phi_t\left(\frac{x}{\ell_i}\right) \tag{8}$$

where T_w is the wall temperature.

In Fig. 3 we show the temperature profile scaled according to (8). We find that for $x/\ell_i < 5$ the data of all four simulations collapse excellently onto a single curve which can be considered as a confirmation of the validity of inner-layer scaling for the temperature profile.

Outer layer

In the outer layer which is the flow region far from

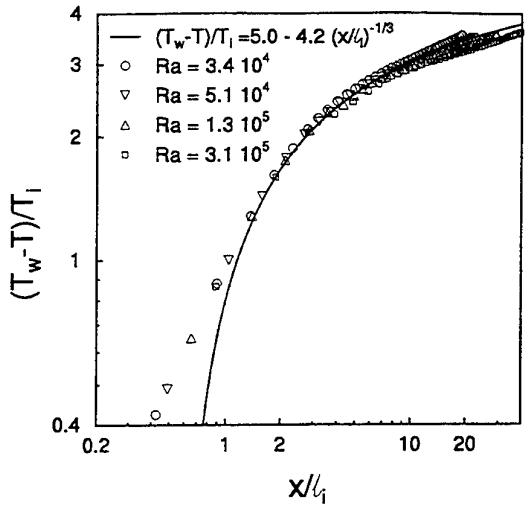


Figure 3: The temperature profile obtained from the four DNS simulations expressed in terms of inner-layer scaling.

the wall, we assume that molecular heat conduction no longer plays a role for the mean temperature. The remaining parameters allow now the following definition of a characteristic velocity (w_o), length (ℓ_o) and temperature (T_o) scale

$$\begin{aligned} w_o &= (g\beta f_t h)^{\frac{1}{3}} = (HNu)^{\frac{1}{3}} \frac{\kappa}{h} \\ \ell_o &= h \\ T_o &= \frac{f_t}{w_o} = Nu\,(HNu)^{-\frac{1}{3}} \Delta T. \end{aligned} \tag{9}$$

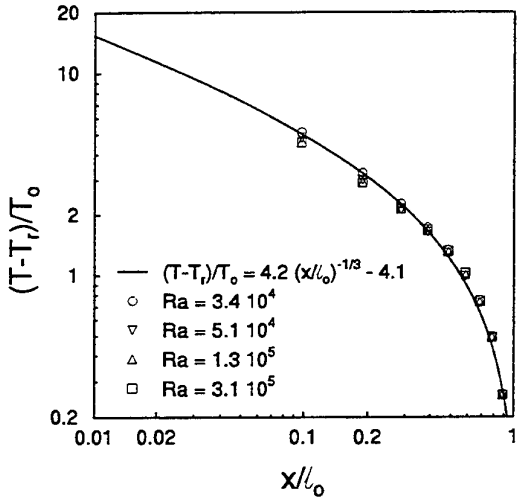


Figure 4: The temperature profile obtained from the four DNS simulations expressed in terms of outer-layer scaling.

With help of these scales we can formulate the following similarity expression for the mean temperature profile valid in the outer layer

$$\frac{T - T_r}{T_o} = F_t\left(\frac{x}{\ell_o}\right). \tag{10}$$

The results of the four simulations expressed in terms of (10) are illustrated in Fig. 4. It is clear that for $x/\ell_o > 0.3$ all temperature data again collapse onto a single curve which is a confirmation of the validity of outer-layer scaling.

Matching

The next step is to assume that there exists a region where both inner- and outer-layer scaling for the temperature profile is valid. George and Capp (1979) called this the buoyant sublayer. The inner layer profile (8) should be matched in this region to the outer layer profile (10). The most straightforward method by which matching can be performed, is by setting the temperature derivative expressed in outer-layer scaling equal to the derivative expressed in inner-layer scaling and taking the limit $\ell_o/\ell_i \to \infty$. Another, more direct method is to observe that in the matching region the temperature profile can no longer depend directly on both κ and h, i.e. the temperature profile can depend only on f_t, $g\beta$ and x. The result is that in the matching region both the inner- and outer-layer profile can be described by the following expression

$$\phi_t \simeq \left(\frac{x}{\ell_i}\right)^{-\frac{1}{3}} \quad \text{and} \quad F_t \simeq \left(\frac{x}{\ell_o}\right)^{-\frac{1}{3}}. \tag{11}$$

From the results shown in Figs. 3 and 4 it follows that the DNS data indeed agree with this matching result.

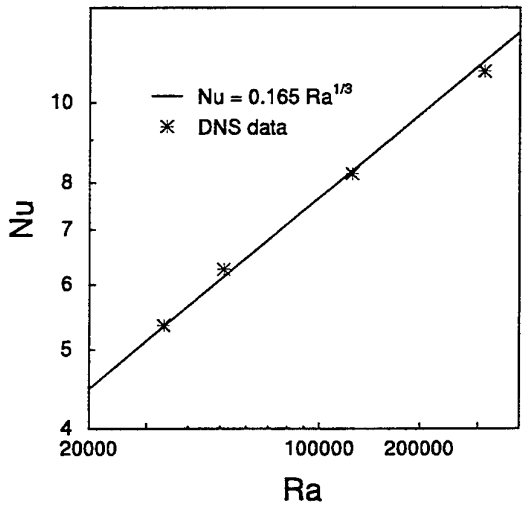


Figure 5: The relation between the Nusselt number Nu and the Rayleigh number Ra as a consequence of matching between inner- and outer-layer scaling (solid line) in comparison with the DNS simulations (symbols).

Another consequence of matching is found by adding the expressions (8) and (10 in the matching layer. As a result of the matching the temperature T cancels and an expression for $T_w - T_r = \Delta T$ results which can be rewritten into

$$Nu = cH^{\frac{1}{3}} \tag{12}$$

where c is a constant.

In Fig. 5 we show the data obtained from our simulations which indeed confirm expression (12) with the value 0.165 for the constant c.

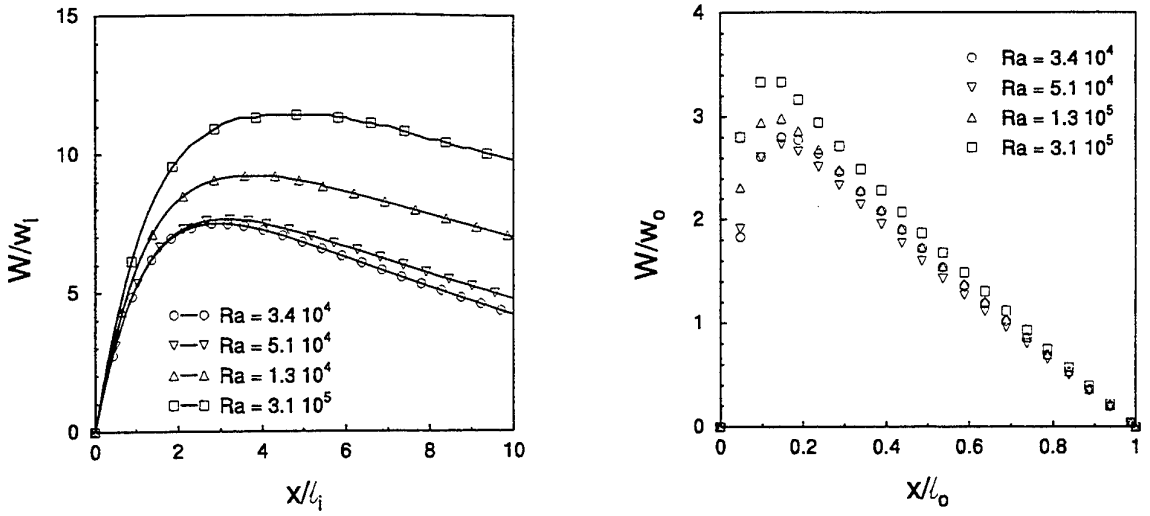


Figure 6: The mean velocity profile obtained from the four DNS simulations expressed in terms of inner- (left) and outer-layer (right) scaling.

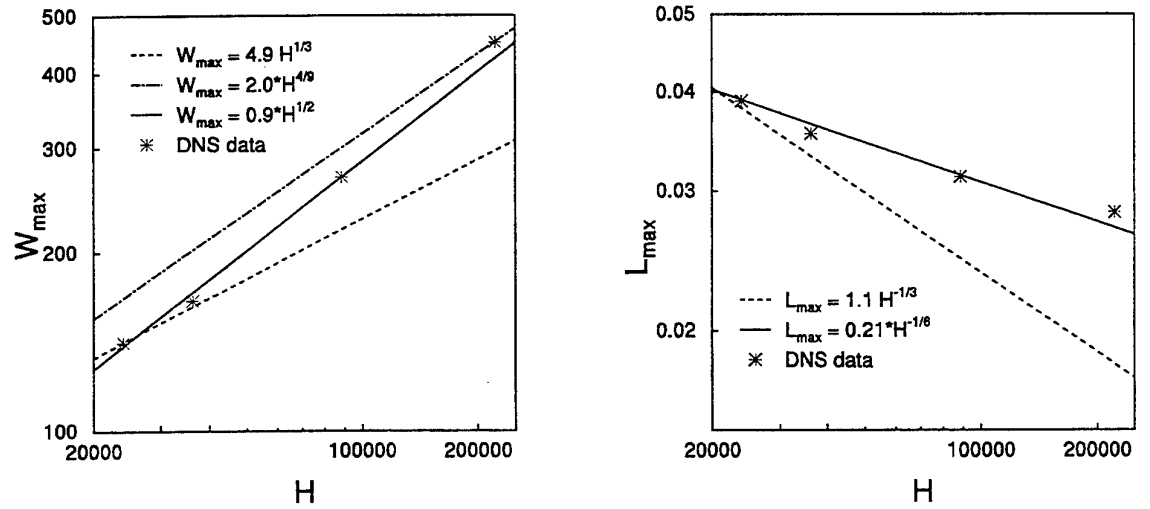


Figure 7: The maximum value of the mean velocity (W_{max}) and the position of this maximum (ℓ_{max}) as a function of the modified Rayleigh number H.

Scaling of the Velocity Profile

For the scaling of the velocity profile it seems appropriate to introduce again the inner and outer layer.

Inner and outer layer

Let us following George and Capp (1979) assume that for the scaling of the velocity profile the same scaling parameters can be used that have been introduced for the scaling of the temperature profile, i.e. (7) and (9). For the mean velocity profile in the inner and outer layer the following expressions then result

$$\frac{\overline{W}}{w_i} = \phi_w\left(\frac{x}{\ell_i}\right) \tag{13}$$

$$\frac{\overline{W}}{w_o} = F_w\left(\frac{x}{\ell_o}\right). \tag{14}$$

The data of the four simulations in terms of these scaling expressions are illustrated in Fig. 6. For the case inner-layer scaling, it is clear that close to the wall, say $x/\ell_i < 1$ the velocity profile are closer to each other than the original profiles shown in Fig. 2. It is however also clear that they do not really collapse onto a single curve. The same remark can be made for the velocity profile in outer-layer scaling when one observes the results in the center region between both walls, i.e. $x/\ell_i > 0.8$. Therefore, our conclusion must be that inner-layer and outer-layer scaling based on the parameters (7) and (9) fails for the mean velocity profile.

To investigate whether perhaps another scaling for the mean velocity is possible, we consider the velocity maximum, ($\overline{W}_{max}$) and the position of this maximum (L_{max}).

Scaling of $\overline{W}_{max}$ and L_{max}

In Fig. 7 our simulation results for the $\overline{W}_{max}$ and L_{max} are given as a function of the modified Rayleigh number H. In the figure we also give the relationships which are valid when $\overline{W}_{max}$ and L_{max} would follow

either inner- or outer-layer scaling. For outer-layer scaling this would imply

$$\overline{W}_{max} \simeq H^{\frac{4}{9}} \quad L_{max} \simeq \text{const.}$$

and for inner-layer scaling

$$\overline{W}_{max} \simeq H^{\frac{1}{3}} \quad L_{max} \simeq H^{-\frac{1}{3}}.$$

We see that neither $\overline{W}_{max}$ nor L_{max} seem to follow inner- or outer-layer scaling. This seems in agreement with the result of Fig. 6 where we found that the mean velocity does not follow either inner- or outer-layer scaling. Instead we find that $\overline{W}_{max}$ and L_{max} seems to fit better to the following scaling relationships

$$\begin{aligned} \overline{W}_{max} &\simeq H^{\frac{1}{2}} \\ L_{max} &\simeq H^{-\frac{1}{6}}. \end{aligned}$$

This result suggests that the mean velocity profile can be scaled in terms of other parameters than the scaling parameters for the temperature profile. This will be a topic of further investigation

CONCLUSIONS

We have presented results of a DNS of the natural convection flow between two infinite, differentially heated vertical walls at four values of the Rayleigh number. With these data we have considered the scaling hypothesis for this flow as proposed by George and Capp (1979). The DNS data confirm the existence of an inner- and outer-layer scaling region for the mean temperature. Matching between these regions leads to a $x^{-1/3}$ behaviour of the mean temperature profile which was also confirmed by the DNS data. The mean velocity profile did not follow scaling rules proposed by George and Capp (1979). The simulation data suggest however that another scaling hypothesis might be valid for the velocity profile.

References

R.B. Bird, W.E. Stewart and E.N. Lightfoot, 1960. Transport phenomena, J. Wiley & Sons, New York.

B. Castaing, G. Gunaratne, F. Heslot, L. Kadanoff, A. Libchaber, S. Thomae, X-Z Wu, S. Zaleski and G. Zanetti, 1989. Scaling of hard thermal turbulence in Rahleigh-Bénard convection. *J. Fluid Mech.*, **204**, 1–30

W.K. George and S.P. Capp, 1979. A theory for the natural convection turbulent boundary layer next to heated vertical surfaces. *Int. J. Heat Mass Transfer*, **22**, 813–826.

R.M. Kerr, 1996. Rayleigh number scaling in numerical convection. *J. Fluid Mech.*, **310**, 139-179.

TURBULENT ENERGY TRANSPORT IN NON-NEUTRAL SHEAR FLOWS

S. Heinz, A. Cadiou and K. Hanjalic
Delft University of Technology
Faculty of Applied Physics, Section Heat Transfer
Lorentzweg 1, 2628 CJ Delft
The Netherlands

ABSTRACT

The description of turbulence as stochastic fluid particle motion provides the one-point statistics of fluctuations with only a few assumptions on pressure and dissipation correlations. This concept is applied to the estimation of turbulent energy transports in stratifed flows by the calculation of third-order moments of the velocity and temperature fields. These terms are known to be essential ingredients of turbulence budget equations for thermal convective flows for instance. General equations for these quantities are derived here and specified for an unsheared convective boundary layer. These relations are shown to be in accord with large-eddy simulation (LES) data. The differences to results obtained by Eulerian transport equations for these terms are discussed.

INTRODUCTION

The consideration of turbulent energy transports is an important ingredient of modelling complex turbulent wall boundary layers as e.g. a convective boundary layer. The parametrization of such third-order terms in second-order budget equations can be tackled successfully by downgradient models,[1] as long as countergradient contributions do not contribute considerably to these budgets. The neglect of such terms leads e.g. to negative values of the vertical flux of turbulent kinetic energy (TKE) in the lower half of the convective boundary layer, whereas it is found to be positive throughout the whole boundary layer in experiments.[2]
Complex algebraic gradient models for the third-order correlations of the velocity and temperature fluctuations can be derived by closures in the transport equations for these terms,[3] but this approach requires the estimation of additional closure parameters. The choice of these parameters determines the different contributions of the variance gradient terms to the third-order moments, that means all these relative weights have to be assumed, which poses a non-trivial problem for complex flows. Secondly, this approach may require clipping procedures for the third-order moments in order to guarantee realizability constraints for second-order moments.[4]
Both these problems can be avoided by applying Lagrangian probability density function (pdf) methods for the calculation of such third-order moments. These stochastic models for the motion of fluid particles and change of their properties can be designed in accord with usual budget equations of turbulence up to second-order.[5] The one-point pdf of turbulent fluctuations is determined by such a Lagrangian model only in dependence on a few assumptions on pressure and dissipation correlations (and consequently only on the parameters used to specify these terms), which appear in the second-order moment equations. Secondly, the realizability problem is avoided, because the moments calculated within this approach are derived from a pdf.[6]
The extension of such Lagrangian pdf methods to stratified flows[7, 8] permits the application of this approach to the explanation of turbulent mixing processes e.g. between a buoyant plume and the surrounding turbulence,[9] or the reflection of mixing processes under convective conditions through turbulent energy transports considered here. This is done, by presenting at first Lagrangian stochastic equations in the next section. Then it is demonstrated, in which way third- and fourth-order moments can be obtained from these equations. These Lagrangian equations (and the derived general expressions for the third-order moments) contain unknown coefficents, which have to be estimated by the demanded consistency with second-order budget equations. This is done by specifying the pressure and dissipation correlations in these budget equations, where the general expressions for the third-order terms are simplified for an unsheared convective boundary layer. The vertical profiles of third-order moments are calculated then by adopting analytical vertical profiles for the required variances. These results are compared with LES data and the differences are discussed to calculations of these quantities in the Eulerian approach.

LAGRANGIAN STOCHASTIC EQUATIONS

The description of buoyant turbulence requires the consideration of a (potential) particle temperature. This quantity will be incorporated in the four dimensional particle state vector $\mathbf{Z}_L(t) = (U_L(t), \Theta_L(t))$, where $U_L(t)$ and $\Theta_L(t)$ are fluid particle velocities and potential temperature (the subscript L denotes a Lagrangian quantity), respectively. The consideration of a linear equation in $\mathbf{Z}_L$ is sufficient for the consistency of a Lagrangian model with turbulence budget equations up to second-order.[7] Such an equations may be written as (I runs from 1 to 3 only over velocity components in contrast to i)

$$\frac{d}{dt} x_L^I(t) = Z_L^I(t), \tag{1a}$$

$$\frac{d}{dt} Z_L^i(t) = \langle a^i \rangle + G^{ij}(Z_L^j - \langle Z_E^j \rangle) + b^{ij}\frac{dW^j}{dt}, \tag{1b}$$

where dW^j / dt is a Gaussian process with vanishing mean values $\langle dW^j / dt \rangle = 0$ and uncorrelated values to different times, $\langle dW^i / dt(t) \cdot dW^j / dt'(t') \rangle = \delta_{ij}\,\delta(t - t')$. The symbol δ_{ij} is the Kronecker delta, $\delta(t-t')$ is the delta function and $\langle \cdots \rangle$ denotes the ensemble average.

In these equations, $\langle a^i \rangle$ is given by the averaged conservation equations for momentum and potential temperature. By adopting the Kolmogorov approximation for the dissipation,[10] the matrix B is determined by

$$B = \frac{1}{4\tau}\begin{pmatrix} C_0\langle q^2\rangle & 0 & 0 & 0 \\ 0 & C_0\langle q^2\rangle & 0 & 0 \\ 0 & 0 & C_0\langle q^2\rangle & 0 \\ 0 & 0 & 0 & C_1\langle (Z_E^4 - \langle Z_E^4\rangle)^2\rangle \end{pmatrix}, \tag{2}$$

from which the matrix b appearing in the stochastic term of (1b) can be obtained by means of the relation $B^{ij} = \frac{1}{2}\, b^{ik} b^{kj}$. C_0 and C_1 in (2) are constants, and the dissipation time scale τ is defined by $\tau = \langle q^2 \rangle / (2\langle \varepsilon \rangle)$, where $\langle \varepsilon \rangle$ denotes the mean dissipation rate of the TKE and $\langle q^2 \rangle$ is twice the TKE. Furthermore, the equations (1b) contain the unknown matrix G, which has to be estimated through the demanded consistency with second-order budget equations of turbulence (see below) and depends on the choice of pressure correlations.

The Lagrangian equations (1a-b) can be also written in terms of a Fokker-Planck equation for the pdf of velocity and temperature fluctuations. The solution of this equation (or of the equations (1a-b)) permits then the calculation of all the moments of this pdf. In order to simplify the following derivations, let us consider now a boundary layer, where the pdf depends only on the vertical coordinate z. Then, the relations

$$\frac{d}{dz} T^{kl3} = \Gamma^{kn} V^{nl} + \Gamma^{ln} V^{nk} + 2B^{kl}, \tag{3}$$

$$\frac{d}{dz} F^{klm3} = \frac{\partial V^{k3}}{\partial z} V^{lm} + \frac{\partial V^{l3}}{\partial z} V^{km} + \frac{\partial V^{m3}}{\partial z} V^{kl} + \Gamma^{kn} T^{nlm} + \Gamma^{ln} T^{nkm} + \Gamma^{mn} T^{nkl} \tag{4}$$

can be derived from the corresponding Fokker-Planck equation for the stationary values of the vertical components $T^{kl3} = \langle z^k z^l z^3 \rangle$ of triple correlations and fourth-order moments $F^{klm3} = \langle z^k z^l z^m z^3 \rangle$, where $z^k = Z_E^k - \langle Z_E^k \rangle$ are the fluctuations of the velocity and potential temperature (related to the superscript 4) fields.

Additionally, the matrix Γ with elements $\Gamma^{ij} = G^{ij} - \partial \langle Z_E^i \rangle / \partial z\, \delta_{j3}$ is applied in (3) and (4), where $\langle Z_E^i \rangle$ denotes the Eulerian mean value of the i-th component of the state vector. V is the matrix of second-order moments, which is given by $V^{ij} = \langle z^i z^j \rangle$.

Assuming suited boundary conditions for the pdf at z = 0, the third- and fourth-order terms are completely determined by the relations (3) and (4). The equations reveal, that in generality non-local parametrizations of third- and fourth-order moments have to be considered. The frequencies Γ and BV^{-1} of all the involved processes are then required in order to solve these equations.

THIRD-ORDER MOMENTS

In order to arrive at analytical results let us calculate now the third-order moments from its equation (4), where the fourth-order moments are approximated by means of the quasi-normality assumption (they are taken as products of second-order moments),[11, 12]

$$F_M^{klmn} = V^{kn}V^{lm} + V^{ln}V^{km} + V^{mn}V^{kl}. \tag{5}$$

It results a system of coupled algebraic equations for 10 triple correlations, if $G^{i2} = 0$ is proposed for all $i \neq 2$. This neglect of couplings corresponds with the consideration of a two-dimensional boundary layer as often done. Proposing furthermore, that $G^{13} = G^{14} = G^{31} = G^{41} = 0$ as justified in the next section, one arrives at a 4- and a 2-dimensional equation system. By adopting the usual notation $w = z^3$ and $\theta = z^4$ for these quantities in the considered approximation, the solutions of these equations read then

$$\langle w^2\theta \rangle = A_{334}S^{334} + A_{344}S^{344} + A_{333}S^{333} + A_{444}S^{444}, \tag{6a}$$

$$\langle w\theta^2 \rangle = B_{334}S^{334} + B_{344}S^{344} + B_{333}S^{333} + B_{444}S^{444}, \tag{6b}$$

$$\langle w^3 \rangle = C_{334}S^{334} + C_{344}S^{344} + C_{333}S^{333} + C_{444}S^{444}, \tag{6c}$$

$$\langle \theta^3 \rangle = D_{334}S^{334} + D_{344}S^{344} + D_{333}S^{333} + D_{444}S^{444}, \tag{6d}$$

as well as

$$\langle q^2 w \rangle = E_{113}S^{113} + E_{114}S^{114} + \langle w^3 \rangle / 2, \tag{6e}$$

$$\langle q^2\theta \rangle = F_{113}S^{113} + F_{114}S^{114} + \langle w^2\theta \rangle / 2, \tag{6f}$$

where $q^2 = 2\, z^1 z^1 + z^3 z^3$ is written for the fluctuating TKE ($z^1 z^1 = z^2 z^2$ due to the considered two-dimensional boundary layer), and the first term of the right-hand side of equation (4) is written as

$$S^{klm} = \frac{\partial V^{lm}}{\partial z} V^{3k} + \frac{\partial V^{km}}{\partial z} V^{3l} + \frac{\partial V^{kl}}{\partial z} V^{3m}. \tag{7}$$

All the coefficients $A_{334} \cdots F_{114}$ can be found in the appendix, where they are given in dependence on the matrix G.

It may be seen from these expressions, that the usually applied downgradient assumption $T^{kl3} \sim S^{kl3}$ is recovered, if $G^{34} = G^{43} = 0$. However, the interaction between the turbulent and buoyant motion is described just by these coefficients (they provide the couplings between the particle velocity and temperature equation), such that their neglect is only justified for a neutrally stratified flow.

By applying the expression (7) for S^{ijk}, the equations (6a) can be rewritten into

$$\langle w^2\theta\rangle = \left\{3A_{333}V^{33} + A_{334}V^{34}\right\}\frac{\partial V^{33}}{\partial z} + 2\left\{A_{334}V^{33} + A_{344}V^{34}\right\}\frac{\partial V^{34}}{\partial z} + \left\{A_{344}V^{33} + 3A_{444}V^{34}\right\}\frac{\partial V^{44}}{\partial z}. \quad (8)$$

The equations (6b-d) can be obtained from (8) by replacing the symbol A by B, C and D respectively. In the same way one obtains the corresponding relation for $\langle q^2 w\rangle$,

$$\langle q^2 w\rangle = 2E_{113}V^{13}\frac{\partial V^{13}}{\partial z} + 2E_{114}V^{13}\frac{\partial V^{14}}{\partial z} + \frac{1}{2}\left\{E_{113}V^{33} + E_{114}V^{34}\right\}\left(\frac{\partial q^2}{\partial z} - \frac{\partial V^{33}}{\partial z}\right) + \frac{1}{2}\langle w^3\rangle, \quad (9)$$

and the equation for $\langle q^2\theta\rangle$ is obtained by replacing E by F and $\langle w^3\rangle$ by $\langle w^2\theta\rangle$ in (9). For G independent of the variances V (see next section), all the coefficients $A_{334} \cdots F_{114}$ in these relations are found to be independent on the variances V.

If the first two terms on the right-hand sides of (9) are neglected for the considered unsheared flow, these equations for the third-order moments have a similar structure as those derived by Canuto et al. [3] The third-order moments are given as linear combinations of the derivatives of $\langle w^2\rangle$, $\langle w\theta\rangle$, $\langle\theta^2\rangle$ and $\langle q^2\rangle$, and the coefficients of these derivatives are proportional to $\langle w^2\rangle$ (the mechanical part) and $\langle w\theta\rangle$ (the buoyant part). The essential difference is given by the fact, that here all the contributions of the different gradients of second-order moments are quantified (see below) without assumptions about their relative importance. Additionally, the realizability is ensured due to the Lagrangian approach, such that no clipping procedure for the third-order terms are required. It is interesting to note, that the additional closure assumptions of Canuto et al. provide terms related to derivatives of $\langle q^2\rangle$ in the equations for $\langle w^2\theta\rangle$, $\langle w\theta^2\rangle$, $\langle w^3\rangle$ and $\langle\theta^3\rangle$ in contrast to all the second-order models applied before and also to the approach presented here.

RELATION TO CLOSURE THEORY

The matrix G to be required in the triple correlations (6a-f) can be estimated by the condition, that the motion of particles and change of their temperatures has to be in consistency with the second-order budget equations of turbulence. This consistency can be established by deriving these budget relations from the Lagrangian theory (1a-b) and comparing these equations with the assumed budget equations of turbulence. Here, no assumption is needed on the third-order terms, which appear also in the Lagrangian equations. Consequently, the matrix G depends on the choice of the pressure and dissipation correlations, and the approximations for these terms determine all the statistical features of the flow.

The estimation of G is possible in accord with arbitrary models for pressure correlations, but the simple model of Rotta is applied now,[13] in order to demonstrate the main features of the approach. If rapid pressure terms related to a small parameter k_2 are neglected (as justified for an unsheared boundary layer considered below), G is given by[7]

$$G = -\frac{1}{4\tau}\begin{pmatrix} k_1 & 0 & 0 & 0 \\ 0 & k_1 & 0 & 0 \\ 0 & 0 & k_1 & -4\beta g\tau \\ 0 & 0 & 0 & 2k_3 - k_1 \end{pmatrix}. \quad (10)$$

In the relation, β is the thermal expansion coefficient, g is the acceleration due to gravity and k_1, k_3 and k_4 are parameters arising from the applied closure assumptions for the pressure and dissipation terms. In generality, one obtains G by the described procedure in dependence on an unknown antisymmetric matrix.[7] This quantity has to be specified by additional assumptions on correlations, but these can be neglected for many cases. In particular, there would be e.g. no influence of this matrix on third-order terms calculated by the relation (3).

For an unsheared boundary layer we have $\Gamma = G$, so that the triple correlations (6a-f) depend only over S^{ijk} on the variances. This feature as well as the proportionality to τ^{-1} are in accord with analytical results of Lumley, but the latter findings are strictly only valid for weakly inhomogeneous flow.[14]

By adopting the expression (10) one finds for (6a-d)

$$\langle w^3\rangle = -\frac{4\tau}{k_1}\left[\frac{\partial V^{33}}{\partial z} + 2\alpha_1\alpha_2(\beta g\tau)^2\frac{\partial V^{44}}{\partial z}\right]\cdot\left\{V^{33} - \alpha_1\beta g\tau V^{34}\right\} + \alpha_1\frac{8\tau}{k_1}\beta g\tau\frac{\partial V^{34}}{\partial z}\left\{V^{33} - 2\alpha_2\beta g\tau V^{34}\right\}, \quad (11a)$$

$$\beta g\tau\langle w^2\theta\rangle = -\alpha_1\tau\frac{\partial V^{33}}{\partial z}\left\{\beta g\tau V^{34}\right\} + 2\alpha_1\tau\beta g\tau\frac{\partial V^{34}}{\partial z}\left\{V^{33} - 2\alpha_2\beta g\tau V^{34}\right\} - 2\alpha_1\alpha_2\tau(\beta g\tau)^2\frac{\partial V^{44}}{\partial z}\left\{V^{33} + \alpha_1\beta g\tau V^{34}\right\}, \quad (11b)$$

$$(\beta g\tau)^2\langle w\theta^2\rangle = 2\alpha_2\tau\beta g\tau\frac{\partial V^{34}}{\partial z}\left\{\beta g\tau V^{34}\right\} + \alpha_2\tau(\beta g\tau)^2\frac{\partial V^{44}}{\partial z}\left\{V^{33} - \alpha_1\beta g\tau V^{34}\right\}, \quad (11c)$$

$$(\beta g\tau)^3\langle\theta^3\rangle = \alpha_1\tau(\beta g\tau)^2\frac{\partial V^{44}}{\partial z}\left\{\beta g\tau V^{34}\right\}, \qquad (11d)$$

where the abbreviations $\alpha_1 = -4/(2k_3 - k_1)$ and $\alpha_2 = -4/(4k_3 - k_1)$ are used. For the relations (6e-f) one obtains now

$$\langle q^2 w\rangle = -\frac{2\tau}{3k_1}\left(\frac{\partial q^2}{\partial z} - \frac{\partial V^{33}}{\partial z}\right)\left\{V^{33} - \alpha_1\beta g\tau V^{34}\right\} + \frac{1}{2}\langle w^3\rangle, \qquad (11e)$$

$$\beta g\tau\langle q^2\theta\rangle = \frac{1}{2}\alpha_1\tau\left(\frac{\partial q^2}{\partial z} - \frac{\partial V^{33}}{\partial z}\right)\left\{\beta g\tau V^{34}\right\} + \frac{1}{2}\beta g\tau\langle w^2\theta\rangle. \qquad (11f)$$

The essential difference to the expressions derived by Canuto et al. for the third-order moments is given by the fact, that the quantitative contributions of the variance gradient terms are calculated here from the Lagrangian theory. This can be seen e.g. in (11a) by extracting a mechanical part $-4\tau V^{33}/k_1$ as well as a buoyant part $4\alpha_1\tau(\beta g\tau)V^{34}/k_1$. The relative contributions of the gradients are then

$$\frac{\partial V^{33}}{\partial z}:\beta g\tau\frac{\partial V^{34}}{\partial z}:(\beta g\tau)^2\frac{\partial V^{44}}{\partial z} = 1 : 0.96 : 0.15 \qquad (12a)$$

and

$$\frac{\partial V^{33}}{\partial z}:\beta g\tau\frac{\partial V^{34}}{\partial z}:(\beta g\tau)^2\frac{\partial V^{44}}{\partial z} = 1 : 0.64 : 0.15 \qquad (12b)$$

for these two parts, respectively, where the below applied values for the closure parameters are used. These ratios have to be assumed in the approach of Canuto et al.

CONVECTIVE BOUNDARY LAYER

The features of the derived third-order relations will be illustrated now for an unsheared convective boundary layer. As a first step for doing this, let us consider the third-order moments which follow from analytical vertical profiles of the variances and TKE dissipation. These profiles are chosen in accordance with the LES data applied by Canuto et al. for the assessments of their results.[2] We estimated for these profiles

$$\frac{V^{34}}{\theta_* w_*} = 1 - \frac{z}{z_i}, \qquad (13a)$$

$$\frac{V^{33}}{w_*^2} = 1.25\left(1 - \frac{z}{z_i}\right)^{2/3}\left(\frac{z}{z_i}\right)^{2/3}, \qquad (13b)$$

$$\frac{V^{44}}{\theta_*^2} = 2.0, \qquad (13c)$$

$$\frac{\langle q^2\rangle}{w_*^2} = 0.3 + 1.25\left(1 - \frac{z}{z_i}\right)^{2/3}\left(\frac{z}{z_i}\right)^{2/3}, \qquad (13d)$$

$$\frac{\tau}{z_i/w_*} = 1.43\left(\frac{z}{z_i}\right)^{0.3}\left\{0.3 + 1.25\left(1 - \frac{z}{z_i}\right)^{2/3}\left(\frac{z}{z_i}\right)^{2/3}\right\}. \qquad (13e)$$

Here, w_* and θ_* are the convective velocity and temperature scales, respectively, and z_i is the boundary layer height. Variations of V^{11} and V^{44} near the surface are neglected, because the profiles of the third-order moments depend for $z/z_i \to 0$ very sensitive on assumptions on these changes.

At first, the applicability of the parametization (5) for the fourth-order moments has to be shown, which was applied for the derivation of the third-order moment relations (11a-f). By adopting (13b), one obtains from (5) the profiles of fourth-order moments presented in Figure 1.

We see, that the applied parametrization (5) reflects qualitatively the tank data measurements apart from small deviations in the upper boundary layer. The same result was found by Luhar et al. by comparing different closure schemes for the simulation of the vertical velocity pdf.[15] Thus, the relations (11a-f) may only be expected to provide the main qualitative features of the third-order moments and alternative closures for the fourth-order moments have to be considered also for more detailed investigations.[16]

The third-order moments are presented in the Figures 2-4 below, where the values $k_1 = 8.3 = k_3 = 6.5$ had been applied for the closure parameters. The parameter k_4 does not enter these relations, because C_1 is not taken into account (second section).

The third-order moment $\langle w^3\rangle/w_*^3$ of velocity fluctuations as well as the normalized vertical flux of TKE $\langle q^2 w\rangle/w_*^3$ agree qualitative rather good with the LES data apart from deviations near the surface. The LES data have a similar behaviour for $z/z_i \to 0$, but weaker expressed due to the applied boundary conditions. As an example for the other third-order moments, the convective flux $\langle w^2\theta\rangle/(w_*^2\theta_*)$ is shown in Figure 4. The behaviour of this moment is again reflected in accord with the LES data, but here the deviations are somewhat stronger. Similar problems are reported by Canuto et al., where e.g. the maximum of this profile was calculated about two times larger than found in the LES.

CONCLUDING REMARKS

The detailed description of micro-processes in a turbulent flow in accord with turbulence budget equations up to second-order determines all the moments of the joint velocity-temperature pdf. The relations (3) and (4) reveal, that relations between these moments have in generality a non-local structure. Algebraic expressions for the third-order moments resulting from this Lagrangian pdf approach are considered here, in order to assess the relation to corresponding expressions obtained in the Eulerian framework through closures of the transport equations for these terms.

The derived relations (11a-f) have a similar structure (the differences are discussed above) as corresponding expressions obtained in the Eulerian approach, but (apart from the realizability, which is ensured due to the Lagrangian approach) they posses an important conceptual advantage over the latter one relations: the contributions of different variance gradient terms are calculated here from the Lagrangian theory

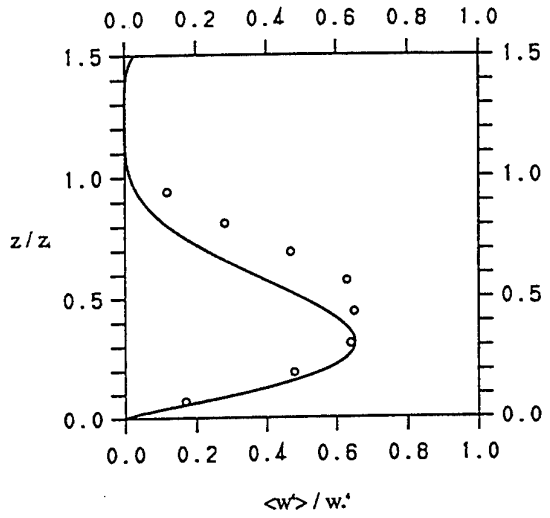


Figure 1. The vertical profiles of the normalized fourth-order moments $\langle w^4 \rangle / w_*^4$ according to the quasi-normality assumption (5). The circles depict tank data measurements presented by Luhar et al.[15]

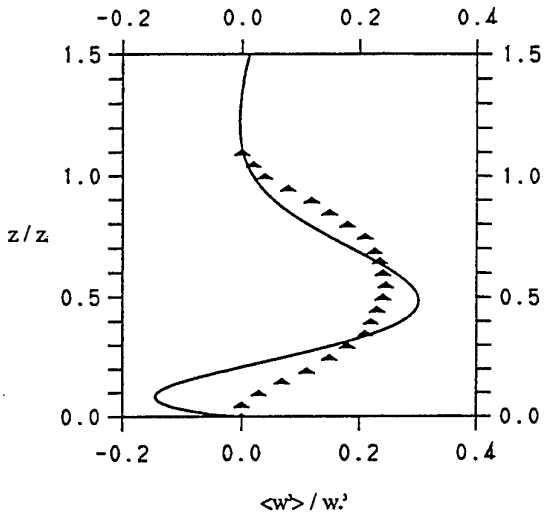


Figure 2. The vertical profile of the normalized third-order moment $\langle w^3 \rangle / w_*^3$ of velocity fluctuations. The triangles depict Nieuwstadt's LES data.[2]

and not assumed. This difference becomes e.g. essential, if different stratified flows have to be considered. The derived ratios between the variance gradient terms are given by the relations (12a-b). Vertical profiles for third-order terms are considered in the last section, where their accordance with LES data is shown.

The presented approach can be applied for the design of advanced turbulence models for stratified flows.[1,3] The effects of more complex pressure correlations and fourth-order parametrizations[16] can be implemented easily, such that an improved adjustment to LES data can be achieved.

APPENDIX

The coefficients appearing in the triple correlation relations (7) and (8) are given by

$$A_{334} = \gamma_2\omega_1, \qquad B_{334} = -2\Gamma^{43}\omega_1,$$

$$A_{344} = -2\Gamma^{34}\omega_1, \qquad B_{344} = \gamma_1\omega_1,$$

$$A_{333} = -\frac{\Gamma^{43}}{3\Gamma^{33}}\gamma_2\omega_1, \qquad B_{333} = \frac{2(\Gamma^{43})^2}{3\Gamma^{33}}\omega_1,$$

$$A_{444} = -\frac{2(\Gamma^{34})^2}{3\Gamma^{44}}\omega_1, \qquad B_{444} = -\frac{\Gamma^{34}}{3\Gamma^{44}}\gamma_1\omega_1,$$

$$C_{334} = -\frac{\Gamma^{34}}{\Gamma^{33}}\gamma_2\omega_1, \qquad D_{334} = \frac{2(\Gamma^{43})^2}{\Gamma^{44}}\omega_1,$$

$$C_{344} = \frac{2(\Gamma^{34})^2}{\Gamma^{33}}\omega_1, \qquad D_{344} = -\frac{\Gamma^{43}}{\Gamma^{44}}\gamma_1\omega_1,$$

$$C_{333} = \frac{1}{3\Gamma^{33}} + \frac{\Gamma^{34}\Gamma^{43}}{3(\Gamma^{33})^2}\gamma_2\omega_1, \qquad D_{333} = -\frac{2(\Gamma^{43})^3}{3\Gamma^{33}\Gamma^{44}}\omega_1,$$

$$C_{444} = -\frac{2(\Gamma^{34})^3}{3\Gamma^{33}\Gamma^{44}}\omega_1, \qquad D_{444} = \frac{1}{3\Gamma^{44}} + \frac{\Gamma^{34}\Gamma^{43}}{3(\Gamma^{44})^2}\gamma_1\omega_1,$$

$$E_{113} = \frac{1+\Gamma^{34}\Gamma^{43}\omega_2}{2\Gamma^{11}+\Gamma^{33}}, \qquad E_{114} = -\Gamma^{34}\omega_2,$$

$$F_{113} = -\Gamma^{43}\omega_2, \qquad F_{114} = \frac{1+\Gamma^{34}\Gamma^{43}\omega_2}{2\Gamma^{11}+\Gamma^{44}}.$$

In these expressions, the quadratic frequencies

$$\omega_1^{-1} = \gamma_1\gamma_2 - 4\Gamma^{34}\Gamma^{43},$$

$$\omega_2^{-1} = \left(2\Gamma^{11}+\Gamma^{33}\right)\left(2\Gamma^{11}+\Gamma^{44}\right) - \Gamma^{34}\Gamma^{43}$$

are used as abbreviations, where

$$\gamma_1 = 2\Gamma^{33} + \Gamma^{44} - \Gamma^{34}\Gamma^{43}/\Gamma^{33},$$

$$\gamma_2 = 2\Gamma^{44} + \Gamma^{33} - \Gamma^{34}\Gamma^{43}/\Gamma^{44}.$$

REFERENCES

[1] K. Hanjalic, "Advanced Turbulence Closure Models: A View of Current Status and Future Prospects", Int. J. Heat and Fluid Flow 15, 178-203 (1994).

[2] F. T. M. Nieuwstadt, P. J. Mason, C. H. Moeng and U. Schumann, "Large-Eddy Simulation of the Convective Boundary Layer: A Comparison of four Computer Codes", Turbulent Shear Flows 8, Ed. F. Durst et al., Springer-Verlag, Berlin, 343-367 (1992).

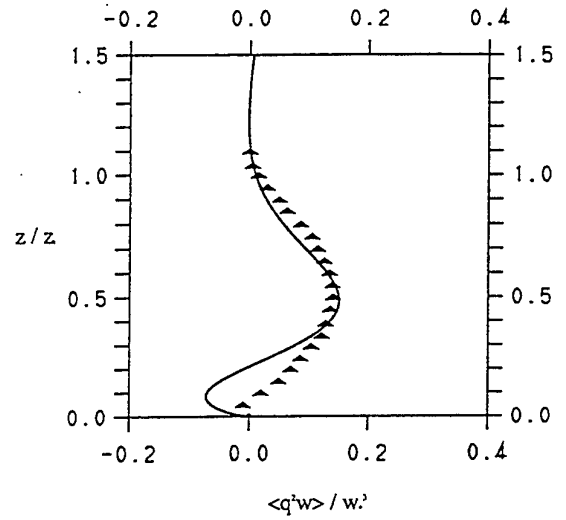


Figure 3. The profile of the normalized vertical flux of TKE $_2$ $\langle q^2 w \rangle / w_*^3$. The triangles depict Nieuwstadt's LES data.[2]

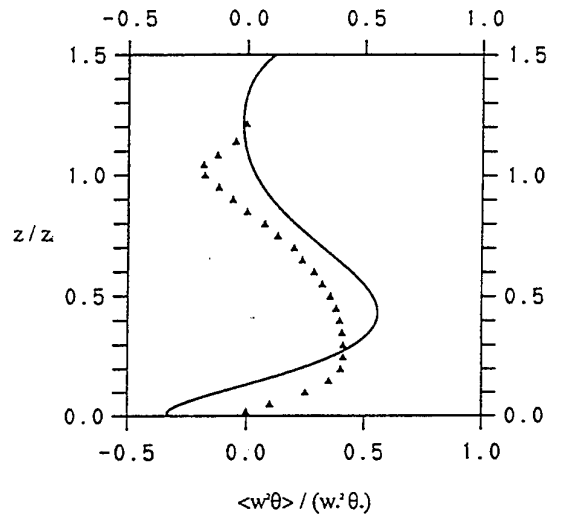


Figure 4. The vertical flux of the convective flux $\langle w^2 \theta \rangle / (w_*^2 \theta_*)$. The triangles depict Nieuwstadt's LES data.[2]

[3]V. M. Canuto, F. Minotti, C. Ronchi, R. M. Ypma and O. Zeman, "Second-Order Closure Model with New Third-Order Moments: Comparison with LES Data", J. Atmos. Sci. 51, 1605-1618 (1994).

[4]J. C. André, G. De Moor, P. Lacarrére, G. Therry and R. du Vachat, "Turbulence Approximation for Inhomogeneous Flows: Part II. The numerical Simulation of a Penetrative Convection Experiment", J. Atm. Sci. 33, 482-491 (1976).

[5]S. B. Pope, "On the Relationship between Stochastic Lagrangian Models of Turbulence and Second-Moment Closures", Phys. Fluids 6, 973-985 (1994).

[6]P. A. Durbin, and C. G. Speziale, "Realizability of Second-Moment Closure via Stochastic Analysis", J. Fluid Mech. 280, 395-407 (1994).

[7]S. Heinz, "Nonlinear Lagrangian Equations for Turbulent Motion and Buoyancy in Inhomogeneous Flows", Phys. Fluids 9, 703-716 (1997).

[8]S. Heinz, "Time Scales of Stratified Turbulent Flows and Relations between Second-Order Closure Parameters and Flow Numbers", submitted to Phys. Fluids.

[9]S. Heinz, "Bouyant Plume Rise calculated by Lagrangian and Eulerian Modelling", Proceedings of the 22nd NATA/CCMS International Technical Meeting on Air Pollution Modelling and its Application, Clermont-Ferrand, France (1997).

[10]A. N. Kolomogorov, "Equations of Turbulent Motion of an Incompressible Fluid', Izv. Akad. Nauk SSSR, Ser. Fiz. 6, 56-58 (1942).

[11]K. Hanjalic and B. E. Launder, "A Reynolds Stress Model of Turbulence and its Application to Thin Shear Flow", J. Fluid Mech. 52, 609-38, (1972).

[12]K. Hanjalic and B. E. Launder, "Contributions towards a Reynolds Stress Closure for Low Reynolds Number Turbulence", J. Fluid Mech. 74, 593-610, (1976).

[13]J. C. Rotta, "Statistische Theorie nichthomogener Turbulenz", Z. Phys. 129, 547-572 (1951).

[14]J. L. Lumley, "Computational Modeling of Turbulent Flows", Adv. Appl. Mech. 18, 123 (1978).

[15]A. K. Luhar, M. F. Hibberd and P. J. Hurley, "Comparison of Closure Schemes used to specify the Velocity PDF in Lagrangian Stochastic Dispersion Models for Convective Conditions", Atm. Env. 30, 1407-18 (1996).

[16]S. Heinz and E. Schaller, "On the Influence of Non-Gaussianity on Turbulent Transport", Boundary Layer Meteorol. 81, 147-166 (1996).

TURBULENT CONVECTION AT LOW PRANDTL NUMBER

S. CIONI[1], J. SOMMERIA AND S. CILIBERTO
Laboratoire de Physique
Ecole Normale Supérieure de Lyon
(URA 1325 CNRS)
46, Allée d'Italie
69364 Lyon
France
[1] email: SCIONI@physique.ens-lyon.fr

ABSTRACT

In this talk experimental results of Rayleigh-Bénard convection in the strongly turbulent regime will be presented.

It will be mainly devoted to the heat flux measurement and a brief review of both numerical and experimental findings concerning this aspect for various Prandtl number will be given.

The present experimental work has been focused on the case of liquid mercury, ($Pr = 0.025$). The heat flux, the statistics of the temperature fluctuations, as well as the structure of the mean flow have been investigated. We report results appeared in J. Fluid Mech. (Cioni *et al.*, 1997), together with more recent measurements in progress. These involve measurements in presence of a vertical magnetic field $|\mathbf{B}| = 0.4$ [T].

INTRODUCTION

Two main challenges arise from the broad litterature on Rayleigh-Bénard convection: the very high Rayleigh number limit and the low-Prandtl one. What happens when very high Rayleigh number are reached is still an open question and our experiment in mercury as well as the recent high-Rayleigh-number findings in helium of Chavanne *et al.* (1997) are recent attempts related to this matter. Moreover in recent years, both experiments (see Cioni *et al.*, 1997, for a review) and numerical (Verzicco & Camussi 1997) works have been devoted to the Rayleigh-Bénard problem at low Prandtl number. The present paper will be mainly devoted to the low Prandtl number convection.

The convective chamber consists of a cylindrical cell of aspect ratio $\Gamma = 1$ ($\Gamma = \frac{diameter}{depth}$). A moveable cold film in the vertical direction allowed us to measure and characterise the temperature field at the smallest scale. Eigth thermistors into the bottom plate as well into the top one allowed us to measure the vertical temperature difference between the two plates and to build a temperature patterns of the latter. The control parameter of this experiment was the heating power as usually done in low Prandtl number experiments. Thus the experimental boundary conditions were fixed heat flux at the bottom and fixed temperature at the top. All these measurements have been performed when steady state conditions were reached. For more details on the experimental aspects the reader is referred to the previous publications.

The experimental results can be summerized as follow.

Large scale flow. A global convective circulation sets in, with velocity scaling in $Ra^{0.42}$ (see Fig. 2b). This is obtained from a frequency of oscillation (see Fig. 2a) related to this velocity. We discuss the scaling for this bulk velocity, and for the Nusselt number, in comparison with various theoretical models. It appears that none is fully satisfactory, when both the dependence in Pr and Ra are considered.

Heat transfers. In mercury a power law in $Nu \sim Ra^{0.26}$ is obtained for the Nusselt number Nu versus the Rayleigh number Ra, for $Ra < 5 \times 10^8$. Beyond this value, transitions to new regimes are observed, but still not clearly characterized. This fit by a power law is in excellent agreement with the result by Rossby (1969), valid down to $Ra = 2000$.

Our measurements in water are in excellent agreement with other experiments with Prandtl number of order 1 (liquids or gas) confirming a 2/7 power law in Rayleigh. By contrast the Nusselt number is about twice smaller in mercury. Comparisons with recent experiments in sodium [2] confirm that Nu increases with Pr at low Pr, while $Nu \simeq cte$ for $Pr > 0.2$.

Scaling laws of temperature field. Study of turbulence intermittency (Cioni *et al.*, 1995) shows that the temperature fluctuations in the bulk behave as a passive scalar in mercury, while it directly influences the turbulence in water, according to the Bolgiano-Obukhov dymamics. We discuss how these spectral laws could be related to the scaling of the convective velocity with Ra.

The rest of the aricle will be devoted firstly to a brief discussion of the large scale flow inside the cell and secondly to the main task of this paper that is the heat flux measuerments.

LARGE SCALE FLOW

The presence of a large scale flow inside a Bérnard convection cell at high Rayleigh number has been shown for the first time by Sano *et al.* (1989) in helium liquid. The cell used in this experiment was a cylindrical cell of aspect ratio one. In our experiment a such mean flow has been detected by its thermal signature in the top and bottom plates, measured by 8 thermistors as shown in Fig. 1.

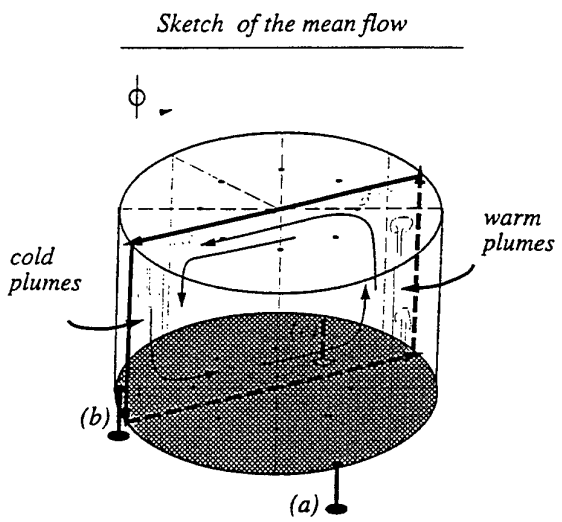


Figure 1: (a) Sketch of the global circulation in mercury at $Ra = 3.5 \times 10^8$. It was detected by the plot of temperature *versus* azimuthal angle ϕ along the top and bottom plates.

Time behaviour

As shown by Sano *et al.* (1989) an oscillation frequency, f_p, observed in the Fourier spectrum of one of the plate thermistor, corresponds to the presence of the global circulation, sketched in Fig. 1. This oscillation was observed in the whole range of Ra investigated ($7 \times 10^6 \langle Ra \langle 2 \times 10^9$).

Some assertions involving the thermal boundary layer instability are given by Sano *et al.* (1989) to explain the mechanism of the oscillation. This interpretation has been made more precise by Villermeaux (1995), who proposed a dynamical model of two unstable modes, in the bottom and top boundary layers, coupled with a delay corresponding to transport by the velocity U as shown experimentally by Ciliberto *et al.* (1996).

The frequency $\omega_p = 2\pi f_p$, normalized by κ/L^2, versus the Ryleigh number is plotted in Fig. 2b. The best fit gives a:

$$\frac{\omega_p L^2}{\kappa} = 0.470\ Ra^{0.424} \qquad (1)$$

Our result is in reasonable agreement with the fit $\frac{\omega_p L^2}{\kappa} = 0.31\ Ra^{0.46 \pm 0.02}$ obtained by Takeshita *et al.* (1996), and shown also in Fig. 2b. Camussi & Verzicco (1997) extend numerically this fit down to $Ra \simeq 4 \times 10^4$.

HEAT FLUX

The study of the heat flux is one of the most important task in studing convection. The general scaling is often assumed on this form

$$Nu \sim Ra^{\alpha}\ Pr^{\gamma}$$

where the Nusselt number represents the non-dimensional convective heat flux, the Rayleigh number is the control parameter equal to $Ra = \frac{g\alpha\Delta L^3}{\nu\kappa}$ and Prandtl number is equal to $Pr = \nu/\kappa$ where α is the thermal expansion coefficient, ν the kinematic viscosity, κ the thermal diffusivity, Δ is the temperature difference between the bottom and top plates, and L is the fluid layer height.

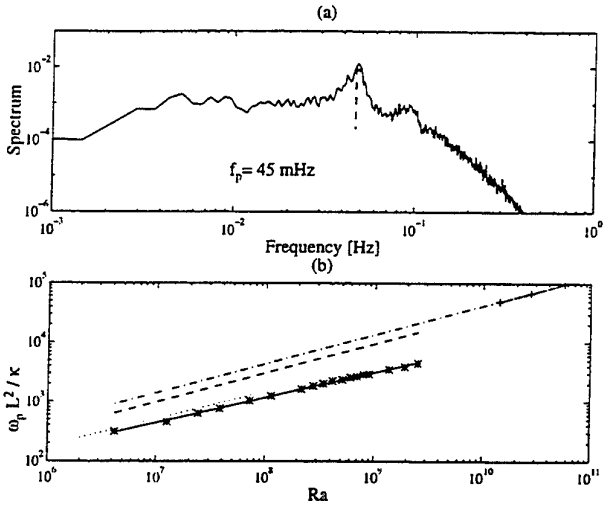


Figure 2: (a) Typical power spectrum of the signal of one thermistor in the bottom plate at $Ra = 8.7 \times 10^8$, showing the peak at the characteristic frequency f_p. This peak corresponds to the circulation frequency of the large scale flow inside the cell. (b) The dependence of the characteristic frequency ω_p, normalized by κ/L^2. *versus* Ra, with the best fit 1 (solid line), compared with the fit of Takeshita *et al.* (1996) (dotted line), of Sano *et al.* (1989) in helium (dashed line); results in water are indicated by (+) and fitted and extrapolated by the dot-dashed line (note that the geometry of this experiment by Ciliberto *et al.*, 1996 is different: a box with square vertical section of 40 x 40 cm and relatively narrow width 10 cm).

Nusselt *vs* Rayleigh

The main goal of our experiment was to extend up to $Ra = 2 \times 10^9$ the two previous works in mercury: Rossby (1968) and Globe and Dropkins (1957). We confirm up to $Ra = 5 \times 10^8$ the Rossby scaling, showing an Rayleigh exponent slightly lower than the 2/7 exponent observed at moderate Prandtl number. This fact is particulary remarkable because Globe and Dropkins proposed a 1/3 exponent for Rayleigh up to $Ra = 2 \times 10^7$. Similar results to ours have been confirmed by Takeshita *et al.* (1997) but for lower Rayleigh.

For Rayleigh larger than $Ra = 2 \times 10^9$ a sharp increase of the Nusselt number was observed (labelled region III in fig. 3) . As stressed by Cioni *et al.* (1997) the presence of the large scale flow plays an important role because this transition could occur. In fact, in contrast with the moderate and large Prandtl number the viscous boundary layer at low Prandtl number is completly nested into the thermal one as experimentally checked by Takeshita *et al.* (1997). So, we can argue that when the amplitude of this mean flow exceeds a given threshold value the viscous boundary layer becomes instable. This leads to a more efficient coupling with the temperature fluctuactions and consequently to a sharp increasing of the heat transfer. This region (III in fig. 3) probably corresponds to a new turbulent regime.

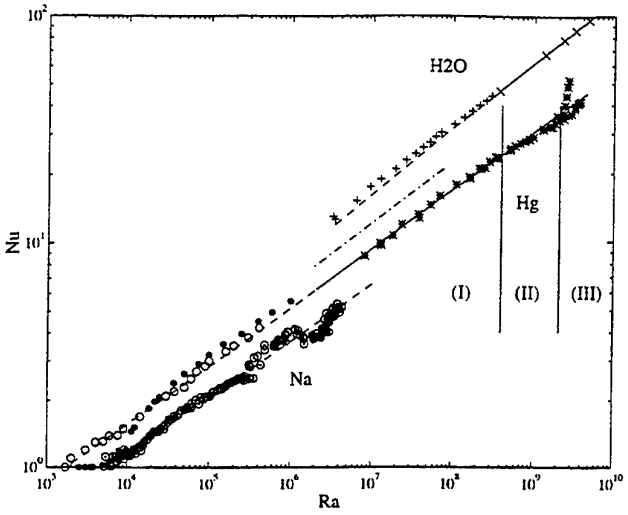


Figure 3: Nusselt *versus* Rayleigh for water (upper curve), mercury (middle curve) and soduim (lower curve). (star) Present experiments in mercury; (cross) Present experiments in water; (plus) Results in water by other autors. (circle) Results in mercury by Rossby, 1969. (dot) Results in mercury by Globe & Dropkin, 1959, (big-dot) numerical findings of Verzicco & Camussi, 1997; the dashed-dot line represents the fit of Takeshita *et al.*, 1996 in mercury. The two solid lines are best fits by power laws for our experiments in water, and in mercury (range I), extended by dashed lines; . Finally, the circle-dot data in sodium come from Hoanyi *et al* (1997). The discepancy of the Verzicco and Camussi data with the Rossby one at low Ra is due to the different aspect ratio.

Nusselt *vs* Prandtl

The other aspect that we studied was the Prandtl number dependence. In fact, if the 2/7 scaling law for the Rayleigh number dependence has been very well checked some problem persist for the Prandtl number exponent.

Table 1: Heat transfer experiments and correlations for thermal convection at high Rayleigh numbers in mercury ($Pr \simeq 0.025$) and sodium[+] ($Pr \simeq 0.005$)

Study	Resuslts Nu	Range in Ra
Kek & Muller[+] (1994)	$0.59Ra^{0.072}$	$2 \cdot 10^3 - 7 \cdot 10^3$
	$0.062Ra^{0.31}$	$1 \cdot 10^4 - 5 \cdot 10^4$
Horanyi *et al.*[+] (1997)	$0.115Ra^{0.25}$	$4 \cdot 10^4 - 1 \cdot 10^6$
	$0.009Ra^{0.41}$	$2 \cdot 10^6 - 4 \cdot 10^6$
Globe & Dropkin (1959)	$0.051Ra^{1/3}$	$2 \cdot 10^5 - 3 \cdot 10^7$
Rossby (1969)	$0.147Ra^{0.257}$	$2 \cdot 10^4 - 5 \cdot 10^5$
Cioni *et al.* (1997)	$0.14Ra^{0.26}$	$5 \cdot 10^6 - 5 \cdot 10^8$
	$0.44Ra^{0.20}$	$4 \cdot 10^8 - 2 \cdot 10^9$
Takeshita *et al.* (1996)	$0.155Ra^{0.27}$	$1 \cdot 10^6 - 1 \cdot 10^8$
Verzicco & Camussi (1997)	$0.14Ra^{0.26}$	$4 \cdot 10^4 - 1 \cdot 10^6$

The well known model of Siggia and Shraimann give for moderate Prandtl number a negative value (-1/7) of the γ exponent. On the other hand, recent result of Castaing group in Grenoble (Chavanne *et al.* 1996) show that for Prandtl number larger than 0.7 there is no dependence on the Prandtl number (see also fig. 4). Moreover, our results

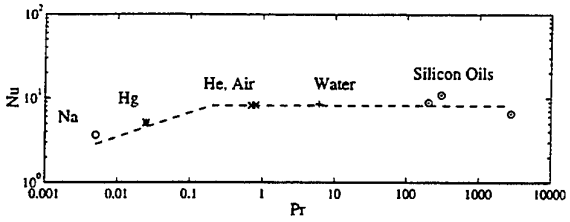


Figure 4: Nusselt *versus* Prandtl at $Ra = 1 \times 10^6$ corresponding to the data given in Tab. 2.

Table 2: Absolute Nusselt number at $Ra = 1 \times 10^6$ for different Prandtl numbers.

Study	Nu	Pr
Horanyi *et al.* (1997)	3.64	0.005
Verzicco & Camussi (1997)	5.08	0.025
Threlfall (1975)	8.20	0.7
Fitzjarrald (1976)	8.28	0.8
Chu & Goldstein (1973)	8.52	6.0
Rossby (1969)	8.93	200
Globe & Dropkin (1959)	10.93	300
Goldstein *et al.* (1990)	6.59	2750

compared with the sodium data of Horanii *et al.* show that for very low Prandtl number the exponent must be positive. A comparison between the sodium data and the mercury one at $Ra = 4 \times 10^6$ shows that $Nu_{Na} \simeq 5.15$ and $Nu_{Hg} \simeq 7.31$ this means a Prandtl number exponent γ equal to 0.22. This trend has been recently checked by Canuto *et al.* (1997).

Cioni *et al.* (1997) propse a phenomenological model yielding for low Prandtl number. We obtain the following scaling:

$$Nu \sim (Ra\ Pr)^{2/7}$$

This physical idea is an adaptation to low Prandtl of the mixing zone model of Castaing *et al.* (1989) and the presence of the mean flow is not crucial.

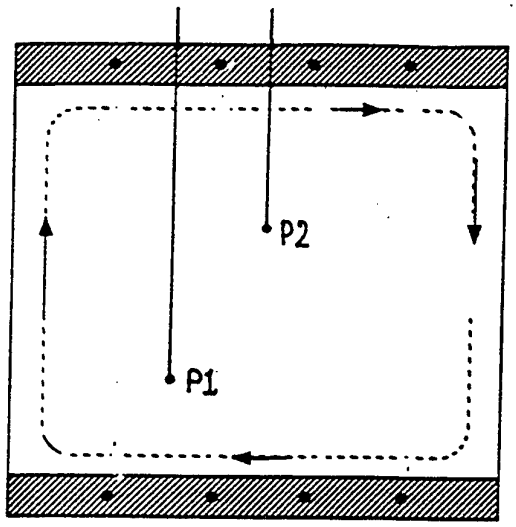
An other analytical relation has been found and qualitatively checked by numerical simulations of Canuto *et al.* (1997), they obtain

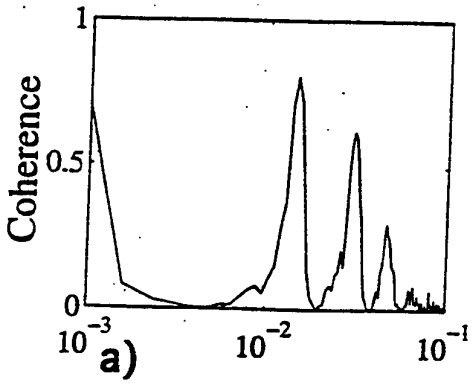
$$10^2 Nu = \frac{7}{2} Pr^{2/7}(1 + Pr^{-1/7} Ra^{-1/9}) Ra^{1/3}$$

From fig. 4 it is clear that a simple power low for the Prandtl number dependence doesn't fit at all the experimental findings in litterature. All these data show clearly that the physical mechanisms that control the turbulent state are thermal convection at low Prandtl number is still unknown.

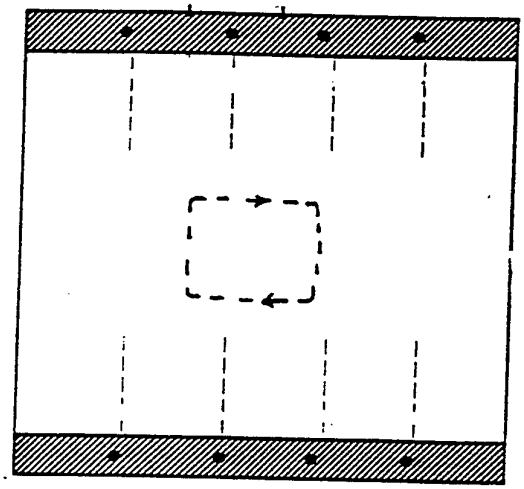
Nusselt *vs* mean flow

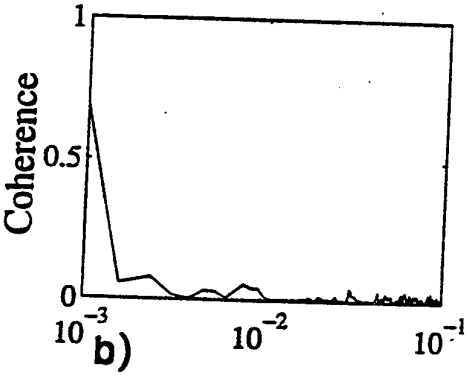
The problem of the influence of the mean flow on the heat flux still awaits answer. A first attempt has been made by Ciliberto *et al.* (1997). They measured the heat flux in two different configurations: with and without the mean flow. They observed that the two configurations exhibit the same value of heat transfer. Figure 5 summerizes this result.


P2
P1


Coherence
1
0.5
0
10^{-3}
10^{-2}
10^{-1}
a)


40 mm




Coherence
1
0.5
0
10^{-3}
10^{-2}
10^{-1}
b)



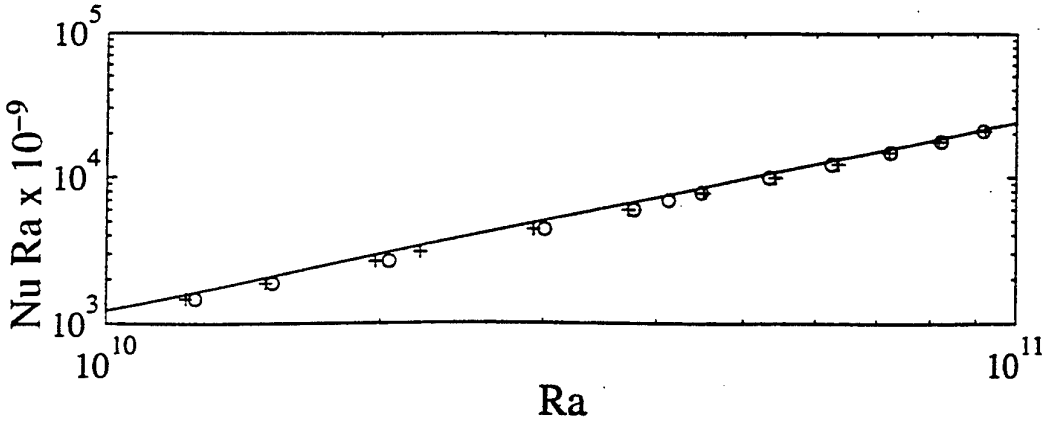

10^5
10^4
10^3
Nu Ra x 10^{-9}
10^{10}
10^{11}
Ra

Fig. 5

Figure 5: (Top-left-side) Schematic drawing of the convective cell. The thermocouples are indicated by (P1,P2). The vertical dashed lines indicate the position of the thin plexiglass screens. (a) The arrows schematically indicate the direction of the mean flow when the screens are not mounted. (b) The mean flow is limited in the central region when the screens are mounted and it cannot extend till the two thermal boundary layers close to the horizontal plates. (Top-rigth-side) Coherence functions of the temperature signals recorded at $Ra = 6.4 \times 10^{10}$ (d=40 cm) by the probes P1 and P2. Figure (a) corresponds to the configuration when the mean flow was present whereas the bottom figure (b) corresponds to the configuration when the mean flow was suppressed by the screens. The shadowgraphs show as the plume (a) start inclined in presence of the mean flow whereas start (b) vertically as the mean flow is confined in the central region of the cell. (Bottom) Dependence of the non-dimensional heat flow $Nu \cdot Ra$ as function of Ra in the range $(2 \times 10^{10} \langle Ra \langle 1.1 \times 10^{11})$: (o) without mean flow, (+) with mean flow. The solid line represents the 2/7 slope.

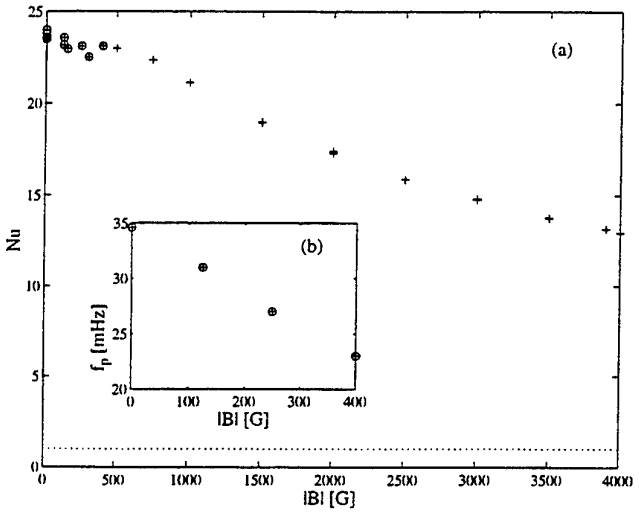


Figure 6: Nusselt number at costant heating power ($W \simeq 320$ *watt*) *versus* the vertical magnetic field $|\mathbf{B}| = B_z$; the frequency peak f_p corresponds to the circulation of the large scale flow inside the cell (see also figure 6). The corresponding Rayleigh number without magnetic field was $Ra \simeq 3.4 \times 10^8$.

Moreover the presence of a vertical magnetic field allows us to study the influence of a strong magnetic field on the properties of turbulent convection. The maximum Chandrasekhar number that we can reach is $Q \simeq 4 \times 10^6$ corresponding to a maximum amplitude of the magnetic field of $|\mathbf{B}| = B_z = 0.4\ [T]$. The Chandrasekkar number Q (Chandasekhar, 1961) is defined as $Q = B_z^2 \sigma L^2 / \rho \nu$ where σ denotes the electrical conductivity and B_z the strength of the vertical magnetic field. More details on the experimental setup with magnetic field will be published elsewhere.

As preliminary results, according to Chandrasekhar (1952) theory the magnetic field inhibits the heat transer through the convective cell (see Fig.6). The nusselt number decrease when magnetic field increase (Nakagawa, 1955 and Jirlow, 1956). Further, the presence of a such field seems to confirm the non-dependence on the overall heat flux from the large scale flow observed by Ciliberto *et al.* (1996). In fact, as shown in fig. 6 for weak amplitude of the magnetic field (lesser than 500 [*Gauss*]) the heat flux is slightly changed (4 %) whereas the strength of the mean flow is considerably reduced (40 %).

REFERENCES

Camussi & Verzicco, 1997, "Convective turbulence in mercury: scaling law and frequency spectra". Preprint.

Canuto V.M., Dubovikov M.S. and Dienstfrey A., 1997, "Turbulent convection in a spectral model", *Physical Rev. Lett.* **78**, 662 - 665.

Castaing B., Gunaratne G., Heslot F., Kadanoff L., Libchaber A., Thomae S., Wu X., Zaleski S. & Zanetti G., 1989 "Scaling of hard thermal turbulence in Rayleigh-Bénard convection", *J. Fluid Mech.* **204**, 1-29.

Chandrasekhar, S., 1961 *Hydrodynamic and Hydromagnetic Stability*, Dover Publications, New York.

Chandrasekhar, S., 1952, "On the inhibition of convection by a magnetic field", *Phil. Mag.*, **43**, 501.

Chavanne X., Chilla F., Chabaud B., Castaing B., Chaussy J., Hébral B., 1996 "High Rayleigh number convection with gaseous helium at low temperature", *J. low temperature Physics* **104**, 110-129.

Chu T. Y. & Golstein R.J., 1973 "Turbulent natural convection in a horizontal water layer heated from below", *J. Fluid Mech.* **60**, 141-159.

Cioni, S., Ciliberto S. and Sommeria, J., 1997, "Strongly turbulent Rayleigh-Bénard convection in mercury: comparison with results at moderate Prandtl number", *J. Fluid Mech.* **335**, 150-81; S. Cioni *et al.*, 1996 "Experimental study of High-Rayleigh-Bénard convection in mercury and water", *Dynamics of Atmospheres and Oceans* **24**, 117-127.

Ciliberto S., Cioni S. & Laroche C., 1997 "Large scale flow properties of turbulent thermal convection", *Phys. Rev. E* **54**, pp 5901.

Cioni S., Ciliberto S. and Sommeria J., 1995 "Temperature structure functions in turbulent convection at low Prandtl number", *Europhysics Letters* **32**, 413-418.

Fitzjarrald D.E., 1976 "An experimental study of turbulent convection in air", *J. Fluid Mech.***73**, 693-719.

Globe S.& Dropkin D., 1959 "Natural-convection heat transfer in liquids confined by two horizontal plates and heated from below", *Journal of Heat Transfer* **31**, 24-28.

Goldstein R.J., Chiang H. D., & See D. L., 1990, "High-Rayleigh-number convection in a horizontal enclosure", *J. Fluid Mech.* **213**, 111-126.

Horanyi, S., Krebs, L. and Müller U., 1997, "Turbulent Rayleigh-Bénard convection in Low Prandtl-number fluids", submitted to *International Journal of Heat and Mass Transfer.*

Jirlow, K., 1956, "Experimental investigation of the inhibition of convection by a magnetic field", *Tellus* **8**, 252-3.

Kek V. & Muller U., 1993 "Low Prandtl number convection in layers heated from below" *Intl. J. Heat Mass Transfer* **36** (11), 2795-2804.

Nakagawa, Y., 1955, "An experiment on the inhibition of thermal convection by a magnetic field", *Nature* **175**, 417-19.

Rossby H.T., 1969 "A study of Bénard convection with and without rotation", *J. Fluid Mech.* **36**, 309-335.

Sano, M., Wu, X.Z. and Libchaber, A., 1989 " Turbulence in helium-gas free convection", *Phys. Rev. A* **40** 6421.

Takeshita, T., Segawa, T., Glazier, J.A. and Sano M., 1996 " Thermal turbulence in mercury " *Phys. Rev Letters* **76** (9), 1465-1468.

Threlfall D.C., 1975 "Free convection in low temperature gaseous helium", *J. Fluid Mech.* **67**, 17-28.

Verzicco, R. and Camussi, R., 1997, "Transitional regimes of low Prandtl thermal convection in a cylindrical cell", *Physics of Fluids*, **9**, 1287-1295.

Villermeaux E., 1995 Memory-induced low frequency oscillations in closed convection boxes *Phys. Rev. Lett.***75**, 4618-4621.

LES OF BUOYANT CAVITY:
SUBGRID SCALE MODELS FOR INHOMOGENEOUS FLOWS

Xianmin Huang, Donald J. Bergstrom
Department of Mechanical Engineering
University of Saskatchewan
57 Campus Drive Saskatoon, Saskatchewan S7N 5A9
CANADA

INTRODUCTION

A three-dimensional buoyant cavity with differentially heated side-walls is an interesting and challenging test problem for computational models intended for buoyant turbulent flows. One application is air flows in rooms with thermally generated wall boundary layers. Since such flows are both typically three-dimensional and unsteady, it is appropriate to consider application of the Large Eddy Simulation (LES) method to this problem. On the other hand, in many ways the turbulent buoyant cavity problem is ill-suited to LES. As the Rayleigh number increases, the boundary layers on the two isothermal side walls become extremely thin, requiring grid resolution in these regions which is comparable to that required for a direct numerical simulation. For the three-dimensional problem, the challenge is to adequately resolve the strongly inhomogeneous near-wall regions, while at the same time modelling the interior of the cavity with a much coarser grid. This presents problems for both the numerical method and the subgrid scale models.

While fully recognising the challenge described above, we would argue that LES still remains an attractive method for this flow. To capture both the near-wall behaviour (with impingement) and effects of buoyancy in a time-average model would probably require a low Reynolds number (LRN) second-moment closure. Such a model would use grid refinement levels in the near-wall region which are comparable to an LES. For a three-dimensional unsteady problem, large computer resources would be required and the use of a time-average closure to resolve the unsteady turbulent motion becomes ambiguous. A LES calculation using similar computing resources would rely less on 'modelling', since it attempts to resolve some of the turbulent scales of motion.

The present paper reports preliminary calculations for LES of buoyancy driven flow in a square cavity using a novel dynamic subgrid scale (SGS) model. Our model formulation uses volume averaging to define the resolved fields. The resultant transport equations are also numerically discretised using a finite volume formulation. Calculations based on a quasi-two-dimensional solution domain indicate that the SGS model does predict enhanced, i.e. turbulent, transport in the narrow wall regions. For comparison we also include the results based on using a dynamic eddy viscosity model for the SGS fields.

FLOW DESCRIPTION

We consider the application of LES to a three-dimensional cubical cavity with two isothermal side-walls. The predominant flow pattern is created by the ascending boundary layer on the hot wall, and descending boundary layer on the cold wall. For a Rayleigh number of $Ra = g\beta\Delta TL^3/\nu\alpha = 10^{10}$, the two boundary layers become turbulent on the vertical isothermal walls. The two wall regions are coupled via fronts of warmer and cooler fluid moving across the top and bottom of the cavity, respectively. The interior region of the cavity appears to be stably stratified with little organised motion.

Relatively few numerical and experimental studies have considered this problem at higher Rayleigh numbers. On the experimental side, Hoogendoorn *et al* (1996) report measurements of the mean and fluctuating velocities along the hot wall of a nearly cubical cavity for a Rayleigh number of $Ra = 4.9 \times 10^{10}$. On the numerical side, direct numerical simulations of the two-dimensional buoyant cavity at similar Rayleigh numbers have been performed by Paolucci (1990) and Xin and Le Quere (1995). To the authors' knowledge, no one has reported a prediction for the three-dimensional problem using LES.

LES MODEL

For the LES model, a volume average formulation is adopted. Following the general approach of Germano *et al* (1991), we introduce a dynamic SGS model which uses a test grid to sample the fluctuating component of the volume average fields. The SGS fluxes are estimated based on this resolved 'turbulent' component of the volume average (or grid-scale) fields. Some aspects of the model formulation are similar to the scale similarity model of Bardina as discussed by Ferziger (1993); we will refer to the new model as the Func-

tional Scale Similarity (FSS) model. For comparison, we have also implemented the dynamic SGS eddy viscosity model of Germano *et al* (1991).

Volume Averaged Equations

The numerical model begins with the conservation laws of mass, momentum, and energy for incompressible flow using the Boussinesq approximation. The transport equations are first volume averaged, where the volume average operator is defined as follows:

$$\widetilde{\Phi} = \frac{1}{\Delta V}\int\int\int \Phi \, dV \tag{1}$$

Here ΔV represents the volume of the control volume under consideration, and Φ is the field to be averaged. We further decompose the velocity, temperature and pressure fields into volume average and fluctuating components, i.e.

$$U_i = \widetilde{U_i} + u_i \; ; \; \Theta = \widetilde{\Theta} + \theta \; ; \; P = \widetilde{P} + p$$

so that the final form of the governing equations becomes:

$$\delta_i(\widetilde{U_i}) = 0 \tag{2}$$

$$\dot{\widetilde{U_i}} + \delta_j(\widetilde{U_i}\widetilde{U_j}) = -\frac{1}{\rho_0}\delta_i(\widetilde{P}) - \beta g_i \widetilde{\Theta}$$

$$+\nu\delta_j(\widetilde{U_{i,j}}) + \delta_j(\tau_{ij} + \xi_{ij}) \tag{3}$$

$$\dot{\widetilde{\Theta}} + \delta_j(\widetilde{\Theta}\widetilde{U_j}) = \alpha\delta_j(\widetilde{\Theta}_{,j}) + \delta_j(\sigma_j + \psi_j) \tag{4}$$

where δ_j is a finite difference operator in the j direction. The volume average transport equations above contain both volume and surface averages. The terms τ_{ij} and σ_j are referred to as the SGS Reynolds stress and the SGS turbulent heat flux, respectively. Although strictly they represent surface average values, we will approximate them by interpolation based on the following volume averaged quantities:

$$\tau_{ij} = -\widetilde{u_i u_j} \tag{5}$$

$$\sigma_j = -\widetilde{\theta u_j} \tag{6}$$

The so called cross-correlation terms ξ_{ij} and ψ_j represent, respectively, momentum and thermal energy fluxes caused by correlations between SGS field fluctuations and large scale motions. We denote them in our theoretical development as:

$$\xi_{ij} = -\overbrace{\widetilde{U_i u_j}}^{j} - \overbrace{u_i\widetilde{U_j}}^{j} \tag{7}$$

$$\psi_j = -\overbrace{\widetilde{\Theta u_j}}^{j} - \overbrace{\theta\widetilde{U_j}}^{j} \tag{8}$$

where "$\overbrace{\;\;}^{j}$" represents the surface average over a control volume surface perpendicular to j-direction. The volume average formulation above in many ways follows the development of Schumann (1975), although he used a staggered grid and his SGS models are quite different from ours. For a finite volume formulation, the LES modelling is closely related to the numerical discretisation.

SGS Model

The purpose of the SGS modelling is to express the SGS Reynolds stress τ_{ij}, SGS turbulent heat flux σ_j, and cross-correlation terms ξ_{ij} and ψ_j solely in terms of the solvable large scale fields. In order to model the SGS Reynolds stress and SGS turbulent heat flux terms dynamically, we consider the expressions for volume averages of products of decomposed fields at both the grid-scale and the test-grid level. The test-grid level volume average has a larger characteristic width. Using decomposition and supersedity, we obtain for the SGS Reynolds stress,

$$\tau_{ij} = -\widetilde{u_i u_j} = -\widetilde{U_i}\widetilde{U_j} + \widetilde{U_i}\widetilde{U_j} \tag{9}$$

$$\tau'_{ij} = -\widehat{u'_i u'_j} = -\widehat{U_i}\widehat{U_j} + \widehat{U_i}\widehat{U_j} \tag{10}$$

where the "angle hat" denotes test-grid averaging, and τ'_{ij} is the SGS Reynolds stress at the test-grid level. By test-grid averaging the first expression, and then subtracting it from the second, we obtain:

$$T_{ij} = \tau'_{ij} - \widehat{\tau_{ij}} = \widehat{\widetilde{U_i}\widetilde{U_j}} - \widehat{\widetilde{U_i}}\widehat{\widetilde{U_j}} \tag{11}$$

where T_{ij}, represents the difference between the SGS Reynolds stresses at the grid-scale and test-grid levels. In a similar manner, we obtain a corresponding equation for the turbulent heat flux:

$$S_j = \sigma'_j - \widehat{\sigma_j} = \widehat{\widetilde{\Theta}\widetilde{U_j}} - \widehat{\widetilde{\Theta}}\widehat{\widetilde{U_j}} \tag{12}$$

where S_j represents the difference between the SGS turbulent heat flux at the grid-scale and test-grid levels. These inter-grid Reynolds stress and turbulent heat flux are only related to large scale fields, and are calculable numerically by test-grid averaging the grid-scale averaged fields.

Recall that our model aims to relate τ_{ij} and σ_j to, T_{ij} and S_j. Specifically, we propose a model for τ_{ij} of the form:

$$\tau_{ij} = \sqrt{C_{ij}C_{jj}}T_{ij} \tag{13}$$

with no summation convention. The coefficient C_{ij} is defined to be the ratio of τ_{ii} over T_{ii} in the j-direction. Local values of the coefficient C_{ij} are calculated using the test-grid information in the manner described below. First, we subtract the "ensemble" mean fields $\widehat{\widetilde{U_i}}$ and $\widehat{\widetilde{\Theta}}$ from the volume average fields $\widetilde{U_i}$ and $\widetilde{\Theta}$ in equations (11) and (12) above for T_{ij} and S_j. This ensures that these functions are the result of temporal fluctuations in the grid-scale fields, and not simply the effect of spatial inhomogeneity.

Next, we postulate a distribution function for the magnitudes of each component of τ_{ij} or σ_j based on eddy length scale. A sample distribution function is given by:

$$f(x) = \begin{cases} A(\frac{x-\eta}{B})^2 e^{-2(\frac{x-\eta}{B})} & \text{if } x > \eta \\ 0 & \text{otherwise} \end{cases} \tag{14}$$

where B is the dominant length scale of the distribution, i.e. the length scale corresponding to the peak value A of the distribution function; η is the smallest length scale of the turbulent fluctuation.

The self-correlation of any field fluctuation can be divided into three contributions based on the length scale: 1) the subgrid portion; 2) the portion between

the subgrid and test-grid; and 3) the solvable portion. In terms of the distribution function, these contributions become:

$$-\tau_{ii} = \int_0^{\Delta_i} f(x)dx \; ; \; -T_{ii} = \int_{\Delta}^{2\Delta_i} f(x)dx$$

$$-t_{ii} = \int_{\Delta_i}^{\infty} f(x)dx$$

where no summation convention is employed, and Δ_i is the characteristic length scale of the surface average in the i-direction, e.g.

$$\Delta_1 = \sqrt{\Delta x_2 \Delta x_3}$$

It is noted that T_{ii} is directly available in the simulation procedure, while t_{ii} can be approximated as:

$$t_{ii} = -(\widetilde{\overline{U_i}} - \widetilde{\overline{U_i}})^2$$

Using the relations above, the specific characteristics of the distribution function, e.g. A and B, can be determined from the local value of the field variables. This in turn enables the coefficients C_{ij} to be calculated using the integral relations above, which is then sufficient to determine τ_{ij} (from equation 13). Following a similar procedure, the coefficient $C_{\theta j}$ can be calculated based on the length scale distribution of the self-correlation of the temperature fluctuation. The SGS turbulent heat flux σ_j can be expressed as:

$$\sigma_j = \sqrt{C_{\theta j} C_{jj}} S_j \tag{15}$$

Cross-Correlation Terms

The volume average transport equations also include cross-correlation terms. For example, in the momentum equation we have:

$$\xi_{ij} = -\overbrace{\widetilde{U_i}u_j}^{j} - \overbrace{u_i\widetilde{U_i}}^{i} \tag{16}$$

where the summation convention is reserved only for the index "j". In analogy to molecular diffusion, the pure flux of $\tilde{\Phi}$ across the control volume surface j due to SGS fluctuation u_j can be expressed by an eddy viscosity model as follows:

$$\alpha_j \frac{\tilde{\Phi}_R - \tilde{\Phi}_L}{\Delta x_j} \tag{17}$$

where the eddy diffusivity α_j is given by

$$\alpha_j = \frac{1}{2} \breve{u}_j \overline{\Delta_j}$$

and Δx_j is the distance between the nodes of two neighbouring control volumes. The mean length scale of the SGS fluctuation, $\overline{\Delta_j}$ can be estimated from the scale distribution of the self-correlation τ_{ii}, while the velocity scale of the fluctuation is approximated by

$$\breve{u}_j = \sqrt{-\tau_{jj}}$$

The final form of the model for the cross-correlation term ξ_{ij} is given by

$$\xi_{ij} = \alpha_j \frac{\widetilde{U_i}^{j+\frac{1}{2}} - \widetilde{U_i}^{j-\frac{1}{2}}}{\Delta X_j} + \alpha_i \frac{\widetilde{U_i}^{i+\frac{1}{2}} - \widetilde{U_i}^{i-\frac{1}{2}}}{\Delta X_i} \tag{18}$$

Following the same procedure, ψ_j can be modelled as:

$$\psi_j = \alpha_j \frac{\widetilde{\Theta}^{j+\frac{1}{2}} - \widetilde{\Theta}^{j-\frac{1}{2}}}{\Delta X_j} \tag{19}$$

Numerically, it is convenient to include the cross-correlation terms by combining the eddy diffusivity α_i $(i = 1,2,3)$ with the molecular viscosity ν or molecular thermal diffusivity α.

Dynamic Eddy Viscosity Model

One of the first applications of dynamic SGS models was by Germano *et al* (1991) who used a Smagorinsky eddy viscosity type model for the SGS fluxes. The test-grid sampling was used to predict a local value for the constant C_S in the eddy viscosity relation,

$$\nu_t = (C_s\Delta)^2|\widetilde{S}| \tag{20}$$

where $\widetilde{S}_{ij}$ is the large-scale strain-rate tensor

$$\widetilde{S}_{ij} = \frac{1}{2}(\widetilde{U}_{i,j} + \widetilde{U}_{j,i}) \tag{21}$$

Germano *et al* used filtering opposed to volume-averaging to formulate their transport equations. They introduce a test-grid which is used to filter the transport equations a second time. The SGS Reynolds stresses on the two grid levels are then compared to obtain the resolved turbulent stress $\mathcal{L}_{ij}$, the counterpart of our T_{ij} above. Assuming that the same functional form, in this case a Smagorinsky model, can be used to characterise the SGS Reynolds stress on both grids, they then develop an expression for the Smagorinsky coefficient $C(x,y,z,t)$ based on the local strain-rates on the two grid levels and the resolved turbulent stress, $\mathcal{L}_{ij}$. In order to avoid cases where C becomes indeterminate or ill-conditioned, they introduce averaging along a homogeneous plane. We closely follow their development in obtaining our dynamic SGS eddy viscosity model, working within a finite volume context. In our case, instead of averaging over a homogenous plane, we locally 'filter' the coefficient in space multiple times to sufficiently smooth the eddy viscosity field, so that sharp cusps associated with ill-conditioned values do not cause numerial divergence. One of the advantages of the dynamic eddy viscosity model is that it allows for local backscatter, where the spectral energy transfer is from the small to the large scale motions. This can present numerical instabilities, but we were able to control them by the local smoothing noted above.

NUMERICAL METHOD

Our Navier-Stokes code uses a fractional-step projection method in a collocated finite volume formulation. The momentum equation is first solved without the pressure gradient term. Next, cell surface fluxes are obtained using the pressure gradient and interpolated values for the velocity based on the provisional fields. A Poisson equation is solved for the pressure correction field, which is then used to update the pressure, node velocity and surface flux velocity fields. The numerical code has been previously tested on three-dimensional lid-driven cavity flows at high Reynolds numbers. The results obtained compared favourably with those obtained by other researchers using different numerical techniques.

RESULTS

Preliminary results of a LES of a buoyant cavity for a Rayleigh number of $Ra = 10^{10}$ are reported below.

Initially, a nearly cubical cavity (of length $1\,m$, depth $0.8\,m$, height $1\,m$) was modelled using a nonuniform grid of $61 \times 41 \times 61$ control volumes. The development of the SGS model was expedited by considering a thin 'quasi-two-dimensional' slice of the cubical cavity, just 3 control volumes deep, as shown in Fig. 1. Homogeneous boundary conditions were implemented on both lateral faces, except for the normal velocity component which was set to zero. Comparisons between the quasi-2D and fully 3D simulations did not evidence significant differences away from the end walls.

For comparison purposes, we also obtained results based on the dynamic eddy viscosity model by restarting the solution fields using the same numerical code but the SGS model of Germano *et al* (1991). As noted above, we smoothed the dynamic coefficient in the eddy viscosity model by averaging the value over a local region of space five times. Excessive smoothing was observed to reduce the level of the SGS transport. Characteristics of the fluctuating velocity field used to begin the calculation were observed to persist for a long time, perhaps indicating a sensitivity of the eddy viscosity model to the initial conditions adopted.

Typical isotherms for the volume average temperature field are shown in Fig. 2 based on the prediction of the FSS model. For comparison, the isotherms predicted by the eddy viscosity model are shown in Fig. 3. In both cases, the disordered flows moving across the top and bottom of the cavity are characterised by irregular temperature distributions. The thermal boundary layers predicted by the FSS model are thicker, and the stratification in the interior of the cavity more developed.

Fig.'s 4 and 5 plot contours of the normalised SGS stress component τ_{13}, and eddy diffusivity coefficient, α_1 used in in the model for the cross-correlation term, respectively. Both fields are highly irregular and evidence peak values which indicate turbulent transport levels much greater than for the laminar case. In contrast, the contours of the SGS eddy viscosity predicted by the model of Germano *et al* (1991) shown in Fig. 6 are much smoother, and indicate turbulent transport which is almost the same order as molecular transport. Negative values of ν_t indicate regions of backscatter, although a 'cut-off' was used to limit the magnitude of the backscatter to $0.9\,\nu_t$.

Fig. 7 plots the prediction for the vertical velocity component at the mid-height of the 'hot' wall. Comparisons are made to both the two-dimensional results of Paolucci (1990) and the experimental measurements of Hoogendoorn *et al* (1996). The FSS model appears to slightly underpredict the level of turbulent transport and hence the thickness of the velocity profile.

Fig. 8. compares the prediction of the SGS eddy viscosity model for the vertical velocity profile at a height of $Z/L = 0.7$ along the hot wall to the data of Hoogendoorn *et al* (1996). In this case, the predicted velocity profile is much thinner than the experimental profile, and the level of turbulent transport predicted by the eddy viscosity model is too low.

CONCLUSIONS

The 3-D buoyant cavity with differentially heated walls remains a difficult flow to predict using LES, mostly due to the thin thermal boundary layers along the isothermal walls. However, from a practical perspective, one can imagine a number of flows in which large almost 'quiescent' regions connect narrow boundary layer regions. For LES to be effective in such flows, the SGS model must be able to accomodate regions of strong inhomogeneity where the grid scale fields are not able to resolve much of the fluctuating turbulent component. Our preliminary results suggest that a SGS model which is based on eddy viscosity relations does not perform well in capturing the development of turbulence in the near-wall regions. On the other hand, it is possible to configure SGS models which do not suffer this limitation. In this regard, the FSS model described above appears promising.

REFERENCES

Ferziger, J.H., 1993, "Subgrid-Scale Modeling" *Large Eddy Simulation of Complex Engineering and Geophysical Flows*, B. Galperin and S.A. Orszag (eds.), Cambridge University Press, 37-54.

Germano, M., Piomelli, U., Moin, P., and Cabot, W.H., 1991, "A Dynamic Subgrid-Scale Eddy Viscosity Model", *Phys. Fluids A*, Vol. 3, 1760-1765.

Hoogendoorn, C.J., Opstelten, I.J., and Dol, H.S., 1996, "Turbulent Natural Convection in a Cubical Cavity", *Proc. Turbulent Heat Transfer Conference*, San Diego, March 10-15.

Paolucci, S., 1990, "Direct Numerical Simulation of Two-Dimensional Turbulent Natural Convection in an Enclosed Cavity", *J. Fluid Mech.*, Vol. 215, 229-262.

Schumann, U., 1975, "Subgrid Scale Model for Finite Difference Simulations of Turbulent Flows in Plane Channels and Annuli", *J. Comp. Physics* 18, 376-404.

Xin, S., and Le Quéré, P., 1994, "Numerical simulation of 2D turbulent natural convection in differentially heated cavities of aspect ratios 1 and 4", *Direct and Large-Eddy Simulation I*, P.R. Voke *et al* (eds.), Kluwer, 424-434.

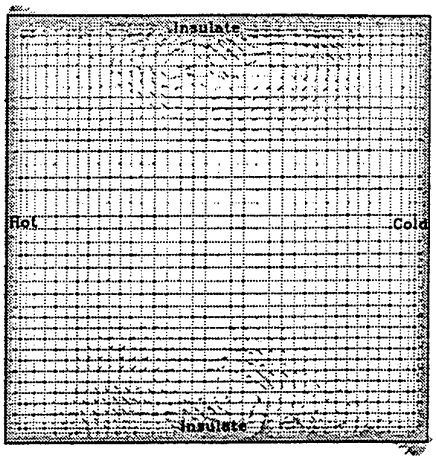


Figure 1: Geometry of BDC flow



Figure 3: Isotherms (Germano's model)



Figure 2: Isotherms (FSS model)

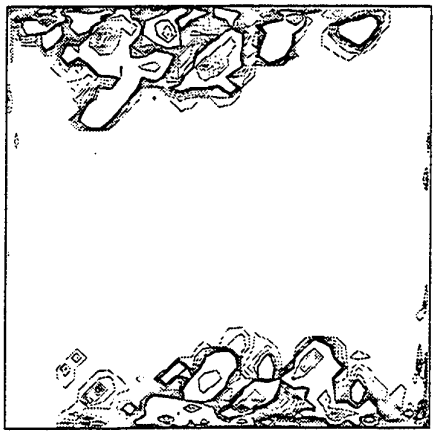


Figure 4: Contour of normalized SGS Reynolds stress $\tau_{13}/U_b^2(-0.0386 \sim 0.0343)$, (FSS model)



Figure 5: Contour of normalized eddy diffusivity $\alpha_1/\alpha(0 \sim 250)$, (FSS model)

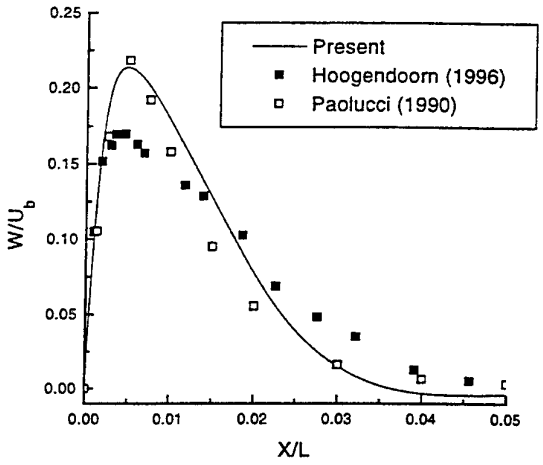


Figure 7: W-velocity profile along horizontal mid-line of hot wall (FSS model)

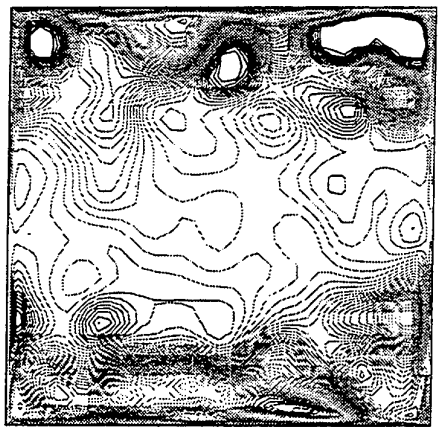


Figure 6: Contour of normalized eddy viscosity $\nu_t/\nu(-0.9 \sim 2.4)$, (Germano's model)

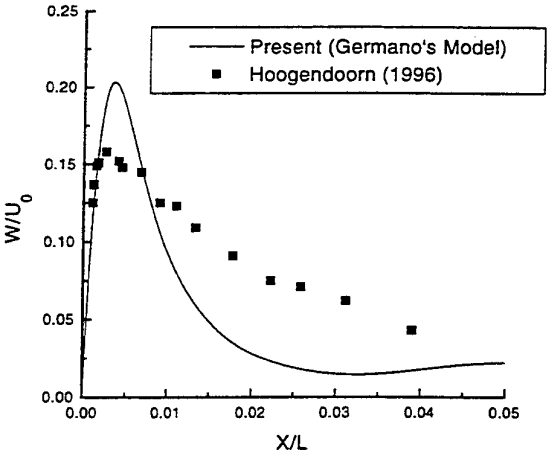


Figure 8: W-velocity profile along horizontal line $Z/L = 0.7$ of hot wall (Germano's model)

SESSION 24 - TWO PHASE FLOWS I

SEDIMENTATION OF SMALL PARTICLES THROUGH A TWO-DIMENSIONAL PLANE MIXING LAYER

T. M. Dreier[1], M. Virant[1], W. Kinzelbach[1]
[1] Swiss Federal Institute of Technology Zürich
Institut of Hydromechanics and Water Resources Management
ETH Hönggerberg
CH-8093 Zürich

INTRODUCTION

The focus of the present investigation is on particle-laden mixing layers.
A mixing layer is formed when two fluid streams of different velocity which are initially separated by a splitter plate start interacting due to shear, as shown in fig. 1. The upper stream can be seeded uniformly with sediment particles. The particles then sink through the mixing layer dominated by large coherent eddies.
The motion of particles is mainly determined by their specific weight and size, as well as by the local rate of change of the velocity of the surrounding fluid.
Shortly after the end of the splitter plate a Kelvin-Hemlholtz instability develops due to shear and leads to large, two-dimensional eddy structures (see e.g. Roshko (1976), Brown et al. (1974)), as shown in fig. 1. The structures grow as they travel downstream until pairing occurs (see fig. 2), i.e. until two adjacent eddies join and form a new larger one. In the region where pairing occurs the flow becomes three-dimensional. The present study is limited to the region of two-dimensional flow.



Figure 1: A mixing layer develops. Visualized by a tracer. (Photography)

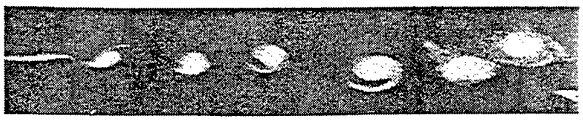


Figure 2: Beginning of the pairing. (Photography)

Martin and Meiburg (1994), Raju and Meiburg (1994) and Druzhinin (1995) performed numerical simulations of particle-laden shear flows and found that the particles avoid the centers of the vortices and accumulate in the region between them, i.e. in their periphery. This redistribution is the response of the particles to the vorticity and strain fields of the flow.
A number of experimental investigations have been performed on the dynamics of mixing layers. But so far only a few experimental studies are available, which look at mixing layers seeded with particles. As far as we are aware the only experimental study in which the correlation of particle and fluid motion is investigated was carried out in air by Lazaro (1992). This experimental investigation involves the dispersion of small particles in a developing, high-Reynolds-number plane mixing layer. No corresponding investigation for particles in water has been undertaken.
The current research project adresses the following questions, which remain unresolved:

How does the interaction between particles and water influence the sedimentation process?
What role does the large scale turbulent motion existing in the mixing layer play in the distribution of particles and how does it affect the sedimentation?

THE EXPERIMENTAL ARRANGEMENT

The experimental arrangement is represented in fig. 3.

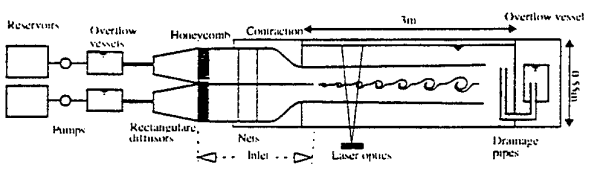


Figure 3: Side view of the experimental arrangement

The water is pumped from two reservoirs into the inlet

via overflow vessels which even out pump-induced variations of the flow. The fluid then enters rectangular diffusers and is conveyed to the test section at different velocities through two independent chambers. The following components are inserted into the two chambers: A honeycomb to reduce the swirl of the fluid, two grids for turbulence reduction, as well as a flow contraction. These measures ensure a low turbulence inlet flow and were required as the variation of the flow velocity has to be small in relation to the sinking velocity of the particles. The inlet flow above the splitter plate is steady and has a rectangular velocity profile with only small deviations near the boundaries.
The next component is the test section, at the end of which the water is drained into an overflow chamber so that the water level remains constant. The optical components for the generation of the light sheet are beneath the test section.

Optical System

The measurement arrangement is shown in fig. 4:

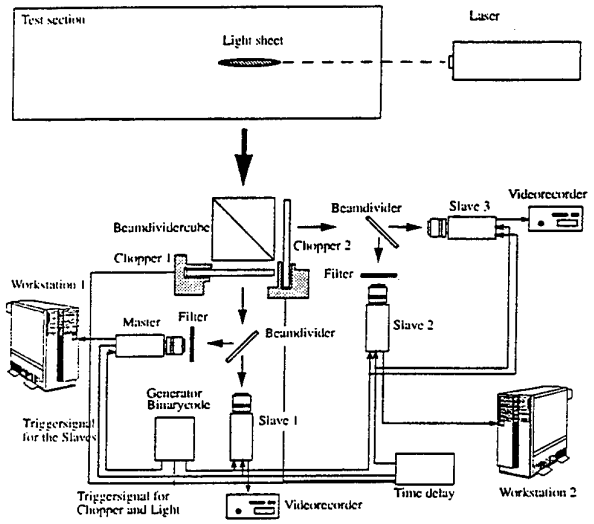


Figure 4: Plan view of the optical system for simultaneous recording of the separate motion of fluid and sediment particles.

The flow markers and the sediment particles are illuminated from below by means of a laser light sheet. The motion of these particles is recorded by four CCD cameras in the same measurement volume. The beam splitter guarantees that all cameras have the same field of view. The sediment consists of quartz sand and the markers are small neutrally- buoyant particles containing fluoresceine and rhodamine. The markers absorb the laser light and emit it again at a larger wavelength. This makes it possible to insert a suitable filter into the beam, which blocks the scattered light so that only the frequency-shifted emitted light can pass the filter. This is why the master camera and slave 2 (see fig. 4) record the movement of the flow markers only.
As a consequence of their small size, the markers emit and reflect only a small amount of laser light. The sensitivity of slave cameras 1 and 3 is therefore reduced to the extent that it detects the scattered light of the sediment particles, but not the light from the markers. The image sequences of the markers are directly digitized and stored onto the hard disks of the two work stations. The image sequences of the sediment are first stored on video tape and digitized at the end of the measurements. To obtain simultaneous images, all slave cameras are triggered by the master camera, whereas slave 2 and slave 3 have a time delay of a multiple of 64 μs . To allow an identification of pairs of simultaneous pictures during processing, a code which is supplied by a binary code generator is inserted on all images.

Test images as reproduced in fig. 5, demonstrate the reliability of the measurement arrangement.

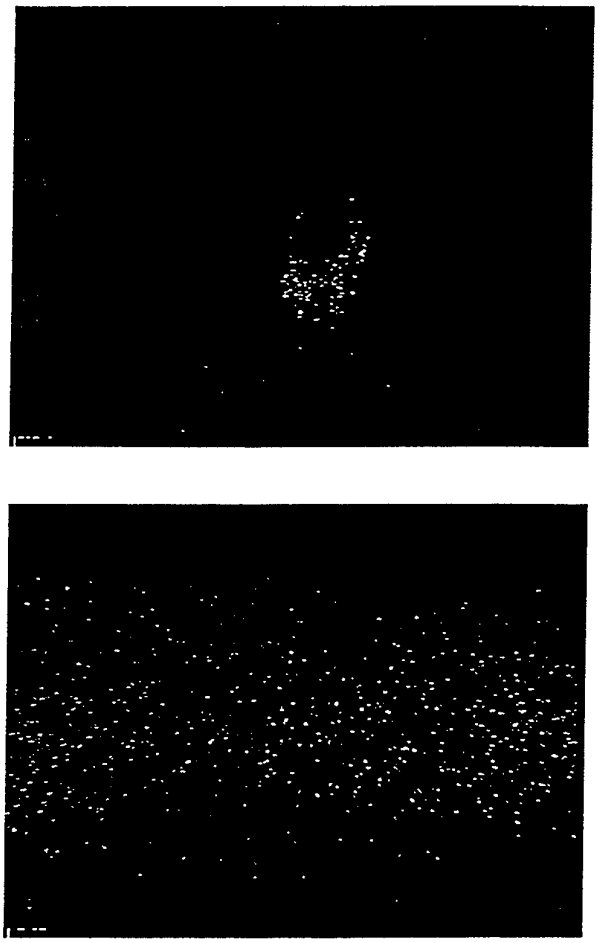


Figure 5: Viewing of flow markers and sediment particles in independent images. The upper picture shows the sediment particles (light of flow markers suppressed) and in the other one the flow markers (light from sediment particles removed by filtering).

Image Processing

The method available for the reconstruction of velocity fields is based on the correlation of groups of particles in a flow field, and was developed at the Institut of Geodesy and Photogrammetry (IGP) at the ETH. From two subsequent digital images, the velocity components as well as the rate of deformation can be determined by a least square matching. For this purpose, the images are subdivided into small surface elements. Each of these surface elements is adapted to the image taken at the next time step by means of a two-dimensional affine transformation until the sum of the squares of the grey-value differences reaches a minimum. From the resulting transformation parameters one can obtain information about the two velocity components, the rotation, the shear and the deformation in the light sheet. In the following section a velocity measurement is represented, which has been obtained by means of the above measurement technique.

The example illustrates the velocity field in the vicinity of a two-dimensional hyperbolic stagnation point, which was generated in a water tank by means of four rollers rotating about their axes (fig. 6).
The hyperbolic stagnation point flow is an extentional flow as it occurs between adjacent eddies of a mixing layer [4]. With this experimental set-up, the potential of the flow measurement technique can be tested under nearly real conditions. For the calculation of the velocity field in the surroundings of the stagnation point, two subsequent pictures of the markers were correlated (fig. 7). The resulting velocity field is shown in fig. 8.

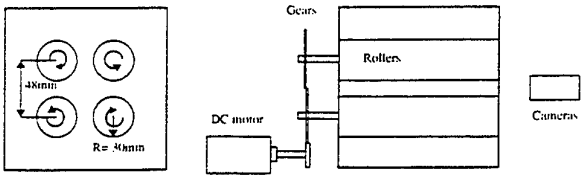


Figure 6: Front and side view of the experimental arrangement to generate a two- dimensional hyperbolic stagnation point flow.

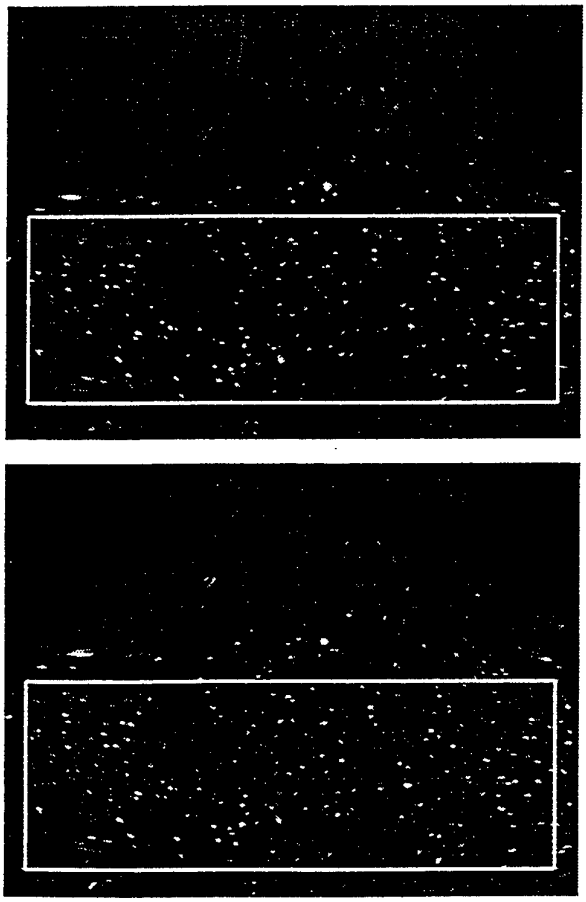


Figure 7: Two subsequent pictures of the markers. The processed part is outlined by the white frame.

DETAILED RESEARCH PLAN

The aim of this study is to verify the theoretical model calculations Martin and Meiburg (1994), Raju and Meiburg (1994) and Druzhinin (1995) related to the accumulation of sediment on the periphery of eddy structures and the accompanying reduction of the sediment concentration in their centers. For this purpose, experimental data will be generated to determine the influence of the inertial and viscous forces on the particles. The necessary experiments are described shortly in the following sections. In the experimental arrangement, two flows with different velocities are initially separated by a splitter plate and then joined in the test section. Markers are added to both fluids. The upper layer is seeded homogeneously over the whole width. The particles then sink through the two-dimensional coherent structures and the motion of the markers and the sediment are recorded simultaneously and separately (fig. 9).

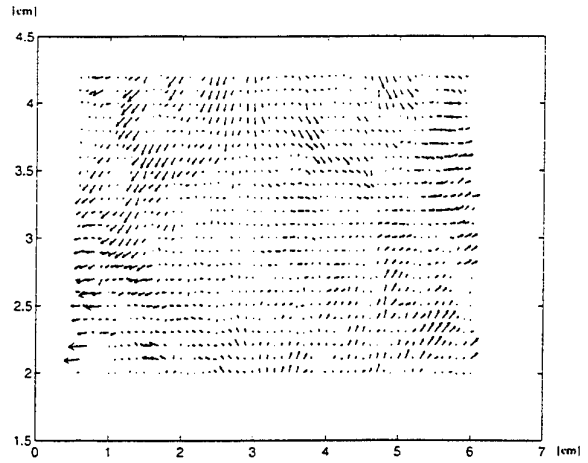


Figure 8: Velocity field generated from the above images. (An arrow of 1cm length corresponds to 3 cm/s)

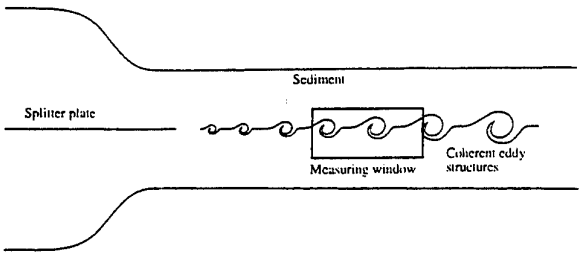


Figure 9: View the experimental procedure

The particle size, the number of particles, and possibly the density of the sediment will be varied as well as the fluid velocity, the velocity difference between the two layers, and the distance of the measurement window from the splitter plate. With these variations the entire region relevant for the particle accumulation can be covered.
Sequences of video images are processed on a workstation. A least-square-matching method is used to generate the two velocity fields. In addition, individual sediment particles will be tracked over several time steps which leads to short particle trajectories. Based on the measured velocity field of the fluid, particle tracks will be simulated. From these data sets probabilities can be computed for the position of particles at a later stage, and compared with the theoretical predictions about the particle redistribution mentioned above.

Acknowledgements : The source code based on the correlation of groups of particles in a flow field was developed at the Institut of Geodesy and Photogrammetry (IGP) at the ETH Zürich, Switzerland, by Dr. Hans-Gerd Maas.

REFERENCES

A. Roshko, 1976, "Structure of turbulent shear flows: A new look", *AIAA J.*, Vol. 14, no. 10

G. L. Brown and A. Roshko, 1974, "On density effects and large structure in turbulent mixing layers", *J. Fluid Mech.*, Vol. 64, part 4

J. E. Martin and E. Meiburg, 1994, "The accumulation and dispersion of heavy particles in forced two-dimensional mixing layers. I. The fundamental and subharmonic cases", *Phys. Fluids*, Vol. 6 (3), March 1994

N. Raju and E. Meiburg, 1995, "The accumulation and dispersion of heavy particles in forced two-dimensional mixing layers. II. The effect of Gravity", *Phys. Fluids*, Vol. 7, 1995

O. A. Druzhinin, 1995, "On the two-way interaction in two-dimensional particle-laden flows: the accumulation of particles and flow modification", *J. Fluid Mech.*, Vol 297, pp. 49-76

Lian-Ping Wang and Martin R. Maxey, 1993, "Settling velocity and concentration distribution of heavy particles in homogeneous isotropic turbulence", *J. Fluid Mech.*, Vol. 256, pp. 27-68

B. J. Lazaro and J. C. Lasheras, 1992, "Particle dispersion in the developing free shear layer" *J. Fluid Mech.* Vol. 235, pp. 143-221

DISPERSION OF SMALL, HEAVY, SPHERICAL PARTICLES IN A THREE-DIMENSIONAL, TEMPORALLY DEVELOPING MIXING LAYER

Bogdan Marcu and Eckart Meiburg
Department of Aerospace Engineering
University of Southern California
Los Angeles, California 90089-1191
USA

ABSTRACT

The effect of the streamwise vortical braid structures on the dispersion of heavy particles in a mixing layer is investigated by means of direct numerical simulations. It is observed that, depending on the particle Stokes number and gravitational effects, the braid vortices can strongly deform the geometry of clear fluid and particle laden regions, thereby altering the concentration, dispersion, and suspension patterns observed in 2-D flows. While local regions of large particle accumulations emerge, the profile of the spanwise and streamwise averaged concentration is generally rendered more uniform by 3-D effects.

INTRODUCTION

Over the last decade, 2-D mixing layers have served as the main test flows for the exploration of the mechanisms by which the large-scale coherent structures of turbulent flows result in the dispersion or accumulation of heavy particles or droplets. In particular, the optimal dispersion of particles with an aerodynamic response time similar to the characteristic time of the flow structures, i.e. a Stokes number St value near unity, has been demonstrated both experimentally[1, 2, 3, 4, 5, 6] and numerically[7, 8, 9]. The ejection of the heavy particles from the vortex cores, and the simultaneous formation of highly concentrated particle bands in the strain field near the braid stagnation point, have been identified as the mechanisms that govern the overall efficiency of the dispersion process. In addition, scaling laws based on local linearizations of the flow field[8, 9] have been able to explain the optimal efficiency of these processes for $St \approx 1$. A more detailed account is provided by many of the references in the recent overview by Crowe, Troutt, and Chung[10].

The observed formation of bands of high particle concentrations in the braid region immediately raises the question as to how 3-D effects can modify the above 2-D picture. Both experimental[11, 12] and numerical[13, 14] investigations have demonstrated the presence of a system of strained counterrotating streamwise vortices in this region, which should affect the concentrated particle bands. A first glimpse of the interesting dynamics displayed by heavy particles in an extensionally strained vortex was provided by the model problem of a Burgers vortex[15]. In this flow, particles with a subcritical value of St can be stably located at the vortex center, whereas supercritical particles tend to orbit around the vortex. The presence of gravity can lead to the existence of several distinct equilibrium points with different stability characteristics. An extension of this investigation to the quasi-2-D problem of a periodic array of extensionally strained counterrotating vortices[16, 17] yielded a wealth of information regarding possible accumulation regions and nonlinear particle dynamics in the mixing layer braid region.

The present investigation aims at integrating the features extracted from the above 2-D and quasi-2-D model flows into a coherent picture of 3-D particle dispersion. Toward this end, we analyze the dispersion of heavy particles in a three-dimensionally evolving, temporally growing mixing layer.

NUMERICAL SIMULATIONS

The assumption of dilute particle concentration allows us to neglect the effect of the particles on the fluid motion, so that the fluid velocity can be obtained in the usual way by means of direct numerical simulation of the Navier-Stokes equations, e.g.[18]. The flow field, initially in the form of a hyperbolic tangent profile, is periodic both in the streamwise and the spanwise directions, which consequently are represented in terms of Fourier modes. In the non-periodic transverse direction, Legendre polynomials are employed in conjunction with a mapping procedure. The Reynolds number, formed with half the difference velocity and the initial vorticity thickness, has a value of 200. The simulation is advanced in time in three fractional steps. In the first step, the convective terms are integrated using an explicit fourth order Runge-Kutta scheme. This is followed by a Crank-Nicolson scheme for the viscous term. The intermediate velocity field obtained from these two steps is corrected to a divergence free field in a a third step. 2-D initial disturbances in the form of the most unstable eigenfunctions are combined with periodic streamwise vortical perturbations in order to trigger an evolu-

tion that approximately reproduces the ROLLUP case analyzed in detail in[18]. The comparison with this case simultaneously serves as validation for our numerical code. The flow is characterized by initially weak counterrotating braid vortices, which amplify under the action of the spanwise Kelvin-Helmholtz vortices until they reach a critical strength that leads to their collapse into nearly round concentrated vortex tubes. The effect of vortex pairing is not considered within the present investigation.

At the beginning of the simulation, the upper stream is seeded with 65,000 heavy particles, whose initial velocity is equal to the local fluid velocity. Subsequently, the motion of these particles is calculated by balancing their inertia with gravitational forces and the Stokes drag exerted on them by the fluid. The resulting dimensionless equation of motion for the particle velocity $\mathbf{v}_p$ as a function of the fluid velocity field $\mathbf{u}(\mathbf{x},t)$ and time t

$$\frac{d\mathbf{v}_p}{dt} = \frac{1}{St}\left[\mathbf{u}(\mathbf{x}_p,t) - \mathbf{v}_p(t)\right] + \frac{1}{Fr^2}\mathbf{e}_g \qquad (1)$$

arises from the well-known Maxey-Riley equation[19] in the limit of large density ratio[2]. Here

$$St = \frac{d^2 \rho_p\, U_0}{18\, \rho_f\, \nu\, \delta_\omega^0} \qquad Fr = \frac{U_0}{\sqrt{\delta_\omega^0 g}} \qquad (2)$$

denote the Stokes and Froude numbers, respectively. ρ_f and ρ_p indicate the densities of the fluid and the particle respectively, d is the particle diameter, U_0 represents half the velocity difference between the free streams, δ_ω^0 indicates the initial vorticity thickness, ν is the fluid kinematic viscosity, and g denotes the gravitational acceleration in the direction $\mathbf{e}_g$. The particle motion in the streamwise x-, the spanwise y-, and the transverse z-direction is obtained by numerically integrating the above equation with a standard predictor-corrector numerical method. For all of the situations reported here, $\mathbf{e}_g$ points in the $-z$-direction.

RESULTS

This short paper aims at explaining the formation of high particle concentration zones in plane mixing layer flows based on particle dynamics observed in these simulations. In a previous study, Marcu and Meiburg[20] presented simulation results for particles characterized by low and $O(1)$ St values. Particles characterized by $St = 0.01$ and $St = 1$ were shown to interact with the three-dimensionally evolving flow, allowing for the formation of bands of high particle concentration. The present investigation aims at extending the St regime to larger values by analyzing the distribution, and in particular the accumulation of particles characterized by $St = 2.5$, both in the presence and in the absence of gravity.

Figure 1 demonstrates the results for $St = 2.5$ in the absence of gravity by displaying instantaneous spanwise and streamwise vorticity contours in various x,z- and y,z-planes, along with the locations of particles contained within a thin slice centered around these planes. While the number of particles ejected into the lower stream is small, layers of high particle concentration form near the folding interface between the upper and the lower streams of fluid. The streamwise vorticity affects the accumulation process throughout the whole flowfield: darker layers of concentrated particles can be observed in both y,z-cuts, cf. figure 1d and e.

Figure 2 shows the particle dispersion for $St = 2.5$ and $Fr = 3.043$. The presence of gravity (pointing in the negative $z-$direction) enhances some of the effects generated by the streamwise vorticity. As the particles fall through the vortical flow structures, they are vigorously redistributed. As shown in the y,z-cuts, the stretched counterrotating

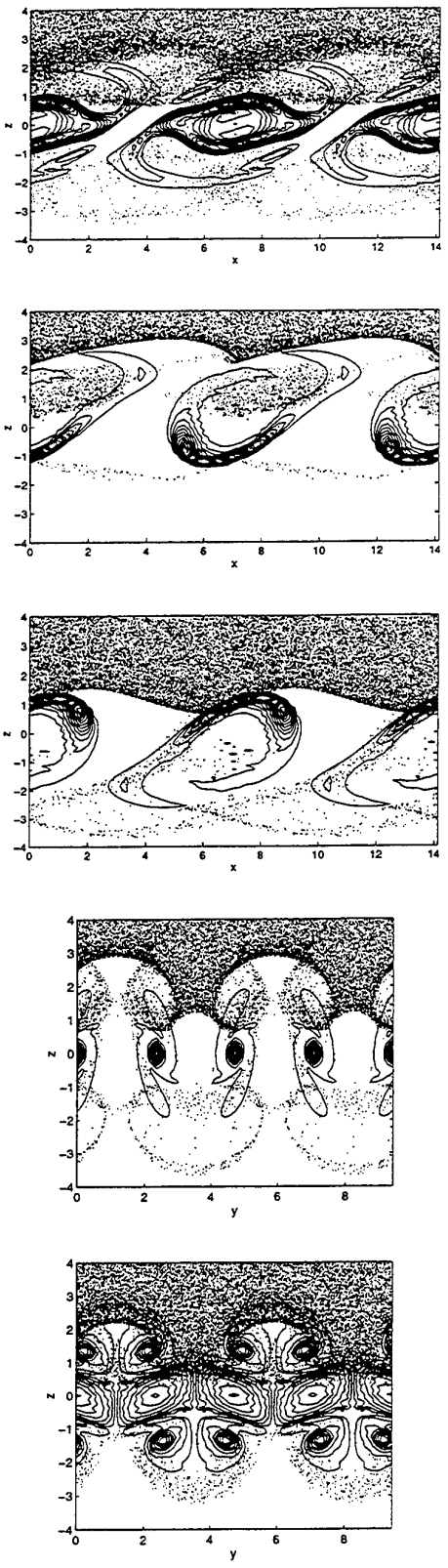


Figure 1: (a). x,z-cut through a streamwise vortex at $t = 16$ for $St = 2.5$ in the absence of gravity. (b). x,z-cut through the upwelling region (c). x,z-cut through the down-welling region. (d). y,z-cut through the center of the braid region (e). y,z-cut through a spanwise roller.

streamwise vortices quickly deplete the particles along the fluid downflow locations while concentrating them in the upflow regions where they remain suspended for a significantly longer time. This process induces the formation of bands of high particle concentration, as shown in figure 2b,

While offering some insight into the particle dispersion process, the x,z- and y,z-cuts shown in the previous figures cannot offer a complete understanding of the particle dispersion field. In the following, the simulation results are presented in three different ways. For evaluating the particle concentration field, the computational domain was divided into 32x32x32 bins, into which the particles are sorted and counted. Thus, a 3-D distribution function f_{3D} for the particle concentration is obtained numerically. This function is normalized by the initial concentration value in the seeded stream. Employing f_{3D}, 2-D plane projections can then be calculated by integrating i)in the $y-$direction, in order to produce the $x,z-$plane projection, ii)in the $z-$direction, to produce the $x,y-$plane projection, and iii)in the $x-$direction, to produce the y,z-plane projection. In the following figures, these plane particle dispersion function projections are plotted on a gray scale, with brighter areas corresponding to higher particle concentrations. In this way, a plane projection image is similar to a snapshot in an experimental apparatus in which particles are illuminated, and thereby seen as white dots on a dark background, so that an accumulation of particles would produce bright areas in the picture. f_{3D} is also integrated over x and y and then normalized, in order to obtain an averaged particle concentration as a function of the vertical coordinate z. In order to compare the particle dispersion produced by a 3-D flow with the dispersion achieved in a 2-D flow, additional numerical simulations were conducted without the initial periodic streamwise vortical perturbations. A corresponding f_{2D} was calculated, normalized in a manner consistent with the 3-D values, and then integrated and plotted together with the 3-D case.

In order to better understand the mechanism of particle accumulation, and to identify the correlation between the zones of high f_{3D} values and the vortical structures, 3-D iso-surface plots were generated for the spanwise and streamwise vorticity and f_{3D}.

One set of such results is presented in figure 7.a for $St = 2.5$, without gravity. The average concentration profiles show significant differences between the dispersion rates achieved by 3-D and 2-D flows. While the 2-D flow produces a strong concentration peak around $z = 1.8$, the 3-D flow partially smoothes out the profile, producing a lower value peak, and displacing it upwards, to $z = 2.7$. Below this peak concentration value, the curve displays a plateau down to $z = 0.5$. The smaller concentration peak at $z = -2.5$ in the 2-D flow is absent in three dimensions.

The peak observed in the averaged concentration profile can easily be correlated to the bright streaks observed in the x,z-plane projection image. The upper stream is more populated with particles, due to the relatively low rate of mixing for this St value. The aerodynamic response time of the particles is relatively long and prevents the vortices from ejecting a large number of them into the lower stream. Nevertheless, the streamwise vorticity generates areas of larger particle accumulation. In the x,y- and y,z-plane projection images, longitudinal streaks and bright spots, respectively, complement the bright structures observed in the xz-plane projection image, which result in the peak in the average concentration profile.

These streaky areas of high particle concentration can be identified in figure 7.b as well. The surfaces aligned in the spanwise direction (light gray) indicate the spanwise rollers, with spanwise vorticity of $\omega_y = 1.0$. The streamwise darker gray surfaces correspond to streamwise vorticity of $\omega_x = -0.7$ while the lighter gray streamwise surfaces indicate streamwise vorticity of $\omega_x = +0.7$. The dark gray

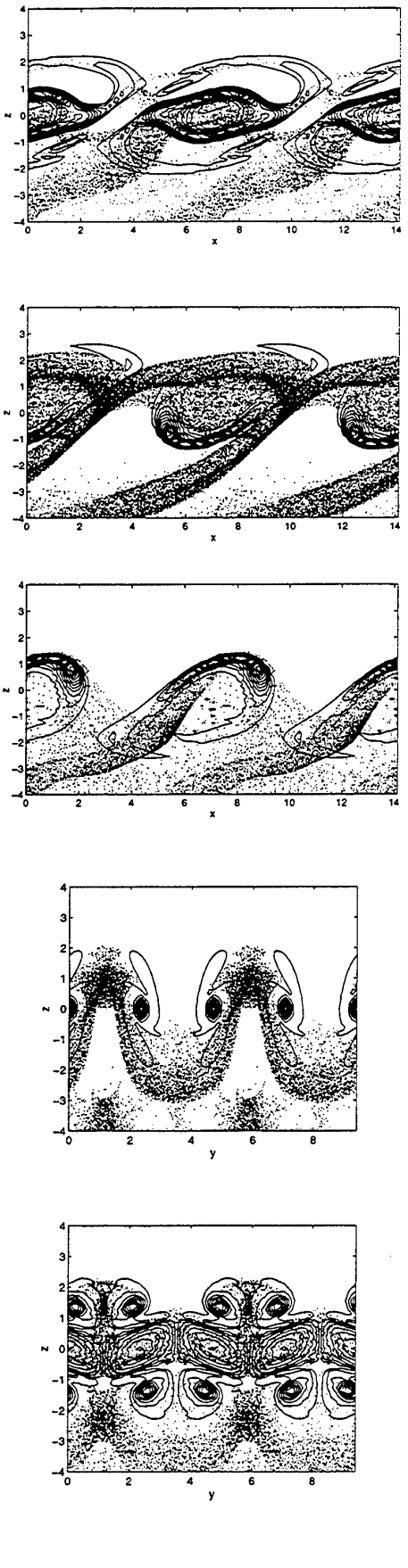


Figure 2: Cuts at the same time and identical locations as in figure 1, for $St = 2.5$, and $Fr = 3.043$.

broken structures correspond to $f_{3D} = 3.5$. It is apparent that the high concentration streaks, although scattered, line up with the streamwise ribs. This accumulation mechanism is due to the combined effect of the Kelvin-Helmholtz vortices, which concentrate the particles in the braids, and the streamwise ribs, which preferentially accumulate the particles at certain spanwise braid locations.

When gravity is introduced to the problem, a stronger and more coherent accumulation of the $St = 2.5$ particles is observed, as shown in figure 7.. The $Fr = 3.043$ value has been chosen based on an accumulation criterion developed by Marcu and Meiburg[16] using a plane projection model of the braid region flow field, in conjunction with a scaling analysis given by Marcu[21].

Figure 7.a shows that the average concentration profile is smoothed again by the 3-D flow, when compared with the 2-D flow. The larger peak located at $z = 0$ for the 2-D flow is replaced by two smaller peaks located at $z = 1$ and $z = -0.7$ for the 3-D flow. It is difficult to correlate these peaks with any high concentration areas in the plane projection images. However, the 3-D plot shown in figure 7.b enables us to explain the distribution. The dark gray surfaces correspond to $f_{3D} = 4$ values, i.e., regions of high particle concentrations. Coherent accumulation structures form in between the streamwise vortices along the upflow regions, as predicted by Marcu and Meiburg[16, 17]. It is interesting to note that for the present parameters the streaks continue uninterrupted along the streamwise direction. Furthermore, these streaks branch out around the spanwise rollers, forming secondary branches reaching below the spanwise rollers. At some of those locations, small areas with f_{3D} values as high as 16 were recorded. These localized, very high concentration areas result in the bright areas observed in the x, y- and y, z-plane projection images.

CONCLUSIONS

In summary, direct numerical simulations indicate that, depending on the St values of the particles and the relative strength of gravity, the extensionally strained streamwise vortices can lead to a substantial modification of the concentration, dispersion, and suspension patterns observed in 2-D simulations. The time-dependent 3-D vorticity field leads to increased stretching and folding of the interface separating clear fluid and particle laden regions, and thereby results in a significantly more complex particle concentration distribution, with local more complex particle concentration distribution, with local areas of high areas of high accumulation. However, peaks observed in 2-D simulations for the transverse profile of the averaged concentration are usually smoothed out by 3-D effects. It is furthermore interesting to note that a particle can have different effective St values with respect to the different vortical structures, so that it can be affected quite differently by them.

ACKNOWLEDGMENTS

We would like to thank Dr. Daniel Chan for his help in generating the computational code. We furthermore gratefully acknowledge NSF support under Grant No. CTS-9196004, and funding through EPRI. Computing resources were provided by the San Diego Supercomputer Center.

REFERENCES

[1] C. T. Crowe, R. A. Gore, and T. R. Troutt. Particle dispersion by coherent structures in free shear flows. *Particulate Science and Technology*, 3:149, 1985.

[2] B. J. Lazaro and J. C. Lasheras. Particle dispersion in a turbulent, plane, free shear layer. *Physics of Fluids A*, 1:1035, 1989.

[3] B. J. Lazaro and J. C. Lasheras. Particle dispersion in the developing free shear layer. Part1: unforced flow. *Journal of Fluid Mechanics*, 235:143, 1992.

[4] B. J. Lazaro and J. C. Lasheras. Particle dispersion in the developing free shear layer. Part2: forced flow. *Journal of Fluid Mechanics*, 235:179, 1992.

[5] E. K. Longmire and J. K. Eaton. Structure and control of a particle-laden round jet. *Journal of Fluid Mechanics*, 236:217, 1992.

[6] K. T. Kiger and J. C. Lasheras. Te effect of vortex pairing on particle dispersion and kinetic energy transfer in a two-phase turbulent shear layer. *Journal of Fluid Mechanics*, 302:149, 1995.

[7] J. N. Chung and T. R. Troutt. Simulation of particles in an axisymmetric jet. *Journal of Fluid Mechanics*, 186:199, 1988.

[8] J. E. Martin and E. Meiburg. The accumulation and dispersion of heavy particles in forced two-dimensional mixing layers. Part 1: The fundamental and subharmonic cases. *Physics of Fluids*, 6:1116, 1994.

[9] N. Raju and E. Meiburg. The accumulation and dispersion of heavy particles in forced two-dimensional mixing layers. Part 2: The effect of gravity. *Physics of Fluids*, 7:1241, 1995.

[10] C. T Crowe, T. R. Troutt, and J. N. Chung. Numerical models for two-phase turbulent flows. *Annual Review of Fluid Mechanics*, 28:11, 1996.

[11] L. P. Bernal and A. Roshko. Streamwise vortex structures in plane mixing layers. *Journal of Fluid Mechanics*, 170:499, 1986.

[12] J. C. Lasheras and H. Choi. Three-dimensional instability of a plane, free shear layer: an experimental study of the formation and evolution of streamwise vortices. *Journal of Fluid Mechanics*, 189:53, 1988.

[13] S. J. Lin and G. M. Corcos. The mixing layer: deterministic models of a turbulent flow. Part 3. The effect of plane strain on the dynamics of streamwise vortices. *Journal of Fluid Mechanics*, 141:139, 1984.

[14] W. T. Ashurst and E. Meiburg. Three dimensional shear layers via vortex dynamics. *Journal of Fluid Mechanics*, 189:87, 1988.

[15] B. Marcu, E. Meiburg, and P. K. Newton. Dynamics of heavy particles in a Burgers vortex. *Physics of Fluids*, 7:400, 1995.

[16] B. Marcu and E. Meiburg. The effect of the streamwise braid vortices on the particle dispersion in a plane mixing layer. Part 1: Equilibrium points and their stability. *Physics of Fluids*, 8:715, 1996.

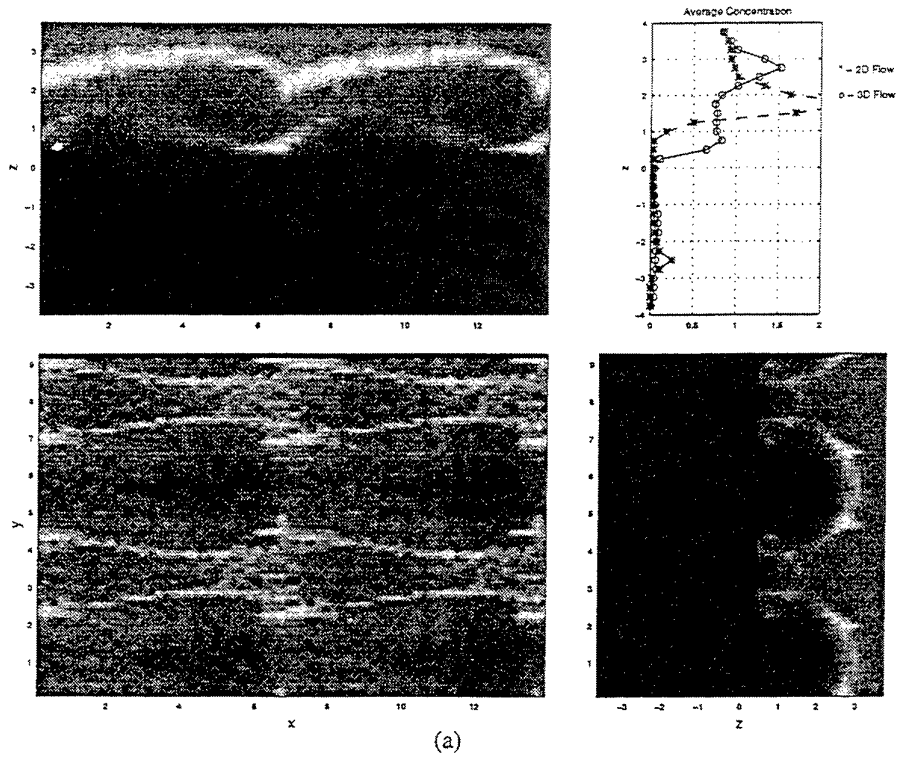
[17] B. Marcu, E. Meiburg, and N. Raju. The effect of the streamwise braid vortices on the particle dispersion in a plane mixing layer. Part 2: Nonlinear particle dynamics. *Physics of Fluids*, 8:734, 1996.

[18] M. M. Rogers and R. D. Moser. The three-dimensional evolution of a plane mixing layer: the Kelvin-Helmholtz rollup. *Journal of Fluid Mechanics*, 243:183, 1992.

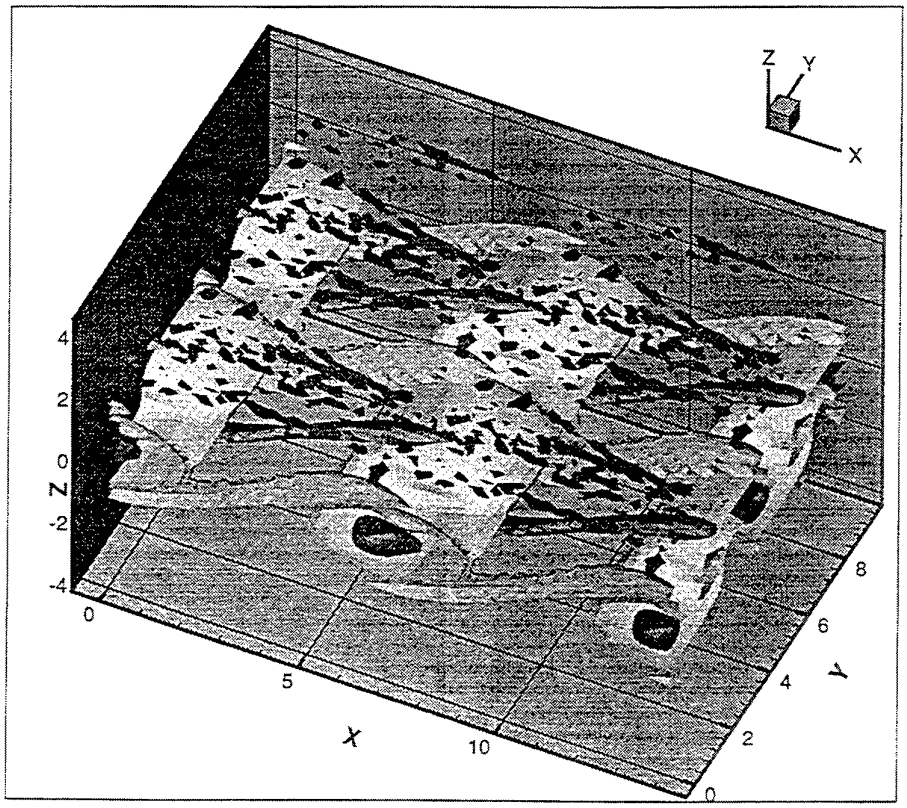
[19] M. R. Maxey and J. J. Riley. Equation of motion for a small rigid sphere in a nonuniform flow. *Physics of Fluids*, 26:883, 1983.

[20] B. Marcu and E. Meiburg. 3-dimensional features of particle dispersion in a nominally plane mixing layer. *Physics of Fluids*, 8:2266, 1996.

[21] B Marcu. *Dynamics of heavy particles within vortical flow structures.* Ph.D. Thesis, University of Southern California, 1996.

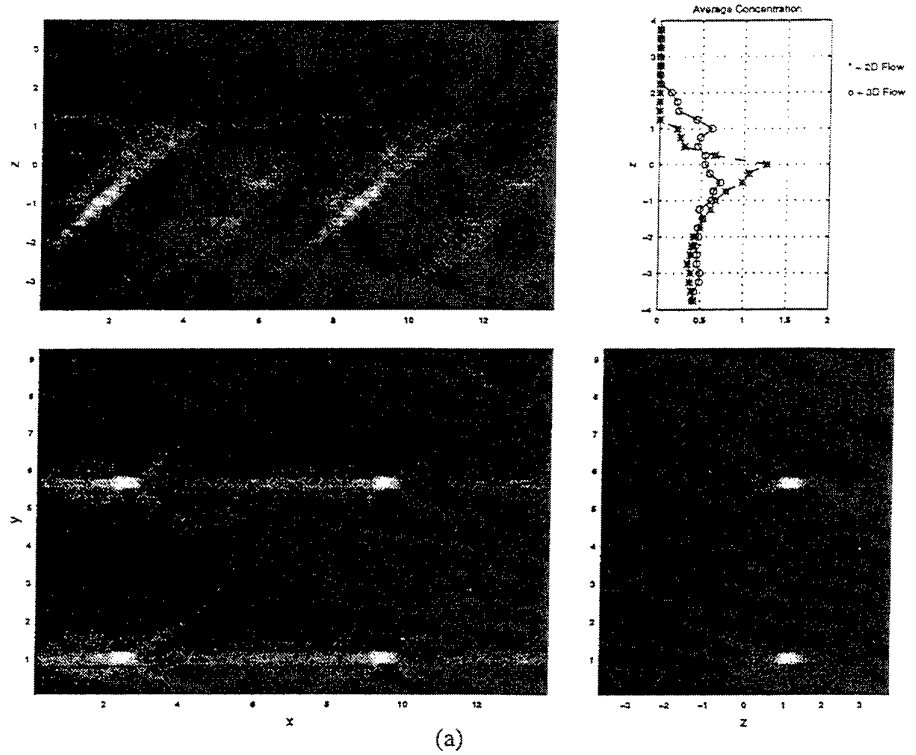


(a)

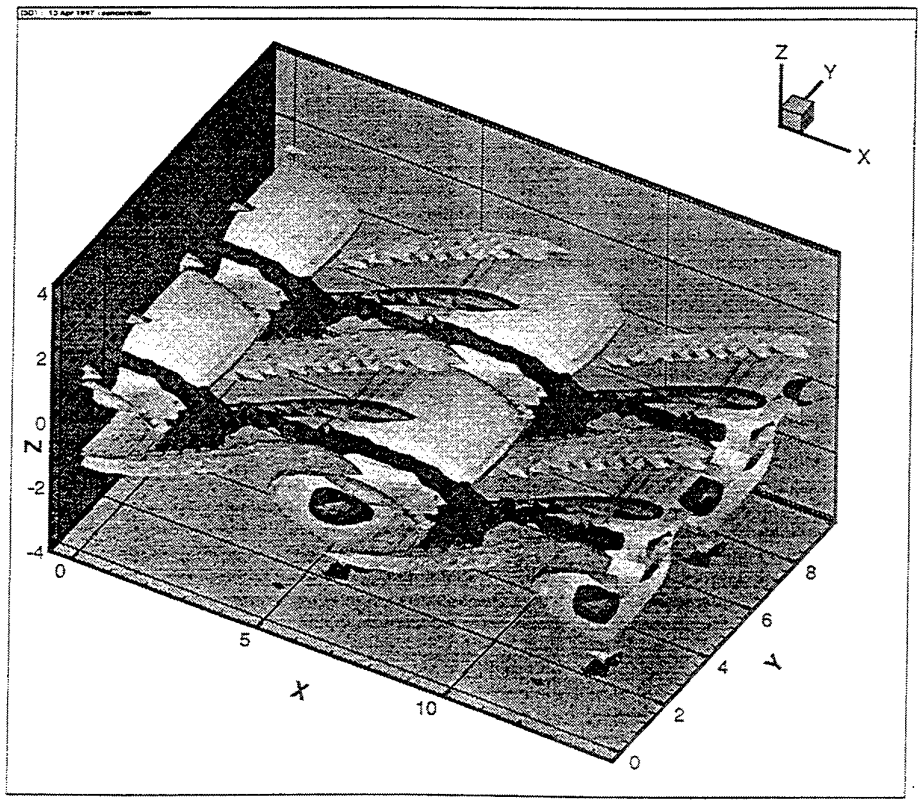


(b)

Figure 3. Particle dispersion for $St = 2.5$, no gravity case. **(a)** plane projection images of the particle dispersion, and the variation of the average particle concentration with the vertical direction (z), a comparative plot for 2-D and 3-D mixing flow. **(b)** three dimensional plot of the flow vorticity structures along with high particle concentration iso-surfaces showing accumulation areas. The normalized concentration value here is 3.5.



(a)



(b)

Figure 4. Particle dispersion for *St = 2.5, Fr = 3.043*. **(a)** plane projection images of the particle dispersion, and the variation of the average particle concentration with the vertical direction (z), a comparative plot for 2-D and 3-D mixing flow. **(b)** three dimensional plot of the flow vorticity structures along with high particle concentration iso-surfaces (blue, or dark colored in gray-scale plots) showing accumulation areas. The normalized concentration value here is 4.0.

LAGRANGIAN STATISTICS OF FLUID/PARTICLE CORRELATED MOTION IN CHANNEL FLOW

Yohei SATO, Itsuro HAYASHI and Koichi HISHIDA

Department of Mechanical Engineering
Faculty of Science and Technology
Keio University
3-14-1, Hiyoshi, Kohoku-ku
Yokohama, 223
JAPAN

ABSTRACT

Motion of solid particles in a fully-developed channel flow of water was investigated by Lagrangian measurement techniques. Digital particle image velocimetry and a CCD camera mounted on a moving shuttle with mean streamwise velocity of particle were used to detect particle motion and fluid along the particle path simultaneously. Five classes of particles were dispersed in the upstream of the test section. It was observed that a force due to fluid pressure gradient and viscous stresses can be dominant in a particle dynamic equation when particle density ratio was close to unity. Lagrangian velocity spectrum of particles which has their density ratio less than unity was found to be higher than that of fluid along the particle path, which is consistent with theory by Mei (1996). Lagrangian autocorrelation of velocity of both heavier particles and fluid decreased rapidly with increasing values of the particle time constant.

INTRODUCTION

Particle motion in a turbulent flow dramatically complicates characterization of the flow and renders the traditional empirical methodology for single-phase flow as far from complete. Many researchers have been fascinated by particle dynamics like Stokes (1851) and Basset (1888) who first established a particle dynamic equation. The most important and fundamental theory in history of turbulence, i.e. the turbulent diffusion theory, by G.I. Taylor (1921), which was developed by Batchelor (1949) and Corrsin (1953) contributed to establishment of the particle dispersion theory (Hardalupas *et al.* 1989, 1990). Theories and accurate modeling are needed to design new or improved products and also to help reach decisions in such matters as mitigation of environment impacts. Only recent direct numerical simulations in isotropic turbulence (Squires and Eaton 1990, 1991, Elghobashi and Truesdell 1992, 1993) have shown well-qualified information and examined validation of theories (e.g. Yudine 1959, Csanady 1963) and models. None of the Lagrangian statistics obtained from the experiments existed, therefore it has been unknown how theories and models work well in wall-bounded flows or shear flows.

The objective of this study was to investigate fluid/particle correlated motion in a turbulent channel flow measured by a digital particle image velocimetry (Sakakibara *et al.* 1993) combined with a CCD camera mounted on a moving shuttle with particle streamwise mean velocity. The exact forces acting on a particle, particle frequency response and Lagrangian correlation in a turbulent channel flow are reported first time and will have contribution to development of theories and models in a field of multiphase flows.

EXPERIMENTAL SETUP

Experimental Facility

The present experiments were performed in a two-dimensional, vertical downflow water channel which was identical to that of Sato (1996) and Sato and Hishida (1996). The channel was vertically oriented so that the gravitational force on the particles was aligned with the direction of flow. Figure 1 illustrates the basic flow and particle supply system. Particles were injected through a long pipe of 4 mm in diameter, which located at the centerline of channel. Water was streamed into the pipe for injecting only polyethylene particles due to their density ratio less than unity. Boundary-layer trips were affixed to both walls at the entrance to a 1.0 m long, 30×250 mm test section. The flow exited the test section into a drain tank, where the particles were collected for reuse. Measurements confirmed that the flow was fully-developed at the channel centerline in the test section and was unmodified by the particle feeder pipe, shown in figure 2. Figure 2 compares profiles of mean streamwise velocity by the Eulerian measurements (Sato and Hishida 1996); included for reference is the log law. All the experiments were run at a centerline mean velocity of 15.5 cm/s, corresponding to a Reynolds number of 5,740 based on channel width. Temperature of water was kept constant by using a heater to avoid varying fluid properties.

Five classes of particles were used in the present set of experiments and their characteristics are compiled in table 1. Particles were chosen to provide being approximately 340 μm in diameter except polystyrene particles of 1,700 μm. The particle size distributions were determined by using successively smaller sieves and the particle sphericity was checked using a microscope.

Experimental Techniques

Lagrangian statistics of both phases were obtained using a digital particle image velocimetry (DPIV) developed by

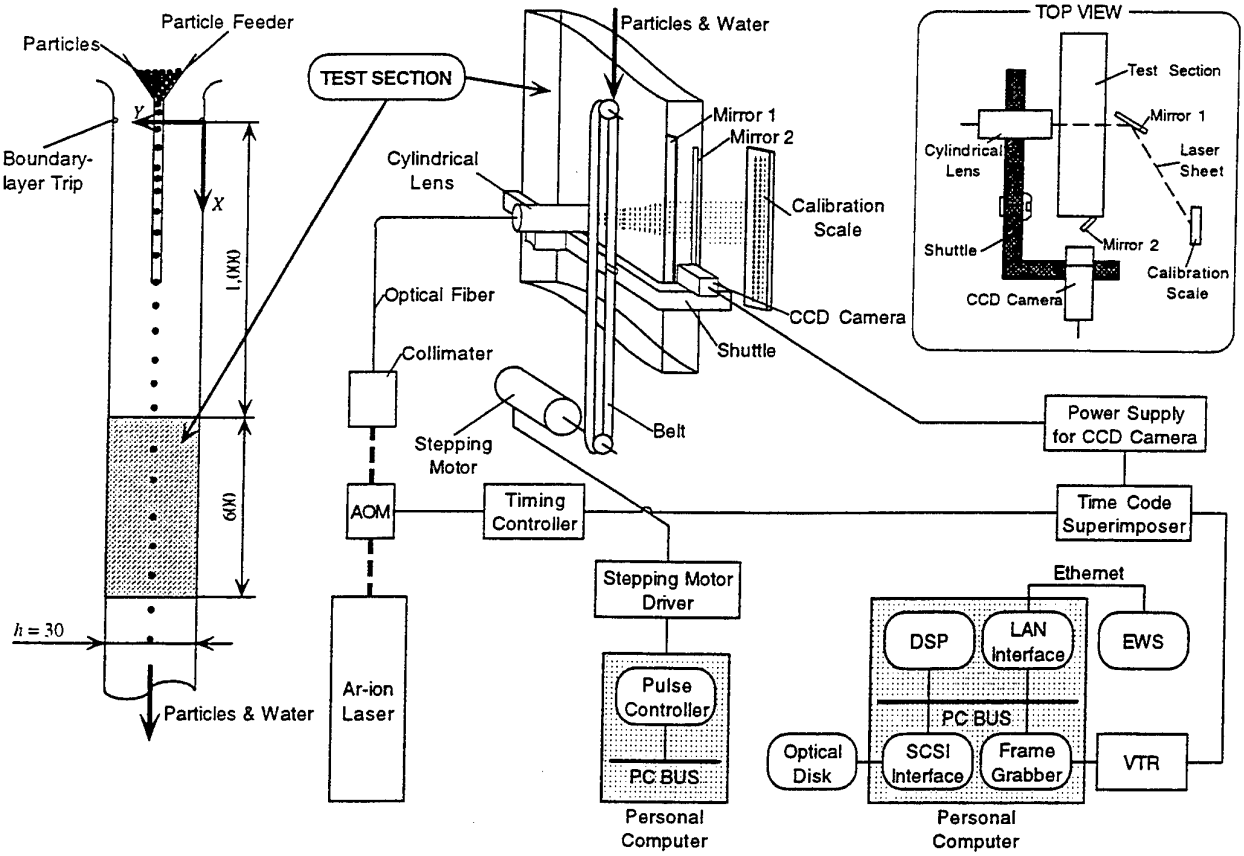


Figure 1. Schematic of experimental apparatus and techniques.

Table 1. Particle properties

Properties		glass	cellulose	polyethylene	polystyrene	polystyrene
number mean diameter	d_p [μm]	454.4	417.7	432.8	423.3	1,720
stan. dev. of diameter	σ_p [μm]	18.9	27.5	26.7	24.8	107.7
density	ρ_p [kg/m^3]	2,590	1,500	918	1,050	1,050
terminal velocity	V_t [mm/s]	68.7	26.6	-6.40	4.10	26.3
particle time constant	τ_p [ms]	7.01	2.71	0.65	0.42	2.68
particle Reynolds number	Re_p	31.1	11.0	2.76	1.78	45.0

Sakakibara *et al.* (1993) and Hishida *et al.* (1996). Shown in figure 1 is a schematic illustration of the digital particle image velocimetry. The illuminated laser light sheet was chopped by an acoustic optical modulator (AOM) cell for synchronizing to the video signal. Velocities were calculated by cross correlation technique between two images. Polyethylene particles of 10 μm (density of 960 kg/m^3) were added as a tracer to the liquid phase. The thickness of the Ar-laser light sheet was 3.0 mm in the test section.

In the present study, a CCD camera and a cylindrical lens were mounted on a moving shuttle in order to establish the Lagrangian measurement techniques which realized detecting particle motion and fluid information around a particle simultaneously. The shuttle moved from top to bottom parallel to the water channel with mean streamwise velocity of particle. A stepping motor was used to control shuttle's velocity and it is necessary to calibrate influence of vibration of shuttle on its velocity. A special calibration scale in which solid marks were randomly distributed as if particle concentration were detected, shown in figure 1, was added to the present system. The CCD camera captured images of flow field in the test section and the calibration scale by using mirror 2, which was illuminated by a laser sheet via mirror 1. Figure 3 displays an image of the instantaneous flow

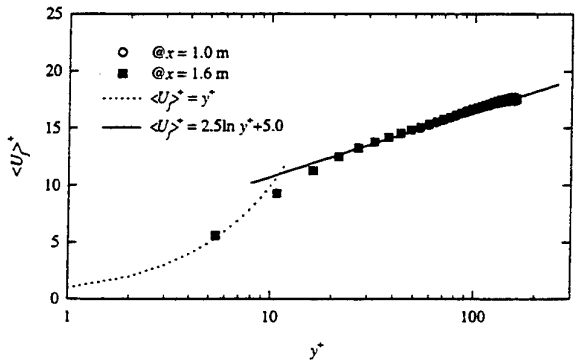


Figure 2. Mean streamwise velocity profiles of water. Both axes are normalized by friction velocity and kinematic viscosity of water.

field and the calibration scale captured by the CCD camera. By using the DPIV system combined with the moving shuttle it is possible to calibrate the shuttle's vibration per unit image. The measurements uncertainty in these experiments due to the velocity calibration was 2.0% for instantaneous velocity measurements.

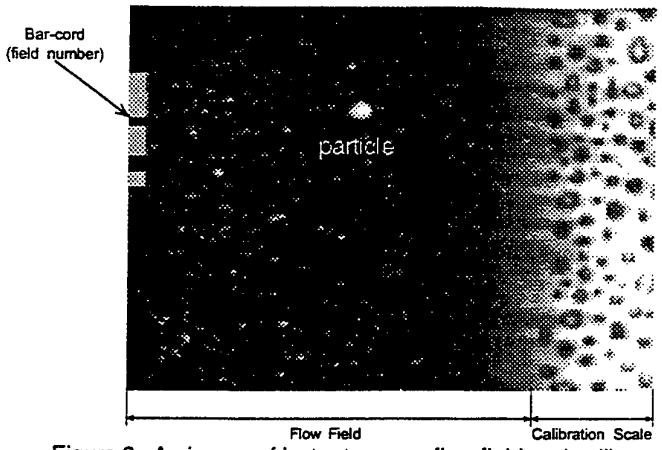


Figure 3. An image of instantaneous flow field and calibration scale captured by a CCD camera.

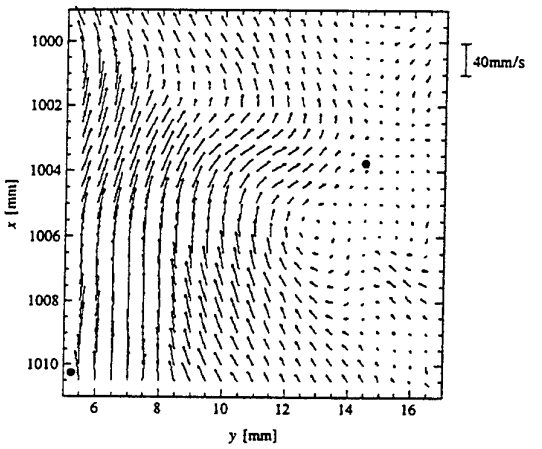


Figure 4. An instantaneous velocity map of fluid seen by particle.

Figure 4 shows an instantaneous velocity map of fluid seen by particle in which the position and the velocity vectors are dimensional in order to show the actual size of the measured region. A particle and surrounding fluid were measured by the CCD camera in a few seconds and then velocities in time series were calculated by using a set of 40 to 60 velocity vector images within an interval of 1/20 s. The Lagrangian statistics were evaluated by averaging 15 to 20 sets of time series data.

In the present experiments fluid velocity along the particle path was evaluated by averaging fluid velocities at four points which were 1.5 mm distant from a particle.

RESULTS AND DISCUSSION

The axes of figures presented in this section have been nondimensionalized values using the centerline mean velocity, $\langle U_c \rangle$, of 0.155 m/s and the channel width, h, of 30 mm.

Forces in Particle Dynamic Equation

Lagrangian measurement techniques can provide the instantaneous informations such as how forces act on a particle in a turbulent shear flow. Exact forces in a particle dynamic equation by Mei (1994) were examined in this subsection. Mei (1994) proposed the following equation for particle Reynolds number less than 173:

$$\frac{d\tilde{u}_{p_i}}{dt} = \underbrace{\left(1-\frac{\rho_f}{\rho_p}\right)g_i}_{f_1} + \underbrace{\frac{18\mu}{d_p^2\rho_p}C_D\left(\tilde{u}_{f_i}-\tilde{u}_{p_i}\right)}_{f_2} + \underbrace{\frac{18\mu}{d_p^2\rho_p}\int_{t_0}^{t}K_B(t-\tau)\frac{d\left(\tilde{u}_{f_i}-\tilde{u}_{p_i}\right)}{d\tau}d\tau}_{f_3} + \underbrace{\frac{1}{2}\frac{\rho_f}{\rho_p}\left(\frac{D\tilde{u}_{f_i}}{Dt}-\frac{d\tilde{u}_{p_i}}{dt}\right)}_{f_4} + \underbrace{\frac{\rho_f}{\rho_p}\frac{D\tilde{u}_{f_i}}{Dt}}_{f_5} + \tilde{f}_{E_i}, \quad (1)$$

where $\tilde{u}_{p_i}$ and $\tilde{u}_{f_i}$ are , respectively, the instantaneous velocity of particle and fluid along the particle path, ρ_p and ρ_f are, respectively, density of particle and fluid, g_i is gravity and μ is fluid viscosity. The first term is the body force (gravity minus buoyancy). The second term is a quasi-steady viscous force in

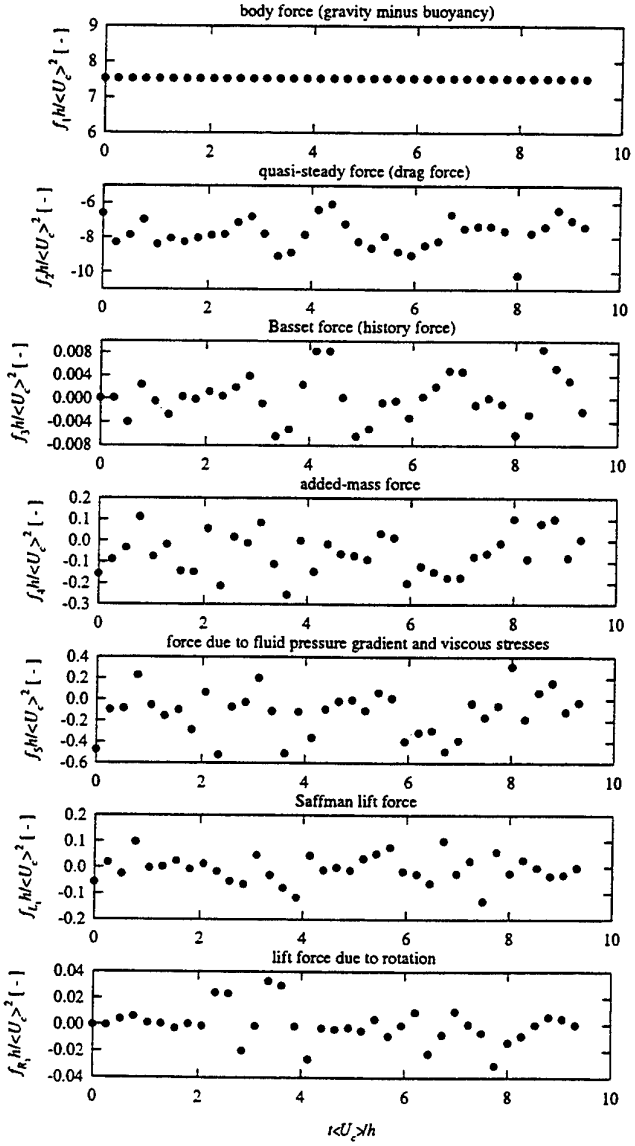


Figure 5. Time development of the forces acting on 450 μm glass particle in the streamwise direction. All the forces are normalized by the centerline mean velocity and the channel width.

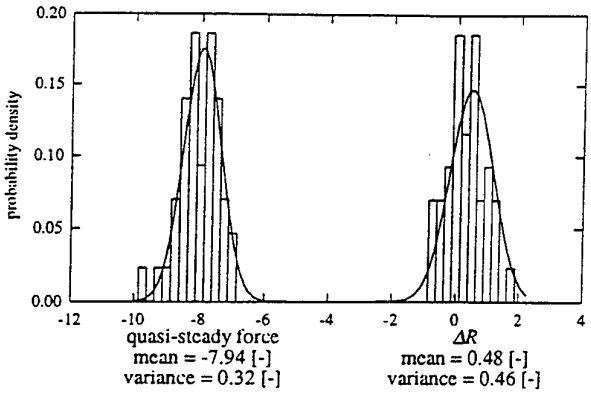


Figure 6. Probability density distributions of the drag force and the residual of equation (1) in the streamwise direction for 450 μm glass particle. The residual was defined as ΔR = left hand side - right hand side of eq. (1).

which the coefficient of drag, C_D, is given by Clift *et al.* (1978). In this paper this term is denoted as the drag force. The third term is called the history force or Basset force in which K_B is the history force kernel (Mei 1994). The fourth term is the added-mass term. The fifth term represents a force due to fluid pressure gradient and viscous stresses. The last term shows any other external body force. In this study the Saffman lift force (1965)

$$\tilde{f}_{L_i} = 1.615\frac{6\mu}{\pi d_p \rho_p}\left(\frac{1}{\nu}\left|\frac{\partial \tilde{u}_{f_i}}{\partial x_j}\right|\right)^{1/2}\left(\tilde{u}_{f_i} - \tilde{u}_{p_i}\right), \tag{2}$$

and the lift force due to rotation (Magnus 1852)

$$\tilde{f}_R = \frac{3}{4}\rho_f \Omega \times \left(V_p - U_f\right)\left[1 + O\left(Re_p\right)\right], \tag{3}$$

are considered as external force.

Figure 5 illustrates the time development of the forces acting on 450 μm glass particle in the streamwise direction which were directly measured first time in experiments. It is necessary to consider an influence of experimental errors on examining exact forces acting on a particle, thus probability density distributions of the drag force and the residual, ΔR, i.e. difference between the left and the right hand side of equation (1), are calculated for aiding discussion. Figure 6 shows the probability density distributions of the above terms in equation (1), which are along the Gaussian distribution. When the gravity acts on particles, the drag and gravity forces are dominant in equation (1) and balance with each other. Small values of the particle density ratio results in slight large values of the added mass force and the force due to fluid pressure gradient and viscous stresses. The experimental results support that the effect of fluid shear on lift force is more significant than that of rotation. Further investigation for other particles indicates that when the particle density ratio becomes close to unity, the force due to fluid pressure gradient and viscous stresses can be dominant in equation (1).

Figure 7 displays the time development of the forces acting on 450 μm glass particle in the transverse direction. It is observed that the force due to fluid pressure gradient and viscous stresses is more significant than other terms. With decreasing values of the particle time constant the drag force shows larger values which is opposite to results in the streamwise direction. For the polyethylene particles the force due to fluid pressure gradient and viscous stresses is about several times the drag force in the transverse direction.

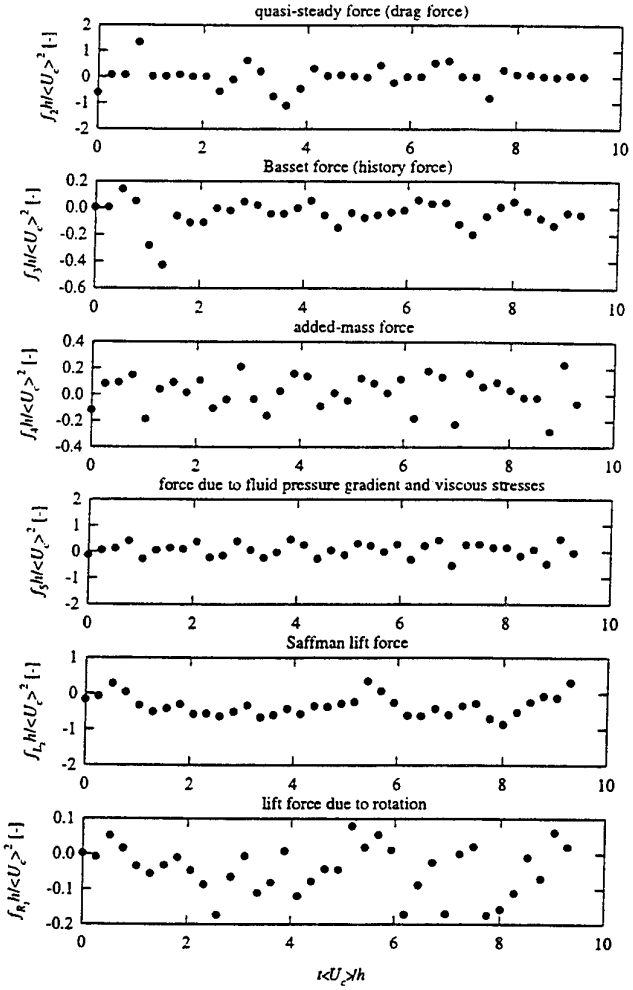


Figure 7. Time development of the forces acting on 450 μm glass particle in the transverse direction. All the forces are normalized by the centerline mean velocity and the channel width.

Particle Frequency Response

Csanady (1963) discussed the response of particles to the high-frequency part of the spectrum with the particle response function:

$$\frac{E^L_{p_i}(\omega)}{E^L_{f@p_i}(\omega)} = \frac{1}{1+\tau_p^2\omega^2}. \tag{4}$$

Equation (4) indicates that the Lagrangian velocity spectrum $E^L_{p_i}(\omega)$ never exceeds that of fluid along the particle $E^L_{f@p_i}(\omega)$. While Mei (1996) derived the following energy transfer function defined as

$$\frac{E^L_{p_i}(\hat{St})}{E^L_{f@p_i}(\hat{St})} = \frac{\left(1+\hat{St}\right)^2 + \left(\hat{St} + \frac{2}{3}\hat{St}^2\right)^2}{\left(1+\hat{St}\right)^2 + \left[\hat{St} + \frac{2}{3}\hat{St}^2 + \frac{4}{9}(r-1)\hat{St}^2\right]^2}, \tag{5}$$

where $\hat{St}$ is a Stokes number in frequency space. Mei's theory has an ability to represent the over-response for buoyant particles ($r = \rho_p/\rho_f < 1$).

Figure 8 depicts profiles of the Lagrangian velocity spectra

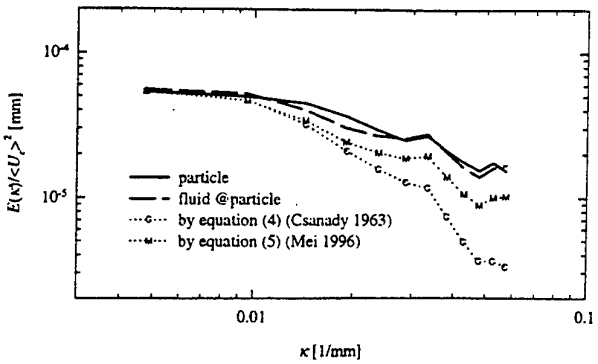


Figure 8. Lagrangian velocity spectra of 450 μm glass particle and fluid along the particle path in the streamwise direction.

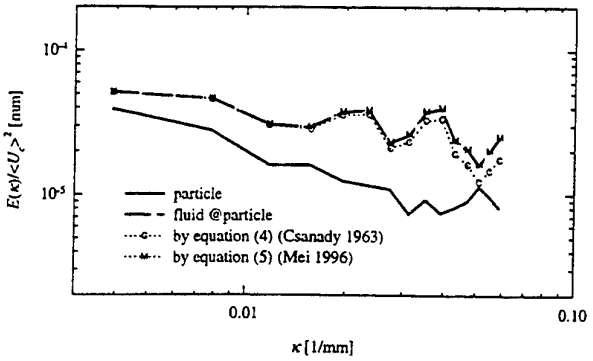


Figure 10. Lagrangian velocity spectra of 430 μm polyethylene particle and fluid along the particle path in the transverse direction.

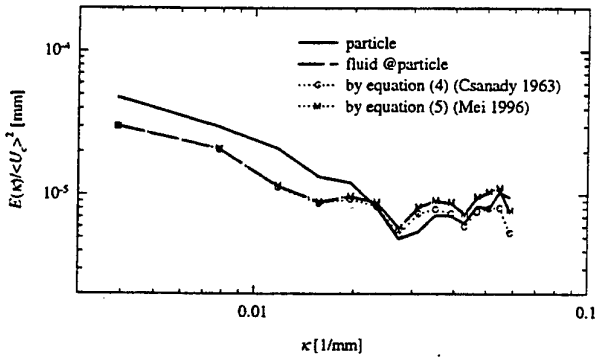


Figure 9. Lagrangian velocity spectra of 430 μm polyethylene particle and fluid along the particle path in the streamwise direction.

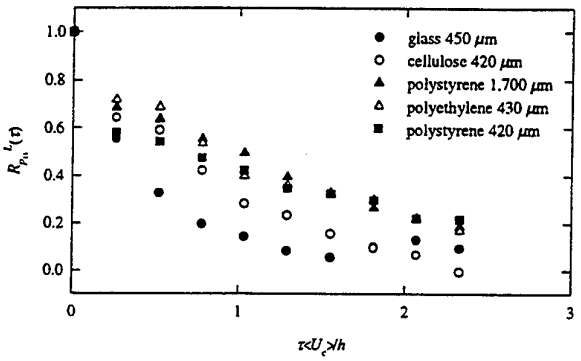


Figure 11. Lagrangian autocorrelation of particle velocity in the streamwise direction.

of 450 μm glass particle and fluid along the particle path in the streamwis direction. The abscissa is the wavenumber, κ, which is related to ω in equation (4) via $\omega = 2\pi\kappa\langle U_c \rangle$. Lines -C- and -M- show the Lagrangian velocity spectrum of particle evaluated by equations (4) and (5), respectively, using the experimental values of fluid spectrum. In the streamwise direction profiles of particle spectrum is close to that of fluid. It means that the glass particles respond well to high-frequency fluctuations of fluid, which seems to contradict Csanady's theory.

Figures 9 and 10 display profiles of the Lagrangian velocity spectra of 430 μm polyethylene particle and fluid along the particle path in the streamwise and transverse direction, respectively. Csanady's theory is not satisfied for the over-response as indicated in figure 9. It is observed from this experiments that particles which have the density ratio less than unity tend to over-response to high-frequency fluctuations of surrounding fluid, which is supported by Mei's theory. However, the particles cannot respond to the transverse fluctuations.

Lagrangian Correlation

It is possible to know how Lagrangian statistics are in a turbulent channel flow by the present measurement techniques. Lagrangian autocorrelations of the particle velocities in the streamwise direction are shown in figure 11. The correlations in non-stationary turbulence are defined as

$$R^L_{P_x}(t_0,\tau) = \frac{\left\langle u_{P_x}(t_0)u_{P_x}(t_0+\tau)\right\rangle}{\left\langle u_{P_x}(t_0)^2\right\rangle^{1/2}\left\langle u_{P_x}(t_0+\tau)^2\right\rangle^{1/2}}. \quad (6)$$

The results from this experiments shows that the velocity autocorrelations of heavy particles decrease faster than those of lighter particles due mainly to the crossing-trajectories effect (Yudine 1959), which is consistent with the experiment in grid-generated turbulence by Snyder and Lumley (1971) and DNS in decaying isotropic turbulence by Squires and Eaton (1991) and Elghobashi and Truesdell (1992). It should be noted that the effects of inertia and drift (gravity) are not isolated in this experiments. It is evident that the correlations do not decrease to zero at long separation times.

Figure 12 displays the Lagrangian correlations of fluid velocity along the particle path in the streamwise direction. It is observed that the correlation of the fluid velocity along the path of the heavier particles decreases more rapidly than does that of the lighter particles, which is probably caused by the heavier particles overshooting the fluid particle paths.

Some models of particle dispersion by turbulence are based on choosing functional forms of the Lagrangian velocity correlation of the fluid velocities along the particle path. Gouesbet *et al.* (1984) used

$$R^L_{f@P_x}(\tau) = \exp\left[\frac{-\tau}{(m^2+1)\tau^L_{f@P_x}}\right]\cos\left[\frac{m\tau}{(m^2+1)\tau^L_{f@P_x}}\right], \quad (7)$$

where $\tau^L_{f@P_x}$ is the Lagrangian time integral scale tensor of the fluid along the particle path. This functional form was originally used by Frenkiel (1953). Lines in figure 12 show the correlation coefficients calculated by equation (7) with the loop parameter m = 0 and 1, and the experimental values of $\tau^L_{f@P_{11}}$. Gouesbet *et al.*

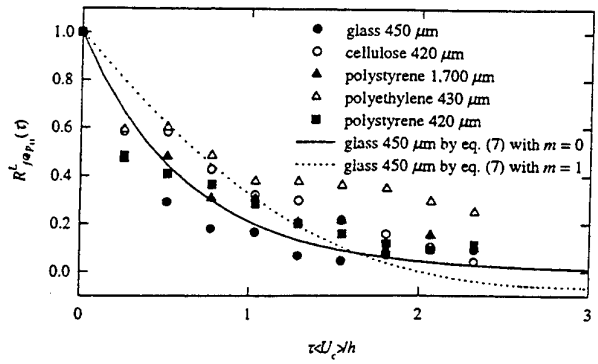


Figure 12. Lagrangian autocorrelation of fluid velocity along the particle path in the streamwise direction.

(1984) has shown that by using equation (7) with $m = 1$ it is possible that heavy particles will disperse faster than fluid elements. However, the experimental evidence indicates that a simple decaying exponential form, i.e. $m = 0$, gives a better result than $m = 1$. Equation (7) was derived in the framework of Tchen's theory for which the effect of an external body force is ignored. As overshooting is not allowed in Tchen's theory it seems unlikely that the correlation of fluid velocities along the particle path will have negative loops. None of the velocity correlations of the fluid along the particle path in the streamwise direction showed negative regions from this experiments.

CONCLUSION

Particle dynamics in a turbulent channel flow have been investigated by the Lagrangian measurement techniques which was developed first time in the present study. Digital particle image velocimetry combined with a system traversing a CCD camera with mean streamwise velocity of particle. Five classes of spherical particles were used to provide varying values of density ratio and particle time constant which have significant effects on particle motion.

Investigations of exact forces acting on particles in a particle dynamic equation by Mei (1994) showed that the drag and the gravity were main forces in the streamwise (gravity) direction. When the particle density ratio was close to unity, the force due to fluid pressure gradient and viscous stresses can be dominant. While in the transverse direction the drag force showed larger values with decreasing values of the particle time constant which was opposite to results in the streamwise direction.

Particles responded well to the high-frequency fluctuations of fluid in the streamwise direction except the over-response of particles which have their density ratio less than unity, supported by Mei's theory. In the transverse direction all the particles were less responsive to fluid fluctuations.

The Lagrangian velocity autocorrelations obtained by the present measurements indicated that the correlations of heavier particles decreased faster than those of lighter particles due to the crossing-trajectories effect. The autocorrelations of fluid along the path of heavier particles decreased more rapidly than did of the lighter particles, which is attributed to overshooting of the heavier particles.

ACKNOWLEDGMENTS

The authors would like to thank Mr. U. Fukuichi for performing experiments. This work was subsidised by the Grant-in-Aid of the Japanese Ministry of Education, Science and Culture (No. 08405019 and No. 4940 for Research Fellowship of the Japan Society for the Promotion of Science for Young Scientists).

REFERENCES

Basset, A.B., 1888, *A Treatise on Hydrodynamics.* Vol. 2, Dover Publications Inc.

Batchelor, G.K., 1949, "Diffusion in a Field of Homogeneous Turbulence," *Austral. J. Sci. Res.*, Vol. 2, pp. 437-450.

Clift, R., Grace, J.R. & Weber, M.E., 1978, *Bubbles, Drops and Particles.* Academic Press, New York.

Corrsin, S., 1953, "Remarks on Turbulent Heat Transfer," *Proc. of the Iowa Thermodynamics Symp.*, Univ. of Iowa, pp. 5-30.

Csanady, G.T., 1963, "Turbulent Diffusion of Heavy Particles in the Atmosphere," *J. Atmos. Sci.*, Vol. 20, pp. 201-208.

Elghobashi, S.E. & Truesdell, G.C., 1992, "Direct Simulation of Particle Dispersion in Decaying Isotropic Turbulence," *J. Fluid Mech.*, Vol. 242, pp. 655-700.

Elghobashi, S.E. & Truesdell, G.C., 1993, "On the Two-Way Interaction between Homogeneous Turbulence and Dispersed Solid Particles. I: Turbulence Modification," *Phys. Fluids A*, Vol. 5, pp. 1790-1801.

Frenkiel, F.N., 1953, "Turbulent Diffusion: Mean Concentration Distribution in a Flow Field of Homogeneous Turbulence," *Adv. Appl. Mech.*, Vol. 3, pp. 61-107.

Gouesbet, G., Berlemont, A. & Picart, A., 1984, "Dispersion of Discrete Particles by Continuous Turbulent Motions. Extensive Discussion of the Tchen's Theory, Using a Two-Parameter Family of Lagrangian Correlation Functions," *Phys. Fluids*, Vol. 27, pp. 827-837.

Hardalupas, Y., Taylor, A.M.K.P. & Whitelaw, J.H., 1989, "Velocity and Particle-flux Characteristics of Turbulent Particle-laden Jets," *Proc. R. Soc. Lond. A*, Vol. 426, pp. 31-78.

Hardalupas, Y., Taylor, A.M.K.P. & Whitelaw, J.H., 1990, "Velocity and Size Characteristics of Liquid-fuelled Flames Stabilised by a Swirl Burner," *Proc. R. Soc. Lond. A*, Vol. 428, pp. 129-155.

Hishida, K., Hanzawa, A., Sakakibara, J., Sato, Y. & Maeda, M., 1996, "Turbulence Structure of Liquid-solid Two-phase Channel Flow (1st Report, Measurements of Two-phase Flow by DPIV)," *Trans. JSME Ser. B*, Vol. 62, pp. 18-25.

Magnus, G., 1852, *Abh. der Akad. der Wissensh.*, Berlin.

Mei, R., 1994, "Flow due to an oscillating sphere and an expression for unsteady drag on the sphere at finite Reynolds number," *J. Fluid Mech.*, Vol. 270, pp. 133-174.

Mei, R., 1996, "Velocity Fidelity of Flow Tracer Particles," *Exp. Fluids*, Vol. 22, pp. 1-13.

Saffman, P.G., 1965, "The Lift on a Small Sphere in a Slow Shear Flow," *J. Fluid Mech.*, Vol. 31, p. 624.

Sakakibara, J., Hishida, K. & Maeda, M., 1993, "Measurements of Thermally Stratified Pipe Flow Using Image-Processing Techniques," *Exp. Fluids*, Vol. 16, pp. 82-96.

Sato, Y., 1996, *Turbulence Structure and Modeling of Dispersed Two-Phase Flows.* Ph. D. Dissertation, Keio Univ..

Sato, Y. & Hishida, K., 1996, "Transport Process of Turbulence Energy in Particle-laden Turbulent Flow," *Int. J. Heat fluid Flow*, Vol. 17, pp. 202-210.

Snyder, W.H. & Lumley, J.L., 1971, "Some Measurements Particle Velocity Autocorrelation Functions in a Turbulent Flow," *J. Fluid Mech.*, Vol. 48, pp. 41-71.

Squires, K.D. & Eaton, J.K., 1990, "Particle Response and Turbulence Modification in Isotropic Turbulence," *Phys. Fluids A*, Vol. 2, pp. 1191-1203.

Squires, K.D. & Eaton, J.K., 1991, "Measurements of Particle Dispersion Obtained from Direct Numerical Simulations of Isotropic Turbulence," *J. Fluid Mech.*, Vol. 226, pp. 1-35.

Stokes, G.G., 1851, "On the Effect of Internal Friction of Fluids on the Motion of Pendulum," *Trans. Camb. Phil. Soc.*, Vol. 9, p. 8. Reprinted in *Mathematics and Physics Papers III*, Cambridge University Press (1922).

Taylor, G. I., 1921, "Diffusion by Continuous Movements," *Proc. R. Soc. Lond. A*, Vol. 20, pp. 196-211.

Yudine, M.I., 1959, "Physical Considerations on Heavy Particle Diffusion," *Adv. Geophys.*, Vol. 6, pp. 185-191.

SIMULATION AND REYNOLDS STRESS MODELING OF PARTICLE-LADEN TURBULENT SHEAR FLOWS

D.B. Taulbee, F. Mashayek, P. Givi, and C. Barré
Department of Mechanical and Aerospace Engineering
State University of New York at Buffalo
Buffalo, New York
U.S.A.

ABSTRACT

Direct numerical simulation (DNS) is conducted of a homogeneous turbulent shear flow laden with mono-size particles. The dispersed phase is simulated in the Lagrangian frame and the carrier phase is considered in the Eulerian manner. The coupling between the two phases is "two-way" which allows investigation of the effects of "the mass loading ratio" and "the particle time constant" on both phases. A new Reynolds stress model (RSM) is developed based on a "two-fluid" methodology in which both the carrier phase and the dispersed phase are considered in the Eulerian frame. Closures are suggested for the unclosed terms (including the pressure-velocity gradient) which manifest the effects of two-way coupling. The results generated by DNS are used to determine the magnitudes of some of the empirical constants appearing in RSM. The final model predictions for all the components of the fluid, the particle, and fluid-particle Reynolds stresses are assessed via detailed comparisons against DNS data.

INTRODUCTION

The objective of this work is twofold: (1) conduct DNS of particle-laden turbulent shear flows, (2) provide a new second-order Reynolds stress model for statistical predictions of two-phase flows. While the DNS results are used to investigate some physical issues pertaining to the structure of such flows, their primary use is to aid the development of RSM. The model is associated with the Reynolds stresses in both phases and the cross-correlation between the velocities of the two phases. Some of the previous contributions in such modeling are due to Shih and Lumley (1986); Zhou (1993); Zhou *et al.* (1994); Simonin *et al.* (1995). Here, DNS data are used rather extensively for both model parameterization (determination of some of the empirical constants appearing in the model), and model assessments. The RSM as proposed here is in the form of full second order transport equations.

One of the first implementation of DNS in two-phase flows is due to Riley and Patterson (1974) who investigate particle dispersion in isotropic turbulence. McLaughlin (1989) simulates particle deposition in a channel, and Squires and Eaton (1991a); Squires and Eaton (1991b) have conducted extensive DNS of stationary and decaying turbulence fields with one- and two-way coupling. Elghobashi and Truesdell (1992); Elghobashi and Truesdell (1993) report the results of similar studies. While there are no reported DNS results on particle-laden homogeneous turbulent shear flows, several large eddy simulation (LES) results of such flows are available (Yeh and Lei, 1991; Simonin *et al.*, 1995). These studies have been very useful for understanding the physics of particle-laden shear flows and for assessment of some of the recent theories pertaining to such flows (Reeks, 1993; Liljegren, 1993). However, the uncertainties associated with the subgrid scale closures as used in LES, does not allow for a through assessment of turbulence closures. This assessment is better furnished via DNS.

DIRECT NUMERICAL SIMULATION

The governing equations considered here are the continuity and Navier-Stokes equations for the continuous fluid phase, coupled with the Lagrangian equations for discrete particles. The particles are assumed to be spherical with diameter smaller than the smallest length scale of the turbulence and to obey an empirically corrected Stokesian drag relation. The particle density is much larger than the fluid density such that only the drag force is significant to the particle dynamics. In addition, the particle volume fraction is assumed to be relatively small and particle-particle interactions are neglected. The fluid velocity and pressure are denoted by $\widehat{U}_i$ and $\widehat{P}$, and the particle position and velocity are denoted as X_i and $\widehat{V}_i$, respectively, where the hat $\widehat{\ }$ indicates the instantaneous quantity. With this nomenclature, the continuity and momentum equations for the fluid, and the Lagrangian equations of motion for a single particle are given by:

$$\frac{\partial \widehat{U}_j}{\partial x_j} = 0 \tag{1}$$

$$\frac{\partial \widehat{U}_i}{\partial t} + \frac{\partial}{\partial x_j}(\widehat{U}_i \widehat{U}_j) = -\frac{1}{\rho_f}\frac{\partial \widehat{P}}{\partial x_i} + \frac{1}{\nu}\frac{\partial^2 \widehat{U}_i}{\partial x_j \partial x_j}$$

$$-\frac{1}{\rho_f \Delta V}\sum^{n_p}\{\frac{f m_p}{\tau_p}(\widehat{U}_i^* - \widehat{V}_i)\}, \qquad (2)$$

$$\frac{dX_i}{dt} = \widehat{V}_i, \quad \frac{d\widehat{V}_i}{dt} = \frac{f}{\tau_p}(\widehat{U}_i^* - \widehat{V}_i), \qquad (3)$$

where x_i and t are the spatial and temporal coordinates, respectively, and ρ_f and ν are the fluid density and kinematic viscosity, respectively. The particle time constant for Stokesian drag of a spherical particle is $\tau_p = \rho_p d_p^2/18\mu$, where ρ_p and d_p are the particle density and diameter, respectively, and μ is the fluid viscosity. The function $f = 1 + 0.15Re_p^{0.687}$ in (2) and (3) represents an empirical correction to Stokesian drag for large particle Reynolds numbers ($Re_p = \rho_f^* d_p|\widehat{U}_i^* - \widehat{V}_i|/\mu$) and is valid for $Re_p \leq 1000$. The superscript $(*)$ indicates the values of the fluid variables at the particle location. The last term in (2) represents the effects of the particle drag which is calculated by volume averaging the contributions from all of the individual particles residing within the cell volume ($\Delta V = (\Delta x)^3$, where Δx is the grid spacing) centered around each grid point ($m_p = \pi\rho_p d_p^3/6$ is the mass of a single particle and n_p is the number of particles within the cell volume).

The carrier phase is simulated by a Fourier pseudo-spectral method, and the particles are tracked individually in a Lagrangian manner. For a given mean shear (S) we have considered five cases to investigate the effects of one- and two-way coupling at various values for the particle time constant (τ_p) and the mass loading ratio (Φ_m), using as many as 6.67×10^5 particles on 96^3 collocation points. To ensure the accuracy of the single phase flow simulation, successful comparisons have been established with the simulation results of Rogers *et al.* (1986), and the experimental data of Tavoularis and Corrsin (1981).

The modification of turbulence by the particles is illustrated in Fig. 1 by considering the temporal variations of the fluid turbulent kinetic energy ($k = \frac{1}{2} < u_i u_i >$, where $<>$ indicates the Eulerian ensemble average over the number of grid points.) and its dissipation rate (ϵ). Both variables are normalized with their corresponding initial values denoted by subscript (0). For all of the cases, initially the fluid turbulent kinetic energy decays due to the absence of the off-diagonal (shear) Reynolds stress term. This term, along with the mean velocity gradient, are responsible for the production of energy in the streamwise direction. After the shear Reynolds stress component is produced by the action of the mean velocity gradient, the kinetic energy starts to increase ($St > 4$). The primary effect of the particles on the fluid is to decrease the turbulent kinetic energy with respect to its single phase value. This is also the case for the dissipation rate as shown in Fig. 1b. The decrease of the kinetic energy and its rate of dissipation in the presence of particles, suggests the existence of an extra dissipation which originates from the drag force.

The equation governing the particle turbulent kinetic energy ($k_p = \frac{1}{2} << v_i v_i >>$, with $<<>>$ denoting the Lagrangian ensemble average) is

$$\frac{dk_p}{dt} = - << v_1 v_2 >> S$$

$$+\frac{<< f >>}{\tau_p}(<< u_i v_i >> - 2k_p). \qquad (4)$$

In deriving (4), the triple correlations between f and velocity components have been neglected after analyzing the

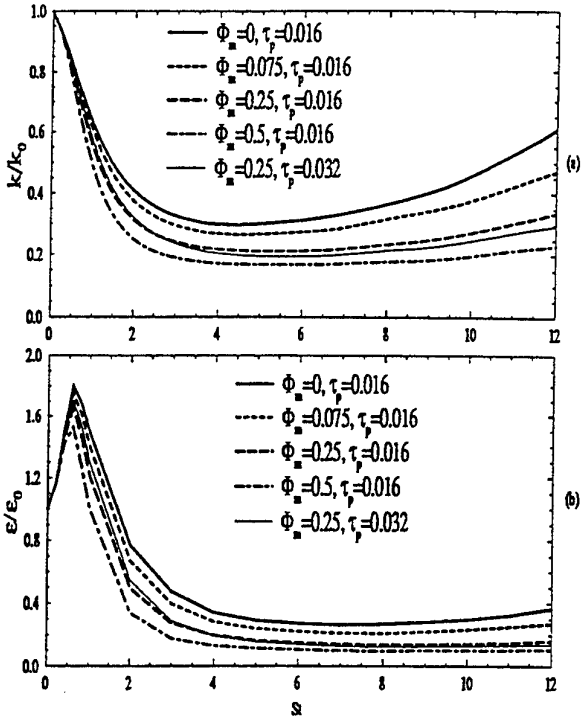


Figure 1: Temporal variations of the fluid turbulent kinetic energy and its rate of dissipation. Both quantities are normalized with their initial values.

DNS data. The first term on the RHS of (4) represents a production by the mean velocity gradient while the second term is due to drag. The temporal evolution of these terms in Fig. 2 indicates that for all of the cases the term due to drag behaves as a dissipation and tends to balance the production. Obviously, during the initial times ($St < 4$), the dissipation overcomes the production and the particle turbulent kinetic energy experiences a rapid decay, similar to those for the fluid. At longer times, Fig. 2 shows that the increase of the mass loading ratio results in the decrease of the magnitude of both the production and dissipation. However, the decrease of the production with the mass loading ratio occurs with a faster rate than that of the dissipation. As a result, the growth rate of the particle turbulent kinetic energy is decreased with the increase of the mass loading ratio. A comparison of cases with different particle time constant values (at the same mass loading ratio) reveals that the initial evolutions of the production and the dissipation terms are more sensitive to the variations of the particle time constant, than are to the variations of the mass loading ratio. During the initial times, the increase of the particle time constant decreases the decay rate of the particle turbulence energy while at long times it results in the decrease of the growth rate of the kinetic energy.

The overall effects of the interaction between the carrier and dispersed phases are summarized in table 1 which shows results at $St = 12$. It is seen that the turbulence non-dimensional time scale Sk/ϵ increases with mass loading indicating the turbulence becomes more sluggish. As observed from the components of the anisotropic tensors, $a_{ij}^f =< u_i u_j > /k - 2\delta_{ij}/3$ and $a_{ij}^p =<< v_i v_j >>$

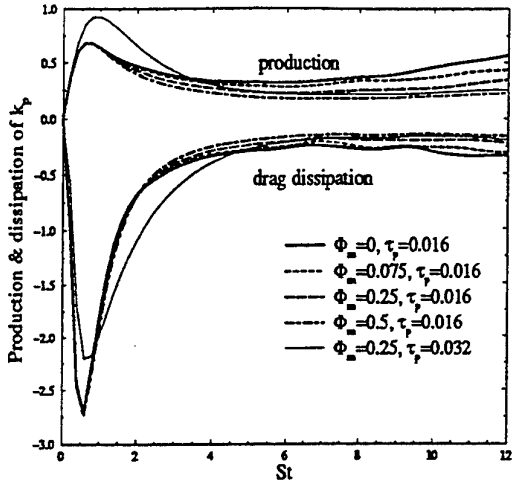


Figure 2: Temporal variations of the production and drag dissipation terms appearing in the particle kinetic energy equation.

Table 1: DNS Results at $St = 12$.

	$\tau_p = 0.016$			$\tau_p = 0.032$
Φ_m	0	0.25	0.5	0.25
Sk/ϵ	4.82	5.88	6.31	5.95
a^f_{11}	0.361	0.533	0.725	0.515
a^f_{22}	-0.291	-0.382	-0.453	-0.418
a^f_{12}	-0.324	-0.325	-0.309	-0.262
a^p_{11}	0.630	0.774	0.890	0.888
a^p_{22}	-0.417	-0.468	-0.509	-0.530
a^p_{12}	-0.414	-0.394	-0.359	-0.352
$\frac{<<v_1^2>>}{<u_1^2>}$	1.037	1.181	1.147	1.197
$\frac{<<v_2^2>>}{<u_2^2>}$	0.546	0.688	0.757	0.500
k_p/k	0.821	0.984	1.025	0.910

$/k_p - 2\delta_{ij}/3$, the normal components of both the fluid and the particle velocity correlations become more anisotropic with increasing mass loading whereas the shear components decrease slightly. Also, the particle normal Reynolds stress in the flow direction is larger than that of the carrier fluid. This is in agreement with the theoretical results of Reeks (1993); Liljegren (1993) and the LES results of Simonin *et al.* (1995), and is due to the lack of small scale dissipation in the dispersed phase as opposed to the fluid phase. Furthermore for large mass loading the kinetic energy of the particles becomes larger than that of the fluid.

REYNOLDS STRESS CLOSURES

In this section a second-order moment Reynolds stress model is proposed for particle-laden flows that includes the effects of two-way coupling between the two phases. The predictions of the model are then compared with the DNS generated data. The model is based on the two-fluid treatment of two-phase flows. Similarly to DNS, we consider the transport of an incompressible fluid (the carrier gas) laden with mono-size particles (the dispersed phase). The governing equations for both phases are expressed in the Eulerian frame by performing volume averaging. For a dilute dispersed phase, typically the volume fraction $\widehat{\Phi} \sim \mathcal{O}(10^{-4})$; the transport equation for the carrier phase simplifies to (2) except the particle drag term becomes $\lambda\Phi(\widehat{U}_i - \widehat{V}_i)/\tau_p$, $\lambda = \rho_p/\rho_f$, due to the volume averaging process. We assume Stokes drag, and the effect of the carrier phase pressure on the particles is negligible. The volume averaged particle equation in the Eulerian form can be written as

$$\frac{\partial \widehat{V}_i}{\partial t} + \widehat{V}_j \frac{\partial \widehat{V}_i}{\partial x_j} = \frac{1}{\tau_p}(\widehat{U}_i - \widehat{V}_i). \tag{5}$$

Following the standard Reynolds decomposition procedure, the flow variables are decomposed into the "ensemble-mean" and fluctuations about the mean: $\widehat{U}_i = U_i + u_i$, $\widehat{V}_i = V_i + v_i$, $\widehat{P} = P + p$ and $\widehat{\Phi} = \Phi + \phi$; and mean flow equations can be obtained by averaging (2) and (5). For the homogeneous shear flow considered here, the fluid velocity is specified with $V_i = U_i$ and with zero void fraction fluxes $\overline{u_i\phi}$ and $\overline{v_i\phi}$. The transport differential equations for other second-order moments are obtained from (2) and (5) by standard methods:

$$\frac{\partial \overline{u_iu_j}}{\partial t} = -\overline{u_iu_l}\frac{\partial U_j}{\partial x_l} - \overline{u_ju_l}\frac{\partial U_i}{\partial x_l} + \psi_{ij} - \epsilon_{ij}$$

$$-\frac{\Phi_m}{\tau_p}[\overline{u_i(u_j - v_j)} + \overline{u_j(u_i - v_i)}], \tag{6}$$

for the carrier phase Reynolds stress,

$$\frac{\partial \overline{v_iv_j}}{\partial t} = -\overline{v_iv_l}\frac{\partial V_j}{\partial x_l} - \overline{v_jv_l}\frac{\partial V_i}{\partial x_l} - \frac{1}{\tau_p}(2\overline{v_iv_j} - \overline{u_iv_j}, -\overline{u_jv_i}), \tag{7}$$

for the dispersed phase Reynolds stress, and

$$\frac{\partial \overline{u_iv_j}}{\partial t} = -\overline{u_iv_l}\frac{\partial V_j}{\partial x_l} - \overline{u_lv_j}\frac{\partial U_i}{\partial x_l} + \chi_{ij}$$

$$+\frac{1}{\tau_p}(\overline{u_iu_j} - \overline{u_iv_j}) - \frac{\Phi_m}{\tau_p}(\overline{u_iv_j} - \overline{v_iv_j}), \tag{8}$$

for fluid-particle velocity covariance. In (6), $\psi_{ij} = \overline{p/\rho_f(\partial u_i/\partial x_j + \partial u_j/\partial x_i)}$ is the pressure-strain correlation, and $\epsilon_{ij} = \overline{2\nu(\partial u_i/\partial x_l)(\partial u_j/\partial x_l)}$ indicates the dissipation rate. In (8), $\chi_{ij} = \overline{p/\rho_f(\partial v_j/\partial x_i)}$ is the pressure-dispersed phase velocity gradient correlation. In these equations, the third-order correlations involving both the velocity and the void fraction fluctuations are neglected.

The pressure terms, ψ_{ij} and χ_{ij} are modeled similarly to the widely utilized closure of Launder-Reece-Rodi (LRR) (Launder *et al.*, 1975). Utilizing Fourier transform methods the Poisson's equation for the pressure can be solved resulting in expressions for ψ_{ij} and χ_{ij} in terms of integrals of two-point velocity correlations. The result for ψ_{ij} contains extra terms, involving fluid-particle velocity correlations, arising from the effects of the particles on the fluid. Following Launder *et al.* (1975) the pressure-strain term ψ_{ij} is formulated as a linear polynomial of the velocity correlations. The coefficients of this polynomial are obtained

by applying the constraints of symmetry, incompressibility, and normalization. The final result for homogeneous flows is

$$\Pi_{ij} = -C_{f1}\epsilon a^f_{ij} + \epsilon\left[\frac{4}{5}S^f_{ij} - 6C_{f2}\left(a^f_{ik}S^f_{kj} + a^f_{jk}S^f_{ki} - \frac{2}{3}a^f_{mn}S^f_{nm}\delta_{ij}\right) - \frac{4+14C_{f2}}{3}(a^f_{ik}\omega^f_{kj} + a^f_{jk}\omega^f_{ki})\right] + C_{f3}\frac{\lambda\Phi}{\tau_p}[2ka^f_{ij} - \overline{u_m v_m}(b^{fp}_{ij} + b^{fp}_{ji})], \quad (9)$$

where C_{f1}, C_{f2} and C_{f3} are empirical constants to be determined, $a^f_{ij} = \overline{u_i u_j}/k - 2\delta_{ij}/3$ and $b^{fp}_{ij} = \overline{u_i v_j}/\overline{u_m v_m} - \delta_{ij}/3$ are the normalized form of the fluid-fluid and the fluid-particle Reynolds stresses, respectively; and $S^f_{ij} = k/(2\epsilon)(\partial U_i/\partial x_j + \partial U_j/\partial x_i)$ and $\omega^f_{ij} = k/(2\epsilon)(\partial U_i/\partial x_j - \partial U_j/\partial x_i)$ are the strain rate and the rotation tensors of the carrier phase, respectively. In (9) the first two terms are the LLR closure for the slow and fast pressure-strain effects, respectively, and the last term depicts the particle effects. Following a similar procedure, a model is derived for the pressure-dispersed phase velocity gradient correlation:

$$\chi_{ij} = -C_{fp1}\frac{\overline{u_i v_j}}{\tau} + C_{fp2}\overline{u_l v_j}\frac{\partial U_i}{\partial x_l} + C_{fp3}\frac{\lambda}{\tau_p}\Phi(\overline{u_i v_j} - \overline{v_i v_j}), \quad (10)$$

where $\tau = k/\epsilon$ is the carrier phase turbulent time scale, and C_{fp1}, C_{fp2}, and C_{fp3} are empirical constants.

Equations (9) and (10) indicate that the proposed closures involve six empirical constants which must be determined. The terms involving C_{f1} or C_{f2} in Eq. (9) are the equivalent of those in LRR. Thus, the magnitudes of these constants are set to be the same ($C_{f1} = 1.75$, $C_{f2} = -0.159$) to ensure that in the limit of one-way coupling Eq. (9) reduces to the equivalent LRR model for single phase flows. The magnitudes of the other four constants are determined by balancing the transport equations for all of the components of the fluid Reynolds stress tensor (Eq. 6) and the fluid-particle covariance tensor (Eq. 8). Note that all of the remaining terms in these equations as well as the terms in models of pressure-strain correlation and pressure-particle velocity gradient correlation are computable directly from the Lagrangian simulations. By considering all of the components and all of the cases a large data bank is furnished to determine and to optimize the values of the remaining four constants. A sample case is shown in Fig. 3 for the energy budget of $<< u_1 v_1 >>$ for $\Phi_m = 0.25$ and $\tau_p = 0.032$s. In this figure, the production, the dissipation rate, and the contribution from drag are calculated from DNS. The values of the pressure-dispersed phase velocity gradient are calculated from the proposed models. The term LHS indicates the derivative of the energy component and is obtained from DNS. This value is compared with $\sum$RHS which is the sum of the production, dissipation rate, and drag contribution (from DNS), and the pressure term (from models). It is observed that the general agreement between the LHS and the $\sum$RHS is good, especially for $St > 2$ when the turbulence is well-developed. Similar comparisons have also been performed for other components for all of the cases. The final (optimized) values of the empirical constants are given in table 2.

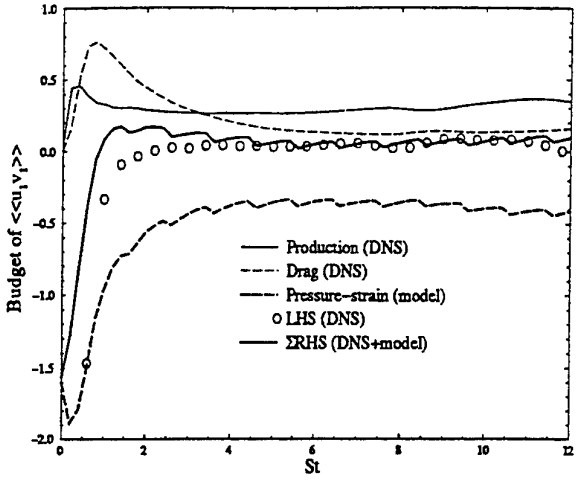


Figure 3: Budget of $<< u_1 v_1 >>$ from the case with $\Phi_m = 0.25$ and $\tau_p = 0.032s$.

Table 2: Empirical constants.

Constant	Magnitude	Basis for choice
C_{f1}	1.75	Launder *et al.* (1975)
C_{f2}	-0.159	Launder *et al.* (1975)
C_{f3}	0.5	Budget of $\overline{u_i u_j}$
C_{fp1}	2.5	Budget of $\overline{u_i v_j}$
C_{fp2}	0.5	Budget of $\overline{u_i v_j}$
C_{fp3}	0.2	Budget of $\overline{u_i v_j}$
C_{ϵ_1}	1.45	Standard k-ϵ
C_{ϵ_2}	1.85	Standard k-ϵ
C_{ϵ_3}	0.8	Overall performance of RSM

The final form of the transport equations for all of the components of the Reynolds stress tensors constitute a set of Reynolds stress models for particle-laden homogeneous shear flows. To close, an equation must be provided for the dissipation rate of the fluid turbulent kinetic energy. The modeled dissipation rate equation can be rationalized from the exact equation for the dissipation rate as obtained from (2). For the present case this equation includes an additional term, $2\lambda\Phi/\tau_p\left[\overline{\nu(\partial u_i/\partial x_j)(\partial u_i/\partial x_j)} - \overline{\nu(\partial u_i/\partial x_j)(\partial v_i/\partial x_j)}\right]$, due to coupling with the dispersed phase. In this expression the first term is the dissipation ϵ and the second term is modeled as the relaxation of the trace of fluid-particle velocity correlation tensor, i.e, $C_{\epsilon 3}\overline{u_m v_m}/\tau$. The final form of the modeled transport equation for the dissipation rate for homogeneous flow is expressed as:

$$\frac{\partial \epsilon}{\partial t} = -C_{\epsilon 1}\frac{\epsilon}{k}\overline{u_1 u_2}\frac{\partial U_1}{\partial x_2} - C_{\epsilon 2}\frac{\epsilon^2}{k} - \frac{\epsilon}{k}\frac{\lambda\Phi}{\tau_p}(2k - C_{\epsilon 3}\overline{u_m v_m}), \quad (11)$$

where $C_{\epsilon 1}$, $C_{\epsilon 2}$, and $C_{\epsilon 3}$ are constants. The values for $C_{\epsilon 1}$ and $C_{\epsilon 2}$ are taken from their single-phase equivalents; $C_{\epsilon 1} = 1.45$ and $C_{\epsilon 2} = 1.85$. The value of constant $C_{\epsilon 3} = 0.8$ is found by comparison with DNS data.

The data generated by DNS for the fluid, particle, and fluid-particle Reynolds stresses are used to assess the

Reynolds stress model. In this assessment the stress and the dissipation rate values at $St = 2$ are taken from DNS as initial values. This time is chosen as the initial time in order to allow the flow and the particles to reach a dynamic equilibrium. All of the cases have been considered; however, the results of only two cases are presented here. Similar trends were obtained for cases with different mass-loading ratios and particle relaxation times.

The numerical procedure involves simultaneous integration of 14 coupled equations (13 for Reynolds stresses and 1 for the dissipation rate). The time derivative term is discretized by a backward finite difference scheme. The decay term is evaluated by averaging between the two successive time levels in order to expedite convergence. By performing two iterations at each time level the resulting technique is similar to the Crank-Nicholson method.

First we consider the case with one-way coupling ($\Phi_m = 0$) for $\tau_p = 0.016$s. The model predictions (lines) are compared with DNS results (symbols) in Fig. 4 for all of the components. The overall agreement is very good; the particle Reynolds stress components (Fig. 4b) show the best overall agreements. This is expected as the transport equations for the particle Reynolds stresses involve no modeling. Small deviations observed in Fig. 4b is due to $\overline{u_i v_j}$ terms. It is noted that the shear components which are of primary importance are predicted very closely to DNS. For this one-way coupling case, Fig. 4a essentially evaluates the performance of the LRR model. Some deviations are observed in the streamwise ($\overline{u_1 u_1}$) component but other components are in reasonably good agreements.

The effects of two-way coupling at $\Phi_m = 0.25$ and $\tau_p = 0.016$s are portrayed in Fig. 5. Again the agreement between the model predictions and DNS results is very promising. Similar to the case with one-way coupling, the largest deviations are observed in the streamwise direction, especially for the fluid. Finally, Fig. 6 shows that the dissipation rate is also calculated very closely to DNS results, for the two cases.

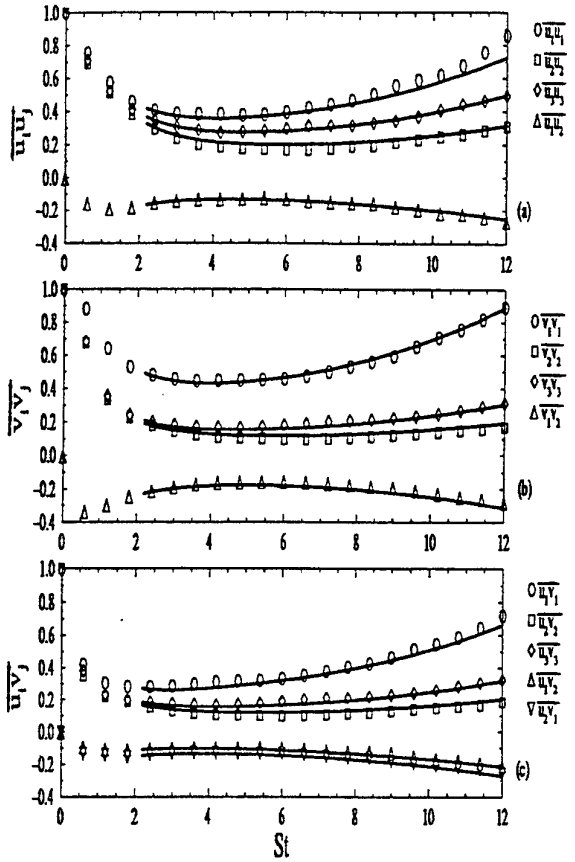


Figure 4: Comparisons of the Reynolds stress model predictions (symbols) with DNS data (lines) for components of the fluid, particle and fluid-particle Reynolds stress tensors in the case with one-way coupling at $\tau_p = 0.016s$.

CONCLUDING REMARKS

This work deals with direct numerical simulation of particle-laden homogeneous shear flow, and proposes a new Reynolds stress model for statistical prediction of two-phase flows. The DNS results are used to assess the performance of the RSM. Reasonable agreement between model and DNS results are observed, especially for the shear (off-diagonal) components which are of primary importance. A very important feature of model is that the effects of the two-way coupling are included in every aspect of the formulation. Work is underway in implementation of the proposed RSM in homogeneous plane-strain flows and their validations via DNS.

REFERENCES

Elghobashi, S. and Truesdell, G. C. (1992). Direct simulation of particle dispersion in a decaying isotropic turbulence. *J. Fluid Mech.* **242**, 655–700.

Elghobashi, S. and Truesdell, G. C. (1993). On the two-way interaction between homogeneous turbulence and dispersed solid particles. I: Turbulence modification. *Phys. Fluids* **5**, 1790–1801.

Launder, B. E., Reece, G. J., and Rodi, W. (1975). Progress in the development of a Reynolds-stress turbulence closure. *J. Fluid Mech.* **68**, 537–566.

Liljegren, L. M. (1993). The effect of a mean fluid velocity gradient on the streamwise velocity variance of a particle suspended in a turbulent flow. *Int. J. Multiphase Flow* **19**, 471–484.

McLaughlin, J. B. (1989). Aerosol particle deposition in numerically simulated channel flow. *Phys. Fluids* **1**, 1211–1224.

Reeks, W.M. (1993). On the constitutive relations for dispersed particles in nonuniform flows. I: Dispersion in a simple shear flow. *Phys. Fluids* **5**, 750–761.

Riley, J. J. and Patterson, G. S. (1974). Diffusion experiments with numerically integrated isotropic turbulence. *Phys. Fluids* **17**, 292–297.

Rogers, M. M., Moin, P., and Reynolds, W. C. (1986). The structure and modeling of the hydrodynamic and passive scalar fields in homogeneous turbulent shear flow. Department of Mechanical Engineering TF-25, Stanford University, Stanford, CA.

Shih, T.-H. and Lumley, J. L. (1986). Second order modeling of near wall turbulence. *Phys. Fluids* **29**, 971–975.

Simonin, O., Deutsch, E., and Boivin, M. (1995). Large

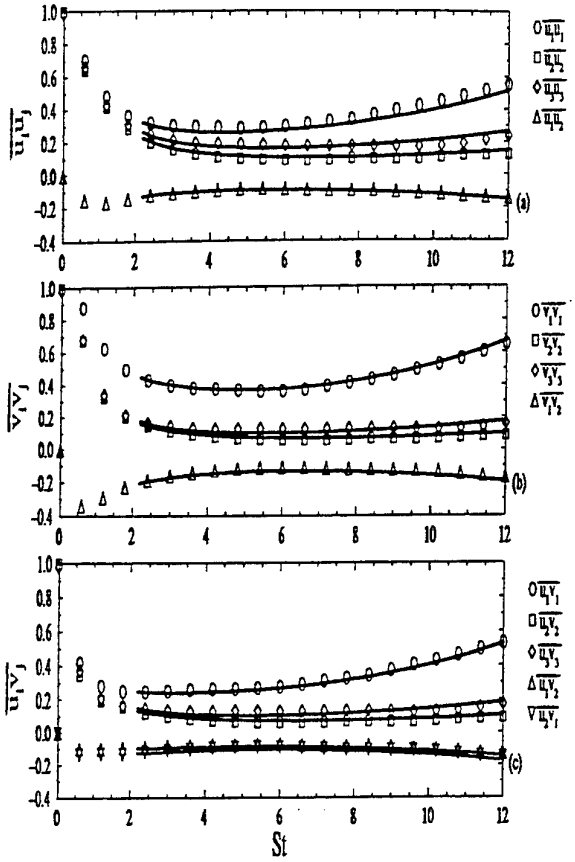


Figure 5: Comparisons of the Reynolds stress model predictions (symbols) with DNS data (lines) for components of the fluid, particle and fluid-particle Reynolds stress tensors for $\Phi_m = 0.25$ and $\tau_p = 0.016s$.

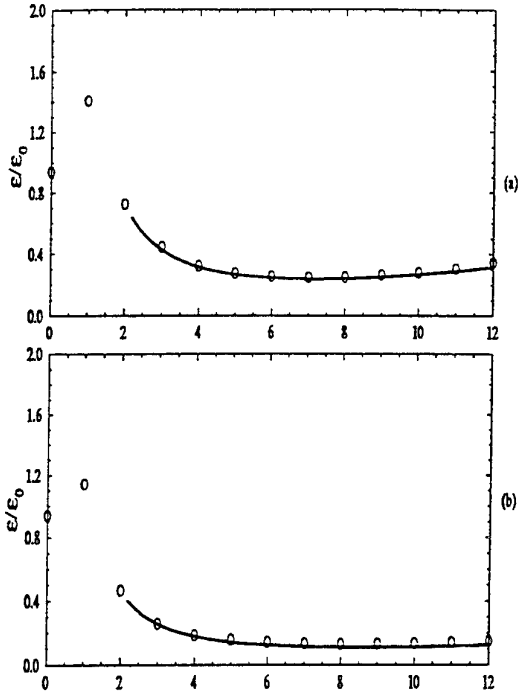


Figure 6: Comparisons of the Reynolds stress model predictions (symbols) with DNS data (lines) for the dissipation rate of the fluid turbulent kinetic energy. (a) $\Phi_m = 0$, $\tau_p = 0.016s$, (b) $\Phi_m = 0.25$, $\tau_p = 0.016s$.

eddy simulation and second-moment closure model of particle fluctuating motion in two-phase turbulent shear flows. In Durst, F., Kasagi, N., Launder, B.E., Schmidt, F.W., and Whitelaw, J.H., editors, *Turbulent Shear Flows 9*, pages 85–115. Springer-Verlag.

Squires, K. D. and Eaton, J. K. (1991a). Measurements of particle dispersion obtained from direct numerical simulations of isotropic turbulence. *J. Fluid Mech.* **226**, 1–35.

Squires, K. D. and Eaton, J. K. (1991b). Preferential concentration of particles by turbulence. *Phys. Fluids* **3**, 1169–1178.

Tavoularis, S. and Corrsin, S. (1981). Experiments in nearly homogenous turbulent shear flow with a uniform mean temperature gradient. Part 1. *J. Fluid Mech.* **104**, 311–347.

Yeh, F. and Lei, U. (1991). On the motion of small particles in a homogeneous turbulent shear flow. *Phys. Fluids* **3**, 2758–2776.

Zhou, L. X., Liao, C. M., and Chen, T. (1994). A unified second-order-moment two-phase turbulent model for simulating gas-particle flows. In Crowe, C. T., Johnson, R., Prosperetti, A., Sommerfeld, M., and Y., Tsuji, editors, *Numerical Methods in Multiphase Flows*, pages 307–313. ASME, FED-Vol. 185, New York, NY.

Zhou, L.X. (1993). *Theory and Numerical Modeling of Turbulent Gas-Particle Flows and Combustion.* CRC Press, Boca Raton, FL.

NUMERICAL STUDY OF PARTICLE MOTION IN A TURBULENT MIXING LAYER USING THE DISCRETE VORTEX METHOD

E. Ory, R. J. Perkins
Laboratoire de Mécanique des Fluides et d'Acoustique
Ecole Centrale de Lyon
36, avenue Guy de Collongue
B.P. 163, 69 131 Ecully Cédex, France

ABSTRACT

Particle dispersion in a two-dimensional mixing layer has been investigated numerically. The time-evolving velocity field was computed using the Discrete Vortex Method (DVM) and the trajectories of heavy particles were then calculated. Profiles of mean velocities agree well with the experimental measurements of Ishima *et al.* (1992). The agreement is less satisfactory for the Reynolds stress, and worst for the fluctuating velocities. The agreement for particle dispersion is more variable. This approach enables us to investigate the interaction between heavy particles and large scale coherent structures.

INTRODUCTION

Many important industrial and environmental processes involve the transport and dispersion of heavy particles by a turbulent flow. Typical examples include flow reactors and combustion chambers. Often it is necessary to predict the dispersion of the heavy particles, and many studies (e.g. Chein & Chung 1987, Chung & Troutt 1988, Ishima *et al.* 1992, Hishida *et al.* 1993 and Marcu & Meiburg 1996a,b) have suggested that the particle dispersion depends strongly on the ability of the particles to follow the motion of large-scale eddies.

Since the publication by Brown & Roshko (1974) of their well-known photographs of a turbulent mixing layer, there has been a great deal of interest in the large-scale, eddy-like structures which occur in certain classes of turbulent shear flow. These photographs confirmed that large-scale coherent structures are indeed intrinsic features of turbulent mixing layers at high Reynolds numbers. Furthermore, sequential merging of vortices provides the primary mechanism for the spreading of the layer in the downstream direction. It is generally considered that these coherent structures dominate the transport of mass, momentum and heat in these flows.

Several of the investigations of particle dispersion in flows dominated by large scale coherent structures have suggested that the particle dispersion can exceed that of fluid elements when the particle response time is of the same order as the time scale of the large coherent structures. Potentially, this effect is relevant to many engineering applications and processes, in which particles or droplets are injected into a turbulent flow, and the objective is to maximize the subsequent dispersion of the particles or droplets. Such results demonstrate the importance of the role played by coherent structures in determining particle dispersion, and suggest that in such flows the characteristic time and velocity scales of the large scale structures (relative to the particle response time and the fall velocity) are the important scaling parameters. This is in contrast to particle dispersion in some other types of turbulent flow (e.g. homogeneous turbulence) where the Kolmogorov scales might provide the most suitable scaling parameters (e.g. Wang & Maxey 1993).

Mixing layers and jets provide useful generic models for this type of problem. For example, Chung & Troutt (1988) developed a DVM of an axisymmetric jet (using ring vortices) and they used this to investigate particle dispersion. However, the enforced axisymmetry in the simulation may have produced large scale structures that were 'too coherent' compared with a real circular jet and this may have exaggerated the importance of the structures.

In order to investigate this, we have developed a DVM of a plane mixing layer. This paper describes (very briefly) the basis of that model, and the use of the model to simulate the experiments of Ishima *et al.* (1992) and Hishida *et al.* (1993). A sketch of their experimental arrangement is shown in **Figure 1**. This comparison between model and experiments (which was not possible for the model developed by Chung & Troutt 1988) is an important preliminary step, before using the model to investigate the interactions between particles and coherent structures in detail.

THE MIXING LAYER

Two parallel, semi-infinite streams of velocity U_1 and U_2 ($U_2 > U_1$) merge at $x = 0$ to create a steady flow $U(x, y)$ which is weakly diverging but self-similar. The velocity difference is given by $\Delta U = U_2 - U_1$, and the average velocity is $\overline{U} = (U_1 + U_2)/2$. The flow can be characterized by the dimensionless velocity ratio $R = \Delta U / 2\overline{U}$ and the Reynolds number $\mathcal{R}_e = \overline{U}l/\nu$ where l is a characteristic length scale and ν is the kinematic viscosity. Goertler (1942) used an eddy viscosity model to develop

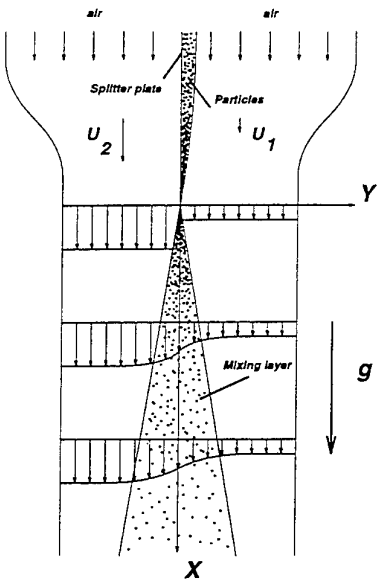


Figure 1: Experimental flow configuration

a similarity solution for the mean velocities :

$$\frac{u - U_1}{U_2 - U_1} = \frac{1}{2}(1 + \mathrm{erf}\,\xi) \tag{1}$$

where $\xi = \sigma y / x$ and σ is a constant which depends on $\left(\overline{U} / \Delta U\right)^{1/2}$. In some cases the self-similar coordinate ξ is replaced by $\eta = (y - y_{0.5}) / \theta$ where $y_{0.5}$ is the value of y at which $u = \overline{U}$, and θ is the momentum thickness of the mixing layer.
The experiments of Ishima *et al.* (1992) and Hishida *et al.* (1993) were performed with: $U_1 = 4\,\mathrm{m.s^{-1}}$, $U_2 = 13\,\mathrm{m.s^{-1}}$, $R = 1.89$ and $\mathcal{R}_e \sim 30\,000$.

THE DISCRETE VORTEX METHOD

In this study we restrict our attention to two-dimensional viscous flow of a fluid with kinematic viscosity ν. Then the equation for the transport and diffusion of vorticity ω can be written:

$$\frac{D\omega}{Dt} = \nu \nabla^2 \omega \tag{2}$$

This leads to a Lagrangian interpretation of the Euler equations, and is the basis for the DVM. This technique is described in detail in a number of reviews and articles (e.g. Chorin 1973, Acton 1976, Ashurst 1979, Leonard 1980), so we only provide a brief description here.
The continuous distribution of vorticity is discretised into a finite number, N_V, of point vortices, each with circulation $\Delta\Gamma_j$, and located at $\mathbf{x}_j$. The complete velocity field is given by the sum of an irrotational background velocity field $\mathbf{U}_B(\mathbf{x})$ and the velocity fields generated by all the point vortices. Each vortex moves at the local velocity, so for a vortex located at $\mathbf{x}_i$, the velocity is given by:

$$\mathbf{u}(\mathbf{x}_i) = \mathbf{U}_B(\mathbf{x}_i) + \sum_{\substack{j=1 \\ j \neq i}}^{N_V} \frac{\Delta\Gamma_j}{2\pi} \frac{(\mathbf{x}_i - \mathbf{x}_j) \wedge \widehat{\mathbf{k}}}{|\mathbf{x}_i - \mathbf{x}_j|^2} \tag{3}$$

where $\widehat{\mathbf{k}}$ is the unit vector out of the plane. This means that the model requires $O(N_v^2)$ calculations per time step. Several approaches have been proposed to reduce the computational time (e.g. Peyret & Taylor 1983, Spalart & Leonard 1981, Clarke & Tutty 1994) but these generally introduce additional numerical diffusion of vorticity. To avoid this, we have computed all vortex interactions directly.
In the inviscid model, the discretised vorticity is modelled by irrotational point vortices, but these introduce problems of numerical stability when vortices approach each other too closely. Therefore, in most practical calculations, the discretised vorticity is modelled by "vortex blobs" - vortices with rotational cores. The two most common forms for this are the Rankine vortex and the Lamb vortex; these simulations have been carried out using Lamb vortices, for which the vorticity distribution is given by:

$$\omega_j(\mathbf{x}) = \frac{\Gamma_j}{\pi\sigma_\omega^2} \exp\left\{-\frac{|\mathbf{x}_j - \mathbf{x}|^2}{\sigma_\omega^2}\right\} \tag{4}$$

It is generally found that, even with the smoothing effect of a rotational core, the two-dimensional vortex model overestimates the fluctuating velocities when compared with experimental measurements. This is because the model neglects the diffusion of vorticity caused by viscosity, and the three-dimensional stretching by the velocity field. For this reason, most implementations of the vortex method include a model for the diffusion of vorticity. Several approaches have been proposed, (see Clarke & Tutty 1994 for a recent survey), but we have adopted a solution in which the core radius grows with time:

$$\frac{d\sigma_\omega^2}{dt} = 4\nu \;\Rightarrow\; \sigma_\omega^2(t) = \sigma_\omega^2(0) + 4\nu t \tag{5}$$

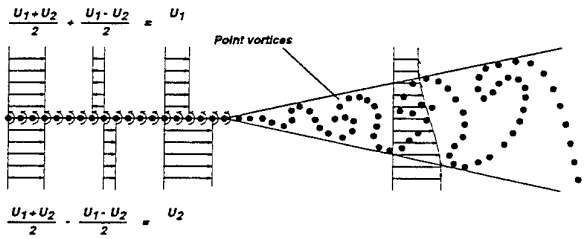


Figure 2: Model of a mixing layer by the DVM

DISCRETE VORTEX MODEL OF A MIXING LAYER

We have used the DVM to construct a two-dimensional model of a mixing layer (see **Figure 2**). The irrotational background velocity field is represented by a uniform flow of velocity $\overline{U}$ together with a semi-infinite bound vortex, with a circulation per unit length $\dot{\Gamma} = U_1 - U_2$. Vortices are shed from the splitter plate at intervals of Δt, with circulation $\Delta\Gamma_i = \dot{\Gamma}\overline{U}\Delta t$ and are advected at the local fluid velocity. The influence of vortices which have left the simulation domain at the downstream boundary ($x = L$) is included through the use of a second semi-infinite bound vortex. Some studies (e.g. Basu *et al.* 1992) have suggested that the simulations can be improved by using several inclined bound vortex sheets at the downstream end; preliminary tests showed that this did not have a significant effect on our calculations.
These simulations were performed for the same conditions as those in the experiments of Ishima *et al.* (1992), with $L = 0.45$ m and $\Delta t = 10^{-4}$ s.
Figure 3 shows the location of the vortices in the domain every 0.001 s (namely 10 time steps). Although the vortices are released at regular intervals they soon begin to

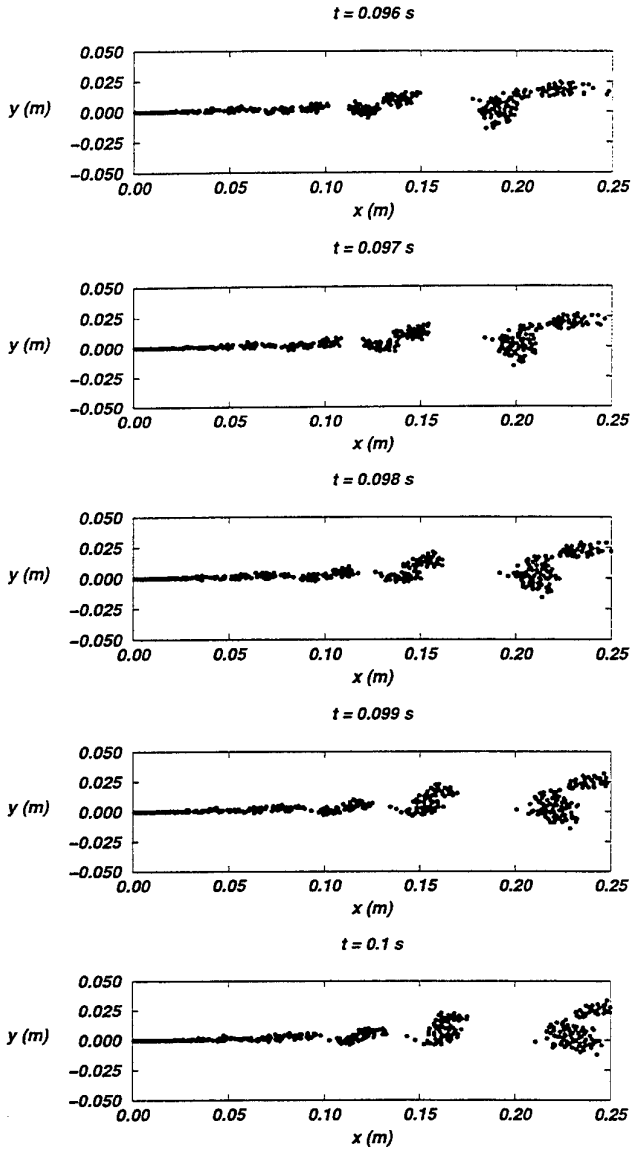


Figure 3: Location of the vortices at five consecutive instants

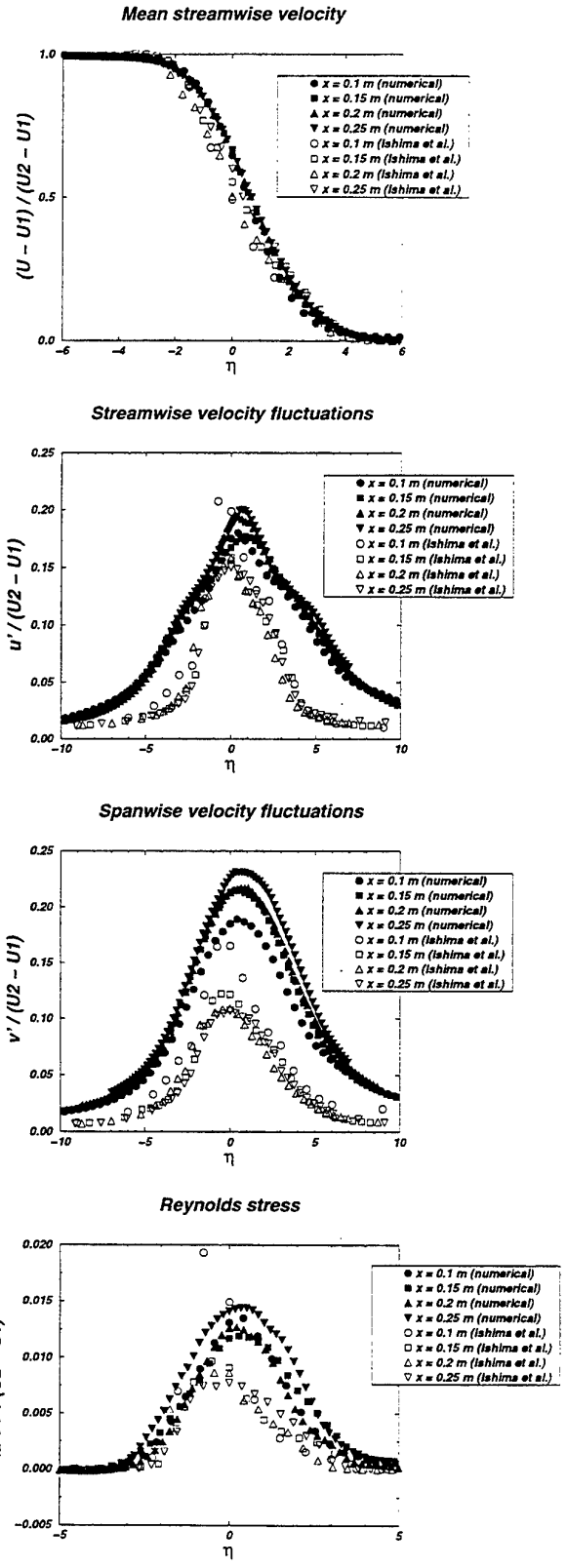


Figure 4: Comparison between numerical and experimental statistical quantities

cluster together, to form larger coherent structures, and the size of such structures continues to increase with distance from the splitter plate, through pairing events. Such a process can be seen at $x \sim 0.15$ m. The structure of the mixing layer resembles, qualitatively, that revealed in the experiments of Brown & Roshko (1974). Profiles of mean and fluctuating velocities and Reynolds stress are shown in **Figure 4**, together with the experimental measurements of Ishima *et al.* (1992).

The computed mean velocities agree well with the measured profiles, and show that the mixing layer is self-similar, at least for $x > 0.1$ m. The computed profiles of u' also appear to be self-similar; the maximum value of u' occurs on the centerline, and agrees well with the measured value. The computed profiles reproduce the same asymmetry with respect to $\eta = 0$ that can be observed in the measured profiles, but away from the centerline, the DVM consistently over-predicts the values of u', compared with experimental results.

The profiles of v' show less evidence of self-similarity, and the centerline values are strongly over-estimated compared with the experimental results. The computed results suggest that v' increases with x, whereas the experimental results show a decrease with x. Once again, both the computed and the measured profiles show a similar asymmetry

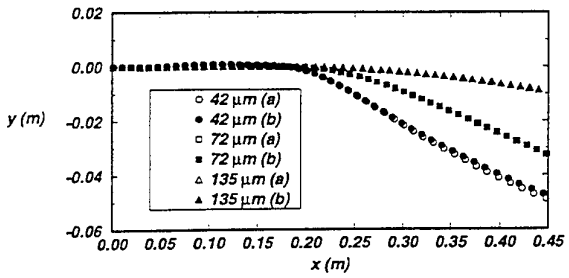


Figure 5: Particle trajectories of three kinds of particles where (a) Buoyancy + Drag, (b) Buoyancy + Drag + Acceleration + Lift

with respect to $\eta = 0$.
The profiles of the Reynolds stress also show less evidence of self-similarity, and the centerline values are overestimated compared with the experimental results. The experimental results show a decrease with x, which is not reproduced in the computed results. On the other hand, the asymmetry in the computed results is similar to that of the experimental results. The over-prediction of the fluctuating velocities (particularly v') and Reynolds stress is a well-known problem with the DVM, and is caused principally by the failure to model the 3-D process of vortex stretching, which enhances the diffusion of vorticity. Consequently, the structures which are formed are too 'coherent', and the fluctuating velocities and Reynolds stress are over-estimated. One possible solution to this problem is to increase the effective viscosity in the model, to enhance the diffusion of vorticity.

PARTICLE DISPERSION

A particle in motion in a turbulent fluid experiences a variety of forces and the complete equation of motion is complicated. However, the forces on a particle are not necessarily all of the same magnitude. For a heavy particle in air, it is often assumed that the lift and pressure gradient forces are small compared with the gravitational and drag forces. For example, the ratio of lift to drag force is given by $F_L / F_D \sim (\phi / 6)(\kappa / \nu)^{1/2}$ where $\kappa (= du / dy)$ is the local velocity gradient. For typical values of the mean shear in these experiments and simulations, $F_L / F_D \sim 10^{-3}$. In order to test the assumption that the lift and added mass forces can be neglected, we have computed some sample particle trajectories using all forces, and compared them with trajectories computed in an identical velocity field, using just drag and buoyancy forces. Typical results are shown in **Figure 5**, which shows that, even for the smallest particles, the contribution from the added mass and lift forces is negligible. As a final check, we have also computed the relative magnitudes of the forces experienced by the particles. These calculations show that, close to the origin of the mixing layer, the added mass force can be of the same order as the buoyancy force (but much less than the drag force), but this decays very rapidly. However the computed lift force is negligible, at all times, and for all the particle sizes.
The equation of motion for the particle can therefore be written :

$$\frac{d\mathbf{u}_p}{dt} = \mathbf{g} + \frac{3C_D}{4\phi\gamma}|\mathbf{u} - \mathbf{u}_p|(\mathbf{u} - \mathbf{u}_p) \qquad (6)$$

where $\mathbf{u}_p$ is the particle velocity, $\mathbf{u}$ is the fluid velocity at the particle location, ϕ is the particle diameter, $\mathbf{g}$ is the gravitational vector, $\gamma (= \rho_p / \rho_f)$ is the relative density of the particle and C_D is the drag coefficient. The value of C_D depends on the particle Reynolds number $\mathcal{R}e_p (= (|\mathbf{u} - \mathbf{u}_p|\phi) / \nu)$ and must be computed from empirical relationships (e.g. Morsi & Alexander 1972).
We have computed particle dispersion for the three types of particle used in the experiments of Ishima *et al.* (1992): $\rho = 2590\,\mathrm{kg.m^{-3}}$, $\phi_1 = 42\,\mu$m, $\phi_2 = 72\,\mu$m, $\phi_3 = 135\,\mu$m, with response times 0.014 s, 0.041 s, and 0.144 s respectively. Once the flow has reached a statistically stationary state, particles are released from the end of the splitter plate, with initial velocities $u_p(0) = 0.9\,\mathrm{m.s^{-1}}$ and $v_p(0) = 0$. Their trajectories are calculated by integrating eq (6), using the fluid velocities obtained from the DVM. At the moment we assume that the particle concentrations are so low that the particles do not modify the flow.

Figure 6 shows the particle and vortex locations at one instant, 0.1 s after the release of the first particle. As expected, the unsteady structure of the mixing layer has most influence on the smallest particles, and almost no influence on the largest particles. Two distinct types of behaviour can be observed for the smallest particles. In the region $x < 0.2$ m, the main effect of the instantaneous structure

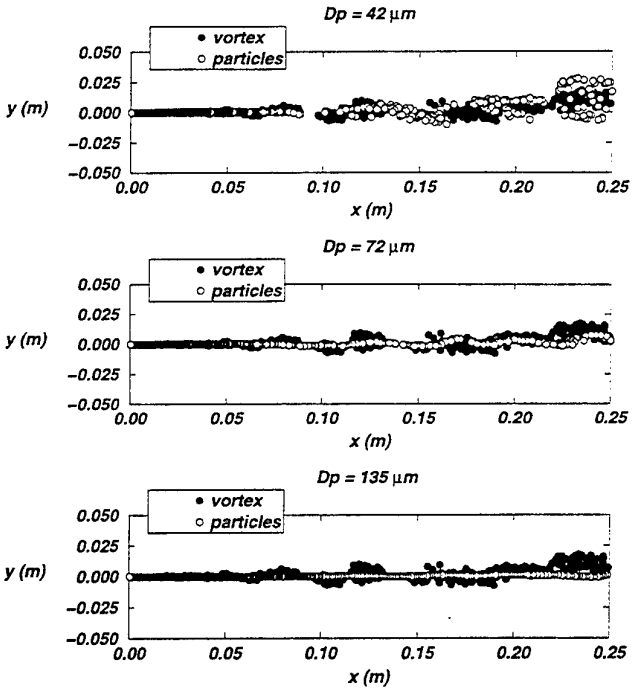


Figure 6: Location of vortices and particles 0.1 s after the first release

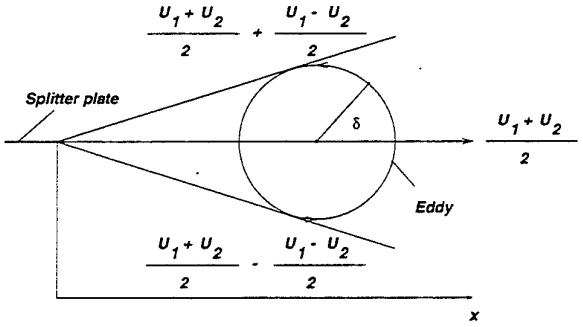


Figure 7: Scheme of an eddy in a mixing layer

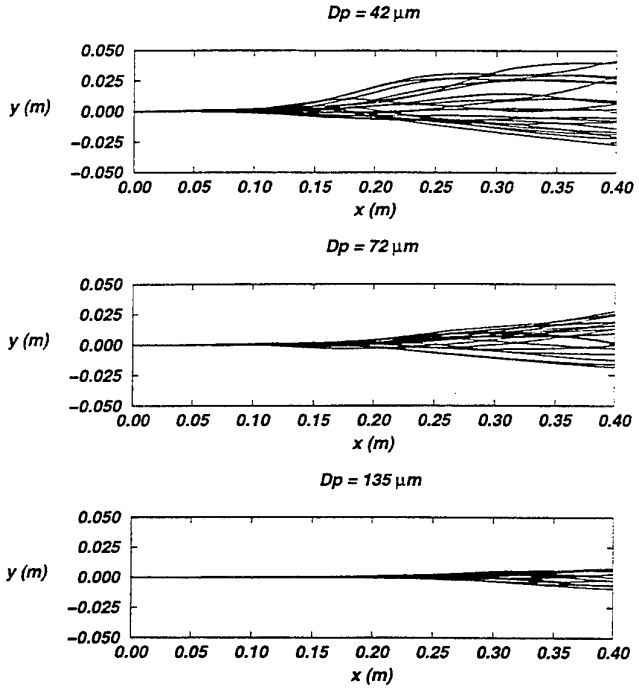


Figure 8: Particles trajectories in a plane turbulent mixing layer

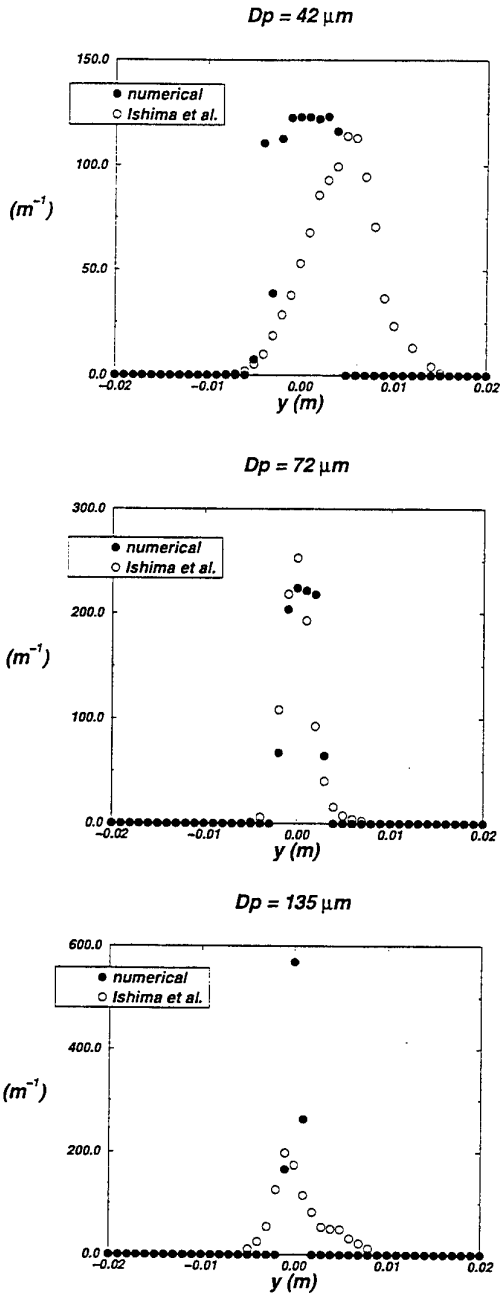


Figure 9: Profiles of particle number density at x = 0.1 m

seems to be to cause a mean deflection of all the particles. However, for $x > 0.2$ m, the particles appear to be clustered around the outside of the large coherent structure. That is, the particle response to the unsteady structure in the mixing layer has changed. This effect can be explained by considering the particle response times, and the typical time scale in the mixing layer which depends on the distance from the origin. A very simple model, based on the turnover time of an eddy in the mixing layer (**Figure 7**) suggests $t_e = (2 / \Delta U) \cdot 2\pi\delta$ ($\sim 0.1\,x$ for this case). Thus we see that the characteristic time scales for the region $0 < x < 0.25$ m are too short for the instantaneous structure to have any real impact on the motion of the two largest classes of particles, but the smallest particles should begin to show some influence of the coherent structures for $x > 0.15$ m. This is confirmed by the results shown in **Figure 6**. Other models and calculations (e.g. Wang & Maxey 1993) have suggested that the particle dispersion should scale on the ratio of the particle response time to the Kolmogorov time scale, rather than the time scale of the large scale structures, as used here. In these experiments and calculations the Kolmogorov time scale τ_k is of the order of $\left(\nu l / u^3\right)^{1/2}$ where l and u are the characteristic length and velocity scales of the large scale eddies in the mixing layer. If we take $l \sim \theta$ (the momentum thickness) and $u \sim \Delta u / 2$ then $\tau_k \sim 5.10^{-5} x^{1/2}$, so within our simulation $\tau_p / \tau_k \geq 500$ at all positions and for all types of particles. This should be contrasted with the conditions studied by Wang & Maxey (1993) when $\tau_p / \tau_k \sim 1$. One important reason for this is the difference in Reynolds numbers. In these simulations the Reynolds number based on the Taylor microscale ($\mathcal{R}_{e_\lambda}$) was of the order of 350, using the preceding estimate for τ_k in the calculation of Wang & Maxey (1993) $21.2 \leq \mathcal{R}_{e_\lambda} \leq 61.5$. This explains why it is the large scale coherent structures, and not the fine scale turbulence, which dominate particle dispersion in these types of flow, and why a scaling based on the ratio τ_p / τ_k is not approximate here.

Some sample particle trajectories are shown in **Figure 8**. These show that the turbulent structure of the mixing layer has no appreciable influence on the largest particles, but the other two show some effects. As expected, the lightest particles respond first, but even they do not show any sign of entrainment into the coherent structures, or rapid ejection from the structures, as has been suggested by other researchers (e.g. Chung & Troutt 1988, Chein & Chung 1987).

Profiles of particle number density at $x = 0.1$ m are shown in **Figure 9**, together with the experimental results. The agreement is very good for the intermediate particles ($\phi_2 = 72\mu$m) but less satisfactory for the other two classes; in both cases the DVM under-estimates the lateral dispersion of the particles, and it fails to reproduce the asymmetry in the experimental profiles. For the 135μm particles,

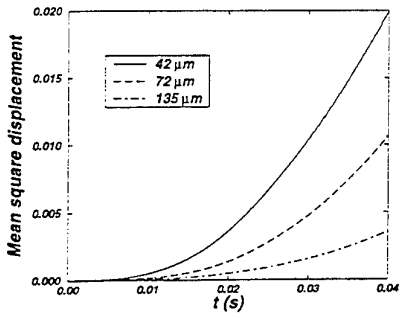


Figure 10: Particle dispersion

this may be caused by the initial conditions. In the DVM, the particles are all released with identical initial velocities, and because the particle inertia is so high, the initial dispersion is very low. However, in the experiments, there must have been some variability in the release conditions. The reasons for the under-estimation of the dispersion of the smallest particles ($\phi_1 = 42\mu m$) are not yet clear. In order to investigate the variation of particle dispersion with distance from the origin of the mixing layer we have also computed the mean square displacement as a function of travel time as shown in **Figure 10**.

LIMITATIONS AND FUTURE DEVELOPMENTS

A numerical study has been performed of particle dispersion in a two-dimensional mixing layer in order to investigate the factors which govern particle motion in turbulent flows.

The profiles of mean velocities agree reasonably well with the measurements of Hishida *et al.* (1993), but the DVM overestimates the fluctuating velocities. This is probably because the model does not include three-dimensional effects such as vortex stretching, which would enhance the diffusion of vorticity, and reduce the coherence of the structures. We are currently investigating ways of correcting this.

When we compare the numerical results obtained with the two-phase flow with the same experiment, we can observe that we obtain comparable conclusions about the dispersion of different sizes of particles but it is necessary now to develop the model to take into account the influence of particles on the flow.

REFERENCES

Acton, W.T. 1976. The modelling of large eddies in a two-dimensional shear layer. *J. Fluid Mech.*, **76**, 561–592.

Ashurst, W.T. 1979. Numerical simulation of turbulent mixing layers via vortex dynamics. *Turbulent Shear Flows,I (ed. F. Durst et al.), Springer*, 402–413.

Basu, A.J., Prabhu A. & Narasimha R. 1992. Vortex sheet simulation of a plane "canonical" mixing layer. *Computers Fluids*, **21**(1), 1–30.

Brown, G.L. & Roshko, A. 1974. On density effects and large structure in turbulent mixing layers. *J. Fluid Mech.*, **64**, 775–816.

Chein, R. & Chung, J.N. 1987. Effects of vortex pairing on particle dispersion in turbulent shear flows. *Int. J. Multiphase Flow*, **13**, 785–802.

Chorin, A.J. 1973. Numerical study of slightly viscous flow. *J. Fluid Mech.*, **57**, 785–796.

Chung, J.N. & Troutt, T.R. 1988. Simulations of particle dispersion in an axisymmetric jet. *J. Fluid Mech.*, **186**, 199–222.

Goertler, H. 1942. Berechnung von aufgaben der freien turbulenz auf grund eines neuen naherungsansatzes. *Z.A.M.M.*, **22**, 244–254.

Hishida, K., Ando, A. & Maeda, M. 1993. Experiments on particle dispersion in a turbulent mixing layer. *Int. J. Multiphase Flow*, **18**(2), 181–194.

Ishima, T., Hishida, K. & Maeda, M. 1992. Effect of particle residence time on particle dispersion in a plane mixing layer. *Trans ASME, J. of Fluid Eng.*, **115**, 751–759.

Leonard, A. 1980. Vortex methods for flow simulations. *J. Comput. Phys.*, **37**, 289–355.

Marcu, B. & Meiburg, E. 1996a. The effect of streamwise braid vortices on the particle in a plane mixing layer. I. Equilibrium points and their stability. *Phys. Fluids*, **8**(3), 715–733.

Marcu, B. & Meiburg, E. 1996b. The effect of streamwise braid vortices on the particle in a plane mixing layer. II. Nonlinear particle dynamics. *Phys. Fluids*, **8**(3), 193–208.

Morsi, S.A. & Alexander, A.J. 1972. An investigation of particle trajectories in two-phase flow systems. *J. Fluid Mech.*, **55**(2), 193–208.

Peyret, R. & Taylor, T.D. 1983. *Computational Methods for Fluid Flow.* Springer-Verlag.

Spalart, P.R. & Leonard, A. 1981. Computation of separated flows by a vortex tracking algorithm. *In: Proceedings of AIAA 14th Fluid and Plasma Conference.*

Wang, L.-P. & Maxey, M.R. 1993. Settling velocity and concentration distribution of heavy particles in homogeneous isotropic turbulence. *J. Fluid Mech.*, **256**, 27–68.

SESSION 25 - JETS II

INVESTIGATION OF MIXING IN A COAXIAL JET CONFIGURATION

Maria Vittoria Salvetti, Giovanni Lombardi, Alessandro Talamelli
Department of Aerospace Engineering
University of Pisa
Via Diotisalvi 2
56126, PISA
ITALY

ABSTRACT

The mixing process in an axisymmetric coaxial jet configuration is analyzed by means of numerical simulation. The evolution of mixing in the initial stage of the flow development, when the dynamics of vorticity is dominated by the large start-up vortex, is compared to the results of previous studies on the mixing process in the formation of an axisymmetric vortex. The effects of Reynolds and Schmidt number are also studied. The influence of the dynamics of vortical structures on the mixing processes have also been analyzed in the full regime, after the initial transient, for different Reynolds numbers. Comparisons between the mixedness parameters computed numerically and those obtained from experimental flow visualizations are shown and discussed.

INTRODUCTION

The flow originated by coaxial jets is of great interest in the design of new industrial burners. In particular, the characterization and control of mixing between the streams is basic to obtain efficient combustion and low pollution.

It has been suggested in the literature that the evolution of the mixing between the two jets is mostly controlled by the dynamics of the vortical structures, forming from the instability of the shear layers. In coaxial jets, the simultaneous presence of two mixing layers leads to non-trivial interactions between these instabilities. Although the flow originated by coaxial jets has been studied extensively, the amount of information presently available on the mixing mechanisms is far from exhaustive.

The aim of the present study is to investigate the mixing mechanisms in a coaxial jet configuration and, in particular, how instantaneous and average mixing are related to the dynamics of the flow. The present analysis is carried out by means of direct numerical simulation of a coaxial jet configuration, for which experimental flow visualizations are also available. Flow visualizations have been obtained by seeding the external jet of a configuration having external to internal radius and velocity ratios R_i/R_e=0.517 and U_i/U_e=0.67. The Reynolds number based on the axis velocity and internal radius is Re=6340. Details on the experimental set-up can be found in (Talamelli *et al.*, 1996).

Although limited to low Reynolds numbers, numerical simulation is useful because it provides simultaneously the time evolution of scalar concentrations and of the vorticity field, so that the effects of the dynamics of vortical structures on the mixing processes can be studied. Furthermore, in the numerical simulation, the simultaneous "seeding" of both the internal and external jets is possible and the analysis of the effect of different flow parameters, such as Reynolds number or Schmidt number, is much easier than in experiments.

NUMERICAL METHOD AND BOUNDARY CONDITIONS

The axisymmetric Navier-Stokes equations in cylindrical coordinates and primitive variables (omitted here for sake of brevity) have been solved. The unknowns are $q_z=U$, $q_r=rV$ and the pressure p, where U and V are respectively the axial and the radial velocity components. The equations have been non-dimensionalized using the radius of the internal jet, R_i, as a length scale, and the centerline axial velocity, U_i, as a velocity scale. The reference Reynolds number is then $Re=R_i\,U_i/\nu$, where ν is the kinematics viscosity.

The spatial discretization of the system of equations is performed on a staggered grid by centered finite differences, second-order accurate.

The advancement in time is carried out by a fractional-step method, in which an intermediate non-solenoidal velocity field is first provisionally calculated; it is then projected into a solenoidal one by a scalar quantity Φ, which is related to the pressure. The momentum equations are advanced in time by a third-order Runge-Kutta scheme, in which non

linear terms are computed explicitly and linear terms implicitly. An approximate factorization technique is used to avoid the inversion of large sparse matrices.

The method is second-order accurate in time and consists of three sub-steps; at each sub-step the scalar Φ is calculated by solving a Poisson equation through trigonometric expansions applied in the axial direction. Details of the numerical method can be found in (Verzicco and Orlandi, 1996) and (Salvetti *et al.*, 1996).

In previous simulations of another coaxial jet configuration (Salvetti *et al.*, 1996), the employed numerical method had given results in good qualitative agreement with experimental flow visualizations in the near-field, where the assumption of axisymmetry is justified. Therefore, the numerical study is focused on the analysis of mixing in the initial flow region, by the solution of the transport equations for two passive scalars:

$$\frac{\partial \xi_i}{\partial t}+\frac{1}{r}\frac{\partial \xi_i q_r}{\partial r}+\frac{\partial \xi_i q_z}{\partial z}=\frac{1}{\mathrm{Re}Sc}\left[\frac{1}{r}\frac{\partial}{\partial r}\left(r\frac{\partial \xi_i}{\partial r}\right)+\frac{\partial^2 \xi_i}{\partial z^2}\right] \quad (1)$$

where ξ_i is the concentration of the passive scalar i, $Sc=\nu/D$ the Schmidt number, assumed to be the same for both scalars, and D the scalar diffusivity.

The computational grid is non-uniform in the radial direction, with points clustered in high-shear regions, and uniform in the z direction. In the present simulations 385 points have been used in the axial direction and 305 in the radial one. The axial and radial dimensions of the computational domain are, respectively, $16R_i$ and 10 R_i.

At the external radial boundary free-slip conditions are assumed. Since we are interested in simulating free jets, it has been verified that the radial dimension of the domain in the present simulations is large enough to avoid spurious effects of free-slip conditions on the dynamics of the jet.

At the inlet of the computational domain (corresponding to the jet outlet), the axial velocity is set to zero at $t=0$, and evolves to a prescribed profile $Q_z(r)$ in a time τ. The evolution law and the value of τ are the same as in (Salvetti *et al.*, 1996) and permit the reproduction of the transient generated by the opening of a valve, or the time required for a motor to reach its final speed in an experiment. The basic stationary velocity profile $Q_z(r)$ is obtained through fifth-order polynomial functions (Salvetti *et al.*, 1996).

In the present simulations the ratio between the maximum velocity of the internal and the external jet is $U_i/U_e=0.67$ and the ratio between the internal and external radius is $R_i/R_e = 0.517$, as in the experiments in (Talamelli *et al.*, 1996). The inlet concentration of the first scalar is 1 in the internal jet and 0 elsewhere, while the other has a concentration at the inlet equal to the unity in the external jet and equal to 0 elsewhere.

In the simulations analyzed in the present paper, after the end of the transient, a random perturbation of zero mean value is superposed on the velocity $Q_z(r)$. Details on its definition may be found in (Salvetti *et al.*, 1996). This perturbation allows the fluctuations of the inlet velocity profile due to the turbulence in the nozzle to be accounted for, even if in an approximate manner, and was shown in (Salvetti *et al.*, 1996) to provide a flow field whose general features are in better agreement with experiments. As regards the radial velocity component, q_r is set equal to zero at the computational inlet.

At the outflow, radiation boundary conditions are applied to each variable q_i and ξ_i:

$$\frac{\partial q_i}{\partial t}+C\frac{\partial q_i}{\partial z}=0 \quad (2)$$

$$\frac{\partial \xi_i}{\partial t}+C\frac{\partial \xi_i}{\partial z}=0 \quad (3)$$

where C is assumed to be constant, equal to $0.6U_i$, and represents the advection speed of the large-scale structures. This assumption leads to simple boundary conditions that have the advantage of satisfying automatically the global conservation of mass, and appear to be appropriate, as shown in (Salvetti *et al.*, 1996).

RESULTS

Initial development of the flow

The analysis of mixing at the initial stage of the development of the flow, after the impulsive start-up, is important for combustion or pulsating jet applications.

At this stage, the vorticity dynamics is dominated by the large start-up vortex, as discussed in (Salvetti *et al.*, 1996), and the situation is "similar" to that of an isolated axisymmetric vortex. Thus, the results obtained in the present simulations can be compared to those of the experimental and numerical studies of mixing in the formation of an axisymmetric vortex ring, carried out respectively in (Cetegen and Mohamad, 1993) and in (Verzicco and Orlandi, 1995). Nevertheless, in the present coaxial jet configuration, the vortical field after the start-up is characterized by the roll-up of both the positive and negative vorticity layers in the external jet. This can be seen, for instance, from the iso-contours of vorticity, obtained at $t=10$ in a simulation at $Re=500$ and $Sc=1$, shown in Fig. 1. Indeed, the large vortex formed from the instability of the external shear-layer is surrounded by a negative vorticity layer, that concentrates in a second smaller vortical structure.

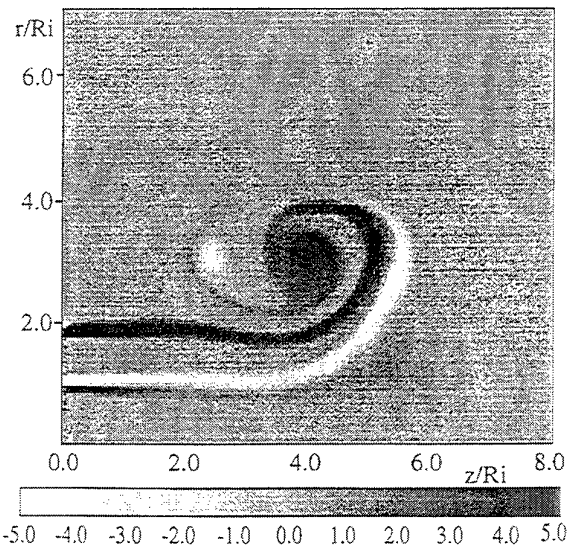


FIG. 1: ISO-CONTOURS OF VORTICITY AT $t = 10$, FOR Re=500.

In (Cetegen and Mohamad, 1993) and in (Verzicco and Orlandi, 1995), the mixedness f has been used as a quantitative measure of the mixing. For non reacting flows the global mixedness f can be defined as:

$$f = \frac{4}{A}\int_A \xi_i(1-\xi_i)dA \qquad (4)$$

where A is the measure of the domain over which the integration is performed and ξ_i is the concentration of one of the inert scalars seeded in the internal and external jets. The mixedness per unit axial and radial length, $F_z(z)$ and $F_r(r)$, have also been calculated, defined as:

$$F_z(z) = \frac{8}{L_r^2}\int_0^{L_r} \xi_i(1-\xi_i)rdr \qquad (5)$$

$$F_r(r) = \frac{4}{L_z}\int_0^{L_z} \xi_i(1-\xi_i)dz \qquad (6)$$

where L_z and L_r are radial and axial dimensions of the domain over which the integration is performed: L_z=16R_i and L_r=6R_i. Thus, in eq. (4), A=$L_z L_r$.

It has been shown in (Cetegen and Mohamad, 1993) and in (Verzicco and Orlandi, 1995) that the mixing is directly proportional to the vortex circulation. Fig. 2 shows the circulation per unit axial length and $F_z(z)$, computed using the concentration of the two scalars, for the same simulation and at the same time instant as in Fig. 1. In agreement with the results presented in (Cetegen and Mohamad, 1993) and (Verzicco and Orlandi, 1995), in the initial stage of the present coaxial jet flow most of the mixing occurs in the large start-up vortex, which corresponds to the maximum of circulation. Nevertheless, significant values of mixedness are found also in correspondence to negative peaks of circulation, due to the negative vorticity layer structures described above (see Fig. 1). As expected, since the start-up vortex forms from the instability of the external jet, most of the mixing is between the scalar injected in the external jet and the surrounding fluid. Indeed, the values of $F_z(z)$ obtained from the concentration of the scalar in the internal jet, are generally much lower than those obtained from the concentration of the other scalar, except than in the negative vorticity layer surrounding the start-up vortex.

As in (Cetegen and Mohamad, 1993) and (Verzicco and Orlandi, 1995), the mixing increases with time. Nevertheless, even in the initial stage of the flow development, the time evolution of global mixedness has a slope directly proportional to global circulation only in a limited time interval. This can be seen from the time evolution of the ratio between f, computed using the concentration of the scalar seeded in the external jet, and global circulation, for the same simulation as previously, shown in Fig. 3. The linear behavior is observed starting from t≅5, when the formation of the start-up vortex is completed, until t≅12, when another vortex forms from the roll-up of the external shear layer.

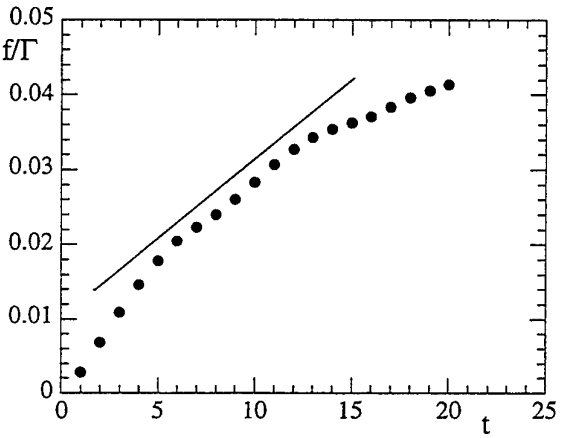


FIG. 3: RATIO BETWEEN GLOBAL MIXEDNESS f AND GLOBAL CIRCULATION Γ AT Re=500 AND Sc=1.

The effects of Re and Sc on the mixing, in the initial stage of development of the flow, have also been studied. In Fig. 4, the time evolution of global mixedness, obtained for Sc=1 and Re=500, 1000, 2000, using the concentration of the scalar seeded in the external jet, are shown. The time evolution of f obtained at Re=500 and Sc=4 is also reported.

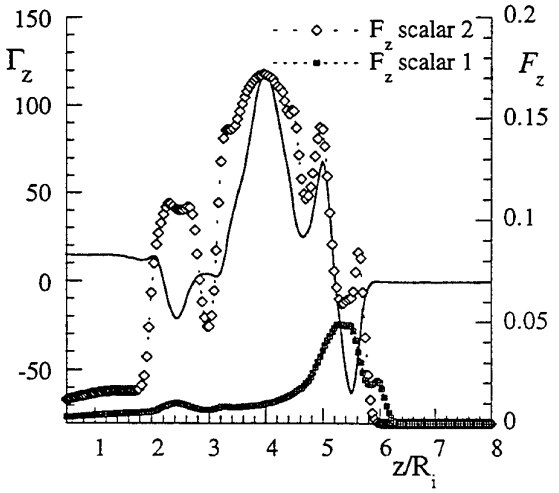


FIG. 2: PER UNIT AXIAL LENGTH CIRCULATION Γ_z AND MIXEDNESS F_z AT t=10, FOR Re=500 AND Sc=1.

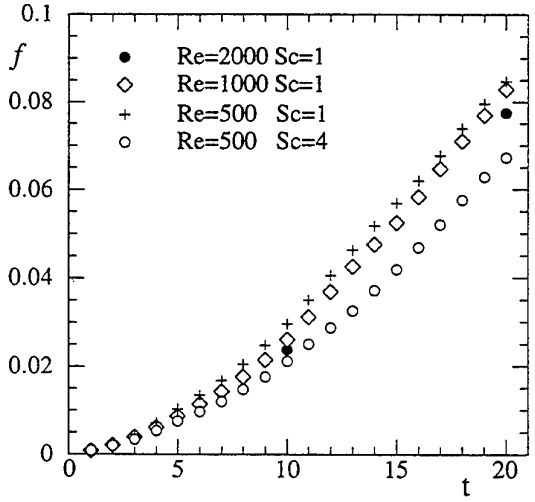
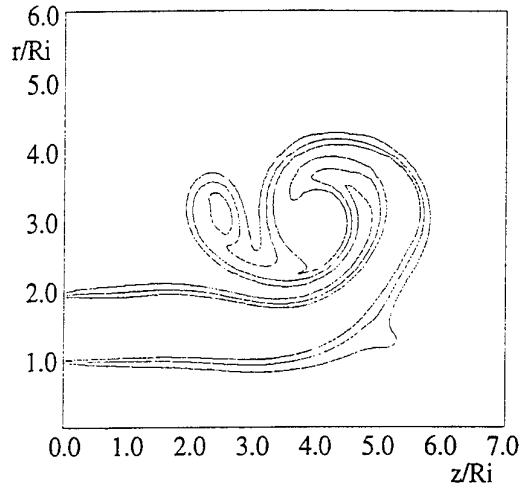
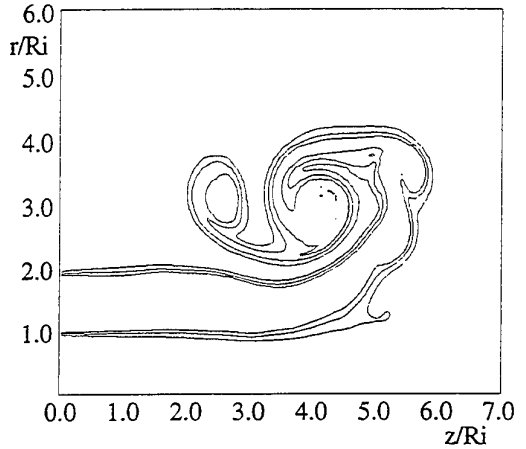


FIG. 4: GLOBAL MIXEDNESS f OF THE SCALAR SEEDED IN THE EXTERNAL JET.



a) Re=500



b) Re=1000

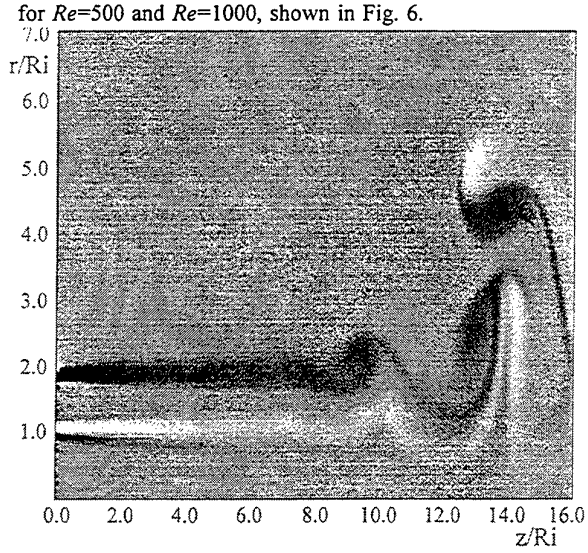
FIG. 5: ISO-LINES OF CONCENTRATION OF THE SCALAR SEEDED IN THE EXTERNAL JET, AT t =10. LINES RANGE FROM 0.1 WITH AN INCREMENT OF 0.3.

At this stage of the flow development, the Reynolds number only slightly affects the global mixedness. This result is not surprising because most of the mixing occurs in the large start-up vortex and the evolution in time of this vortex is independent of the Reynolds number, as shown also in (Salvetti *et al.*, 1996). Nevertheless, a slight decrease of global mixedness is observed as the Reynolds number increases. This is the result of two opposite effects. The first one can be observed, for instance, from the isolines of concentration of the scalar seeded in the external jet, obtained at t=10, for Re=500 and Re=1000, reported in Fig. 5. Though the shape of the isolines, and then the contact area, is very similar in the two different cases, it is more lobed for the higher Re, and this would tend to increase the mixing. On the other hand, the diffusion of the scalar is clearly higher for lower Reynolds numbers and, hence, the region in which mixing is significant narrows as the Re increases; as a result, the global mixedness decreases.

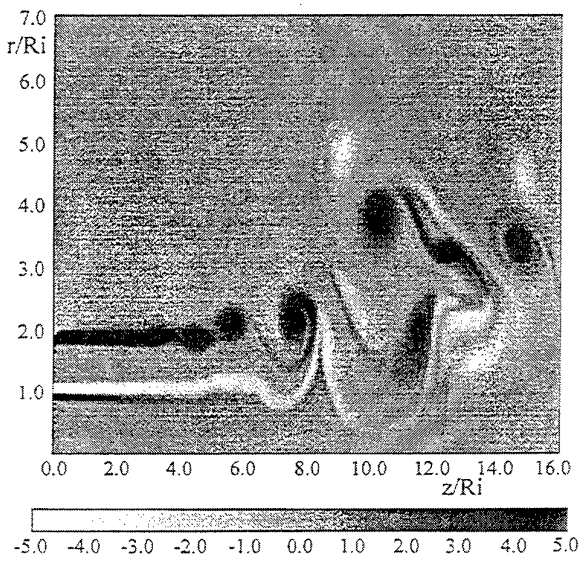
As concerns the dependence on Schmidt number, the latter effect is even more predominant, yielding a more remarkable decrease of f.

Analysis of mixing after the initial transient and comparison with the experiments

The dynamics of vorticity, after the initial transient, is clearly highly dependent on the Reynolds number, as can be seen for instance from two typical vorticity fields obtained at t=170, for Re=500 and Re=1000, shown in Fig. 6.



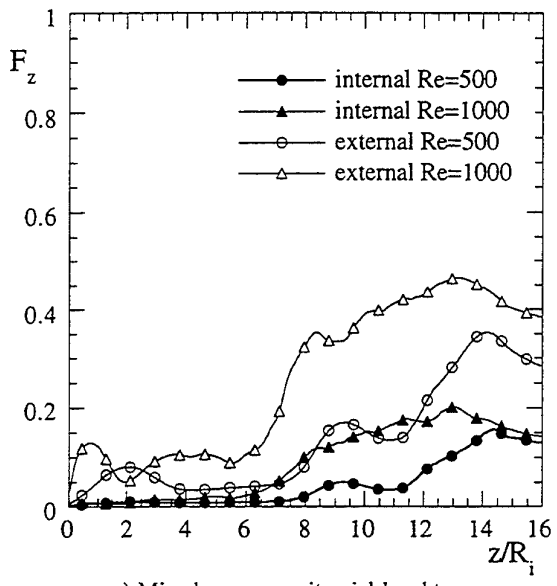
a) Re=500



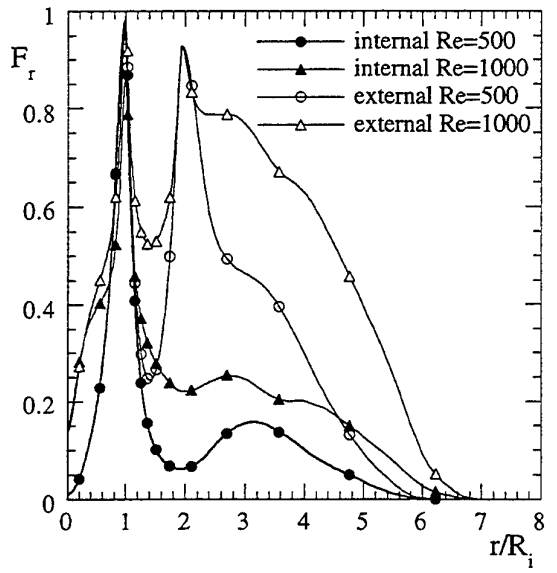
b) Re=1000

FIG. 6: ISO-CONTOURS OF VORTICITY, AT t=170.

Since mixing is deeply related to the dynamics of the large vortical structures, the mixedness parameters are affected by the Reynolds number. $F_z(z)$ and $F_r(r)$, computed from the scalar concentrations, averaged in a time interval ranging from t=100 and t=180, are shown in Figs. 7a and 7b, for Re=500 and Re=1000. For both Reynolds numbers, the comparison between the mixedness parameters obtained from the concentrations of the two different scalars indicate that, as expected, the mixing between the two streams occurs mainly in the shear-layers between the two jets and that most of the mixing is between the external jet and the surrounding fluid. For the higher Re, since the roll-up of the shear-layers

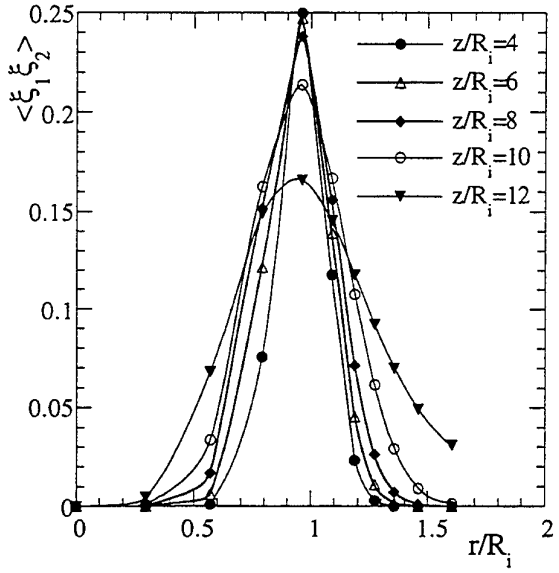


a) Mixedness per unit axial lenght

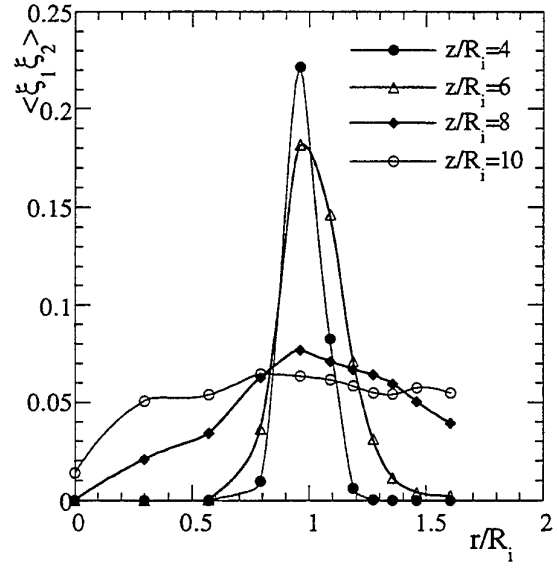


b) Mixedness per unit radial lenght

FIG. 7: MIXEDNESS PARAMETERS COMPUTED FROM MEAN SCALAR CONCENTRATIONS.



a) *Re*=500



b) *Re*=1000

FIG. 8: CORRELATION BETWEEN SCALAR CONCENTRATIONS AT DIFFERENT AXIAL LOCATIONS.

occurs closer to the jet outlet, the zone in which vortical structures are present is larger than for the lower *Re* (Fig. 6). Therefore, the zone in which mixing is significant is larger and this yields higher mixedness values.

If we are interested in the mixing occurring between the two jets only, a clearer evaluation can be obtained from the time correlation between the internal and external scalar concentrations. The radial distributions of this correlation are shown at different axial locations in Fig. 8a and 8b, for *Re*=500 and *Re*=1000 respectively. As discussed previously, the mixing between the two layers mainly occurs in the shear-layers between the two jets and, moving downstream, the thickness of the zone in which mixing is significant increases noticeably in correspondence of the roll-up of the shear layers.

In agreement with the analysis of Fig. 7, for the higher *Re*, since the roll-up of the shear-layers occurs closer to the jet outlet, at a given axial location, the zone of mixing between the two scalars is significantly larger than for the lower *Re*. Time signals of scalar concentration, recorded in numerical simulations, have also been analyzed by a new wavelet cross-correlation technique (Onorato *et al.*, 1997), that provides a clear characterization of spectral and instantaneous contribution to the correlation between the two signals; the results are not shown in the present paper due to lack of space.

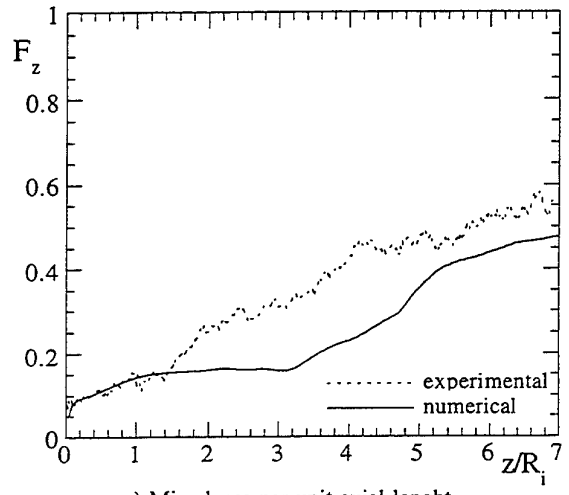
The previous results show that mixing phenomena are, as expected, related to the dynamics of vorticity. Nevertheless, except than in the initial phase of the flow development, analyzed above, the correlation between mixing and

circulation appears to be quite low, for all the Reynolds numbers. This can be seen from the table below, in which the correlation coefficients between per unit axial length mixedness and circulation are shown, for different Reynolds numbers and different stages of the flow development. In the computation of these coefficients, averaging is carried out in space over the computational domain and in time over the intervals specified in the table.

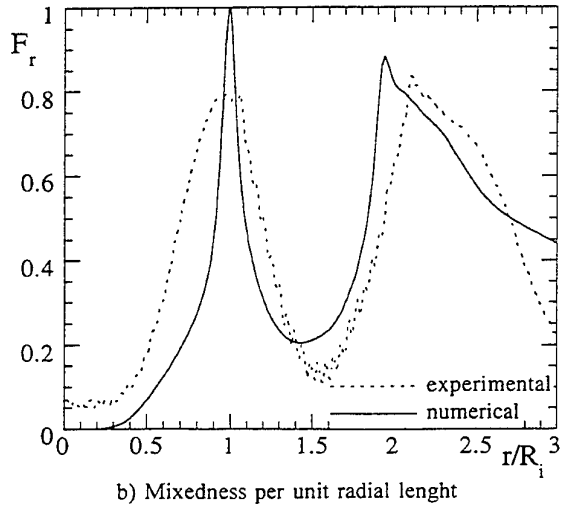
	Re=500	*Re=1000*	*Re=2000*
t = 0-20	*0.79*	*0.77*	*0.73*
t = 100-180	*0.25*	*0.34*	*0.28*

TAB. 1: CORRELATION COEFFICIENTS BETWEEN PER UNIT AXIAL LENGTH MIXEDNESS AND CIRCULATION.

In order to make a qualitative comparison between the numerical simulation and experimental flow visualizations, in Fig. 9a and 9b, $F_z(z)$ and $F_r(r)$, computed from the experimental images are shown. In this case, ξ_i is a parameter indicating the concentration of the seeding particles, obtained by the gray level in the experimental image: ξ_i is averaged on several images. The integration in Eqs. (5) and (6) is now carried out on the width of the experimental image: $L_z=7R_i$ and $L_r=3R_i$. The values of the mixedness per unit axial and radial length, computed from the time averaged concentration of the passive scalar seeded in the external jet, are also shown in Figs. 9a and 9b, for a simulation at Re=2000 and Sc=1. In spite of the axisymmetry assumption and lower Reynolds number, reasonable agreement is observed with experimental values.



a) Mixedness per unit axial lenght



b) Mixedness per unit radial lenght

FIG. 9: COMPARISON BETWEEN EXPERIMENTAL AND NUMERICAL MIXEDNESS PARAMETERS.

CONCLUDING REMARKS

The mixing process in an axisymmetric coaxial jet configuration has been analyzed by means of numerical simulation. Transport equations have been solved for two passive scalars, "seeded" in the internal and in the external jet respectively.

In the initial stage of the flow development, when only the large start-up vortex is present, the global mixedness has been found to increase in time proportionally to the circulation. This is in agreement with the results of previous studies on the mixing process in the formation of an axisymmetric vortex ring. Since the dynamics of vorticity at this initial stage is independent of the Reynolds number, the mixing is only slightly affected by *Re*. The effect of the Schmidt number is more significant.

Conversely, in the full regime, the Reynolds number strongly affects the dynamics of vorticity and, hence, the mixing. Nevertheless, for all the Reynolds numbers, the mixing between the two streams occurs mainly in the shear-layers between the two jets and most of the mixing is between the external jet and the surrounding fluid.

Comparisons between the mixedness parameters computed numerically and those obtained from experimental flow visualizations show that, in spite of the axisymmetry assumption and lower Reynolds number in the simulations, reasonable agreement is observed with experimental values.

ACKNOWLEDGEMENTS

Authors gratefully acknowledge Ing. G. Mordacci and Ing. A. Tanzini, of ENEL-CRT, for providing the experimental flow visualizations.

REFERENCES

Cetegen, B.M., Mohamad, N., 1993, "Experiments on liquid mixing and reaction in a vortex," *J. Fluid Mech.*, vol. 249, pp. 391.

Onorato, M.Jr., Salvetti, M.V., Buresti, G., Petagna, P, 1997, "Wavelet cross-correlation analysis od DNS velocity signals in a coaxial jet," *Eur. J. Mech B/Fluids, vol. 16, no. 4.*

Salvetti, M.V., Orlandi, P., Verzicco, R., 1996, "Numerical Simulations of Transitional Axisymmetric Coaxial Jets," *AIAA Journal*, vol. 34, no. 4, pp. 736-743.

Talamelli, A., Buresti, G., Mordacci, A., Tanzini, G., 1996, "Large scale vortical structures in a turbulent coaxial jet," *Proc. of 8th International Symposium on Applications of Laser Techniques to Fluid Mechanics*, vol. II, Lisbon.

Verzicco, R., Orlandi, P., 1995, "Mixedness in the formation of a vortex ring," *Phys. Fluids*, vol. 7, no. 6, pp. 1513-1515.

Verzicco, R., Orlandi, P., 1996, "A finite-difference scheme for the three-dimensional incompressible flows in cylindrical coordinates," *J. of Comput. Phys.*, vol. 123, pp. 402-414.

Flow regimes and mixing in the near field of large velocity ratio coaxial jets.

Hichem Rehab, Emmanuel Villermaux and Emil J. Hopfinger
LEGI/IMG
BP53X
38041 Grenoble-Cedex 09
France

ABSTRACT

The near flow field structure of large outer to inner velocity ratio coaxial jets has been investigated. Two flow regimes are identified according to the velocity ratio between the streams. For moderate velocity ratios, the flow structure is characterized by a central potential cone whose length varies as A/r_u where A is a constant depending on the initial conditions. Above a certain critical value of the velocity ratio r_{uc}, a transition to a recirculation regime occurs. The recirculation regime installed favours a precocious mixing in the near field. The mean concentration in the recirculating cavity is nearly constant and the concentration fluctuations are weak reflecting the flow homogeneity in the backflow region. Simple models, based on mass conservation and the intensity of entrainment across the mixing layers, are consistent with the experimental results.

INTRODUCTION AND MOTIVATION

Coaxial jets are used in many engineering applications as for instance in combustion chambers of rocket engines, where slow speed (U_1) liquid oxygen injected in the central jet is mixed with high speed (U_2) gaseous hydrogen injected in the annular jet. The present paper is concerned with the near field flow structure of coaxial turbulent water jets and is aimed at understanding the flow dynamics in the limit of large annular to central velocity ratios ($r_u = \frac{U_2}{U_1} > 1$) and high Reynolds numbers (the Reynolds number is defined from momentum conservation as $Re = \frac{U_2 D_2}{\nu}[1 - (D_1/D_2)^2]^{1/2}$, where D_1 and D_2 are the inner and the outer exit diameters respectively, when $r_u >> 1$ and ranges from 10^4 to 10^5).

The near field flow behavior is investigated through both the velocity and the concentration fields. Two flow regimes have been identified depending on whether the velocity ratio r_u is larger or smaller than a critical value r_{uc}. When $r_u < r_{uc}$, the flow structure is characterized by a central potential cone invaded progressively by the fast annular dominating stream. This invasion is associated with a periodic pinch-off of the central cone at its downstream end at a frequency f giving a Strouhal number of $St = \frac{fD_2}{U_2} = 0.3$ characteristic of the preferred jet mode. Above r_{uc}, a transition to a reverse flow regime occurs. This regime is characterized by a recirculating flow of wake type, whose dynamics is governed by the annular stream only. The bubble size increases with r_u and reaches approximately D_1 for $r_u = \infty$. The mean backflow intensity is proportional to U_2 and is measured to be $U_R \approx 0.3U_2$ for $r_u = \infty$. When the reverse flow intensity is large enough ($U_R/U_2 > 0.15$) the recirculation cavity oscillates at a characteristic low frequency relatively to the preferred jet mode, giving a Strouhal number of $St = \frac{fD_1}{U_2} \approx 0.035$ (Rehab et al., 1997).

We pay a particular attention here to the characterization of the mixing ability in both regimes. Quantitative visualizations have been made by a laser induced fluorescence technique. Disodium fluorescein dye is used as a high Schmidt number $Sc \approx 2000$ passive tracer. The spatial resolution of the images is fixed by the thickness of the laser sheet, which corresponds also to the size of a pixel. For the Reynolds numbers used ($Re \approx 10^4$) and this value of the Schmidt number, the pixel size corresponds to a scale



Figure 1: Instantaneous picture of the flow structure for $r_u = 4$. The annular jet (dark) is seeded with fluorescent dye and the laser light sheet cuts through the central plane. View from $x = 0$ to $x/D_1 = 3$.

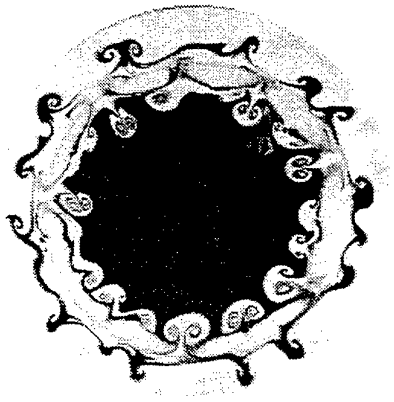


Figure 2: Instantaneous cross-section picture of the flow structure for $r_u = 4$ at $x/D_1 = 1$. The central jet (dark) is seeded with fluorescent dye.

equivalent to Kolmogorov scale and is about 40 times larger than the Batchelor scale.

MODERATE VELOCITY RATIOS - $r_u < r_{uc}$

In this regime the flow structure is characterized by two axisymmetric shear layers separated by two potential cones (Fig.1). The annular potential cone where U_2 is approximately constant, has a length essentially fixed by the diameter ratio $\beta = \frac{D_2}{D_1}$ and is slightly dependent on r_u. The central potential cone length x_{p1}, determined from mean velocity variations along the axis, is strongly dependent on r_u and decreases as r_u is increased. The measurements give $\frac{x_{p1}}{D_1} \approx \frac{8}{r_u}$, indicating that the velocity ratio r_u represents the most significative parameter of the flow.

This experimental law can be explained as follows: the mass conservation implies that all the fluid injected through the central jet is entrained across the surface of the inner cone of length x_{p1} with an entrainment velocity u_e assumed to be uniform along the central cone surface. The entrainment process is carried out by spanwise and streamwise coherent structures of the inner and the outer mixing layers (Fig.2). Hence, the mass balance is given by:

$$\frac{\pi D_1^2}{4}\,\overline{U_1} = \frac{\pi D_1}{2}\sqrt{\left(\frac{D_1}{2}\right)^2 + {x_{p1}}^2}\; u_e, \qquad (1)$$

where $\overline{U_1}$ is the inner jet bulk velocity. The overall entrainment rate is, for large values of r_u, essentially fixed by the turbulent intensity within the dominant outer mixing layer that is $u' \approx \alpha U_2$ with $\alpha = 0.17$ (Hussain & Zedan, 1978). The entrainment velocity is expressed by $u_e \approx C\alpha U_2$ with $C \approx 0.5$ (Rehab et al., 1997). Using these values and expressions in equation (1) we obtain $\frac{x_{p1}}{D_1} \approx \frac{1}{2C\alpha r_u} \approx \frac{6}{r_u}$ which is in good agreement with the experimental behavior. The value of the numerical constant here depends on both the initial flow conditions and the geometry of the coaxial injectors.

The same reasoning can be made for the scalar field. Fig.3 represents the mean concentration distributions C along the jet axis normalized by the initial mean concentration C_0 at the inner nozzle exit. It is observed, that the mean normalized concentration is constant along the inner unmixed region, then decreases in the mixing zone where the two streams meet on the axis. The unmixed zone corresponds to the inner potential cone. The mean concentration decreases as the inner jet is diluted by the outer clear stream. We characterize the inner unmixed zone by a dilution length L_s which corresponds to a certain value of the dilution level C_s/C_0 on the axis. Figure

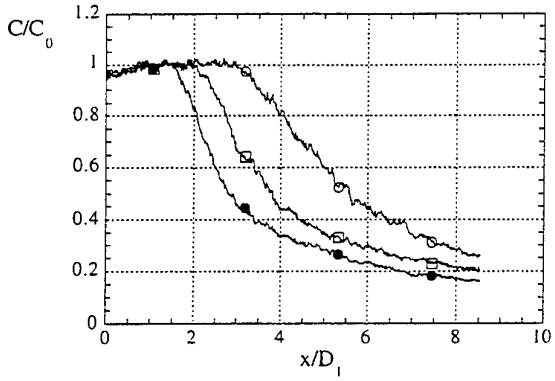


Figure 3: Mean concentration evolutions along the axis; (a), as a function of $\frac{x}{D_1}$; •, $r_u = 2$; □, $r_u = 3$; ○, $r_u = 4$.

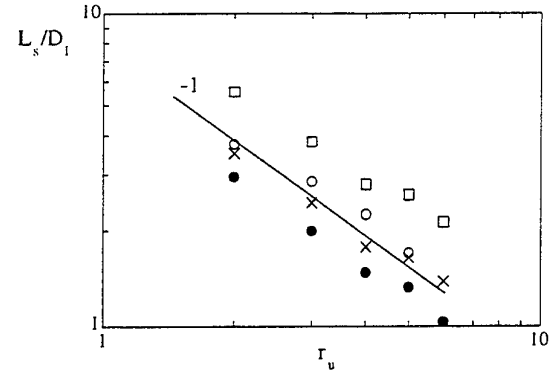


Figure 4: Dependence of the central dilution length L_s on the velocity ratio r_u. •, $C/C_0 = 1$; ×, $C/C_0 = 0.9$; □, $C/C_0 = 0.5$; ○, determined from the velocity field.

4 represents the evolutions of the dilution length L_s as a function of the velocity ratio r_u for three values of the dilution rate $C_s/C_0 = 1, 0.9$ and 0.5. Then it appears that L_s can be represented by a law of the form

$$\frac{L_s}{D_1} = \frac{A_s}{r_u} \qquad (2)$$

independently, in law, of the dilution rate C_s/C_0. The numerical constant A_s is, in turn, a function of the dilution level and increases as C_s/C_0 decreases. For instance, it is found that $\frac{L_s}{D_1} = \frac{12}{r_u}$ for $C_s/C_0 = 0.5$ while for $C_s/C_0 = 1$, $\frac{L_s}{D_1} = \frac{6}{r_u}$.

Also included in Fig.4, are the results of the inner potential cone length obtained from the axial mean velocity field and which gives also a power law evolution on r_u. A good agreement is found with the dilution length evolution. In particular, the potential cone length extracted from mean velocities (Rehab et al. 1997) giving $\frac{x_{p1}}{D_1} = \frac{8}{r_u}$ is in excellent agreement with the dilution length corresponding to $C_s/C_0 = 0.9$. Represented as a function of the correlation $\frac{x}{D_1} r_u$, the mean concentration profiles of Fig.5 show a perfect superposition thus confirming the importance of the velocity ratio r_u as the main parameter.

The dilution length law (2) can be explained, again, by a mass conservation argument. The mass balance of tracer is $Q_{e0}C_0 = Q_{es}C_s$, where

$Q_{e0} = \frac{\pi D_1^2}{4}\overline{U_1}$ and $Q_{es} = \frac{\pi D_1}{2}\sqrt{\left(\frac{D_1}{2}\right)^2 + L_s^2}\; u_e$; L_s is the dilution length and $\frac{C_s}{C_0}$ is the dilution level. We then obtain $\frac{L_s}{D_1} \approx \frac{C_0}{C_s}\frac{6}{r_u}$, giving $L_s = x_{p1}$ for $C_0 = C_s$, in good agreement with the experimental results.

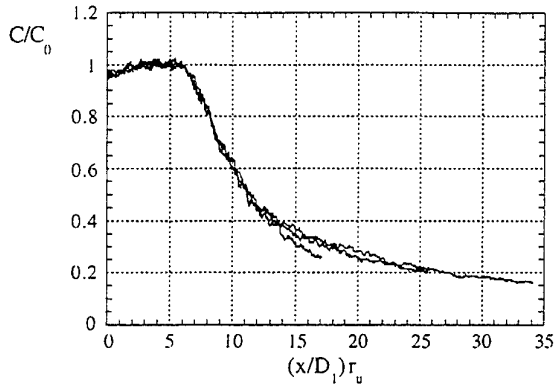


Figure 5: Mean concentration evolutions along the axis as a function of the similarity parameter $\frac{x}{D_1} r_u$ The central jet is seeded with fluorescein.

This result indicates that the large scale mixing of the two streams occurs downstream of $x \approx L_s$ and closer to the nozzle exits when r_u is large. The mean concentration decreases markedly in the reattachement region by dilution. The mean concentration has reached one third of its initial value on the axis at $\frac{x}{D_1} r_u \approx 15$.

LARGE VELOCITY RATIOS - $r_u \geq r_{uc}$

The flow regime when $r_u \geq r_{uc}$ is characterized by the truncation of the central potential cone and the formation of a recirculating flow bubble (Villermaux et al., 1994).

The transition mechanism is based on the entrainment process in the mixing layer. The entrainment is maintained by a radial pressure difference $\Delta P = \rho u'^2/2$ across the entrainment interface with $u' = \alpha(U_2 - U_1)$. As long as the inner incident kinetic pressure $\rho U_1^2/2$ is larger than ΔP, there is no recirculating flow. At the threshold, when r_u reaches r_{uc}, the inner kinetic pressure is not able to overcome the adverse pressure jump ΔP and a reverse flow towards the inner jet exit occurs. The recirculation sets in when: $\frac{\alpha^2}{2}\rho(U_2 - U_1)^2 = \frac{1}{2}\rho\overline{U_1}^2$, giving $r_{uc} = \frac{1}{\alpha\frac{\overline{U_1}}{U_1}} + 1 \approx 7$ with $\alpha = 0.17$, in good agreement with the observed experimental critical value. The same reasoning can be made when the streams have different densities. In that case, the critical velocity ratio is replaced by a critical momentum flux ratio (Villermaux et al. 1994).

Figure 6 shows the mean concentration evolutions C/C_0 along the axis for $r_u = 4, 8$ and 15. These curves are deduced from mean images where the annular stream is seeded at the same concentration C_0 and maintained at a constant velocity $U_2 = 0.4$ m/s ($Re \approx 7200$). The mean concentration increases from nearly zero in the central clear zone to higher concentration values ($C/C_0 \approx 0.4$ for $r_u = 4$) in the pinching zone. As r_u increases and for $r_u = 8$, which represents approximately the critical velocity ratio, Fig.6 shows a mean concentration peak at approximately $C/C_0 \approx 0.55$, above which the concentration decreases by dilution within the clear fluid medium. This peak is reached at the stagnation point ($x/D_1 \approx 1.6$), of the recirculation cavity that just forms.

For $r_u = 15$ and since the recirculation bubble size gets larger as r_u increases, the maximum mean concentration level $C/C_0 \approx 0.64$ extends on $1 < x/D_1 < 1.6$ which represents approximately the backflow cavity size . The mean concentration distribution for $r_u = 15$ presented in Fig.7 shows clearly the invasion of the inner jet and the higher mean concentration level in the very near field of the coax-

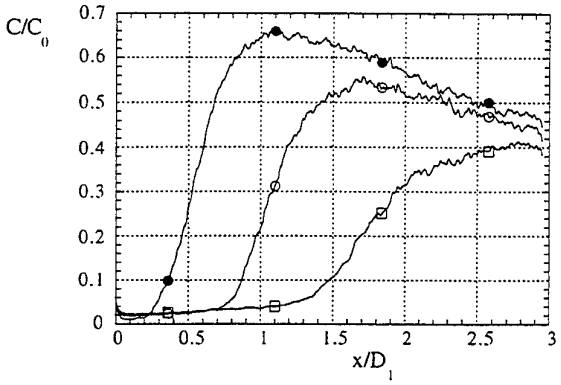


Figure 6: Mean normalized concentration evolutions along the axis; as a function of $\frac{x}{D_1}$ □, $r_u = 4$; ○, $r_u = 8$; •, $r_u = 15$. The annular jet is seeded with fluorescein.

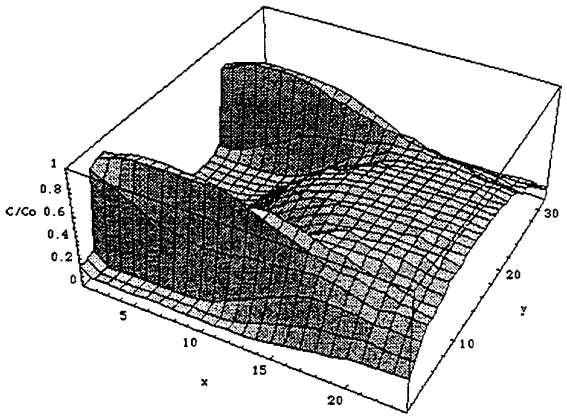


Figure 7: Mean normalized concentration distribution from $x = 0$ to $x/D_1 = 1.5$ and $y = -D_2/2$ to $y = D_2/2$ for $r_u = 15$. The annular jet is seeded with fluorescein.

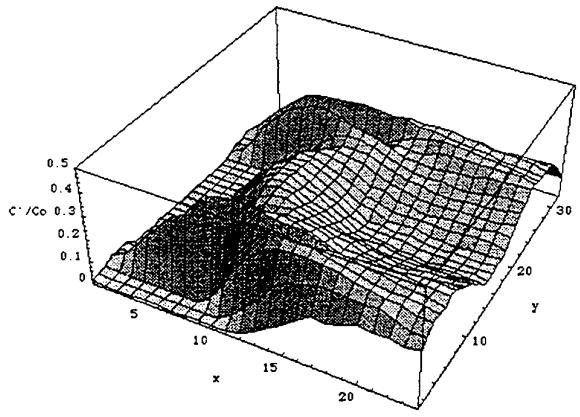


Figure 8: Fluctuation normalized concentration distribution from $x = 0$ to $x/D_1 = 1.5$ and $y = -D_2/2$ to $y = D_2/2$ for $r_u = 15$. The annular jet is seeded with fluorescein.

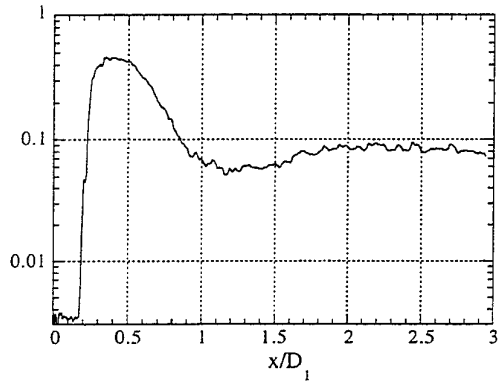


Figure 9: Intensity of segregation $I = \frac{C'^2}{C(1-C)}$; distribution along the axis for $r_u = 15$.

ial jets. As expected, the recirculation regime favours the mixing of the two streams in the very near field of coaxial jets. The normalized rms concentration distribution (Fig.8) reveal weak concentration fluctuations beyond the upstream stagnation point ($C'/C_0 \approx 0.15$ for $r_u = 15$) and indicative of the good mixing between the two streams which occurs there. The recirculating regime ($r_u > r_{uc}$) is then a simple way to realize an early and efficient mixing in the coaxial jets near field.

This is further confirmed by the evolution of the intensity of segregation I defined as $I = \frac{C'^2}{C(1-C)}$; $(0 < I < 1)$, when its evolution on the axis is studied. By contrast with the evolution of C'^2 alone, I gives the true progress of the mixing at a molecular level when the mean concentration C is itself variable in space. $I = 1$ when the scalar is stirred but remains segregated, and $I = 0$ when the homogeneity at the molecular level has been reached.

The values of I near 1 capture the frontier of the recirculation bubble near $x/D_1 \approx 0.2$, and the inside of the bubble where I is 10 times weaker around $x/D_1 \approx 1$, reflect the smoothness and the homogeneity of the scalar field there.

REFERENCES

Hussain, A. K. M. F. and Zedan, M. F. 1978, "Effects of the initial condition on the axisymmetric free shear layer: Effects of the initial momentum thickness". *Phys. Fluids* **21**, (7), 1100-1112.

Rehab, H., Villermaux, E. and Hopfinger, E.J. 1997, "Flow regimes of large velocity ratio coaxial jets". *To appear in J. Fluid Mech.*.

Villermaux, E., Rehab, H. and Hopfinger, E.J. 1994, "Breakup regimes and self-sustained pulsations in coaxial jets". *Meccanica.* **29**, 393-401.

ON SIMILARITY OF A PLANE TURBULENT JET IN A CO-FLOWING STREAM

John C. LaRue and Thang Ly
Mechanical and Aerospace Engineering
UC Irvine
Irvine, CA 92697
USA

Hamid Rahai and Pin Yao Jan
Mechanical Engineering department
Calif. State University, Long Beach
Long Beach, CA 90840
USA

ABSTRACT

The flow downstream of a plane jet is investigated for a ratios of excess centerline to freestream velocity that range from 4.7 to 0.27. The lower value is similar though slightly higher than values where some evidence of wake-type similarity has been observed. In the present study only jet-type similarity is observed. The type of similarity is determined using a novel approach which yields values not only for the virtual origin and decay coefficient but also for the exponent in similarity formulation for the decay of the centerline velocity excess and the growth of the half-width. Experimental values of 0.485 and 0.95 are obtained respectively. In contrast, jet-type similarity analysis yields values of respectively, 0.5 and 1.0.

INTRODUCTION

A plane jet in a co-flowing stream begins its evolution with downstream distance as two plane mixing layers separated by fluid with properties that correspond to the jet-exit flow. Eventually, the two mixing layers begin to merge and jet fluid which is unmixed with the freestream begins to appear only intermittently in the central region of the flow. Further downstream and after a transition or interaction region where the mixing layers interact and merge, the flow may exhibit an approximate jet-type similarity (cf. Bradbury (1965) and Bradbury and Riley (1967)). If it does exhibit an approximate jet-type similarity region, further downstream, the flow will pass through another transition region and then reach a position where the flow should exhibit a wake-type similarity (cf. Bilger (1968)). At relatively low ratios of the jet exit to freestream velocity, Bilger (1968) suggests that the region of approximate jet-type similarity may not form and the flow will consist of developing, transitional and wake-type similarity regions. In both similarity regions, profiles of the mean velocity and other statistical properties of the velocity field should become similar when suitably normalized.

Bradbury and Riley (1967) present the downstream decay of the mean centerline velocity and root mean square (rms) downstream velocity fluctuations and the downstream growth of the half width for free stream to jet velocity ratios of 0.16 to 0.6 and jet heights of 3.17 and 9.51 mm to as far downstream as 250 jet heights. Ratios of the freestream velocity divided by the excess velocity on the centerline vary from about 0.22 to 10. The downstream variation of the centerline velocity excess shows some evidence of a change from jet-type similarity to wake-type similarity with increasing freestream to jet velocity ratios greater than 0.36. Specifically, it appears that the rate of change with downstream distance of the mean velocity excess on the centerline changes with downstream distance from a value of about 0.16 which is consistent with jet-type similarity to a value of about 0.41 which is taken to be consistent with wake-type similarity. However, profiles of the rms of the fluctuating velocities and the Reynolds stresses are not presented and, consequently, it is not known if the profiles of the higher order statistics are similar. In addition, for each ratio of the freestream to jet velocity, different values of the virtual origin are used and the data are collected in different ranges of downstream distance normalized by the momentum thickness.

Kotsovinos (1976) has shown that it is likely that the use of different downstream ranges will lead to different values for the rate of change of the mean velocity excess as well as the virtual origin. Thus, some of the difference in the decay coefficients reported by Bradbury and Riley (1967) may be due to the use of different data ranges. Further Koptsovinos (1976) concludes that the spreading rate for a plane jet issuing into a quiescent stream may not vary linearly with downstream distance. This is inconsistent with the prediction of similarity theory as presented by Townsend (1976) and Tennekes and Lumley (1972). However, Libby (1996) suggests an alternate similarity formulation which is consistent with the observation of Kotsovinos (1976).

Everitt (1972) presents results for the plane jet in a co-flowing stream to 314 slot heights downstream of the jet exit where the ratio of the freestream velocity to excess mean centerline velocity reaches about 0.158. This value is about 60% larger than the maximum value of 0.093 for the ratio of the freestream to centerline deficit velocity in a plane wake where wake-type similarity is observed (cf. Townsend (1949) and (1976)). The normalized rms longitudinal velocity does not appear to reach a constant value and thus, wake-type similarity while perhaps approached in the Everitt (1972) study, does not appear to have been observed.

The downstream distance required for the two mixing layers to begin to merge depends on the turbulence level and flow characteristics at the jet exit (cf. Flora and Goldschmidt (1969), Hussain and Clark (1977) and Goldschmidt and Bradshaw (1981). For example, the growth rates of the longitudinal turbulence intensity and the nondimensional entrainment rates are higher for a jet exit flow with a laminar boundary layer in comparison to a jet exit flow with a fully turbulent boundary layer. With respect to similarity behaviour, these observations suggest that jet initial conditions will have an effect on the apparent or virtual origin of the turbulence but not necessarily on the relative centerline intensities, the normalized Reynolds stresses and other suitably normalized properties at distances far downstream of the jet exit.

In the present study, the range of measurements extends to about 880 slot heights or 88 momentum thicknesses downstream of the jet exit. The results include not only the centerline decay of the mean velocity and rms of the longitudinal fluctuations but also the rms of the transverse velocity fluctuations and maximum Reynolds stresses. Profiles of the mean velocity, the rms of the longitudinal and transverse velocity fluctuations and the Reynolds stresses have also been obtained but only the profiles of the rms of the longitudinal velocity fluctuations are presented here. The type of similarity is assessed using a novel approach that provides not only the virtual origin, the proportionality coefficients in the similarity expressions, but also the optimal value of the exponent.

The results presented herein correspond to one flow condition of three that are planned or have been carried out. For this case, the ratio of the jet exit to freestream velocity is chosen to be about 4.8. This leads to a range of ratios of the freestream to centerline excess velocity of 0.27 to 4.7. These values all exceed values for the velocity ratio where wake-type similarity (specifically for the flow downstream of circular cylinders) would be observed. Future studies will use lower values for the freestream to jet velocity ratio so that wake-type similarity can conceivably be observed. Thus, for the present study, only jet-type similarity should be observed.

Similarity Theory

Detailed discussions of wake-type and jet-type similarity are presented in Townsend (1976) and Tennekes and Lumley (1972). Therefore only a brief review of similarity theory and the most relevant consequences are presented here. For this discussion and all the results presented subsequently, the x axis is taken to be in the downstream direction with origin at the jet exit, the y axis is taken to be normal to the x axis and flow center plane with origin at the center plane and the z axis is taken to be normal to the plane formed by the x and y axes. Similarity theory predicts that

$$\begin{aligned} U &= U_f + U_s f(y/\delta) \\ \overline{uv} &= U_s^2 g_{12}(y/\delta) \\ \overline{u^2} &= U_s^2 g_1(y/\delta) \\ \overline{v^2} &= U_s^2 g_2(y/\delta) \end{aligned} \qquad (1)$$

where U is the mean velocity, U_f is the freestream velocity, $U_s \equiv |U_{cl} - U_f|$, U_{cl} is the centerline velocity, δ is the y location where $U(\delta) = 0.5(U_{cl} - U_f)$ and u and v are, respectively, the fluctuating velocities in the x and y coordinate directions. From Egn. 1, it is easy to see that the following relationships must be satisfied: $\overline{u_{cl}^2}/U_s^2 = const.$, $\overline{v_{cl}^2}/U_s^2 = const.$, and $\overline{uv}_{max}/U_s^2 = const.$

For $U_s >> U_f$, jet-type similarity can occur where

$$\delta \propto x \text{ and } U_s \propto x^{-1/2} \qquad (2)$$

For $U_s << U_f$, wake-type similarity can be observed where

$$\delta \propto x^{1/2} \text{ and } U_s \propto x^{-1/2} \qquad (3)$$

Libby (1996) also provides and alternative formulation for flows that are similar and suggests a generalization of Eqns. 2 and 3 where

$$\frac{U_s}{U_f} = \frac{f_0(0)}{\tilde{x}_1^{1/2}} + \frac{f_1(0)}{\tilde{x}_1} + \ldots \qquad (4)$$

where $\tilde{x}_1 \equiv \left(\frac{x - x_{0,U}}{\theta}\right)$.

EXPERIMENTAL FACILITIES AND CONDITIONS

All results presented herein are obtained using a NACA 0020 airfoil that is placed horizontally on the centerplane of the UCI large wind tunnel, which has a test section cross-section of 61 by 91 cm and a length of 6.71 m. In the central part of the test section at a mean velocity of 10 *m/s*, the mean velocity is found to vary by less that 1% and the free stream turbulence intensities at the entrance and exit of the test section are found, respectively, to be 0.17% and 0.22%. The temperature in the wind tunnel varies by less than $\pm 1C$ during the course of a data collection period.

The airfoil has a chord of 25.4 cm, a thickness of 5.08 cm and spans the width of the test section. The center of the airfoil is hollow and consists of an air supply manifold which is supplied from a high pressure, regulated, compressed air source, a plenum, a screen section to damp out velocity fluctuations, a contraction section and a two dimensional channel with a width of 60 cm. a height, h=3.175 mm, and a length of 16.5 cm which exits at the trailing edge of the airfoil. For all tests, the jet centerline exit velocity is about 20 m/sec and the freestream velocity is about 4.1 m/sec. The Reynolds number for the channel is about 4.1×10^3. Thus, the flow at the exit of the jet is turbulent channel flow in contrast to the top hat type profile used in the studies of Bradbury (1965) and Bradbury and Riley (1967).

The resulting momentum thickness, θ, is about 3.5 cm and is computed by numerical integration of the mean velocity profiles between $\pm 3\delta$ using the following:

$$\theta = \int_{-3\delta}^{3\delta} \frac{U}{U_f}\left(1-\frac{U}{U_f}\right)dy \qquad (5)$$

An increase of the limits of integration to $\pm 3.5\delta$ leads to less than a 1% change in the computed value of the momentum thickness. A summary of the flow conditions for each profile is shown in Table 1.

Most of the data presented herein are obtained using an X-wire probe which consists of two TSI T1.5 hot wire sensors operated at overheats of 1.7 by means of TSI Model 1050 constant temperature anemometers (CTA). Based on the square wave test, the frequency response is computed to be about 50 *kHz* at 25 *m/s*. The calibration methodology is based on that described by Bradshaw (1971). Pre- and post-calibrations are performed and data are presented only when the pre- and post-calibration coefficients yield values for the mean and rms of the fluctuating velocities that differ by less than 1%.

The output voltage from the CTA's are each used as the input to two precision buck and gain amplifiers which are used to match the signal level to the allowable dynamic range of the analogue to digital converter. All signals are low-pass filtered at 4 kHz. For each CTA, the output of one of the associated buck and gain amplifiers is connected to an analogue differentiator. The output of the differentiator and the undifferentiated signal from each CTA are connected to a Computer Boards Inc. (CBI) SSH-16 sample and hold board and then to a CBI CIO-AD16F 12 bit analogue to digital converter which is mounted in a PC clone and controlled by means of DataLog
acquisition software. The hot wire data are sampled at 8000 samples per second for each channel of data. At each position, about 20 seconds of data are recorded and subsequently archived on a Pinnacle Micro RCD 1000 recordable CD-ROM drive. The data are analyzed using DataReady analysis software.

To assess the two dimensionality of the flow, vertical profiles of the statistical properties of the velocity field at the furthest downstream position, i.e. at x/d = 976, are obtained at various transverse positions. The half width at this location is about 5.8 cm. The mean centerline velocity and the rms of the fluctuating velocity are found to vary by less than 2% over a central region of 23.2 cm in span-wise extent. If the large scale structures are assumed to be about $1/2\delta$ in transverse extent, the two-dimensional portion of the flow can be estimated to be about eigth times the size of the large scale structure. Thus, the region of two-dimensionality normal to the x-y plane should be adequate to ensure that the flow at this position is two-dimensional.

RESULTS

The mean velocity profiles are shown on Figs. 1a-1c. In the central region of the flow, i.e. for $y/\delta \le 1.5$, the mean velocity profiles appear to be nearly similar starting at $x/\theta = 0.32$. However, for $y/\delta \ge 1.5$ and $x/\theta \le 11$, a velocity deficit which arises from the boundary layer on the airfoil can be observed. Thus, the flow can be similar only for $x/\theta > 11$

We next consider the downstream evolution of the inverse of the normalized velocity excess. We assume that the inverse of the normalized velocity excess raised to a power $1/n_U$ is linearly related to the downstream position as shown in the following:

$$\left(\frac{U_f}{U_s}\right)^{1/n_U} = A_U\left(\frac{x-x_{0,U}}{\theta}\right) \qquad (6)$$

If the exhibits jet-type or wake type similarity, based on Eqns. 3 or 4, n_U should equal unity. To find the value of n_U that provides the best description of the measured data, a value of n_U is chosen and the corresponding values of the coefficient, A_U and virtual origin, $x_{0,U}$ are obtained using the method of least squares. The optimal values for the exponent, coefficient and virtual origin are those that minimize the rms of the difference, σ_U, between computed and measured values of U_f/U_s where

$$\sigma_U = \sqrt{\frac{1}{N}\sum_i^N\left[\left(\frac{U_f}{U_s}\right)_{c,i} - \left(\frac{U_f}{U_s}\right)_{m,i}\right]^2} \qquad (7)$$

where the subscript m refers to a measured value, c refers to a value computed using the coefficients obtained from the method of least squares at values of the downstream position that correspond to measured values.

Fig. 2 shows a plot of σ_U versus n_U. It is easy to see that the optimal value for n_U is about 0.485—a value acceptably close to the value of 0.5 predicted by similarity theory. The corresponding values for A_U and $x_{0,U}/\theta$ are, respectively, 0.27 and -3.82.

Motivated by the similarity form of the centerline variation of the mean velocity as indicated in Eqns. 3 and 4, the square of the inverse of the normalized centerline velocity excess as a function of downstream distance is shown on Fig. 3. For $x/\theta \ge 16$, and consistent with similarity theory, the decay of square of the inverse of the centerline velocity excess appears to vary linearly with downstream distance. The solid line shown on Fig. 3 represents a least square fit through the data in the range $16 \le x/\theta \le 88$.

The optimal exponent, n_δ, coefficient, A_δ, and virtual origin, $x_{0,\delta}/\theta$, can be found following the same procedure used to find the corresponding coefficients for the decay of the inverse of the centerline velocity excess and equations that correspond to Eqns. 6 and 7. Specifically, the optimal values for the exponent, coefficient and virtual origin are those that minimize the rms of the difference, σ_δ, between computed and measured values of δ/θ. Fig.4 shows a plot of σ_δ versus n_U. It is easy to see that the optimal value for n_δ is about 0.95—a value acceptably close to the value of 1.0 predicted by similarity theory for a jet-type similarity. The corresponding values for A_δ and $x_{0,\delta}/\theta$ are, respectively, 0.017 and -34.4. For plane jets issuing into quiescent or very low speed co-flows, $A_\delta \approx 0.1$ (cf. Rodi (1972)). Thus, consistent with the observations of Bradbury and Riley (1967), the effect of an increase in the co-flow or free stream velocity relative to the jet exit velocity is to reduce the rate of growth of the half- width.

The downstream variation of δ/θ is shown on Fig. 5. It would appear that the linear variation predicted by similarity theory does not begin until about $x/\theta = 28$ where it can be seen that the half-width grows linearly with downstream position. Thus, it appears that even as far downstream as

$x/d = 888$ or equivalently $x/\theta = 88$, the flow exhibits jet-type similarity but not wake-type similarity.

The centerline decay of the normalized variance of the downstream and transverse fluctuating velocities are shown on Figs. 6 and 7. The developing region which is taken to correspond to the region of increasing normalized velocity variance can be seen to extend to about $x/\theta \approx 10$. This region is followed by a transition region where the normalized variance decreases with increasing downstream distance which extends to about $x/\theta \approx 60$. Further downstream, the normalized velocity variances appear to become nearly constant, i.e. consistent with similarity, and the normalized values of the variance for the downstream and vertical velocity fluctuations are, respectively 0.062 and 0.048. These values are, respectively about 10% and 25% than the corresponding values reported by Gutmark and Wygnanski (1976) for a plane jet issuing into a quiescent flow.

The downstream variation of the maximum of the normalized Reynolds stress is shown on Fig. 8. The developing region extends from the jet exit to about $x/\theta \approx 10$ where the normalized Reynolds stress reaches its maximum. With increasing downstream distance, the Reynolds stress gradually decreases through the transition region until about $x/\theta \approx 55$. With further increases in the downstream position, the Reynolds stress appears to be nearly a constant of about 0.024. In contrast to the difference found between the normalized variance for the present and previous studies, the normalized Reynolds stress for $x/\theta \geq 55$ is nearly equal to the corresponding values reported by Bradbury (1965) and Gutmark and Wygnanski (1976). This agreement must be considered fortuitous rather than indicating that the present flow is similar to that of the two referenced studies.

The transverse profiles of the normalized downstream velocity variance are shown in Figs. 9a-c. The expected variation in the profile shapes is observed on Fig. 9a which shows profiles extending from very near the jet exit to $x/\theta \approx 12$. The variation of the profiles in the transition region shown on Fig. 9b is less than observed in the developing region but the profiles do not become similar until the furthest two stations which are presented on Fig. 9c.

CONCLUSIONS

1. The transverse profiles of the velocity excess and the downstream variation of normalized half-width and the normalized inverse of the square of the centerline velocity excess are consistent with jet-type similarity for $\frac{x}{\theta} > 16$.

The exponent in the similarity expression for the downstream variation of square of the inverse of the normalized centerline velocity excess is found to be 0.485 which is close to the value of 0.5 predicted by similarity theory.

The exponent in the similarity expression for the downstream variation of the half-width is found to be 0.95 which again is close to the value of unity predicted by similarity theory for jet-type similarity.

The rate of growth of the half-width is about one-sixth that of a plane jet in a quiescent stream. The observed slower growth rate of the half-width of a jet in a co-flowing stream is consistent with the observations of Bradbury and Riley (1967).

Values of the virtual origin in the similarity expressions for the downstream variation of the square of the inverse of the centerline velocity excess and the half-width differ significantly. The virtual origin for the former is -3.82 while that of the latter is -34.4. It is not surprising that the two virtual origins differs as the virtual origin for the half-width may have a greater dependence on the low momentum fluid in the boundary layer that forms on the airfoil.

The downstream decay of the centerline values of the longitudinal and transverse fluctuating velocities as well as the maximum Reynolds stress exhibit similarity for $\frac{x}{\theta} > 60$. The transverse profiles of the variance of the longitudinal velocity fluctuations are also similar starting at about this location. Thus, consistent with other studies in plane jet flows, statistical features of the flow associated with the fluctuating quantities require considerable more downstream distance to become similar than do the mean flow quantities.

Only jet-type similarity is observed even though the ratio of the centerline to freestream velocity reaches 0.27. While this value is similar to the value where Bradbury and Riley (1967) find wake-type similarity, it is consistent with the lack of wake-type similarity found by Everitt (1972) at the even lower value of 0.158 for the velocity ratio. Based on the cylinder results of Townsend (1949) and (1976), it appears that velocity ratios less than 0.1 may be required over an extended downstream distance to observe wake-type similarity in a plane jet flow. This may be difficult to achieve because of the excess jet momentum needed to overcome the momentum deficit in the boundary layer on the airfoil.

REFERENCES

Bilger, R.E., "The turbulent plane jet-wake," Proceedings of the Conference on Hydraulics and Fluid Mechanics, pp. 159-162, 1968.

Bradbury, L.J.S., "The structure of a self-preserving turbulent plane jet." J. Fluid Mech., Vol. 23, pp. 31-64, 1965.

Bradbury, L.J.S., and J. Riley, "The spread of a turbulent plane jet issuing into a parallel moving airstream," J. of Fluid Mech., Vol. 27, pp. 381-394, 1967.

Bradshaw, P., "An introduction to turbulence and its measurement," Pergamon Press, New York, 1971.

Everitt, K., "The spread of turbulent jets and wakes," Ph.D. thesis, University of London, 1972.

Flora, J.J. and V. W. Goldschmidt, "Virtual origins of a free plane turbulent jet," AIAA J., Vol. 7, pp. 2344-2346, 1969.

Goldschmidt, V. W. and P. Bradshaw, ""Effect of nozzle exit turbulence on the spreading or (widening) rate of plane free jets," ASME Paper 81-FE-22, 1981.

Gutmark, E. and I. Wygnanski, "The planar turbulent jet," J. Fluid Mech. Vol. 73, pp. 465-495, 1976.

Hussain, A.K.M.F. and A. Ray Clark, "Upstream influence on the near field of a plane turbulent jet," Physics of Fluids, Vol. 20, pp. 1416-1426, 1977.

Kotsovinos, N. E. "A note on the spreading rate and virtual origin of a plane turbulent jet," J. of Fluid Mech., Vol. 77, pp. 305-311, 1976.

Libby, P. A., "Introduction to turbulence," Taylor and Francis, Washington, D.C., 1996.

Tennekes, H. and J. L. Luml;ey, "A first course in turbulence," The MIT Press, Cambridge, MA, 1972.

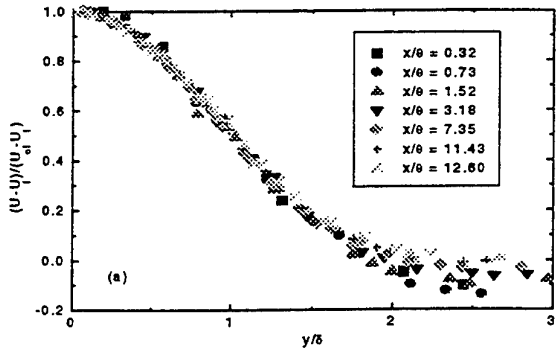
Townsend, A. A., 'The fully developed turbulent wake of a circular cylinder," Australian J. Sci. Res., Vol. 2A, pp. 451-468, 1949.

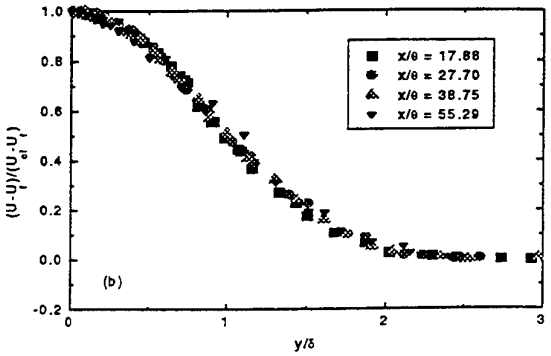
Townsend, A. A., "The structure of turbulent shear flow," Second Edition, Cambridge University Press, New York, 1976.

Table 1. Flow Parameters

x/h^1	$U_f^{(2)}$	U_{cl}	Us	U_f/U_f	θ / h	δ / h
4	4.08	18.85	14.77	4.85	12.39	0.43
8	4.21	14.82	10.61	4.72	11.01	0.72
16	4.02	11.05	7.03	4.95	10.54	1.32
32	4.15	8.86	4.71	4.78	10.07	2.34
72	4.13	6.94	2.81	4.87	9.79	4.73
120	4.12	6.28	2.16	4.88	10.50	7.00
144	4.05	6.15	2.1	4.74	11.42	7.56
192	4.14	5.89	1.75	4.78	10.73	9.24
288	4.16	5.62	1.46	4.79	10.40	11.01
400	4.18	5.45	1.27	4.77	10.32	13.11
592	4.20	5.29	1.09	4.72	10.71	15.86
848	4.22	5.15	0.93	4.65	10.82	20.60
888	4.29	5.20	0.91	4.62	10.15	20.90

1. $h = 3.175$mm
2. All velocities have units of *m/s*





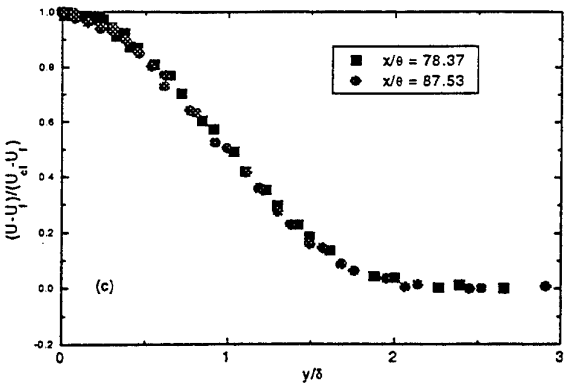


Figure 1. Transverse profiles of the mean velocity

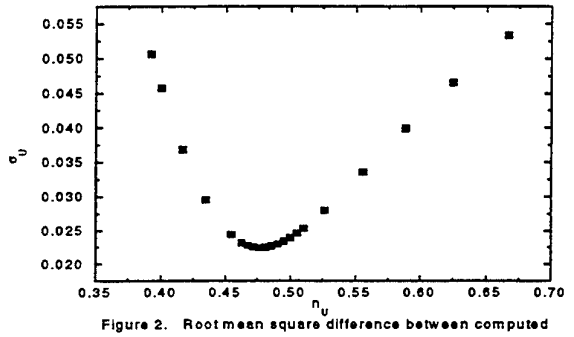


Figure 2. Root mean square difference between computed and measured values of (U_f/U_s).

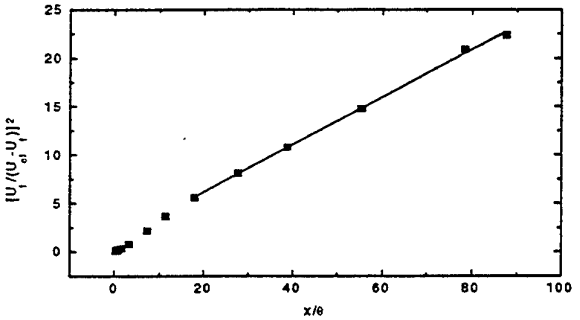


Figure 3. Downstream variation of the square of the inverse of the normalized centerline velocity excess.

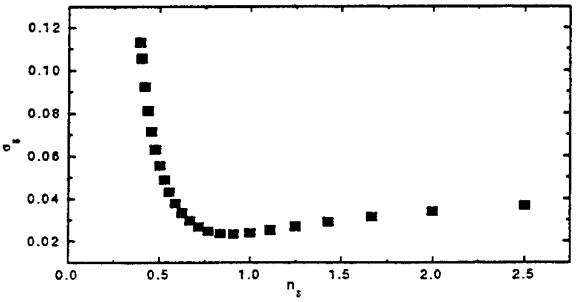


Figure 4. Root mean square of the difference between the computed and measured half width as a function of the exponent in the similarity relationship.

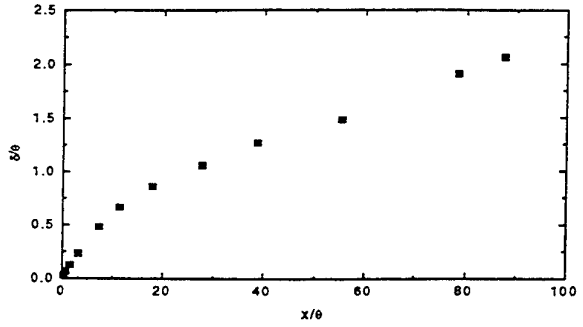


Figure 5. Normalized half-width as a function of downstream distance.

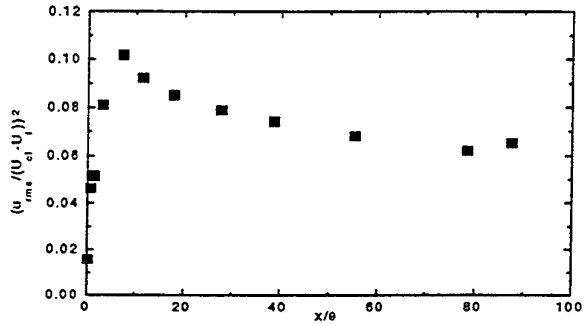


Figure 6. Downstream decay of the square of the normalized centerline rms velocity, $(u_{rms}/(U_{cl}-U_l))^2$.

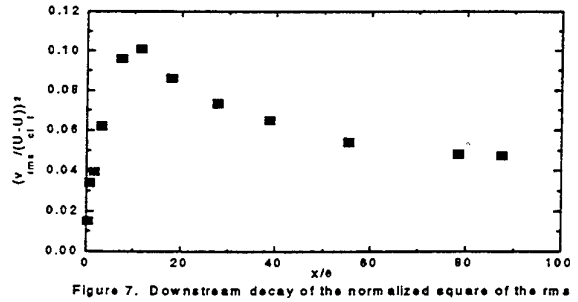


Figure 7. Downstream decay of the normalized square of the rms of the vertical velocity fluctuations, $(v_{rms}/(U_{cl}-U_l))^2$.

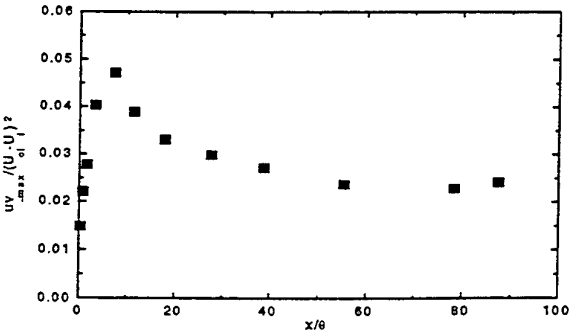
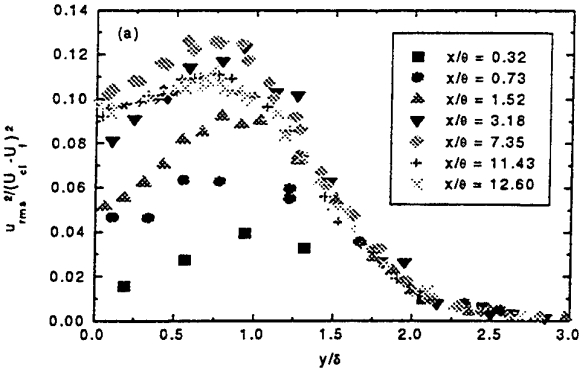
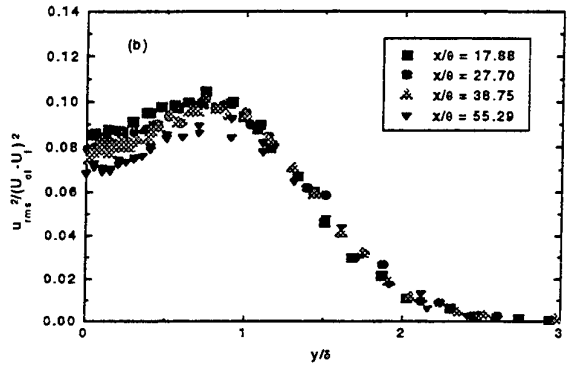


Figure 8. Downstream variation of maximum normalized shear stress.





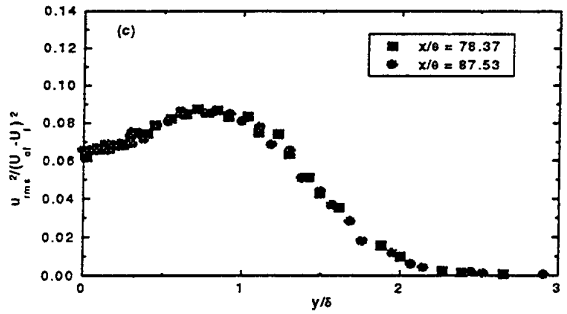


Figure 9. Transverse variation of the sqaure of the normalized rms of the downstream fluctuating velocity, u_{rms}.

THE INFLUENCE OF INLET CONDITIONS ON A LARGE EDDY SIMULATION OF A TURBULENT PLANE JET

Claus Weinberger, Jann Rewerts, Johannes Janicka
Fachgebiet Energie– und Kraftwerkstechnik
Technische Hochschule Darmstadt
Petersenstr. 30
D–64287 Darmstadt
Germany

ABSTRACT

A turbulent plane jet at Re=10000 is investigated using large eddy simulation based on Schumanns 'volume balance procedure'. The Smagorinsky model is used to describe the unresolved scales. The simulation results with an inlet condition prescribed as an inflowing 'top hat' profile with superimposed weak random fluctuations are compared with time-dependent inlet profiles of a pre-calculated channel flow simulation. The computed mean quantities and the turbulence intensities are compared with experimental data in the far field of the jet as well as near the exit. The analysis shows a better representation of the physics when using the channel flow as the inlet condition. Random excitation at the same *rms*-level yields a strong underprediction of the turbulent intensities in the near field. It is assumed that this behaviour is due to the typical time scale of the excitation.

INTRODUCTION

Turbulent plane jets have been widely investigated experimentally and numerically. Experimental work has been done to analyze the mean jet characteristics in the self-preservation region as well as in the near field of the nozzle (Miller and Comings 1957, Gutmark and Wygnanski (1976), Everitt and Robins (1978), Thomas and Goldschmidt (1986)). Recent numerical investigations were based on second-order one-point closure models to turbulence. Launder et al. (1975) presented computed results of the turbulent plane jet using their well-known linear model. Shih et al. (1992) developed a non-linear second order closure for boundary-free shear flows. A systematic comparison of second-order closure models applied to the selfpreservation region of plane and round jets was conducted by Pfuderer et al. (1996) and showed the limitations of one-point closure models for the prediction of jets.

The first application of a large-eddy simulation (LES) to a practical engineering problem is dated as early as 1970 (Deardorff (1970)) but only for some years LES has been adapted to investigate turbulent plane jets (Dai et al. (1995), Hoffmann (1996), Meinke et al. (1996), Weinberger and Janicka. (1996)). Unfortunately it is quite difficult to compare the aforementioned works. On the one hand the analysis of the computation based on different quantities which were chosen for the evaluation. On the other hand different configurations were used especially concerning the inlet conditions. Hoffmann (1996) as well as Weinberger and Janicka (1996) set a 'top hat' profile for the mean axial velocity with surperimposed random disturbances. Dai et al. (1995) prescribe a parabolic mean profile and sinuoidal fluctuations. Finally Meinke et al. (1996) pick the inlet conditions out of a channel flow.

These studies reveal that LES is capable to describe the main characteristics of this type of flow such as mean velocity profiles, the spreading and the dominant frequency at the end of the potential core. Additionally the observed symmetrical arrangement of vortices near the nozzle and their asymmetrical arrangement beyond the potential core are captured. However, the turbulence intensities in the selfpreservation region show discrepancies compared to measurements. The computation of Hoffmann (1996) overpredicts all turbulence intensities by approximately 25 % whereas the shear stress is captured quite well. The same tendency is observed by Weinberger and Janicka (1996) concerning the spanwise and vertical fluctuations whereas the agreement of the streamwise intensity is fairly good. These discrepancies are somewhat surprising because the inlet profile with the superimposed weak random fluctuations is comparable to the inflow conditons in experiments (Gutmark and Wygnanski (1976), Thomas and Goldschmidt (1986)).

The objective of this work is to investigate the influence of the inlet conditions on the incompressible plane jet calculations. Simulations with a flat profile and artificial disturbances are compared with a simulation in which the ingoing velocities and turbulent intensities are obtained from a pre-calculated channel flow simulation. It is clear that the first case is characterized by a transitional process to turbulent flow. However, it is commonly expected that in the far field of the jet the results are independent of the inlet conditions and selfpreservation is achieved.

NUMERICAL TECHNIQUE

In LES the large scale structures of a turbulent flow are resolved whereas a model is applied to the unresolved subgrid scales (SGS). To decompose the velocity and pressure fields the 'volume balance procedure' developed by Schumann (1975) is adopted. It is based on a grid volume integration of the Navier Stokes equations and leads to quantities which can be interpreted as discretely located volume and surface averages. They represent the resolved fields. The surface average is indicated as

$$\overline{\phi}^{\Delta A} = \frac{1}{\Delta A}\int\int \phi \; dA \,, \tag{1}$$

and the volume average is

$$\overline{\phi}^{\Delta V} = \frac{1}{\Delta V}\int\int\int \phi \; dV. \tag{2}$$

This procedure applied to the incompressible Navier Stokes equations yields the following equations for the large scales:

$$\begin{aligned}\frac{\partial}{\partial t}\int \overline{u_i}^{\Delta V} dV = &- \oint_A \overline{u_i}^{\Delta A_j}\overline{u_j}^{\Delta A_j} dA_j - \oint_A \frac{\overline{p}^{\Delta A_i}}{\overline{\rho}^{\Delta A_i}} dA_i \\ &+ \oint_A (\overline{\tau_{ij}}^{\Delta A_j} + \overline{\tau_{ijSGS}}^{\Delta A_j}) dA_j,\end{aligned} \tag{3}$$

where u_i denotes the velocity, p the pressure, ρ the density, τ_{ij} the stress tensor and τ_{ijSGS} the subgrid scale stress. The surfaces of each volume cell are indicated as ΔA_j. The manipulated Navier Stokes equations are solved on staggered grids on the basis of the pipe flow simulation code FLOWSI developed at Lehrstuhl für Fluidmechanik, TU München (Schmitt 1982). For the integration in time the explicit second-order Adams-Bashforth scheme is applied providing an intermediate solution $\overline{u_i}^{\Delta V,*}$. The divergence free velocity field at the new time level $n+1$ is obtained via a correction step

$$\overline{u_i}^{\Delta V,n+1} = \overline{u_i}^{\Delta V,*} - \frac{\Delta t}{\overline{\rho}^{\Delta A_i}} \frac{\partial \overline{\Psi}^{\Delta A_i,n+1}}{\partial x_i} \tag{4}$$

with

$$\overline{\Psi}^{\Delta A_i,n+1} = \overline{p}^{\Delta A_i,n+1} - \overline{p}^{\Delta A_i,n}. \tag{5}$$

Taking the divergence of (4) yields a Poisson equation for the pressure correction $\overline{\Psi}^{\Delta A_i,n+1}$. It is discretized with a second-order central difference scheme and solved with a direct 2D-elliptic solver which utilizes a FFT in the homogeneous direction.

SUBGRID SCALE MODEL AND REQUIREMENTS ON LES

The eddy viscosity model proposed by Smagorinsky (1963) is used to represent the unknown subgrid scale stresses, denoted by a double prime, in terms of the resolved fields:

$$\overline{\tau_{ijSGS}}^{\Delta A_j} = -\overline{u_i'' u_j''}^{\Delta A_j} = 2\nu_t \overline{S_{ij}}^{\Delta A_j} - \frac{1}{3}\overline{u_k'' u_k''}^{\Delta A_j}\delta_{ij}, \tag{6}$$

$$\nu_t = (C_s\Delta)^2 \sqrt{\frac{1}{2}\overline{S_{ij}}^{\Delta A_j}\overline{S_{ij}}^{\Delta A_j}}, \tag{7}$$

where ν_t represents the subgrid eddy viscosity. S_{ij} is the strain rate tensor and $\Delta = ((\Delta x^2 + \Delta y^2 + \Delta z^2)/3)^{0.5}$ is a characteristic subgrid length scale. It should be noted that the Smagorinsky model has a strictly dissipative character, i.e. kinetic energy is only transferred from the large scales to the subgrid scales. This is in contrast to the observed back scattering of energy to the mean flow (Hsiao and Huang 1990).

The simulations revealed that it is very important not to damp the highly oscillating fluctuations of the computed large scales. Therefore a non-dissipative fourth-order Lagrange interpolation scheme was used to calculate the convective fluxes inside the computational domain whereas a second-order interpolation scheme is adopted at the boundaries. The diffusive terms are discretized to second-order accuracy. The Smagorinsky constant is set to $C_s = 0.075$. Higher values lead to a higher damping which prevents the formation of large structures. On the other hand the computation gets unstable when using lower values.

Table 1: CONFIGURATION.

Name	comp. domain	grid points
TH-RL	25.7 x 6.28 x 20	257 x 16 x 70
TH-RH	25.7 x 6.28 x 30	257 x 16 x 80
CH-CH	25.7 x 6.28 x 20	257 x 16 x 70
channel flow	16 x 6.28 x 1	128 x 64 x 10

CONFIGURATION AND BOUNDARY CONDITIONS

A turbulent plane jet is simulated with a Reynolds number $Re = U_o B/\nu = 10000$ where U_o denotes the bulk velocitiy at the inlet, B the width of the nozzle and ν the kinematic viscosity. The extension of the computational domain (see Figure 1) in axial (x), homogeneous (y) and vertical (z) direction non-dimensionalized by the nozzle width and the number of points are listed in Table 1. The inlet conditions consising of top-hat profiles with superimposed random fluctuations are denoted 'TH-RL' and 'TH-RH' for a low *rms*−level of 0.5% and a mean *rms*−level of about 5%, respectively. The latter excitation is similar to channel turbulence and its distribution was set. For run 'CH-CH' the inlet velocity is extracted from a simulated channel flow with its charateristic mean profile, turbulent quantities and the developed correlations. Beyond the nozzle region the grid is smoothly stretched in vertical direction. The dimensionless time step is $\Delta t = 0.02$.

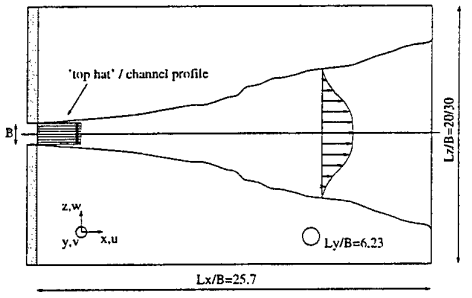


Fig. 1: COMPUTATIONAL DOMAIN.

The channel flow simulation is seperately performed at same Reynolds number. The grid resolution in vertical direction is prescribed by the jet simulation whose configuration parameters are determined by memory and computation time limitations. The mean velocity profile as well as the turbulence intensities show a fairly good agreement with measurements. However, the coarse vertical resolution causes discrepancies especially near the wall. It turned out to be necessary to resolve the spanwise direction with 64 points. The reduction to 16 points of the jet simulation is done by taking each fourth point. Thus the integral length scale information is maintained. The jet inlet profile is taken from the middle of the channel.

When setting the boundary conditions it is focused on not to prescribe any data known in advance, e.g. founded on similarity considerations. Neumann conditions for all velocities and the pressure were found to deal quite well with the arising negative velocities at the outflow boundary. At the upper and lower boundary the pressure is set to zero. The tangential velocities are constantly extrapolated. Periodic boundary conditions are applied in the homogeneous direction.

RESULTS AND DISCUSSION

The instantaneous results provided by the LES are averaged after reaching the beginning of the statistical stationary state. Statistical data is obtained from 1200 samples which is additionally averaged in the homogeneous direction. The presented results are non-dimensionalized by the centreline velocity $\overline{u_c}$ and the velocity half-width z_{05}. Mean quantities and turbulence intensities of the large scales are compared with measured data from Gutmark and Wygnanski (1973), Everitt and Robins (1978) and Thomas and Goldschmidt (1985) labeled 'GuWy', 'EvRo', 'ThoGo', respectively. These experiments had 'top-hat'-profiles with inlet turbulent intensities of about 0.2%. In the plots large scale fluctuations are denoted by a prime.

Spectral Considerations

The near field of a jet is characterized by the so-called 'potential core'. It covers the region in which the centerline velocity is unaffected. The potential core is bounded by the adjacent shear layers in which vortices are generated due to the instability of an initial fundamental frequency. At the end of the potential core the shear layers coalesce. Consequently this is the point where the centerline velocity begins to decay and the jet starts to spread.

On the basis of the fundamental instability linear and non-linear interactions of fluctuations cause the generation of further spectral modes, e.g. harmonics or subharmonics. The end of the potential core is dominated by a preferred frequency in the spectrum of the axial velocity. It represents the number of vortices per unit length of the jet (Namer and Ötügen (1988)). The non-dimensionalized form is the Strouhal number $St = fB/U_0$. In Figure 2 the frequencies of the peak values in the velocity spectra along the axis are to be seen. The profiles are shifted upstream when strongly exciting the ingoing velocities (runs TH-RH, CH-CH) without creating other characteristic frequencies downstream $x/B \approx 3$. This indicates that the instability mechanism, i.e. the order of the generated frequencies is neither affected by the mean inlet profile nor by the level of exciting.

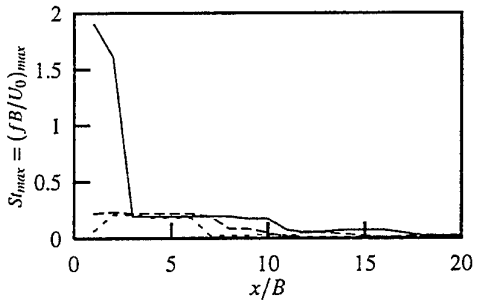


Fig. 2: MAXIMUM AMPLITUDE IN THE SPECTRUM OF AXIAL VELOCITY ALONG AXIS. — TH-RL; -- TH-RH; ··· CH-CH.

Mean Flow Field

The mean axial velocity profiles at $x/B = 20$ are presented in Figure 3. All simulations agree very well with measured selfpreserved profile. Selfpreservation is already reached downstream $x/B \approx 12$. Figure 4 shows the velocity half-width which grows linearly with nearly $0.1 \cdot x$ in all runs. The spreading rate of run CH-CH is somewhat lower as also observed by Hussain and Clark (1977) who experimentally investigated the influence of inlet conditions on plane jets. They also compared channel flow data and laminar profiles at the inlet.

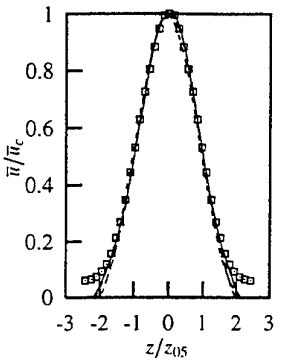


Fig. 3: MEAN AXIAL VELOCITY ACROSS JET — TH-RL; -- TH-RH; ··· CH-CH; □ GUWY.

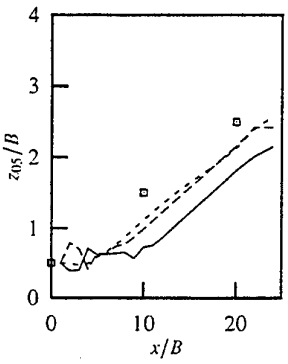


Fig. 4: VELOCITY HALF-WIDTH ALONG AXIS — TH-RL; -- TH-RH; ··· CH-CH; □ 0.1 x.

Hence the mean quantities such as the mean velocity and the spreading rate as well as the principal generation of jet-typical frequencies turn out to be independent of the inlet conditions even near the nozzle.

Compared to the simulation TH-LH the end of the potential core in the configurations TH-RH and CH-CH is located farther upstream. As aforementiond the order of the created frequencies does not differ. On the other hand the content of energy of the dominant frequencies is increased when superimposing higher fluctuations leading to an accelerated saturation of the participated harmonics and subharmonics. The preferred mode and consequently the end of the potential core is reached faster.

Results in the Near Field

The near field data provided by Gutmark and Wyngnanski (1976) is not relevant for the comparison in this work. In their work a Reynolds number of 30000 was used contrary to 10000 in the presented simulations. Namer and Ötügen (1988) investigated the influence of the Reynolds number on the near field. The far field results turned out to be independent.

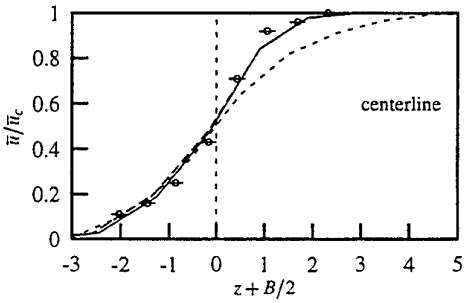


Fig. 5: MEAN AXIAL VELOCITY ACROSS JET NEAR THE NOZZLE ($x/B = 2$). — TH-RL; -- TH-RH; ··· CH-CH; ○ THOGO.

Figure 5 presents the mean axial velocity across the jet at $x/B = 2$. The block profiles of TH-RL and TH-RH are smerged due to the turbulent diffusive terms which are determined by gradients of the mean velocities. The velocity profiles are in good agreement with the measured ones of Thomas and Goldschmidt (1986). Similar results are obtained for $x/B = 3.5$ (not shown). Run CH-CH leads to a wider profile.

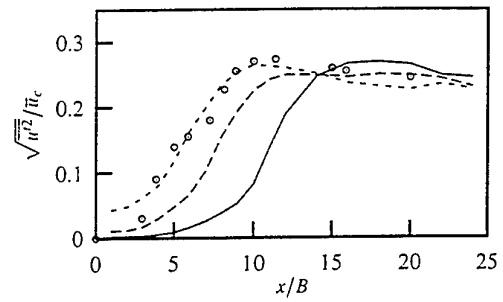


Fig. 6: STREAMWISE FLUCTUATIONS ALONG AXIS; — TH-RL; -- TH-RH; ··· CH-CH; o THOGO.

The development of the streamwise fluctuations along the axis of run CH-CH fits very well with the experiments of Thomas and Goldschmidt (1985), see Figure 6. In run TH-RH the increase of the disturbance level sets on further downstream. The difference between the cacluations TH-RH and TH-RL is due to the minor exciting level of the latter one. With decreasing Reynolds numbers the peak of the axial fluctuations near the exit became more distinct (Thomas and Goldschmidt (1985)).

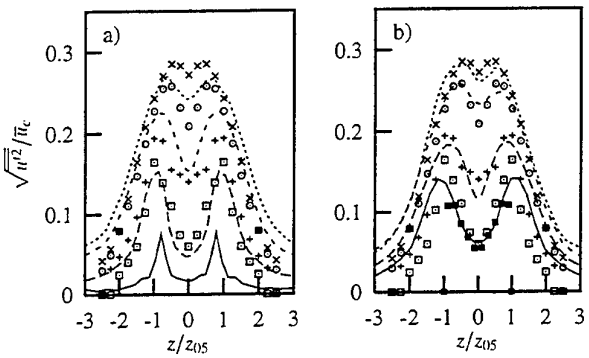


Fig. 7: STREAMWISE FLUCTUATIONS NEAR NOZZLE a) RUN TH-RH, b) RUN CH-CH; LINES: SIM., POINTS: THOGO; —, □ $x/B = 3.5$; --,+ $x/B = 5$; ···,o $x/B = 8$; ····,× $x/B = 11$; ■ CHANNEL FLOW

Figure 7a presents the profiles in the near field of the jet at $x/B = 3.5$, 5, 8 and $x/B = 11$.

The measurements of Thomas and Goldschmidt (1985) show that that there is a strong increase of axial fluctuations on the first nozzle widths downstream the exit. Starting from the initial *rms*−value of about 0.2% the measured intensity level reaches 5% on the centerline at $x/B = 3.5$. In the shear layer the fluctuations are approximately 50 % higher than the channel fluctuations near the wall. This indicates a strong production of axial fluctuations on the first nozzle widths downstream the exit.

It is to be seen that the shear layer fluctuations of run TH-RH downstream $x/B = 5$ nearly reaches the maximum value of the shear layer whereas the centerline value is underpredicted. Concerning run TH-RL all streamwise fluctuations near the nozzle (not shown) are far too low.

The excellent agreement in the near field characteristics from the exit to $x/B \approx 11$ is to be seen in Figure 7b. This result is somewhat surprising. Firstly the initial *rms*-levels of CH-CH and TH-RH are the same. Secondly Thomas and Goldschmidt (1985) got flat initial velocity profiles with a fluctuation intensity of less than 0.2 %. Thus the jet underwent a transition-like process. Therefore this configuration resembles more run TH-RL and TH-RH, respectively, contrary to the fully developed inflow in CH-CH.

The production of axial fluctuations is determined by mean gradients of the velocity. The mean axial velocity is captured quite well by the simulations with even better results for TH-RL and TH-RH. Therefore it is assumed that the essential features of the turbulence production in the shear layers are represented.

The transport of turbulence intensity from its location of production in the shear layers to the core of the jet also seems to be sufficiently represented because of the good agreement between run CH-CH and the measurements over the long distance from $x/B = 3.5$ to $x/B = 11$.

The reason can be found in the prescribed initial excitation in combination with the purely dissipative Smagorinsky model. The temporal excitation is characterized by a typical time scale τ. The Taylor hypothesis yields the related length scale $L = \overline{u}_{inlet}\tau$. With the assumption $\varepsilon = k^{3/2}/L$ one obtains an expression for the dissipation

$$\varepsilon_{inlet} \sim \frac{I^3 \overline{u}_{inlet}^2}{\tau}, \tag{8}$$

where the turbulent kinetic energy k is substituted by the excitation level I. I corresponds to the *rms*−value which is equal in the simulations TH-RH and CH-CH. In TH-RH and TH-RL the fluctuations are superimposed at each time step Δt_{Sim} of the simulation. Hence, the typical time scale can be determined by $\tau \approx 0.5\Delta t_{Sim} \ldots \Delta t_{Sim}$. This is in contrast to run CH-CH where τ is excactly the integral time scale $T_{Channel}$ of the developed channel flow. Because of $\Delta t_{Sim} \ll T_{Channel}$ one obtains

$$\varepsilon_{TH-RL/H} \gg \varepsilon_{CH-CH}. \tag{9}$$

This may explain the low fluctuation intensities when exiciting randomly.

Figure 8 shows time series of the fluctuations of the centerline velocity for different x/B−positions. The same excitation levels are to be seen at $x/B = 0.1$. At $x/B = 0.3$ the randomly generated fluctuations are smoothed so that the effective *rms*-level of the inlet flow is strongly reduced resulting in a delayed onset of turbulent intensities. In contrast to this behaviour the profile of $u'(t)$ of run CH-CH is maintained until $x/B \approx 1$. Thus approximation 9 is confirmed. At $x/B = 8$ time correlations have developed due to the generation of large scale structures.

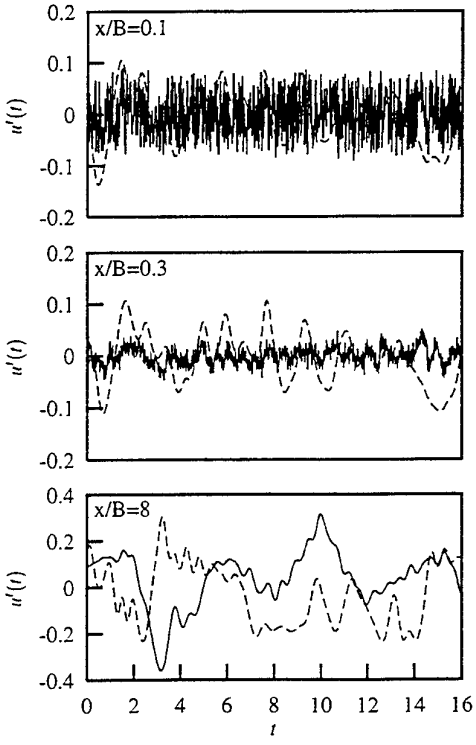


Fig. 8: DEVELOPMENT OF STREAMWISE FLUCTUATIONS AT $x/B = 0.1, 0.3$ AND $x/B = 8$. — TH-RH; -- CH-CH.

It is to be investigated if less-dissipative subgrid-scale models and random excitations with defined time scales yield better results. However, it is believed that the laminar-like disturbances found in experiments do not have the character of white noise. The spectrum of the axial velocity of Thomas and Goldschmidt (1985) contains distinct frequencies $St = 0.25, 0.34$ and $St = 0.46$ already at $x/B = 1$. The corresponding function of the velocity in time is therefore rather smooth which is approximately represented by the developed channel flow fluctuations.

Analysis of Structures

The isosurfaces of the vorticity component ω_y of run CH-CH and TH-RL are shown in Figure 9a and 9b, respectively. Compared to run TH-RL the higher excitation level of run CH-CH leads to fluctuations of the vorticity right behind the exit. This corresponds to higher values fo the kinetic energy of the large scales. The break-down of vortices occurs much faster causing the aforementioned faster increase of the turbulent intensities. The forming structures of run CH-CH look smoother and are orientated in the streamwise direction more regularly. Until $x/B = 25$ these differences maintain which let expect that the turbulent intensities in this region are still influenced by the inlet conditions.

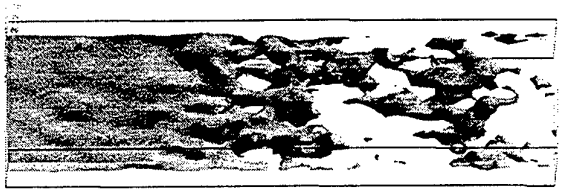


Fig. 9a: ISOSURFACE OF VORTICITY ω_y (RUN CH-CH).



Fig. 9b: ISOSURFACE OF VORTICITY ω_y (RUN TH-RL).

Results in the Far Field

Figure 10 a)-d) presents the turbulence intensities as well as the shear stress in the far field of the jet ($x/B = 20$). They are compared with the selfpreserved profiles of Gutmark and Wygnanski (1976) and Everitt and Robins (1978).

The calculated axial fluctuations lie within the experimental scatter. Concerning the spanwise intensities good results are obtained in TH-RH and CH-CH whereas the lateral fluctuations are overpredicted by all simulations. The turbulent intensities of the simulation TH-RL are approximately equal or higher than those of TH-RH and strongly overpredict the measured level for $\overline{v'^2}$. The same trend is to be seen concerning the results of TH-RH and CH-CH. It is believed that the lack of excitation at the nozzle hinders the break-down of the vortices to small-scale turbulence resulting in an overprediction of kinetic energy at the large scales.

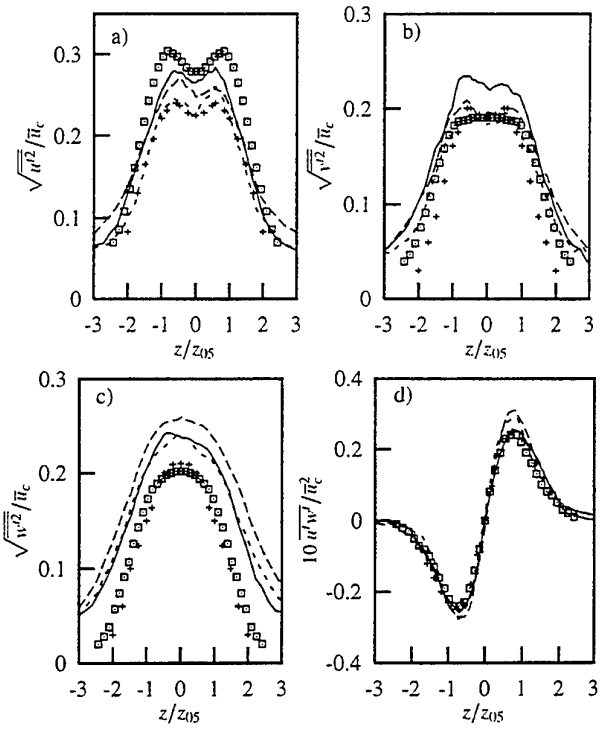


Fig. 10: TURBULENT INTENSITIES ACROSS JET (C_s = 0.075). a) STREAMWISE FLUCT., b) SPANWISE FLUCT., b) LATERAL FLUCT., d) SHEAR STRESS — TH-RL; -- TH-RH ; ··· CH-CH; □ GUWY; + EVRO.

In shear stress (Figure 10 d) is captured quite well by all simulations corresponding to the correct prediction of the spreading rate.

Variation of the Smagorinsky Constant

Figure 11 shows that the inlet conditions affect the turbulence intensities until $x/B = 25$. In order to evaluate the influence of the Smagorinsky constant computation TH-RH is performed with $C_s = 0.1$. An overall improvement in the far field is achieved (Figure 11).

CONCLUSION

A large eddy simulation of a turbulent plane jet with a 'top hat' profile with superimposed randomly generated disturbances was compared with a simulation in which the inflowing time-dependent turbulent profiles were extracted from a pre-calculated channel flow computation.

Selfpreserved profiles of the axial velocity develop already downstream $x/B = 11$. Mean quantities like the normalized mean axial velocity profile as well as the spreading rate turned out to be independent of the inlet conditions. As far as this first investigation shows the mean profile of the inlet velocity have a minor influence in the near field due to a rather fast turbulent diffusive smerging.

Random excitations together with the use of the dissipative Smagorinsky model lead to a decrease of the effective disturbance level. Apparently the implicit prescription of a time scale yields high dissipation rates and therefore immediate smoothing right behind the nozzle. The onset of turbulence fluctuations is delayed. When prescribing channel flow turbulence with its characteristic integral time scale an excellent agreement with measured turbulent intensities near the exit is achieved.

Additionally measurements show that even with laminar-like inflow conditions typical frequencies are built up right behind the nozzle. This character of the developing flow is better rep-

resented when prescribing disturbances with distinct frequencies represented by channel flow turbulence.

The turbulent intensities in the far field ($x/B = 20$) still depend on the inlet conditions. Far low excitation levels at the exit yield higher large scale fluctiuations as a lack of sufficient small-scale turbulence.

However, more detailed studies and especially a more extended computation region on axial direction should be performed to gain more insights.

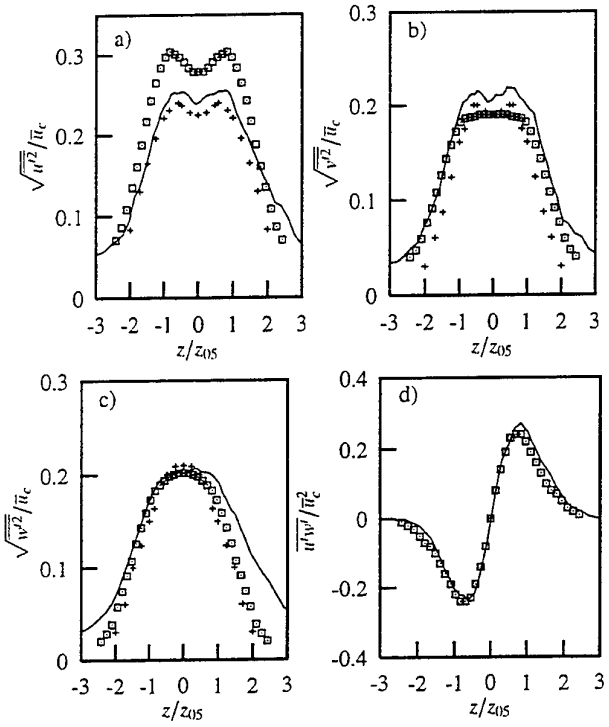


Fig. 11: TURBULENT INTENSITIES ACROSS JET (C_s = 0.1). a) STREAMWISE FLUCT., b) SPANWISE FLUCT., b) LATERAL FLUCT., d) SHEAR STRESS — TH-RH; □ GUWY; + EVRO.

REFERENCES

Crow, S. C., and Champagne, F. H., 1971, "Orderly Structure in Jet Turbulence," *J. Fluid Mech.*, Vol. 48, part 3, pp. 547–591.

Dai, Y., Kobayashi, T., and Taniguchi, N., 1995, "Investigation of Organized Structures in Plane Turbulent Jet Flow by Using Large Eddy Simulation," *Proceedings, 10th Symposium on Turbulent Shear Flows*, Vol. 1.

Everitt, K. W., and Robins, A. G., 1978, "The Development and Structure of Turbulent Plane Jets," *J. Fluid Mech.*, Vol. 88, part 3, pp. 563–583.

Gutmark, E., and Wygnanski, I., 1976, "The Planar Turbulent Jet," *J. Fluid Mech.*, Vol. 73, part 3, pp. 465–495.

Heskestad, G., 1965, *J. Appl. Mech.*, Vol. 32, p. 721.

Hoffman, G., 1996, "Engineering Application of Large Eddy Simulation to Turbulent Free and Wall-Bounded Shear Layers," Ph.D. Thesis, TU München, Germany.

Hsiao, F.-B., and Huang, J.-M., 1990, "On the Evolution of Instabilities in the Near Field of a Plane Jet," *Phys. Fluids A*, Vol. 2 (3), pp. 400–412.

Hussain, A.K.M.F., Clark, R., 1977, "Upstream influence on the near field of a plane turbulent jet." *Phys. Fluids*, Vol. 20, (9), pp. 1416–1426.

Launder, B. E., Reece, G. J., and Rodi, W., 1975, "Progress in the Development of a Reynolds-Stress Turbulence Closure," *J. Fluid Mech.*, Vol. 68, part 3, pp. 537–566.

Meinke, M., Abdelfattah, A., Rister, Th., and Schulz, C., 1996, "Simulation of Turbulent Flows for Complex Geometries," *Finite Volumes for Complex Applications. Problems and Perspectives*, F. Benkhaldoun, and R. Vilsmeier, eds., pp. 99–114.

Miller, D. R., and Comings, E. W., 1957, "Static Pressure Distribution in the Free Turbulent Jet," *J. Fluid Mech.*, Vol. 3, pp. 1–10.

Namer, I., and Ötügen, M. V., 1988, "Velocity Measurements in a Plane Turbulent Air Jet at Moderate Reynolds Numbers," *Exp. Fluids*, Vol. 6, pp. 387–399.

Pfuderer, D. G., Eifert, C., and Janicka, J., 1996, "A Comparison of Linear and Non-Linear Second-Order Closure Models Applied to Plane and Round Jets," *Proceedings, Engineering Turbulence Modelling and Experiments*, W. Rodi, and G. Bergeles, eds., Elsevier, Vol. 3.

Schmitt, L., 1982, "Numerische Simulation turbulenter Grenzschichten (LES). Teil 1: Grundlagen," Bericht Nr. 82/2, Lehrstuhl für Fluidmechanik, TU München, Germany.

Schumann, U., 1975, "Subgrid Scale Model for Finite Difference Simulations of Turbulent Flow in Plane Channels and Annuli," *J. Comp. Phys.*, Vol. 18.

Shih, T.-H., Chen, J.-Y., and Lumley, J. L., 1992, "Second-Order Modelling of Boundary-Free Turbulent Shear Flows," AIAA *Journal*, Vol. 30 (6), pp. 1553–1560.

Smagorinsky, J., 1963, "General Circulation Experiments with the Primitive Equations," *Mon. Weath. Rev.*, Vol. 91, p. 99.

Thomas, F. O., and Goldschmidt, V. W., 1986, "Structural Characteristics of a Developing Turbulent Planar Jet," *J. Fluid Mech.*, Vol. 163, pp. 227–256.

Weinberger, C., and Janicka, J., 1996, "Large Eddy Simulation of a Turbulent Planar Jet," *Finite Volumes for Complex Applications. Problems and Perspectives*, F. Benkhaldoun, and R. Vilsmeier, eds., pp. 503–510.

LARGE EDDY SIMULATIONS OF THREE-DIMENSIONAL SPATIALLY EVOLVING ROUND JETS

G.Urbin[1], **C.Brun**[1,2], **O.Métais**[2]
[1] CEA DRN/DTP
17 rue des Martyrs
38054 Grenoble cedex 09

[2] LEGI/IMG
BP53
38041 Grenoble-Cedex 09
France

INTRODUCTION

Jets are prototype shear flows well suited for the study of large-scale and microscale turbulent mixing. In the last five years, the progress in the experimental methods for detection and identification has made possible a detailed investigation of the complex three-dimensional coherent vortices imbedded within the flow. For instance, the influence of the entrainment of the secondary streamwise vortices has been studied by Liepmann and Gharib (1992). On the numerical side, several simulations of two-dimensionnal or temporally evolving jets have been performed. Very few have however investigated the three-dimensionnal spatial development of the round jet. We here present a statistical and topological numerical study of the spatial growth of the round jet from the nozzle up to twelve diameters downstream. The use of large-eddy simulations (LES) techniques allow us to reach high values of the Reynolds number: here, Re is taken around 20000. The advantage of these techniques is that high Reynolds number flows can be simulated with a moderate number of resolution points and a reasonable computer cost. Our goal here is to demonstrate the ability of the LES to properly reproduce the coherent vortex dynamics in the transitional region of the jet. We also show the possibility of controlling the jet behaviour by manipulating the inflow conditions.

SUBGRID-SCALE MODELS AND NUMERICAL TOOLS

One of the major challenge for the LES is to allow the laminar-turbulent transition to take place. Indeed, most of the subgrid-scale models dissipate the kinetic energy even if the flow is not turbulent, and therefore prevents the proper growth of the instabilities. Here, we have used two distinct subgrid-scales models which act only in the regions where the flow presents an important level of small-scale three-dimensional turbulence. These are modified versions of the structure function model originally proposed by Métais and Lesieur (1992): the "selective" and "filtered" structure-function models (see Lesieur and Métais, 1996, for details). Those two models have demonstrated their ability to simulate the transition towards turbulence in flows such as the weakly-compressible boundary-layer flow over a flat plate (see Ducros *et al.*, 1996), or the spatially growing mixing layer (Silvestrini, 1996). Note that the dynamic model proposed by Germano *et al.* (1991) has also managed to simulate transitional shear-flows (see Abba et al 1996, for the round jet).

In the present work, we compare the results given by two very distinct numerical codes solving the three-dimensional incompressible Navier-Stokes equations:

- The first code is an industrial software called TRIO-VF developed for thermal-hydraulics applications at the Commissariat a l'Energie Atomique de Grenoble by Grand *et al.* (1988). It has been thoroughly validated in many LES of various flows (see e.g. Silveira-Neto *et al.*, 1993, for the backward facing step). It uses the finite volume method on a structured mesh. Temporal discretisation is a first order Euler scheme; spatial discretisation is a third order Quick Sharp scheme. Zero pressure gradient is assumed at the outflow.
- The second code (SPECOMPACT) mixes 2D pseudo-spectral methods in the radial homogeneous flow direction and 6^{th} order compact finite-differences schemes (see Lele, 1992) in the axial one. Non-reflective outflow boundary conditions are approximated by a multi-dimensional extension of Orlansky's discretization scheme. Temporal discretization is performed by means of a low-storage 3rd order Runge-Kutta scheme (see Gonze, 1993, for details). The high-precision of the numerical methods used in this second code implies a very low numerical diffusion allowing to precisely study the subgrid-scale models effects.

NUMERICAL EXPERIMENTS

The experimental studies by Michalke and Hermann (1982) have clearly pointed out the capital effect of the inflow momentum boundary layer thickness θ and of the ratio D/θ (D : jet diameter) on the jet donwstream development. It was shown that the detailed shape of the mean velocity profile strongly influences the nature of the coherent vortices appearing near the nozzle (see Cohen and

Wygnanski, 1987): either axisymmetric structures (vortex rings) or helical structure can indeed develop. Here, we compare two simulations (with or without coflow) at $D/\theta = 20$ and confront our numerical results with experimental data. We have restrained ourself to relatively small values of D/θ after having checked that a correct resolution of the shear zone at the border of the nozzle is crucial to correctly reproduce the initial development of the instabilities.

Cartesian coordinates have been prefered to cylindrical coordinates since the former will allow us to consider, in future works, more complex geometries of industrial interest (multi-jets for instance). Furthermore, phenomena like side jets, can be well-resolved even in regions far from the jet axis.

We consider a computational domain starting at the nozzle and extending up to $16D$ downstream (for the TRIO simulation) and to $10D$ downstream (for the SPECOMPACT simulation). The section perpendicular to the jet axis consists of a square $10D * 10D$, which has been shown to be sufficient to avoid jet confinement. We use a coarse spatial resolution of $48 * 48 * 88$ points for TRIO taking advantage of the possibility of mesh refinement within the jet shear-layer (stretched mesh). Conversely, $288*288*101$ points are used for SPECOMPACT and the mesh is regularly distributed.

The two runs do not start with the same inflow conditions. For the SPECOMPACT run, the mean and fluctuation velocity profiles are taken from experimental results at $Re = 21000$ performed by Djeridane (1994). The fluctuations, which correspond to a fully-developed turbulent pipe flow of turbulent intensity 15%, are modeled by stochastic perturbations. For the TRIO run, the jet is forced upstream by a top-hat profile to which is superposed a weak 3D white noise ("natural forcing"). The intensity of the noise mimics experimental measurements performed at the nozzle (see Liepmann and Gharib, 1992 for instance): we choose 1% for the rate of turbulence level at the center and 5% near the border. The Reynolds number is 25000. With the TRIO code, the case of the jet excited with specified inflow perturbations at the nozzle will be presented in the laset section.

STATISTICAL RESULTS

In order to reach a good statistical convergence, the statistics evaluation is performed over a period of 100 D/W_{noz} with the TRIO code and of 40 $D/(W_{noz} - W_{cof})$ with the SPECOMPACT code (W_{noz} inlet bulk velocity; W_{cof} coflowing velocity). Statictics are compared with experimental results. Figure 1a shows the downstream evolution of the mean axial velocity on the jet axis. The fall around $Z/D = 5$ (SPECOMPACT) and around $Z/D = 6$ (TRIO) indicates the end of the potential core. The computed values falls within the experimental range. The subsequent velocity decrease is somewhat overestimated by the LES indicating an overprediction of the jet spreading rate. This is more pronounced for the results with the TRIO code: this may be due to the different inflow conditions for the two runs. Notice that the same overestimation has been observed in the recent LES by Olsson and Fuchs (1996) using the dynamic model proposed by Germano *et al.* (1991). The late decay rate corresponds however with the experimental one.

The mean radial velocity profile (Figure 2) confirm the previous tendencies. At first, both the jet expansion and the axial velocity decays are underestimated by the numerical simulations. The two quantities are subsequently overestimated as compared with the experimental results.

The compilation of various laboratory experiments on turbulent round jets reveals an important scatter in the experimental data for the downstream evolution of fluctuating quantities like the r.m.s. axial velocity. This in-

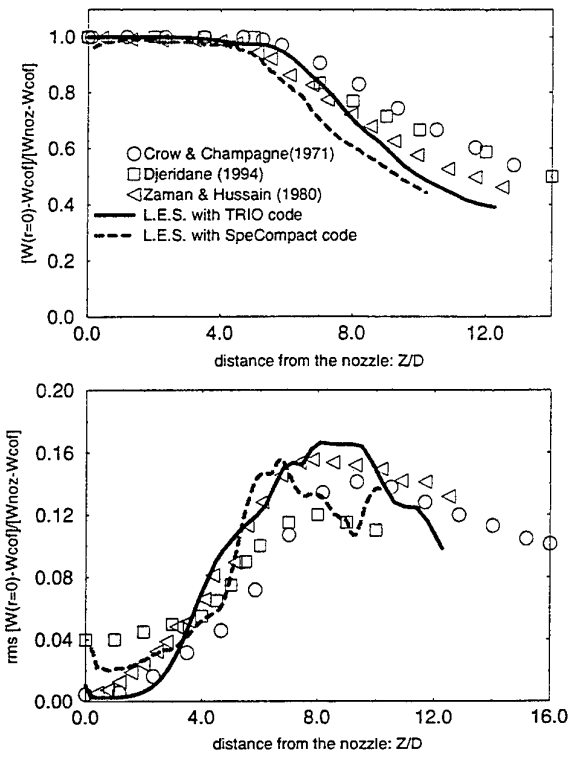


Figure 1: Numerical and experimental results comparisons. Centerline axial velocity: time averaged (a) and r.m.s.(b) (W_{cof} is the coflowing velocity, W_{noz} is the inlet bulk velocity)

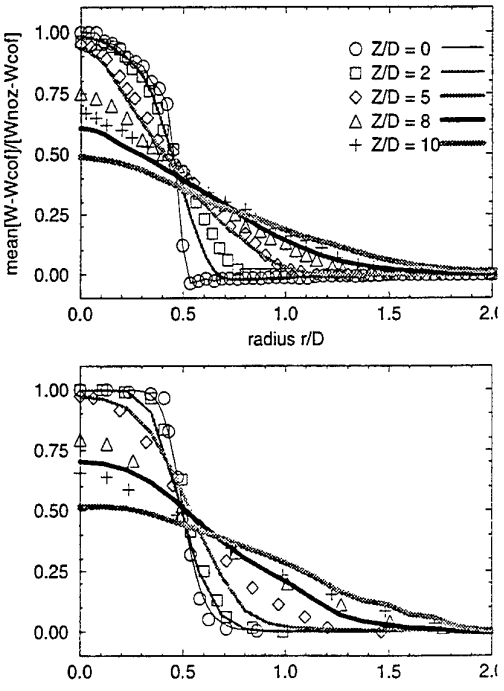


Figure 2: Transversal mean axial velocity profiles at various stations Z/D. Top: SPECOMPACT code (lines) compared with Djeridane's (1994) experiment (symbols). Bottom: TRIO code (lines) compared with Moore 's (1977) experiment.

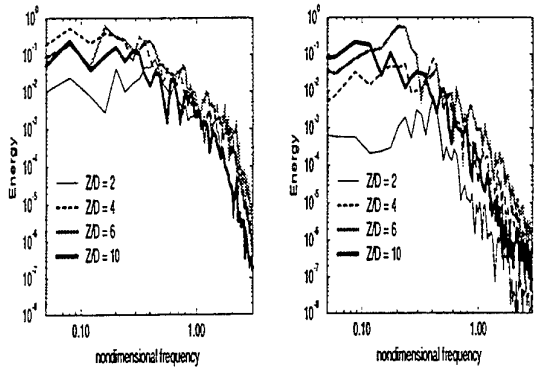


Figure 3: Frequency spectra of the fluctuating axial velocity at different downstream locations and around $r/D = 0.5$. left: SPECOMPACT; right: TRIO

dicates a very strong sensitivity of the jet developement to inflow fluctuations. Such a sensitivity will be clearly demonstrated in the last sections devoted to the controlled jet. Considering our "artificial" inflow conditions (white noise), we may consider that the evolution of the r.m.s. fluctuating axial velocity away from the nozzle is well reproduced by the numerics (see Figure 1 b). In an adjustement stage, the inlet fluctuations first decrease. Further away from the inlet, the flow becomes unstable within the jet shear layer leading to a strong increase of the fluctuations. Those reach a maximum intensity around $Z/D = 6$ for the SPECOMPACT case and $Z/D = 8$ for the TRIO case. Further downstream, the fluctuation amplitude decays, sign of a (almost) fully-developped turbulent flow.

Spectral analysis

For the two computations, we have applied fast Fourier transform to periodized temporal longitudinal velocity samples taken in the shear layer zone (around $r/D = 0.5$) at $Z/D = 2$, 4, 6 and 10 (Figure 3). Nondimensionalization is based on the jet diameter and the inlet bulk velocity providing a Strouhal number $St = fd/W_{noz}$. The same behaviour is observed in both simulations. For $Z/D \geq 2$ a first frequency peak emerges around $St = 0.4$ in both cases. A subharmonic energetic frequency is also present around $St = 0.2$. The dominant observed frequency is in good agreement with the experimental value ($0.3 < Str_D < 0.5$ Hussain & Zaman 1981). Past the potential core ($Z/D = 6$), the energy spectrum reaches a maximum amplitude, and the subharmonic peak around $St = 0.2$ has become dominant. This indicates vortex pairing yielding large-scale structures advected in the jet. At $Z/D = 10$, the subharmonic frequency saturates and the high frequency energy decreases due to dissipative effects. Note that a $f^{-5/3}$ Kolmogorov range is not reached at the outlet of the computational domain indicating that a fully developped turbulent state is not yet achieved. The spectral slope is steeper than 5/3 with approximately $f^{-2.5}$ (SPECOMPACT case) and f^{-4} (TRIO case) behaviours. The steeper slope obtained with the TRIO code may be associated with the coarser grid inducing a high frequency damping outside the refined mesh regions.

COHERENT VORTICES

We here characterize the coherent structures with the aid of both high vorticity regions and low-pressure regions. Figure 4 a) and b) (TRIO case) shows that the Kelvin-Helmholtz instability along the jet border yields, further downstream, vortex structures mainly consisting in axisymmetric rings (Figure 4 a). We have found that these structures are, however, not always present and al-

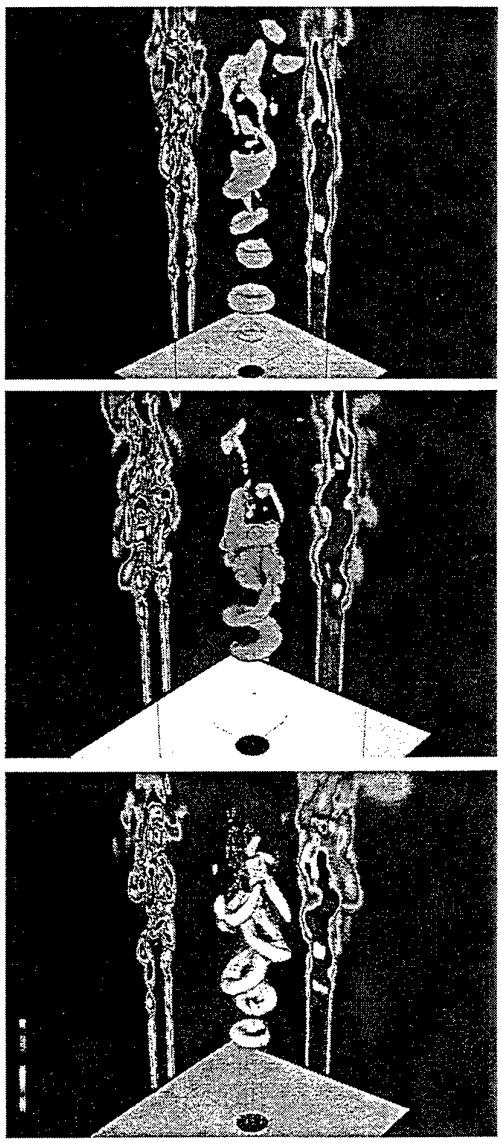


Figure 4: Natural jet: instantaneous visualization (TRIO-VF code) at three different times. Low pressure isosurface in light gray; YZ cross-section (through the jet axis) of the vorticity modulus ($min = 0$; $max = 8W_{noz}/D$); XZ cross-section of the velocity modulus ($min = 0$; $max = 1.2W_{noz}$).

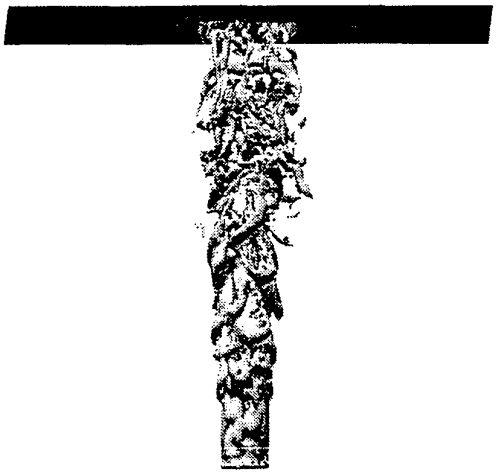


Figure 5: Instantaneous visualization: vorticity modulus isosurface ($max = 3(W_{noz} - W_{cof})/D$), and XY cross-section at the outlet $Z/D = 10$ (SPECOMPACT code).

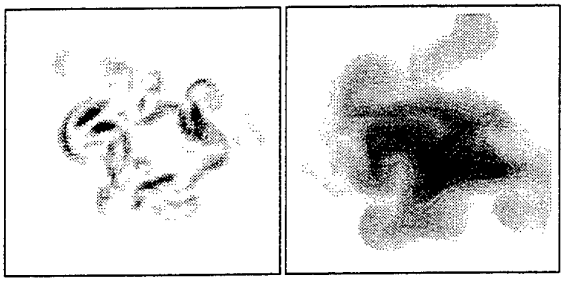


Figure 6: Focus on transversal cross-sections of the vorticity modulus (left) and axial velocity (right) at $Z/D = 4.5$ (SPECOMPACT code).

ternate with vortices of helicoidal shape (Figure 4 b). We then follow the structures further downstream. The 3D low pressure isosurface visualization shows an original vortex arrangement subsequent to the varicose mode growth: the "alternated-pairing". We have checked that, during their advection downstream, the vortex rings axis tends to deviate from the jet axis. The inclination angle of two consecutive vortices appears to be of opposite sign eventually leading to a local pairing with an alternate arrangement (Figure 4 c). Note that such a structure was previously observed by Comte *et al.* (1992) in a direct simulation of a temporally evolving round jet at low Reynolds number ($Re = 2000$).

Figure 5 displays a vorticity modulus isosurface obtained in the SPECOMPACT run. We observe similar topological organization as on Figure 4 c) with alternatively inclined vortex loops. In the vorticity field close to the nozzle, a detailed investigation of the longitudinal vorticity reveals pairs of counter-rotating vortices linked with the primary rings and responsible for the creation of side jets (Figure 6 a). These yield a transverse finger shape stretching of the velocity field (Figure 6 b)).

EXCITED JET

As opposed to the previous "natural" unexcited jet, we now excite the jet with specified inflow perturbations at the nozzle. The simulations are performed with the TRIO code.

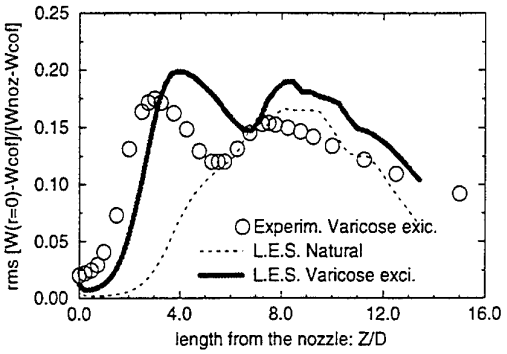


Figure 7: Jet with varicose mode excitation. Comparison with experimental results of Crow and Champagne (1971): centerline axial velocity r.m.s. fluctuations

Varicose excitation

Numerous experimental visualizations have been performed with an axisymmetric excitation of the jet. Crow and Champagne (1971) were the first to notice that the jet response is maximal with a preferred mode frequency corresponding to Str_D between 0.3 and 0.5. We here reproduce such an excitation of the varicose mode by imposing a periodic perturbation (alternatively low-speed and high speed) to the axial velocity at the nozzle:

$$W(r) + \epsilon\, W_{noz}\, sin\left(\frac{Str_D W_{noz}}{D} time\right) \qquad (1)$$

This is superposed to the white random perturbation of the previous case. The periodic fluctuation level is $\epsilon = 1\%$, and its imposed frequency corresponds to $Str_D = 0.35$.

Comparisons of the axial velocity fluctuations with experimental results, show that, as opposed to the unexcited jet, a strong and fast amplification of the instability appears, resulting in a first peak at $Z/D = 4$ (Figure 7). This saturation is followed by a decrease until a second peak is reached. Note that the above behaviour is in good correspondance with experimental observations.

The visualizations show that the varicose mode is now present at every instant at the beginning of the jet $Z/D < 6$. The vortex structures are more intense than in the natural case with well marked and organized pressure trough (Figure 8 top). The Figure 8 (bottom) shows that the rings resulting from the varicose mode are linked together with longitudinal vortices. These have already been observed experimentally at moderate Reynolds number flow (Lasheras, Lecuona and Rodriguez, 1991; Monkewitz and Pfitzenmaier, 1991, and Liepmann and Gharib, 1992). Here, we also find them at our high Reynolds $Re = 25000$. These longitudinal vortices are known to entrain and eject fluid outside, thus creating transverse side jets and "branches". The latter were studied numerically, in temporal simulations of Martin and Meiburg (1991), Abid and Brachet (1992) at low Reynolds number. Notice that, in these works, they were directly excited with a specified azimuthal excitation of the vortex rings: this is at variance with the present study. Here, we evaluate their number to be between 3 to 7 at the end of the potential core. Furthermore, the maximum vorticity magnitude within the longitudinal structures is about 40% of the vorticity of the associated rings.

One possible explanation for the origin of these longitudinal vortices is an azimuthal oscillation of the vortex lines at the stagnation points between consecutive primary rings followed by a strong stretching mechanism by the latter (Lasheras, Lecuona and Rodriguez, 1991). The number of longitudinal structures should therefore be directly linked

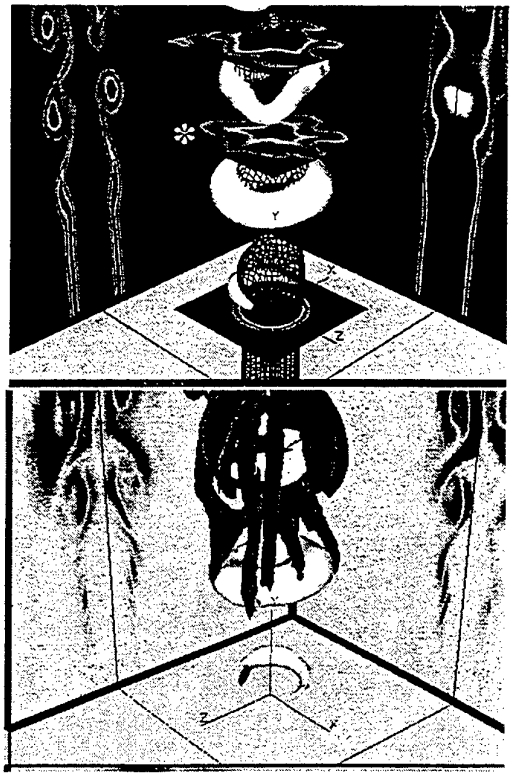


Figure 8: Jet with varicose mode excitation: top) same visualizations as Figure 6 plus three cross-sections of the axial velocity component in planes perpendicular to the jet axis. bottom) black and grey: positive and negative longitudinal vorticity isosurfaces corresponding to $\omega_z = \pm 1.2 W_{noz}/D$. YZ and XZ cross-sections (through the jet axis) of the longitudinal vorticity component ($min = -4.W_{noz}/D$; $max = +4.W_{noz}/D$

to the azimuthal oscillations of the primary rings. Many studies have been devoted to the instability of isolated vortex rings. Widnall *et al.* (1974) have predicted that, for a vortex ring of radius R and of core size a, the most unstable azimuthal mode n is given by $n = R/a\alpha$. α is equal to 2.7, for a smooth vorticity distribution inside the core, given by

$$\omega(r) = [(|r| - R)^2 - a^2]^2 \qquad (2)$$

R_{ring} and a_{ring} deduced from the numerical results are respectively $R_{ring} = 0.59D$ and $a_{ring} = 0.11D$. For this parameter couple (R_{ring}, a_{ring}), the ring should develop an instability with approximately 15 waves, as opposed to our 3 to 7. Further investigations are therefore needed to determine the nature of the azimuthal instability giving rise to the longitudinal vortices.

Alternated pairing excitation

As mentioned above, when the toroidal structures are advected downstream, they display alternated localized pairings. Since this vortex arrangement seems to be characteristic of the jet topology, we next propose to preferentially excite it from the nozzle. The excitation method is based on the same principle as previously described.

$$W(r) + \epsilon\, W_{noz}\, sin\left(\frac{Str_D W_{noz}}{D} time\right)\, sin\left(\frac{Y}{D}\right) \qquad (3)$$

where $r = \sqrt{X^2 + Y^2}$ is the radial distance from the jet axis. The perturbation intensity is here $\epsilon = 5\%$. Its frequency is the same as before except that now half of the

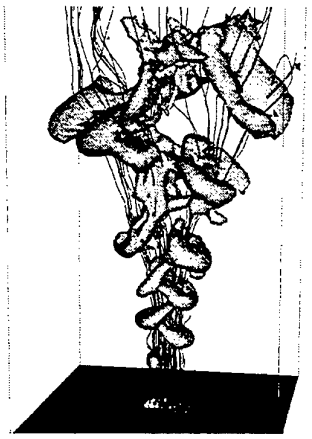


Figure 9: Bifurcation of a "Alternated pairing" mode excited jet. instantaneous vizualisation of streamlines emerging from the nozzle. Low pressure isosurface in grey ($P = 25\% P_{min}$).

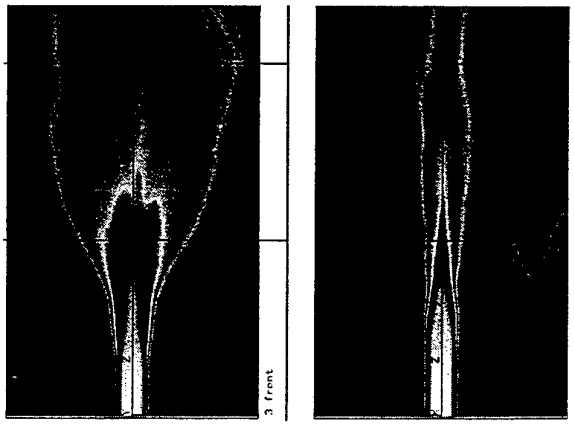


Figure 10: "Alternated pairing" mode excited jet. Time averaged axial velocity (only 55 adimensional times are represented): a) XZ plane; b) YZ plane ($min = 0$; $max = 1.0 W_{noz}$)

jet presents a speed excess, while a speed defect is imposed on the other half, and this alternatively. Note that this perturbation has a preferred direction, chosen along the Y axis. The resulting structures are shown on Figures 9.

Inclined vortex rings exhibiting localized pairing persist far downstream till $Z/D = 10$. The striking facts are the very distinct spreading rates in the Y and X directions. The spreading rate is here to be taken to be the angle between the jet borders at half velocity ($W(r_{1/2}) = W(r = 0)/2$). In the XZ plane, the spreading rate is increased, and reaches $50° - 55°$ at $Z/D = 6$. Conversely, it is close to zero ($3°$ at $Z/D = 6$) in the YZ plane (Figure 10). Notice that, because of such a development, this jet is now affected by the lateral boundaries downstream $Z/D = 8$.

The present jet exhibits strong similarities with the "bifurcating" jet of Lee and Reynolds (1985). They have experimentally showed, that a properly-combined axial and helical excitations can cause a turbulent round jet to split into two distinct jets. Such a bifurcation is indeed observed here (see figure 10). The streamlines originally concentrated close to the nozzle tend to clearly separate for $Z/D > 4$. Furthermore, the alternatively inclined vortex-rings seem to separate and move away from the jet centerline to form a Y-shaped pattern. As in the present simulation, the exprimental jet was observed to rapidly spread in

one preferential axial plane, while spreading was inhibited in the perpendicular plane. The measured spreading rate in the former plane was $40° - 70°$, depending on the excitations characteristics. This is in good correspondance with our computed value. A more precise comparison would require to push our lateral boundaries away. One of the important technological application of this peculiar excitation resides in the ability to polarize the jet in a preferential direction.

CONCLUSION

We have simulated the three-dimensional spatial growth of a free-round jet using L.E.S. based upon the filtered and selective structure function subgrid-scale models. By using two distinct numerical codes, we were able to investigate the influence on the results of the numerical discretization and of the grid stretching. In the natural jet case (white noise perturbation at the inflow), we have studied the influence of the inflow mean velocity and perturbation velocity profiles on the flow developement. With both numerical codes, we are able to reproduce the primary and secondary vortex coherent structures and to obtain a good statistical agreement with experimental results. As far as coherent structures dynamics are involved, the LES show an alternance between axisymmetric vortex rings and helicoidal structures. Further downstream, the rings yield an original flow structure consisting in localized alternated pairings. In agreement with several experimental results, we have next clearly showed how a specific excitation (axisymmetric, alternate, etc) of the jet at the nozzle renders possible the control of the jet vortical structures and yields a strong modification of its statistics. This demonstrates that LES constitute a very good tool to validate flow control techniques.

Acknowledgements : Some of the computations were carried out at the IDRIS (Institut du Développement et des Ressources Informatique Scientifique, Paris). Part of this work was supported by the DRET under contract 95/2557A.

REFERENCES

Abba, A., Bucci, R., Cercignani, C., and Valdettaro, L., 1996, "Large eddy simulation of turbulent jet: Test case LES3", In *The second ERCOFTAC workshop on direct and large eddy simulation*, Grenoble 16-19 september 1996, Kluwer Academic Publishers.

Abid, M., and Brachet, M.E., 1992, "Mécanisme de génération des jets latéraux dans les jets axisymetriques forcés", *C.R.Acad.Sci.Paris.*.

Cohen, J., and Wygnansky I., 1987, "The evolution of instabilities in the axisymmetric jet, partl : the linear growth of disturbances near the nozzle", *J.Fluid Mech.*, **176**, pp. 191–219.

Comte, P., Fouillet, Y., and Lesieur, M., 1992, "Simulation numérique des zones de mélange compressibles", *Revue scientifique et technique de la defense*, 3ème trimestre, pp. 43–63.

Crow, S.C. , and Champagne, F.H., 1971, "Orderly structure in jet turbulence", *J.Fluid Mech*, **48**, pp. 547–591.

Djeridane,T., 1994, "Contribution à l'étude experimentale de jets turbulents axisymétriques à densité variable", *Thèse de l'Université d'Aix-Marseille II.*

Ducros, F., Comte P., and Lesieur, M., 1996, "Large-eddy simulation of transition to turbulence in a compressible boundary layer over a flat plate: I-low Mach number", *J. Fluid Mech.*, **326**, pp. 1–36.

Germano M., Piomelli U., Moin P., and Cabot W., 1991, "A dynamic subgrid-scale eddy-viscosity model", *Phys. Fluids A.*, **3** (7), pp. 1760-65.

Gonze, M.A., 1993, "Simulation Numérique des Sillages en Transition à la Turbulence", PhD thesis. National Polytechnic Institute, Grenoble.

Grand, D., Coulon, N., Magnaud, J.P., and Villand, M., 1988, "Computation of flow with distributed resistance and heat sources", In *Proc. Third Intl. Symp. on Refined Flow Modelling and Turbulence Measurements, Nipon Toshi Center Tokyo* (ed. Y. Iwasa), pp. 487–494.

Hussain, F., and Zaman K.B.M.Q., 1981, "The "preferred mode" of the axisymmetric jet", *J.Fluid Mech*, **110**, pp. 39–71.

Lasheras, J.C., Lecuona A., and Rodriguez, P., 1991, "Three dimensionnal structure of the vorticity field in the near region of laminar co-flowing forced jets", In *The Global Geometry of Turbulence*, edited by J.Jimenez (Plenum Press, New-York).

Lee, M., Reynolds, W.C., 1985, "Bifurcating and blooming jets at high Reynolds number", *Fifth Symp. on Turbulent Shear Flows*, Ithaca, New York 1.7-1.12.

Lele, S.K., 1992, "Compact finite difference schemes with spectral-like resolution", *J. Comput. Phys.*, **103**, pp. 16–42.

Lesieur, M., and Métais, O., 1996, "New trends in large-eddy simulations of turbulence", *Annu. Rev. Fluid Mech.*, **28**, pp. 45–82.

Liepmann, D., and Gharib, M., 1992, "The role of streamwise vorticity in the near-field entrainment of round jets", *J.Fluid Mech*, **245**, pp. 643–668.

Martin, J.E., and Meiburg, E., 1991, "Numerical investigation of three-dimensionally evolving jets subject to axisymmetric and azimuthal perturbations", *J.Fluid Mech*, **230**, pp. 271–318.

Métais, O., and Lesieur, M., 1992, "Spectral large-eddy simulation of isotropic and stably stratified turbulence", *J.Fluid Mech*, **239**, pp. 157–194.

Michalke, A., and Hermann, G., 1982, "On the inviscid instability of a circular jet with external flow. *J.Fluid Mech*, **114**, pp. 343–359.

Monkewitz, P.A., and Pfizenmaier, E., 1991, "Mixing by 'side jets' in strongly forced and self-excited round jets", *Phys. Fluids A*, **3** (5), pp. 1356–1361.

Moore, C.J., 1977, "The role of shear-layer instability waves in jet exhaust noise", *J.Fluid Mech*, **80**, pp. 321–367.

Olsson, M. , and Fuchs, L., 1996, "Large eddy simulation of the proximal region of a spatially developing circular jet", *Phys. Fluids*, **8** (8), pp. 2125–2137.

Silveira-Neto A., Grand D., Métais, O., and Lesieur, M., 1993, "A numerical investigation of the coherent vortices in turbulence behind a backward-facing step. *J. Fluid Mech.*, **256**, pp. 1–25.

Silvestrini, J., 1996, "Simulations des grandes échelles des zones de mélange: application à la propulsion solide des lanceurs spatiaux couches limites compressibles", PhD thesis. National Polytechnic Institute, Grenoble.

Widnall, S.E., Bliss, D.B., and Tsai, C., 1974, "The instability of short waves on vortex ring", *J.Fluid Mech*, **66** (1), pp. 35–47.

SESSION 26 - SEPARATED FLOWS I

Large Eddy Simulation: A Dynamic One-Equation Subgrid Model for Three-Dimensional Recirculating Flow

Lars Davidson
Dep. of Thermo and Fluid Dynamics, Chalmers University of Technology
S-412 96 Gothenburg, Sweden

ABSTRACT

Standard dynamic subgrid models have numerical stability problems. The remedy is to average in some homogeneous flow direction(s) or to introduce some artificial clipping. Thus this type of models do not seem to be applicable to real three-dimensional flow without introducing *ad hoc* user modifications. In the present study a new one-equation subgrid model is presented which reduces the need of this type of user-modifications. The present model is a modification of the model presented in Ref. [5]. The model is applied to recirculating flow in an enclosure.

INTRODUCTION

Germano *et al.* [10, 11] propose a dynamic subgrid model in which the constant in the Smagorinsky model is not arbitrarily chosen (or optimized), but where it is computed. The dynamic models which have been developed have problems with negative values of the C-coefficient. When a negative C occurs it is believed to represent *backscatter*, i.e. spectral flow of energy from subgrid scales to resolved scales. This means that the production term in the transport equation for subgrid kinetic energy $P_{k_{sgs}} = -\tau^a_{ij}\bar{u}_{i,j}$ becomes negative, and feeds energy back to the resolved scales. The problem is that negative diffusion (negative C) causes numerical problems. These can be handled as long as the total (i.e. viscous plus turbulent) diffusion is positive. However, large negative, turbulent diffusion remains a problem. It is not only negative values on C that causes numerical problems. It exhibits very strong gradients and "fluctuates wildly" [23]. In a ventilated enclosure, for example, the author has found that C varies typically in the range ± 4 which should be compared with a standard value of the Smagorinsky constant $C_S^2 = 0.01$. In the literature [23, 19, 24, 20, 2, 22, 6, 17, 18] it has been found that in order to achieve numerical stability present dynamic subgrid models require either that there exist a homogeneous flow direction or that the dynamic coefficient is clipped at some arbitrary limit in an *ad hoc* manner. Thus the model does not seem to be applicable to real three-dimensional flows where no homogeneous flow direction exists.

An attempt to improve this restriction was presented by Ghosal *et al.* [13, 12] where they try to optimize the equation for C globally, but still with the constraint that $C > 0$. This optimization leads to an integral equation (Fredholm's integral equation of the second kind) which is very expensive to solve numerically. They report that it increases the CPU time by 50% [1].

In the present work a new one-equation dynamic subgrid model is applied to recirculating flow in an enclosure. It is an modification of the model presented in Ref. [5].

THE ONE-EQUATION MODEL

If we follow Germano [9] and introduce *generalized* central moments the transport equation for the subgrid kinetic energy k_{sgs} reads [4]

$$\frac{\partial k_{sgs}}{\partial t} + (\bar{u}_j k_{sgs})_{,j} = -\mathcal{T}_f(u_i,u_j)\bar{u}_{i,j} - \left\{\frac{1}{2}\mathcal{T}_f(u_j,u_i,u_i) + \mathcal{T}_f(u_i,p)\right\}_{,j} + \nu(k_{sgs})_{,jj} - \nu\mathcal{T}_f(u_{i,j},u_{i,j}). \quad (1)$$

The dynamic coefficient C in the production term

$$P_{k_{sgs}} = -\tau^a_{ij}\bar{u}_{i,j}$$
$$\tau^a_{ij} \equiv \mathcal{T}_f(u_i,u_j) = -2C\Delta k_{sgs}^{\frac{1}{2}}\bar{S}_{ij} \quad (2)$$

is computed in a similar way as in the standard dynamic model [10, 11, 13, 12], i.e.

$$C = -\frac{\mathcal{L}_{ij}M_{ij}}{2M_{ij}M_{ij}};\ \mathcal{L}_{ij} = \widehat{\bar{u}_i\bar{u}_j} - \widehat{\bar{u}}_i\widehat{\bar{u}}_j$$
$$K = k_{sgs} + \frac{1}{2}\mathcal{L}_{ii}$$
$$M_{ij} = \widehat{\Delta}\widehat{K^{\frac{1}{2}}}\widehat{\bar{S}}_{ij} - \Delta\widehat{k_{sgs}^{\frac{1}{2}}\bar{S}_{ij}} \quad (3)$$

where $\mathcal{L}_{ij}$ denotes the *dynamic* Leonard stresses, and where $K \equiv \frac{1}{2}T_{ii}$ is the subgrid kinetic energy on the test level [13, 12, 4]. The diffusion constant can also be computed dynamically as in Refs. [13, 12]. In the present study the standard gradient hypothesis is used with the turbulent Prandtl number set to one. The dissipation term $\varepsilon_{k_{sgs}}$

is estimated as

$$\varepsilon_{k_{sgs}} \equiv \nu \mathcal{T}_f(u_{i,j}, u_{i,j}) = C_* \frac{k_{sgs}^{\frac{3}{2}}}{\Delta}. \quad (4)$$

In order to estimate C_* attention is turned to the transport equation for K. The equations for k_{sgs} and K read in symbolic form

$$C_{k_{sgs}} - D_{k_{sgs}} = P_{k_{sgs}} - C_* \frac{k_{sgs}^{\frac{3}{2}}}{\Delta} \quad (5)$$

$$C_K - D_K = P_K - C_* \frac{K^{\frac{3}{2}}}{\widehat{\Delta}}. \quad (6)$$

where C and D on the left-hand sides denote convection and diffusion, respectively. Apply the test filter to Eq. 5. In Ref. [5] an ASM-like expression was used, which was found to have an undesired positive feedback feature, which made it necessary to restrict the variations in the C_*-coefficient. Here we use a modified relation. The transport of k_{sgs} is set proportional to that of K so that

$$\widehat{P}_{k_{sgs}} - \frac{1}{\Delta}\widehat{C_* k_{sgs}^{\frac{3}{2}}} = \left(P_K - C_* \frac{K^{\frac{3}{2}}}{\widehat{\Delta}} \right), \quad (7)$$

and we obtain

$$C_*^{n+1} = \left(P_K - \widehat{P}_{k_{sgs}} + \frac{1}{\Delta}\widehat{C_*^n k_{sgs}^{\frac{3}{2}}} \right) \frac{\widehat{\Delta}}{K^{\frac{3}{2}}}. \quad (8)$$

The dissipation cannot be negative which requires that we limit C_* to positive values, i.e. $C_* \geq 0$. In Eq. 8 C_* is kept inside the filtering process. Following Piomelli [20] the dynamic coefficient under the filter is taken at the old time-step.

To ensure numerical stability a *constant* value of C in space ($\langle C \rangle_{xyz}$) is used in the momentum equations, which is determined by requiring that the production in the whole computational domain should remain the same, i.e.

$$\langle 2C\Delta k_{sgs}^{\frac{1}{2}} \bar{S}_{ij} \bar{S}_{ij} \rangle_{xyz} = 2\langle C \rangle_{xyz} \langle \Delta k_{sgs}^{\frac{1}{2}} \bar{S}_{ij} \bar{S}_{ij} \rangle_{xyz} \quad (9)$$

The idea is to include all local dynamic information through the source terms of the transport equation for k_{sgs}. This is probably physically more sound since large local variations of C appear only in the source term, and the effect of the large fluctuations in the dynamic coefficients will be smoothed out in a natural way. This means that the need to restrict or limit the dynamic coefficient is reduced or may not be necessary altogether. However, *if* we have to restrict the dynamic coefficients in the k_{sgs} equation this does not affect the results as much as if the coefficient in the original dynamic model is restricted. The reason is that in the one-equation model the coefficients affect the stresses only in an indirect way (the source terms are part of a transport equation) whereas in the original dynamic model the dynamic C-coefficient is linearly proportional to the stresses. It is extremely important to use subgrid models which are numerically stable and where the need to introduce *ad hoc* modification is limited as far as possible, if we want to develop turbulence models applicable to general flow situations.

The spatial variation of C is included via the production term in the modelled k_{sgs} equation. In this way backscatter is taken into account in an indirect way. Although it is not fed *directly* back to the resolved flow, it influences the resolved flow via the kinetic subgrid energy. A negative production reduces k_{sgs} and this effect influences the neighborhood through convection and diffusion of k_{sgs}.

The new model can be summarized as follows:

1. The equation for the kinetic subgrid energy is solved (Eq. 1);

2. The production term (see Eq. 2) is computed using the *local* dynamic coefficient (Eq. 3) without any averaging or restrictions;

3. The turbulent Prandtl number in the diffusion term is set to one;

4. The local dynamic coefficient in front of the dissipation term is computed from Eq. 8;

5. The subgrid stresses in the momentum equation are computed using a *homogeneous* values $\langle C \rangle_{xyz}$ of the dynamic coefficient determined from Eq. 9; $\langle C \rangle_{xyz}$ is also used in the diffusion term in the k_{sgs} equation.

6. The boundary condition for k_{sgs} is zero at all boundaries.

The boundary conditions for k_{sgs} does not seem to affect the results much, and the reason is that the equation is dominated by its source terms, production and dissipation (see Fig. 8b).

Some limits on C_* *are* used. It is not allowed to go negative (this occurs in approximately 25% of the nodes). A limit is also used to prevent C_* from growing too large. Presently an arbitrary value of 10 is used; this limit is reached in approximately 0.3% of the nodes. It is presently not clear if this limit is needed at all. Note that the present formulation for C_* in Eq. 8 is considerably better than that used in Ref. [5].

THE NUMERICAL METHOD

An implicit, two-step time-advancement methods is used. When the filtered Navier-Stokes equation for $\bar{u}_i$

$$\frac{\partial \bar{u}_i}{\partial t} + \frac{\partial}{\partial x_j}(\bar{u}_i \bar{u}_j) = -\frac{1}{\rho}\frac{\partial \bar{p}}{\partial x_i} + \nu \frac{\partial^2 \bar{u}_i}{\partial x_j \partial x_j} - \frac{\partial \tau_{ij}}{\partial x_j} \quad (10)$$

is discretized it can be written

$$\bar{u}_i^{n+1} = \bar{u}_i^n + \Delta t H\left(u_i^n, u_i^{n+1}\right) - \frac{1}{\rho}\alpha \Delta t \frac{\partial p^{n+1}}{\partial x_i} - \frac{1}{\rho}(1-\alpha)\Delta t \frac{\partial p^n}{\partial x_i} \quad (11)$$

where $H\left(u_i^n, u^{n+1}\right)$ includes convection and the viscous and subgrid stresses, and $\alpha = 0.5$ (Crank-Nicolson). Equation 11 is solved which gives $\bar{u}_i^{n+1}$ which does not satisfy continuity. An intermediate velocity field is computed by subtracting the implicit part of the pressure gradient, and the resulting Poisson equation is solved employing an efficient multigrid method. For more details, see Refs. [5, 16, 8, 7].

RESULTS

A steady computation is first carried out using the CALC-BFC code and the $k-\varepsilon$ model [3]. These results are used as initial start fields in the LES calculations. The predictions are compared with Laser-Doppler measurements of Restivo [21] (also available in Ref. [15]). The geometry is given by (see Fig. 1):

$$L/H = 3,\ W/H = 1,\ h/H = 0.056,\ t/H = 0.16$$
$$Re = \frac{U_{in} h}{\nu} = 5000.$$

where W is the extent of the domain in the z direction. We have used $H = 3$ m, $U_{in} = 0.455$ m/s, and air of 20°C. Inlet boundary conditions are set as

$$\bar{u}_{in} = U_{in} + rnd \cdot u_{rms,exp} \quad (12)$$
$$\bar{v}_{in} = rnd \cdot u_{rms,exp},\ \bar{w}_{in} = rnd \cdot u_{rms,exp}$$

Homogeneous inlet profiles are used for all variables. Note that the random function rnd is called at different times

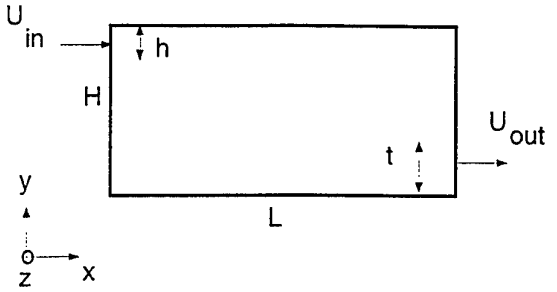


Figure 1: Ventilated enclosure.

for $\bar{u}_{in}$, $\bar{v}_{in}$ and $\bar{w}_{in}$, which means that the fluctuations are not correlated so that $(\overline{\bar{u}\bar{v}})_{in} = (\overline{\bar{u}\bar{w}})_{in} = (\overline{\bar{v}\bar{w}})_{in} = 0$.

At the outlet the exit velocity is computed from global continuity and it is taken as constant over the outlet. Zero gradient is set for the remaining variables.

At all six walls traditional wall functions [3] are used if $y^+ > 11$. Along the ceiling these are never used as the boundary layer is well resolved ($y^+ < 3$ for the first node).

A $96 \times 64 \times 64$ grid has been used. A hyperbolic tangent function is used in x and z direction, whereas geometric stretching is used in the y direction. At the position $x/H = 2$ (see Fig. 6) 17 nodes are located inside the velocity maximum, $y_{1/2}$ corresponds to $y/H = 0.89$, and for the near-wall node $y^+ \simeq 2$. For more details, see Ref. [5]. The number of time steps used in each calculation is typically 40000 using a maximum CFL number of approximately two. This corresponds to approximately 2200 seconds. The streamwise average of the peak velocity in the wall jet along the ceiling is close to $U_{av} = 0.5U_{in}$ (= 0.228 m/s). Thus the time it takes for a fluid particle to move from the inlet to the opposite wall can be estimated as $L/U_{av} \simeq 40$ seconds, which means that $2200/40 = 55$ characteristic time units (L/U_{av}) are covered in a simulation. Averaging has been performed during the last 19 000 time steps. Tests presented in [3] show that this is more than enough. Unless otherwise stated all results presented have been obtained with the new dynamic one-equation model.

In Fig. 2 the time averaged $\bar{u}$ velocities are compared with experiments, and as can seen the agreement is good. The predicted peak velocity in the wall jet is in good agreement with experiments, much better than for the one-equation model presented in Ref. [5]. The original dynamic model [10, 11, 3] is compared with the new dynamic one-equation model. As can be seen the one-equation model performs better.

In Fig. 3 instantaneous velocity vector plots are shown. Looking at the wall jet in side view (Fig. 3a) we see the characteristic wavy pattern. This accounts for the entrainment process between the wall jet and its surrounding. If we are used to Reynolds Averaged Navier-Stokes (RANS) we can easily misinterpret the effect of turbulent (or, as in LES, subgrid) viscosity. In RANS a high turbulent viscosity gives a smeared out, diffusive velocity profile due to high diffusion of momentum in the normal direction (y). In LES it is vice versa. A high subgrid viscosity damps the resolved fluctuations which are responsible for diffusion of time-averaged momentum in the y direction and the result is a more pointed velocity profile due to reduced diffusion of momentum.

The time history of $\bar{u}$ is shown in Fig. 4. It can be seen that there is a large difference between the turbulence in the wall jet (Fig. 4a) and that in the middle of the room (Fig. 4b). The magnitude of the fluctuations in the wall jet is larger and there are much higher frequencies. In Fig. 4b the flow is not fully turbulent.

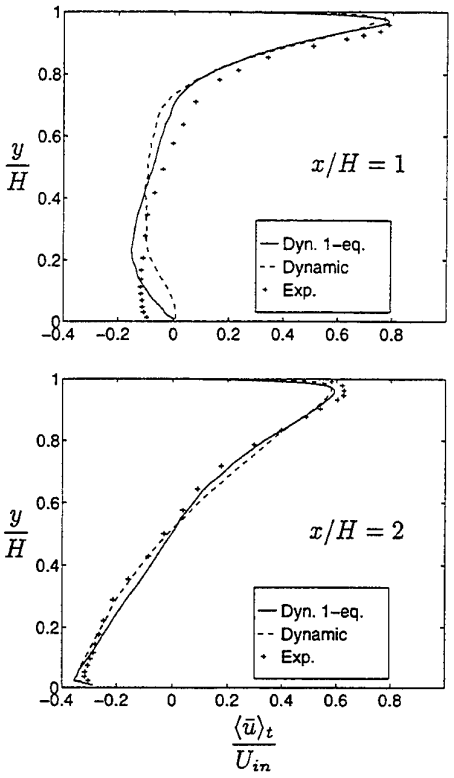


Figure 2: Time averaged velocity profiles. Symmetry plane $z/H = 0.5$. Lines: predictions; +: experimental mean velocity [21] (see also [15].

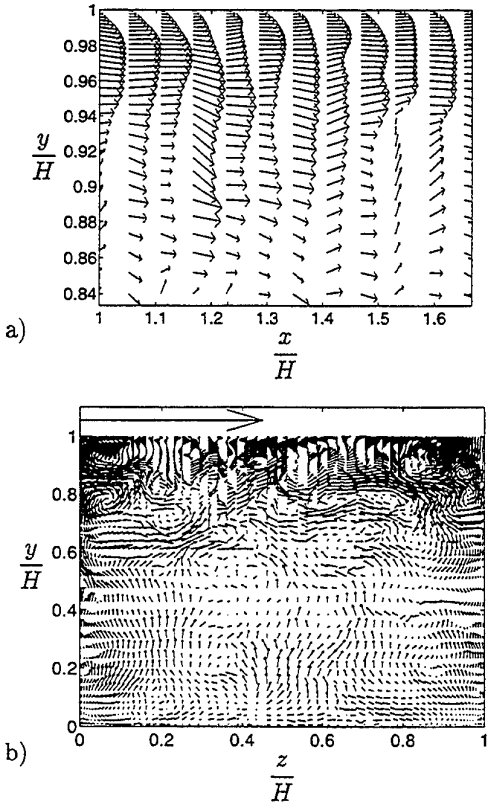


Figure 3: Vector plots. a) $z/H = 0.5$. b) $x/H = 1.5$. Reference arrow above the figure shows $U/U_{in} = 1$.

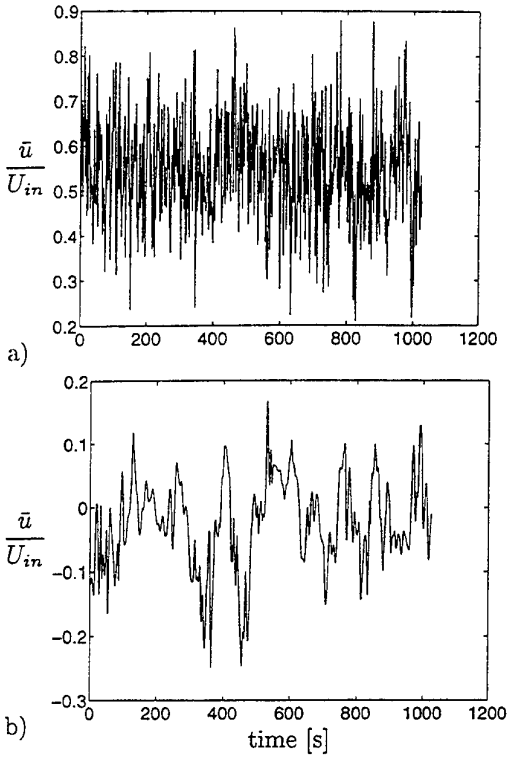


Figure 4: Time history of $\bar{u}$ at two chosen cells. $z/H = 0.5$. a) $x/H = 1.0, y/H = 0.92$. b) $x/H = 1.0, y/H = 0.5$

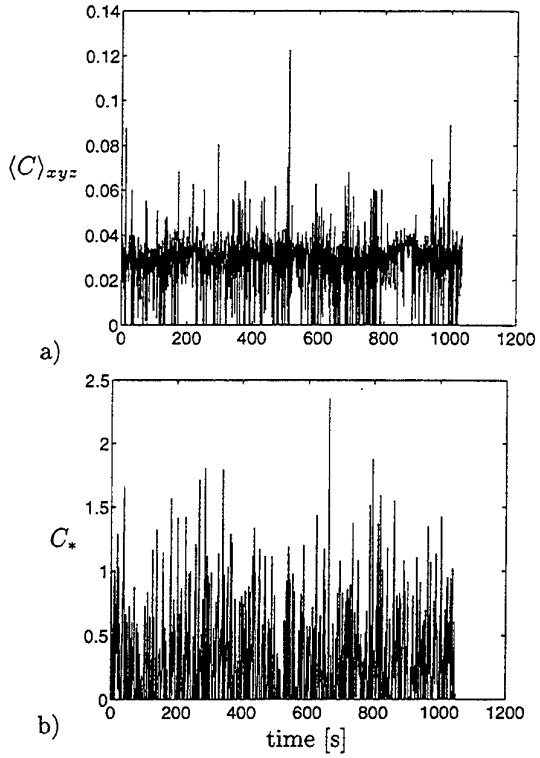


Figure 5: Time history of the dynamic coefficients. a) The dynamic coefficient $\langle C \rangle_{xyz}$. b) The dynamic coefficient C_* at one chosen cell $x/H = 2.0, y/H = 0.92, z/H = 0.5$.

From the time history of the homogeneous dynamic coefficient $\langle C \rangle_{xyz}$ in Fig. 5a we find that the time averaged value is close to 0.04 which corresponds to a value of the Smagorinsky constant $C_S = 0.2$. The $\langle C \rangle_{xyz}$ coefficient sometimes (at approximately 3% of the time steps) wants to go negative, but it is clipped at zero. The C_* coefficient connected with the dissipation term in the k_{sgs} equation is presented in Fig. 5b. Its behavior is more stochastic than $\langle C \rangle_{xyz}$, because it is local. It often tends to zero, but it rarely hits the upper bound which has been set to 10. In fact, at $x/H = 2$ the C_* coefficient never becomes larger than approximately 3. Possibly the upper limit is not needed at all. Here it is clearly seen that the present model works much better than that presented in Ref. [5].

Wall jet

The flow along the ceiling is a wall jet. Thus it could be interesting to compare the predictions with wall jet data. The experiments of Karlsson *et al.* [14] have been chosen. The Reynolds number in the wall jet experiment is higher ($Re = 10000$) than in the present study.

In Fig. 6 the streamwise mean velocities, computed with the standard dynamic model and the one-equation dynamic model, are compared with experiments, and the agreement is very good. If we, however, compare the width and the maximum velocities this picture changes. The predicted wall jet spreads too much compared with experiments (see Table 1), which agrees with the comparison in Fig. 2. The peak velocity, however, agrees well with experiments, in particular for the predictions with the one-equation model. The reason for the rather poor agreement in the spreading rate could be due to insufficient grid resolution. It could also be that the subgrid models (both the dynamic and the dynamic one-equation model) give too low a subgrid viscosity. As a results this would give too large exchange of momentum in the y direction due to too little damping (by the subgrid stresses) of the resolved fluctuations.

	x/h	U_{max}/U_{in}	$d\delta_{1/2}/dx$	$y_{1/2}/h$
1-eq. model	17.9	0.786	-	2.01
1-eq. model	35.7	0.592	0.111	4.01
dyn. model	17.9	0.739	-	2.20
dyn. model	35.7	0.581	0.126	4.46
Exp.	20	0.771	-	1.88
Exp.	40	0.566	0.08	3.48

Table 1: Comparison with wall jet data [14]

The stresses in the wall jet are shown in Fig. 7. Generally, the stress levels are too low, both the normal ones and the shear stress. The stress changes sign near the wall and the location agrees well with the experimental one; the positive peak, however, is under-predicted. The dynamic Leonard stress $\mathcal{L}_{12}$ (see Eq. 3) is also included, and it is almost as large as the resolved stress. It can be seen that the subgrid stress (also included in Fig. 7) is much smaller than the resolved stress, except close to the wall. Actually, at $x/H = 2$, the time averaged subgrid turbulent viscosity is of the same order as the viscous one ($\langle \nu_{sgs} \rangle_t < 4\nu$), whereas the instantaneous value can be much higher ($\nu_{sgs,max} \simeq 26\nu$).

In Fig. 8a turbulent kinetic energies are presented. We find that the subgrid energy k_{sgs} is rather large. It is much larger than for the model presented in Ref. [5]. The reason is that the dissipation in the present study is much smaller due to a smaller C_* coefficient. The dynamic Leonard kinetic energy is a large fraction of the resolved kinetic energy. In Fig. 8b the time averaged production and dissipation term in the k_{sgs} equation are shown. As can be seen they are fairly much in balance. The spatial variation of $\langle C_* \rangle_t$ at $x/H = 2$ is also included. It has values close to 0.5 except close to the wall where it attains values around

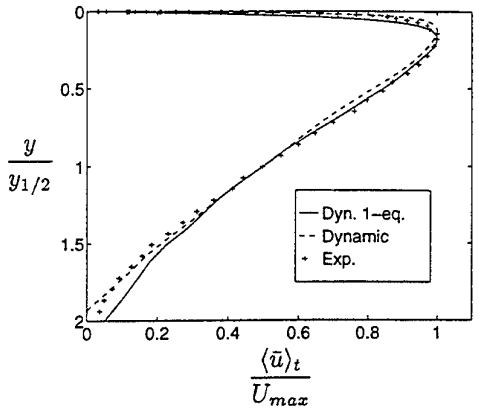


Figure 6: Time averaged velocity. $z/H = 0.5$. LES: $x/H = 2$ ($x/h = 35.7$); exp: $x/h = 40$. Solid line: 1-eq. dynamic model; dashed line: dynamic model; +: experiments [14].

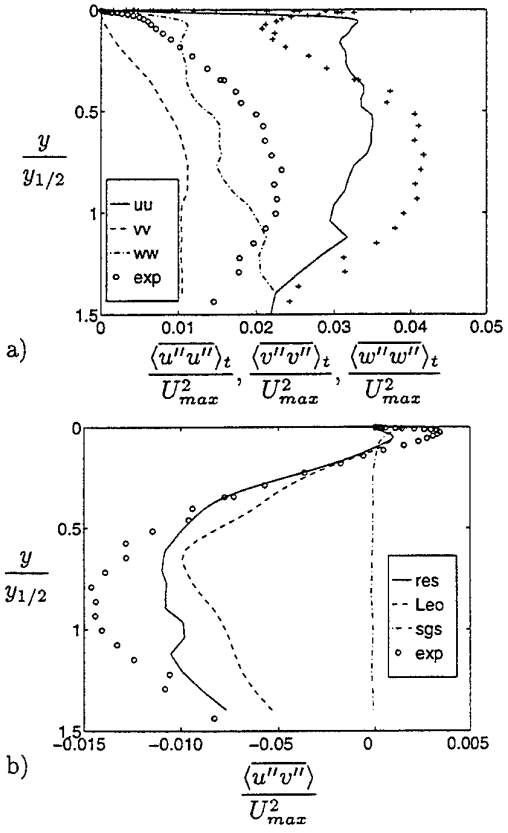


Figure 7: Resolved stresses. Symmetry plane $z/H = 0.5$. LES: $x/H = 2$ ($x/h = 35.7$); exp: $x/h = 40$. a) Solid line: $\langle u''u'' \rangle_t / U_{max}^2$; dashed line: $\langle v''v'' \rangle_t / U_{max}^2$; dash-dotted line: $\langle w''w'' \rangle_t / U_{max}^2$. +: experimental $\overline{u^2}/U_{max}^2$; o: experimental $\overline{v^2}/U_{max}^2$ [14]. b) Solid line: shear stress $\langle u''v'' \rangle_t / U_{in}^2$; dashed line: dynamic Leonard stress $\langle \mathcal{L}_{12} \rangle_t / U_{in}^2$; dash-dotted line: subgrid shear stress $\langle \tau_{12} \rangle_t / U_{in}^2$; o: experimental $\overline{uv}/U_{max}^2$[14].

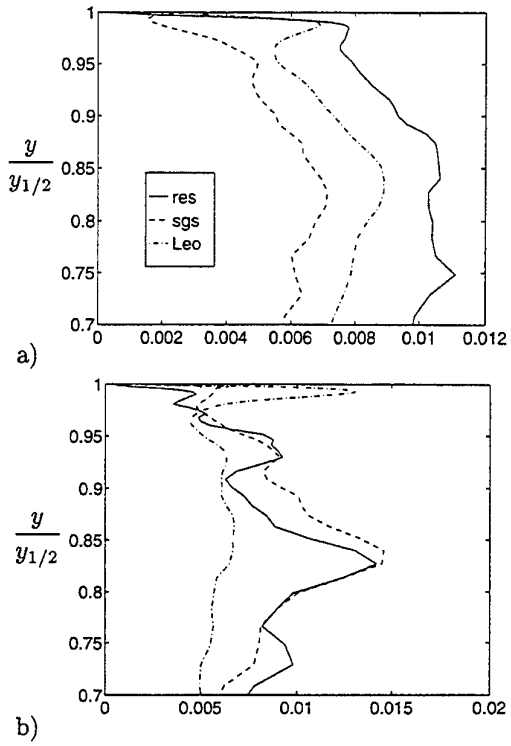


Figure 8: Symmetry plane $z/H = 0.5$. $x/H = 2$. a) Kinetic turbulent energies. Solid line: resolved turbulent kinetic energy $\frac{1}{2}\langle u_i'' u_i'' \rangle_t / U_{in}^2$; dash-dotted line: kinetic energy of dynamic Leonard stresses $\frac{1}{2}\langle \mathcal{L}_{ii} \rangle_t / U_{in}^2$; dashed line: turbulent kinetic subgrid energy $\langle k_{sgs} \rangle_t / U_{in}^2$. b) Terms in the subgrid kinetic energy equation. Solid line: production $\langle P_k \rangle_t$; dashed line: dissipation $\langle C_* k_{sgs}^{1.5} / \Delta \rangle_t$; dash-dotted line: $0.01 \langle C_* \rangle_t$.

1.3.

CONCLUSIONS

A contribution towards a development of a new dynamic subgrid one-equation model has been presented. The general idea is to include dynamic information in the source terms of an equation for the turbulent kinetic subgrid energy k_{sgs} rather than directly in the momentum equations. In the momentum equation a *homogeneous* value (keeping the time dependence) of the local dynamic coefficient is used. In this way numerical stability is greatly enhanced since the large oscillation in the local dynamic coefficients enter as source terms in the k_{sgs} equation, and they are naturally smoothed out through convection and diffusion. This model naturally accounts for back-scatter since the production term in the k_{sgs} equation is permitted to go negative.

The proposed new one-equation model gives closer agreement with experimental data than the standard original dynamic model.

References

[1] AKSELVOLL, K., AND MOIN, P. Large eddy simulation of turbulent confined coannular jets and turbulent flow over a backward facing step. Report no. TF-63, Stanford University, Dept. Mech. Eng., 1995.

[2] BALARAS, B., BENOCCI, C., AND PIOMELLI, U. Finite-difference computations of high Reynolds num-

ber flow using the Dynamic subgrid-scale model. *Theor. and Comp. Fluid Dyn. 7* (1995), 207–216.

[3] DAVIDSON, L. Implementation of a large eddy simulation method applied to recirculating flow in a ventilated room. Report, ISSN 1395-7953 R9611, Dep. of Building Technology and Structural Engineering, Aalborg University, 1996.[1]

[4] DAVIDSON, L. Large eddy simulations: A note on derivation of the equations for the subgrid turbulent kinetic energies. Rept. 97/11, Dept. of Thermo and Fluid Dynamics, Chalmers University of Technology, Gothenburg, 1997.[1]

[5] DAVIDSON, L. LES of recirculating flow without any homogeneous direction: A dynamic one-equation subgrid model. In *2nd Int. Symp. on Turbulence Heat and Mass Transfer* (Delft, 1997), pp. 481–490.[1]

[6] DAVIDSON, L., AND NIELSEN, P. Large eddy simulations of the flow in a three-dimensional ventilated room. In *5th Int. Conf. on Air Distributions in Rooms, ROOMVENT'96* (Yokohama, Japan, 1996), S. Murakami, Ed., vol. 2, pp. 161–168.[1]

[7] EMVIN, P. *The Full Multigrid Method Applied to Turbulent Flow in Ventilated Enclosures Using Structured and Unstructured Grids.* PhD thesis, Dep. of Thermo and Fluid Dynamics, Chalmers University of Technology, Gothenburg, 1997.

[8] EMVIN, P., AND DAVIDSON, L. Development and implementation of a fast large eddy simulations method. Rept., Dept. of Thermo and Fluid Dynamics, Chalmers University of Technology, Gothenburg, 1997.[1]

[9] GERMANO, M. Turbulence: the filtering approach. *Journal of Fluid Mechanics 238* (1992), 325–336.

[10] GERMANO, M., PIOMELLI, U., MOIN, P., AND CABOT, W. A dynamic subgrid-scale eddy viscosity model. *Phys. Fluids A 3* (1991), 1760–1765.

[11] GERMANO, M., PIOMELLI, U., MOIN, P., AND CABOT, W. Erratum. *Phys. Fluids A 3* (1991), 3128.

[12] GHOSAL, S., LUND, T., MOIN, P., AND AKSELVOLL., K. Corrigendum. *Journal of Fluid Mechanics 297* (1995), 402.

[13] GHOSAL, S., LUND, T., MOIN, P., AND AKSELVOLL., K. A dynamic localization model for large-eddy simulation of turbulent flows. *Journal of Fluid Mechanics 286* (1995), 229–255.

[14] KARLSSON, R., ERIKSSON, J., AND PERSSON, J. LDV measurements in an plane wall jet in a large enclosure. In *Laser Techniques and Applications in Fluid Mechanics* (1993), D. D. o. R.J. Adrian, F. Durst, M. Heitor, M. Maeda, and J. H. J.H. Whitelaw, Eds., Springer-Verlag, pp. 311–332.

[15] NIELSEN, P. Specification of a two-dimensional test case. Report, ISSN 0902-7513 R9040, Dept. of Building Technology and Structural Engineering, Aalborg Universitetscenter, Aalborg, 1990.

[16] NILSSON, H. A parallel multiblock extension to the CALC-BFC code using PVM. Rept. 97/11, Dept. of Thermo and Fluid Dynamics, Chalmers University of Technology, Gothenburg, 1997.[1]

[17] OLSSON, M. *Large Eddy Simulation of Turbulent Jets.* PhD thesis, Dep. of Mechanics, Royal Institute of Technology, Stockholm, 1997.

[18] OLSSON, M., AND FUCHS, L. Large eddy simulation of the proximal region of a spatially developing circular jet. *Phys. Fluids A 8* (1996), 2125–2137.

[19] PIOMELLI, U. High Reynolds number calculations using the dynamic subgrid-scale stress model. *Phys. Fluids A 5* (1993), 1484–1490.

[20] PIOMELLI, U., AND JUNHUI, L. Large-eddy simulation of rotating channel flow using a localized dynamic model. *Phys. Fluids 7* (1995), 839–848.

[21] RESTIVO, A. *Turbulent Flow in Ventilated Rooms.* PhD thesis, University of London, Imperial College of Science and Technology, Mechanical Engineering Department, 1979.

[22] VOKE, P., GAO, S., AND LESLIE, D. Large-eddy simulations of plane impinging jets. *Int. J. Numer. Meth. Engng. 38* (1995), 489–507.

[23] YANG, K.-S., AND FERZIGER, J. Large-eddy simulation of turbulent obstacle flow using a dynamic subgrid-scale model. *AIAA J. 31* (1993), 1406–1413.

[24] ZANG, Y., STREET, R., AND KOSEFF, J. A dynamic mixed subgrid-scale model and its application to turbulent recirculating flows. *Phys. Fluids A 5* (1993), 3186–3196.

[1] available as postscript file at http://www.tfd.chalmers.se/~lada

NUMERICAL AND MODELLING INFLUENCES ON LARGE EDDY SIMULATIONS FOR THE FLOW PAST A CIRCULAR CYLINDER

Michael Breuer
Institute of Fluid Mechanics
University of Erlangen-Nürnberg
Cauerstr. 4
D-91058 Erlangen
Germany

ABSTRACT

In the present work the turbulent flow past a circular cylinder ($Re = 3,900$) has been computed by LES. The objective was not to investigate the physical phenomena of this flow in detail but to study numerical and modelling aspects which influence the quality of LES solutions. Concerning the numerical method the most important component is the discretization of the non-linear convective fluxes. Five different schemes have been investigated. Moreover, the influence of different grid resolutions has been examined. On the modelling side two aspects play an important role, namely the near-wall model and the subgrid scale model. Due to the restriction to low Reynolds numbers in this study no-slip boundary conditions were used at solid walls. Therefore only the second aspect was taken into account. Two different subgrid scale models have been applied. Additionally, computations without any subgrid scale modelling have been carried out in order to prove the performance of the models.

INTRODUCTION

Turbulent flows past bluff bodies are in general very complicated including complex phenomena such as separation, reattachment or vortex shedding. An appropriate description by Reynolds-averaged Navier-Stokes equations combined with statistical turbulence models is difficult to achieve. In contrast to statistical turbulence models direct numerical simulations require no extra assumptions but will not be applicable to engineering flows in the near future. The concept of large eddy simulation (LES) offers a suitable way of solving such flow problems. In LES the large eddies strongly depending on the special flow configuration and its boundary conditions are resolved numerically whereas only the fine-scale turbulence has to be modeled by a subgrid scale model.

However, before LES can be used for applications of practical relevance we have to learn more about all influences on the quality of LES solutions. This includes numerical aspects like discretization schemes or resolution requirements as well as modelling aspects like subgrid scale models or near-wall models. Due to extremely large computation times detailed studies on this important topic are rare. There have been attempts to distribute the load to different groups by organizing workshops on LES for specified test cases. One of these was the "Workshop on LES of Flows past Bluff Bodies" at Tegernsee, June 1995. The results have been published by Rodi et al. (1997). However, despite the large number of contributions it was quite difficult to draw any concrete conclusions. Different groups applied different numerical methods on grids with varying resolutions using different subgrid scale models and wall boundary conditions. Much of what was learned in terms of how the various factors affect the results was derived from those cases in which a single group made multiple simulations that differ in just one factor.

The objective of the work reported here is to continue such efforts in order to learn more about LES and the important factors affecting the quality of the solution. In contrast to the test cases of the LES workshop at Tegernsee (flow past a square cylinder and flow past a cubical obstacle) which could be tackled by Cartesian grids, a geometrically and physically more complex flow problem is considered, namely the flow past a long, circular cylinder. In contrast to its square counterpart this configuration requires curvilinear body-fitted grids and the separation point on the surface is not fixed by the geometry.

DESCRIPTION OF THE LES METHOD

Finite Volume Method

For LES the three-dimensional, time-dependent Navier-Stokes equations are filtered in order to separate the large scale and the small scale motions. In this study an incompressible fluid is assumed. A box filter is applied as filter kernel. The governing equations can be found in Breuer and Rodi (1994). The code (**LESOCC** = **L**arge **E**ddy **S**imulation **O**n **C**urvilinear **C**oordinates) used to solve the filtered equations is based on a 3-D finite volume method for arbitrary non-orthogonal, body-fitted grids (Breuer et al., 1994, 1996, 1996a-b). The surface integrals are approximated by the midpoint rule, which is equivalent to the product of the integrand at the cell face center and the cell face area: $F_{i+\frac{1}{2}} = \int_{S_{i+\frac{1}{2}}} f \cdot dS \approx f_{i+\frac{1}{2}} \cdot S_{i+\frac{1}{2}}$

This approximation is of second order accuracy in space if the value of f is known at the location $i+\frac{1}{2}$. For a cell-centered (non-staggered) grid arrangement as used in **LESOCC** the values of f at the cell faces are not available and have to be obtained by interpolation. In order to examine the influence of the interpolation scheme especially for the non-linear convective fluxes five different options have been investigated. For simplification these schemes are described here under the assumption of a uniform Cartesian grid and a positive flow direction. Then the approximation for the value at the east cell face is as given in Table 1.

Scheme	*Value at cell face:* $f_{i+\frac{1}{2}} =$	$\mathcal{T}$
Hybrid	$\begin{cases} \frac{1}{2}(f_i + f_{i+1}) : Pe_{i+\frac{1}{2}} \leq 2 \\ f_i \quad\quad\quad : otherwise \end{cases}$	Δx^2 Δx
CDS-2	$\frac{1}{2}(f_i + f_{i+1})$	Δx^2
HLPA	$f_i + \gamma(f_{i+1} - f_i)\left(\frac{f_i - f_{i-1}}{f_{i+1} - f_{i-1}}\right)$ $\gamma = \begin{cases} 1 : 0 < \frac{f_i - f_{i-1}}{f_{i+1} - f_{i-1}} < 1 \\ 0 : otherwise \end{cases}$	Δx^2 Δx
Quick	$\frac{3}{8}f_{i+1} + \frac{3}{4}f_i - \frac{1}{8}f_{i-1}$	Δx^3
CDS-4	$-\frac{1}{16}f_{i+2} + \frac{9}{16}f_{i+1} + \frac{9}{16}f_i - \frac{1}{16}f_{i-1}$	Δx^4

Table 1: Overview of all interpolation schemes

The Hybrid scheme is a combination of two different approximations. It switches between the upwind differencing scheme (UDS) and the central differencing scheme (CDS-2) depending on the local value of the Peclet number. For LES the Peclet number is in general larger than two. Therefore the leading truncation error term $\mathcal{T}$ of this scheme is proportional to the grid spacing Δx. The Hybrid scheme satisfies the boundedness criterion unconditionally. However, it is known to be numerically quite diffusive and therefore not well suited for LES. Nevertheless, it is added here for completeness. The CDS-2 scheme linearly interpolates the value at the cell face which leads to a truncation error term proportional to the square of the grid spacing Δx^2. This scheme has often been used for LES computations. The HLPA scheme (hybrid linear/parabolic approximation) was proposed by Zhu (1991) and combines a second order upstream-weighted approximation with first order upwind differencing under the control of a convection boundedness criterion. Zhu claims that HLPA is capable of yielding low diffusive and always bounded solutions. Especially the first property makes it worth investigating this scheme in the context of LES. The Quick scheme originally proposed by Leonard (1979) is a logical improvement of the CDS-2 scheme. Instead of a straight line between the nodes i and $i+1$ a parabola is used to approximate the function f. To construct this polynomial three instead of two nodes have to be taken into account. The third point is taken from the upstream side which is in accordance with the nature of convection. By performing Taylor series expansions it can be shown that this quadratic interpolation has a third order leading truncation error term. However, it is important to mention that the Quick scheme is still of second order accuracy if it is used in conjunction with the midpoint rule approximation of the surface integral. Although this restriction holds true for other higher order interpolations the CDS-4 scheme was implemented which is the natural extention of CDS-2 and Quick. It fits a third order polynomial through four nodes. Two nodes are taken from the upstream side and two nodes from the downstream side. Similarly to CDS-2 the CDS-4 scheme is a symmetric interpolation which does not depend on the flow direction like the Hybrid or the Quick scheme. Again, in combination with the midpoint rule this scheme has formally the same order of accuracy as CDS-2, Quick and in most cases HLPA. However, in spite of this fact large differences will be observed in the quality of LES results if these different schemes are used for LES computations. This will demonstrate that the numerical dissipation produced by the scheme for the convective fluxes is of much greater relevance for LES than its formal order of accuracy in space itself. This topic will be discussed below. Finally it should be mentioned that all viscous fluxes are approximated by central differences of second order accuracy, which fits the elliptic nature of the viscous effects.

Time advancement is performed by a predictor-corrector scheme. A low-storage multi-stage Runge-Kutta method (3 sub-steps, second order accurate in time) is applied for integrating the momentum equations in the predictor step. Within the corrector step the Poisson equation for the pressure correction (SIMPLE method) is solved implicitly by an incomplete LU decomposition method which is accelerated by a FAS multigrid technique. Explicit time marching works well for LES with small time steps which are necessary to resolve turbulence motion in time. Due to a higher stability limit of the Runge-Kutta scheme, much larger time steps ($CFL = O(1)$) can be used than with the previously applied Adams-Bashforth scheme. This leads to a reduction in computing time by a factor of about two.

Subgrid scale models

The filtering procedure provides the governing equations for the resolvable scales of the flow field. They include an additional term for the non-resolvable subgrid scale stresses which describe the influence of the small-scale structures on the larger eddies. For modelling these non-resolvable subgrid scales two different models are applied, namely the well known Smagorinsky model (1963) with Van Driest damping ($l = C_s\Delta(1 - exp(-y^+/25)^3)^{0.5}$) near solid walls as well as the dynamic model originally proposed by Germano et al. (1991). All computations based on the Smagorinsky model have been done with a Smagorinsky constant of $C_s = 0.1$. Following a suggestion of Lilly (1992) a least-squares approach is used to determine values for ${C_s}^2$. Depending on the flow problem different kinds of averaging procedures can be applied in the dynamic approach. For homogeneous flows averaging can be performed in the corresponding direction. For fully inhomogeneous flows only an averaging procedure in time is applicable. Here a recursive lowpass digital filter is chosen (Breuer and Rodi, 1994). In case of the flow past a circular cylinder it is necessary to average in the homogeneous direction as well as in time (filter parameter $\epsilon = 10^{-3}$) in order to get a stable solution. Additionally, negative eddy viscosities are clipped. Moreover, computations have been performed without any subgrid scale model.

DETAILS OF THE TEST CASE

The flow past a long, circular cylinder is an appropriate test case for the intended investigations. First a low (subcritical) Reynolds number of 3,900 (based on cylinder diameter D and free-stream velocity u_∞) is chosen. It is known from experiments that for this Reynolds number transition takes place in the free shear layers. The flow problem has already been simulated and analyzed by Beaudan and Moin (1994). For this low Reynolds number no-slip boundary conditions are used at solid walls, whereas for high Reynolds number computations two different wall function approaches are available in **LESOCC** (Breuer and Rodi, 1994, 1996). In the spanwise direction of the cylinder periodicity of the flow is assumed. At the inflow plane constant velocity is imposed (no perturbations added). A convective boundary condition given by $\frac{\partial u_i}{\partial t} + u_\infty \frac{\partial u_i}{\partial x} = 0$ is used at the outflow boundary.

Various curvilinear, O-type grids have been generated for this investigation. Table 2 gives an overview of these different grids and the corresponding number of control volumes as well as the size of the domain. All grids except one consist of 165 x 165 control volumes in the cross-

Run	*Grid*	*Domain*	*Scheme*	*SGS Mod.*	L_r/D	C_d	$C_{P_{back}}$	Θ_1	Θ_2	Θ_3
A	$165 \times 165 \times 1$	$30D \times \pi D$	CDS-2	–	–	1.625	−2.008	100.7	138.2	–
B1	$165 \times 165 \times 32$	$30D \times \pi D$	Hybrid	Smago.	0.397	1.486	−1.665	95.2	126.0	–
B2	$165 \times 165 \times 32$	$30D \times \pi D$	HLPA	Smago.	0.630	1.319	−1.432	91.4	115.5	–
B3	$165 \times 165 \times 32$	$30D \times \pi D$	Quick	Smago.	1.686	0.969	−0.867	86.7	121.5	150.6
B4	$165 \times 165 \times 32$	$30D \times \pi D$	CDS-2	Smago.	1.115	1.099	−1.049	87.9	112.0	147.3
B5	$165 \times 165 \times 32$	$30D \times \pi D$	CDS-4	Smago.	1.214	1.071	−1.011	87.6	113.7	150.6
C1	$165 \times 165 \times 32$	$30D \times \pi D$	CDS-2	–	0.994	1.144	−1.115	88.6	111.3	150.6
C2=B4	$165 \times 165 \times 32$	$30D \times \pi D$	CDS-2	Smago.	1.115	1.099	−1.049	87.9	112.0	147.3
C3	$165 \times 165 \times 32$	$30D \times \pi D$	CDS-2	Dynam.	1.197	1.071	−1.011	87.7	113.4	148.8
D1	$165 \times 165 \times 64$	$30D \times \pi D$	CDS-2	–	0.870	1.156	−1.164	89.3	116.7	–
D2	$165 \times 165 \times 64$	$30D \times \pi D$	CDS-2	Smago.	1.043	1.097	−1.069	88.5	119.0	–
D3	$165 \times 165 \times 64$	$30D \times \pi D$	CDS-2	Dynam.	1.372	1.016	−0.941	87.4	–	–
E1	$165 \times 165 \times 64$	$30D \times 2\pi D$	CDS-2	Smago.	1.114	1.089	−1.036	87.9	113.2	146.2
E2	$209 \times 165 \times 32$	$120D \times \pi D$	CDS-2	Smago.	1.106	1.081	−1.023	88.0	112.7	148.9
Experiments (Son and Hanratty, 1969; Norberg, 1987; Cardell, 1993)					1.33 ±0.2	0.98 ±0.05	−0.90 ±0.05	87.0 ±2.0	–	–

Table 2: Overview of all simulations

sectional plane. Primarily two grids have been used in this study which only differ in the number of control volumes in the spanwise direction (32 for **B/C** and 64 for **D**). The size of the integration domain for these grids is $30D$ in the cross-section and πD in the direction of the cylinder axis. Additionally, three other version are used. The first (Run **A**) is for a 2-D computation with only one control volume in spanwise direction. The second (Run **E1**) is for a test with a larger domain in spanwise direction whereas the third (Run **E2**) covers a four times larger domain in the cross-sectional plane. The internal region of this grid (radius $\leq 15D$) is exactly the same as for the other grids. The additional points in the radial direction are added to extend the grid to its new outer size. In all cases the grid points are clustered in the vicinity of the cylinder (geometrical series with a stretching factor of 1.03) and in the wake region.

Statistics are in general compiled over periods of at least $100D/u_\infty$ time units or approximately 22 vortex shedding cycles. In most cases even longer periods of more than $200D/u_\infty$ time units have been computed to prove convergence of the statistics. Of course additional averaging has been performed in spanwise direction.

RESULTS AND DISCUSSION

Three–dimensional effects

In order to show the necessity for three–dimensional computations for LES a 2–D simulation has been carried out in addition to 3–D simulations. For the 2–D case the same code and the same cross–sectional grid with only one control volume in spanwise direction is used. Table 2 gives an overview of all simulations. For investigations on the impact of three–dimensionality simulation **A** has to be compared with Run **C1**. Both simulations have been carried out with the CDS–2 scheme and no subgrid scale model. Fig. 2 shows the streamlines of the time–averaged flow field. Totally different streamline patterns can be observed for the 2–D (**A**) and the 3–D simulation (**C1**). The largest difference is given by the absence of an attached recirculation region behind the cylinder in the 2–D case. In spite of nearly the same averaging time for the 2–D and 3–D simulations the 2–D flow field is more asymmetric than the 3–D one. Even increasing the averaging time does not improve the 2–D results significantly. The reason for this strange behavior can only be detected by observations of the instantaneous flow structure past the cylinder. Contrary to the 3–D LES asymmetric vortex shedding with a non–zero mean lift coefficient is observed in the 2–D case. This phenomenon is shown in Fig. 1 by a plot of the instantaneous pressure distribution. The vortices which shed from the cylinder move downstream along an axis which is inclined with reference to the symmetry line. Irregularly the axis of the vortex street changes from positive to negative angles and the other way round. Similar observations have been reported in the literature. Due to this behavior the asymmetric time–averaged streamlines can be explained.

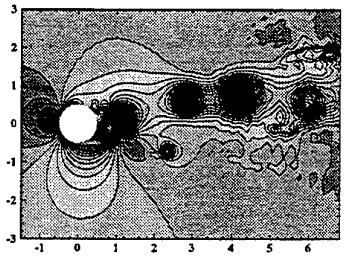


Figure 1: 2–D LES (Run **A**): Instantaneous pressure distribution for the flow past a circular cylinder, Re = 3,900.

In contrast to experimental measurements and 3–D LES the 2–D simulation shows an (unphysical) positive time–averaged streamwise velocity distribution at all centerline stations downstream of the cylinder. In the 3–D case (**C1**) the flow field consists of a large recirculation region behind the cylinder and two additional, small separation bubbles attached to the downstream face of the cylinder. As a result of this flow structure the computed drag coefficient C_d and the back–pressure coefficient $C_{P_{back}}$ are much too high in the 2–D case compared with experimental measurements (e.g. Norberg (1987), $C_d = 0.98 \pm 0.05$ and $C_{P_{back}} = -0.9 \pm 0.05$). The large deviations between 2–D and 3–D results indicate that three–dimensional structures strongly influence the near–wake of the flow. Beaudan and Moin (1994) have already pointed out that these structures consist of pairs of counter–rotating streamwise vortices, which cannot be captured by a 2–D calculation. This is an illustrative proof that 2–D LES (as well as DNS) is worthless due to the impact of three–dimensionality of the flow even in case of (nearly) two–dimensional flow problems.

Influence of discretization scheme

The second aspect which has been investigated is the influence of different approximations for the convective fluxes in the filtered Navier–Stokes equations. For that reason five different simulations (Run **B1–5**, see Table 2) have been carried out which differ only according to this detail. All simulations are based on the grid with $165 \times 165 \times 32$ control volumes and the Smagorinsky model with $C_s = 0.1$. Fig. 2 shows a first qualitative comparison of the time–

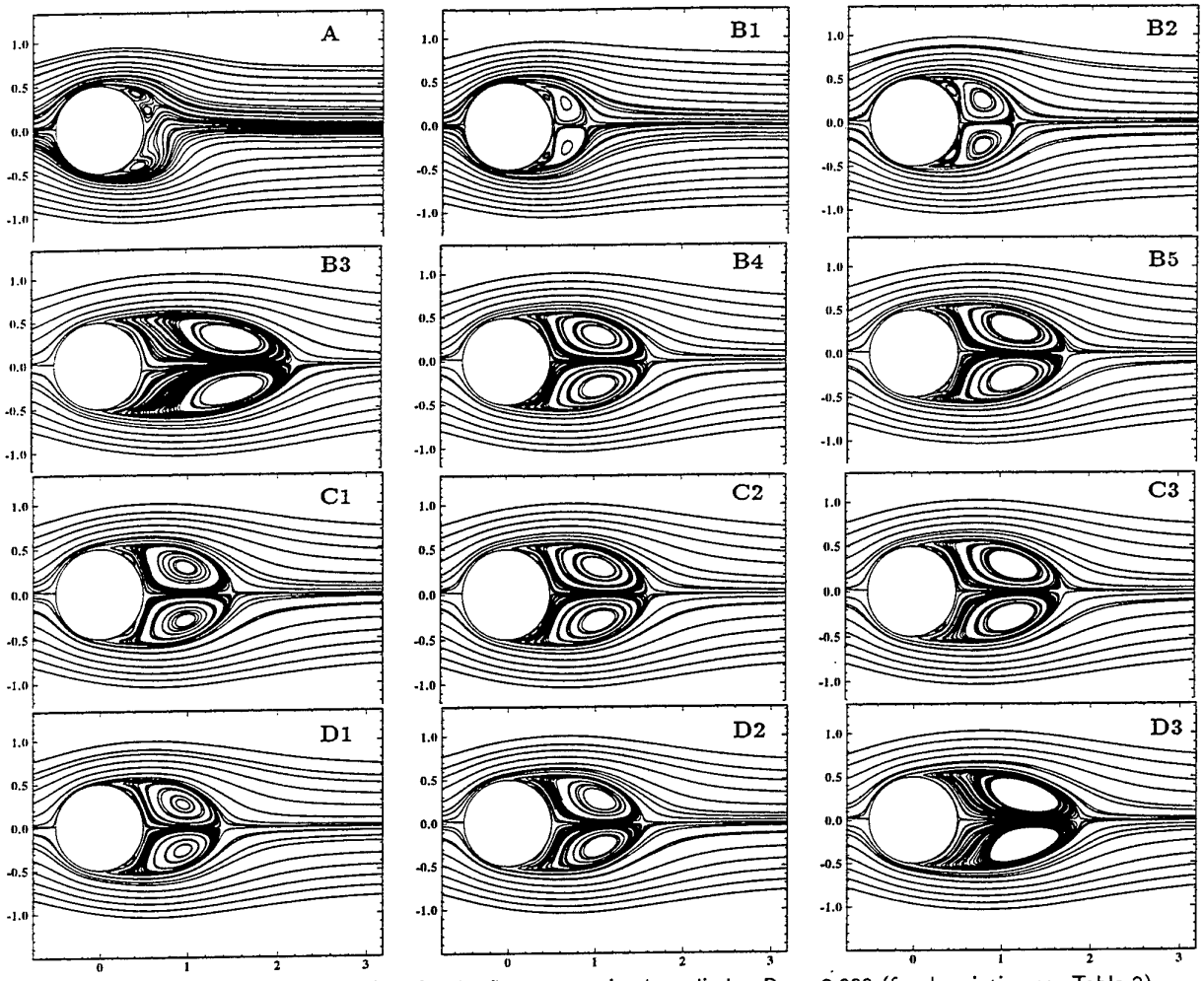


Figure 2: Time–averaged streamlines for the flow past a circular cylinder, Re = 3,900 (for description see Table 2).

averaged streamlines. Although it is already known in the LES community that the discretization scheme plays a dominant role for the quality of the solution it is worth demonstrating this important issue by illustrative applications. As shown in Fig. 2 the structure and the length of the recirculation bubbles behind the cylinder are strongly influenced by the numerical scheme. In all simulations a recirculation region behind the cylinder exists. Additionally, two small counter–rotating vortices attached to the backward side of the cylinder can be observed. Therefore three angles can be determined: the primary separation angle Θ_1, the reattachment angle Θ_2, and the secondary separation angle Θ_3. The values are listed in Table 2 in conjunction with the recirculation length L_r/D, the drag coefficient C_d, and the back–pressure coefficient $C_{P_{back}}$. The Strouhal number of the vortex shedding frequency has not been added to Table 2 because for all simulations the computed values are found to be within the experimental range of $St = 0.215 \pm 0.005$ determined by Cardell (1993). Apparently, this quantity is not very sensitive to the parameters of the simulation. Rodi et al. (1997) already pointed out that accurate prediction of the Strouhal number is not necessarily an indication of a quality simulation.

As known from measurements (e.g. Son and Hanratty, 1969) separation should take place before the apex of the cylinder at approximately $\Theta_1 = 85 \pm 2$. In Run **B1** (Hybrid scheme) separation is postponed for about 10 degrees. The recirculation length is only one third of the experimental value resulting in a much too high back–pressure coefficient and drag value. Simulation **B2** shows a similar trend. However, the results are quantitatively slightly better but still not in good agreement with measured values. Run **B3** based on the Quick scheme shows an opposite behavior. Here the computed recirculation length is about 27 % larger than the experimental value and the back–pressure and drag coefficients are even smaller than in experiment. This is a totally unexpected result. As already mentioned above the Quick scheme combined with the midpoint rule is of second order accuracy. It generates a disperse third order error term as well as a dissipative fourth order error term thats acts like an additional subgrid scale model. Similarly to the dissipative second order error term of the Hybrid and the HLPA scheme the fourth order term is expected to add numerical diffusion to the problem leading, at least in part, to shorter recirculation zones. However, the Quick scheme shows the opposite result and actually no explanation can be offered for this behavior.

The best results compared with experiments available (e.g. Ong and Wallace, 1996) are achieved by the CDS–2 and the CDS–4 scheme. The error terms of both schemes do not have any even component (second or fourth order derivatives) which damp out high frequency components in the solution. The results of CDS–4 (**B5**) are in slightly better agreement with experimental observation than those of CDS–2 (**B4**). However, the variations between these two results are much smaller than among the others. In Fig. 3 the time–averaged axial velocity distribution along the centerline is plotted in comparison with measurements by Lourenco and Shih (1993) and Ong and Wallace (1996). This figure summarizes the observations based on the streamline plots. Additionally, the distribution of the resolved turbulent kinetic energy k is shown.

The Hybrid scheme (**B1**) and the HLPA scheme (**B2**) generate the largest maxima of k quite close to the cylinder in a distance of about $0.5D$ and $0.75D$, respectively. Additional peaks of k can be observed directly in the vicinity of the wall. The maxima of k produced by CDS-2 (**B4**) and CDS-4 (**B5**) are smaller than for **B1** and **B2** and their locations farther downstream. The lowest maximum is achieved by the Quick scheme (**B3**). In all simulations the position of the maxima coincides quite well with the recirculation length L_r/D. However, the high levels of k especially for **B1** and **B2** have to be explained because they seem to be contradictory to the high numerical diffusion produced by these approximations. In the circular cylinder flow we see strong vortex shedding behind the cylinder, accompanied by turbulent fluctuations. Due to this large-scale vortex shedding the resolved turbulent kinetic energy k is a sum of the quasi-periodic oscillations and the resolved turbulent fluctuations. In order to separate these two effects it would be necessary to perform phase-averaging which is associated with several problems as described by Breuer and Pourquie (1996). However, looking at instantaneous flow fields of **B1–5** (not shown here) the apparent contradiction turns out fine. In case of **B1** and **B2** the simulated flow looks like laminar vortex shedding showing nearly no turbulent fluctuations as expected for LES of a turbulent flow. That means that the high levels of k for these simulations are almost completely generated by the quasi-periodic vortex shedding and not by turbulent fluctuations. This observation is consistent with the high level of numerical diffusion typical for upwind schemes (**B1–2**). Simulations **B4** and **B5** generate instantaneous flow fields as expected for the flow past a cylinder at a subcritical Reynolds number. The vortex shedding motion is superimposed by strong turbulent fluctuations. Again, the result of Run **B3** is difficult to explain. Turbulent motions can be observed. However, exact splitting of quasi-periodic and turbulent components cannot be achieved without phase-averaging.

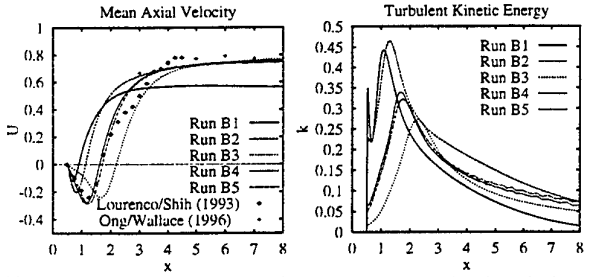


Figure 3: Mean axial velocity and total resolved turbulent kinetic energy along the centerline for Run **B1–5**.

Influence of subgrid scale modelling

In comparison with these large variations of the results applying different numerical schemes Fig. 2 indicates a rather small influence of subgrid scale modelling (Run **C1–3**). This is a series of three simulations in which only the model for the non-resolvable subgrid scale stresses has been varied. In Table 2 the computed integral quantities are listed. Simulation **C1** without any subgrid scale model shows the shortest recirculation length and the highest back-pressure and drag coefficient of all **C**-cases. Switching on the Smagorinsky model (**C2**) results in slightly improved values. The recirculation length increases and accordingly the drag decreases. This trend continues if the dynamic model (**C3**) is applied instead of the Smagorinsky model. The distribution of the pressure coefficient C_p and the friction coefficient C_f on the surface of the cylinder is plotted in Fig. 4 for **C1–3**. In the front part of the cylinder nearly no differences in the results can be observed. Because the flow is laminar in this region subgrid scale modelling does not have any influence (as expected). However, on the backward side small deviations occur especially for the pressure distribution. The results obtained with the Smagorinsky (**C2**) and dynamic models (**C3**) are close to each other and show better agreement with experimental values for $Re = 3,000$ (Norberg, 1987) than **C1** without any subgrid scale model. The size of the separation and reattachment regions on the cylinder is similar in all simulations.

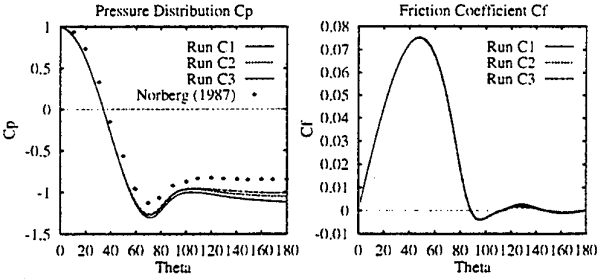


Figure 4: Pressure coefficient C_p and friction coefficient C_f using different subgrid scale models (Run **C1–3**).

In Fig. 5 the time-averaged axial velocity as well as the resolved turbulent kinetic energy k along the centerline are plotted for Run **C1–3**. As observed before the location of the maximum of k corresponds fairly well with the recirculation length. It appears that k is reduced when the Smagorinsky model is switched on. Surprisingly, k is further reduced when the Smagorinsky model is replaced by the dynamic approach.

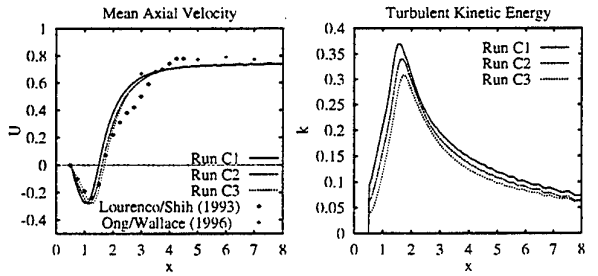


Figure 5: Mean axial velocity and total resolved turbulent kinetic energy along the centerline for Run **C1–3**.

Influence of resolution

In order to investigate the influence of the spanwise resolution a new series of simulations **D1–3** has been carried out which differs from **C1–3** only by the doubled number of control volumes. Again, Fig. 2 shows the streamline plots of the time-averaged flow and Table 2 lists the computed integral parameters. The largest deviation between a **D**- and a corresponding **C**-result occurs for the simulation applying the dynamic model (**C3/D3**). In Fig. 6 the turbulent kinetic energy k is plotted along the centerline as well as the pressure distribution on the surface. In comparison with the results of series **C** sketched in Fig. 5 k increases for all subgrid scale models and the deviations between the results achieved with different models do not decrease on improving the spanwise resolution. For the pressure distribution the deviations are even emphasized. However, Run **D3** shows a fairly good agreement with the measurements of Norberg (1987) as well as with the integral quantities listed in Table 2.

Fig. 7 shows total Reynolds stress profiles in the near wake ($x/D = 1.54$) obtained from **D1–3**. For all simulations the streamwise Reynolds stress $\overline{u'u'}$ is fairly well predicted in comparison with measurements of Lourenco and Shih (1993). The dynamic model **D3** yields slightly better results. However, the cross-stream Reynolds stress $\overline{v'v'}$ is highly overpredicted in the simulation without any subgrid scale model **D1** and with Smagorinsky model **D2**. This result is totally contradictory to the observations of

Beaudan and Moin (1994) who found underpredicted values of this quantity. Again, the dynamic model (**D3**) shows an excellent agreement with the measurements according to the simulations of Beaudan and Moin (1994).

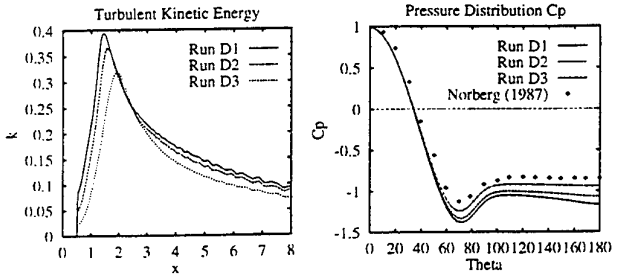


Figure 6: Total resolved turbulent kinetic energy along the centerline and pressure coefficient C_p along the cylinder surface for Run **D1–3**.

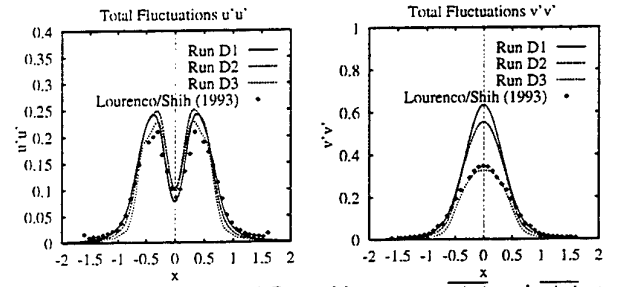


Figure 7: Total resolved Reynolds stresses $\overline{u'u'}$ and $\overline{v'v'}$ at $x/D = 1.54$ for Run **D1–3**.

Finally, two more aspects have been investigated. First the domain of integration is doubled in the spanwise direction (Run **E1**) by doubling the number of grid points compared with **C2** while keeping the spanwise cell size constant. According to the computed integral parameters this modification does not improve the results significantly. Another test (Run **E2**) increases the domain of integration four times in the radial direction while keeping the internal grid unchanged (as described above). Also this modification is rather irrelevant to the computed results indicating that the previously used domain size is fully sufficient.

CONCLUSIONS

The strong impact of three–dimensionality for LES calculations as well as the important aspect of low–diffusive discretization schemes for the convective fluxes have been presented and discussed. The investigation confirms the statement that the numerical dissipation produced by a scheme is more crucial for LES than its formal order of accuracy. Furthermore, the influence of subgrid scale modelling and spanwise resolution has been studied in detail. Drawing conclusions from the investigations above the dynamic model (**D3**) yields the best solution which agrees fairly well with experimental measurements. Finally, the important role of spanwise resolution has to be emphasized which has often been underestimated for LES of flow problems with a homogeneous direction.

ACKNOWLEDGEMENT

Financial support by the Bayerische Forschungsstiftung in the Bavarian Consortium of High–Performance Scientific Computing (FORTWIHR II) is gratefully acknowledged.

REFERENCES

Beaudan, P., Moin, P., 1994, *Numerical Experiments on the Flow past a Circular Cylinder at a Sub–Critical Reynolds Number,* Report No. TF–62, Thermosciences Division, Dept. of Mech. Engineering, Stanford University.

Breuer, M., Rodi, W., 1994, *Large–Eddy Simulation of Turbulent Flow through a Straight Square Duct and a 180° Bend,* Fluid Mech. and its Appl., vol. **26**, Direct and Large–Eddy Simulation I, Sel. papers from the First ERCOFTAC Workshop on DNS & LES Guildford, Surrey, U.K., 27 - 30 March 1994, eds. P.R. Voke, L. Kleiser & J.P. Chollet, Kluwer Academic Publishers, Dordrecht.

Breuer, M., Pourquie, M., 1996, *First Experiences with LES of Flows past Bluff Bodies,* Proc. of the 3rd Intern. Symp. of Engineering Turbulence Modelling and Measurements, Heraklion–Crete, Greece, May 27–29, 1996, Engineering Turbulence Modelling and Exp. **3**, pp. 177–186, W. Rodi & G. Bergeles (eds.), Elsevier Science, Amsterdam.

Breuer, M., Rodi, W., 1996, *Large–Eddy Simulation of Complex Turbulent Flows of Practical Interest,* In: 'Flow Simulation with High–Performance Computers II', ed. E.H. Hirschel, Notes on Numerical Fluid Mechanics, vol. **52**, pp. 258–274, Vieweg Verlag, Braunschweig.

Breuer, M., Pourquie, M., Rodi, W., 1996a, *Large–Eddy Simulation of Internal and External Flows,* 3rd Int. Congress on Indust. and Applied Mathem., Hamburg, 3–7 July, 1995, Spec. Issue of ZAMM, "Issue 4: Applied Sciences –Especially Mechanics (Minisymp.)", eds. E. Kreuzer & O. Mahrenholtz, ISBN 3–05–501747–1, pp. 235–238, Akademie Verlag, Berlin.

Breuer, M., Lakehal, D., Rodi, W., 1996b, *Flow around a Surface Mounted Cubical Obstacle: Comparison of LES and RANS–Results,* IMACS–COST Conf. on CFD, 3–D Complex Flows, Lausanne, Switzerland, Sept. 13–15, (1995), In: 'Comp. of 3D Complex Flows', eds. M. Deville, S. Gavrilakis and I.L. Rhyming, Notes on Numerical Fluid Mech., vol. **53**, pp. 22–30, Vieweg Verlag, Braunschweig.

Cardell, G.S., 1993, *Flow past a Circular Cylinder with a Permeable Splitter Plate,* Ph.D. Thesis, Graduate Aeronautical Lab. California Inst. of Technology.

Germano, M., Piomelli, U., Moin, P., and Cabot, W.H., 1991, *A Dynamic Subgrid Scale Eddy Viscosity Model,* Phys. Fluids A **3** (7), pp. 1760–1765.

Leonard, B.P., 1979, *A Stable and Accurate Convection Modelling Procedure Based on Quadratic Upstream Interpolation,* Comput. Methods Appl. Mech. Engrg., vol. **19**, pp. 59–98.

Lilly, D.K., 1992, *A Proposed Modification of the Germano Subgrid–scale Closure Method,* Phys. Fluids A **4** (3), pp. 633–635.

Lourenco, L.M., Shih, C., 1993, *Characteristics of the Plane Turbulent Near Wake of a Circular Cylinder, A Particle Image Velocimetry Study,* private communication, (data taken from Beaudan and Moin, 1994).

Norberg, C., 1987, *Effects of Reynolds Number and Low–intensity Free–Stream Turbulence on the Flow around a Circular Cylinder,* Publ. No. 87/2, Dept. of Applied Thermosc. and Fluid Mech., Chalmer Univ. of Technology, Gothenburg, Sweden.

Ong, L., Wallace, J., 1996, *The Velocity Field of the Turbulent Very Near Wake of a Circular Cylinder,* Experiments in Fluids, vol. **20**, pp. 441–453, Springer Verlag, Berlin.

Rodi, W., Ferziger, J.H., Breuer, M., Pourquié, M., 1997, *Status of Large Eddy Simulation: Results of a Workshop,* to appear in: Journal of Fluids Engineering, June 1997, Workshop on LES of Flows past Bluff Bodies, Rottach–Egern, Tegernsee, Germany, June 26–28, 1995.

Smagorinsky, J., 1963, *General Circulation Experiments with the Primitive Equations, I, The Basic Experiment,* Mon. Weather Rev. **91**, pp. 99–165.

Son, J., Hanratty, T.J., 1969, *Velocity Gradients at the Wall for Flow around a Cylinder at Reynolds Numbers from* 5×10^3 *to* 10^5, J. Fluid Mech., vol. **35**, pp. 353–368.

Zhu, J., 1991, *A Low–Diffusive and Oscillation–Free Convection Scheme,* Communications in Applied Numerical Methods, vol. **7**, pp. 225–232.

RESPONS OF SEPARAED FLOWS OVER A BACKWARD-FACING STEP TO LOCAL FORCING

Kyung Bin Chun
Samsung Motors Inc.
493, Banwol-ri, Taean-eup, Hwasung-kun, Kyungki-do, 445-970
Korea

Hyung Jin SUNG
Department of Mechanical Engineering
Korea Advanced Institute of Science and Technology
373-1 Kusong-dong, Yusong-ku, Taejon, 305-701
Korea

ABSTRACT

An experimental study was made of the flow over a backward-facing step in a wind tunnel as well as in a water channel. Excitations were given to separated flow by means of a sinusoidally oscillating jet issuing from a thin slit near the separation line. To characterize the lare-scale vortex evolution due to the local forcing, a flow visualization was performed by a dye tracer method with fluorescent ink. Small localized forcing near the separation edge enhanced the shear layer growth rate and prodced a large roll-up vortex at the separation edge. A large vortex in the shear layer gave rise to a higher rate of entrainment, which led to a reduction in reattachment length as compared with the unforced flow.

INTRODUCTION

Flows with separation and reattachment have been long subjects of fluids engineering research. The presence of a separated flow, together with a reattaching flow, gives rise to increased unsteadiness, pressure fluctuations, structure vibrations and noise. Also they tend to enhance heat and mass transfer and augment mixing. In particular, reattaching flows cause large variations of the local heat transfer coefficients as well as substantial flow noise augmentation. Thus, control of separated and reattaching flows is expected to have a wide application in fluids engineering.

A literature survey reveals that there have been many attempts to control or lessen the unfavorable behavior associated with separated and reattaching flows. Several methodologies have been applied by many researchers (Nagib et al., 1985; Roos and Kegelman, 1986; Bhattacharjee et al., 1986; Obi et al., 1993; Kiya et al., 1993; Sigurdson, 1995). Among the techniques in the literature, the introduction of a local forcing in the vicinity of the separation edge has been contemplated (Kiya et al., 1993; Sigurdson, 1995; Chun and Sung, 1996). These experimental efforts utilized a small-amplitude localized jet flow close to the separation edge. The jet flow contained a well-defined single-frequency pulsation. It was demonstrated that, by means of small localized perturbation near the separation edge, overall characteristics of the separated and reattaching flows were altered significantly. The afore-said method of controlling the separated and reattaching flow presents a promising ground for further study. The idea is that unfavorable characteristics may be reduced by the introduction of a small, localized perturbation near the vicinity of the separation edge. The success of the prior experiments suggests a need to extend experimental studies into the feasibility of separation control. In view of the relatively simple configuration, turbulent flow over a backward-facing step was selected for further experimental study.

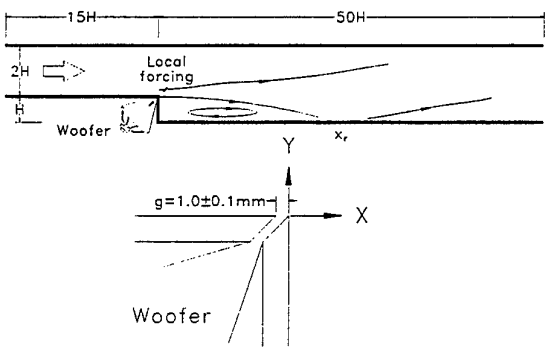


Figure 1: Test section and definition of axis.

EXPERIMENTAL PROCEDURES

Wind tunnel

The dimensions of the inlet channel were: the spanwise width $W = 625mm$, height $2H = 100mm$, and the length in the streamwise direction was $750mm$. Figure 1 shows a schematic view of the configuration of the test section. The step height (H) of a backward-facing step was $50mm$ and the aspect ratio was equal to 12.5. A $300mm$ woofer acoustic speaker was mounted inside the chamber. A sinusoidal velocity fluctuation was introduced through a spanwise thin slit along the separation line. The width of the slit g, was equal to $1.0 \pm 0.1mm$. The forcing amplitude (A_o) was defined as the ratio of the difference of total velocity (Q) due to oscillation to the mean free stream velocity (U_o): $A_o = (Q_{forced} - Q_{unforced})/U_o$. The total velocity Q was equal to $(U^2 + V^2)^{1/2}$, where U and V are the time-mean velocity fluctuation components near the separation point. The exper-

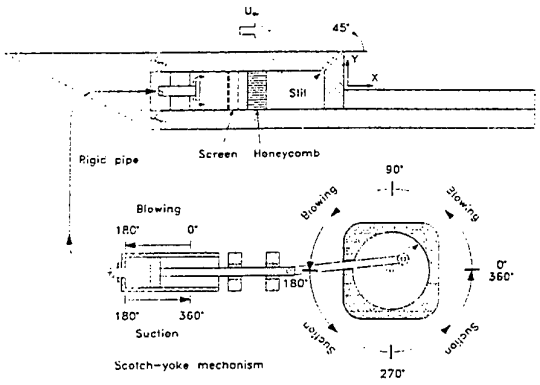


Figure 2: Test section and local forcing system.

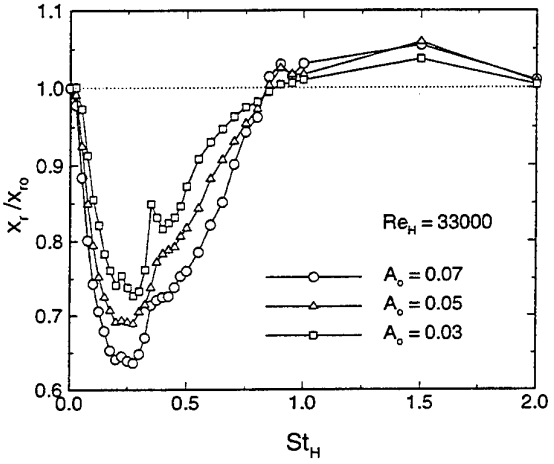


Figure 3: Normalized reattachment x_r/x_{ro} against St_H, at $Re_H = 33000$.

iment was carried out over the ranges of St_H ($0 \leq St_H \leq 5.0$) and A_o ($0.03 \leq A_o \leq 0.07$) at moderate Reynolds numbers ($13000 \leq Re_H \leq 33000$).

Water channel

A test rig of the present backward-facing step was immersed in a uniform main flow. As shown in Fig. 2, the step height was $H = 20mm$ and the spanwise width was $250mm$. Since the aspect ratio was 12.5, the two dimensional flow assumption can be applicable to a reasonable accuracy in the central portion of the test section. The local forcing was also introduced by a sinusoidally oscillating jet through a spanwise thin slit along the separation line. The slit width was equal to $g = 2.0 \pm 0.1mm$. The forcing was driven by a scotch-yoke system. As seen in Fig. 2, the slit was connected to a square cavity in which water was sinusoidally forced through a rigid pipe. A dye tracer method with fluorescent ink was employed in the present flow visualization. A 4W Argon-ion laser was used as a light source. Photographs were taken with an ASA-3200 film with the exposure time (1/125-1/250s). The moving image was managed by a CCD camera with a suitable diaphram and the recorded in a S-VHS video recorder. A three-beam, two-color LDV system (TSI 9100-8) was used to measure the velocity components in the recirculating region. In order to find the reattachment length (x_r), the forward-flow time-fraction (γ_p) in the vicinity of the wall was measured by a splitter

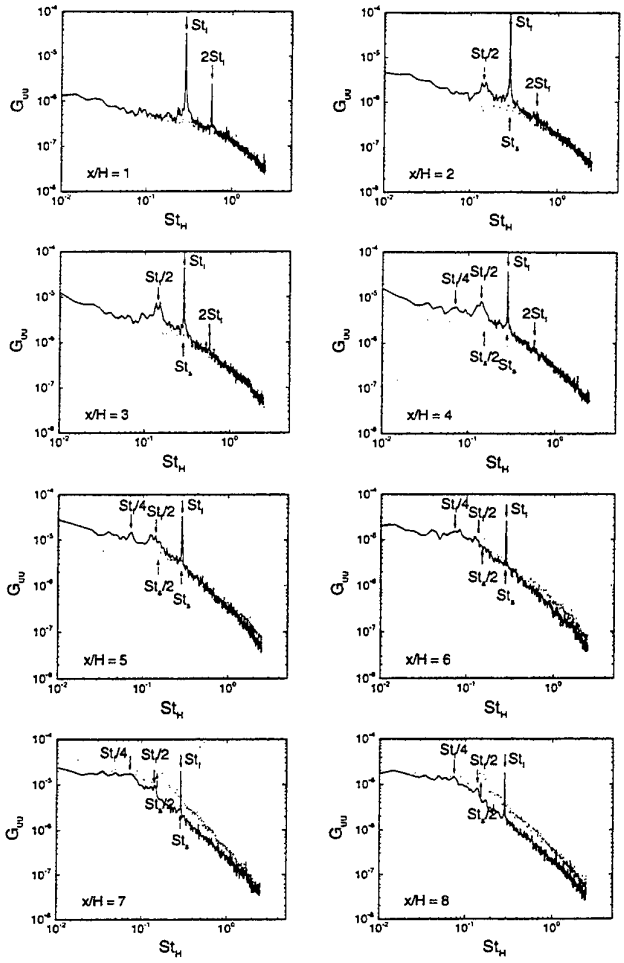


Figure 4: Velocity spectra along the streamwise position at $Re_H = 33000$.

film probe (TSI-1288). For an effective flow visualization, the Reynolds number was fixed at $Re_H = 1200$ at the fixed local amplitude $A_o = 0.3$. The forcing frequency was varied in a range of $0.3 \leq St_H \leq 1.0$.

RESULTS AND DISCUSSION

As a measure of effectiveness of the local forcing, the normalized reattachment length x_r/x_{ro} at $Re_H = 33000$ was plotted and shown in Fig. 3. Here, x_{ro} denotes the time-mean reattachment length without local forcing ($A_o = 0$). As seen in Fig. 3, the effect of local forcing on the reattachment length is substantial. At a high forcing level ($A_o = 0.07$), the reattachment has a single minimum approximately at $St_H = 0.27$. The forcing amplitude (A_o) affects only the size of reattchment length, i.e., the reattchment length decreases generally with increasing forcing levels.

However, a closer inspection of Fig. 3 for lower forcing amplitude ($A_o = 0.03$) discloses that double minima of x_r/x_{ro} are observed at about $St_H \cong 0.27$ and $St_H \cong 0.40$. These two distinct minima also have been detected by other researchers (Nagib et al., 1985; Kiya et al., 1993). The smaller reduced frequency ($St_H \cong 0.27$) is related to the shedding-type instability in the separated shear layer and is associated with the momentum exchange induced by the modulation of the separated shear layer (Nagib et al., 1985). For a large value of the reduced frequency ($St_H \cong 0.40$), the dominating mechanism is the formation and shedding of energetic vortices caused by local forcing. This effect may be related to the shear layer instability in the initial boundary

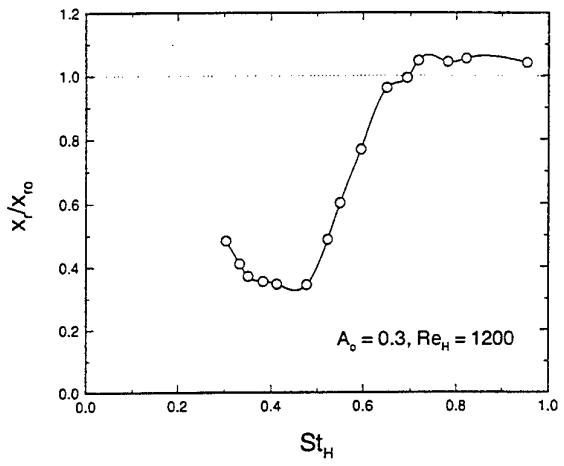


Figure 5: Normalized reattachment x_r/x_{ro} against forcing frequency St_H.

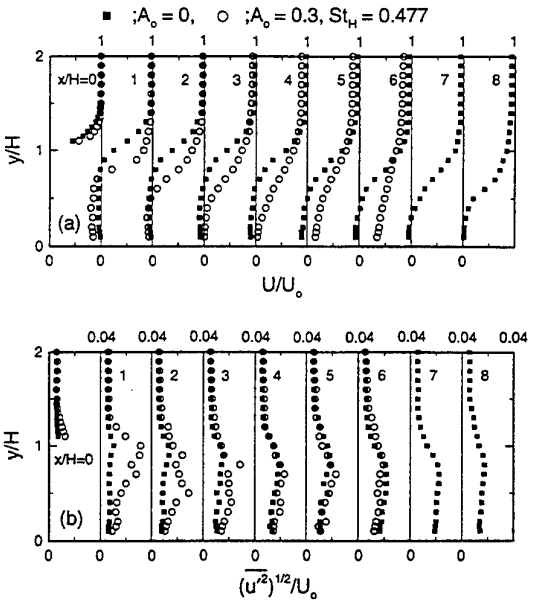


Figure 6: Profiles of U/U_o and $(\overline{u'^2})^{1/2}/U_o$ at $Re_H = 1200$, (a) mean velocity (b) turbulence intensity.

layer. It is known that the local forcing increases the shear-layer growth rate and produces a large roll-up vortex at an earlier separation edge. A large vortex in the shear layer produces a higher rate of entrainment, which leads to the reduction of the reattachment length as compared to the unforced flow ($A_o = 0$).

In an effort to understand the mechanism of the effect of local forcing, the spectra of streamwise velocity fluctuations were measured and presented in Fig. 4 as a function of downstream distance. The spectra were obtained at the position $U/U_{max} = 0.95$, where the value of streamwise velocity was 95% of the maximum velocity. Comparisons are made for two cases : i) $A_o = 0$, and, ii) $A_o = 0.07$ and $St_H = 0.275$. The spectra of $A_o = 0$ are plotted with dotted lines and the spectra of $A_o = 0.07$ and $St_H = 0.275$ with solid lines. The notation St_f in Fig. 4 denotes the reduced forcing frequency ($St_f = f_f H/U_o$) and St_s is the reduced shedding frequency ($St_s = f_s H/U_o$). Here, the shedding frequency f_s was obtained near the reattachment position in unforced flow.

Near the separation edge ($x/H = 1.0$), no significant peak is displayed for the unforced flow ($A_o = 0$); whereas, a sharp peak is exhibited at the forcing frequency (St_f). It can be observed that the energy levels for both cases are relatively low. At $x/H = 2.0$, a spectrum peak corresponding to the first subharmonics ($St_f/2$) of the forcing frequency begins to emerge. This suggests that a large-scale vortex amalgamation takes place in the separated shear layer apparently due to the local forcing. This vortex merging causes the increase in turbulence intensities so that the overall turbulence levels are significantly enhanced. The vortex-shedding frequency (St_s) in the unforced flow may be observed, which is nearly coincident with the present forcing frequency ($St_s \cong St_f$). This result is supportive of Sigurdson's argument that the most effective forcing frequency for minimum reattachment length is generated at or near the frequency of the shedding for unforced flow.

As the flow is convected downstream, the peak value of St_f is gradually attenuated. Conversely, the peak value of $St_f/2$ becomes larger as a function of downstream distance. At $x/H = 4.0$, the second subharmonics ($St_f/4$) appears, which suggests a second vortex merging. This process results in an increase in turbulence levels. After reattachment, however, no further vortex-pairings are detected and the energy levels also are diminished. For $x/H = 6.0$, the turbulence energy levels are even lower than for the case of the unforced flow. Although two vortex-pairings are present in the forced flow ($St_f/2, St_f/4$), only one subharmonics ($St_s/2$) appears in the unforced flow ($4.0 \leq x/H \leq 8.0$). The first vortex-merging creates an increase of turbulence levels, where the turbulence levels are higher than those of the forced flow until the reattachment ($x/H = 8.0$).

Next, the normalized reattachment length x_r/x_{ro} for water channel is displayed in Fig. 5. The lower limit of the forcing frequency was set by practical loboratory constraints. At a particular forcing frequency $St_H = 0.4$, the reattachment length is reduced significantly. However, as St_H increases further $St_H \geq 0.8$, the reattachment length is even larger than that of the unforced flow ($A_o = 0$).

In order to see the effect of local forcing on the time-averaged flow, a detailed measurement was made at $Re_H = 1200$ for two cases ($A_o = 0$ and $A_o = 0.3, St_H = 0.477$). Contrary to the air flow case, the measurement in the recirculating region behind a backward-facing step was possible by using the present two-component LDV system. In the prior wind tunnel experiment (Chun and Sung, 1996), the hot-wire anemometer was employed, i.e., the profiles in the recirculating region could not be measured. As seen in Fig. 6(a), a relatively large effect by local forcing is displayed on the development of the separated flow ($1 \leq x/H \leq 6$). In the near-region of separation ($x/H = 0$), the mean velocity profiles are only slightly modified by local forcing. However, significant changes are detected in the shear layer region ($1 \leq x/H \leq 3$). After reattachment ($x/H = 3$), the flow is gradually redeveloped. Figure 6(b) represents the time-averaged turbulence energy levels. The influence of local forcing on the turbulence energy levels is pronounced in the recirculating region. As opposed to the mean velocity profiles in Fig. 6(a), after reattachment ($x/H \geq 3$), it is shown that the turbulence intensity is recovered more rapidly. This suggests that the amalgamation of the rolled-up vortices induced via local forcing can increase turbulent intensity levels within the separated shear layer.

The sequential pictures for one period of local forcing ($0° \leq \phi \leq 360°$) are presented in Fig. 7 for three forcing cases. These forcing cases, respectively, are prototypical of the qualitatively distinct conditions: no forcing case ($A_o = 0$), the minimum reattachment length case ($A_o = 0.3, St_H = 0.477$) and the maximum reattachment case ($A_o = 0.3, St_H = 0.650$). For $A_o = 0$, the flow at the separation edge is flapped downstream by the shear layer instability at $x/H = 4 \sim 5$. A closer inspection near the corner step discloses that a corner flow exists near $x/H \leq 1$. Moreover, the weak flow circulation are clearly captured within the recirculating region ($0 \leq x/H \leq 4$). After reattachment, the large-scale vortices are separated and redeveloped downstream. When the effective local forcing is per-

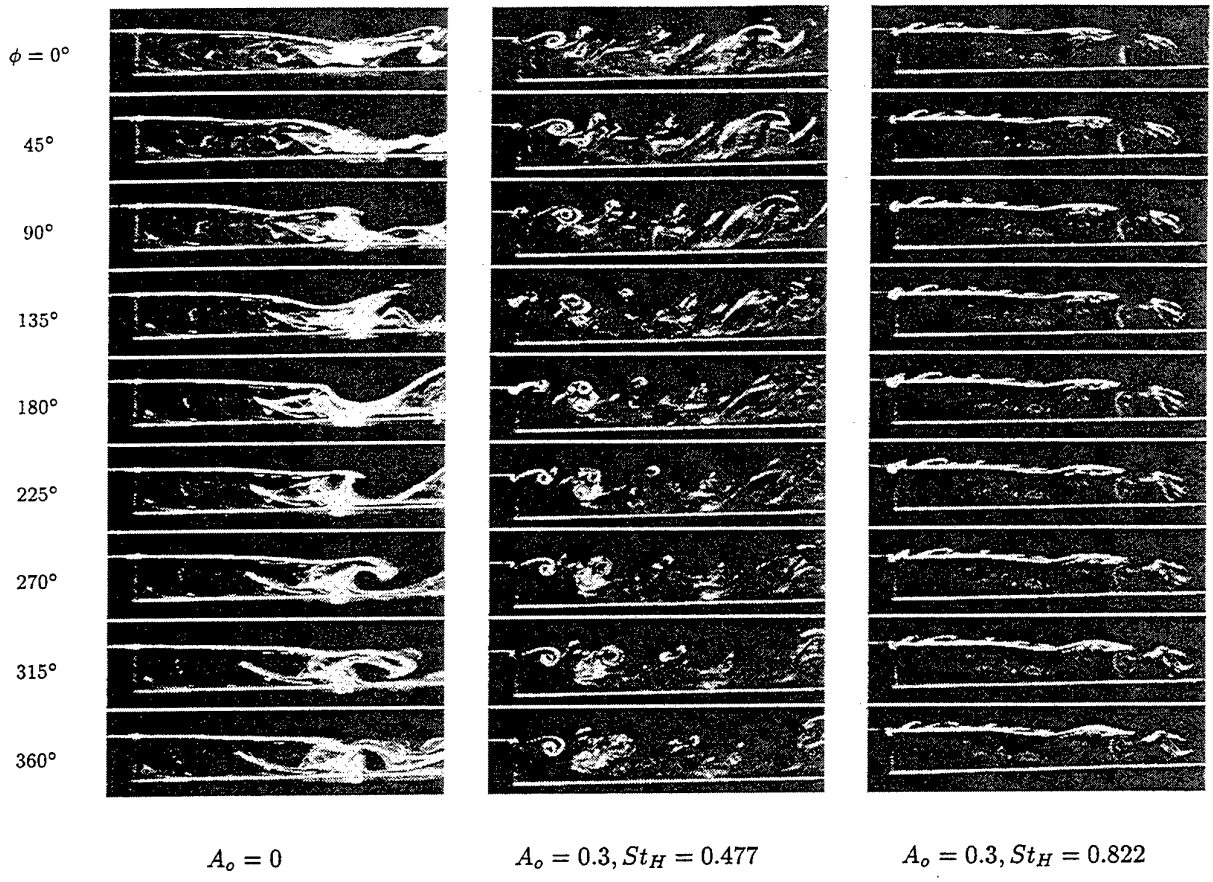


Figure 7: Time evolution of large-scale vortices, $Re_H = 1200$.

turbed ($A_o = 0.3, St_H = 0.477$), the rolled-up vortex due to local forcing is clearly seen at $0 \leq x/H \leq 1$. As time elapses, the rolled-up vortex is merged with the prior one and then convected downstream. However, when the forcing condition is $A_o = 0.3, St_H = 0.650$, the recirculating region is not influenced by the local forcing. The disturbed flow is simply propagated downstream along the dividing streamline.

The enlarged view of the initial rolled-up vortex formation is displayed in Fig. 8. A closer inspection of the flow near the separation edge reveals that, in a local suction stage ($0° \leq \phi \leq 90°$), a rolled-up vortex is just generated from the inlet wall layer at the separation edge. As time proceeds, this rolled-up vortex is convected downstream. However, when a local blowing is commenced ($\phi \geq 105°$), the inlet rolled-up vortex is influenced by the local issuing jet. It is clearly seen that a jet flow due to the local blowing penetrates into the initial rolled-up vortex. A new rolled-up vortex formation is shown, which is then splitted into a pair of vortices, i.e., the upper and lower vortex. As stated above, the upper vortex is merged with the pre-staged lower vortex, which increases flow mixing in the recirculating region.

CONCLUSIONS

The effect of local forcing on the turbulent flow over a backward-facing step was significant. The amalgamation of the rolled-up vortices increased the turblence intensity levels. In the present flow visualization, the initial rolled-up vortex was splitted into two vortices with different rotations. The upper vortex was merged with the prior lower one, while the new lower onw was convected downstream. These amalgamation of the rolled-up vortices can increase flow mixing, which results in shortening of the reattachment length.

REFERENCES

Bhattacharjee, S., Scheelke, B., and Troutt, T. R., 1986, "Modifications of vortex interactions in a reattaching separated flow", *AIAA J.*, Vol. 24, pp. 623–629.

Brederode, V. and Bradshaw, P., 1978, "Influence of the side walls on the turbulent center-plane boundary-layer in a squareduct", *J. Fluids Eng.*, Vol. 100, pp. 91–96.

Chun, K. B. and Sung, H. J., 1996, "Control of turbulent separated flow over a backward-facing step by local forcing", *Exp. Fluids*, Vol. 21, pp. 417–426.

Eaton, J. K. and Johnston, J. P., 1980, "Turbulent flow reattachment: An experimental study of the flow and structure behind a backward-facing step", Report MD-39, Thermoscience Division, Department of Mechanical Engineering, Standard University.

Kiya, M., Shimizu, M., Mochizuki, O., Ido, Y., and Tezuka, H., 1993, "Active forcing of an axisymmetric leading-edge turbulent separation bubble", AIAA paper (AIAA-93-3245), July 6-9, Orlando, FL, USA.

Kiya, M., Shimizu, M., Mochizuki, O., and Ido, Y., 1993, "The forced turbulent separation bubble", in *9th Symposium on Turbulent Shear Flows*, August 16-18, Kyoto, Japan.

Nagib, H. M., Reisenthel, P. H., and Koga, D. J., 1985, "On the dynamical scaling of forced unsteady separated flows", in *AIAA Shear Flow Control Conference*, AIAA-85-0553, March 12-14, Boulder, Colorado.

Roos, F. W. and Kegelman, J. T., 1986, "Control of coherent structures in reattaching laminar and turbulent shear layers", *AIAA J.*, Vol. 24, pp. 1956–1963.

Sigurdson, L. W., 1995, "The structure and control of a turbulent reattaching flow", *J Fluid Mech.*, Vol. 298, pp. 139–165.

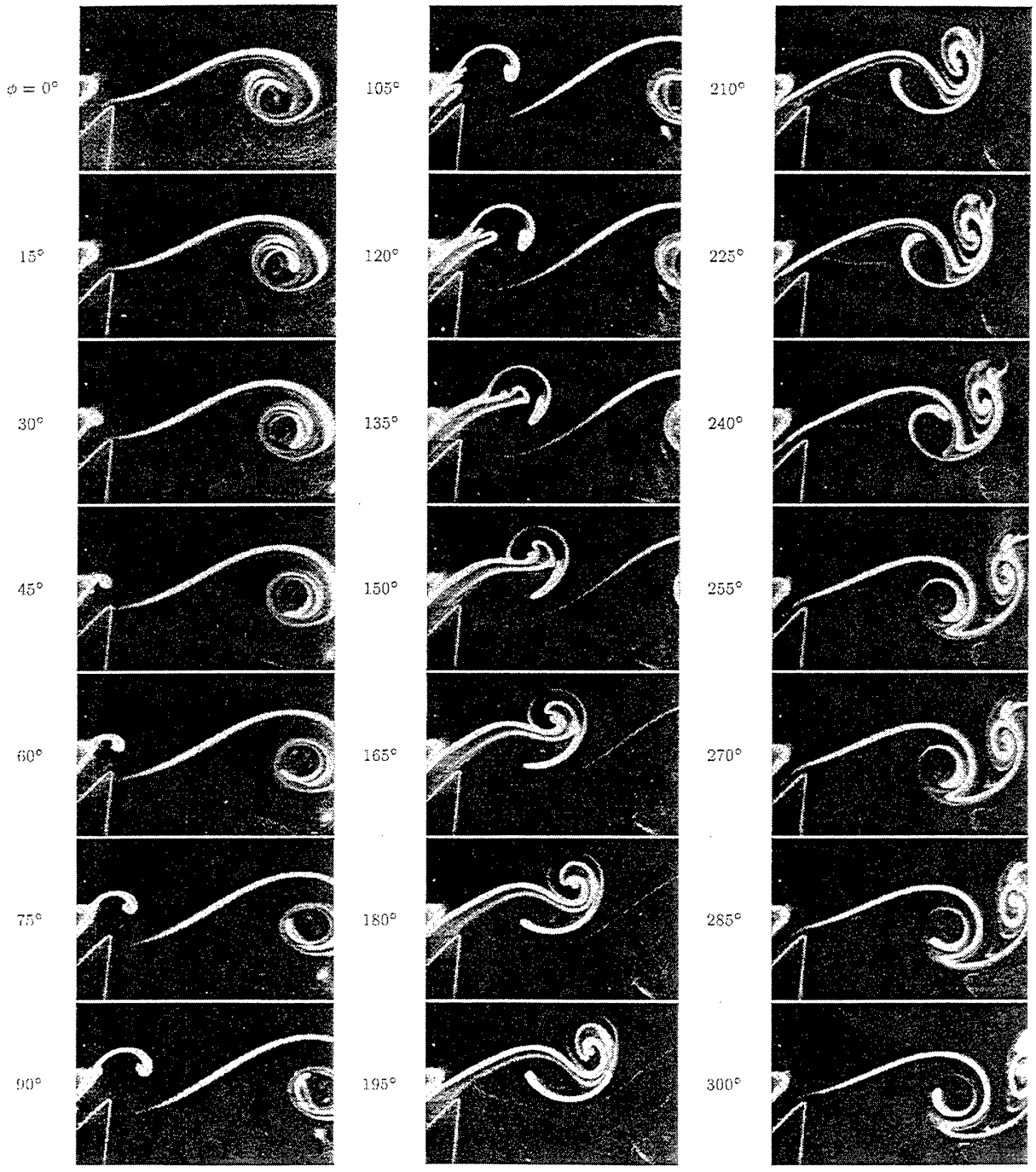


Figure 8: Detailed evolution of initial rolled-up vortex at $A_o = 0.3, St_H = 0.477$.

AN EXPERIMENTAL INVESTIGATION OF THE FLOW AROUND A TWO-DIMENSIONAL SQUARE PRISM IN THE PROXIMITY OF A SOLID WALL: EFFECT OF THE GAP SIZE

Robert J. Martinuzzi and Kenjo C.Q .Wu
Department of Mechanical & Materials Engineering
The University of Western Ontario
London, Ontario, N6A 5B9
Canada

ABSTRACT

Results are reported for an experimental study of the flow around a two-dimensional, square prism placed in the vicinity of a solid wall with a cylinder face mounted normal to the on-coming flow at a Reynolds number of 23,000 (based on the prism side dimension, D, and the free-stream velocity) for several wall-to-prism gap heights. The nominal boundary layer thickness was 1.5D at the cylinder location. Velocity data were acquired using a two-component Laser Doppler Velocimeter and a Hot-Wire Anemometer. Oil-film and light-sheet visualization techniques were used to document flow behavior. Three distinct flow topologies are identified based on the gap height. For large gaps, the influence of the wall results in a deflection of the far wake flow. For intermediate gap heights ranging from 2D to 0.3D, the vortex shedding frequency increases while the drag decreases and local separation of the wall boundary layer may be observed. For smaller gaps, vortex shedding activity could not be detected.

INTRODUCTION

Bluff body flows are of fundamental interest because of the complex nature of the interactions between the turbulent and the large-scale, often periodic coherent flow structures in the wake region. The understanding gained from such studies finds application in dispersion problems (eg. Pollutant transport, cooling of electronic components) or in wind engineering. Albeit most practical geometries result in complicated three-dimensional flows, the study of two-dimensional configurations is a valuable diagnostic tool for investigating the physical mechanisms underlying very complex phenomena. While much literature is dedicated to the study of two-dimensional bluff bodies either mounted on the surface of a solid wall or suspended in a uniform flow, bluff bodies in the proximity of solid walls have received much less attention. This study concentrates on documenting one such flow as a function of the separation of a square cylinder from a solid wall.

At high Reynolds numbers, the flow around two-dimensional bluff bodies suspended in a uniform flow field is characterized by a highly turbulent wake dominated by the periodic shedding of large-scale vortices. The downstream extent of the near wake recirculation region is of the order of the obstacle dimension normal to the flow. For square cylinders normal to the flow, the separation streamline originates at the leading edges and does not reattach on the obstacle. The mean velocity and turbulent fields are symmetric about the prism streamwise centre plane (Bearman and Gradham, 1980; Lyn *et al.*, 1995). For two-dimensional, surface mounted bluff bodies, there is a separation vortex-system at the windward base of the obstacle. The wake is highly turbulent and the recirculation extends much further downstream than for the suspended case (Shofield and Logan, 1990). Quasi-periodic shear layer flapping activity is observed in the wake. For square prisms, the flow separates at the leading edge and will reattach on the obstacle top face only if the on-coming boundary layer thickness is significantly larger than the obstacle height (Castro, 1978).

Flows around bluff bodies in the proximity of solid walls show characteristics of both suspended and wall-mounted configurations. The resulting flow field depends on: (1) the shape of the geometry; (2) the Reynolds numbers, Re; (3) the channel blockage ratio; (4) the free stream turbulence level, Tu; (5) the wall-to-prism separation, S; and (6) the on-coming wall boundary layer thickness, δ. Wolochuk *et al.* (1996) , using hot-wire anemometry (HWA) show that the vortex shedding frequency, expressed in terms of the Strouhal number St, is much lower for square prisms than for triangular prisms at the same Re. The results of an HWA study of flow past suspended cylinders by West and Aspelt (1982) show that: (I) an increase of Re from $5x10^3$ to $5x10^4$ results in a decrease of St (0.207 to 0.190) and an increase in the drag coefficient , C_D (1.26 to 1.32); (ii) both St and C_D increase for blockage ratios greater than 6%. Wolochuk *et al.* (1996) show that an increase of Tu from 2.5% to 10% results in a 2.4% increase in St. It has also been shown that the onset of vortex formation and shedding will only occur above a critical gap height. Grass *et al.* (1984) report that, for the flow around a circular cylinder of diameter D, vortex shedding could not be observed below $S/D \approx 0.3$ for boundary layer thickness $\delta/D < 2.5$ and $S/D = 0.5$ for $\delta/D \geq 3.5$. Taniguchi and Miyakoshi (1990) report critical gap heights of $S/D \approx 0.3$ for $\delta/D < 0.4$ and 0.8 at $\delta/D \approx 1$.

The forces induced on a square cylinder placed in the proximity of a solid wall were investigated by Devarakonda and Humphrey (1995) for a thin boundary at a Reynolds number Re_D=10,000 (based on the prism side length, D, and free stream velocity, U_∞); blockage ratio of 13.75% and Tu=1.7%. It was found that while the lift coefficient increases, the drag coefficient decreases with decreasing gap height. Durao *et al.* (1991) investigated a similar flow (Re_D= 13,600; Tu=3%; blockage ratio of 12.8% and δ/D=0.8) using Laser-Doppler Velocimetry (LDV) and reported that vortex shedding activity is suppressed for gap heights smaller than S/D≈0.375. Above the critical gap height, it was found that St was independent of Re_D or S/D. Bosch *et al.* (1996) and Bosch and Rodi (1996) conducted both experimental and numerical studies of vortex shedding past a square cylinder near a wall at Re_D=22,000; blockage ratio of 12.8%; Tu=3% and δ/D=0.8. It was observed that vortex shedding occurs for S/D≥0.5, the flow is steady for S/D=0.25 and an intermediate flow behavior is observed for S/D=0.375.

This study presents results for the flow around a two-dimensional square prism at Re_D=23,000; $\delta/D\approx1.5$; Tu=2% and a total flow blockage ratio of 5.5%. Detailed velocities field measurements were performed for wall-to-prism separations of S/D= 0.25, 0.5, 1, 2, 4 and ∞ (remote wall). Flow visualization experiments and shedding frequency measurements were made for these and other gap heights as well.

EXPERIMENTAL SETUP AND CONDITIONS

The experiments were conducted in a suction-type, open-circuit subsonic wind-tunnel. The geometry and nomenclature are summarized in Fig. 1. The inlet nozzle has a smooth gradual contraction ratio of 6:1. Air is drawn at the inlet through a fine meshed screen grid and a honeycomb flow straightener. The test section consists of transparent plexiglas frame, with an internal square cross-section of 18". The test model, a square cylinder made of steel to ensure sharp edges, is placed at the working-section mid height (y/h=0.5) and 40D downstream of the test section entrance with one face perpendicular to the on-coming flow. The square cylinder side dimensions are D=1" and the span is 18D. A smooth flat plate with a serrated leading edge was used to obtain a controlled, fully-turbulent boundary layer. The square prism was placed at L=33.5D downstream of the plate leading edge. The boundary layer thickness, measured in the absence of the obstacle, was δ=1.5D at the location L.

MEASUREMENT TECHNIQUES

The mean velocity and the Reynolds stress fields were measured using a two-component LDV system, operated in back-scatter mode, with a 4 W Argon-Ion laser light sources. A Bragg-cell and downmixer (shift frequencies 5 and 10 MHZ) were used for direction discrimination. The optic probe (2.6x beam expander and 733 mm focal lens) was attached to a computer-controlled traversing mechanism to allow positioning within ±0.2 mm. Signals were processed using two IFA 550 (TSI Inc.) signal processors. A 50 μs coincidence window was set as velocity-pair validation criterion. A water-glycerine mixture was atomized to seed the flow. The typical particle size was less than 5μm (see Domnick and Martinuzzi, 1994) The particles were injected upstream of the channel inlet to avoid interference. Typical data rates was ranged from 1kHz to 5kHz and 30,000 events were recorded at each point. Shedding frequencies were determined using LDV (FFT with time-history method) and HWA(even time sampling). Measurements were repeated several times for several different locations in the obstacle wake. The frequency corresponding to the spectral peak was associated with vortex shedding activity. The drag coefficient was calculated from

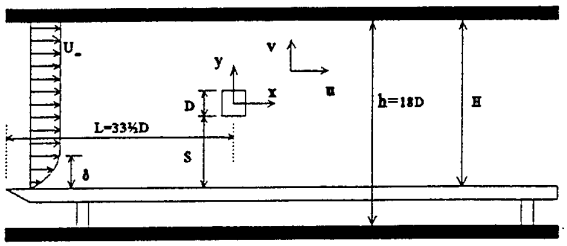


Fig.1: Definition of the flow geometry and nomenclature.

the integration of the momentum equation for several profiles in the wake region.

Surface flow patterns were also investigated using an oil-film visualization technique. The oil-film consisted of a kerosene, graphite and transmission oil mixture. Results were recorded on photographic film. The transient flow field behavior was also observed using a laser light-sheet technique.

The uncertainty in the velocity measurements was estimated based on detector electronic resolution and the statistical variance of the velocity data. Flow statistics were calculated by post-processing the acquired velocity data with an arrival-time weighting technique to compensate for bias affects. The uncertainty estimates for the mean velocity components are $0.015U_\infty$ in the free stream region and $0.03U_\infty$ in the wake region, where the velocity fluctuations were very large. The Reynolds stresses have uncertainties of 5% in the free stream and 8-10% in the wake region. The uncertainty bounds for the Strouhal number and drag coefficients is shown in the figures as error bars.

RESULTS

The Mean Flow Field

The measured mean streamwise, u, and vertical, v, velocity components for gap heights S/D=2, 1, 0.5 and 0.25 are represented as vectors in Fig. 2. Surface flow patterns, obtained on the solid wall with an oil-film technique, are shown in Fig. 3 for several gap heights. Analysis of the data indicates that they are at least three topologically distinct mean flow regimes based on gap height.

For large wall-to-prism separations (S/D≥4), the influence of the wall on the flow field is small. The present results for the remote wall case (S/D→∞) are not shown here since these are very similar to those extensively discussed by Lyn *et al.* (1995). Generally, the flow field is symmetric about the centre-plane, y/D=0. The flow separates at the leading edges and does not reattach on the prism lateral faces (y/D=±0.5). Over each of these faces, a topological node can be identified corresponding to the centre of a bound recirculation vortex. Two counter-rotating vortices can be identified in the near wake the recirculation region.The reverse flow region extends to x/D≈0.9 along y/D=0, at which location a free saddle point is located. A free saddle point is also located over each of the trailing edges which indicates that flow from the wake can penetrate the separation region over the lateral faces. This return flow gives rise to a very small secondary recirculation region which is observed as a thin dark band of pigment accumulation during the oil-film experiments. The results for the gap height S/D=4 are very similar to those for S/D→∞. The flow in the gap region is slightly faster than over the cylinder which results in a

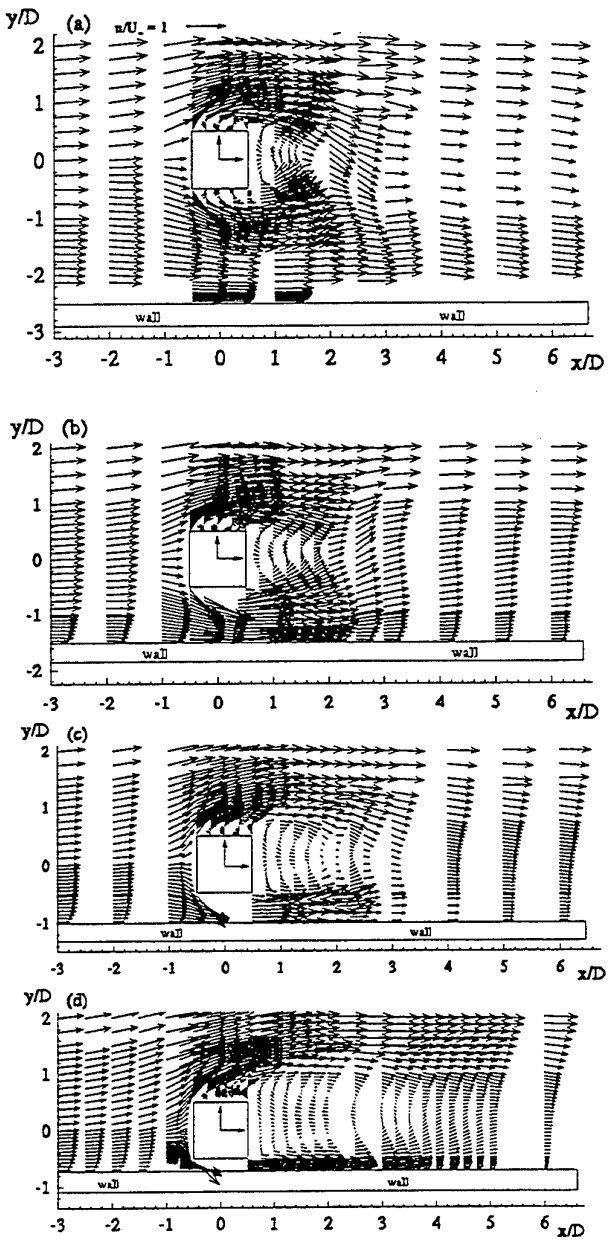


Fig. 2-Time-averaged vector representation of mean velocity: a) S/D=2; b) S/D=1; c) S/D=0.5 and d) S/D=0.25.

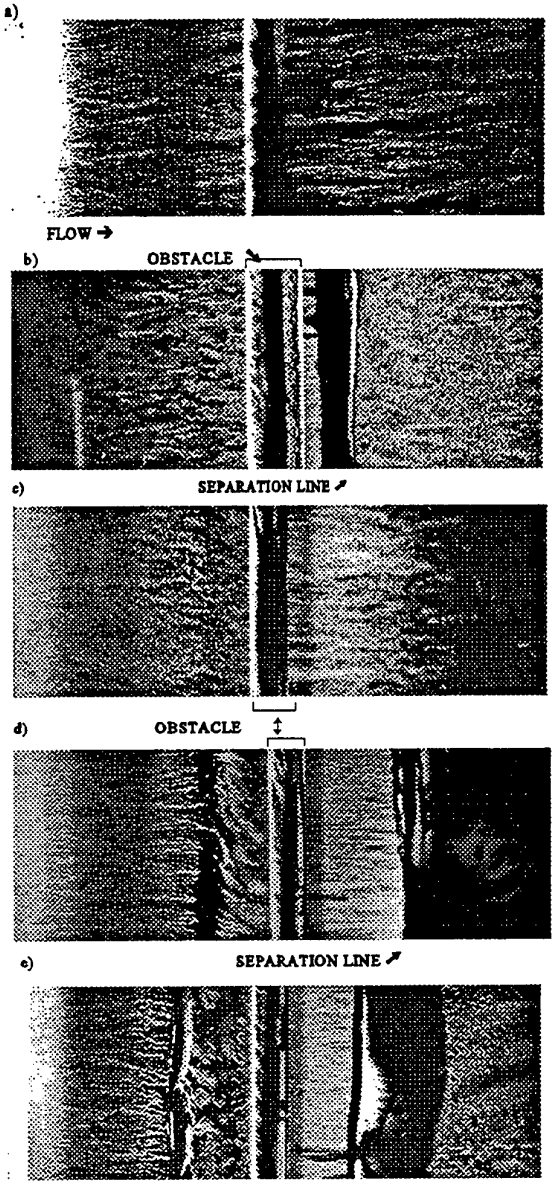


Fig. 3 - Flow patterns of the oil-film visualization: a) S/D=2; b) S/D=1; c) S/D=0.5; d) S/D=0.25 and e) S/D=0.19.

slight upwash in the far wake most noticeable in the region $2.5<x/D<4$. The flow field in the recirculation regions around the cylinder remains symmetric (see Wu and Martinuzzi, 1997).

The topological structure and behavior of the flow field changes significantly as the gap height is reduced. For example, for $0.5 \le S/D \le 2$, while vortex shedding activity was clearly detected, only one free saddle points could be identified (Fig. 2a-c). For S/D=0.25, only the free saddle point was observed (Fig. 2d) and the flow did not exhibit any periodicity. In general, the presence of the obstacle in the wall vicinity resulted in a thickening of the on-coming boundary layer. Although the acceleration of the fluid through the gap increases with decreasing S/D, the ratio of the mass flow rate through the gap to that deflected over the obstacle decreases (i.e. the upstream origin of the stagnation streamline drops further below y=0 as S/D decreases).

For the cases, S/D=1 and 2, the fluid stream from the gap expands quickly, by reasons of continuity, upon entering the wake region. Consequently, the structure of the near wake recirculation region is distorted away from the solid wall. The location of the vortex cores is clearly shifted upwards. The flow over the top face of the obstacle is very similar to that for the suspended cylinder. The flow separates at the leading edge and does not reattach. This leads to a small secondary recirculation at the obstacle trailing edge (see the thin pigment accumulation line near the trailing edge in Fig. 3a,b) and a free saddle point above the trailing edge. On the lower face, the flow again separates at the leading edge, but

reattaches on the face, as seen clearly in Fig. 2a for S/D=2. Measurements could not be made for S/D=1 on the bottom face due to optical access restrictions. However, the velocity vectors at the trailing edge strongly suggest that the flow reattaches on the bottom face for S/D=1 as well (see Fig. 2b). Thus, a free saddle point cannot exist below the trailing edge. The flow fields for S/D=1 and 2 are thus topologically different from those at S/D=4 or S/D=∞. This result differs from that reported by Bosch *et al.* (1996). Whereas the far wake flow for S/D=2 is characterized by a downwash (flow towards the wall), that for S/D=1 shows a clear upwash. This difference is further emphasized by the appearance of a separation bubble along the solid wall between x/D≈0.9 and 2. (see pigment accumulation in Fig. 3b). Although the vector diagrams of Fig. 2b do not clearly show this boundary layer separation, the measured values for $\overline{u'v'}$-profiles show an inflection point and a sign change near the wall in the region 1<x/D<2 (see Fig. 4) which is consistent with the appearance of a recirculation zone. Further evidence is provided by observation using the light-sheet technique. The flow pattern in Fig. 5 shows smoke lifting from the wall at approximately x/D≈1 and the entire wake flow is moving upwards. This pattern was a dominant occurance for S/D=1 but was not observed for S/D=2.

The flow field for S/D=0.5 (Fig. 2c,3c) is topologically similar to that for S/D=2. The flow does not reattach on the top face of the obstacle but does on the bottom face. The near wake flow is also skewed away from the wall. The mean reverse flow zone extends much further downstream for S/D=0.5 than for S/D=2 or 1. The far wake flow is also directed towards the wall (downwash) and the lack of pigment accumulation along the solid wall suggests that the boundary layer does not separate.

The velocity measurements of Durao *et al.* (1991) for S/D=0.5 differ in several important aspects from the present. First, the reverse flow over the top face shows no vortical structure in the earlier study. Thus, there is no free saddle point over the trailing edge. These differences imply smaller stream line curvature and consequently higher pressure on the prism back face. The recirculation vortex core is located higher than in the present study (y/D≈0.6 vs. Y/D≈0.4), and the absence of downwash in the far wake flow.

The mean flow field structure for S/D=0.25 (Fig. 2d, 3d) is topologically very different from those previously discussed. Although the flow over the top face does not reattach , the top recirculation region does not show a developed vortex core (node point) and , consequently, the free saddle over the trailing edge has also disappeared. It thus follows that the wake recirculation now extends to the leading edge of the obstacle. The near wake recirculation is nearly twice as long as that for S/D=0.5. The far wake flow clearly shows an upwash. Similarly to the case S/D=1, the presence of an upwash coincides with a local separation of the wall boundary layer observed from the pigment accumulation in Fig. 3d at x/D≈3.2. A similar separation bubble was also observed by Durao *et al.* (1991). The pigment accumulation upstream of the obstacle suggests the possible existence of an upstream separation. However, the velocity measurement in this region are still inconclusive. The surface flow patterns for S/D=0.19 (Fig. 3e) are topologically similar to those for S/D=0.25 and thus the flow structure is expected to be qualitatively similar.

The streamwise velocity component along the plane y=0 is shown in Fig. 6 for several S/D cases. The recirculation region Fig. 6 extends to x/D≈0.9 for S/D≥4 which is in agreement with values reported earlier in the literature. For S/D=2, 1, 0.5 and 0.25, the recirculation extends to x/D≈1.2, 1.3, 1.6 and 3, respectively. Bosch *et al.* (1996) measured x/D=1.1 for S/D=0.75 which is in close

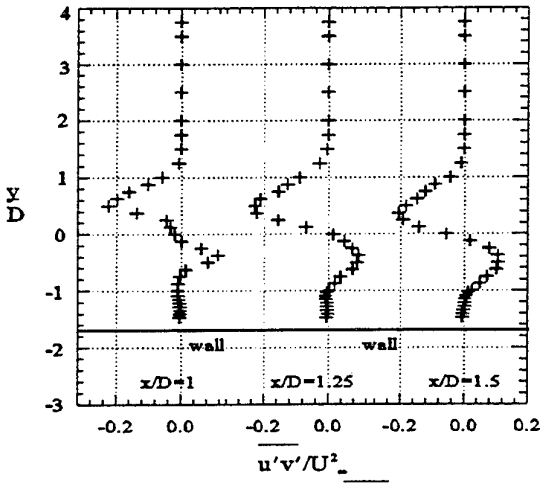


Fig. 4 - Reynolds stress (u'v') for S/D=1.

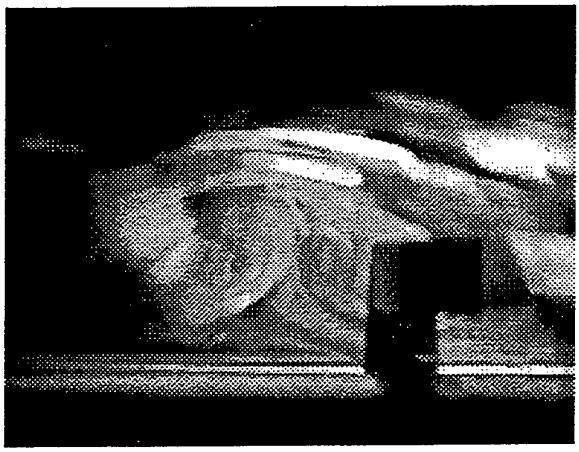


Fig. 5-Laser light-sheet visualization for S/D=1.

agreement. Durao *et al.* (1991) measured x/D=2.4 and 3.7 for S/D=0.5 and 0.25, respectively, which is significantly longer. The present results also suggest that the velocity recovery region increases dramatically as S/D increases, which is probably due to the influence of the wall. For wall bounded obstacles, the recirculation region extends to approximately 8D.

Shedding Frequency and Drag

The frequency, *f*, associated with vortex shedding is presented in Fig.7 in terms of the Strouhal number, St=fD/U∞, as a function of gap size. The error bars enclose the range of all measured values. Data from other studies in the literature are included for comparison. St increases montonically with decreasing gap height from 0.133 at S/D→∞ to 0.157 at S/D=0.3. For gap heights S/D≤0.25, vortex shedding activity could not detected. The power spectral density function (psdf) show well defined, narrow peaks for measurements at S/D≥0.5. When comparing psdf measured at the same location relative to the obstacle, it was observed that the magnitude (strength) of the psdf-peak decreased with decreasing S/D, which indicates a reduction in the energy of fluctuations of the shed vortices. For S/D≤0.375, the psdf showed peak broadening suggesting intermittent vortex shedding activity. Observations from laser light-sheet visualization experiments are consistent with this interpretation. Bosch *et al.* (1996) also report

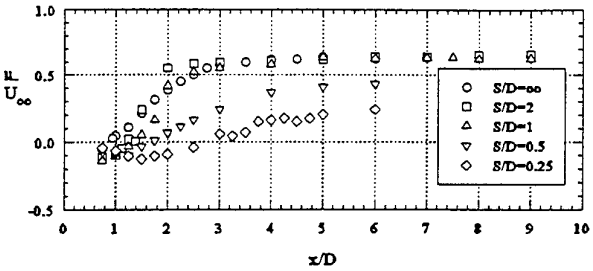


Fig. 6 - Time-averaged centerline u-velocity as a function of S/D=1.

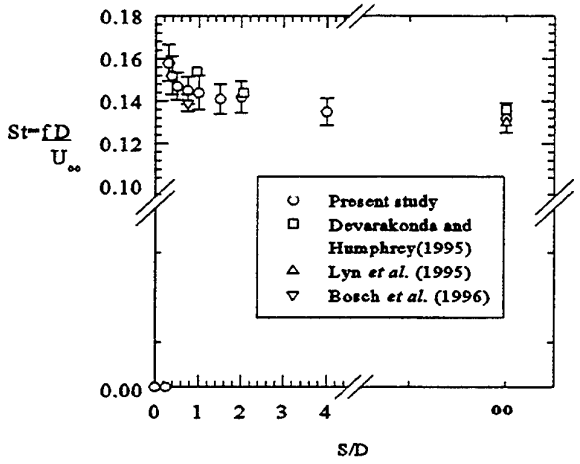


Fig. 7 - Shedding frequency as a function of the gap height.

this behavior, however, they could not detect vortex shedding below S/D=0.35. The results of Durao *et al.* (1991) show no vortex shedding activity below S/D=0.375 and that St is independent of S/D. The major difference already observed for the flow field structure are consistent with different dynamic behavior.

The drag coefficients as a function of S/D are shown in Fig. 8, where the error bars enclose the range of the all measurement values. The present results for S/D→∞ (C_D=2.04±0.03) agree well with those of previous studies, since these were conducted at higher blockage ratios (13% vs. 5.5%). Devarakonda and Humphrey (1995) calculated C_D by integration of the measured surface pressure distributions. They report that C_D mainly decreases due to an increase of the pressure on the leeward face. The present results are consistent with this observation. As S/D is reduced below 1, the length of the recirculation region grows resulting in smaller streamline curvature, which dictates that the pressure gradient normal to the streamlines also decreases. Specifically, the pressure in the near wake will thus increase with decreasing gap height while the pressure on the windward face is essentially that of stagnation and remains unchanged.

The Turbulent Field

The structure of the turbulent field is discussed in terms of the isoline contours of the Reynolds stresses , u'^2, v'^2 and $u'v'$. Results for S/D=0.25 and S/D=1 are shown in Fig. 9 as examples. For S/D→∞ the isolines are symmetric about the plane y/D=0. The maxima for u'^2_{max} occur at x/D≈0.8, y/D=±0.6 and v'^2_{max} at y/D=0, x/D=2.2. The ratio u'^2_{max}/v'^2_{max}=0.6 is lower than the value of 0.71 reported by Durao *et al.* (1991). The Reynolds shear stress $u'v'$

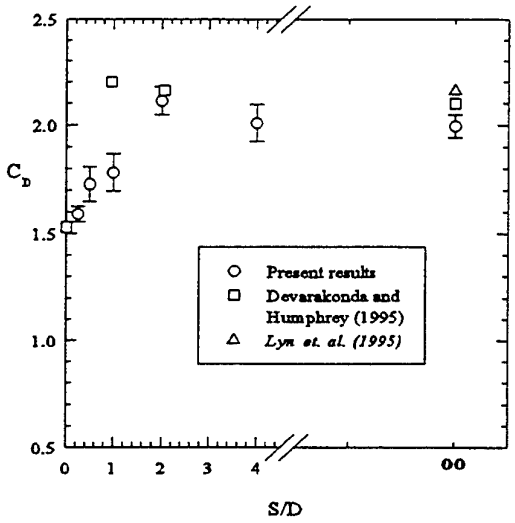


Fig. 8 - Drag coefficient as a function of the gap height (S/D).

approaches a maximum value of $0.13U_\infty^2$ near x/D=2.2 and y/D=±0.8. The turbulent field remain essential unchanged for S/D=4.

The locations for $\overline{u'^2}_{max}$ is generally in the vicinity of the maximum strain rate, ∂u/∂y, in the shear layer. As S/D decreases, the u'^2 field becomes less symmetric. The higher values of u'^2 are found along the top shear layer. The location of u'^2_{max} shifts downstream and upwards as the recirculation region expands with decreasing S/D. On the bottom side of the prism, the location of u'^2_{max} moves downstream and towards the wall.

The main contribution to the production of $\overline{v'^2}$ is the term $v'^2(\partial v/\partial y)$. The location and magnitude of v'^2_{max} will then be in the vicinity of the maximum for that production term. This location will generally coincide with that of the free saddle point for the velocity field at the end of the wake recirculation. The value for u'^2_{max}/v'^2_{max} decreases from 0.6 at S/D=4 to 0.4 at S/D=1. This trend implies an increase of fluctuations in the v-direction and is in opposition to the results reported by Duaro *et al.* (1991). As S/D is further reduced, the influence of the wall is observed as a strong damping of the v-fluctuation and the ratio u'^2_{max}/v'^2_{max} increases to 1.3 at S/D=0.25. The location for $u'v'_{max}$ is generally directly above and below those for v'^2_{max}. Since the main contribution to the $u'v'$ production term is $v'^2(\partial u/\partial y)$. The magnitude for $u'v'$ generally decrease with S/D as v'^2_{max} decreases due to damping of vertical fluctuations in the vicinity of the wall. The absolute maximum for $u'v'$ occurs in the shear layer above the v'^2_{max}. The values of $u'v'$ are generally higher along the top shear layer (see Fig. 4).

CONCLUSIONS

The results for an investigation of the flow field around a square cylinder mounted in the proximity of a solid wall were summarized for several gap heights. The blockage ratio, 5.5% and the on-coming boundary layer thickness, δ/D=1.5, are significantly different from similar investigations found in the literature (12.5% and 0.8, respectively).

Analysis of the mean velocity field suggests that three distinct

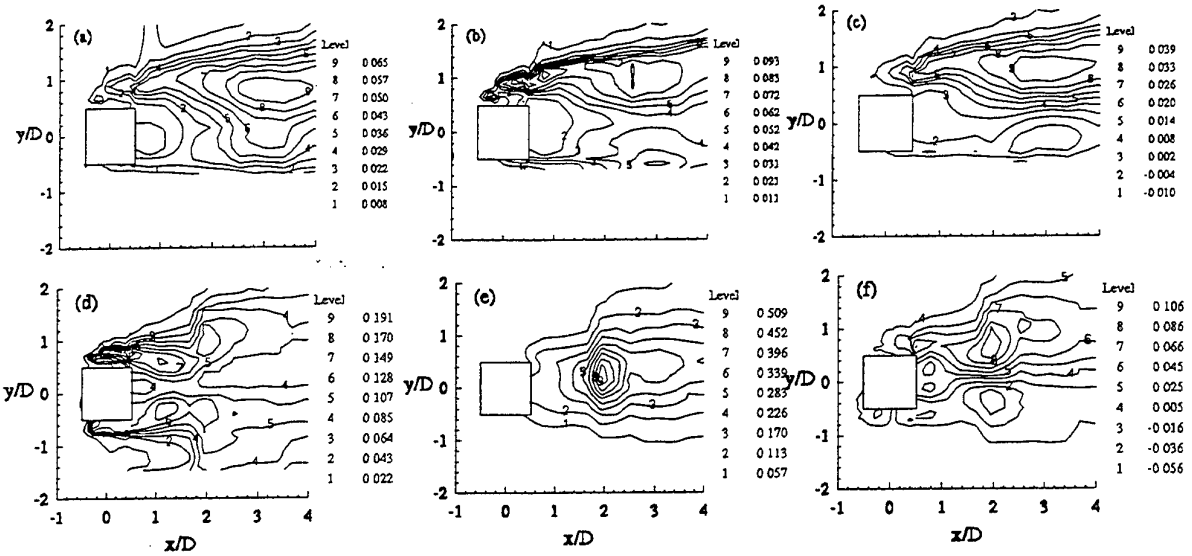


Fig. 9-Isoline contours (normalized with U^2_∞): S/D=0.25: a) $\overline{u'^2}$, b) $\overline{v'^2}$, c) $\overline{-u'v'^2}$; S/D=1: d) $\overline{u'^2}$, e) $\overline{v'^2}$, f) $\overline{-u'v'^2}$.

topological flow regimes exist based on the wall-to-prism separation. For largeseparation (S/D≥4) the presence of the obstacle has little influence on the wall boundary layer. The near wake turbulent field remains symmetric about the plane y=0.

For intermediate gap heights (0.5≤S/D≤2), the presence of the obstacle results in a thickening of the wall boundary layer. The near wake turbulent field is asymmetric. The flow which separates at the leading edges does not reattach on the obstacle top face but does on the bottom face resulting in a topologically different flow. It is also observed that separation of the solid wall boundary layer is accompanied by an upwash of the wake flow. The vortex shedding frequency increases while the drag coefficient decreases with decreasing S/D.

For smaller gap heights (S/D<0.3), no vortex shedding could be detected. The flow over the cylinder top face no longer shows a well defined vortex. In the wake, there is an upwash and separation of the wall boundary layer is observed.

ACKNOWLEDGMENTS

This work has been partially supported by grants from the Natural Sciences and Engineering Research Council of Canada.

REFERENCE

Bearman, P. W. and Graham, J. M. R., 1980, "Vortex shedding from bluff bodies in oscillatory flow," *J. Fluid Mech.*, Vol. 99, pp. 225-245.

Bosch, G. and Rodi, W., 1996, "Simulation of vortex shedding past a square cylinder near a wall," *Int. J. Heat and Fluid Flow*, Vol. 17, pp. 267-275.

Bosch, G., Kappler, M. and Rodi, W., 1996, "Experiments on the Flow Past Cylinder Placed near a Wall," *Exp. Thermal and Fluid Science*, Vol. 13, pp. 292-305.

Castro, I. P., 1979, "Relaxing wakes behind surface-mounted obstacles in rough wall boundary layer," *J. Fluid Mech.*, Vol. 93, part 4, pp. 631-659.

Devarakonda, R. and Humphrey, J. A. C., 1995, "Turbulent flow in the near wakes of single and tandem prisms," *10th Symposium on Turbulent Shear Flows*, The Pennsylvania State Univ., pp. 18.1-18.6.

Domnick, J and Martinuzzi, R., 1994, "A cheap and effective alternative for particle sedding fluid in LDA-application," *Exp. Fluids*, 16, 292-295.

Durao, D. F. G., Gouveia, P. S. T., and Pereira, J. C. F., 1991, "Velocity characteristics of the flow around a square cross section cylinder placed near a channel wall," *Exp. Fluids*, 11, pp. 341-350.

Grass, A. J., Raven, P.W. J., Stuart, R. J. and Bray, J. A., 1984, "The Influence of Boundary Layer Velocity Gradients and Bed Proximity on Vortex Shedding from Free Spanning Pipelines," *ASME J. Energy Res. Tech.* Vol. 106, pp. 70-78.

Lyn, D. A., Einav, S., Rodi, W. and Park, J.-H., 1995, "A laser-Doppler velocimetry study of ensemble-averaged characteristics of the turbulent near wake of a square cylinder," *J. Fluid Mech.* Vol. 304, pp. 285-319.

Schofield, W.H. and Logan, E., 1990, "Turbulent Shear Flow Over Surface Mounted Obstacles," *ASME J. Fluids Engineering*, Vol. 112, pp. 376-385.

Tanigushi, S. and Miyakoshi, K., 1990, "Fluctuating fluid forces acting on a circular cylinder and interference with a plane wall, effects of boundary layer thickness," *Exp. Fluids*, 9, 197-204.

West, G. S. and Apelt, C. J., 1982, "The effects of tunnel blockage and aspect ratio on the mean flow past a circular cylinder with Reynolds numbers between 10^4 and 10^5," *J. Fluid Mech.*, Vol. 114, pp. 361-377.

Wolochuk, M. C., Plesniak, M. W., and Braun, J. E., 1996, "The Effects of Turbulence and Unsteadiness on Vortex Shedding From Sharp-Edged Bluff Bodies," *ASME J. Fluids Engineering*, Vol. 18,pp.18-25.

Wu, K.C.Q and Martinuzzi, R.J., 1997, "Experimental Study of the Turbulent Wake Flow Behind a Square Cylinder Near a Wall". To appear in the *proc. of ASME FED '97 Summer Meeting*, Vancouver, B.C. Canada.

Topology of coherent vortices in the reattachment region of a backward- facing step

F. Delcayre
LEGI/IMG, BP53, 38041 Grenoble-Cedex 09, France.

ABSTRACT

Turbulent reattaching flows over a backward-facing step have motivated many experimental and numerical (k-ε, LES and DNS) investigations in the past few years. A reason for this growing interest is obviously the variety of phenomenon occuring in the reattachment region. Previous studies have mainly contributed to the statistical characterization of this flow. In their review, Eaton & Johnston [3] insisted on the rapid decay of Reynolds stresses and turbulent energy in the reattachment zone as well as the low frequency flapping in this reattachement region. The causes involved in these phenomenon are not yet fully understood. Flow visualizations of a separation bubble by Kiya et al [7] have shown the existence of large-scale structures which were found to be a key feature of the flow dynamics. The present paper proposed a numerical investigation of these coherent structures by means of Large Eddy Simulations.

INTRODUCTION

The flow over a backward-facing step is a combination of two sorts of turbulence : turbulent free shear flows and turbulent wall flows.
Eaton & Johnston [3] made an excellent review of this flow. They provided a very complete database of the previous works. Thus, a lot of investigations have been done on the parameters which influence the mecanism of reattachment and three parameters seem to influence a lot this mecanism: the initial boundary thickness $\frac{\delta_e}{H}$, the expansion ratio R and the Reynolds number. Westphal et al [14] showed that, whereas the reattachment length is sensitive to the inflow conditions, the reattachement process is quasi-independent of these conditions using the renormalised coordinate $X = \frac{x - X_r}{X_r}$.
A more recent experimental work on the flow over a backward-facing step is the work carried out by Jovic & Driver [6] on a double expansion with an aspect ratio $R = 6$ and with a low Reynolds number $Re_H = 5000$. This database was useful for the validation of the Direct Numerical Simulation of Le & Moin [8] and the Large Eddy Simulations of Akselvoll & Moin [1].
The recent work carried out by Le et al [9] is certainly the more detailed and complete calculation of this flow on the statistical point of view. One of the aim of this study was to validate different turbulent models.
This paper is focused on the dynamic of the flow and pay more attention on the topology of the flow.

NUMERICAL AND EDDY VISCOSITY MODELLING ASPECTS

A finite volume approach with staggered grid is used. Pressure is then defined at the centre of the cells and velocity components at the cells interface. The integration method is derived from the SOLA-ICE algorithm (Harlow et al [4]). Second order central differencing is used for the continuity equation and for pressure gradients and dissipative terms in the momentum equation. Velocity at cells interface which are required to evaluate convective fluxes are interpolated by the QUICK-SHARP scheme (Leonard [10]). The Poisson equation solution is obtained iteratively by solving a linear system with a conjugate gradient method with SSOR preconditioner. Finally, time advancement scheme is a low storage third-order Runge-Kutta scheme (Williamson [15]) with a CFL condition on the time step.
LES of such a flow have been carried out in conditions close to an experiment performed by Jovic & Driver [6]. The subgrid model retained is the selective-structure function model (Lesieur & Métais [11]) in its four-point version in planes parallel to the lower wall. The calculations were performed with an inlet velocity profile obtained from Spalart's [13] boundary layer simulation at Re_θ=670 (Re_{δ^*}=1000) where θ and δ^* are the momentum and displacement thick-

θ and δ^* are the momentum and displacement thicknesses. For this particular profile, the boundary layer thickness is $\delta \approx 6.1\delta^* = 1.2H$. Thus, the step-height Reynolds number corresponding to this profile is: $Re_H = \frac{U_0 H}{\nu} \approx 5100$.

The inlet fluctuations are generated by a 3D random white noise of an amplitude about 1.25% on the shear zone in the inlet area. The inlet velocity profile is imposed 0.3H upstream the step. The computational domain extent is 15H downstream the step, the spanwise direction size is 4H and in the vertical direction an expansion ratio of 1.2 is chosen which corresponds to a domain height of 6H. Consequently, the mesh size of such a computational domain is $97 \times 34 \times 46$. Using the inlet wall shear velocity $u_{\tau 0} = 4.9 \times 10^{-2} U_0$, it is then possible to determine the grid spacing using wall units. Only the spanwise grid spacing is constant and gives a $\Delta z^+ = 30$. In the other directions, the grid spacing is not uniform. In the streamwise direction, the mesh is stretched to increase the number of cells down the separation point. With this kind of mesh, the minimum streamwise resolution $\Delta x^+_{min} = 11$ is achieved just on the corner of the step. The maximum streamwise resolution is at the exit boundary, $\Delta x^+_{max} = 70$. A non-uniform mesh distribution was used in the vertical direction with fine grid near the wall and at the location of the step, the minimum resolution is $\Delta y^+_{min} = 3.75$ and the maximum resolution $\Delta y^+_{max} = 110$.

RESULTS

Statistics

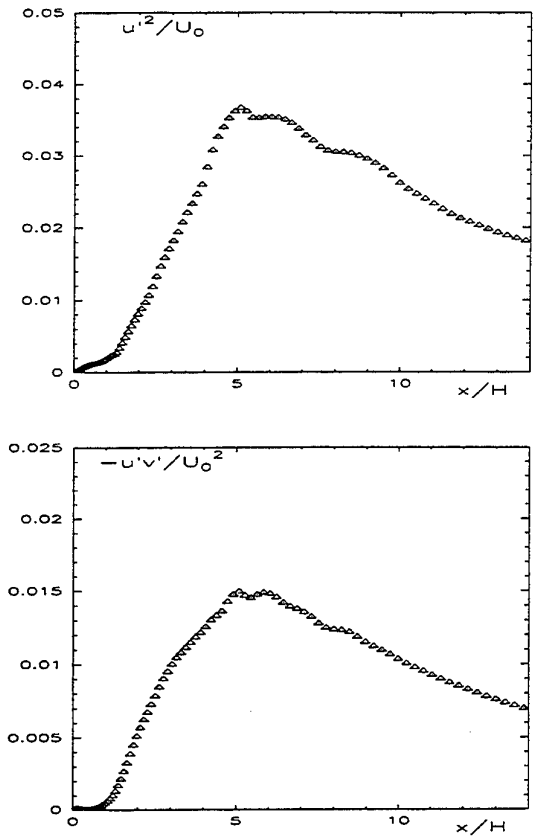


Figure 1: *Evolution of maxima of turbulence intensity and Reynolds stresses*

General behavior.

Le & Moin [8] have shown the difficulty to obtain a correct reattachment length: this requires to simulate deterministically (calculating a channel flow) the boundary layer upstream of the step. The reattachment length X_R found in this Large Eddy Simulation X_R is 7.2 H which is far from the experimental measurement ($X_r = 6.15H$). Indeed, without the turbulent structures, the transition of the shear layer will be larger and then the reattachement length larger too. In spite of this discrepancy, the calculation reproduces well the main properties described by Eaton & Johnston [3](Fig. 1).

Eaton & Johnston [3] provided a large amount of data for turbulent flows over a backward-facing step. In their review, they emphasized that this flow has a number of unusual mean properties in the downstream direction. One of the most interesting behavior is the rapid decay of Reynolds stresses and turbulence energy in the reattachment zone.

Consistently with this review, turbulence-intensity and Reynolds stresses ($-\overline{u'v'}$) firstly increase abruptly 1H downstream the step and reach a peak one step length before the reattachment and then decrease rapidly. The value of the maximum of turbulence intensity ($\overline{u'^2}/U_0^2$) is about 0.038 which is the typical value found by Eaton et al. [3]. For the Reynolds stress ($-\overline{u'v'}$) the maximum value, 0.015, is very close from the typical values found for free mixing-layers.

The sudden decay observed is subject to controversy among the research community. Some authors argued that the large eddies shed behind the step are torn in two in the reattachment zone. Therefore, this phenomenon would be responsible of this decrease. But, most of the authors disagreed with this argument and visualizations of the flow in the next section are contradictory with this hypothesis. Indeed, it seems to be the three-dimensional effects which are responsible of this behavior generating a sudden appearance of small scales in the flow. The topological study in the next section will help the understanding of this phenomenon.

Mean profiles.

A comparison between the experiment of Jovic & Driver [6], the DNS of Le & Moin [8] and the LES carried out in this work is plotted at the reattachment point in Fig. 2. Here, statistical quantities are averaged over the spanwise direction, using the periodicity condition, and time. The agreement between these three set of data is good.

The renormalised coordinate $X = \frac{x - X_r}{X_r}$ is used to compare the statistical results obtained in the calculation with the results obtained by Le et al [8] in their DNS. This scaling is classically used when there is a discrepancy on the reattachment length between two experiences.

The mean streamwise velocity profiles show inflexional point for $X = 0.66$ which means that the turbulent boundary layer is not yet developing in the exit

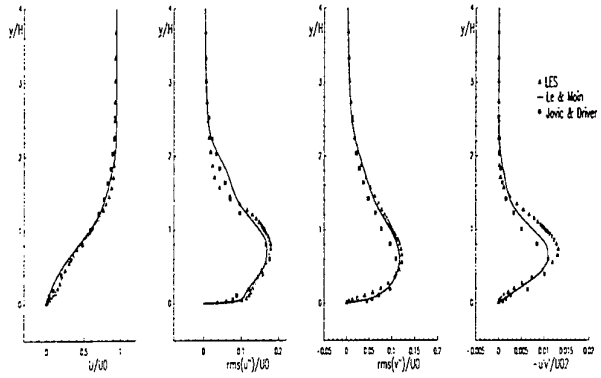


Figure 2: *Statistical quantities at the reattachment length*

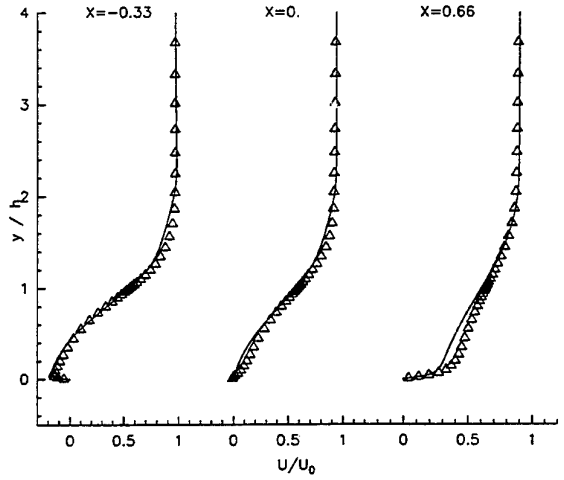


Figure 3: *Mean streamwise velocity profiles*

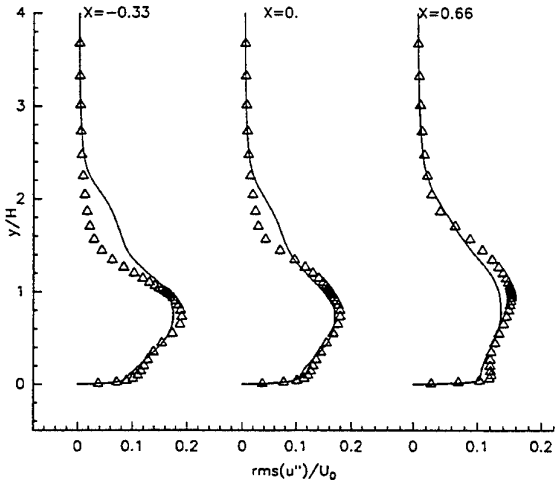


Figure 4: *Turbulent streamwise intensity profiles*

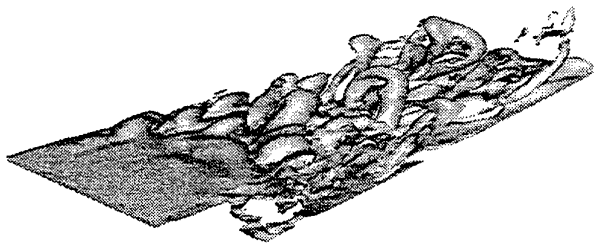


Figure 5: *Overall view of the backward-facing step flow (vorticity modulus* $\|\vec{\omega}\|$*=1.5* $\frac{U_0}{H}$*)*

boundary (Fig. 3). Topological study in the next section will show the persistance of shear layer structures downstream the reattachment which could explain this behavior.
Turbulent intensity are helpful to understand the flow (Fig. 4). In the streamwise intensity profile, it can be seen firstly the development of the shear layer with typical values of mixing layers. At the end of the domain, it is possible to see the development of a peak in the near wall region. This peak is a proof of the redevelopment of the boundary layer.
For the others statistics, a good statistical agreement has been obtained.

Topological study of the flow

Overall views.

The advantage of numerical investigation is to provide instantaneous data on each velocity components and pressure. In the case of a LES, it is possible to characterize large scale coherent motions by means of vorticity or pressure isosurfaces, as shown in Fig. 5 and 6.
For the detached shear layer, the boundary layer separates at the corner of the step and a free mixing-layer arises. Then Kelvin-Helmoltz billows are shed behind the step. These vortices become quickly 3D with the growth of oblique modes which leads to helical pairing (Fig. 7).
Thus, these spanwise vortices are highly threedimensionalized by the development of this instability and are then stretched into big longitudinal Λ shaped vortices. These vortices impinge the wall and are strained into big arch-like vortices. They are eventually dissipated as they are convected downstream. The shape of these vortices is very similar to the structure shown by Kiya et al. [7] in their experiments.
The results obtained with a quasi two-dimensional noise are in contradiction with the results obtained by previous workers in the case of a free mixing layer (Comte et al [2]). The helical pairing is still the predominant instability in backward facing step flows whereas it almost vanishes in free mixing layers. This is an important difference which characterises the flow over a backward-facing step. Since the inflow is quasi 2D, spanwise perturbation can only exist by a feedback excitation produced in the recirculation zone.

Three-dimensionalization of the flow.

A key feature of the flow over a backward-facing step is the transformation of an initially spanwise vorticity field in a field where streamwise vorticity predominates. It is then important to study the transition toward turbulence in this flow. For this purpose another

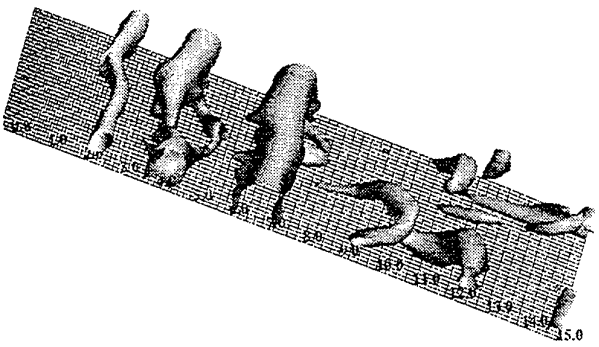


Figure 6: *Overall view of the backward-facing step flow (iso-pressure surfaces* $P = -0.09\rho_0 U_0^2 = P_{min} + 0.65(P_{max} - Pmin))$

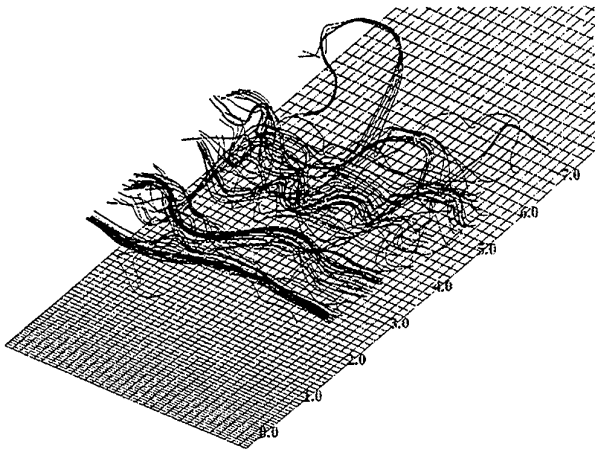


Figure 7: *Three-dimensional effects on vortex lines*

way to visualize the coherent structures shed behind the step is used. It consists in separating the regions where the strain rate is lower than the vorticity magnitude. The strain rate is particularly high in the shear zone at the beginning of the shear layer. A criteria based on this differenciation will be useful in this area to understand how Kelvin-Helmoltz billows develop. Hunt et al [5] defined a criteria based on a Q quantity where $Q = (\Omega_{ij}\Omega_{ij} - S_{ij}S_{ij})/2$. Ω_{ij} is the antisymetric part of $\partial u_i/\partial x_j$ and S_{ij} the symetric part. The positivity of Q will define the zones where rotation is predominant (the vortices cores).
Flow visualizations of the vorticity modulus field filtered by the Q criteria and coloured by the ω_x value show the general tendency of the flow to transform a spanwise vorticity field to a streamwise vorticity field. With the duplicated domain, it is obvious that the helical pairing phenomenon is a characteristic of this flow (Fig. 8). Thus, the topology of the flow is completely changed 3H downstream the step.
The transition toward turbulence over a backward-facing step is a transformation of spanwise vortices to streamwise vortices enhanced by an important oscillation of the Kelvin-Helmoltz vortices.
A statistical study on the orientation angle of vorticity vectors was done. The angle θ was characterised as follows: $\theta = tan^{-1}(\frac{\omega_y}{\omega_x})$. The interval of variation

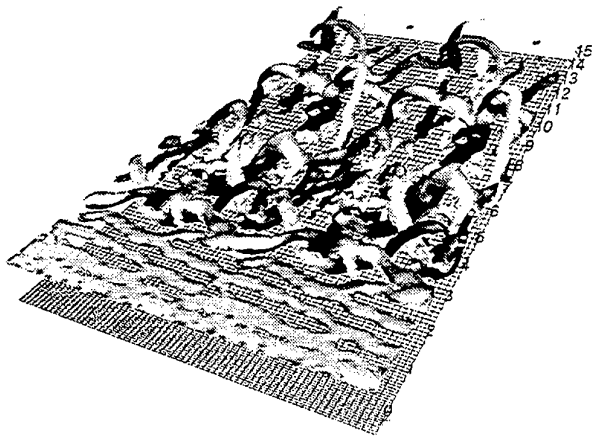


Figure 8: *Overall view of the vorticity modulus* ($||\vec{\omega}||$=1.5 $\frac{U_0}{H}$) *with Q criteria coloured by* ω_x *(black)* $-1.5\frac{U_0}{H} < \omega_x < +1.5\frac{U_0}{H}$ *(white). Domain duplicated.*

of this angle is included in $[-\pi, \pi]$. The evaluation of this angle was weighted with the magnitude of the projected vorticity vector: $\omega_{xy} = \frac{(\omega_x^2+\omega_y^2)}{<\omega_x^2+\omega_y^2>}$ where <> significates a spanwise averaging. Moin & Kim [12] used this procedure to analize the structure of vorticity field in a turbulent channel flow.

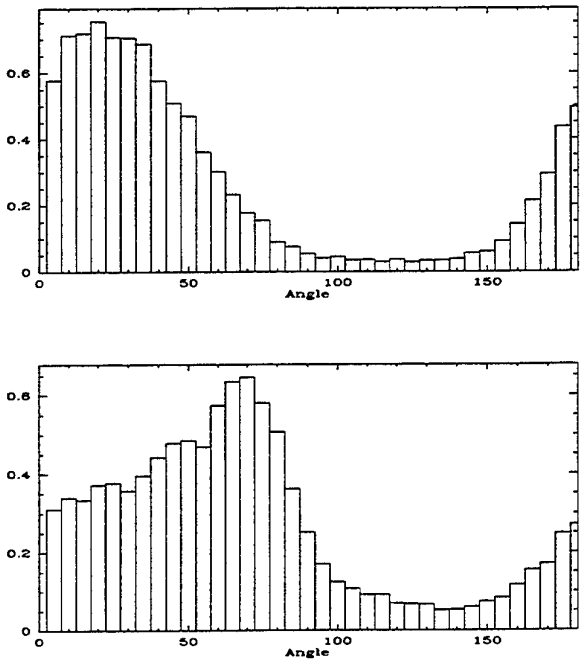


Figure 9: *Pdf of the angle of coherent structures upstream (above) and downstream (below) the reattachment*

Using Probability Density Functions in the different areas it is then possible to define this angle which will correspond to the peaks on the pdf. An interesting remark is that the π periodicity on the pdf is clearly obtained and then shows that a quasi complete statistical convergence has been obtained. In the rest of this section, using this periodicity only the part where

Θ is positive is studied.
The evolution of this angle was firstly studied in the streamwise direction and in the direction normal to the wall. It is then possible to see the evolution of this angle. At the beginning of the flow, the maximum more probable angle is located in the shear layer and corresponds to the longitudinal vortices stretched between the Kelvin-Helmoltz vortices. The value of this angle is approximately $35° - 40°$ (Fig. 9).
The value of this angle increases going downstream the flow. Downstream the reattachment values of $70° - 75°$ are obtained. The extension of the Λ-shaped vortices is 1H and the angle of these structures increases from the wall to the mean flow.
Animations of the vorticity modulus field show that the Λ-shaped vortices rearrange in a staggered manner. Their occurence downstream the reattachment is highly correlated with enlargement and shrinking of the recirculation bubble and correspond to the degenerescence of the Kelvin-Helmoltz vortices which, after various pairing, are convected downstream. They are relatively fast dissipated with a persistance of the longitudinal component of the vorticity.

Strouhal numbers.

It has been shown that the flow over a backward-facing step is characterised by a shedding of different sorts of vortices. Pressure fluctuations spectra in different positions (Fig. 10) are used to characterise the quasi periodic behavior of the flow (Le et al [9]).

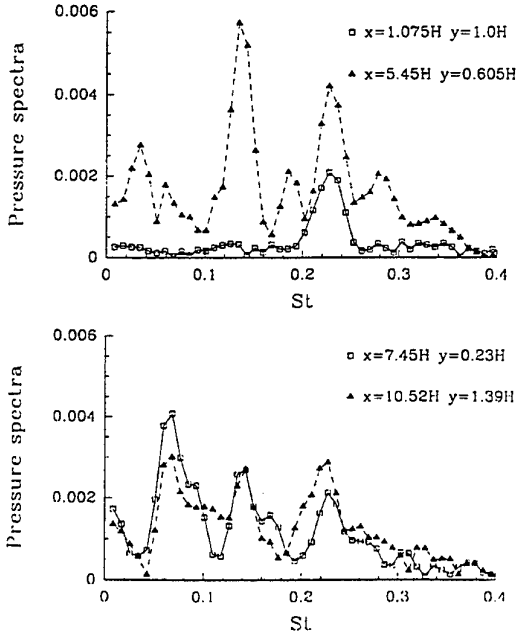


Figure 10: *Spectra of spanwise averaged pressure fluctuations at different positions*

There are three dominant frequencies in the different areas of the flow. Pressure fluctuations spectra show a peak ($St_1 \approx 0.23$) in the first region ($x < 2H$) of the flow. It is the frequency of the Kelvin-Helmoltz shedding. Then, the frequency of the pairing appears ($St_2 \approx 0.12$). In the region of the reattachment another frequency emerges ($St_3 \approx 0.07$) which corresponds to a flapping oscillation of the recirculation bubble whose mechanism is not very well understood. Finally, downstream the reattachment zone the three Strouhal number have approximately the same content of energy. The same results are obtained with power spectras of velocity fluctuations.

CONCLUSION

Large Eddy Simulations with the selective structure function model (Lesieur & Métais [11]) in the configuration of the backward-facing step is used to study the flow on its statistical and topological behavior. Thanks to Le et al [9]'s study, it has been possible to compare the statistical results obtained in this simulation. Whereas the reattachment length is relatively far from the experiment of Jovic & Driver [6] (certainly due to the simplicity of the inlet profiles) using renormalised coordinate the statistical agreement is good. It has been possible to obtain the general behavior of these statistical quantities described by Eaton & Johnston [3] which characterise the flow over a backward-facing step.
Thanks to flow visualisations, it has been possible to describe accurately the problem of vortex topology in a turbulence behind a backward-facing step. The different Strouhal numbers associated with the different vortices are in good agreement with previous workers. The helical pairing is the predominant instability in the flow and even imposing quasi twodimensional perturbations this mode is obtained. Then, it has been shown that the transition toward turbulence over a backward-facing step is characterised by the transformation of spanwise vortices onto streamwise vortices. The Kelvin-Helmoltz vortices are turned into Λ-shaped vortices which impinge the wall and are elongated into big arch like vortices. Topology study of the vortices downstream the reattachement was done with pdf on the angle of these large scale structures and their presence may justify the slow readjustment of the mean velocity profile to a canonical boundary layer profile.

ACKNOWLEDGEMENTS

Computations were carried out at the IDRIS (Institut du Développement et des Ressources en Informatique Scientifique, Paris).

REFERENCES

[1] K. Akselvoll and P. Moin. Large eddy simulation of turbulent confined coannular jets and turbulent flow over a backward facing step. TF 63, Stanford University, 1995.

[2] P. Comte, M. Lesieur, and E. Lamballais. Large- and small-scale stirring of vorticity and a passive scalar in a 3-d temporal mixing layer. *Phys. Fluids A*, 4(12):2761–2778, 1992.

[3] J.K. Eaton and J.P. Johnston. A review of research on subsonic turbulent flow reattachment. *AAIA Journal*, 19(9):1093–1100, 1981.

[4] F. Harlow and A. Amsden. A numerical fluid dynamics calculation for all flow speed. *J. Comp. Phys.*, 8:197, 1971.

[5] J. C. R. HUNT, A. A. WRAY, and P. MOIN. Eddies, stream, and convergence zones in turbulent flows. *Center for Turbulence Research Rep.*, **CTR-S88**:193, 1988.

[6] S. JOVIC and M. DRIVER. Backward-facing step measurement at low reynolds number $re_h = 5000$. NASA Technical Memorandum 108807, Ames Research Center, 1994.

[7] M. KIYA and K. SASAKI. Structure of a turbulent separation bubble. *J. Fluid Mech.*, **137**:83–114, 1983.

[8] H. LE and P. MOIN. Direct numerical simulation of turbulent flow over a backward-facing step. TF 58, Stanford University, 1994.

[9] H. LE, P. MOIN, and J. KIM. Direct numerical simulation of turbulent flow over a backward-facing step. *J. Fluid Mech.*, **330**:349–374, 1997.

[10] B. P. LEONARD. Simple high-accuracy resolution program for convective modelling of discontinuities. *Int. J. Numer. Methods Fluids*, **8**:1291–1398, 1988.

[11] M. LESIEUR and O. MÉTAIS. New trends in large-eddy simulations of turbulence. *Annu. Rev. Fluid Mech.*, **28**, 1996.

[12] P. MOIN and J. KIM. The structure of the vorticity field in turbulent channel flow. part 1. analysis of instantaneous fields and statistical correlations. *J. Fluid Mech.*, **155**:441–464, 1985.

[13] P. R. SPALART. Direct simulation of a turbulent boundary layer up to $r_\theta = 1410$. *J. Fluid Mech.*, **187**:61–98, 1988.

[14] R. V. WESTPHAL, J. P. JOHNSTON, and J. K. EATON. Experimental study of flow reattachment in a single-sided sudden expansion. MD 41, Stanford University, 1984.

[15] J. H. WILLIAMSON. Low-storage runge-kutta schemes. *J. Comp. Phys.*, **35**:48–56, 1980.

SESSION 27 - TWO PHASE FLOWS II

PRIMARY INSTABILITY IN LIQUID-GAS SHEAR LAYERS

L. Raynal[(1)], E. Villermaux[(1)], J. C. Lasheras[(2)] and E. J. Hopfinger[(1)]
[(1)] LEGI/IMG
BP53X
38041 Grenoble-Cedex 09
France

[(2)] AMES-UCSD
9500 Gilman Drive
La Jolla, CA 92093
USA

ABSTRACT

The primary instability of a low-speed liquid jet under the action of a high-speed gas stream has been experimentally investigated. This was done using two sets of experiments, the first one involving a two-dimensional flow, while the second one was performed in an axisymmetric round jet.

This interfacial instability is of the form of two-dimensional waves which are amplified and advected downstream. Measurements of the convection velocity, the frequency and the wavelength have been performed for a wide range of liquid and gas velocities. It is shown that these quantities scale with the convection velocity, known from large density difference mixing layers, and the vorticity layer in the gas stream. Surface tension is of no importance.

The results are shown to be in good agreement with linear stability analysis, taking into account the large density discontinuity and assuming that all the initial vorticity is in the gas stream.

INTRODUCTION

The atomization of liquid jets has been investigated for many years, motivated by the wide range of applications of two-phase combustion encountered for instance in diesel or liquid propellant rocket engines. Nevertheless, the fundamental processes of liquit jet instability which leads to the breakup of the liquid and the formation of droplets is still not well understood.

The atomization of a liquid jet can be divided into two distincts regions. The first one, close to the exit section, is the region where primary breakup occurs; inertia effects, assisted or not by a co-flowing gas stream, causes the liquid to disintegrate into ligaments leading to the formation of drops with a wide size distribution. The second one is located farther downstream where the drops may be further broken up. This process is referred as secondary breakup. Since the pionneer works of Kolmogorov (1949) and Hinze (1949), the breakup of drops has received much attention, see e.g. the review of Hsiang and Faeth (1992). Less work has been done on the fundamental process involving the primary breakup. Arai and Hashimoto (1985) and Mansour and Chigier (1991) have measured the oscillation frequency of a two-dimensional liquid sheet in a co-flowing gas stream, but do not provide a physical explanation of their results.

In the present paper, it is shown that the mechanism involved in primary instabilities developing at the liquid-gas interface is similar to a large density difference shear layer and is well described by a linear Kelvin-Helmholtz stability analysis.

EXPERIMENTAL APPARATUS

The two sets of experiments are shown in Fig.1. The first set-up (Fig.1a) consists in a plane liquid-gas shear layer of finite thickness, while the second (Fig.1b) corresponds to axisymmetric liquid-gas coaxial jets. The ranges of stream velocities investigated are, for the liquid (suffix 1) $U_1 = 0.1$ to $1\,m/s$, and the gas (suffix 2) $U_2 = 10$ to $100\,m/s$ in the two dimensional case, and 0.5 to $5\,m/s$ and 15 to $200\,m/s$ in the axisymmetric case. In both sets of experiments the fluids used are air and water. The gas and liquid sheet thicknesses are $H = 10\,mm$ in the planar configuration, while the liquid jet diameter, D_1, is $7.6\,mm$ and the gas annular outer diameter, D_2, is $11.4\,mm$ in the axisymmetric configuration. The injectors used are convergent nozzles with high enough contraction ratios (between 6 and 10) to ensure in all conditions studied that the gas and liquid streams are practically laminar at the exit sections.

The non-dimensional numbers involved in the problem are: the Reynolds numbers $Re_i = \frac{\rho_i U_i D_h}{\mu_i}$ $_{i=1,2}$, where D_h designates the hydraulic diameter of the jet, $D_h = 2H$ or D_i depending if we consider the planar or the axisymmetric configuration, the Weber number, $We = \frac{\rho_2 U_2^2 D_h}{\sigma}$, where σ is the surface tension, and the momentum flux ratio, $M = \frac{\rho_2 U_2^2}{\rho_1 U_1^2}$, whose importance in atomization problems

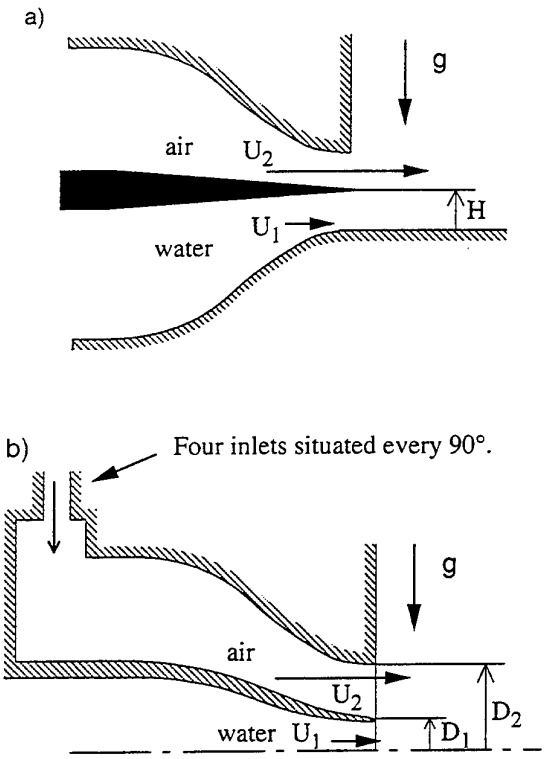


Figure 1: Experimental setup, a) plane setup, b) axisymmetric setup.

has been shown by Hopfinger and Lasheras (1994). Re_i is always greater than 2×10^3 so that flows quickly become turbulent. The Weber number varies from 30 to more than 3000 and M covers the range 0.1-115 in the axisymmetric case and reaches up to 1200 in the planar case. As $M > 1$ in most cases, the gas stream dominates the whole two-phase flow.

Measurements of the interfacial wave frequency have been done using a Position Sensitive Detector (PSD). A $1\,mW$ laser beam is projected normal to the liquid interface; the beam is tramsmitted through the liquid sheet and impacts the PSD sensitive surface ($12 \times 12\,mm^2$) at a instantaneous location mainly depending on the local slope of the interface. Thus, the frequency of the PSD signal gives the frequency of interest. This frequency is determined from the most energetic peak in the power sprectrum of the signal. In most cases, peaks are, at least, one decade above their base so that frequencies are unambiguously determined. In the case of the axisymmetric experimental setup, a very similar technique using laser beam light attenuation was used, giving results with similar accuracy as in the planar case.

In order to measure the convection velocity of the interfacial waves, a hot-film was placed at various distances, d, downstream of the laser beam. Cross correlations betweeen the hot-film and the PSD signals were computed to determine the time shift, Δt, between the two sensors as a function of the distance between them. The convection velocity, U_c, is given by the slope of the curve $d(\Delta t)$. For given fixed values of velocities, U_1 and U_2, three different measurements corresponding to three different values of d, at least, were made to minimize the experimental uncertainty.

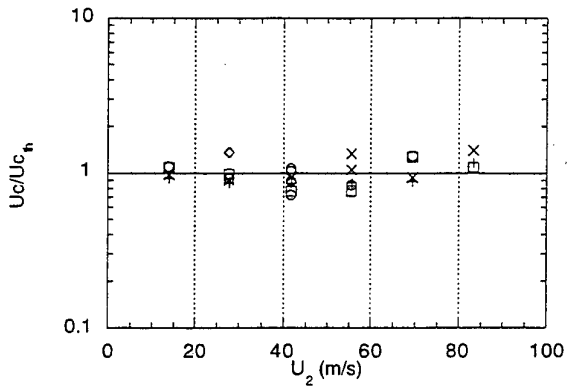


Figure 2: Measured convection velocity divided by U_{cth} whose expression is given by equation 1. $U_1 =$ ∘0.11, □0.28, ◇0.55, × 0.83 + 1.11 m/s.

EXPERIMENTAL RESULTS

Convection velocity

In the case of homogeneous mixing layers, it is well known that the convection velocity of the coherent spanwise, two-dimensional eddies is approximately given by $\frac{U_1+U_2}{2}$ (see e.g. Brown and Roshko 1974). Several studies have been done with streams of different densities but still with one phase. Using of mixture of helium and nitrogen, Bernal and Roshko (1986) propose that the convection velocity of the spanwise structures is in that case :

$$U_c = \frac{\sqrt{\rho_1}U_1 + \sqrt{\rho_2}U_2}{\sqrt{\rho_1} + \sqrt{\rho_2}} \qquad (1)$$

Equation (1), due to Brown (1974) was later justified by Dimotakis (1986) involving the continuity of the pressure at the interface in a frame moving at the convection velocity.

Our experimental results are compared to Eq.(1) for the whole ranges of liquid and gas velocities as shown in Fig.2. The measured convection velocities, U_c, nondimensionalized by the theoretical velocity given by Eq.(1) (designated in the figure as U_{cth}), are plotted against the gas velocity, U_2. The measurements presented here have been carried out in the two-dimensional setup only. One observes a very good collapse of nearly all data around a value of 1, so that Eq.(1) represents a very good model for this velocity in the two-phase flow of interest. Thus, in the following, U_c designates the convection velocity given by Eq.(1), in place of the experimental values.

Characteristic frequency

The results obtained in the two-dimensional setup are shown in Fig.3. The interfacial wave frequency, f, is plotted against the gas velocity, U_2, for different liquid velocities, U_1. One observes that for the first four liquid velocities, which corresponds to an increase of U_1 by a factor of 4, the collapse of the different data is rather good. This indicates that a limit regime is reached where the liquid velocity has no direct influence. It can be seen from Eq.(1) that, when the gas velocity is high enough, meaning that the momentum flux ratio is high enough, the convection

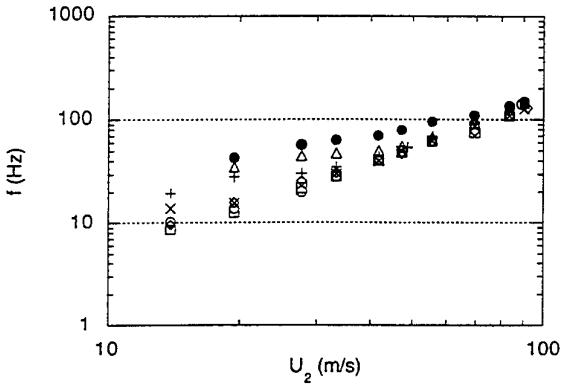


Figure 3: Characteristic frequency versus the gas velocity. U_1 = ○0.069, □0.11, ◇0.19, × 0.28, + 0.55, △ 0.83, • 1.11 m/s.

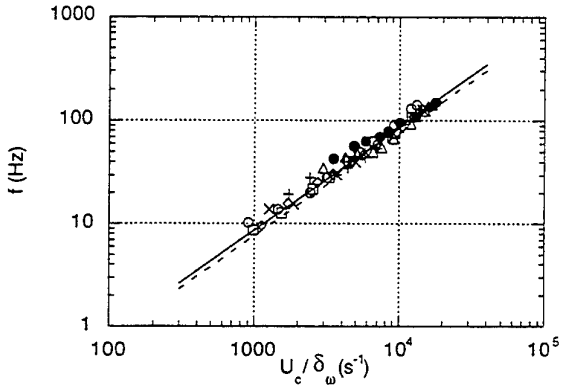


Figure 5: Characteristic frequency versus the flow frequency $\frac{U_c}{\delta_\omega}$. Same symbols as in Fig.3, experimental — $f = 8.7 \times 10^{-3} \frac{U_c}{\delta_\omega}$, theoretical - - - $f = 7.6 \times 10^{-3} \frac{U_c}{\delta_\omega}$.

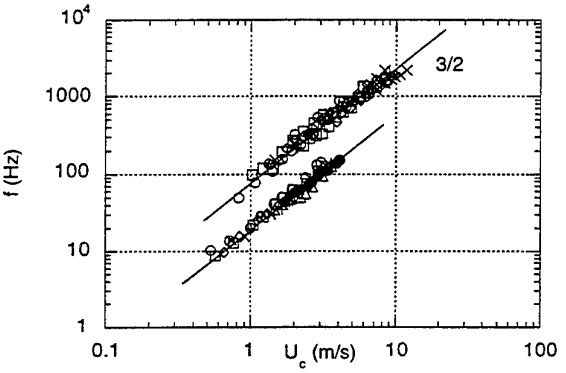


Figure 4: Characteristic frequency against the convection velocity. Lower group, planar case, $0.069 < U_1 < 1.1\,m/s$, upper group, axisymmetric case, $0.5 < U_1 < 5\,m/s$.

velocity is simply given by $U_c = \sqrt{\frac{\rho_2}{\rho_1}} U_2$. When increasing the liquid velocity, the frequency increases for moderate gas velocity, and again above a certain value of U_2, it collapses with the values obtained for lower liquid velocities. Although not plotted here, the same trends are observed in the frequencies measurements in the axisymmetric setup.

The interfacial wave frequency is the ratio of the distance between two consecutive structures divided by the convection velocity. When plotting the frequency versus the convection velocity, it is observed that the influence of the liquid velocity is entirely taken into account via U_c. Figure 4 shows that frequencies, obtained in both experimental setups, as a function of the convection velocity, collapse into two curves. In this representation, these two curves depend on the experimental set-up, but no more on the liquid velocities. This result proves that the wavelength of the instability is independent of the liquid velocity. As the power of the curve $f(U_c)$ is well represented by 3/2 (see Fig.4), the characteristic length that fixes the wavelength of the instability should be proportional to $U_2^{-1/2}$ since no influence of the liquid velocity is expected. As previoulsy said, convergent nozzles were used, resulting in laminar boundary layers, whose thicknesses follow a power law with U_2. The vorticity thickness, δ_ω, defined by :

$$\delta_\omega = \frac{U_2}{\frac{dU}{dy}|_{max}} \tag{2}$$

where $\frac{dU}{dy}|_{max}$ is the maximum shear in the gas velocity profile at the exit section, has been actually measured in the two-dimensional experimental setup as :

$$\frac{\delta_\omega}{H} = \frac{8.5}{\sqrt{Re_2}} \tag{3}$$

Figure 5 shows the frequency of the interfacial instability plotted against $\frac{U_c}{\delta_\omega}$. This group is entirely given by the flow exit conditions and has the dimension of a frequency. It is actually observed that the data collapse well into a single curve giving a non dimensional Strouhal number:

$$\frac{f\delta_\omega}{U_c} = 8.7 \times 10^{-3} \tag{4}$$

In the axisymmetric case, the dependence of δ_ω on Re_2 was not measured. The results of Fig.4 imply however that δ_ω is smaller in the axisymmetric case. This is consistent with the fact that the gas inlet dimensions are about five times less in the axisymmetric case than in the planar case.

The form of the law and the numerical value in equation 4 can be represented by a kelvin-Helmholtz type intability analysis.

LINEAR STABILITY ANALYSIS

These calculations have been carried out considering the usual temporal linear stability analysis approximations, inviscid, parallel streams, infinitesimal perturbations (see Chandrasekhar 1961 for more details) and we assume no effect of surface tension (case of large Weber number). The velocity and density profiles used in this analysis are shown in figure 6. The velocity increases gradually while there is

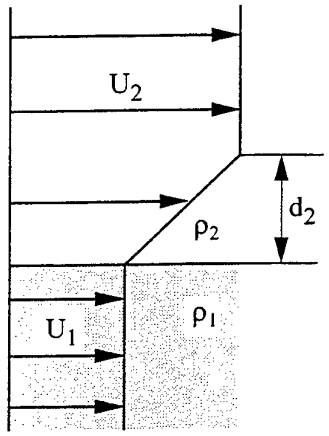


Figure 6: Velocity and density profiles used in the linear stability analysis.

a true discontinuity of the density profile. The density ratio, $S = \frac{\rho_2}{\rho_1}$, is varied from 1 to 1/1000, and the vorticity thickness in the air stream is given by the thickness of the gas boundary layer, d_2.

Figure 7 shows the curves of the amplification rate, ω_i, versus the wave number, k, for different values of S. One clearly sees, that decreasing S leads to a pronounced decrease in ω_i and of the unstable wavenumber range. Nevertheless, there are still wavenumbers for which $\omega_i > 0$, meaning that the flow is still unstable. Figure 8 shows the non-dimensional selected modes, corresponding to the most amplified mode, in terms of wavenumber, kd_2, (or wavelength, $\lambda = \frac{2\pi}{k}$), pulsation, $\frac{\omega_r d_2}{U_2 - U_1}$, (or frequency, $f = \frac{\omega_r}{2\pi}$), amplification rate $\frac{\omega_i d_2}{U_2 - U_1}$ and group velocity, $\frac{d\omega_r}{dk}\frac{1}{U_2 - U_1}$. It is seen that the wavenumber decreases as the density ratio increases, for $\frac{\rho_1}{\rho_2} \geq 10$ this decrease is fairly given by:

$$kd_2 \simeq 1.3\sqrt{\frac{\rho_2}{\rho_1}} \tag{5}$$

The decrease of the group velocity, which has to be compared with the convection velocity, follows also closely this $-1/2$ power law. Notice that the decrease of the wavenumber, resulting in an important increase in the wavelength, justifies, a posteriori, the fact that the surface tension plays no role in this instability. The meaningful Weber number, for this instability, should actually be expressed with the wavelength of the instability instead of the liquid jet diameter. This Weber number thus increases with the square-root of the density ratio implying that the surface tension effects become less important as this ratio increases.

For $S = 1.2 \times 10^{-3}$, the value of interest in the case of water-air shear layers, the selected wavelength, corresponding to the most amplified wavenumber, is such that the expected theoretical non dimensional frequency of the instability is:

$$\left.\frac{f\delta_\omega}{U_c}\right|_{th} = \frac{1.38}{2\pi}\sqrt{\frac{\rho_2}{\rho_1}} = 7.6 \times 10^{-3} \tag{6}$$

This result is shown in Fig.5 as a dotted line. Notice that although slightly below the experimental data points, it nevertheless represents a good prediction. This value should actually be compared to the experimental value of

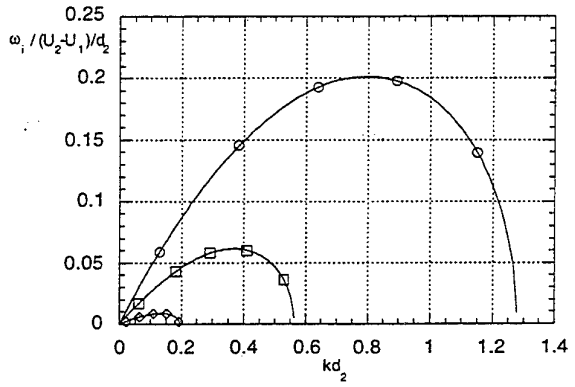


Figure 7: Amplification rate versus wavenumber. $S = \circ 1, \square 1/10, \diamond 1/100$.

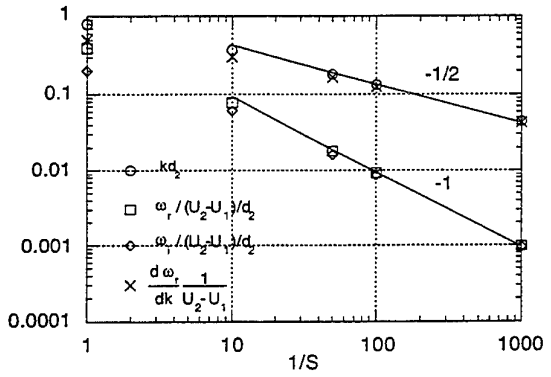


Figure 8: Selected modes for S varying from 1 to 1/1000.

8.7×10^{-3} (see Eq.(4)). Considering all the approximations used in our linear analysis, agreeement with the experimental results is indeed very good. The same conclusion holds for the group velocity. The calculation has been made assuming that $\frac{U_2}{U_1} >> 1$, this limit corresponding to the experimental case, and it provides:

$$\frac{d\omega_r}{dk}\frac{1}{U_2} = 0.043 \tag{7}$$

which has to be compared with Eq.(1) in the limit $\frac{U_2}{U_1} >> 1$. For $\frac{U_2}{U_1} = 100$, representative value of the experimental conditions, Eq.(1) gives $\frac{U_c}{U_2} = 0.040$.

CONCLUSION

The instability developing at a liquid-gas interface in a two-dimensional mixing layer and a coaxial liquid-gas jet have been experimentally investigated. It is found that the convection velocity of the interfacial spanwise structures is in good agreement with the formula given by Bernal and Roshko (1986) obtained for non-homogeneous gaseous mixing layers (see Eq.(1)). The frequency of the interfacial

instability is shown to be determined by the shear in the gas stream, and to be given by the nondimensional relation $\frac{f\delta_\omega}{U_c} = 8.7 \times 10^{-3}$ in close agreement with the results of a linear stability analysis of inviscid paralell flows in the absence of surface tension.

Acknowledgements

This work has been made possible through the financial support of the SEP (Société Europénne de Propulsion) under contract $n°910023$.

REFERENCES

Arai, T. and Hashimoto, H. 1985, *Proceedings of the 3rd International Conference on Liquid Atomization and Spray Systems* London **VI.B.14**, 1-7.

Bernal, L.P. and Roshko, A. 1986, "Streamwise vortex structure in plane mixing layers". *J. Fluid Mech.* **170**, 499-525.

Brown, G. L. 1974, "The entrainment and large structures in turbulent mixing layers.", in *Proc. 5th Australasian Conference on Hydraulics and Fluid Mechanics*, 352-359.

Brown, G. L. and Roshko, A. 1974, "On density effects and large scale structures in turbulent mixing layers.", *J. Fluid Mech.*, **64 (4)**, 775-815.

Chandrasekhar, S. 1961, Hydrodynamic and hydromagnetic stability. Dover Pub. Inc., New-York.

Dimotakis, P.E. 1986, "Two-dimensional shear layer entrainment". *AIAA* **24 (11)**, 1791-1796.

Hinze, J.O. 1949, "Critical speeds and sizes of liquid globules", *Appl. Sci. Res.*, **A1**, 273-288.

Hopfinger, E.J. and Lasheras, J.C. 1994, "Breakup of a water jet in high velocity co-flowing air", in *Proceedings of the 6th International Conference on Liquid Atomization and Spray Systems*, Rouen. **1-15**, 110-117.

Hsiang, L.P. and Faeth, G.M. 1992, "Near-limit deformation and secondary breakup", *Int. J. Mutltiphase Flow*, **18-5**, 635-652.

Kolmogorov, A.N. 1949, "On the breakage of drops in a turbulent flow", in *selected works of A.N. Kolmogorov "Mathematics and Mechanics"*, V.M. Tchekomirov Ed. Kluwer Acad. Pub. Dordrecht.

Mansour, A. and Chigier, N. 1991, Dynamic behavior of liquid sheets. *Phys. Fluids A3*, **(12)**, 2971-2980.

ON THE ANALYSIS OF SHEAR-DRIVEN LIQUID BREAK-UP PROCESSES

by

Isabel S. Carvalho, Manuel V. Heitor and Dina Santos

Department of Mechanical Engineering
Instituto Superior Técnico
Av. Rovisco Pais
1096 Lisboa Codex
Portugal

ABSTRACT

The process of liquid sheet disintegration and break-up into a spray is studied making use of a flat liquid film surrounded by a mixing layer for variable strain levels. The work considers a liquid sheet with an aspect ratio of 114 and a liquid velocity up to 6 m/s and allows to study the basic phenomena typical of air blast atomisation. The results include the quantification of convergence lengths, disintegration frequency and spray and deflection angles, for velocity ratios of the air flows in each side of the liquid sheet between 0 and 4, and show that the disintegration of the liquid sheet is associated with a periodic process, which is mainly dependent on the absolute air velocity and the air-liquid momentum ratio.

INTRODUCTION

The basic mechanisms involved in air blast atomisation have been studied for a number of years making use of planar liquid films and major achievements have been reported since Fraser et al. (1963) and Dombrowski and Jonhs (1963), namely by Mansour and Chigier (1990, 1991), Eroglu and Chigier (1991), Stapper et al. (1992) and Lozano et al. (1996). These studies were conducted in quiescent ambient and/or between two co-flowing air streams of similar velocity, and although the results have contributed to improve knowledge of basic processes and regimes associated with liquid break-up and atomisation, the experimental conditions used do not fully represent the shear behaviour of the more practical configurations. Moreover, streamwise vorticity was shown to considerably influence the break-up process (e.g., Lozano et al, 1996; Chigier and Reitz, 1996), but its effect on the disintegration process has not been quantified in a systematic way. This has motivated the present work, for which vorticity generation can be easily controlled by varying the velocity gradient established through a liquid sheet of large aspect ratio.

The present work involves the analysis of the flow downstream a 2-D planar liquid film surrounded by a mixing layer for variable strain levels, which was made possible by injecting the liquid sheet between two independently controlled air flows. The ultimate objective is to improve knowledge of the liquid break-up mechanisms and their relation with the atomisation quality in air blast nozzles of practical relevance.

The next section describes the flow configuration and the experimental techniques used throughout the work. The third section presents and discusses the results and the main findings are summarised in the last section.

EXPERIMENTAL METHOD

Figure 1 shows a schematic diagram of the liquid film generator, which consists of: i) an inner liquid flow, with an exit thickness of t = 0.7 mm, and an aspect ratio of l/t= 114; and ii) outer air flows, with a thickness of 7 mm, which are passed along either sides of the liquid film to produce a shear force at the air-liquid interface. Air can be fed through the left and right channels separately, thus allowing the air velocity ratio to be varied between 0 and 4, with absolute average velocities up to 40 m/s. The impingement angle of the air flows towards the liquid film is 30 deg. Water was used as the test liquid, and the results reported here are for a liquid velocity up to 6 m/s.

Different visualisation techniques were used throughout the work, which include laser light sheet illumination obtained by spreading a laser beam with a cylindrical lens, with individual images acquired by a 35 mm camera operating with 400 ASA films, and exposure time varying between 4 ms and 66 ms. In addition, back white lighting of the flow was used, making use of a strobelight operating at different frequencies. Flow images were acquired by a CCD video camera, each frame corresponding to an individual image of the flow, with an exposure time of 1.2 μs.

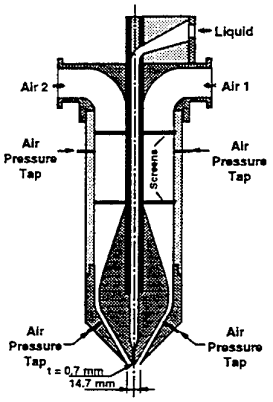


Figure 1. Schematic diagram of the flat liquid film generator

The oscillatory frequency of the liquid sheet prior to break-up, as identified before in the literature, was analysed by matching the strobelight frequency ,f_s, with that of the flow, for $0<f_s(Hz)<250$. The analysis allowed to identify the fundamental frequency of the sheet oscillation, as well as related harmonics, and sample results are presented here with the purposes of contributing to the qualitative analysis of the liquid break-up process. A comprehensive analysis of the liquid sheet oscillatory motions is presented elsewhere.

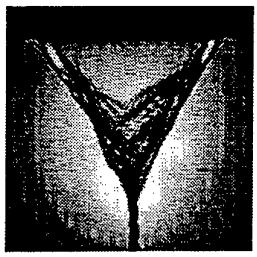
RESULTS AND DISCUSSION

The results of the work discussed in this paper are presented in three parts, namely : i) for a liquid sheet in the absence of air flow; ii) for a liquid sheet surrounded by two sheets of high-speed air of similar flow rate; and iii) for a liquid sheet in a mixing layer formed between two air sheets of different velocity. The results presented in the first two parts allow to assess the present flow field in terms of those previously reported in the literature , while the last part introduces new data on the analysis of the disintegration of liquid sheets typical of practical airblast atomisation . The novelty derives from the need to better control the atomisation of liquid sheets, namely by increasing the shear-generated vorticity created at the liquid interphases.

Figure 2 presents sample results obtained in the absence of air, which characterise a convergent sheet bounded by thick rims that are drawn together by surface tension forces, as first described by Mansour and Chigier (1990).

The convergence length, L_c, increases with the liquid film velocity, U_L, as shown in Figure 2 b), where L_c is plotted versus the relative velocity ($U_R = U_a - U_L$). The results must be extrapolated with care due to their dependence on the geometry of the sheet generator, but show a clear linear increase of the convergence length as the liquid flow rate increases, which is in qualitative agreement with the results of Mansour and Chigier (1990). The central part of the film keeps a smooth appearance for small liquid velocities U_L, although it exhibits small ripples near the exit for U_L = 2.1 m/s, Re_L = 1628. As the liquid mass flow rate increases, this effect is more pronounced and at U_L = 2.9 m/s (Re_L = 2249) the liquid surface becomes clearly disturbed over all its extension. Following again Mansour and Chigier (1990), it is interesting to note that these disturbances are dampened on the downstream region, because turbulent energy production ceases at the nozzle exit and the liquid sheet tends to laminarize as a result of viscous dissipation of turbulent energy.

a)



b)

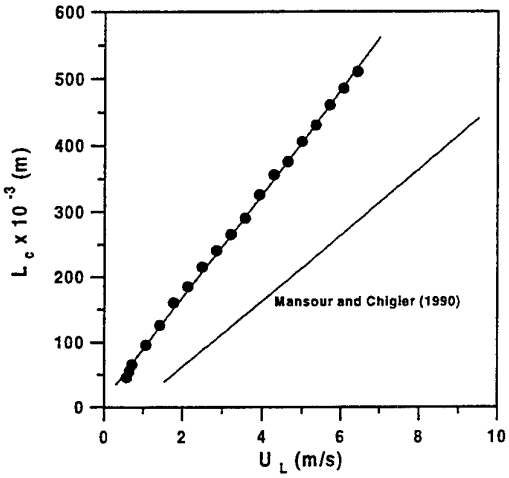


Figure 2. Analysis of the convergence length of the liquid film (l=80 mm; t=0.7 mm), for $U_1=U_2=0$

a) Flow visualisation

b) L_c as a function of the liquid velocity, U_L

When the liquid film is surrounded by two sheets of air flow, the aerodynamic forces become stronger and the surface tension forces cannot contradict the increase of the growth rate of the initial disturbance, thus the liquid film starts to disintegrate closer to the nozzle exit. Consequently, for high enough values of air mass flow rate, a convergence length no longer can be defined and a break-up length is quantified instead.

Figures 3 and 4 show two different views of the liquid film for different air flow rates and U_L = 0.9; 1.6 m/s, which exhibit similar liquid surface characteristics to those reported before by Mansour and Chigier (1991) and Lozano et al (1996). The results obtained for high liquid velocities resemble those characterise by "cellular" break-up, in that the liquid sheet issuing from the nozzle is drawn up into small, but ordered "cell" structures. As the shear strength is increased, namely by decreasing the liquid velocity, the sheet gives rise to

streamwise ligaments, which are formed very close to the nozzle. The analysis shows that a spanwise wave is superimposed on top of the streamwise ligaments, which grow together and, as a result, gives rise to the type of distorted waves discribed by Mansour and Chigier (1991) downstream of the initial sinusoidal wave.

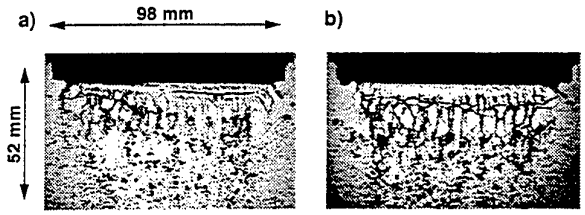


Figure 3. Front view (strobelight visualization) of the flat liquid film for $U_1=U_2=20$ m/s
a) $U_L = 0.9$ m/s
b) $U_L = 1.6$ m/s

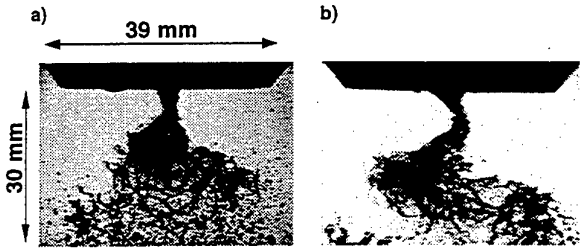


Figure 4. Side view (strobelight vizualization) of the flat liquid film for $U_1=U_2=20$m/s
a) $U_L = 0.9$ m/s; b) $U_L = 1.6$ m/s

It should also be noted that the mixing process between the two air flows is strongly influenced by the turbulence field produced by the aerodynamic and geometrical exit conditions. The near exit region is influenced by the velocity ratio between the two co-flowing air streams and by the geometry of the separation wall between them, which is, very thin in the present case. In addition, the characteristics of the boundary layers at the exit plane will influence the characteristics of the air-liquid interface. In the present configuration the atomising air has a velocity component in a direction normal to the liquid film and, as a consequence, the interaction between the liquid and the atomising air is enhanced. For low liquid velocities, the liquid film emerging from the nozzle is rapidly torn into small fragments by the immediate interaction between the liquid and the impinging air streams, as already suggested by Lefebvre (1992).

As clearly shown in Figure 4, disintegration occurs when the wave amplitude reaches a critical value, as previously described by Dombrowski and Johns (1963), and fragments of the liquid are torn off from the "outer layers" of the liquid film. The fragments rapidly contract into unstable ligaments under the action of surface tension and drops are formed as a result of ligament break up, as illustrated in Figure 3. According to this mechanism, the growing waves protrude into the coflowing air stream, promoting the interaction between the air and the liquid and causing the crests of the waves to become detached and form ligaments, which subsequently break into drops.

It is important to note that the previous analysis of liquid sheets surrounded by a co-flow of high-speed air have shown that vorticity created by the sharp interphase velocity gradients plays a prominent role in the liquid break-up process, which is oscillatory in nature and dominated by contrast frequencies. Based on the measurement technique described above, sample results of the sheet oscillation frequency are plotted in figure 5, as a function of the liquid velocity. The results characterise the sinusoidal mode of oscillation described by Mansour and Chigier (1991) and Lozano et al (1996) and show that the frequency oscillation is affected by the liquid velocity only for $U_L > 1$m/s.

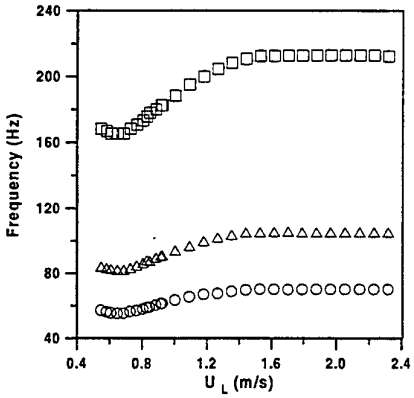


Figure 5. Vibration frequency of the liquid sheet as a function of the liquid velocity for $U_1=U_2=20$ m/s

The characteristics of typical oscillating liquid sheets and of the downstream spray are easily observed in the side view of figure 4, which clearly identify two distinct modes of operation. First, the liquid film may oscillate left and right, and drops are torn away from the liquid surface at the extreme radial positions (i.e., far away form the geometrical axis of the liquid film). Second, the liquid film seems to keep vertically aligned with the liquid exit, and drops are spread symmetrically from both sides of the liquid surface with a very precise frequency. Both modes are alternatively present, and were identified for a large frequency range, above 44 Hz.

The analysis above validates the comparison between the present flow and those reported previously in the literature, which reflect the importance of streamwise vorticity in the formation of liquid ligaments and droplets. We now turn to the analysis of the process of liquid disintegration in the presence of increased shear, by surrounding the liquid sheet with two air flow sheets at different flow rates. As a result, the liquid flow and dispersed phase downstream of the nozzle becomes significantly assymmetric and may be characterized, as in figure 6, through consideration of a deflection angle, β, in addition to the typical spray angle, $\propto$.

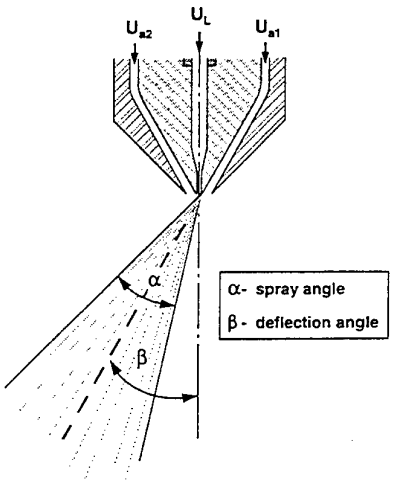


Figure 6. Schematic diagram of the liquid sheet analysis for $U_1 > U_2$

The criterion to measure these angles was to follow the crests of the major liquid perturbations, but not considering the droplets surrounding the liquid sheet. In general, the analysis has shown a substantial decrease in the spray angle, as the liquid flow rate was increased. This agrees with the observations of Mansour and Chigier (1990) and is explained since the specific energy of air per unit volume of liquid leaving the nozzle is reduced. Increasing the liquid flow rate results in the decrease of the air-liquid relative velocity at the interface, which is accompanied by a reduction of the amplitude of oscillations of the liquid sheet, with a corresponding decrease in the spray angle.

Prior to the quantitative analysis of the spray and deflection angles, it is important to note that under non-symmetric mixing conditions, the liquid sheet break-up process follows the mechanism described above. Figure 7 shows sample front views of the present flow for different air velocity ratios $(U_1-U_2)/U_1$, which identify the "cellular" and "streamwise ligament" break-up processes identified before. Figure 8 shows the related side views and it is important to note the stabilizing effect on the flow, as the velocity gradient across the liquid sheet is increased, namely in the near nozzle region. Nevertheless, this does not alter the oscillatory nature of the breakup process, which is characterized again by the presence of ligaments oriented in the spanwise direction, as a result of the growth of spanwise sinusoidal waves that form on the liquid sheet as it exists the nozzle.

Figure 9 shows measured spray angles plotted as a function of the liquid velocity for different air flow rates. The results were obtained with exposure times of the order of 1s and the related uncertainty is estimated to be $\pm$ 10^0 (approximately 10%). For all operating conditions, a region of maximum spray angle occurs, followed by a sharp decrease for higher values of liquid velocity. The maximum value of spray angle is displaced to higher values of liquid velocity as the air flow rate increases, the maximum value decreasing with the air flow rate, as observed by Mansour and Chigier (1991) and Lozano et al (1996) for similar and higher air velocities.

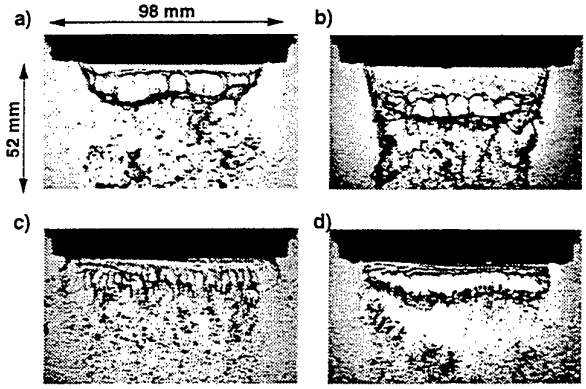


Figure 7. Front view (strobelight visualisation) of the flat liquid film for $U_1>U_2$
a) U_L = 0.9 m/s; U_1= 20 m/s; U_2= 0
b) U_L = 0.9 m/s; U_1= 39 m/s; U_2= 0
c) U_L = 1.6 m/s; U_1= 20 m/s; U_2= 0
d) U_L = 1.6 m/s; U_1= 39 m/s; U_2= 0

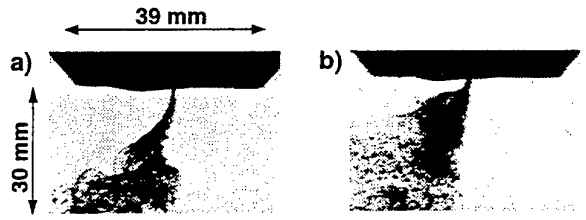


Figure 8. Side view (strobelight visualization) of the flat liquid film for $U_1 > U_2$
a) U_1= 20 m/s; U_2= 0
b) U_1= 39 m/s; U_2= 0

It is important to note that a temporary change in the spray structure was detected as the liquid velocity was increased, which is accompanied by highly unsteady sprays for a very narrow range of U_L. The process appears to be dependent on the air flow rate, with the spray angles varying around ±15-20°. For a small increase in liquid velocity, very poor atomisation is obtained and the spray angle undergoes another sharp decrease.

The deflection angles, as shown in Figure 10a), decrease with increasing liquid velocity for a constant value of air flow rate, with the results suggesting a well-behaved nature of the liquid disintegration process under non-symmetric mixing conditions. The results are found to be represented as a function of the reciprocal of the air-to-liquid momentum ratio, as in figure 10b). This behaviour was also found by Carvalho and Heitor (1995) with reference to the atomisation of an axissymmetric liquid sheet formed between turbulent coaxial jets and the analysis calls for the importance of the present results in order to improve knowledge of practical air

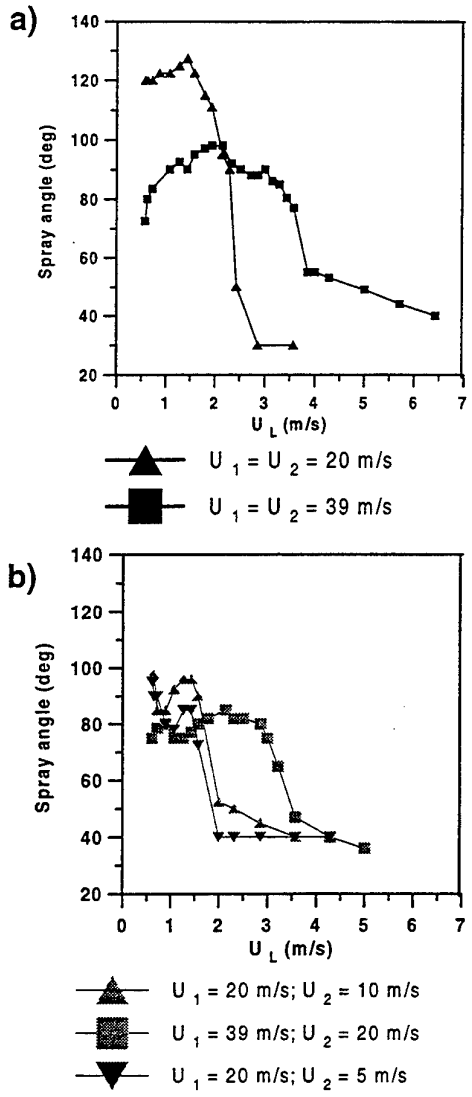


Figure 9. Analysis of the spray angle (following the definition of Figure 6) as a function of the liquid velocity
a) $U_1=U_2$
b) $U_1>U_2$

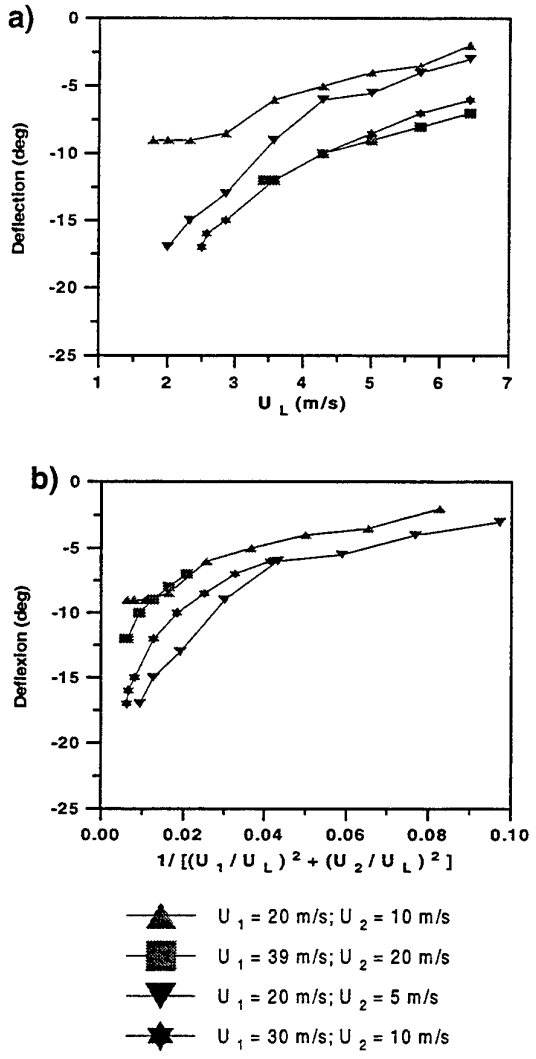


Figure 10. Analysis of the spray deflection for $U_1>U_2$, as a function of the liquid velocity and air/liquid momentum ratio
a) Spray defection as a function of the liquid velocity, U_L
b) spray deflection as a function of air/liquid momentum ratio

blast prefilming atomizers. Another interesting observation is that even under strong shear conditions across the liquid sheet, when the droplets are generated mainly from streamwise oriented filaments, the presence of longitudinal waves causes intermittent droplet clouds.

CONCLUSIONS

The disintegration process of a flat liquid film under symmetric and non symmetric mixing conditions is studied by means of different visualisation techniques. The ultimate objective is to improve knowledge of shear-driven atomisation processes, in a way that allows to study the basic phenomena typical of air blast atomisation.

The results quantify the process of liquid disintegration and breakup for a liquid sheet with an aspect ratio of 114, a thickness of 0,7 mm and liquid velocities in the range 0.9 to 6m/s, and show that the deterioration of the liquid film is associated with a periodic process mainly dependent on the air velocity. The principal cause of instability is due to the interaction of the film with the surrounding air flow, whereby rapidly growing waves are imposed on the liquid surface. Disintegration occurs when the wave amplitude reaches a critical value and fragments of sheet are torn off. The fragments rapidly contract into unstable ligaments under the action of surface tension and drops are produced as the latter subsequently break down. The process seems to be strongly dependent on the "energy" associated with the air flows, although the results show that the gas-to-liquid momentum ratio is the key parameter in the atomisation process, namely under non-symmetric mixing conditions.

ACKNOWLEDGEMENTS

The assistance of Mr. J. Coelho in the preparation of this paper is gratefully appreciated. Financial support has been provided through the BRITE/EURAM programme of the European Commission under the contact AERO-CT95/0122

The authors are pleased to acknowledge the research grant of Dina Santos from the PRAXIS XXI program of the Portuguese Ministry of Science and Technology.

REFERENCES

Carvalho, I.S. and Heitor, M.V. 1995, "Liquid film break-up and drolet characterisation in strongly swirling jet floes. In: "Advances in Multiphase Flows", eds. A. Serigawa et al., Elsevier Sci. Publ., pp. 119-128.

Chigier, N. and Reitz, R.D. 1996, "Regimes of Jet Breakup and Breakup Mechanisms. (Physical Aspects). In: Recent Advances in Spray Combustion: Spray Atomization and drop Burning Phenomena," Volume I., Progress in Astronautics and Aeronautics, Vol.166, pp.109-136.

Dombrowski, N. and Johns, W.R. 1963, "The Aerodynamic Instability and Disintegration of Viscous Liquid Sheets," Chemical Engng. Sci., **18**, pp.203-214.

Eroglu, H. and Chigier, N. 1991, "Liquid Sheet Instability in Coflowing Air Stream," ICLASS-91, 15-18 July, Gaithersburg, MD, USA. pp. 679-686.

Fraser, R.P., Dombrowski, N. and Routley, J.H. 1963, "The Atomization of a Liquid Sheet by an Impinging Air Stream," Chemical Engng. Sci., **18**, pp.339-353.

Lefebvre, A. H. 1989, Atomization and Sprays. Hemisphere Publishing Corporation.

Lefebvre, A.H. 1992, "Energy Considerations in Twin-Fluid Atomization," Trans. ASME, J.Engng. Gas Turbines Power, **114**, pp.89-96.

Lozano, A., Call, C.J., Dopazo, C. and Garcia-Olivares, A. 1996, "Experimental Study of the Atomization of a Planar Liquid Sheet," Atomization and Sprays, **6**, pp.77-94.

Mansour, A. and Chigier, N. 1990, "Disintegration of Liquid Sheets," Phys. Fluids A, **3(12)**, pp. 2971-2980.

Mansour, A. and Chigier, N. 1991, "Dynamic Behavior of Liquid Sheets," Phys. Fluids A, **2(5)**, pp. 706-719.

Rizk, N.K. and Lefebvre, A.H. 1980, "The Influence of Liquid Film Thickness on Airblast Atomization," Trans. ASME, J. Engng. Power, **102**, pp.706-710.

Stapper, B. E., Sowa, W. A. and Samuelsen, G.S. 1992, "An Experimental Study of the Effects of Liquid Properties on the Breakup of a Two-Dimensional Liquid Sheet," Trans. ASME, J. Engng. Gas Turbine Power, **114**, pp.39-45.

DISPERSION OF BUBBLES IN A SHEAR FLOW

C. Martínez, J.C. Lasheras
Department of Applied Mechanics in Engineering Sciences
University of California, San Diego
9500 Gilman Drive
La Jolla, CA, 92093-0411
U.S.A.

ABSTRACT

An experimental characterization of the dispersion of bubbles in a plane, turbulent mixing layer using a combination of Phase Doppler Particle Analizer (PDPA) and laser scattering measurements is presented. It is shown that for bubbles with Stokes Numbers based on the turnover time of the large eddies equal to or less than one, their mean, lateral dispersion is independent of their size. This is shown to be the case even for downstream distances well beyond the mixing transition where the shear layer exhibits a wide range of eddy scales, and the Stokes Number of the bubbles based on the smaller scales are greater than one.

INTRODUCTION

The characterization of particle-turbulence interaction is of fundamental importance to a wide variety of flows and applications. Dispersion of small, heavy spherical particles in temporally evolving shear flows has been studied numerically and experimentally in the last decade. It is well known that the behaviour of free shear layers is dominated by the presence of large-scale, coherent vortices (Brown & Roshko 1974), whose pairing and amalgamation determine the growth of the turbulent mixing region (Winant & Browand 1974). The receptivity to forcing the primary instability which leads to the formation of these large eddies makes the free shear layer one of the most interesting turbulent flows with which to study the motion of small particles in turbulent flows as well as to analyze the role of the coherent structures in the dynamics of the dispersion process.

Particles of different density than the base flow can exhibit different dispersion characteristics in turbulent flows. Although the above is true for particles denser and lighter than the base fluid, their dispersion mechanism has been shown to be very different. Experimental studies of liquid droplets dispersing in a gaseous, free shear layer (Lázaro & Lasheras 1989, 1992a and 1992b) have shown that small-sized particles behave almost as fluid particles while particles greater than a critical size are flung out to the edge of the vortex leaving their core depleted. Lázaro and Lasheras also found a similarity in the spreading rate of the droplet concentration depending on their size by normalizing the downstream distance and the particle concentration thickness of each droplet size family using a particle viscous relaxation length defined as:

$$L_D = \frac{\rho_p U_\infty d_p^2}{18\rho\nu} \tag{1}$$

When the particles are much lighter than the base flow (i.e. bubbles), their interaction with the large-size coherent eddies of the shear layer has been shown to lead to the opposite phenomena whereby, depending on their size, the bubbles accumulate in the core of the large eddies (Rightley 1995). Numerical simulations of the motion of bubbles in a planar, free shear layer by Ruestsch and Meiburg (1993) have also shown that the concentration of bubbles accumulating in the vortex cores increases with the bubble Stokes number. However, numerical simulations by Crowe et al (1992) found little, or no effect, of the Stokes number in the dispersion characteristics of the bubbles, a result which they attributed to the fast relaxation time of the bubbles. In spite of the above studies, there is a lack in the experimental characterization of the dispersion of bubbles in a planar, turbulent shear layer. In particular, one of the important issues which remains unsolved is the determination of the maximum bubble size for which the bubbles can be assumed on the average to disperse as fluid particles. Although the turbulent shear layer exhibits a wide spectrum of frequencies, it is well known that most of the turbulent kinetic energy is contained in the large-scale, coherent vortices. Thus, it is reasonable to assume that the mean dispersion of the bubbles will be dominated by their interaction with these large eddies. One can conclude therefore, only particles with a viscous, relaxation time larger than the turnover time of these large coherent eddies should have a mean dispersion different from fluid particles. The above simplified argument will only hold true if one neglects the effect of the interaction of the bubbles with the wide range of eddy scales also present in the shear layer, an issue which remains unsolved. Thus, in order to study the range of bubble sizes below which the mean dispersion characteristics of the bubbles are equal to that of fluid particles, we have conducted a series of detailed experiments where bubbles with viscous relaxation times equal

or smaller than the turnover time of the large-scale eddies developing in the mixing layer have been analyzed. In our study, we combine PDPA measurements with light scattering measurements to obtain detailed measurements of the evolution of the bubble concentration field as a function of the bubble size. These measurements are then used to determine the optimum diameter of the bubbles below which their mean dispersion is independent of their size. These results are shown to be relevant to the implementation of various measurement techniques such as hydrogen bubble visualizations, LDV and PIV measurements.They also have important implications in the design of industrial processes such as two-phase flow chemical reactors, particle separators, etc....

Experimental Facility and Measurement Techniques

The experimental set-up consists of a horizontal shear layer produced by two water streams which meet at the trailing edge of a thin splitter plate (Figure 1). The water is supplied from two 1000 gallon reservoirs which feed two independent constant head tanks. The water channel entrance is equipped with various elements to attenuate the turbulence and to damp out the surface waves produced by the supply jets discharging into the channel. A variety of honeycomb sections and screens are carefully placed in the upper, slow stream to homogenize the flow. The lower, fast stream uniformly loaded with bubbles is therefore undisturbed to avoid an undesired accumulation of bubbles on the screens and to prevent changes in the flow conditions with time. Both streams are driven through a 3:1 area contraction nozzle before discharging into the test section. The water at the end of the test section is collected into two tanks where the bubbles have time to settle down, before the flow is recirculated back into the main reservoirs.

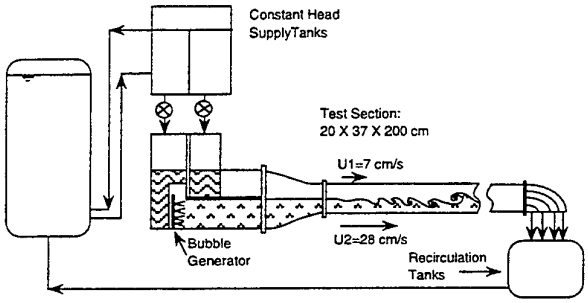


Figure 1: Experimental Facility

The bubbles are generated by injecting water, saturated with CO_2 from a water tank pressurized at 60 psi, through an array of small nozzles drilled into a grid of brass tubes evenly distributed along the width of the entrance of the lower stream in the channel (see Figure 1). The turbulence produced by the small jets mixes the bubbles into the flow, thereby reaching a homogeneous bubble concentration at the entrance of the test section. Accumulation of bubbles on the plate which separates the upper and lower layer is removed by suction before they reach the edge of the splitter plate to avoid the introduction of undesired perturbations into the flow.

Two different optical measurement techniques are used to characterize the evolution of the bubbles in the shear layer and to study their dispersion characteristics according to their size: digital image processing of time-averaged measurements of the 90° scattered light by the particles (Figure 2), and Phase Doppler sizing and velocimetry (PDPA).

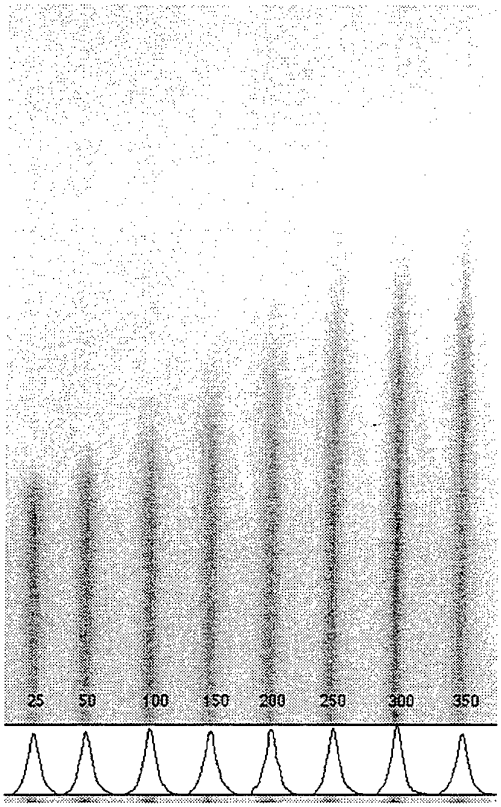


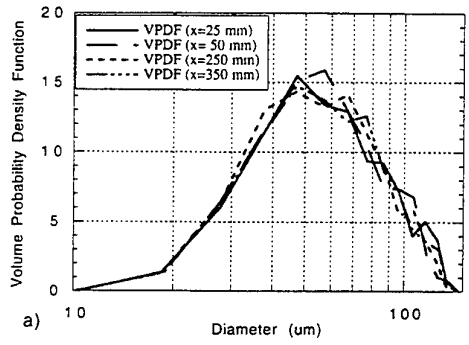
Figure 2: Evolution of the concentration of bubbles in the shear layer. Intensity of the scattered light at distances from 25 to 350 mm from the trailing edge of the splitter plate is shown. The cross-section gaussian profile of the laser beam can be seen at each feestream location.

Initial Conditions

The flow conditions chosen for our study are a turbulent, free shear layer with mean freestream velocities of $U_1 = 7cm/s$ and $U_2 = 28cm/s$ (Figure 1). The convective velocity of the large eddies forming in the mixing layer is $U_c = \frac{U_1+U_2}{2} = 17.5cm/s$. The most unstable frequency of the naturally evolving shear layer was experimentaly found to be approximately 2 Hz, which together with the above convective velocity gives a wavelength of the large eddies of about 8.75 cm. A uniform concentration of polidispersed size bubbles with sizes ranging from 10 to 150 μm is injected in the lower, fast stream. A vertical traverse of the bubble-laden freestream performed under the splitter plate (Figure 4) shows a uniform initial concentration of bubbles (void fraction). In addition, very few variations of the probability density function and mean diameters (D_{32}, D_{10}) of the bubbles across the freestream were detected (Figure 3). Therefore,we can conclude that our bubble generation and injection mechanism produces a steady bubble-laden flow containing bubbles with a wide range of diameters which are uniformly distributed across the free stream. Furthermore, the initial bubble void fraction and the bubble size distribution function are the same everywhere across the free stream indicating that gravitational settling is negligible in our experiments.

Experimental Techniques

The characterization of the evolution of the bubble field was made using several optical techniques: digital image processing of the intensity of the 90° scattered light by



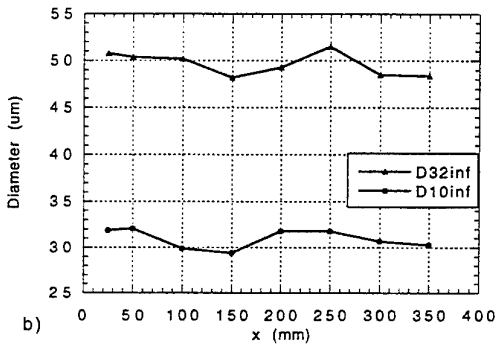
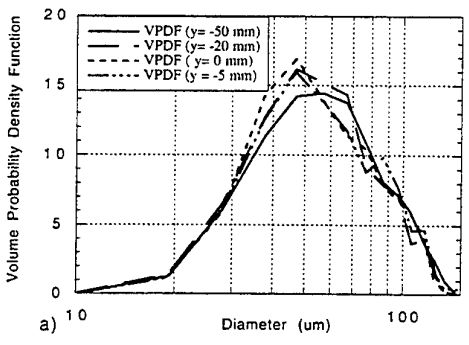


Figure 3: Freestream Conditions: a) Axial evolution of the Probability Density Function. b) Axial evolution of Mean and Sauter Mean Diameter.



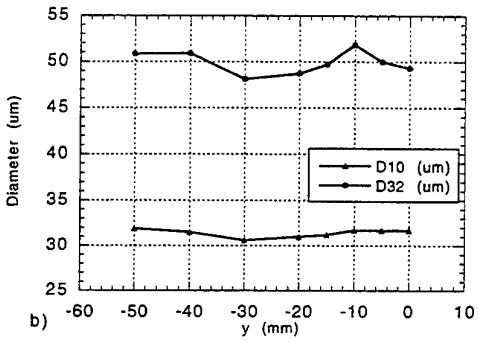


Figure 4: Initial Conditions: a) Vertical evolution of the Probability Density Function. b) Vertical evolution of Mean and Sauter Mean Diameter.

the bubbles, and PDPA particle sizing and velocimetry. The light scattered by the cloud of bubbles as a vertical laser beam is shined through the mixing layer is collected at 90° by a CCD camera and processed with a NIH 1.60 image processing package. Time average of the scattered light at different downstream positions from the splitter plate allows us to measure the lateral spreading rate of the concentration of bubbles (Figure 2). When the scattering medium is diluted and made up of spherical bubbles whose mean spacing is much larger than their diameter, multiple scattering effects can be neglected. Under these conditions Lázaro 1989 has shown, using the MIE scattering theory that:

$$\ln \frac{I}{I_o} = -3L\bar{\alpha}_b \int_0^\infty \frac{Pdf(D)}{D} dD \tag{2}$$

where $\bar{\alpha}_b$ and $Pdf(D)$ are the concentration of bubbles and the volume probability density function respectively, I is the scattered light intensity, I_o is the intensity of the incident beam, L is the propagation length or length along the path of the laser beam, and D is the diameter of the bubbles. Defining the attenuation parameter as $\zeta_b = ln\frac{I}{I_o}$ we calculate the normalized concentration of bubbles as:

$$\frac{\bar{\alpha}_b}{\bar{\alpha}_{b\infty}} = \frac{\zeta_b \int_0^\infty \frac{Pdf(D)}{D} dD|_\infty}{\zeta_{b\infty} \int_0^\infty \frac{Pdf(D)}{D} dD} \tag{3}$$

where ∞ refers to a reference free stream conditions. A Phase Doppler Particle Analyzer system was used to measure simultaneously the local instantaneous two components of the velocity and the size of the bubbles. Therefore the probability density functions needed in equation (3) are measured to compute the concentration of the bubbles, $\bar{\alpha}_b$, and its evolution within the mixing layer. By distinguishing the velocity data by size, we were able to calculate the mean value and rms of the velocity of the bubbles depending on their diameter, and to calculate the spatial variation of the time average concentration of bubbles of each size $\bar{\alpha}_b(D)$ as follows:

$$\frac{\bar{\alpha}_b(D)}{\bar{\alpha}_{b\infty}(D)} = \frac{Pdf(D)|_\infty}{Pdf(D)} \frac{\zeta_b}{\zeta_{b\infty}} \tag{4}$$

Theoretical considerations

The unsteady equation of motion for a small spherical particle of radius r_b and mass m_b is given by:

$$m_b \frac{d\mathrm{V}}{dt} = (m_b - m_f)\mathrm{g} - 6\pi r_b \mu_f (\mathrm{V} - \mathrm{u}) + m_f \frac{D\mathrm{u}}{Dt} - \frac{1}{2} m_f \frac{d(\mathrm{V} - \mathrm{u})}{dt} \tag{5}$$

where the terms on the right hand side of equation (5) are buoyancy, viscous Stokes drag, effects of pressure gradient and added mass. In this equation we have neglected the Basset history term and other effects, such as Faxen correction, etc. V is the bubble velocity, u is the velocity of the fluid and m_f is the mass of the carrier fluid contained in a volume of the same size as the volume of the bubble. In the case of small bubbles where $m_b \ll m_f$ equation (5) simplifies to:

$$\frac{d\mathrm{V}}{dt} = -2\mathrm{g} - \frac{9\nu_f(\mathrm{V} - \mathrm{u})}{r_b^2} + 3\frac{D\mathrm{u}}{Dt} \tag{6}$$

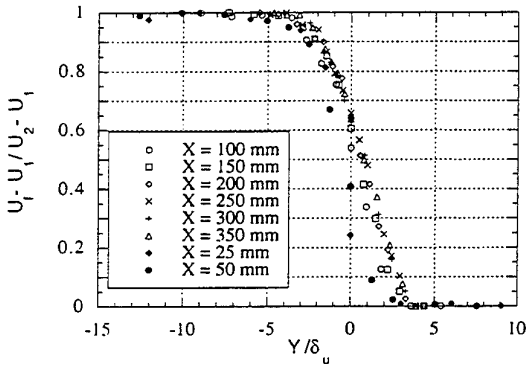


Figure 5: Similar profiles of velocity

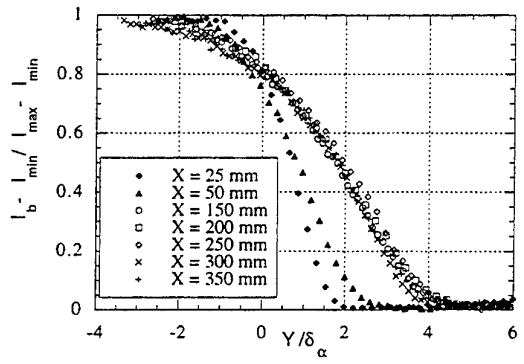


Figure 6: Similar profiles of global concentration of bubbles

For the flow conditions and size of bubbles presented above, one can define the following characteristic times which govern the bubble motion:

$$\begin{aligned} \tau_b &= \frac{d_b^2}{36\nu_f} \\ \tau_f &= \frac{\delta}{\Delta U} \\ \tau_g &= \frac{\delta}{V_T} \end{aligned} \tag{7}$$

where τ_b, τ_g are relaxation (viscous) and buoyant times respectively, and τ_f is the eddy turnover time (corresponding to the large eddies). $V_T = \frac{-d^2 g}{18\nu_f}$ is the terminal velocity of the bubble in still fluid, δ is the characteristic length of the large scales (taking as the momentum thickness of the shear layer), and $\Delta U = U_2 - U_1$ is the difference between the freestream velocities. In addition to the fluid time (or turnover time) defined with the large scale eddies, we can define a similar turnover time for each of the scales present in the shear layer. This leads to a wide range of time scales spaning from the Kolmogorov turnover time, τ_k, to the τ_f defined in equation (7). The Stokes number is defined as the ratio between the bubble relaxation time and the turbulent flow time:

$$S_t = \frac{d^2 \Delta U}{36\nu_f \delta} \tag{8}$$

For the bubbles to follow the flow and behave as passive scalars, τ_b must be smaller than any flow characteristic times for all ranges of scales, i.e. the Kolmogorov turnover time, τ_k.

Selecting a characteristic length of $\delta = 7mm$, diameter of bubbles of $d = 100\mu m$ and $\Delta U = 21cm/s$ we can calculate the values of the different time scales from equation (7):
$\tau_b \approx 3x10^{-4}\, s$
$\tau_f \approx 3.5x10^{-2}\, s$
$\tau_g \approx 1.25 s$
and thus the Stokes number, $S_t = \frac{\tau_b}{\tau_f} = 8x10^{-3}$. Smaller eddies whose time scales are smaller than τ_f may be able to accumulate certain classes of bubbles depending on their size. In our case, where gravity plays an unimportant role, bubbles are expected to follow the fluctuations produced by the large, coherent structures in the shear layer. Increasing the size of the bubble to $\tau_b \approx \tau_f$, will decrease τ_g as d^2, and bubbles will escape the mixing layer due to buoyant effects.

Results

From the dimensionless profiles of the mean longitudinal component of the velocity and bubble concentrations we have calculated several parameters to characterize the lateral spreading of the bubbles and compared it to that of the longitudinal momentum. For this comparison, we have specifically selected the following parameters:

The 10% Level Thickness of the axial velocity, δ_{L_u}, or the difference between the vertical coordinate of the locations where the velocity drops from 90% to 10% of the freestream value

$$\delta_{Lu} = y(U_n = 0.1) - y(U_n = 0.9); \tag{9}$$

the momentum thickness, δ_u, defined as:

$$\delta_u = \int_{-\infty}^{\infty} U_n(1 - U_n)dy \tag{10}$$

where $U_n = \frac{U - U_1}{U_2 - U_1}$.
the 10% Concentration Level Thickness, $\delta_{L\bar{\alpha}}(D)$

$$\delta_{L\bar{\alpha}}(D) = y(\bar{\alpha}_n = 0.1) - y(\bar{\alpha}_n = 0.9), \tag{11}$$

and the Concentration Integral Thickness, $\delta_{\bar{\alpha}}(D)$, define as:

$$\delta_{\bar{\alpha}}(D) = \int_{-\infty}^{\infty} \bar{\alpha}_n(D)(1 - \bar{\alpha}_n(D))dy \tag{12}$$

where $\bar{\alpha}_n(D) = \frac{\bar{\alpha}(D)}{\bar{\alpha}_{\infty(D)}}$. It is important to notice that, as it was shown in equation (4), $\delta_{L\bar{\alpha}}(D)$ and $\delta_{\bar{\alpha}}(D)$ depend on the diameter of the bubble in general.

The evolution of the mean streamwise velocity and the intensity of the light scattered by the bubbles is shown in figures 5 and 6 where the vertical distance, y, has been normalized by the respective integral thickness. Observe that in both cases self similar profiles occurs at 50 mm downstream from the splitter plate in both cases. Thus, it is clear from these results that the shear layer has already developed after this point and it is well beyond the mixing transition.

Experimental data obtained with a Phase Doppler System at different downstream locations allows us to study the motion of the microbubbles as they are convected within the mixing region. Figure 7 shows the evolution of the volume probability density function, Pdf(D), measured at various vertical positions at a downstream distance of 20 cm from the trailing edge of the splitter plate. Very few

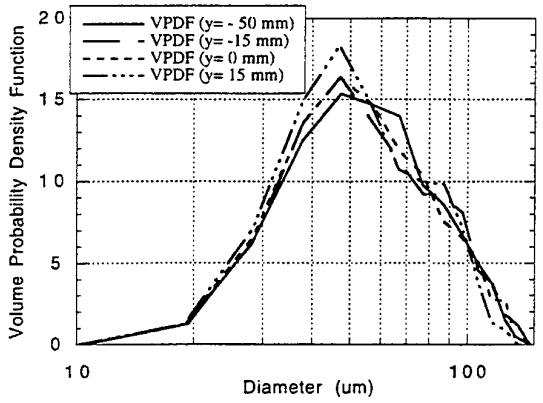


Figure 7: Probability Density Function of the volume of bubbles at x= 200 mm

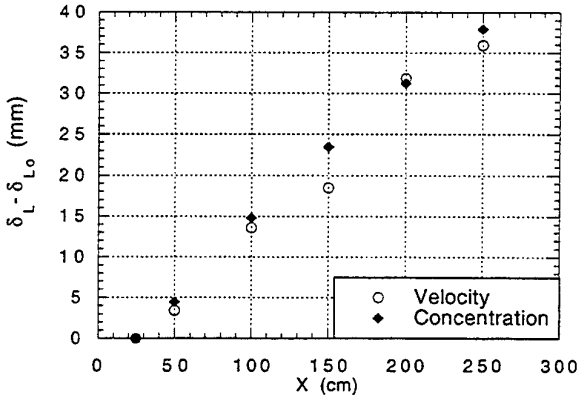


Figure 9: Evolution of the Level Thickness (δ_{Lo} = the initial value

changes are significant, and any fluctuations are within the instrument uncertainty (see figures 3 and 4). Additional measurements of the probability density functions at different downstream location show similar features. Therefore, since no modifications are found in the lateral and longitudinal evolution of the probability density functions of the bubbles, the term $\frac{Pdf(D)|_\infty}{Pdf(D)}$ in equation (4) remains approximately equal to one, and the concentration profiles of the bubble size families can be aproximated by the attenuation profiles:

$$\frac{\bar{\alpha}_b}{\bar{\alpha}_{b\infty}} \approx \frac{\zeta_b}{\zeta_{b\infty}} \tag{13}$$

Comparison of the 10% level thickness and integral thickness (figures 8 and 9) calculated from the velocity and concentration of bubbles profiles shows identical results in both cases. Smaller eddies with turnover time smaller than the viscous relaxation time of the bubbles may present a higher concentration of bubbles in their cores, but on the time averaged measurements presented here this effect is wiped out by the influence of the large eddies with a turnover time higher than the bubble relaxation time.

CONCLUSION

We have shown that the mean dispersion of bubbles in a turbulent mixing layer is independent of the bubble size if the bubble viscous relaxation time is an order of magnitude smaller than the turnover time of the large, coherent eddies which dominate the evolution of the turbulent mixing layer. Furthermore, we have found that on the average, these microbubbles disperse as fluid particles, even in downstream regions where the mixing layer is well past the mixing transition and exhibits the coexistence of a wide range of turbulent scales, some of which having eddy turnover times smaller than the bubble's viscous relaxation time.

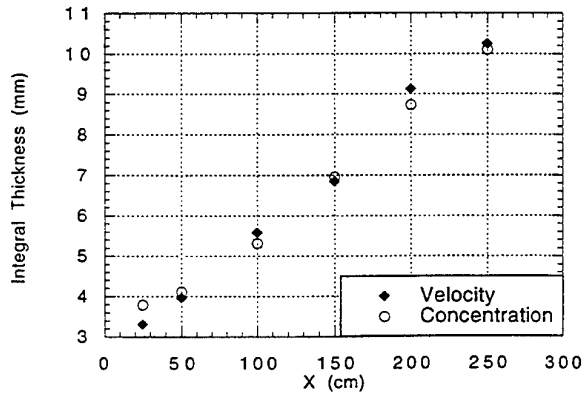


Figure 8: Evolution of Integral Thickness

These results are attributed to the fact that although depending on their size, bubbles may concentrate in the small scales, their interaction with the large scale eddies dominates their mean, lateral dispersion. These results are consistent with numerical simulations of bubbles in turbulent mixing layers which found that in the absence of gravitational settling, their mean dispersion is only a function of their Stokes Number based on the large scale eddies.

Acknowledgements : The authors gratefully acknowledge the support of the ONR under contract # N00014-91-J-1252 and also the support of a Fellowship from the Consejo Asesor the Investigación de la Diputación General de Aragón (Spain) to Carlos Martínez.

REFERENCES

Brown, G.L. and Roshko, A. (1974). On density effects and large structure in turbulent mixing layers. *Journal of Fluid Mechanics,* 64:775-816.

Elghobashi, S.E. and Truesdell, G.C. (1993). On the two-way interaction between homogeneous turbulence and dispersed solid particles.i: turbulence modification. *Physics of Fluids a,* 5:1790-1801.

Lance, M and Bataille, J. (1991). Turbulence in the liquid phase of a uniform bubbly air-water flow. *Journal of Fluids Mechanics,* 93:135-159.

Lázaro, B.J. (1989). Particle Dispersion in Turbulent Free Shear Flows. PhD thesis, University of Southern California.

Lázaro, B.J. and Lasheras, J. C. (1989). Particle dispersion in a turbulent,plane, free shear layer. *Physics of Fluids A,* 1(6):1035-1044.

Lázaro, B.J. and Lasheras, J. C. (1992a). Particle dis-

persion in the developing free shear layer.Part 1. Unforced flow. *Journal of Fluid Mechanics,* 235:143-178.

Lázaro, B.J. and Lasheras, J. C. (1992b). Particle dispersion in the developing free shear layer.Part 2. Forced flow. *Journal of Fluid Mechanics,* 235:179-221.

Maxey, M.R. and Riley, J.J (1983). Equation of motion for small rigid sphere in a non-uniform flow. *Physics of Fluids,* 26(4):883-889.

Rightley, P. M. (1995). Bubble dispersion and interphase coupling in a free shear flow. PhD thesis, University of California, San Diego.

Ruestch, G.R. and Meiburg, E. (1993). On the motion of small spherical bubbles in two-dimensional vortical flows. *Physics of Fluids,* 5(10):2326-2341.

Sene, K.J., Hunt, J.C.R. and Thomas, N.M. (1994). The role of coherent structures in bubble transport by turbulent shear flows. *Journal of Fluids Mechanics,* 259:219-240.

Winant, C.C. and Browand, F. K. (1974). Vortex pairing: The mechanism of turbulent-mixing growth at moderate reynolds Number. *Journal of Fluids Mechanics,* 63:237-255.

LARGE EDDY SIMULATION OF TURBULENT GAS-SOLID FLOWS IN A VERTICAL CHANNEL AND EVALUATION OF SECOND-ORDER MODELS

Qunzhen Wang[1]
[1] Department of Aerospace Engineering
Pennsylvania State University
University Park, PA 16802, USA

Kyle D. Squires[2]
[2] Department of Mechanical and Aerospace Engineering
Arizona State University
Tempe, Arizona 85287-6106, USA

Olivier Simonin[3,4]
[3] Laboratoire National d'Hydraulique / EDF
6 Quai Watier 78400 Chatou, FRANCE
[4] Institut de Mécanique des Fluides / INPT
Allée Camille Soula 31400 Toulouse, FRANCE

ABSTRACT

Large eddy simulation (LES) has been used for prediction of the particle-laden turbulent flow in a vertical channel. Calculations were performed at a Reynolds number based on friction velocity and channel half-width of 180. Subgrid-scale stresses in the fluid were closed using the Lagrangian dynamic eddy viscosity model. Particle motion was governed by drag. Particle-particle collisions were neglected and the fluid was not modified by the presence of the particles. Results for a particle density ratio of 2118 are presented in this paper, statistics of the dispersed phase were obtained from the trajectories of 250,000 particles. The simulation results were used to perform an *a priori* evaluation of closure model assumptions in the two-fluid model of Simonin (1991a). In general, there is good agreement between LES results and closure assumptions used for the unknown terms in the particle kinetic stress and fluid-particle covariance transport equations. Turbulent momentum transfer from the fluid in the particle kinetic stress equation is accurately predicted. In the fluid-particle covariance equation the greatest discrepancies in closure of the momentum transfer term occur in the near-wall region, indicating the model used for the fluid turbulent time scale must be improved. Closure models for triple correlation transport of the kinetic stress and fluid-particle covariance are also reasonable.

INTRODUCTION AND BACKGROUND

In two-fluid modeling of turbulent two-phase flows separate mean transport equations are derived for both the continuous and dispersed phases. As is well known, this procedure leads to closure problems due to the presence of turbulent correlations and interphase transfer terms. Of particular importance to prediction of gas-solid flows are the closure approximations used to model the particle kinetic stress tensor (the second-order moments of the particle velocity fluctuations) and fluid-particle velocity correlations (e.g., see Simonin 1991a). The assumptions of gradient transport and local equilibrium are often applied to model these correlations, generally assuming the particle kinetic shear stresses are proportional to the local mean shear of the dispersed phase and normal stresses are dominated by fluid drag (e.g., see Elghobashi & Abou-Arab 1983).

One of the main problems with models based on gradient transport for the shear stress and equilibrium for the normal stresses is that analyses and simulation results show that the Boussinesq approximation is not satisfactory. Reeks (1993) and Liljegren (1993) have shown that the particle shear stresses depend explicitly upon the shearing of both phases. Reeks (1993), Simonin *et al.* (1995), and Wang & Squires (1996) showed that the particle stress tensor anisotropy increases with the particle relaxation time and is significantly greater than the fluid one. These complex features are contained in the approach proposed by Simonin (1991a), which is based on separate transport equations for the components of the kinetic stress tensor and for the fluid-particle velocity covariance. This approach accounts for particle-turbulence interactions, the production by mean velocity shear, the mean and turbulent transport by the particle velocity, and the influence of inter-particle collisions. While the particle kinetic stress transport model has been applied with success to many experimental gas-solid flow configurations (e.g, jets, mixing layers, vertical channel, swirling flows, etc.), one of the primary difficulties with evaluating the closure approximations in such an approach is that there is a lack of detailed experimental measurements. In a previous study using the results from large eddy simulation, Simonin *et al.* (1995) validated the model derivation and closure assumptions in homogeneous turbulent shear flows. While very useful for both better understanding particle interactions with turbulence as well as evaluating closure models, measurements or simulation results from non-homogeneous flows are required to more fully validate the model. The objective of this work is to present results from large eddy simulation of the simplest non-homogeneous particle-laden turbulent shear flow—fully developed channel flow—and to use LES results to evaluate closure approximations in the two-fluid model of Simonin (1991a).

SIMULATION OVERVIEW

LES of the fully developed turbulent flow between plane channels driven by a uniform pressure gradient is considered in this work. The effect of the subgrid scales on the resolved eddies is parameterized using the Lagrangian dynamic eddy viscosity model developed by Meneveau *et al.* (1996). The governing equations are solved numerically

on a staggered grid using the fractional step method (e.g., see Wu *et al.* 1995). The calculations were performed at a Reynolds number $Re_\tau = u_{1,\tau}\delta/\nu_1 = 180$, where $u_{1,\tau}$ is the friction velocity, δ the channel half-width, and ν_1 is the fluid kinematic viscosity. The channel domain and grid resolution are the same as that used by Wang & Squires (1996), who showed that prediction of the gas-phase turbulent carrier flow are in good agreement with DNS results and experimental measurements.

Gas-solid channel flow in the dilute regime is considered in which particle-particle collisions are neglected and the coupling is one-way, i.e., from fluid to particles only. Particle motion was governed by nonlinear drag using a correlation from Clift *et al.* (1978),

$$\rho_2 \frac{du_{2,i}}{dt} = -\rho_1 \frac{3}{4}\frac{C_D}{d}|\mathrm{v}_r|v_{r,i}\,, \qquad (1)$$

where ρ_2 and ρ_1 are the particle and fluid density, respectively. The particle velocity is $u_{2,i}$, the fluid velocity along the particle trajectory is $u_{1,i}$, d is the particle diameter, $v_{r,i} = u_{2,i} - u_{1,i}$ the relative velocity between particle and fluid, and $|\mathrm{v}_r| = |v_{r,i}v_{r,i}|$ is the magnitude of the slip velocity. Note that the effects of gravitational acceleration were neglected. The drag coefficient C_D is expressed in terms of the particle Reynolds number Re_p as $C_D = 24\left[1 + 0.15Re_p^{0.687}\right]/Re_p$ where $Re_p = |\mathrm{v}_r|d/\nu_1$. Fourth-order Lagrange polynomials were used to interpolate the fluid velocity to the particle position. For particles that moved out of the channel in the streamwise or spanwise directions periodic boundary conditions were used to reintroduce it in the computational domain. The channel walls were assumed perfectly smooth with a particle undergoing an elastic collision when its center was one radius from the wall.

Properties of the dispersed phase were obtained by following the trajectories of 250,000 particles. The trajectories of a large ensemble are required in order to present statistics for the dispersed phase in the same manner as for the fluid, i.e., by averaging over homogeneous planes. Numerical experiments demonstrate adequate statistical convergence is obtained using this sample size (see Wang & Squires 1996). The particle radius in wall units was fixed at 0.50 and a variation in the particle response time was obtained by considering density ratios $\rho = \rho_2/\rho_1$ of 529, 2118, and 8471. For the sake of brevity, only results for $\rho = 2118$ are presented in this paper.

From an arbitrary initial condition the Eulerian velocity field was first time advanced to a statistically stationary state. The particles were then assigned random positions throughout the channel. The initial particle velocity was assumed to be the same as the fluid velocity at the particle location. Particles were then advanced in the flow field to a new equilibrium condition in which particle motion was independent of initial conditions. Similar to the fluid flow, statistics of the particle velocity were averaged over the two homogeneous directions, both channel halves, and time.

RESULTS AND DISCUSSION

Particle Kinetic Stress Equation

As shown by Simonin *et al.* (1995), the equation governing the transport of the particle kinetic stresses can be derived from the particle equation of motion,

$$\left[\frac{\partial}{\partial t} + U_{2,m}\frac{\partial}{\partial x_m}\right]\langle u''_{2,i}u''_{2,j}\rangle_2 = P_{2,ij} + D_{2,ij} + \Pi_{2,ij}\,, \qquad (2)$$

where $U_{k,i} = \langle u_{k,i}\rangle_k$ is the mean velocity, and $u''_{k,i} = u_{k,i} - \langle u_{k,i}\rangle_2$ is the fluctuating velocity ($k = 1$ for the continuous phase and $k = 2$ for the dispersed phase). In this paper $\langle\cdot\rangle_k$ denotes averaging with respect to phase k, i.e., time and ensemble averaging over the grid when $k = 1$ and over the particle positions when $k = 2$. The first term on the right-hand side of (2) represents production by the mean gradient of the particle velocity,

$$P_{2,ij} = -\langle u''_{2,i}u''_{2,m}\rangle_2 \frac{\partial U_{2,j}}{\partial x_m} - \langle u''_{2,j}u''_{2,m}\rangle_2 \frac{\partial U_{2,i}}{\partial x_m}\,, \qquad (3)$$

while the second term represents transport by the particle velocity fluctuations,

$$D_{2,ij} = -\frac{1}{\alpha_2}\frac{\partial}{\partial x_m}\left[\alpha_2\langle u''_{2,i}u''_{2,j}u''_{2,m}\rangle_2\right]\,, \qquad (4)$$

where α_2 is the volume fraction of the dispersed phase. The last term represents the momentum transfer rate from the fluid turbulence and is expressed as,

$$\Pi_{2,ij} = -\left\langle \frac{\rho_1}{\rho_2}\frac{3}{4}\frac{C_D}{d}|\mathrm{v}_r|\left[v_{r,i}u''_{2,j} + v_{r,j}u''_{2,i}\right]\right\rangle_2\,. \qquad (5)$$

The momentum transfer $\Pi_{2,ij}$ can be either a production or destruction term depending on the relative magnitude of the particle kinetic stress $\langle u''_{2,i}u''_{2,j}\rangle_2$ and the fluid-particle covariance $\langle u''_{1,i}u''_{2,j}\rangle_2$. The part of $\Pi_{2,ij}$ corresponding to production of the kinetic stress is that from the fluid-particle covariance,

$$\Pi^p_{2,ij} = \left\langle \frac{\rho_1}{\rho_2}\frac{3}{4}\frac{C_D}{d}|\mathrm{v}_r|\left[\langle u''_{1,i}u''_{2,j}\rangle_2 + \langle u''_{1,j}u''_{2,i}\rangle_2\right]\right\rangle_2\,, \qquad (6)$$

while the destruction is,

$$\Pi^d_{2,ij} = -\left\langle \frac{\rho_1}{\rho_2}\frac{3}{2}\frac{C_D}{d}|\mathrm{v}_r|\left[\langle u''_{2,i}u''_{2,j}\rangle_2\right]\right\rangle_2\,. \qquad (7)$$

While the production term $P_{2,ij}$ in (2) can be calculated directly from the mean flow and particle kinetic stresses, the other two terms on the right-hand side of (2) need to be modeled in a second-order closure. Following Simonin *et al.* (1995), the components of the momentum transfer representing production and destruction of the kinetic stress can be approximated as,

$$\Pi^p_{2,ij} \approx \frac{1}{\tau^F_{12}}\left[\langle u''_{1,i}u''_{2,j}\rangle_2 + \langle u''_{1,j}u''_{2,i}\rangle_2\right]\,, \qquad (8)$$

and

$$\Pi^d_{2,ij} \approx -\frac{2}{\tau^F_{12}}\langle u''_{2,i}u''_{2,j}\rangle_2\,, \qquad (9)$$

where τ^F_{12} is the mean particle relaxation time evaluated in terms of an average drag coefficient,

$$\tau^F_{12} = \frac{\rho_2}{\rho_1}\frac{4}{3}\frac{d}{\langle C_D\rangle_2}\frac{1}{\langle|\mathrm{v}_r|\rangle_2}\,, \qquad (10)$$

where,

$$\langle C_D\rangle_2 = C_D\left(\langle Re_p\rangle_2\right)\,, \qquad \langle Re_p\rangle_2 = \frac{\langle|\mathrm{v}_r|\rangle_2 d}{\nu_1}\,, \qquad (11)$$

(Simonin *et al.* 1995).

Shown in Figure 1 is the comparison of the exact evaluation of $\Pi_{2,ij}$, $\Pi^p_{2,ij}$, and $\Pi^d_{2,ij}$ from the LES to the approximations (8) and (9) for $\rho = 2118$. Note that in (8) and (9) the particle kinetic stresses and fluid-particle covariance are evaluated from the LES results. There is very good agreement as can be clearly seen in the figure. Though not shown here, the momentum transfer term $\Pi^p_{2,ij}$ and $\Pi^d_{2,ij}$ are larger for the lighter particles due to their increased responsiveness to fluid motions. In addition, in

the wall-normal and spanwise directions an equilibrium between production and destruction exists, with $\Pi^p_{2,ij}$ and $\Pi^d_{2,ij}$ nearly in balance because the particle velocity fluctuations in the directions orthogonal to the mean shear are dominated by the interaction with the fluid turbulence. Thus, according to the expressions of the momentum transfer term (8) and (9), the normal and spanwise particle velocity variances are nearly equal to the corresponding fluid-particle velocity correlations.

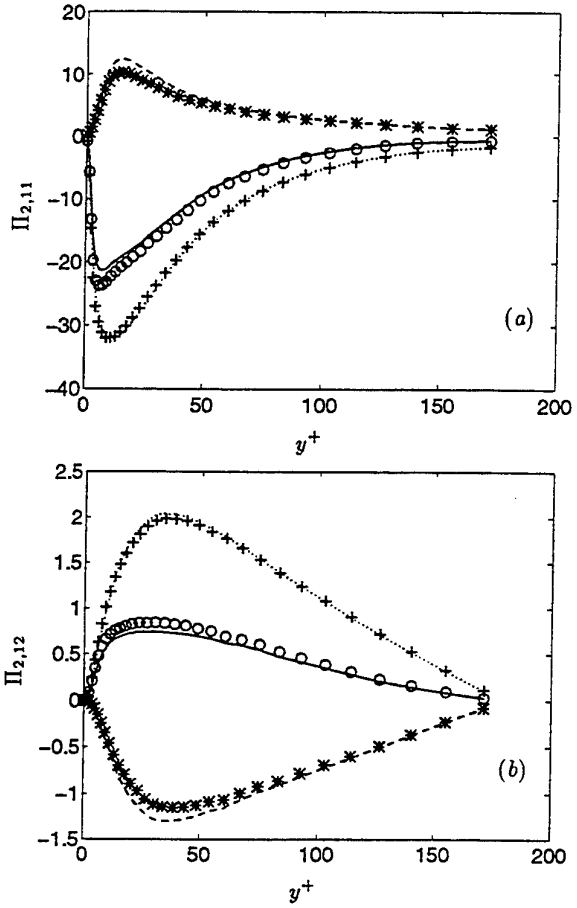


Figure 1: Momentum transfer terms $\Pi_{2,ij}$, $\Pi^p_{2,ij}$, and $\Pi^d_{2,ij}$, $\rho = 2118$. (a) $i = j = 1$; (b) $i = 1$, $j = 2$. $\Pi_{2,ij}$: o LES; —— Eqn. (8) + Eqn. (9). $\Pi^p_{2,ij}$: * LES; ---- Eqn. (8). $\Pi^d_{2,ij}$: + LES; ····· Eqn. (9).

Fluid-Particle Covariance Equation

Figure 1 shows that the models (8) and (9) for the momentum transfer term $\Pi_{2,ij}$ are accurate. The production part of the momentum transfer term $\Pi^p_{2,ij}$ in (8) is written in terms of the fluid-particle covariance $\left\langle u''_{1,i}u''_{2,j}\right\rangle_2$, which requires a closure approximation in a two-fluid model. The covariance $\left\langle u''_{1,i}u''_{2,j}\right\rangle_2$ represents the correlation between the particle velocity fluctuation and the fluid velocity fluctuation measured at the particle position. Similar to the approach outlined in Haworth & Pope (1986), the fluid velocity fluctuation viewed by the particles is assumed to obey a generalized Langevin equation. This in turn allows derivation of the transport equation for $\left\langle u''_{1,i}u''_{2,j}\right\rangle_2$ from the closed fluid-particle joint pdf equation (Simonin 1996),

$$\left[\frac{\partial}{\partial t} + U_{2,m}\frac{\partial}{\partial x_m}\right]\langle u''_{1,i}u''_{2,j}\rangle_2$$

$$= P_{12,ij} + P_{21,ji} + D_{12,ij} + \Pi_{12,ij} + \Phi_{12,ij} - \frac{1}{3}\varepsilon_{12}\delta_{ij} \quad (12)$$

The first two terms on the right-hand side represent production by the mean gradient of particle and fluid velocities, respectively,

$$P_{12,ij} = -\langle u''_{1,i}u''_{2,m}\rangle_2 \frac{\partial U_{2,j}}{\partial x_m} , \quad (13)$$

$$P_{21,ji} = -\langle u''_{2,j}u''_{1,m}\rangle_2 \left[\frac{\partial U_{1,i}}{\partial x_m} + \frac{\partial V_{d,i}}{\partial x_m}\right] , \quad (14)$$

where $V_{d,i}$ is the turbulent drift velocity (e.g., see Simonin *et al.* 1993). The third term on the right-hand side of (12) represents transport by particle and fluid velocity fluctuations,

$$D_{12,ij} = -\frac{1}{\alpha_2}\frac{\partial}{\partial x_m}\left[\alpha_2\langle u''_{1,i}u''_{2,j}u''_{2,m}\rangle_2\right] . \quad (15)$$

The fourth term represents the production rate due to interphase momentum transfer (i.e., particle dragging by fluid motion),

$$\Pi_{12,ij} = -\left\langle \frac{3}{4}\frac{\rho_1}{\rho_2}\frac{C_D}{d}|\mathbf{v}_r|\left[v_{r,j}u''_{1,i}\right]\right\rangle_2 , \quad (16)$$

By definition, $\Phi_{12,ij}$ is a return to isotropy term and ε_{12} is the dissipation rate. These terms account for molecular viscosity, turbulent pressure strain-rate, and relative velocity between the fluid and particle motion (the so-called crossing trajectories effect).

Similar to $\Pi_{2,ij}$ in the particle kinetic stress equation, the momentum transfer term $\Pi_{12,ij}$ in the fluid-particle covariance equation can be either a production or destruction term depending the the relative magnitude of the Reynolds stress $\langle u''_{1,i}u''_{1,j}\rangle_2$ and the fluid-particle covariance $\left\langle u''_{1,i}u''_{2,j}\right\rangle_2$. Therefore, (16) can also be divided into a production part and a destruction part,

$$\Pi^p_{12,ij} = \left\langle \frac{\rho_1}{\rho_2}\frac{3}{4}\frac{C_D}{d}|\mathbf{v}_r|\left[u''_{1,i}u''_{1,j}\right]\right\rangle_2 , \quad (17)$$

$$\Pi^d_{12,ij} = -\left\langle \frac{\rho_1}{\rho_2}\frac{3}{4}\frac{C_D}{d}|\mathbf{v}_r|\left[u''_{1,i}u''_{2,j}\right]\right\rangle_2 . \quad (18)$$

Using the mean particle relaxation time τ^F_{12}, (17) and (18) are approximated as,

$$\Pi^p_{12,ij} \approx \frac{1}{\tau^F_{12}}\langle u''_{1,i}u''_{1,j}\rangle_2 , \quad (19)$$

and

$$\Pi^d_{12,ij} \approx -\frac{1}{\tau^F_{12}}\left\langle u''_{1,i}u''_{2,j}\right\rangle_2 . \quad (20)$$

Figure 2 show the comparison of $\Pi_{12,ij}$ as well as the production part $\Pi^p_{12,ij}$ and the destruction part $\Pi^d_{12,ij}$ from the LES and that from (19) and (20). As also the case in Figure 1, the covariances in (19) and (20) are evaluated using the LES results. It is evident that, similar to the approximation of $\Pi_{2,ij}$ in Figure 1, there is good agreement, indicating (19) and (20) are accurate approximations. Although the comparison is not shown in this manuscript for the components and for the other density ratios, $\Pi_{12,ij}$ is comparable to the production and destruction parts and both $\Pi^p_{12,ij}$ and $\Pi^d_{12,ij}$ increase for lighter particles.

According to the generalized Langevin model retained by Simonin *et al.* (1995), the return to isotropy and dissipation term are given by,

$$\Phi_{12,ij} - \frac{1}{3}\varepsilon_{12}\delta_{ij} = -\frac{1}{\tau^t_{12}}\langle u''_{1,i}u''_{2,j}\rangle_2 - \beta_2 P_{21,ji} , \quad (21)$$

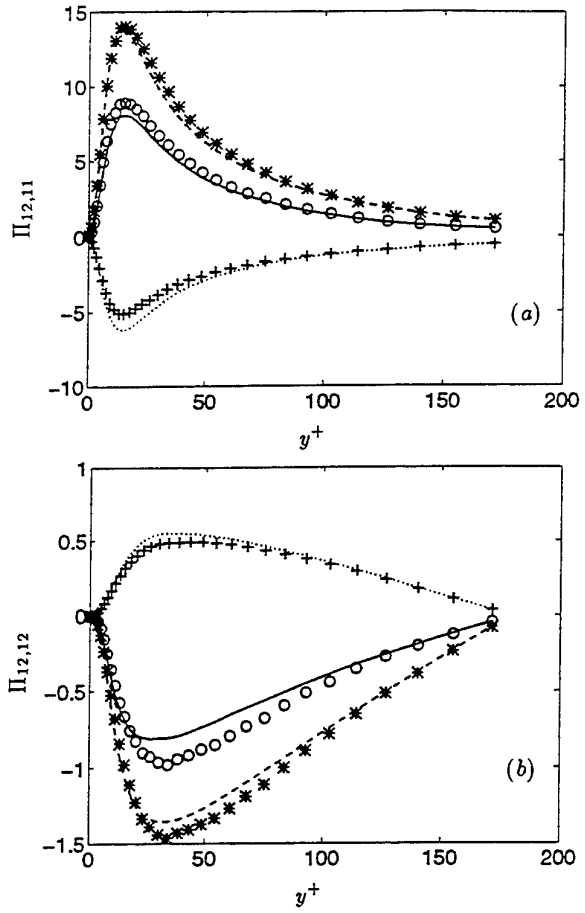


Figure 2: Momentum transfer terms $\Pi_{12,ij}$, $\Pi^p_{12,ij}$, and $\Pi^d_{12,ij}$, $\rho = 2118$. (*a*) $i = j = 1$; (*b*) $i = 1$, $j = 2$. $\Pi_{12,ij}$: o LES; Eqn. (19) + Eqn.(20); $\Pi^p_{12,ij}$: * LES; Eqn. (19); $\Pi^d_{12,ij}$: + LES; Eqn. (20).

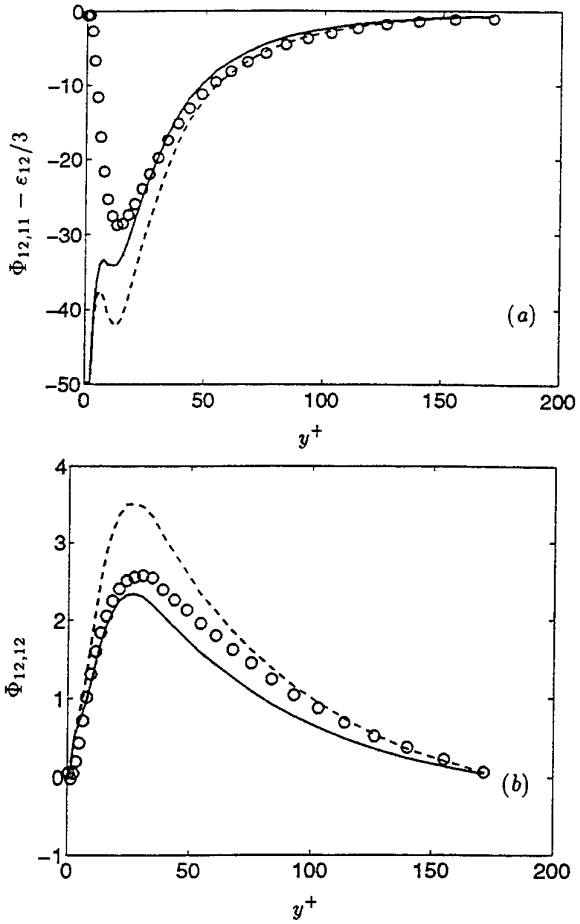


Figure 3: $\Phi_{12,ij} - \delta_{ij}\varepsilon_{12}/3$ from Eqn. (21), $\rho = 2118$. (*a*) $i = j = 1$; (*b*) $i = 1$, $j = 2$. o LES; ——— $\beta_2 = 0$; ---- $\beta_2 = 0.6$.

where

$$\varepsilon_{12} = \frac{1}{\tau^t_{12}} q_{12} + \beta_2 P_{21,mm} \ , \tag{22}$$

where τ^t_{12} is a time macroscale of the fluid turbulence viewed by the particles. In general, τ^t_{12} should account for the crossing trajectories effect (Simonin *et al.* 1993). However, based on results for non-settling particles in homogeneous flows, τ^t_{12} is approximated here as,

$$\tau^t_{12} = \frac{1}{\beta_1} \frac{q_1^2}{\varepsilon_1} \ , \tag{23}$$

where $\beta_1 = 2.05$ based on single-phase flow modeling (Haworth & Pope 1986). In the simplified Langevin model, $\beta_2 = 0$ in (21), while rapid distortion gives $\beta_2 = 0.6$ (Haworth & Pope 1986).

Figure 3 show the comparison of $\Phi_{12,ij} - \varepsilon_{12}\delta_{ij}/3$ from LES and that from (21). It is again evident that there is good agreement between LES results and the model prediction. In the near wall region, while $\Phi_{12,12}$ from (21) agrees well with the LES results, the streamwise component exhibits a larger discrepancy due to the fact that $\langle u''_{1,1} u''_{2,1} \rangle_2$ increases more rapidly with distance from the wall than the time scale τ^t_{12}. Thus, the model for τ^t_{12} requires improvement in the near-wall region. The figure also shows that the results for $\beta_2 = 0.6$ offers a relatively small change compared to those obtained using $\beta_2 = 0$.

Velocity Triple Correlations

In both the transport of the particle kinetic stress (2) and the fluid-particle covariance (12), triple correlation transport requires a model. Similar to the approach of Hanjalic & Launder (1972), Simonin (1991b) derived the triple particle velocity correlation from the corresponding transport equation neglecting mean transport and influence of the mean velocity gradient and also using a quasi-Gaussian approximation for the quadruple particle velocity correlations. For non-colliding particles the resulting expression is,

$$\begin{aligned} \langle u''_{2,i} u''_{2,j} u''_{2,k} \rangle_2 \approx & \langle u''_{1,i} u''_{2,j} u''_{2,k} \rangle_2 \\ & - \frac{\tau^F_{12}}{3} \langle u''_{2,i} u''_{2,m} \rangle_2 \frac{\partial \langle u''_{2,j} u''_{2,k} \rangle_2}{\partial x_m} \\ & - \frac{\tau^F_{12}}{3} \langle u''_{2,j} u''_{2,m} \rangle_2 \frac{\partial \langle u''_{2,k} u''_{2,i} \rangle_2}{\partial x_m} \\ & - \frac{\tau^F_{12}}{3} \langle u''_{2,k} u''_{2,m} \rangle_2 \frac{\partial \langle u''_{2,i} u''_{2,j} \rangle_2}{\partial x_m} \end{aligned} \tag{24}$$

For practical purposes, Simonin (1991b) proposed a Boussinesq approximation for the fluid-particle-particle velocity correlation consistent with the asymptotic limit case of particles following the fluid turbulent motion, which leads to,

$$\langle u''_{2,i} u''_{2,j} u''_{2,k} \rangle_2 \approx -K^t_{2,im} \frac{\partial \langle u''_{2,j} u''_{2,k} \rangle_2}{\partial x_m}$$

$$-K^t_{2,jm}\frac{\partial\langle u''_{2,k}u''_{2,i}\rangle_2}{\partial x_m} - K^t_{2,km}\frac{\partial\langle u''_{2,i}u''_{2,j}\rangle_2}{\partial x_m}, \qquad (25)$$

and, similar to the approach in Daly & Harlow (1970), (25) is approximated as

$$\langle u''_{2,i}u''_{2,j}u''_{2,k}\rangle_2 \approx -K^{t'}_{2,km}\frac{\partial\langle u''_{2,i}u''_{2,j}\rangle_2}{\partial x_m}. \qquad (26)$$

The dispersion tensors $K^t_{2,km}$ and $K^{t'}_{2,km}$ in (25) and (26) are specified in terms particle-particle and fluid-particle velocity correlations,

$$K^{t'}_{2,ij} = \tau^F_{12}\langle u''_{2,i}u''_{2,j}\rangle_2 + K^t_{12,ij} \qquad (27)$$

with

$$K^t_{12,ij} = \beta_1 C_s \tau^t_{12}\langle u''_{1,i}u''_{2,j}\rangle_2 \qquad (28)$$

(Simonin 1991b). Based on models for single-phase turbulence, $C_s = 0.11$ following Hanjalic & Launder (1972) or $C_s = 0.22$ following Daly & Harlow (1970).

Shown in Figure 4 is a representative comparison of two components of the triple correlation $\langle u''_{2,i}u''_{2,j}u''_{2,2}\rangle_2$ from the LES to that from (24), (25), and (26). Note that of the 27 components in $\langle u''_{2,i}u''_{2,j}u''_{2,k}\rangle_2$, only four are non-zero in the channel. In general, (24) is more accurate than (25) and (26) since (24) is an intermediate approximation in terms of the fluid-particle velocity triple-correlation $\langle u''_{1,i}u''_{2,j}u''_{2,k}\rangle_2$. Though not shown here, for $\langle u''_{2,3}u''_{2,3}u''_{2,2}\rangle_2$ the agreement with LES results is better when (25) is used compared to (26) whereas (26) yields slightly more accurate predictions of $\langle u''_{2,1}u''_{2,2}u''_{2,2}\rangle_2$.

For triple correlation transport in the fluid-particle covariance equation (12), similar to the model for $\langle u'_{1,i}u'_{1,j}u'_{1,k}\rangle_1$ proposed by Hanjalic & Launder (1972), the triple correlation term $\langle u''_{1,i}u''_{2,j}u''_{2,k}\rangle_2$ in the fluid-particle covariance equation can be modeled as,

$$\langle u''_{1,i}u''_{2,j}u''_{2,k}\rangle_2 \approx -\beta_1 C_s \tau^t_{12}\left[R_{12,im}\frac{\partial\langle u''_{2,j}u''_{2,k}\rangle_2}{\partial x_m}\right.$$

$$\left.+R_{12,jm}\frac{\partial\langle u''_{2,k}u''_{2,i}\rangle_2}{\partial x_m} + R_{12,km}\frac{\partial\langle u''_{2,i}u''_{2,j}\rangle_2}{\partial x_m}\right], \qquad (29)$$

where $R_{12,km} = \langle u''_{1,k}u''_{2,m}\rangle_2$. A simpler model can be derived similar to that of Daly & Harlow (1970) used in single phase flows, i.e.,

$$\langle u''_{1,i}u''_{2,j}u''_{2,k}\rangle_2 \approx -K^t_{12,km}\frac{\partial\langle u''_{2,i}u''_{2,j}\rangle_2}{\partial x_m}, \qquad (30)$$

(Simonin 1991b).

Figure 5 show the comparison of the triple correlation $\langle u''_{1,i}u''_{2,j}u''_{2,k}\rangle_2$ from the LES and that from (29) and (30). The agreement between the model predictions and LES results, while not perfect, is comparable to that in single-phase turbulence For $\langle u''_{1,1}u''_{2,1}u''_{2,2}\rangle_2$ the agreement with LES results is improved when (29) is used, while both (29) and (30) yield reasonable predictions for the other components.

SUMMARY

Large eddy simulation has been used for calculation of a vertically oriented, particle-laden channel flow. Statistics of the dispersed phase were acquired by averaging over the trajectories of 250,000 particles. LES results were

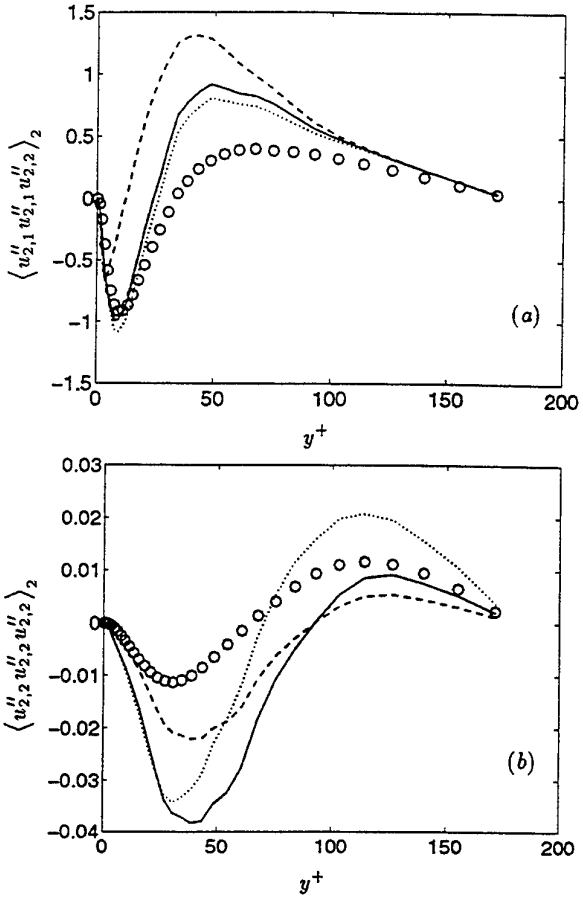


Figure 4: Particle velocity triple correlation $\langle u''_{2,i}u''_{2,j}u''_{2,2}\rangle_2$, $\rho = 2118$. (a) $i = j = 1$; (b) $i = j = 2$. o LES; ····· Eqn. (24); —— Eqn. (25); ---- Eqn. (26).

used to evaluate closure assumptions in the two-fluid model of Simonin (1991b). In general, there is good agreement between LES results and closure assumptions for the unknown terms in the particle kinetic stress and fluid-particle covariance transport equations. The momentum transfer term is accurately predicted in the kinetic stress equation. In the fluid-particle covariance transport equation, the momentum transfer is also accurate, with the greatest discrepancy occurring near the wall. Improvements to the model used for the fluid turbulent time scale τ^t_{12} are required in order to resolve the over-prediction. Triple correlation transport is also reasonably predicted, with an accuracy comparable to that in single-phase turbulence.

It is important to point out that the current investigation was an *a priori* study in the sense that closure assumptions in the model were evaluated using the 'exact' second-order moments, i.e., the fluid Reynolds stresses, particle kinetic stresses, and fluid-particle covariance from the LES results. An *a posteriori* approach would require an accurate Reynolds stress transport model for the fluid turbulence. This would in turn permit an evaluation of the closure models for predicting the kinetic stresses and fluid-particle covariance.

It is also worth remarking that the two-fluid approach considered in this paper requires that transport equations be carried for three different velocity correlation tensors. In practice, to simplify the model for applications an algebraic closure could be adopted for the fluid-particle velocity correlation tensor, i.e., solution of a transport equation for $q_{12} = \langle u''_{1,i}u''_{2,i}\rangle_2$ together with a generalized Boussinesq

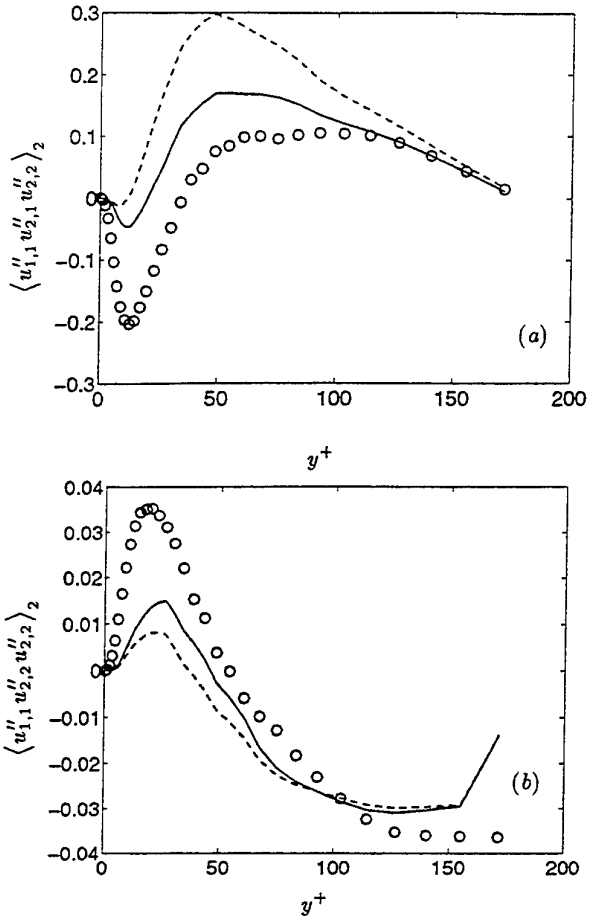


Figure 5: Fluid-particle-particle velocity correlation $\langle u''_{1,i}u''_{2,j}u''_{2,2}\rangle_2$, $\rho = 2118$. (*a*) $i = j = 1$; (*b*) $i = 1$, $j = 2$. ∘ LES; —— Eqn. (29); ---- Eqn. (30).

approximation for the separate components of $\langle u''_{1,i}u''_{2,i}\rangle_2$. Such an approach has been validated in simple homogeneous shear slow and needs to be next validated in non-homogeneous flows such as the channel.

One of the interesting features correctly predicted by the model is the large anisotropy of the particle kinetic stress tensor (see also Simonin *et al.* 1995, Wang & Squires 1996). Inter-particle collisions, not considered in the current study, which induce a redistribution of energy among the normal components, may be very important even in dilute flows and should be taken into account in future studies.

Finally, it is also important to comment that LES is a very powerful tool and well suited for development and validation of two-phase flow models for engineering applications. LES calculations provide a very detailed description of both phases and are very well-defined, crucial elements for validating lower-level closure models. LES therefore appears to be a very powerful approach for development and validation of closure models for additional effects also not considered in this work, e.g., interphase heat and mass transfer, modification of fluid turbulence by particles (two-way coupling), and prediction of two-phase flows in more complex geometries.

Acknowledgments

This work was supported by the National Institute of Occupational Safety and Health (Grant Number OH03052-03).

REFERENCES

[1] Clift, R., Grace, J.R. and Weber, M.E., 1978, *Bubbles, Drops and Particles*, Academic Press, New York

[2] Daly, B.J. and Harlow, F.H., 1970, "Transport equations in turbulence", *Phys. Fluids* **13**, pp. 2634-2639.

[3] Elghobashi, S.E. and Abou-Arab, T.W., 1983, "A two-equation turbulence model for two-phase flows", *Phys. Fluids* **26**(4), pp. 931-938.

[4] Hanjalic, K. and Launder, B.E., 1972, "A Reynolds stress model of turbulence and its application to thin shear flows", *J. Fluid Mech.* **52**, pp. 609-638.

[5] Haworth, D.C. and Pope, S.B., 1986, "A generalized Langevin model for turbulent flows", *Phys. Fluids* **29**, pp. 387-405.

[6] Liljegren, L.M., 1993, "The effect of a mean fluid velocity gradient on the streamwise velocity variance of a particle suspended in a turbulent flow", *Int. J. Multiphase Flow* **19**, pp. 471-484.

[7] Meneveau, C., Lund, T.S. and Cabot, W.H., 1996, "A Lagrangian dynamic subgrid-scale model of turbulence", *J. Fluid Mech.* **319**, pp. 353-385.

[8] Reeks, M.W., 1993, "On the constitutive relations for dispersed particles in nonuniform flows 1. dispersion in a simple shear flow", *Phys. Fluids* **5**, pp. 750-761.

[9] Simonin, O., 1991a "Second-moment prediction of dispersed phase turbulence in particle-laden flows", *Eighth Symposium on Turbulent Shear Flows*, pp. 7-4-1 – 7-4-6.

[10] Simonin, O., 1991b, "Third-moment closure", Annexe 3, Rapport EDF HE 44/91.24.

[11] Simonin, O., 1996, "Continuum modeling of dispersed two-phase flows", in *Combustion and Turbulence in Two-Phase Flows*, 1995-1996 Lecture Series Programme, von Karman Institute, Belgium.

[12] Simonin, O., Deutsch, E. and Minier, J.P., 1993, "Eulerian prediction of the fluid/particle correlated motion in turbulent two-phase flows", *Appl. Sci. Res.*, **51**, pp. 275-283.

[13] Simonin, O., Deutsch, E. and Boivin, M., 1995, "Large eddy simulation and second-moment closure model of particle fluctuating motion in two-phase turbulent shear flows," in *Turbulent Shear Flow 9*, F. Durst, N. Kasagi, B.E. Launder, F.W. Schmidt, J.H. Whitelaw, editors, Springer-Verlag (Heidelberg), pp. 85-115.

[14] Wang, Q. and Squires, K.D., 1996, "Large eddy simulation of particle-laden turbulent channel flows", *Phys. Fluids* **8**, pp. 1207-1223.

[15] Wu, X., Squires, K.D. and Wang, Q., 1995, "On extension of the fractional step method to general curvilinear coordinate systems", *Num. Heat Transfer, Part B: Fundamentals*, **27**(2), pp. 175-194.

NUMERICAL INVESTIGATION OF TURBULENT HEAT TRANSFER MECHANISMS AT A GAS-LIQUID INTERFACE

V. De Angelis, P. Lombardi, S. Banerjee

Department of Chemical & Nuclear Engineering
University of California Santa Barbara
Santa Barbara, California

INTRODUCTION

Prediction of scalar transfer rates at the interface between immiscible, turbulent streams has been of central importance in many industrial operations such as gas absorption, condensation, evaporation, extraction and aeration. Recently, gas, moisture and heat transfer at the ocean-atmosphere interface has begun to receive attention. The primary motivation has come from the need to parametrize coupling fluxes between the ocean, and atmosphere, general circulation models used in long term climate studies.

Gas and moisture transfer at continuous interfaces between turbulent air and water streams are controlled by layers $\sim O(10^{-2}mm)$ and $\sim O(1mm)$ thickness, respectively. This suggests that direct numerical and large eddy simulations could be used to clarify microphysical processes controlling scalar transfer rates, since such scales are resolvable with available computational resources.

To this end, numerical procedures using a pseudospectral method, together with a projection algorithm, have been developed and applied to coupled gas-liquid flows. The initial studies focused on flows under conditions where interface deformations were small – a situation corresponding to a series of laboratory experiments where detailed measurements of the near-interface turbulence characteristics were made. The simulations agreed very well with measurements.

The next step was to calculate gas flow over wavy solid surfaces, where the wavelengths corresponded to those of capillary waves. The simulation maintained spectral accuracy, and agreed with experimental data, which included waves of sufficient steepness that separation occurred behind the crests. Finally, simulations were conducted for conditions under which capillary waves developed at the interface – the physical properties being those of air and water at atmospheric conditions.

The program of simulations, supported, where possible, by experiments, clarified that the scalar transfer rates on each side of the interface were correlated with the sweeps on each side, i.e. fourth quadrant events which bring high speed fluid close to the interface, forming regions of high shear stress and high scalar transfer rates. Furthermore, the simulations, and experiments indicated that the sweep frequency could be expressed in terms of the frictional drag, but not in terms of the total drag, which includes form drag. From this, using surface renewal theory, it was found that simple parametrizations for the scalar transfer rates could be derived in terms of the frictional drag, with no adjustable parameters.

It appeared that capillary wave characteristics mainly affect the scalar transfer rates by affecting the frictional drag, i.e. indirectly, by affecting sweep frequencies. The scalar transfer sublayers, in themselves, are so thin that the curvature of the surface due to capillary waves has little direct effect. Parametrizations based on these considerations are in excellent agreement with large-scale laboratory experiments, some of which were done after the parametrizations were proposed.

2 STRUCTURE OF NEAR-INTERFACE TURBULENCE

2.1 Flat Gas-Liquid Interfaces

Lombardi et al. (1996) did a direct numerical simulation where the gas and liquid were coupled through continuity of velocity and stress boundary conditions at the interface. The interfacial plane shows regions of high shear stress and low shear stress, with low shear stress regions corresponding to the low speed regions and the high shear stress to the high speed regions. The low shear stress regions are streaky in nature with high shear stress islands. At the edges of the high shear stress regions, vortices are seen to spinup on both sides of the interface. These are

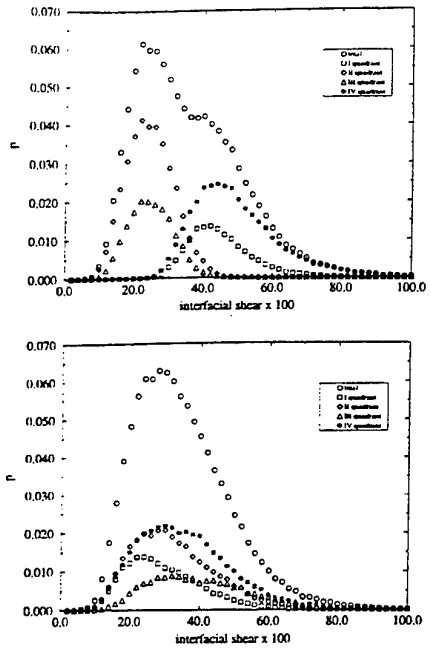


Figure 1: Probability of strongly coherent events classes according to quadrant as a function of interfacial shear stress in the region over which the events occur

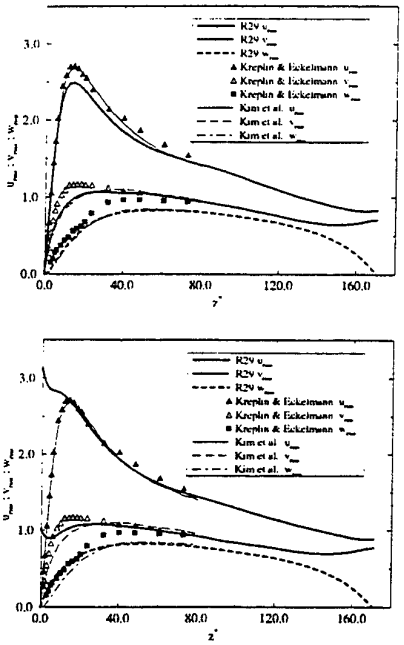


Figure 2: Results from direct numerical simulation on rms velocity fluctuations, cases air-water interface

initially in the plane normal to the interface but subsequently are stretched in the quasi-streamwise direction by the mean flow. These quasi-streamwise vortices are known to play a major role in the ejection-sweep processes observed in wall turbulence, and they do the same at the gas-liquid interface. At this point it is worth considering how the high shear stress regions form.

This can be clarified by considering a quadrant analysis of the velocity field over the interface in which velocity fluctuations in each quadrant of the Reynolds stresses are correlated with shear stress at the interface. In the first quadrant both the streamwise and interface normal velocity fluctuations are positive. In the second, the streamwise component is negative but the interface normal component is positive. This corresponds to an ejection of low speed fluid. In the third quadrant both the streamwise and the interface-normal velocity fluctuations are negative, and in the fourth the streamwise component is positive whereas the interface-normal component is negative. The fourth quadrant then corresponds to a sweep in which high-speed fluid is brought towards the interface. Consider now the correlation of each quadrant of such velocity fluctuations with the interfacial shear stress shown in Figure 1 (top) on the gas side. It is clear that sweeps, i.e., in the fourth quadrant, lead to the high shear stress regions whereas ejections lead to the low shear stress regions. This is what is observed in wall turbulence at a solid boundary and therefore the gas sees the liquid surface much like a solid boundary.

However, if we look at Figure 1 (bottom), it is immediately clear that no such correlation exists on the liquid side.

In fact, all the quadrants have similar behavior with regard to the shear stress regions that occur below the high speed sweeps on the gas side, i.e., the motions that bring high speed fluid from the outer regions to the interfaces on the gas side leads to high shear stress at the interface. Conversely, ejections on the gas side which take low speed fluid away from the interface into the outer flow, strongly correlate with low shear stress regions. The liquid does not behave in this way and does not dominate the pattern of shear stress on the interface. This is of some importance as we will show in a later section.

The difference between the gas and the liquid phases in the near interface region is further clarified by observing the velocity fluctuations on each side of the interface as shown in Figure 2. The top portion of the Figure is for the gas whereas the bottom Figure is for the liquid. The gas, as is evident, behaves much like flow over a solid wall. The fluctuations are almost identical to that at a solid boundary, in all directions – streamwise, spanwise, and wall-normal. On the other hand, the liquid, as evident from the bottom Figure, has the largest fluctuations in the streamwise and spanwise directions right at the interface itself. It sees the interface virtually as a free slip boundary, except for the mean shear.

Certain other aspects of turbulence on each side of a gas-liquid interface are worth considering. Clearly ejections and sweeps may be expected to play an important role in determining scalar transfer rates so their frequency of occurrence is of some importance. In the wall region, it is known that ejections and sweeps have a spacing in time that lies between a non-dimensional time of $30 - 90$ with 90 being the upper-limit which corresponds to assemblages of ejections and sweeps termed bursts. This is shown in Figure 3 for wall and shear-generated, interfacial turbulence as a function of the shear Reynolds number. Rashidi and Banerjee (1990) found that on the liquid side

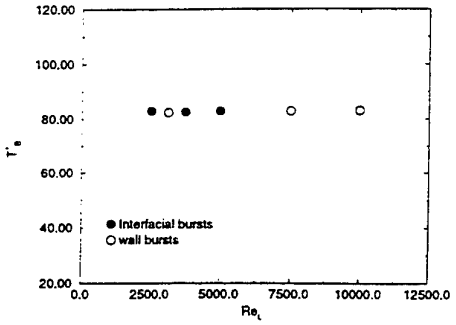


Figure 3: Scaling of interfacial and wall bursts. The time between bursts is scaled with the local shear stress and viscosity.

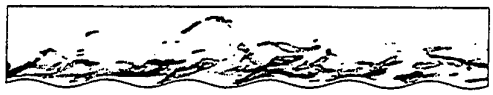


Figure 4: Quasi-streamwise vortices scalar indicator

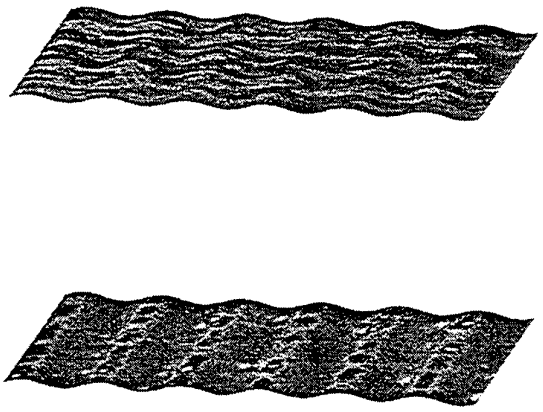


Figure 5: top: Streaky structure at a wavy wall bottom: Shear stress at a wavy wall

of a sheared interface this type of parametrization held. In Figure 3 the time between interfacial bursts is also plotted as a function of the shear Reynolds number and the behavior at a macroscopic level is very similar to that at a solid boundary. Thus the qualitative behavior is similar, though within the bursts themselves there are substantial differences between the gas and the liquid sides. This finding, with regard to the time between bursts, which remain about the same as in wall turbulence, is of considerable importance in predicting scalar transfer as discussed later.

2.2 Turbulence structure near wavy surfaces

The previous discussion focused on turbulence phenomenon for coupled gas-liquid flows with flat interfaces – a situation close to the experiments of Rashidi and Banerjee (1990). To understand the effect of waves on the gas side – where such effects may be expected to be more important than on the liquid side, flow over a surface with two-dimensional waves (with spanwise crests and troughs) was investigated. The flow situations correspond to the experiments of Buckles and Hanratty (1984), so the results could be checked.

To allow the pseudospectral method to be used for flows over wavy boundaries it was necessary to map the flow field into a rectangular domain. This was done with a nonorthogonal transformation that stretched the surface normal coordinate. To maintain spectral accuracy in the simulations, the usual solution procedure [see Lam and Banerjee (1992)] had to be modified. A projection algorithm was adopted – the details being available in De Angelis et al. (1997).

The waves introduced a streamwise length scale as indicated by the vortex structure shown in Figure 4 (here a scalar vortex indicator based on the eigenvector corresponding to the complex eigenvalues of the rate of deformation tensor is used to show the quasi-streamwise vortices near the surface). However, when the phase average velocities are removed from the instantaneous field then typically streaky regions of high speed - low speed flow and shear stress are seen, as indicated in Figure 5 (top) and 5 (bottom). The streak spacing is $\sim$ 100 in units nondimensionalized with the frictional drag (removing the form drag component from the total drag). This suggests that turbulence phenomena near the wavy surface may scale with frictional drag. rather than the total drag. On examining the time between sweeps and bursts, a time non-dimensionalized with the frictional drag, i.e. $t^+ = t\tau_i/\mu$, is seen to be between 30 and 90, in agreement with what happens at a flat wall. Here τ_i is the frictional drag, i.e. the form drag has been removed from the total.

3 SCALAR TRANSFER RATES

Scalar transfer rates were calculated using the velocity fields discussed in the previous sections. The evolution equation is:

$$\frac{\partial T}{\partial t} + \nabla(\mathrm{u}T) = \frac{1}{ScRe}\nabla^2 T \qquad (1)$$

Equation (1) is solved using pseudospectral methods, e.g. Fourier modes in the two horizontal directions and Chebyshev polynomials in the wall-/interface-normal direction.

For the computations in which Sc (or Pr) are $\sim O(1)$ the spacing of the collocation points used for the velocity field simulation, were also used for the scalar flux calculations, i.e. the scalar concentration equation was solved using the same number of modes in each direction. However, the simulations for higher Sc (or Pr) number required a much finer spacing of collocation points in the interface-normal direction. To achieve this, the region resolved with Chebyshev modes was limited to regions in which significant mean gradients were espected.

Moreover the Chebyshev collocation points were mapped and concentrated in the interface region.

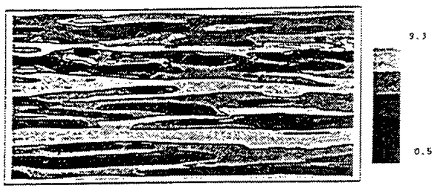


Figure 6.a: Mass flux $Sc = 10$, on the gas side

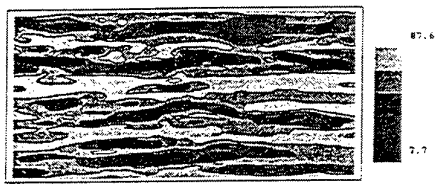


Figure 6.b: Shear stress at the interface

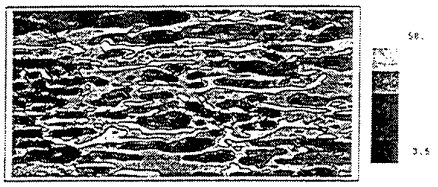


Figure 7.a: Mass flux $Sc = 25$ on the liquid side

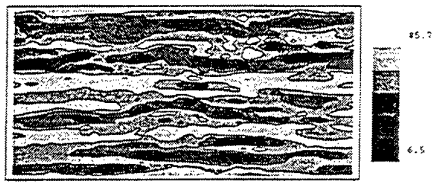


Figure 7.b: Shear stress at the interface

Equation (1) was solved in a mapped domain, defined by the transformation:

$$\begin{cases} x_1 = \xi_1 \\ x_2 = \xi_2 \\ x_3 = g(\xi_3) - h(\xi_3) f(\xi_1, \xi_2, \tau) \\ t = \tau \end{cases} \quad (2)$$

The function $g(\xi_3)$ allows the redistribution of the Chebyshev collocation points in the normal direction. The function $h(\xi_3)$ allows Equation (1) to be solved with spectral methods in the wavy interface case – $f(\xi_1, \xi_2, \tau)$ describes the shape of the waves. More details on the mapping can be found in De Angelis et al. (1997). Here it suffices to say that given the transformation in Equation (2), the physical domain $X \equiv (x_1, x_2, x_3, t)$ is mapped into a computational domain $\Xi \equiv (\xi_1, \xi_2, \xi_3, \tau)$ that is a rectangular parallelepiped with uniform grid spacing in the ξ_1 and ξ_2 directions. The grid spacing in the ξ_3 direction corresponds to Chebyshev collocation points.

3.1 Simulation Results: Flat Interface

The cases studied with the resolved regions and the 1^{st} and the 2^{nd} grid spacings normal to the interface are as follows in Table I, which also contains calculated nondimensional scalar transfer velocities β^+.

Table I: Scalar Transfer Calculation Parameters

Sc	z^+_{max}	Nodes	Δz_1^+	Δz_2^+	β^+
0.7	171	65	0.096	0.3	0.097
10	43	65	0.024	0.08	0.016
3.65	171	129	0.024	0.08	0.053
25	43	129	0.006	0.02	0.020

Contours of the instantaneous scalar fluxes at interfaces are shown in Figures 6 and 7, and compared with the shear stress at the interface for the gas and the liquid side calculations respectively. It is immediately evident that the gas side fluxes correlate well with the shear stress. On the other hand, the flux field on the liquid side, shows a much finer structure (see Figure 7) and no such correlation exists.

It is of interest therefore to understand what processes control the liquid side fluxes. Figure 8 shows the instantaneous Reynold stresses $u'w'$, the interface normal velocity w', and the scalar transfer coefficient $\beta_l^+ = \beta/u_l^*$ as a function of time in wall units. This is shown for one point at the interface but is typical of all points. It is clear that when $u'w'$ is strongly positive and w' is positive (corresponding to a sweep) the scalar coefficient is high. The correlation with the instantaneous Reynolds stress is self-evident, and the sweep essentially renews the interfacial region, giving rise to high scalar transfer rates. Since, on the liquid side, sweeps do not correlate with the high shear stress areas at the interface, therefore strong correlation between scalar transfer rates and interfacial shear stress patterns is not to be expected.

The time period between sweeps can also be estimated from the numerical simulation. On the gas and the liquid side there are between 1 and 3 sweeps, corresponding to 1 "burst", in about 90 non-dimensional time units ($tu_\star^2/\nu$), where $u_\star = \sqrt{\tau_i/\rho}$ and τ_i is the interfacial shear stress (equal for both phases). For the gas side, the result is to be expected, but the liquid side results indicate that the main turbulence phenomena in the two field are uncoupled. This follows because the density and viscosity of the gas and the liquid are different and the dimensional time between the sweeps and bursts are, therefore, very different.

3.2 Simulation Results: Wavy Surface.

The temporally and spatially varying velocity field obtained in the simulation for gas flow over wavy surfaces was provided for solution of the species concentration equation and the scalar transfer rate was determined. To date the calculations have been done with $Sc = 1$ and for the gas side, as the scalar concentration gradients are spread over the thickest layer in this case – and hence could be expected to be most affected by the wavy surface.

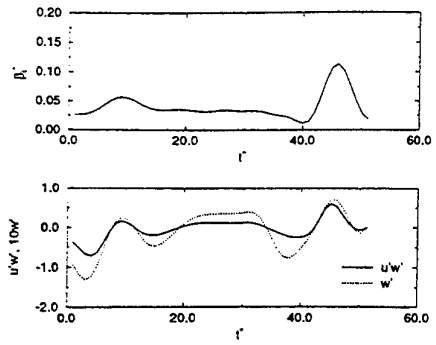


Figure 8: Time history for the liquid of β^+ and Reynolds stress

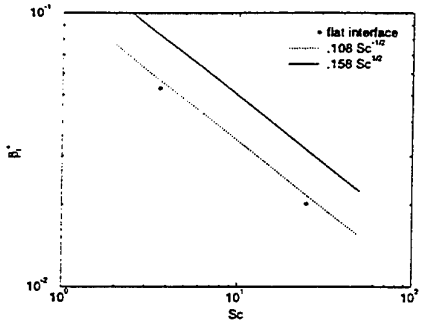


Figure 9: Mass transfer coeff. vs Sc number for the liquid

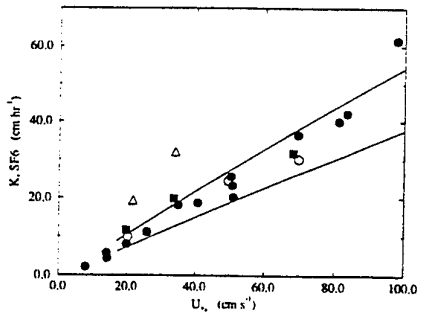


Figure 10: Comparison of Equation (4) with the data by Wanninkhof and Bliven

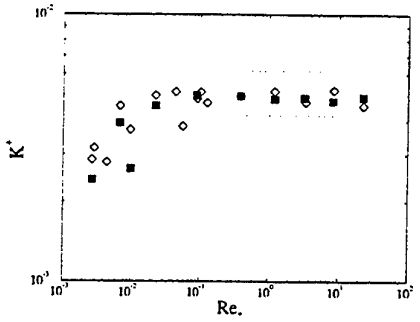


Figure 11: Comparison of Equation (4) with wind-wave tank gas transfer data (from Ocampo-Torres)

The objective of the simulation was to determine the value of β^+ for comparison with the flat interface cases in Table I. Since the surface is wavy, a portion of the total surface stress is due to the form drag, and a portion is due to the frictional drag. The direct numerical simulation allows each component of the drag to be estimated. If we define a velocity scale based on frictional drag as u_* and based on frictional plus form drag as as $\hat{u_*}$, then the simulation gives, $\beta^+ = 0.077$ and $\hat{\beta}^+ = 0.063$.

3.3 Scalar Flux Parametrization

The surface renewal theory of Danckwerts (1951) may be used to parametrize scalar transfer rates on the liquid side, with a time between renewals being between 30 and 90 shear-stress-based non-dimensional time units. The theory was originally developed for "mobile interfaces" in the sense that liquid motions parallel to the interface were relatively unimpeded.

The scalar transfer rate is then:

$$\overline{\beta} = (D/\tau)^{1/2} \tag{3}$$

with $\tau^+ = 30$ to 90 (ν/u_*^2) based on the preceding discussion. This leads to

$$\frac{\overline{\beta_l} Sc^{0.5}}{u_l^*} = 0.108 \text{ to } 0.158 \tag{4}$$

This equation was derived by Banerjee (1990), based on the conjecture that sweeps/bursts controlled scalar transfer rates and that sweep/burst frequencies were similar at a sheared liquid interface to those observed in wall turbulence. Both conjectures are supported by the simulations and experiments.

Equation (4) is compared with simulation results for two different Schmidt numbers in Figure 9. It is clear that the numerical values agree with the predictions and the Schmidt number dependence is correctly predicted. Equation (4) is also compared with wind-wave tank data for SF_6 and CO_2 transfer rates from Wanninkhof and Blivens (1991) and Ocampo-Torres et al. (1994) in Figures 10 and 11 respectively. Again the agreement is good noting that u_* is probably somewhat over estimated as the form drag was not separated out.

Turning now to the gas side, the gas sees the liquid much like a solid surface as discussed earlier. So a form of the surface renewal theory modified for such applications, e.g. by Banerjee (1971) amongst others, is necessary. This leads to a different dependence in the Schmidt number, and the modified expression is:

$$\frac{\overline{\beta_g} Sc^{2/3}}{u_g^*} = 0.07 \text{ to } 0.09 \tag{5}$$

Figure 12 compares the expression with DNS results. It is clear that the Schmidt number dependency is correctly predicted, and the numerical values are within the range of Equation (5). Also shown in the figure is β_g^+ and $\hat{\beta}_g^+$ for gas flow over a wavy surface with $Sc = 1$. It is clear that if the frictional drag is used to nondimensionalize β_g, then the results are in line with Equation (5), and the wave effects are captured in this formulation. However if β_g is nondimensionalized with the total drag, i.e. $\hat{\beta}$, then the value of the LHS of Equation (5) lies well below

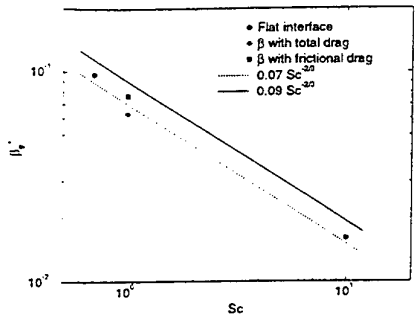


Figure 12: Mass transfer coefficient vs Sc number, Gas

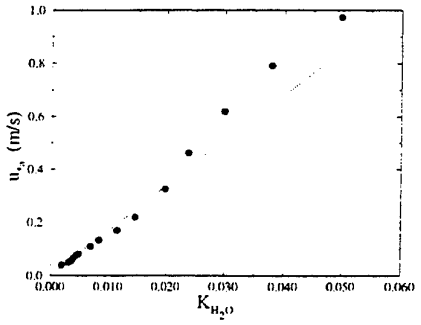


Figure 13: Mass transfer coefficient v.s. u_* from Ocampo-Torres et al. (1994)

the prediction. The lower bound of Equation (5) is also compared with the moisture transfer data of Ocampo-Torres et al. (1994) in Figure 13. The agreement, again, is good.

4. CONCLUSIONS

Direct numerical simulations of scalar transfer between two immiscible turbulent streams indicates that the controlling mechanisms are sweeps/bursts on both sides. For air-water flows the controlling phenomena are not coupled in the sense that the sweep/burst frequencies scale, on each side separately with the respective friction velocities, based on frictional drag and kinematic viscosities. Because the density and viscosity on each side are different, the sweep/burst frequency is also different. The simulations also give quantitative estimates of the scalar fluxes and transfer coefficients on each side of the interface, as well as clarify the dependence on Schmidt number.

On the air side, the transfer velocities are seen to vary with $Sc^{-2/3}$, whereas on the liquid side they vary with $Sc^{-1/2}$. On both sides they are proportional to the frictional velocity (derived from the frictional drag at the interface), though the constants of proportionality are somewhat different.

Parametrizations for the scalar transfer coefficient based on surface renewal theory, using time between sweeps and bursts to give the renewal rate – as suggested by the DNS, give the correct dependence on the Schmidt number and the correct values of the proportionality constants.

Computations have been done for air flow over wavy surfaces, and fully-coupled air-water flows with deformable interfaces. The scalar transfer calculations have not been completed as yet, but the available calculations done for $Sc = 1$ on the air side for flow over a wavy surface – a case where wave effects would be expected to be at a maximum – indicate that the same parametrizations as for the flat interface case holds. This is to be expected since the scalar concentration gradients are only significant in very thin layers – of much smaller scale than capillary wave lengths. The main effect of waves then arise, through the effects on interfacial frictional drag.

Furthermore, comparison of the parametrizations with wind-wave tank scalar transfer experiments are in good agreement suggesting that wave effects are captured, and arise through the effects on frictional drag.

ACKNOWLEDGEMENT

We wish to acknowledge the continuing support of the EU through contract EV5V-CT93-0291, and of the US DOE through contract DE-FG-03-85ER13314.

REFERENCES

S. Banerjee (1971), "A note on turbulent mass transfer at high Schmidt numbers", *Chem. Eng. Science*, **26**, 989-990.

S. Banerjee (1990), "Turbulence structure and transport mechanisms at interfaces", 9^{th} *Int. Heat Transfer Conference*, 395.

J. Buckles and T. Hanratty (1984), "Turbulent flow over large-amplitude wavy surfaces", *J. Fluid Mech.*, **140**, 27-44.

P.V. Danckwerts (1951), "Significance of liquid film coefficients in gas absorption", *Ind. Eng. Chem.*, **43**, 1460, 1951.

V. De Angelis, P. Lombardi, and S. Banerjee (1997), "Direct numerical simulation of turbulent flow over a wavy wall", *Phys. Fluid*, in press.

K. Lam and S. Banerjee (1992), "On the condition of streak formation in a bounded turbulent flow", *Phys. Fluid*, **A4**(2), 306-320.

P. Lombardi, V. De Angelis, and S. Banerjee (1996) "Direct numerical simulation of near-interface turbulence in coupled gas-liquid flow", *Phys. Fluid*, **8**, 1643-1665.

F.J. Ocampo-Torres, F.J. Donelan, J.M. Woollen, and J.R. Koh (1994), "Laboratory measurements of mass transfer of carbon dioxide and water vapor for smooth and rough flow conditions", *Tellus Series B*, 46:16.

M. Rashidi and S. Banerjee (1990), "The effect of boundary conditions and shear rates on streaks formation and breakdown in turbulent channel flow", *Phys. Fluid*, **A2**, 1827.

R.H. Wanninkhof and L.F. Bliven (1991), "Relationship between gas exchange, wind speed, and radar backscatter in a large wind wave tank", *J. of Geophys. Res.*, **96(C2)**, 2785-2796.

SESSION 28 - DNS AND LARGE EDDY SIMULATION II

LARGE EDDY SIMULATIONS OF COMPRESSIBLE FLOWS ON HYBRID MESHES

F. DUCROS, F. NICOUD, and T. SCHÖNFELD

CERFACS - F31057 Toulouse Cedex

France

INTRODUCTION

The understanding of the flow structure and the mechanisms leading to turbulence is crucial for many fundamental and industrial applications such as aeronautical design for example. Numerical simulations have become a reliable tool to predict turbulent flows, either through turbulence modeling (providing steady or unsteady results) or instationary flow calculations (Direct Numerical Simulation (D.N.S.) or Large-Eddy Simulation (L.E.S.)). However, turbulence models are often unable to well predict the instationary behaviour of flows whereas D.N.S. is structurally limited to extremely low and therefore unrealistic Reynolds numbers.

L.E.S. thus appears to be a very attractive tool for the handling of turbulent flows, provided they are able to describe flows in complex geometries. Although complex geometries can be handled by structured multiblock method, this approach can result in a large number of grid points. An alternative is the use of unstructured or hybrid grids, which consist of a combination of different cell types.

This paper covers efforts made in developing numerical tools at CERFACS for the handling of compressible flows in unstructured and hybrid meshes using L.E.S.. Although the calculations performed here can be reproduced using a structured code (see Eggels *et al.* 1994 for example), we will show results that demonstrate the capabilities of our method.

A CLASSICAL FORMULATION FOR THE L.E.S. APPROACH

The L.E.S. approach is based on the filtering of the complete compressible Navier-Stokes equations (due to the finite mesh-size), which thus exhibit sub-grid scale tensors and vectors describing the interaction between non-resolved (sub-grid scales corresponding to wavenumbers greater than the cutoff wavenumber k_c) and resolved motion. The commutativity between the filtering operator and the time and space derivatives is supposed in the present work. This is justified in the sense that the second-order errors (in terms of $\mathcal{O}(\Delta^2)$,where Δ stands for the grid spacing) implicitely neglected by this commutation (Ghosal and Moin 1995) are of the same order as the truncation errors of the numerical method (see below).

The influence of non-resolved scales on the resolved motion is taken into account by means of a sub-grid scale model based on the introduction of a turbulent viscosity ν_t (Ducros *et al* 1995), which gives:

$$\mathcal{T}_{ij} - \frac{1}{3}\mathcal{T}_{ll}\delta_{ij} = 2\bar{\rho}\nu_t\tilde{S}_{ij} \qquad (1)$$

where $\mathcal{T}_{ij} = -\overline{\rho u_i u_j} + \bar{\rho}\tilde{u}_i\tilde{u}_j$ is the sub-grid scale tensor and $\tilde{S}_{ij} = \frac{1}{2}(\left(\frac{\partial\tilde{u}_i}{\partial x_j} + \frac{\partial\tilde{u}_j}{\partial x_i}\right) - \frac{2}{3}\frac{\partial\tilde{u}_l}{\partial x_l}\delta_{ij})$, where $\tilde{u}_i$ and $\bar{\rho}$ are the resolved velocity and density, $\bar{}$ and $\tilde{}$ standing for the filtering due to the mesh and its Favre's notation counterpart. The sub-grid energy flux is treated in the same manner:

$$Q_i = -\overline{(\rho e + p)u_i} + (\bar{\rho}\tilde{e} + \bar{p})\tilde{u}_i \approx \bar{\rho}\kappa_t\frac{\partial\tilde{T}}{\partial x_i}, \qquad (2)$$

where $\kappa_t = \nu_t/Pr_t$ and $Pr_t = 0.6$: the constant turbulent Prandtl number is justified by the low compressible cases we treat here, for which temperature can be considered as a passive scalar. $\bar{p}$, $\tilde{e}$ and $\tilde{T}$ denote the resolved pressure, total energy and temperature.

EDDY VISCOSITY MODELS

We implement two different eddy viscosity models; one is the well-known Smagorinsky model, defined by:

$$\nu_{t1} = (C_1\delta)^2\sqrt{2\tilde{S}_{ij}\tilde{S}_{ij}} \quad . \qquad (3)$$

where $C_1 = \sqrt{4C_K^{-3/2}/3\sqrt{6}\pi^2} = 0.18$. $C_K = 1.4$ is the Kolmogorov constant and δ stands for the local cut-off length ($\delta \approx \pi/k_c$) . Many methods can be found to evaluate $C1$. Lilly (1967) precribes a sub-grid dissipation equal to the dissipation rate of an incompressible homogeneous turbulence ϵ ($\epsilon =< 2\nu_t\tilde{S}_{ij}\tilde{S}_{ij} >$) and found $C1$ by assuming that $< \tilde{S}_{ij}\tilde{S}_{ij} >^{3/2} =< (\tilde{S}_{ij}\tilde{S}_{ij})^{3/2} >$.

Here, assuming that ν_t is independant of wavenumber k and that all dissipation is provided by the eddy-viscosity, one gets $\epsilon = 2\nu_t \int_0^{k_c} k^2 E(k)dk$, which now involves

$$\nu_t = \frac{2}{3} C_K^{-3/2} \sqrt{\frac{E(k_c)}{k_c}} \quad , \tag{4}$$

(Lesieur 1990). Then, as $\langle 2\nu_t \tilde{S}_{ij} \tilde{S}_{ij} \rangle = 2\nu_t \int_0^{k_c} k^2 E(k)dk$, Equation (4), together with the previous equality and $E(k) = C_k \epsilon^{(2/3)} k^{-5/3}$ directly leads to equation (3).

The second model is a Smagorinsky model defined on high-pass filtered velocity fields, following to previous works concerning the filtered structure function model (Ducros *et al.* 1996, Lesieur and Métais 1996):

$$\nu_{t2} = (C_2 \delta)^2 \sqrt{2HP(\tilde{S}_{ij})HP(\tilde{S}_{ij})} \quad , \tag{5}$$

where $HP(\tilde{S}_{ij})$ stands for the resolved strain rate defined on high-pass filtered velocity fields.

Here the high-pass filtered velocity fields are obtained using a compact estimation of the fourth-order derivatives of conserved variables taken from a Jameson's type artificial viscosity formulation (Schönfeld and Rudyard 1994). As in Ducros et al. (1996), the transfer function of the high-pass filter is numerically evaluated, which gives:

$$\frac{E_{HP}(k)}{E(k)} = a \left(\frac{k}{k_c} \right)^b \quad , \tag{6}$$

where $E_{HP}(k)$ stands for the energy spectrum of the filtered field and $a \approx 0.35$ and $b \approx 6.66$ are two constants determined numerically. The constant C_2 is then determined using the same method as C_1, *ie* by prescribing:

$$\epsilon = \langle 2\nu_t HP(\tilde{S}_{ij})HP(\tilde{S}_{ij}) \rangle = 2\nu_t \int_0^{k_c} k^2 E_{HP}(k)dk \quad , \tag{7}$$

which gives

$$C_2 = \left(\frac{2}{3} C_k^{-3/2} \sqrt{\frac{3b+4}{6a}} \frac{1}{\pi^2} \right)^{1/2} \approx 0.37 \quad . \tag{8}$$

As stressed in Ducros *et al.* (1996), a valuable information concerning the behaviour of sub-grid scale models for transitional flows is provided by the answer of a given model to a discrete longitudinal sine wave $u = U sin\ \omega$, $\omega = \pi k / k_c$ in the long wave limit $k_c \longrightarrow \infty$. This limit corresponds to a signal that is well captured by the mesh and stands for laminar and transitional part of the flows. In our case and for this one-dimensional signal, one can easily check that ν_{t1} and ν_{t2} scale respectively on ω^2 and ω^4. This a-priori better behaviour of the second model during transitional stages will be confirmed hereafter.

NUMERICAL TOOL

The complete Navier-Stokes equations are solved in their conservative form using the *AVBP* code developed at CERFACS and Oxford University (Schönfeld and Rudgyard 1994). We thus solve

$$\frac{\partial \vec{w}}{\partial t} + \nabla \vec{F} = \mathcal{D}(\mu \vec{\nabla}.\vec{w}) \quad , \tag{9}$$

where $\vec{F} = \vec{F}(\vec{w})$, $\vec{w}$ denotes the flux of conserved quantities and $\mathcal{D}(\mu \vec{\nabla}.\vec{w})$ stands for the dissipative part of Navier-Stokes equations. Frequently, numerical methods for unstructured meshes are based on the finite element approach (Hughes and Mallet 1986 for example), and therefore do not require the calculation of second derivatives for the dissipative operator. In our case, the dissipative operator $\mathcal{D}(\mu \vec{\nabla}.\vec{w})$ requires such calculations over any type of elements, which is not straightforward and will be detailed in a forthcoming publication (Nicoud *et al* 1997).

The *AVBP* code is based on the *COUPL* [1] parallel library, which uses cell-vertex finite-volume techniques based on arbitrary unstructured grids, and provides many schemes for the advective part of equation (9). The underlying numerical method for all the calculations presented here is an explicit Lax-Wendroff scheme, that is second order in both time and space, which justifies the previous approximation concerning the commutativity of filter and space derivatives.

A first application of D.N.S. using this code was performed by Nicoud *et al* (1996) and shows the capability of the code to describe a minimal turbulent channel flow with and without flow injection.

For the present applications, the sub-grid scale models ν_{t1} and ν_{t2} are implemented in the *AVBP* code in a general manner, δ being systematically taken as the third of the cell volume, which may be questionnable in case of highly distorted meshes.

RESULTS

We first validate the behaviour of the two previous models for the very simple case of a freely decaying compressible homogeneous turbulence; then we treat the more complicated case of a turbulent pipe flow.

Homogeneous Isotropic Turbulence

The initial condition consists in a divergence free velocity field of which energy is concentrated at large scales. The Reynolds number is set to infinity and the resolution is only of 20^3 grid points. During the simulation, the spectra fill up and exhibit a self similar decay once the fully turbulent regime is reached (see Fig. 1). Enstrophy is growing up

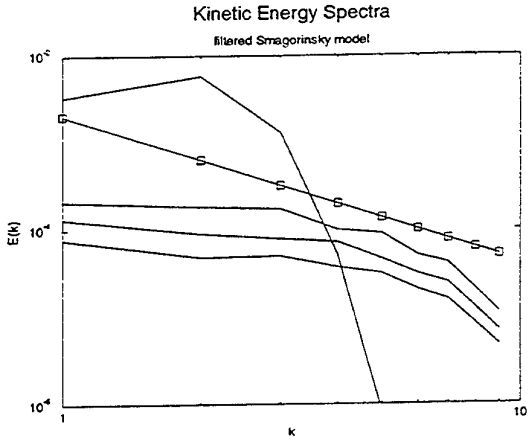


Figure 1: Time evolution of kinetic energy spectra using the ν_{t2} model in homogeneous turbulence, together with a $k^{-5/3}$ law.

to a certain level which is higher for the filtered model (Fig. 2, bottom). After this time the kinetic energy is decaying according to a $t^{-1.6}$ law, which is in reasonable agreement with theoretical and experimental results $t^{-1.4}$ (Lesieur 1990) (Fig. 2, top). The larger production of enstrophy in the case of the filtered Smagorinsky model ν_{t2}, together with the better conservation of kinetic energy before dissipation state is reached, suggests an improved capability of the filtered model to handle transitional flows and can be connected to the previous analysis in terms of

[1] Cerfacs and Oxford University Parallel Library

longitudinal sine wave. Note that this filtered Smagorinsky

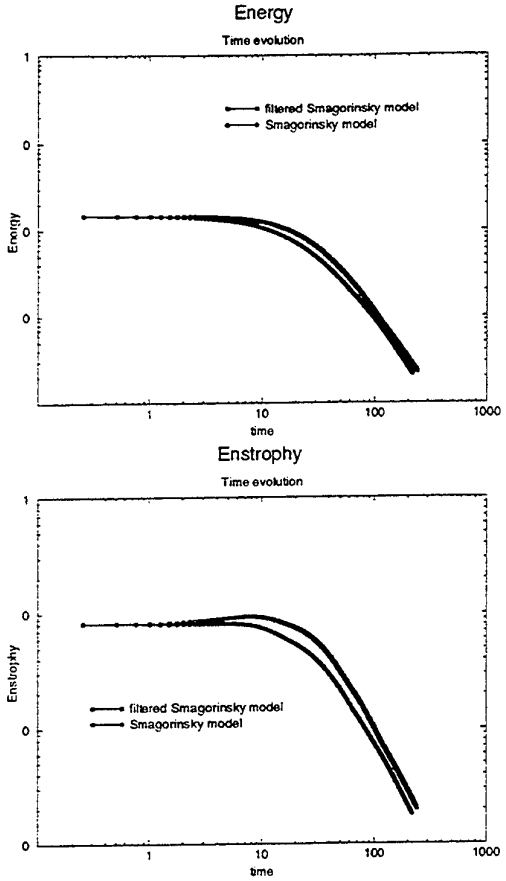


Figure 2: Time evolution of kinetic energy (left) and of enstrophy (right) for both models in freely decaying turbulence.

model is insensitive to large scales of motion, which means that the turbulent viscosity is scaled only on the energy contained in the small resolved scales. This enables us to suppress one of the classical drawbacks of the Smagorinsky model: spurious dissipation for the large scales of motion.

Application to a Turbulent Pipe Flow

General Conditions. We now use the code with the filtered Smagorinsky model ν_{t2} for the simulation of a turbulent pipe flow of radius R and length $4 \times R$, periodic in the streamwise direction x; r and θ are used to denote the radial and azimutal directions respectively. The Mach number is about 0.25 and the Reynolds number is $Re_{U_b} = 5000$, based on the bulk velocity U_b obtained in the turbulent regime and on the radius R. Initial condition consists of a Poiseuille flow, together with a white noise of small amplitude (0.1%) that will trigger the transition through non linear effects. A source term is added to the Navier-Stokes equations to simulate a pressure gradient corresponding to the fully turbulent state; this term comes from a empirical evaluation and reads:

$$\frac{\partial p}{\partial x} = \frac{\lambda}{2R} \frac{\rho U_b^2}{2} \qquad (10)$$

with $\lambda = 0.3164 Re_{U_b}$ (Schlichting 1979).

This calculation has been performed using two different hybrid meshes, with the following features:

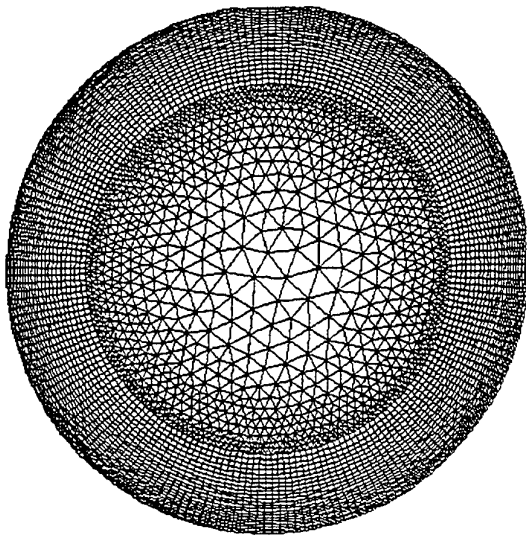


Figure 3: Zoom of the mesh taken for the pipe flow for calculation 2, with 240 000 cells.

Mesh	δ_x^+	δ_θ^+	r^+ first point
1	≈ 28	≈ 17.6	≈ 5
2	≈ 28	≈ 8.8	≈ 2.1

Table 1. Grids spacing in wall units.

The two simulations give comparable qualitative results but provide better statistics for the fine mesh (mesh 2): only this second calculation will be presented below. A view of the mesh is given in Fig. 3 for this case. The radius scales on $R^+ = 281$; along a given radius, one has 23 structured hexahedral cells near the wall, the remaining inner part of the pipe being filled with prisms. The combination of element types shows the advantage of hybrid meshes which allow to reduce the computational costs by meshing the pipe core region with a relative small number of cells. 200 points are used in the θ direction (only 100 points for the first simulation) and 40 points are needed in the x direction, which gives a total of 240000 nodes (6000 nodes in each section, whereas the first calculation requires a total of 62 000 nodes, that is 1550 nodes per section).

Notice that such a flow calculation was already performed using Direct Numerical Simulation at a lower Reynolds number (Re_{U_b} equal 3500) by Eggels *et al.* (1994). In this case, the incompressible Navier-Stokes equations were solved using a second-order scheme formulated in a cylindrical coordinate system, which requires about 12200 points in each section for the considered Reynolds number. The mesh of Eggels *et al.* is equally spaced in both radial ($\delta_r^+ \approx 1.88$) and streamwise direction ($\delta_x^+ \approx 7.03$). It results from these considerations that the limiting time step from this calculations scales to $\approx 6.\ 10^{-3} R/U_b$ whereas its scales to $\approx 3.\ 10^{-3} R/U_b$ in our case: this shows that, despite the relative low Mach number of our simulation, the choice for a unstructured mesh in this case allows to obtain a time stepping similar to an incompressible calculation on a regular structured grid.

Transition To Turbulence. The complete calculation using the ν_{t2} model requires about 50 hours on 32 processors of a Cray T3D machine to achieve the complete transition to turbulence and to accumulate statistics. Fig. 4 shows the time evolution of the mean total kinetic

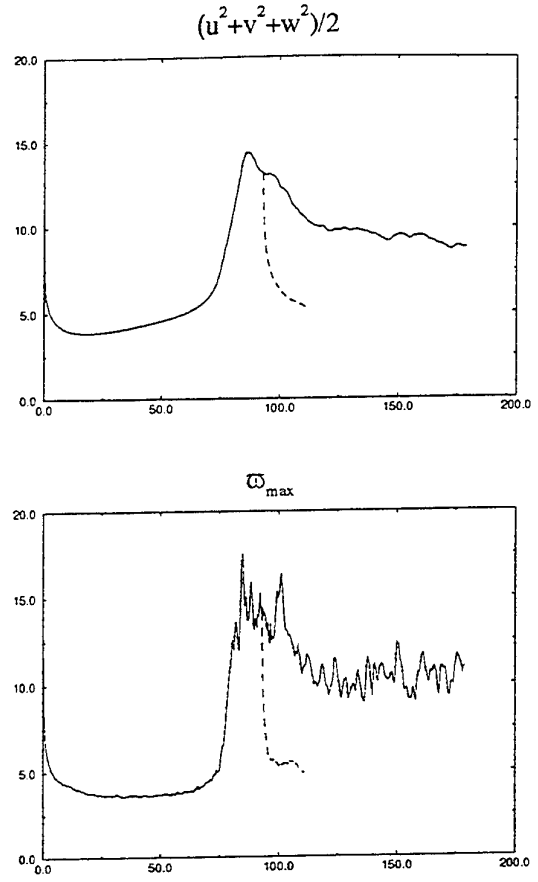


Figure 4: Time evolution of kinetic energy (top) and of maximum of vorticity (bottom) for both models during transition in the pipe, (log-linear plot).

energy and of the maximun of vorticity during the calculation: the time is expressed in R/U_b and the total time simulated corresponds to 44 advection times through the pipe at the speed U_b. After a short period of decrease of energy ($0 < t < 10R/U_b$) due to the fact that the white noise we prescribe at $t = 0$ is not well adapted to the flow, instabilities develop very slowly up to $t = 75R/U_b$ (see time evolution of the vorticity in Fig. 4), then transition to turbulence occurs through an exponential growth of instabilities. Notice that the restart of the calculation at $t = 85R/U_b$ with the ν_{t1} model leads to complete relaminarization of the flow, which is physically not acceptable and confirms the poor behaviour of the classical formulation of Smagorinsky's model.

Visualisations. The visualisations provided here are performed at the end of our calculation. For all visualisations, the mean flow is moving from the fore- to the background and one fourth of the pipe has been cut off and removed in order to enable an insight of the motion in the core region of the pipe. Fig. 5 exhibits classical parietal turbulent motion, *i.e.* ejections of relative low speed fluid from the wall to the upper part of the layer, connected with hairpin vortices: all these coherent structures are well-known and have already be found numerically (Spalart, 1988, Eggels *et al.*, 1994, Ducros *et al.*, 1996). Notice the relative sparse distribution of such structures in the core region of the pipe that is also observed in Eggels *et al.* (1994) justifies the use of a relatively coarse grid in this region. Notice that the transition from hexahedras to prisms is not visible in Fig. 5 (no distortion of the structures is observed), which suggests that this particular aspect of the method is numerically well treated for all the terms involved in the resolution of Navier-Stokes equations. This will be confirmed by the statistics presented below.

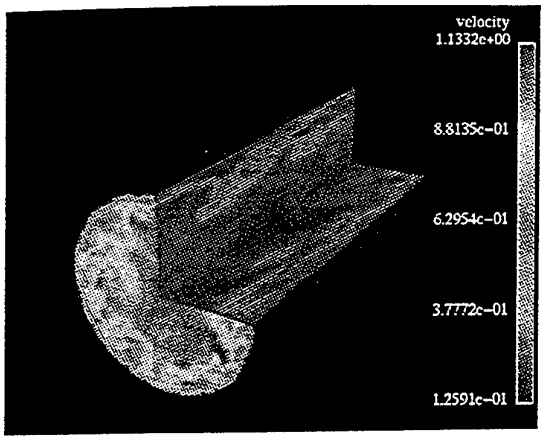


Figure 5: Slice on the total velocity in the turbulent pipe at $t \approx 175R/U_b$. Ejection and swept events are materialised by clear contours stretched from the wall.

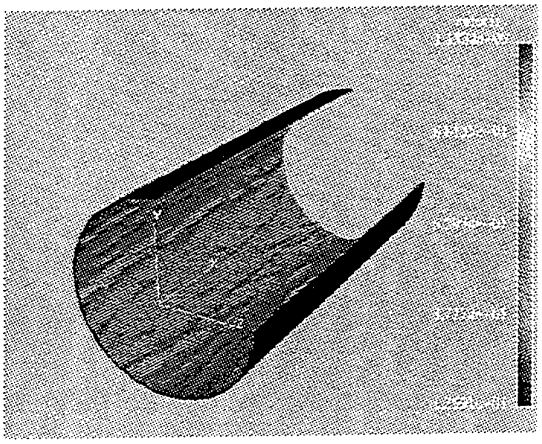


Figure 6: Iso-surface $(q^2)^{1/2} = 0.05U_b$ (black) and $(q^2)^{1/2} = 0.37U_b$ (grey) at turbulent state.

The behaviour of the flow is now investigated using three pictures of isosurfaces of the total velocity (Fig. 6, 7, 8) and one picture of the vorticity modulus (Fig. 9). The first picture (Fig. 6) shows the near wall motion, where Λ shape structures are visible and almost aligned along the x-direction, which is reminiscent of streaky patterns usually observed (Robinson 1990). Fig. 7 clearly shows ejection of low speed fluid from the wall. Fig 9 exhibits evidences of turbulent motions at very small scales near the wall, which are well captured by the mesh and the eddy viscosity model, whereas turbulence in the core region of the pipe develops at a greater scale (Fig 8).

Statistics. During the transition to turbulence, the mean streamwise velocity profil changes from a laminar Poiseuille to a turbulent flow, of which the shape is very close from what is observed in a turbulent channel flow. Once the fully turbulent regime has been reached with no further changes in the mean streamwise velocity (*i.e.* among $t \approx 125R/U_b$), we accumulated statistics over

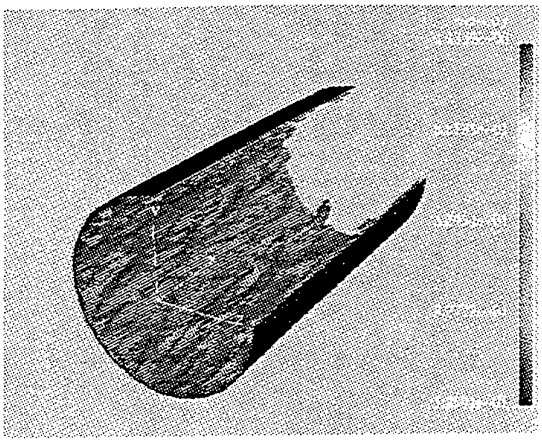


Figure 7: Same view as before, plus iso-surface $(q^2)^{1/2} = 0.65U_b$ (grey).

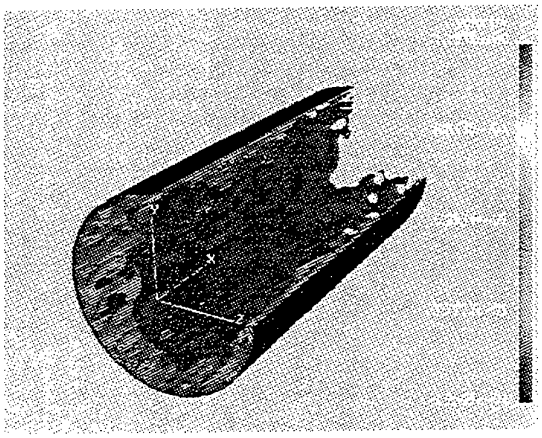


Figure 8: Same view as before, plus iso-surface $(q^2)^{1/2} = 1.0U_b$ (black).

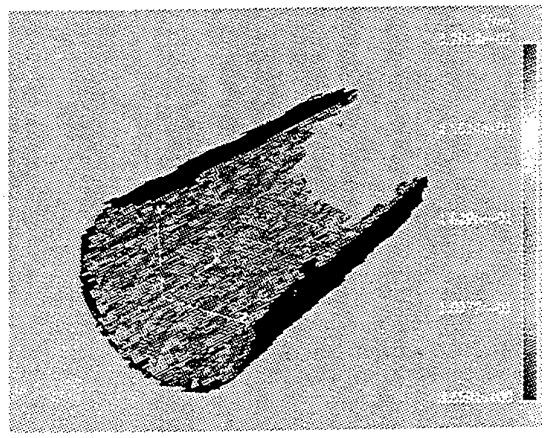


Figure 9: Iso-surface $(\omega^2)^{1/2} = 3U_b/R$ (black) and $(\omega^2)^{1/2} = 7U_b/R$ (grey).

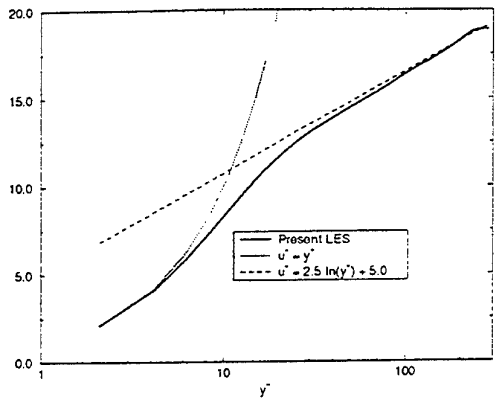


Figure 10: Mean streamwise velocity profil in wall units, together with the laminar and the usual logarithmic law $U^+ = 1/\kappa ln y^+ + C$.

$50R/U_b$ time unit. The mean streamwise velocity expressed in wall units is plotted in Fig. 10, the mean turbulent intensities and the Reynolds stresses are plotted in Fig. 11. Unfortunately, since no experimental data for comparison is available, we compare our results with the numerical and experimental results at a lower Reynolds number of Eggels *et al.* (1994). For y^+) 30, our results show that the streamwise velocity nearly follows a classical logarithmic law almost up to the centerline of the pipe flow. The results are plotted against the classical logarithmic law $U^+ = 1/\kappa\ lny^+ + C$ with a von Kármán's constant $\kappa = 0.4$ and $C = 5$, which is classically observed in plane channel flow (Kim *et al.* 1987). However, as reported in Eggels *et al.* (1994), both values of von Kármán's constant and of C do not mach exactly the usual values given above for the turbulent pipe flow: this has been verified both numerically and experimentaly. In our case, the best fit for these constants seems to be $\kappa = 0.35$ and $C \approx 3.6$, that is very close to Eggels *et al.* evaluation for κ but different for C (Eggels *et al.* propose $C = 4.8$). Although many observations concerning this scatter around the value of C suggest that this value depends strongly on curvature effects (Huffman and Bradshaw 1972), the problem of the dependency of von Kármán's constant in such configurations remains an open question. As regards the mean turbulent intensities, we observe that our L.E.S. predicts a peak of streamwise velocity $u'^{+2} \approx 7$ for $y^+ \approx 12.5$, whereas Eggels *et al.* give 7.45 for $y^+ \approx 14$. This slight departure is confirmed when looking at other velocity components: $u_\theta'^{+2} \approx 1.7$ at $y^+ \approx 38$ ($u_\theta'^{+2} \approx 1.1$ at $y^+ \approx 44$ for Eggels *et al.*) and $u_r'^{+2} \approx 1.2$ at $y^+ \approx 65$ ($u_\theta'^{+2} \approx 0.72$ at $y^+ \approx 60$ for Eggels *et al.*). Our estimation of the Reynolds tensor is $u_r'^{+} u'^{+} \approx -1$ whereas Eggels *et al.* found -0.7. We think these discrepancies may be explained by at least three facts:

- Reynolds number effects, which may be very important within the range of considered Reynolds numbers.
- the relative low resolution at the wall: $y^+ \approx 0.94$ for the first point in Eggels *et al.* calculation whereas we only have $y^+ = 2.1$.
- maybe the non ideal scaling of our eddy viscosity model near the wall, which does not scale in y^3, as suggested in previous studies (Germano *et al.* 1991).

This last point is already under investigation.

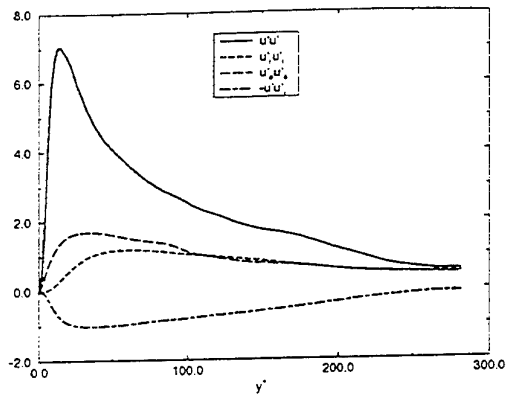


Figure 11: Mean turbulent intensities and Reynolds stress in wall units.

CONCLUSION

This paper addresses the problem of computing unsteady turbulent compressible flows using the L.E.S. approach for hybrid meshes, which allows to easily handle arbitrary complex geometries.

The work covers two new aspects of L.E.S. turbulent modeling:

- first, our results to the pipe flow suggest that L.E.S. in complex geometries are available, despite the fact that our approach tends to be pragmatic: some aspects of the L.E.S. formulation in complex geometries are passed over here (commutativity between space and filter is supposed, anisotropy of the mesh considered only through the local volume of the cells, etc...);
- secondly it takes benefit from previous works allowing the development of sub-grid scales models able to treat transitional as well as fully turbulent flows, and thus proposes a new sub-grid scale model developed on the basis of the Smagorinsky model.

Some problems implicitely related to unstructured codes are clearly posed, among them the necessity to formulate a suitable dissipative operator for L.E.S.: some explanations concerning this point will be given in a forthcoming paper. Finally, let us recall that the use of hybrid meshes can lead to a significant reduction of the number of grid points or cells for some classes of problems; as seen previously, the time step can also be effected by the use of hybrid meshes. This opens some perspectives like computation of unsteady flows in real aeronautic configurations, such as air-intakes or wings, which are already in process.

Acknowledgements : We would like to thank M. Rudgyard (Oxford University Computing Laboratory) for the fruitful discussions concerning the dissipative operator in unstructured meshes. This work was supported by CERFACS.

REFERENCES

Ducros, F., Comte, P., et Lesieur, M., 1995, "Large-eddy simulation of a spatially growing boundary layer over an adiabatic flat plate", *Int. J. Heat and Fluid Flow*, Vol. 16, pp. 341-348.

Ducros F., Comte P., et Lesieur M., 1996, "Large-eddy simulation of transition to turbulence in a weakly-compressible boundary layer over a flat plate", *J. of Fluid Mech.*, Vol. 326, pp. 1-36.

Eggels, J.G.M., Unger, F., Weiss M.H., Westerweel., J., Adrian, R. J., Friedriech, R., Nieuwstadt, F. T. M., 1994 "Fully developed turbulent pipe flow: a comparison between direct numerical simulation and experiment", *J. of Fluid Mech.*, Vol. 268, pp.175-209.

Germano, M., Piomelli, U., Moin, P., Cabot, W., 1991, "A dynamic subgrid-scale eddy viscosity model", *Phys. fluids*, A 3, Vol. 7, pp. 1760-1765

Ghosal S. and Moin P., 1995, "The basic equation for the large eddy simulation of turbulent flow in complex geometry", *J. of Comp. Physiscs*, Vol. 118, pp. 24-37.

Huffman, G.D., Bradshaw, P., 1972, "A note on Von Kármán's constant in low Reynolds number turbulent flows", *J. Fluid Mech.*, Vol. 177, pp. 133-166.

Hughes,T. J. R., Mallet, M., 1986, "A new finite element formulation for computational fluid dynamics: III. The generalized streamline operator for multidimentional advective-diffusive systems", *Comp. Meth. Appl. Mech. Eng.*, Vol. 58, pp. 305-328.

Kim, J., Moin, P., Moser, R. 1987 "Turbulence statistics in fully turbulent channel flow at low Reynolds number", *J. Fluid Mech.*, Vol. 177, pp. 133-166.

Lesieur, M., 1990, *Turbulence in Fluids* Second revised edition, Kluwer Academic Publishers.

Lesieur, M., Métais, O., 1996 New trends in Large-Eddy Simulations of Turbulence, *Annu. Rev. Fluid. Mech.*, Vol. 28, pp. 45-82.

Lilly, D K, 1967 "The representation of small scale turbulence in numerical simulations experiments", proceedings of the IBM Scientific Computing Symposium on Environmental Sciences, Yorktown Heights.

Nicoud., F., Ducros, F., Rudgyard, M., Schonfeld T., 1997 "Dissipative operators for non structured and hybrid meshes: application to L.E.S.", preprint CERFACS and Oxford University.

Nicoud, F.C., Ducros, F., Schönfeld T., "Towards direct and large eddy simulation of compressible flows in complex geometries", *Notes in Numerical Fluid Mech., to appear.*

Robinson, S. K., 1991 "Coherent motions in the turbulent boundary layer", *Annu. Rev. Fluid Mech.*, Vol. 23, pp. 601-639.

Schlichting, H, 1979, "Boundary layer theory", Mc-Graw Hill publisher.

Schönfeld, T., Rudgyard, M., 1994, A cell-vertex approach to local mesh refinement for 3-D Euler equations, *AIAA 94-0318.*

Spalart, P., 1988 "Direct simulation of a turbulent boundary layer up to $R_\theta = 1410$", *J. Fluid. Mech.*, Vol. 187, pp. 61-98.

SPECTRAL-DYNAMIC MODEL FOR LES OF FREE AND WALL SHEAR FLOWS

E. Lamballais[1][2], M. Lesieur[1], J. H. Silvestrini[1][3]

[1] LEGI/IMG
BP53, 38041 Grenoble Cedex 09
France

[2] LEA/CEAT
43, Route de l'Aérodrome, 86036 Poitiers Cedex
France

[3] CPGMAp/UFRGS
Av. Bento Goncalves 9500, 91501-970 Porto Alegre - RS
Brasil

ABSTRACT

Using EDQNM nonlocal interactions theory, we propose spectral eddy coefficients allowing to account for non-developed turbulence in the subgrid-scales. This spectral-dynamic model is applied with success to LES of a mixing layer at $Re_{\delta_i} = 2000$ and rotating/non-rotating turbulent channel flows at $Re = 6666$ and 14000. A generalization of the model in physical space, in terms of mixed structure-function and hyperviscosity models, is also proposed.

THE SPECTRAL-DYNAMIC MODEL

We start by considering the large-eddy simulation (LES) problem from a spectral point of view, with a sharp cutoff above k_c in Fourier space (in a context of homogeneous and isotropic turbulence). Following the concept of spectral eddy viscosity introduced by Kraichnan [11], Chollet & Lesieur [6] have proposed to use $[E(k_c,t)/k_c]^{\frac{1}{2}}$ to normalize the eddy viscosity in a subgrid-scales model ($E(k,t)$ is the spectral density of the kinetic energy), in writing

$$\nu_t(k,k_c,t) = K(k/k_c)\ \nu_t^\infty(k_c,t) \tag{1}$$

with

$$\nu_t^\infty(k_c,t) = 0.267\ \left[\frac{E(k_c,t)}{k_c}\right]^{\frac{1}{2}}. \tag{2}$$

In this model, the constant value 0.267 was obtained in assuming that $E(k)$ follows a Kolmogorov law extending about the cutoff, and the spectral dependence of eddy viscosity was adjusted with the expression

$$K(k/k_c) = 1 + 34.5\ e^{-3.03(k_c/k)}\ . \tag{3}$$

In (3), $K(k/k_c)$ displays a strong overshoot (cusp-behaviour) in the vicinity of $k/k_c = 1$, as shown by Kraichnan [11]. The eddy-diffusivity was found to behave qualitatively the same [7], with a corresponding turbulent Prandtl number $P_r^t = \nu_t^\infty/\kappa_t^\infty$ approximately constant and equal to 0.6.

On the basis of the EDQNM nonlocal interactions theory (see [6, 7, 18, 17]), one can express for $k \ll k_c$ spectral eddy viscosities $\nu_t^\infty(k_c,t)$ and diffusivities $\kappa_t^\infty(k_c,t)$ in a more general manner, using leading-order expansions in powers of the small parameter k/k_c. They are respectively equal to

$$\nu_t^\infty(k_c,t) = \frac{1}{15}\int_{k_c}^\infty \theta_{0pp}\left[5E(p,t) + p\frac{\partial E}{\partial p}\right]dp \tag{4}$$

and

$$\kappa_t^\infty(k_c,t) = \frac{2}{3}\int_{k_c}^\infty \theta_{0pp}^T\ E(p,t)\ dp\ , \tag{5}$$

where θ_{kpq} and θ_{kpq}^T are are nonlinear triple-correlation relaxation times of EDQNM theory. The eddy coefficients may now be evaluated in a less restrictive context than previously. Assuming that the kinetic energy spectrum follows a power law $E(k) \propto k^{-m}$ instead of a Kolmogorov law, ν_t^∞ may be expressed (for $0 < m < 3$) as

$$\nu_t^\infty(k_c,t) = 0.31\ C_k^{-\frac{3}{2}}\ \frac{5-m}{m+1}\ (3-m)^{\frac{1}{2}}\ \left[\frac{E(k_c,t)}{k_c}\right]^{\frac{1}{2}} \tag{6}$$

with the associated turbulent Prandtl number

$$P_r^t = 0.18\ (5-m)\ . \tag{7}$$

The m-dependence of the eddy viscosity and diffusivity (normalized by $[E(k_c,t)/k_c]^{\frac{1}{2}}$) is presented in figure 1. One can observe on this graph that ν_t^∞ and κ_t^∞ decrease monotonously in the interval $0 < m < 3$. It is interesting to note that ν_t^∞ is reduced by more than 50 % with respect to its value for $m = 5/3$, as soon as $m > 2.2$, and multiplied at least by a factor of 2 if $m < 1$.

In the "spectral dynamic model" used for the LES presented below, we define the spectral eddy viscosity with the aid of eqs (1) and (6). Thus, the k–dependence of the eddy-viscosity have been conserved through (3). It is important to keep the cusp, which accounts for local and semi-local interactions in the neighbourhood of k_c. Indeed, this avoids the spectral-gap assumption between resolved and subgrid-scales, which is inherent to any eddy-viscosity assumption in physical space. Using the spectral-dynamic

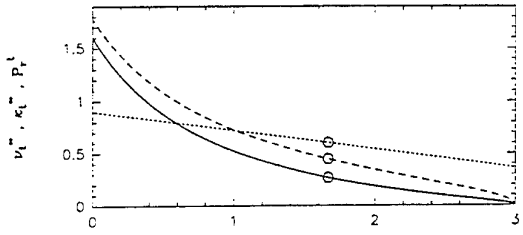


Figure 1: Variation of eddy viscosity, eddy diffusivity (normalized by $[E(k_c,t)/k_c]^{\frac{1}{2}}$) and turbulent Prandtl number with m, the slope of the kinetic-energy spectrum in the neighbourhood of the cut-off wave number k_c. Symbols correspond to values obtained when considering a Kolmogorov law ($m = 5/3$).
——— : ν_t^∞, - - - - : κ_t^∞, ... : P_r^t

model permits to reduce automatically the eddy viscosity without any empirical correction (like adjustment of constant(s) in the model) in two situations :

- for transitional or moderate Reynolds number flows, where no inertial zone can exist in the kinetic energy spectrum ;
- for near-wall region of fully turbulent flows, where kinetic energy spectra are steeper than Kolmogorov, even at high Reynolds number.

Note finally that (6) is only valid for $m \leq 3$. For $m > 3$, our choice was to set the eddy-viscosity equal to zero. From a practical viewpoint, this may be justified in considering that if the kinetic energy spectrum is steep enough, there is no energy pile-up at high wave numbers, so that no subgrid-scales modelling is really needed.

APPLICATION TO MIXING LAYER

Flow configuration and numerical aspects

We have carried out a LES of a temporal mixing layer at $Re_{\delta_i} = U\delta_i/\nu = 2000$, where δ_i is the initial vorticity thickness equal to $2U/\omega_i$ and ω_i the initial maximal vorticity modulus. Pseudo-spectral methods are used to solve the filtered Navier-Stokes equations, enforcing periodic boundary conditions in the streamwise (x) and spanwise (z) directions, while free-slip conditions are imposed in the transverse direction (y) by means of sine/cosine expansions. The temporal derivative is approximated by a third-order low-storage Runge-Kutta scheme [23].

Initial conditions consist in a basic hyperbolic-tangent velocity profile and a small Gaussian isotropic perturbation of kinetic energy $10^{-4}U^2$. The computational domain is cubic of side $L_x = L_y = L_z = 4\ \lambda_a$ (where $\lambda_a = 7\ \delta_i = 2\pi/k_a$ is the wavelength of the most amplified streamwise mode predicted by linear stability theory). Hence two pairings of Kelvin-Helmholtz vortices are allowed. Aliasing errors [4] were minimized by taking more collocation points in physical space (120^3) than Fourier modes (96^3).

The simulation was stopped at $t = 60\ \delta_i/U$, the time of the second pairing of Kelvin-Helmholtz structures. No confinement effects on the mixing layer were observed (see [22] for a complete description of the simulation). At this time, the Reynolds number based on the local vorticity thickness δ (defined as $2U/|\langle\omega_z\rangle(y=0)|$) was $Re_\delta = 20000$.

Model validation and results

In this temporal mixing layer LES, the spectral-dynamic model is used in its "standard version" defined by equations

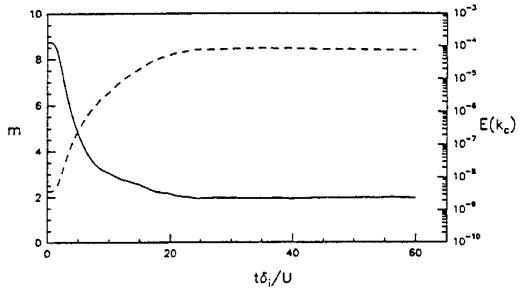


Figure 2: Temporal variation of the three-dimensional kinetic energy spectrum slope m (—) and of the kinetic energy at the cutoff wave number $E(k_c)$ (- - -).

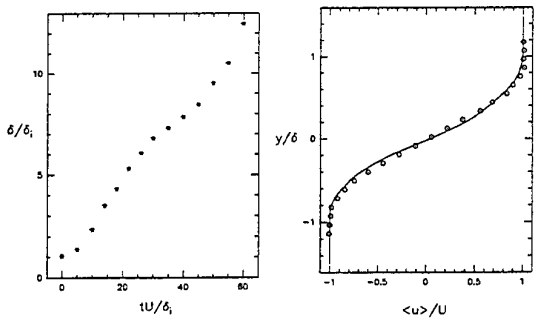


Figure 3: Temporal evolution of the local vorticity thickness δ (left) and comparison of mean streamwise velocity (straight line) with self-similar mixing layer experimental data of Bell & Mehta (symbols) [2] (right).

(1),(3) and (6). The spectrum slope m is calculated at each time step, from the three-dimensional kinetic energy spectrum, using a least-square method applied to wave numbers ranging between $k_c/2 < k < k_c$.

Figure 2 shows the temporal evolution of m and $E(k_c)$ for the whole simulation. The spectrum slope decreases initially from the high value ($m \approx 9$) defined in the initial conditions. At $t = 10\ \delta_i/U$, that is, when Kelvin-Helmholtz vortices roll-up, we have $m \approx 3$. It means that the eddy-viscosity was inactive (see equation 6) at this instant, and all the dissipation was due to molecular viscosity. It allows the growth of instabilities not to be influenced by eddy viscosity, which is certainly desirable. Between $t = 10$ and $30\ \delta_i/U$ (moment of the first pairing), the slope m falls from 3 to 2. After that, m remains very close to 2 until the end of the simulation.

Statistics of the recorded velocity profiles were used to determine the temporal evolution of the local vorticity thickness, and compared with experimental data of self-similar mixing layers of Bell & Mehta (1990) ([2]). The l.h.s. of figure 3 shows $\delta(t)$. A fairly linear growth is established very early at a rate of $d\delta/(Udt) = 0.19$. During the first pairing ($t \approx 30$), the spreading slows down, and afterwards it starts again rising at the same rate. In spite of the differences in the spatial growth of mixing layers reported in several works [21], and also between the spatial and the temporal problem, the growth rate we found for the latter is very close the traditionally accepted mixing layer spatial growth of 0.18 reported in Brown & Roshko's experiments [3].

The r.h.s. of figure 3, and figure 4, show respectively the mean streamwise velocity and velocity components variances at the end of the simulation ($t = 60\ \delta_i/U$). The agreement between numerical and experimental data is remarkable. The slight lack of convergence for $\langle u'u'\rangle$ and

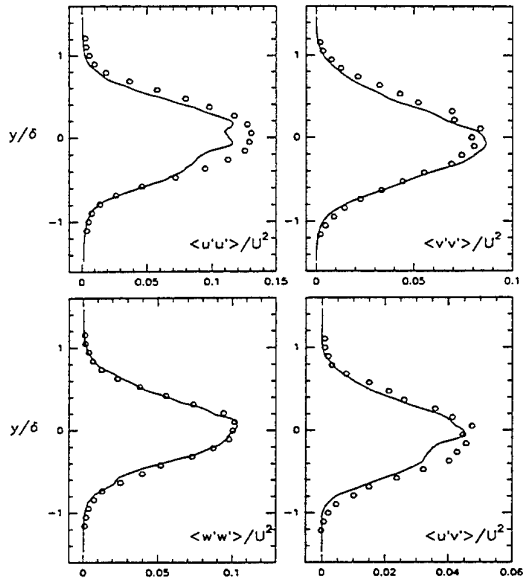


Figure 4: Comparison of the velocity fluctuations variances with self-similar mixing layer experimental data of Bell & Mehta [2].

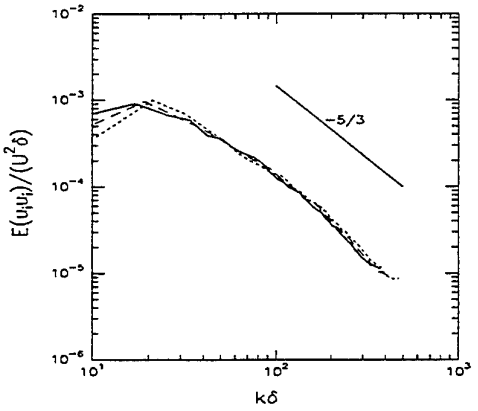


Figure 5: Normalized three-dimensional kinetic energy spectra at $t = 50$ (—), 55 (- - -) and 60 δ_i/U (- - -).

$\langle u'v' \rangle$ is explained by the fact that only spatial averages in the periodic directions were calculated.

Figures 3 and 4 seem to indicate that a self-similar state was established at the end of the simulation. This fact is confirmed by the normalized three-dimensional kinetic energy spectrum, which is presented in figure 5 (the normalization is made by the local scale δ). The good collapse of the different spectra for $t = 50$, 55 and 60 $\delta_i/$ is a good indicator that a self-similar regime is attained. Another confirmation may be established transforming the streamwise distance needed to establish the self-similar regime in Bell & Mehta experiences in elapsed time. There is however a slight problem concerning the spectral slope in the neighbourhood of k_c, which is close to 2, as already stressed. Indeed, mixing-layer experiments at this Reynolds find a $-5/3$ exponent over a quite long range in small scales. We had already observed this defect in isotropic turbulence with the plain spectral-cusp model, and it seems here that the extra reduction of the eddy-viscosity brought by the slope -2 is not sufficient to create exactly a $k^{-5/3}$ cascade across k_c.

Since, except for the ultraviolet spectra, the statistics are in good agreement with experimental data, it is worth looking at the three-dimensional vortical structure. Figure 6 shows a perspective view of isosurfaces of vorticity modulus, with a threshold value of $|\omega_i|$, at $t = 14$ (left-side) and 60 δ_i/U (right-side). The l.h.s. shows a dislocated array of rolling-up Kelvin-Helmholtz vortices, similar to the configuration found in previous DNS simulations [8] and laboratory experiments [5], and called "helical pairings". Secondaries streamwise vortices are also stretched by the deformation field between the K-H vortices. The r.h.s. picture is taken when a self-similar regime has established. This state is characterized by the presence of intense small-scale vortices, with no preponderant orientation. The large scales are not identifiable by visualization of vorticity isosurfaces but instead we found their signature in the structures of low pressure (see figure 7). It seems that we have here one big quasi two-dimensional vortex stretching thinner longitudinal vortices. However, the spanwise width of the domain is now too small to contain the wavelength of the helical-pairing instability, which should scale on δ.

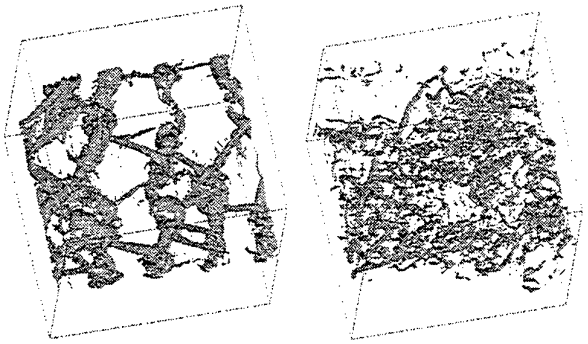


Figure 6: Perspective views of the mixing layer at $t = 14$ (left) and 60 δ_i/U (right) showing isosurfaces of the vorticity modulus with a threshold value of ω_i.

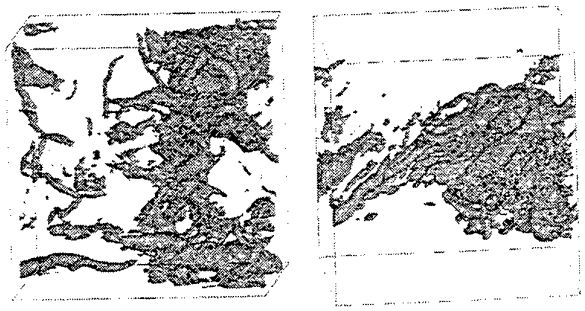


Figure 7: Top (left) and side (right) views of low-pressure isosurfaces at $t = 60$ δ_i/U.

CHANNEL FLOW

Flow configuration

Here, we consider the turbulent plane channel flow submitted (or not) to spanwise rotation. Let $\langle \vec{u} \rangle = (\langle u \rangle, 0, 0)$ be the mean relative velocity in a Cartesian coordinates system (x, y, z) associated to the rotating frame. x, y and z are respectively the streamwise, wall-normal and spanwise directions, the rotation vector being $\vec{\Omega} = (0, 0, \Omega)$ (see figure 8).

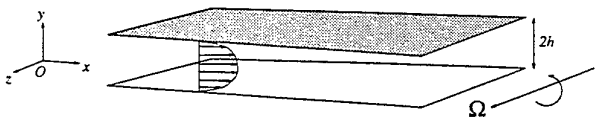


Figure 8: Schematic view of the rotating channel.

The half-channel height is noted h and the bulk velocity U_m. Non-dimensional parameters used here are the Reynolds number $Re = \frac{U_m\ 2h}{\nu}$ and the global Rossby number $Ro_g = \frac{3\ U_m}{2\Omega\ h}$. Small values of the latter concern strong rotation regimes where Coriolis forces dominate inertial forces, while infinite global Rossby number corresponds to no rotation. Note that the 3/2 factor in the global Rossby expression is present to conserve the same definition as in previous work where transitional rotating channel flow was considered [14]. In a laminar situation (Poiseuille flow), this global Rossby corresponds to the ratio of the vorticity at the wall $\left(\frac{3\ U_m}{h}\right)$ upon the solid-body rotation vorticity 2Ω.

Model adaptation

An adaptation of the model formulation is necessary to treat the direction of inhomogeneity y. In the present case, two-dimensional spectra $E_{2d}(y, k_{2d}, t)$ have been used, with $k_{2d} = \sqrt{k_x^2 + k_z^2}$. A slope $m(y,t)$ of each kinetic-energy spectrum given in a plane $y = cste$ is then defined, in such way that the spectral-eddy viscosity takes the final form

$$\nu_t^{\infty +}(y, k_{2d}, t) = 0.31\ C_k^{-\frac{3}{2}}\ \frac{5 - m(y,t)}{m(y,t)+1}\ [3 - m(y,t)]^{\frac{1}{2}}$$
$$\times (1 + 34.5e^{-3.03(k_c/k_{2d})})\ \left[\frac{E(y, k_c, t)}{k_c}\right]^{\frac{1}{2}}$$

Note that the spectral formulation used in this model concerns only horizontal directions. Numerically, $m(y,t)$ is evaluated using a least-square method applied on a spectral range of highest wave numbers. For simulations presented here, a quite large number of wave numbers has been used $(k_c/2 < k_{2d} < k_c)$, but we have verified that this number can be reduced without significant modification of the results.

A last remark concerns the use of a two-dimensional spectrum instead of a three-dimensional one. In an isotropic turbulence context, a 3D-spectrum $E(k) = c_1\ k^{-m}$ may be deduced from a 2D-spectrum $E_{2d}(k_{2d}) = c_2\ k_{2d}^{-m}$ by integration : it is found

$$\frac{c_1}{c_2} = \left\{ \frac{\Gamma(\frac{1}{2})\Gamma(\frac{1}{2}(m+1))}{3\Gamma(\frac{1}{2}m+1)} - \frac{\Gamma(\frac{1}{2})\Gamma(\frac{1}{2}(m+1))}{6\Gamma(\frac{1}{2}m+2)} \right\} \quad (8)$$

With the aid of this expression, it is possible to evaluate the 3D-spectrum at the cutoff wave number $E(k_c)$. Note however that this correction is not fully justified if the y-direction is inhomogeneous, as in the present situation. From a practical point of view, it has been observed that use of the correction factor given by (8) in the subgrid-scale model has a negligible effect on the final result.

Non-rotating channel results

We use here a mixed spectral-compact code having spectral accuracy (see [13] for details). We first present two LES of non-rotating channel flows at $Re = 6666$ (case A) and $Re = 14000$ (case B). The grid refinement close to the wall allows to simulate accurately the viscous sublayer, with a resolution of $(64 \times 65 \times 32)$ for case A, and $(128 \times 96 \times 64)$ for case B.

Figure 9 shows the mean velocity profile in case A, compared with the LES of Piomelli [19] using the dynamic model of Germano [9]. The latter is known to be in good agreement with experiments or DNS at this low Reynolds number. Present results coincides, with for instance correct values for the Karman constant or the friction velocity.

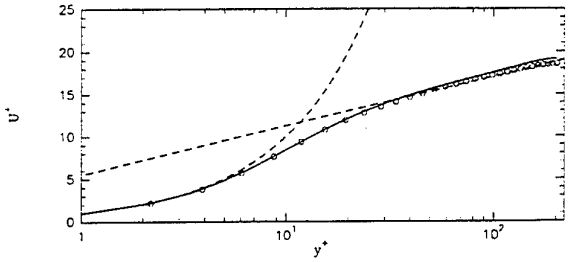


Figure 9: Case A ($h^+ = 204$), comparison of the mean velocity profile (straight line) versus Piomelli's [19] dynamic-model simulations (symbols).

Figure 10 shows for case A the rms velocity fluctuations, compared with Piomelli's results. The agreement is still very good, with a correct prediction of the longitudinal velocity fluctuations peak, corresponding to a maximum intensity for the high an low-speed streaks.

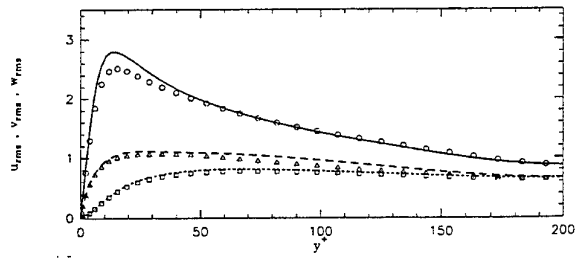


Figure 10: Same as Figure 9, but for the rms velocity fluctuations, from top to bottom longitudinal, spanwise and transverse velocities.

The same velocity statistics as for case B are presented on figure 11 and compared with DNS [1] data at approximately the same Reynolds number. It can be seen that mean velocity and turbulence intensities obtained by present LES are in good agreement with (unfiltered) DNS results. Notice that LES allows in this case to reduce the computational cost by a factor of 100 with respect to DNS.

Quality criteria based only on statistics may be insufficient. Indeed, we have observed that a simulation without any subgrid-model (at the same Reynolds number and resolution) gives statistics of the velocity field (mean value, variances and Reynolds stresses) not dramatically affected, while kinetic energy spectra or instantaneous vorticity fields are very unrealistic. Figure 13 presents a vorticity visualization in the LES, compared with a DNS at lower Reynolds. The coherence of the large-scale motion in terms of hairpin ejections and streaks at the wall is preserved in LES. It is clear also that the LES does indicate features expected from turbulence at higher Reynolds number, and displays much more vortical activity in the small scales than the DNS. The small (resolved) scale activity thus predicted is susceptible of enhancing mixing or chemical reactions in LES of turbulent transport or combustion for instance.

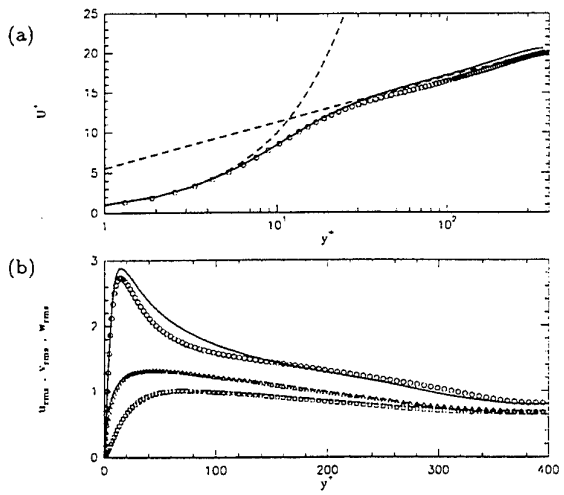


Figure 11: Turbulent channel flow, comparisons of present LES using spectral-dynamic model (straight lines, $h^+ = 389$) with the DNS [1] (symbols, $h^+ = 395$); a) mean velocity, b) rms velocity components.

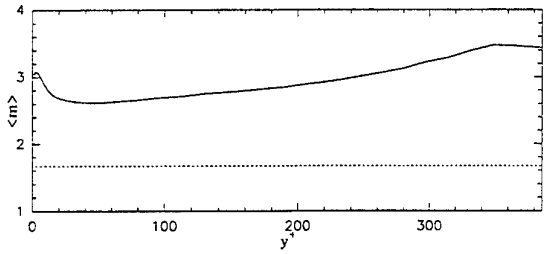


Figure 12: Profile of $\langle m \rangle$, the mean value of the kinetic-energy spectrum slope for a given y-position.

We have thus shown that the spectral-dynamic model gives a good near-wall behaviour in turbulent wall flows, without use of any "hand-tuned" constant in the eddy-viscosity formulation. To illustrate the importance of the eddy-viscosity correction, we present on Figure 12 the profile of the spectral exponent $m(y,t)$ averaged with time. It can be noticed first that spectra are clearly steeper than Kolmogorov in the whole channel. In addition, we see that m is very close to 3 or higher in the viscous region, corresponding to a very low (or zero) value of the eddy viscosity. This permits correct near-wall statistics. Dynamics models in physical space present the same advantage, but not via an explicit control of the energy distribution in the highest wave numbers. However, one should check on the experiments at this Reynolds number whether the quite steep velocity spectra obtained here are realistic, or if they are an artefact of the model.

Rotating channel results

The spectral-dynamic model has been applied also to the rotating turbulent channel [13, 15], where results in good qualitative agreement with DNS at lower Reynolds numbers [13, 14] were obtained. The spectral dynamic model is tested here for a very strong rotation, corresponding to $Ro_g = 2$. For such a rotation rate, DNS have shown that a quasi-laminar zone develops in the cyclonic region while, in the anticyclonic region, the vortex organization of the flow differs strongly from the non-rotating case. For present LES with higher Reynolds number, the same tendencies can be observed (see Figure 14). For instance, a pdf analysis of the angle made by hairpins with the horizontal plane (not presented here) shows that vortices in the anticyclonic region lean more and more towards the wall as the Rossby number diminishes, while becoming more coherent.

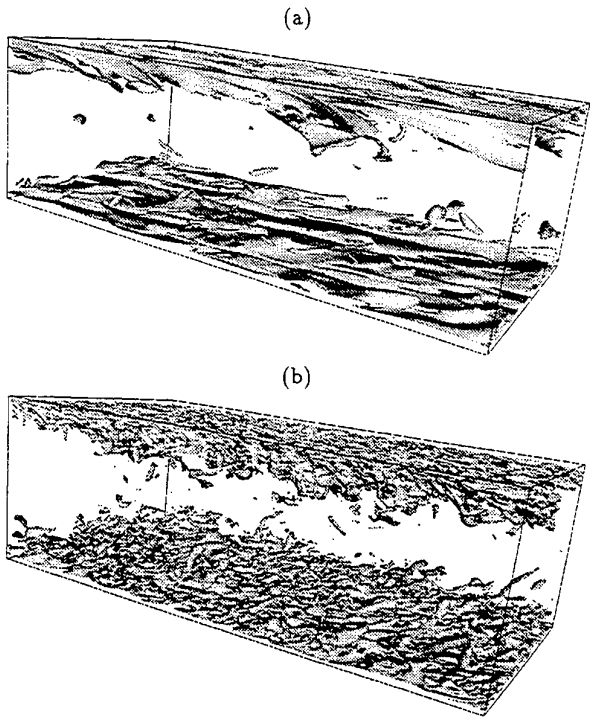


Figure 13: Turbulent non-rotating channel flow, isosurface of the vorticity modulus $\omega = 4.5\ U_m/h$ (the flow goes from left to right); a) DNS at $Re = 5000$, b) LES at $Re = 14000$.

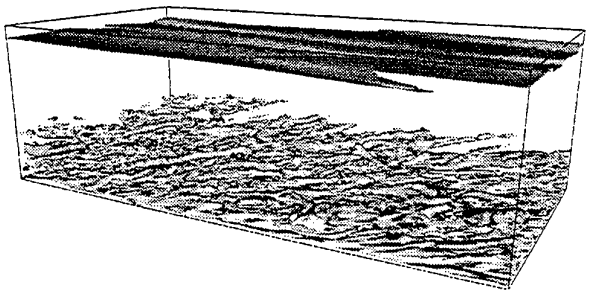


Figure 14: Turbulent rotating channel flow, isosurface of the vorticity modulus $\omega = 3.375\ U_m/h$ (the flow goes from left to right); LES at $Re = 14000$ and $Ro_g = 2$.

To our knowledge, no equivalent DNS nor experiments at identical Reynolds number and rotation rate as our present LES are given in the literature. Validation of the present simulation is therefore not yet feasible. It may be however interesting, at the same Rossby number, to compare DNS at lower Reynolds number ($Re = 5000$) with present LES at $Re = 14000$. Here, we concentrate our attention on the reduction of the cyclonic friction velocity (noted $u_{\tau c}$) with respect to its value without rotation (noted u_τ^∞) for the same Reynolds number. We find that this reduction is more marked for $Re = 14000$ (LES) than for $Re = 5000$ (DNS), with $u_{\tau c}/u_\tau^\infty$ respectively equal to 0.49 and 0.59. For moderate rotation ($18 < Ro_g < 25$), Johnston *et al.* [10] have reported the same tendency, i.e. a reduction of the normalized cyclonic wall friction with the increase of the Reynolds number ($Re = 10300$ and $Re = 11400$). Cy-

clonic friction velocity was found to be lower in these experiments than in DNS [12, 13]. On the other hand, and for similar rotation rates, Launder & Tselipidakis [16] in calculations using a one-point closure model, and Piomelli & Liu [20] with LES, have noticed on the contrary an increase with the Reynolds number of the normalized friction velocity. Hence, further computations (very high resolution DNS) or experiments are needed to decide about this point.

RETURN TO PHYSICAL SPACE

In fact, the function $K(x)$ defined in (3) can be put under the form $K(x) = 1 + \nu_n^* x^{2n}$, with $2n \approx 3.7$ [7]. Determining ν_n^* on the basis of subgrid-energy conservation, and approximating $2n$ by 4, one can propose an equivalent of the spectral-cusp model in physical space as

$$0.661 \frac{\partial}{\partial x_j}\left[\nu_t^{SF}\left(\frac{\partial \bar{u}_i}{\partial x_j}+\frac{\partial \bar{u}_j}{\partial x_i}\right)\right]+0.014\,\Delta x^4\,\nu_t^{SF}(\nabla^2)^3\bar{u}_i \quad (9)$$

for the eddy-viscous operator in the momentum equation. Here, ν_t^{SF} is the eddy-viscosity of the structure-function model [18]. Multiplying the above operator by $\tilde{A} = (\sqrt{12}/5)[(5-m)/(m+1)]$, we obtain in physical space a model equivalent to the spectral-dynamic model.

Acknowledgments : Computations were carried out at the IDRIS (Institut du Développement et des Ressources en Informatique Scientifique, Paris). This work was sponsored by *Institut Universitaire de France*, CNRS, INPG and UJF.

REFERENCES

[1] R. A. Antonia, M. Teitel, J. Kim, and L. W. B. Browne. Low-Reynolds-number effects in a fully developed turbulent channel flow. *J. Fluid Mech.*, **236**:579–605, 1992.

[2] J. Bell and R. Mehta. Development of a two-stream mixing layer from tripped and untripped boundary layers. *AAIA Journal*, **28**:2034–2042, 1990.

[3] G. Brown and A. Roshko. On density effects and large structure in turbulent mixing layers. *J. Fluid Mech.*, **64**:775–816, 1974.

[4] C. Canuto, M. Y. Hussaini, A. Quarteroni, and T. A. Zang. *Spectral Methods in Fluid Dynamics.* Springer-Verlag, New York, 1988.

[5] C. Chandrsuda, R. Mehta, A. Weir, and P. Bradshaw. Effect of free-stream turbulence on large structure in turbulent mixing layers. *J. Fluid Mech.*, **85**:693–704, 1978.

[6] J. P. Chollet and M. Lesieur. Parameterization of small scales of the three-dimensional isotropic turbulence utilizing spectral closures. *J. Atmos. Sci.*, **38**:2747–2757, 1981.

[7] J.P. Chollet and M. Lesieur. Modélisation sous maille des flux de quantité de mouvement et de chaleur en turbulence tridimensionnelle isotrope. *La Météorologie*, **29-30**:183–191, 1982.

[8] P. Comte, M. Lesieur, and E. Lamballais. Large- and small-scale stirring of vorticity and a passive scalar in a 3-d temporal mixing layer. *Phys. Fluids A*, **4**(12):2761–2778, 1992.

[9] M. Germano. Turbulence : the filtering approach. *J. Fluid Mech.*, **238**:325–336, 1992.

[10] J. P. Johnston, R. M. Halleen, and D. K. Lezius. Effects of spanwise rotation on the structure of two-dimensional fully developed turbulent channel flow. *J. Fluid Mech.*, **56**:533–557, 1972.

[11] R. H. Kraichnan. Eddy viscosity in two and three dimensions. *J. Atmos. Sci.*, **33**:1521–1536, 1976.

[12] R. Kristoffersen and H. I. Andersson. Direct simulations of low-Reynolds-number turbulent flow in rotating channel. *J. Fluid Mech.*, **256**:163–197, 1993.

[13] E. Lamballais. *Simulations numériques de la turbulence dans un canal plan tournant.* PhD thesis, Institut National Polytechnique de Grenoble, 1996.

[14] E. Lamballais, M. Lesieur, and O. Métais. Effects of spanwise rotation on the vorticity stretching in transitional and turbulent channel flow. *Int. J. Heat and Fluid Flow*, **17**(3):324–332, 1996.

[15] E. Lamballais, O. Métais, and M. Lesieur. Influence of a spanwise rotation upon the coherent-structure dynamics in a turbulent channel flow. In *Proc. 2nd Ercoftac Workshop on Large Eddy Simulation*, Grenoble, France, 1996.

[16] B. E. Launder and D. P. Tselepidakis. Application of a new second-moment closure to turbulent channel flow rotating in orthogonal mode. *Int. J. Heat and Fluid Flow*, **15**(1):2–10, 1994.

[17] M. Lesieur. *Turbulence in fluids.* Kluwer Academic Publishers, third edition, 1997.

[18] O. Métais and M. Lesieur. Spectral large-eddy simulation of isotropic and stably stratified turbulence. *J. Fluid Mech.*, **239**:157–194, 1992.

[19] U. Piomelli. High Reynolds number calculations using the dynamic subgrid-scale stress model. *Phys. Fluids A*, **5**:1484–1490, 1993.

[20] U. Piomelli and J. Liu. Large-eddy simulation of rotating channel flows using a localized dynamic model. *Phys. Fluids A*, **7**(4):839–848, 1995.

[21] J. H. Silvestrini, P. Comte, and M. Lesieur. DNS and LES of incompressible mixing layers developing spatially. In *Proc. 10th Symp. on Turbulent Shear Flows*, pages S3–25, 1995.

[22] J.H. Silvestrini. *Simulation des grandes échelles des zones de mélange; application à la propulsion solide des lanceurs spatiaux.* PhD thesis, Institut National Polytechnique de Grenoble, 1996.

[23] J. H. Williamson. Low-storage runge-kutta schemes. *J. Comp. Phys.*, **35**:48, 1980.

LARGE EDDY SIMULATION OF TURBULENT CHANNEL FLOWS

C.Fureby, A.D.Gosman, G.Tabor, H.G.Weller,
Mechanical Engineering Department,
Imperial College of Science, Technology and Medicine,
Exhibition Road, London SW7 2BX, U.K.

N.Sandham,
Queen Mary & Westfield College,
London, U.K.

M.Wolfshtein
Technion – Israel Institute of Technology,
Haifa, Israel

ABSTRACT

In order to be of use in engineering situations, LES models must be able to reproduce near-wall flows. We approach this by refining the mesh close to the wall in a manner that reflects the anisotropic nature of near-wall turbulence. This requires the SGS modelling to be able to deal with anisotropic meshes as well as the anisotropic turbulence near the walls. The technique is then applied to fully-developed turbulent flow in a channel. We show that the first and second order statistical moments of the resolvable velocity are well reproduced, with the differential stress model of Deardorff performing particularly well.

INTRODUCTION

Large Eddy Simulation (LES) is based on the decomposition of the dependent variables into large- or Grid Scale (GS) components and small- or Sub Grid Scale (SGS) scale components, which represent the unresolved fraction of the turbulence, with the effect of the latter on the former being accounted for by SGS models. Away from walls LES performs well even on fairly coarse grids, i.e. when the cut-off wavenumber lies in the inertial range but biased towards the the integral scale. Recently, much effort has been devoted to incorporating near-wall modelling into LES (e.g. Cabot (1995)) : this is particularly directed towards applications at very high Reynolds numbers. However, a refined treatment of the near wall region is desirable in many cases, since near-wall effects are often important in the dynamical evolution of the entire flow field. Parameters such as the wall friction and heat transfer coefficients depend heavily on near-wall effects. Furthermore it is important to reproduce the interscale energy transfer between the unresolved fraction of the flow and the macroscopic flow. This is known to be difficult using wall models or damping functions of the van Driest type. If we are interested in complex geometries, it is advantageous to avoid concepts like 'distance to the wall' or 'wall-normal vectors', since they introduce interpretational problems as well as resulting in untenable behaviour.

Close to the wall the characteristic length scales of the most energetic eddies decrease. If the grid is unable to resolve these length scales, then anisotropies in the turbulent flow will be anisotropies of the SGS motion, and necessitating the solution of the full differential stress equation for the SGS stress tensor. In this study we investigate the possibility of resolving the near-wall region to capture the dynamics of this region, with specific reference to fully developed turbulent channel flow. As described above, the turbulent length scales become anisotropic close to the wall, with the perpendicular scale l_y tending to zero whilst the other scales l_x, and l_z parallel to the wall remain finite. We utilise a computational cell with sides $(\Delta_x, \Delta_y, \Delta_z) \propto (l_x, l_y, l_z)$ adequate to resolve the structures in the buffer layer. Δ_y is increased through the log-law region in order to coarsen the grid and provide more isotropic cells in the bulk of the flow. Since the refinement will be in one direction only, the number of additional cells necessary will be modest, and hence the problem will remain computationally tractable. However this does imply that the SGS modelling must be able to deal with mesh anisotropy. We investigate a number of different SGS models, mostly based on the eddy-viscosity concept. However the assumption of isotropy implicit in this type of model may be inappropriate given the anisotropic mesh and turbulence involved in this case. Accordingly we also use a differential stress model which does not rely on this assumption.

LES MODELS

In LES it is assumed that the dependent variables can be divided into GS and SGS components, i.e. $\mathbf{v} = \overline{\mathbf{v}} + \mathbf{v}'$, where $\overline{\mathbf{v}} = G * \mathbf{v} = \int_D G(\zeta, \Delta)\mathbf{v}(\zeta, t)d^3\zeta$, and

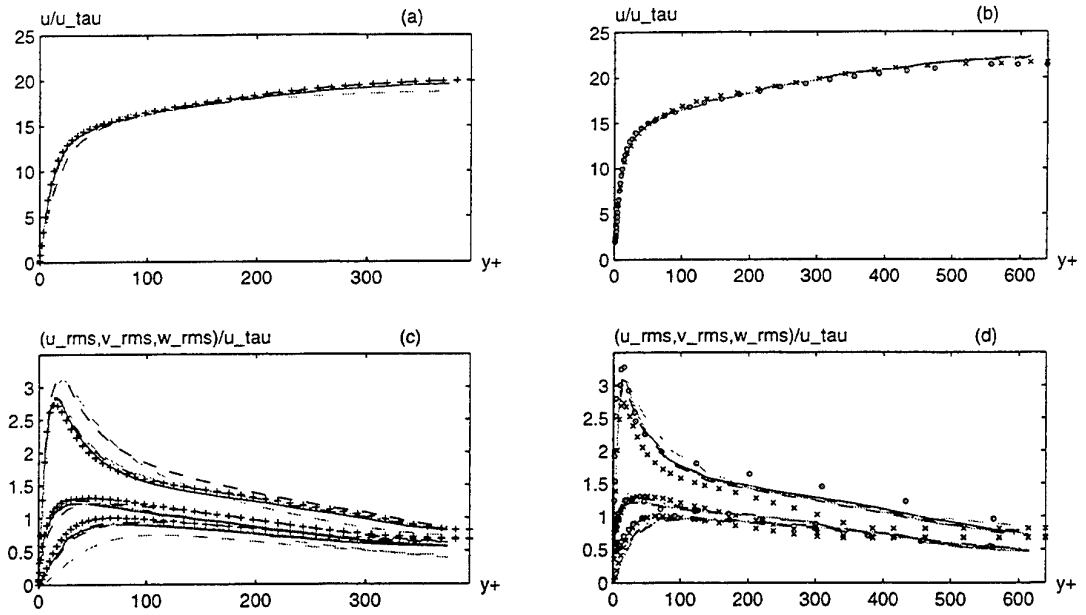


Figure 1: Profiles of resolvable streamwise velocity $\langle \overline{v} \rangle_x$ (a. $\mathcal{R}e_\tau = 395$, b. $\mathcal{R}e_\tau = 640$) and second order velocity moments T_{xx}, T_{yy} and T_{zz} (c. $\mathcal{R}e_\tau = 395$, d. $\mathcal{R}e_\tau = 640$). The circles represent experimental data (Wei and Willmarth (1989)), the plusses DNS data (Kim et al. (1987)), and the crosses MK's LES data (Moin and Kim (1982)). The lines are profiles from our LES : A1 (grey solid line), A2 (black dashed line) B1 (black dash-dotted line), B2 (grey dashed line), and C (black solid line). The grey dashed line is model C on the coarser mesh.

D is the computational domain. The kernel $G(\mathbf{x}, \Delta)$ is any function with the properties $\int_D G(\zeta, \Delta) d^3\zeta = 1$, $G(\mathbf{x}, \Delta) \geq 0$, $\lim_{\Delta \to 0} G(\mathbf{x}, \Delta) = \delta(\mathbf{x})$, and $G(\mathbf{x}, \Delta) \in C^n(\mathcal{R}^3)$ having compact support. In the absence of body forces, convolving the incompressible Navier Stokes equations (NSE) with G gives

$$\nabla . \overline{\mathbf{v}} = 0, \qquad (1)$$
$$\partial_t \overline{\mathbf{v}} + \nabla . (\overline{\mathbf{v}} \otimes \overline{\mathbf{v}}) = \nabla . (\overline{\mathbf{S}} - \mathbf{B}),$$

given that $[G*, \nabla]\mathbf{v} = 0$: $\mathbf{v}$ is the velocity field, ν the molecular viscosity, $\mathbf{S} = -p\mathbf{I} + 2\nu\mathbf{D}$ with p the specific pressure, and $\mathbf{D} = \frac{1}{2}(\nabla \mathbf{v} + \nabla \mathbf{v}^T)$. The convolution process generates an additional term, the SGS stress tensor :

$$\mathbf{B} = \overline{\mathbf{v} \otimes \mathbf{v}} - \overline{\mathbf{v}} \otimes \overline{\mathbf{v}} = \mathbf{L} + \mathbf{C} + \mathbf{R}, \qquad (2)$$

where $\mathbf{L}$ is the Leonard stress, $\mathbf{C}$ the cross stress and $\mathbf{R}$ the Reynolds stress tensor (e.g. Fureby et al. (1997)). A balance equation for $\mathbf{B}$ can be derived from the exact and filtered NSE :

$$\partial_t \mathbf{B} + \nabla . (\mathbf{B} \otimes \overline{\mathbf{v}}) = \mathbf{P} + \mathbf{M} + \mathbf{\Pi} + \mathbf{E}, \qquad (3)$$

where $\mathbf{P} = -\left(\overline{\mathbf{L}}\mathbf{B}^T + \mathbf{B}\overline{\mathbf{L}}^T\right)$ is the production. Here $\mathbf{M}$ is the generalised triple correlation, $\mathbf{\Pi}$ the pressure-velocity gradient tensor, and $\mathbf{E}$ the dissipation tensor.

The GS components are morphologically dependent on the geometry of the flow via the boundary conditions. The effect of the SGS components on the GS motion must be separately modelled, which is achieved by supplying a model for $\mathbf{B}$ in terms of the GS velocity field. This model should also accurately predict the interscale energy transfer $e(\Delta) = -\mathbf{B}.\overline{\mathbf{D}}$, in order to permit coarse grid solutions of (1). Two different approaches to the modelling of $\mathbf{B}$ are used, either based on the conventional eddy-viscosity concept, or using a full balance equation for $\mathbf{B}$.

SGS Models of Eddy-Viscosity Type

The simplest SGS models are based on the hypothesis that the deviatoric part of $\mathbf{B}$ is locally aligned with $\overline{\mathbf{D}}_D = \overline{\mathbf{D}} - \frac{1}{3} tr(\overline{\mathbf{D}})\mathbf{I}$, whilst the normal stresses are assumed to be isotropic and thus representable through the SGS kinetic energy k. Consequently,

$$\mathbf{B} = \frac{2}{3} k \mathbf{I} + 2\nu_k \overline{\mathbf{D}}_D, \qquad k \equiv \frac{1}{2} tr(\mathbf{B}) \qquad (4)$$

where the SGS kinetic energy k, and the SGS viscosity ν_k must be specified for the model to be complete. The best-known model of this class is that of Smagorinsky (1963), with

$$k = c_I \Delta^2 \|\overline{\mathbf{D}}\|^2, \qquad \nu_k = c_D \Delta^2 \|\overline{\mathbf{D}}\|, \qquad (5)$$

where $c_I \simeq 0.20$ and $c_D \simeq 0.01$. This model will be referred to as Model A1.

An exact balance equation for k can be derived by contracting the exact balance equation for $\mathbf{B}$ (3). Redistribution effects do not contribute to the k equation in isochoric flows, and it can be assumed that diffusive and dissipative effects can be modelled as $\nabla.(\nu_k \nabla k)$ and $\epsilon = c_\epsilon k^{3/2} \Delta^{-1}$ respectively. This gives

$$\partial_t k + \nabla . (k \overline{\mathbf{v}}) = -\mathbf{B}.\overline{\mathbf{D}} + \nabla . (\nu_k \nabla k) - \epsilon,$$
$$\nu_k = c_k \Delta k^{1/2} \qquad (6)$$

with $c_k \simeq 0.05$ and $c_\epsilon \simeq 1.05$. This is the one-equation eddy-viscosity model (Yoshizawa (1986)), hereafter referred to as model B1.

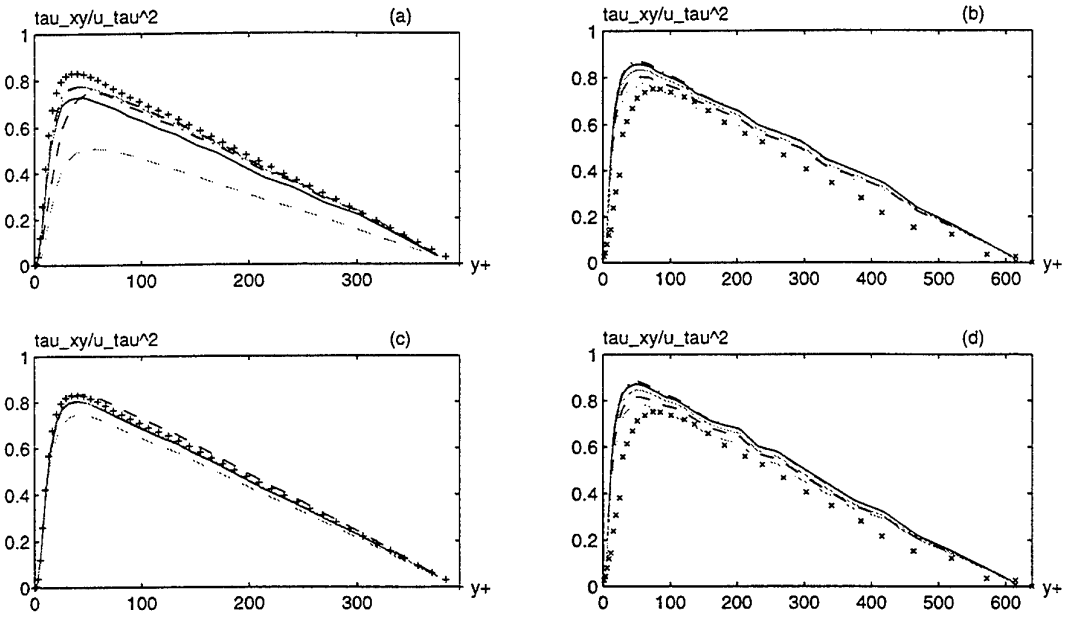


Figure 2: Resolved Reynolds stress T_{xy} (top) and total stress $T_{xy} + \langle B \rangle_{xy}$ (bottom) for the various SGS models. The left hand column is for $\mathcal{R}e_\tau = 395$, the right hand one $\mathcal{R}e_\tau = 640$. Legends as for Figure 1.

Traditionally, additional modifications to the SGS viscosity expressions in (5) and (6) have been included. Most common are damping functions of van Driest type, e.g. Moin and Kim (1982), or wall functions for very high $\mathcal{R}e$. These modifications are motivated either by the desire to account for near-wall effects, or to ensure the proper asymptotic behaviour for the SGS shear stresses in the neighbourhood of the wall. We have experimented with adding such damping functions to models A1 and B1, but have found that they degrade rather than improve the results, as well as running counter to the idea of this paper. This approach will therefore not be discussed further in this paper.

Another approach to the modelling of anisotropic turbulence is that of the dynamic model, first suggested by Germano et al. (1994). The idea here is to sample information on the GS level to evaluate the model coefficients by filtering (1) a second time with a kernel of width $\Delta' > \Delta$. There are several possible ways to proceed. The conventional approach utilises the Germano identity to construct an overdetermined system, which, after additional simplifications, can be solved to determine the model coefficients. This has been applied to evaluate c_I and c_D in model A1 to produce model A2. The drawback of this procedure is that additional averaging, either in homogeneous directions, along streamlines or in local regions of the flow (the method used here), is necessary to avoid excessive fluctuations in the resulting model coefficients. An alternative approach has recently been proposed by Kim and Menon (1995), in which the scale similarity assumption is used to derive expressions for the model coefficients. This has been applied to evaluate c_k and c_ϵ in model B1 to produce model B2.

Full SGS Stress Equation Models

An alternative to modelling $\mathbf{B}$ using the eddy viscosity concept is to solve the full differential stress equation (3). Such a model is more likely to be able to cope with grid or flow anisotropies. In order to complete the model we must model the terms $\mathbf{M}$, $\mathbf{\Pi}$ and $\mathbf{E}$ in equation (3). The first successful attempt was made by Deardorff (1973); we use a variant of this model in which $\mathbf{M}$ is approximated by a gradient hypothesis, as $\nabla.(\nu_k \nabla \mathbf{B})$. The pressure velocity-gradient term $\mathbf{\Pi}$ is split into a return to isotropy term $\mathbf{\Pi}^{(1)} = -c_M k^{1/2} \Delta^{-1} \mathbf{B}_D$ and a mean strain term $\mathbf{\Pi}^{(2)} = \frac{2}{5} k \overline{\mathbf{D}}_D$, whilst $\mathbf{E} = -\frac{2}{3}\epsilon \mathbf{I}$. This is model C :

$$\partial_t \mathbf{B} + \nabla.(\mathbf{B}_\otimes \overline{\mathbf{v}}) = \mathbf{P} + \nabla.(\nu_k \nabla \mathbf{B}) \\ -c_M k^{1/2} \Delta^{-1} \mathbf{B}_D + \frac{2}{5} k \overline{\mathbf{D}}_D - \frac{2}{3}\epsilon \mathbf{I}, \quad (7)$$

where $\nu_k = c_k \Delta k^{1/2}$, $\epsilon = c_\epsilon k^{3/2} \Delta^{-1}$, $c_k \simeq 0.07$, $c_M \simeq 4.15$ and $c_\epsilon \simeq 1.05$. Note that by combining the terms $\mathbf{\Pi}^{(1)}$ and $\mathbf{E}$, a generalised dissipation tensor of the form $-\frac{\sqrt{k}}{\Delta}(c_M \mathbf{B}_D + \frac{2}{3} c_\epsilon k \mathbf{I})$ is generated. This can be reformulated in terms of the SGS anisotropy tensor $\mathbf{A} = k^{-1}\mathbf{B} - \frac{2}{3}\mathbf{I}$, to yield $\mathbf{\Pi}^{(1)} + \mathbf{E} = -\epsilon(\frac{c_M}{c_\epsilon}\mathbf{A} + \frac{2}{3}\mathbf{I})$. Consequently, the effective dissipation is tensorial and linearly dependent on $\mathbf{A}$, thereby providing an improved treatment of flow and grid anisotropies.

Computational Details

In this study we use a second-order-accurate energy-conserving finite-volume code in which the pressure-momentum system is decoupled using the PISO method. The momentum equation is discretised in time using the Crank-Nicholson scheme, which is second-order accurate. The resulting system is solved using the Conjugate Gradient method with incomplete preconditioning. Simulations have been performed on a range of Reynolds numbers up to $\mathcal{R}e_\tau = 1280$: results are presented here for $\mathcal{R}e_\tau = 395$ and $\mathcal{R}e_\tau = 640$. To minimise the computational cost a small domain is preferable : we use a channel with dimensions in

wall units of 1580 and 750 in the streamwise ($\mathbf{e}_x$) and spanwise ($\mathbf{e}_z$) directions. A strategy for mesh generation must be devised. The mesh should resolve the buffer layer sufficiently to perform LES of the turbulent structures there, which implies a mesh grading and becoming more two-dimensional towards the walls. However we cannot construct the mesh directly according to these principles. An approximate mesh can be set up, and the details of cell dimension and grading manipulated in order to generate the best possible profiles for the low order statistical moments of the velocity. Good results can be obtained if $\Delta x^+ \simeq 35$, $\Delta z^+ \simeq 20$ and $\Delta y^+ \in [2, 20]$, keeping the aspect ratio below $\sim 10 - 15$ and adopting an anisotropic finite-volume equivalent of the filter in terms of a Laplace operator (e.g. Aldama (1994)). Note that DNS and experimental results indicate that the vortical streaks in the near-wall turbulence have a spacing of ~ 100 wall units, which suggests that our resolution is just adequate for LES. In addition, we have performed calculations using the differential stress model C on a mesh which has been coarsened by a factor of 2 in both the x and z directions, thus reducing the resolution by a factor of 4. The flow is driven by a constant mass flow in the $\mathbf{e}_x$ direction and has periodic boundary conditions in the $\mathbf{e}_x$ and $\mathbf{e}_z$ directions. Comparisons can be made between our LES results and experimental, DNS and other LES data for this case, principally in terms of the first and second order statistical moments $\overline{\mathbf{v}}$ and $\overline{\mathbf{v}}'$, but also in terms of the morphology of the turbulent structures found in the flow. In addition we are able to investigate turbulent structures and the scaling behaviour of the flow at higher $\mathcal{R}e$ than is possible with DNS.

RESULTS

First and Second Order Moments

Some results are shown in figure 1 for various moments of the velocity for $\mathcal{R}e_\tau = 395$ (left hand column) and $\mathcal{R}e_\tau = 640$ (right hand column). The different lines correspond to different SGS models, compared to DNS from Kim et al. (1987), experimental data from Wei and Willmarth (1989) and LES data from Moin and Kim (1982) (hereafter MK), which is plotted using various symbols. The profiles are generated by by time averaging over a time interval of $50h/u_\tau$ for $\mathcal{R}e_\tau = 395$ and $40h/u_\tau$ for $\mathcal{R}e_\tau = 640$, followed by combined streamwise and spanwise averaging over the entire channel : these averaging procedures are denoted $\langle\cdot\rangle$. The profiles were found to be symmetric across the channel centreline to within 0.5%, which demonstrates that the time averaging was sufficient for an adequate statistical sample. Accordingly only half the channel profile is plotted. Only minor differences between the models are apparent for the streamwise component $\langle\overline{v}\rangle_x$ (figures 1a, 1b); these are limited to the wall proximity region $y^+ \leq 90$ (this region contains the viscous sublayer, the buffer layer and part of the logarithmic region. We will refer to the rest of the domain – i.e. the rest of the logarithmic region and the wake region – as the outer region). In the wall proximity region, we generally find that models involving transport equations for $\mathbf{B}$ or k generate better profiles than purely algebraic models such as A1. The profiles generated on the coarser mesh are not significantly different from the refined version, i.e. there is a degree of mesh independence for the first order statistics. We also find that the dynamic models A2, B2 do not provide significant improvements over their non-dynamic counterparts, contrary to the findings of other authors e.g. Germano et al. (1994).

Turbulence intensities are investigated by examining the individual components of the resolvable turbulent stress tensor $\mathbf{T} = \langle\langle(\overline{\mathbf{v}} - \langle\overline{\mathbf{v}}\rangle) \otimes (\overline{\mathbf{v}} - \langle\overline{\mathbf{v}}\rangle)\rangle\rangle$; figures 1c, 1d show profiles of these components for the two different cases. The agreement between our LES and the DNS or experimental data is still good, although variations between different models are beginning to appear. For the $\mathcal{R}e_\tau = 395$ case, model B1 systematically overpredicts the streamwise component T_{xx} by about 8% (spanwise average) compared to the DNS data, an effect which is common to all our models at lower $\mathcal{R}e_\tau$. At $\mathcal{R}e_\tau = 640$, our results overpredict this component compared with MK's LES, but underpredict the experimental profile of Wei and Willmarth (1989). Closer inspection of the wall proximity region reveals that the peak in T_{xx} is in very good agreement with the experimental data both in magnitude and position ($y^+ \simeq 12 - 20$) : the agreement with the MK data is less good (the peak being found to be at $y^+ \simeq 15 - 25$). T_{zz}, T_{yy} are generally flatter than the DNS data would indicate, either due to inadequate spatial resolution, or because too large a fraction of the fluctuations resides in the unresolved scales. However the error is comparable to the difference between DNS and experiment.

Figure 2 shows profiles of the resolvable shear stress T_{xy} (top) and the total shear stress $T_{xy} + \langle\mathcal{B}\rangle_{xy}$ (bottom). At $\mathcal{R}e_\tau = 395$, the resolved fraction of the flow is dominant over the SGS contribution in the wake region, and so there is little difference between the various SGS models. This is not the case in the viscous sublayer and buffer layer, and so there are significant differences between the profiles of T_{xy} in this region. Model C predicts the lowest values of T_{xy} generally. Including the SGS shear stress – the exact value from model C, an estimate from the modelling for the other models – generates very close agreement indeed between the different models and between our models and the literature LES data. Model A2 overpredicts the shear stress, whilst the others agree precisely. At $\mathcal{R}e_\tau = 640$, agreement with the MK data is less good, with the shear stresses (both resolvable and total) calculated to be above the values from the MK data. On the coarser mesh, the difference between our calculated resolvable shear stress and the actual shear stress is more significant, showing that the SGS model represents a significant part of the shear stress when the mesh is coarser. This effect is more significant close to the wall, which is understandable since the mesh coarsening was parallel to the wall. Including the effect of the SGS shear stress improves the agreement with the other models. We note that the differences between models decline as we move into the wake region, again because of the reduced importance of the SGS modelling in this region.

Near Wall Flow

Figure 3. shows profiles of turbulence production (3a, b) and dissipation (3c, d) for the two cases. For LES we can estimate the total production as

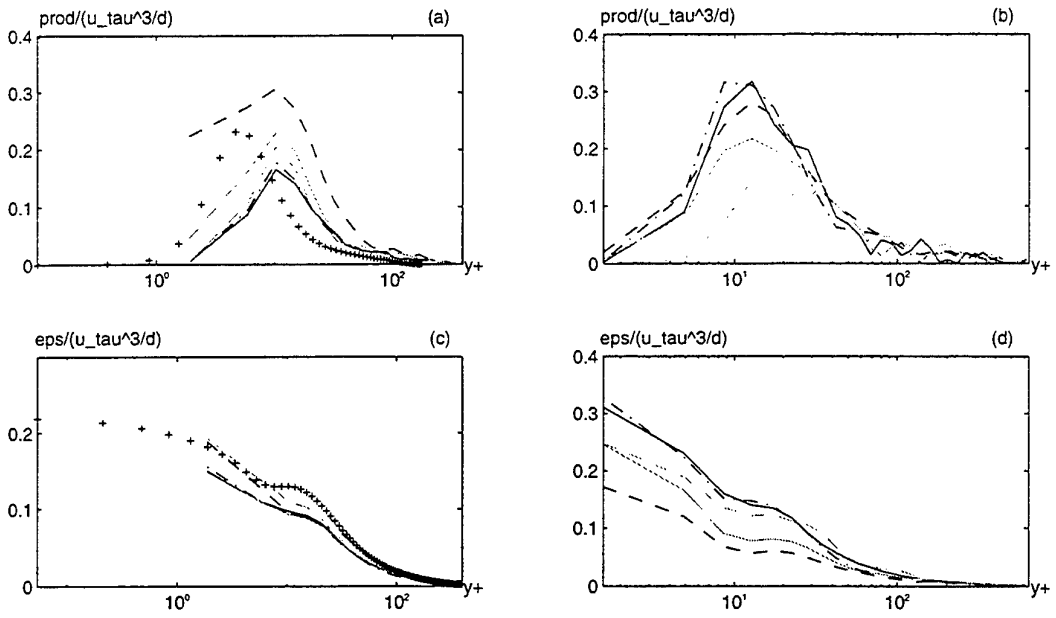


Figure 3: Turbulence production $\langle(\mathbf{T}+\mathbf{B}).\overline{\mathbf{D}}\rangle$ (top) and dissipation $2\nu\langle|\omega'|^2\rangle + \varepsilon_{sgs}$ (bottom). The left hand column is for $\mathcal{R}e_\tau = 395$, the right hand one $\mathcal{R}e_\tau = 640$. Legends as for Figure 1.

$\langle(\mathbf{T}+\mathbf{B}).\overline{\mathbf{D}}\rangle$. For a linear viscous fluid, and assuming isotropy, we can write the dissipation as $\varepsilon = 2\nu\langle|\omega'|^2\rangle$, and again we can estimate the total dissipation from the LES as $2\nu\langle|\omega'|^2\rangle + \varepsilon_{sgs}$. Production and dissipation are third order statistical moments, and so we should expect lower accuracy in our simulations. However these quantities are important for the physics of turbulence in channels, and so we should still examine them. None of the models predict the position of the peak production correctly, although the magnitude is reasonably predicted. Preliminary investigation suggests that this is simply an issue of insufficient resolution in the buffer layer. Models A1 and A2 provide fair estimates of the variation in production across the channel. Models B1 and B2 overestimate the overall production by about 5% (compared with the value from DNS), with the overestimate being as high as 20% in the wall proximity region (Model B1). Model C produces the best estimate, which is probably because this model can deal with non-local and hereditary effects better than the others, as well as its ability to treat anisotropies discussed earlier. Again, calculations on the coarser mesh show little deviation from the common behaviour of all models. All the models considered fail to reproduce the dissipation correctly, as shown in figures 3c, d. We have separately examined the resolved dissipation, which is responsible for around half of the total dissipation, and found that it has the right general behaviour, with a plateau near $y^+ \simeq 20$, but the wrong magnitude. This suggests that the SGS contribution is critically important to the overall dissipation, but is poorly reproduced by all the models considered here. The least inaccurate dissipation profile is generated by model C, indicating that the ability to treat anisotropy effects is important. Conceivably, model C is able to minimise the contamination of the resolved scales by the unresolved scales.

The fact that the wall proximity region is the source for the majority of the production suggests that we should look more closely at the coherent structures in this region. This can be done by examining isosurfaces defining peaks in $\overline{\mathbf{v}'}$ or in the vorticity, which map out the coherent regions close to the walls as streaks with a well-defined spacing. The algebraic models A1 and A2 give a streak spacing of about 130 (in wall units) whilst the one-equation models B1 and B2, and the differential stress model C give a value close to 110. This is in very good agreement with experimental data and DNS, which give values around 100 wall units. However the MK LES gives a streak spacing of around 250 wall units, wildly in excess of our results. The length of the streaks is between 800 and 1000 wall units, and they have diameters of ~20 wall units, again in good agreement with experiment and DNS : these dimensions appear to be fairly independent of SGS model. The mean streak spacing is observed to decrease slowly with increasing $\mathcal{R}e$, whilst their length increases somewhat. This motivates further study of the one-equation and differential stress models. Very close to walls, transport of energy by convection becomes negligable, and so diffusive transport processes will be dominant (Durbin (1993)). One-equation models are able to model the diffusion better, whilst the modelled balance equations for the SGS stress tensor in model C are also able to take account of the anisotropic nature of this diffusion. In more traditional approaches, using a van Driest damping function, the streak spacing is greater, at about 300 and 200 respectively (see also Horiuti (1985)), thereby affecting some of the fundamental physical processes in the near-wake region.

It can be shown that $\mathbf{B}$ must be positive definite and symmetric : in order to be realisable, any model for $\mathbf{B}$ should share these features (Fureby and Tabor (1997)). The necessary and sufficient conditions for this can be expressed in terms of the invariants of $\mathbf{B}$, i.e. $I = \frac{1}{2}\mathrm{tr}\mathbf{B} \geq 0$, $II =$

$\frac{1}{2}((\mathrm{tr}\mathbf{B})^2 - \mathrm{tr}(\mathbf{B}^2)) \geq 0$ and $III = \det\mathbf{B} \geq 0$. The first two inequalities indicate that k must be non-negative, and that the Schwartz inequality must be satisfied. In general these requirements are found to be adequately satisfied for all our models, although for the one-equation and differential stress models (B1, C) $I \geq 0$ has to be artificially enforced in a small fraction of the control volumes, since the discretisation scheme used can spuriously produce negative k when fluid is advected towards large k values. The third inequality is related to the anisotropy of the flow, with $\det\mathbf{B} = 0$ representing the two-dimensional turbulence limit, when one of the eigenvalues will be zero. Only model B2 satisfies $III \geq 0$, with the other models producing non-realisable regions predominantly in the viscous sublayer and buffer layer, the error being significantly smaller for model C than for the others. The affected volumes are small, representing less than 1% of the total volume, and appear to be uncorrelated with flow structures such as rate of strain. However the concentration of realisability errors in the near wall region suggests that the turbulence generation mechanisms in these regions may be incorrectly represented by the models.

CONCLUSIONS

The ability to accurately predict wall-bounded flows is important for engineering applications of LES. Typical approaches to the problem of near-wall flows have involved the introduction of wall functions. However, if we are interested in complex geometries the SGS models used should avoid concepts like 'distance to the wall' or 'wall-normal vectors' since they introduce interpretational problems as well as resulting in untenable behaviour. We have investigated an alternative, which is to refine the mesh perpendicular to the wall in a manner that reflects the anisotropy of near-wall turbulence. We believe that this is a more natural way of coping with the presence of the wall : it has the added benefit of resolving the boundary layer, which may be of interest. Parameters such as wall friction and heat transfer coefficients depend heavily on near wall effects. Furthermore, in many applications it is important to reproduce the interscale energy transfer between the unresolved fraction of the flow and the macroscopic flow. This is known to be difficult using wall models or damping functions of the van-Driest type. For the simple case investigated here, the mesh has been constructed by hand : it is conceivably possible to quantify the requirements for the mesh to be effective near the walls and to combine this with automatic mesh refinement, thus allowing the mesh to evolve during the calculation to optimise the solution.

For this to work, the SGS model must be able to cope with mesh anisotropies as well as flow anisotropies. We have compared two families of models : ones based on an eddy viscosity concept, which implicitly assume isotropy, and models based on a differential SGS stress equation, of which we have picked a simplified version of the Deardorff model. We compare these models on a fully developed turbulent channel at several Reynolds numbers, and find that whilst all the models behave creditably, the differential stress model is better able to model the near-wall flow. The streak spacing is better predicted as well. Finally, we investigate the realisability of all these models, and find that nearly all the models have problems with the third invariant III near the walls. This may be linked to the modelling of the production of turbulence in the buffer layer. In all, we have shown that it is possible to perform very good simulations on wall-bounded flows without wall modelling by producing a near-optimal computational mesh. In addition, whilst the primary influence on the accuracy of the simulations is the mesh, specific parameters of the flow do show differences between the various SGS models.

Acknowledgements

This work is supported by the EPSRC under Grants No. 43902 and K20910. We would also like to thank the Taub computer centre, Technion, Israel, for providing computing resources.

REFERENCES

Aldama, A., 1994 "Leonard and Cross-Term Approximations in the Anisotropically Filtered Equations of Motion", In *Large Eddy Simulation of Complex Engineering and Geophysical Flows*, B.Galperin and S.Orszag, editors, C.U.P., chapter 24, pp. 539 - 557.

Cabot, W., 1995 "Large Eddy Simulations with Wall Models", In *Annual Research Briefs*, Center for Turbulence Research.

Deardorff, J. W., 1973, "The Use of Subgrid Transport Equations in a Three-Dimensional Model of Atmospherical Turbulence", *J.Fluids Engng. Trans ASME*, 156, pp.55.

Durbin, P. A., 1993, "A Reynolds Stress Model for Near-Wall Turbulence", *J.Fluid Mech.*, 249, pp.465 - 498.

Fureby, C. and Tabor, G., 1997 "Mathematical and Physical Constraints on Large Eddy Simulations", To appear in Theor.Comp.Fluid Dyn.

Fureby, C. , Tabor, G. , Weller, H. , and Gosman, A. D., 1997 "A Comparative Study of Sub Grid Scale Models in Homogeneous Isotropic Turbulence", To appear in : Physics of Fluids.

Germano, M. , Piomelli, U. , Moin, P. , and Cabot, W. H., 1994, "A Dynamic Sub Grid Scale Eddy Viscosity Model", *Phys.Fluids A*, 3, pp.1760.

Horiuti, K., 1985, "Large Eddy Simulation of Turbulent Channel Flow by One Equation Modelling", *J.Phys.Soc.Japan*, 54(8), pp.2855 - 2865.

Kim, W.-W. and Menon, S., 1995 "A New Dynamic One-Equation Subgrid-Scale Model for Large Eddy Simulations", Technical Report 95 - 0356, AIAA.

Kim, J. , Moin, P. , and Moser, R., 1987, "Turbulence Statistics in Fully Developed Channel Flow at Low Reynolds Number", *J.F.M.*, 177, pp.133 - 166.

Moin, P. and Kim, J., 1982, "Numerical Investigation of Turbulent Channel Flow", *J.F.M.*, 118, pp.341 - 377.

Smagorinsky, J. , 1963, "Numerical Study of Small-scale Intermittency in Three-Dimensional Turbulence", *Mon.Weather Rev.*, 91, pp.99 - 164.

Wei, T. and Willmarth, W. W., 1989, "Reynolds-number Effects on the Structure of a Turbulent Channel Flow", *J.F.M.*, 204, pp.57 - 95.

Yoshizawa, A., 1986, "Statistical Theory for Compressible Turbulent Shear Flow with the application to Subgrid modelling", *Phys.Fluids A.*, 29(7), pp.2152 - 2164.

A NUMERICAL SIMULATION ON THE INTERACTION BETWEEN TANGLED POLYMERS AND TURBULENT STRUCTURES

Yoshimichi Hagiwara, Yukimasa Takashina, Mitsuru Tanaka and Hidetoshi Hana
Department of Mechanical and System Engineering
Kyoto Institute of Technology
Matsugasaki, Kyoto 606
Japan

ABSTRACT

We have developed a new model representative of tangled polymers by using a cluster of beads and springs. Direct numerical simulation has been conducted for a liquid turbulent channel flow with three clusters. The computational results show that the elongation of polymers and the suppression of polymer diffusion are predicted by the present model. The time derivative of the turbulence energy is found to be affected by the reaction force resulting from the elongation of the cluster. It is found that the vorticity in a small eddy-dominant region is noticeably attenuated by the cluster. This suggests that the development of a small eddy into a large one could be arrested by the tangled polymers.

INTRODUCTION

It is known that the drag for turbulent liquid duct flow is reduced by adding a small amount of specific polymers, such as polyoxyethylene and polyacrylamide, to the flow. In order to clarify the mechanism of the drag-reduction phenomena, Massah and Hanratty (1996) and Kajishima *et al.* (1996) conducted direct numerical simulations. They adopted a finitely extendable nonlinear elastic (FENE) bead-spring as representative of a polymer molecule. It consisted of two beads and a beads-connecting spring with a nonlinear spring constant. They obtained the additional dissipation of the turbulence energy (Massah and Hanratty) and the relaxation of longitudinal vortices (Kajishima *et al.*) due to a number of bead-spring models. These results are useful for understanding the drag reduction of the turbulent flow with polymers.

However, the experimental results on polyoxyethylene solutions under shear flow regions obtained by Miyamoto (1994) cannot be explained by the FENE bead-spring. He discovered that the polymer molecules were tangled in the three dimensions in the form of mesh-like structures. The structures were found to vary with the shear rate, γ, and be kept in the case where γ is up to 1000 [1/s]. No other models have yet been developed for understanding these phenomena.

In the present study, we develop a model that expresses a group of polymer molecules tangled by using a cluster of beads and springs. A direct numerical simulation for the turbulent channel flow is carried out by introducing a cluster into two different eddy-dominant regions and a shear-dominant region. We discuss the deformation of the cluster configuration and the effect of the clusters on the local values of turbulence energy, the vorticity and the shear stress.

COMPUTATIONAL METHOD

Model for Tangled Polymers

Cluster of Beads and Springs. We considered a group of tangled polymers. Visualised images obtained by Miyamoto (1994) showed that the thicker parts of the polymers (hereafter called nodes) were connected by thin straight parts. We assumed that the nodes and the rest are replaced by spherical beads with various sizes and springs with nonlinear spring constant, respectively. It was also assumed that the beads have the same density as that of the solvent and that the springs have no volume. Two neighboring beads were assumed to be connected by the spring. On the other hand, if the distance between two beads was longer than a certain length, l_c, these beads were assumed not to be connected directly by a spring. We recognised the formation and the disappearance of the mesh-like structure by adding and subtracting springs between two nodes, respectively. Thus, a cluster of the beads and springs was assumed to represent a group of tangled polymers in the present study. Figure 1 illustrates part of the connection of the cluster.

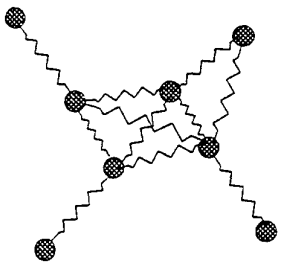


Fig. 1 Cluster of beads and springs

Table 1 Dimensions of computational domain and grid arrangement

case	L_1/h	L_3/h	N_1	N_2	N_3	$\Delta X_1 u^*/\nu$	$\Delta X_2 u^*/\nu$	$\Delta X_3 u^*/\nu$	$Re^*=u^*h/\nu$
Present	4.0	2.0	64	50	48	8.75	1.42～14.0	5.83	140
Suzuki & Kawamura(1994)	6.4	3.2	128	66	128	9.0	0.80～11.8	4.5	180
Satake & Kasagi(1993)	1.25π	0.375π	48	97	36	12.3	0.127～7.63	4.9	150
Rai & Moin(1991)	4π	2π	192	101	192	11.8	NA	5.9	180
Kajishima *et al.*(1996)	7.68	3.84	64	64	64	18.0	0.9～9.0	9.0	150
Massah *et al.*(1993)	12.7	6.33	128	65	128	14.8	NA	7.42	150

Motion of Beads. The drag force, F_D, calculated by the Stokes law of resistance and the restitution force of the spring, F_S, were considered to act on the beads. The equation of motion for the m-th bead is as follows:

$$\rho\frac{4\pi r^3}{3}\frac{\partial U^m}{\partial t} = -F_D^m + F_S^m$$
$$= -6\pi\mu r(U^m - U) + \sum_{n=1}^{M}\frac{k}{1-(l_{mn}-l_{mn0})^2/l_{mn0}^2}\frac{l_{mn0}-l_{mn}}{l_{mn}}(X^m - X^n), \quad (1)$$

where ρ is the bead density, r is the bead radius, U^m and U are the velocities of the bead and the solvent flow respectively, μ is the solvent viscosity, M is the total number of beads for the cluster of polymers, l_{mn} and l_{mn0} are the distance between the bead and the n-th bead and its initial value respectively, X is the coordinate of the bead, and k is the spring constant.

The time increment, Δt, for the discretised expression of Eq. (1) was determined so that the increment was much shorter than the polymer relaxation time (Massah *et al.*, 1993), $\lambda = 6\pi\mu r/k$, and the bead relaxation time, $\tau = \rho(4/3)\pi r^3/6\pi\mu r = 2r^2/9\nu$ (ν is the kinematic viscosity). Therefore, the bead velocity was obtained explicitly by the discretised expression of Eq.(1). The locations of the beads were calculated from the bead velocity thus obtained.

In the present study, r was assumed to be equal to $0.14\nu/u^*$. λ and Δt were set equal to $0.12\nu/u^{*2}$ and $0.00028\nu/u^{*2}$, respectively. We assumed that M was equal to 60 and that the beads and springs for a cluster were initially in a spherical region of $12\nu/u^*$ in diameter. l_c was set equal to $5\nu/u^*$.

Solvent Flow

Momentum Equation. The reaction force to F_D was assumed to act on the solvent flow. The momentum equation of the flow is given as follows:

$$\frac{DU}{Dt} = -\nabla\frac{P}{\rho} + \frac{\mu}{\rho}\nabla^2 U + \frac{1}{\rho V}\sum_{m=1} F_D^m , \quad (2)$$

where P is the pressure and V is a cell volume for the reaction force.

Computational Domain. The present study dealt with a turbulent channel flow of the solvent in a space between two flat plates at the distance of $2h$. The origin of coordinates was on one plate. The X_1, X_2 and X_3 axes were positioned in the direction of the main flow, normal to the plates and in the transverse direction to the main flow, respectively. The Reynolds number based on h and the friction velocity, u^*, was 140.

The computational domain was assumed to be a box of $4h \times 2h \times 2h$. The domain was divided into a total of $64 \times 50 \times 48$ cells. The cell dimension is identical either in the X_1 direction or the X_3 direction. It increases in the X_2 direction based on a geometric progression. The velocity components were defined at the centre of the cell surfaces (hereafter called grid points) and the pressure was given at the centre of the cell. In table 1, the box length, L, the number of grid points, N, the grid spacing, Δ, and the Reynolds number, Re^*, based on u^* and h are compared with the single-phase counterparts used in other simulations using finite difference schemes (Suzuki and Kawamura, 1994; Satake and Kasagi, 1993; Rai and Moin, 1991) and the counterparts with the FENE bead-spring models (Kajishima *et al.*, 1996; Massah *et al.*, 1993).

Discretisation. The second-order central difference scheme based on the interpolation method (Suzuki and Kawamura, 1994; Kajishima, 1994) was applied for the finite differencing of the convection terms of the momentum equations. In the interpolation method, the gradient form of the convection term was evaluated not at the velocity grid point but at half the grid-spacing in the direction of convection from the grid point. Then the interpolated value of two adjacent gradient forms in the direction of convection was assigned at the grid point between the two points where the forms were evaluated. This evaluation satisfies numerical consistency between the mass continuity and the momentum convection. Suzuki and Kawamura (1994) reported that the computational result of low-order turbulence quantities using this scheme shows good agreement with the counterpart obtained using the spectral method. The convection terms for the velocity, U_1, are expressed as follows;

$$U_1\frac{\partial U_1}{\partial X_1}\Big|_{i+1/2,j,k} + U_2\frac{\partial U_1}{\partial X_2}\Big|_{i+1/2,j,k} + U_3\frac{\partial U_1}{\partial X_3}\Big|_{i+1/2,j,k}$$
$$= \frac{1}{2}[(U_1\frac{\partial U_1}{\partial X_1}\Big|_{i+1,j,k} + U_1\frac{\partial U_1}{\partial X_1}\Big|_{i,j,k})$$
$$+ (U_2\frac{\partial U_1}{\partial X_2}\Big|_{i+1/2,j+1/2,k} + U_2\frac{\partial U_1}{\partial X_2}\Big|_{i+1/2,j-1/2,k})$$
$$+ (U_3\frac{\partial U_1}{\partial X_3}\Big|_{i+1/2,j,k+1/2} + U_3\frac{\partial U_1}{\partial X_3}\Big|_{i+1/2,j,k-1/2})]$$
$$= \frac{1}{2}[(\frac{U_1|_{i+3/2,j,k} + U_1|_{i+1/2,j,k}}{2}\cdot\frac{U_1|_{i+3/2,j,k} - U_1|_{i+1/2,j,k}}{\Delta X_1}$$
$$+ \frac{U_1|_{i+1/2,j,k} + U_1|_{i-1/2,j,k}}{2}\cdot\frac{U_1|_{i+1/2,j,k} - U_1|_{i-1/2,j,k}}{\Delta X_1})$$
$$+ (\frac{U_2|_{i+1,j+1/2,k} + U_2|_{i,j+1/2,k}}{2}\cdot\frac{U_1|_{i+1/2,j+1,k} - U_1|_{i+1/2,j,k}}{(\Delta X_2|_{j+1} + \Delta X_2|_j)/2}$$
$$+ \frac{U_2|_{i+1,j-1/2,k} + U_2|_{i,j-1/2,k}}{2}\cdot\frac{U_1|_{i+1/2,j,k} - U_1|_{i+1/2,j-1,k}}{(\Delta X_2|_j + \Delta X_2|_{j-1})/2})$$
$$+ (\frac{U_3|_{i+1,j,k+1/2} + U_3|_{i,j,k+1/2}}{2}\cdot\frac{U_1|_{i+1/2,j,k+1} - U_1|_{i+1/2,j,k}}{\Delta X_3}$$
$$+ \frac{U_3|_{i+1,j,k-1/2} + U_3|_{i,j,k-1/2}}{2}\cdot\frac{U_1|_{i+1/2,j,k} - U_1|_{i+1/2,j,k-1}}{\Delta X_3})], \quad (3)$$

where U_2 and U_3 are the velocity components in the X_2 and X_3 directions, respectively. The second-order central difference scheme without the interpolation method was applied for the finite differencing of the viscous terms of the momentum equations.

Using the successive over-relaxation method, the velocity components and the pressure were simultaneously adjusted so that

the conservation of mass was satisfied.

The third-order Adams-Bashforth scheme was used for the time integration of the discretised equations because the scheme has very low dispersion errors (Dimas and Triantafyllou, 1994).

In the discretised form of Eq. (2), the reaction force to F_D for each bead was distributed to eight neighbouring centres of cells with a spatial interpolation method. Similarly, the fluid velocity near a bead in the right-hand side of Eq. (1) was estimated from the counterparts at eight neighbouring grid pints with the spatial interpolation method.

Initial and Boundary Conditions. The result of a preliminary computation without the cluster after the flow reached a statistically steady state was adopted as the initial velocity field of the present study. A sinusoidal velocity fluctuation in the three directions superimposed on linear velocity distribution had been given as the initial velocity field for the preliminary computation.

The nonslip condition was imposed on the plates. The complete elastic collision was assumed between the beads and the plate. The periodical boundary condition was given for velocity components and pressure in the X_1 and X_3 directions.

IDENTIFICATION OF TURBULENT STRUCTURE

We identified eddy-dominant regions and shear-dominant regions from the database as the initial condition in order to decide a location for giving a cluster of the beads and the springs to the database. We adopted a zone classification method of turbulent structure developed by Kevlahan (1993) for the search of the regions. The method is based on the values of pressure, speed and the parameter defined by the rate of strain tensor, S_{lm}, and the vorticity tensor, Ω_{lm}, in the following manner:

$$S_{lm}=\frac{1}{2}\left(\frac{\partial U_l}{\partial X_m}+\frac{\partial U_m}{\partial X_l}\right),\quad \Omega_{lm}=\frac{1}{2}\left(\frac{\partial U_l}{\partial X_m}-\frac{\partial U_m}{\partial X_l}\right),\quad \Sigma=\frac{S_{lm}^2-\Omega_{lm}^2}{S_{lm}^2+\Omega_{lm}^2}. \quad (4)$$

The criteria are as follows;

eddy or donor eddies: $\Sigma<-1/3$, $|\Omega|\geq\frac{1}{2}|\Omega|_{RMS}$.

shear: $-1/3\leq\Sigma\leq 1/3$, $|S|\geq\frac{1}{2}|S|_{RMS}$ or $|\Omega|\geq\frac{1}{2}|\Omega|_{RMS}$.

convergence: $\Sigma>1/3$, $|S|\geq\frac{1}{2}|S|_{RMS}$.

streaming: $|u|>u_{RMS}$, $|S|<\frac{1}{2}|S|_{RMS}$, $|\Omega|<\frac{1}{2}|\Omega|_{RMS}$.

RESULTS AND DISCUSSION

Validation of Schemes

The ensemble averages of the mean velocity, the turbulence intensities and the shear stress over space and time for $640\nu/u^{*2}$ were calculated. Figure 2 shows the mean velocity normalised by the friction velocity, $\overline{U}_1^+(=\overline{U}_1/u^*)$, as a function of the wall unit, X_2^+ ($=X_2u^*/\nu$). Figures 3(a), 3(b) and 3(c) indicate turbulence intensities of streamwise, wall-normal and transverse component, respectively.

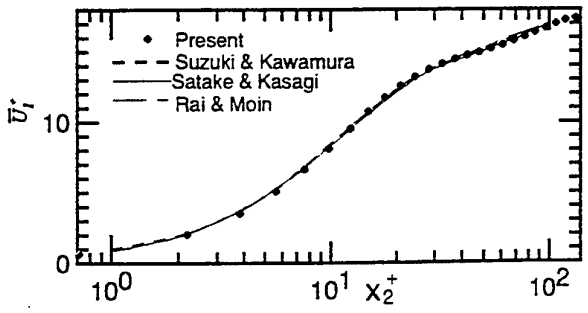


Fig. 2 Mean velocity profile

Figure 4 shows the distribution of the Reynolds shear stress. The present computation results show good agreement with the counterparts in the simulation results of other researchers (Suzuki and Kawamura, 1994; Satake and Kasagi, 1993; Rai and Moin, 1991). These figures suggest that the present computation is validated.

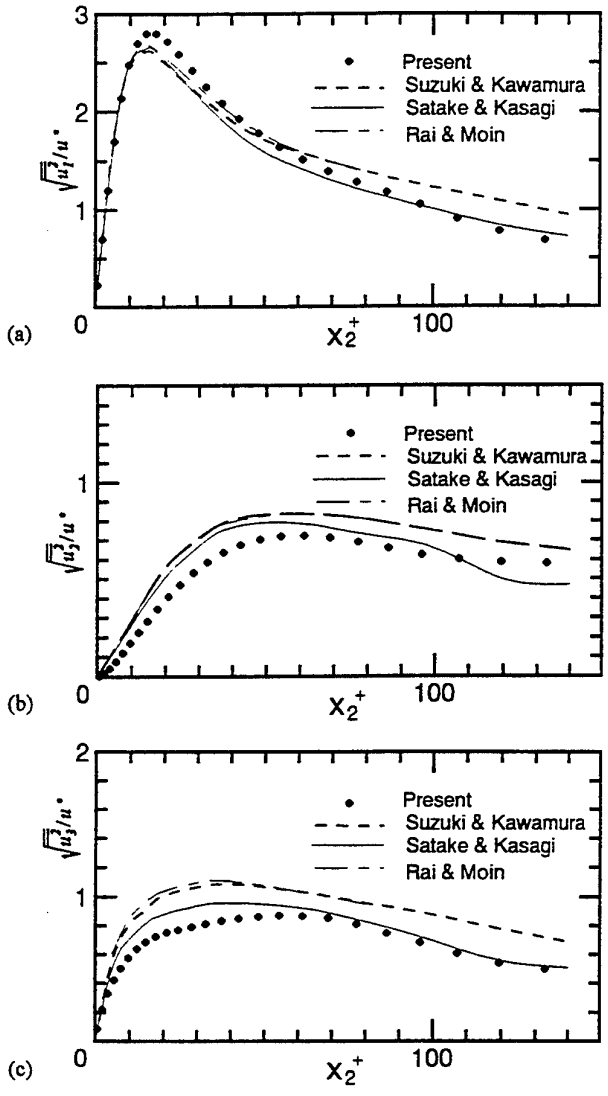


Fig. 3 Turbulence intensities (a) streamwise component, (b) wall-normal component, (c) transverse component

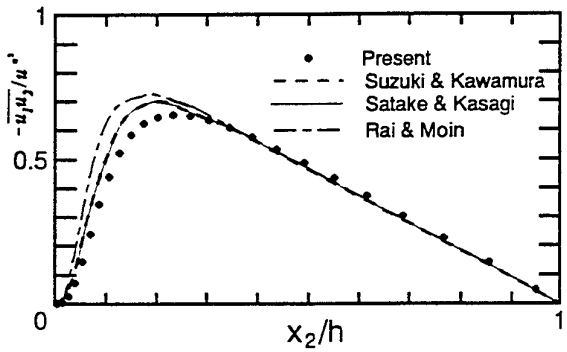


Fig. 4 Reynolds shear stress

Polymers in a Shear-dominant Region

Mean Shear Rate. The centre of the cluster was set at $X_2^+ = 6$ in a shear-dominant region at the initial state. The dimensionless spatial-mean shear, γ^+ ($=\gamma\nu/u^{*2}$) over the initial spherical region for the cluster was 0.78. γ^+ was expected to be smaller than that in the experiment conducted by Miyamoto.

Deformation of Cluster. Figure 5 shows the location of the beads. Figure 5(a) illustrates the initial position of the beads in a shear-dominant region. The positions of the beads at t^+ [$= tu^{*2}/\nu$] = 2.8 are shown in Fig. 5(b). Almost all the beads in this figure are found to be concentrated in a specific region. The rest of the beads represent the break of polymers. In Fig. 5(c), the positions of the beads at the same time are shown for the case without any interaction between the beads and the solvent flow. The beads in this case are considered as tracer particles. The tracer particles are found to be diffused mainly in the streamwise direction. This is due to the mean shear of the flow. By comparing Fig. 5(b) with Fig. 5(c), the diffusion of the beads was found to be suppressed by the springs.

Forces Due to Cluster. Figure 6 depicts time change in the summation of the reaction force, F_{Di}^+ (i=1,2,3) [$=\sum_{m=1} F_{Di}^m/\rho\nu^2$] due to the beads in a cell downstream of the initial location of the cluster (hereafter called monitoring cell). When t^+ was equal to 1.1, the centre of the cluster passed through the centre of the monitoring cell. The summation of the reaction force in each direction became stronger as the cluster approached and then deteriorated after the cluster passed through the monitoring cell. The reaction force in the X_2 direction was always the strongest among three forces.

Time Derivative of Turbulence Energy. Time derivative of the turbulence energy is expected to be affected by the forces due to the cluster, based on the equation of the turbulence energy, K [$= u_iu_i/2u^{*2}$], at a time written as follows:

$$\frac{\partial K}{\partial t} = -U_i\frac{\partial K}{\partial X_i} + (Pro) + (Diff) - (Diss) + \frac{1}{\rho V}\sum_{m=1} F_{Di}^m u_i \ , \qquad (5)$$

where (*Pro*), (*Diff*) and (*Diss*) represent the production, diffusion and dissipation terms of the turbulence energy, respectively. Figure 7 indicates the dimensionless time derivative of the turbulence energy, $\partial K^+/\partial t^+$, at the monitoring cell as a function of time for the cases with and without the cluster. It is found that a tendency of decreasing in $\partial K^+/\partial t^+$ was attenuated during which the aforementioned reaction force acted on the flow. This is because the last term in Eq.(5) took positive values during the period, which is mainly caused by positive values of u_2 and high positive values of F_{D2} shown in Fig. 6.

The decreasing tendency of the time derivative was enhanced after the cluster passed through the monitoring cell and the reaction forces became zero. It is expected that diffusion or dissipation of turbulence energy contributes to the change in the tendency. This suggests that the force due to the cluster exerts an influence of turbulence structure in the shear-dominant region.

Polymers in a Large Eddy-dominant Region

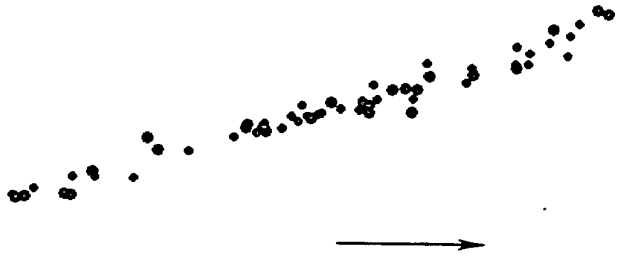
Deformation of Cluster. The centre of the cluster was set at $X_2^+ = 33$ in a large eddy-dominant region at the initial state. Figure 8 illustrates the positions of the beads in an eddy-dominant region at $t^+ = 2.8$ with the counterpart of the tracer particles. The darker and brighter spheres in the figure represent the beads and the tracer particles, respectively. Noticeable deformation of the cluster



(a) $t^+ = 0$ X_1 direction



(b) $t^+ = 2.8$ X_1 direction



(c) $t^+ = 2.8$, tracer particles X_1 direction

Fig. 5 Location of beads

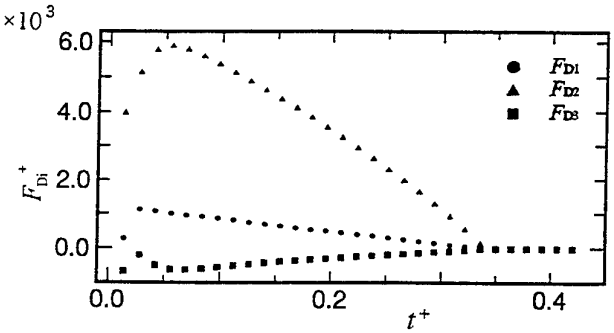


Fig. 6 Time change in reaction force

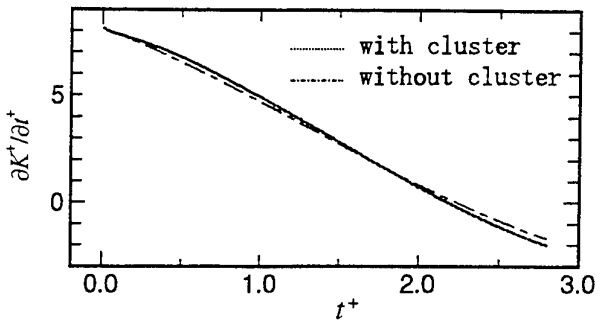


Fig. 7 Time derivative of turbulence energy

seen in this figure. This is because fluid vortical motion in the eddy-dominant structure did not contain strong mean shear effective for the deformation of the cluster.

Forces Due to Cluster. Figure 9 depicts time change in the summation of the reaction force due to the beads in a different monitoring cell in the eddy-dominant region. The summation of the reaction force in each direction shows a similar tendency to the counterpart for the cluster in the shear-dominant structure except the sign of F_{D3}.

Time Derivative of Vorticity. Since the reaction force of each bead was distributed to several centres of cells, the summation of reaction forces to the adjacent cell to the monitoring cell was not the same as that shown in Fig. 9. These forces formed a nonconservative force-field. Therefore, the forces affect vorticity transport. Figure 10 indicates the dimensionless time derivative of the voriticity, $2\partial\Omega_{23}^+/\partial t^+$, at the monitoring cell as a function of time for the cases with and without the cluster. It is found that the time change in $2\partial\Omega_{23}^+/\partial t^+$ was slightly enhanced by the approach of the cluster and that it was attenuated after the cluster passed. This tendency was also obtained for the other vorticity components.

Polymers in a Small Eddy-dominant Region

Deformation of Cluster. The centre of the cluster was set at $X_2^+ = 24$ in a small eddy-dominant region at the initial state. Figure 11 illustrates the positions of the beads in an eddy-dominant region at $t^+ = 2.8$ with the counterpart of the tracer particles. The darker and brighter spheres in the figure represent the beads and the tracer particles, respectively. Similar to the result for the large eddy-dominant region shown in Fig. 8, the cluster was found not to be affected by the small eddy-dominant structure.

Forces Due to Cluster. Figure 12 depicts time change in the summation of the reaction force due to the beads in a different monitoring cell in the small eddy-dominant region. The time variation of F_{D2} was similar to that of the same force in the other cases. On the other hand, F_{D1} showed the opposite tendency F_{D2}, and F_{D3} had little change. These differences in the time change in the forces are considered to be based on the small-scale structure.

Time Derivative of Vorticity. We focused on the vorticity component of $2\Omega_{23}$ which increased through the computation for the case without the cluster. The present small eddy-dominant structure is expected to develop into a larger structure. Figure 13 indicates the dimensionless time derivative of the vorticity, $2\partial\Omega_{23}^+/\partial t^+$, at the monitoring cell as a function of time for the cases with and without the cluster. It is found that the tendency of decreasing in the time derivative was enhanced by the approach of the cluster and that it was attenuated after the cluster passed. These tendencies are more

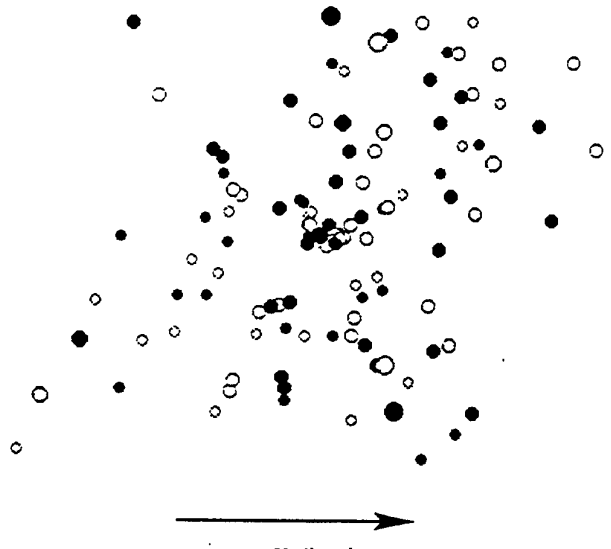


Fig. 8 Location of beads ($t^+ = 2.8$)

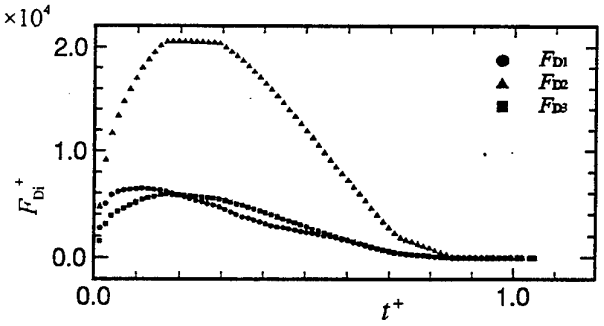


Fig. 9 Time change in reaction force

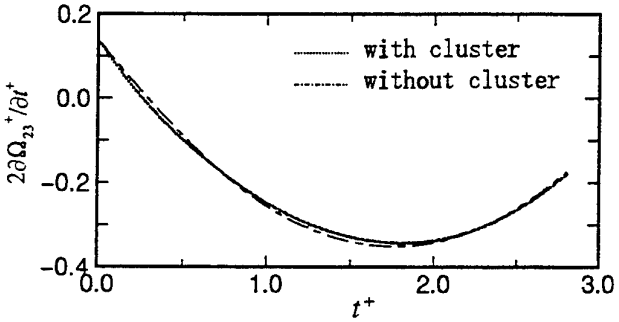


Fig. 10 Time derivative of vorticity

noticeable than the counterparts obtained for the larger eddy-dominant structure. This suggests that small-scale eddies which may be developed into a lager one could be arrested by the tangled polymers.

Spatial Distribution of Vorticity. Figure 14 shows the region (A) of $\Omega_{23}^+ > 17$ in the small eddy-dominant structure and the beads. The regions of lower and higher vorticities due to the beads are also shown in the figure by brighter area (B) and darker area (C), respectively. The lower region of vortices is found to be located around the beads in the neighbourhood of the eddy-dominant structure. This represents local mechanism for small-scale eddies to be arrested by tangled polymers.

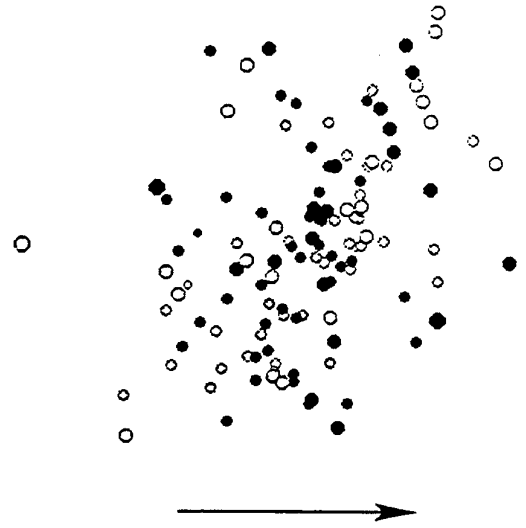


Fig. 11 Location of beads

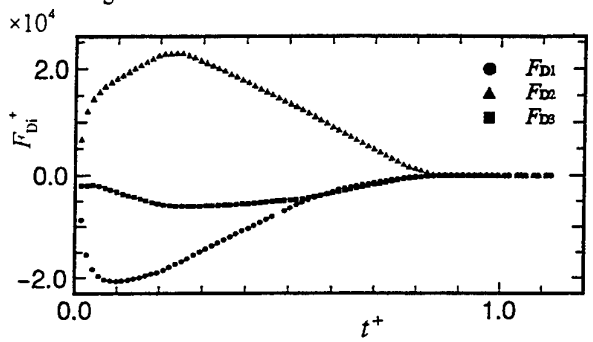


Fig. 12 Time change in reaction force

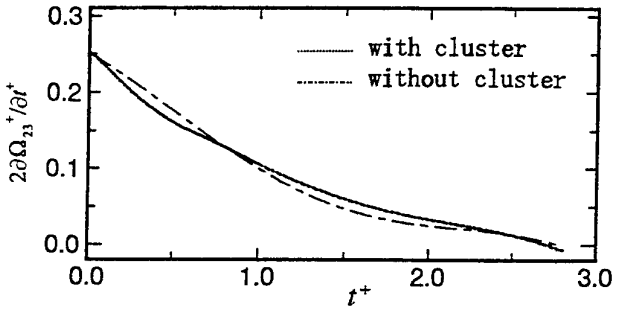


Fig. 13 Time derivative of vorticity

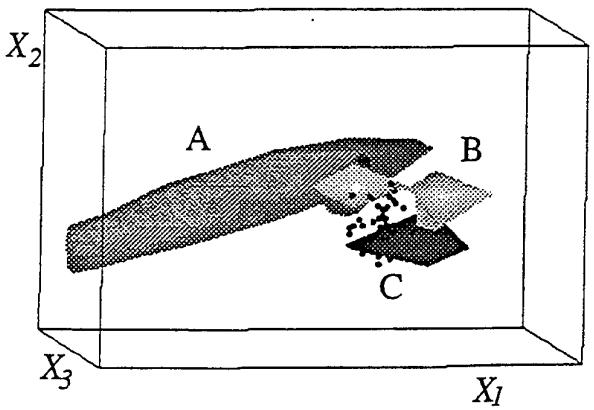


Fig. 14 Spatial distribution of vorticity

CONCLUSIONS

The numerical simulation was carried out for turbulent channel flow with the clusters of beads and springs as representatives of tangled polymer molecules. The main conclusions obtained are as follows.

(1) The elongation of the polymers and the suppression of diffusion of the polymers due to the mean shear of the flow were predicted by our model using the cluster of beads and springs.

(2) The time derivative of the turbulence energy was affected by the reaction force resulting from the elongation of the cluster.

(3) The vorticity was noticeably attenuated by the tangled polymers in a small scale eddy-dominant region. This suggests that the development of a small eddy into a large one could be arrested by the tangled polymers.

The present authors thank Professor M. Maxey at Brown University, USA for his comments on the computational schemes.

REFERENCES

Dimas, A. A. and Triantafyllou, G. S., 1994, "Nonlinear Interaction of Shear Flow with a Free Surface," *J. Fluid Mechanics*, Vol. 260, pp. 211-246.

Gyr, A. and Bewersdorff, H. W., 1995, Drag Reduction of Turbulent Flows by Additives, Kluwer Academic Publishers, Dordrecht.

Kajishima, T., 1994, "Conservation Properties of Finite Difference Method for Convection (in Japanese)," *Trans. Japan Soc. Mech. Eng.*, Vol. 60B, pp. 2058-2063.

Kajishima,T. *et al.*, 1996, "Direct Numerical Simulation of Turbulent Flow of Non-Newtonian Fluid by the Discrete Element Model (in Japanese)," *Proceedings 1st Symp. of Japan Soc. for Comp. Eng. & Sci.*, Vol. 1, pp. 461-464.

Kevlahan, N. K. R., 1993, "Rapid Distortion of Turbulent Structures," *Applied Scientific Research*, Vol. 51, pp. 411-415.

Massah, H. *et al.*, 1993, "The Configurations of a FENE Bead-spring Chain in Transient Rheological Flows and in a Turbulent Flow," *Physics of Fluids*, Vol. A5, pp. 881-890.

Massah, H. and Hanratty, T. J., 1996, "The Implications of Computer Studies of the Behavior of a FENE Bead-spring in a Turbulent Field," ASME *Proceedings FED Summer Meeting 1996*, Vol. 2, pp. 183-190.

Miyamoto, H., 1994, "Experiment for Visualization of Polymer Chains in High-polymer Aqueous Solutions under Shear Flow Regions (in Japanese)," *Trans. Japan Soc. Mech. Eng.*, Vol. 60B, pp. 2038-2043.

Suzuki, T. and Kawamura, H., 1994, "Consistency of Finite-diffence Scheme in Direct Numerical Simulation of Turbulence (in Japanese)," *Trans. Japan Soc. Mech. Eng.*, Vol. 60B, pp. 3280--3286.

IDENTIFICATION OF VORTICAL STRUCTURES BY A NON LOCAL CRITERION: APPLICATION TO PIV MEASUREMENTS AND DNS-LES RESULTS OF TURBULENT ROTATING FLOWS

M. Michard, L. Graftieaux, L. Lollini, N. Grosjean
Laboratoire de Mécanique des Fluides et d'Acoustique
UMR 5509, ECL-UCB-CNRS
Ecole Centrale de Lyon
36, avenue Guy de Collongue
BP 163 - 69131 Ecully Cedex
France

INTRODUCTION

In this study, we present an alternative approach to classical criteria (Weiss 1991, Jeong & Hussain 1995) for the identification and the localization of large vortical structures in turbulent flows. This problem often deals with measurements of instantaneous velocity fields performed by Particle Image Velocimetry (P.I.V.) as well as post-processing of numerical results obtained by Large Eddy Simulations or Direct Numerical Simulations. Identification methods of vortices are often based on dynamic criterion using vorticity, or some quantities related to velocity gradients. The identification method proposed in this paper is based on purely geometrical considerations regarding the flow structure in the neighborhood of the center of a vortex, and is not concerned with dynamical properties of the flow field. The non-local character of the adopted criterion is appropriate to the post-processing of P.I.V. measurements for the following reasons. First, P.I.V. measurements in complex flows may be subjected to the presence of noise, due to the difficulty to ensure a uniform seeding of the flow. Second, the spatial resolution of P.I.V. is generally not sufficient for solving the small scales of the flow. Thus, adjacent velocity vectors may be poorly correlated and any purely local quantity like vorticity may present very high values. These very large values of vorticity can hide the presence of large scale vortical motions embedded in the small scale turbulent field. Moreover, in a large number of flows, there is no reason for correlating regions of high vorticity with the presence of vortices. The efficiency of the present criterion has been tested in a first step on some analytical laminar flows in order to investigate the influence of some computation parameters, like the ratio between the vortex size and the mesh size. Then, we used the criterion in order to characterize in a statistical manner the large scale velocity fluctuations of a strongly turbulent swirling flow obtained downstream of a cylinder head of a internal combustion engine. Finally, the same criterion has been used to identify large scale vortices in D.N.S. of rotating turbulence.

CRITERION'S DEFINITION AND TESTING

Definition

To introduce this quantity, let us first consider the case of a two-dimensional vortex. The basic idea is that we expect streamlines to be closed in the neighborhood of the vortex center, at least in a frame moving with the vortex center velocity. Figure 1 shows an example with a two-dimensional vortex ; $\boldsymbol{r}$ and α denote respectively the radius vector and the angle between $\boldsymbol{r}$ and velocity $\boldsymbol{u}$ at point M. Let P be the center of the vortex and M a point moving along a closed streamline around P. $\sin\alpha$, which is the intensity of the normalized cross-product $\boldsymbol{r} \times \boldsymbol{u}$, generally always keeps a constant sign. The mean value of $\sin\alpha$ along the streamline is either positive or negative but non-zero and is maximum at the center of the vortex. Furthermore, this quantity tends to zero when computed outside the vortex. On the other hand, in the case of a random velocity field where no organized structures exist, $\sin\alpha$ is a zero-mean value.

We generalize this idea for a three-dimensional flow by computing the vector function $\boldsymbol{f}$ given by

$$\boldsymbol{f}(\boldsymbol{x}_p) = \frac{1}{V}\int_{\boldsymbol{x}\in V} \frac{(\boldsymbol{x}-\boldsymbol{x}_p)\times\boldsymbol{u}(\boldsymbol{x})}{|\boldsymbol{x}-\boldsymbol{x}_p|\,|\boldsymbol{u}(\boldsymbol{x})|}d\boldsymbol{x} \qquad (1)$$

where V is a volume surrounding P (see figure 1). This function is called Normalized Angular Momentum (N.A.M.) and its modulus varies in the range $[0:1]$. P.I.V. data are two-dimensional and thus only require the computation of the component of $\boldsymbol{f}$ orthogonal to the measured velocities. Only in a few cases the complete vector $\boldsymbol{f}$ will be needed (three-dimensional numerical data for example). In the following, they will be referred to as $\boldsymbol{f}_{2D}$ and $\boldsymbol{f}_{3D}$ respectively. In the limit of a very small volume V, $|\boldsymbol{f}_{2D}|$

tends towards a characteristic function which value is zero everywhere except at the vortex center where $|f_{2D}| = 1$.

Application to discrete velocity fields

The flow predicted by Direct Numerical Simulations or measured by P.I.V. is discrete and it is thus necessary to modify equation (1). In the following, we have adopted the definition

$$f(P) = \frac{1}{(2N+1)^3} \sum_i \frac{\boldsymbol{r}_i \times \boldsymbol{u}(M_i)}{|\boldsymbol{r}_i| \, |\boldsymbol{u}(M_i)|}. \qquad (2)$$

$(2N+1)^3$ is the number of points M_i in the volume V round the point P. The ability to detect an extremum of $|f|$ will depend on some basic geometrical parameters. These parameters are the characteristic length size of the vortex L, the mesh size L_M and the size L_V of the computational volume. For regular meshes, N is the ratio $L_V/2L_M$. It is the number of layers round the point P and it is an important parameter for the computation of the N.A.M. (see figure2).

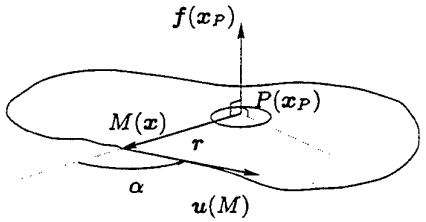


Figure 1: Normalized Angular Momentum : definition sketch.

Tests

The different criteria have been tested on several analytical 2D laminar flows, namely the pure shear, the solid-body rotation and the Taylor-Green vortices. In the case of three-dimensional vortices, we tested the criterion on the spherical Hill's vortex.

The pure shear. We have checked that, in the case of a pure shear flow ($u_x = Sy$, $u_y = u_z = 0$), the criterion is identically zero everywhere (the vorticity is uniform, namely $-S$).

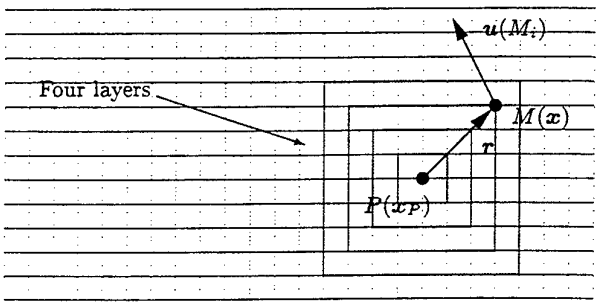


Figure 2: Definition sketch for the computation of N.A.M. on a reduced volume ($N = 4$).

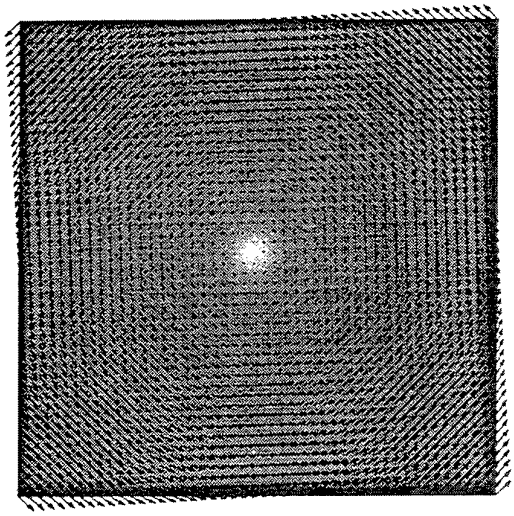


Figure 3: N.A.M. field ($N = 3$) in the case of solid-body rotation.

Solid body rotation. In this case too, vorticity is uniform, whereas the extremum of $|f_{2D}|$ is well correlated with the vortex center location (figure 3).

The Taylor-Green vortices. This test shows the ability of the criterion for identifying the vortices but also points out the influence of the size of the computational domain. The present is done on square Taylor-Green cells, with different computational sizes (N = 1, 2, 4, 6, 8 and 12 layers). Note that, in all these cases, the centers of the vortices are identified but also that the smaller is the computational domain size L_V, the sharpener is the shape of the criterion profile (see figure 4).

The spherical Hill's vortex. For a detailed description of the spherical Hill's vortex, the reader may refer to the books of Panton (1984) or Saffman (1992) for example. Let us say that in such a vortex ring, the one non-zero component of vorticity, namely the ω_θ component, is proportional to distance to the vortex axis. That is to say

$$\omega_\theta = Cr.$$

Thus, in such a flow, vorticity is unable to identify the vortex structure, as it is shown in figure (5), whereas the three-dimensional isosurfaces of the normalized angular momentum clearly mark the vortex structure.

POST-PROCESSING OF P.I.V. MEASUREMENTS

Measurements have been done by P.I.V. in a highly turbulent swirling flow downstream a cylinder head of a internal combustion engine (Michard *al.*, 1996). A set of 3000 instantaneous velocity fields in the plane of the swirl have been measured. In order to be sure that the criterion is able to determine accurately the instantaneous swirl center location, we have in a first step removed the small fluctuating filed by applying a low-pass filter to each measured raw velocity field. An example of filtered velocity field is shown in figure (6), where we compare the spatial fields of vorticity and N.A.M. ($N = 3$). It clearly appears that it is

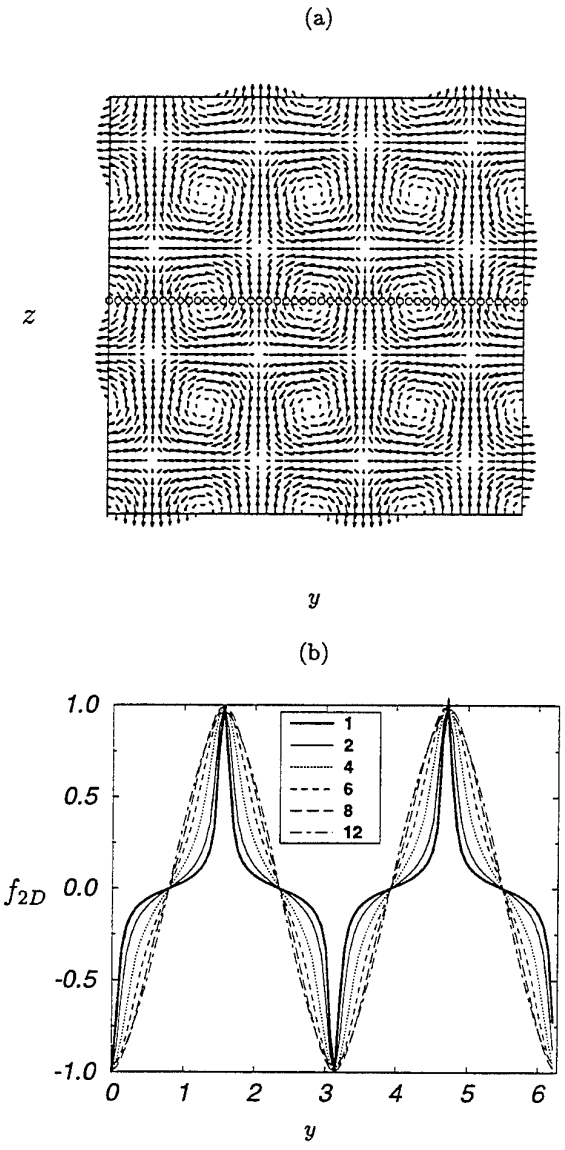


Figure 4: Test on the Taylor-Green cells (a). Profiles (b) along the marked cross section (a) of the one component f_{2D} of N.A.M. for different computational domain sizes (namely 1, 2, 4, 6, 8 and 12 layers).

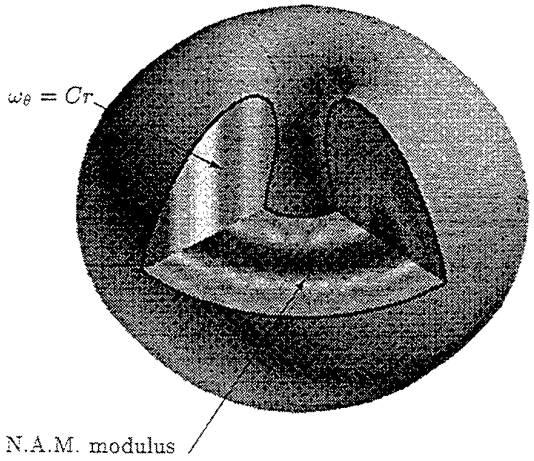


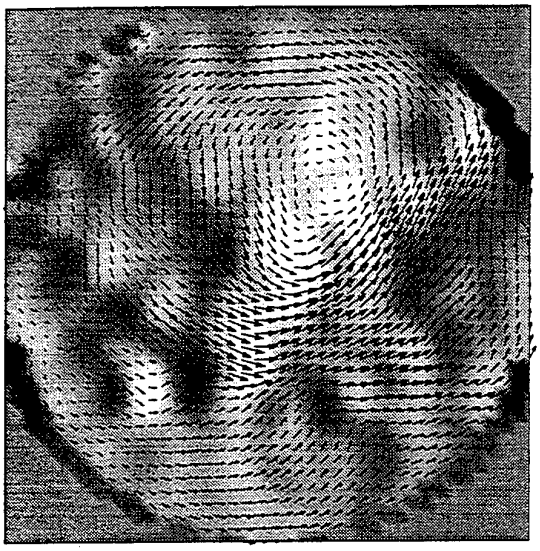
Figure 5: Test on the Hill's spherical vortex. The vorticity has only one component $\omega_\theta = Cr$ where r is the distance to the vortex axis.$0.2 \leq \|f_{3D}\| \leq 0.6$.

not possible to correlate regions of high vorticity with the swirl center position, whereas the maximum of N.A.M. is accurately located at the swirl center location. We compare in figure (7) the spatial repartition of N.A.M. of the raw and filtered velocity fields. This figure shows that the criterion is able to accurately detect the swirl center location of the raw field despite of fluctuations due to the small scale turbulent field. By modifying the parameters of the low-pass filter, we have checked that the measured swirl center location is weakly sensitive to the small scale velocity fluctuations. We present in figure (8) the probability density function of the swirl center coordinates in the plane of the swirl (coordinates have been normalized by the radius R of the duct). The p.d.f. has been computed by applying the criterion to a set of 3000 measured velocity fields. The ratio between the 'root mean square' value of the swirl center coordinates and the radius R of the duct lies in the range 0.22 to 0.25. The shape of the p.d.f. is similar to the results obtained by Volkert *et al.* (1996) in a rapid compression machine used to investigate the interaction of compression and rotation on turbulence. While turbulence levels obtained in this latter experiment are low and the swirl center determination is easy to achieve, the swirling motion in the present experiment is not easy to detect. The results concerning the p.d.f. of the swirl center location are now used in order to estimate the apparent fluctuations caused by the swirl center precessing motion and to correct Laser Doppler Anemometry data with this estimation.

POST-PROCESSING OF NUMERICAL DATA (Direct Numerical Simulations)

The numerical velocity fields are results of DNS of "diffusive" turbulence subjected to solid body rotation. These simulations were undertaken to try to reproduce the experiment of Hopfinger, Browand & Gagne (1982). This experiment was carried out to lead to a better understanding of cyclones genesis under the effect of the Coriolis force. It

(a)



(b)

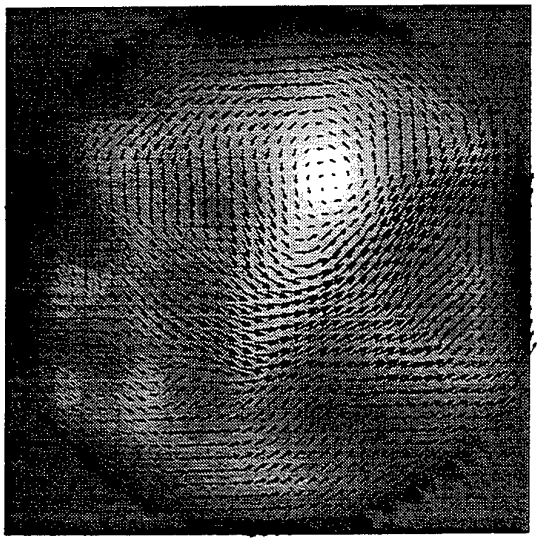
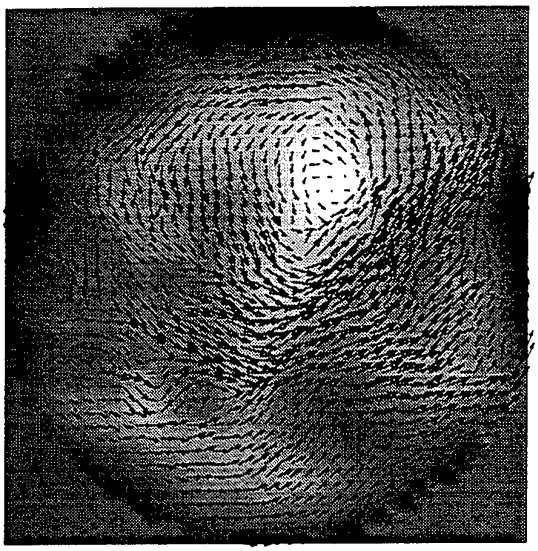


Figure 6: Comparison between vorticity field (a) and N.A.M. field (b) ($N = 3$).

(a)



(b)

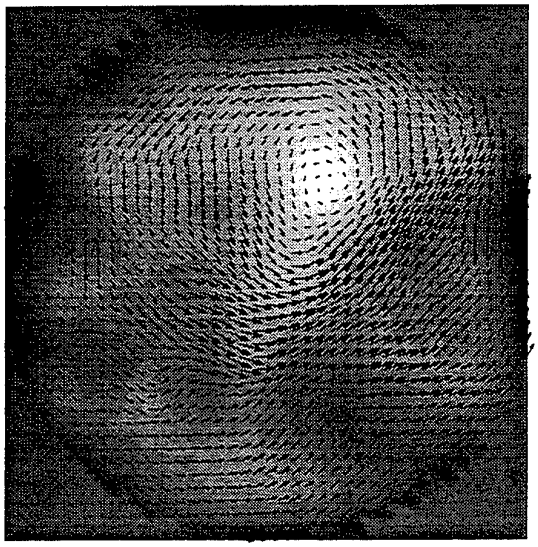


Figure 7: N.A.M. of the raw field (a) and the filtered field (b) ($N = 3$).

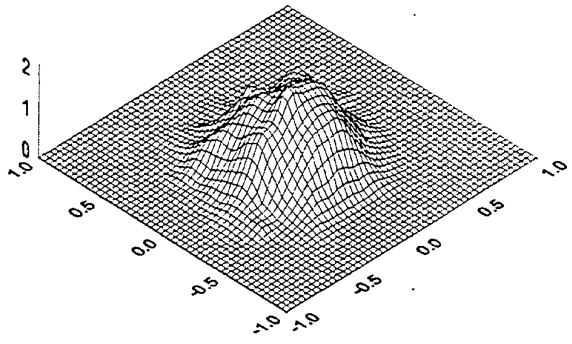


Figure 8: Probability density function of the swirl center location.

has shown that quasi two-dimensional vortices with axes approximatively parallel to the background rotation axis appear (as observed in atmospheric or oceanic flows). The simulation used here were undertaken with a high rotation rate so that the Coriolis force is dominant and we expect many vortices to appear. For further details, the reader may refer to Lollini & Cambon (1996).

It is of great interest for us to characterize these vortices, in terms of number, intensities and cyclonic or anticyclonic characters. We observed that vorticity is not an appropriate tool for localizing the vortices in such a case, and there are two reasons for this. First, as already mentioned for P.I.V. data post-processing, this local quantity may be maximum where the local shear is high and not necessarily at the center of a vortex. Second, the strongly inhomogeneous character of the flow leads to strong spatial variations of vorticity. This is a problem to perform 3D isosurfaces visualizations of vorticity.

In the previous section, we have shown the ability of the 2D criterion for detecting vortices in two-dimensional flows. With our 3D numerical velocity fields, we can now test the complete criterion (see definition 1), which has been used to mark the spherical Hill's vortex structure (figure 5). Figure 9 shows the result of the computation of the N.A.M. modulus on the three-dimensional velocity field. We plotted the vorticity contours on three parallel planes (orthogonal to the background rotation) and isolated two vortices (a cyclonic and an anticyclonic) thanks to the 3D isosurfaces of N.A.M. modulus. Note that even though the two "vortex tubes" are well correlated with the patches of low and high vorticity, vorticity is not smooth enough to determine accurately the vortices locations. Furthermore, this tool is of great interest in this particular case for example because it allows to point out the well known Ekman pumping effect (near the upper wall, the fluid either rising or going down in a anticyclonic or cyclonic vortex respectively).

This identification method will make easier the temporal study of three-dimensional structures like these shown on figure 9. It will allow to follow them in space and time and thus to observe their behaviors and evaluate the characteristic lifetimes of these structures.

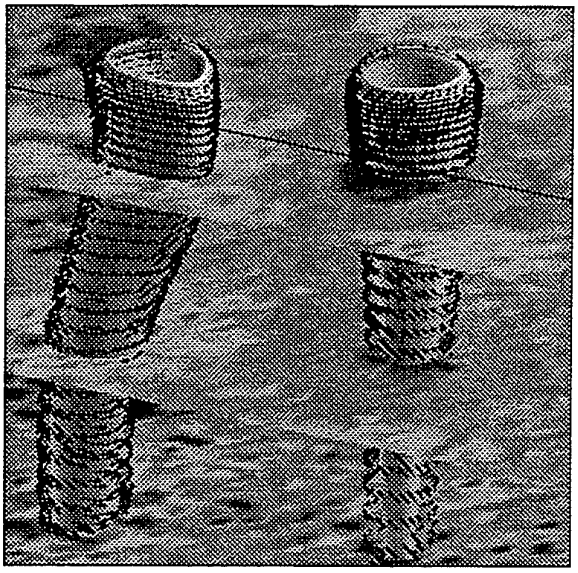


Figure 9: Visualization of N.A.M. modulus on three-dimensional vortices obtained by Direct Numerical Simulation (Lollini & Cambon 1996).

CONCLUSIONS

Measurements noise as well as the poor spatial resolution of P.I.V. data make difficult the computation of local quantities (*e.g.* vorticity). Through its non local character, the Normalized Angular Momentum criterion allows to find with a good accuracy the center of vortical structures, even in strongly turbulent flows. The method is at present used to characterize the precessing motion of a swirling flow over a very large number of PIV velocity fields and different experimental conditions. The N.A.M. criterion is used to characterize in a statistical manner not only the center position p.d.f., but also the spatial extend and intermittency of the swirling motion.

The extension of the criterion for three-dimensional velocity has been successfully undertaken and should identify vortices whatever their orientations (hairpin vortices in turbulent boundary layer for example). An easy and accurate study of organized structures (lifetime, stability, size, motion) could be gained from the implementation of this criterion.

The mathematical properties of the normalized angular momentum defined by equation (1) are under investigation. The first problem is to relate the N.A.M. function properties to the local topology of streamlines in the case of a 2D steady incompressible laminar flow. If the vortices are convected with a velocity which order of magnitude is greater than the order of magnitude of a characteristic velocity inside the vortex, streamlines are not closed and equation (1) needs to be modified. We suggest the following definition

$$\boldsymbol{f}(\boldsymbol{x}_p) = \frac{1}{V}\int_{\boldsymbol{x}\in V} \frac{(\boldsymbol{x}-\boldsymbol{x}_p)\times(\boldsymbol{u}(\boldsymbol{x})-\boldsymbol{u}_C(\boldsymbol{x}))}{|\boldsymbol{x}-\boldsymbol{x}_p|\,|(\boldsymbol{u}(\boldsymbol{x})-\boldsymbol{u}_C(\boldsymbol{x}))|}d\boldsymbol{x}$$

where $\boldsymbol{u}_C(\boldsymbol{x})$ is a local convective velocity given by

$$\boldsymbol{u}_C(\boldsymbol{x}) = \frac{1}{V}\int_{\boldsymbol{x}\in V} \boldsymbol{u}(\boldsymbol{x})d\boldsymbol{x}$$

Acknowledgments

D. Safsaf is gratefully acknowledged for his helpful technical assistance in P.I.V. measurements.

P.I.V. measurements were performed with the Dantec Flowman software with a 1K×1K cross-correlation Kodak camera.

The authors are grateful to Dr. C. Cambon for helpful discussion.

REFERENCES

Hopfinger E.J., Browand F.K. and Gagne Y., 1982, "Turbulence and waves in a rotating tank", *J. Fluid Mech.*, 125:505-534.

Jeong J. and Hussain F., 1995, "On the identification of a vortex", *J. Fluid Mech.*, 285:69-94.

Lollini L. and Cambon C., 1996, "Numerical simulations of inhomogeneous turbulence generated by an oscillating grid and subjected to solid-body rotation", in *Computation and visualization of three-dimensional vortical and turbulent flows*, French-German Workshop, Munich.

Michard M., Simoens S., Grosjean N. and Safsaf D., 1996, "Caractérisation du mouvement de précession d'un tourbillon à l'aide de la Vélocimétrie par Images de Particules", $5^{ème}$ *Congrès Francophone de Vélocimétrie Laser*, Rouen.

Panton R.L., 1984, "Incompressible Flow", John WILEY & Sons.

Saffman P.G., 1992, "Vortex Dynamics", *Cambridge University.*

Volkert J., Tropea C., Domann R. and Hubner W., 1996, "Combined application of Particle Image Velocimetry (P.I.V.) and Laser Doppler Anemometry (L.D.A.) to swirling flows under compression.", 8^{th} *Int. Symp. on Appl. of Laser Techniques to Fluid Mechanics*, Lisbon, July 8-11.

Weiss J., 1990, "The dynamic of enstrophy transfer in two-dimensional hydrodynamics", *Physica*, 273-293.

SESSION 29 - COMPRESSIBLE FLOWS I

MIXING ENHANCEMENT IN SUPERSONIC RECTANGULAR JETS

M. Samimy, J.-H. Kim, and P. S. Clancy
Department of Mechanical Engineering
The Ohio State University
Columbus, Ohio 43210, USA

ABSTRACT

Rectangular nozzles with one modified trailing edge were used to generate large scale streamwise vortices in order to enhance mixing in supersonic jets. The modifications are simple cut-outs in the plane of the nozzle wall, and act to induce streamwise vortices. The mixing performances of a rectangular nozzle, with design Mach number 2 and with various trailing edges, were evaluated using flow visualizations in flow regimes ranging from moderatley overexpanded M_j =1.5 to moderately underexpanded M_j = 2.5. The results indicate that the overall mixing can be significantly increased in underexpanded operating regimes with modifications in just one trailing edge. The results, however, are not as clear-cut in overexpanded flow regimes. The trailing edge modifications do not significantly alter the overall mixing in the ideally expanded flow regime. This is consistent with the hypothesis that only in off-design flow regimes streamwise vortices would be generated due to the induced cross-stream velocity.

INTRODUCTION

It has been known for quite sometime that large scale structures in free shear flows -- ring type rollers in axisymmetric flows and spanwise rollers in two-dimensional flows -- become much less organized and more three-dimensional as the compressibility level is increased (Elliott et al 1992, Clemens and Mungal 1992, and Samimy et al 1992). This results in the loss of entrainment capability of these structures, thus lower gross mixing (e.g. Papamoschou and Roshko 1988), and also in much lower Reynolds stresses (Samimy and Elliott 1990, Goebel and Dutton 1991, and Bonnet et al. 1993) in highly compressible flows. Therefore, it is difficult to use spanwise/ring type large scale structures to control mixing in free shear flows. In contrast, streamwise vortices seem to be unaffected or much less affected by compressibility (Samimy et al. 1993, Zaman et al. 1994, and Reeder and Samimy 1996). Streamwise vortices are generated in highly underexpanded jets due to Taylor-Gortler type instability (Novopashin and Perepelkin 1989, Krothapalli et al.1991, and Arnette et al. 1993). They could also be generated by simple devices such as tabs in not only underexpanded jets but also in the ideally expanded flow regimes (Ahuja and Brown 1989, Samimy et al. 1993, and Zaman et al. 1994). The main thrust of the current work is to generate large scale streamwise vortices using trailing edge modifications in rectangular nozzles in order to enhance mixing and reduce noise in supersonic jets. Since the modifications are on the plane of the nozzle, thus parallel to the flow, it is anticipated that the thrust loss would be much less in comparison with that of the devices such as tabs. In this paper, only the mixing enhancement aspect of the research will be discussed.

Jets from modified axisymmetric nozzles have been studied by Norum (1983), Wlezien and Kibens (1988), and Krothapalli et al. (1990), and from modified rectangular nozzles by Raman (1996). However, all these researchers have concentrated on the noise issue. Detailed flow visualizations and flow measurements are needed to complement the noise results and to explore the effects of nozzle trailing edge modifications on the flow structure and mixing. Such investigations are the goal of the present work.

The work herein is focused on rectangular nozzles because they have superior mixing and noise characteristics relative to axisymmetric nozzles (e.g. Seiner 1991 and Gutmark et al. 1991). For the work presented in this paper, we have chosen a half-nozzle with a splitter plate on one side to ensure that the flow reaches nozzle design Mach number, before approaching the trailing edge modifications (Fig. 1). The design Mach number for the results presented in this paper is Mach 2. The modifications are simple cut-outs in the splitter plate. The optimum cut-out

geometry would be the one that generates a pair of large and strong streamwise vortices with a significant separation distance. Intuitively, this would be a 45° cut-out, and that is the angle of all the cut-outs used to date in this work. In addition, for a Mach 2 jet issuing into ambient air, the convective Mach number is approximately 0.85. This corresponds to an angle of 45° for the most amplified oblique instability according to theoretical work of Sandham and Reynolds (1991).

EXPERIMENTAL FACILITY AND TECHNIQUES

All the experiments were conducted at the Aeronautical and Astronautical Research Laboratory at The Ohio State University. The air, which is supplied by two four-stage compressors, is filtered, dried, and stored in two cylindrical tanks with a total capacity of 42.5 m^3 at 16.5 MPa pressure. The air is then throttled down to the required stagnation pressure using control valves. The air enters the 19 cm diameter and 120 cm long stagnation chamber radially, then turns 90° by a squirter and passes through a perforated plate before entering the nozzle. The rectangular nozzle, with an aspect ratio of 3 (2.54 cm high and 7.52 cm wide), is attached to the stagnation chamber using a specifically designed faceplate which provides a matching profile for the nozzle inlet.

Schematics of the baseline nozzle and the four nozzles with modified trailing edges used in these experiments are shown in Fig. 1. As was discussed earlier, the baseline nozzle is a half-nozzle with a splitter plate of 1 mm thick on one side (Fig. 1a) and the supersonic nozzle of 44 mm thick on the opposite side. The thickness for the other two sides is approximately 19 mm. This design was selected to ensure that the flow reaches the nozzle design Mach number of 2.0, before approaching the trailing edge modifications. The splitter plate modifications are combinations of simple serrations on the splitter plate. The angle of serrations is 45°. Each nozzle was operated at five nozzle pressure ratios corresponding to fully expanded jet Mach numbers of 1.5, 1.75, 2.0 (design Mach number), 2.2, and 2.5.

Cross sectional and streamwise images of the jet were acquired by using the laser sheet illumination technique. The scattering particles are water/ice clusters with diameters on the order of 50 nm that are formed when the moist and warm ambient air is entrained into and mixed with the dry and cold jet air. A beam from the second harmonic (λ = 532 nm) of a frequency doubled Nd:YAG pulsed laser was used as the light source. The pulse width of the laser is 9 nsec, so the flow is effectively frozen while an instantaneous image is acquired. For each case, 50 instantaneous images are collected by an ICCD camera and is stored on the hard disk of a 486 personal computer. Average images are calculated from these 50 instantaneous images.

EXPERIMENTAL RESULTS

Our previous results in the ideally expanded flow regime indicated that the modified nozzle trailing edge geometries had only a slight effect on the overall mixing (Martens et al. 1996), and a negligible effect on the farfield noise (Samimy et al. 1997). However, at off-design conditions nozzles 3 and 4 shown in Fig. 1 seemed to be the most effective from both mixing enhancement and noise reduction view points (Samimy et al. 1997). Therefore, we will concentrate on these two nozzles and compare their performance with the baseline nozzle in the flow visualization results presented below. Since the effect of the modifications was minor for the ideally expanded condition, it is believed that the 45°cut-outs did not trigger nor significantly enhance the oblique instabilities in the mixing layer of the jet, even though, as discussed before, the 45° angle was the optimum angle based on previous theoretical and computational results.

Figures 2 and 3 show the instantaneous images of the jet cross section for the baseline nozzle, nozzle 3, and nozzle 4 at x/D_{eq} = 2 and 8, respectively, for five operating conditions ranging from moderately overexpanded M_j = 1.5 (top row) to moderately underexpanded M_j = 2.5 (bottom row). For these images, the exposure time is the pulse duration of the laser, which is 9 ns, and is short enough to effectively freeze the flow. The images mark the mixing region where the moist ambient air has been mixed with the cold and dry jet air to generate condensed water/ice particles that scatter the laser light. These particles are very small, having a diameter on the order 50 nm, and are expected to follow the flow. These instantaneous images are typical, and all contain structures with scales as large as and often even larger than the average thickness of the mixing layer, and extend quite beyond the instantaneous mixing region, particularly for the x/D_{eq} = 8 case. The overall deformations are relatively stationary for the x/D_{eq} = 2 location, with modified but recognizable jet cross sections. However, in the x/D_{eq} = 8 case, one cannot identify the type of cross section in many of the instantaneous images.

Average images (average of 50 instantaneous images) corresponding to the instantaneous images of Figs. 2 and 3 are shown in Figs. 4 and 5. The deformations of the jet cross sections due to the modifications of the nozzle trailing edge are very distinct and interesting. For the modified nozzles, the direction of the deformations changes from the overexpanded cases to the underexpanded cases. This is intuitive, since the direction of the cross flow (with respect to the axes of the nozzle), changes from overexpanded cases to underexpanded cases as the flow exiting the nozzle passes through either an expansion fan or a compression wave, respectively. The deformation of the baseline nozzle cross section, and the development of the jet cross section between x/D_{eq} = 2 and 8, can be easily understood based on the cross flow established by the trailing edge modifications, and the resultant streamwise vortices due to the cross flow and corner vortices. These images can be used to analyze the mixing characteristics and performance of the modified nozzles from four different view points: 1) the streamwise vortices generated by these modified nozzles, 2) the extent of the average mixing layer, 3) the overall interfacial region between the jet and the ambient air, and 4) the overall mixing region determined from instantaneous images. Each of these will briefly be discussed below.

Figure 6 shows the schematic of the expected distribution of cross-stream velocity component and the resultant streamwise vortices for the baseline nozzle, nozzle 3, and nozzle 4 for both

overexpanded and underexpanded regimes. The hypothesized vortex patterns of Fig. 6 can be identified, to various degree, in Figs. 2-5. Obviously, the magnitude of the velocity and the strength of the associated streamwise vortices would depend on the degree of over- or under-expansion. It is known that a pair of streamwise vortices is generated at each corner of a rectangular nozzle (Zaman 1994). As is seen in Figs. 2-5, the corner vortices are sufficiently strong at $M_j = 2.5$ to substantially deform the jet cross section. It seems that as a result of pairing of each set of adjacent corner vortices by $x/D_{eq}= 2$, only two pairs of streamwise vortices exist at both $x/D_{eq}= 2$ and 8, and they that are stretching the jet along the major axis. The streamwise vortices due to cut-outs are weaker and also much closer to each other in the overexpanded cases, in comparison with the underexpanded cases. This renders them less effective in deforming the jet cross section, except for the $M_j =1.75$ case, in which case the jet is screeching and flapping. Figure 7 shows instantaneous streamwise images on the minor axis plane extending from $x/D_{eq}= 0$ to 4 for nozzles 3 and 4 operating at $M_j = 1.75$. It shows the effects of a pair of streamwise vortices pulling the ambient air into the jet (for nozzle 4) and streching the jet in the normal to the jet axis direction (for nozzle 3) consistent with the schematic of these vortices shown in Fig. 6.

A change in the extent of the average jet mixing layer observed in the images shown in Figs. 4 and 5 would indicate whether the trailing edge modifications have increased or decreased the mixing in the jet mixing layer. However, large scale unsteadiness in the flow would exaggerate the mixing level. For example, images for $M_j = 1.5$ and 1.75 for the baseline nozzle shown in Fig. 5 indicate thicker mixing layer in comparison with that of nozzle 3. However, the jet is screeching and flapping in both these baseline cases (Samimy et al. 1997). Figure 8 shows several instantaneous image of the baseline nozzle at $M_j = 1.75$ that clearly indicate the effects of this flapping motion and the alternating preferential entrainment and mixing in one side or the other on the mixing layer. Because of this flapping motion, the average jet mixing layer thickness may appear to have increased when in actuality the thickness increase is due to the flapping motion.

The trailing edge modifications substantially distort the jet cross section. The extent and the type of distortion depend upon the degree of under- or over-expansion of the jet and the type of trailing edge. Obviously, this distortion increases the interfacial area between the jet and the ambient fluids, and thus increases the mixing between two fluids. It has been shown in subsonic flows that this increase in interfacial region could substantially increase the mixing (Belovich at al. 1996). Thus one could use the circumferential length of the mixing layer as a measure of mixing.

Since the instantaneous images, samples of which shown in Figs. 2 & 3, are digital. One can obtain a semi-quantitative overall mixing performance by determining the overall mixing region for each instantaneous image, then calculating an average overall mixing over 50 images. Figure 9 shows the overall mixing region obtained from 50 sets of images, a set of which is shown in Figs. 2 & 3. To calculate the overall mixing region, a threshold intensity (I_{thresh}) value is determined from the minimum and maximum intensities (I_{min} & I_{max}) in an instantaneous image; $I_{thresh} = I_{min} + 0.05(I_{max} - I_{min})$. When the intensity of a pixel is greater than this value, the pixel is counted as a part of the mixing region. The instantaneous mixing region is obtained by adding all the pixels registering an intensity above the threshold intensity. Then the average overall mixing region is obtained over 50 instantaneous images. It should be noted that this is an approximate measure of the mixing performance of the nozzles, and a good tool for comparison purposes. It is by no means a quantitative technique for mixing measurements. In overexpanded cases, the nozzle trailing edge modifications do not seem to have a significant effect on mixing. In underexpanded cases, both nozzle 3 and nozzle 4 enhance mixing, but nozzle 3 performs much better than nozzle 4. Considering both mixing performance and noise performance, nozzle 3 seems to be superior to nozzle 4. It should be mentioned that vortex generating tabs are also less effective in overexpanded cases (Samimy et al. 1993 and Zaman et al. 1994).

CONCLUSIONS

Rectangular nozzles with one modified trailing edge were used to generate large scale longitudinal vortices in order to enhance mixing and reduce noise in a supersonic jet. These modifications are simple cut-outs in the plane of the nozzle wall, and act to generate streamwise vortices. The cut-outs make a 45° angle with the spanwise direction. Intuitively, this is the optimum angle to generate strong large scale streamwise vortices. In addition, for a Mach 2 jet issuing into ambient air, the convective Mach number is approximately 0.85. This corresponds to an angle of 45° for the most amplified oblique instability. In choosing this cut-out angle, the goal was not only to generate streamwise vortices, but also to excite oblique spanwise structures.

The mixing performances of various trailing edges in a nozzle with design Mach number 2 were evaluated using flow visualizations in flow regimes ranging from moderately overexpanded $M_j =1.5$ to moderately underexpanded $M_j = 2.5$. The results indicate that with modifications made in just one trailing edge, the mixing performance is improved significantly in underexpanded regimes. However, the conclusion is not as straight forward in overexpanded regimes. In the ideally expanded regime, the trailing edge modifications do not significantly alter the overall mixing level. This is consistent with the hypothesis that streamwise vortices are generated only in off-design flow regimes due to the induced cross-stream velocity component.

The work presented herein shows the capability of modified nozzles to enhance mixing in supersonic jets. A better understanding of the complex flowfields associated with the modified supersonic jets is needed to optimize their capabilities. Detailed velocity and vorticity measurements using PDV (Clancy and Samimy 1997), are underway to further explore the physics of these flows.

ACKNOWLEDGMENTS

The support of the research by NASA Lewis Research Center through Grants NAG3-1724 and NAG3-1986 with Dr. K.B. Zaman as the technical monitor is greatly appreciated.

REFERENCES

Ahuja, K.K. and Brown, W.H., 1989, "Shear flow control by mechanical tabs," AIAA Paper 89-0994.

Arnette, S.A., Samimy, M., and Elliott, G.S., 1993, "On streamwise vortices in high Reynolds number supersonic axisymmetric jets," Phys. Fluids A, Vol. 5, 187-202.

Belovich, V. M., Samimy M., and Reeder, M.F., 1996, "Dual Stream Axisymmetric Mixing in Presence of Axial Vorticity," Journal of Propulsion and Power, Vol. 12, No. 1, pp. 178-185.

Bonnet, J.P., Debisschop, J.R, and Chambres, O., 1993 "Experimental studies of the turbulent structure of supersonic mixing layer," AIAA Paper 93-0217.

Clancy, P.S. and Samimy, M., 1997, "Multi-component velocimetry using planar Doppler velocimetry in high speed flows," AIAA Paper 97-0497.

Clemens, N.T. and Mungal, M.G., 1992, "Two- and three-dimensional effects in the supersonic mixing layer," AIAA J., Vol. 30, No. 4, 937-981.

Elliott, G.S., Samimy, M., and Arnette, S.A., 1992, "Study of compressible mixing layers using filtered Rayleigh scattering based visualizations," AIAA J., Vol. 30, No. 10, 2567-2569.

Goebel, S.G. and Dutton, C.J., 1991, "Experimental study of compressible turbulent mixing layers," AIAA J., Vol. 29, 538-546.

Gutmark, E., Schadow, K.C., and Wilson, K.J., 1991, "Effect of convective Mach number on mixing of coaxial circular and rectangular jets," Phys. Fluids A, Vol. 3, No. 1, 29-36.

Gutmark, E., Schadow, K.C., and Yu, 1995, "Mixing enhancement in supersonic free shear flows," Ann. Rev. Fluid Mech., Vol. 27, 375-417.

Krothapalli, A., McDaniel, J., and Baganoff, D., 1990, "Effects of slotting on the noise of an axisymmetric supersonic jet," AIAA J., Vol. 28, 2136-2144.

Krothapalli, A., Buzyna, G., and Lourenco, L., 1991, "Streamwise vortices in an underexpanded axisymmetric jet," Phys. Fluids A, Vol. 3, 1848-1851.

Martens, S., Samimy, M., and Milam, D.M., 1996, "Mixing enhancement in supersonic jets via trailing edge modifications," Proceedings of Fluid Engineering Division Summer Meeting: FED-Vol. 237, Vol. 2, San Diago, California, 485-490.

Norum, T.D., 1983, "Screech suppression in supersonic jets," AIAA J., Vol. 21, No. 2, 235-240.

Novopashin, S.A. and Perepelkin, A.L., 1989, "Axial symmetry loss of a supersonic turbulent jet," Phys. Lett. A, Vol. 135, 290-293.

Papamoschou, D. and Roshko, A., 1988, "The compressible turbulent shear layer: an experimental study," J. Fluid Mech., Vol. 197, 453-477.

Raman, G., 1996, "Screech tones from rectangular jets with spanwise oblique shock-cell structures," AIAA Paper No. AIAA-96-0643.

Reeder, M.F. and Samimy, M., 1996, "The evolution of a jet with vortex-generating tabs: real-time visualization and quantitative measurements," J. Fluid Mech., Vol.311, 73-118.

Samimy, M. and Elliott, G.S., 1990, "Effects of compressibility on the characteristics of free shear layers," AIAA J., Vol. 28, No. 3, 439-445.

Samimy, M., Reeder, M.F., and Elliott, G.S., 1992, "Compressibility effects on large structures in free shear flows," Phys. Fluids A, Vol. 4, No. 6, 1251-1258.

Samimy, M., Zaman, K.B.M.Q., and Reeder, M.F., 1993, "Effect of tabs on the flow and noise field of an axisymmetric jet," AIAA J., Vol. 31, 609-619.

Samimy, M., Kim, J.-H., and Clancy, P., 1997, "Supersonic Jet Noise Reduction and Mixing Enhancement Through Nozzle Trailing Edge Modifications," AIAA Paper 97-0146.

Sandham, N.D. and Reynolds, W.C., 1991, "Three-dimensional simulations of large eddies in the compressible mixing layers," J. Fluid Mech., Vol. 224, 133-158.

Seiner, J.M, 1991, "Fluid dynamics and noise emission associated with supersonic jets," in Studies in Turbulence, Gatski, B., Sarkar, S., and Speziale, C.G. (Ed.).

Wlezien, R.W. and Kibens, V., 1988, "Influence of nozzle asymmetry on supersonic jets," AIAA J., Vol. 26, No. 1, 27-33.

Zaman, K.B.M.Q., 1994, "Effects of delta tabs on mixing and axis switching in jets from axisymmetric nozzles," AIAA Paper 94-0186.

Zaman, K.B.M.Q., Samimy, M., and Reeder, M.F., 1994, "Control of an axisymmetric jet using vortex generators," Phys. Fluids, Vol. 6, 778-793.

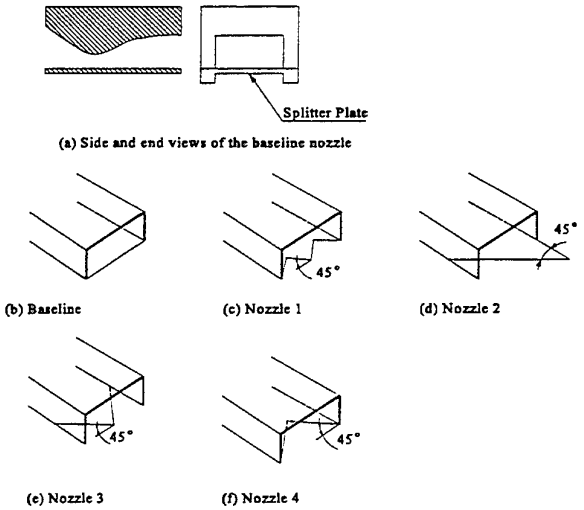
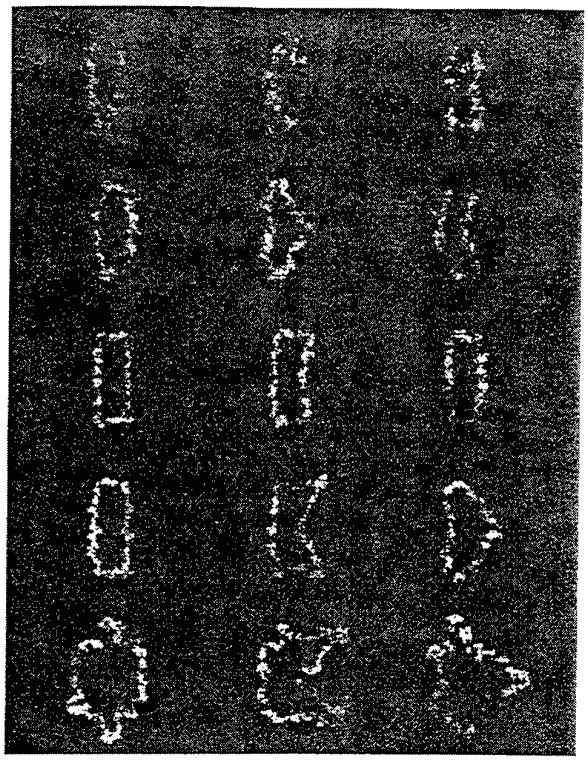
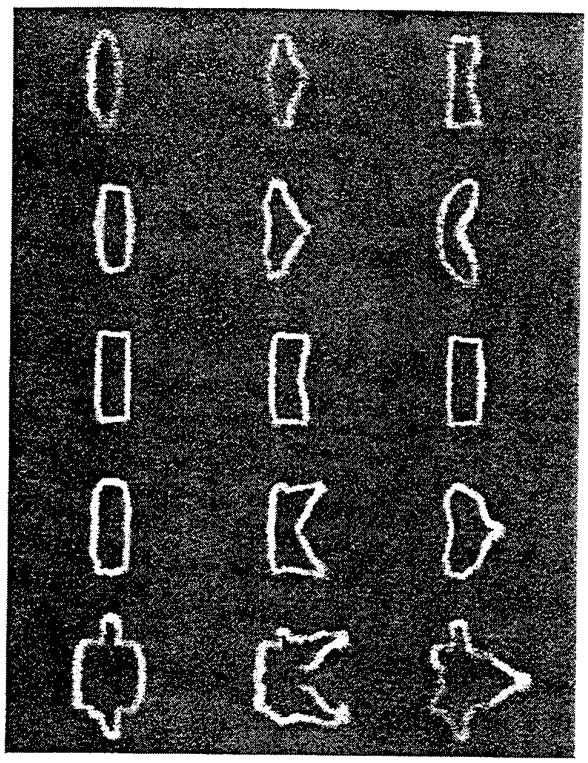


Fig. 1 Schematic of the nozzle configurations (Thick lines represent thick lips in (b)-(f)).



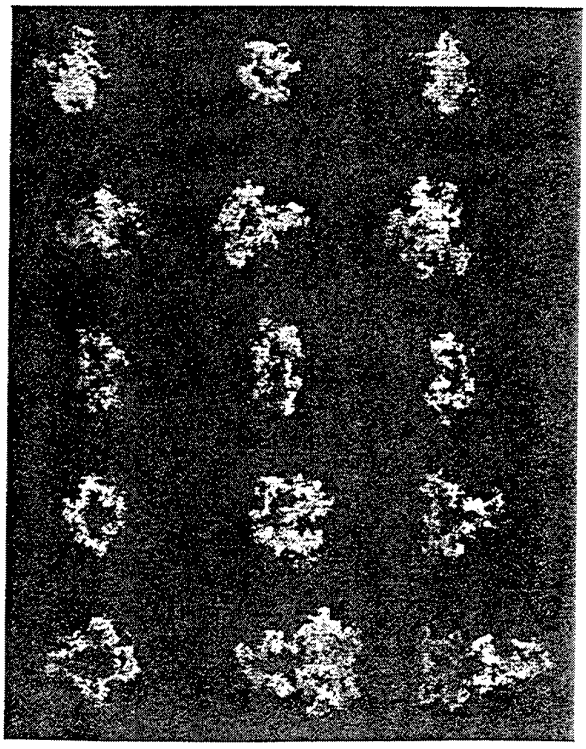
Baseline Nozzle Nozzle 3 Nozzle 4

Fig. 2 Instantaneous cross sectional images at $2D_{eq}$. (Rows 1-5 are for M_j=1.5, 1.75, 2.0, 2.2, and 2.5, respectively)



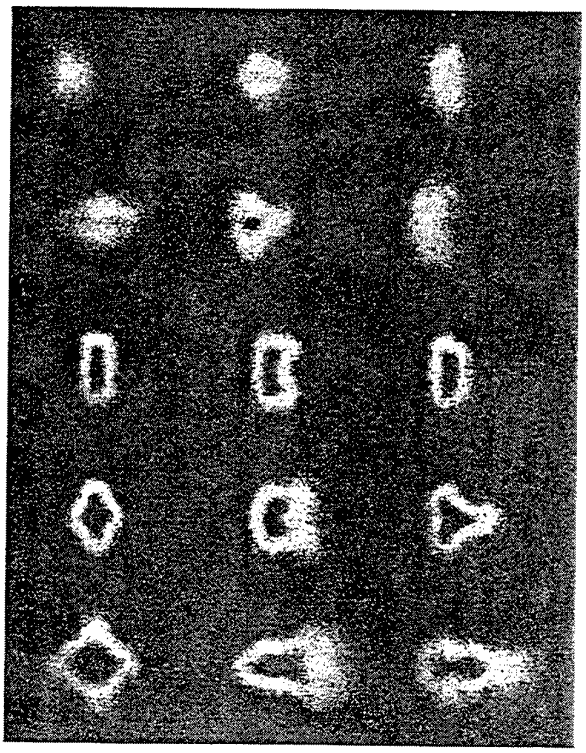
Baseline Nozzle Nozzle 3 Nozzle 4

Fig. 4 Average cross sectional images at $2D_{eq}$.



Baseline Nozzle Nozzle 3 Nozzle 4

Fig. 3 Instantaneous cross sectional images at $8D_{eq}$. The scale of Figs. 2 & 4 relative to Figs. 3 & 5 is 1.6:1.



Baseline Nozzle Nozzle 3 Nozzle 4

Fig. 5 Average cross sectional images at $8D_{eq}$.

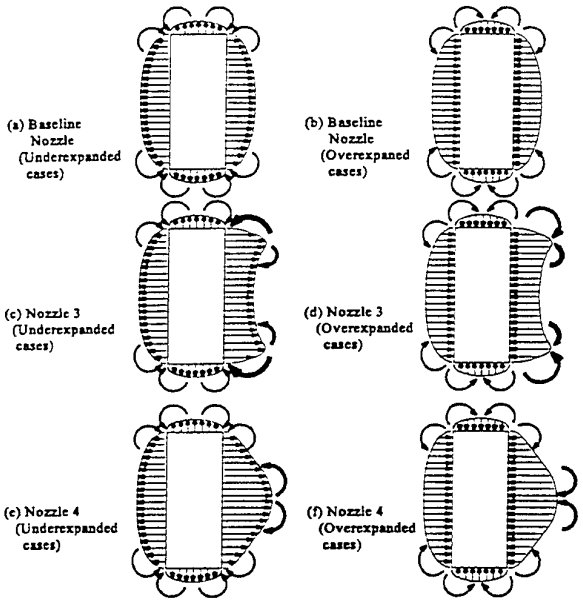


Fig. 6 Schematic of the anticipated cross-stream velocity distributions at the vicinity of the nozzle exit and the expected induced streamwise vortices.

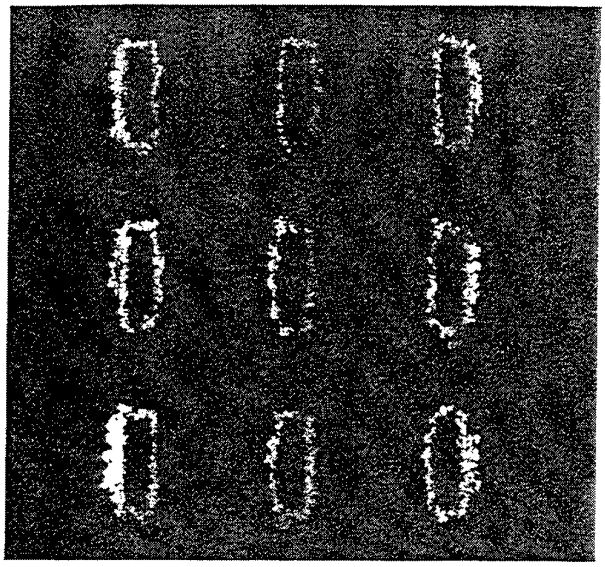
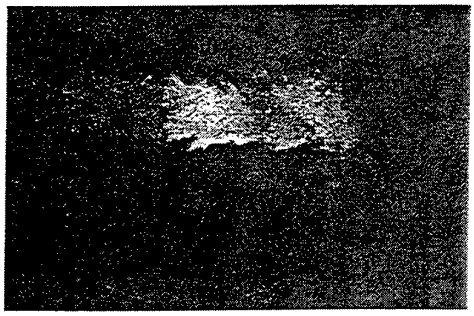
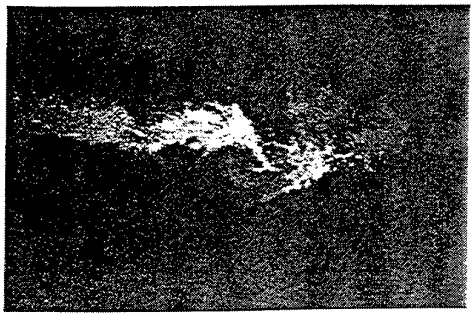


Fig. 8 Instantaneous images showing the effect of flapping motion of the jet for the baseline nozzle at M_j=1.75. Images are not connected in time.



(a) Nozzle 3



(b) Nozzle 4

Fig. 7 Instantaneous streamwise images on the minor axis plane for M_j=1.75 from x/D_{eq} =0 to 4.

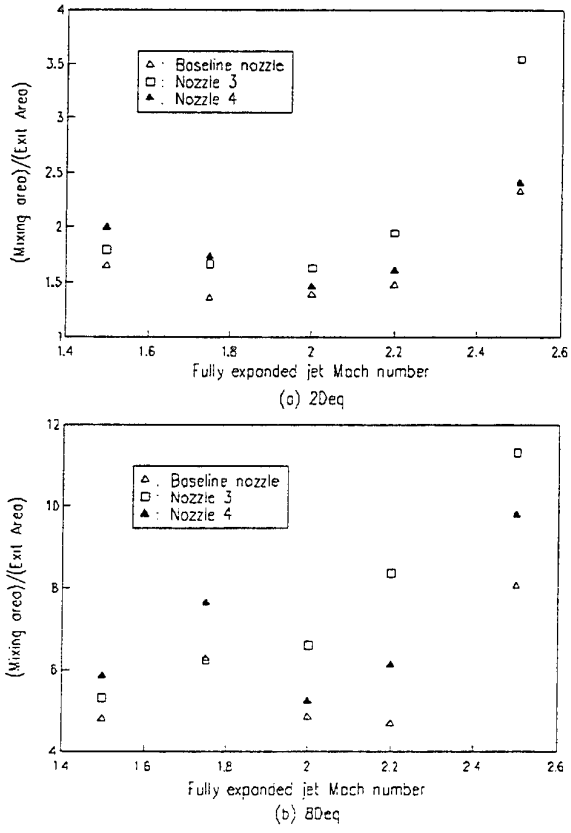


Fig. 9 Variations of mixing regions with the fully expanded jet Mach number at 2 and 8 D_{eq}.

AMPLIFICATION/ATTENUATION OF TURBULENCE IN A HEATED JET/SHOCK WAVE INTERACTION

L. Jacquin, P. Geffroy

ONERA
29 Avenue de la Division Leclerc
92 190 Chatillon
France

See late papers

LOCALIZATION AND ANALYSIS OF LARGE SCALE STRUCTURES BY A WAVELET TRANSFORM TECHNIQUE IN A SUPERSONIC TURBULENT MIXING LAYER

P. Dupont, P. Muscat, J.P. Dussauge

I.R.P.H.E.,Unité Mixte Universités-CNRS 6594

12 Avenue Général Leclerc

Marseille 13003

ABSTRACT

The space time description of the organized structures in a supersonic mixing layer with a convective Mach number of 0.62 is given. Fourier analysis is shown to give only global information. A method based on wavelet transform is proposed to perform a space-time analysis localized in time. It is used to detect and to analyze these structures, in particular to determine the convection velocity associated with large scales. Characteristic time and length scales are given and compared with the scales deduced from the spectral analysis. The results are used to separate the contribution of the large scales to the turbulent signal.

INTRODUCTION

In supersonic and turbulent mixing layers, compressibility causes a drastic reduction of the spread rate, and therefore may affect the properties of the large scale eddies. In subsonic cases it has been shown that periodic structures are developed in the layer and seem to govern its spatial evolution. Previous work (Dupont, Muscat, Dussauge, 1995a, Clemens and Mungal, 1995 among others) has confirmed that these large scale structures remain quasi-periodic in a mixing layer even at convective Mach number of 0.62. As they play a key role in turbulent diffusion and mixing it can be suspected that the behavior of the flow unsteadiness at low frequency is affected by compressibility and contributes to the reduction of the Reynolds stresses and of the mixing process in compressible mixing layers. If many studies have already been carried out on coherent structures in compressible layers, quantitative information on their spatial behavior and their energetic content are limited. Most of experimental results have been obtained by optical methods (visualization by a contaminant in one of the flows, Bonnet et al., 1993, Clemens and Mungal, 1995), and show that their aspect is strongly affected when the convective Mach number is greater than 0.5. In fact, for higher Mach number, it becomes quite difficult, even with planar flow visualizations, to detect the structures (Clemens and Mungal, 1995, Bonnet et al., 1993, Chambre 1997, Samimy et al. 1992) which are no more two dimensional. For this reason, we have developed signal processing tools based on two points measurements to localize and analyze the large scale structures in a supersonic turbulent mixing layer.

EXPERIMENTAL SET UP

A mixing layer with a supersonic-subsonic combination is investigated. The experiment was conducted in the continuous supersonic wind tunnel at IRPHE. The incoming supersonic flow present particularly low levels of pressure or velocity fluctuations (respectively less than 0.8 and 0.3%) which means that acoustic excitations due to the wind tunnel are probably negligible. The subsonic flow presents levels respectively equal to 0.8 and 1%. The initial supersonic boundary layer is turbulent and fully developed. The convective Mach number is 0.62. It was controlled that in the explored part of the flow, the mixing layer is also fully developed. Presented measurements were realized at a distance of 400 times the initial momentum thickness θ_0. Main parameters of the flow are reported in the following table :

M_1	M_2	s	q	Mc	θ_0(mm)	R_δ
1.83	0.38	0.26	0.65	0.6	0.73	$8.7\,10^4$

where s and q are respectively the velocity and density ratio.

Two-point measurements were performed with Dantec « Streamline » constant temperature hot-wire anemometers. The bans width of the anemometers was of 100 kHz. The longitudinal separation of the probes ξ, was about the half of the thickness of the layer (δ_ω=23.8 mm, ξ=9 mm). As a characteristic convection time is $\xi/U_C \approx 20\mu s$, signals were sampled at a frequency of 1MHz and up to $1.2*10^6$ points per channel were acquired.

SPECTRAL ANALYSIS

It has been shown (Dupont, Muscat, Dussauge, 1995a) that there are peaks at characteristic frequencies f_c on the power

spectral density (Figure 1) : they were understood as the indication of quasi periodic structures at large scale. The Strouhal number deduced was $S_t=f_c\delta/U_c\approx 0.18$, where U_c is the isentropic convection velocity.

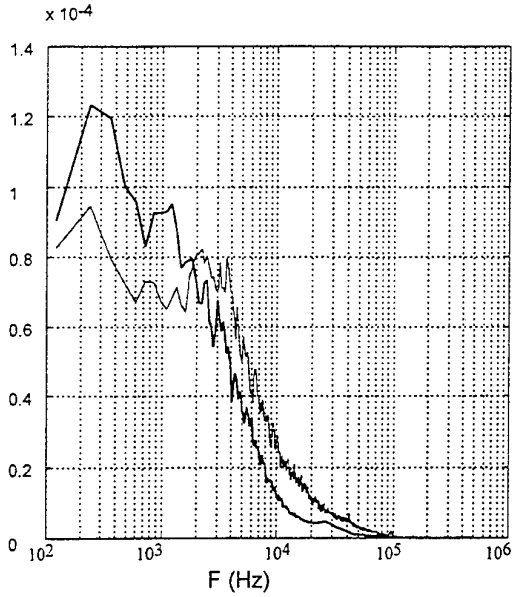


Figure 1 : Power Spectral Density (PSD) of the turbulent signal —— ; of the convection velocity, ——— near the supersonic edge of the mixing layer ; x=280mm

The experimental determination of the dispersion relationship provided the measurement of the group velocity U_g. Two behaviors have been observed across the layer, depending on the frequency range. For frequencies around f_c, U_g was found to keep a value close to the isentropic convection velocity U_c, while higher frequencies have a group velocity which is between the isentropic velocity and the mean local velocity. This suggests the existence of two media, one following Taylor's hypothesis, and the second one keeping a constant convection velocity. Then, the knowledge of the instantaneous convection velocity of the fluid motions can lead to identify the passage of the large eddies. Classically, convection velocity can be deduced from the space time intercorrelation function $R(\xi,\tau)$ or from its Fourier transform. Now, a similar information is required, but localized in time, and a new intercorrelation function of time should be defined : $R(\xi, \tau, t)$. Its properties should be comparable with $R(\xi,\tau)$:

$$R(\zeta,\tau)=\int R(\zeta,\tau,t)dt$$

The wavelet transform is used to define this localized intercorrelation function and to separate the information relative to the energetic scales, and to select parts in the signal depending on their convection velocity.

ANALYSIS OF THE COHERENT STRUCTURES

Localized space-time intercorrelation

When two-point measurements are considered, wavelet coefficients computed at a given scale a can be used as a time series to consider only this scale in the signal and then to apply classical signal analysis (Wang, Brasseur, Smith and Smits 1994). It is also possible to build for each signal a variance $E_{l,x}$ localized in time and scale (Daubechies, 1992) :

$$E_{l,x}(t,a)=C_\psi^{-1}\frac{|W_x(t,a)|^2}{a^2}$$

where $W_x(t,a)$ is the wavelet coefficient at scale a and time t of the signal in spatial position x. C_ψ is a characteristic constant of the generating wavelet.

Liandrat (1995), improves the localization by accounting for the influence cone of the wavelet . He defines a local mean variance on the finite temporal support of all dilated wavelets $\chi_a(t)$:

$$E_{m,x}(t,a)=E_{l,x}(t,a)\otimes\chi_a(t)$$

where $\otimes$ denotes the convolution operator.

We generalized this last approach to define a quantity equivalent to a cross-correlation function localized in time and scale (Muscat et al., 1997):

$$C(t,\tau,\xi,a)=C_\psi^{-1}\mathrm{Re}\left[W_x(t,a)W^*_{x+\xi}(t+\tau,a)\right]\otimes\chi_a(t)$$

where the symbol * denotes the complex conjugate. In turbulent signals with large bandwidth spectra, it is not sufficient to take into account only one time scale. If Σa is the band of considered time scales $[a_{min}\ a_{max}]$, we define :

$$C(t,\tau,\xi,\Sigma a)=\int_{a_{min}}^{a_{max}}C(t,\tau,\xi,a)da$$

$C(t,\tau,\xi,\Sigma a)$ is the contribution of the time scale band Σa, at time t, to the total correlation $C(\tau,\xi)$. Then the localized cross-correlation coefficient is :

$$R(t,\tau,\xi,\Sigma a)=C(t,\tau,\xi,\Sigma a)\Big/\left(E_{m,x}(t,\Sigma a)\,E_{m,x+\zeta}(t+\tau,\Sigma a)\right)^{1/2}$$

For each time t, the cross-correlation coefficient $R(t,\tau,\xi,\Sigma a)$ has a maximum for some time lag τ_{opt}. Then a convection velocity depending on time and scale band can be defined :$U_c(t,\Sigma a)=\xi/\tau_{opt}(t,\xi,\Sigma a)$. The value $R(t, \tau_{opt}, \xi, \Sigma a)$ is the level, localized in time, of the spatial correlation for the considered time scales. It can be shown that the intercorrelation at optimal lag time of a pass band signal $R(\tau_{opt}, \xi, f)$ is equal to the coherence function at the same frequency f. In the same manner, $R(t, \tau_{opt}, \xi, \Sigma a)$ can be understood as a local coherence function, $\mathrm{coh}(t, \Sigma a, \xi)$.

Coherent structures detection

The measurements presented in this paper were performed in the supersonic part of the flow where mean local speed and isentropic convection velocity differ significantly. They are respectively equal to 330 and 485 ms^{-1}.

The considered scales are chosen to agree with the spatial filtering produced by the probe separation (Dupont et al. 1995b). The equivalent cut-off frequency is estimated from the coherence function and only time scales longer than the inverse frequency are taken into account in the analysis. The time scales analyzed range between 20μs and 1000μs; on the energy spectrum, the correspondent frequencies represent 80% of the total energy of the signal. An example of $U_c(t)$ vs time is given in Figure 2.

The energy spectrum $Su_c(f)$ of the convection velocity $U_c(t)$ is presented together with the spectrum of the total signal S(f) in Figure 1. The characteristic peaks, around the characteristic frequency f_c, observed on both spectra, are then associated with a repetition in time of turbulent zones composed of smaller scales.

The signal $U_c(t)$ is used to localize the coherent structures (medium 1) from the rest of the flow (medium 2). On the high velocity side, the passage of eddies correspond to a local decrease of $U_c(t)$. Then, medium 1 (respectively medium 2) is associated with the minimums (respectively the maximums) of $U_c(t)$ placed between two derivatives of large amplitude, consecutively negative, then positive (respectively positive, then negative), see Figure 2. Thus, no conditions on the absolute value of $U_c(t)$ is used to select the media.

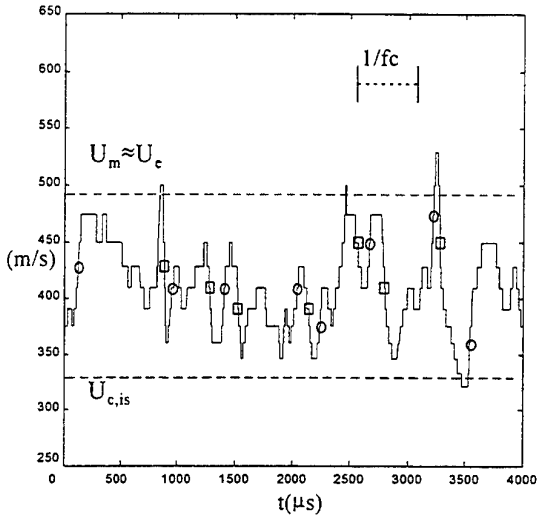


Figure 2: Time history of the convection velocity $U_c(t)$. Same location as in Figure 1. U_e :external velocity, U_m : mean velocity (Pitot measurements), $U_{c,is}$:isentropic estimate of the convection velovcity. O location of the maximum of the derivative $\partial U_c/\partial t$. □ location of the minimum of the derivative $\partial U_c/\partial t$.

This method of detection gives three basic quantities associated to each structure : their convection velocity (U_c), the time duration before the next one (t_d) and their time of flight (t_f). These time scales are defined using the evolution of $U_c(t)$ between two consecutive gradients localized a the instants t_{G-} and t_{G+}. To locate the middle of the structure, $U_c(t)$ is considered as a weighting function : $p_j=(U_{max}-U_{cj})/\Sigma p_i$, where U_{max} is the maximum convection velocity in the interval $[t_{G-}\ t_{G+}]$ and the instant of passage is chosen as : $t_i=p_j t_j$ for $t_{G-}<t_j<t_{G+}$, which is the weighted time between the two gradients. The standard deviation of t is : $\sigma_t=[p_j(t_j-t_i)^2]^{1/2}$, and the convection velocity of the structure is the average value of $U_c(t)$ in the interval $[t_i-\sigma_t\ \ t_i+\sigma_t]$. Finally, the flying time of the structure is choosen such as :

$$(U_{max}-Uc_i)\ t_{fi}=\int_{t_{G-}}^{t_{G+}}(U_{max}-U)dt$$

In this manner, no arbitrary threshold is necessary to define velocity and time scales, and the evolution of $U_c(t)$ can be automatically taken into account. Of course, in some cases, structures will not be localized, mainly due to the method to estimate the gradients. But as it can be seen on Figure 2, most of the eddies are expected to be detected, which means that statistical quantities deduced from time duration can be safely used.

We present now some statistical properties of these quantities. They have been estimated with 3158 events which is reasonable to obtain good estimates.

Temporal and spatial scales of coherent structures

The mean value of the convection velocity of the coherent part of the flow U_{c1}=353ms^{-1} and is close to the isentropic estimate (+6%). Its shape is roughly Gaussian with a standard deviation of 45 ms^{-1} (see Figure 3). This confirms the results obtained with the group velocity of the dispersion relationship of the convection velocity (Dupont, Muscat, Dussauge, 1995a).

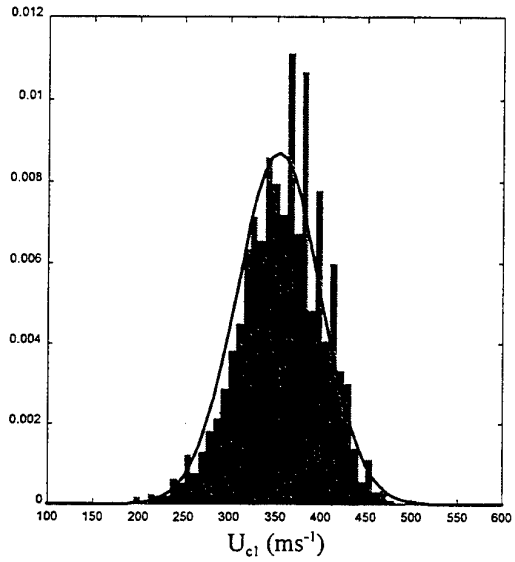


Figure 3: PDF of the convection velocity of the coherent structures; ——— Normal law

If each structure (i) is supposed to have a mean convection velocity equal to the estimated one ($U_{c1,i}$) over the duration time t_d, the distance between two structures is given by $\Lambda_i=U_{c1,i}t_{d,i}$, and the inverse of t_d corresponds to the passage frequencies of the structures. Characteristic temporal and spatial scales associated with the coherent structures are deduced from the time of flight: t_f^{-1}, corresponds to a characteristic frequency associated with the structure and its size is given by : $\lambda_i=U_{c1,i}t_{fi}$. Λ is independent of the transverse position y, but λ depends both on y and on the possibly random vertical location of the different structures.

The probability density function (PDF) of t_d^{-1} and t_f^{-1} can be compared to the spectra of the signal. They are presented in Figure 4, together the spectra of the signal, as function of the dimensionless variable $K\delta/(2\pi)$, where K is the estimated wave number : $K=\omega/U_c$.

The low frequency peaks already mentioned appear to be effectively characteristic duration times. The mean value of t_d leads to a Strouhal number of 0.17 which is in very good agreement with the Strouhal number already evaluated. We observe that the distance between structures range from 2.5 to 10 mixing layer thicknesses. It is clear that even if some wavelengths have a larger probability, the distribution of size is quite continuous and remains close to a lognormal distribution (which correspond to a normal law in the logarithmic representation of the Figure 4). It can be noted that each missed eddy in the detection process implies an artificially large t_d (ie small t_d^{-1}) and would give a PDF asymmetric towards the left hand side. Such an asymmetry is actually not observed (see Figure 4) which gives some confidence in the detection process.

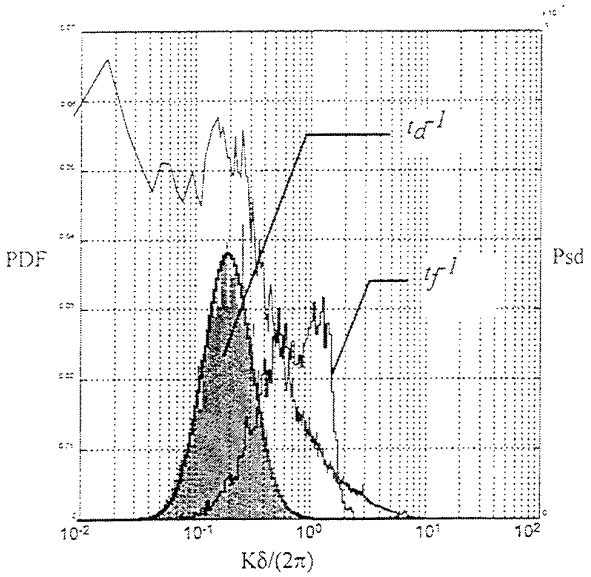


Figure 4 : comparison between the PSD of the turbulent signal —; the PDF of t_d^{-1}, of t_f^{-1} and the lognormal law fitted on t_d^{-1} ——

That is in qualitatively good agreement with a model proposed for a two-dimensional subsonic fully developped turbulent mixing layer (Bernal, 1988), which relates the growth of the mixing layer with the amalgamation mechanism of the large eddies. Bernal proposed a statistical model in the case $U_{c1,i}$=Cte. It gives a lognormal law for the PDF of Λ, and therefore for t_d^{-1} too. When the layer is in a self-similar state for the unsteady motions, Λ/x is independent of the considered section. The standard deviation σ of the logarithm of Λ is found to be related to the more frequent type of amalgamation : σ= 0.276 if pairings are dominant, 0.162 for tearing and 0.436 for tripling. Previous experimental and numerical results (Ramaprian et al. 1989, Bernal, 1988) showed that pairing can be the dominant process of amalgamation in subsonic mixing layers. In our case, we found a standard deviation of 0.48, much larger than the theoretical value of 0.276. As previously mentionned, the existence of characteristic peaks in the PDF indicates that self similarity is not completely reached. Nevertheless, it seems that a more complex evolution than in subsonic cases can be expected. This is consistent with previous visualizations (Clemens and Mungal, 1995) which show that three dimensional structures become predominant when M_c increases.

In the previous results, isentropic estimate of the convection velocity was used to transform the temporal case to a spatial one. As proposed before, direct estimation of length scales is possible with the measured convection velocity of each structure. The same representation as in Figure 4 is used to present the PDF of Λ (Figure 5).

It is clear than same results are obtained, in particular the same lognormal behaviour with about the same standard deviation (σ_Λ= 0.49). Similarly, the same Strouhal number of 0.165 is deduced from the average value of Λ ($S_{tr}=\delta/\Lambda$). Then it seems reasonable to consider than the main merging process which occurs in this flow is not a pairing process, but rather a tripling process. However, the model proposed by Bernal, is purely two dimensional, it may be not well fitted to for compressible mixing layer at M_c >0.5.

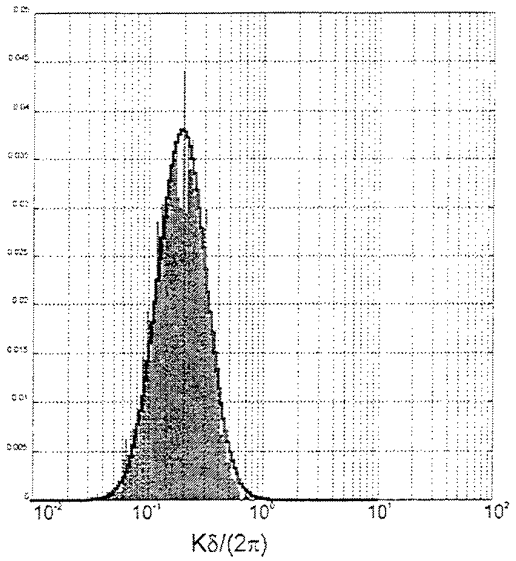


Figure 5 : PDF of δ/Λ and the lognormal law (—).

As found for the time duration, characteristic flying time are identified, both on the PDf of t_f^{-1} and on the spectra of the signal. They correspond to eddy sizes between one and three layer thicknesses.

Nevertheless, to find a Strouhal number comparable to the subsonic one with same Reynolds numbers (Browand and Troutt, 1985) is of interest. As a matter of fact, if we make the assumption, as in the Bernal's model, that the growth of the layer is mainly controlled by the evolution of the large coherent eddies, in a self similarity state, we have : Λ/x=Cte. In order to compare incompressible (referenced 0) and compressible mixing layers with same velocity and density ratio we can write : $\Lambda/\Lambda_0=(S_{tr0}/S_{tr})*\delta/\delta_0$. The ratio δ/δ_0 is also the ratio of the spreading rates δ'/δ'_0. This ratio is the normalized spreading rate and is generally assumed to be a function of the convective Mach number only : $\Phi(M_c)$. Hence we obtain $\Lambda/\Lambda_0=(S_{tr0}/S_{tr})*\Phi(M_c)$, where $\Phi(M_c)$ is a decreasing function of M_c. In a self similar state, the mean value Λ at a given station is related to the number of amalgamations whose have been necessary to create the actual structures. Then, the description of the quantity $(S_{tr0}/S_{tr})*\Phi(M_c)$ would give informations on the reduction or not of the amalgamation processes when M_c is increasing.

Conditional analysis

The previous results have shown that the observation of the time history of $U_c(t)$ is an efficient tool to detect coherent structures in a compressible mixing layer. Characteristic size of eddies have been put in evidence. It is now examined if quantities other than convection velocity, can be associated with the large coherent structures.

A conditional analysis has been performed to separate the information relative to media (1) and (2). For each medium the mean convection velocity (U_{ci}), the level of energy (E_i) and the spectra deduced from wavelets coefficients (S_{wi}) have been obtained.

As already mentioned, the mean convection velocity deduced from the parts of the signal associated with the large quasi periodic structures is in good agreement with the isentropic estimate and with the low frequency group velocity (±6%). On

the opposite, medium 2 has a mean convection velocity equal to the local mean velocity (±4%) (see Figure 6). Nearly the same level of energy has been obtained for the two mediums. The conditional spectra are shown Figure 7 : it is clear that the same temporal scales are involved in both media. These two results show that a criterion based on the local level of energy or on the local partition of energy cannot be efficient to detect the periodic scales of a mixing layer in the case of a fully turbulent flow.

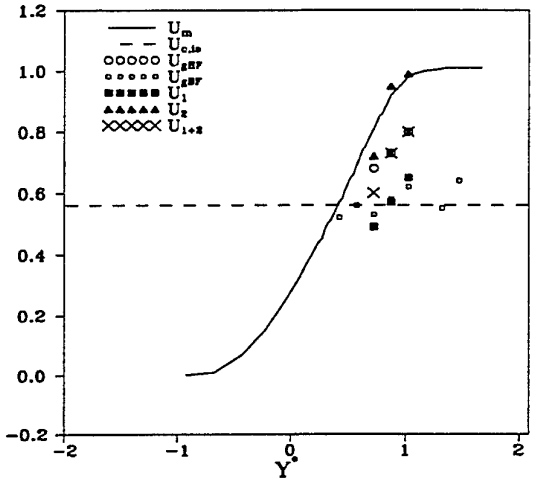


Figure 6: Dimensionless velocity profiles. $U_{g,BF}$ and $U_{g,HF}$ are group velocities of the signal in the low frequency and in the high frequency ranges.

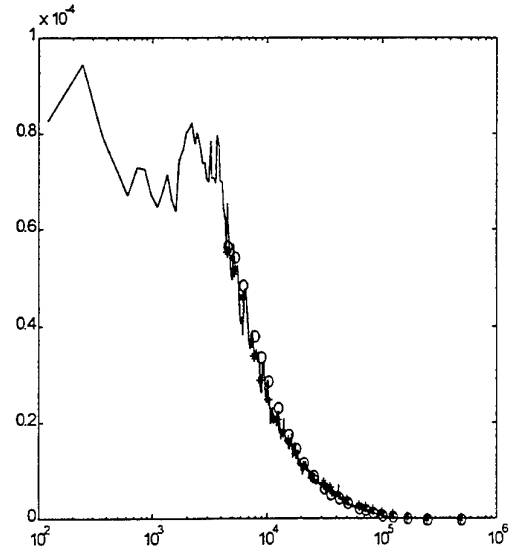


Figure 7 Power spectral density of the fluctuations in the media 1 (O) and 2 (✱) compared to the spectrum of the signal.

The existence of two media with same time scales, but with different convection velocity can be taken into account to reinterpret the dispersion relationships deduced from the Fourier analysis. It may be shown that when two non dispersive media (same phase velocity for each frequency) are considered with finite non-zero convection velocities respectively denoted U_{c1} and U_{c2}, the resulting signal is not dispersive and has a convection velocity such as : $U_{c1+2}=2U_{c1}U_{c2}/(U_{c1}+U_{c2})$. This relation was applied to the present measurements ; the results are given in Figure 6 and there is very good agreement with the group velocity deduced from the experimental dispersion relationship.

Finally, the average value of $R(t, \tau_{opt}, \xi, \Sigma a)$ is nearly the same in each medium and has practically the value of the coherence function considered at an equivalent frequency. This shows that the spatial decay of coherence due to the cascade of turbulence for the considered energetic scales is roughly the same in the different parts of the flow.

CONCLUSIONS

In this work, we proposed a method to localize and analyze large coherent structures in a compressible turbulent mixing layer. It is based on the evaluation of the convection velocity related to the energetic scales of the layer. It relies on the assumption that coherent part can have a convection velocity different than the rest of the flow. Results confirmed that the isentropic convection velocity is an appropriate estimate in a mixing layer at M_c=0.62. Characteristic time and length scales have been obtained. These different informations have been used to reinterpret results obtained from the Fourier analysis : spectra and dispersion relationship. It appears that models based on representations of amalgamations phenomena are still relevant for such flows, but with some differences compared to subsonic cases. In particular the preferential merging process seems not to be a pairing process but rather a tripling mechanism. The values of the parameters for the pairing and tripling were taken by reference to two dimensional analysis. These values are probably altered by the three dimensional effects occurring at a convective Mach number of 0.62.

Finally, conditional analysis of the coherent and no-coherent part of the flow have shown that each medium contains the same energy with similar spectra and the same spatial decay of coherence.

REFERENCES

BERNAL L.P., 1988 " The statistics of the organized vortical structure in turbulent mixing layers". *Phys. Fluids* 31(9) ,pp 2533-2543

BONNET J.P., DEBISSCHOP J.R. &.CHAMBRES O., 1993 "Experimental studies of the turbulent structures of supersonic mixing layers" *A.I.A.A. Paper* 93-0217

CHAMBRES O.1997 " Analyse experimentale de la modelisation de la turbulence en couche de melange supersonique". Thèse de Doctorat de L'Université de Poitiers.

BROWAND F.K. and TROUTT T.R. 1985 "The turbulent mixing layer : geometry of large vortices", *J. Fluid Mech.* 158, pp. 489-509

1995CLEMENS N.T., MUNGAL M.G., 1995 "Large-scale structure and entrainment in the supersonic mixing layer". *J. Fluid Mech.* 284, pp. 171-216.

DAUBECHIES I., 1992 "Ten Lectures on Wavelets". *SIAM.* Philadelphia, Pennsylvania, U.S.A.

DUPONT P , MUSCAT P & DUSSAUGE J.P., 1995a " Time and space-time statistics in a supersonic mixing layer". Second symposium on transitional and turbulent compressible flows, *Joint ASME/JSME Fluids Engineering Conference*, Hilton Heads, S.C. , August 1995.

DUPONT P , MUSCAT P & DUSSAUGE J.P., 1995b "Properties of energetic scales in a supersonic mixing layer". *IUTAM Symposium on Combustion in Supersonic Flows,* Poitiers, October 1995.

LIANDRAT J., 1995 : "Some Algorithms for Turbulence Analysis and Modeling", in *Wavelets, Theory and Applications*, Oxford Univ.Press

MUSCAT P., DUSSOULLIEZ P., DUPONT P. & LIANDRAT J. 1997. "Coherent structures detection method using wavelet transform". *I.U.T.A.M. Symposium on simulation and Identification of organized structures in flows*, Lyngby, may 1997.

RAMAPRIAN B.R., SANDHAM M.D., MUNGAL M.G. and REYNOLDS W.C., 1989, "Passive scalar tagging for the study of coherent structures in the plane mixing layer", *Phys. Fluids* vol.1, n°12, pp. 2034-2041.

SAMIMY M., ELLIOT G.S. & ARNETTE S.A. 1992 "Identification of Large Structures in Compressible Mixing using Filtered Rayleigh Scattering". *I.U.T.A.M. Eddy Structure Identification in Free Turbulent Shear Flows*, Poitiers, October 1992.

WANG Q., BRASSEUR J.G., SMITH R.W., SMITS A.J. 1994 "Multi-dimensional continuous wavelet transforms and applications to turbulence data", Submitted to *Proc. Royal Soc.*

Validation of a pseudo-sound theory for the pressure-dilatation in DNS of compressible turbulence

J.R. Ristorcelli
ICASE, NASA Langley Research Center
Hampton, VA USA 23693

G.A. Blaisdell
School of Aeronautics and Astronautics
Purdue University, IN USA 47907

Introduction

The validation of an analytical development for the pressure dilatation, $< pd >$, appearing in the single point closures for compressible turbulence, given in Ristorcelli (1995, 1997), is the subject of this article. The analysis is relevant to shear flows with negligible bulk dilatation and low M_t^2. These restrictions are satisfied in a wide number of flows ranging from simple shear layers of theoretical interest, Papamoschou and Roshko (1988), to the complex shear layers associated with supersonic mixing enhancement, Gutmark *et al.* (1995). In most of these supersonic shear layers a Mach number based on the fluctuating velocity of the fluid particle is small. A Mach 4 mean flow with a turbulence intensity of 8 *per cent* has a turbulent Mach number of $M_t = 0.32$. The square of this turbulent Mach number, the appropriate perturbation expansion parameter arising from the Navier-Stokes equations, $M_t^2 \sim 0.1$, is small. The existence of this small parameter, M_t^2, allows some analytical results.

This article addresses the validation using recent DNS results for compressible turbulence of the pressure dilatation, $< pd >$, which appears in the equation for the kinetic energy of a compressible turbulence. The article is primarily a study of the analysis of Ristorcelli (1995, 1997) in the light of recent DNS by Blaisdell. The representations were obtained using simple scaling arguments about the effects of compressibility and a singular perturbation idea and the methods of statistical fluid mechanics. While the results are expressed in the context of a statistical turbulence closure they provide, with very few phenomenological assumptions, an interesting and clear physical model for the scalar effects of compressibility. For a homogeneous turbulence with quasi-normal isotropic large scales the expressions derived are – in the small turbulent Mach number *squared* limit – exact. The analytical results, which do not have any unspecified empirical coefficients, are in good agreement with DNS results. The analytical results, which are a rigorous consequence of the low M_t^2 assumptions, are shown to predict the proper scalings in homogeneous compressible turbulence.

Preliminaries

It has been shown, Ristorcelli(1995, 1997) that a low fluctuating Mach number expansion for the compressible Navier Stokes equations produces a diagnostic relationship for the dilatation. The small parameter in these expansions is the square of the fluctuating turbulent Mach number: γM_t^2 and $M_t = \tilde{u}/c_\infty$ where $\tilde{u} = 2k/3 =< u_j u_j > /3$ and $c_\infty^2 = \gamma P_\infty/\rho_\infty$. To leading order the density fluctuations are given, in nondimensional units, by the solenoidal pressure fluctuations, $\gamma\rho_1 = p_{inc} = p_1$ and the continuity equation becomes a *diagnostic* relation for the fluctuating dilatation,

$$-\gamma d \;=\; p_{,t} + v_k p_{,k} \,. \tag{1}$$

The subscript on p_1 has been dropped. It is seen that one does not need to obtain a solution to the evolution equation for the compressible velocity field, w_i, in order to obtain its dilatation, $d = w_{i,i}$. A very nice result. The dilatation is diagnostically related to the *local* fluctuations of the pressure and velocity; it is the rate of change of the incompressible pressure field $p_{1,jj} = (v_i v_j)_{,ij}$, following a fluid particle. Constitutive relations for the pressure-dilatation can be found by taking the appropriate moments of the diagnostic relation for the dilatation to produce,

$$-2\gamma < pd > \;=\; \frac{D}{Dt} < pp > . \tag{2}$$

The near field compressibility effects, as manifested in $< pd >$, have been directly linked to the solenoidal portions of the velocity field. This fact has been exploited to obtain expressions for the pressure-dilatation covariances, Ristorcelli (1995, 1997). The following representation for the pressure-dilatation covariance were obtained:

$$\begin{aligned} < pd > = \quad & -\chi_{pd} M_t^2 \,[P_k - \bar{\rho}\epsilon + T_k] \\ & + \tfrac{3}{4}\chi_{pd} M_t^4 \gamma(\gamma-1)(P_T + \bar{\rho}\epsilon + T_T)] \\ & - \bar{\rho} k \;\; M_t^2 \; \chi_{pd}^T \; \tfrac{D}{Dt}\mathcal{T} \end{aligned}$$

$$\chi_{pd} \;=\; \frac{2 I_{pd}}{1 + 2 I_{pd} M_t^2 + \frac{3}{2} I_{pd} M_t^4 \gamma(\gamma-1)}$$

$$\chi^r_{pd} = \frac{I^r_{pd}}{1 + 2I_{pd}M_t^2 + \frac{3}{2}I_{pd}M_t^4\gamma(\gamma-1)}$$
$$I_{pd} = \frac{2}{3}I^s_1 + I^r_{pd}\,[3\hat{S}^2 + 5\hat{W}^2]$$
$$I^r_{pd} = \frac{1}{30}(\frac{2}{3})^3\,\alpha^2 I^r_1. \qquad (3)$$

Note that $\mathcal{T} = [3\hat{S}^2 + 5\hat{W}^2]$. The nondimensional strain and rotation rates are given by: $\hat{S}^2 = (Sk/\epsilon_s)^2$, $\hat{W}^2 = (Wk/\epsilon_s)^2$ where $S = \sqrt{S_{ij}S_{ij}}$ and $W = \sqrt{W_{ij}W_{ij}}$. The strain and rotation tensors are defined in analogy with the incompressible case, *i.e.*, traceless $S_{ij} = \frac{1}{2}[U_{i,j} + U_{j,i} - \frac{2}{3}D\delta_{ij}]$, $W_{ij} = \frac{1}{2}[U_{i,j} - U_{j,i}]$. Here $M_t = \tilde{u}/c_\infty$ where $\tilde{u} = 2k/3 = < u_j u_j > /3$ and $c^2_\infty = \gamma P_\infty/\rho_\infty$ and α comes form the Kolmogorov scaling realtion $\ell = \alpha(2k/3)^{3/2}/\epsilon_s$. The constants, denoted by the I_i, in these expressions are given by integrals of the longitudinal correlation function, f: $I^s_1 = \int_0^\infty \xi f'^2 d\xi$, and $I^r_1 = 2\int_0^\infty \xi f d\xi$. A quick of order of magnitude estimate for the integrals can be made using $f = e^{-\xi^2\pi/4}$. The following values are found: $I^s_1 = \frac{1}{2}$, $I^r_1 = \frac{4}{\pi} = 1.273$. The values found from high Reynolds number wind tunnel data are similar: $I^s_1 = 0.300$, $I^r_1 = 1.392$, Zhou (1995).

Isotropic decay

For the isotropic decay the expression for the pressure dilatation becomes

$$< pd >= \chi_{pd} M_t^2\, \epsilon_s\,. \qquad (4)$$

Here $\bar{\rho}$ has been set to unity. The sign of $< pd >$ is positive indicating a net tranfer of energy from potential to kinetic modes. Rearranging to isolate the scaling produces

$$\frac{< pd >}{M_t^2\,\epsilon_s} = \chi_{pd} = \frac{\frac{4}{3}I^s_1}{1 + \frac{4}{3}I^s_1 M_t^2}. \qquad (5)$$

Terms of order M_t^4 have been dropped. Earlier estimates given in Ristorcelli (1995), shown above, indicate $I^s_1 = 0.5 - 0.3$. The theory therefore predicts an asymptote for χ_{pd} as the turbulent Mach number vanishes:

$$\chi_{pd} \to 0.666 - 0.40 \qquad as \qquad M_t^2 \to 0. \qquad (6)$$

The DNS results, shown in Figure 1, were provided by Blaisdell for three different initial turbulent Mach numbers. As a service to the reader the figure identifies two definitions of the turbulent Mach number: that used by Blaisdell *et al.* (1993) in his simulations, M^b_t, and that which comes from the perturbation theory of Ristorcelli (1995, 1997). They are recent compressible DNS reflecting a consistent set of initial conditions described in Ristorcelli and Blaisdell (1997).

The agreement with the DNS shown in Figure 1 is very good. The theory has been proven without *a posteriori* adjustment of constants. The actual values of the constant could in principal be calculated from the DNS. As they are expected to be weakly dependent on initial conditions these tact is not followed further - what has been presented is sufficient for verification. Moreover the slow portion of the pressure dilatation is nominal compared to the rapid portion which is the most important contributor in the shear flows of interest.

Homogeneous shear

The pressure-dilatation in the homogeneous shear is now investigated. The instantaneous pressure-dilatation is seen in Figure 2. Also shown are its averaged values following the procedure of Sarkar (1992). Here the time integral of the pressure-dilatation has been taken: the vertical axis being $-\frac{1}{St}\int \frac{<pd>}{\epsilon_s} d(St)$. The oscillations in the pressure-dilatation associated with the relaxation from initial conditions are not seen. There is, nonetheless, a build up of the oscillations which has been linked to the compressible component of the pressure field, Sarkar (1992), Blaisdell and Sarkar (1993). No explanation for this behavior is known.

For a homogeneous shear the expression for the pressure-dilatation can be simplified. For a simple shear $\mathcal{T} = 8\hat{S}^2$ and, neglecting terms of order M_t^4, produces

$$< pd >= -\chi_{pd} M_t^2\,[P_k - \epsilon] \; - k\;\; M_t^2\;\chi^r_{pd}\; 8\frac{D}{Dt}\hat{S}^2. \qquad (7)$$

For Blaisdell's homogeneous shear, in which $S = const.$, the expression can be rearranged

$$< pd >= \quad -\chi_{pd} M_t^2\;\epsilon_s[\tfrac{P_k}{\epsilon_s} - 1]$$
$$-16\chi^r_{pd}\;M_t^2\epsilon_s\;(\tfrac{Sk}{\epsilon_s})^2\tfrac{D}{D(St)}\;\tfrac{Sk}{\epsilon_s}. \qquad (8)$$

Note that the coefficent of the first term, χ_{pd}, ignoring the small slow pressure contribution, scales as $\chi_{pd} \sim (\frac{Sk}{\epsilon_s})^2$; accounting for the definitions of the χ's the pressure dilatation can be rewritten as

$$< pd >\sim \quad -[\alpha^2(\tfrac{Sk}{\epsilon_s})^2 M_t^2\;\epsilon_s(\tfrac{P_k}{\epsilon_s} - 1)]\;I^r_1$$
$$[1 + \tfrac{1}{\frac{P_k}{\epsilon_s} - 1}\tfrac{D}{D(St)}\;\tfrac{Sk}{\epsilon_s}]. \qquad (9)$$

As the flow evolves it is expected that $I^r_1 \to const.$ and $1 + \frac{1}{\frac{P_k}{\epsilon_s} - 1}\frac{D}{D(St)}\;\frac{Sk}{\epsilon_s} \to 1$. The scaling of $< pd >$ with the term in the first set of brackets will be investigated.

"Non-equilibrium" aspects of $< pd >$

The homogeneous shear DNS is not an equilibrium flow. Using $\frac{Sk}{\epsilon_s}$ as an indicator of the non-equilibrium nature of the flow one sees that $\frac{D}{Dt}\frac{Sk}{\epsilon_s} \to 0$ only in the very latest stages of the DNS, see Figure 3 bottom plot. Two regions of the flows evolution are accordingly distinguished: a nonequilibrium earlier portion in which $D/Dt\;\hat{S} \neq 0$, and a structural equilibrium portion for which $D/Dt\;\hat{S} \to 0$. If the flow is in structural equilibrium, $\frac{Sk}{\epsilon_s} \to const$, one obtains the simplest form of the pressure-dilatation: call it

$$< pd >_{se} = -\chi_{pd} M_t^2\,[P_k - \epsilon]\,. \qquad (10)$$

Let this be called the structural equilibrium form of the pressure-dilatation (which does not mean that the flow is in equilibrium as $P_k \neq \epsilon$).

Figure 3 indicates the relative contributions of the two terms making up the the pressure-dilatation model. It is seen at small times, according to the pseudo-sound theory, that both terms make non-negligible contributions to the pressure-dilatation. As the structural equilibrium is approached, $D/Dt\;\hat{S} \to 0$, and the second term's importance, as might be expected, becomes negligible. This is manifested in the second graph were the ratio of $< pd >_{se}$ to the total $< pd >$ approaches unity. Also shown is the *per centage* time rate of change of the relative strain $\frac{\epsilon_s}{Sk}\frac{D}{Dt}\frac{Sk}{\epsilon_s}$. The curves are noisy as they involve differentiation of numerical data; the trends are nonetheless unmistakeble.

Pressure-dilatation scalings

The appropriately scaled integrals of $< pd >$ will now be taken. In this way one can establish whether the scalings predicted by the model are correct. In the late stages of Blaisdells DNS, about three or four eddy turniovers past inception, $St > 10$, it appears that a structural equilibrium is being approached. In this region the scaling suggested by

$$< pd >\sim -[\alpha^2(\frac{Sk}{\varepsilon_s})^2 M_t^2\;\epsilon_s(\frac{P_k}{\epsilon_s} - 1)]\;I^r_1 \qquad (11)$$

is investigated. After the scaling $< pd >$ the time integral $\frac{1}{St-St_0}\int(\,)d(St)$ will be taken - let the symbol $\int_{ST}$ denote this averaging operation. The integrals

$$
\begin{aligned}
I_0 &= \int_{ST} < pd > \\
I_1 &= \int_{ST} \frac{< pd >}{\epsilon_s} \\
I_2 &= \int_{ST} \frac{< pd >}{\epsilon_s[\frac{P_k}{\epsilon} - 1]} \\
I_3 &= \int_{ST} \frac{< pd >}{M_t^2\epsilon_s[\frac{P_k}{\epsilon} - 1](\frac{Sk}{\epsilon})^2} \\
I_4 &= \int_{ST} \frac{< pd >}{\alpha^2 M_t^2\epsilon_s[\frac{P_k}{\epsilon} - 1](\frac{Sk}{\epsilon})^2}.
\end{aligned}
$$

The integrals are shown in the Figure. The integration starts at $St = 9$; the integrals are normalized by their values at $St = 10$. If the scaling suggested by the analysis of Ristorcelli Ristorcelli (1995, 1997) is correct the last integral, I_4, will be approximately constant reflecting the fact that the time integral $\frac{1}{St}\int I_1^T d(St) \sim I_1^T$ and $\frac{D}{Dt}\hat{S} \to 0$ as the equilibrium portions of the DNS are attained. Inspection of I_4 in Figure 4 shows this to be the case. The period of time $10 < St < 16$ corresponds to about one eddy turnover time, k/ϵ.

The gradient Mach number

The largest relative collapse of the scaled integrals of $< pd >$ occurrs with the quantities $M_t^2(\frac{Sk}{\epsilon})^2$ - the collapse from I_2 to I_3. The quantity $M_t^2(\frac{Sk}{\epsilon})^2$ can be thought of as the square of the gradient Mach number and the pressure-dilatation is seen to be a strong function of this quantity. Sarkar (1995) has defined a gradient Mach number: $M_g = S\ell/c$ in which the transverse two-point correlation of the longitudinal velocity as the length scale at the end of the simulations. In this article ℓ will be taken as the traditionally defined longitudinal length scale that occurs in the Kolmogorov scaling: $\ell = \alpha(2k/3)^{3/2}/\epsilon_s$. In which case a mean strain Mach number is defined:

$$M_S = \frac{S\ell}{c} = \alpha\frac{2}{3}\frac{Sk}{\epsilon_s}M_t = \alpha\frac{2}{3}\hat{S}M_t \simeq \frac{2}{3}\hat{S}M_t. \qquad (12)$$

In fact the curve overshoots the optimum collapse (a horizontal line): the gradient Mach number is increasing faster than $< pd >$.

The Kolmogorov scaling coefficient

The collapse, I_4, is much better when the Kolmogorov coefficient is included. A new feature associated with compressibility, that of the Kolmogorov scaling coefficient, α, is thus apparent. The values used for α come from Blaisdell's DNS: the longitudinal integral length scale, ℓ, k and ϵ_s are calculated from the DNS and then the the Kolmogorov relationship, $\epsilon = \alpha(\frac{2}{3}k)^{3/2}/\ell$ is used to find α. Blaisdell has calculated the two-point correlation of the solenoidal field at select points during the simulation.

The pressure-dilatation model is sensitive to variations in the Kolmogorov scaling parameter: in fact it is decreasing as rapidly as M_S is increasing. The definition for the mean gradient Mach number given above, $M_S = \frac{2}{3}\frac{Sk}{\epsilon_s}M_t$, implicitly assumes $\alpha \simeq 1$. M_t and $\frac{Sk}{\epsilon_s}$ are not new quantities for describing turbulence in single point closures; α, however, is new. This distinction is made in order to recognize α as a new independent quantity.

The Kolmogorov constant is thought to be a universal constant for high Reynolds number in isotropic turbulence; for nonideal finite Reynolds number anisotropic turbulence it is *a flow specific quantity*. It is this fact that makes creating a turbulence model from the analysis of Ristorcelli (1995, 1997) difficult: a choice for α must be made and for any given flow the choice is not, *a priori*, known. The value of α can be thought of as describing some large scale structural aspects of the flow: it, after all, relates the kinetic energy, its cascade rate and the two-point correlations.

Summary and Conclusions

In all likelyhood there are many aspects of compressibility that will contribute to the unusual and dramatic stabilizing effects of compressibility. It is unlikely that any one term in a statistical closure will account fully for the physical mechanism(s) responsible. This article has focused on one of these effects, the pressure-dilatation. The present analysis treats only the "scalar" effects of compressibility - the reduction k through the dilatational covariances in the energy budget; it cannot account for the reduction in the shear anisotropy, b_{12}, or the normal anisotropy, b_{22}, so important to the production mechanism for the shear stress, $< v_1v_2 >$. To account for these more substantial structural effects appears to require a compressible pressure-strain representation accounting for the effects of compressibility. This has been indicated in Blaisdell and Sarkar (1992), Vreman *et al.* (1996), Simone *et al.* (1997).

The pressure-dilatation is found to be a nonequilibrium phenomena. It scales as $M_t^2(\frac{Sk}{\epsilon_s})^2[P_k/\epsilon_s - 1]$. For it to be important requires both 1) the square of the gradient Mach number, M_S^2, to be nonnegligible and 2) $P_k \neq \epsilon$. In as much as the pressure-dilatation can be either positive or negative its dependence on the gradient Mach number indicates that the gradient Mach number can be either a stabilizing or destabilizing. These predictions are consistent with the DNS of Simone *et al.* (1997) who observes such behavior as related to the anisotropy, b_{12}.

Except for the well-established Kolmogorov scaling, $\ell \sim (\frac{2}{3}k)^{3/2}/\epsilon_s$, and the quasi-normal assumption, no additional phenomenological assumptions are made. The pressure dilatation is a function of the Kolmogorov scaling coefficient and this is expected to be an important feature in models for compressible flows. The Kolmogorov coefficient is a flow dependent quantity: there is little known about its dependence in non-ideal - anisotropic, strained, inhomogeneous - flow situations. The appearance of the Kolmogorov coefficient, in as much as it links the energy, the spectral flux and a two-point length scale, is an indication of dependence on large scale structure.

References

Blaisdell, G.A. (1996). Personal communication.

Blaisdell, G.A., N.N. Mansour, W.C. Reynolds (1993). Compressibility effects on the growth and structure of homogeneous turbulent shear flow. *J. Fluid Mech.* 256:443.

Blaisdell, G.A., S.S. Sarkar (1993). Investigation of the pressure-strain correlation in compressible homogeneous turbulent shear flow. ASME FED-vol 151, Transitional and Turbulent Compressible Flows.

Gutmark, E.J., K.C. Schadow, K.H. Yu (1995). Mixing enhancement in supersonic free shear layers. *Ann. Rev. Fluid Mech.* 27:375.

Papamoschou, D., A. Roshko (1988). The compressible turbulent shear layer: an experimental study. *J. Fluid Mech.* 197:453.

Ristorcelli, J. R., (1995). "A pseudo-sound constitutive relationship and closure for the dilatational covariances in compressible turbulence: an analytical theory." ICASE report 95-22, to appear *J. Fluid Mech.* (1997).

Ristorcelli, J.R., G. Blaisdell (1996). "Consistent initial conditions for the DNS of compressible turbulence" w/ G.

Blaisdell, ICASE Report 96-49, to appear *Phys. Fluids* (January 1997).

Sarkar, S. (1992). The pressure-dilatation correlation in compressible flows. *Phys. Fluids A* 12:2674.

Sarkar, S. (1995). The stabilizing effect of compressibility in turbulent shear flow. *J. Fluid Mech.* 282:163.

Simone, A., G.N. Coleman, C. Cambon (1997). The effect of compressibility on turbulent shear flow: a rapid-distortion-theory and direct-numerical-simulation study. *J. Fluid Mech.* 330:307.

Vreman, W.A., N.D. Sandham, K.H. Luo (1996). Compressible mixing layer growth rate and turbulence characteristics. *J. Fluid Mech.* 320:235.

Zhou, Y. (1994). personal communication.

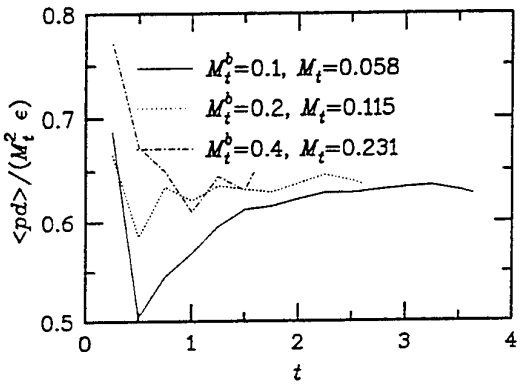


Figure 1: The isotropic decay.

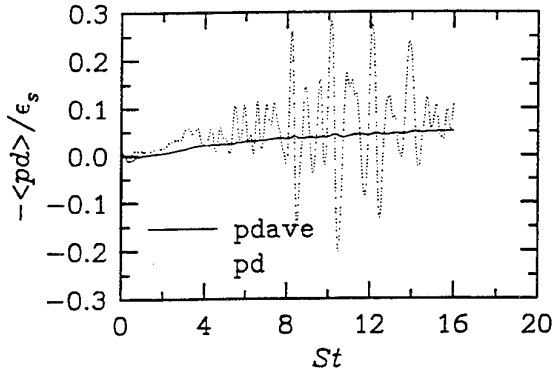


Figure 2: The instantaneous and averaged pressure dilatation - Blaisdell's rjr_s1 DNS.

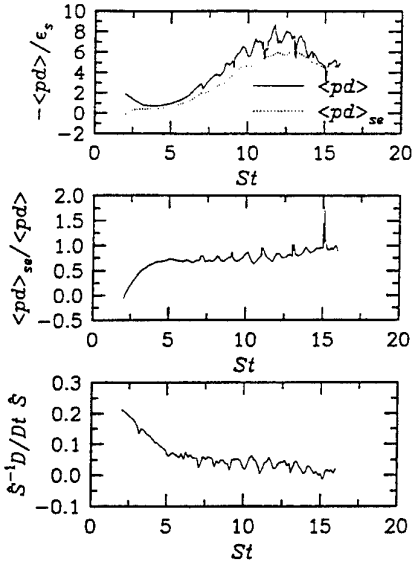


Figure 3: Contribution of the equilibrium portion of the pressure-dilatation to the pressure dilatation as predicted by the pseudo-sound analysis.

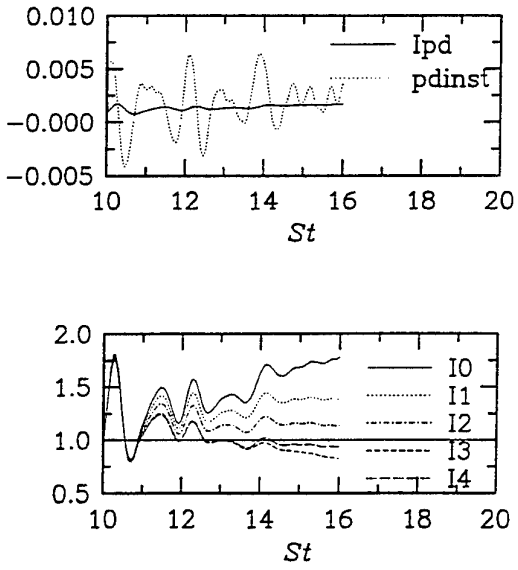


Figure 4: Integral scalings for the pressure dilatation in homogeneous shear.

PREDICTION OF 3D SUPERSONIC FLOWS INCLUDING CROSSFLOW SEPARATION USING LOW-REYNOLDS NUMBER TURBULENCE MODELS

Hugues Deniau, Frédéric Thivet, Jean-Marc Moschetta
ONERA/CERT, Aerothermodynamics Department
B.P. 4025 - 31055 Toulouse Cedex 4
France

ABSTRACT

This paper deals with the capability of a wide range of turbulence models to predict the crossflow separation and the skin friction in 3D supersonic flows around slender bodies at angle of attack. Well-known algebraic and two-equation models are briefly presented. Reynolds-Stress Models (RSM) are then reviewed, focusing on the principles they are building on. Existing low-Reynolds nonlinear RSM are shown to be unable to predict a flat plate boundary layer for high-Reynolds number. Two ways are followed to supply this deficiency: the first one consists of building a new low-Reynolds nonlinear RSM, fitted to correctly predict the flat plate boundary layer; the second one consists of building two-layer low-Reynolds linear RSM / high-Reynolds nonlinear RSM models. Computed results around ogive-cylinders are presented and compared to each other and to experimental data. Two-layer RSM are shown to be valid for moderate and high angles of attack, even when two-equation models failures arise.

INTRODUCTION

The design of missiles flying at supersonic speeds in a controlled manner heavily relies on the understanding and prediction of flowfields at high angle of attack. Due to their efficiency and ability to compute most of the complex phenomena involved, the PNS equations are widely used in this design process. A PNS solver, named Torpedo [8], has been recently developed and validated for laminar flows. However, one of the most important and difficult aspects for accurately computing realistic flows is the modeling of the turbulence features of such flows. This is especially true for the numerical simulation of flows around a missile body since the vortices developing on the leeward side of the body are highly sensitive to the turbulence model used. The goal of this paper is to study the capability of a wide range of turbulence models to predict flows around an ogive-cylinder at angle of attack.

TURBULENCE MODELING

Various models are considered and compared to one other, ranging from algebraic to Reynolds-Stress Models (RSM). In this paper, we focus our attention to a few of them and in particular to the low-Reynolds RSM:

- algebraic model: Baldwin-Lomax model including the modification proposed by Degani and Schiff for slender body calculations.
- two-equation models: several variants of the k–ε model (Launder and Sharma, Nagano and Tagawa, Shih) and Menter k–ω model.
- Reynolds Stress Models: they are divided into two groups: the linear models (near-wall SSG, Launder and Shima, Hanjalić and Jakirlić) and the nonlinear ones (Launder-Tselepidakis)

Algebraic model

The Baldwin-Lomax model is widely used in Navier-Stokes computations because it does not require to evaluate boundary layer thickness. The turbulent length scale is computed as the distance from the wall where the function $f = y|\Omega|D(y^+)$ reaches its maximum, where $D(y^+)$ is the van-Driest wall function, y represents the distance to the closest wall and $|\Omega|$ is the vorticity magnitude.

The modification proposed by Degani and Schiff consists of taking the maximum closest to the wall.

Two-equation models

Two-equation $k-\varepsilon$ models make use of an equation for the turbulent kinetic energy k and another for either the real dissipation rate ε (Nagano-Tagawa or Shih) or the isotropic dissipation rate $\tilde{\varepsilon}$ (Launder-Sharma), which is defined as: $\tilde{\varepsilon} = \varepsilon - 2\nu \left(\partial\sqrt{k}/\partial x_l\right)\left(\partial\sqrt{k}/\partial x_l\right)$.

The greatest advantage in using the isotropic dissipation instead of the real one lies in the homogeneous wall condition $\tilde{\varepsilon} = 0$, which is numerically much more stable. The last two-equation model is the so-called BSL $k-\omega$ model by Menter. It contains a transport equation for k and another for the specific dissipation rate ω. These equations are obtained from the standard $k-\varepsilon$ model reformulated in terms of $k-\omega$ and coupled with Wilcox $k-\omega$ model by a special blend function. The latter is designed in such

a way that the $k-\varepsilon$ model applies mainly in the outer part of the boundary layer and $k-\omega$ in the inner part. As opposed to the first three models, no wall function needs to be added.

RSM MODELS

High-Reynolds Renolds-Stress-Models

The evolution equation for the Reynolds stress $\overline{u_i u_j}$ can be written into a classical form:

$$\underbrace{\frac{\partial \rho U_l \overline{u_i u_j}}{\partial x_l}}_{convection} = \underbrace{P_{ij}}_{production} + \underbrace{\Phi_{ij}}_{redistribution} - \underbrace{\varepsilon_{ij}}_{dissipation} + \underbrace{\mathcal{D}_{t\,ij}}_{turbulent\ diffusion} + \underbrace{\mathcal{D}_{v\,ij}}_{viscous\ diffusion} \quad (1)$$

Φ_{ij}, ε_{ij} and $\mathcal{D}_{t\,ij}$ must be modeled. The pressure-strain correlation Φ_{ij} accounts for the fact that the energy associated with the different Reynolds stresses is not equally distributed, which results in differences when using RSM or two-equation models.

The redistribution term Φ_{ij} is split into slow and rapid parts $\Phi_{ij,1}$ and $\Phi_{ij,2}$. $\Phi_{ij,2}$ is evaluated using an expansion with respect to the anisotropy tensor components $a_{ij} = \overline{u_i u_j}/k - 2/3\delta_{ij}$ under the assumption that the flow is homogeneous and weakly anisotropic. According to the order of expansion, one can obtain either linear models such as the Launder-Reece-Rodi (**LRR**) and Speziale-Sarkar-Gatski (**SSG**) models or nonlinear models such as the Fu-Launder-Tselepidakis (**FLT**) model. Model constants are determined in such a way that some mathematical properties are satisfied, or lead to numerical results that match experiment, or on the basis of realisability in the case of nonlinear models.

Near-Wall modeling

Low-Reynolds $k-\varepsilon$ / high-Reynolds RSM.

Most authors use high-Reynolds RSM coupled with a low-Reynolds $k-\varepsilon$ model. In this approach, the transport equations for Reynolds stresses are solved only from the logarithmic layer where they are specified through algebraic relations [7]. This method does not account for anisotropy effects in the near-wall layer and assume the existence of an equilibrium layer in complex three dimensional flows. In the present study, only low-Reynolds RSM are used, so that the Reynolds-Stress equations are integrated up to the wall.

Low-Reynolds linear RSM. Various models are available in the literature, depending on the choice for the pressure-strain correlation model and for the wall damping functions. In most low-Reynolds RSM, the pressure-strain correlation model is based on a linear model. The difference between these models lies in the feature of the wall proximity effects, which either depends on viscosity only (this approach is adopted in the near-wall SSG model [11]) or on the turbulence structure as well (Launder-Shima (**LS**) [5] and Hanjalić-Jakirlić (**HJ**) [3]). The motivation for the second approach is twofold: 1) wall-effects are not confined in the viscous sublayer but affect the boundary layer up to $y^+ = 60$, and 2) wall-effects affect the normal Reynolds stress differently, since the turbulence reaches a two-component limit at the wall. This selective behavior cannot be reproduced by a simple function of viscosity.

In the first class of models, near-wall effects are modeled by making the model constants dependent on the turbulent Reynolds number R_t only. For the second class, near-wall effects depend on the local values of the anisotropy tensor invariants $A_2 = a_{ik}a_{ki}$, $A_3 = a_{ik}a_{kj}a_{ji}$ and on the flatness parameter $A = 1 - 9/8(A_2 - A_3)$ which vanishes when the turbulence reaches a two component limit state.

For example, in the near-wall SSG model, $\Phi_{ij,1}$ is damped at the wall by the factor $1 - f_w(R_t)$ with:

$$f_w = 1 - \exp\left[-(R_t/B)^2\right] \text{ and } B = 200, \quad (2)$$

as opposed to **HJ** where this term is written:

$$\Phi_{ij,1} = \left[1 - f_w + 2.6AF^{1/4}\min\left(1\,,\,(R_t/140)^4\right)\right]\varepsilon a_{ij} \quad (3)$$

with $F = \min(0.6\,,\,A_2)$ and $f_w = 1 - \sqrt{A}E^2$ where E is the flatness parameter of the anisotropic dissipation tensor $e_{ij} = \overline{\varepsilon_{ij}}/\varepsilon - 2/3\delta_{ij}$.

Low-Reynolds nonlinear RSM. However, it is known that the linear model for pressure-strain correlation does not correctly predict the anisotropy effects and the disaligment between turbulent and viscous shear stress: the use of nonlinear models seems to be interesting. The modeling of wall proximity effects in nonlinear RSM models comes up against several difficulties:

- the knowledge of energy-transfer between the Reynolds stresses is insufficient;
- models obtained in homogeneous turbulent flows are not able to mimic energy transfer in the vicinity of the wall, where the turbulence features are strongly anisotropic and inhomogeneous.

Such low-Reynolds RSM are nevertheless built by a careful term-by-term fit to each component of Reynolds stress balance obtained by DNS. Unfortunately, these models (Launder-Tselepidakis (**LT**) [6], Launder-Li [4] or Shih-Mansour [12]) are unable to predict a high Reynolds number flow on a flat plate. Between $x/L = 0$ and $x/L = 0.2$, a first calculation with **HJ** model leads to a fully turbulent boundary layer. The calculation is then carried on with the **LT** model. Figure 1 shows the evolution of the flatness parameter A and the ratio $\overline{uv}/k$. The boundary layer obviously tends to relaminarize. This is due to an over-damping of the $\Phi_{ij,1}$ term in the vicinity of the wall. As a consequence, the level of the normal stress $\overline{v^2}$ and the production of $\overline{uv}$ are too small and the turbulence is destroyed in the wall region.

This loss of generality seems to indicate that the energy transfer between the Reynolds stresses at the wall are ill-modeled by homogeneous turbulence models. This fact is confirmed by recent DNS studies performed by Kim and by Perot and Moin [10]. The latter showed that $\Phi_{ij,1}$ tends to increase the anisotropy level at the wall by contrast to what happens in homogeneous turbulence. This behaviour may be explained by noticing that the energy transfer is due to viscosity. Perot and Moin propose to use the f_{ij} tensor to model $\Phi_{ij,1}$ in the near-wall region. ($f_{ij} = \varepsilon_{ij} - \nu\partial^2\overline{u_i u_j}/\partial x_k \partial x_k$).

We propose a low-Reynolds number extension of the FLT model designed as **LTm** model, which is simply built to fit the results obtained with **HJ** for a flat plate boundary layer. This model is similar to those proposed by Launder and Li except for the damping function applied to $\phi_{ij,1}$ and for the expression of the dissipation tensor in the near-wall region (we adopt the same approach as in **HJ** by using the flatness parameter E). Applications will show that this model gives results similar to those obtain with other RSM.

Low-Reynolds linear RSM / high-Reynolds nonlinear F

In this study, we propose to use a two-layer approach where the boundary layer is split into two parts. In the fully turbulent region, a high-Reynolds nonlinear model is used, while in the viscous sublayer we use one of the low-Reynolds linear models.

COMPUTATIONAL APPROACH

Principle of discretization

Calculations are performed with a non-iterative PNS solver. The discretization of the crossflow inviscid fluxes is carried out by an extension of the TVD upwind scheme of Roe-Osher-Chakravarthy for the PNS equations. When solving the turbulent transport equations, special attention is paid to the numerical treatment of the source term. A hybrid explicit/implicit formulation is proposed which allows a better stability [1].

Special treatment for $k-\varepsilon$

$k-\varepsilon$ models which make use of an equation for the real turbulent dissipation are found to be more sensitive to the wall boundary condition for ε and/or mesh refinement. This behaviour is due to the fact that the calculated value of kinetic energy does not behave as y^2 as it should (y denoting the distance from the wall). When using an evolution equation for $\tilde{k}$ instead of k, this sensitivity is significantly reduced. $\tilde{k}$ is derived from k by: $k = \tilde{k} f_2^d$ where $f_2^d = \left(1-\exp\left(-y^+/5\right)\right)^2$. The damping function f_2 of the sink term in the NT model can be expressed as $f_2 = f_2^d * f_2^g$, f_2^g ensuring that the model reproduces the decay of homogeneous turbulence. By subsituting this expression for k in Nagano-Tagawa equations, one obtains:

$$\frac{\partial \rho U_i \tilde{k}}{\partial x_i} = \frac{(P-\rho\varepsilon)}{f_2^d} + \frac{\partial}{\partial x_j}\left[\left(\mu+\frac{\mu_t}{\sigma_k}\right)\frac{\partial \tilde{k}}{\partial x_j}\right] - \frac{\tilde{k}}{f_2^d}\frac{\partial \rho U_i f_2^d}{\partial x_i} + \frac{\tilde{k}}{f_2^d}\frac{\partial}{\partial x_j}\left[\left(\mu+\frac{\mu_t}{\sigma_k}\right)\frac{\partial f_2^d}{\partial x_j}\right] + \frac{2}{f_2^d}\left(\mu+\frac{\mu_t}{\sigma_k}\right)\frac{\partial f_2^d}{\partial x_j}\frac{\partial \tilde{k}}{\partial x_j}$$

$$\frac{\partial \rho U_i \varepsilon}{\partial x_i} = C_{\epsilon 1}\frac{\varepsilon}{\tilde{k} f_2^d}P - \rho C_{\epsilon 2} f_2^g \frac{\varepsilon^2}{\tilde{k}} + \frac{\partial}{\partial x_j}\left[\left(\mu+\frac{\mu_t}{\sigma_\epsilon}\right)\frac{\partial \varepsilon}{\partial x_j}\right]$$

Wall conditions for $\tilde{k}$ and $\partial\varepsilon/\partial n$ are derived by assuming that the source term of the equation for $\tilde{k}$ is bounded at the wall. Results will show that the mesh sensitivity is reduced by this treatment.

Discretization of nonlinear models

When using a nonlinear RSM model, the transport equations for the Reynolds stresses are expressed in term of the anisotropy tensor components to improve stability. Nevertheless, no simple wall conditions exist for these components, and we must split the boundary layer into two parts: RSM equations are solved in terms of Reynolds stresses in the inner layer and in terms of anisotropy tensor components in the outer layer. The location of the matching between both formulations of the same model does not influence the solution.

APPLICATIONS

Geometry and flow conditions

We consider the computation of the supersonic turbulent flow around an ogive-cylinder at three angles of attack (10, 15, 20°). It is intended to evaluate the ability of the selected turbulence models to adequatly compute three-dimensional phenomena such as crossflow separation. The freestream conditions are those of the experiment of Pagan and Molton [9], ($M_\infty = 2$, $Re_D = 1.61\,10^5$, $T_\infty = 183\,K$, $T_w = 307\,K$) where $D = 0.03m$ is the cylinder diameter. For the measurement of the skin friction coefficient, the Reynolds number was $Re_D = 1.61\,10^6$.

Study of algebraic and two-equation models

To illustrate the importance of this $\tilde{k}-\varepsilon$, the influence of a mesh refinement in the wall vicinity on the stagnation pressure field at the marching station $x/D = 7$ is presented on figure 4. The mesh sensitivity is dramatically reduced by using the $\tilde{k}-\varepsilon$ version.

Side-by-side comparisons of computational and experimental results are presented for the algebraic Baldwin Lomax model with Degani-Schiff correction and for low-Reynolds $k-\varepsilon$ models. The prediction of the stagnation pressure level in the core of the vortex with the $k-\varepsilon$ model is noticeably improved at 10° as well as at 15° (Fig. 7). The improvement is more obvious for the wall pressure coefficient, as shown on figure 5. This trend is confirmed for higher angle of attack: see for instance the stagnation pressure contours on figure 7.

Two-equation models give similar results and are in good agreement with experimental data for 10° angle of attack, except for the Shih's model, which has been calibrated on DNS, and seems to have difficulty to predict such high-Reynolds number flows (Fig. 5). The Menter $k-\omega$ model gives results similar to other two-equation models (Fig. 5,7), and seems to be numerically more stable.

The agreement with experimental data is less satisfactory for higher angles of attack. In particular, the wall pressure coefficient plateau and the primary vortex shape are not adequatly reproduced (Fig. 6, 7, 9).

Study and comparison of RSM models

In the case of Reynolds Stress models for which wall effects lie on viscosity only, the wall function must be fitted to the ogive-cylinder test case: the value of B in equation (2) is taken equal to 100 instead of 200, since this last value tends to reduce drastically the turbulence level.

At the opposite, the other class of models needs no adjustment: they appear to be more general; however, they make use of wall functions which depend on the anisotropy tensor invariants, which can give rise to numerical instability. These models are less robust than the first ones.

For the three different angles of attack, all RSM models give similar results. The improvement in the prediction of the primary vortex shape and of the wall pressure coefficient if compared with two-equation models can be noticed (Fig. 6 and 9). The differences between both results can be explained by the decrease of the turbulent kinetic energy in the vortex core predicted by RSM models: the anisotropy reduces the turbulent level in the vortex core (Fig. 10).

For 10° of angle of attack, the turbulent kinetic energy level predicted by RSM or two-equation models are very similar. These results confirm that at moderate angles of attack, the crossflow is governed by the boundary-layer, although at high angles of attack, the primary vortex behaves as a free vortex.

Two results obtained with the **LTm** are presented. The model is validated on the Owen's axisymetric ogive [2] (Fig.2): the $\overline{uv}$ profile obtained with **LTm** or **LS** are similar and in good agreement with experimental data. This low-Reynolds nonlinear model is able to predict the 3D flowfield around Pagan and Molton's ogive cylinder as well as linear models (Fig. 3).

Two-layer RSM models have been validated on a flat plate and on the axisymetric ogive (Fig.2). The use of nonlinear models in the outer layer affects the primary vortex (Fig. 8). The improvement due to the RSM models as regard to the two-equation models for the prediction of the

skin friction coefficient is clearly demonstrated in figure 11. In this figure, the effect of the model used in the viscous layer is also pointed out: the best results are obtained with the **HJ/FLT** two-layer RSM.

CONCLUSION

A three-dimensional PNS solver has been developed for the computation of 3D turbulent flows. Various turbulence models have been selected and adapted to the PNS equations, ranging from algebraic to RSM models. Special attention have been devoted to the wall region treatment and to numerical robustness. An original two-layer low-Reynolds RSM / high-Reynolds RSM approach has been proposed and validated. The improvement due to Reynolds Stress Models for the computation of 3D flowfield with large crossflow separation is obviously demonstrated for moderate and high angles of attack. Nevertheless, for a moderate angle of attack (10°), algebraic and two-equation models give satisfactory results.

Acknowledgments : This research was financially supported by Aerospatiale-Missiles and by the french Ministry of Defense (DGA/DRET)

REFERENCES

[1] Deniau, H., Lafon, A., and Moschetta, J., 1995, "Progress in the Development and Validation of Turbulence Models for the Computation of 3D Supersonic Flows with Crossflow Separation," *33rd Aerospace Sciences Meeting & Exhibit*, AIAA Paper 95-0090.

[2] Horstman, C.C., and Owen, F.K., 1972, "Turbulent Properties of a Compressible Boundary Layer," *AIAA Journal*, Vol. 10, pp. 1418-1424.

[3] Jakirlić, S., Hanjalić, J., and Durst, F., 1993, "Computation of Accelerating 3D Turbulent Boundary Layers by a Second Moment Closure," *Refined Flow Modelling and Turbulence Measurements, 5th IAHR International Symposium*, Presses de l'École Nationale des Ponts et Chaussées, Paris, pp. 57-64.

[4] Launder, B.E., and Li, S.P., 1994, "The Elimination of Wall-Topography Parameters from Second-Moment Closure," *Physics of Fluid*, Vol. 6, pp. 999-1006.

[5] Launder, B.E., and Shima, N., 1989, "Second-Moment Closure for the Near-Wall Sublayer: Development and Application," *AIAA Journal*, Vol. 27, pp. 1319-1325.

[6] Launder, B.E., and Tselepidakis, D.P., 1991, "Directions in Second-Moment Modelling of Near-Wall Turbulence," *29th Aerospace Sciences Meeting & Exhibit*, AIAA Paper 91-0219.

[7] Leschziner, M.A., 1995, "Computation of Aerodynamics Flows with Turbulence-Transport Models based on Second-Moment Closure," *Computers and Fluids*, Vol. 24, pp. 377-392.

[8] Moschetta, J., Lafon, A., and Deniau, H., 1995, "Numerical Investigation of Supersonic Vortical Flow about a Missile Body," *Journal of Spacecraft and Rockets*, Vol. 32, pp. 765-770.

[9] Pagan, D., Molton, P., and Delery, J., 1990, "Basic Experiment on a Supersonic Vortex Flow around a Missile Body," *Journal of Spacecraft and Rockets*, Vol. 29, pp. 373-378.

[10] Perot, B., and Moin, P., 1995, "Shear-Free Turbulent Boundary Layer. Part 2. New Concepts for Reynolds Stress Transport Equation Modelling of Inhomogeneous Flows," *Journal of Fluid Mechanics*, Vol. 295, pp. 229-245.

[11] So, R.M., Aksoy, H., Sommer, T.P., and Yuan, S.P., 1994, "Development of a Near-Wall Reynolds-Stress Closure based on the SSG Model for the Pressure Strain," Technical report, NASA Report 4618.

[12] Shih, T.H., and Mansour, N.N., 1990, "Modelling of Near-Wall Turbulence," *First International Symposium on Egineering Turbulence Modelling and Measurements*, Rodi et al., ed., Elsevier Science Publishers, Amsterdam.

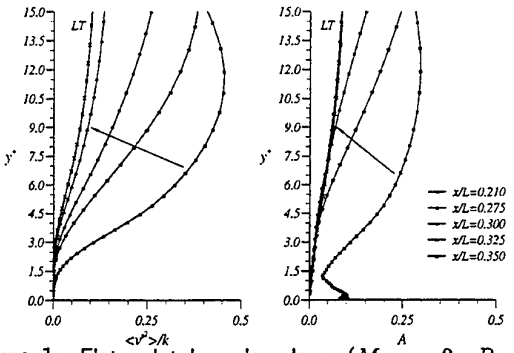


Figure 1: Flate plat boundary layer ($M_\infty = 2$, $Re_L = 1.6\,10^6$, $L = 1m$): evolution of the ratio $\overline{v^2}/k$ and the flatness parameter A

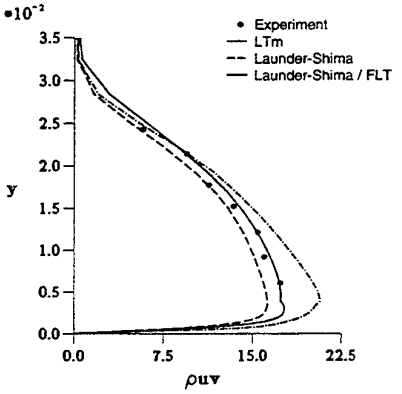


Figure 2: Owen's experiment ($M_\infty = 7.2$, $Re_L = 1.09\,10^7$, $L = 1m$): $\overline{\rho uv}$ profile at marching station $2.25m$, Comparisons of RSM models

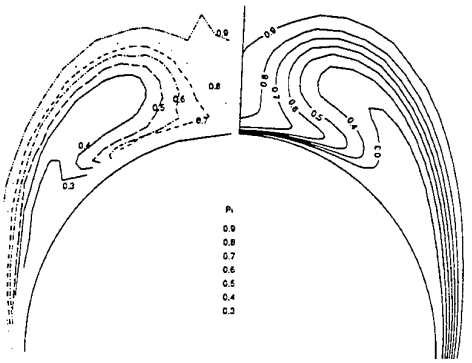
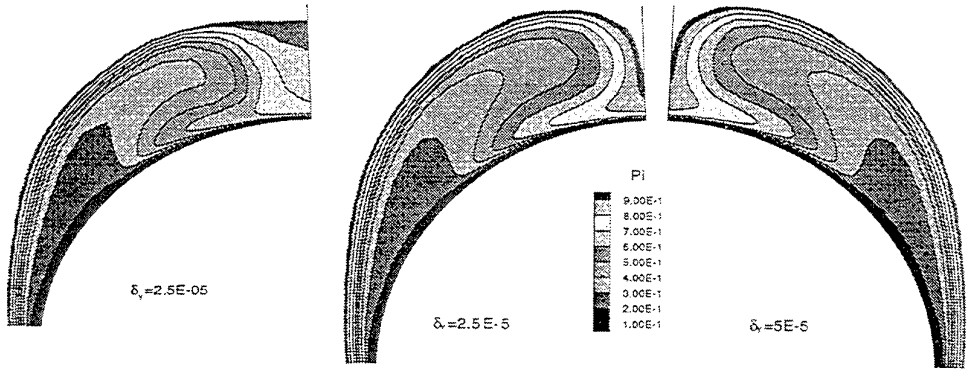


Figure 3: Ogive-Cylinder at 10° angle of attack: Stagnation pressure contours at the marching station $x/D = 7$, performance ot **LTm** model



Nagano-Tagawa: original model

Nagano-Tagawa: $\tilde{k} - \varepsilon$ version

Figure 4: Ogive-Cylinder at 10° angle of attack: Stagnation pressure contours at the marching station $x/D = 7$: Study of mesh-sensitivity

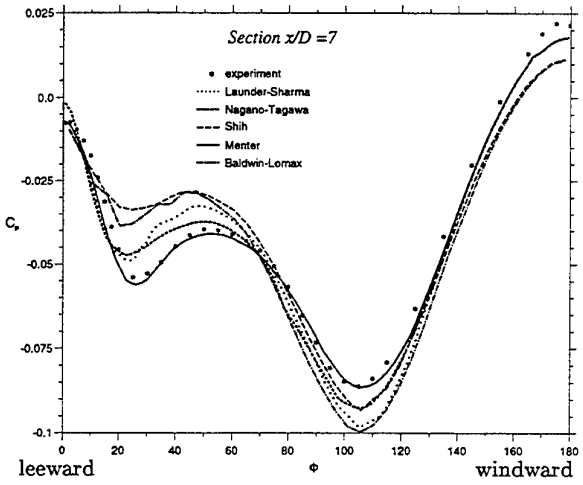


Figure 5: Ogive-Cylinder at 10° angle of attack: Wall pressure coefficient at the marching station $x/D = 7$: Comparisons of two-equation and algebraic models

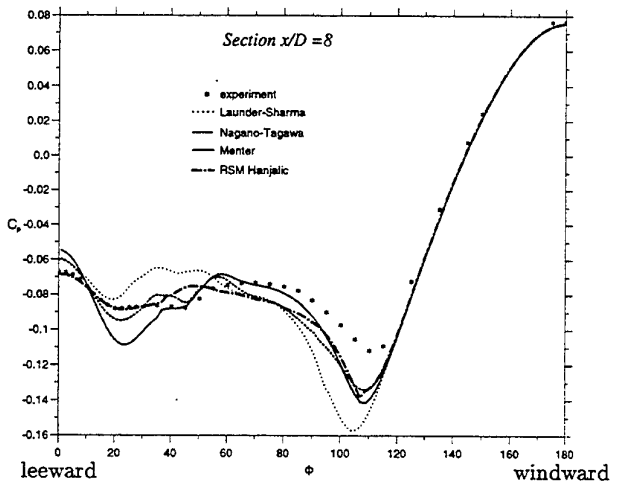


Figure 6: Ogive-Cylinder at 15° angle of attack: Wall pressure coefficient at the marching station $x/D = 8$: Comparisons of two-equation and RSM models

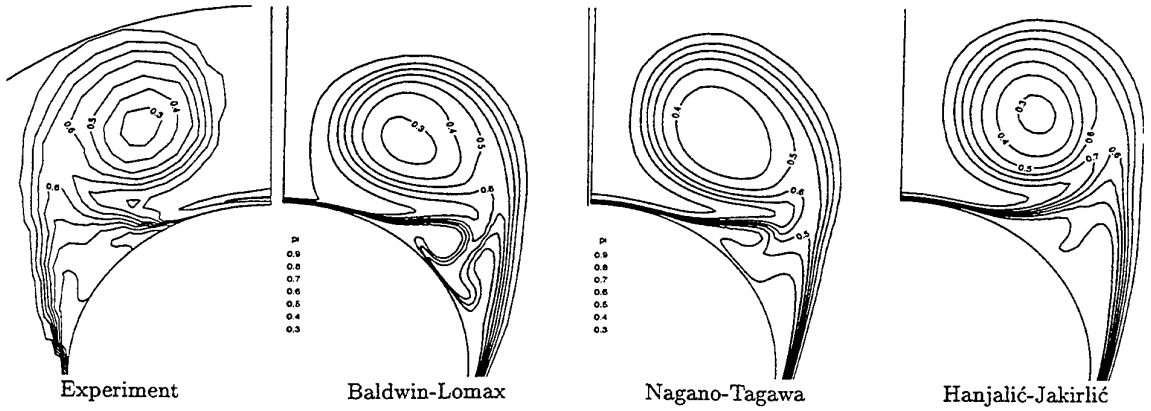


Figure 7: Ogive-Cylinder at 15° angle of attack: Stagnation pressure contours at the marching station $x/D = 8$: Comparison of algebraic, two-equation and RSM models

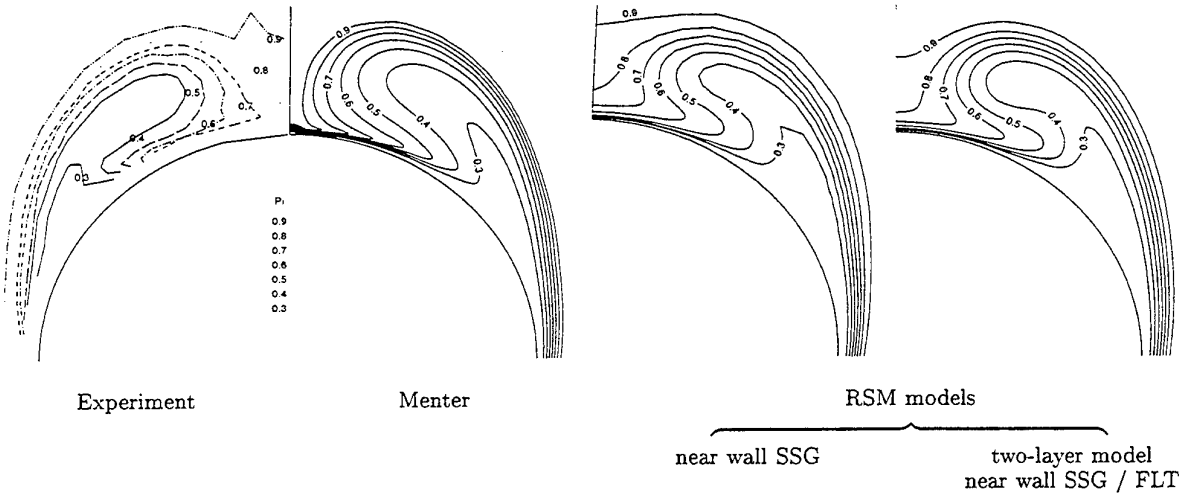


Figure 8: Ogive-Cylinder at 10° angle of attack: Stagnation pressure contours at the marching station $x/D = 7$: Comparison of two-equation and RSM models, validation of the two-layer approach

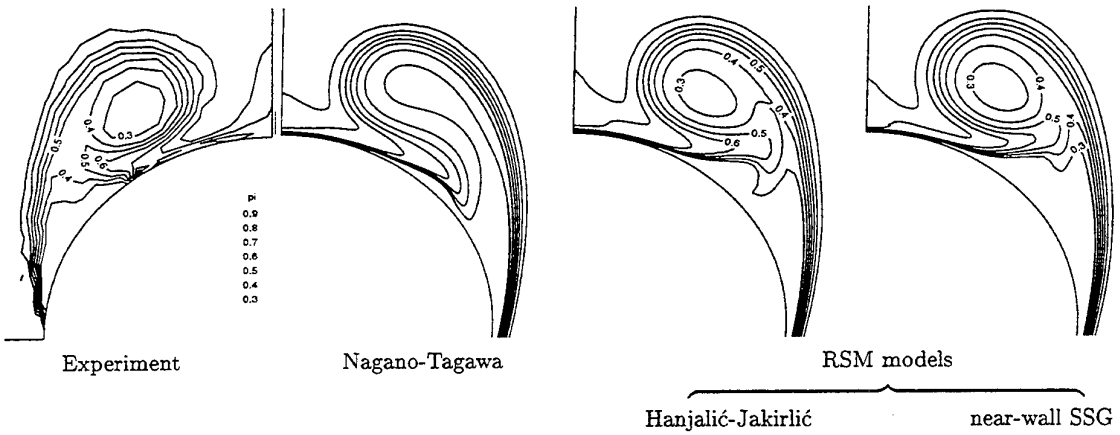


Figure 9: Ogive-Cylinder at 15° angle of attack: Stagnation pressure contours at the marching station $x/D = 6$: Comparison of two-equation and RSM models

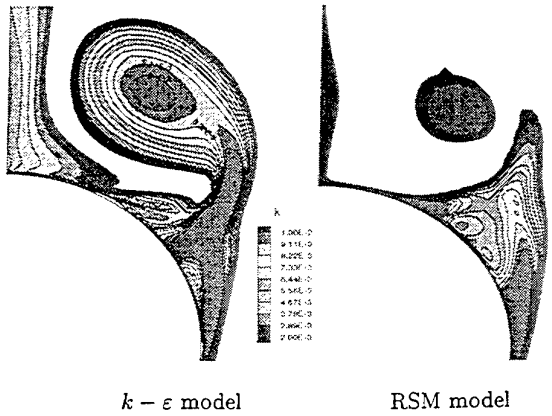


Figure 10: Ogive-Cylinder at 15° angle of attack: Turbulent kinetic energy contours at the marching station $x/D = 8$

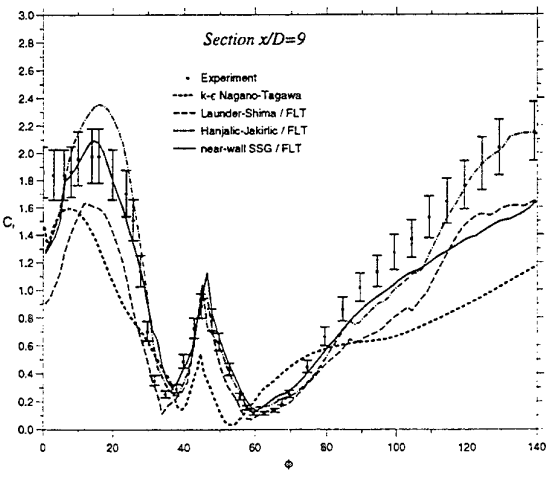


Figure 11: Ogive-Cylinder at 10° angle of attack $Re_D = 1.61\,10^6$: Skin friction coefficient at the marching station $x/D = 9$: Comparisons of two equations and RSM models

SESSION 30 - SEPARATED FLOWS II

MEASUREMENTS IN AN UNSTEADY SEPARATED FLOW USING HOT WIRE RAKES

AUBRUN Sandrine, HA MINH Hieu, BOISSON Henri
Institut de Mécanique des Fluides de Toulouse, UMR CNRS - INP/UPS N° 5502,
av du professeur Camille Soula, 31400 TOULOUSE, FRANCE

CARLES Pierre
Université Pierre et Marie Curie, Laboratoire de Modelisation en Mécanique,
4 place Jussieu, 75252 PARIS Cedex 05, FRANCE

COULOMB Jean
Centre d'Essais Aéronautique de Toulouse,
23, av H. Guillaumet,31056 TOULOUSE cedex, FRANCE

ABSTRACT

Our study consists in identifying the characteristics of a two-dimensional unsteady incompressible separated flow behind a backward-facing step. The Reynolds number based on step height is about 10^5. An experimental apparatus using simple or X hot wires rakes is set up for measuring the transverse and the longitudinal instantaneous velocities simultaneously in several points in shear layer, where coherent structures are formed and convected. Then, characteristics of coherent structures are captured by means of several conditional methods.

INTRODUCTION

The study of unsteady phenomena in separated flows is of current interest owing to existence of strong instabilities developing large scale vortical structures in the separated zone (aero-acoustic strain in materials, perturbation in combustion chambers). The physical nature of these structures is not well known yet and, up to now, numerical approaches have not been able to correctly predict their characteristics because of difficulties in extracting the organized motion from Reynolds' averaging of turbulent flows. The experimental approach seems to be the best way to analyze coherent structures (CS). Similar approaches have been already elaborated in the case of mixing layers and wakes (Bonnet et al. (1992), Giralt et al. (1992), Hussain et al. (1993)). The challenge is to extend these methods to a case more complex due to the high rate of curvature of the mixing layer.

DIFFICULTIES

By definition, CS's are considered as an accumulation of spatially phase-correlated vorticity. Further studies prove that their main features, although globally deterministic, present significant random discrepancy. It is the case, for instance, of their exact shape, spatial extent and trajectory. It follows that with a one-point measurement apparatus, it is not possible to precisely locate the CS relatively to the probe. Multipoint measurements overcome this difficulty since one captures all the spatial extent in a given section of the CS at each time step.

Moreover, we can build a detection signal of CS transit based on its whole spatio-temporal extent, instead of relying on any external signal which could create a false detection.

However, this introduces a scale of analysis and a space resolution which can occult some of characteristic scales and thus, some of physical properties of these structures.

EXPERIMENTAL APPARATUS

The rearward facing step model is fixed in the middle of the wind-tunnel S10 of C.E.A.Toulouse (figure 1). The test volume is 1 m wide by 2.2 m height by 2 m long. The plate where initial boundary layer is developing is 0.45 m, the reattachment plate is 1.2 m and the step height is 65 mm. The aspect ratio is more than 10 and so, ensure that we simulate a flow in an infinitely high tunnel. Reference velocity is 40 m/s (Reynolds number based on step height is about $1.7\ 10^5$, Mach number 0.12).

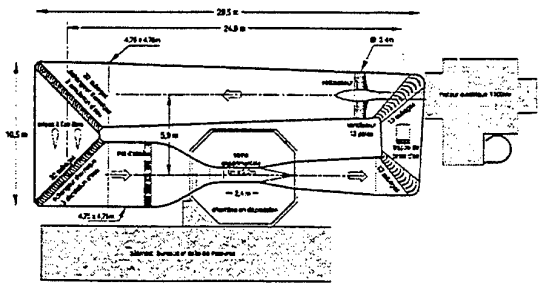


FIGURE 1 : WIND TUNNEL S10 OF C.E.A.T.

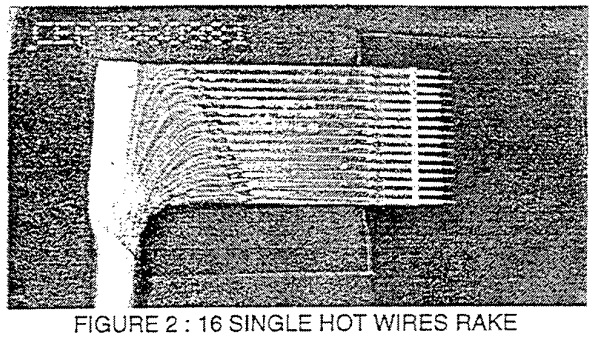


FIGURE 2 : 16 SINGLE HOT WIRES RAKE

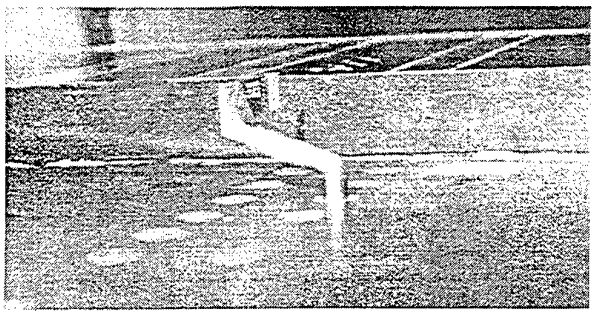


FIGURE 3 : HOT WIRE RAKE "IN SITU",ON A BENT SUPPORT

Some preliminary Laser Doppler Velocimetry measurements gave access to mean velocity fields and help to check flow bidimensionality as well as to find reattachment length (Xr = 5.7 H) and where to place the rakes in the flow. Then, an experimental study was developed using 16 single hot wires or 8 X hot wires rakes in the mean-gradient direction behind the backward facing-step (figures 2 and 3). The instantaneous streamwise and transversal velocity measurements for a sampling frequency about 12 kHz allowed a good definition of the CS's transit in this area. In addition, measurements with a lower sampling frequency and long duration enable more precise spectral analysis.

In this study, we present results based on measurements performed with a rake of 8 X hot wires located at X = 1.2 H. Intervals between wires are $0.24\delta_\omega$ and the rake covers all the shear layer extend in the transverse direction ($1.8\delta_\omega$ = 25 mm where δ_ω is the vorticity thickness in the studied section). The power density spectrum of velocity signal (figure 4) exhibited a concentration of energy around 370 Hz in the shear layer. We associate this bump to the CS transit. The shape of this spectrum confirms that natural CSs keep random characteristics and that a spectral analysis or a conditional method based on an external signal detection are not sufficient.

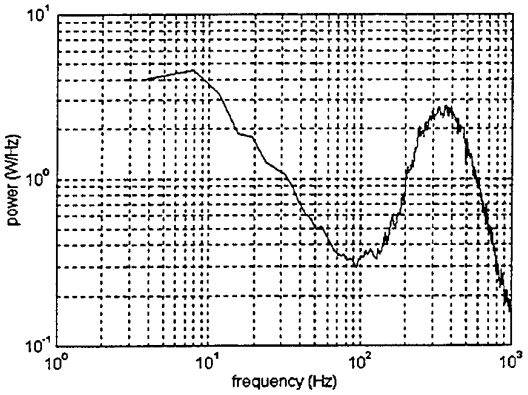


FIGURE 4 : POWER SPECTRAL DENSITY OF A VELOCITY SIGNAL IN THE SHEAR

DEFINITIONS

A time and space dependent signal F can be decomposed as follows :

$$F(t,y) = \overline{(F)}(y) + f(t,y)$$
$$= \langle F \rangle (t,y) + f'(t,y)$$
$$= \overline{(F)}(y) + \tilde{f}(t,y) + f'(t,y)$$

where $\overline{(F)}$ is the signal's time average and $\langle F \rangle$ its the coherent part. $\tilde{f}(t,y)$ is deduced from $\overline{(F)}$ and $\langle F \rangle$ and represents the coherent perturbation around time average. f and f' are the remaining parts through averaging. f' is considered as a completely incoherent signal.

For a discrete time series of simultaneous F signal at N y locations separated by Δy, during T with a time step Δt, we define :

$$F(t,y) = F(i*\Delta t, j*\Delta y) = F_{i,j}$$
with i=1,2,...,T/Δt and j=1,...,N

DETECTION OF COHERENT STRUCTURES

Two signal processing methods were applied to these measurements. Advantage was taken from the complementarity of these methods to provide correct physical interpretations of data.

Vorticity-based method

The first method was based on the instantaneous spanwise vorticity (using the Taylor hypothesis in the flow direction and finite difference schemes for evaluating derivative terms) and gave us a time display of the vorticity along the transversal length of the rake. We applied a numerical filter (LP without phase difference) to visualize high vorticity areas. Even if this investigation was not the panacea, vorticity peaks were, by definition, the best CS detectors and could clearly be identified from contour plots.

Practically, we used a method very close to the vorticity-based conditional sampling technique developed by Hayakawa : From a discrete time series of simultaneous U and V signals at N locations separated by Δy, during T with a time step Δt, we define the instantaneous vorticity :

$$\Omega_{z\,i,j} = -\frac{1}{Uc}\frac{V_{i+1,j} - V_{i-1,j}}{2 * \Delta t} - \frac{U_{i,j+1} - U_{i,j-1}}{2 * \Delta y}$$

Uc is the average convection velocity of CS in the longitudinal direction (Uc = 0.5*Umax in our study).

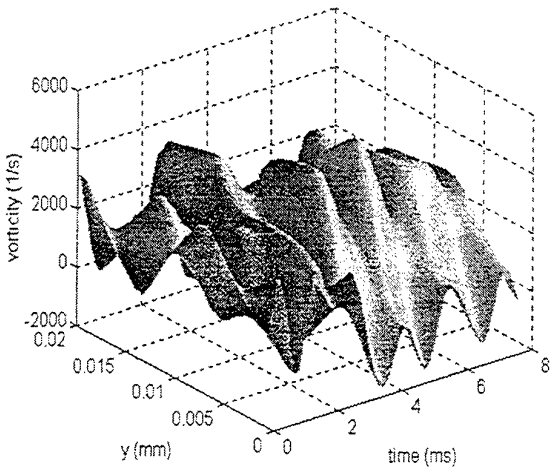


FIGURE 5 : SMOOTHED VORTICITY FIELD

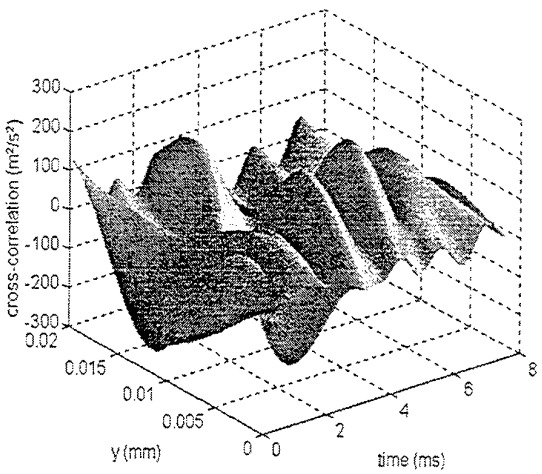


FIGURE 6 : SMOOTHED CROSS-CORRELATION FIELD

We obtained a spatio-temporal map of vorticity field (figure5).

"Profile recognition" method

Theory. The second method is similar to "pattern recognition" technique. Assuming that the transit of a CS in this kind of flow is typically characterized by an overvelocity (with respect to the local time mean longitudinal velocity) in the top of the CS and an undervelocity in the bottom, we build an indicative reference velocity profile of the CS's transit in the studied area. For each time step, we compute the spatial cross-correlation between this reference profile and the instantaneous profile. The cross-correlation function is :

$$Cuu_{ref\,n,j} = \sum_{i=1}^{N} u_{i,j}\, u_{ref\,i+n,j} \qquad \text{with n = -N to N}$$

We use the correlation function instead of the correlation coefficient to keep the strength of CS's : the instantaneous profile must look like the reference profile but also should present the amount of over- and under-velocity magnitudes.

So, we obtain a spatio-temporal map of space correlation field (figure 6) and, if a strong correlation zone (time and space spread) is detected, we class it as a CS's transit. Again, we used a low pass numerical filter to investigate high correlation areas.

Reference profile. Inevitably, we have to choose a reference profile. To minimize subjectivity, the method relies on a "POD profile" : the Proper Orthogonal Decomposition was performed from the correlation matrix corresponding to the long time signal. It was possible to identify most energetic modes of the decomposition related to the CSs and to establish an average basic form to be used in the profile recognition. We also applied an iterative method to this reference profile : we included each new detected profile in the reference profile using weighted averages (figure 7). It is interesting to remark that, for different initial profiles, the iterative profile tends towards an unique solution.

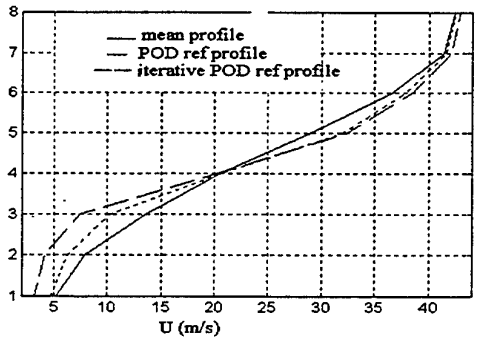


FIGURE 7 : REFERENCE PROFILES

Comparison

We have performed tests in order to check if these two methods had the same sensitivity to CS's transit. For its purpose, we computed the space-time correlation between the vorticity field and the space correlation field inferred from the "profile recognition" (figure 8).

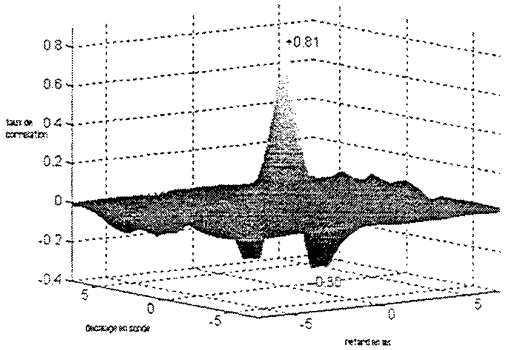


FIGURE 8 : CROSS-CORRELATION BETWEEN VORTICITY FIELD AND SPATIAL CORRELATION FIELD

A high correlation peak was obtained at exactly zero space and time delay. It proved that, even if the spatial step is large, the transversal location of vorticity and correlation maxima are in good agreement. In time direction, the high correlation area was well located on zero delay. Meanwhile, the peak correlation was not very high. Detailed analysis of time series Ω and $C_{u,uref}$ showed that in spite of very similar time variation, there were magnitude distortions. For instance, figure 9 shows that for probe number 4 (j = 4), even though vorticity and correlation are very aligned and in phase, they are not simply proportional.

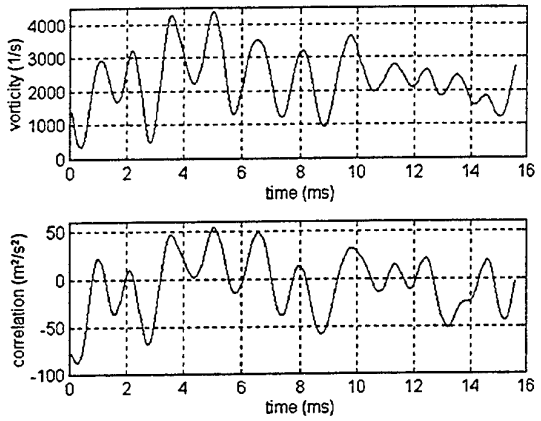


FIGURE 9 : COMPARISON BETWEEN VORTICITY AND CORRELATION SIGNAL ON PROBE 4

Detection approach

To isolate CS features from the complete motion, we imposed a threshold (Th) on vorticity or cross-correlation maps to select areas where their magnitude was strong. Positions (y_c, t_c) of maximum amplitude in these areas were supposed to be CSs centers :

$$\Omega(t_c, y_c) > Th \quad \underline{\text{AND}} \quad \Omega(t_c, y_c) = Max_{local}(\Omega(t, y))$$

Then, we obtained a spatio-temporal matrice I that indicate center positions :

$$\text{if } I_{i,j} = 1,\ t_c = i\Delta t \text{ and } y_c = j\Delta y$$
$$\text{else } I_{i,j} = 0$$

PHASE AVERAGE

The application of phase average on instantaneous signals allowed to extract the coherent motion <F> and the pure random motion f. Furthermore, the coherent motion was assumed to be the coherent structure motion.

We chose not to class as the same event structures centered on different transverse positions. These CSs could indeed have distinct features. So, to determine the mean coherent structure centered on a fixed transverse position, we aligned original unfiltered realizations of all transverse positions with respect to each center of reference position and then, we applied ensemble-average on U and V. For instance, to educe the mean coherent structure centered on probe 4, the detection signal was reduced to vector $I_{i,4}$. For τ time delay with respect to the structure center, the phase-average operator was :

$$\left\langle F(t,y)\right\rangle_4 = \frac{1}{N}\sum_{t=t_1}^{t_N} F(t+\tau, y) \text{ with} \{t_1,...,t_N\} = \{I_{i,4}=1\}$$

The procedure of "realignment" proposed by Hayakawa was also implemented : phase-average <Ω> or $<C_{u,uref}>$ is used to detect new CS centers and possibly correct those already found. This correction should reduce possible time delays between phase average CS and each detected realization.

RESULTS

Vorticity-based method

We present (figure 10, at end of article) the morphology of mean coherent structures centered on the fourth and fifth wires. As expected, the vorticity peak was well defined and centered on the trigger point. The mean structure centered on the fifth wire seemed to be more distorted than the one centered on the fourth wire and presented protrusions at its extremities. This characteristic is probably due to phase difference within the structure, i.e., meanly, structures centered on the fifth wire possessed a natural tilt.

To check that these vorticity peaks were really due to vortical structures but not only to transverse gradient, we present coherent streamwise and transverse velocity fields $\tilde{u}$ and $\tilde{v}$.

Indeed, locations of over and under velocities are representative : the transverse gradient is optimal for $\tilde{u}$, and the streamwise one for $\tilde{v}$.

The last two plots depict the morphology of mean structure in a convected frame. To obtain these fields, we subtracted the average convection velocity of structures Uc from the streamwise coherent velocity <U>. It is interesting to notice that if we subtract the experimental convection velocity, the structure is not centered on the vorticity peak. On the other hand, if we subtract from the time-mean velocity of the reference position to the phase averaged velocity, the structure is well centered on the vorticity peak where it was educed. This means that averaged structures are convected at their center velocity. Indeed, the global convection velocity includes all structures and so, behave as a spatio-temporal average of the real phenomena.

Finally, selection of events during the detection stage is not based any structure size criteria. Nevertheless, some structures are completely occulted by this technique : long CS could go undetected because their peak vorticity value was under the prescribed threshold. Even, a small structure creating a high but short vorticity peak could be smoothed out by filtering. So, a natural selection of CS's morphology is imposed by using a vorticity-based conditional sampling.

"Profile recognition" method

In conditions of these experiments, the phase average process based on the "profile recognition" method did not permit to attain a converged solution.Even though both detection maps were in good agreement, the application of a threshold to select

suitable events leads to completely different averaged results. In order to interpret this difference, we scrutinized each detection stage. We notice that both small and large CSs were educed and averaged together. Although we fixed a reference CS transit signature, velocity magnitude of detected profile was also relevant, and further subclassed of CSs might be found.

We plan to implement an additional criteria based on the CS extent to avoid averaging CSs which present too many discrepancies.

CONCLUSION

These both conditional methods have allowed us to study coherent structures which develop in the shear layer produced by separated flow behind a backward facing step. The behavior of this shear layer in the studied section is closed to the plane mixing layer. The morphology of the conditional CS is in good agreement with Hayakawa and Bellin results. It confirms the habit to consider the curved shear layer as a plane mixing layer in the first sections. The "profile recognition" method still needs further improvements but, it is really hopeful since it permit to study several occuring CS morphologies. Furthermore, it would present a great advantage since it doesn't require the transversal velocity measurements. The experimental apparatus is, therefore, highly simplified, and the spatial resolution enhanced. Nevertheless, with existing experimental means and using the detection based on filtered vorticity peaks, we have obtained information about the decomposition between coherent motion and incoherent background. These results could improve the semi- deterministic approach in two manners : they can give information to theoreticians to conceive new models or revise old ones, and can be a good data bank to validate some simulations of this unsteady flow.

AKNOWLEDGEMENTS

The author gratefully aknowledge Dr D. Faghani for fruitful discussions and suggestions.I would like also to thank J.P. Bonnet and J. Delville who advised and designed the hot wires rakes. The measurements were supported by the C.E.A.T. (Centre d'Essais Aéronautique de Toulouse).

REFERENCES

Bellin S., 1991, "Etude experimentale des structures cohérentes d'une couche de mélange plane turbulente de fluide incompressible". Thesis.

Bellin S., Delville J., Vincendeau E., Garem J.H., Bonnet J.P., 1992, "Large scale structure characterization in a 2D mixing layer by Pseudo Flow Visualisation and Delocalised Conditional Sampling." in Bonnet J.P. and Glauser M.N. Eds., 1992, "Eddy structure identification in free turbulent shear flows", Proceedings of the IUTAM Symposium - POITIERS October 1992, Kluwer Academic Publishers.

Ferre J.A., Giralt F., 1992, "A pattern recognition approach to the analysis of turbulent signals." in Bonnet J.P. and Glauser M.N. Eds., 1992, "Eddy structure identification in free turbulent shear flows", Proceedings of the IUTAM Symposium - POITIERS October 1992, Kluwer Academic Publishers.

Hayakawa M., 1993, "vorticity-based conditional sampling for identification of large-scale vortical structures in turbulent shear flows". in Bonnet J.P. and Glauser M.N. Eds., 1993, "Eddy structure identification in free turbulent shear flows", Proceedings of the IUTAM Symposium - POITIERS October 1992, Kluwer Academic Publishers.

Hussain A.K.M.F. and Hayakawa M., 1987, "Eduction of large-scale organized structures in turbulent plane wake.", J. Fluid Mech. (1987), vol 180, pp.193-229

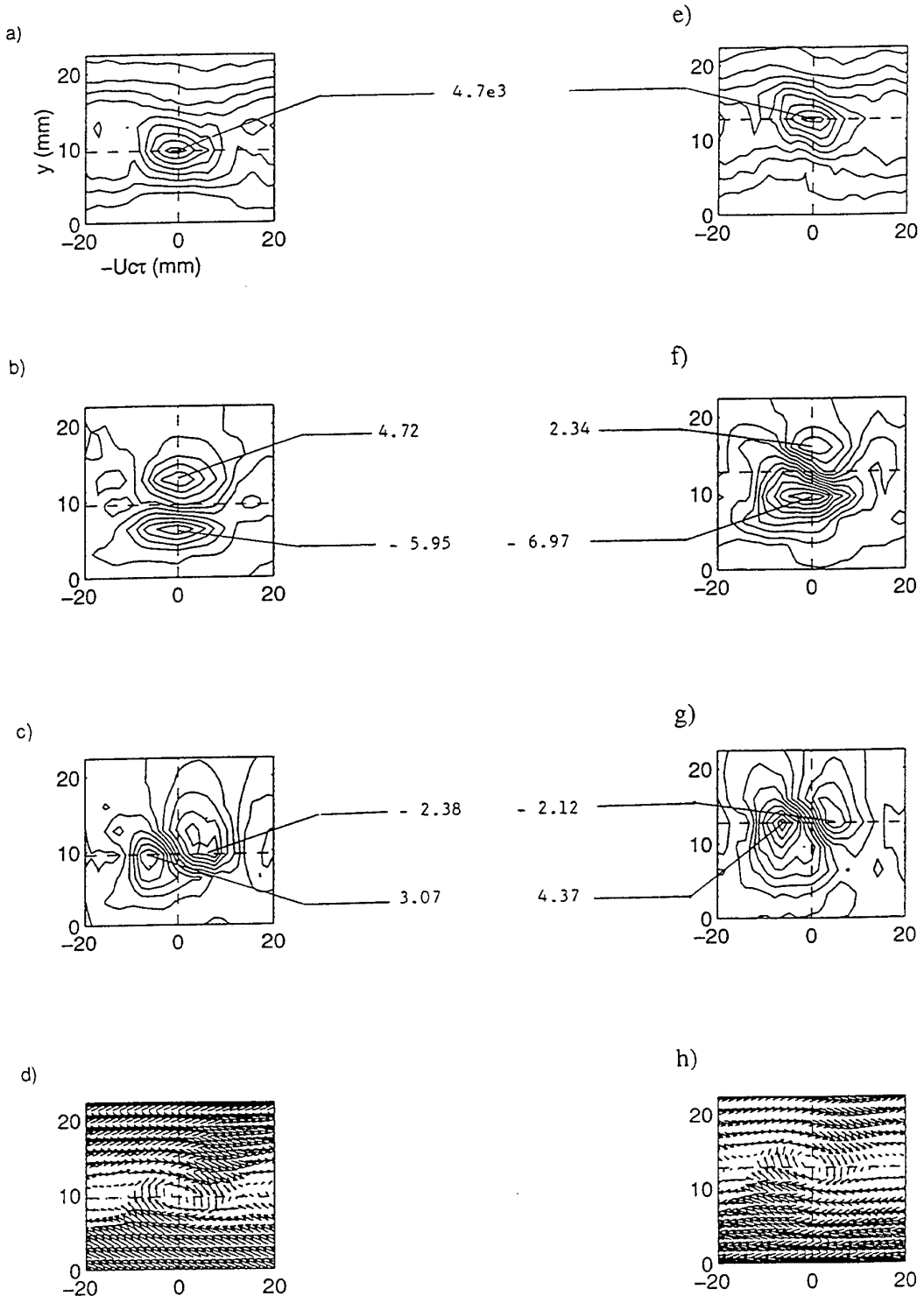


FIGURE 7 : MORPHOLOGY OF PHASE-AVERAGED STRUCTURE CENTERED ON THE FOURTH (a to d) AND FIFTH(e to h) WIRES.

a) and e) $\langle \Omega(\tau, y) \rangle$. b) and f) $\tilde{u}(\tau, y)$ .c) and g) $\tilde{v}(\tau, y)$. d) and h) vector field of structure.

AN INVESTIGATION ON THE FLUCTUATIONS OF THE REATTACHMENT POINT DOWNSTREAM A BACKWARD FACING STEP USING PARTICLE TRACKING VELOCIMETRY

Giovanni P. Romano, Stefano Pomponio
Department of Mechanics and Aeronautics
"La Sapienza" University, Via Eudossiana 18, 00184 Roma, ITALY

Giorgio Querzoli
Department of Civil Engineering
"Tor Vergata" University, Roma, ITALY

ABSTRACT

The flow field downstream a backward facing step is investigated using a multi-point measurement technique as the Particle Tacking Velocimetry. The near-step region (from 0 to about 11 step heights along the streamwise direction) is considered for Reynolds numbers between 200 and 3000 (using the step height). Eulerian and Lagrangian statistics are used to determine the average reattachment length and its variation in time. The results indicate that on the average this length decreases for increasing Reynolds numbers (unless lower than 500). The fluctuation of the reattachment length is as large as 3 step heights and slightly decreases with the Reynolds number. The distribution of the instantaneous reattachment point is skewed towards small values for small Reynolds numbers and becomes almost symmetrical when the Reynolds number increases. The fluctuation of the reattachment point seems to be influenced by the large scale structures for Reynolds numbers lower than 1000, while by a sort of low frequency "flip-flop" of the shear layer for larger Reynolds numbers.

INTRODUCTION

The flow field downstream a simple geometrical configuration, as the step in the channel, is extremely complex due to the combined effects of the step discontinuity and of the rigid boundaries on the flow dynamics. The interest on such a flow field is justified not only from the viewpoint of fundamental research, but also on the basis of the large number of applications in hydraulic and mechanical engineering. Among the others, the behaviour of contaminants and pollutants in the region between the step and the reattachment point (the point where the separation line arrives at the wall) is investigated. Therefore, besides of Eulerian statistics, special attention is given to the Lagrangian description of turbulence.

Due to the relatively easy boundary conditions and to the strict requirements on the description of the flow field, the Backward Facing Step (BFS) has been used as a benchmark problem for several numerical codes. However, there are several discrepancies between numerical and experimental results, that are only partially explained by the different parameters as the Reynolds number, the step expansion ratio (that is the ratio between the channel heights downstream and upstream of the step), the wall layer thickness to step height ratio and the two-dimensionality of the flow field (Askelvoll and Moin, 1993). As a consequence, there is an effective demand for accurate, whole field and instantaneous measurements on the BFS.

Despite the large number of papers devoted to the subject, there are a few whole field measurements. In the following, the attention will be focused on the interaction between the flow and the bottom channel wall. The question is if and how large scale structures are responsible for the fluctuations of the average position of the reattachment point. The most of the experiments on the BFS concerned with single-point measurements. The extensive investigation of Armaly *et al.* (1983) (in air) pointed out the effect of the Reynolds number on the reattachment length, X_r: for $Re=Uh/\nu$ (where U is the mean velocity before the step, h the step height and ν the kinematic viscosity) less than 1000 it increases almost linearly up to $X_r/h\approx19$. For larger Reynolds numbers it decreases to $X_r/h\approx7$. These results

have been confirmed by other authors (for example Sinha *et al.*, 1981, Kasagi *et al.*, 1992). However, they are strongly dependent on the step expansion ratio and on the layer thickness at the step: for example there is a 20% difference in the reattachment length from the measurements of Armaly *et al.* (1983) (expansion ratio equal to 2) ($X_r/h\approx8$), to those of Kasagi *et al.* (1992) (expansion ratio equal to 1.5) ($X_r/h\approx6.5$) roughly at the same Reynolds number. Also when considering these effects, a strong discrepancy between mostly of the results obtained in air and water is still present. The latter show reattachment lengths more than two times lower than the former at small Reynolds numbers (Durst and Tropea, 1981, Adams and Johnston, 1988). Due to the different approaches involved this result seems not to be simply due to numerical or experimental problems.

In this paper the flow field over a BFS in water is investigated in the region between the step and the reattachment point for Re between 100 and 3000. The aim of the paper is to give some clarification on the mechanisms responsible for the fluctuations of the reattachment point using a well established multi-point technique as the Particle Tracking Velocimetry: to this end, Eulerian and Lagrangian statistics are considered.

EXPERIMENTAL SET UP

The step is placed into a water channel (height=2cm (h_1), width=10 cm (l)) at about x/h_1=80 from the contraction (5:1). The step height is h=1cm, so that the expansion ratio is h_2/h_1=1.5 and the channel width to step height ratio is l/h=10. The displacement thickness and the momentum thickness before the step (measured using a Laser Doppler Anemometer) decrease as the Reynolds number and are equal to 0.15h and to 0.08h at $Re\approx2500$. The momentum thickness Reynolds number is approximately 200. The turbulence intensity of the free stream is equal to 5%.

Flow Visualization is performed by inserting Fluorescein as close as possible to the step. The measurement section is illuminated by a spanning laser beam using a rotating polygonal mirror. The Schmidt number is about 2000. Extensive LDA measurements were performed in the past (Romano and Tumbiolo, 1995): the reattachment length was $X_r/h\approx7$ at $Re\approx7500$ in reasonable agreement with results of Armaly *et al.* (1983) and of Westphal *et al.* (1984) at similar Reynolds numbers. The agreement was observed up to x/h=20.

The two velocity components on the light plane are measured using a PTV system (Cenedese and Paglialunga, 1990). The measurement plane is obtained by using the rotating mirror. Its angular velocity is selected to have one image of tracers on each frame (single exposure PTV). The mirror scans the measurement section with a velocity more than 100 times higher than the maximum velocity: therefore, the error related to the use of a scanning mirror is negligible.

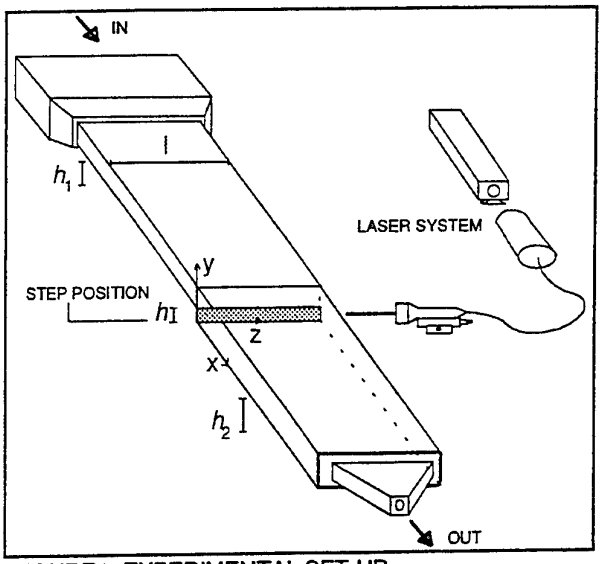


FIGURE1. EXPERIMENTAL SET-UP.

The light sheet thickness is about 0.3cm (0.3h): such a large value is required to "track" the seeding particles also when three-dimensional motions are involved. Pollen particles (mean size equal to 40 μm, density equal to 1.02 that of the water, relaxation time scale equal to 3×10^{-4} s) are used as seeders: they are able to follow velocity fluctuations up to about 1 kHz. Images of the flow field are acquired by means of a videocamera connected to a videorecorder at 50 frames per second. They are acquired at a 512×512×8 bit resolution. Image analysis is performed by "tracking" each particle along its trajectory during consecutive frames. Tracking consists of the detection of each particle barycentre and of the analysis of its displacements using some maximum velocity and acceleration as validation parameters (Cenedese and Querzoli, 1994). About 50 images of particles are obtained on each video frame on a (10×3)cm^2 measurement region: for PTV this is a rather high data density. The relative error on PTV is given by the digit error, that is about 5% of the mean velocity (Romano, 1995).

RESULTS

Visualizations

In Figure 2, flow visualizations on the (x,y) plane at different Reynolds numbers are presented. For Re<200 instabilities are not observed, whereas for Re=300 the Kelvin-Helmholtz (K-H) instability appears. In comparison to free flows, the spanwise vortices are deformed by the presence of the wall: the x-size is more than two times larger than that along y (respectively more than 2h and less than 1h). This interaction is outlined in the visualization at Re=500 where very long inclined layers of flow from the wall are observed.

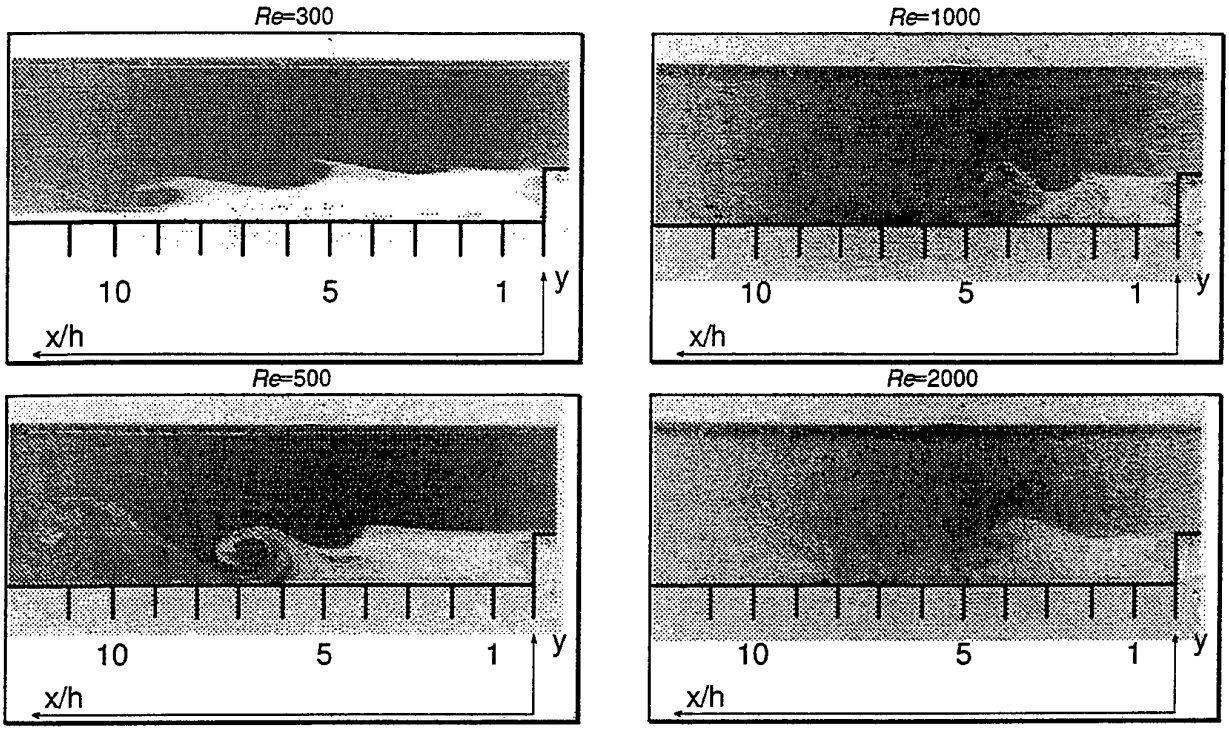


FIGURE 2. FLOW VISUALIZATION AT DIFFERENT REYNOLDS NUMBERS. FLOW FROM RIGHT TO LEFT.

They derive from the interaction of large scale structures with the wall. At higher Reynolds number the K-H vortex size decreases to less than $1h$ along x, whereas is practically unchanged along y. Their appearance is moved towards the step. For Re>1000 large scale instabilities are not clearly detected.

These observations are confirmed when measuring the variation of the vertical vortex size (a) along x. In Figure 3 this size is given for different Reynolds numbers. It changes almost linearly with the distance from the step and the slope increasing as the Reynolds number. On the other hand, the horizontal vortex size (not shown) reaches a maximum (corresponding to the point closer to the wall) and then decreases. It is usually two times larger than the vertical vortex size and it decreases as the Reynolds number. In Figure 3 it is also noticed that the position where the vortices initially appear moves towards the step when the Reynolds number increases. At the same time, such vortices lose their shape rapidly, so that at high Reynolds number they disappear earlier. The position of the vortex centre is followed in time: in Figure 4 the non-dimensional x and y positions (x_c/h and y_c/h) are plotted as functions of the time $t^*=tU/h$. While the first increases linearly in time, the second decreases down to a minimum (roughly equal to $0.6 \div 0.7$ h), corresponding to the minimum distance from the wall, and then starts to increase (not for Re=500). The y-position seems to depend on the Reynolds number more than that in x. These conclusions agree with those obtained by Shen and Ma (1996) by Image Velocimetry.

In Figure 5 the non-dimensional number of vortices per unit time (nh/U) is plotted *vs* the Reynolds number: the overall increase shows that, when the Reynolds number increases, there is not only an higher number of convected vortices, but rather an effective increase of the number of generated vortices.

Particle Tracking Velocimetry

In Figure 6 examples of PTV trajectories at three Reynolds numbers are shown: about 800 trajectories are overlapped during 100 frames (about 2s of total image acquisition time). At small Reynolds number, particles does not arrive at the wall within the test section, while this happens for higher Reynolds numbers. The previous trajectories are used to obtain averaged quantities in a Eulerian frame of reference and to follow instantaneous particles in a Lagrangian one.

Mean velocity isocontours, for the same Reynolds numbers used in Figure 6, are given in Figure 7. These plots contain all the information that can be obtained by classical single point techniques. However, they are obtained by averaging about 9000 frames corresponding to only 6 minutes of total acquisition time. The reattachment length (determined by computing the distance where the point corresponding to zero axial velocity arrive at the wall) is given in Figure 8 together with results by Armaly *et al.* (1983) (obtained in air using LDA). Also taking into account a 20% difference dependent on the different expansion ratio, present data strongly differ from those by Armaly *et al.* (1983).

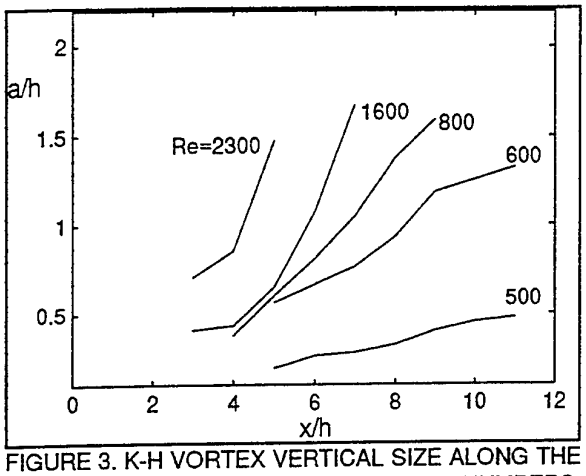


FIGURE 3. K-H VORTEX VERTICAL SIZE ALONG THE X-DIRECTION AT DIFFERENT REYNOLDS NUMBERS

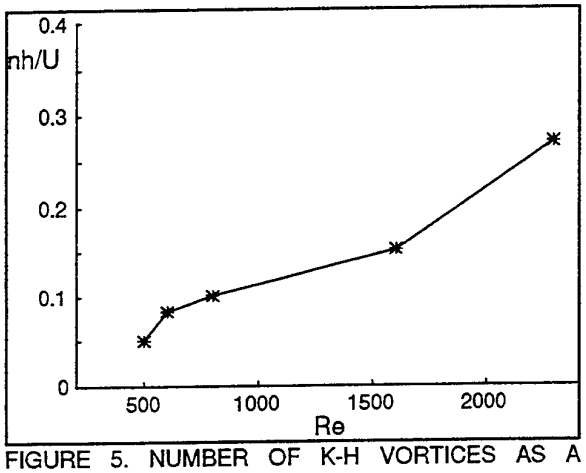


FIGURE 5. NUMBER OF K-H VORTICES AS A FUNCTION OF THE REYNOLDS NUMBER.

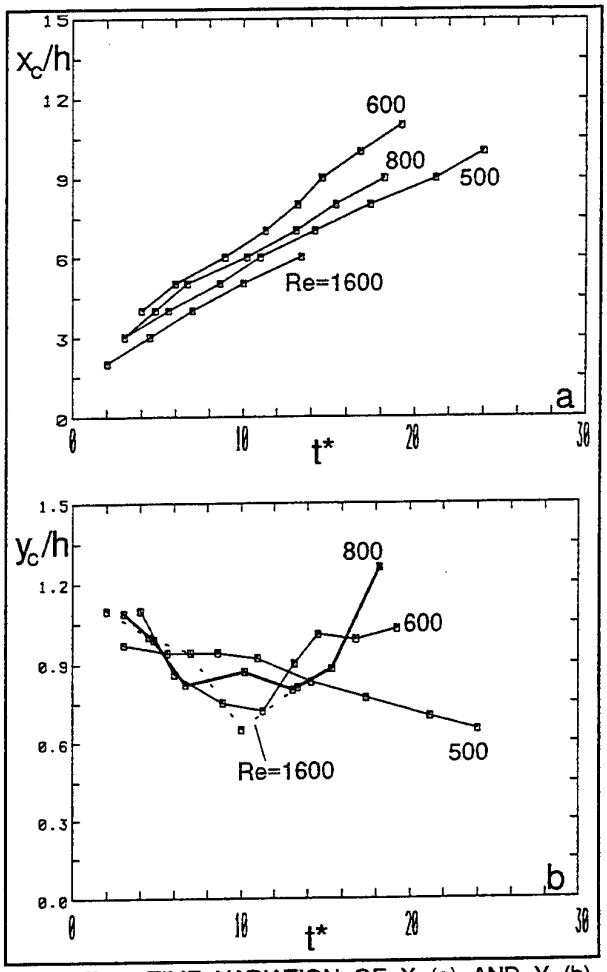


FIGURE 4. TIME VARIATION OF X (a) AND Y (b) POSITIONS OF K-H VORTICES ($t^*=tU/h$).

This difference is similar to that obtained when comparing two-dimensional numerical simulations and experiments. However, present data, although obtained on a plane, are representative of a real 3D flow. This point deserves further attention in future investigations.

Such plots cannot allow to investigate the instantaneous variations of the reattachment point that have been preliminary noted in PTV images (on the order of ±30% of the average). To investigate this variation, trajectories are followed in time in a Lagrangian frame and their minimum distance from the wall is detected and recorded. This minimum distance from the wall along a trajectory is assumed to represent the "instantaneous" reattachment length. In Figure 9 the variation in time of this instantaneous reattachment point is given for *Re*=2500. The average value is equal to 6.4*h* in agreement with that given in Figure 8. However, it oscillates between 4*h* and 9*h* (±40%). The power spectrum of this signal (not shown) displays a first line at about 10Hz and a second at 0.03 Hz: the first value is close to the frequency due to the passage of K-H vortices.

Indeed, at this Reynolds number this last frequency is given roughly by U/1.5*h* (1.5*h* is the vortex size as given in Figure 3), that is larger than 10 Hz. On the other hand, the low frequency is not observed for *Re*<1000. Therefore, the variation of the reattachment point for *Re*>1000 is not due only to the instantaneous passage of K-H vortices but also to a low frequency oscillation that could correspond to a "flapping" of the outflow not observed in free-shear layers (Eaton and Johnston, 1980). The probability density distributions of the instantaneous reattachment lengths are given in Figure 10 for three Reynolds numbers. At small values the standard deviation is equal to about 1.7h and the distribution has a negative skewness. This means that frequently the reattachment length is high (in comparison to the average), but sometimes there are particles arriving at the wall at small distances from the step. For larger Reynolds numbers the standard deviation of the distribution slightly decrease (is equal to 1.4*h* at *Re*=2500), while the distribution is non (or slightly) positively skewed. This means that more frequently than before particles arrive close to the step.

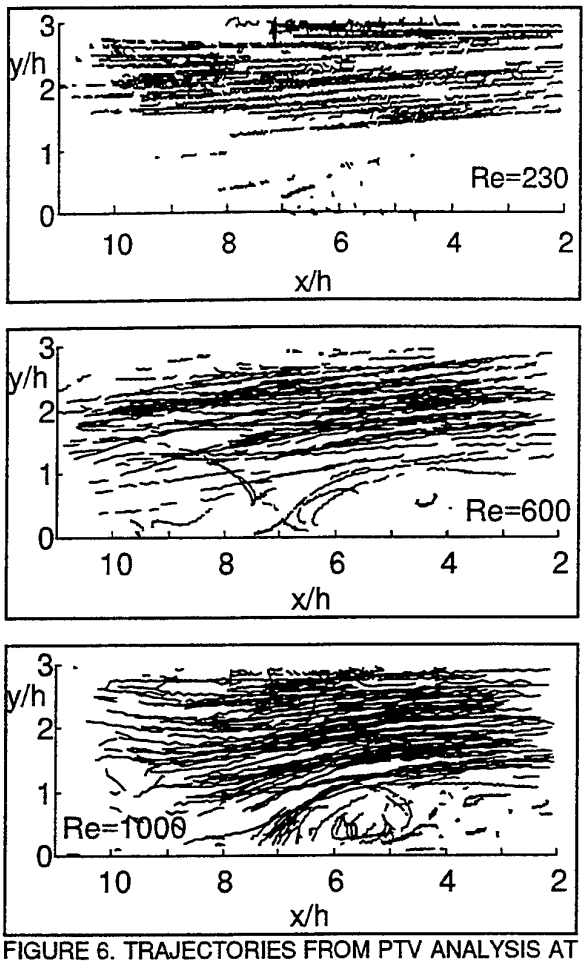


FIGURE 6. TRAJECTORIES FROM PTV ANALYSIS AT DIFFERENT REYNOLDS NUMBERS. FLOW FROM RIGHT TO LEFT.

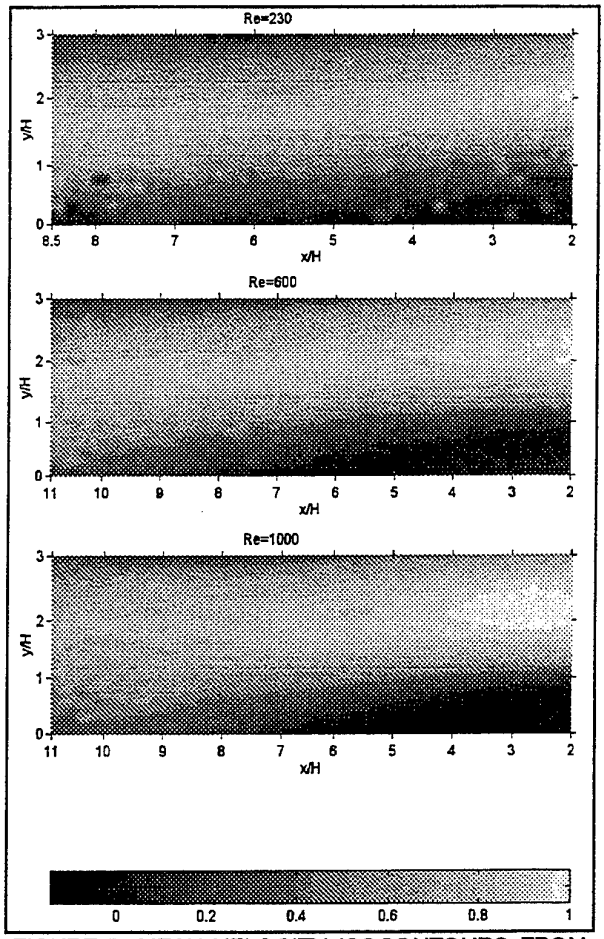


FIGURE 7. MEAN VELOCITY ISOCONTOURS FROM PTV AT DIFFERENT REYNOLDS NUMBERS. FLOW FROM RIGHT TO LEFT

CONCLUSIONS

In this paper average and instantaneous values of the reattachment point are derived. The average reattachment length decrease as the Reynolds number (except for *Re*<500) in disagreement with other results. The instantaneous variation of the reattachment point seems to derive from a sort of flapping that cause the mean flow to move away from the wall and to approach again the wall alternatively. This is a sort of "flip-flop" device that partially hides the effect of large scale vortices on the fluctuations of the reattachment point for Reynolds numbers larger than 1000. This fact is confirmed by visualizations of particle behaviour on large time intervals.

REFERENCES

Adams E.W. and Johnston J.P. 1988 "Effects of the separating shear layer on the reattachment flow structure " Experiments in Fluids, 6, 493-499

Armaly B.F., Durst F., Pereira J.C.F. and Shonung B. 1983 "Experimental and theoretical investigation of backward facing step flow." *J. Fluid Mech.* **127**, 473-496

Askelvoll K. and Moin P. 1993 "Large eddy simulation of a backward facing step flow" *Eng. Turbulence Models and Exp. 2*, W. Rodi and F. Martelli eds., Elsevier

Cenedese A. and Paglialunga A. 1990 "Direct digital analysis of a multiexposed photograph in PIV" *Experiments in Fluids*, **8**, 273-280

Cenedese A. and Querzoli G. 1994 "Lagrangian study of the convective boundary layer using image analysis" Proceedings of the 7th International Symposium on Applications of Laser Anemometry to Fluid Mechanics, Lisbon, Portugal

Durst F. and Tropea C. 1981 "Turbulent backward-facing step in two dimensional ducts and channels" Proceedings 3rd International Symposium on Turbulent Shear Flows, Davis, USA

Eaton J.K. and Johnston J.P. 1980 "Turbulent flow reattachment: an experimental study of the flow and structure behind a backward facing step." *Rep. MD-39*, Dept. of Mechanical Engineering, Stanford University

Kasagi N., Matsunaga A. and Kawara S. 1992 "Turbulence measurement in a separated and reattaching flow over a backward-facing step with the aid of three-dimensional particle tracking velocimetry" *Journal of Wind Engineering*, **52**, 523-528

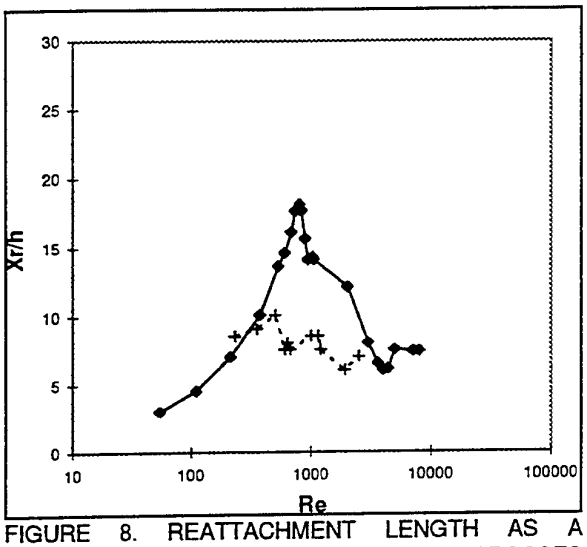


FIGURE 8. REATTACHMENT LENGTH AS A FUNCTION OF THE REYNOLDS NUMBER. CROSSES INDICATE PRESENT RESULTS, DIAMONDS RESULTS BY ARMALY ET AL. (1983)

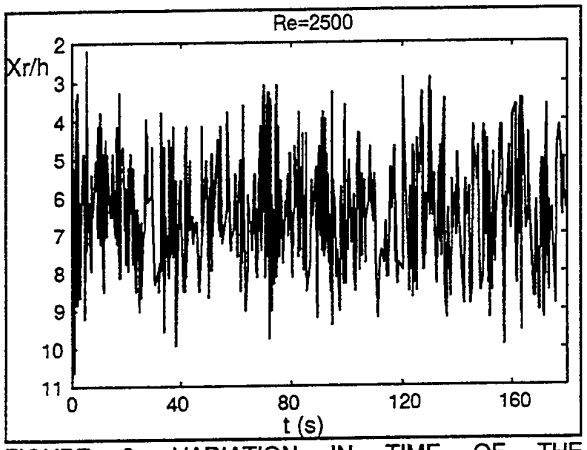


FIGURE 9. VARIATION IN TIME OF THE INSTANTANEOUS REATTACHMENT POINT.

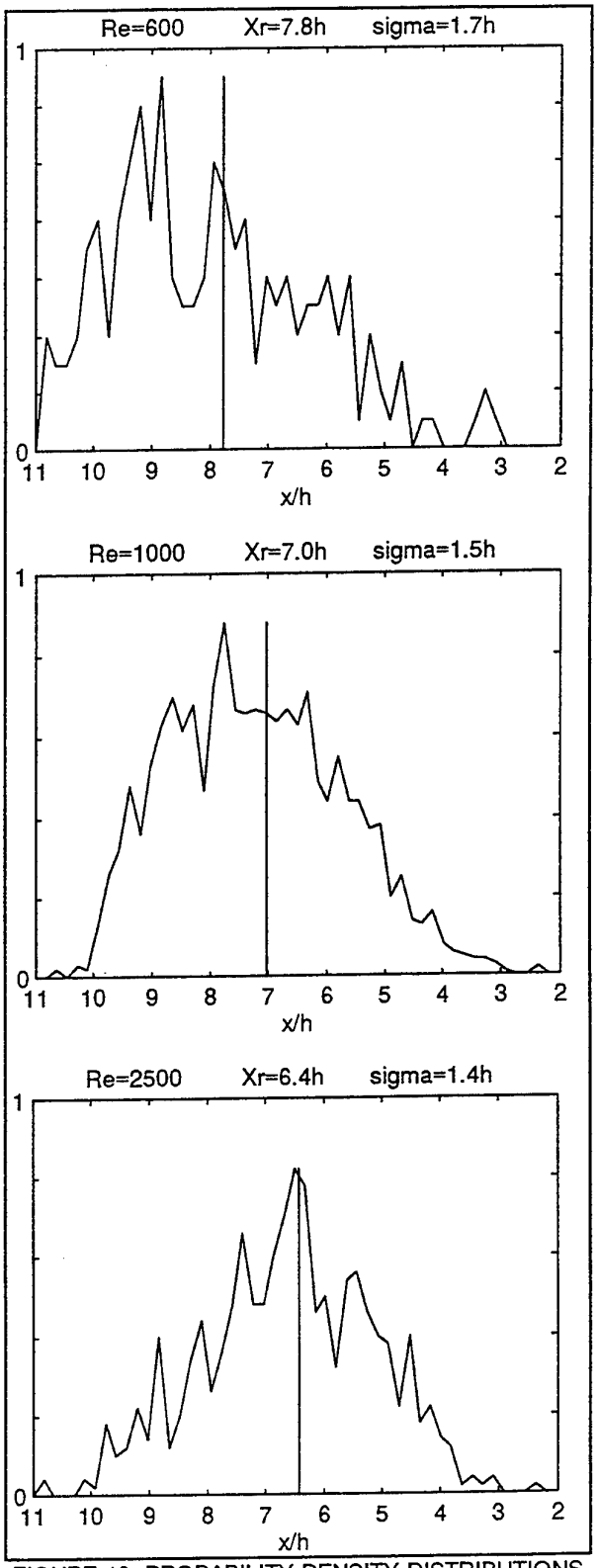


FIGURE 10. PROBABILITY DENSITY DISTRIBUTIONS OF INSTANTANEOUS REATTACHMENT POINT FOR DIFFERENT REYNOLDS NUMBERS

Romano G.P. and Tumbiolo A. 1995 "Experimental study of the fluid-dynamic field downstream a sudden expansion", PhD Thesis

Romano G.P. 1995 "The use of colors in PIV" Proceedings of the International Conference on PIV, Fukui, Japan

Shen G.X. and Ma G.Y. 1996 "The investigation on the properties and structures of starting vortex flow past a backward-facing step by WBIV technique" *Experiments in Fluids*, **21**, 57-65

Sinha S.N., Gupta A.K. and Oberai M.M. 1981 "Laminar flow over backsteps and cavities" *AIAA Journal*, **19**, 2 1527-1530

Westphal R.V., Johnston J.P. and Eaton J.K. 1984 "Experimental study of flow reattachment in a single-sided sudden expansion". *Rep. MD-41*, Dept. of Mechanical Engineering, Standford University

DIRECT AND REYNOLDS-AVERAGED NUMERICAL SIMULATIONS OF A TRANSITIONAL SEPARATION BUBBLE

Philippe R. Spalart
Boeing Commercial Airplane Group
P.O. Box 3707
Seattle, WA 98124
U.S.A.

Michael Kh. Strelets
Federal Scientific Center "Applied Chemistry"
St. Petersburg 197198
Russia

ABSTRACT

The laminar boundary layer on a flat surface is made to separate by applying suction through an opposite boundary, causing approximately a 25% deceleration. The detached shear layer transitions to turbulence, reattaches, and evolves towards a normal turbulent state. Temperature is treated as a passive scalar with an isothermal wall. The flow is studied by Direct Numerical Simulation (DNS), and by a Reynolds-Averaged (RANS) approach with a one-equation turbulence model and spontaneous ("trip-less") transition. In the transition region, both show a negative surge in skin friction. The agreement on skin friction, displacement thickness, and pressure is quite good, which we attribute to the simple nature of transition "by contact" due to flow reversal. In contrast, the heat-transfer surge is greatly under-predicted by the model. The detailed transition mechanism, and the possible dependence of the DNS solution on the weak incoming disturbances and on the presence of a hard opposite boundary, are scrutinized. We argue that the flow, although transitional, is fully specified by its total deceleration, two Reynolds numbers, and the Prandtl number. This makes DNS-RANS comparisons meaningful.

INTRODUCTION

Transition to turbulence occurs in a wide variety of manners. Much of the research has addressed transition by gradual amplification of small disturbances, such as cross-flow vortices or TS waves, because such cases make the location of transition most uncertain. Progress in stability methods should displace DNS transition work, and steer it towards flows dominated by elliptic (steep spatial growth) and nonlinear effects, such as the present one. Wings with moderate Reynolds numbers and low sweep angles often cause their boundary layer to separate while still laminar; the detached shear layer may become turbulent rapidly enough to achieve reattachment, creating a "short bubble". This is well known in classical aerodynamics, and revealed by a "flat spot" on the pressure distribution as the bubble alters the effective shape of the airfoil. It appears that transition is inevitable, except at the smallest Reynolds numbers (chord Reynolds numbers below about 70,000, see Lissaman 1983), but the length of the bubble is not obvious. This is of importance for high-lift devices on airliners, particularly in wind-tunnel tests. Some high-performance low-Reynolds-number airfoils plan on a short bubble, and provide a "transition ramp".

The wall heat transfer in separation bubbles appears to break the usual analogy with momentum transfer (Spalart and Coleman 1997), making skin-friction measurement particularly difficult, and providing an additional challenge in turbulence modeling. Heat transfer is also used to detect transition in experiments. Finally, the turbine blades in turbo-machines are very sensitive to heat transfer, have low sweep, and moderate Reynolds numbers. On the other hand, they are exposed to high freestream turbulence levels, which we are not considering here.

For this paper, we set out to create a transitional separation bubble under simple conditions, easy to reproduce numerically if not experimentally. Very few of the experiments provide the ceiling shapes and suction/blowing rates needed to calculate the flows (airfoil experiments such as Crouch and Saric 1986 do, but they have less detail and are less attractive for DNS). A transitional bubble is somewhat more physically interesting than a fully-turbulent one (such as Spalart and Coleman 1997) and achieves reattachment more promptly even in an adverse pressure gradient. This slightly relieves the need for high Reynolds numbers, which is helpful in a DNS. We speculate that this flow transitions by what we loosely call an absolute instability (Huerre and Monkewitz 1985); the initial three-dimensionality is also of interest.

In order to deserve attention, the DNS is to have a low level of disturbances in the entry region and to be accurate while having a high enough Reynolds number to create viable turbulence. "Low-Reynolds-number effects" are a nuisance when using DNS results to test turbulence models. It also appeared that, unlike transition by gradual amplification, this kind of transition could, possibly, be amenable to Reynolds-averaged calculations (Shur *et al.* 1996). We believe transition of transport-equation turbulence models "by contact" should be understood, as it happens spontaneously in complex calculations. We had evidence that laminar separation can be followed by transition, but not that the rate at which transition occurs is accurate. This led us to the present joint study. By "transition" of a turbulence model we mean that the Reynolds stresses it provides go from being zero, or at least negligible relative to the viscous stresses, to much larger than the viscous stresses.

SPECIFICATION OF THE FLOW

The boundary conditions are identical to those of Pauley, Moin, and Reynolds (1990), expect of course for the third dimension. A viscous wall at $y = 0$ creates the boundary layer, and an inviscid boundary at $y = Y$ controls the pressure gradient. At the inviscid boundary, the boundary condition in the streamwise velocity u is either no-stress, or zero vorticity; this has little importance, since fluid only leaves the domain through this boundary. A suction velocity $V(x)$ at Y is specified, which is non-zero only in the vicinity of a "slot" near $x = X$. These conditions can be closely duplicated in an experiment (provided side-wall problems are solved), unlike those we used for a turbulent bubble (Spalart and Coleman, 1997, had suction followed by blowing, so that the vorticity of the injected fluid would matter). If U_0 is the velocity upstream in the channel, the deceleration is measured by the ratio

$$S \equiv \frac{1}{YU_0} \int_{-\infty}^{\infty} V(x)\, dx.$$

If the V distribution is sufficiently localized near X, compared with Y, the boundary layer is sensitive only to the above integral (we used a Gaussian with width $0.24Y$). If the inflow and outflow boundaries are far enough not to matter, the boundary conditions are reduced to three non-dimensional parameters: S, and the Reynolds numbers $R_Y \equiv YU_0/\nu$ and $R_X \equiv XU_0/\nu$. Here, X is measured from the virtual origin of the incoming Blasius boundary layer, and ν is the molecular viscosity. Heat transfer adds another parameter, the molecular Prandtl number Pr which we set to 0.71, and the type of wall condition which we made isothermal.

Pauley *et al.* presented two-dimensional results for S in the range $[0.09, 0.22]$, R_X in the range $[6\ 10^4, 24\ 10^4]$, and $R_Y \approx R_X/5$. They obtained periodic vortex shedding in 2D solutions. We also find the threshold for flow reversal and shedding to be near $S = 0.12$. For the transitional case we chose $S = 0.3$, $R_X = 10^5$, $R_Y = R_X/3$, in order to produce a large enough bubble and a fairly high Reynolds number. For a given S and R_X, a larger R_Y makes the pressure rise more gradual. For a Blasius region to exist before the pressure rise, which we require to facilitate comparisons, R_Y must be less than about half of R_X.

CALCULATION METHODS

The DNS code is close to that of Spalart and Coleman (1997). It is spectral in space and mixed third/second-order in time. The inflow and outflow are treated by a fringe method, with additional damping terms to suppress disturbances in the fringe, similar to our other transition studies. The resolution is at least as fine as that proven in fully turbulent boundary layers (Spalart 1988). This flow is more demanding, since we demand low disturbance levels upstream. The grid was refined beyond the usual turbulence values in the x and y directions, based on observations of the spurious fluctuations in the irrotational region, which are never exactly zero. The grid spacing is 0.0094 in the x direction, 0.005 in z and variable in y with about 100 points within the boundary layer at its thickest ($\delta \simeq 0.5$). Periodic spanwise conditions are applied with a period equal to $0.6Y$, which is about 7 times the displacement thickness at the outflow, or 8 times the total thickness of the detached laminar shear layer.

The initial condition of the DNS contained 3D random perturbations; their details and level are not relevant in the developed solution. The approach to steady state was verified in the integral quantities, and established based on the temperature-deficit equilibrium, shown below. The fringe terms were adjusted to provide a Blasius entry region

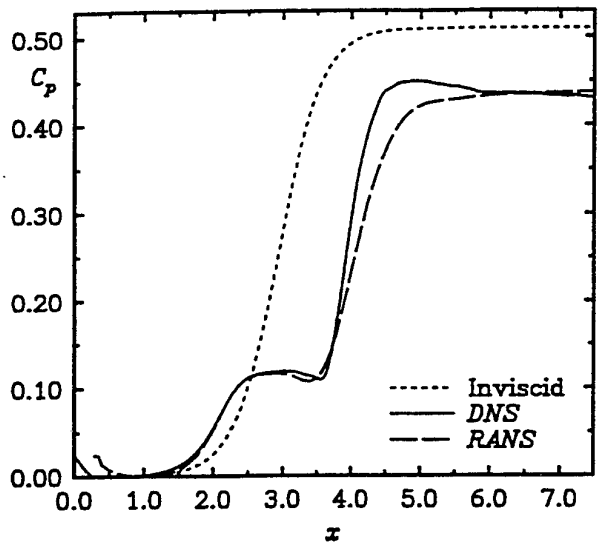


Figure 1: Wall pressure coefficient.

with the desired virtual origin. The outflow conditions are not critical, as shown by the smoothness of the curves in this and other fringe simulations.

The RANS solver uses the upwind-difference scheme of Rogers and Kwak (1990). This is an implicit flux-difference splitting scheme of 3rd-order accuracy for the convective terms, and second-order for the viscous terms. The method is implemented by line Gauss-Seidel relaxation. The S-A eddy-viscosity transport equation (Spalart and Allmaras, 1994) is solved jointly with the RANS equations with first-order accuracy for the convective terms. Finally, the temperature equation is solved independently. A non-uniform grid (with clustering in the vicinity of the wall and suction region) is used with the total number of grid points 201×101. The spacing in x is between 0.03 and 0.05. The maximum value of the normalized near-wall grid spacing, Δy^+, in the turbulent region is no higher than 0.6. The ratio of neighboring steps is less than 1.05 for x, and less than 1.2 for y. Grid studies give error estimates below 5% for quantitites such as the skin-friction peak. The constants c_{t3} and c_{t4} were also varied, because they are arbitrary to some extent, and have some control over spontaneous transition; in this flow, they had no effect.

The RANS solution uses the "Trip-Less" approach of Shur *et al.* (1996); the eddy viscosity is zero in the entry region and transition occurs only because reverse flow carries non-zero values upstream in the bubble. This was achieved by setting non-zero inflow values during the first iterations, and then setting zero inflow values until a new steady state was reached. The 2D RANS solution has a stable steady state, unlike 2D solutions without turbulence model, such as those of Pauley *et al.* (1990). The transitional RANS solution appears to be unique.

RESULTS, INTEGRAL QUANTITIES

We present pressure coefficients in figure 1. From here on, lengths are normalized with Y and velocities with U_0. The DNS fringes leave a "useful region" that covers roughly $[0.5, 7.5]$ in the x direction. By "inviscid wall pressure", in the figure, we mean the pressure that would exist with a slip condition on the lower wall. It has a smooth rise from $C_p = 0$ to $S(2 - S)$, centered at $x = 3$. The viscous C_p reaches only about 0.43, instead of 0.51, because the displacement thickness is near 0.08 downstream of the bubble, which lessens the deceleration. The displacement

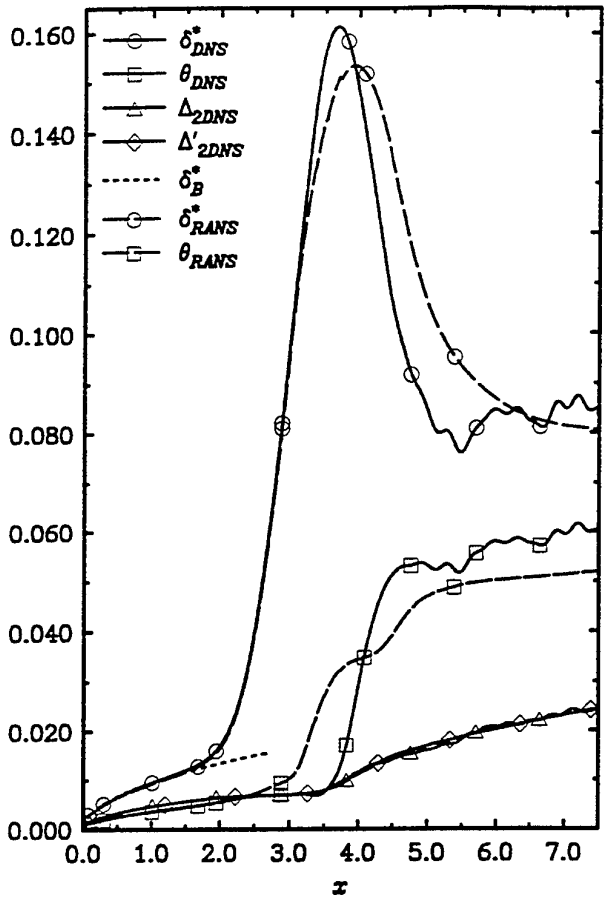


Figure 2: Boundary-layer thicknesses.

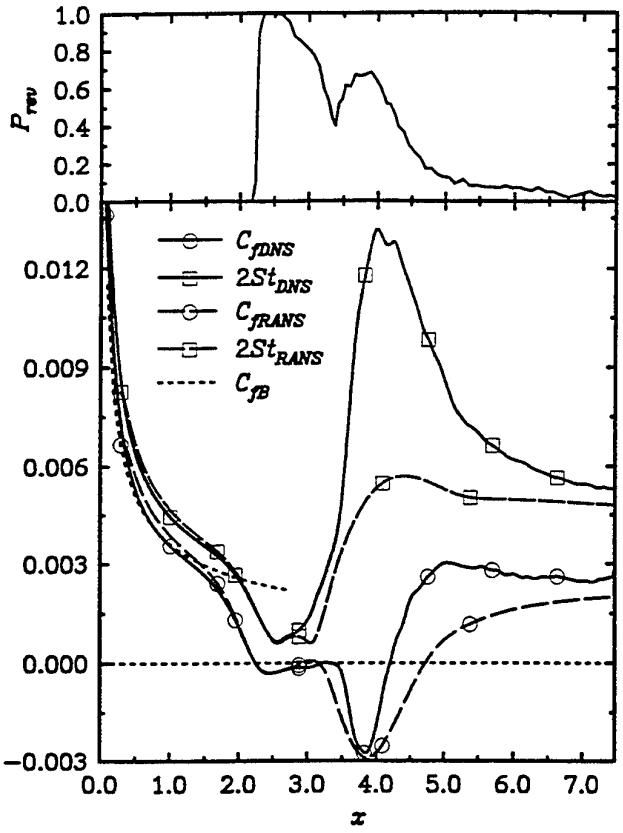


Figure 3: Wall transfer coefficients, based on U_0, and probability of reverse wall shear (upper graph).

effect at the bubble itself creates the expected flat spot, followed by a rapid rise. Note also the anticipated rise near $x = 2$, caused by the concave curvature of the streamlines. This was observed in experiments, by comparing with a tripped case, which remained attached and therefore close to the inviscid C_p (Gaster 1966). The agreement between DNS and RANS is better than expected.

We present thicknesses in figure 2. In the definition of the velocity thicknesses δ^* and θ, the velocity U is ill-behaved outside the viscous region, because of pressure gradients, and is replaced by the pseudo-velocity $\overline{U}(x,y) \equiv -\int_0^y \omega_z(x,y')\,dy'$. On the other hand, the true velocity is used in the temperature-deficit thickness $\Delta_2 \equiv \int_0^Y U(1-T)\,dy$, T being well-behaved. We use the notation T and t' for the mean and root-mean-square temperatures. Δ_2 is very valuable as a check of equilibrium, with no need for boundary-layer assumptions. The quantity Δ_2' is the right-hand-side of the integrated temperature equation (Coleman and Spalart 1997). It matches Δ_2 very well, although the time sample we were able to collect in time for the conference leaves some roughness beyond $x \approx 4$. The figure also shows agreement with the Blasius distribution for δ^*. DNS and RANS agree quite well on δ^*, which is consistent with the pressure. However, θ rises earlier in the RANS, and is about 14% too low downstream.

The wall-transfer coefficients in figure 3 are more sensitive, and exhibit appreciable differences between the two methods. Both have a negative surge of skin friction around $x = 3.8$, which we did not foresee but is justified by the steep pressure rise, following a region with essentially zero values. The recovery to positive values is too slow with RANS, missing the local maximum near $x = 5$. This was not expected, as models often approach "standard" states faster than they should, but it is consistent with results of the S-A model behind a backward-facing step. At $x = 7.5$, the DNS gives $R_\theta \simeq 1500$, $C_f' \simeq 0.0044$ (both based on the local edge velocity $\overline{U}(x,\infty)$ rather than on U_0), and $H \equiv \delta^*/\theta \simeq 1.41$. These values are not far from normal in zero pressure gradient, as we would expect $C_f' \simeq 0.0039$, $H \simeq 1.44$. The RANS gives $R_\theta \simeq 1300$, $C_f' \simeq 0.0035$, $H \simeq 1.55$ (at $x = 7.5$, δ^* and H are still dropping). A longer recovery region would be desirable, but $R_\theta \simeq 1500$ is not far from the current limit of DNS. The Blasius curve C_{fB} is also shown.

The Stanton number is more challenging. The RANS completely misses the large surge at transition, which would of course be quite a concern in jet-engine applications. Recall that the S-A model simply uses a constant turbulent Prandtl number equal to 0.9. The agreement improves downstream. Notice how mismatched the momentum and temperature boundary layers are in that region: Δ_2 is less than half of θ, whereas in a simple boundary layer it would be a little larger. Correlatively, $2St'$ is near 0.0071, which far exceeds C_f; this will slowly close the gap between Δ_2 and θ.

The upper graph shows the probability for the wall shear stress to be negative. It jumps from 0 to 1 near $x = 2.25$, revealing the very weak dependence on time and on the spanwise coordinate. In the turbulent part of the bubble, it is quite below 1, much like in bubbles with turbulent entry (Alving and Fernholz 1996). It then decays quite slowly as a result of elevated turbulence levels, relative to the mean skin friction, and is still non-zero at $x = 7.5$.

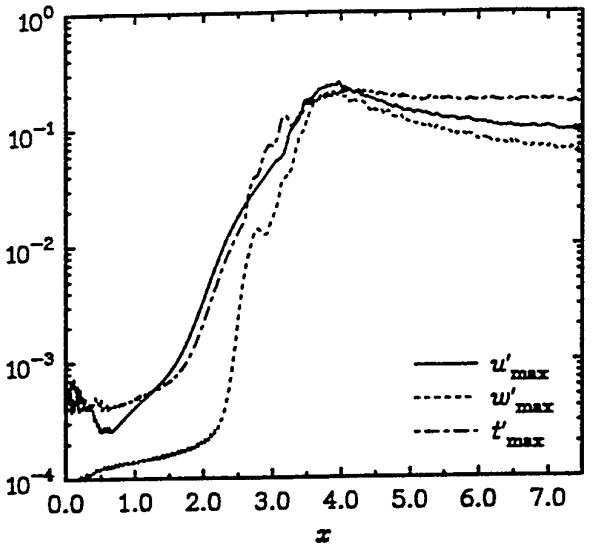


Figure 4: Peak rms in boundary layer.

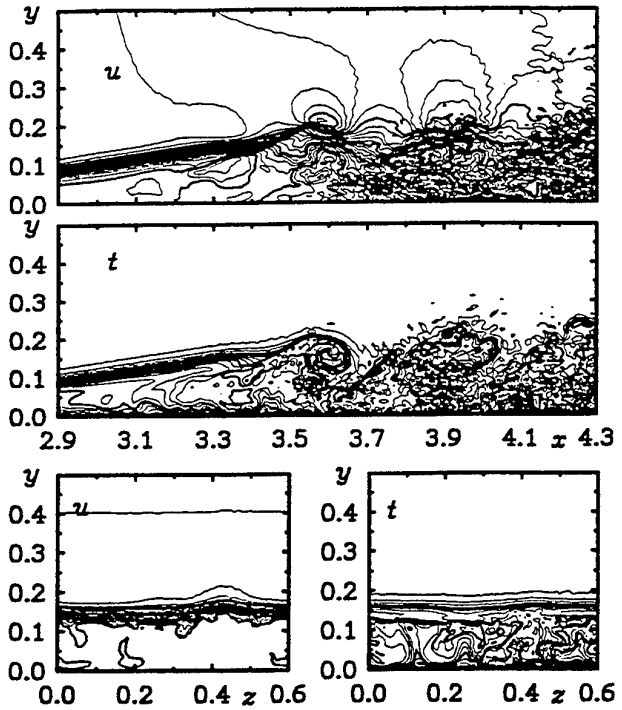


Figure 5: Instantaneous velocity and temperature from the DNS. Side views, and end views at $x = 3.5$.

RESULTS, LOCAL QUANTITIES

These results all come from the DNS. Figure 4 shows the peak values of u', w', and t' within the boundary layer. All are well below 0.1% in the Blasius region, indicating that the damping of the turbulence through the fringe was quite effective. However, some authors report effects on bubble length at least down to 0.2% (Mayle 1991), so that it is difficult to guarantee that residual fluctuations play no role. Typical levels outside the boundary layer are 0.03%. At separation, $x \simeq 2.25$, w' increases by a factor of 50, indicating a dramatic rise of the three-dimensionality. The peaks of u' and t' then smoothly rise to near 10% at $x = 3.5$, with w' lagging. After transition, the peak u' decays from about 3.7 in wall units at $x = 5$ to the usual 2.7 at $x = 7.5$. However, a normal log layer is not established; U^+ at $y^+ = 100$ is less than 15. Other workers have also found the wall-unit profiles to be lower than normal even far downstream of reattachment (Castro and Epik 1996).

The sustained spatial growth rate $d(\log u')/dx$ upstream of transition is between 2 and 4, with two spikes near 6. Growth is steep even upstream of $x = 1$, where the Blasius boundary layer is stable ($R_{\delta^*} = 314$). The instantaneous side views in figure 5 show a sudden change from a very smooth shear layer to a rolled-up vortex, with small-scale activity throughout the layer. End views in the same region reveal no remarkable large three-dimensional flow structures, suggesting that a typical secondary instability is not taking place. Michalke (1965) points out that the mixing-layer instability, with a ratio $R \equiv |U_2 - U_1|/(U_1 + U_2)$ equal to 1, grows by a factor of 35 in one wavelength (U_1 and U_2 being the velocities on either side of the layer). Here, R is about 1.06, giving an even larger growth ratio, so that the convective instability comes close to explaining the very sudden appearance, visually, of rolls. The absolute instability of Huerre and Monkewitz (1985) may not add much to Michalke's, particularly since the R ratio does not reach their critical value ($R = 1.315$) until $x \simeq 3.63$, well into the transition region. The present shear layer has a vorticity thickness $\delta_\omega \equiv |U_2 - U_1|/\omega_{max}$ of about 0.045, and Michalke's analysis would predict a wavelength of about 0.3; this agrees with figure 5. The Reynolds number $|U_2 - U_1|\delta_\omega/\nu$ is about 1,500; therefore, viscous effects are much weaker than wall-proximity effects.

It appears that the Kelvin-Helmholtz instability is involved, but the possible dependence of the DNS results on incoming disturbances is difficult to establish beyond any doubt. Numerical errors are of course never zero, and they do propagate upstream. However, they are dominated by very short waves, with typical wavelengths of a few grid spacings, say about 0.05 here. Thus, they are not likely to foster the wavelength 0.3. Similarly, the dominant period in time represents about 500 time steps. The "hard" ceiling (prescribed normal velocity) at a height of 1 reflects pressure signals, but appears too distant to dictate the wavelength 0.3. Of course, the reflection preserves the frequency, and the base flow undergoes noticeable changes (such as 0.05 in C_p) on the scale of 0.3 in x. Therefore, receptivity is present. We could study this further by creating receptivity in the laminar region, for instance with a suction and/or blowing "slot". Reflections against the inflow boundary are of course not zero, but the very low disturbance level at $x = 0$ suggests that they play no role.

In figure 6 we show the profiles which underlie the transition. The mean velocity only reaches very small negative values, which is consistent with the small skin friction for $x < 3.5$. Crouch and Saric (1986) had larger values. The profiles of u' and $|\partial U/\partial y|$, each normalized by its local maximum, are instructive. We think of a "flapping" shear layer as having a dependence of the type $u(x, y, z, t) = \widetilde{u}(y - \tilde{y})$ where the function $\widetilde{u}$ depends on x only, and $\tilde{y}(x, z, t)$ is a statistical variable with small variations. For such a dependence, the rms of u is proportional to the slope of U: $u' \propto |U_y|$. This behavior is clear in figure 6. At $x = 2$, the shear layer does not yet have pure flapping behavior. At $x = 2.5$, the shapes match very well except close to the wall. At $x = 3$ and $x = 3.5$, "true" turbulence near the wall is growing, but the outer part still exhibits flapping behavior. We see that the growth rates in the [2,4] range for $x < 3.5$ apply to the flapping motion (which sets the u' peak), not to the shorter waves which eventually cause transition.

In figure 7 we show contours of the primary averaged quantities. The mean streamlines and the U and T con-

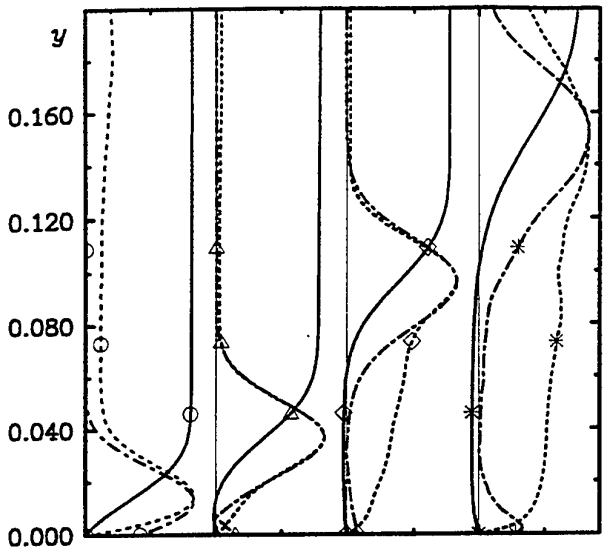


Figure 6: Profiles in DNS. —, U; - - -, $u'/u'_{\max}$; - — -, $|U_y|/U_{y\max}$. ∘, $x = 2$; △, $x = 2.5$; ◇, $x = 3$; ∗, $x = 3.5$. Each profile is displaced by 1.2

tours exhibit the thin laminar detached shear layer, followed by a sudden widening as transition begins near $x = 3.5$. They are very reminiscent of Gaster's measurements (1966). The peak negative mean velocity is -0.16, at $(x, y) = (3.75, 0.013)$. The concave streamline curvature, which we invoked earlier to explain the early pressure rise, is very noticeable near $x = 2.5$; the same applies near $x = 4.5$. The length of the bubble is 1.9, giving a Reynolds number of 63,000 based on the upstream velocity. This compares well with the value of 50,000 quoted by Lissaman (1983). The temperature and vorticity rms are confined to the boundary layer, but the velocity rms contains irrotational fluctuations and therefore extends much farther up. The temperature rms has a complex behavior, quite unlike that of u', including a local minimum at $(x, y) = (3.75, 0.12)$ and high near-wall values. The double-peak behavior is even more pronounced for t' than for u'.

The rms of vorticity (all three components added) rises to very high values near $x = 3.75$, as intense small-scale turbulence is generated. ω' then decays throughout the recovery region. We also show the pseudo-shear-stress $\overline{u_i u_j} S_{ij} / \sqrt{2 S_{ij} S_{ij}}$, designed to equal the familiar $-\overline{u'v'}$ in parallel regions, but to be insensitive to axis rotation. It can be viewed as the production of turbulent kinetic energy, normalized by the strain tensor. It take very high values, near 0.017, at transition. Over the recovery region, it decays to values near 0.0014, consistent with the skin friction ($C_f \simeq 0.0026$). Small regions of negative production are found, particularly very near the wall at $x = 4$. Spalart and Coleman (1997) also found such regions, but had concerns that their flow might have unrealistic distortions.

CONCLUSIONS

We believe we have obtained the DNS of a well-defined and reproducible transition mechanism in a separation bubble. The results of the RANS are better than could be expected, considering how crudely turbulence models treat transition; we had predicted that RANS would predict transition, but give the wrong bubble length. If the length is correct, the model might be useful to predict short and long bubbles on airfoils. Of course, our considerations on receptivity imply that any success of turbulence models would be somewhat fortuitous. This is because receptivity occurs at a distance through pressure signals, whereas the models only involve local diffusion. It would not be the first time a turbulence model gives a fair answer without a deep reason for doing so. It is also fortunate that the RANS solution is not sensitive to the negotiable constants in the turbulence model. On the other hand, the heat transfer prediction is as poor as we could fear; we intend to analyse the reasons for this, beginning with the turbulent Prandtl number. We also intend to carry another temperature field, with prescribed wall heat transfer; this will be closer to most experiments.

In the future we intend to obtain a longer and later sample to obtain smooth curves up to $x = 7.5$, and to test at least one other turbulence model. We will calculate growth rates for instabilities in profiles such as those in figure 6. We will conduct a 2D "DNS" like that of Pauley *et al.* (1990) to see how long it tracks the 3D DNS; this will suggest in which region three-dimensionality is essential. A very interesting and very costly extension would be to gradually reduce S until transition is not sustained any more. It may or may not coincide with the S value that gives flow reversal, and would be a further and severe test of the turbulence models. We could also reduce the Reynolds number in an attempt to obtain "bursting" and a 'long bubble" (Gaster 1966).

Acknowledgements : We greatly benefited from discussions with Dr. J. D. Crouch. The RANS calculations were done by Drs. M. Shur and A. Travin.

REFERENCES

Alving, A. E., and Fernholz, H. H., 1996, "Turbulence measurements around a mild separation bubble and downstream of reattachment". *J. Fluid Mech.* **322**, 297.

Castro, I. P., and Epik E., 1996, "Boundary-layer relaxation after a separated region". *Exp. Therm. Fluid Sci.* **13**, 4, 338.

Crouch, J. D., and Saric, W. S., 1986, "Oscillating hot-wire measurements above an FX63-137 airfoil". AIAA-86-0012.

Gaster, M., 1966, "The structure and behavior of laminar separation bubbles". AGARD CP 4.

Huerre, P., and Monkewitz, P. A., 1985, "Absolute and convective instabilities in free shear layers". *J. Fluid Mech.* **159**, 151.

Lissaman, P. B. S. 1983. "Low-Reynolds-number airfoils". *Annu. Rev. Fluid Mech.* **15**, 223.

Mayle, R. E. 1991. "The role of laminar-turbulent transition in gas turbine engines". *J. Turbomach.* **113**, 509.

Michalke, A. 1965. "On spatially growing disturbances in an inviscid shear layer". *J. Fluid Mech.* **23**, 521.

Pauley, L. L., Moin, P., and Reynolds, W. C., 1990, "The structure of two-dimensional separation." *J. Fluid Mech.* **220**, 397.

Rogers, S.,E., and Kwak, D., 1990, "Upwind difference scheme for the time-accurate incompressible Navier-Stokes equations". *AIAA J.* **28**, **2**, 253.

Shur, M. L., Spalart, P. R., Strelets, M. Kh., and Travin, A. K., 1996, "Navier-Stokes simulation of shedding turbulent flow past a circular cylinder and a cylinder with a backward splitter plate". Third Eur. CFD Conf., Paris.

Spalart, P. R., 1988, "Direct simulation of a turbulent boundary layer up to $R_\theta = 1410$". *J. Fluid Mech* **187**, 61.

Spalart, P. R., and Allmaras, S. R., 1994, "A one-equation turbulence model for aerodynamic flows". *Rech. Aérosp.* **1**, 5.

Spalart, P. R. and Coleman, G. N., 1997, "Numerical study of a separation bubble with heat transfer". *Eur. J. Mech. B* **16**, 2.

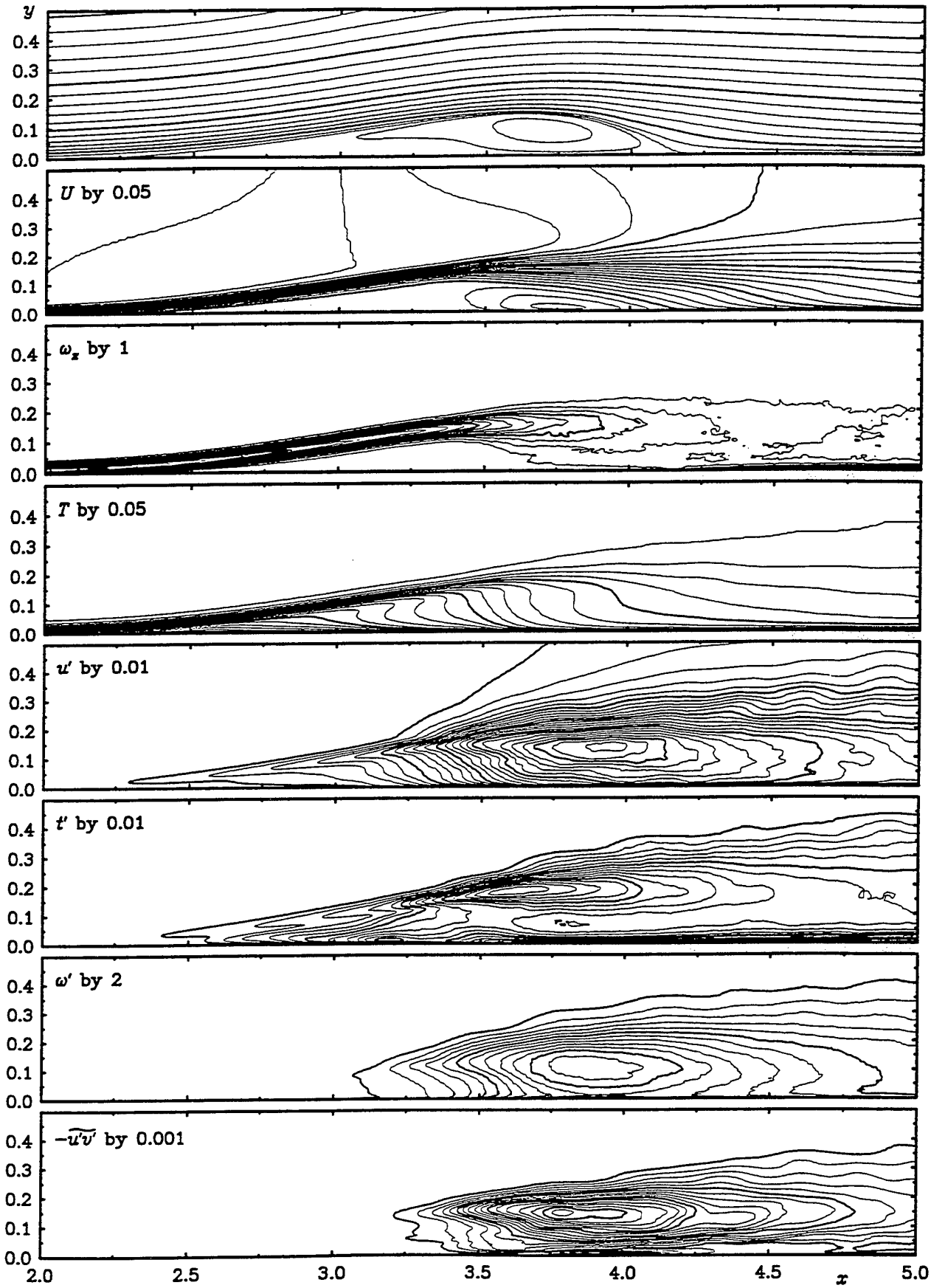


Fig. 7. DNS Reynolds–averaged quantities. Each frame gives quantity name and contour interval.

COMPUTATIONS OF SEPARATING AND REATTACHING FLOWS USING A LOW-REYNOLDS-NUMBER SECOND-MOMENT CLOSURE

T.J. Craft
Department of Mechanical Engineering
UMIST, P.O. Box 88
Manchester
UK

ABSTRACT

The paper describes further developments to the low-Reynolds-number second-moment closure of Craft & Launder (1996), focussing in particular on the prediction of separating and reattaching flows. The flows considered are the axisymmetric diffuser flows of Stieglmeier et al (1989), and the backward facing step flows reported by Driver & Seegmiller (1983) and Le et al (1997). It is shown that modifications to the pressure strain model allow the large shear stress values found experimentally in the recirculation region to be captured, whilst an elaboration of the (algebraic) approximation for the triple moments improves the prediction of the recirculation and recovery region.

INTRODUCTION

One of the drawbacks of the most widely used Reynolds stress models is their use of wall normal distances and vectors to account for wall-proximity effects. This clearly hinders their application to flows with non-planar or multiple walls, where these geometry-specific quantities may be difficult, or impossible, to define uniquely. Following the work of Launder & Tselepidakis (1993) and Launder & Li (1994), Craft & Launder (1996) made some initial proposals in extending the realizable stress model, which had been developed at UMIST by Fu (1988), to account for low-Reynolds-number and near-wall effects without the need to introduce any geometry-dependent quantities. This was achieved by employing "normalized turbulence lengthscale gradients", which allowed the model to identify the direction in which strong inhomogeneity was present. Promising results were obtained for a number of flows including sheared and shear-free boundary layers, and impinging flow.

The present contribution extends the testing and development of this model by considering a number of cases where the geometry of the flow induces separation and reattachment. This is an important further test of the modelling procedures, since the non-planar walls help to ascertain whether the use of the above lengthscale gradients in place of wall-normal vectors can be expected to produce the desired effect in more complex geometries.

The axisymmetric diffuser flow studied experimentally by Stieglmeier et al (1989) results in a relatively weak recirculation, whilst the backward facing step flows test the model's ability to predict a larger recirculation zone. The DNS of Le et al (1997) is particularly useful in this respect, since it provides full Reynolds stress budgets in what is a relatively complex flow situation.

The following sections describe the modelling details, highlighting further developments to those reported by Craft & Launder (1996), and present the predictions of the flows currently under consideration.

MODELLING APPROACH

The Reynolds stress transport equations can be written as

$$\frac{D\overline{u_i u_j}}{Dt} = P_{ij} + \Pi_{ij} - \varepsilon_{ij} + d_{ij} \qquad (1)$$

where the production term $P_{ij} = -(\overline{u_i u_k}\partial U_j/\partial x_k + \overline{u_j u_k}\partial U_i/\partial x_k)$ does not require any modelling.

In the present work, the dissipation ε_{ij} is modelled as in Craft & Launder (1996). The form of this is designed to give isotropic values in high-Reynolds-number regions far from walls. Close to a wall, however, it utilises the fact that there are significant gradients of the turbulent kinetic energy, k, in order to return the correct wall-limiting values derived by Launder & Reynolds (1983).

Pressure-Correlations

For reasons given in Craft & Launder (1996), the pressure correlation, Π_{ij} is split into a redistributive and a non-redistributive part by

$$\Pi_{ij} = \phi^{*}_{ij} - \overline{u_i u_j}/k\, d^{p}_{k} \tag{2}$$

where $d^{p}_{k} = -(1/\rho)\partial(\overline{pu_k})/\partial x_k$ is the pressure-diffusion of the turbulent kinetic energy, and the correlation between fluctuating pressure and velocity, $\overline{pu_k}$, is modelled as

$$\overline{pu_k} = -\rho(0.5 d_k + 1.1 d^{A}_{k})(\nu\varepsilon k A A_2)^{1/2} \times [c_{pd1} A_2 + c_{pd2} R_t^{-1/4} \exp(-R_t/40)] \tag{3}$$

with $c_{pd1} = 1.0 + 2.0\exp(-R_t/40)$ and $c_{pd2} = 0.4$, which gives a reasonable fit to the available DNS data. The invariants of the Reynolds stress anisotropy tensor, A_2 and A, are defined as $A_2 = a_{ij}a_{ij}$, $A_3 = a_{ij}a_{jk}a_{ki}$, $A = 1 - 9/8(A_2 - A_3)$, where $a_{ij} = \overline{u_i u_j}/k - 2/3\delta_{ij}$, and $R_t = k^2/(\nu\varepsilon)$ is the turbulent Reynolds number.

The redistributive part of Π_{ij} is modelled as

$$\phi^{*}_{ij} = \phi^{*}_{ij1} + \phi^{*}_{ij2} + \phi^{inh}_{ij} \tag{4}$$

where

$$\phi^{*}_{ij1} = -c_1\tilde{\varepsilon}[a_{ij} + c'_1(a_{ik}a_{kj} - 1/3 A_2\delta_{ij})] - \tilde{\varepsilon} f'_A a_{ij}$$

$$\begin{aligned}
\phi^{*}_{ij2} = {} & -0.6\,(P_{ij} - 1/3\delta_{ij}P_{kk}) + 0.3 a_{ij}P_{kk} \\
& - 0.2\left[\frac{\overline{u_k u_j}\;\overline{u_l u_i}}{k}\left[\frac{\partial U_k}{\partial x_l} + \frac{\partial U_l}{\partial x_k}\right] - \frac{\overline{u_l u_k}}{k}\left[\overline{u_i u_k}\frac{\partial U_j}{\partial x_l} + \overline{u_j u_k}\frac{\partial U_i}{\partial x_l}\right]\right] \\
& - c_2\,[A_2\,(P_{ij} - D_{ij}) + 3 a_{mi}a_{nj}\,(P_{mn} - D_{mn})] \\
& + c'_2\left\{\left(\frac{7}{15} - \frac{A_2}{4}\right)(P_{ij} - 1/3\delta_{ij}P_{kk}) \right. \\
& + 0.1\,[a_{ij} - 1/2\,(a_{ik}a_{kj} - 1/3\delta_{ij}A_2)]\,P_{kk} \\
& - 0.05 a_{ij}a_{lk}P_{kl} \\
& + 0.1\left[\left(\frac{\overline{u_i u_m}}{k}P_{mj} + \frac{\overline{u_j u_m}}{k}P_{mi}\right) - 2/3\delta_{ij}\frac{\overline{u_l u_m}}{k}P_{ml}\right] \\
& + 0.1\left[\frac{\overline{u_l u_i}\;\overline{u_k u_j}}{k^2} - 1/3\delta_{ij}\frac{\overline{u_l u_m}\;\overline{u_k u_m}}{k^2}\right]\left[6D_{lk} + 13k\left[\frac{\partial U_l}{\partial x_k} + \frac{\partial U_k}{\partial x_l}\right]\right] \\
& \left. + 0.2\frac{\overline{u_l u_i}\;\overline{u_k u_j}}{k^2}(D_{lk} - P_{lk})\right\}
\end{aligned}$$

$$\begin{aligned}
\phi^{inh}_{ij} = {} & f_{w1}\frac{\varepsilon}{k}(\overline{u_l u_k}d^{A}_{l}\delta_{ij} - 3/2\,\overline{u_i u_k}d^{A}_{j} - 3/2\,\overline{u_j u_k}d^{A}_{i})d^{A}_{k} \\
& + f_{w2}\frac{\varepsilon}{k^2}\overline{u_l u_n}(\overline{u_n u_k}d^{A}_{k}\delta_{ij} - 3/2\,\overline{u_i u_n}d^{A}_{j} - 3/2\,\overline{u_j u_n}d^{A}_{i})d^{A}_{l} \\
& + f'_{w1}\frac{k^2}{\varepsilon}\left(\overline{u_k u_l}\frac{\partial\sqrt{A}}{\partial x_k}\frac{\partial\sqrt{A}}{\partial x_l}\delta_{ij} - 3/2\,\overline{u_i u_k}\frac{\partial\sqrt{A}}{\partial x_k}\frac{\partial\sqrt{A}}{\partial x_j} - 3/2\,\overline{u_j u_k}\frac{\partial\sqrt{A}}{\partial x_k}\frac{\partial\sqrt{A}}{\partial x_i}\right)
\end{aligned} \tag{5}$$

where

$$D_{ij} = -(\overline{u_i u_k}\partial U_k/\partial x_j + \overline{u_j u_k}\partial U_k/\partial x_i)$$

$$\tilde{\varepsilon} = \varepsilon - 2\nu(\partial k^{0.5}/\partial x_j)^2$$

$$c_1 = 3.1 f_A f_{Rt}\min(A_2^{0.5}, 0.5) \quad c'_1 = 1.1$$

$$f_{w1} = 2.0 f'_{Rt} \quad f'_{w1} = 0.22 \quad f_{w2} = 0.1 + 0.8 A_2 f''_{Rt}$$

$$f_{Rt} = \min(R_t/160, 1) \quad c'_2 = \min(0.6, A)$$

$$f'_{Rt} = \min(1, \max(0, 1 - (R_t - 55)/20))$$

$$f''_{Rt} = \min(1, \max(0, 1 - (R_t - 50)/85))$$

$$f_A = \begin{cases} (A/14)^{1/2} & A < 0.05 \\ A/0.7^{1/2} & 0.05 < A < 0.7 \\ A^{1/2} & A > 0.7 \end{cases}$$

$$f'_A = A^{0.5} f_{Rt} + A(1 - f_{Rt})$$

The quantities d_i and d^{A}_{i} are the normalized length-scale gradients defined as

$$d_i = \frac{N_i}{0.5 + (N_k N_k)^{0.5}} \text{ where } N_i = \frac{\partial(k^{1.5}/\varepsilon)}{\partial x_i} \tag{6}$$

$$d^{A}_{i} = \frac{N^{A}_{i}}{0.5 + (N^{A}_{k} N^{A}_{k})^{0.5}} \text{ where } N^{A}_{i} = \frac{\partial(k^{1.5}A^{0.5}/\varepsilon)}{\partial x_i} \tag{7}$$

These are designed to indicate the *direction* in which strong inhomogeneity exists: if the lengthscale gradients are large, the values of d_i and d^{A}_{i} are close to unity, whilst they become negligible in regions of small inhomogeneity.

In the earlier work of Craft & Launder, the coefficient c_2 in ϕ^{*}_{ij2} was taken as $\min(0.55, A^{1.5})$. The purpose of the factor $A^{1.5}$ was to reduce the effect in the near-wall region where, in its absence, the terms multiplied by c_2 contribute a very large sink term for the shear stress. In the backward facing step flow currently under consideration, the data shows that a large shear stress is generated immediately following separation from the step. Furthermore, the budget of $\overline{uv}$, reported by Le et al (1997), shows that there is substantial generation of the shear stress in this region, which is not quite balanced by the pressure-strain process. In the computations, however, as the flow leaves the step, the parameter A increases, as a result of the turbulence no longer being close to 2-component, and the pressure-strain contribution becomes too large, resulting in underprediction of the shear stress. After investigating a number of alternative methods of reducing c_2 in the near-wall region, the present calculations employ a form dependent upon both A and the strain parameter $S \equiv k/\varepsilon(S_{ij}S_{ij})^{1/2}$ where $S_{ij} = \partial U_i/\partial x_j + \partial U_j/\partial x_i$. The form adopted is $c_2 = \min(0.55, 3.2A/(1+S))$, which was found to give almost identical results to the earlier version in simple plane channel flows.

Turbulent Diffusion

For the turbulent diffusion of the stresses, Craft & Launder (1996) employed the proposal of Hanjalic & Launder (1972) to model the triple moments as

$$\overline{u_i u_j u_k} \propto -\frac{k}{\varepsilon}\left[\overline{u_i u_l}\frac{\partial\overline{u_j u_k}}{\partial x_l} + \overline{u_j u_l}\frac{\partial\overline{u_i u_k}}{\partial x_l} + \overline{u_k u_l}\frac{\partial\overline{u_j u_i}}{\partial x_l}\right] \tag{8}$$

Whilst this gives good agreement with the data near both shear and shear-free surfaces, it has the drawback that, towards the centre of a channel flow (where the cross-stream and spanwise stresses $\overline{v^2}$ and $\overline{w^2}$ are nearly equal) it predicts significantly more diffusion of $\overline{v^2}$ than of $\overline{w^2}$. At high Reynolds numbers this can be sufficient to give $\overline{v^2} > \overline{w^2}$ on the channel centreline. Moreover, when applied to the step flows, it was found to lead to a very strong backflow in the recirculation region, and very late recovery of the flow.

The formulation presently adopted for the triple moments is based on an algebraic simplification of their transport equations, which can be written as

$$\frac{D\overline{u_i u_j u_k}}{Dt} = P^1_{ijk} + P^2_{ijk} + \phi_{ijk} + d_{ijk} - \varepsilon_{ijk} \qquad (9)$$

where the production terms

$$P^1_{ijk} = \overline{u_i u_j}\frac{\partial \overline{u_k u_l}}{\partial x_l} + \overline{u_i u_k}\frac{\partial \overline{u_j u_l}}{\partial x_l} + \overline{u_k u_j}\frac{\partial \overline{u_i u_l}}{\partial x_l} \qquad (10)$$

$$P^2_{ijk} = -\overline{u_i u_j u_l}\frac{\partial U_k}{\partial x_l} - \overline{u_i u_k u_l}\frac{\partial U_j}{\partial x_l} - \overline{u_k u_j u_l}\frac{\partial U_i}{\partial x_l} \qquad (11)$$

are exact.

Invoking the Millionshtchikov (1941) approximation for the fourth order moments appearing in the diffusion term d_{ijk}, leads to

$$d_{ijk} = -\frac{\partial}{\partial x_l}(\overline{u_i u_j}\,\overline{u_k u_l} + \overline{u_i u_k}\,\overline{u_j u_l} + \overline{u_k u_j}\,\overline{u_i u_l}) \qquad (12)$$

whilst ε_{ijk} is modelled as $-2\varepsilon\overline{u_i u_j u_k}/k$ from a simplification of the form proposed by Kawamura et al (1995).

The pressure correlations ϕ_{ijk} are modelled as

$$\phi_{ijk} = \phi_{ijk1} + \phi_{ijk2} + \phi^{inh}_{ijk}$$

where

$$\phi_{ijk1} = -c_{t1}\varepsilon\overline{u_i u_j u_k}/k$$

$$\phi_{ijk2} = -c_{t2}P^2_{ijk} + c'_{t2}\left(\overline{u_i u_j u_l}\frac{\partial U_l}{\partial x_k} + \overline{u_i u_k u_l}\frac{\partial U_l}{\partial x_j} + \overline{u_k u_j u_l}\frac{\partial U_l}{\partial x_i}\right)$$

$$\phi^{inh}_{ijk} = c_{tw}\left(\frac{\partial \overline{u_i u_n}}{\partial x_r}\delta_{jk} + \frac{\partial \overline{u_j u_n}}{\partial x_r}\delta_{ik} + \frac{\partial \overline{u_k u_n}}{\partial x_r}\delta_{ji}\right)\overline{u_l u_r}d^A_l d^A_n$$

represent a return to isotropy term, a mean-strain dependent term, and an inhomogeneity related term respectively, and the coefficients are taken as

$$c_{t1} = 4.2 \quad c_{t2} = 1.0 \quad c'_{t2} = 0.2A \quad c_{tw} = 0.5$$

The coefficient c_{t2} was taken as unity since inclusion of the P^2_{ijk} term tended to cause numerical instabilities in the code. The other coefficients were tuned to give good agreement with available boundary layer data, whilst not causing the problems outlined above at the centreline of a plane channel flow. The final model for the triple moments was then obtained by neglecting the lhs of equation (9), and solving the resultant algebraic relations for the triple moments.

Dissipation Rate Equation

The dissipation rate equation employed is a simplified version of that proposed by Craft & Launder (1996), and is a transport equation for the "homogeneous" dissipation rate, $\tilde{\varepsilon}$, which can be written as

$$\frac{D\tilde{\varepsilon}}{Dt} = c_{\varepsilon 1}\frac{\tilde{\varepsilon}P_{kk}}{2k} - c_{\varepsilon 2}\frac{\tilde{\varepsilon}^2}{k} - c'_{\varepsilon 2}\frac{(\varepsilon - \tilde{\varepsilon})\tilde{\varepsilon}}{k} + \frac{\partial}{\partial x_l}\left(\left(\nu\delta_{lk} + c_\varepsilon\overline{u_l u_k}\frac{k}{\varepsilon}\right)\frac{\partial\tilde{\varepsilon}}{\partial x_k}\right) + c_{\varepsilon 3}\nu\overline{u_i u_j}\frac{k}{\varepsilon}\frac{\partial^2 U_k}{\partial x_i \partial x_l}\frac{\partial^2 U_k}{\partial x_j \partial x_l} + c_{\varepsilon 5}A^{1/2}(1-A)\frac{\varepsilon}{\sqrt{k}}\overline{u_i u_j}\frac{\partial A}{\partial x_i}\frac{\partial}{\partial x_j}\left(\frac{k^{3/2}A^{1/2}}{\varepsilon}\right) \qquad (13)$$

with coefficients given in table 1.

Table 1: Coefficients in the $\tilde{\varepsilon}$ equation.

$c_{\varepsilon 1}$	$c_{\varepsilon 2}$	$c'_{\varepsilon 2}$	$c_{\varepsilon 3}$
1.0	$\frac{1.92}{1+0.7A_d A_2^{0.5}}$	1.0	0.875

$c_{\varepsilon 5}$	c_ε	A_d
1.0	0.18	$\max(A, 0.25)$

RESULTS

Figure 1 shows the predicted mean velocity and normal stresses in a plane channel flow at a Reynolds number Re_τ of 495 compared to the DNS data of Kim (1989). The model clearly returns good predictions of the stress anisotropy in the near-wall region.

The two-dimensional flows reported here have been computed using a modified and extended version of the STREAM code (Lien & Leschziner 1993), which is a finite volume solver, with a fully collocated grid arrangement, employing the SIMPLE pressure correction with Rhie & Chow (1983) interpolation to avoid chequerboarding. The diffuser flows employed a grid fo 100 (axial) by 80 (radial) nodes, and the step flows meshes of up to 120x120 nodes, which were found to give grid-independent results.

Axisymmetric Diffuser Flows

Before considering the backstep flows, attention is first given to the axisymmetric diffuser flows studied experimentally by Stieglmeier et al (1989). The geometry of these cases is shown in figure 2, and the inlet condition is fully-developed pipe flow at a Reynolds number of 15600, which was obtained from a separate calculation using a version of the parabolic code PASSABLE (Leschziner 1982).

The predicted vector plot for the 14° expansion is shown in figure 3, and the predicted velocity profiles using both the present model and the Launder-Sharma (1974) k-ε model are shown in figure 4. The recirculation zone appears to be well predicted by the present model, as are the shear and normal stress profiles shown in figure 5.

In the downstream region, the turbulence levels towards the centre of the pipe are somewhat underpredicted, whilst in the near-wall region, the radial stress,

$\overline{v^2}$, appears to be slightly overpredicted, leading to the small disagreement seen in the mean velocity profiles in figure 3.

For the larger diffuser angle of 18°, the results are very similar as can be seen from figures 6 and 7 showing the mean velocity and normal stress profiles.

Backward Facing Step Flows

Figure 8 shows the predicted mean velocity profiles for the backstep flow simulation of Le et al (1997) at a Reynolds number of 5100. The recirculation region is again well-predicted, although there are slight discrepancies between the predicted and simulated profiles further downstream in the flow recovery region. The shear and normal stress profiles, shown in figures 9 and 10, indicate that the high peak values found in the recirculation region are well captured, as are the $\overline{v^2}$ profiles further downstream. However, the streamwise stress $\overline{u^2}$ tends to be underpredicted in the recovery region, as does the shear stress $\overline{uv}$.

Finally, for the backstep flow of Driver & Seegmiller (1983), figures 11 and 12 show that the recirculation zone is again well-predicted, with a sharp peak in the turbulence energy immediately following separation. Further downstream, in the recovery region, the turbulence energy is again slightly underpredicted in the near-wall region, leading to a too slow recovery of the mean velocity profile.

CONCLUSIONS

The low-Reynolds-number stress modelling work of Craft & Launder (1996) has been extended and tested further in a number of recirculating flows involving non-planar walls. The results are in reasonable agreement with the experimental and simulation data, giving confidence that the model can be applied to more complex geometries without the need to include quantities such as wall-normal vectors and distances. The immediate recirculation regions are well-predicted by the model, although some further refinement is needed in the recovery region, where the model currently predicts too slow a recovery of the flow.

Acknowledgements

The author would like to thank the Royal Society of London for funding this work through a University Research Fellowship.

References

Craft, T.J., Launder, B.E. 1996 *Int. J. Heat Fluid Flow* **17**, 245-254.

Driver, D.M., Seegmiller, H.L. 1983 *AIAA J.* **23**, 163.

Fu, S. 1988 Ph.D. Thesis, Faculty of Technology, University of Manchester.

Kawamura, H., Sasaki, J., Kobayashi, K. 1995 Proc. 10th Turbulent Shear Flows Symposium, Pennsylvania State University.

Kim, J. 1989 Personal Communication.

Hanjalic, K., Launder, B.E. 1972 *J. Fluid Mech.* **51**, 301.

Launder, B.E., Sharma, B.I. 1974 *Lett. Heat Mass Transfer* **1**, 131.

Launder, B.E., Reynolds, W.C. 1983 *Phys. Fluids* **26**, 1157.

Launder, B.E., Tselepidakis, D.P. 1993 in *Turbulent Shear Flows 8*, p81, Springer.

Launder, B.E., Li, S-P. 1994 *Phys. Fluids* **6**, 999.

Le, H., Moin, P., Kim, J. 1997 *J. Fluid Mech.* **330**, 349-374.

Leschziner, M.A. 1982 Report TF/82/11, Dept. of Mech. Eng., UMIST.

Lien, F-S., Leschziner, M.A. 1993 in *Turbulent Shear Flows 8*, p431, Springer.

Millionshtchikov, M.D. 1941 *C.R. Acad. Sci. SSSR* **32**, 619-621.

Rhie, C.M., Chow, W.L. 1983 *AIAA J.* **21**, 1525.

Stieglmeier, M., Tropea, C., Weiner, N., Nitsche, W. 1989 *J. Fluids Eng.* **111**,465.

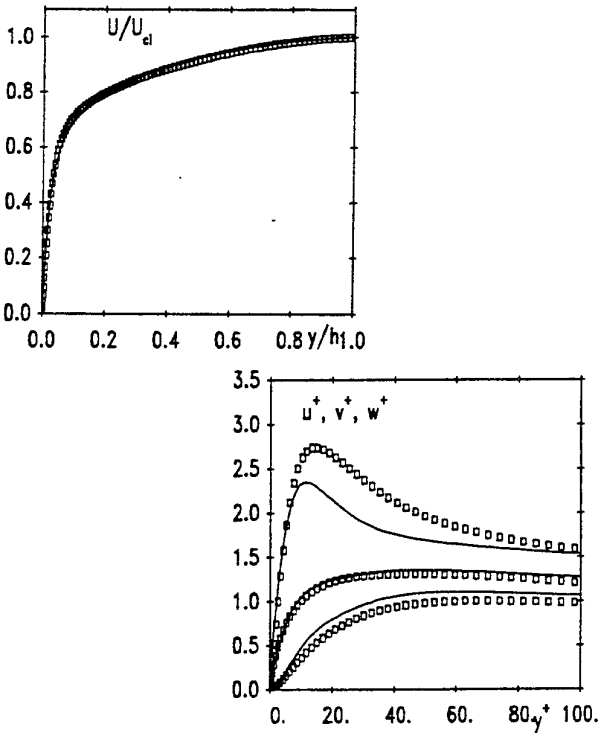


Figure 1: Mean velocity and normal stress profiles in plane channel flow.

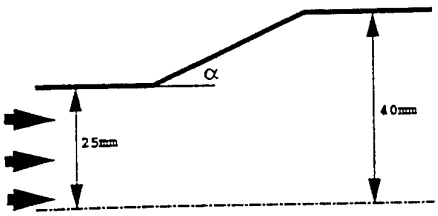


Figure 2: Diffuser case geometry.

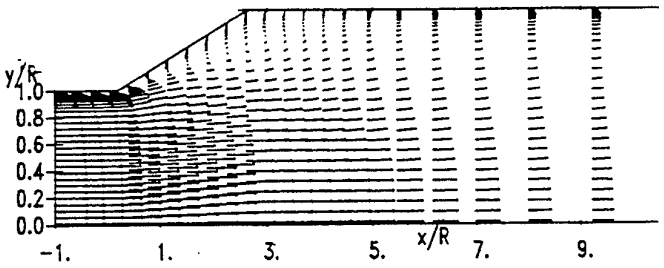


Figure 3: Vector plot of the 14° diffuser.

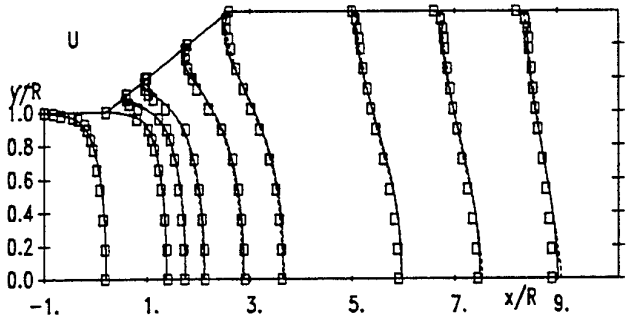
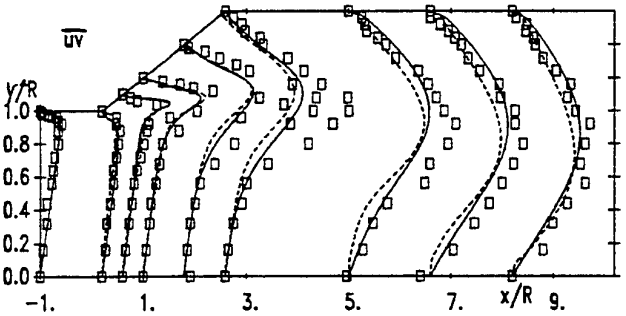
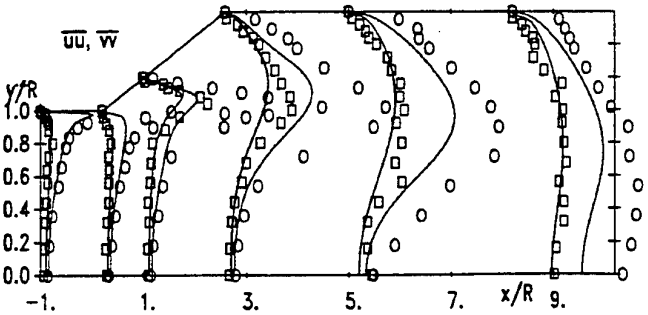


Figure 4: Mean velocity profiles in the 14° diffuser.

——— Present Model
- - - - Launder-Sharma k-ε





——— Present Model - - - - Launder-Sharma k-ε

Figure 5: Shear and normal stress profiles in the 14° diffuser.

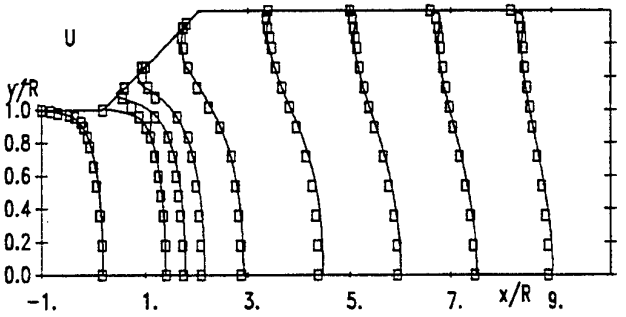


Figure 6: Mean velocity profiles in the 18° diffuser.

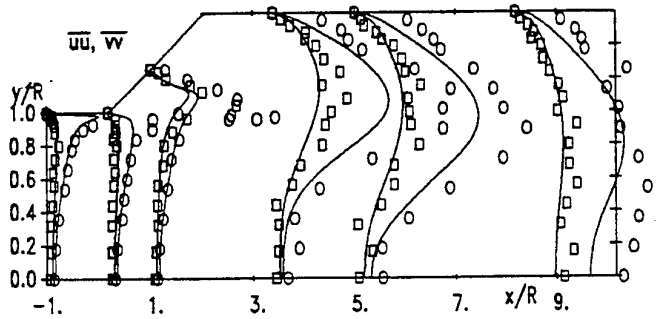


Figure 7: Normal stress profiles in the 18° diffuser.

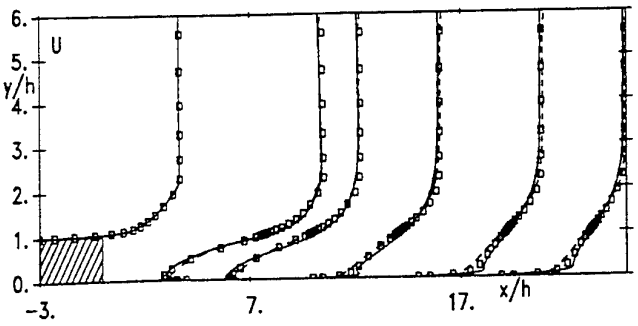


Figure 8: Mean velocity profiles in the backstep flow of Le et al.

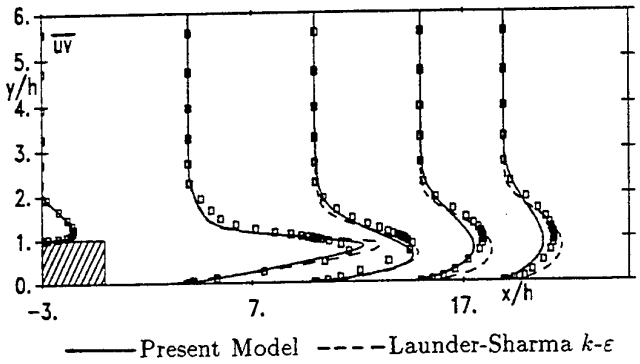


Figure 9: Shear stress profiles in the backstep flow of Le et al.

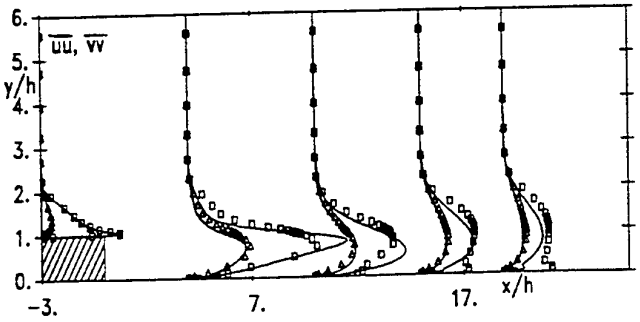


Figure 10: Normal stress profiles in the backstep flow of Le et al.

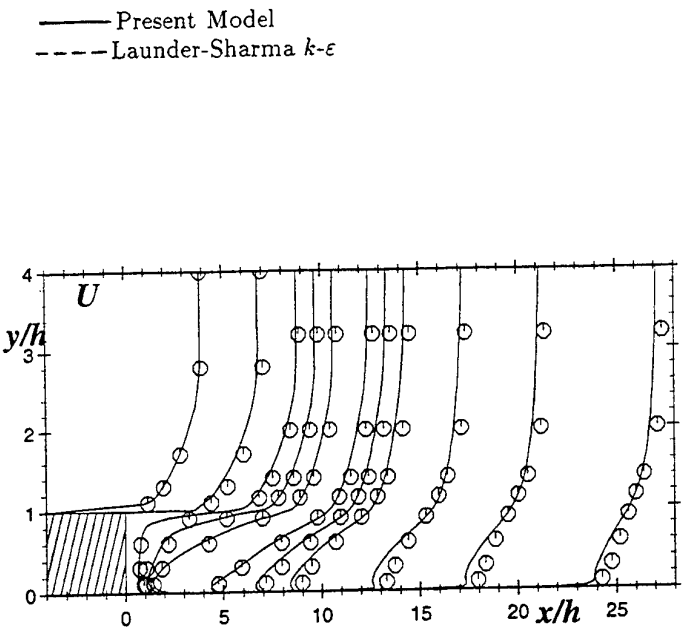


Figure 11: Mean velocity profiles in the backstep flow of Driver & Seegmiller.

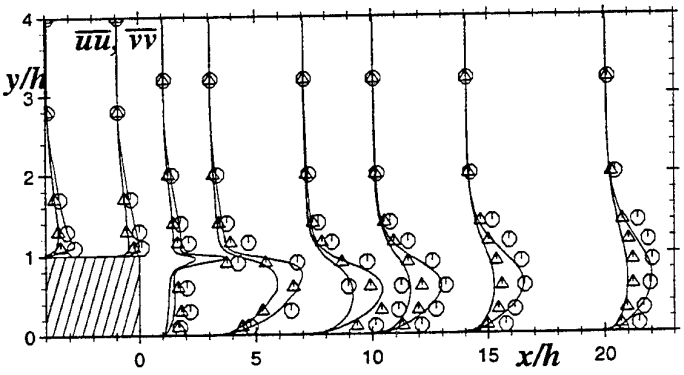


Figure 12: Normal stress profiles in the backstep flow of Driver & Seegmiller.

LARGE EDDY SIMULATION OF PERTURBED TURBULENT WALL FLOWS

A. Dejoan, E. Vedy and R. Schiestel
Institut de Recherche sur les Phénomènes Hors Equilibre (I.R.P.H.E.)
1 rue Honnorat
13003 Marseille
France

ABSTRACT

Large eddy simulations of turbulent flows near walls have been performed to investigate the influence of perturbations produced either by a geometrical accident or by the way of superimposed unsteady boundary conditions.

The flows under consideration are the flow downstream a step, the pulsed channel flow and the channel flow perturbed by periodic blowing-suction at the wall.

The numerical method is an hybrid dicretization using fourth order hermitian difference in non-homogeneous directions and Fourier pseudo- spectral expansions in homogeneous directions.

The characteristics of the flow are analysed through phase -averaged quantities showing lag effects and through instantaneous 3D fields showing structural effects.

INTRODUCTION

The present study is dealing with perturbed turbulent flows due to geometrical effects or to unsteadiness. Both cases can produce noticeable variations from the usual quasi-equilibrium turbulence found for instance in tubes and boundary layers over a plat plate. These flows are thus particularly interesting for providing databases useful to develop and refine turbulence modelling methods.

The flow downstream of a backward-facing step is a well known example of imposed geometrical perturbation. This flow has been studied experimentally by several investigators (see Jovic *and al.* (1995), Eaton *and al.* (1981), Durst *and al.* (1983)). The flowfield is indeed very complex where the presence of a recirculating zone influences the properties of the shear layer. At the reattachment, the flow is very unsteady with very large structures that are moving through this zone. Further downstream there is a relaxation zone after which the flow recovers equilibrium. This flow has long been a ticklish matter for turbulence modelling. The development of DNS and LES allowed further investigations for analysing the mechanisms in this flow and also to obtain numerical databases that supplement experimental measurements.

Unsteady turbulent flows occur in various situations encountered in industrial applications. There are for instance important manifestations of hysteresis which are significant for applications in aeronautics. We can cite also pulsed flows in ducts and boundary layers, influence of wall vibrations on a turbulent flow, forced vortex shedding flow from obstacles ... Several experimental studies have been developed since the past fifteen years (see Le *and al.* (1994)) that allowed insight into the structure and characteristics of unsteady turbulent flows. If classical time-averaged quantities are often found to be almost the same as the value expected in the corresponding steady flow , this fact must not mask that substantial changes can be found in the behavior of the flow. As regards detailed turbulence characteristics, intensity and structure, important changes may occur when the frequency of oscillation is increased past a critical level for which there is interaction between the oscillating motion and the turbulent flow structure itself. Analysis of the turbulence field can be made using phase averaging that enables a three terms decomposition generalizing the Reynolds decomposition.

The present study uses large eddy simulation to investigate perturbed turbulent flows of the two types described before. The backward-facing step, which has been already extensively studied by numerous authors, is mainly used here for testing the LES method. Unsteady flows considered include the pulsed channel flow for which experimental comparisons are available and the channel flow with wall perturbations produced by superimposed periodic blowing-suction.

GOVERNING EQUATIONS AND NUMERICAL PROCEDURE

After filtering of the instantaneous Navier-Stokes equations, the following system of the momentum and continuity equations is derived

$$\begin{aligned} \frac{\partial \overline{\mathbf{U}}}{\partial t} &= -\overline{\overline{\mathbf{U}}.\nabla\overline{\mathbf{U}}} - \nabla\overline{P} - \nabla\overline{\overline{\tau}} + \nu\Delta\overline{\mathbf{U}} \\ \nabla\overline{\mathbf{U}} &= 0 \end{aligned} \qquad (1)$$

where the overbar denotes filtering.

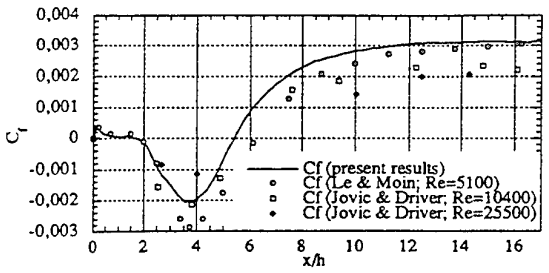


Figure 1: friction coefficient C_f in a flow downstream of a backward-facing step in a boundary layer.

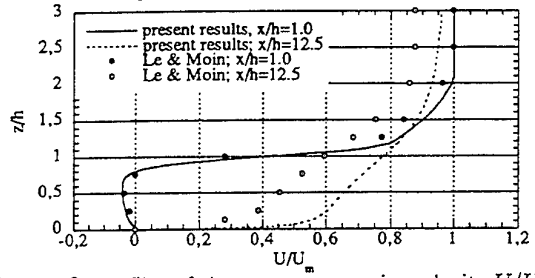


Figure 2: profiles of the mean streamwise velocity U/U_m at x/h=1.0 and at x/h=12.5.

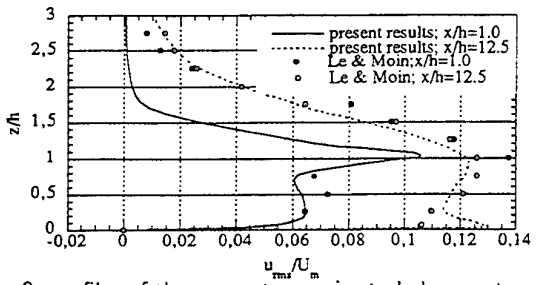


Figure 3: profiles of the mean streamwise turbulence intensity u_{rms}/U_m at $x/h = 1.0$ and at $x/h = 12.5$.

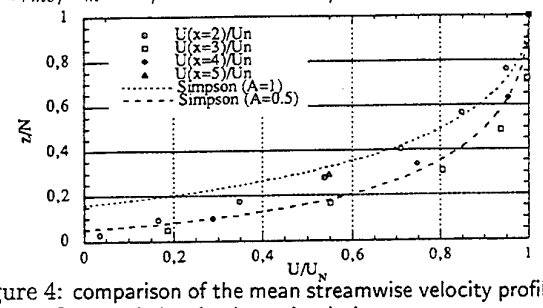


Figure 4: comparison of the mean streamwise velocity profile with the Simpson's law in the recirculation zone.

The subgrid stresses are defined by:

$$\bar{\bar{\mathbf{R}}} = \overline{\mathbf{u}' \otimes \overline{\mathbf{U}}} + \overline{\overline{\mathbf{U}} \otimes \mathbf{u}'} + \overline{\mathbf{u}' \otimes \mathbf{u}'} \tag{2}$$

$$\bar{\bar{\tau}} = \bar{\bar{\mathbf{R}}} - \frac{2}{3}\,\mathrm{trace}(\bar{\bar{\mathbf{R}}}).\bar{\bar{\mathbf{I}}} \tag{3}$$

The deviatoric part (3) must be modelled. The closure used here is the Smagorinsky model which suppose proportionality with the filtered strain-rate tensor $\overline{S}_{ij}$.

$$\tau_{ij} = -2\nu_t \overline{S}_{ij}$$

Near the wall damping is introduced according to the following formulation:

$$\nu_t = \begin{cases} (C_s l)^2 \sqrt{2\overline{S}_{ij}\overline{S}_{ij}} & \text{pour } \zeta \le \zeta_c \\ C_2 \frac{l^4}{\nu} 2\overline{S}_{ij}\overline{S}_{ij} & \text{pour } \zeta \ge \zeta_c \end{cases} \tag{4}$$

with

$$l = \left[\prod min(\Delta_m, l^*)\right]^{1/3} \quad , C_s = 0.2 \quad , C_2 = \frac{C_s^2 \nu}{27\kappa u_*}$$

$$l^* = \begin{cases} \frac{0.1}{C_s}\delta & \text{pour } \zeta \ge \frac{0.1\delta}{\kappa} \\ \frac{\kappa\zeta}{C_s} & \text{pour } \zeta \le \frac{0.1\delta}{\kappa} \end{cases} \tag{5}$$

where Δ_m denotes the filter width in the (m) direction, δ the width of the wall shear layer, ζ is the distance from the wall and κ the Von Karman constant.

The governing equations are solved on a staggered grid and the non-linear terms are discretized using a skew-symmetric form. The space derivatives are obtained by Fourier pseudo-spectral development in homogeneous directions and are obtained by fourth order hermitian finite difference schemes in non-homogeneous directions.

Time advancement uses fractional step method with Adams-Bashforth scheme for the non-linear terms and a Crank-Nicolson scheme for the viscous terms. Pressure linkage is solved by an approximate Poisson equation that guarantees fourth order accuracy with internal iterations.

Several versions of the numerical code have been developped depending on the number of homogeneous directions (1 or 2 in the present applications). In the inhomogeneous directions the mesh is strongly refined near the wall by using a change of space variable.

The numerical method has been tested in the case of plane channel (see Viazzo *et al.* (1995)).

THE FLOW DOWNSTREAM OF A BACKWARD FACING STEP IN A BOUNDARY LAYER

In the present simulation, the Reynolds number based on the maximum inflow velocity U_m and the step height h is equal to Re_h=13800. This choice has been dictated by the inlet boundary conditions built on an already existing simulation in a plane channel. The dimensions of the streamwise, spanwise and vertical directions are $20h$, $3\pi h/2$ and $5h$. The simulations make use of 380 928 grid points ($NX = 96$, $NY = 64$, $NZ = 62$) and the mesh is refined near the lower wall (minimum step size is $\Delta_z/h = 0.0064$) and near the vertical step wall (minimum step size is $\Delta_x/h = 0.07$). The statistical results have been obtained using a total integration time tU_m/h=300.

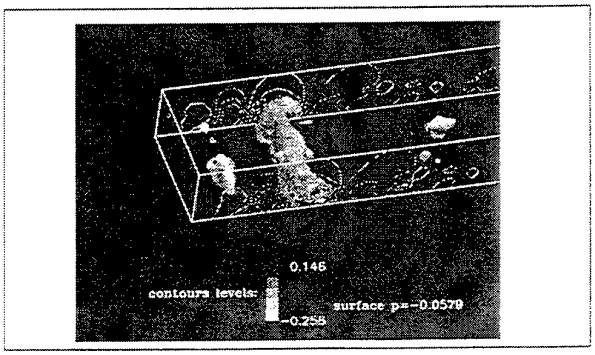


Figure 5: perspective view of the low pressure surfaces downstream of the step.

The reattachment length is an important primary test for

the calculation method. Figure (1) shows the distribution of friction coefficient versus the distance from the step. Good overall agreement is found with the experiments of Jovic and Driver, 1995 and the DNS of Le and Moin, 1994 even if the Reynolds numbers are somehow different.

Indeed the reattachment length is known to have strong dependance on Reynolds number in the lower range but it varies only slightly in the range $Re_h \geq 5000$. The calculated reattachment lenght is slightly underpredicted due to the above mentionned Reynolds number effects.

A secondary recirculation bubble is also found near the step wall, according to experimental and DNS results. Streamwise mean velocity profiles are given on figure (2) for two downstream locations. In spite of some discrepancies appearing between the Le and Moin DNS and the present predictions, mainly attributed to Reynolds number effects, the shape of the profiles is found to be correct.

Inflectional profiles are still found in the second section $x/h = 12.5$ showing that equilibrium is not yet reached. The same remarks hold for the turbulence intensity distributions given on figure (3).

The profiles exhibit a first small local maximum of energy near the wall probably linked to reverse flow effects and a larger peak located in the shear layer.

In the recirculation zone, no universal wall law exists and it is interesting to compare with the empirical relation proposed by Simpson (see Le *and al.* (1994)):

$$\frac{U}{U_n} = 1 - A\left[\frac{y}{N} - log\left(\frac{y}{N}\right) - 1\right] \qquad (6)$$

where A is a numerical constant and N is the distance to the wall of the maximum reverse flow. The values of A adequate for approximating reasonably the numerical results represented on figure (4) lies between 0.5 and 1.

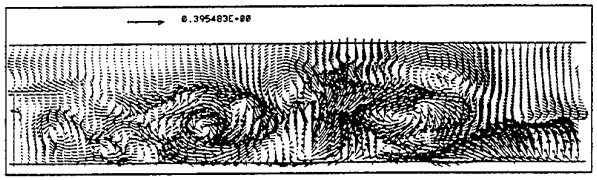


Figure 6: fluctuating velocity vectors in the x-z plane.

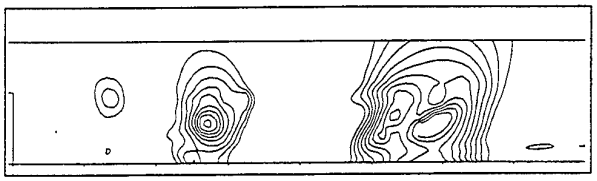


Figure 7: pressure fluctuations contours in the x-z plane; 12 levels $p'/\rho U_m^2$ from -0.138 to 0.0.

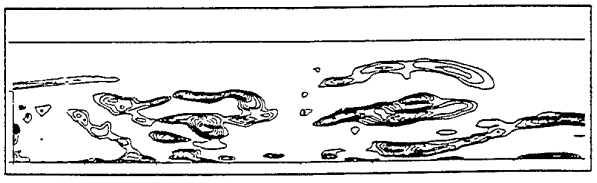


Figure 8: contours of the spanwise vorticity component; 12 levels $\omega_y h/U_m$ from 0.0 to 4.4.

Figure (5) gives an instantaneous perpective view of large eddies revealed by low pressure isosurfaces. The motion of vortices shedding from the step gives rise to large scale temporal oscillations. These large eddies looks quasi-two dimensional, they grow in the shear layer before interacting with the wall. Further insight is given on figures (6), (7) and (8) that put in corrsespondance three instantaneous views in a longitudinal section: the velocity vector field showing the presence of big rolls, the spanwise vorticity component that presents maximum values at the same locations and negative values of pressure fluctuations which is known to be a very good indicator of large eddies.

PULSED CHANNEL FLOW

The second type of perturbed turbulent flow considered here is the unsteady periodic channel flow with forced pressure gradient oscillations . Several experimental and numerical investigations (see Binder *and al.* (1995), Rida *and al.* (1991), Tardu *and al.* (1994)) are available in the scientific literature for detailed comparaisons. These previous studies have shown that the time averaged mean flow and the turbulent quantities seem to be unaffected by the imposed periodical oscillations.

At the high frequencies, the phase averaged quantities follow the Stokes solution while at relatively low frequencies this is no longer true near the wall and also further from the wall.

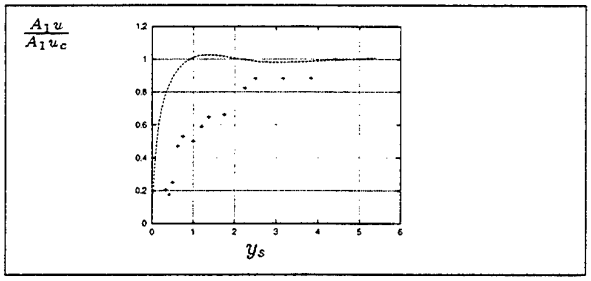


Figure 9: relative amplitude of fundamental mode of the periodic velocity oscillations vs non-dimensional distance y_s from the wall. (+) Binder and Kueny; (-) present simulation.

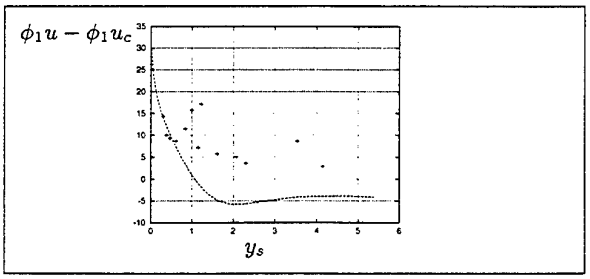


Figure 10: phase of fundamental mode of the periodic velocity oscillations vs non-dimensional distance y_s from the wall. (+) Binder and Kueny; (-) present simulation.

Binder and Kueny 1981, have shown also that the Stokes thickness l_s^+ non-dimensionalized with the mean viscous sublayer thickness is the leading parameter:

$$l_s^+ = l_s \frac{u_*}{\nu} \ , \ l_s = \sqrt{\frac{\nu}{\pi f}} \qquad (7)$$

where f is the frequency of the imposed oscillations and u_* the friction velocity at the wall.

The mean Reynolds number based on the channel halfwidth and the mean bulk velocity has been fixed to $Re_h = 13800$. The dimensions of the computational domain with respect to the streamwise, spanwise and vertical

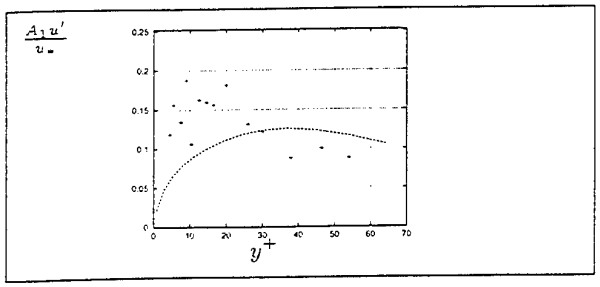


Figure 11: amplitude of fundamental mode of the periodic variations of the turbulent intensity vs y_s. (+) Binder and Kueny; (-) present simulation.

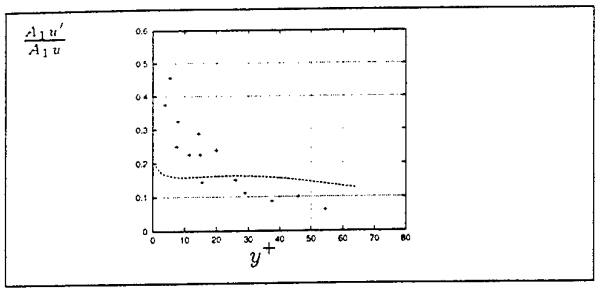


Figure 12: relative amplitude of the periodic variations of the turbulent intensity vs y^+. (+) Binder and Kueny; (-) present simulation.

directions are $4\pi h$, πh, $2h$. This simulation supposes that both x and y coordinates are homogeneous directions with periodic conditions. This grid is composed of $256 \times 128 \times 62$ numbers of points.

The value of l_s has been selected on the basis of the analysis of Binder and Kueny 1981, in order to create situations for which the oscillating flow interacts with turbulence. The value $l_s^+ = 12.9$ has been considered and the amplitude of the superimposed oscillating velocity $a_{\tilde{u}_c}$ (relative amplitude of the modulation) is 0.05.

The statistical treatment has been carried on five periods to obtain the phase averaged quantities from the databases.

The numerical results confirm previous findings already cited indicating that the mean velocity profiles in pulsed flow are practically always indistinguishable from the steady state profile. The same is true for the turbulence intensities.

The periodic velocity oscillations (with $l_s^+ = 12.9$) are analysed in figures (9) and (10) which compare respectively, the amplitude A_1 and the phase shift Φ_1 of the first mode of the velocity versus the non-dimensional distance from the wall $y_s = y/l_s$. The calculations give near the wall a steep gradient of amplitude which is characteristic of low frequency cases while further from the wall a local maximum is found like in Stokes flow. Phase shift presents a rapid decrease from the wall that also recalls a Stokes flow behaviour while measured quantities are more scattered.

The periodic variations of the turbulent intensity is shown on figures (11) and (12). The calculated amplitudes of the variations of the turbulence intensity $\sqrt{u'u'}$ given on (10) present an order of magnitude comparable with the experimental values; the maximum value obtained for the ratio $\frac{A_1 u'}{u_*} / \frac{\tilde{u}_c}{u_c} \approx 3.5$ shows that the oscillation of the normal stress is larger then the forcing of the mean flow.

On figure(12) these turbulent intensity variations are compared to the local amplitude of mean velocity. The calculated values are rather moderate compared to experiments but considering the value of turbulent intensity $\sqrt{u'u'}/\overline{u}$=0.08 it appears that there is still an amplification of the turbulent intensity with respect to the imposed velocity oscillation.

Another comparison has been made with the experimental case of Binder *et al.* 1995. realized for a larger amplitude. Figure (13) shows that the ratio $a_{\widetilde{u'u'}}/2a_{\tilde{u}}$ is very close to unity, suggesting that the turbulence response follows closely the forcing amplitude without attenuation. The comparison is almost satisfactory even if the amplitude is very different for the experimental case.

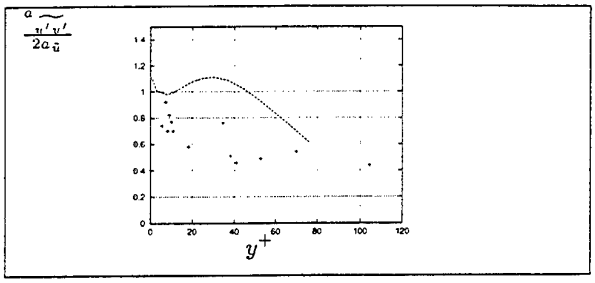


Figure 13: amplitude profiles of the modulation of the longitudinal turbulent intensity. (+) Binder, Kueny and Blackwelder; (-) present simulation.

The figure (14) is an illustration of the large phase shift found between the longitudinal normal stress and the phase averaged velocity gradient that acts in the corresponding transport equations for the normal stress. This results suggest that even if large eddy simulations offer a great hope for unsteady turbulence prediction, subgrid scale models that are based on subgrid viscosity, are likely to be limited because they postulate instantaneous alignment of the subgrid scale stresses with the phase averaged mean rate of strain. Introduction of finite time response of turbulence would be desirable.

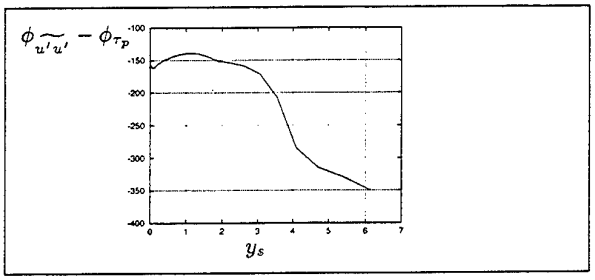
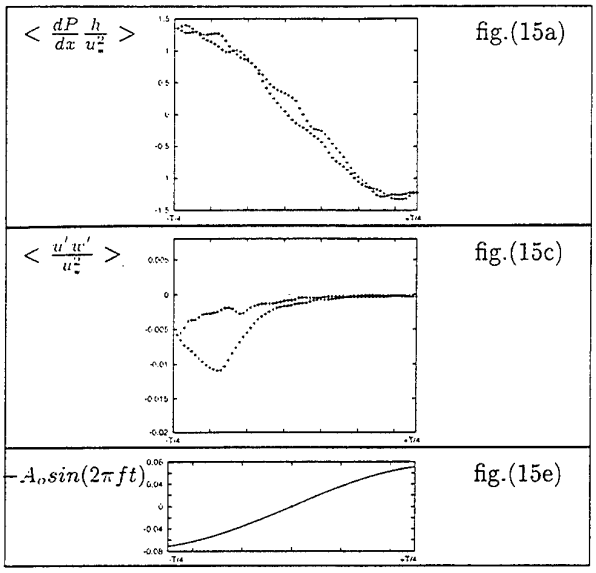


Figure 14: phase of the fundamental mode of the periodic turbulent intensity oscillations vs non-dimensional y_s distance from the wall . (-) present simulation.

TURBULENT CHANNEL FLOW WITH IMPOSED SINUSOIDAL WALL PERTURBATION

This case consists in a flow between two parallel flat plates submitted to periodic blowing and suction in time and space on one wall. The investigation of this type of unsteadiness is of great interest for the fundamental study of coherent structures and their impact on turbulence control.

Many studies in boundary layer blowing and suction exist in the literarure in the steady case (see Antonia *et al.* (1987), Miyake *and al.* (1995), Kajishima *and al.* (1992). In the configuration considered here, the lower wall is seen as permeable with an imposed normal velocity varying si-



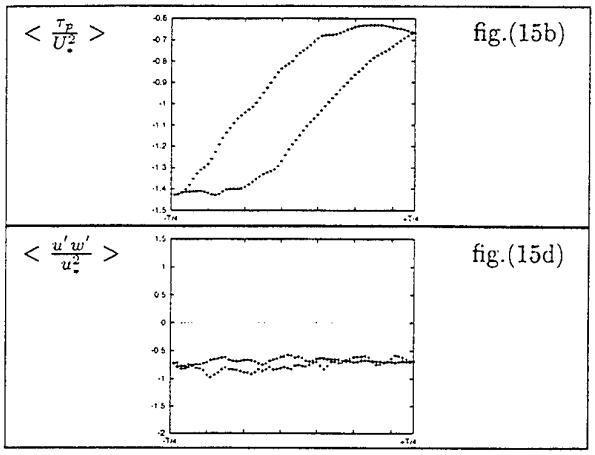
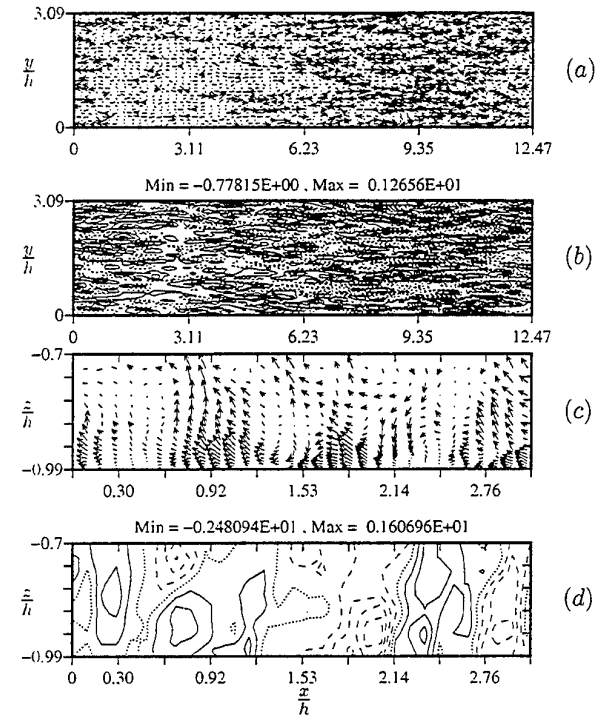
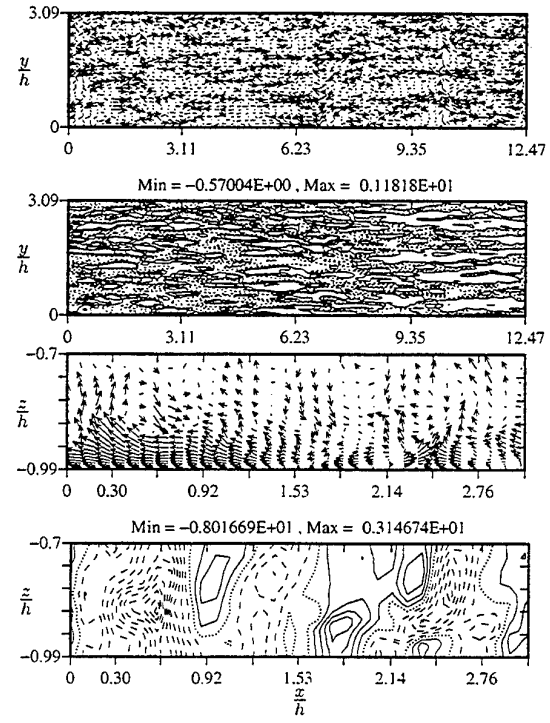
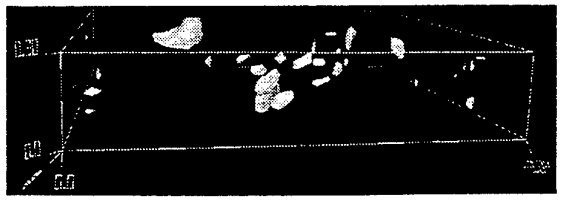


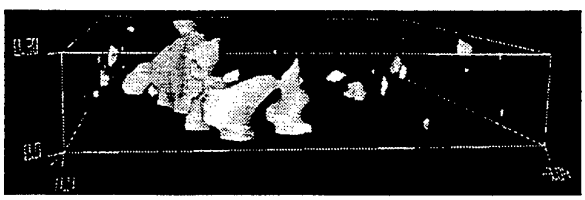
Figure 15: hysteresis of (a) pressure gradient, (b) shear stress, (c) turbulent shear stress at $z+ = 0.885$, (d) turbulent shear stress at $z+ = 30.04$ and (e) superimposed perturbation for $x/h = 3\pi$.







Figure(16): $t = T/4$.



Figure(17): $t = T/2$.

Figures(16) and (17): (a): fluctuating velocity vectors at $Z^+ = 0.885$; (b): fluctuation of the streamwise velocity at $Z^+ = 0.885$; (c): fluctuating velocity vectors at $y = H_y/2$; (d): pressure fluctuations at $y = H_y/2$; (e): perspective view of the low pressure fluctuation level $p'/\rho u_*^2 = -0.47$.

nusoidally in time and space:

$$w_{wall}(x,y) = A_o sin\,(2\pi ft)\, sin\,(\kappa_1 x) \qquad (8)$$

where f is the frequency of the perturbation and $2\pi/\kappa_1$ is the wavelength of the longitudinal perturbation. Their values are : $A_o = 0.075u_*$, $f = 2u_*/h$ and $\kappa_1 = 1/2$.

The number of grid points and the computational box are the same as the pulsed channel case. This numerical simulation which allows a high resolution near the wall, has been made on a total of thirteen periods and on this time interval a sample of 1690 points has been extracted.

As in previous case, it is found that the time mean values are almost unaffected by the wall perturbations compared to the ones obtained in a steady channel flow. However important differences may be found if one looks at the phase average quantities.

Figures (15a) to (15e) show hysteresis plots for several quantities including pressure gradient, wall shear stress and turbulent shear stress very near the wall. All the quantities are strongly affected by the periodic blowing-suction.

A strong lag effect is seen on the shear stress distribution at the particular x position represented.

Figures (15c) and (15d) show the hysteresis diagram for the turbulent shear stress at different wall distances, indicating that the influence of the wall perturbation strongly decays far from the wall. The same behavior has been observed for the others turbulent quantities.

Structural properties are illustrated on figures (16a to 16e) and (17a to 17e) for two different phases ($t = T/4$ corresponding to maximum blowing in the $0 \leq x \leq 2\pi h$ region and maximum suction in the $2\pi h \leq x \leq 4\pi h$ region, and $t = T/2$ corresponding to $w_{wall} = 0$).

Figure (16a) clearly show that the blowing zone is characterized by a strong decay of turbulence fluctuations with a tendancy to relaminarization. This remark is confirmed by the contour plots presented on figure (16b) suggesting encreased turbulence in the suction zone and damped fluctuations in the blowing zone.

Subsequent figures consider longitudinal x-z vertical sections. Velocity vectors plots in projection on the vertical plane are put in correspondance with pressure contours. The longitudinal distance represented is limited to one fourth of the wavelength starting from $x = 0$. So, figures (16c) (16d) show relatively low fluctuations levels. The contrary is found on figures (17c) (17d), with high turbulence fluctuations near the wall and high levels of pressure fluctuations. It is also possible to notice on these two figures a good correspondance between turbulent vortex and instantaneous pressure minimum.

Perspective views of the turbulent structures determined by low-pressure iso-surface are shown on figure (16e) and (17e) for these two phases ($T/2$ and $T/4$) at the same location in space. For $t = T/2$, horse-shoe vortices are found like in a fully developed channel flow, while for $t = T/4$, the vortices obtained with the same pressure level are scarce with no apparent organization.

CONCLUSIONS REMARKS

In this contribution, we have applied large eddy simulation to study various perturbed turbulent flows. Like in pulsed flows, the phase-averaged quantities show that lag effects occur in the turbulent interactions producing non-equilibrium situations.

These situations are often accompanied by structural effects such as coherent structures. Present simulations have shown the ability of large eddy simulations to investigate the statistical and structural properties of perturbed flows and in particular to give informations to improve statistical modelling. One has to mention however that the strong lag effect found will not be captured properly by the Smagorinsky model still used here and that transport equation subgrid scale model is desirable and now under investigation.

Acknowledgements : the authors wish to acknowledge the support by the IDRIS in Paris providing computer resources on the Cray C98

REFERENCES

Akselvoll, K., and Moin, P., 1993, "Large eddy simulation of a backward-facing step flows" *Engineering Turbulence Modelling and experiments 2, Ed. by Rodi, W. and Mortelli, F. Elsevier* , pp. 303–313.

Antonia, R., A., Fulachier, L., Krishnamoorthy, L., V., Benabib, T., and Anselmet, A., 1988, "Influence of wall suction on the organized motion in a turbulent boundary layer", *J. of Fluid Mech.*, Vol. 190 , pp. 217–240.

Arnaly, B.F., Durst, F., Pereira,J.C.F., and Schönung, B., 1983, "Experimental and theoretical investigation of backward-facing step", *J. of Fluid Mech.*, Vol. 127 , pp. 473–496.

Binder, G., and Kueny, J.L., 1981, "Measurements of the periodic velocity oscillations near the wall in unsteady turbulent channel flow", *Unsteady turbulent shear flows, IUTAM Symposium Toulouse, France. Springer Verlag, Ed. by Michel, R., Cousteix, J., and Houdeville,R.* , pp. 100–108.

Binder, G., Tardu, S., and Vezin, P., 1995, "Cyclic modulation of Reynolds stress and length scales in pulsed turbulent channel flow", *Proc. Roy, Soc. London* , Vol. A(451) , pp. 121–139.

Durst,F., and Tropea, C., 1983, "Flows over Two-dimensional Backward-facing steps", *Structure of Complex Turbulent Shear Flow, IUTAM Symposium Marseille 1982, Ed. by Dumas, R., Fulachier, L., Springer* , pp. 41–42.

Eaton, J.K., and Johmston, J.P., 1981, "A review of research on subsonic turbulent flow reattssachment", *IAAJ.*, Vol. 19 (9), pp. 1093–1100.

Jovic, S., and Driver, D., 1995 "Reynolds number effect on the skin friction in separated flows behind a backward-facing step", *Experiments in Fluids*, Vol. 18 (6), pp. 464–467.

Kajishima, T., and Miyake, Y., 1992, 'Large Eddy Simulation of a Turbulent Channel Flow with a Periodic Pressure gradient" *JSME International Journal*, Series II, Vol. 35 (1).

Le, H., and Moin, P., 1994, "Direct numerical simulation of turbulent flow over a backward-facing step", *Report No TF-58, Thermoscience Division, Dept. of Mech. Engng., Stanford University, Stanford California.*

Miyake, Y. Tsujimoto, K., and Beppu, H., 1995, "Direct numerical simulation of a turbulent flow in a channel having a periodic pressure gradient", *J. Heat and Fluid Flow*, Vol. 16 , pp. 333–340.

Rida, S., and Dang, T., 1991, "Direct simulation of turbulent pulsed channel flows", *8th Symp. on Turbulent Shear Flows, Münich.*

Schiestel, R., and Viazzo, S., 1995, "A Hermitian-Fourier numerical method for solving the incompressible Navier-Stokes equations", *J. Computers and Fluids*, Vol. 24 (6), pp. 739–752.

Tardu, S., F., Binder, G., and Blackwelder, R., F., 1994, "Turbulent channel flow with large-amplitude velocity oscillations", *J. of Fluid Mech.*, Vol. 267 , pp. 109–151.

Viazzo, S., and Schiestel, R., 1995 "Simulation des grandes échelles turbulentes en canal à l'aide d'un schéma hermitien", *C.R.Acamd. Sciences* , Tome 321 (Serie IIb), pp. 225–232.

SESSION 31 - ROTATION AND CURVATURE FLOWS I

MODELING OF TURBULENT SWIRLING FLOWS

Tsan-Hsing Shih, Jiang Zhu and William W. Liou
Center for Modeling of Turbulence and Transition,
ICOMP, NASA Lewis Research Center, Cleveland, OH 44142.

Kuo-Huey Chen
The University of Toledo, Ohio.

Nan-Suey Liu
NASA Lewis Research Center, Cleveland, OH 44135.

John L. Lumley
Cornell University, Ithaca, New York

ABSTRACT

Flows in an aircraft engine combustor are typically swirling for better fuel-air mixing and flame stabilizing. It has been long recognized that eddy viscosity turbulence models are unable to appropriately model swirling flows. Therefore, it has been suggested that, for modeling of swirling flows, a second order closure scheme should be considered for its ability in modeling of rotation and curvature effects. However, this scheme will require solving many complicated second moment transport equations (six Reynolds stresses plus other scalar fluxes and variances), which is not an easy task for CFD implementations and also requires large computer resources for a general combustor swirling flow. This paper is devoted to a development of a cubic Reynolds stress-strain model for turbulent swirling flows, inspired by the work of Launder's group at UMIST. Using this type of models, one only needs to solve two turbulence equations, one for turbulent kinetic energy k and the other for dissipation rate ε. The cubic model developed in this paper is based on a general Reynolds stress-strain relationship (Shih and Lumley, 1993). Two flows have been chosen for model evaluation. One is a fully developed rotating pipe flow, and the other is a more complex flow with swirl and recirculation.

INTRODUCTION

For better fuel-air mixing and flame stabilizing in a combustor, a swirling flow is often applied. Therefore, accurate modeling of turbulent swirling flows is important to an engine combustor design. Commonly used turbulence models in engineering calculations are eddy viscosity models which include zero-equation and two-equation models (e.g., mixing length models and k-ε models). However, this kind of eddy viscosity models have been long recognized that they are often not appropriate for predicting swirling flows. In fact, the deficiency of eddy viscosity models for swirling flows can be analytically shown by using a fully developed rotating pipe flow (Fu, 1995). The measured swirl velocity in the pipe varies approximately as the square of the normalized radius (r^2), but eddy viscosity models give an exact linear profile of the swirl velocity, which describes a solid body rotation.

To avoid this kind of deficiency of eddy viscosity models, a second order closure scheme has been suggested for modeling of swirling flows for its ability to simulate the effects of mean rotation and curvature. However, this requires solving many complicated second moment transport equations, which include six Reynolds stresses plus other scalar fluxes and variances. Because of this complication and of also requiring for large computer resources, second moment transport equation models have not been successfully implemented in CFD for a general combustor swirling flow.

Recent developments in nonlinear Reynolds stress-strain models bring a practical method for the calculations of combustor flows for its potential in simulating turbulent swirling flows with only two modeled turbulence transport equations (Craft et al, 1993). Further development and evaluation of these models are of great interest to both CFD development and modern aircraft engine combustor design.

The model developed in this paper is based on a general Reynolds stress-strain relationship which is an explicit expression for the Reynolds stresses in terms of a tensorial polynomial of mean velocity gradients. It is derived from a generalized Cayley-Hamilton relation. This general formulation contains terms up to the sixth power of the mean velocity gradient with eleven undetermined coefficients. Obviously, for any practical application, we need to truncate this polynomial. Shih, Zhu and Lumley (1995) suggested a

quadratic formulation and determined the three relevant coefficients by using the realizability constraints of Reynolds stresses and a result from rapid distortion theory analysis. This quadratic model works quite successfully for many complex flows including flows with separation. However, our recent calculations of swirling flows show that the swirl velocity is not appropriately predicted, which verifies the finding from Launder's group at UMIST. Launder (1995) pointed out that "the weaknesses of the linear eddy viscosity model can not be rectified by introducing just quadratic terms to the stress-strain relation." In this paper, we retain the cubic terms from a general Reynolds stress-stain formulation and determine the coefficients by using a similar method used in Shih et al's quadratic model and the measured data from rotating pipe flows. Modeled k-ε equations are used together with the cubic Reynolds stress-strain model for mean flow calculations. The first test flow is a fully developed pipe flow rotating about its own axial axis with various rotation rates (Imao, Itoh and Harada, 1996). The second test flow is a more complex flow with swirl and recirculation (Roback and Johnson, 1983). These two flows both have detailed experimental data on mean velocity components. The comparisons between the experimental data and computational results from models will be reported in detail.

CUBIC REYNOLDS STRESS MODEL

A cubic Reynolds stress model, used in this study for modeling of turbulent swirling flows, is derived from a general formulation of Reynolds stress-strain relation. The detailed derivation is reported in a NASA CR by Shih et al (1997). The resultant cubic model can be expressed in terms of mean velocity gradients, $U_{i,j}$, or in terms of mean strain and rotation rates, S_{ij} and Ω_{ij}. Here, we list both of them for the convenience in their applications.

In terms of mean velocity gradients, the cubic model of Reynolds stresses is

$$
\begin{aligned}
-\rho\overline{u_i u_j} &= -\frac{2}{3}\rho k\,\delta_{ij} \\
&+C_\mu\frac{\rho k^2}{\varepsilon}\left(U_{i,j}+U_{j,i}-\frac{2}{3}U_{k,k}\,\delta_{ij}\right) \\
&+B_1\frac{\rho k^3}{\varepsilon^2}\left(U_{k,i}U_{k,j}-U_{i,k}U_{j,k}\right) \\
&+B_2\frac{\rho k^4}{\varepsilon^3}\left[-\frac{1}{2}I_S\left(U_{i,k}U_{k,j}+U_{j,k}U_{k,i}-\frac{2}{3}\Pi_1\delta_{ij}\right)\right. \\
&-\frac{1}{2}I_S\left(U_{k,i}U_{k,j}+U_{i,k}U_{j,k}-\frac{2}{3}\Pi_2\delta_{ij}\right) \\
&\left.+U_{k,i}U_{k,p}U_{p,j}+U_{k,j}U_{k,p}U_{p,i}-\frac{2}{3}\Pi_3\,\delta_{ij}\right] \qquad (1)
\end{aligned}
$$

where "$,j$" means tensorial derivative with respect to j. I_S is the first principal invariant of S_{ij}, i.e., S_{kk}. The invarints Π_1, Π_2 and Π_3 are defined as follows

$$\Pi_1 = U_{i,j}U_{j,i}\,,\ \Pi_2 = U_{i,j}U_{i,j}\,,\ \Pi_3 = U_{i,k}U_{i,p}U_{p,k} \quad (2)$$

The three coefficients C_μ, B_1 and B_2 are

$$C_\mu = \frac{1}{4.0 + A_S\frac{kU^*}{\varepsilon}} \qquad (3)$$

$$B_1 = \frac{\sqrt{1-9C_\mu^2\left(\frac{kS^*}{\varepsilon}\right)^2}}{1+6\frac{k^2}{\varepsilon^2}\Omega^*\,S^*} \qquad (4)$$

$$B_2 = \frac{1.3\mu_T}{\frac{\rho k^4}{\varepsilon^3}\frac{|7(S^*)^2+(\Omega^*)^2|}{4}} \qquad (5)$$

in which μ_T is the eddy viscosity in Eq. (18), and

$$
\begin{aligned}
&A_S = \sqrt{6}\cos\phi, \quad \phi = \frac{1}{3}\arccos(\sqrt{6}W^*), \\
&W^* = \frac{S^*_{ij}S^*_{jk}S^*_{ki}}{(S^*)^3}, \quad U^* = \sqrt{(S^*)^2+(\Omega^*)^2}, \\
&S^* = \sqrt{S^*_{ij}S^*_{ij}}, \quad \Omega^* = \sqrt{\Omega_{ij}\Omega_{ij}} \qquad (6)
\end{aligned}
$$

In terms of mean strain and rotation rates, Eq. (1) can be written as

$$
\begin{aligned}
-\rho\overline{u_i u_j} &= -\frac{2}{3}\rho k\delta_{ij} + C_\mu\frac{\rho k^2}{\varepsilon}2S^*_{ij} \\
&+2B_1\frac{\rho k^3}{\varepsilon^2}\left(S_{ik}\Omega_{kj}-\Omega_{ik}S_{kj}\right) \\
&-2B_2\frac{\rho k^4}{\varepsilon^3}\left(\Omega_{ik}S^2_{kj}-S^2_{ik}\Omega_{kj}+\Omega_{ik}S_{km}\Omega_{mj}\right. \\
&\left.-\frac{1}{3}\Omega_{kl}S_{lm}\Omega_{mk}\delta_{ij}+II_S S^*_{ij}\right) \qquad (7)
\end{aligned}
$$

where

$$
\begin{aligned}
&S^*_{ij} = S_{ij}-\frac{1}{3}S_{kk}\delta_{ij}, \quad S_{ij} = \frac{1}{2}\left(U_{i,j}+U_{j,i}\right), \\
&\Omega_{ij} = \frac{1}{2}\left(U_{i,j}-U_{j,i}\right), \quad S^2_{ij} = S_{ik}S_{kj} \qquad (8)
\end{aligned}
$$

II_S is the second principal invariant of S_{ij}:

$$II_S = \frac{1}{2}\left(S_{kk}S_{mm}-S^2_{kk}\right) \qquad (9)$$

Note that in the above equations, S_{kk} means $S_{11}+S_{22}+S_{33}$ and S^2_{kk} means $S_{1p}S_{p1}+S_{2p}S_{p2}+S_{3p}S_{p3}$ in which each term contains a summation operator on the subscript "p".

TURBULENT SWIRLING FLOWS

The model proposed in the previous section will be used for modeling of swirling flows in this study. The first flow is a fully developed rotating pipe flow (Imao, Itoh and Harada, 1996). This flow was used for model development; however, a pipe flow with various axial rotating rates is still a critical test case for the model. The second flow is a more complex swirling flow with recirculation and separation (Roback and Johnson, 1983), which is often encountered in an aircraft engine combustor.

Rotating pipe flow

A fully developed rotating pipe flow provides a very clean test case for checking turbulence model's ability in modeling of swirling flows. Commonly used eddy viscosity models fail to predict this flow. One can show that any eddy viscosity model will produce a solution of solid body rotation for a rotating pipe flow, while experimental data shows that the flow is not a solid body rotation. Experiments further show that the characteristics of a pipe flow changes significantly with the axial rotation rate. For example, for a fixed mass flux, the axial rotation will strongly reduce the pressure drop. In other words, for a fixed pressure drop, the axial rotation will increase the total mass flux. However, the standard eddy viscosity models show no such changes at all.

In a fully developed turbulent pipe flow, all the axial gradients, $\partial/\partial x$ and azimuthal derivatives $\partial/\partial\theta$ are zero, and so is the radial velocity $V = 0$. The non-zero velocity components are the axial velocity U and tangential (or swirl) velocity $W = r\Omega$, where Ω is the angular velocity. Equations for this flow are very simple:

$$\frac{\partial r\rho U}{\partial t} = -r\frac{\partial \overline{P}}{\partial x} + \frac{\partial}{\partial r}\left[(\mu+\mu_T)r\frac{\partial U}{\partial r}\right] + \frac{\partial r\tau_{xr}}{\partial r} \tag{10}$$

$$\frac{\partial r^2\rho W}{\partial t} = \frac{\partial}{\partial r}\left[(\mu+\mu_T)r\frac{\partial rW}{\partial r}\right] - 2\frac{\partial}{\partial r}\left[(\mu+\mu_T)rW\right] + \frac{\partial r\tau_{\theta r}}{\partial r} \tag{11}$$

$$\frac{\partial r\rho k}{\partial t} = \frac{\partial}{\partial r}\left[\left(\mu+\frac{\mu_T}{\sigma_k}\right)r\frac{\partial k}{\partial r}\right] + rP_k - r\rho\varepsilon \tag{12}$$

$$\frac{\partial r\rho \varepsilon}{\partial t} = \frac{\partial}{\partial r}\left[\left(\mu+\frac{\mu_T}{\sigma_\varepsilon}\right)r\frac{\partial \varepsilon}{\partial r}\right] + C_{\varepsilon 1}\, rP_k\frac{\varepsilon}{k} - C_{\varepsilon 2}\,\frac{r\rho\varepsilon^2}{k} \tag{13}$$

or

$$\frac{\partial r\rho \varepsilon}{\partial t} = \frac{\partial}{\partial r}\left[\left(\mu+\frac{\mu_T}{\sigma_\varepsilon}\right)r\frac{\partial \varepsilon}{\partial r}\right] + C_1\, rS\,\varepsilon - C_2\,\frac{r\rho\varepsilon^2}{k+\sqrt{\nu\varepsilon}} \tag{14}$$

where $S = \sqrt{2S_{ij}S_{ij}} = \sqrt{\left(\frac{\partial U}{\partial r}\right)^2 + \left(\frac{\partial W}{\partial r} - \frac{W}{r}\right)^2}$. The nonlinear parts of turbulent stresses, τ_{xr} and $\tau_{\theta r}$, from the proposed cubic model, Eq. (1) or Eq. (7), are

$$\tau_{xr} = 0 \tag{15}$$

$$\tau_{\theta r} = -B_2\frac{\rho k^4}{\varepsilon^3}\left[W\left(\frac{\partial U}{\partial r}\right)^2 + W\frac{\partial W}{\partial r}\left(\frac{\partial W}{\partial r} - \frac{W}{r}\right)\right] \tag{16}$$

and the corresponding production rate of turbulent kinetic energy P_k is

$$P_k = \mu_T\left[\left(\frac{\partial U}{\partial r}\right)^2 + \left(\frac{\partial W}{\partial r} - \frac{W}{r}\right)^2\right] - B_2\frac{\rho k^4}{\varepsilon^3}\frac{W}{r}\left(\frac{\partial W}{\partial r} - \frac{W}{r}\right)\left[\left(\frac{\partial U}{\partial r}\right)^2 + \frac{\partial W}{\partial r}\left(\frac{\partial W}{\partial r} - \frac{W}{r}\right)\right] \tag{17}$$

where

$$\mu_T = C_\mu\, f_\mu\frac{\rho k^2}{\varepsilon} \tag{18}$$

$$f_\mu = \left[1 - exp(-a_1R_k - a_3R_k^3 - a_5R_k^5)\right]^{1/2} \tag{19}$$

and $a_1 = 1.7 * 10^{-3}$, $a_3 = 1 * 10^{-9}$, $a_1 = 5 * 10^{-10}$, $R_k = \rho\sqrt{k}y/\mu$. Other model constants used in this paper are standard: $\sigma_k = 1$, $\sigma_\varepsilon = 1.3$, $C_{\varepsilon 1} = 1.44$ and $C_{\varepsilon 2} = 1.92$. Depending on particular modeled k-ε equations, C_μ and f_μ may have different formulations proposed by different researchers. For example, if Eq. (14) (Shih et al, 1995) is used together with

$$C_1 = max\left\{0.43,\ \frac{\eta}{5+\eta}\right\}$$
$$C_2 = 1.9$$
$$\eta = \frac{S\,k}{\varepsilon}$$

then f_μ needs to be adjusted. In this paper we have used the following near wall damping function:

$$f_\mu = 1 - \frac{1}{1 + 0.1R_k + 0.15R_k^2} \tag{20}$$

From Eq. (11), it is easy to show that any eddy viscosity model will produce a solution of solid body rotation, i.e., $W/W_{wall} = r/R$, where W_{wall} is the swirl velocity of the wall and R is the radius of the pipe. It can also be shown that any quadratic Reynolds stress models will have no contributions to the component $\tau_{\theta r}$ for a fully deveied rotating pipe flow. Therefore, they will also produce a solution of solid body rotation, just like an eddy viscosity model does. Eqs. (10-14) can be easily and accurately solved by a parabolic code. Figures 1 - 3 show the results of the present cubic model with Eqs. (12) and (14) compared with the measurements by Imao, et al (1996). The results from the standard k-ε model are also included for comparisons. In Figures, the rotation parameter N is defined as $N = W_{wall}/U_m$, where U_m is the average velocity of the pipe. The Reynolds number based on U_m and R is 20000. As shown in these figures that the standard k-ε model has totally missed the effect of axial rotations on pipe flow. In contrast, the present cubic Reynolds stress model can capture all the effects of the axial rotation on the pipe flow: it increases the centerline velocity and changes the axial velocity profile towards parabolic shape, it maintains non-solid body swirl velocity profile, it reduces the relative turbulent kinetic energy k/U_m^2.

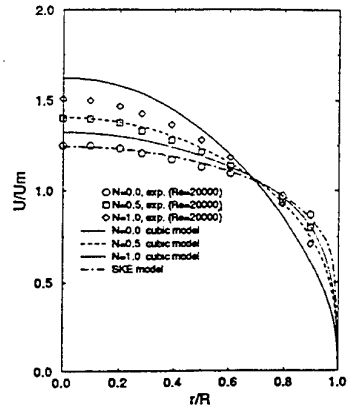


Figure 1: Axial velocity profile in a rotating pipe

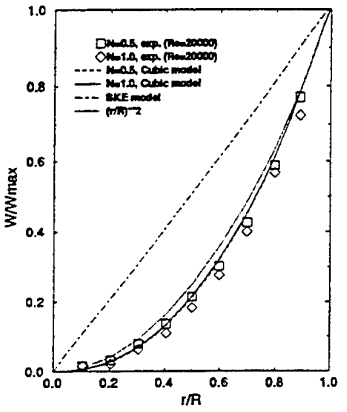


Figure 2: Tangentail velocity profile in a rotating pipe

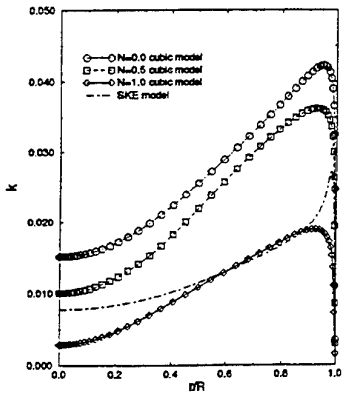


Figure 3: Effect of rotation on turbulent kinetic energy $\frac{k}{U_m^2}$

Complex swirling flow

A confined swirling coaxial jet was experimentally studied by Roback and Johnson (1983). Figure 4 shows the general features of the flow. At the inlet, an inner jet and an annular jet are ejected into an enlarged duct. Besides an annular separation due to sudden expansion of the duct, a central recirculation bubble is created by flow swirling. This flow feature is often observed in an aircraft engine combustor. In this figure, calculated velocity vectors in an axisymmetric plane from the cubic model is compared with the one from the standard k-ε model. Solutions were obtained by two Navier-Stokes codes. One is CORSAIR (Liu et al, 1996) and the other is FAST-2D (Zhu, 1991). Eq. (13) and Eq. (14) are respectively used in this calculation. Numerical results from the two codes are quite close to each other. Figure 5 compares the calculations of the centerline velocity from standard k-ε eddy viscosity model (SKE) and the present cubic model with the experiment. The negative velocity indicates the central recirculation. It is seen that both models predict the strength of central recirculation quite well, but the present model predicts the rear stagnation point much better than does the SKE model. This is also reflected in Figure 4 that the recirculation bubble from the cubic model is larger than that from the standard k-ε model. Figures 6, 7, 8 show the comparison of calculated and measured mean velocity profiles at x=51mm. Both models give reasonably good profiles which are within experimental scatter. However, significant differences of tangential velocity profile between the two models have been found in the downstream region. For example, Figure 9 shows the swirl velocity profile at x=305mm. SKE model predicts a nearly solid body rotation, whereas the cubic model shows a non-solid body rotation which is consistent with the experimental observation.

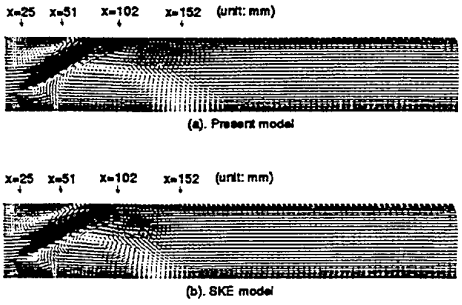


Figure 4: Velocity vectors in an axisymmetric plane. (a) from present model, (b) from standard k-ε model.

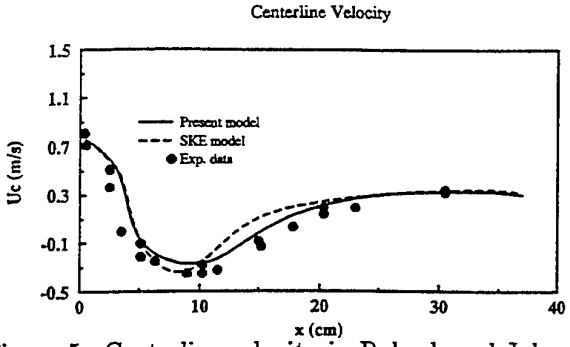


Figure 5: Centerline velocity in Roback and Johson flow

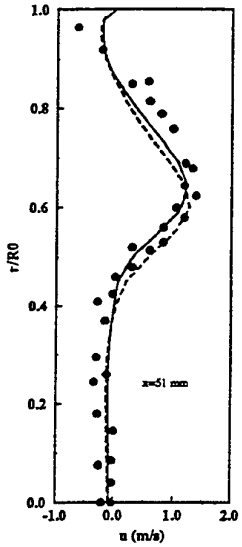


Figure 6: Axial velocity profile at $x = 51mm$

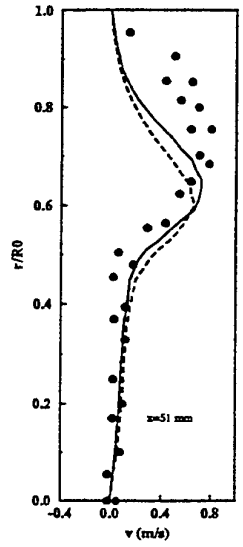


Figure 7: Radial velocity profile at $x = 51mm$

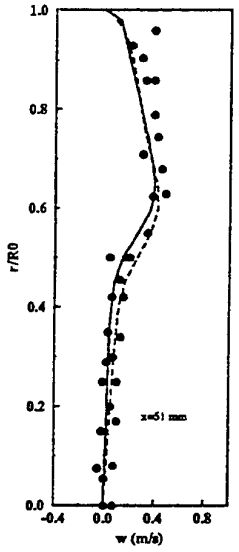


Figure 8: Tangential velocity profile at $x = 51mm$

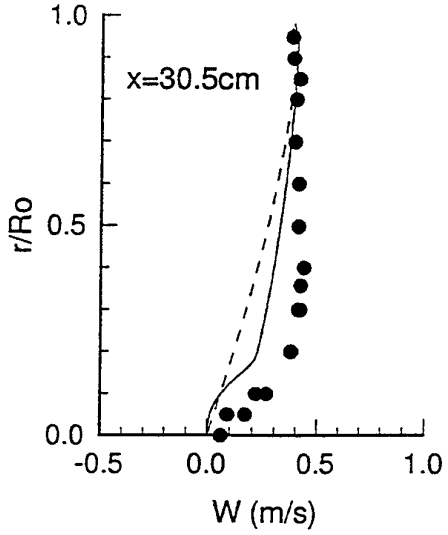


Figure 9: Tangential velocity profile at x=305mm

CONCLUSION AND DISCUSSION

This study shows that nonlinear cubic Reynolds stress-strain models with modeled k-ε equations have the potential to simulate turbulent swirling flows encountered in aircraft engine combustors. The model proposed in this paper appears simple and numerically robust in CFD applications which the engine industry is particularly interested in. However, further evaluations against other flows are needed in order to find the flow range of model's validity and possible further improvements.

The cubic Reynolds stress model can be combined with existing k-ε model equations, yet the best combination needs further studies and evaluations.

The proposed cubic model appears the simplest among other cubic or higher order models; however it still needs about 15% more CPU time than a linear k-ε eddy viscosity model does for a general 2D axisymmetric swirling flow. We expect that if a higher order model (e.g., fourth or fifth) is used, then the CPU time for calculating Reynolds stresses will siginicantly increase and the model may become impratical for a general 3D swirling flow.

REFERENCES

Craft T.J., Launder B.E. and Suga K., 1993, "Extending the applicability of eddy viscosity models through the use of deformation invariants and nonlinear elements." 5th IAHR Conference on Refined-Flow Modelling and Turbulence Measurement, Paris, 7-10 September 1993.

Fu S. and Wang C., 1995, "Second-Moment Closure Modelling of Turbulence in Non-Inertia Frame." Proceedings of the Mathematical Modelling of Turbulent Flows. Edited by Hisaaki Daiguji and Yutaka Miyake, Japan Society of Computational Fluid Dynamics, 95-110.

Imao, S. and Itoh, M., 1996, "Turbulent characteristics of the flow in an axially rotating pipe," *Int. J. Heat and Fluid Flow* 17: 444-451.

Launder, B.E., 1995, "An introduction to single-point closure methodology," Proceedings of the ER-COFTAC/IUTAM Summer School, in Stockholm, 12-20 June, 1995.

Liu, N.-S. Quealy, A., Kundu, K., Brankovic A., Ryder, R. and Van Dyke, K., 1996, "Multi-Disciplinary Combustor Design System and Emissions Modeling," NASA 1996 CAS workshop Proceedings, Ames Research Center, NASA, Aug. 13-17, 1996.

Roback, R. and Johnson, B.V., 1983, "Mass and momentum turbulent transport experiments with confined swirling coaxial jets," NASA CR 168252.

Shih, T.-H. and Lumley, J. L., 1993, "Remarks on turbulent constitutive relations." *Math. Comput. Modelling* **18**, 9–6.

Shih, T.-H., Zhu, J. and Lumley, J. L., 1995, "A new Reynolds stress algebraic equation model." *Comput. Methods Appl. Mech. Engrg.* 125 (1995) 287-302.

Shih, T.-H., Liou, W.W., Shabbir, A., Yang, Z. and Zhu, J., 1995, "A new k-ε eddy viscosity model for high Reynolds number turbulent flows," *Comput. Fluids* 24 (3) 227-238.

Shih, T.-H., Zhu, J., Liou, W.W., Chen, K.-H., Liu, N.-S. and Lumley, J. L., 1997, "Modeling of turbulent swirling flows," NASA CR 1997 to appear.

Zhu, J, 1991, "A computer program for numerical simulation of two-dimensional incompressible flows with complex boundaries," Rep. 690, Institute for Hydromechanics, University of Karlaruhe.

EDQNM AND DNS PREDICTIONS OF ROTATION EFFECTS IN STRAINED AXISYMMETRIC TURBULENCE

O. Leuchter
Office National d'Etudes et de Recherches Aerospatiales (ONERA)
92320 Châtillon
France

C. Cambon
LMFA (UMR-CNRS 5509), Ecole Centrale de Lyon (ECL)
69130 Ecully
France

ABSTRACT

The effects of rotation on strained homogeneous turbulence are analysed on the basis of nonlinear spectral calculations using a refined EDQNM closure model, and by direct numerical simulation (DNS). The results globally confirm the tendencies observed in laboratory experiments: Rotation significantly inhibits the strain-induced anisotropization of the Reynolds-stress tensor, as a consequence of an enhanced level of the rapid pressure-strain correlations, and increases the anisotropy of the integral lengthscales relative to the rotation axis. Satisfactory agreement is achieved between EDQNM and DNS results. The DNS calculations reveal the existence of streamwise vortical structures of high intensity, as a consequence of the stretching of the flow by axisymmetric strain.

INTRODUCTION

Various types of rotation-strain coupling have been investigated in recent years at ONERA, in the framework of basic research on rotation effects in homogeneous turbulence. Plane and axisymmetric configurations have been analysed, both experimentally and numerically. The numerical approach has mainly focussed on nonlinear spectral calculations based on the EDQNM closure approach developed in cooperation with the ECL. This rather fundamental research activity was primarily motivated by the need for more refined single-point closure models able to predict rotation effects correctly. Actually, most of the Reynolds stress models available in the literature are not sensitive to rotation in axisymmetric flows.

Rotation acts on strained axisymmetric turbulence primarily through linear mechanisms. In homogeneous flow, it is essentially the strong action of rotation on the rapid pressure terms which causes the turbulence structure to be modified. The closure of the rapid pressure-strain correlation therefore still remains one of the main tasks in one-point turbulence modelling.

Rapid distortion theory (RDT) is an appropriate background for analysing and understanding the linear rotation effects, since it provides exact numerical solutions for the pressure-strain correlations in the rapid limit. RDT calculations show that it is the large enhancement that rotation produces on the *rotational part* of the rapid pressure-strain correlation that is responsible for the reduction of anisotropy observed in the experiments. RDT also elucidates the mechanism by which rotation enhances the strain-induced anisotropy of the integral lengthscales relative to the axial direction.

Nonlinear spectral calculations based on the standard (EDQNM-1) closure model qualitatively confirm these tendencies, except that the anisotropy level is significantly reduced due to the nonlinear damping effects. The purpose of the present work is to provide more refined nonlinear spectral predictions of axisymmetric rotation-strain coupling with a more elaborate two-point closure model (the EDQNM-2 model), and to compare the results with Direct Numerical Simulations (DNS).

FLOW CHARACTERISTCS

Homogeneous turbulence in solid-body rotation is subject to axisymmetric contraction with a constant strain rate D. The mean flow is described by the following velocity-gradient tensor:

$$\lambda_{ij} \equiv (\frac{\partial U_i}{\partial x_j}) = \begin{pmatrix} D & 0 & 0 \\ 0 & -D/2 & -\Omega \\ 0 & \Omega & -D/2 \end{pmatrix} , \qquad (1)$$

where Ω is the (time-dependent) rotation rate, which varies during the straining process ($t > 0$) according to $\Omega = \Omega_0.e^{Dt}$. Ω_0 is the initial rate of solid-body rotation before the strain is applied.

The flow has been investigated experimentally in a facility developed at ONERA for the purpose of basic research on rotating turbulence. The initial solid-body rotation of rate Ω_0 is generated by a rotating honeycomb, coupled with a grid turbulence generator, and the strain is superimposed in a subsequent contracting duct of appropriate shape (see ref.[1] for details). Ducts of different lengths, but with the same contraction ratio ($C = 4$) allow the strain rate D to be varied for a given axial velocity. The rotation rate

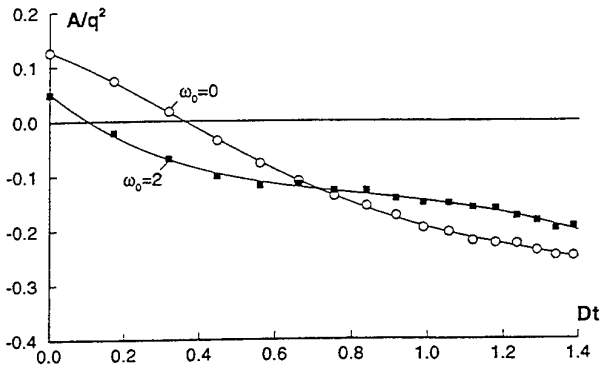


Figure 1: Experiment: Axisymmetric anisotropy

can be varied continuously between 0 and a maximum of 2π rad/s. The distortion described by eq.(1) is suitably reproduced in the experiments near the flow axis. For the nominal conditions, the Taylor microscale Reynolds number ($Re_\lambda = (q^2/3)^{1/2}\lambda/\nu$) is of the order of 40, and the flow is characterized by the parameters $\omega_0 = \Omega_0/D$ and $\tau_0 = 2\epsilon_0/Dq_0^2$. The latter represents the ratio between the characteristic linear time ($t_L = 1/D$) and the characteristic nonlinear time (eddy turnover time $t_{NL} = q_0^2/2\epsilon_0$), where $q_0^2/2$ is the kinetic energy at $t = 0$ and ϵ_0 the corresponding dissipation rate. Typical values for both parameters are $\omega_0 = 0$, 1 or 2, and $\tau_0 = 0.5$, 1 or 2.

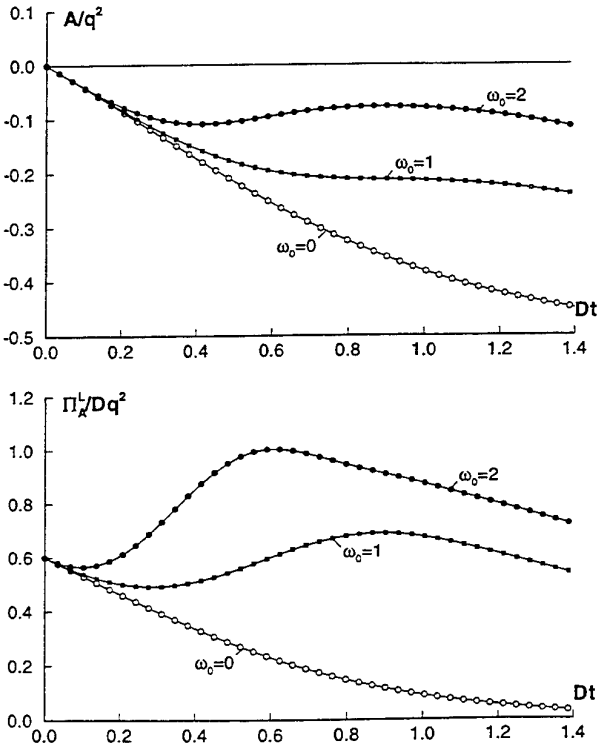


Figure 2: RDT results: Anisotropy (upper figure), Pressure-strain correlation (lower figure)

The measurements showed that the strain-induced increase of the rotation strongly affects the structure of the turbulence. As shown in Figure 1, the variation of the (normalized) axisymmetric anisotropy ($A/q^2 = (\overline{u^2} - \overline{v^2})/q^2$) during the straining process is significantly reduced in the presence of rotation (here $\omega_0 = 2$), compared to the non-rotating reference case of pure axisymmetric strain ($\omega_0 = 0$). Rotation simultaneously increases the corresponding pressure-strain correlation and the anisotropy of the axial lengthscales (not shown).

These tendencies are confirmed by (spectral) Rapid Distortion Theory (RDT) and its nonlinear extension based on the EDQNM-1 closure, while (single-point) second order closure models do not predict this behavior correctly, as they are strictly insensitive to rotation in axisymmetric flow. Figure 2 shows, for sample RDT results, the anisotropy A and the corresponding rapid pressure-strain correlation Π_A^L normalized by Dq^2. The initial conditions are isotropic, unlike the experiments. The huge amplification of the linear pressure terms and the concomitant reduction of the anisotropy appear clearly to be the most relevant linear rotation effects.

NUMERICAL METHODS

EDQNM-2 Model

The principle of the EDQNM-2 model has been outlined in ref.[3] for the general case, and applied to the particular case of solid-body rotation in ref.[4]. Recently, an extended version of the model has been developed for the case of rotation- strain coupling as defined by eq.(1), see ref.[5].

The EDQNM-2 model differs from the standard (EDQNM-1) model by the fact that the rotational mean velocity gradients are explicitly taken into account in the spectral equations for the third-order moments. The starting point is the Craya equation for the second-order spectral tensor Φ_{ij}, defined as the Fourier transform of the two-point velocity correlation tensor in physical space:

$$\frac{\partial \Phi_{ij}}{\partial t} - \lambda_{lm} k_l \frac{\partial \Phi_{ij}}{\partial k_m} = -(\lambda_{im}\Phi_{mj} + \lambda_{jm}\Phi_{im}) + \\ +2\lambda_{lm}\frac{k_l}{k^2}(k_i\Phi_{mj} + k_j\Phi_{im}) - 2\nu k^2 \Phi_{ij} + T_{ij} \qquad (2)$$

The terms on the right-hand side represent the production, the "rapid" pressure-strain correlation, the viscous term, and the nonlinear transfer term, respectively. Only the nonlinear term T_{ij} (which also contains the "slow" pressure-strain correlation) needs to be closed. Instead of Φ_{ij}, we use the scalar variables e and Z defined by

$$e = \frac{1}{2}\Phi_{ii}, \qquad Z = \frac{1}{2}\Phi_{ij} N_i^* N_j^* \qquad (3)$$

where N and N^Λ are the complex eigenvectors of the rotation matrix relative to the wavevector k, see ref.[3], [4].

Equation (2) is then replaced by the scalar equations

$$\frac{de}{dt} + 2\nu k^2 e + D.L^e = T^e, \\ \frac{dZ}{dt} + (2\nu k^2 - 4i\Omega\mu)Z + D.L^Z = T^Z \qquad (4)$$

The scalar e represents the energy density and $Z = Z_r + iZ_i$ the complex deviator in planes normal to the wavevector k. The quantities L^e and L^Z stand for the linear contributions due to the strain, and μ is the cosine of the angle between the rotation vector Ω and the wave vector k. The time derivatives in eq.(4) are to be considered as convective derivatives along the spectral trajectories (in accordance with RDT and DNS using distorted Fourier modes).

By analogy with eq.(3), the nonlinear terms T^e and T^Z are defined by:

$$T^e = \frac{1}{2}T_{ii}, \qquad T^Z = \frac{1}{2}T_{ij}N_i^* N_j^* \qquad (5)$$

These involve triple correlations, which can be written in the following symbolic form:

$$< \hat{u}\hat{u}\hat{u} > (t) = \{g \cdot g \cdot g\}(t) < \hat{u}\hat{u}\hat{u} > (t_0) + \int_{t_0}^{t} \{g \cdot g \cdot g\}(t-t') < \hat{u}\hat{u}\hat{u}\hat{u} > (t')dt' \quad (6)$$

The g's represent the Green functions relative to the linear operator in the spectral equations for the velocity fluctuations. By neglecting the direct effect of strain in the nonlinear terms, the individual Green functions can be expressed analytically (see ref.[4]) as:

$$g_{ij}(t-t') = Re[N_i N_j^* \cdot e^{(2i\Omega\mu - \nu k^2)(t-t')}] \quad (7)$$

For nonrotating flows, they reduce to the usual (EDQNM-1) form:

$$g_{ij}(t-t') = (\delta_{ij} - \frac{k_i k_j}{k^2}) \cdot e^{-\nu k^2 (t-t')} \quad (8)$$

With the classic EDQNM closure assumptions, eq.(6) takes the final (symbolic) form:

$$< \hat{u}\hat{u}\hat{u} > (t) = \sum \{< \hat{u}\hat{u} >< \hat{u}\hat{u} >\}(t) \times \times \int_{-\infty}^{t} \{g^* \cdot g^* \cdot g^*\}(t-t')dt' \quad (9)$$

where $g^*(t) = g(t).e^{-\eta t}$. η stands for the usual eddy damping term of the basic isotropic EDQNM model. In equation (9) the transient term (first term in eq.(6)) is neglected, and the initial conditions for the triple correlations are taken at $t = -\infty$. The Markovian assumption is also adopted. The effect of rotation on the third-order moments is represented by the triple product of the Green functions in the integral of eq.(9), giving rise to rather sophisticated expressions for the characteristic eddy damping time, compared to those usually considered in the basic EDQNM closure. It is this term which allows initially isotropic turbulence, subjected to solid-body rotation, to develop axisymmetric anisotropy, in accordance with numerical simulations, whereas the initial isotropy would be conserved with the standard EDQNM-1 model.

Equation (4) is solved numerically with an implicit solver for the linear terms and an explicit treatment for the nonlinear terms. The latter requires remeshing at every (nonlinear) time step for flow cases involving axisymmetric strain. The calculations start at $t = 0$ from isotropic initial conditions corresponding to a specified energy spectrum $E_0(k)$. The initial conditions for e and Z are then $e_0 = E_0(k)/4\pi k^2$ and $Z_0 = 0$. For comparison with experiments, the initial energy spectrum is adjusted in such a way that the corresponding values of the initial energy ($q_0^2/2 = \int E_0(k)dk$) and the initial dissipation rate ($\epsilon_0 = 2\nu \int k^2 E_0(k)dk$) coincide with the experimental values.

The calculations start with given values of the strain rate D and the initial rotation rate Ω_0, expressed through the ratio $\omega_0 = \Omega_0/D$. The maximum value of t is $t_{max} = ln(C)/D$, where C is the total contraction of the flow. As in the experiments, C is fixed at a value of 4, yielding for the non-dimensional time Dt a maximum value of $Dt_{max} = ln(4) \approx 1.39$. The physical-space statistics are deduced from the solution of eq.(4) by simple integration in Fourier space.

Direct Numerical Simulation

The Direct Numerical Simulations are made with a pseudo-spectral method in a cubic box of length 2π, using distorted Fourier modes, with periodic boundary conditions in the three directions. The method is described in detail in ref.[6]. The simulations, performed with a resolution of 128^3 mesh points, are made for the following flow cases, consistent with eq.(1):

- isotropic decay,
- solid-body rotation,
- pure axisymmetric strain,
- rotation coupled with axisymmetric strain.

The velocity field is initialized in a preliminary calculation of isotropic decay starting (at $t = -0.5$) from random-phase Fourier modes with a specified energy spectrum of the form:

$$E(k) \sim (\frac{k}{k_m})^n exp\left[-\frac{n}{2}[(\frac{k}{k_m})^2 - 1]\right]. \quad (10)$$

The proportionality factor is such that the total energy is 1. The adjustable constant n lies typically between 2 and 4, and k_m is the wave number for which $E(k)$ is maximum. The values retained in the present calculations are $n = 2$ and $k_m = 8$. Figure 3 shows the initial energy spectrum (at $t = -0.5$, solid line) according to eq.(10), together with the final spectrum obtained at the end of the relaxation period ($t = 0$, symbols).

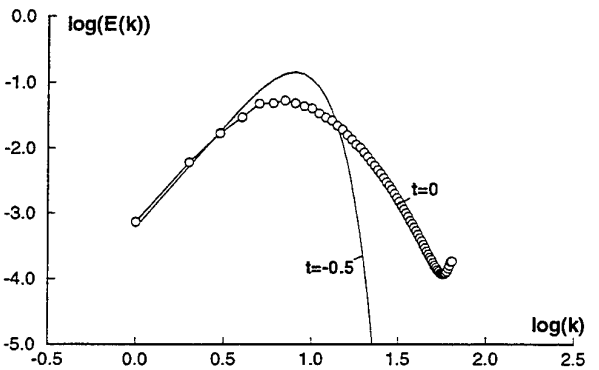


Figure 3: Energy spectra (relaxation period)

The relaxation to turbulence is characterized by the variation of the velocity-gradient skewness factor

$$S_k = \frac{\overline{(\partial u_1/\partial x_1)^3}}{[\overline{(\partial u_1/\partial x_1)^2}]^{3/2}}, \quad (11)$$

considered to be representative for the building-up of the third-order correlations which generate the spectral energy transfer. Once the skewness factor reaches its asymptotic level, the rotation (and/or strain) is imposed (at $t = 0$). The energy has by then dropped from 1 to 0.58, and the microscale Reynolds number Re_λ from 51 to 26. The value of $k_{max}\eta$ during the whole relaxation period remains close to 1, which can be considered an adequate limit concerning space resolution. At the end of the relaxation process, the following values for the various lengthscales are obtained (computational units):

- integral lengthscale $L_f = 0.324$
- dissipation lengthscale $L_\epsilon = (q^2/3)^{3/2}/\epsilon = 0.287$
- Taylor microscale $\lambda = (5\nu q^2/\epsilon)^{1/2} = 0.166$

- Kolmogorov scale $\eta = (\nu^3/\epsilon)^{1/4} = 0.014$,

showing in particular that the largest scales are adequately small (as required), compared to the dimensions of the computational box.

The calculations are performed (as for the EDQNM calculations) between $t = 0$ and $t_{max} = ln(C)/D$. Two values of the ratio $\omega_0 = \Omega_0/D$ are considered for the case of rotation-strain coupling: 1 and 2. The ratio τ_0 between the characteristic linear and nonlinear times at t=0 ($\tau_0 = 2\epsilon_0/Dq_0^2$) takes the values 0.523 and 1.046, which could also be achieved in the experiments (see above). Accordingly, the ratio between the total flow time (t_{max}) and the initial eddy turnover time ($t^* = 2\epsilon_0/q_0^2$) takes the values 0.725 and 1.45, respectively. For the lower value, the linear mechanisms are more significant. The initial Rossby number at $t = 0$ ($Ro_0 = 2\epsilon_0/\Omega_0 q_0^2 = \tau_0/\omega_0$) then varies between 0.25 and 1.

In view of comparing DNS with EDQNM-2 calculations, the latter start with the same energy spectrum $E_0(k)$ as in the DNS (Figure 3), and with isotropic initial conditions corresponding to $e_0(k) = E_0(k)/4\pi k^2$ and $Z_0(k) = 0$.

The physical-space statistics are calculated at selected time steps by space averaging over the computational volume.

Since the level of the initial Reynolds number at $t = 0$ can be easily reproduced in the experiments, comparisons between experimental and numerical results are in principle feasible. It must, however, be noted that rotation is suddenly imposed at $t = 0$ in the calculations (together with the strain), whereas in the experiments the turbulence develops during the initial period ($t < 0$) in the presence of solid-body rotation. This results in different initial states in the experiments, depending on the value of ω_0. Direct comparisons between numerical and experimental results are therefore to be considered with care.

RESULTS AND DISCUSSION

EDQNM-2 Results

The EDQNM-2 results are relative to nominal conditions of the experiments ($Re_\lambda \approx 40$, $\tau_0 \approx 2$), except that the calculations start from isotropic conditions. Like in the experiments, the turbulent energy decay is found to be slightly reduced in the presence of rotation ($\omega_0 = 2$), compared to the non-rotating reference case of pure strain, obviously due to nonlinear effects.

Figure 4 shows the (normalized) anisotropy $A/q^2 = (\overline{u^2} - \overline{v^2})/q^2$ and the corresponding linear pressure-strain correlation Π_A^L normalized by Dq^2. The results are plotted against the non-dimensional time Dt (as in Figs. 1 and 2) for $\omega_0 = 0$ and $\omega_0 = 2$. They show that the level of the rapid pressure-strain correlation is strongly amplified by the rotation, similarly to what Figure 2 shows for RDT (where $\tau_0 = 0$). It can be seen that the strong amplification of Π_A^L remains the dominant feature of rotation effects for this type of flow, irrespective of the value of τ_0. The corresponding reduction of the (negative) anisotropy is similar to that shown in Figure 2 for RDT, but both the amount of anisotropy produced by pure strain and the variation due to the rotation are significantly reduced here, due to the nonlinear damping effects.

Figure 4 shows in addition the results obtained with the standard EDQNM-1 model (solid lines). These clearly show that the neglect of rotation effects in the EDQNM eddy relaxation term leads to rather unrealistic predictions, especially concerning the continuous growth of the rapid pressure-strain correlation.

The EDQNM-2 results also reveal strong rotation effects on the anisotropy of the integral lengthscales L_u and L_v relative to the axial direction (see the following section for more details).

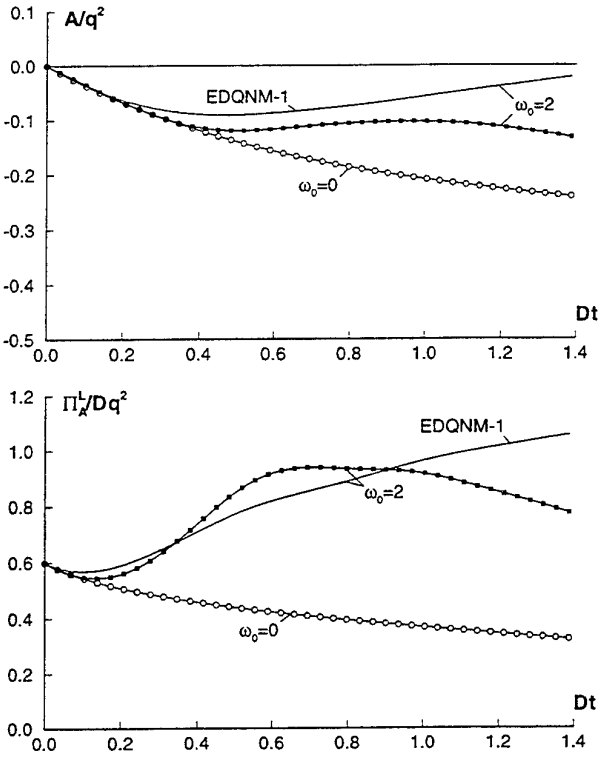


Figure 4: EDQNM-2 results: Anisotropy (upper figure) Pressure-strain correlation (lower figure)

Comparison between EDQNM-2 and DNS

EDQNM and DNS results are first compared for the basic reference case of isotropic decay (Figure 5). Here (and in the following figures) DNS results are represented by symbols, and EDQNM-2 results by solid lines.

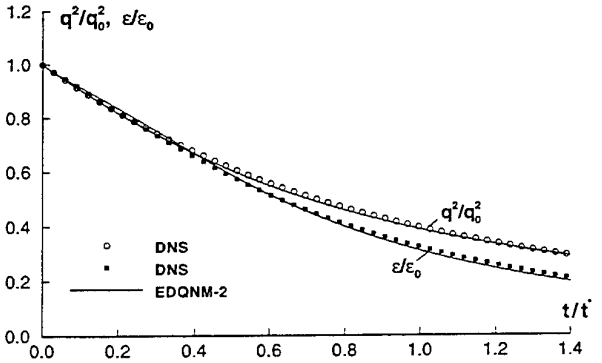


Figure 5: Comparison between EDQNM-2 and DNS: Isotropic decay

The turbulent kinetic energy $q^2/2$ and the dissipation rate ϵ, normalized by their respective initial values ($q_0^2/2 = 0.582$ and $\epsilon_0 = 0.844$), are plotted against the non-dimensional time t/t^*, where t^* is the eddy turnover time at $t = 0$ (here $t^* = 0.689$) The value $t/t^* = 1.4$ corresponds to $\tau_0 \approx 1$. The agreement between the two calculations is seen to be satisfactory. It should be noted that, for this basic reference case, no mesh deformation is required, and

that the EDQNM closure reduces to the basic EDQNM-1 version.

In the following, the comparisons between EDQNM-2 and DNS are made for $\tau_0 = 0.52$, opposing the case of rotation-strain coupling ($\omega_0 = 2$) to the reference case of pure strain ($\omega_0 = 0$). In computational units, the strain and rotation rates are then $D = 2.773$ and $\Omega_0 = 5.545$. (In the following figures, the initial rotation rate Ω_0 is represented by R)

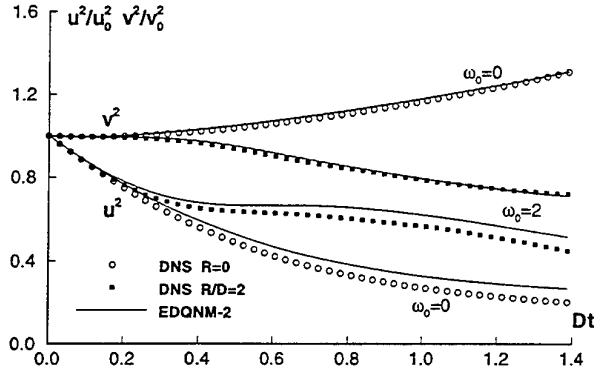


Figure 6: Comparison between EDQNM-2 and DNS: Normal stresses $\overline{u^2}$ and $\overline{v^2}$

Figure 6 shows the variations of the normal stresses $\overline{u^2}$ and $\overline{v^2}$, and Figure 7 that of the kinetic energy, normalized by their respective initial values at t=0. In the case of pure strain, $\overline{u^2}$ is seen to be decreased and $\overline{v^2}$ to be increased, as a consequence of the opposite signs of the corresponding production terms. This leads to increasing negative anisotropy $A = \overline{u^2} - \overline{v^2}$, whereas the turbulent energy varies only moderately. When rotation is added to the strain, $\overline{u^2}$ increases and $\overline{v^2}$ decreases with respect to the pure-strain situation, with the consequence of inhibiting the strain-induced growth of negative anisotropy (as evidenced in Figs. 2, 4 and 8), and accentuating the energy decay. Figures 6 and 7 show satisfactory agreement between EDQNM-2 and DNS results, especially for the variation of the transverse component $\overline{v^2}$.

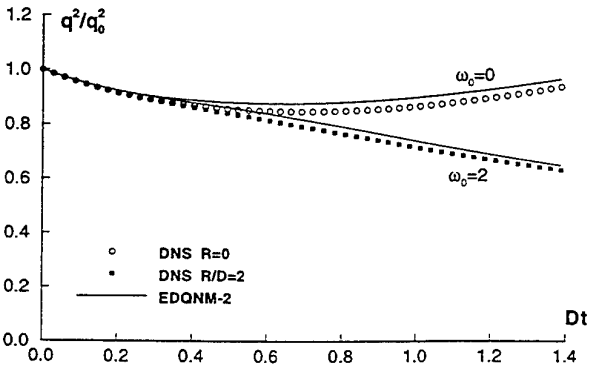


Figure 7: Comparison between EDQNM-2 and DNS: Kinetic energy

The variations of the anisotropy and the corresponding rapid pressure-strain correlations are shown in Figure 8. The strain-induced anisotropization in the pure-strain case, as well as the rotation-induced variation in the case of rotation-strain coupling are seen to be noticeably larger than those shown in Figure 4, due to the lower level of the Reynolds number and to the lower value of τ_0, which reinforces the linear effects (to compare also with Fig. 2).

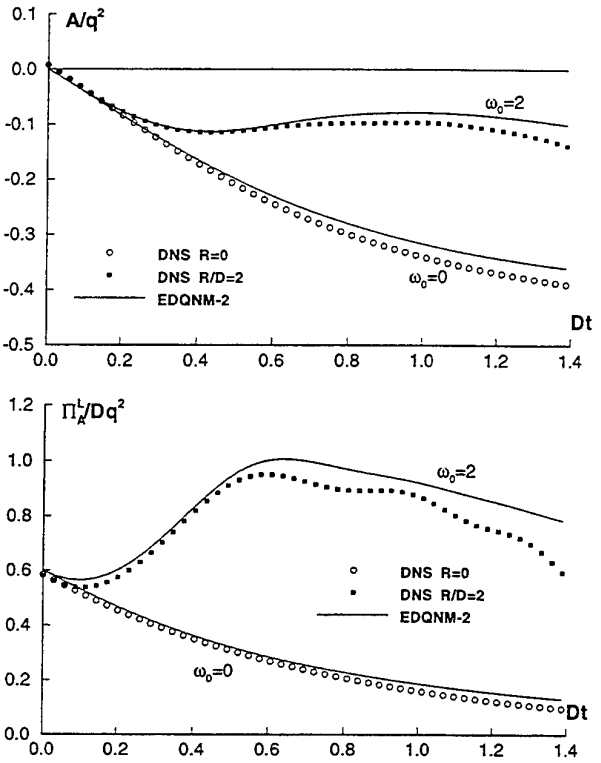


Figure 8: Comparison between EDQNM-2 and DNS: Anisotropy (upper figure) Pressure-strain correlation (lower figure)

From Figure 6 through 8, it can be seen that the DNS results reproduce the EDQNM-2 predictions reasonably well, except for the pressure-strain correlations in the last period of the straining process, where the differences become more significant. This could be a consequence of some non-axisymmetric anisotropy developing in the DNS, but also due to the strong stretching effect of axisymmetric strain.

Figure 9 illustrates the effects of rotation on the equatorial energies E_u and E_v and the corresponding integral lengthscales L_u and L_v, normalized by their respective initial values. These quantities are deduced from the integrals of Φ_{11} and Φ_{22} (or Φ_{33}) over the equatorial plane $k_1 = 0$, respectively:

$$L_u = \frac{E_u}{\overline{u^2}} = \frac{\pi}{\overline{u^2}} \int\int_{k_1=0} \Phi_{11} dk_2 dk_3,$$
$$L_v = \frac{E_v}{\overline{v^2}} = \frac{\pi}{\overline{v^2}} \int\int_{k_1=0} \Phi_{22} dk_2 dk_3 \ . \qquad (12)$$

Axisymmetric strain without rotation produces (essentially through linear mechanisms) a sharp increase of E_v, with a simultaneous decrease of E_u, so that the ratio E_v/E_u, starting from the isotropic value 0.5, becomes much larger than 1 at the end of the straining process. In the presence of rotation, this tendency is further accentuated, essentially through nonlinear effects on E_v. It is interesting to note that within the EDQNM-1 approximation rotation would have no effect on E_v.

Similar trends are observed for the lengthscales, according to eq.(12). Figure 9 shows in effect that there is a strong increase in L_v in the case of axisymmetric strain

and rotation-strain coupling, whereas L_u is much less affected and remains approximately at its initial value. It is to note that the increasing effect of rotation on L_v cumulates the direct effect on E_v with the effect of decreasing $\overline{v^2}$.

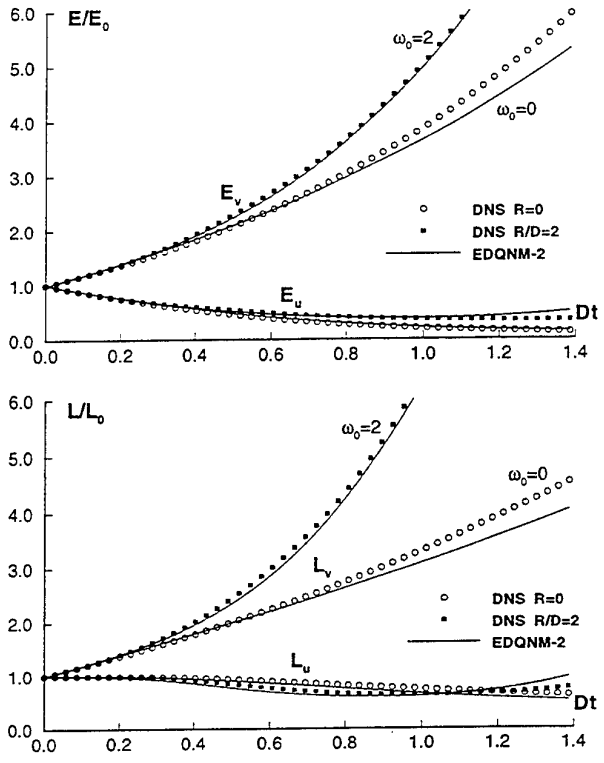


Figure 9: Comparison between EDQNM-2 and DNS:
Equatorial energies (upper figure)
Integral lengthscales (lower figure)

Figure 10 shows DNS plots of axial vorticity ω_x in the y, z plane normal to the rotation axis, for the case of rotation-strain coupling with $\omega_0 = 2$. Solid lines are for positive and dashed lines for negative vorticity. The distance between two successive iso-lines corresponds to 0.4 times the rms value (σ_ω) of ω_x. The level of σ_ω is 3.6 times higher in Figure 10 than for the case of pure rotation. As can be seen from Figure 10, the combined action of strain and rotation generates isolated vortical structures of high intensity, in contrast to the pure rotation case where the vortical structures are much less ordered and appear more chaotic. Figure 10 thus confirms the trend towards two-dimensional flow, suggested by the particular behavior of the equatorial energies and the lengthscales shown in Figure. 9.

CONCLUSION

The combined effects of rotation and strain on axisymmetric homogeneous turbulence are analysed in the framework of a nonlinear spectral approach based on a refined EDQNM closure model. The new model takes rotational mean velocity gradients into account in the spectral equations for the third-order moments. The results show substantial improvements in the prediction of the rapid pressure term, which is one of the crucial problems in the field of turbulence modeling based on single-point closure. The inhibition, by rotation, of the strain-induced anisotropization of the Reynolds stresses is well predicted by the model. Future effort in this field should be devoted to generalizing the EDQNM-2 model for inclusion of the irrotational

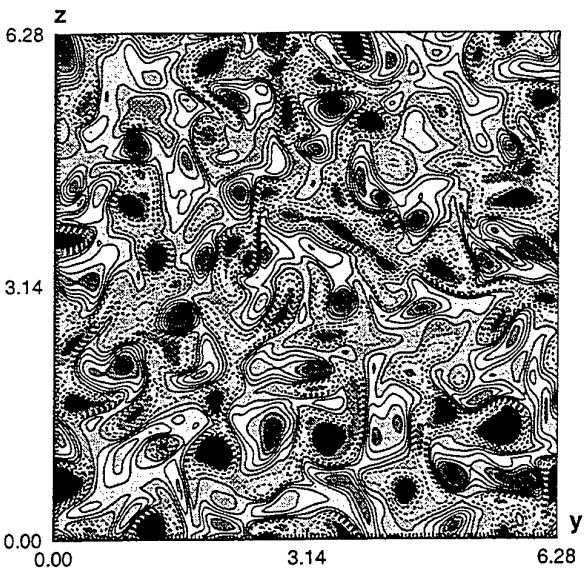


Figure 10: DNS: Iso-vorticity plots, $\omega_0 = 2$

velocity gradients in the equation for the third-order moments.

The EDQNM results compare favorably with DNS calculations, which confirm the most relevant rotation effects predicted within the refined two-point closure approach. In particular, the tendency to two-dimensionality as evidenced by the behavior of the integral lenthscales is supported by vorticity plots of the DNS results.

Both predictive methods appear to be useful tools for analysing and enlightening the linear and nonlinear mechanisms by which rotation acts on the turbulence. They are thus valuable guides for finding new modelling concepts in physical space for turbulent flows subjected to strong rotation effects. In spite of its intrinsic limitation to low Reynolds number flows, DNS appears as a useful complementary tool for assessing modelling concepts for refined two-point closure approaches of the EDQNM-2 type.

REFERENCES

[1] Leuchter, O., Dupeuble, A., Rotating homogeneous turbulence subjected to axisymmetric contraction. *Ninth Symp. on Turb. Shear Flows*, Kyoto, August 1993

[2] Leuchter, O., Bertoglio, J.P., Non-linear spectral approach to rotating turbulence in the presence of strain. *Tenth Symp. on Turb. Shear Flows*, Penn. State Univ., August 1995

[3] Cambon, C., Teissèdre, C., Jeandel, D., Étude d'effets couplés de déformation et de rotation sur une turbulence homogène, *J. Méc. Théor. Appl.* 4, No.5, pp.629-657, 1985

[4] Cambon, C., Jacquin, L., Spectral approach to non-isotropic turbulence subjected to rotation, *J. Fluid Mech.*, **202**, pp. 295-317, 1989

[5] Leuchter, O., Cambon, C., Spectral analysis of rotation effects on axisymmetrically strained turbulence with an improved EDQNM model, *Sixth Europ. Turb. Conf.*, Lausanne, 1996 (TP ONERA 1996-96)

[6] Dang Tran K., Direct Numerical Simulation of homogeneous strained turbulence, *VKI Lecture Series 1986-5 on "Computational Fluid Dynamics"*, Rhode-St-Genèse, March 1986

EXPERIMENTS FOR THE EFFECTS OF CURVATURE AND PRESSURE GRADIENT ON THE TURBULENT WAKE OF A FLAT PLATE

A.R. Starke, R.A.W.M. Henkes, M.J. Tummers
Faculty of Aerospace Engineering
Delft University of Technology
Kluyverweg 1, 2629 HS Delft
The Netherlands

ABSTRACT

In an earlier study (Tummers, 1995) experimental data were presented for the turbulent near wake of a flat plate subjected to an adverse pressure gradient. This paper presents new data on the simultaneous effects of curvature and adverse pressure gradient. The results are compared with new data for the wake under zero pressure gradient. The measurements were performed with a three-component laser-Doppler velocimeter, and include the mean velocity, Reynolds stresses and triple velocity correlations. Temporal correlation functions of the streamwise velocity component were measured to determine the dissipation length scales. These data can be used as a testcase for turbulence models.

INTRODUCTION

The research of turbulent wakes is motivated by industrial needs for a better description of the flow around airfoils in high-lift conditions. In that situation the strong wake behind the wing interacts with the flow over the flaps. The prediction of these flows by turbulence models is complicated by the combined effects of pressure gradient and curvature. The development of turbulence models requires reliable experimental data for the mean velocities and turbulence statistics obtained in basic configurations.

It is known that an adverse pressure gradient results in a larger spreading rate of the wake and in larger Reynolds stresses. Curvature affects the flow through the combination of the direction of the curvature and the mean-velocity gradient. When the mean velocity increases with increasing distance from the centre of the local curvature radius the flow is stabilized, which will result in a decrease of the spreading of the wake and a lower production of turbulent kinetic energy compared to the part of the wake where the velocity decreases with increasing distance from the centre of the curvature.

Experimental studies for the effects of curvature on turbulent wakes are reported by, for example, Hah & Lakshminarayana (1982), Nakayama (1987) and Weygandt & Mehta (1995). Measurements were taken in the wakes of various bodies in different experimental set-ups using hot-wire probes. All these studies confirm that even a mild curvature has a significant effect on the mean velocities and the turbulence statistics in the wake. Since the development of advanced turbulence models requires accurate experimental data to verify their performance, it was decided to use an LDA system, which is a non-intrusive method, for the acquisition of a reliable data-set on the effects of curvature and pressure gradient on the turbulent wake of a flat plate. The main objective of the present study is to obtain accurate initial conditions that are required for numerical methods. These data will be used to investigate the performance of advanced turbulence models in wakes that are subjected to curvature and pressure gradients.

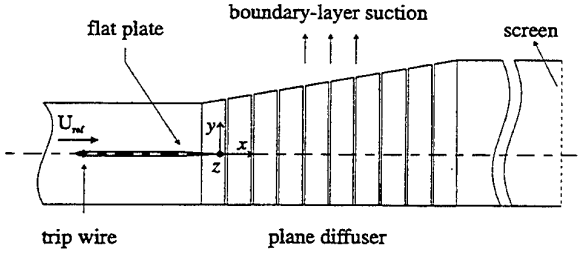


Figure 1: The flow configuration.

EXPERIMENTAL SET-UP

Test configuration

The measurements were performed in the turbulent wake of a flat plate, which has a 600 *mm* chord and a thickness of 18 *mm*. The plate has an elliptic nose and the last 110 *mm* is tapered to form a sharp trailing edge of 0.2 *mm*. The boundary layers on both sides of the plate were tripped with wires at 6% chord from the leading edge. The plate was positioned at zero angle of attack in the test section of an open-return-type wind tunnel, as shown in Figure 1. The test section was followed by a channel with adjustable side walls. A reference pressure p_{ref}, defined as the dif-

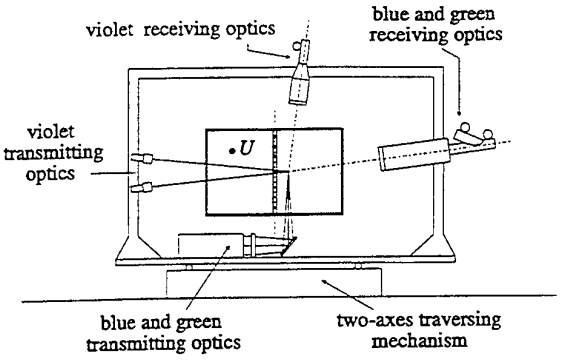


Figure 2: The experimental set-up.

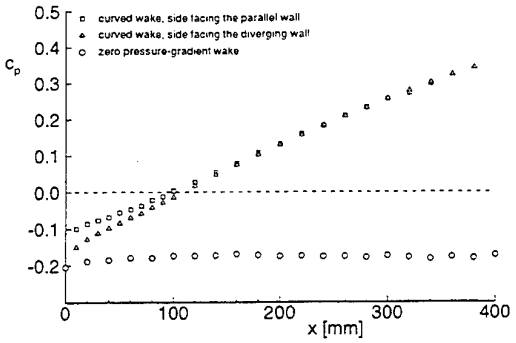


Figure 3: The static pressure distribution.

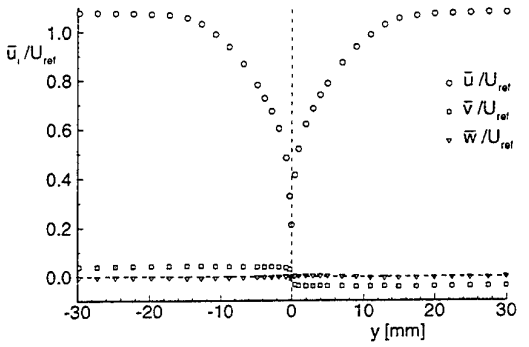


Figure 4: The mean velocity components at $x = 2.5\,mm$.

ference between the static pressure in the settling chamber and in the test section, together with the air density and the contraction ratio of the wind tunnel, were used to determine a reference velocity U_{ref}. All measured data were made dimensionless using this velocity. The wind tunnel was operated at a velocity of approximately 10 m/s, corresponding to a chord-Reynolds number of 4×10^5.

The experiments were performed in two different configurations. First, a zero pressure-gradient wake is investigated. Cross-stream traverses are performed at twelve downstream stations ranging from $x = 0\ mm$ to $x = 420\ mm$. At these stations mean velocities and turbulence statistics are measured. Furthermore, a centreline traverse is performed in this configuration. Secondly, a lateral and an adverse pressure gradient are introduced by adjusting one of the side walls. This results in a wake that initially curves towards the diverging wall. In this configuration ten cross-stream traverses are performed between $x = 0\ mm$ and $x = 420\ mm$.

Instrumentation

The flow field was measured using a three-component, dual-beam LDA system, which is shown in Figure 2. The green and the blue colours of a 5 Watt Argon-ion laser were used to measure the streamwise and the lateral components of the velocity vector simultaneously, while the third velocity component was measured independently using the violet colour of the laser. To detect possible instantaneous flow reversal, one beam of each colour was led through a Bragg cell causing a 40 MHz frequency shift. To increase the spatial resolution, the receiving directions were set almost perpendicular to the transmitting optical axes. Small pinholes placed in front of the photomultipliers reduced the effective length of the measurement volumes to 0.2 mm. The width of the measurement volumes was 0.12 mm. The output signals of the photomultipliers were electronically down-mixed and then processed by Burst Spectrum Analyzers. In addition the pressure field in the test section was measured with a static pressure probe.

EXPERIMENTAL RESULTS

Pressure distribution

Pressure measurements were performed in the undisturbed flow outside the wake. The static pressure coefficients c_p, which is defined with respect to p_{ref} and $\frac{1}{2}\rho U_{ref}^2$, are given in Figure 3. It can be seen that the static pressure remains constant in downstream direction, except for a short region near the trailing edge where a small rise in the pressure can be observed. The curved wake has a clear normal pressure gradient over the initial part of the wake. This pressure gradient balances the centrifugal forces which arise due to the curvature of the mean stream lines. In streamwise direction the curved wake encounters an almost constant adverse pressure gradient.

Mean flow characteristics

Zero pressure-gradient wake.

Figure 4 shows the components of the mean velocity vector at $x = 2.5\ mm$. Both the streamwise and the lateral velocity component are seen to be distributed symmetrically around the x-axis. At all measured stations the measured spanwise velocity ranged between $\overline{w}/U_{ref} = -0.004 \pm 0.006$, which indicates that the flow is almost two-dimensional.

Figure 5 shows the development of the mean streamwise velocity in downstream direction. The boundary layer at the trailing edge has a shape factor $H = 1.55$, which is slightly higher than the value $H = 1.4$ that is normally found for a turbulent boundary layer in a zero pressure gradient. The difference is caused by the fact that the boundary layer is subjected to a mild adverse pressure gradient induced by the tapered part of the plate. However, the static pressure remains practically constant along the edge of the wake, as was shown in Figure 3. The initial stations behind the trailing edge of the plate show a rapid destruction of the inner layers of the wall-bounded flow at the plate: the sharp gradient of the mean velocity can be seen to develop into the more wake-like profile within approximately 20 mm length downstream.

Figure 6 presents the development of the displacement

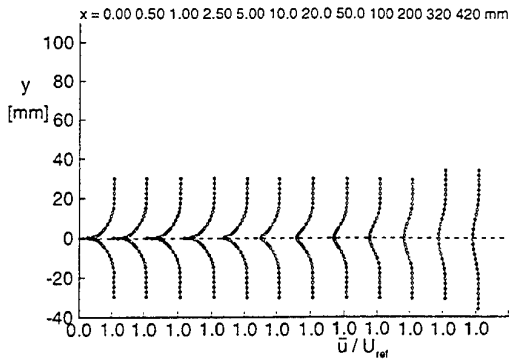


Figure 5: The mean streamwise velocity in the zero pressure-gradient wake.

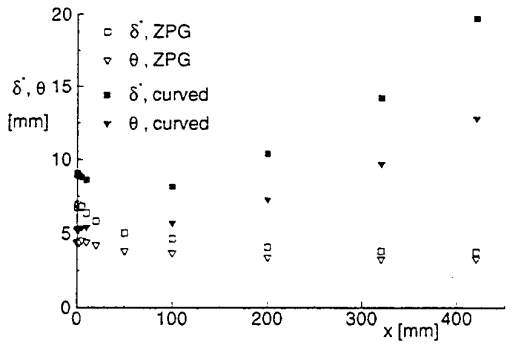


Figure 6: The displacement thickness and the momentum-loss thickness.

thickness and the momentum-loss thickness, defined by

$$\delta^* = \int_{-\infty}^{\infty} \left(1 - \frac{\overline{u}}{U_\infty}\right) dy, \tag{1}$$

$$\theta = \int_{-\infty}^{\infty} \frac{\overline{u}}{U_\infty} \left(1 - \frac{\overline{u}}{U_\infty}\right) dy. \tag{2}$$

Although the static pressure along the edge of the wake is practically constant, the momentum-loss thickness shows a clear change in downstream direction. The momentum-loss thickness decreases from $\theta = 4.4\ mm$ at the trailing edge to a constant value of $\theta = 3.3\ mm$ far downstream. A varying momentum-loss thickness in a zero pressure-gradient wake is also reported by Ramaprian et al. (1982). Their results indicate a 7% decrease in the momentum-loss thickness in the near wake. They hypothesized that this was due to the separated flow behind the relatively thick (1 mm) trailing edge. Hayakawa & Iida (1992) found a 10% variation in the momentum-loss thickness behind the trailing edge. This was partly explained by the inspection of the momentum-integral equation which was extended with a term for the mean streamwise velocity fluctuations. The variation in the momentum-loss thickness was coupled to the measured variation in the mean streamwise velocity fluctuations. However, this does not explain the substantial decrease of θ in the present experiment. Also the relatively thin trailing edge is presumed to have negligible effect on the momentum-loss thickness. In our opinion the change of θ in the near wake is caused by the tapering of the trailing edge of the plate. The curvature of the stream lines that leave the tapered trailing edge into the symmetrical wake corresponds to a normal pressure gradient within the wake near the trailing edge of the plate. From the local balance between centrifugal forces and pressure forces it can be concluded that the normal pressure increases going from the outer edge of the beginning of the wake towards the trailing-edge position. A local streamwise favourable pressure gradient is therefore introduced at the start of the wake, since the static pressure will become constant throughout the wake further downstream. This local favourable pressure gradient results in an additional acceleration of the mean flow near the centreline and a decrease of the momentum-loss thickness. As a consequence it is not possible to apply the thin shear-layer approximation to the present flow, since this would result in a constant momentum-loss thickness as prescribed by the initial conditions.

Figure 7 shows the centreline velocity expressed in wall-coordinates, defined as

$$x^+ = \frac{u_\tau x}{\nu}, \qquad u^+ = \frac{\overline{u}}{u_\tau}. \tag{3}$$

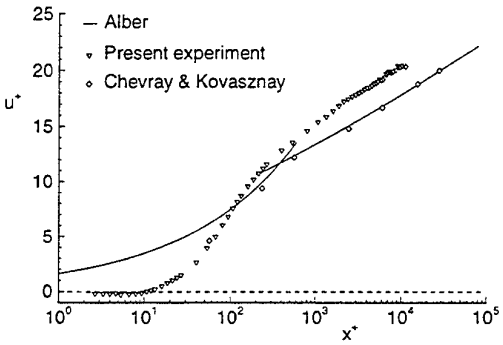


Figure 7: The development of the centreline velocity.

The friction velocity, u_τ, has been evaluated from the mean-velocity profile at the trailing edge using a Clauser chart. Directly downstream of the trailing edge there is a 0.4 mm long backflow region, caused by the finite thickness of the plate. Further downstream the centreline velocity grows logarithmically. The additional acceleration of the flow due to the tapered trailing edge causes the increase of the centreline velocity in comparison to the analytical solution of Alber (1980) for the development of a zero pressure-gradient wake behind a flat plate. The figure also shows the experimental data by Chevray & Kovasznay (1969), who used an extremely thin plate with a trailing edge angle of less than 0.07°, compared to 4.64° in the present study.

The spreading rate is one of the main parameters in wakes. In a zero pressure-gradient wake the velocity scale, u_0, and the length scale, l_0, are known to grow with streamwise distance as $x^{-1/2}$ and $x^{+1/2}$, respectively. These scales are usually defined as the defect velocity at the centreline and the y-coordinate at which the velocity defect reaches half its value at the centreline. This leads to a constant spreading rate in the far wake where the velocity defect is small compared to the free-stream velocity. The spreading rate defined as

$$S = \frac{1}{2} \frac{U_\infty}{u_o} \frac{dl_0}{dx} \tag{4}$$

is plotted in Figure 8. The present experiment does not extend far enough downstream to reach the self-similar far-wake conditions. Therefore, no asymptotic value for the spreading rate can be deduced. However, the spreading rate at the last measured station equals $S = 0.092$, which is roughly in agreement with the value $S = 0.087$ that is

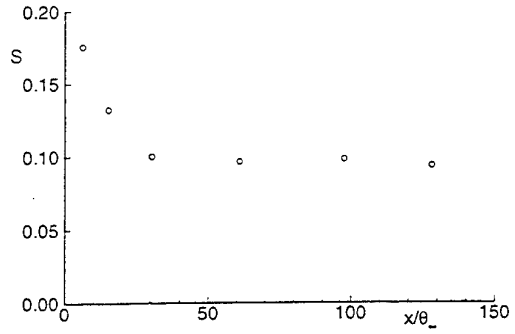


Figure 8: The spreading rate for the zero pressure-gradient wake.

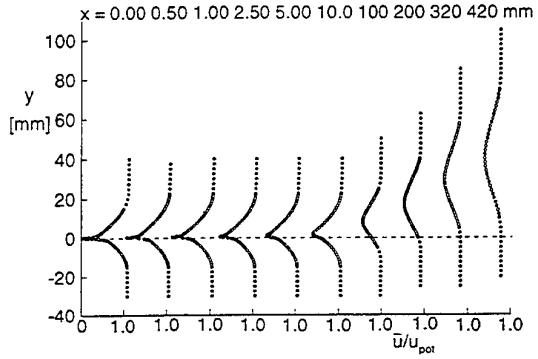


Figure 9: The mean streamwise velocity in the curved wake.

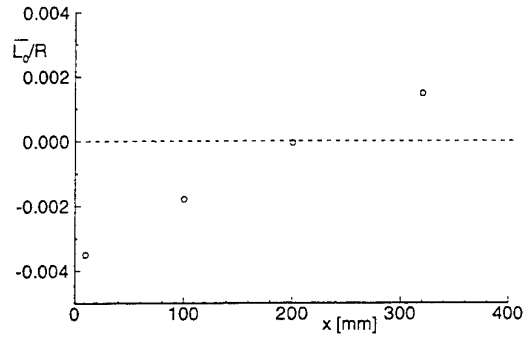


Figure 10: The curvature parameter.

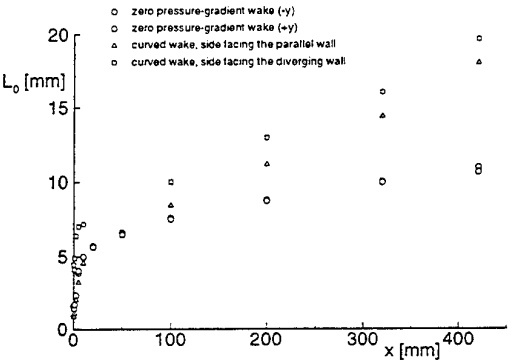


Figure 11: The development of the half width of the wake.

reported by Wygnanksi (1986) for the far wake of a flat plate with a tapered trailing edge.

Curved wake.

The components of the mean velocities and the turbulence quantities depend on the orientation of the coordinate axes. A curvilinear $s-n$ coordinate system is chosen in the curved flow. Here, s is defined as the streamwise distance from the trailing edge of the plate on the line that connects the maxima in the velocity defect of each downstream station. The n-coordinate is measured perpendicular to this reference line. All velocities in a traverse are rotated to this direction. Furthermore, the mean-velocity components are scaled with the local potential flow velocity, rather than with the local free-stream velocity, since in a curved wake the free-stream velocity differs on both sides of the wake. The potential flow velocity varies approximately linear across the wake:

$$u_{pot} = u_{p_0}\left(1 - \frac{n}{R}\right). \tag{5}$$

Here, u_{p_0} is the interpolated value of the potential flow at the centreline of the wake. Note that this scaling also implies a redefinition of the displacement thickness and the momentum-loss thickness for the curved wake: the free-stream velocity U_∞ in the definition of eq. (1) and eq. (2) is now replaced by the interpolated potential flow velocity u_{pot}.

The local radius of curvature, $R(x)$, is determined from the balance between the centrifugal and the pressure forces acting on the wake:

$$\frac{\partial \overline{p}}{\partial n} = \frac{\rho \overline{u}^2}{R}. \tag{6}$$

This formulation is in agreement with the conservation of y-momentum as described by the Navier-Stokes equations under the thin shear-layer approximation. Figure 10 shows the curvature parameter which is defined as the ratio between the average half width of the wake and the local radius of curvature: $\overline{l_0}/R(x)$. Negative values indicate that the wake curves towards the diverging test-section wall. At $x = 200\ mm$ an inflection point occurs when the curvature parameter changes sign. From here on the side of the wake facing the parallel test-section wall is destabilized by the curvature, whereas the side of the wake facing the diverging test-section wall is stabilized. The maximum absolute value of the curvature parameter equals 0.0035 and occurs near the trailing edge of the plate. This value is quite small compared to other studies, where maximum values in the range $0.014 < \overline{l_0}/R(x) < 0.056$ are reported.

The development of the mean streamwise velocity component for the curved wake is shown in Figure 9. Note that the y-coordinate is plotted on the vertical axis instead of the s-coordinate. This was done to show the transverse shift of the wake towards the diverging test-section wall. The velocity profiles are asymmetrical at the trailing edge. This is caused by the adverse pressure gradient which is induced in the boundary layer at only one side of the plate, namely the one facing the diverging wall. As shown in Figure 1 the divergence of this wall starts at an upstream position of the trailing edge of the plate. As a result the half width of the wake is larger at the side of the wake facing the diverging wall. Further downstream an increased spreading of the wake at the side which is destabilized by the curvature, as reported in the literature, is hardly noticeable in the present experiments, owing to the relatively large radius of curvature.

Figure 11 shows the half width in both the zero pressure-

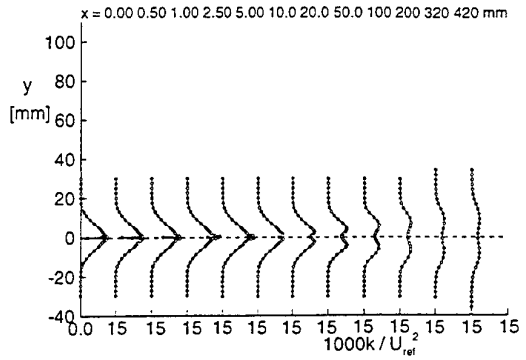


Figure 12: The turbulent kinetic energy in the zero pressure-gradient wake.

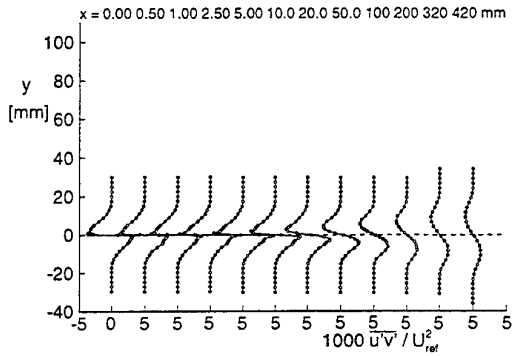


Figure 13: The Reynolds shear stress in the zero pressure-gradient wake.

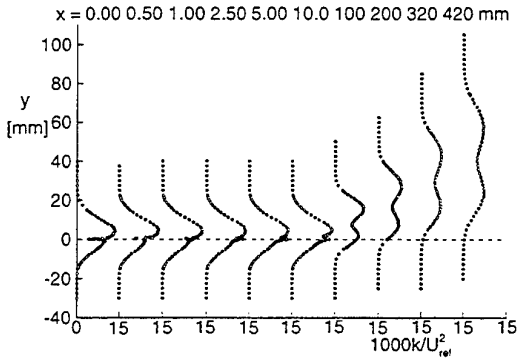


Figure 14: The turbulent kinetic energy in the curved wake.

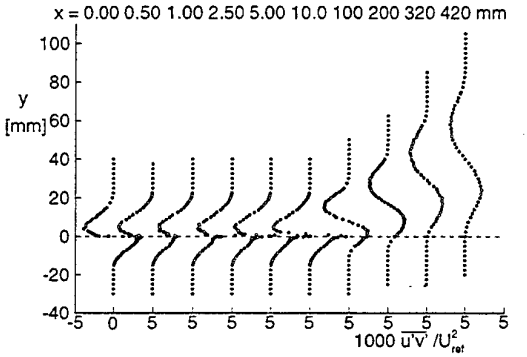


Figure 15: The Reynolds shear stress in the curved wake.

gradient wake and the curved wake. The adverse pressure gradient that is encountered by the curved wake leads to a larger spreading of the wake compared to the zero pressure-gradient wake.

The displacement thickness and the momentum-loss thickness are shown in Figure 6, for both wakes. The displacement thickness first decreases behind the flat plate and starts to increase further downstream. The momentum-loss thickness is observed to grow steadily in downstream direction in the curved wake. The decrease in the momentum-loss thickness in the zero pressure-gradient wake is not observed in the curved wake. However, close to the trailing edge the momentum-loss thickness appears to grow slower than further downstream, which might be caused by the effect of the tapered trailing edge on the internal pressure field.

Turbulence quantities

Zero pressure-gradient wake.

Figure 12 shows the development of the turbulent kinetic energy in the zero pressure-gradient wake. Initially a maximum in the turbulent kinetic energy occurs near the wall. Further downstream this maximum decreases monotonically, while it moves away from the centreline of the wake. A similar behaviour is found for the Reynolds shear stress, which is shown in Figure 13.

Curved wake.

Figures 14 and 15 show the turbulent kinetic energy and the Reynolds shear stress in the curved wake. The adverse pressure gradient on the side of the wake facing the diverging wall of the test section introduces asymmetric initial profiles. Both quantities can also be seen to develop asymmetrically. The level of the turbulent kinetic energy and the Reynolds shear stress is higher than in the zero pressure-gradient wake.

Figure 16 shows the maximum values of the turbulent kinetic energy for the zero pressure-gradient wake and for both sides of the curved wake. Initially the maximum in the turbulent kinetic energy decays faster at the side of the wake facing the parallel wall than at the side of the wake facing the diverging wall. However, after the inflection point in the radius of curvature the maximum in the turbulent kinetic energy increases at the side of the wake facing the parallel wall while it decreases on the other side.

Integral time scale

Temporal autocorrelation functions were determined from the randomly sampled LDA-data by means of the slotting technique (Mayo, 1974). Integration of these functions yields the integral time scale T, which gives information on the large-scale structures in the flow field. Application of Taylor's hypothesis on frozen turbulence then gives the integral length scale, L_T as

$$L_T = \overline{u} \times T. \tag{7}$$

An estimate for the dissipation rate of the turbulent kinetic energy from the experimental data can now be obtained from:

$$\epsilon \propto \frac{k^{3/2}}{L_T}. \tag{8}$$

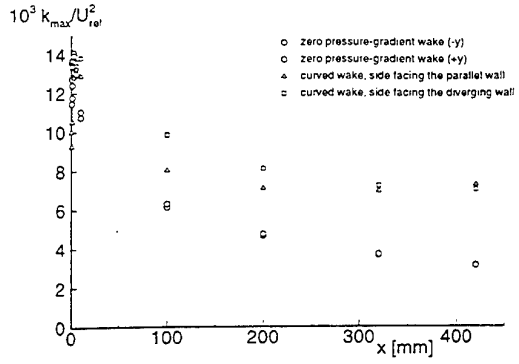


Figure 16: The maximum values of the turbulent kinetic energy in both wakes.

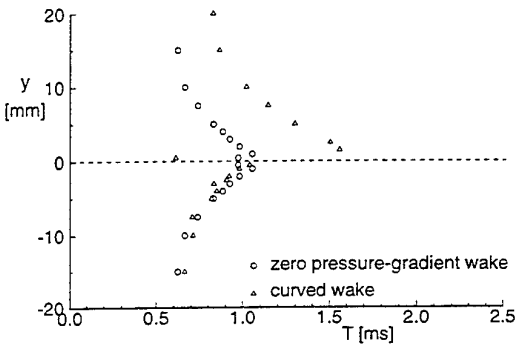


Figure 17: The integral time scale at $x = 0\ mm$.

This relation is based on the balance between production and dissipation of turbulent kinetic energy, using dimensional analysis. Figure 17 shows the integral time scale at the trailing edge of the plate for both configurations. In the zero pressure-gradient wake the integral time scale has been measured at one side of the wake only. The resulting time scales are mirrored in the x-axis for easier comparison with the curved wake. Both wakes have almost identical time scales at the side of the wake facing the parallel wall. A maximum occurs near the wall and the integral time scale slowly decreases outwards. At the side of the curved wake facing the diverging wall the integral time scale is larger than on the opposite side of the wake. Although not shown in the figure, it was found that the integral time scale rises steeply near the edge of the wake, since the autocorrelation function of the undisturbed flow goes to one for all time lags. This results in an unbounded value for the integral time scale.

Figure 18 shows the dissipation rate profile that has been evaluated from the experiments. A sharp peak is observed near $y = 0$, which falls to zero towards the edge of the wake. The dissipation rate at the side of the curved wake facing the diverging wall is clearly higher than on the opposite side. This is caused by the adverse pressure gradient at this side of the plate which enhances the production of turbulent kinetic energy. The assumed balance between production and dissipation will then also lead to a higher dissipation rate.

CONCLUSIONS

Experiments were presented for the combined effect of curvature and streamwise pressure gradient on the turbulent wake of a flat plate. The configuration was designed

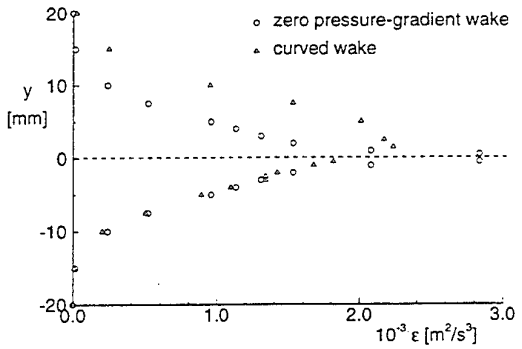


Figure 18: The dissipation rate of the turbulent kinetic energy at $x = 0\ mm$.

such that the boundary layers on both sides of the plate are asymmetric when reaching the trailing edge. In the initial part of the wake a weak curvature is present, whereas further downstream a mild adverse pressure gradient has been established.

The effect of curvature on the mean velocity components and the turbulence in the wake is primarily visible in a shift of the wake centre line to the diverging tunnel wall and in the asymmetric development of the maximum of the turbulent kinetic energy. Compared to the presented wake experiments for a zero pressure gradient, the presence of an adverse pressure gradient causes a higher spreading rate and higher Reynolds stresses on both sides of the wake. Computations with turbulence models for this new experimental test case are underway.

REFERENCES

Alber, I.E., 1980, "Turbulent wake of a thin, flat plate." *AIAA Journal*, vol. 18, no. 9, pp. 1044-1051.

Chevray, R. and Kovasznay, L.S.G., 1969, "Turbulence measurements in the wake of a thin flat plate." *AIAA Journal*, vol. 7, no. 8, pp. 1641-1643.

Hah, C. and Lakshminarayana, B. 1982, "Measurement and prediction of mean velocity and turbulence structure in the near wake of an airfoil." *J. Fluid Mech.*, 115, pp. 251-282.

Hayakawa, M. and Iida, S., 1992, "Behaviour of turbulence in the near wake of a thin flat plate at low Reynolds numbers." *Phys. Fluids A*, vol. 4, no. 10, pp. 2282-2291.

Mayo, W.T., 1974, "A discussion of limitations and extensions of power spectrum estimation with burst counter LDV systems." *Proc. Second Int. Workshop on Laser Velocimetry (Purdue University)*, pp. 90-104.

Nakayama, A., 1987, "Curvature and pressure-gradient effects on a small-defect wake." *J. Fluid Mech.*, 175, pp. 215-246.

Ramaprian, B.R., Patel, V.C. and Sastry, M.S., 1982, "The symmetric turbulent wake of a flat plate." *AIAA Journal*, vol. 20, no. 9, pp. 1228-1235.

Tummers, M.J., Passchier, D.M. and Henkes, R.A.W.M., 1995, "Experimental investigation of the wake of a flat plate in an adverse pressure gradient and comparison with calculations." *10th Symposium on Turbulent Shear Flows*, vol. 1, pp. 6.7-12.

Weygandt, J.H. and Mehta, R.D., 1995, "Three-dimensional structure of straight and curved plane wakes." *J. Fluid Mech.*, 282, pp. 279-311.

Wynanski, I., Champagne, F., Marasli, B., 1986, "On the large scale structures in two-dimensional, small-deficit, turbulent wakes." *J. Fluid Mech.*, 168, pp. 31-71.

CALCULATIONS OF THE FLOW THROUGH A U-BEND

M.M. Gibson

Thermofluids Section
Mechanical Engineering Department
Imperial College, London SW7 2BX, UK

R.D. Harper

Century Dynamics
Hurst Road, Horsham
West Sussex, RH12 2DT, UK

ABSTRACT

The U-bend in question represents on a greatly magnified scale the interior cooling duct of a gas-turbine blade. The paper reports the results of two-dimensional calculations based on the q-ζ two-equation low-Reynolds-number turbulence closure. These results are compared with published experimental data taken from smooth-wall and rib-roughened ducts, and with the results obtained using a conventional k-ε model with wall functions.

INTRODUCTION

The k-ε turbulence model owes its pre-eminent position in computational fluid dynamics to the discovery by Spalding (1969) and his contemporaries that there was no need to modify the length-scale equation (in this case the ε-equation) in order to handle wall flows, provided always that the problem of resolving the low-Reynolds-number turbulence close to the wall was avoided by the use of 'wall functions'. For this reason the promising k-W and k-kL models of Gibson and Spalding (1972) and Ng and Spalding (1972) were discarded in favour of a model which not only employed a variable which appeared explicitly in the k-equation, had a recognisable physical attribute (energy dissipation), but was perceived at the time to be computationally more convenient.

Although the high-Reynolds-number k-ε model has given good service over the years, it is now difficult to justify the continued use of wall functions, particularly in applications where the existence of universal wall laws is doubtful, and as arguments for computational economy become weaker. Wall functions endure mainly because the problem of integrating the turbulence equations to the wall has yet to be satisfactorily solved. The choice of ε as a variable adds to the difficulties: it has no natural boundary condition at the wall, so that one must be derived from assumed limiting behaviour of the turbulence fluctuations as $y \rightarrow 0$. And if the assumed wall value ε_w is subtracted to form a new variable, $\tilde{\varepsilon} = \varepsilon - \varepsilon_w$, which is zero at the wall, this quantity is found to vary as y^2 as $y \rightarrow 0$, thus necessitating the use of an excessively fine grid for computations through the sublayers, as well as the need to calculate spatial derivatives of the turbulence energy, k. Other 'wall' terms are also needed, whose exact form is uncertain, and which destroy the attractive simplicity of the high-Reynolds-number model, which is one of its chief merits. There is, in short, no advantage in persisting with the ε-equation except the many years of experience built into it, much of which may still be employed in the formulation of more useful equations.

Alternatives include equations for the turbulent vorticity, $\omega \equiv \varepsilon/k$, and its reciprocal, the time scale $\tau \equiv k/\varepsilon$. And there are other variables fitting the general form of $k^m \varepsilon^n$. Spalding (1991) has pointed out that the question of which of these is best has never been seriously investigated. We have found that there is much to be said for the use of the new variable, $\zeta \equiv \tilde{\varepsilon}/2\sqrt{k}$, especially when the k-equation is replaced by one for $q \equiv \sqrt{k}$. ζ is then identified as the dissipation rate of q. Both variables are zero at the wall and are well behaved in that they vary linearly with distance from it for small y. ζ lies between ω and ε in the progression $\omega \equiv \tilde{\varepsilon}/k$, $\zeta \equiv \tilde{\varepsilon}/2\sqrt{k}$ and $\tilde{\varepsilon}$, meeting the empirical condition that for simplicity in the high-Reynolds-number form the exponent of $\tilde{\varepsilon}$ in the general variable above should be unity. $\zeta \propto \sqrt{(\omega\varepsilon)}$ apparently acquires the merits of the earlier models without, it seems, many of the defects.

Gibson and Dafa'Alla (1995) used DNS of channel flow and boundary layers to validate the model, which was then applied to the calculation of the flow over two-dimensional fences and ribs by Gibson and Harper (1995). In a further development, Gibson and Harper (1997) used the corresponding low-Reynolds-number q-ϑ and ζ-ϑ equations in a four-equation closure to calculate the heat transfer from an impinging jet. Finally, Dafa'Alla et al (1996, 1997) have applied the model to boundary layers with periodic variation of free-stream velocity.

THE MATHEMATICAL MODEL

We start from the turbulence constitutive equation:

$$-\overline{u_i u_j} = \nu_t\left(\frac{\partial U_i}{\partial x_j}+\frac{\partial U_j}{\partial x_j}\right)-\frac{2}{3}\delta_{ij}k \qquad (1)$$

where ν_t is the kinematic eddy viscosity:

$$\nu_t \equiv C_\mu f_\mu q L \qquad (2)$$

In this definition q is the square root of the turbulence kinetic energy ($q \equiv \sqrt{k}$), L is the length scale, C_μ is a constant and f_μ is a low-Reynolds-number damping function.

An equation for q is derived in the usual way from the Navier-Stokes equations as follows:

$$U_i\frac{\partial q}{\partial x_i} = \frac{\partial}{\partial x_j}\left\{\left(\nu+\frac{\nu_t}{\sigma_q}\right)\frac{\partial q}{\partial x_j}\right\}+Q-\zeta \qquad (3)$$

where Q is the rate of production of q:

$$Q \equiv \frac{-\overline{u_i u_j}}{2q}\frac{\partial U_j}{\partial x_j} \qquad (4)$$

and ζ is the rate of destruction. An equation for ζ is used to evaluate the length scale from:

$$L \equiv \frac{q^2}{2\zeta} \qquad (5)$$

where the factor of two, which was originally inserted for imagined convenience, has now become a bit of a nuisance. Recognising that the turbulence time scale is q/ζ, it is easy to make up a ζ-equation on the lines of the familiar equation for ε. The result is:

$$U_i\frac{\partial \zeta}{\partial x_i} = \frac{\partial}{\partial x_j}\left\{\left(\nu+\frac{\nu_t}{\sigma_\zeta}\right)\frac{\partial \zeta}{\partial x_j}\right\}+\frac{\zeta}{q}\left(C_{\zeta 1}f_{\zeta 1}Q-C_{\zeta 2}f_{\zeta 2}\zeta\right)+\psi' \qquad (6)$$

where the Cs are constants, the fs are low-Reynolds-number damping functions, and the last term accounts for sources of ζ which become significant only in the immediate vicinity of a wall. The eddy viscosity, equation (2), is now expressed as:

$$\nu_t \equiv C_\mu f_\mu \frac{q^3}{2\zeta} \qquad (7)$$

Note that reference has been made only in passing to the k-ε model and that no knowledge of that model is needed to formulate the q-ζ closure. The authors and their colleagues now recognise that the care taken in their earlier papers to relate the two new equations to the old ones has been counter-productive in that many potential users and particularly journal referees were concerned that the ε and ζ equations did not transform exactly into one another, that in order to get equation (6) from the ε and k equations certain terms have to be neglected. This is true but it does not matter. These critics regard the ε equation as sacrosanct, forgetting that it is a made-up equation just like equation (6), no better and no worse, at least in principle. In practice, however, it turns out that the ζ equation is usually easier to handle and generally gives the better results.

The equations contain a number of constants and functions to be determined by reference to experimental data and the results of numerical simulations at low Reynolds number. It is convenient now to make use of the experience gained with the established models, a useful short cut, as the ζ-equation and ε-equation constants are related by:

$$C_\zeta f_\zeta = 2C_\varepsilon f_\varepsilon - 1 \qquad (8)$$

or $C_\zeta = 2C_\varepsilon - 1$ when the f-functions are unity outside the viscous layers, C_μ is unchanged, and the damping functions may be assumed to have the same forms. For the time being the standard k-ε model constants $C_{\varepsilon 1} = 1.44$, $C_{\varepsilon 2} = 1.92$ are used so that $C_{\zeta 1} = 1.88$, $C_{\zeta 2} = 2.84$, with $\sigma_q = 1.0$ and $\sigma_\zeta = \sigma_\varepsilon = 1.3$.

Mainly we have used the low-Reynolds-number functions of the Launder and Sharma (1974) k-ε model because they are functions of the turbulence Reynolds number:

$$R_t \equiv \frac{q^3}{2\nu\zeta} \qquad (9)$$

and do not depend explicitly on the distance from the wall, which is often difficult to establish in general recirculating flow. Thus, in the ζ-equation (6) we generally put $f_{\zeta 1} = 1.0$ and

$$f_{\varepsilon 2} = 1-0.3\exp\left(-R_t^2\right) \qquad (10)$$

For damping the eddy viscosity:

$$f_\mu = \exp\left\{\frac{-A_\mu}{\left(1+R_t/50\right)^2}\right\} \qquad (11)$$

with $A_\mu = 6.0$ instead of the Launder-Sharma value of 3.4 so as to give the best results for channel flows and boundary-layers (Gibson and Dafa'Alla 1995). Equation (11) generally gives satisfactory results in spite of its failure precisely to match the limiting conditions at the wall. Improved versions, still dependent only on R_t, are given by Dafa'Alla et al (1996, 1997). We also follow Launder and Sharma (1974) in writing:

$$\psi' = \frac{\nu\nu_t}{q}\left(\frac{\partial^2 U_i}{\partial x_j \partial x_k}\right)\left(\frac{\partial^2 U_i}{\partial x_j \partial x_k}\right) \qquad (12)$$

CALCULATIONS

The computer code is based upon general curvilinear structured meshes fitted to the boundary of a geometry in the x-y plane but retaining the rectilinear form in the z-direction. An arbitrary flow geometry is transformed into a 'computational space' which is a rectangular difference grid independent of the physical geometry. All variables are co-located at the grid nodes. The pressure field is determined using the SIMPLE algorithm but the mass flux vectors it is used to compute are modified by using a pressure-smoothing algorithm to avoid decoupling the pressure and velocity fields. A TVD scheme was used for discretisation and the equations solved using either a conjugate gradient method or Gauss-Siedel line-by-line approach. In view of the resources immediately available only two-dimensional computations were attempted in the first instance. These were made on the symmetry plane of the duct shown in Figure 1. For calculations with the standard k-ε model with wall functions grid-independent solutions were obtained on a 1297 x 62 grid. For the low-Reynolds-number q-ζ model a 2469 x 139 grid was found to be necessary. Further details are given by Harper (1996), together with the results of heat-transfer calculations.

Measured and calculated distributions of the x-wise mean velocity component, U, the cross-stream component, V, and the shear stress, $\overline{uv}$, are compared in Figures 2, 3 and 4. Here the points represent the experimental data of Iacovides et al (1996), the continuous lines the results of low-Re q-ζ calculations, and the dotted lines those of the k-ε wall-function method. Recall that the flow has been

treated as two-dimensional and secondary flow produced in a duct of finite aspect ratio does not appear. On balance, where the computations differ, the low-Reynolds-number method is superior, as might perhaps be expected. On the other hand, the results also demonstrate the extraordinary ability of wall functions to deliver at least qualitatively correct results for flows with separated regions where the ability of the law-of-the-wall, however modified, is debatable to say the least. The pressure loss is predicted more accurately by the low-Reynolds-number method. The table below shows the pressure-loss coefficients calculated by the two methods for the region $-6.9D < x < 7.55D$.

Pressure-Loss Coefficient

	Smooth	Ribbed	Ratio
k-ε-wall-function	1.20	3.68	3.07
q-ζ low-Re	1.86	4.16	2.24
Experimental data	1.90	4.77	2.51

CLOSURE

The study is one of a series designed to test the practicability of the q-ζ turbulence model. On the whole we are reasonably well satisfied with the model performance, particularly in relation to numerical robustness, although it conceded that there is more to be done. Attention is now to be centred on the use of more realistic damping functions which meet the limiting conditions of turbulence at the wall.

ACKNOWLEDGEMENT

This work was mainly supported by European Gas Turbines Limited, Lincoln, England. The authors are grateful to Mr J.M. Hannis of EGT for his encouragement and advice.

REFERENCES

Dafa'Alla, A.A., Juntasaro, E. and Gibson, M.M., 1996, "Calculation of Oscillating Boundary Layers with the q-ζ Turbulence Model," Engineering Turbulence Modelling and Measurements, Vol. 3, (ed. W. Rodi and G. Bergeles), Elsevier, pp 141-150.

Dafa'Alla, A.A., Juntasaro, E. and Gibson, M.M., 1997, "Computations of Periodic Turbulent Boundary Layers with Moderate Adverse Pressure Gradient," Int. J. Heat Fluid Flow (to appear).

Gibson, M.M. and Dafa'Alla, A.A., 1995, "A Two-Equation Model for Turbulent Wall Flow," AIAA J., Vol. 33, pp. No. 8, pp. 1514-1518.

Gibson, M.M. and Harper, R.D., 1995, "Calculations of Separated Flows with the Low-Reynolds-Number q-ζ Turbulence Model," Proc. Tenth Turbulent Shear Flows Symposium, Pennsylvania State University.

Gibson, M.M. and Harper, R.D., 1997, "Calculation of Impinging-Jet Heat Transfer with the Low-Reynolds-Number q-ζ Turbulence Model," Int. J. Heat Fluid Flow, Vol. 18, No. 1. pp. 80-87.

Gibson, M.M. and Spalding, D.B., 1972, "A Two-Equation Model of Turbulence applied to the Prediction of Heat and Mass Transfer in Wall Boundary Layers," ASME paper 72-HT-15 at 1972 AIChE-ASME Conference.

Harper, R.D., 1996, "Computation of Heat Transfer in Turbulent Separated Flows," PhD thesis, Imperial College.

Iacovides, H., Jackson, D.C., Kelemenis, H.Ji, G., Launder, B.E. and Nikas, K., 1996, "LDA Study of the Flow Development through an Orthogonally Rotating U-Bend of Strong Curvature and Rib-Roughened Walls," Proc. 41st ASME Gas Turbine and Aeroengine Congress, Birmingham, Paper No. 96-GT-476.

Launder, B.E. and Sharma, B.I., 1974, "Application of the Energy-Dissipation Model of Turbulence to the Calculation of the Flow near a Spinning Disk," Letters in Heat and Mass Transfer, Vol. 1, pp. 131-138.

Ng, K.H. and Spalding, D.B., 1972, "Turbulence Model for Boundary Layers near Walls," Phys. Fluids, Vol. 15, pp. 20-30.

Spalding, D.B., 1969, "The Prediction of Two-Dimensional Steady Turbulent Flows," Imperial College, MED Rep. EF-TN-A-16.

Spalding, D.B., 1991, "Kolmogorov's Two-Equation Model of Turbulence," Proc. Roy. Soc., Vol. A434, pp. 211-216.

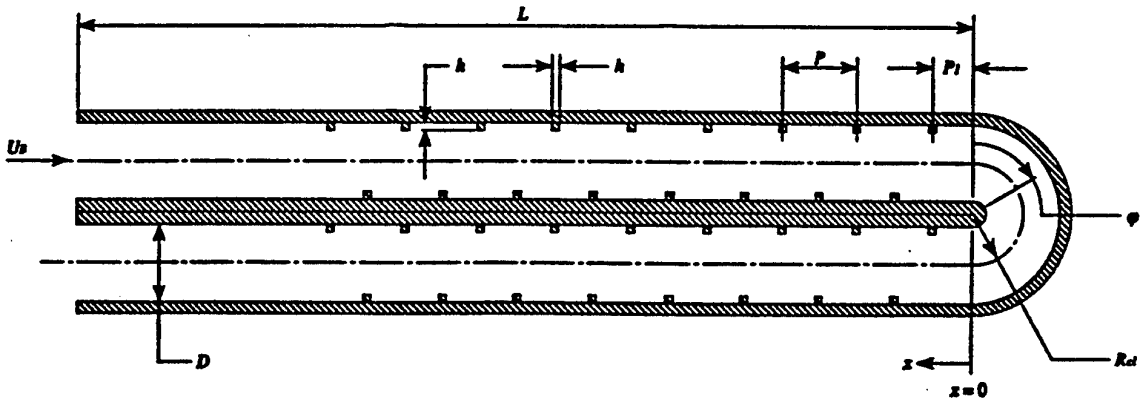


Figure 1. Section through the symmetry plane of the rib-roughened U-bend.
L = 600 mm, D = 50 mm, h = 5 mm, P = 50 mm.

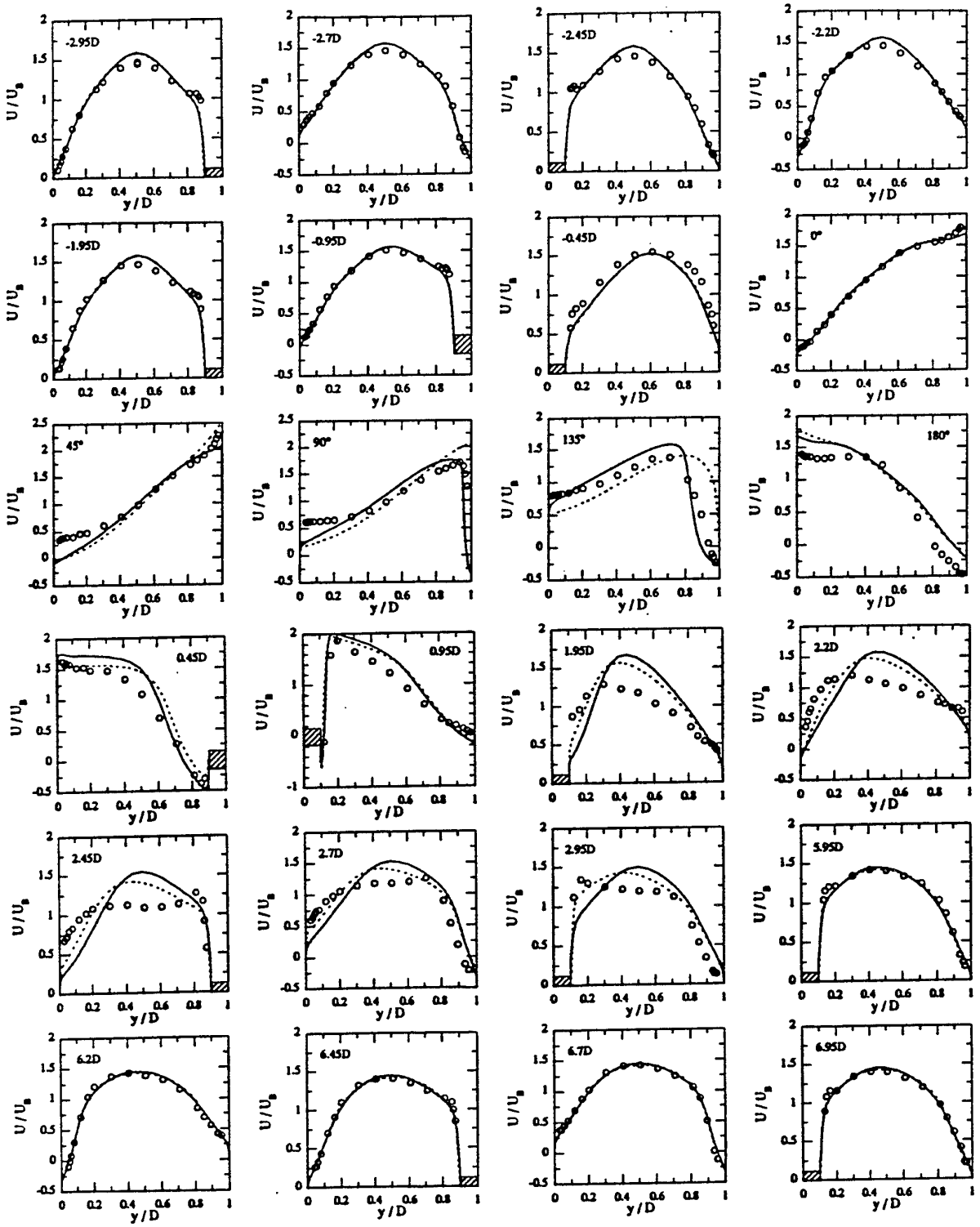


Figure 2. Measured and predicted distributions of the streamwise velocity component U normalised by the bulk velocity. o o o o o Experimental data from Iacovides et al (1996), ——— q-ζ model, - - - - - - k-ε model with wall functions.

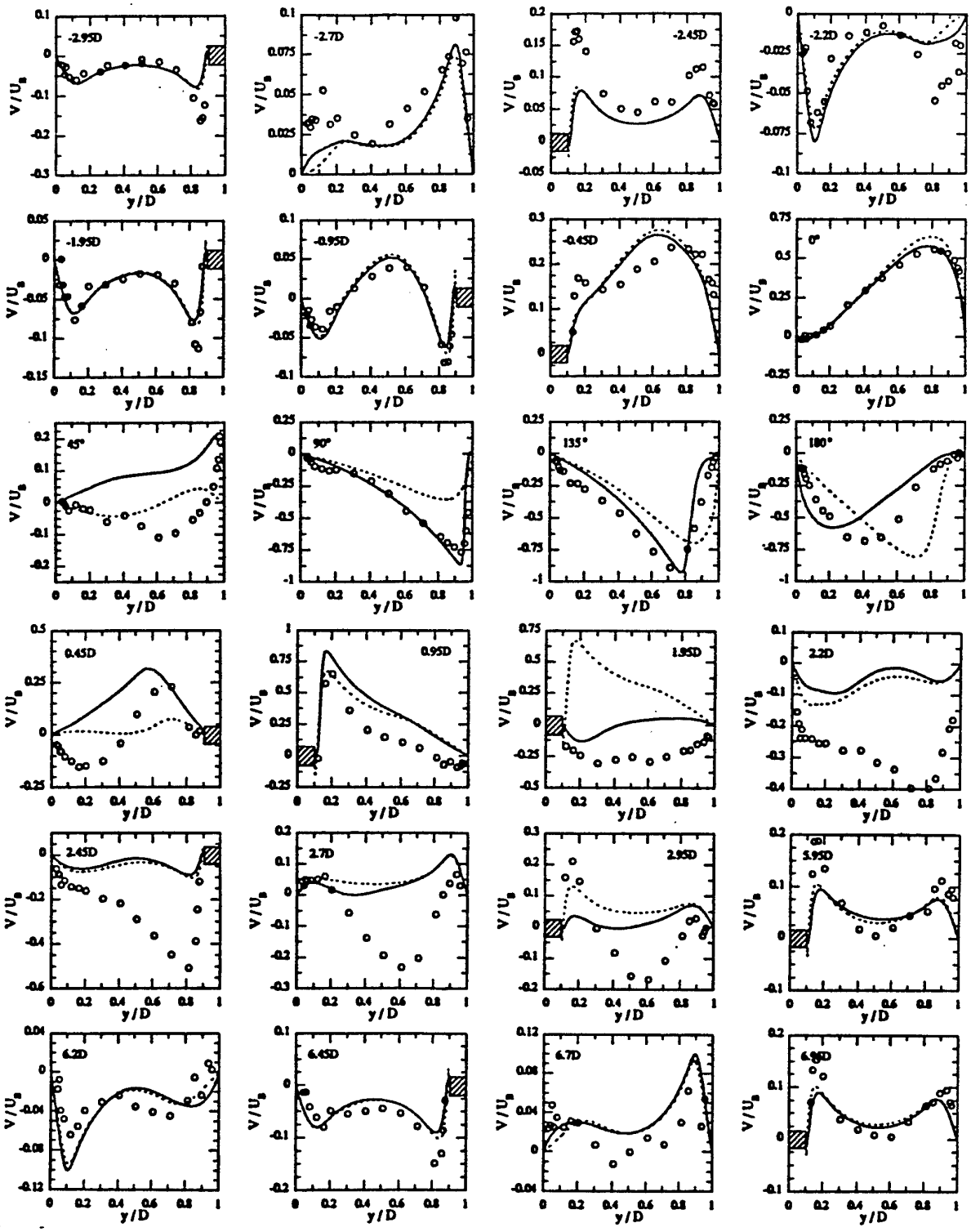


Figure 3. Measured and predicted distributions of the velocity component V normalised by the bulk velocity.
o o o o Experimental data from Iacovides et al (1996), ——— q-ζ model, - - - - - - k-ε model with wall functions.

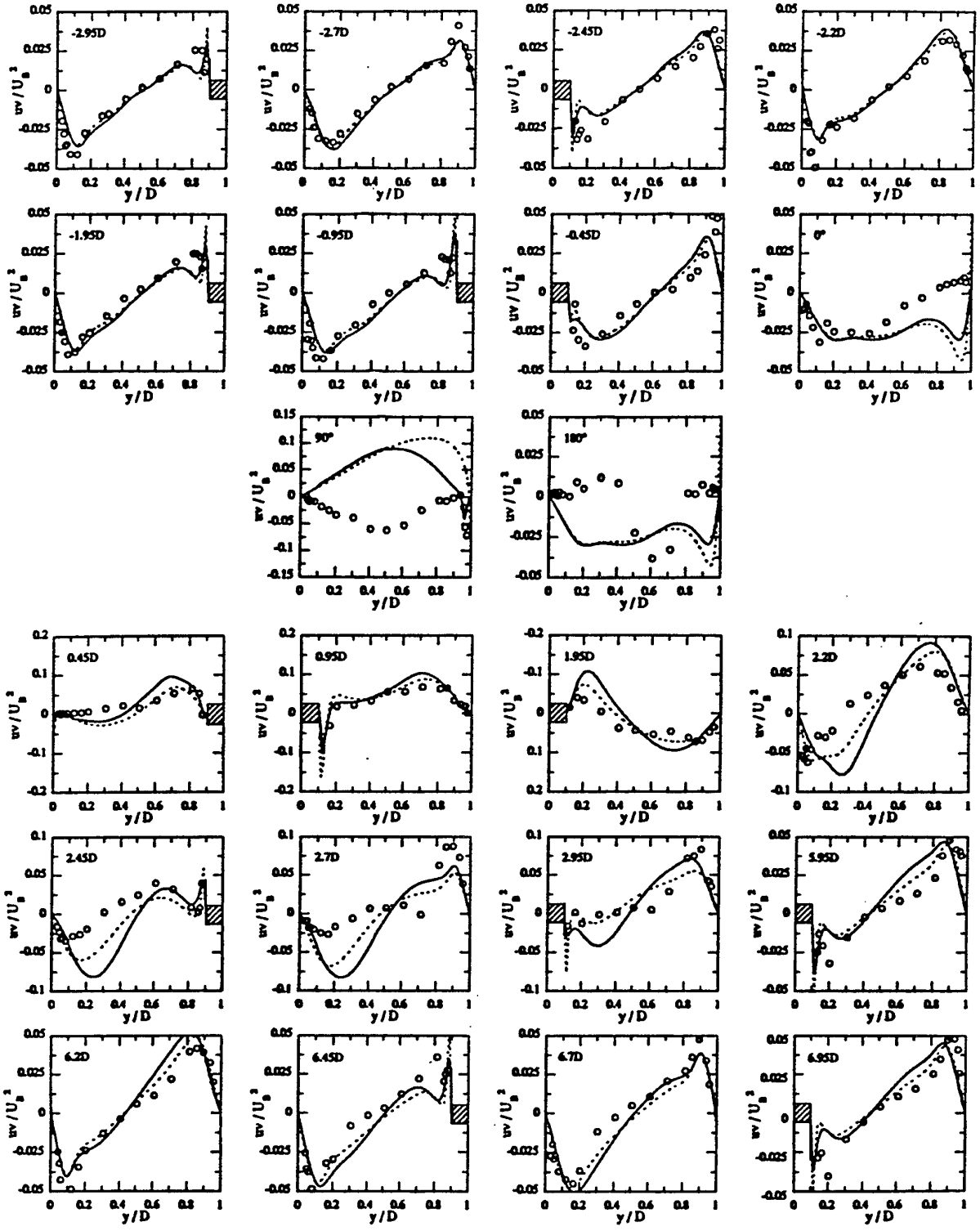


Figure 4. Measured and predicted distributions of the shear stress $\overline{uv}$.
o o o o Experimental data from Iacovides et al (1996), ———— q-ζ model, - - - - - - k-ε model with wall functions.

THE DISSIPATION RATE TRANSPORT EQUATION AND SUBGRID-SCALE MODELS IN ROTATING TURBULENCE

R. Rubinstein, Ye Zhou
Institute for Computer Applications in Science and Technology
NASA Langley Research Center
Hampton, Virginia 23681
USA

B. A. Younis
Department of Civil Engineering
City University
Northampton Square
London EC1V 0HB
UK

INTRODUCTION

Kraichnan's (1959) Direct Interaction Approximation (DIA) and related closures (Kraichnan, 1964, Kaneda, 1968) remain the only deductive turbulence theories. Although a study of a simple inhomogeneous flow, like channel flow, using these closures would be of the greatest theoretical and practical interest, the complexity of the calculations required to implement them has precluded any but preliminary results (Dannevik, 1992).

Practical application of DIA therefore requires some compromise between rigor and usefulness. The most comprehensive attempt to extract turbulence models from DIA remains the two-scale theory (TSDIA) of Yoshizawa (1984, 1996) in which inhomogeneity, anisotropy, and nonstationarity are introduced by perturbing about a state of homogeneous, isotropic, stationary turbulence.

Yoshizawa's procedure leads to formulas for quantities familiar in single point phenomenological turbulence closures like the eddy viscosity. A typical result is the expression for eddy viscosity

$$\nu = \frac{4}{15}\int d\mathbf{k}\int_0^\infty d\tau\; G(k,\tau)Q(k,\tau) \tag{1}$$

in terms of the DIA descriptors of isotropic turbulence: the response function $G(k,\tau)$ and correlation function $Q(k,\tau)$. The isotropy of the lowest order field implies that these descriptors are scalars, homogeneity permits introduction of the wave-vector argument $\mathbf{k}$, and stationarity in time makes them functions of time difference τ only. Yoshizawa (1984) shows how the familiar eddy viscosity formula of single-point turbulence modeling is deduced from this formula, by substituting Kolmogorov scaling forms for G and Q.

DIA FOR ROTATING TURBULENCE

Eq. (1) suggests that an eddy viscosity for turbulence subject to any external agency can be derived, provided that appropriate formulas for G and Q are known. Rotation is a particularly simple external effect, since the energy remains an inviscid invariant under rotation, and a steady state with constant energy flux remains possible. Since Kolmogorov scaling may no longer apply we first outline how DIA can be used to investigate the properties of this steady state. For rotating turbulence, the DIA equations of motion take the form

$$\begin{aligned} &\dot G_{ij}(\mathbf{k},t,s) + 2P_{ip}(\mathbf{k})\Omega_{pq}G_{qj}(\mathbf{k},t,s) \\ &+ \int_s^t dr\;\eta_{ip}(\mathbf{k},t,r)G_{pj}(\mathbf{k},r,s) = 0 \end{aligned} \tag{2}$$

$$\begin{aligned} &\dot Q_{ij}(\mathbf{k},t,s) + 2P_{ip}(\mathbf{k})\Omega_{pq}Q_{qj}(\mathbf{k},t,s) \\ &+ \int_s^t dr\;\eta_{ip}(\mathbf{k},t,r)Q_{pj}(\mathbf{k},r,s) \\ &= \int_s^t dr\; G_{ip}(\mathbf{k},t,r)F_{pj}(\mathbf{k},s,r) \end{aligned} \tag{3}$$

where the eddy damping η and forcing F are defined by

$$\begin{aligned} \eta_{ir}(\mathbf{k},t,s) &= \int_{\mathbf{k}=\mathbf{p}+\mathbf{q}} d\mathbf{p}d\mathbf{q}P_{imn}(\mathbf{k})P_{\mu rs}(\mathbf{p})\times \\ &\quad G_{m\mu}(\mathbf{p},t,s)Q_{ns}(\mathbf{q},t,s) \end{aligned} \tag{4}$$

$$\begin{aligned} F_{ij}(\mathbf{k},t,s) &= \int_{\mathbf{k}=\mathbf{p}+\mathbf{q}} d\mathbf{p}d\mathbf{q}P_{imn}(\mathbf{k})P_{jrs}(\mathbf{k})\times \\ &\quad Q_{ns}(\mathbf{p},t,s)Q_{mr}(\mathbf{q},t,s) \end{aligned} \tag{5}$$

In Eqs. (4) and (5),

$$\begin{aligned} P_{imn}(\mathbf{k}) &= k_m P_{in}(\mathbf{k}) + k_n P_{im}(\mathbf{k}) \\ P_{im}(\mathbf{k}) &= \delta_{im} - k^{-2}k_i k_m \end{aligned}$$

The solution of these equations in complete generality is not known. A useful simplification, EDQNM, effectively replaces the response equation Eq. (2) by a phenomenological hypothesis, and solves a simplified, Markovianized version of the correlation equation Eq. (3) (Cambon and Jacquin, 1986).

A perturbative solution of these equations is suggested by Leslie's (1972) treatment of shear turbulence: treat the

rotation terms as small, and perturb about an isotropic turbulent state. This approach is adopted by Shimomura and Yoshizawa (1986) who derive a TSDIA theory in which inhomogeneity and rotation both appear as small parameters.

The complementary limit is also of interest. Namely, in the response equation, balance the time derivative by the rotation term, and treat the eddy damping as small. This linear theory of the response equation treats strongly rotating turbulence as a case of *weak turbulence* (Zakharov *et al*, 1992) in which nonlinear decorrelation of Fourier modes is dominated by linear dispersive decorrelation (Waleffe, 1993). The result is conveniently expressed in terms of the *Craya-Herring* basis

$$\begin{aligned} \mathbf{e}^{(1)}(\mathbf{k}) &= \mathbf{k}\times\mathbf{\Omega}/\mid \mathbf{k}\times\mathbf{\Omega}\mid \\ \mathbf{e}^{(2)}(\mathbf{k}) &= \mathbf{k}\times(\mathbf{k}\times\mathbf{\Omega})/\mid \mathbf{k}\times(\mathbf{k}\times\mathbf{\Omega})\mid \end{aligned}$$

or the equivalent basis of Cambon and Jacquin (1989), and the corresponding tensors

$$\begin{aligned} \xi^0_{ij} &= e^{(1)}_i e^{(2)}_j - e^{(1)}_i e^{(2)}_j \\ \xi^1_{ij} &= e^{(1)}_i e^{(2)}_j + e^{(1)}_i e^{(2)}_j \\ \xi^2_{ij} &= e^{(1)}_i e^{(1)}_j - e^{(2)}_i e^{(2)}_j \\ \xi^3_{ij} &= e^{(1)}_i e^{(1)}_j + e^{(2)}_i e^{(2)}_j \end{aligned} \tag{6}$$

Note that $\xi^3_{ij} = P_{ij}(\mathbf{k})$.

The leading order solution of Eq. (2), obtained by dropping the eddy damping term, is

$$\begin{aligned} G_{ij}(\mathbf{k},t,s) &= \{\cos(\mathbf{k}\cdot\mathbf{\Omega}(t-s)/k)P_{ij}(\mathbf{k}) \\ &+ \sin(\mathbf{k}\cdot\mathbf{\Omega}(t-s)/k)\xi^0_{ij}(\mathbf{k})\}H(t-s) \end{aligned} \tag{7}$$

where H is the unit step function. Let us adopt the *fluctuation-dissipation* hypothesis relating the two-time correlation function to the response function and single-time correlation function

$$\begin{aligned} Q_{ij}(\mathbf{k},t,s) &= G_{im}(\mathbf{k},t,s)Q_{mj}(\mathbf{k}) \\ &+ G_{jm}(\mathbf{k},s,t)Q_{mi}(\mathbf{k}) \end{aligned} \tag{8}$$

Conditions under which this approximation is reasonable are discussed by Woodruff (1992). Substituting Eqs. (7) and (8) in Eq. (3) shows that the single-time correlation function must take the general form containing all of the ξ tensors of Eq. (6)

$$Q_{ij}(\mathbf{k}) = \sum Q^p(\mathbf{k})\xi^p_{ij}(\mathbf{k}) \tag{9}$$

which is equivalent to the form of the correlation function noted by Cambon and Jacquin (1989).

The DIA inertial range energy balance (Kraichnan, 1971), which states that a steady state with constant energy flux exists, is

$$\begin{aligned} \varepsilon &= [I^+ - I^-]P_{imn}(\mathbf{k})\int_0^\infty d\tau\ 2P_{\mu rs}(\mathbf{p})\times \\ &\quad G_{m\mu}(\mathbf{p},\tau)Q_{ns}(\mathbf{q},\tau)Q_{ir}(\mathbf{k},\tau) \\ &- P_{jrs}(\mathbf{k})G_{ij}(\mathbf{k},\tau)Q_{ns}(\mathbf{p},\tau)Q_{mr}(\mathbf{q},\tau) \end{aligned} \tag{10}$$

where the integration operators in Eq. (10) are defined by

$$\begin{aligned} I^+(k_0) &= \int_{k\geq k_0} d\mathbf{k}\int_{\mathbf{k}=\mathbf{p}+\mathbf{q};p,q\leq k_0} d\mathbf{p}d\mathbf{q} \\ I^-(k_0) &= \int_{k\leq k_0} d\mathbf{k}\int_{\mathbf{k}=\mathbf{p}+\mathbf{q};p,q\geq k_0} d\mathbf{p}d\mathbf{q} \end{aligned}$$

and $\tau = t - s$ denotes time difference. The time integrals in Eq. (10) will take the form

$$\begin{aligned} &\Theta(\mathbf{k},\mathbf{p},\mathbf{q}) = \\ &\Omega^{-1}\delta(\pm\mathbf{p}\cdot\mathbf{\Omega}/p\Omega \pm \mathbf{q}\cdot\mathbf{\Omega}/q\Omega \pm \mathbf{k}\cdot\mathbf{\Omega}/k\Omega) \end{aligned} \tag{11}$$

Thus, wave-vector integrations take place over resonant triads only (Waleffe, 1993) and these integrals scale as Ω^{-1} (Zhou, 1995).

Introduce the *ansatz*

$$Q^p(\mathbf{k}) = k^{-\alpha-2}f^p(\mathbf{\Omega}\cdot\mathbf{k}/k\Omega) \tag{12}$$

for the functions in Eq. (9). In view of Eq. (11), the energy balance Eq. (10) requires $\alpha = 2$. The goal of this work is a two-equation model of the standard form. Accordingly, we only attempt to quantify the overall effect of rotation on turbulent energy transfer, ignoring the *polarization* of turbulence (Cambon and Jacquin, 1989) by rotation and the distribution of energy in k space. It will suffice to summarize the scaling laws in terms of the 'equivalent' isotropic energy spectrum given by Zhou (1995),

$$E(k) \sim \sqrt{\varepsilon\Omega}k^{-2} \tag{13}$$

It is of interest to exhibit the eddy damping correction to the leading order results represented by Eqs. (7) and (13). Namely, substituting these results in Eq. (4) for the eddy damping factor,

$$\eta \sim k^2\int_k^\infty dp\ \frac{1}{\Omega}\sqrt{\varepsilon\Omega}p^{-2} \sim k\sqrt{\varepsilon/\Omega} \tag{14}$$

The corrections to the time scale and energy spectrum have the form

$$\begin{aligned} \Theta &\sim \frac{1}{\Omega}\{1+O(\Omega^{-3/2})\}^{-1} \\ E &\sim \sqrt{\varepsilon\Omega}k^{-2}\{1+O((k^2\varepsilon/\Omega^3)^{1/2}\} \end{aligned} \tag{15}$$

The low rotation rate expansion of Shimomura and Yoshizawa (1986) gives the complementary expansions in positive powers of Ω,

$$\begin{aligned} \Theta &\sim \varepsilon^{-1/3}k^{-2/3}\{1+O(\Omega)\} \\ E &\sim \varepsilon^{2/3}k^{-5/3}\{1+O(\Omega/\varepsilon^{1/3}k^{2/3}\} \end{aligned} \tag{16}$$

The expansions in Eqs. (15) and (16) could be consolidated into Padé approximations for the energy spectrum and decorrelation time applicable for any rotation rate.

Locality of energy transfer

The scaling law of Eq. (13) is purely formal: to prove that a steady state scales this way, the convergence of the integral in Eq. (10) must be demonstrated. Divergence would imply strong dependence on the cutoff at large or small scales, and would therefore alter the scaling law (Kraichnan, 1959). Even if the dependence on $\Omega^{1/2}$ is known, Eq. (13) cannot be asserted on dimensional grounds: dimensional analysis assumes that k is the only relevant length scale; it therefore postulates the locality which convergence of the flux integral proves.

Since a convergence proof would require both the tensor forms Eq. (9) and the exact forms of the functions $f^p(\mathbf{\Omega}\cdot\mathbf{k}/k\Omega)$, Eq. (13) is only hypothetical. But it is easily proven that the flux integral with isotropic functions with the scalings of Eq. (15) does converge. This fact provides some support for asserting the locality of energy transfer in a rotating inertial range and using the scaling laws of Eq. (15) to develop turbulence models.

SUBGRID-SCALE MODELS

Since the lowest order field in TSDIA is arbitrary, the transport properties of weakly strained strongly rotating turbulence can be derived by perturbing about the steady rotating turbulent state just described instead of perturbing about a Kolmogorov steady state. In carrying out this program, it should be stressed that formulas like Eq. (1) for the eddy viscosity are the result of evaluating an integral over interacting triads in the distant interaction limit. This is consistent with the properties of strongly rotating turbulence since distant triads with $k/p, k/q \to 0$ satisfy the resonance condition as well.

Again, since our goal is to evaluate the over-all effect of rotation on turbulent energetics, we will evaluate the eddy viscosity integral using the isotropic expressions of Eq. (15). It follows by substituting these results in Eq. (1) that in strongly rotating turbulence, to leading order

$$\nu = C_\nu^\Omega \Delta \sqrt{\varepsilon/\Omega} \tag{17}$$

where Δ is the filter size. Corrections for finite rotation rates are suggested by Eq. (15). Setting Δ equal to the integral scale of turbulence leads to the single point result

$$\nu \sim \frac{K}{\Omega} \tag{18}$$

Equating the dissipation rate to the resolved production gives

$$\varepsilon = C_\nu^\Omega \sqrt{\varepsilon/\Omega} \Delta S^2 \tag{19}$$

where $S^2 = S_{ij}S_{ij}/2$ and S_{ij} is the strain rate. Solving Eq. (19) for ε and substituting in Eq. (17),

$$\nu = (C_\nu^\Omega)^2 \frac{S^2\Delta^2}{\Omega} \tag{20}$$

which is the Smagorinsky model for strongly rotating turbulence.

This calculation supplements the evaluation by Shimomura and Yoshizawa (1986) of the sub-grid scale viscosity in weakly rotating turbulence. But the effect of rotation becomes weaker with decreasing scale size; accordingly, the weak rotation correction of Shimomura and Yoshizawa may be appropriate even in some rapidly rotating flows.

The additional production and dissipation mechanisms present in meteorological flows are often modeled by Richardson number modifications of the subgrid-scale viscosity. Thus, if the energy balance at the grid scale is written as

$$\nu S^2 (1 - R_f) = \varepsilon \tag{21}$$

and Kolmogorov scaling

$$\nu = C\varepsilon^{1/3}\Delta^{4/3} \tag{22}$$

can be assumed, then Eqs. (21) and (22) give

$$\nu = C\Delta S^2 \sqrt{1 - R_f} \tag{23}$$

If strong rotation is also present, as in a rotating buoyant flow, Eqs. (17), (18), and (21) imply

$$\nu = (C_\nu^\Omega)^2 \frac{S^2\Delta^2}{\Omega}(1 - R_f) \tag{24}$$

Note the difference between the Richardson number dependence in Eq. (23), corresponding to no rotation, and in Eq. (24), corresponding to strong rotation.

DISSIPATION TRANSPORT EQUATION

Our earlier work (Rubinstein and Zhou, 1996) attempts to implement Leslie's (1972) suggestion that the dissipation rate transport equation be derived from the expression Eq. (10) for energy transfer into the inertial range. A complete treatment would require TSDIA in order to evaluate the essentially inhomogeneous diffusion effects. The present account will be limited to the production and destruction terms, which are amenable to a homogeneous theory.

The starting point is then the DIA equations Eqs. (2)-(3) in which the strain rate term

$$\mathcal{S}_{im}(t) = \frac{\partial U_i}{\partial x_m} - 2k^{-2}k_i k_p \frac{\partial U_p}{\partial x_m} + \delta_{im} k_s \frac{\partial U_s}{\partial x_r}\frac{\partial}{\partial k_r}$$

is added to the rotation term. Differentiating the time dependent form of Eq. (10) with respect to time, and assuming stationarity of the lowest order TSDIA field,

$$\begin{aligned}
\dot{\varepsilon} = {} & [I^+ - I^-]P_{imn}(\mathbf{k})\{P_{mrs}(\mathbf{p})Q_{ns}(\mathbf{q}) \times \\
& Q_{ir}(\mathbf{k}) - P_{irs}(\mathbf{k})Q_{ns}(\mathbf{p})Q_{mr}(\mathbf{q}) + \int_0^\infty d\tau[\\
& P_{\mu rs}(\mathbf{p})\dot{G}_{m\mu}(\mathbf{p},\tau)Q_{ns}(\mathbf{q},\tau)Q_{ir}(\mathbf{k},\tau) \\
- \; & P_{jrs}(\mathbf{k})\dot{G}_{ij}(\mathbf{k},\tau)Q_{ns}(\mathbf{p},\tau)Q_{mr}(\mathbf{q},\tau) \\
+ \; & P_{\mu rs}(\mathbf{p})G_{m\mu}(\mathbf{p},\tau)\dot{Q}_{ns}(\mathbf{q},\tau)Q_{ir}(\mathbf{k},\tau) \\
- \; & P_{jrs}(\mathbf{k})G_{ij}(\mathbf{k},\tau)\dot{Q}_{ns}(\mathbf{p},\tau)Q_{mr}(\mathbf{q},\tau) \\
+ \; & P_{\mu rs}(\mathbf{p})G_{m\mu}(\mathbf{p},\tau)Q_{ns}(\mathbf{q},\tau)\dot{Q}_{ir}(\mathbf{k},\tau) \\
- \; & P_{jrs}(\mathbf{k})G_{ij}(\mathbf{k},\tau)Q_{ns}(\mathbf{p},\tau)\dot{Q}_{mr}(\mathbf{q},\tau)]\}
\end{aligned} \tag{25}$$

The time-dependent form of this equation might be of interest in the context of non-equilibrium turbulence modeling. Note that the first two terms, distinguished by the absence of any time integration, arise from a quasi-normal hypothesis. The remaining terms are corrections due to DIA.

We follow the program outlined before: to find the dissipation rate transport equation in weakly rotating turbulence, we will substitute Kolmogorov scaling forms for the descriptors G and Q; to find this transport equation in strongly rotating turbulence, we will substitute descriptors appropriate to strong rotation.

The destruction term

The destruction terms D_ε are those which are independent of strain. Consider first the destruction term in non-rotating turbulence. The quasi-normal terms can be shown (Rubinstein and Zhou, 1996) to contribute

$$D_\varepsilon = -C_{\varepsilon 2}\frac{\varepsilon^2}{K} \tag{26}$$

when expressed in terms of single-point quantities. The most important conclusion is that the integral which leads to Eq. (26) is convergent in the large k limit. This implies that there is no Reynolds number dependence in the destruction term. The remaining terms in Eq. (25) lead to the same result. The third term, for example, has the form

$$[I^+ - I^-]\eta(p)\Theta(k,p,q)P(\mathbf{k})P(\mathbf{p})Q(q)Q(k)$$

Since the combination $\eta\Theta$ is homogeneous of degree zero, the convergence of the integral is not changed, and the form Eq. (26) again follows.

To evaluate the destruction term in strongly rotating turbulence, we observe first that the terms of lowest order in Ω are the quasi-normal terms which we have already analyzed (Rubinstein and Zhou, 1996). Substituting the energy spectrum with the scaling of Eq. (15) in these terms,

there results

$$D_\varepsilon = -C_{\varepsilon 2}^{\Omega}\varepsilon\Omega \tag{27}$$

The constant $C_{\varepsilon 2}^{\Omega}$ is expressed as a convergent integral. The result of Eq. (27) agrees in the strong rotation limit with the rotation correction proposed by Bardina *et al* (1985). Dimensional analysis obviously cannot predict this limit, and other limits for D_ε have been proposed.

The production term

The production terms P_ε depend on the mean velocity gradient. The contribution of lowest order in the mean velocity gradient obviously depends on $S^2 = S_{ij}S_{ij}/2$, where S_{ij} is the strain rate.

Beginning again with turbulence without rotation, we find at once that there can be no production term without weak breaking of the isotropy of small scales (Xu and Speziale, 1996). This weak anisotropy is introduced using Leslie's (1972) perturbative DIA theory of shear turbulence. Expanding the single time correlation function in a power series in the strain rate,

$$Q_{ij}(\mathbf{k},t) = Q_{ij}^{(0)}(\mathbf{k},t) + Q_{ij}^{(1)}(\mathbf{k},t) + \cdots$$

where $Q^{(0)}$ is the correlation function of isotropic turbulence and setting $G_{ij} = G_{ij}^{(0)}$ the response function of isotropic turbulence, Leslie found

$$\begin{aligned} Q_{ij}^{(1)}(\mathbf{k},t) = \int_0^t ds\{\ & G^{(0)}(k,t,s) \\ (\quad & -\frac{\partial U_i}{\partial x_r} + 2k_ik_pk^{-2}\frac{\partial U_p}{\partial x_r})Q_{rj}^{(0)}(k,t,s) \\ + \quad & G^{(0)}(k,t,s)(-\frac{\partial U_j}{\partial x_r} + 2k_jk_pk^{-2}\frac{\partial U_p}{\partial x_r}) \times \\ & Q_{ri}^{(0)}(k,t,s) \\ + \quad & G^{(0)}(k,t,s)k_r\,\frac{\partial U_r}{\partial x_n}\,\frac{\partial}{\partial k_n}\,Q_{ij}^{(0)}(k,t,s) \\ - \quad & Q_{ij}^{(0)}(k,t,s)k_r\,\frac{\partial U_r}{\partial x_n}\,\frac{\partial}{\partial k_n}G^{(0)}(k,t,s)\} \end{aligned} \tag{28}$$

Nonzero contributions to production are possible from terms which contain the combination $SQ^{(1)}$. These terms will contibute production of dissipation terms proportional to quadratic invariants of the mean velocity gradient $S_{ij}S_{ij}$ and $W_{ij}W_{ij}$ where W_{ij} is the antisymmetric part of the mean velocity gradient. For example, the third term in Eq. (15) contributes

$$\begin{aligned} P_\varepsilon &= [I^+ - I^-]\mathcal{S}\Theta P(\mathbf{k})P(\mathbf{p})Q^{(1)}(\mathbf{q})Q^{(0)}(\mathbf{k}) \\ &= [I^+ - I^-]\mathcal{S}\Theta^2 P(\mathbf{k})P(\mathbf{p})\mathcal{S}Q^{(0)}(\mathbf{q})Q^{(0)}(\mathbf{k}) \end{aligned} \tag{29}$$

where indices have been dropped. The second power of Θ in Eq. (29) arises from the time integration in Eq. (28) required to express $Q^{(1)}$ in terms of $Q^{(0)}$. The contribution to P_ε of Eq. (29) differs from a contribution from the quasi-normal terms only in the factors of Θ. As these factors scale like $k^{-2/3}$, they do not introduce any high wavenumber divergence, and we find that in terms of single-point quantities, they contribute

$$P_\varepsilon \sim KS^2 \sim \frac{\varepsilon}{K}\nu\nabla U^2 \tag{30}$$

where ∇U^2 denotes terms quadratic in the mean velocity gradient. These terms must be proportional to the invariants $S_{ij}S_{ij}$ or to $W_{ij}W_{ij}$

The occurrence of terms proportional to $W_{ij}W_{ij}$ in Eq. (30) would lend theoretical support to the procedure of 'sensitizing to irrotational strains' introduced by Hanjalić and Launder (1980). Since such a term cannot appear in energy production P_K, we conclude that P_K and P_ε may not be related by the proportionality

$$P_\varepsilon = C_{\varepsilon 1}\frac{\varepsilon}{K}P_K \tag{31}$$

Further evidence against the proportionality of Eq. (31) occurs if the series for P_ε is taken to higher order in ∇U by substituting the higher order terms in Leslie's expansion Eq. (28) in Eq. (25). The result,

$$P_\varepsilon = \nu\frac{\varepsilon}{K}\{O(\nabla U)^2 + \frac{K}{\varepsilon}O(\nabla U)^3 + \cdots\} \tag{32}$$

can be compared term by term with the result of substituting Yoshizawa's (1984) expansion of the Reynolds stress in the definition of energy production,

$$P_K = \nu\{O(\nabla U)^2 + \frac{K}{\varepsilon}O(\nabla U)^3 + \cdots\} \tag{33}$$

There is no reason to anticipate term-by-term equality of the series in braces in Eqs. (32) and (33).

Evaluating Eq. (29) using the descriptors Eq. (15) of strongly rotating turbulence leads to the scaling

$$P_\varepsilon \sim \Omega^{-1}\varepsilon\nabla U^2 \sim \frac{\varepsilon}{K}\nu(\Omega)\nabla U^2 \tag{34}$$

where $\nu(\Omega)$ denotes the rotation-dependent viscosity with the strong rotation limit Eq. (18).

INTERPOLATION FORMULAS

In principle, the series expansions of ν, D_ε and P_ε, in positive powers of Ω following Shimomura and Yoshizawa (1986) for weak rotation, and in negative powers of Ω for strong rotation, can be continued to arbitrary order. The problem arises to interpolate rationally between these limits to obtain a model valid at intermediate rotation rates. Thus, for the turbulent viscosity, we can pose a series approximations of Padé type

$$\nu = C_\nu\frac{K^2}{\varepsilon}\{\frac{1}{1+C_1(\Omega K/\varepsilon)^2}\}^{1/2} \tag{35}$$

$$= C_\nu\frac{K^2}{\varepsilon}\{\frac{1+D_1(\Omega K/\varepsilon)^2}{1+C_1(\Omega K/\varepsilon)^2+C_2(\Omega K/\varepsilon)^4}\}^{1/2} \tag{36}$$

$$= \cdots$$

which reduce to the usual eddy viscosity formula with $O(\Omega)^2$ corrections for low rotation rates, or to the limiting form given by Eq. (18) for strong rotation. The constants C_i and D_i could be determined, in principle, by matching to the high and low rotation rate expansions constructed above.

The lowest order interpolation, Eq. (35), when used with analogs for D_ε and P_ε does not prove satisfactory in computations. At moderate rotation rates, the reduction in ε brought about by the modified dissipation rate transport equation causes the leading factor in ν to increase, unless the constant C_1 is made extremely large. Only when Ω is asymptotically large does the factor in braces become small enough to reduce the turbulent viscosity.

This defect may be due to the property of Eq. (35) that the strong rotation limit fixes the constant C_1, which then also determines the rotation correction in the weak rotation limit. It appears that these limits are not consistent. The more complex model of Eq. (36) may be more satisfactory, but further investigation is essential in order to at least suggest the size of the constants.

Acknowledgements : This work was completed while the authors were in residence at the Institute for Computer Applications in Science and Engineering (ICASE) at NASA Langley Research Center.

REFERENCES

Bardina, J., Ferziger, J. H., and Rogallo, R. S., 1985, "Effect of rotation of isotropic turbulence: computation and modeling," *J. Fluid Mech.* Vol. 154, p. 321.

Cambon, C., and Jacquin, L., 1989, "Spectral approach to non-isotropic turbulence subjected to rotation," *J. Fluid Mech.* Vol. 202, p. 295.

Cambon, C., Jacquin, L., and Lubrano, J. L., 1992, "Toward a new Reynolds stress model for rotating turbulent flows," *Phys. Fluids A* Vol. 4, p. 812.

Dannevik, W. P., 1986, "Efficient solution of non-Markovian covariance evolution equations in fluid turbulence," *J. Sci. Comput* Vol. 1, p. 151.

Hanjalić, K. and Launder, B. E., 1980, "Sensitizing the dissipation rate equation to irrotational strains," *J. Fluids Eng.* Vol. 102, p. 34.

Leslie, D. C., 1972, *Modern Developments in the Theory of Turbulence*, Oxford University Press.

Kaneda, Y., 1981, "Renormalized expansions in the theory of turbulence with the use of the Lagrangian position function," *J. Fluid Mech.* Vol. 107, p. 131.

Kraichnan, R. H., 1959, "The structure of isotropic turbulence at very high Reynolds number," *J. Fluid Mech.* Vol. 5, p. 497.

Kraichnan, R. H., 1965, "Lagrangian-history closure approximation for turbulence," *Phys. Fluids* Vol. 8, p. 575.

Kraichnan, R. H., 1971, "Inertial range transfer in two and three dimensional turbulence," *J. Fluid Mech.* Vol. 47, p. 525.

Rubinstein, R. and Zhou, Y., 1996, "Analytical theory of the destruction terms in dissipation rate transport equations," *Phys. Fluids* Vol. 8, p. 3172.

Shimomura, Y., and Yoshizawa, A., 1986 "Statistical analysis of anisotropic turbulent viscosity in a rotating system," *J. Phys. Soc. Japan* Vol. 55, p. 1904.

Waleffe, F., 1993, "Inertial transfers in the helical decomposition," *Phys. Fluids* Vol. 5, p. 677.

Woodruff, S. L., 1992, "Dyson equation analysis of inertial-range turbulence," *Phys. Fluids A*, Vol. 5, p. 1077.

Xu, X. H. and Speziale, C. G., 1996, "Explicit algebraic stress model of turbulence with anisotropic dissipation," *AIAA J.* Vol. 34, p. 2186.

Yoshizawa, A., 1984, "Statistical analysis of the deviation of the Reynolds stress from its eddy viscosity representation," *Phys. Fluids* Vol. 27, p. 3177.

Yoshizawa, A. and Yokoi, N., 1995, "Statistical analysis of the effects of helicity in inhomogeneous turbulence," *Phys. Fluids* Vol. 7, p. 12.

Yoshizawa, A., 1996, "Simplified statistical approach to complex turbulent flows and ensemble-mean compressible turbulence modeling," *Phys. Fluids*

Zakharov, V. E., L'vov, V. S., and Falkovich, G., 1992, *Kolmogorov Spectra of Turbulence* I, Springer.

Zhou, Y., 1995, "A phenomenological treatment of rotating turbulence," *Phys. Fluids* Vol. 7, p. 2092.

SESSION 32 - COMPRESSIBLE FLOWS II

COMPUTATIONS OF COMPRESSIBLE TURBULENT SHEAR FLOWS WITH MULTIPLE-TIME-SCALE MODELS

A. Hadjadj, D. Vandromme

LMFN-CORIA, UMR 6614 CNRS
INSA de Rouen, BP 8
76801 ST Etienne du Rouvray,
France

and

L. De Chantérac

DRET-DGA
26, Boulevard Victor, 00460 Armée,
France

ABSTRACT

This paper concerns computations of compressible turbulent shear flows with multiple-scale models. Several improvements in computations of shear flows (mixing layer, afterbody flow including near wall turbulent boundary layer and supersonic jet) at high convective Mach number are obtained with multiple-scale models. The multiscale modeling permits to understand better the physics concerning regions of strong nonequilibrium turbulent flows. In this study, two aspects have been examined ; the **compressibility** caused by strong Mach number variations and the **anisotropy** of turbulent flow. The results show that the RSM model with multiscale formulation is able to integrate simultaneously these two effects. This model is proved numerically stable and gives better results compared to those issued from a classical second-moment closure.

NOMENCLATURE

$E(\kappa)$	: energy spectral density
M_c	: convective Mach number
σu	: $\sqrt{u''^2}$
$U_i, \widetilde{u_i''}$	: mean and fluctuating velocity components
U^*	: dimensionless velocity
y^*	: $(y - y_0)/\delta_\omega$
δ_ω	: vorticity thickness
δ_b	: visual thickness of shear layer
κ	: wave number
ρ	: density

INTRODUCTION

The aerothermodynamics phenomena over space launch vehicles or missiles are a challenging problem on space and aeronautical applications. These physical phenomena can affect strongly the engine's aerodynamic performances and, in consequence, its conception and operating mode.
The physical problems found on this geometry type are primarily the result of the interaction of two primary flows; one issued from a propulsive jet at high speed and high temperature, and the other caused by the exterior air flow at low speed and low temperature. The complexity and the usual misunderstanding of these physical phenomena coupled with the turbulence modeling problem of complex compressible flows motivated the present study.

In turbulence modeling, the classical two-equation $k - \epsilon$ model and its variants have been the most widely used models in engineering calculations. However, one of the weaknesses of this model is the use of a single-time scale (or a single-length scale) to describe the turbulent field. Indeed, the usual turbulence models based on one-point closures suppose a local equilibrium neglecting the spectrum characteristic turbulence fluctuation. In reality, turbulence is characterized by a wide spectrum of fluctuations and the turbulent interactions are associated with different parts of this evolving spectrum. One approach to take into account this physical reality is the multiple-time-scale turbulence modeling (see Schiestel 1987, Wilcox 1988 and Kim 1991).
In this work, we propose the introduction of several scales characterizing different process of turbulence interaction by using multiple-time-scale models.

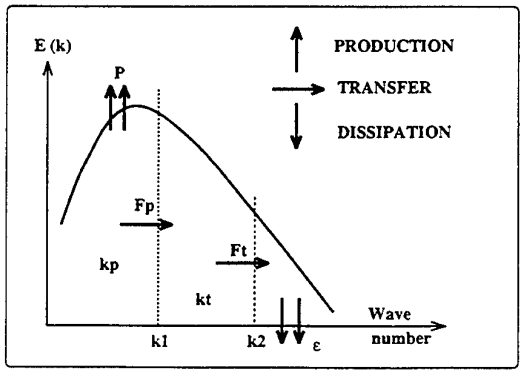


Figure 1: *Sketch of spectral partitioning*

The multiscale turbulence modeling consists in partitioning the energy spectrum into several regions, each characterized by a different time scale. Thus different mechanisms

such as the return to isotropy, dissipation, diffusion, and viscosity can be modeled using the various characteristic scales. In the simplified split-spectrum used by Kim et al. (1991), turbulent transport is described by using two time scales : the first corresponds to the large eddies and describes generation of turbulent kinetic energy, and the second corresponds to the smaller-scale eddies and describes dissipation rate. Figure 1 shows a sketch of a typical spectrum arising in a shear-flow at high Reynolds numbers. The turbulent energy can be partitioned into three regions : production region, characterized by the turbulent kinetic energy k_p and the energy transfer rate ϵ_p, transfer region, characterized by the turbulent kinetic energy k_t and the dissipation rate ϵ_t and dissipation region, where the turbulent kinetic energy is dissipated into heat.

TURBULENCE MODELING

The turbulence modeling the most widely used is based on the eddy viscosity concept. However, this approach is questionable for many flows, especially for turbulence anisotropy and compressible shear flows. A second-moment closure permits a finer description of the turbulence behaviour.
The second-order models are based on the solution of Reynolds-stress tensor and dissipation-rate equations. The first Reynolds-stress model was introduced by Launder, Reece and Rodi in 1975. This model is based on incompressible Navier-Stokes equations and uses the Reynolds average for all variables.
Wilcox and Rubesin proposed a new formulation of the second-order closure replacing the equation of the dissipation rate ϵ by an equation of rotational ω^2, keeping entirely the same stress closure Π_{ij}. Their model has shown some improvements for flow geometries at strong curvature.
Recently, Wilcox proposed a second-order model with multiscale formulations. Indeed, this approach consists in modeling two different flow regions, which are :

- ▷ **Large eddies** : contain most of the energy of the turbulence, contain very little vorticity, and transport the Reynolds stress tensor.
- ▷ **Small eddies** : Contain a lot of vorticity, a very small energy, are isotropic, and dissipate into heat.

The modeled Reynolds stress equations with multiscale formulation are :

$$\frac{\partial}{\partial t}\overline{\rho}\widetilde{u_i''u_j''} + \frac{\partial}{\partial x_k}\overline{\rho}\widetilde{U}_k\widetilde{u_i''u_j''} = \underbrace{-\overline{\rho}\widetilde{u_i''u_k''}\frac{\partial \widetilde{U}_j}{\partial x_k} - \overline{\rho}\widetilde{u_j''u_k''}\frac{\partial \widetilde{U}_i}{\partial x_k}}_{Production\ P_{ij}}$$

$$\underbrace{+\hat{\alpha}\left(P_{ij} - \frac{2}{3}P\delta_{ij}\right) + \hat{\beta}\left(Q_{ij} - \frac{2}{3}P\delta_{ij}\right) + \hat{\gamma}\rho k\left(S_{ij} - \frac{1}{3}S_{kk}\delta_{ij}\right)}_{Linear\ Redistribution}$$

$$\underbrace{-\beta^* C_1\ \omega\left(\overline{\rho}\widetilde{u_i''u_j''} - \frac{2}{3}\rho k\delta_{ij}\right)}_{Quadratic\ Redistribution} \qquad (1)$$

$$\underbrace{+\frac{\partial}{\partial x_k}\left[C_s'\frac{k}{\epsilon}\widetilde{u_k''u_l''}\frac{\partial}{\partial x_l}\widetilde{u_i''u_j''}\right]}_{Turbulent\ Diffusion}$$

$$\underbrace{-\frac{2}{3}\beta^*\rho\omega k\delta_{ij}}_{Destruction}$$

At this system, three supplementary equations are added, which are :

- ▷ Total turbulent kinetic energy equation :

$$\frac{D(\rho k)}{Dt} = P - \beta^*\rho\omega k + \frac{\partial}{\partial x_k}\left[(\mu + \sigma^*\mu_t)\frac{\partial k}{\partial x_k}\right] \qquad (2)$$

- ▷ Turbulent kinetic energy equation for large eddies :

$$\frac{D(\rho k_p)}{Dt} = (1 - \hat{\alpha} - \hat{\beta})P - \beta^*\rho\omega k\left(\frac{k_p}{k}\right)^{3/2} \qquad (3)$$

- ▷ Dissipation-rate equation ω :

$$\frac{D(\rho\omega)}{Dt} = \gamma\frac{\omega}{k}P - \beta^*\rho\omega^2 + \frac{\partial}{\partial x_k}\left[(\mu + \sigma^*\mu_t)\frac{\partial \omega}{\partial x_k}\right] \qquad (4)$$

The tensors P_{ij} and Q_{ij} are given by :

$$P_{ij} = -\overline{\rho}\widetilde{u_i''u_k''}\frac{\partial \widetilde{U}_j}{\partial x_k} - \overline{\rho}\widetilde{u_j''u_k''}\frac{\partial \widetilde{U}_i}{\partial x_k}$$

$$Q_{ij} = -\overline{\rho}\widetilde{u_i''u_k''}\frac{\partial \widetilde{U}_k}{\partial x_j} - \overline{\rho}\widetilde{u_j''u_k''}\frac{\partial \widetilde{U}_k}{\partial x_i}$$

where

$$P = -\overline{\rho}\widetilde{u_m''u_n''}\frac{\partial \widetilde{U}_n}{\partial x_m}$$

Finally, the ten closure coefficients appearing in the model are :

$$\hat{\alpha} = 42/55 \quad \hat{\beta} = 6/55 \quad \hat{\gamma} = 1/4$$
$$\beta = 3/40 \quad \gamma = 4/5 \quad \sigma = 1/2$$
$$\beta^* = 9/100 \quad \sigma^* = 1/2 \quad C_1 = 1 + 4\left(\frac{k_p}{k}\right)^{3/2}$$

For a 2D flow, the model contains six transport equations. Theses ones coupled with Navier-Stokes equations (mass, momentum and energy conservations) make a total of ten equations to solve.
In this study, we examine the performances of the previous model, called **RSM multiscale**, and applied to a wide range of turbulent flows.

COMPUTATIONAL RESULTS

In this paper, we examine the performance of multiple-time-scale models on complex flows at high speed including afterbody flows. The computations are performed by an explicit-implicit time-dependent finite volume technique with a flux-splitting formulation.

Concerning the test cases under study, the flowfield is simulated numerically by solving axisymmetric and 2D Navier-Stokes equations in combination with different turbulent models: Jones and Launder $k-\epsilon$ model [5], a variety of multiple-time-scale models [6,7], including the partial equations for Reynolds stress transport [13].

As a first step in turbulence modeling, the performances of the previous models are compared and analyzed critically for a wide range of turbulent flows including supersonic mixing layers [3], near wall turbulent boundary layer with zero adverse pressure gradient [8] and supersonic exhaust jet [9]. The second step of the study is to provide a more comprehensive testing and evaluation of these models for realistic afterbody configurations for which detailed measurements are available [1].

Equilibrium boundary layer flow

The experimental data for the fully developed boundary layer flow over a flat plate can be found in ref [8] (see Klebanoff 1953). The inlet freestream velocity is 15 m/s, the boundary layer thickness is 76 mm and the Reynolds number is about 10^6.

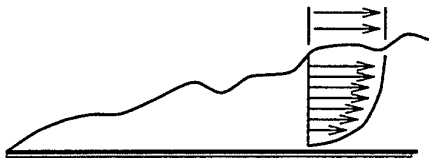


Figure 2: *The flat plate boundary layer*

Figure 3 shows the normalized mean velocity profile for a flat plate turbulent boundary layer.

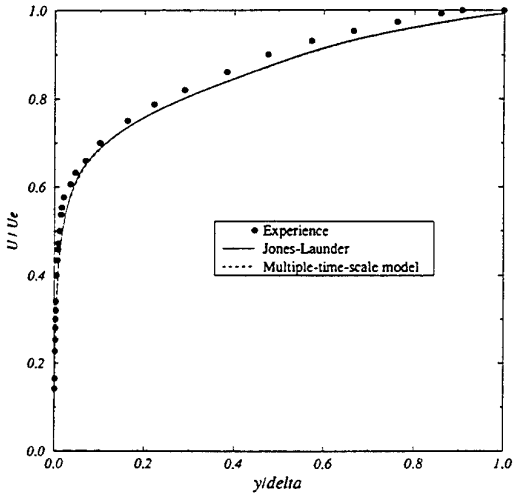


Figure 3: *The flat plate boundary layer, prediction of normalized velocity profile*

In this graph, numerical results of multiple-time-scale and $k-\epsilon$ turbulence models show good agreement with experimental data. Indeed for an equilibrium flow, the predictions using the multiple-time-scale model are not significantly different from those obtained with a single-time-scale one. Similar results have been obtained by Schiestel (1983) and Gleize et al. (1996).

Compressible mixing layer

In this study, we are interested in the mixing layer studied experimentally by Goebel et Dutton in a supersonic wind-tunnel at the University of Illinois at Urbana-Champaign. A wide variety of conditions has been investigated with freestream velocity ratios ranging from 0.16 to 0.79, freestream density ratios ranging from 0.57 to 1.55, and convective Mach numbers ranging from 0.20 to 1.0. This range of convective Mach numbers permits to illustrate the region of significant compressibility effects.

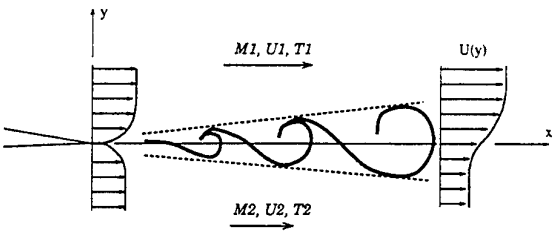


Figure 4: *Shear-layer geometry*

Furthermore, we examine in detail the flow configuration with convective Mach number $M_c = 0.46$ and Reynolds number $R_e = 12.10^6\ m^{-1}$, whose operating conditions are as following :

M_1, M_2	U_1, U_2 (m/s)	P (Pa)	U_2/U_1	ρ_2/ρ_1
1.91, 1.36	700, 399	46000	0.57	1.55

When a mixing layer is fully developed, it is possible to obtain similarity profiles. The existence of such a zone is verified due to the curve $U^* = f(Y^*)$ (see figure 5).

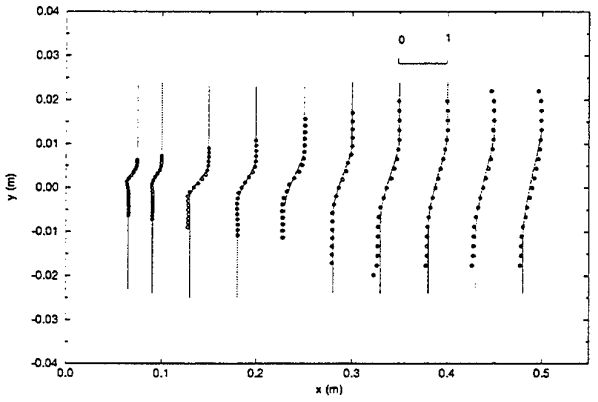


Figure 5: *Development of the normalized mean velocity U^*, multiscale models*

The near-wake region of the splitter plate is characterized by a transition from boundary layer flow to a fully developed mixing layer. In this region, the turbulence and mean flow are strongly unbalanced. The turbulent interactions mechanism depends on the nature of the incident boundary layers and on the geometry of the edge of the splitter plate. Locally, a subsonic pocket can appear with a recirculation zone, trapped between two supersonic flows.

From figure 5, it can be seen that the multiscale models (with or without Reynolds stress transport) are the

aptest to describe the transition zone in very good agreement with experimental data. However, the classical $k-\epsilon$ model shows a deficit for the first four stations (see Hadjadj 1997).

▷ **Compressibility effect**

In this section, we analyze the capacity of the used turbulent model to predict the compressibility effects. So, we have calculated six mixing layers varying the convecting Mach number from 0.2 to 1.15 and keeping constant the freestream velocity ratio $r=0.57$, the freestream density ratio $s = 1.55$ and the nominal Reynolds number $R_e=12.10^6\ m^{-1}$.

In the graph 6, we present the results obtained with the classical $k-\epsilon$ model and those obtained with the compressible RSM multiscale model. In this way, the normalized growth rate, function of the convective Mach number, are compared to different experimental results correlated with the empirical curve.

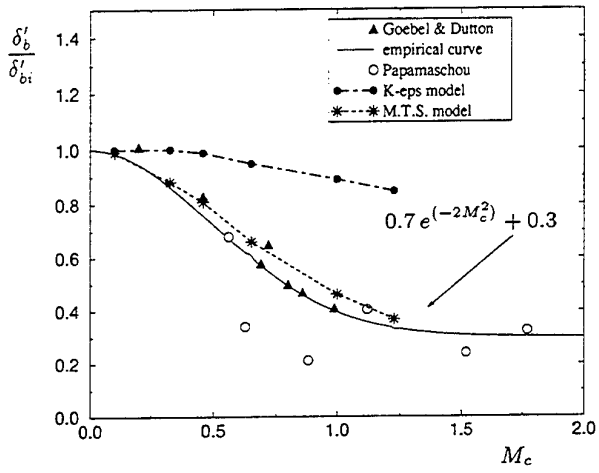


Figure 6: *Normalized shear layer spread rate vs. convective Mach number*

We remarque that beyond the convective Mach number $M_c=0.5$, the curve decreases and tends to an asymptotic value for high convective Mach numbers. The RSM multiscale model gives a normalized growth rate very close to the experimental data, while the incompressible $k-\epsilon$ model gives a constant growth rate for different convective Mach numbers. This result shows the capacity of the RSM multiscale model to predict correctly the compressibility effects.

▷ **Anisotropy behavior**

Afterwards, we examine the Reynolds stress tensor. The classical $k-\epsilon$ model is based on the isotrope viscosity hypothesis, which is unable to describe the Reynolds stress behaviour. Indeed, the calculation underestimates the fluctuating longitudinal velocity component $-\widetilde{u''}$ and overestimates the fluctuating transversal velocity $-\widetilde{v''}$ component along the mixing layer.

Figure 7 compares computed and measured variations of the maximum ratio of the Reynolds tensor $-\widetilde{u''^2}/k$, $-\widetilde{v''^2}/k$ and the turbulent shear stress $-\widetilde{u''v''}/k$ for a supersonic mixing layer at convective Mach number equal to 0.46. As shown, the multiple-time-scale model accounts for the disalignment of the Reynolds-stress-tensor and gives satisfactory results when the turbulence approaches an asymptotic state.

We notice a disparity of 15 % for $-\widetilde{u''^2}/k$ and 30 % for $-\widetilde{v''^2}/k$ compared to experimental data. This result, even if it does not coincide totally with experimental points, is completely acceptable, in comparison to the classical second order model that produces double disparities from experimental data (see Hadjadj 1997).

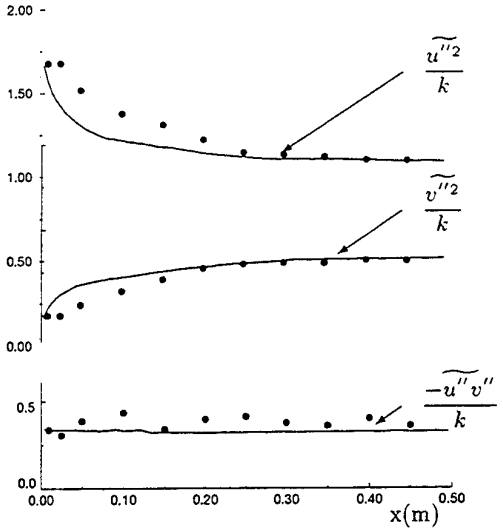


Figure 7: *Evolution of the maximum ratio of the Reynolds tensor along the mixing layer*

However, the turbulent shear stress $-\widetilde{u''v''}/k$ is practically constant and equal to its equilibrium value.

Axisymmetric afterbody flow

The next step of this study has to do with realistic afterbody configurations. The test case under-investigation is the S3Ch single-flux axisymmetric nozzle (see Bailly et al. 1994). The existing availability of experimental results (mean profiles and turbulent quantities) permits an accurate validation of turbulence models using CFD.

The operating conditions for the selected test case are :

- **Internal flow**
  - stagnation pressure : $P_t = 3.15\,10^5$ Pa
  - stagnation temperature : $T_t = 900$ K (hot jet)
  - pressure ratio : $P_t/P_a = 4.80$
- **External flow**
  - $M_\infty = 0.8$
  - stagnation pressure : $P_t = 10^5$ Pa
  - stagnation temperature : $T_t = 300$ K
  - incident boundary layer thickness ($\delta \simeq 8\,mm$) à $x = -218\,mm$

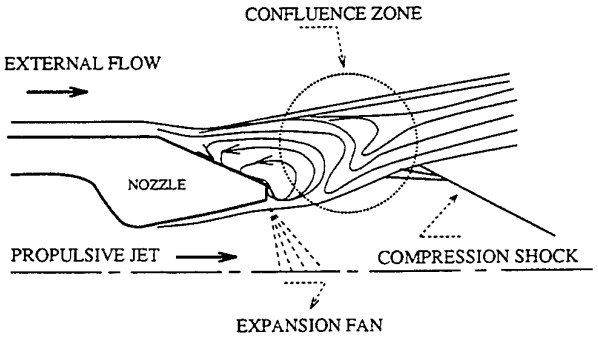
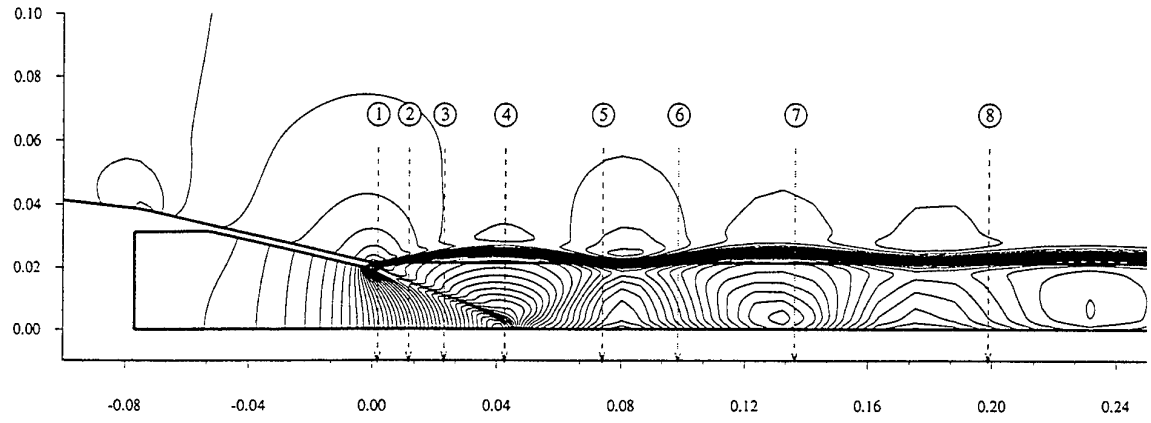


Figure 8: *Afterbody flow with supersonic underexpanded jet*



Stations	1	2	3	4	5	6	7	8
x (mm)	4.20	8.70	21	42	74	100	135	200
x/D_{col}	0.11	0.22	0.53	1.07	1.88	2.54	3.43	5.08

Figure 9: *Locations of Laser Doppler Velocimetry survey*

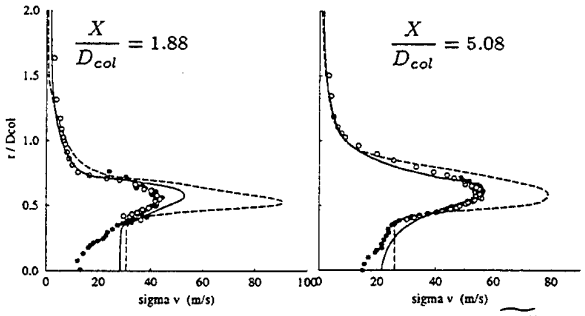


Figure 10: *Fluctuating radial velocity,* $-\widetilde{v''}$

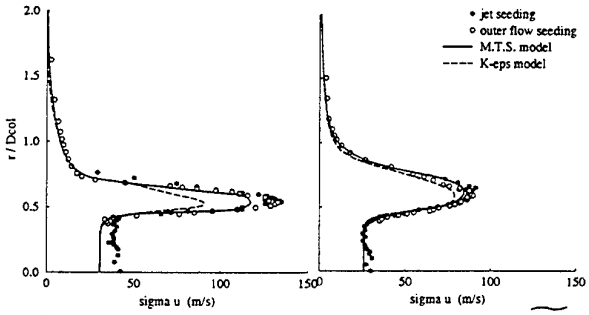


Figure 11: *Fluctuating longitudinal velocity,* $-\widetilde{u''}$

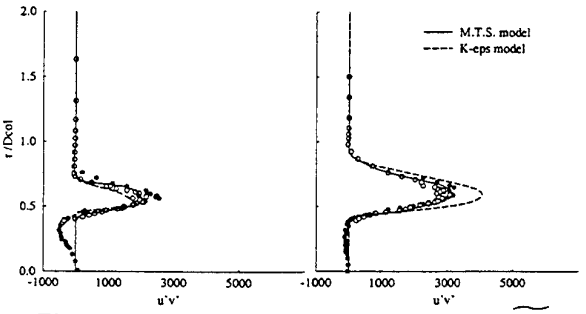


Figure 12: *Turbulent shear stress profile,* $-\widetilde{u''v''}$

The flow issuing from the converging nozzle has a higher pressure than the outer flow. Therefore, the jet is under-expanded and adapts itself to the environment through a train of Mach cells. The structure of such a flow is schematically shown in figure 8. The flow near the trailing edge of the nozzle is largely affected by the nature of the two incoming jets, and can influence the engine's performances.

Figure 9 shows different locations of a 2D Laser Doppler Velocimetry (LDV) survey. In this case, the LDV provides information on both mean velocity and turbulence profiles at each location : starting from $x/D_{col}=0.11$ to $x/D_{col}=5.08$, where D_{col} is a nozzle throat diameter. The first four locations, situated at $x/D_{col} \leq 1.07$, concern the region close to the nozzle exit including the compression shock and the confluence zone. The last two stations concern the far jet downstream of the nozzle.

The numerical results of mean velocity profiles, obtained with the RSM multiscale model, are of excellent quality and show a very good agreement between computation and experimental data.

On the figures 10, 11 and 12, we present the results of the turbulent quantities (fluctuating longitudinal and radial velocity with the turbulent shear stress profile) at two differents locations ($x/D_{col}=1.88$ and $x/D_{col}=5.08$).

The comparison between the experimental and the numerical data shows that the $k-\epsilon$ model predict discrepancies of 36 % for σu and 53 % for σv component. These discrepancies are substantially reduced at 4 % and 7 % respectively with the RSM model (see figures 10, 11 and 12).

Practically, in both near wake zone and mixing layer region the RSM multiscale model predicts well the maximum of turbulent intensity having the good spread rate.

CONCLUSION

This work deals with the validation of multiscale turbulence models, with or without transport of Reynolds stress tensor, in the case of compressible shear flows. The computational results showed that:

- The multiscale models are able to predict correctly the physical process in regions where the flow is in turbulent nonequilibrium (in the transition zone downstream to the separation flat plate, near wake region ...).
- The RSM multiscale model, with compressible correction, is able to reproduce in a very satisfactory way the effects of compressibility (The normalized growth rate decreases rapidly with increasing convective Mach number).
- Taking into account the processes of turbulent diffusion, this latter model describes quite fairly the anisotropic phenomena of the Reynolds tensor, especially next to the wake region. The levels of speed fluctuations are better taken into account than the ones issued from a classical second order closure.
- Finally, it is important to notice that the multiscale models do not depend on the position of the wave partitioning at the entrance of the calculation domain. In deed, whatever might be the energy level initially attributed to the large and small eddies, these models give the same equilibrium value for energy. This value is around 65% for the large eddies and 35 % for the small ones, in the case of supersonic mixing layer.

The next step of the study is to provide a more comprehensive testing and evaluating of the multiple-time-scale models subjected to stringent boundary layer separation flow, especially for shock wave/turbulent boundary layer and shock/shock interactions.

Acknowledgements : This research has been supported by the DRET-DGA under Contract No 94/2502, Opération MARCO. The authors would like to thank Dr G. Rollin and Dr T. Mauffret from SNECMA for their collaboration. Computations were carried out at the CRIHAN (Centre de Resources Informatiques de HAute Normandie, Rouen).

REFERENCES

Bailly, D., Francois, C., Pilon, J. A. and Regard, D., Qualification en subsonique des écoulements issus de la tuyère de référence et de la tuyère ventillée, *Rapport de synthèse final No 51/3482 AY, ONERA, 1994*

Gleize, V., Schiestel, R. and Couaillier, V., Multiple scale modeling of turbulent nonequilibrium boundary layer flows, *Phys. Fluids 8 (10), October 1996*

Goebel, S. G. and Dutton, J. C., Experimental study of compressible turbulent mixing layers, *AIAA J. VOL. 29, No. 4, 1991*

Hadjadj, A., Analyse physique et simulation numérique des écoulements compressibles, application aux tuyères de propulseurs, *Thèse de Doctorat, Université de Rouen, 1997*

W. P. Jones, W. P. and Launder, B. E., The prediction of laminarization with a two-equation model of turbulence, *Int. J. Heat Mass Transfer 15, 301, 1972*

Kim, S. W., Calculation of divergent channel flows with a multiple-time-scale turbulence model, *AIAA Journal, VOL. 29, No. 4, April, 1991*

Kim, S. W., Numerical investigation of separated transonic turbulent flows with a multiple-time-scale turbulence model, *NASA TM 102499, ICOMP-90-04, 1990*

Klebanoff, P. S., Characteristics of turbulence in a boundary layer with zero pressure gradient, *NACA report, 1247, 1953.*

Mistral, S., Jacquin, L., Gefroy, L. and Losfeld, G., Etude d'un jet supersonique coaxial chauffé : Résultats expérimentaux *Rapport Technique No. 51/1147AY ONERA. 1991*

Schiestel, R., Multiple scale concept in turbulence modeling, Journal de Mécanique théorique et appliquée, VOL. 2, No. 3, 1983

Schiestel, R., Multiple-time-scale modeling of turbulent flows in one point closures, *Phys. Fluids 30 (3), March 1987*

Vandromme, D., Contribution à la modélisation et à la prédiction d'écoulements turbulents à masse volumique variable, *Thèse d'Etat, Université de Lille, 1983*

Wilcox, D. C., Multiscale model for turbulent flows, *AIAA Journal, VOL. 26, No. 11, November 1988*

Zeidan, B. and Djilali, N., Multiple-time-scale turbulence model computations of flow over a square rib, AIAA Journal, VOL. 34, No. 3, 1995

MODELING OF INHOMOGENEOUS COMPRESSIBLE TURBULENCE USING A TWO-SCALE STATISTICAL THEORY

Fujihiro Hamba
Institute of Industrial Science
University of Tokyo
Roppongi, Minato-ku, Tokyo 106
Japan

ABSTRACT

Turbulence models for compressible flows are investigated using a statistical theory called the two-scale direct-interaction approximation. Inertial-range spectra for velocity and density variances are assumed to derive models for several correlations systematically; they include the dilatation dissipation, mass flux, Reynolds stress, and pressure-dilatation correlation. Model expressions are shown to contain two important parameters: the turbulent Mach number and the density variance normalized by the mean density. Typical terms are material derivatives of the turbulent kinetic energy and its dissipation rate as well as the mean velocity divergence. Direct numerical simulation data of isotropic and homogeneous shear turbulence are used to examine models for the dilatation dissipation. The normalized density variance is shown to be useful to explain results from two runs of isotropic turbulence with different initial conditions.

INTRODUCTION

Turbulence modeling plays an important role in the study of high-speed flows in engineering and aerodynamic problems; they include flows in supersonic combustion engines and over hypersonic transport aircraft. The enhancement of the kinetic energy dissipation by the dilatational terms is one of the typical compressibility effects. Zeman (1990) and Sarkar *et al.* (1991) proposed that the dilatation dissipation is proportional to the solenoidal dissipation and is a function of the turbulent Mach number. Sarkar (1992) also modeled the pressure-dilatation correlation using the turbulent Mach number. Zeman (1991) related the correlation to the rate of change of the pressure variance. Recently, Sarkar (1995) performed DNS of homogeneous shear flows to show that the reduced growth rate of kinetic energy is primarily due to a reduction of the turbulence production and that the gradient Mach number is important for understanding this compressibility effect.

Using a statistical theory Yoshizawa (1990) pointed out that compressibility effects are tightly linked with density fluctuations. He proposed a three-equation model that consists of transport equations for the kinetic energy, its dissipation, and the density variance (Yoshizawa 1992). Taulbee and VanOsdol (1991) also modeled transport equations for the density variance and the mass flux. Fujiwara and Arakawa (1993) proposed another type of three-equation model involving the sum of the normalized compressible turbulent kinetic energy and the density variance.

Yoshizawa (1990) used a statistical theory called the two-scale direct-interaction approximation (TSDIA) to derive compressible turbulence models. This method was originally developed for incompressible turbulence (Yoshizawa 1984). The TSDIA consists of two main procedures. First, two-scale variables are introduced and the direct-interaction approximation (DIA) is applied to express statistical quantities in terms of two-time velocity correlations in wavenumber space. Second, by using inertial-range spectra, expressions are simplified to derive one-point closure models. However, the second procedure has not been carried out for compressible turbulence because detailed inertial-range spectra are not available. Instead, Yoshizawa (1992) applied dimensional analysis to results of the first procedure. He also proposed an alternative simplified approach that treats the governing equations in physical space (Yoshizawa 1995). Several model expressions were obtained and an important effect of density fluctuations was clarified by these methods. Some ambiguity still remains; since several nondimensional parameters are involved in compressible turbulence, statistical quantities cannot be uniquely modeled only by dimensional analysis.

The energy spectrum for compressible turbulence has been examined theoretically and numerically to some extent. Moiseev *et al.* (1981) theoretically obtained a spectral form that depends on the turbulent Mach number. Kida and Orszag

(1990) showed that the spectrum of the solenoidal component in their DNS is very close to that for incompressible flows whereas the spectrum of the compressible component depends strongly on the turbulent Mach number. Bataille and Bertoglio (1993) used eddy-damped quasi-normal Markovian theory to examine inertial-range spectra of weakly compressible turbulence. Although more study needs to be done to understand inertial-range behavior, these findings help us to assume some spectral forms for compressible turbulence.

In this work, we introduce inertial-range spectra of density and velocity variances to simplify results of the first procedure of TSDIA. A deviation from the Kolmogorov spectrum is assumed for the spectrum of the compressible velocity variance. The dependence on nondimensional parameters is systematically obtained by the simplification. We apply the TSDIA to several correlations included in the mean-field equations to propose a three-equation model. We examine models for the dilatation dissipation using DNS of isotropic and homogeneous shear turbulence.

FUNDAMENTAL EQUATIONS

The motion of a viscous compressible fluid is described by the equations for the density ρ, the velocity u_i, and the internal energy e

$$\frac{\partial \rho}{\partial t}+\frac{\partial}{\partial x_i}(\rho u_i)=0 \tag{1}$$

$$\frac{\partial}{\partial t}(\rho u_i)+\frac{\partial}{\partial x_j}(\rho u_j u_i)=-\frac{\partial p}{\partial x_i}+\frac{\partial}{\partial x_j}(\mu s_{ji}) \tag{2}$$

$$\frac{\partial}{\partial t}(\rho e)+\frac{\partial}{\partial x_i}(\rho e u_i)=-p\frac{\partial u_i}{\partial x_i}+\mu s_{ji}\frac{\partial u_i}{\partial x_j}+\frac{\partial}{\partial x_i}\left(\lambda\frac{\partial \theta}{\partial x_i}\right) \tag{3}$$

where μ is the viscosity, λ is the thermal conductivity, and θ is the temperature. The deviatoric part of the strain rate tensor, s_{ij}, is given by

$$s_{ij}=\frac{\partial u_i}{\partial x_j}+\frac{\partial u_j}{\partial x_i}-\frac{2}{3}\frac{\partial u_k}{\partial x_k}\delta_{ij} \tag{4}$$

For the perfect gas the pressure p and the internal energy e are written as

$$p=\rho R\theta=(\gamma-1)\rho e,\quad e=c_v\theta \tag{5}$$

where $\gamma=c_p/c_v$. Here, R is the specific gas constant and c_v and c_p are the specific heats at constant volume and pressure, respectively.

We divide a physical quantity f into the mean F and the fluctuation f'

$$f=F+f',\quad F=\langle f\rangle \tag{6}$$

where f denotes ρ, u_i, e, p, s_{ij}, and θ. Some mean quantities are denoted by an overbar as $\bar{\rho}$. By taking the ensemble average of (1)-(3), we obtain the equations for the mean quantities $\bar{\rho}$, U_i, and E. Those equations contain several correlations such as the mass flux $\langle\rho' u_i'\rangle$ and the Reynolds stress $\langle u_i' u_j'\rangle$. The correlations need to be modeled to close the mean-field equations.

Yoshizawa (1990) pointed out that compressibility effects are tightly linked with the density fluctuations; he proposed a three-equation model that consists of the equations for the turbulent kinetic energy $K(=\langle u_i'^2\rangle/2)$, its dissipation rate ε, and the density variance $K_\rho(=\langle\rho'^2\rangle)$. The equations for K and K_ρ can be written as

$$\frac{DK}{Dt}=-\langle u_i' u_j'\rangle\frac{\partial U_i}{\partial x_j}-\varepsilon+\frac{1}{\bar{\rho}}\left\langle p'\frac{\partial u_i'}{\partial x_i}\right\rangle-\frac{1}{2}\frac{\partial}{\partial x_j}\langle u_i'^2 u_j'\rangle$$

$$-\frac{1}{\bar{\rho}}\frac{\partial}{\partial x_i}\langle p' u_i'\rangle+\frac{1}{\bar{\rho}^2}\langle\rho' u_i'\rangle\frac{\partial P}{\partial x_i} \tag{7}$$

$$\frac{DK_\rho}{Dt}=-2K_\rho\frac{\partial U_i}{\partial x_i}-2\langle\rho' u_i'\rangle\frac{\partial\bar{\rho}}{\partial x_i}-2\bar{\rho}\left\langle\rho'\frac{\partial u_i'}{\partial x_i}\right\rangle-\frac{\partial}{\partial x_i}\langle\rho'^2 u_i'\rangle$$

$$-\left\langle\rho'^2\frac{\partial u_i'}{\partial x_i}\right\rangle \tag{8}$$

The correlations included in (7) and (8) as well as the ε equation itself need to be modeled in terms of the mean quantities and the three variables.

Model expressions shown later contain two nondimensional parameters: the turbulent Mach number M_t ($=\sqrt{2K}/\bar{c}$ where $\bar{c}$ is the mean sound speed) and the normalized density variance $\rho_n^2(=K_\rho/\bar{\rho}^2)$. By adopting K_ρ as one of the basic quantities we can use ρ_n^2 as a parameter independent of M_t. Modeling with the two parameters is expected to be more flexible than that with M_t only.

TWO-SCALE STATISTICAL THEORY

Here, we give a brief summary of the procedure of the TSDIA. Its mathematical details were given in Yoshizawa (1992).

We first introduce two time and space variables using a small-scale parameter δ as

$$\xi(\equiv x),\quad X(\equiv\delta x),\quad \tau(\equiv t),\quad T(\equiv\delta t) \tag{9}$$

Here, the fast variables ξ and τ describe the rapid variations of the fluctuating field whereas the slow variables $\mathbf{X}$ and T describe the slow variations of the mean field. A quantity f can be written as

$$f=F(X,T)+f'(\xi,X,\tau,T) \tag{10}$$

Using the Fourier transform with respect to ξ we express f' as

$$f'(\xi,X,\tau,T)=\int dk f(k,X,\tau,T)\exp\left[-ik\cdot(\xi-U\tau)\right] \tag{11}$$

This representation is equivalent to the viewpoint that the fluctuating motion consists of many small eddies moving with the mean velocity $\mathbf{U}$. Hereafter, the dependence of $f(\mathbf{k},\mathbf{X},\tau,T)$ on $\mathbf{X}$ and T is not written explicitly.

Applying (9)-(11) to the equations for ρ', u_i', and p' (or e') we obtain a system of equations for the fluctuating field in wavenumber space. We expand the fluctuation $f(\mathbf{k},\tau)$ in powers of δ:

$$f(k,\tau)=\sum_{n=0}^{\infty}f_n(k,\tau) \tag{12}$$

Substituting (12) into the system of equations and equating quantities in each order of δ we have an equation for each quantity $f_n(\mathbf{k},\tau)$. By introducing the Green's functions for ρ_0, u_{0i}, and p_0. we can formally solve the equations for $f_n(n\geq 1)$ in terms of the lower-order quantities.

A correlation included in the mean-field equations can be written as

$$\langle f'(x,t)g'(x,t)\rangle=\int dk\langle f(k,\tau)g(-k,\tau)\rangle/\delta(0)$$

$$=\int dk\left(\langle f_0 g_0\rangle+\langle f_1 g_0\rangle+\langle f_0 g_1\rangle+\cdots\right)/\delta(0) \tag{13}$$

Here, $\delta(0)$ denotes the delta function $\delta(k)$ where the one-dimensional wavenumber k equals 0.

Substituting the formal solution for f_n and g_n ($n\geq 1$) and applying the DIA we obtain a model expression for the correlation. It is written in terms of the mean field as well as the basic correlations and the Green's functions defined by

$$Q_\rho(k,\tau,\tau')=\langle\rho_0(k,\tau)\rho_0(-k,\tau')\rangle/\delta(0)=Q_\rho(k,\tau,\tau') \tag{14}$$

$$Q_{ij}(k,\tau,\tau')=\langle u_{0i}(k,\tau)u_{0j}(-k,\tau')\rangle/\delta(0)$$

$$= D_{ij}(\mathbf{k})Q_s(k,\tau,\tau') + \Pi_{ij}(\mathbf{k})Q_c(k,\tau,\tau') \quad (15)$$

$$G_p(k,\tau,\tau') = \left\langle \hat{G}_p(k,\tau,\tau') \right\rangle = G_p(k,\tau,\tau') \quad (16)$$

$$G_{ij}(k,\tau,\tau') = \left\langle \hat{G}_{ij}(k,\tau,\tau') \right\rangle$$

$$= D_{ij}(\mathbf{k})G_s(k,\tau,\tau') + \Pi_{ij}(\mathbf{k})G_c(k,\tau,\tau') \quad (17)$$

$$G_e(k,\tau,\tau') = \left\langle \hat{G}_e(k,\tau,\tau') \right\rangle = G_e(k,\tau,\tau') \quad (18)$$

where

$$D_{ij}(\mathbf{k}) = \delta_{ij} - k_i k_j / k^2, \quad \Pi_{ij}(\mathbf{k}) = k_i k_j / k^2 \quad (19)$$

For example, the expression for the eddy viscosity can be written as

$$\nu_e \approx \int_0^\infty dk \int_{-\infty}^{\tau} d\tau' G_s(k,\tau,\tau') Q_s(k,\tau,\tau') + \cdots \quad (20)$$

The expression includes wavenumber and time integrals of two-time correlations and Green's functions. It is too complicated to be a practical model; some simplification is necessary.

Following the TSDIA for incompressible turbulence, we assume inertial-range forms for the fundamental statistical quantities as

$$Q_a(k,\tau,\tau') = \sigma_a(k)\exp\left[-\omega_a(k)|\tau-\tau'|\right], \quad a = (\rho,s,c) \quad (21)$$

$$G_b(k,\tau,\tau') = H(\tau-\tau')\exp\left[-\omega_b'(k)(|\tau-\tau'|)\right], \quad b = (\rho,s,c,e) \quad (22)$$

where

$$\sigma_\rho(k) = C_{\sigma\rho} M_t^2 \bar{\rho}^2 \varepsilon_d \varepsilon^{-1} k^{-3-\alpha-2\beta} k_m^{\alpha+2\beta} H(k-k_m) \quad (23)$$

$$\sigma_s(k) = C_{\sigma s} \varepsilon^{2/3} k^{-11/3} H(k-k_m) \quad (24)$$

$$\sigma_c(k) = C_{\sigma c} \varepsilon_d \varepsilon^{-1/3} k^{-(11/3)-\alpha} k_m^{\alpha} H(k-k_m) \quad (25)$$

$$\left[\omega_s(k), \omega_s'(k)\right] = \left[C_{\omega s}, C_{\omega s}'\right] \varepsilon^{1/3} k^{2/3} \quad (26)$$

$$\left[\omega_\rho(k), \omega_\rho'(k), \omega_c(k), \omega_c'(k), \omega_e'(k)\right]$$

$$= \left[C_{\omega\rho}, C_{\omega\rho}', C_{\omega c}, C_{\omega c}', C_{\omega e}'\right] M_t^{-1} \varepsilon^{1/3} k^{(2/3)+\beta} k_m^{\beta} \quad (27)$$

Here, $C_{\sigma a}$, $C_{\omega a}$, and $C'_{\omega b}$ are model constants, H(k) and H(τ) are the unit step functions, k_m is the wavenumber of the energy-containing range, and ε, ε_d, and M_t are the dissipation, the dilatation dissipation, and the turbulent Mach number defined by

$$\varepsilon = \bar{\nu}\left\langle s_{ji}' \frac{\partial u_i'}{\partial x_j} \right\rangle, \quad \varepsilon_d = \frac{4}{3}\bar{\nu}\left\langle \left(\frac{\partial u_i'}{\partial x_i} \right)^2 \right\rangle, \quad M_t = \frac{\sqrt{2K}}{\bar{c}} = \left(\frac{2\bar{\rho}K}{\gamma P} \right)^{1/2} \quad (28)$$

respectively. For the solenoidal quantities σ_s, ω_s, and ω'_s the spectra are the same as those for incompressible turbulence. The compressible part of energy spectrum, σ_c is proportional to ε_d. This is because the ratio of the compressible to solenoidal parts of turbulent kinetic energy is shown to be proportional to the ratio of the dilatational to solenoidal dissipations. The spectrum is steeper than the Kolmogorov one by α. Moiseev *et al.* (1981) showed the deviation α is a function of M_t. Here, we do not include such M_t dependence but consider α an unknown numerical parameter. The deviation from the incompressible inertial-range form is also introduced into ω(k) for compressible quantities. We assume that time scales for compressible quantities are shorter than those for incompressible ones; the ratio is of the order of M_t.

For example, substituting the above spectral forms into (20), we obtain a one-point closure model for the eddy viscosity as a function of k_m and ε. By converting k_m into K and ε we have a usual expression proportional to K^2/ε.

RESULTS

Dilatation Dissipation

We applied the procedure of the previous section to $\langle \rho'\rho' \rangle$ to obtain an expression for the density variance; it is a function of the mean field $\bar{\rho}$, U_i, and P as well as the quantities K, ε, ε_d, and M_t. Since the transport equation for K_ρ is solved in the K-ε-K_ρ model, the modeling of K_ρ itself is not necessary. Instead, the expression can be considered a model for ε_d. Expanding ε_d in terms of the other quantities we have

$$\varepsilon_d = C_{\varepsilon d1} \frac{\rho_n^2}{M_t^2} \varepsilon \left[1 + C_{\varepsilon d7} M_t \left(2\frac{K}{\varepsilon}\frac{\partial U_i}{\partial x_i} + \frac{1}{4}\frac{K}{\varepsilon\bar{\rho}}\frac{D\bar{\rho}}{Dt} - \frac{1}{4}\frac{K}{\varepsilon P}\frac{DP}{Dt} \right.\right.$$

$$\left.\left. + \frac{3}{2\varepsilon}\frac{DK}{Dt} - \frac{K}{\varepsilon^2}\frac{D\varepsilon}{Dt} + \frac{K}{\varepsilon K_\rho}\frac{DK_\rho}{Dt} \right) \right] \quad (29)$$

where ρ_n^2 is the normalized density variance defined by

$$\rho_n^2 = K_\rho / \bar{\rho}^2 \quad (30)$$

and $C_{\varepsilon d1}$ and $C_{\varepsilon d7}$ are model constants. Hereafter, C_{an} denotes a model constant where 'a' represents a physical quantity and 'n' is the number of the term.

The factor before the square bracket in (29) shows the ratio $\varepsilon_d/\varepsilon$ is proportional to ρ_n^2/M_t^2. Yoshizawa (1992) pointed out that this quantity is important in characterizing the compressibility effect and introduced a parameter χ(= ρ_n^2/M_t^2). Yoshizawa (1995) paid attention to the importance of the parameter χ and proposed the model:

$$\varepsilon_d/\varepsilon_s = C_{\varepsilon dY}\chi \quad (31)$$

where $\varepsilon_s = \varepsilon - \varepsilon_d$ and $C_{\varepsilon dY}$ is a model constant. This model is the same as (29) to the first order.

The modeling of ε_d was originally investigated by Sarkar *et al.* (1991) and Zeman (1990). Sarkar *et al.* (1991) used asymptotic analysis and DNS to model ε_d as follows

$$\varepsilon_d/\varepsilon_s = C_{\varepsilon dS} M_t^2 \quad (32)$$

Zeman (1990) assumed the existence of shock-like structure in flow fields to derive the model

$$\varepsilon_d/\varepsilon_s = C_{\varepsilon dZ} F(M_t, K_{Mt}) \quad (33)$$

where K_{Mt} is the flatness factor of M_t and $F(M_t, K_{Mt})$ is a complicated integral. He also derived a simple algebraic expression for use in practice (Blaisdell and Zeman 1992)

Blaisdell *et al.* (1991) used DNS of decaying isotropic turbulence to examine the above two models. They carried out two simulations that had the same initial values of M_t but different initial ratios of compressible to solenoidal velocity variances. In spite of the same turbulent Mach number the two simulations showed different values of $\varepsilon_d/\varepsilon$. They concluded that the development of $\varepsilon_d/\varepsilon$ in isotropic turbulence depends more on its initial values than on the turbulent Mach number and that simulations of isotropic turbulence cannot be used to validate the proposed models. However, Yoshizawa's model as well as the present model show that $\varepsilon_d/\varepsilon$ depends not only on M_t but also on ρ_n^2. As was pointed out by Yoshizawa (1995) the difference in $\varepsilon_d/\varepsilon$ in the two simulations can be attributed to the difference in ρ_n^2. The assumption that $\varepsilon_d/\varepsilon$ depends only on M_t seems too restrictive to capture the behavior of decaying isotropic turbulence. In the K-ε-K_ρ model we use the two parameters M_t and ρ_n; the development of ρ_n^2 is obtained from the transport equation for K_ρ.

Mass Flux

Since ensemble averaging is used in this work, the mean-velocity equation contains the mass flux; its modeling is

necessary. Taulbee and VanOsdol (1991) examined the transport equation for the mass fluctuating velocity $\langle\rho' u_i'\rangle/\bar{\rho}$ and modeled terms included in the equation. Instead of the transport equation we model the mass flux itself. It can be modeled as

$$\langle\rho' u_i'\rangle = -C_{\rho u1} M_t \frac{K^2}{\varepsilon}\frac{\partial\bar{\rho}}{\partial x_i}\left[1-2\frac{\rho_n^2}{M_t^2}+C_{\rho u3}\left(\frac{K}{\varepsilon}\frac{\partial U_i}{\partial x_i}+\frac{3}{\varepsilon}\frac{DK}{Dt}-\frac{5}{4}\frac{K}{\varepsilon^2}\frac{D\varepsilon}{Dt}\right)\right]-\frac{10+15\alpha}{10+6\alpha}C_{\rho u1}\frac{\rho_n^2}{M_t}\frac{K^2}{\varepsilon}\left[-\frac{17}{8}\frac{\partial\bar{\rho}}{\partial x_i}+\left(\frac{17}{8}-\frac{5}{2\gamma}\right)\frac{\bar{\rho}}{P}\frac{\partial P}{\partial x_i}+\frac{9}{4}\frac{\bar{\rho}}{K}\frac{\partial K}{\partial x_i}-\frac{3}{2}\frac{\bar{\rho}}{\varepsilon}\frac{\partial\varepsilon}{\partial x_i}+\frac{3}{2}\frac{\bar{\rho}}{K_\rho}\frac{\partial K_\rho}{\partial x_i}\right] \quad (34)$$

The term with the first square bracket depends on the gradient of mean density; it corresponds to the gradient-diffusion approximation. The eddy diffusivity is proportional to $M_t K^2/\varepsilon$. It is smaller than the eddy diffusivity in incompressible flows by a factor of M_t. The eddy diffusivity for the mass flux includes nonequilibrium effects due to DK/Dt and Dε/Dt as well as compressibility effects due to ρ_n^2/M_t^2 and $\partial U_i/\partial x_i$.

On the other hand, the term with the second square bracket also depends on the gradients of mean quantities other than $\bar{\rho}$; this effect is called cross diffusion. For example, when the gradients of $\bar{\rho}$ and P are small and the isentropic relations hold, the profile of P is proportional to that of $\bar{\rho}$; the pressure gradient term simply represents the modification of the eddy diffusivity. However, when the temperature changes rapidly due to heat release, the profiles of density and pressure may be different; in such a case the cross diffusion effect due to the pressure gradient can be important in the mass flux model.

Using the simplified approach Yoshizawa (1995) derived a model for the mass flux as follows

$$\langle\rho' u_i'\rangle = -\left[1+\frac{3(\gamma-1)}{\gamma}\frac{\sigma_\rho^2}{\sigma_e}\right]\frac{\nu_t}{\sigma_\rho}\frac{\partial\bar{\rho}}{\partial x_i}-\frac{3}{\gamma}\chi\nu_t\bar{\rho}\frac{1}{E}\frac{\partial E}{\partial x_i}-\frac{3}{2}\frac{K_\rho}{\bar{\rho}}\frac{\nu_t}{K}\frac{DU_i}{Dt} \quad (35)$$

where $\nu_T=(2/3)C_u(K^2/\varepsilon)$ and σ_ρ, σ_e, and C_u are model constants. If we assume that $P=(\gamma-1)\bar{\rho}E$ and $DU_i/Dt = -(1/\bar{\rho})\partial P/\partial x_i$ we can see that the second and third terms on the right-hand side correspond to the cross-diffusion term due to the mean pressure in (34). The major difference between (34) and (35) lies in the dependence of the eddy-diffusivity on M_t; the diffusivity of the former is of $O(M_t)$ whereas that of the latter is of O(1). This difference stems from the different dependence of the time scale for density fluctuations on M_t.

Reynolds Stress

Yoshizawa (1995) pointed out that compressibility effects are not incorporated into the Reynolds stress up to the order of δ; this order corresponds to the eddy-viscosity approximation. We calculated the Reynolds stress up to the order of δ^2 to obtain

$$\langle u_i' u_j'\rangle = \frac{2}{3}K\delta_{ij}-C_{uu1}\frac{K^2}{\varepsilon}\left(\frac{\partial U_i}{\partial x_j}+\frac{\partial U_j}{\partial x_i}\right)^*\times\left[1-2\frac{\rho_n^2}{M_t^2}+C_{uu4}\left(\frac{23}{49}\frac{K}{\varepsilon}\frac{\partial U_i}{\partial x_i}+\frac{1}{\varepsilon}\frac{DK}{Dt}-\frac{5}{12}\frac{K}{\varepsilon^2}\frac{D\varepsilon}{Dt}\right)\right]$$

$$+C_{uuA}\frac{K^3}{\varepsilon^2}\left[\frac{62}{105}\left(\frac{\partial U_i}{\partial x_k}\frac{\partial U_j}{\partial x_k}\right)^*+\frac{2}{35}\left(\frac{\partial U_k}{\partial x_i}\frac{\partial U_k}{\partial x_j}\right)^*+\frac{34}{105}\left(\frac{\partial U_i}{\partial x_k}\frac{\partial U_k}{\partial x_j}+\frac{\partial U_j}{\partial x_k}\frac{\partial U_k}{\partial x_i}\right)^*+\frac{7}{15}\frac{D}{Dt}\left(\frac{\partial U_i}{\partial x_j}+\frac{\partial U_j}{\partial x_i}\right)^*\right]$$

$$+C_{uu10}M_t\frac{K^3}{\varepsilon^2}\left[\frac{\partial}{\partial x_i}\left(\frac{1}{\bar{\rho}}\frac{\partial P}{\partial x_j}\right)+\frac{\partial}{\partial x_j}\left(\frac{1}{\bar{\rho}}\frac{\partial P}{\partial x_i}\right)\right]^* \quad (36)$$

where

$$\left(f_{ij}\right)^* \equiv f_{ij}-\frac{1}{3}f_{kk}\delta_{ij} \quad (37)$$

Except for the isotropic part, $(2/3)K\delta_{ij}$, the expression consists of three parts. The first part represents the modification of the eddy viscosity due to compressibility and nonequilibrium effects. The second part corresponds to nonlinear models that have already been investigated for incompressible flows (Speziale 1987). The third part represents the compressibility effect due to a mean pressure gradient.

The modification of the eddy viscosity due to DK/Dt and Dε/Dt has already been proposed for incompressible flows (Yoshizawa and Nisizima 1993). Yoshizawa (1995) also mentioned its importance for compressible flows. Expression (36) suggests that we should take into account not only the nonequilibrium effect but also the compressibility effects due to the density variance and mean-velocity divergence. Sarkar (1995) showed that the reduced growth rate of turbulence energy in homogeneous shear flows is primarily due to the decrease in turbulence production. Since the production term includes the Reynolds stress, compressibility effects on the Reynolds stress need to be modeled appropriately. In the present model the direct effect of compressibility on the eddy viscosity is expressed by ρ_n^2/M_t^2 in (36) because the mean-velocity divergence vanishes for homogeneous shear flows. For inhomogeneous turbulence the mean-velocity divergence can play an important role when the flow speed rapidly changes in the streamwise direction as in a shock wave. If the flow speed decreases and the divergence is negative, the eddy viscosity becomes smaller than the usual estimate, K^2/ε.

Although the third part is smaller than the second part by a factor of M_t, its expression is interesting in the sense that it does not include the mean velocity. Each term in the square bracket can be divided into the two terms: $(1/\bar{\rho})\partial^2 P/\partial x_i^2$ and $-(1/\bar{\rho}^2)(\partial\bar{\rho}/\partial x_i)(\partial P/\partial x_i)$. A term similar to the latter can be seen in the K equation (7). The importance of this term in the K equation was discussed by Yoshizawa (1995). Similarly the transport equation for the Reynolds stress contains such a term. Therefore, the gradients of mean density and pressure can affect the Reynolds stress.

Pressure-Dilatation Correlation

The pressure-dilatation correlation has been investigated as a typical compressibility effect. In this work we obtained a model expression as

$$\left\langle p'\frac{\partial u_i'}{\partial x_i}\right\rangle = C_{pd1}\frac{\rho_n^2}{M_t}\gamma P\frac{\varepsilon}{K}+C_{pd2}\frac{\rho_n^4}{M_t^3}\gamma P\frac{\varepsilon}{K}-C_{pd3}\frac{\rho_n^2}{M_t}\left(\gamma P\frac{\partial U_i}{\partial x_i}+3\frac{\gamma P}{K}\frac{DK}{Dt}-\frac{5}{4}\frac{\gamma P}{\varepsilon}\frac{D\varepsilon}{Dt}\right)+2\rho_n^2\frac{\gamma P}{\bar{\rho}}\frac{D\bar{\rho}}{Dt}$$

$$-\rho_n^2\gamma\frac{DP}{Dt}+C_{pd8}\frac{\rho_n^2}{M_t}\frac{K^2}{\varepsilon}\gamma\bar{\rho}^2\frac{\partial}{\partial x_i}\left(\frac{P}{\bar{\rho}^3}\frac{\partial\bar{\rho}}{\partial x_i}-\frac{\gamma-1}{\gamma}\frac{1}{\bar{\rho}^2}\frac{\partial P}{\partial x_i}\right) \quad (38)$$

By assuming some relations for basic model constants such as $C_{\omega\rho}$ and $C_{\omega c}$ we found that the constant C_{pd1} vanishes. If the assumption does not hold exactly, the constant can have a small nonzero value.

Using the simplified approach Yoshizawa (1995) proposed a model as

$$\left\langle p'\frac{\partial u_i'}{\partial x_i}\right\rangle=-C_{pdY1}\bar{\rho}\varepsilon\chi+C_{pdY2}\bar{\rho}K\chi\frac{\partial U_i}{\partial x_i}+C_{pdY3}\frac{\bar{\rho}K\chi}{E}\frac{DE}{Dt} \quad (39)$$

The third term on the right-hand side corresponds to the two terms that include $D\bar{\rho}/Dt$ and DP/Dt in the present model. Each term in (39) is proportional to χ whereas terms in (38) show a different dependence on ρ_n and M_t. Using the first and third terms in his model Yoshizawa (1995) explained the property of the pressure-dilatation correlation whose value is positive for decaying isotropic turbulence and negative for homogeneous shear turbulence. The present model contains terms with Dk/Dt and $D\varepsilon/Dt$. The terms can also explain the different sign of the correlation because of the difference in the development of energy in the two flows.

Sarkar (1992) modeled the pressure dilatation in the form of a power series in M_t as follows

$$\left\langle p'\frac{\partial u_i'}{\partial x_i}\right\rangle=C_{pdS1}M_t\bar{\rho}\left(\left\langle u_i'u_j'\right\rangle-\frac{2}{3}K\delta_{ij}\right)\frac{\partial U_i}{\partial x_j}+C_{pdS2}M_t^2\bar{\rho}\varepsilon_s$$

$$+C_{pdS3}M_t^2\bar{\rho}K\frac{\partial U_i}{\partial x_i} \quad (40)$$

This model is different from the above two models in that this does not contain the density variance. The first term on the right-hand side has a similar factor to the production term in the K equation. Yoshizawa (1995) discussed that such a term can overestimate the pressure-dilatation correlation in a turbulent channel flow in which the shear is strong but the correlation is very small. On the other hand, the present and Yoshizawa's models contain the density variance; it is expected to explain the small value of the correlation.

Comparison to DNS Data

Blaisdell *et al.* (1991) performed DNS of decaying isotropic and homogeneous shear turbulence. Using the DNS data we compare models for the dilatation dissipation. Although the TSDIA assumes inertial-range spectra, the simulations are at low Reynolds numbers and do not show an inertial range. The DNS results must include some low Reynolds number effects. The values of model constants in this paper may change for higher Reynolds number flows. Nonetheless, we believe that by comparing the models to the DNS we can better understand compressible turbulence.

We examined four simulations of isotropic turbulence and nine simulations of homogeneous shear flow. Here, we will show results of three simulations; their initial conditions are given in Table 1.

The parameter χ_c in Table 1 denotes the ratio of the compressible to total velocity variance $\left\langle u_{ci}'u_{ci}'\right\rangle/\left\langle u_j'u_j'\right\rangle$. Figures 1 and 2 show the time history of the ratio $\varepsilon_d/\varepsilon$ for cases idc128 and ie128. The initial values of M_t are the same for the two cases whereas those of ρ_n and χ_c are different. The solid lines denote the DNS results, the dashed lines denote the values predicted by Sarkar's model (32), and the dotted lines denote those by the present model (29). The model constant in Sarkar's model is given by C_{edS}=1. On the other hand, values of constants in the present model have not been obtained yet because the values of the basic constants, such as $C_{\sigma c}$ and α, are not known. Here, to examine overall agreement with DNS data, the model constants are set at C_{ed1}=1 and C_{ed7}=0 in (29). In Figs. 1 and 2 the DNS results for the two cases are very different; the value of $\varepsilon_d/\varepsilon$ for ie128 in Fig. 2 is much greater than that for idc128 in Fig. 1. Since Sarkar's model contains only M_t, the predicted values for the two cases are almost the same; they decrease in time monotonically. On the other hand, the present model contains M_t and ρ_n^2; it predicts different values of $\varepsilon_d/\varepsilon$ for the two cases. The value for idc128 increases in time like the DNS result. The model explains the effect of the initial condition in terms of the density variance. Similar results were obtained for the other two simulations using a higher

TABLE 1. INITIAL CONDITIONS FOR DNS OF ISOTROPIC AND HOMOGENEOUS SHEAR TURBULENCE BY BLAISDELL ET AL. (1991).

Case	Flow	M_t	ρ_n	χ_n
idc128	isotropic	0.3	0	0
ie128	isotropic	0.3	0.15	0.25
sha192	shear	0.4	0	0

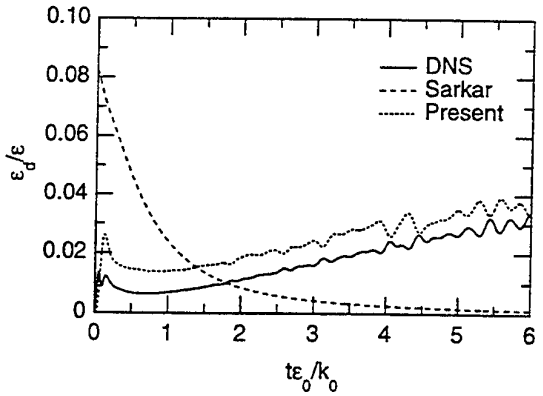


FIGURE 1. TIME HISTORY OF THE RATIO OF DILATATION DISSIPATION TO TOTAL DISSIPATION FOR CASE IDC128.

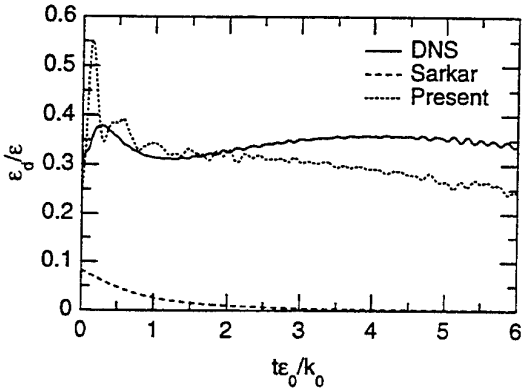


FIGURE 2. TIME HISTORY OF THE RATIO OF DILATATION DISSIPATION TO TOTAL DISSIPATION FOR CASE IE128.

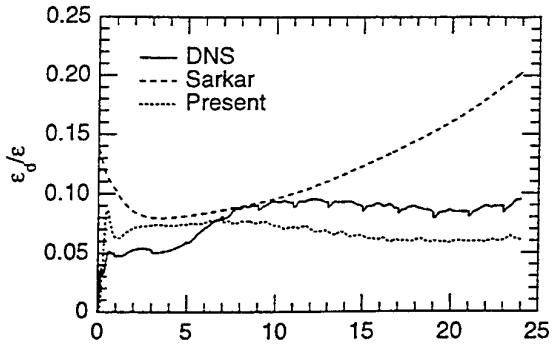


FIGURE 3. TIME HISTORY OF THE RATIO OF DILATATION DISSIPATION TO TOTAL DISSIPATION FOR CASE SHA192.

turbulent Mach number, M_t=0.7 (not shown). Fujiwara (1996) also illustrated the initial condition effects solving the K-ε-F model where F is the sum of the nondimensional density variance and compressible kinetic energy.

Contrary to isotropic turbulence the effect of initial conditions were shown to disappear for homogeneous shear turbulence. Time histories of $\varepsilon_d/\varepsilon$ for simulations with different initial conditions tend to overlap as time increases. Here, we show results of a case denoted sha192; in this case the largest number of grid points was used and its results are considered the most reliable. Figure 3 shows the time history of $\varepsilon_d/\varepsilon$ for case sha192. The difference between the present and Sarkar's models is smaller than that for isotropic turbulence. However, the DNS result shows almost a constant value after St=10 whereas Sarkar's model predicts a continually increasing value after St=3. The present model shows the same tendency as the DNS although the value is smaller. Other simulations with M_t=0.5 extend to St=15 and show qualitatively similar profiles as in Fig. 3. Therefore, the parameter ρ_n is concluded to be important for modeling the dilatation dissipation.

CONCLUDING REMARKS

Model expressions obtained in this work need to be examined further by comparing to DNS of homogeneous and inhomogeneous turbulence. Since the TSDIA is a method based on derivative expansions, expressions contain several terms including higher-order terms. Some terms should be selected so that model expressions are simple but contain essential compressibility effects. Model constants also should be estimated by DNS.

We assumed inertial-range spectra of the density and velocity variances. The spectral forms are not as established as those for incompressible flows. If details of inertial-range spectra are obtained in other theories or experiments, we can include them into this analysis. The relationship to incompressible models in the limit of zero Mach number also needs to be considered to improve the models.

ACKNOWLEDGMENT

I would like to thank Prof. G. A. Blaisdell for providing his DNS data.

REFERENCES

Bataille, F. and Bertoglio, J.-P., 1993, "Short and Long Term Behaviour of Weakly Compressible Turbulence," In FED-Vol. 151, *Transitional and Turbulent Compressible Flows*, ASME, pp. 139-145.

Blaisdell, G. A., Mansour, N. N., and Reynolds, W. C., 1991, "Numerical Simulations of Compressible Homogeneous Turbulence," Rep. TF-50, Dept. of Mech. Engr., Stanford University.

Blaisdell, G. A. and Zeman, O., 1992, "Investigation of the Dilatational Dissipation in Compressible Homogeneous Shear Flow," In *Proc. of Summer Program*, Center for Turbulence Research, NASA Ames/Stanford Univ., pp. 231.

Fujiwara, H., 1996, "Compressibility Effects on Shear Turbulence," Ph. D. thesis, University of Tokyo.

Fujiwara, H. and Arakawa, C., 1993, "Direct Numerical Simulation and Modeling of Compressible Isotropic Turbulence," In *Ninth Symp. on Turbulent Shear Flows*, Kyoto, pp. 22-2-1.

Kida, S. and Orszag, S. A., 1990, "Energy and Spectral Dynamics in Forced Compressible Turbulence," *J. Sci. Comp*, Vol. 5, pp. 85-125.

Moiseev, S. S., Petviashvily, V. I., Toor, A. V., and Yanovsky, V. V., 1981, "The Influence of Compressibility on the Selfsimilar Spectrum of Subsonic Turbulence," *Physica*, 2D, pp. 218-223.

Sarkar, S., 1992, "The Pressure-Dilatation Correlation in Compressible Flows," *Phys. Fluids* A, Vol.4, pp.2674-2682.

Sarkar, S., 1995, "The Stabilizing Effect of Compressibility in Turbulent Shear Flow," *J. Fluid Mech.*, Vol 282, pp. 163-186.

Sarkar, S., Erlebacher, G., Hussaini, M. Y., and Kreiss, H. O., 1991, "The Analysis and Modelling of Dilatational Terms in Compressible Turbulence," *J. Fluid Mech.*, Vol. 227, pp. 473-493.

Speziale, C. G., 1987, "On Nonlinear K-l and K-ε Models of Turbulence," *J. Fluid Mech.*, Vol. 178, pp. 459-475.

Taulbee, D. and VanOsdol, J., 1991, "Modeling Turbulent Compressible Flows: The Mass Fluctuating Velocity and Squared Density," AIAA Paper, No. 91-0524.

Yoshizawa, A., 1984, "Statistical Analysis of the Deviation of the Reynolds Stress from its Eddy-Viscosity Representation," *Phys. Fluids*, Vol. 27, pp. 1377-1387.

Yoshizawa, A., 1990, "Three-Equation Modeling of Inhomogeneous Compressible Turbulence Based on a Two-Scale Direct-Interaction Approximation," *Phys. Fluids* A, Vol. 2, pp. 838-850.

Yoshizawa, A., 1992, "Statistical Analysis of Compressible Turbulent Shear Flows with Special Emphasis on Turbulence Modeling," *Phys. Rev.* A, Vol. 46, pp. 3292-3306.

Yoshizawa, A., 1995, "Simplified Statistical Approach to Complex Turbulent Flows and Ensemble-Mean Compressible Turbulence Modeling, *Phys. Fluids*, Vol. 7, pp. 3105-3117.

Yoshizawa, A. and Nisizima, S., 1993, "A Nonequilibrium Representation of the Turbulent Viscosity Based on a Two-Scale Turbulence Theory," *Phys. Fluids* A, Vol. 5, pp. 3302-3304.

Zeman, O., 1990, "Dilatation Dissipation: The Concept and Application in Modeling Compressible Mixing Layers," *Phys. Fluids* A, Vol. 2, pp. 178-188.

Zeman, O., 1991, "On the Decay of Compressible Isotropic turbulence," *Phys. Fluids* A, Vol. 3, pp. 951-955.

AN IMPROVED TWO-POINT CLOSURE FOR WEAKLY COMPRESSIBLE TURBULENCE AND COMPARISONS WITH LARGE-EDDY SIMULATION

G. Fauchet, L. Shao, R. Wunenburger* and J.P. Bertoglio

Laboratoire de Mécanique des Fluides et d'Acoustique, U.M.R. C.N.R.S. 5509
Ecole Centrale de Lyon, 36 av. G. de Collongue, 69130 Ecully, France
⋆ Present address: Physique et Mécanique des Milieux Hétérogènes,
U.R.A. C.N.R.S. 857, E.S.P.C.I., 10 rue Vauquelin, 75231 Paris, France

ABSTRACT

A new two-point closure for weakly compressible isotropic turbulence is proposed. The model has the same structure that the EDQNM closure previously extended to compressible turbulence (Bataille et al (1993)), but is based on different assumptions concerning two-time correlations. The results of the new model are nearly identical to the ones of the EDQNM theory in the case of incompressible turbulence, whereas in the case of compressible turbulence they significantly differ. In the limit of small turbulent Mach numbers, the scalings of the quantities associated with the purely compressible part of the field are found to be strongly altered. Direct and Large-Eddy Simulations are also performed in the case of weakly compressible isotropic turbulence maintained statistically stationary by injecting energy in the large scales. Comparisons with the theory confirm the scalings at low Mach number and show good qualitative agreement when the Mach number is increased. Quantitative comparisons of the spectra lead to a reasonable agreement.

INTRODUCTION AND BASIC EQUATIONS

The aim of the present paper is to investigate the dynamics of weakly compressible isotropic turbulence within the framework of two-point closure theories and to compare the results with Direct and Large-Eddy Simulations. In a previous work, the Direct Interaction Approximation (DIA) was extended to weakly compressible turbulence (Marion et al (1988)). Then, the DIA equations were used as a starting point to derive the Eddy Damped Quasi Normal Markovian (EDQNM) model for weakly compressible isotropic turbulence (Bataille et al (1993) and Bertoglio et al (1996)). Among the results obtained with the EDQNM model, at low turbulent Mach number (M_t), the dilatational dissipation was found to scale as $M_t^2 Re^0$. More recently, it was shown by Wunenburger (1994), using a simplified form of the model, that the results were largely depending on one of the assumptions introduced when deriving the one-time EDQNM model from the two-time DIA closure, namely the assumption on the relaxation terms introduced in the two-time correlation equations (or in the response function equations). In the EDQNM approach, a linear relaxation is postulated.

In the present paper, a new one-time model is derived from the DIA formulation, introducing a different type of relaxation. The new relaxation term leads to a Gaussian shape for two-time correlations of the solenoidal field (whereas the usual relaxation leads to an exponential form). For incompressible turbulence, it is shown that the results are not significantly affected by this alteration. In contrast, in the case of compressible turbulence, results concerning the dilatational part of the field are largely modified.

Direct and Large Eddy Simulations are also performed in order to check the validity of the statistical models. Comparisons are proposed in the case of statistically stationary isotropic turbulence which has the advantage of being independent of the initial conditions.

In the basic set of equations, a low Mach number approximation is introduced ($M_t \ll 1$) to simplify the Navier-Stokes equations for weakly compressible turbulence. After Fourier transforming and splitting the velocity field into a solenoidal component u^s and a dilatational component u^c, where u^s is divergence free and u^c is curl free, the simplified set of equations is:

$$\frac{\partial}{\partial t} p(\vec{K}) = -i\rho_o C_o^2 K_i u_i^c(\vec{K}) \qquad (1)$$

$$\left(\frac{\partial}{\partial t} + \nu K^2\right) u_i^s(\vec{K}) =$$

$$-i\int P_{ij}(\vec{K})Q_l u_j(\vec{P})u_l(\vec{Q})\delta(\vec{K}-\vec{P}-\vec{Q})d\vec{P}d\vec{Q} \quad (2)$$

$$\left(\frac{\partial}{\partial t}+\nu' K^2\right) u_i^c(\vec{K}) = -i\frac{K_i}{\rho_o}p(\vec{K})$$
$$-i\int \Pi_{ij}(\vec{K})Q_l u_j(\vec{P})u_l(\vec{Q})\delta(\vec{K}-\vec{P}-\vec{Q})d\vec{P}d\vec{Q} \quad (3)$$

where ρ_o is the mean density, C_o is the sound speed (both assumed to be constant), p is the pressure fluctuation, ν and ν' are the molecular viscosities, with $\nu' = 4/3\nu$, $\vec{K}$ is the wave-vector. P_{ij} and Π_{ij} respectively denote the projector onto the plane orthogonal to the wave-vector, and the projector along the wave-vector direction. M_t is defined as: $M_t = u'/C_o$.

Equations (1), (2) and (3) are used as the starting point to develop our statistical models. They also constitute the basic set of equations for the numerical simulations.

THE MODIFIED MODEL: CASE OF INCOMPRESSIBLE TURBULENCE

Formally, in the case of incompressible turbulence, the DIA formulation is :

$$(\frac{\partial}{\partial t}+\nu K^2)\Phi(K,t,t') = \int < G(K,t',t'') > \Phi(P,t,t'')\Phi(Q,t,t'')dt'' \quad (4)$$

$$(\frac{\partial}{\partial t}+\nu K^2) < G(K,t,t') >= \int < G(K,t',t'') >< G(P,t,t'') > \Phi(Q,t,t'')dt'' \quad (5)$$

where $\Phi(K,t,t')$ is the two-time two-point velocity correlation and $< G(K,t,t') >$ is the averaged response function (response of the velocity at K and t to a perturbation at t' (t'$\leq$t)).

One-time models, such as the EDQNM, are derived from the two-time DIA by applying the following procedure:

- deduce the equation for the one-time correlation by taking the limit t' $\rightarrow$ t in equation (4). It comes:

$$(\frac{\partial}{\partial t}+2\nu K^2)\Phi(K,t) = \int < G(K,t,t'') > \Phi(P,t,t'')\Phi(Q,t,t'')dt'' \quad (6)$$

- link the two-time correlations that remain in the right hand side of (6) to the one-time correlations, introducing a new function R(K,t,t'):

$$\Phi(K,t,t') = R(K,t,t')\Phi(K,t') \quad (7)$$

- introduce the "Markovianization" assumption: i.e. assume that, in the right hand side of (7), $\Phi(K,t'')$ has a weak dependency with respect to time (compared with the characteristic time of the response function). Then the equation for the one-time correlation reads:

$$(\frac{\partial}{\partial t}+2\nu K^2)\Phi(K,t) = \int \Theta_{KPQ}\Phi(P,t)\Phi(Q,t) \quad (8)$$

where

$$\Theta_{KPQ} = \int < G(K,t,t'') > R(P,t,t'')R(Q,t,t'')dt''$$

is a characteristic time of the triad {K,P,Q}.

- assume modeled forms for $< G >$ and R.

The EDQNM model is obtained if, in the last step of the above procedure, the following assumptions are injected:

- the non linear term appearing in the right hand side of (5) is expressed by a linear relaxation term $-\mu(K) < G(K,t,t') >$ where μ is an eddy damping coefficient. This leads to:

$$< G(K,t,t') >= \exp((-\mu(K)-\nu K^2)(t-t'))$$

- R is assumed to be equal to $< G >$.

- the eddy damping coefficient is expressed in order to obtain a $K^{-5/3}$ behaviour of the spectrum in the inertial range. A form usually retained is:

$$\mu(K) = \lambda\sqrt{\int_0^K P^2 E(P)dP} \quad (9)$$

where λ is a constant related to the Kolmogorov constant ($\lambda = 0.355$ is generally used).

The approach proposed in the present paper consists in expressing the functions $< G >$ and R differently. It is known that for statistically stationary turbulence, $R(K,t,t+\tau)$ has to be an even function of τ and that the exponential form resulting from the EDQNM assumptions does not satisfy this condition. This question was raised by Kraichnan (1964) who also noticed that this inconsistency could be corrected by introducing another formulation for R:

$$R(K,t,t') = \exp(-\alpha(K)(t-t')^2). \quad (10)$$

The aim of the present approach is to propose, and to extend to compressible turbulence, a model consistent with this Gaussian shape. As a matter of fact, it was shown by Kraichnan (1971) that, in case of incompressible turbulence, the use of Gaussian functions for $< G >$ and R, instead of exponential forms, was resulting in only minor changes in the predictions of the closure. This probably explains that the problem has received little attention in the field of turbulence modeling. The situation being different in the case of compressible turbulence, attention is here focused on this point.

A systematic (and easy to extend to compressible turbulence) route to obtain (10) is to replace the right hand side of equation (5) by a modeled term $-2\alpha(K)\ (t-t') < G(k,t,t') >$. This leads to:

$$< G(K,t,t') >= \exp(-\alpha(K)(t-t')^2 - \nu K^2(t-t'))$$

and Kraichnan's expression for R is recovered if R is assumed to be the limit of $< G >$ when ν tends to 0. Following this procedure, equation (8) is not modified. Solely the form of the characteristic time Θ is changed.

It can be shown that the new damping coefficient α is linked to μ by $4\alpha = \Pi\gamma\mu^2$, where γ is found to be equal to 2.68, following Kraichnan's approach (1971).

THE MODIFIED MODEL FOR WEAKLY COMPRESSIBLE TURBULENCE

In the DIA equation for weakly compressible turbulence (Marion et al (1988)), the following quantities are introduced:

- $\Phi^{\alpha\beta}(K,t,t')$ correlation between the α-mode at K and t and the β-mode at t',
- $< G^{\alpha\beta}(K,t,t') >$ averaged response function (response of the α-mode at K and t to a perturbation of the β-mode at t' (t'$\leq$t)),

where α and β stand for the different modes $\{u^s$, u^c and p$\}$. When the procedure described in the previous section is applied to compressible turbulence, the resulting closed set of equations is identical to the one of the EDQNM model (Bataille et al (1993)). Only the characteristic times are modified (their expressions are given in Appendix). In the response function equations, three damping coefficients are introduced: α^{ss}, α^c and α^p. α^{ss}, associated with the solenoidal mode, is taken equal to the damping coefficient for incompressible turbulence α. The coefficients α^c and α^p associated with the dilatational modes are simply assumed to be proportional to α^{ss}: $\alpha^c = \alpha^p = r\alpha^{ss}$.

COMPARISON BETWEEN EDQNM AND THE MODIFIED MODEL

In the case of incompressible turbulence, as noticed by Kraichnan (1971), the results of the model are very weakly dependent on the choice of the assumption concerning the two-time correlations. This can be observed in figure 1 where the numerical predictions of the EDQNM and modified models are compared, in the case of a turbulent field maintained statistically stationary by injecting energy in the large scales. Only the smallest scales of the turbulence spectrum are slightly modified.

In the case of weakly compressible turbulence, results are analyzed with a forcing applied to the solenoidal part of the field. The behaviours of the different spectra E^{ss}, E^{cc}, E^{pp} and $E^{p'p'}$ are studied, as well as the scalings for the compressible turbulent kinetic energy $q_c^2/2$ and for the dilatational dissipation ϵ^d. These quantities are defined as:

$$\begin{aligned}
\int E^{ss}(K)dK &= \tfrac{1}{2} < u^s u^s > &= \tfrac{1}{2}q_s^2 \\
\int E^{cc}(K)dK &= \tfrac{1}{2} < u^c u^c > &= \tfrac{1}{2}q_c^2 \\
\int E^{pp}(K)dK &= \tfrac{1}{2\rho_o^2 C_o^2} < pp > & \\
\int E^{p'p'}(K)dK &= \tfrac{1}{2\rho_o^2 C_o^2} < p'p' > & \\
\int E^{pp}_{inc}(K)dK &= \tfrac{1}{2\rho_o^2 C_o^2} < p_{inc}p_{inc} > & \\
\int 2\nu K^2 E^{ss}(K)dK &= \epsilon^s & \\
\int 2\nu' K^2 E^{cc}(K)dK &= \epsilon^d &
\end{aligned}$$

where p_{inc} is the "incompressible pressure" (solution of a Poisson equation) and $p' = p - p_{inc}$.

In the limit of a very small turbulent Mach number, an asymptotic expansion of the present model can be performed. Assuming a Kolmogorov type of spectrum for E^{ss}, this analytical analysis leads to the results summarized in table I.

	EDQNM	modified model
$E^{cc}(K)$	$M_t^2 R_e^1 K^{-11/3}$	$M_t^4 R_e^0 K^{-3}$
$E^{pp}(K)$	$M_t^2 R_e^1 K^{-11/3}$	$M_t^2 R_e^0 K^{-7/3}$
$E^{p'p'}(K)$	$\approx E^{cc}(K)$	$M_t^6 R_e^0 K^{-11/3}$
$\lim_{M_t\to 0} E^{pp}(K)$	$\neq E^{pp}_{inc}(K)$	$E^{pp}_{inc}(K)$
q_c^2/q_s^2	$M_t^2 R_e^1$	$M_t^4 R_e^0$
ϵ^d/ϵ^s	$M_t^2 R_e^0$	$M_t^4 R_e^{-1} \ln(R_e)$

table I

Comparisons with the results of the EDQNM model, also given in table I, show that different scalings are obtained. It has to be pointed out that both the compressible turbulent kinetic energy and the dilatational dissipation are found to scale as M_t^4, whereas in the case of the EDQNM model they are proportional to M_t^2. The slopes of the different spectra are also affected. It is also interesting to notice that in the limit $M_t \to 0$, the pressure spectrum tends to the pressure spectrum in incompressible turbulence, which was not the case with the EDQNM model. The obtained scalings and the fact that equipartition of energy between the u^c and p' modes is not obseved, indicate that the modified model reproduces the "pseudo-sound" regime (Ristorcelli 1995).

In figure 2, results of the numerical integration of the modified model are plotted at low Mach number (M_t=10^{-2}). They validate the results of the analytical analysis, the different slopes of the spectra being in agreement with those given in table I. In figure 2, it can also be observed that the spectrum of the solenoidal velocity is not affected by compressibility effects. In figure 3, the dilatational dissipation is plotted as a function of the Mach number. At low M_t, the $M_t^4 Re^{-1}\ln(Re)$ scaling is observed, whereas for M_t larger than 10^{-1} discrepancies begin to appear, indicating that turbulence is leaving the pseudo-sound regime, to enter an acoustic regime, equipartition between the u^c and p' modes beginning to be observed (results not shown here).

LARGE EDDY SIMULATION TECHNIQUE

In order to provide comparisons, Large Eddy Simulations (LES) are performed. In this case, equations (1) (2) and (3) are directly used. For LES, the molecular viscosity in (2), ν, is replaced by $\nu + \nu_t$, where ν_t is a subgrid eddy viscosity, evaluated using a Chollet-Lesieur (1981) formulation, built on the spectral energy density of the solenoidal velocity at the cut-off wavenumber $E^{ss}(K_c)$. To account for low Reynolds number effects, the modification introduced by Chollet (1983) is used. On the compressible mode, we also introduce an eddy viscosity. Its expression is built on the purely compressible energy at the cut-off:

$$\nu_{tc} = 0.267\sqrt{E^{cc}(K_c)/K_c} \qquad (11)$$

This formulation would require further justifications, but it was shown, by comparing results of LES on fine and coarse grids, that it leads to acceptable results.

With the aim to get statistically steady isotropic turbulence, an external force is used to supply energy into the turbulent field at large scales. In order to avoid

excessive disturbance of the compressible mode, the forcing is applied only to the solenoidal part of the field. The force is therefore solenoidal. It is added to the right hand side of equation (2). It is stochastically generated and time correlated with a memory time T_{nl}. The force is obtained by a Langevin equation (cf Shao et al (1996)).

The time correlation of the force is:

$$< f_i(t) f_i(t') > \propto \exp\left(-\frac{|t-t'|}{T_{nl}}\right) \quad (12)$$

A second type of forcing, generated using two Langevin equations, was also used. In this case, the two-time correlation of the force has a zero derivative at $t = t'$.

$$< f_i(t) f_i(t') > \propto \left(1 + \frac{|t-t'|}{T_{nl}}\right) \exp\left(-\frac{|t-t'|}{T_{nl}}\right) \quad (13)$$

The set of equations (1)-(3) is solved using a pseudo spectral code. Time integration is achieved with a 4^{th} order Runge-Kutta scheme. The forcing is applied to a range of wave-numbers between 0 and 58 m^{-1}. Statistically stationary turbulence is obtained. The effect of the memory time T_{nl} is analyzed in figure 4 where the compressible kinetic energy is plotted as function of T_{nl}. Clearly, the compressible kinetic level is drastically reduced when T_{nl} increases. However, for large enough memory time, an asymptotic state is obtained and the results become independent of T_{nl}. In figure 4, we also compare results obtained with the two types of forcing techniques (respectively satisfying (12) and (13)). It appears that the asymptotic level is the same with the two forcings (the asymptote being reached faster when the second one is used).

All the results presented below are for T_{nl} large enough for the asymptote to be reached, so they are considered as independent of the forcing. More specifically, the second type of forcing is used with T_{nl} approximatively equal to 5 turbulent turn-over times.

The LES computations were run on a 64^3 grid. The Mach number was changed by varying the value of the sound speed. Seven values of M_t were investigated, ranging from M_t=4 10^{-2} to M_t=0.45. The influence of the Reynolds number was studied by varying the value of the molecular viscosity. Three values of Re_L (based on the integral length scale) were investigated: $Re_L \simeq 80$, $Re_L \simeq 800$ and $Re_L \simeq 4000$. It has to be pointed out that in the lowest Reynolds number case, all the important scales of the turbulent motion were nearly resolved so that, in this case, the LES was nearly a DNS. For validation purpose, a DNS on a 128^3 grid was also performed (at M_t= 0.2 and Re_L=80).

SIMULATION RESULTS AND COMPARISON WITH THE MODEL

In figures 5 and 6, the compressible kinetic energy $q_c^2/2$ and the dilatational dissipation ϵ^d are plotted against the turbulent Mach number for different Re_L. At low Mach number ($M_t \leq 0.1$), a M_t^4 scaling is obtained for both q_c^2 and ϵ^d. The compressible kinetic energy level is found to be independent of the Reynolds number. The dilatational dissipation is found to scale as $M_t^4 Re_L^{-1} \ln(Re_L)$. This is in agreement with the results of the modified statistical model presented in table I. At higher Mach number, the behaviours

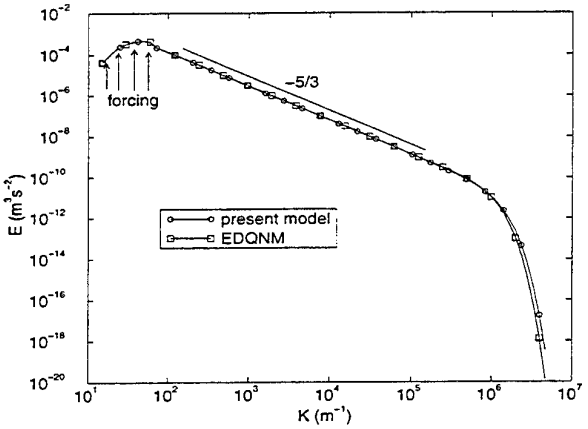


Figure 1: Comparison between the present model and EDQNM in the case of incompressible turbulence. Turbulent kinetic energy spectrum; Re_L=10^8.

change. This is also in agreement with the results of our statistical model.

In figures 7, 8, 9 and 10, a comparison between spectra obtained with LES (or DNS in case of fig. 8) and with the present statistical model is proposed. Both $E^{ss}(K)$ and $E^{cc}(K)$ are plotted at different Mach and Reynolds numbers. The overall agreement appears to be satisfactory. It has to be pointed out that all the model results presented here were obtained with r=0.125 (ratio between the damping coefficients on the compressible and solenoidal modes). The influence of this parameter is illustrated in figure 10, where results obtained with r=1 are also plotted: r appears to play a significant role, especially when the Reynolds number becomes high.

CONCLUSION

The improved two-point closure for compressible turbulence appears to lead to results that significantly differ from those of the EDQNM model. The different scalings associated with the compressible modes are modified. The results of the new model are corroborated by LES results.

Acknowledgments

The authors would like to thank M. Lesieur for providing computational material used in the statistical part of this study, and the CNRS IDRIS computer center for facility provided on a Cray C98.

REFERENCES

Bataille F. & Bertoglio J.P., 1993, "Long time behaviour study and decay of a compressible turbulence", *11 Symp. on Turb. Shear Flows*, Kyoto, August 93.

Bertoglio J.P., Bataille F. & Marion J.D., 1996, "Two-point closures for weakly compressible turbulence", *under revision for Phys. of Fluids.*

Chollet J.P., 1983, "Statistical closure to derive sub-grid-scale modeling for large eddy simulations of three dimensional turbulence", *Technical Note TN 206*, NCAR.

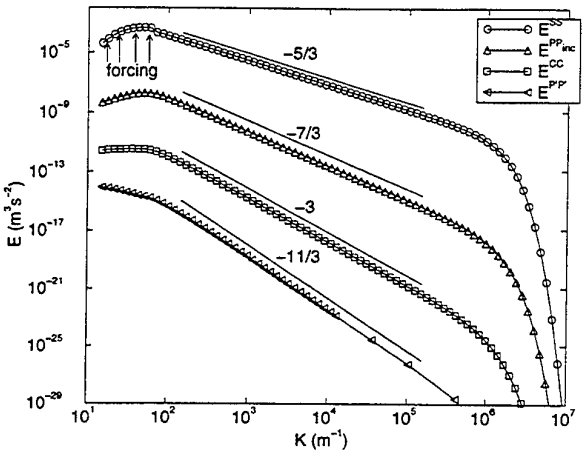


Figure 2: Results of the present model at M_t=10^{-2}: turbulent kinetic energy spectra, incompressible and compressible pressure spectra; Re_L=10^8.

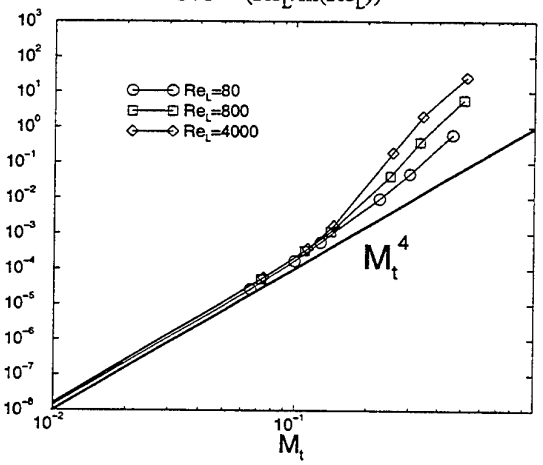


Figure 3: Normalized dilatational dissipation as function of M_t for different Reynolds numbers (model results).

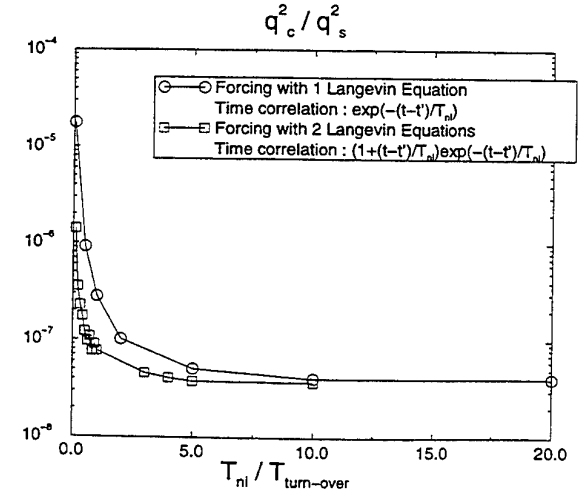


Figure 4: Normalized compressible kinetic energy as function of T_{nl}. Case Re_L=300, M_t = 0.15 (LES results).

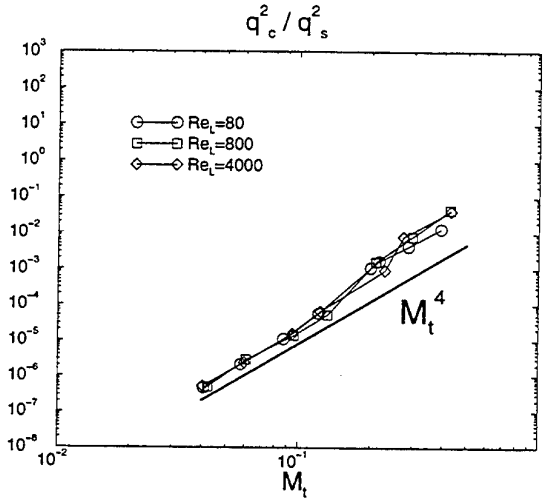


Figure 5: Compressible kinetic energy as function of M_t for different Reynolds numbers (LES results).

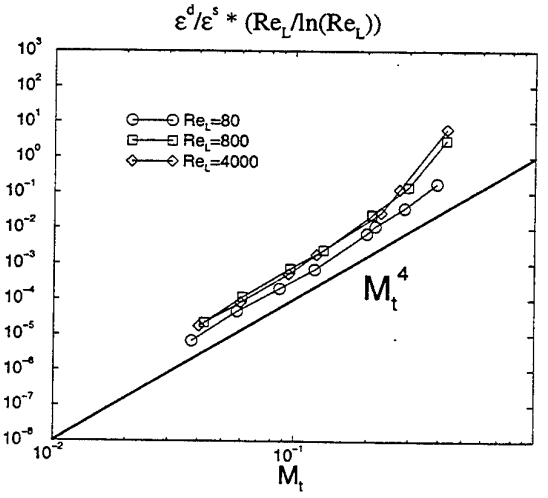


Figure 6: Normalized dilatational dissipation as function of M_t for different Reynolds numbers (LES results).

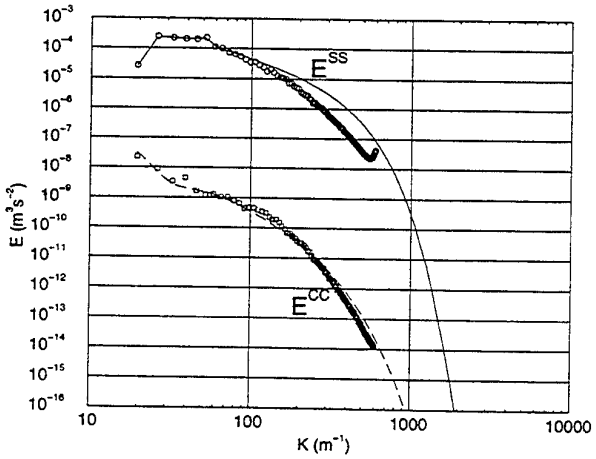


Figure 7: Comparison between LES (symbols) and model (lines); Re_L=80, M_t=0.1 .

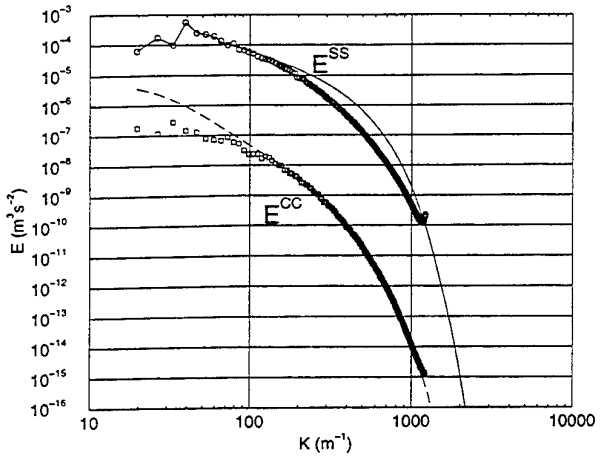


Figure 8: Comparison between DNS (symbols) and model (lines); Re_L=80, M_t=0.2 .

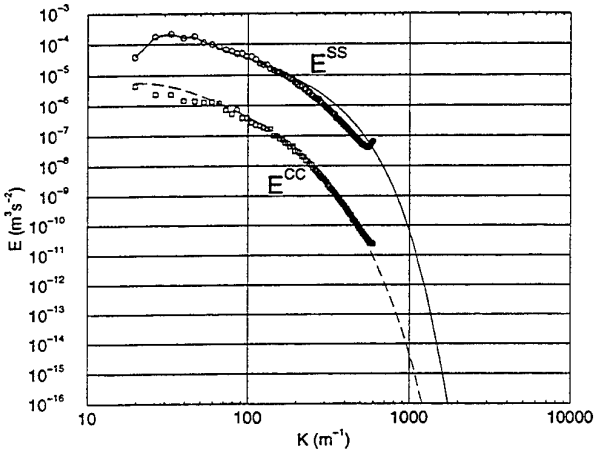


Figure 9: Comparison between LES (symbols) and model (lines); Re_L=80, M_t=0.45 .

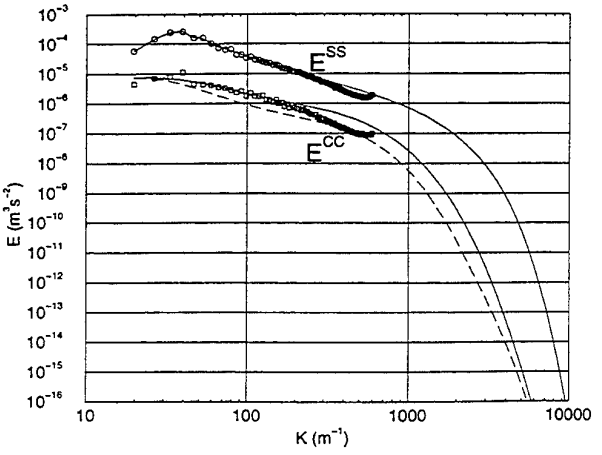


Figure 10: Comparison between LES (symbols) and model (lines); Re_L=800, M_t=0.45 (r=1 —; r=0.125 - -).

Chollet J.P. & Lesieur M., 1981, "Parameterization of small scales of three-dimensional isotropic turbulence utilizing spectral closures", *J. Atm. Sci.*, Vol. 38, pp. 2747-2757.

Kraichnan R. H., 1964, "Approximation for steady-state isotropic turbulence", *Phys. Fluids*, vol. 7, pp. 1163-1168.

Kraichnan R. H., 1971, "Inertial-range transfer in two- and three-dimensional turbulence", *J. Fluid. Mech.*, vol. 47, part 3, pp. 525-535.

Marion J.D., Bertoglio J.P. & Mathieu J., 1988, "Spectral study of weakly compressible isotropic turbulence; part I: Direct Interaction Approximation", *C.R.A.S.*, t. 307, Série II, pp. 1487-1492.

Ristorcelli J.R., 1995, "A pseudo-sound constitutive relationship for the dilatational covariances in compressible turbulence", *ICASE Report 95.*

Shao L. & Bertoglio J.P., 1996, "Large Eddy Simulations of weakly compressible isotropic turbulence", *ETC VI*, Lausanne, July 96.

Wunenburger R., 1994, "Etude spectrale d'une turbulence isotrope homogène stationnaire faiblement compressible", *Rapport E.N.S.L.*

APPENDIX

The characteristic times appearing in the statistical models for weakly compressible turbulence are:

$$\Theta^{\beta\gamma\delta}_{KPQ} =$$

$$\sum_{\epsilon_\beta\in\{-1,1\}} \sum_{\epsilon_\gamma\in\{-1,1\}} \sum_{\epsilon_\delta\in\{-1,1\}} A(\eta,b,a) \cdot \left(d^\beta + \epsilon_\beta g^\beta(K)\right)\left(d^\gamma + \epsilon_\gamma g^\gamma_o(P)\right)\left(d^\delta + \epsilon_\delta g^\delta_o(Q)\right)$$

$$\begin{aligned} \eta &= \eta^\beta(K) + \eta^\gamma_o(P) + \eta^\delta_o(Q) \\ b &= \epsilon_\beta b^\beta(K) + \epsilon_\gamma b^\gamma_o(P) + \epsilon_\delta b^\delta_o(Q) \\ a &= \alpha^\beta(K) + \alpha^\gamma(P) + \alpha^\delta(Q) \end{aligned}$$

This general expression is valid for both EDQNM and the modified model, but the definitions of the different functions differ. They are given here in the case of the modified model:

$$\eta^{ss}(K) = \nu K^2$$
$$\eta^{cc}(K) = \eta^{cp}(K) = \eta^{pc}(K) = \eta^{pp}(K) = \nu' K^2/2$$
$$\alpha^{cc}(K) = \alpha^{cp}(K) = \alpha^{pc}(K) = \alpha^{pp}(K) = r\alpha^{ss}(K)$$
$$b^{ss}(K) = 0$$
$$b^{cc}(K) = \sqrt{(\eta^{cc}(K))^2 - K^2 C_o^2}$$
$$b^{cp}(K) = b^{pc}(K) = b^{pp}(K) = b^{cc}(K)$$
$$d^{ss} = d^{cc} = d^{pp} = 1; d^{cp} = d^{pc} = 0$$
$$g^{ss}(K) = 0$$
$$g^{cc}(K) = g^{pp}(K) = \eta^{cc}(K)/b^{cc}(K)$$
$$g^{cp}(K) = g^{pc}(K) = -KC_o/b^{cp}(K)$$
$$\eta^\beta_o(K) = \lim_{\nu,\nu'\to 0} \eta^\beta(K)$$
$$b^\beta_o(K) = \lim_{\nu,\nu'\to 0} b^\beta(K)$$
$$g^\beta_o(K) = \lim_{\nu,\nu'\to 0} g^\beta(K)$$

$$A(\eta,b,a) = \frac{\sqrt{\Pi}}{8a} \exp((\frac{\eta+b}{a})^2) erfc(\frac{\eta+b}{a}).$$

VALIDATION OF LINEAR AND NON-LINEAR LOW-RE TURBULENCE MODELS IN SHOCK/BOUNDARY LAYER INTERACTION

G. Barakos and D. Drikakis
UMIST
Department of Mechanical Engineering
PO Box 88
Manchester M60 1QD
United Kingdom

ABSTRACT

Validation of linear and recently developed non-linear eddy-viscosity models in transonic flows featuring shock/boundary layer interaction and separation, is presented. The accuracy of the models is assessed against experimental results for two transonic flow cases, one over an axisymmetric bump and another in a channel with a bump on the lower wall. Discretisation of the mean flow and turbulence transport equations is obtained by a characteristics-based scheme, third-order of accuracy. For the time integration an implicit unfactored method is used. The study reveals that the numerical predictions for the shock/boundary layer interaction are improved by the present non-linear models.

INTRODUCTION

Shock/boundary layer interaction appears in many aeronautical applications, such as flows in compressor passages, around turbomachinery blades and external flows over aircraft wings or helicopter blades. The aerodynamic performance in these applications depends strongly on the location and strength of the shocks, as well as on the flow separation, induced by the shock/boundary layer interaction. Accurate prediction of such flow phenomena is of primary technological importance and their simulation remains a challenging problem due to the complex physics involved.

Past research has revealed that the accuracy of the numerical calculations is mainly dictated by the accuracy of the turbulence model. Experience using algebraic turbulence models has shown that such modelling of turbulence did not provide satisfactory results in most cases. Linear low-Re two-equation models seem to offer the best balance between accuracy and computational cost, but are not able to capture effects arising from normal-stress anisotropy. At present non-linear models seem to be one of the principal routes for advanced modelling of turbulence beyond the linear eddy-viscosity models. Such models take into account streamline curvature and swirl, as well as history effects. Non-linear models are still being refined and validated for steady flows, mainly two-dimensional and incompressible, while limited experience has been acquired from applications to compressible flows.

The objectives of the present study is to validate, in flows with shock/boundary layer interaction, two- and three-equation non-linear eddy-viscosity models (EVM) recently developed at UMIST by Craft, Launder and Suga (Craft *et al.*, 1996; Suga, 1995). The accuracy of the models is assessed in contrast to experimental results for two transonic flow cases and calculations using linear eddy-viscosity models.

NUMERICAL METHOD

The compressible Navier-Stokes equations for a two-dimensional curvilinear coordinate system (ξ, η), in conjunction with the transport equations of the turbulence model, are written in matrix form as:

$$\frac{\partial U}{\partial t} + \frac{\partial E}{\partial \xi} + \frac{\partial G}{\partial \zeta} = \frac{\partial R}{\partial \xi} + \frac{\partial S}{\partial \zeta} + H \qquad (1)$$

U is the six-component vector of the conservative variables:

$$U = J\left(\rho, \rho u, \rho w, e, \rho k, \rho \tilde{\epsilon}\right)^T \qquad (2)$$

where ρ is the density, u, w are the velocity components in the x and z directions, respectively, e is the total energy per unit volume, k is the turbulent kinetic energy and $\tilde{\epsilon}$ the isotropic part of the turbulent dissipation rate.
The matrix $H = J\tilde{H}$ has non-zero entries for the source terms of the turbulence model equations, as well as for terms due to the axisymmetric formulation. J is the Jacobian of the transformation from Cartesian to curvilinear coordinate system.
The inviscid (E,G) and viscous (R,S) flux vectors are written as:

$$E = J\left(\tilde{E}\xi_x + \tilde{G}\xi_z\right), \quad G = J\left(\tilde{E}\zeta_x + \tilde{G}\zeta_z\right) \qquad (3)$$

$$R = J\left(\tilde{R}\xi_x + \tilde{S}\xi_z\right), \quad S = J\left(\tilde{R}\zeta_x + \tilde{S}\zeta_z\right)$$

In the above relations $\tilde{E}$, $\tilde{G}$ and $\tilde{R}$,$\tilde{S}$ are the inviscid and viscous Cartesian flux vectors, respectively.

The total energy per unit volume ϵ is the sum of the specific internal energy (i), kinetic energy ($\frac{1}{2}\rho(u^2+w^2)$) and turbulent kinetic energy k:

$$\epsilon = \rho i + \frac{1}{2}\rho\left(u^2+w^2\right) + \rho k \tag{4}$$

The pressure is evaluated by the equation of state for an ideal gas.

A third - order upwind scheme along with a characteristics - based flux averaging (linear locally one - dimensional Riemann solver) is used to calculate the inviscid fluxes at the cell faces (Drikakis and Durst, 1994, Eberle *et al.*, 1992). Limiters based on the squares of pressure derivatives have been used for the detection of shocks and contact discontinuities.

An implicit-unfactored solver (Barakos and Drikakis, 1996) has been employed for the solution of the equations. A sequence of approximations q^ν such that:

$$\lim_{\nu>1} q^\nu \rightarrow U^{n+1}$$

is defined between two time steps n and $n+1$. Using implicit time discretisation and after linearising the fluxes around the sub-iteration state ν the following form is derived:

$$\frac{\Delta q}{\Delta t} + (A^\nu_{inv}\Delta q)_\xi + (C^\nu_{inv}\Delta q)_\zeta - (A^\nu_{vis}\Delta q)_\xi - (C^\nu_{vis}\Delta q)_\zeta = RHS \tag{5}$$

where

$$RHS = -\left(\frac{q^\nu - U^n}{\Delta t} + E^\nu_\xi + G^\nu_\zeta - R^\nu_\xi - S^\nu_\zeta - H^\nu\right) \tag{6}$$

$$\Delta q = q^{\nu+1} - q^\nu \tag{7}$$

and

$$A_{inv} = \frac{\partial E}{\partial U},\ C_{inv} = \frac{\partial G}{\partial U},\ A_{vis} = \frac{\partial R}{\partial U},\ C_{vis} = \frac{\partial S}{\partial U} \tag{8}$$

At each time step the final system of algebraic equations is solved by a point Gauss-Seidel relaxation scheme.

According to the present method the transport equations for the turbulence model are solved coupled with the fluid flow equations. This strategy provides fast convergence and compact numerical implementation. Alternatively, the transport equations for the turbulence model can be solved with a fourth-order Runge-Kutta explicit scheme. This option has also been implemented into the present Navier-Stokes code. The above formulation is quite general since the implementation of another two-equation turbulence model requires slight modifications regarding the incorporation of the damping functions, closure coefficients and boundary conditions.

TURBULENCE MODELLING

In the present study two linear $k-\epsilon$ models have been employed: the Launder-Sharma (1974) and the Nagano-Kim (1988). The main objective is, however, to validate the non-linear models recently developed at UMIST. The first is a two-equation model proposed by Craft *et al.* (1996) and the second is a three-equation $k-\epsilon-A_2$ model proposed by Suga (1995).

Linear eddy-viscosity models of the $k-\epsilon$ type, make use of the Boussinesq approximation and require the solution of two transport equations; one for the kinetic energy of turbulence, k, and one for the turbulent dissipation rate, ϵ.

The stress tensor t_{ij} is modeled using the Boussinesq approximation:

$$t_{ij} = \bar{t}_{ij} + \tau^R_{ij} \tag{9}$$

where

$$\bar{t}_{ij} = \mu\left(\frac{\partial u_i}{\partial x_j} + \frac{\partial u_j}{\partial x_i}\right) - \frac{2}{3}\mu\frac{\partial u_k}{\partial x_k}\delta_{ij}, \tag{10}$$

$$\tau^R_{ij} = \mu_T\left(\frac{\partial u_i}{\partial x_j} + \frac{\partial u_j}{\partial x_i}\right) - \frac{2}{3}\mu_T\frac{\partial u_k}{\partial x_k}\delta_{ij} - \frac{2}{3}\rho_k\delta_{ij} \tag{11}$$

and μ_T is the eddy-viscosity of the fluid.

On the other hand, non-linear eddy-viscosity models use an expansion of the Reynolds stress components in terms of the mean strain-rate and rotation tensors:

$$S_{ij} = \left(U_{i,j} + U_{j,i}\right)/2, \quad \Omega_{ij} = \left(U_{i,j} - U_{j,i}\right)/2 \tag{12}$$

For the $k-\epsilon$ non-linear EVM by Craft *et al.* (1996) the transport equations for the k and $\tilde{\epsilon}$ are:

$$\frac{D\rho k}{Dt} = d_k + P_k - \rho\epsilon \tag{13}$$

$$\frac{D\rho\tilde{\epsilon}}{Dt} = d_{\tilde{\epsilon}} + C_{\epsilon 1}P_k\frac{\tilde{\epsilon}}{k} - C_{\epsilon 2}\frac{\rho\tilde{\epsilon}^2}{k} + P_{\epsilon 3} + S_\epsilon \tag{14}$$

The diffusion terms are given by:

$$d_k = \frac{\partial}{\partial x_k}\left\{\left(\mu + \frac{\mu_T}{1.0}\right)\frac{\partial k}{\partial x_l}\right\} \tag{15}$$

$$d_{\tilde{\epsilon}} = \frac{\partial}{\partial x_k}\left\{\left(\mu + \frac{\mu_T}{1.3}\right)\frac{\partial \tilde{\epsilon}}{\partial x_l}\right\} \tag{16}$$

The production term P_k and the near wall term $P_{\epsilon 3}$ are:

$$P_k = \rho c_\mu f_\mu \tilde{\epsilon}\tilde{S}\tilde{\Omega} \tag{17}$$

$$P_{\epsilon 3} = 0.0022\frac{\tilde{S}\mu_T k^2}{\tilde{\epsilon}}\left(\frac{\partial^2 U_i}{\partial x_k \partial x_l}\right)^2, \quad \tilde{R}_t < 250 \tag{18}$$

$$P_{\epsilon 3} = 0, \quad \tilde{R}_t \geq 250 \tag{19}$$

The coefficients $c_{\epsilon i}$ in the dissipation equation take the values: $c_{\epsilon 1} = 1.44$, $c_{\epsilon 2} = 1.92\left\{1 - 0.3exp\left(-\tilde{R}_t^2\right)\right\}$. Finally the length-scale (Yap) correction S_ϵ is:

$$S_\epsilon = max\left[0.83\left(\frac{k^{3/2}}{2.5\tilde{\epsilon}y} - 1\right)\left(\frac{k^{3/2}}{2.5\tilde{\epsilon}y}\right)^2\frac{\rho\tilde{\epsilon}^2}{k}, 0\right] \tag{20}$$

where y is the wall-distance. Due to the marginal improvement, provided in most flow cases, by quadratic non-linear expansions of the anisotropy of the Reynolds stress tensor, $a_{ij} \equiv \frac{\overline{u_i u_j}}{k} - \frac{2}{3}\delta_{ij}$, a cubic expansion has been suggested by Craft *et al.* (1996):

$$a_{ij} = -\frac{\mu_T}{\rho k}S_{ij} + c_1\frac{\mu_T}{\rho\tilde{\epsilon}}\left\{S_{ik}S_{kj} - \frac{1}{3}S_{kl}S_{kl}\delta_{ij}\right\} + c_2\frac{\mu_T}{\rho\tilde{\epsilon}}\left(\Omega_{ik}S_{kj} + \Omega_{jk}S_{ki}\right) + c_3\frac{\mu_T}{\rho\tilde{\epsilon}}\left(\Omega_{ik}\Omega_{jk} - \frac{1}{3}\Omega_{lk}\Omega_{lk}\delta_{ij}\right)$$

$$+c_4\frac{\mu_T k}{\rho\tilde{\epsilon}^2}\left(S_{ki}\Omega_{lj}+S_{kj}\Omega_{li}\right)S_{kl} \quad (21)$$

$$+c_5\frac{\mu_T k}{\rho\tilde{\epsilon}^2}\left(\Omega_{il}\Omega_{lm}S_{mj}+\right.$$

$$\left.S_{il}\Omega_{lm}\Omega_{mj}-\frac{2}{3}S_{lm}\Omega_{mn}\Omega_{nl}\delta_{ij}\right)$$

$$+c_6\frac{\mu_T k}{\rho\tilde{\epsilon}^2}S_{ij}S_{kl}S_{kl}+c_7\frac{\mu_T k}{\rho\tilde{\epsilon}^2}S_{ij}\Omega_{kl}\Omega_{kl}$$

This cubic expansion has been utilised here to calculate the components of the Reynolds stress tensor $-\overline{\rho\ u_i u_j}$. In the above, S_{ij} and Ω_{ij} are the strain and vorticity tensors, while $\tilde{S}$ and $\tilde{\Omega}$ are their normalised invariants:

$$\tilde{S}\equiv\frac{k}{\tilde{\epsilon}}\sqrt{S_{ij}S_{ij}/2},\quad \tilde{\Omega}\equiv\frac{k}{\tilde{\epsilon}}\sqrt{\Omega_{ij}\Omega_{ij}/2} \quad (22)$$

where the coefficients c_i take the values: $c_1=-0.1, c_2=0.1, c_3=0.26, c_4=-10c_\mu^2$. The eddy viscosity is calculated by: $\mu_T=c_\mu\rho f_\mu\frac{k^2}{\tilde{\epsilon}}$, where

$$c_\mu=\frac{0.3\left[1-exp\left\{-0.36exp\left(0.75\eta\right)\right\}\right]}{1+0.35\eta^{1.5}} \quad (23)$$

$$f_\mu=1-exp\left\{-\left(\frac{\tilde{R}_t}{90}\right)^{1/2}-\left(\frac{\tilde{R}_t}{400}\right)^2\right\} \quad (24)$$

$$\eta=max\left(\tilde{S},\tilde{\Omega}\right) \quad (25)$$

Such functional form of c_μ has been found to be beneficial in flows far from equilibrium and has also been employed in the work by Liou and Shih (1995) for shock/boundary layer interaction problems.

To obtain a better representation of the turbulence anisotropy the three equation model by Suga (1995) utilises an additional transport equation for the second invariant A_2 of the Reynolds stress anisotropy tensor. As reported by Suga (1995), inclusion of the third equation makes the numerical results comparable to those obtained by differential Reynolds stress models. In addition, the CPU time is slightly increased, while the model becomes free the wall-distance. The transport equation for the invariant $A_2\equiv a_{ij}a_{ij}$ is:

$$\frac{DA_2}{Dt}=dA_2-2\frac{A_2}{k}P_k+2\frac{a_{ij}}{k}P_{ij}+2\frac{a_{ij}}{k}\phi_{ij}+$$

$$2\frac{A_2}{k}\epsilon-2\frac{a_{ij}}{k}\epsilon_{ij} \quad (26)$$

The diffusive part dA_2 is modelled as:

$$dA_2=\frac{\partial}{\partial x_k}\left\{\left(\nu\delta_{kl}+0.22f_g\overline{u_k u_l}\frac{k}{\tilde{\epsilon}}\right)\frac{\partial A_2}{\partial x_l}\right\} \quad (27)$$

and the pressure-strain term ϕ_{ij} can be found in the work of Suga (1995). Once A_2 is calculated, the effective values of S_{ij} and Ω_{ij} can be also calculated as:

$$S_{ij}^*=r_\eta S_{ij},\quad \Omega_{ij}^*=r_\eta\Omega_{ij} \quad (28)$$

where

$$r_\eta=1+\left[1-exp\left\{-\left(\frac{A_2}{0.5}\right)^3\right\}\right]\left[1+4\sqrt{exp\left(\frac{-\tilde{R}_t}{20}\right)}\right] \quad (29)$$

These are subsequently used in the cubic expansion of a_{ij}.

The structure of the transport equations for k and $\tilde{\epsilon}$ remains the same as for the two-equation non-linear model, but the production and diffusion terms are different:

$$P_k=P_{\tilde{\epsilon}}=\rho c_\mu f_\mu\tilde{\epsilon}\tilde{S}\tilde{\Omega} \quad (30)$$

$$d_k=\frac{\partial}{\partial x_k}\left\{\left(\mu\delta_{kl}+0.22f_g\overline{u_k u_l}\frac{\rho k}{\tilde{\epsilon}}\right)\frac{\partial k}{\partial x_l}\right\} \quad (31)$$

$$d_{\tilde{\epsilon}}=\frac{\partial}{\partial x_k}\left\{\left(\mu\delta_{kl}+0.18f_g\overline{u_k u_l}\frac{\rho k}{\tilde{\epsilon}}\right)\frac{\partial\tilde{\epsilon}}{\partial x_l}\right\} \quad (32)$$

$$c_{\epsilon 1}=1+0.15\left(1-A^*\right) \quad (33)$$

$$c_{\epsilon 2}=\frac{1.92}{1+0.7\left(1-\frac{1}{1+\tilde{R}_t^2/400}\right)\sqrt{A_2}max\left(0.25,A^*\right)} \quad (34)$$

$$P_{\epsilon 3}=1.2\frac{\mu\mu_T}{\rho}\frac{\partial^2U_i}{\partial x_k\partial x_j}\frac{\partial^2U_i}{\partial x_k\partial x_j}+$$

$$1\frac{\mu\mu_T}{k\rho}\frac{\partial k}{\partial x_k}\frac{\partial U_i}{\partial x_l}\frac{\partial^2U_i}{\partial x_k\partial x_l} \quad (35)$$

$$S_\epsilon=\frac{\rho\tilde{\epsilon}\tilde{\epsilon}}{k}exp\left(-\tilde{R}_t^2/4\right)+$$

$$35\left(\frac{\partial U_i}{\partial x_m}\frac{\partial l}{\partial x_l}\frac{\partial l}{\partial x_m}\right)\left(\frac{\partial U_p}{\partial x_q}\frac{\partial l}{\partial x_p}\frac{\partial l}{\partial x_q}\right)\frac{\rho k\tilde{\epsilon}}{\tilde{\epsilon}} \quad (36)$$

RESULTS AND DISCUSSION

Test Cases

The shock/boundary layer interaction over a bump is one of the most well known flow configurations used for the validation of turbulence models. Such cases have been the subject of various efforts like the BRITE/EURAM EUROVAL project (Haase *et al.*, 1993) and the AFSOR-HTTM-Stanford conference (Kline *et al.*, 1980).

Two transonic flow cases involving shock/boundary layer interaction have been considered in this work. The first one was identified as Case 8611 at the 1980 AFSOR-HTTM-Stanford conference. The experimental data have been contributed by Johnson *et al.* (1982). A schematic representation of the flow configuration is shown in Figure 1(a). A free stream is allowed to form a boundary layer around a cylinder having an attached bump. The bump's leading edge is smoothed and at its origin a coordinate system has been considered. The bump is assumed symmetric around the cylinder and its length c has been used as the characteristic length of the problem. A detailed description of the bump geometry can be found in the work of Bachalo and Johnson (1979). Because the axisymmetric configuration provides a flow, free of three-dimensional effects the above case is considered as one of the very few two-dimensional cases available for validation of turbulence models in transonic flow conditions (Marvin and Huang, 1996). The working fluid is air flowing at $M_\infty=0.875$ while the Reynolds number per unit length was $Re/m=13.6\ 10^6/m$. The experimental data obtained at the Ames transonic wind tunnel (Johnson *et al.*, 1982) revealed a shock over the bump at about $x/c=0.63$, as well as separation of the boundary layer occurring between $x/c=0.7$ and $x/c=1.1$. This case has been extensively utilised for the validation of numerical techniques and turbulence models.

The second test case has been submitted by Délery to the 1980-81 Stanford Conference (Délery, 1980; Kline *et al.*, 1981). In Figure 1(b) a schematic of the geometry is shown, while the exact description can be found in the work by Kline *et al.* (1981). For this case the inlet Mach number is 0.63. The flow is accelerated over the bump until a Mach number close to 1.4 is achieved. The downstream pressure which is controlled by an adjustable second throat yields the existence of a normal shock wave above the bump trailing edge. The pressure gradient induced by the shock is strong enough to create boundary layer separation on the lower wall. Downstream of the separation point, the flow becomes again supersonic and a second shock quasi-normal to the lower wall is formed. The two shocks join each other above the interaction zone and form a single normal shock which interacts with the boundary layer on the upper wall. The separation and reattachment points were found to be at $x = 0.260m$ and $x = 0.325m$, respectively, away from the leading edge of the bump. The reservoir conditions for this problem are $P_o = 95000\ N/m^2$ and $T_o = 300\ K$. A comparison between various calculations using different models and numerical schemes can be found in the work by Haase *et al.* (1993)

For both test cases surface pressure, as well as LDV measurements are available and, thus, it is possible to assess the accuracy of the models by comparing the velocity, and turbulent shear stress profiles at various positions.

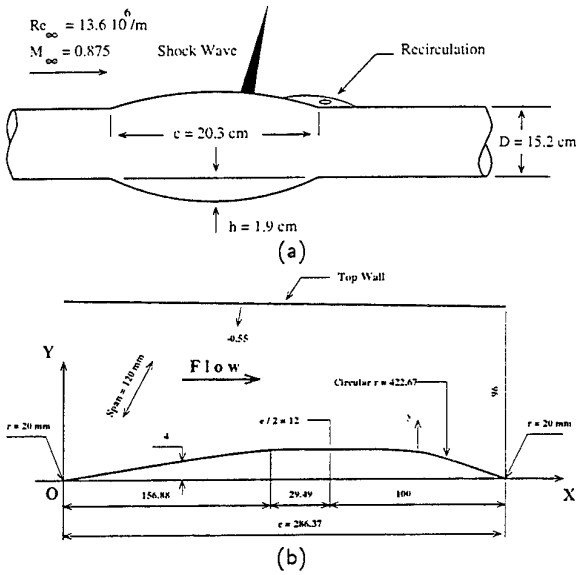


Figure 1: Schematic representation of the test cases, (a) Johnson *et al.* (1982) case and (b) Délery's (1983) case C.

Results

For the first case the linear $k-\epsilon$ model by Launder and Sharma (1974), as well as the two and three-equation non-linear models have been employed. Several discretisation grids have been tested and finally results on the grid 160×80 have been used for the comparisons.

The predicted surface pressure distributions are shown in Figure 2. As shown all models capture satisfactory the shock position and the pressure distribution before the shock. Differences are encountered at the pressure plateau after the shock where the flow is separated. The non-linear models are able to capture better the pressure distribution apparently due to the functional form of the c_μ coefficient. Results are shown in Figure 3 for the velocity and turbulent shear stress profiles using the above models. The non-linear models provide better results both upstream ($x/c = 0.75$) and downstream ($x/c = 1.0$) of the shock wave. The non-linear models capture better (Figure 3) the development of the maximum turbulent shear stress and, thus, predict better the boundary layer separation.

The Nagano-Kim (1988) linear model and the two and three-equation non-linear models were employed for the second test case. A 121×121 grid has been used. In previous computations (Haase *et al.*, 1992) this grid was found to be adequate for obtaining grid independent solution. For all calculations the exit pressure was fixed to 60 KPa. As expected, the exit pressure is an important parameter to control the position of the shock. In this work the value of 60 KPa was found adequate for calculations with the linear and non-linear models.

As can be seen from the pressure distribution (Figure 4) the predictions obtained by the linear and non-linear models are in fair agreement with the experimental data before and after the interaction zones. Most of the differences are encountered in the recirculation region.

In Figure 5 the velocity profiles are compared with the experimental data. The linear models underpredict the separation region and, consequently, the pressure and strength of the λ-shock are underestimated.

The non-linear models predict better the flow near the interaction region as can be seen from the velocity profiles and Figures 6,7 where the shock structures predicted by the linear (Nagano-Kim) and non-linear $k-\epsilon-A_2$ models are shown.

More information about the accuracy of the models can be obtained by comparing the shear stress profiles (Figure 5). The linear models tend to underestimate the magnitude of the turbulent shear stress while the non-linear models give slightly better predictions. All models fail however, to predict the shear stress magnitude indicated by the experimental data. This is striking in particular for the $k-\epsilon-A_2$ model which is sensitive to the anisotropy of the turbulent flow and, thus, was expected to give better predictions for the stress levels. Examining the experimental data by Délery it was found that the measurements indicate a magnitude of the u' velocities about 16 times more than the w'. As reported in the work by Benay et al. (1989) such anisotropy is apparent and is mainly due to oscillations of the shock structure that magnify the turbulence. It is known that shock waves are sources of anisotropy which is convected downstream, but this phenomenon needs further investigation.

The calculation for the linear model requires 610 CPU minutes on an HP 9000/700 workstation. For the nonlinear model the CPU time was increased to 890 CPU minutes. A summary of the required CPU time is shown in Table 1.

CONCLUSIONS

Validation and assesment of linear and non-linear two and three-equation models has been obtained in transonic flows with shock-boundary layer interaction inducing separation. It was found that the linear eddy-viscosity models underestimate the separated flow regions and the strength of the shock structures. On the other hand the present non-linear eddy-viscosity models were found to give consistently better predictions for the mean flow and turbulence quantities. The price to be paid is an increase of the CPU time.

Acknowledgements : The financial support through CEC (COP-94-1239) and EPSRC (GR/L18457) is gratefully acknowledged.

REFERENCES

Bachalo,W.D. and Johnson, D.A., 1979, "An Investigation of Transonic Turbulent Boundary Layer Separation Generated on an Axisymmetric Flow Model", *AIAA Pa-*

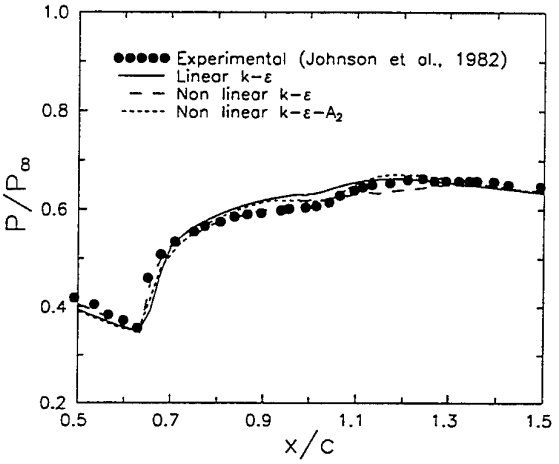


Figure 2: Comparison between experimental data and numerical results for the surface pressure distribution over the axisymmetric bump (Case 8611).

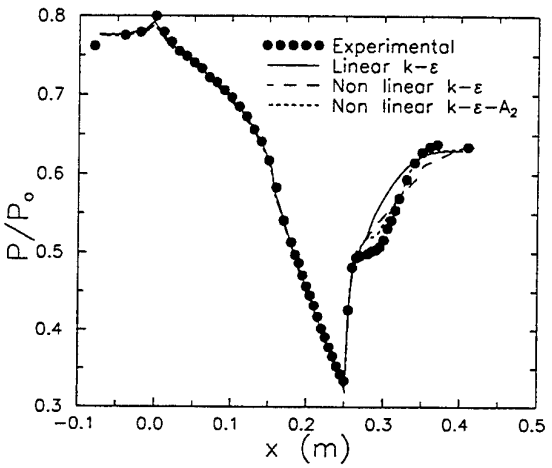


Figure 4: Comparison between experimental data and numerical results for the surface pressure distribution along the bump (Délery's Case C).

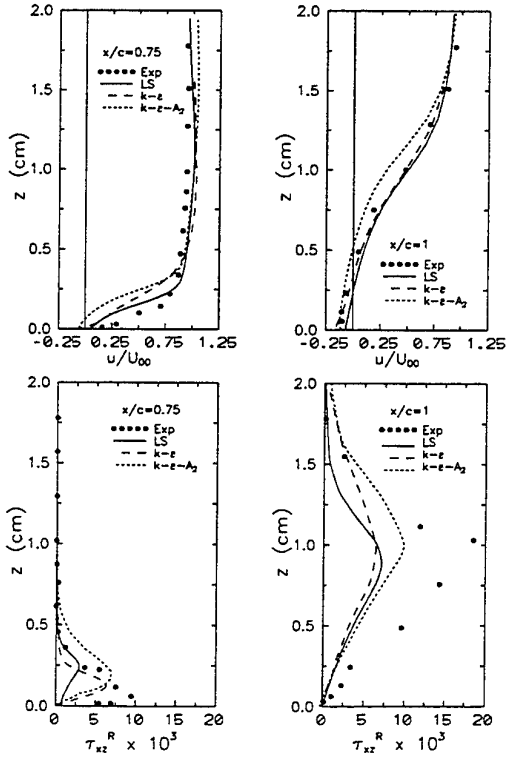


Figure 3: Comparison between experimental data and numerical results for the velocity and turbulent shear stress profiles (case 8611); Launder-Sharma model (LS) against non-linear $k-\epsilon$ and $k-\epsilon-A_2$ models.

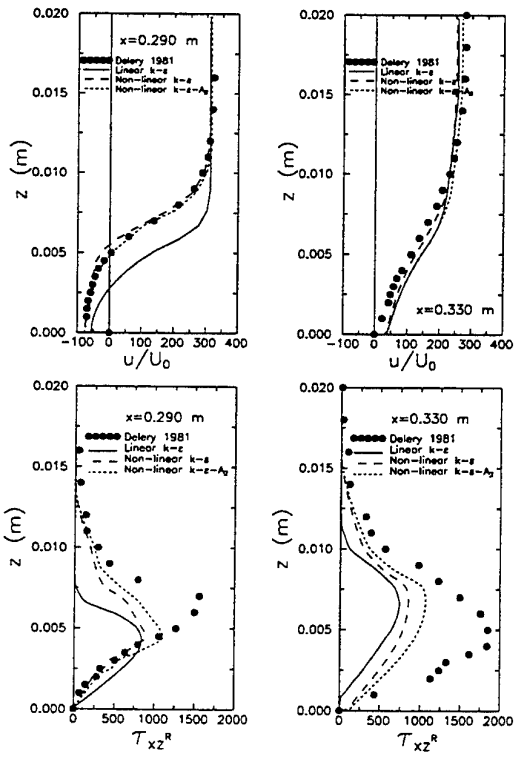


Figure 5: Comparison between experimental data and numerical results for the velocity and turbulent shear stress profiles (Délery's Case C); Nagano-Kim model against non-linear $k-\epsilon$ and $k-\epsilon-A_2$ models.

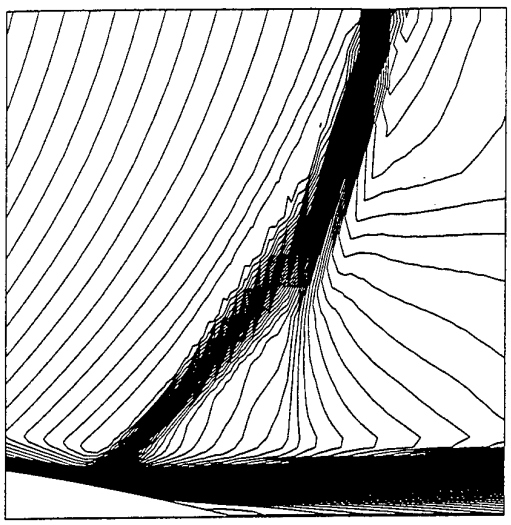


Figure 6: Prediction of the λ–structure using the Nagano-Kim $k-\epsilon$ model (Délery's Case C).

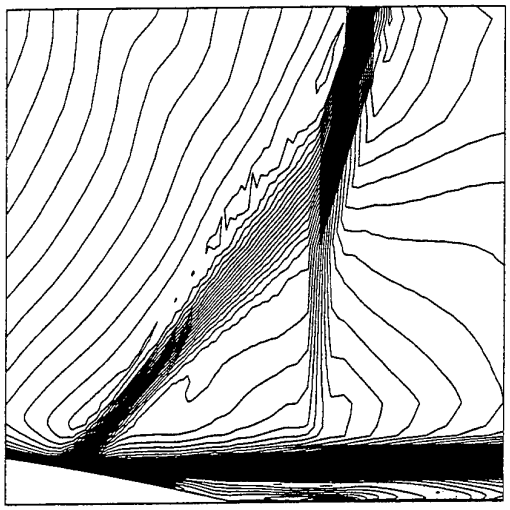


Figure 7: Prediction of the λ–structure using the non-linear $k-\epsilon-A_2$ model (Délery's Case C).

Model	Case 8611	Délery's Case C
Linear $k-\epsilon$	610	1090
Non-Linear $k-\epsilon$	890	1332
Non-Linear $k-\epsilon-A_2$	1028	1803

Figure 8: Work units required for computation of the two flow cases. A work unit corresponds to a minute of CPU time on a HP 9000/700/99 workstation.

per 79-1479.

Barakos, G. and Drikakis, D., 1996, "Implicit Unfactored Implementation of Two-Equation Turbulence Models in Compressible Navier-Stokes Methods", *Int. J. Num. Meth. Fluids* (*submitted*).

Benay, R., Cöet, C. and Délery, J.,1989, "A Study of Turbulence Modelling in Transonic Shock-Wave Boundary-Layer Interactions", *Turbulent Shear Flows*, Vol.6, 194, Springer, Berlin.

Craft, T.J., Launder, B.E. and Suga, K., 1996, "Development and Application of a Cubic Eddy-Viscosity Model of Turbulence", *Int. J. Heat and Fluid Flow*, Vol. 17, pp. 108–115.

Délery, J.M., 1983, "Experimental Investigation of Turbulence Properties in Transonic Shock-wave/Boundary-Layer Interactions", *AIAA J.*, Vol. 21, pp. 180–185.

Délery, J.M., 1980, "Modern Measurement Techniques in Shock Boundary Layer Interactions", *VKI LS=1080-8*, Belgium.

Drikakis, D. and Durst, F., 1994, "Investigation of Flux Formulae in Transonic Shock Wave/Turbulent Boundary Layer Interaction", *Int. J. Num. Meth. Fluids*, Vol. 18, pp. 385–413.

Eberle, A., Rizzi, A. and Hirschel, E.H., 1992, "Numerical Solutions of the Euler Equations for Steady Flow Problems", Springer Verlag, Wiesbaden.

Haase, W., Brandsma, F., Elsholz, E., Leschziner, M. and Schwambron, D. (Eds.),1993, "Euroval, A European initiative on Validation of CFD codes", Notes on Numerical Fluid Mechanics, Vol. 42, Vieweg Verlag.

Johnson, D.A., Horstman, C.C. and Bachalo, W.D., 1982, "'Comparison Between Experiment and Prediction for a Transonic Turbulent Separated Flow", *AIAA J.*, Vol. 20, pp. 737–744.

Kline, S.J., Cantwell, B.J. and Lilley, G.M. (eds.), 1981, "The 1980-81 AFSOR/HTTM-Stanford Conference on complex Turbulent Flows: Comparison of Computation and Experiment", Vol. I. Objectives, Evaluation of Data, Specification of Test Cases, Discussion and Position Papers", Stanford University, USA.

Launder, B.E. and Sharma, B.I., 1974, "Application of the Energy-Dissipation Model of Turbulence to the Calculation of Flow Near a Spinning Disk", *Letters in Heat and Mass Transfer*, Vol. 1, pp. 131–138.

Liou, W.W. and Shih, T.H., 1996, "Transonic Turbulent Flow Predictions with Two-Equation Turbulence Models", NASA CR-198444, ICOMP-96-02, NASA, Lewis, OH, USA.

Marvin J.G. and Huang, G.P.,1996, "Turbulence Modeling - Progress and Future Outlook", Keynote Lecture presented at the 15th international Conference on Numerical Methods in Fluid Dynamics, June 1996, Monterey, CA, USA.

Nagano, Y. and Kim, C., 1988, "A Two-Equation Model for Heat Transport in Wall Turbulent Shear Flows", *J. Heat Transfer*, Vol. 110, pp. 583–589.

Speziale C.G., 1987, "On Nonlinear $K-l$ and $K-\epsilon$ Models of Turbulence", *J. Fluid Mechanics*, Vol. 178, pp. 459–475.

Suga, K., 1995, "Development and Application of a Non-Linear Eddy Viscosity Model Sensitized to Stress and Strain Invariants", Ph.D. Thesis, UMIST, Manchester.UK.

COMPUTATION OF TURBULENT SHOCK WAVES USING SECOND-MOMENT CLOSURES

Gilles Brun[1], Jean-Marc Hérard[2], Denis Jeandel[1], Markus Uhlmann[1]

[1]Ecole Centrale de Lyon.
36, avenue Guy de Collongue. 69131. Lyon . France.

[2]Electricité de France. Direction des Etudes et Recherches.
Département Laboratoire National d'Hydraulique.
6, quai Watier. 78400. Chatou. France

ABSTRACT

We present herein some new results on second order modelling of turbulent compressible flows. Emphasis is given on suitable ways to compute non conservative convective systems arising from physical modelling, focusing on Finite-Volume schemes. It is shown that trustable computations of these systems cannot be achieved when using Euler-based approximate (or exact) Riemann solvers, though this is implicitely stated by many workers in the field.

INTRODUCTION

It is claimed herein that the accurate computation of turbulent compressible flows, using second order closures, requires the development of specific approximate Riemann type solvers to account for first-order differential terms. Emphasis is given herein on a simple objective and strongly realisable model arising from the literature, but the methodology applies to more complex closures arising from the literature (Shih and Lumley, 1985 ; Fu et al, 1987). Steady computations of turbulent flows with such closures are usually performed with help of Euler based Riemann solvers, which means that the influence of the turbulence on the behaviour of the whole system is highly negligible. Actually, this is not an adequate strategy, even when using two-equation closures, as pointed out before in (Hérard, 1995b). This is even more true when investigating systems which have been proposed to account for the dynamical behaviour of the Reynolds stress tensor.

In the first two sections, governing equations and basic properties are described. These results enable us to propose in the third section a simple but efficient way to compute time-dependent solutions including shocks, using either structured or unstructured meshes. The fourth section is devoted to the presentation of sample computational results of turbulent shock-tube experiments, which confirm the capabilities of the adequate scheme, and the failure of "Euler" type approximate Riemann solvers.

GOVERNING EQUATIONS

The basic set of equations is based on standard Favre's averaging of Navier-Stokes equations (Favre, 1965), and we refer to Vandromme and Ha Minh (1986) ,Vandromme (1991), Sarkar and Lakshmanan (1991) for instance for details on modelling features . The set of equations is (overbar and tilde notations have been droped, except for turbulent mass fluxes <u">) :

$$(\rho)_{,t} + (\rho U_i)_{,i} = 0 \tag{1}$$

$$(\rho U_i)_{,t} + (\rho U_i U_j)_{,j} + (p\,\delta_{ij})_{,j} + (R_{ij})_{,j} = -(\Sigma_{ij}^{visc})_{,j} \tag{2}$$

$$(E)_{,t} + (E\,U_j)_{,j} + (U_i(p\,\delta_{ij}+R_{ij}))_{,j} = \ldots - (U_i(\Sigma_{ij}^{visc}))_{,j} + \left(\sigma_E\left(\frac{p}{\rho}\right)_{,j}\right)_{,j} + \left(\frac{\Phi_{jj}^k}{2}\right)_{,k} - \left(\langle u_i'' \rangle\, p\right)_{,i} \tag{3}$$

$$(R_{ij})_{,t} + (R_{ij}\,U_k)_{,k} + R_{ik}U_{j,k} + R_{jk}U_{i,k} = \ldots \Phi_{ij} - \frac{2}{3}\left(\frac{\varepsilon}{I}\right)\mathrm{trace}\,(R)\,\delta_{ij} + \left(\Phi_{ij}^k\right)_{,k} - \langle u_i'' \rangle\, p_{,i} - \langle u_i'' \rangle\, p_{,i} \tag{4}$$

$$R_{ij} = \langle \rho\, u_i'' u_j'' \rangle \tag{5}$$

$$\Sigma^{v}_{ij} = -\mu\,(U_{i,j} + U_{i,j} - \frac{2}{3} U_{l,l}\delta_{ij}) \qquad (6)$$

$$p = (\gamma-1)\,(E - \frac{\rho U_j U_j}{2} - \frac{1}{2} R_{jj}) \qquad (7)$$

It is recalled that admissible states are such as :

$$n_i\, R_{ij}(x,t)\, n_j \geq 0 \qquad (8a)$$

$$\rho(x,t) \geq 0 \quad ; \quad p(x,t) \geq 0 \qquad (8b)$$

Given any vector $\mathbf{n}$ in IR^3 with unit norm, we introduce :

$$R_{nn} = \mathbf{n}^t\, \mathbf{R}\, \mathbf{n} \qquad (9a)$$

$$U_n = \mathbf{U}^t\, \mathbf{n} \qquad (9b)$$

ρ stands for the mean density, $\mathbf{U}$ is the mean velocity, E denotes the mean total energy and P is the mean pressure. The Reynolds stress tensor is $\mathbf{R}$, and K is the turbulent kinetic energy (K = trace($\mathbf{R}$) : 2) ; γ is the ratio of specific heats and σ_E is positive ; μ is the molecular viscosity.

Solutions of the whole closed set should be such that (8a-8b) holds. Moreover, the set of governing equations should be strongly realisable (see Fu et al (1987), Hérard (1994ab, 1995a, 1996), Lumley (1978), Pope (1985), Shih and Lumley (1985), Shih et al (1994) for details). Lumley (1978) proposed a "slow" model to account for Φij, which is in agreement with previous constraints, and also fulfills the objectivity requirement (Speziale, 1979). More recently, two slightly distinct proposals were suggested by Shih and Lumley (1985), and Fu, Launder, Tselepidakis (1987), in order to account for "rapid terms". We focus on Lumley's closure, and in addition assume that the mass flux is modeled according to :

$$\langle u_i'' \rangle = \tau \frac{R_{ij}}{\rho} \rho_{,j}$$

BASIC RESULTS

Entropy inequality

We introduce the state variable $\mathbf{W}^t = (\rho, \rho U, \rho V, \rho W, E, R_{11}, R_{22}, R_{33}, R_{12}, R_{13}, R_{23})$, and define : $\eta = -\rho\, \mathrm{Log}(p\rho^{-\gamma})$, and : $f^{nv}_{\eta}(\mathbf{W}) = \mathbf{U}\,\eta$. Then :

Proposition :
Regular solutions W of the set ((1) to (4) are such that :

$$\eta_{,t} + \nabla.\,(f^{nv}_{\eta}(\mathbf{W})) + \nabla.(\,f^{v}_{\eta}(\mathbf{W},\nabla\mathbf{W})) = S_{\eta}(\mathbf{W},\nabla\mathbf{W}) \leq 0$$

The source term may be written as (setting T= P/ρ) :

$$S_{\eta}(\mathbf{W},\nabla\mathbf{W}) = -\frac{(\gamma-1)}{T}\left(\frac{\sigma_E}{T} T_{,i}T_{,i} + \varepsilon - \Sigma^{visc}_{ij}(U_{i,j}+U_{j,i})\right) - (\gamma-1)\langle u_i'' \rangle\, \rho_{,i}$$

This entropy inequality enables to connect states through genuinely non linear fields in a physical way. The reader is referred to Brun et al (1997) for proof. It obviously requires that the Reynolds stress tensor is realisable.

Hyperbolicity

Focusing now on statistically two-dimensional turbulence, and hence assuming that : $R_{13} = R_{23} = 0$, $W = 0$, $\varphi_{,3} = 0$, whatever φ stands for, we may introduce a new "2D" state variable $\mathbf{Z}^t = (\rho, \rho U, \rho V, E, R_{11}, R_{22}, R_{33}, R_{12})$. The non conservative convective subset, reads:

$$\mathbf{Z}_{,t} + \sum_{i=1}^{2} (\mathbf{F}_i(\mathbf{Z}))_{,i} + \sum_{i=1}^{2} \mathbf{A}^{nc}_i(\mathbf{Z})\, \mathbf{Z}_{,i} = 0 \qquad (10)$$

For realisable states, we set : $c_1 = \left(\frac{\gamma p}{\rho} + 3\frac{R_{nn}}{\rho}\right)^{1/2}$, and : $c_2 = \left(\frac{R_{nn}}{\rho}\right)^{1/2}$, and we get :

Proposition :
The two-dimensional non conservative first-order differential set (10) is a non strictly hyperbolic system as soon as states are in agreement with (8a, 8b). The eigenvalues are :

$$\lambda_1 = U_n - c_1$$
$$\lambda_2 = U_n - c_2$$
$$\lambda_3 = \lambda_4 = \lambda_5 = \lambda_6 = U_n$$
$$\lambda_7 = U_n + c_2$$
$$\lambda_8 = U_n + c_1$$

In a one-dimensional framework, the 1-wave and the 8-wave are Genuinely Non Linear ; other fields are Linearly Degenerate.

The eigenvalue problem is "ill-conditioned", due to the fact that the turbulent Mach number, which is proportional to $(K/P)^{1/2}$ is usually much smaller than one.

Solution of the 1D Riemann problem

If σ stands for the speed of a travelling discontinuity, the following approximate jump conditions arise (we set : $[\varphi] = \varphi_R - \varphi_L$, and: $\overline{\varphi} = (\varphi_R + \varphi_L)/2$) :

$$-\sigma[\rho] + [\rho U] = 0 \qquad (11a)$$

$$-\sigma[\rho U] + [\rho U^2 + R_{11} + P] = 0 \qquad (11b)$$

$$-\sigma[\rho V] + [\rho U V + R_{12}] = 0 \qquad (11c)$$

$$-\sigma[E] + [U\,(E+R_{11}+P)] + [V\,R_{12}] = 0 \qquad (11d)$$

$$-\sigma[R_{33}] + [U\,R_{33}] = 0 \qquad (11e)$$

$$-\sigma[R_{11}] + [U\,R_{11}] + 2\,\overline{R_{11}}[U] = 0 \qquad (11f)$$

$$-\sigma[R_{22}] + [U\,R_{22}] + 2\,\overline{R_{12}}[V] = 0 \qquad (11g)$$

$$-\sigma[R_{12}] + [U\,R_{12}] + \overline{R_{11}}[V] + \overline{R_{12}}[U] = 0 \qquad (11h)$$

(see Smoller (1983) for fundamentals of conservative hyperbolic systems, and Le Floch (1988) , Le Floch and Liu (1992), for theoretical results within the frame of non

linear hyperbolic systems in non conservative form). Owing to the entropy inequality : $-\sigma[\eta]+[F_\eta]\leq 0$, it may be proved that (see Brun et al (1997), Uhlmann (1997)) :

Proposition :
Assuming the above mentioned approximate jump conditions (11) hold, t he 1D-Riemann problem associated with the non linear non conservative hyperbolic system (10) has a unique entropy-consistent solution, provided that some condition on the data on each side of the initial discontinuity holds. The realisability of the Reynolds stress tensor is preserved, through contact discontinuities, and through genuinely non linear fields.

A counterpart of the latter result within the frame of two-equation compressible models was detailed in Forestier et al (1997), Hérard et al (1995).

NUMERICAL ALGORITHM

The computation of viscous fluxes, which are present on the right hand side of equations (2) and (3), only requires the implementation of centered schemes. Moreover, suitable ways to implement source terms (right hand side in equation (4)) were discussed in a previous work (Hérard, 1995a). Since no Roe-type approximate Riemann solver (Roe, 1981) based on a state average may be exhibited here (see Brun et al (1997) for details), we present below a modified version of the latter, which is based on the scheme previously described in (Hérard, 1995b). We define : $\mathbf{Z}^t=(\rho,\rho U,\rho V,E,R_{11},R_{22},R_{33},R_{12})$, and $\mathbf{B_1(Z)}$:

$$\mathbf{B}_1(\mathbf{Z})=\frac{d\mathbf{F}_1}{d\mathbf{Z}}(\mathbf{Z})+\mathbf{A}_1^{nc}(\mathbf{Z}) \qquad (12)$$

We recall that :

$$\mathbf{F}_1^t(\mathbf{Z})=(\rho U,\ \rho U^2+p+R_{11},\ \rho UV+R_{12},\ U(E+p+R_{11})+VR_{12},..$$
$$U\,R_{11},\ U\,R_{22},\ U\,R_{33},\ U\,R_{12}) \qquad (13)$$

Integrating equation (10) over cell Ω_i provides :

$$\mathbf{vol}\ (\Omega_i)(\mathbf{Z}_i^{n+1}-\mathbf{Z}_i^n)+\Delta t\int_{\Gamma_i}\mathbf{F}_1^{num}(\mathbf{Z}^n)\,d\Gamma+\Delta t\,\mathbf{S}_i(\mathbf{Z}^n)=0 \qquad (14)$$

where :

$$\mathbf{S}_i^t(\mathbf{Z}^n)=(0,0,0,0,2(R_{11})_i^n\int_{\Omega_i}U_{,x}^n\,d\Omega,\ 2(R_{12})_i^n\int_{\Omega_i}V_{,x}^n\,d\Omega,$$
$$0,\ (R_{11})_i^n\int_{\Omega_i}V_{,x}^n\,d\Omega+(R_{12})_i^n\int_{\Omega_i}U_{,x}^n\,d\Omega) \qquad (15)$$

All terms in (15) are computed using centred schemes. The numerical flux in the integral on the left hand side of (14), is then set as :

$$(\mathbf{F}_1^{num})_{ij}(\mathbf{Z}^n)=\frac{1}{2}((\mathbf{F}_1)(\mathbf{Z}_i^n)+(\mathbf{F}_1)(\mathbf{Z}_j^n))$$
$$-\frac{1}{2}\,|\mathbf{B}_1((\mathbf{Z}_i^n+\mathbf{Z}_j^n)/2)|\,(\mathbf{Z}_j^n-\mathbf{Z}_i^n) \qquad (16)$$

using standard notations. Hence the scheme (14) is complete.

A slightly different scheme was also recently derived, which is based on the proposal by Gallouet (1996), Gallouet and Masella (1996), Masella et al (1996). This second scheme takes advantage of both Godunov's basic idea and Roe's approximate Riemann solver (Roe, 1981), and has been extensively investigated within the frame of Euler equations (Masella, 1996), and some hyperbolic two-phase flow models (Masella, 1996 ; Combe and Hérard, 1997).

COMPUTATION OF SHOCK WAVES

We present below numerical results obtained with the scheme detailed in the previous section. The resulting flow contains a symmetrical double shock wave. This test case is much interesting since it enables to examine the behaviour of the scheme near a wall boundary when dealing with impinging jets. There exists a strong coupling between various Reynolds stress components, but also between mean variables and second-moments. Riemann invariants U, (p+R11) are- well preserved through the 2-wave, the 3-4-5-6 wave and the 7-wave. It must also be emphasised that the mean density does not vary across the 2-wave and the 7-wave, according to theoretical results. Additional notations are introduced in one figure:

$$V^+=V+\frac{R_{12}}{(\rho\,R_{11})^{1/2}}\ ;\ V^-=V-\frac{R_{12}}{(\rho\,R_{11})^{1/2}}$$

It is emphasized that V^+ (respectively V^-) remains constant through the 2-wave (respectively the 7-wave). The normal component of the velocity U behaves as its counterpart in Gas Dynamics ; the tangential velocity V is non trivial, due to the strong shear induced by the non-zero component R_{12}. All Reynolds stress components (except R_{33}) have been plotted in the second figure ; it may be checked that the determinant $(R_{11}R_{22}-(R_{12})^2)$ remains positive.

Results presented here allow the comparison with results obtained using an "Euler" based approximate Riemann solver, where the computation of first-order convective fluxes which do not involve the Reynolds stress tensor is done using an upwinding technique based on the following system :

$$(\rho)_{,t}+(\rho U_i)_{,i}=0$$

$$(\rho U_i)_{,t}+(\rho U_iU_j)_{,j}+(p\,\delta_{ij})_{,j}=0$$

$$(E)_{,t}+((E+P)\,U_j)_{,j}=0$$

$$(R_{ij})_{,t}+(R_{ij}\,U_k)_{,k}=0$$

whereas the remaining first-order differential terms are computed using centered schemes. Obviously, the computed

solution of a double shock wave shows that the Euler-based solver cannot recognize the two new waves, and the whole results in a spurious oscillation for variables which should vary across these two new waves, according to the theoretical results.

CONCLUSION

The computation of turbulent compressible flows with second-moment closures requires using specific algorithms. Otherwise spurious solutions may develop, if Euler-based schemes are used. Accurate prediction of slow internal waves can be achieved provided that fine meshes and (or) second order MUSCL type extension is implemented. The scheme which has been described in this contribution accounts for non conservative first order differential terms. This is compulsory in order to prevent occurence of negative values of the mean pressure. The approximate Riemann solver enables to preserve the realisability of the whole Reynolds stress tensor (i.e. the positivity of fundamental minors). Other suitable ways to compute shock waves were detailed in (Buffard and Hérard , 1996) when focusing on one or two-equation turbulence models. These results may be extended to the frame of second-moment closures.

REFERENCES

Brun, G., Hérard, J.M., Jeandel, D., Uhlmann, M., 1997, "Suitable Reynolds stress closures and their numerical solution in compressible flow" *in preparation.*

Buffard, T., Hérard, J.M., 1997, "A conservative fractional step method to solve non isentropic Euler equations", *Computer Methods in Applied Mechanics and Engineering,* vol. 144, n° 3-4, pp. 199-225.

Buffard, T., Hérard, J.M., 1996, "Approximate Riemann type solvers to compute turbulent compressible one and two-equation models" *ASME FED, vol. 238,* pp. 189-196.

Combe, L. , Hérard, J.M., 1997, "Computation of two-phase flows on unstructured meshes" Proceedings on the 10th *Int. Conf. on Numerical Methods in Laminar and Turbulent Flows*, Swansea, UK, july 21-25, 1997.

Favre, A. , 1965, "Equations des gaz turbulents compressibles" *Jour. Mec.,* vol. 4, pp. 391-421.

Eymard, R., Gallouet, T., Herbin, R., 1997, "Finite Volume methods" *Handbook for Numerical Analysis*, P.G. Ciarlet and P.L. Lions editors.

Forestier, A., Hérard, J.M., Louis, X., 1997, "A Godunov type solver to compute turbulent compressible flows" *C.R. Acad. Sci. Paris,* I-324.

Fu, S, Launder, B.E., Tselepidakis, D.P., 1987, "Accomodating the effects of high strain rates in modelling the pressure strain correlations"*UMIST report TFD 87/5* .

Gallouet, T. , 1996, "Rough schemes for complex hyperbolic systems" Proceedings of the *First Int. Symp. on Finite Volumes for Complex Applications*, Rouen-France, 15-18 july 1996.

Gallouet, T., Masella, J.M., 1996, A rough Godunov scheme" *C. R. Acad. Sci. Paris,,* I-323, pp. 77-84.

Godunov, S.K., 1959, "A difference method for numerical calculation of discontinuous equations of hydrodynamics" *Math Sb.*, Vol. 47, pp. 217-300.

Hérard, J.M., 1994ab, "Basic analysis of some second moment closures". a. Part I : incompressible isothermal turbulent flows" *Theoretical and Computational Fluid Dynamics*, vol. 6, n°4, pp. 213-233 . b. Part II : incompressible turbulent flows including buoyant effects" *Coll.ection des Notes internes DER 94NB00053.*

Hérard, J.M. , 1995a, "Realisable second-moment closures and a priori suitable algorithms" *Turbulence , Heat and Mass Transfer 1*, K. Hanjalic and J.C.F. Pereira editors, pp. 154-160.

Hérard, J.M., 1995b, " An approximate Riemann solver to compute a non conservative hyperbolic system derived from a turbulent compressible model " *EDF report HE-41/95/009/A*, in French.

Hérard, J.M., 1996, "Realisable non degenerate second-moment closures for incompressible turbulent flows" *C. R. Acad. Sci. Paris*, t.322, IIb, pp. 371-377.

Hérard, J.M., Forestier, A., Louis, X., 1995, "A non strictly hyperbolic system to describe compressible turbulence" *Collection des Notes internes DER 95NB00003.*

Le Floch, P., 1988, "Entropy weak solutions to non linear hyperbolic systems in non conservative form" *Comm. in Part. Diff. Eq.*13(6), pp. 669-727.

Le Floch, P., 1988, Liu, T.P., 1992, "Existence theory for non linear hyperbolic systems in non conservative form" *C.M.A.P. report 254.*

Lumley, J.L., 1978, "Computational modelling of turbulent flows" *Advances in Applied Mechanics*, vol. 18, pp. 123-176.

Masella, J.M., 1997, PhD thesis, Université Paris VI, Paris, France, May 29, 1997.

Masella, J.M., Faille, I., Gallouet, T., 1996, "On a rough Godunov scheme" submitted for publication in the *Int. J. for Comp.utational Fluid Dynamics.*

Pope, S.B. , 1985, " PDF methods for turbulent reactive flows " *Prog. Energy Combust Sci.*, vol. 11, pp. 119-192.

Roe, P.L., 1981, "Approximate Riemann solvers, parameter vectors and difference schemes" *J. Comp. Physics* , vol 43.

Sarkar, S., Lakshmanan, B. , 1991, " Application of a Reynolds stress turbulence model to the compressible shear layer" *AIAA journal*, vol. 29, pp. 743-749.

Shih, T., Lumley, J.L., 1985, "Modeling of pressure corelation terms in Reynolds stress and scalar flux equations" *Cornell University report FDA-85-3.*

Shih, T., Shabbir, A., Lumley, J.L., 1994, "Realisability in second moment turbulence closures revisited" *NASA Technical Memorandum 106469* .

Smoller, J., 1983, "Shock waves and reaction diffusion equations" *Springer-Verlag* .

Speziale, C.G., 1979, "Invariance of turbulent closure models" *Physics of Fluids A*, vol. 22, n° 6, pp. 1033-1037.

Uhlmann, M., 1997, PhD thesis, Ecole Centrale de Lyon, Lyon, France, April 17, 1997.

Vandromme, D., 1991, "Turbulence modelling for compressible flows and implementation in Navier-Stokes solvers" Lecture series, Von Karmann Institute for Fluid Dynamics .

Vandromme, D., Ha Minh, H., 1986, "About the coupling of turbulence closure models with averaged Navier-Stokes equations" *J. Comp. Physics* , vol 65, n° 2, pp. 386-409 .

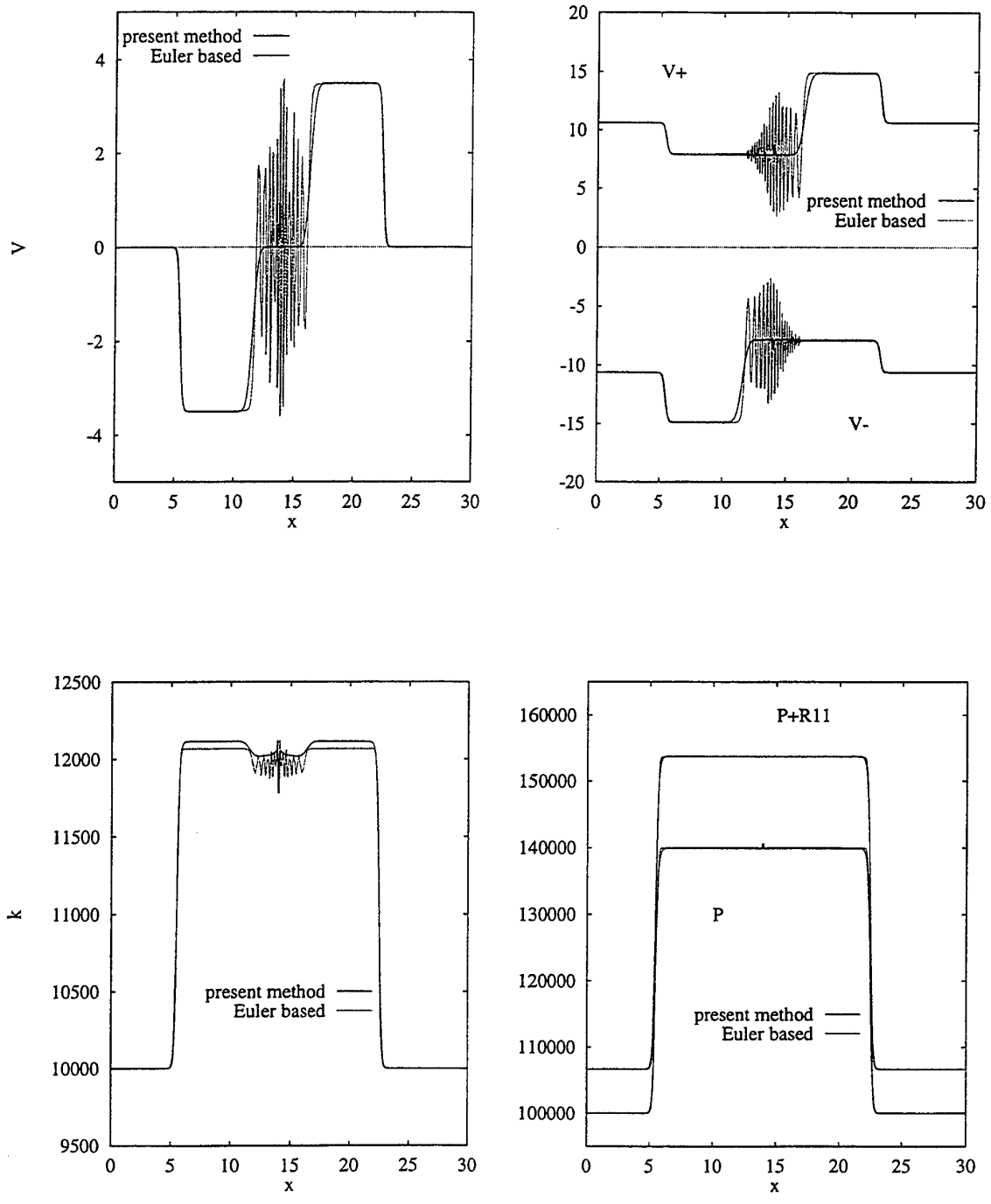


Figure 1 : double shock wave

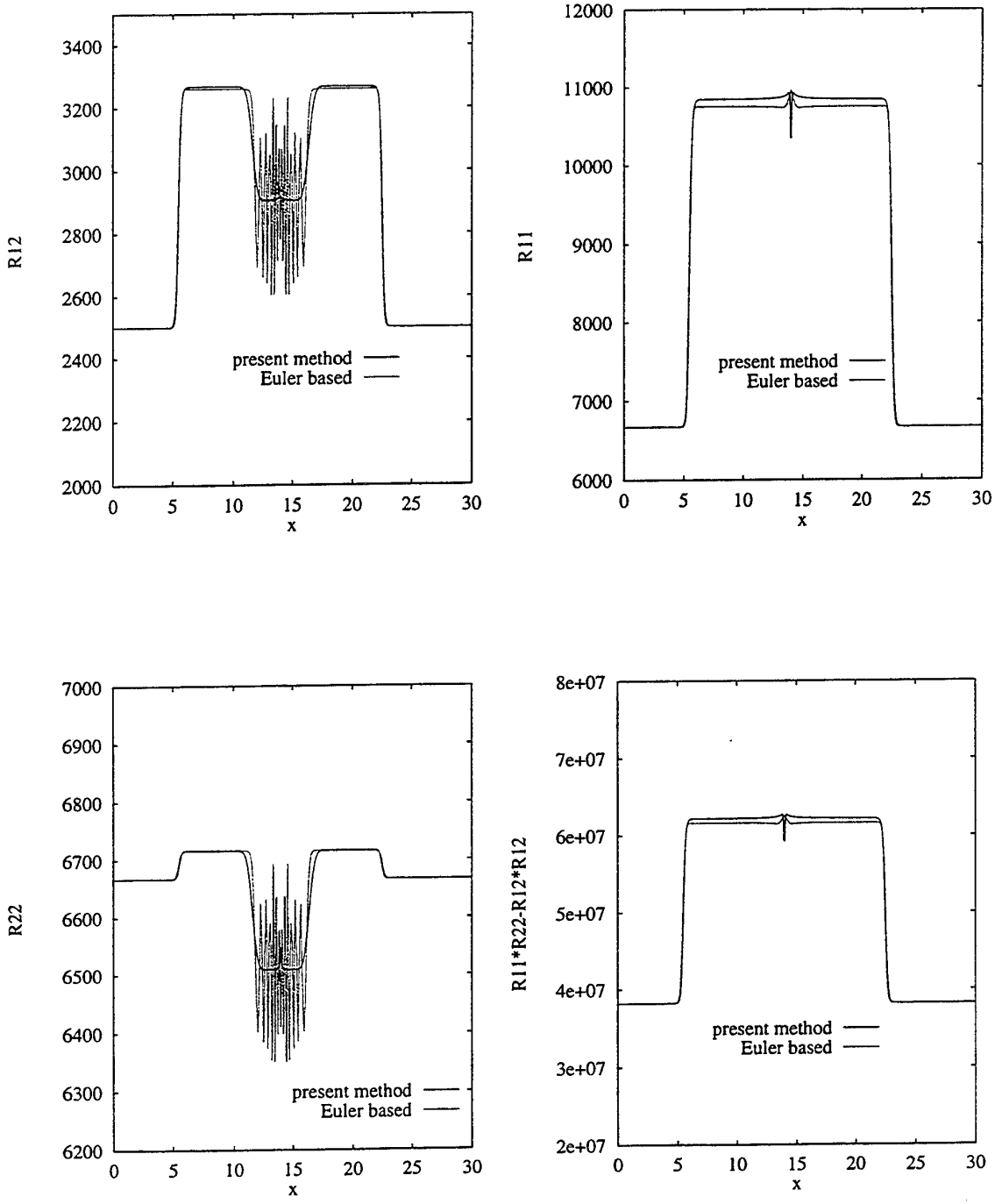


Figure 2 : double shock wave (continuing)

SESSION 33 - WALL FLOWS III

DIRECT NUMERICAL SIMULATION OF DECELERATED WALL-BOUNDED SHEAR FLOWS

Gary N. Coleman[1], John Kim[1] and Philippe R. Spalart[2]

[1]UCLA Mechanical & Aerospace Engrg., 48-121 Engr. IV, Box 951597, Los Angeles, California, 90095-1597, USA

[2]Boeing Commercial Airplane Group, P.O. Box 3707, MS 67-LM, Seattle, Washington, 98124-2207, USA

ABSTRACT

Fully developed turbulent two-dimensional channel flow is subjected to mean strains that represent the effect of pressure gradients in two- and three-dimensional boundary layers. This is done by applying irrotational temporal deformations to the flow domain of a conventional channel direct numerical simulation code. The velocity difference between the inner and outer layer is controlled by accelerating the walls in the streamwise-spanwise plane, allowing duplication of the defining features of both the inner and outer regions. Strains imitating infinite-swept-wing and two-dimensional adverse-pressure-gradient (APG) boundary layers are considered. We find that while both alter the structure of the turbulence, the influence of the APG dominates over that of the pure skewing. When the APG strain acts alone, behavior observed in the corresponding experiments is produced – namely an increase in turbulence intensity in the outer layer accompanied by diminished energy near the wall. The strained-channel flows, whose statistics depend only on time and one spatial dimension, are expected to be useful both as a means of addressing fundamental physical questions and also to test and develop turbulence models for spatially evolving pressure-driven boundary layers.

INTRODUCTION

The most obvious result of subjecting a turbulent boundary layer to an adverse pressure gradient (APG) is a reduction in the surface shear stress. But besides causing the mean skin friction to approach zero as the flow develops in the downstream direction, the bulk deceleration $\partial U/\partial x < 0$ is also responsible for deforming the turbulence in the region away from the wall (cf. figure 1*a*,*b*). While the importance of the inner-layer modification is clear – leading to a drop in production of turbulent kinetic energy, for example – the strain applied to the outer layer is also likely to be significant (Smits & Wood 1985, Bradshaw 1988). The objective of this study is to explore the relative importance of the inner- and outer-layer alterations introduced by adverse pressure gradients in two- and three-dimensional boundary layers. By obtaining a deeper understanding of the physics of APG boundary layers, we hope to contribute to the refinement and development of practical turbulence models applied to APG flows of general interest.

APPROACH

Our attention is directed toward the nonequilibrium flow created by suddenly imposing a mean strain field to turbulence that had previously been in a statistically stationary state. Specifically, incompressible turbulent two-dimensional (2D) plane channel flow is subjected to spatially uniform irrotational strains characteristic of those induced in the outer region of engineering boundary layers by pressure gradients. We are thus able to capture the essential physics of spatially developing pressure-driven shear layers using a temporally evolving flow. Advantages of this approach, which is described in detail in Coleman, Kim & Spalart (1996; hereinafter referred to as CKS) and represented schematically for the case of a 2D APG strain in figure 1, include having a single well-defined initial condition (instead of dealing with the uncertainty associated with inflow and outflow boundary conditions), being able to generate statistics by averaging over two homogeneous directions and both halves of the channel, and being able to use an unsteady one-dimensional problem to test and develop turbulence models for spatially evolving flows.

Solutions are obtained using direct numerical simulation (DNS); since all relevant scales of motion are resolved, no turbulence or subgrid-scale model is required. In contrast to previous DNS studies of strained flows, which assumed that both the strain and the turbulence were homogeneous (Rogallo 1981), here we apply a uniform strain to turbulence between two no-slip surfaces. The imposed strain field is given by the divergence-free irrotational deformation,

$$A_{ij} \equiv \frac{\partial U_i}{\partial x_j} = \begin{bmatrix} \partial U/\partial x & 0 & \partial U/\partial z \\ 0 & \partial V/\partial y & 0 \\ \partial W/\partial x & 0 & \partial W/\partial z \end{bmatrix}, \quad (1)$$

where

$$A_{11} + A_{22} + A_{33} = 0 \qquad \text{and} \qquad A_{13} = A_{31}. \quad (2)$$

Each point of the flow volume is affected by the strain (figure 1*c*). This amounts to distorting the entire computational domain consisting of the two walls at $y = \delta(t)$ (where δ is the channel half-width, which when $A_{22} \neq 0$ will be a function of time) and the periodic boundaries in x and z. The fact that the walls deform complicates the comparison between the near-wall regions of the present and actual pressure-driven boundary layers. However, since the magnitude of the irrotational outer-layer strains are typically much smaller than the mean shear near the wall, and because the appropriate behavior of the near-wall rotational gradients can be approximated in a straightforward manner (see below), the significance of this formal inconsistency is limited. It is convenient at this point to differentiate between the irrotational and vortical mean fields observed by the turbulence. The former is prescribed by imposing the various A_{ij} components in (1); the latter is due to wall-normal variations of the mean velocity $\overline{\mathbf{u}}(y)$ between the no-slip channel walls. Note that the applied irrotational strains will affect both the turbulence and the rotational mean, since the streamwise and spanwise shear, $\partial\overline{u}/\partial y$ and $\partial\overline{w}/\partial y$ respectively, are the components of mean vorticity (i.e. both the perturbation and mean vorticity will be altered by A_{ij}). In order to subject the turbulence near the walls to the correct rotational mean gradient the following strategy is employed: the walls are accelerated in the x-z plane such that the difference between the mean channel centerline velocity $(\overline{u}_c, \overline{w}_c)$ and the wall velocity (u_w, w_w) varies in time at the same rate that the

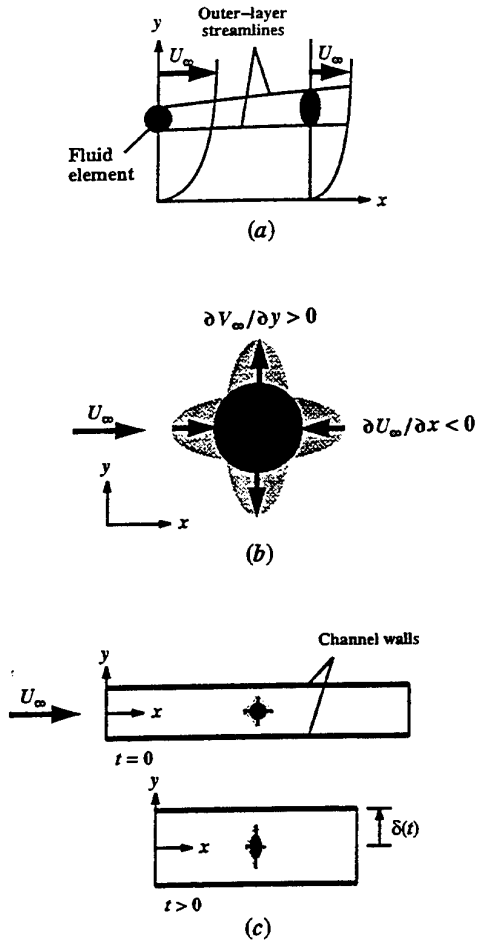


FIGURE 1. Schematic of 2D APG boundary layer. (*a*) Spatially developing analog. (*b*) Strain applied to fluid element at $x = 0$ of spatially developing flow and at $t = 0$ of strained channel DNS. (*c*) Initial and deformed domain of strained-channel DNS.

outer-layer velocity in the spatial flow changes as it convects downstream. For example, when the 2D APG strain given by $A_{11} = -A_{22} < 0$ is applied, the *difference* between the mean streamwise velocity at the centerline and the wall, $\overline{u}_c - u_w$, follows $\overline{u}_{c(0)} \exp(A_{11} t)$ (since we desire $\partial(\overline{u}_c - u_w)/\partial t = (\overline{u}_c - u_w) A_{11}$). This accounts for the bulk deceleration caused by an APG by diminishing the mean surface shear stress, and creates an 'inner layer' that propagates outward in time. In practice, instead of accelerating the walls the same result can be obtained by keeping the walls stationary and imposing a spatially uniform time-dependent pressure gradient that creates the same $\overline{u}_c(t)$ history. Since the two approaches are identical, for ease of visualization the DNS data presented below, which were generated with the moving-wall procedure, are plotted as if the nonzero pressure gradient had been used.

Three cases will be considered, defined by the strain-rate components summarized in table 1. The rationale for these choices will be explained below. The DNS results are obtained using a modified version of the spectral channel code of Kim, Moin & Moser (1987). It imposes the three principal strain rates in Cartesian coordinates, so that the numerical domain remains a right parallelopiped for all time; the off-diagonal (skewing) components in (1)

Case	A_{13}	A_{11}	A_{22}	A_{33}	$Re_\tau(0)$
I	0.99	−0.99	1.98	−0.99	180
Ia	0.99	0	0	0	180
II	0	−0.3	+0.3	0	400

TABLE 1: Case parameters.
(Strain magnitudes given in terms of initial u_τ/δ.)

are obtained by utilizing initial fields that flow through the domain at an angle with respect to the principal strain axes (cf. figure 2*c* of CKS). Two sets of numerical parameters are employed. For the runs that include nonzero A_{13}, an initially square domain of size $8\pi\delta/3 \times 8\pi\delta/3$ is used, with number of effective grid (quadrature) points of 256 x 256 in planes parallel to, and 129 in the direction normal to, the walls. Even though the initial Reyolds number for this run is the same as that used by Kim *et al.* (1987) for their 2D study ($Re_\tau = u_\tau\delta/\nu \approx 180$, where u_τ is the wall-friction velocity and ν the kinematic viscosity), the 3D nature of the present flow requires a much greater computational expense. For the run with no skewing (which implies that the principal-strain axes are aligned with the streamwise-spanwise directions), a higher Reynolds number is used, $Re_\tau(0) \approx 400$, and the initial streamwise and spanwise domain size L_x and L_z is $2\pi\delta$ and $\pi\delta$, respectively; the required number of streamwise n_x, wall-normal n_y, and spanwise n_z quadrature points is $(n_x, n_y, n_z) = (256, 193, 192)$.

Because of the time-dependence of the results, the 'mean' quantities presented below (denoted by an overbar) are obtained by averaging over planes parallel to the walls, over both halves of the channel and (unless explicitely stated otherwise) over at least four ensembles of each case. Multiple simulations were performed using the same strain parameters for statistically independent realizations of the 2D Poiseuille initial conditions.

RESULTS: INFINITE-SWEPT-WING STRAIN

We begin by imposing the most general deformation allowed by (1). The resulting flow, denoted Case I, duplicates the full complexity of a three-dimensional (3D) boundary layer, since lateral irrotational skewing ($A_{13} = A_{31}$), streamwise deceleration ($A_{11} < 0$), lateral convergence ($A_{33} < 0$) and wall-normal divergence ($A_{22} > 0$) are all present. This strain field thus corresponds to that found in the 3D boundary layer experiments of van den Berg *et al.* (1975) and Bradshaw & Pontikos (1985); in the present study the initial flow direction is oriented at 45 deg to the principal strain axes in the x-z plane, which implies that instead of the 35 deg sweep angle of the 'infinite swept wing' experiments, the effective sweep angle is 45 deg, and A_{11} and A_{33} are equal. The strain rates used here are larger than the experimental values, with the skewing equal to 0.99 of the initial ratio of the wall-friction velocity to the channel halfwidth. The experimental values are roughly 0.2 to 0.3 as large. Other details about the solution procedure (including the relationship between the mean centerline and wall velocities used to enforce the effective no-slip condition of the spanwise velocity; see figure 2) are the same as those employed for the 3D cases discussed in CKS.

The evolution of the Case I mean spanwise velocity is illustrated in figure 2. Two characteristics of pressure-driven 3D boundary layers can be seen: the growth of the layer thickness due to the streamwise deceleration/wall-normal divergence (i.e. the APG), and the 'instant' appearance of spanwise shear (mean streamwise vorticity) in

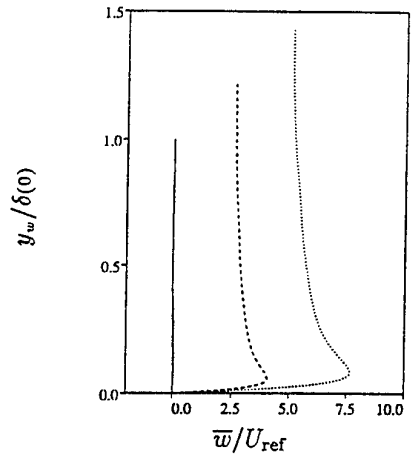


FIGURE 2. Mean spanwise velocity for Case I: ——— , $A_{13}t = 0$; - - - - , $A_{13}t = 0.10$; ····· , $A_{13}t = 0.18$. Reference velocity $U_{\rm ref} = 0.73u_{\tau(0)}$; distance from the wall $y_w = \delta - |y|$.

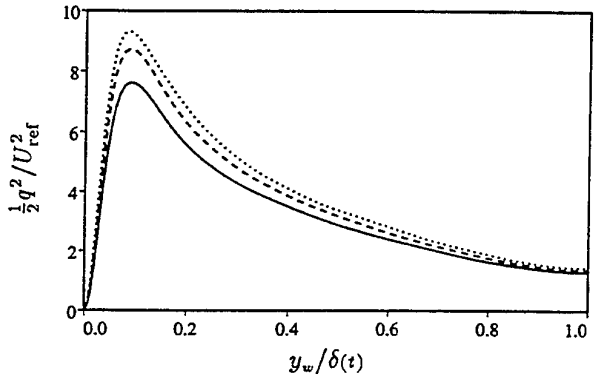


FIGURE 3. Turbulent kinetic energy $q^2/2 = \overline{u_i'u_i'}/2$ for Case I: symbols as in figure 2.

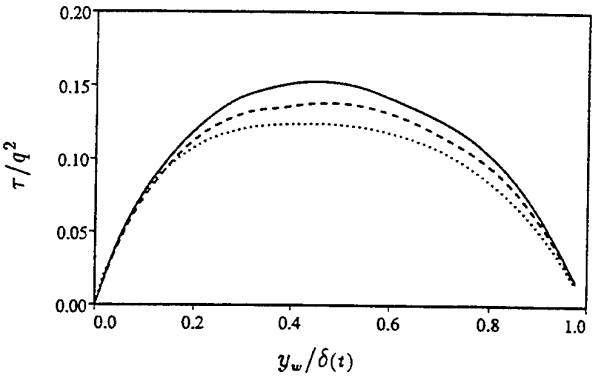


FIGURE 4. Structure parameter $a_1 = \tau/q^2$ for Case I: symbols as in figure 2. Reynolds shear stress $\tau = (\overline{u'v'}^2 + \overline{v'w'}^2)^{1/2}$.

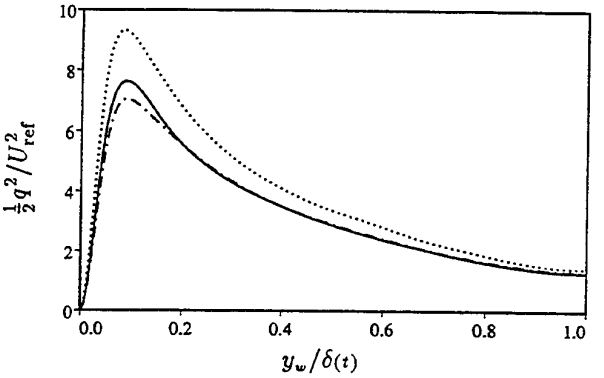


FIGURE 5. Turbulent kinetic energy $q^2/2 = \overline{u_i'u_i'}/2$ for Cases I and Ia: ——— , Case I and Ia initial condition, $A_{13}t = 0$ ($\alpha = 0\,\text{deg}$); ····· , Case I at $A_{13}t = 0.18$ ($\alpha = 10\,\text{deg}$); —·— , Case Ia at $A_{13}t = 0.20$ ($\alpha = 11.5\,\text{deg}$). Skewing angle $\alpha = \arctan(A_{13}t)$.

the outer layer, due to the A_{13}-induced skewing of the mean spanwise vorticity. This latter 'inviscid skewing' mechanism dominates the behavior of the outer-layer mean velocity to the extent that when viewed in hodograph form (not shown) the $\overline{u}$ versus $\overline{w}$ curve is closely approximated by the Squire-Winter-Hawthorne expression (Bradshaw 1987). The strain also alters the turbulent kinetic energy $q^2/2 = \overline{u_i'u_i'}/2$, causing it to increase across the entire layer (figure 3), and profoundly affects the relationship between q^2 and the turbulent shear stress $\tau = (\overline{u'v'}^2 + \overline{v'w'}^2)^{1/2}$. As shown in figure 4, the structure parameter ratio $a_1 = \tau/q^2$ is uniformly decreased by the applied strain. The significance of this reduction is twofold. From a fundamental point of view it implies that the efficiency of kinetic energy extraction from the mean by the turbulence has become less efficient. From a practical point of view it indicates an inaccuracy in turbulence models that assume a_1 is constant for all flows.

Structure parameter values smaller than that found in 2D layers have been observed in many 3D boundary layers – both shear- and pressure-driven, and equilibrium and nonequilibrium varieties (Bradshaw & Pontikos 1985, Moin *et al.* 1990, Schwarz & Bradshaw 1994, Eaton 1995, Johnston & Flack 1996). Some have proposed that this reduction is primarily a result of the spanwise shear. This hypothesis can be directly tested by comparing data from Cases I and Ia. Since the latter imposes the same skewing component upon the same initial conditions, but does so without also applying the normal components present in the Case I swept-wing straining field, the difference between the two simulations will be solely the result of non-skewing 'APG effects'. In figure 5, which contrasts the kinetic energy profiles after the same amount of total skewing ($\alpha \approx 10\,\text{deg}$), we see that all of the kinetic energy increase found in Case I is due to the principal strain components. In fact, when A_{11}, A_{22}, and A_{33} are zero, the only change in q^2 is a near-wall reduction, presumably because of the finite $\partial\overline{w}/\partial y$ below the peak in the crossflow (figure 2). The Case Ia results are therefore consistent with the previously observed *stabilizing* behavior associated with conversion of a 2D equilibrium boundary layer to a nonequilibrium one by addition of mean flow three-dimensionality (Bradshaw & Pontikos 1985, Moin *et al.* 1990, CKS). While this phenomenon is of great interest due to its paradoxical nature (since addition of a strain typically causes the turbulence to become *more* energetic), the present findings imply that it is of limited significance in practice – since in engineering boundary layers skewing is rarely if ever unaccompanied by an APG. A comparison of the evolution of the structure parameter under the Case I and Ia strain fields further indicates the dominance of APG over pure-skewing effects. Figure 6 reveals only a slight change of a_1 due solely to nonzero A_{13}, while the change produced (after the same mount of skewing) by the full strain field is much more profound. We conclude that for strain magnitudes of order u_τ/δ the infinite-swept-wing flow is less sensitive to pure skewing than to strains caused

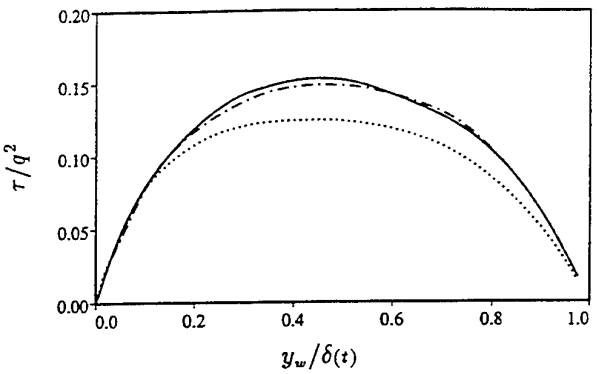


FIGURE 6. Structure parameter $a_1 = \tau/q^2$ for Cases I and Ia: symbols as in figure 5.

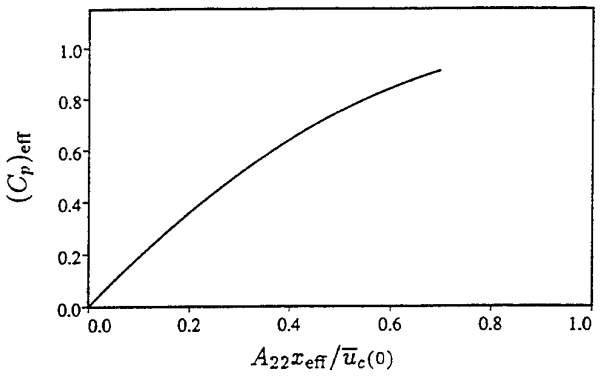


FIGURE 7. Effective pressure coefficient variation for 2D-APG strain runs. C_p based on initial mean centerline velocity $\overline{u}_c(0)$.

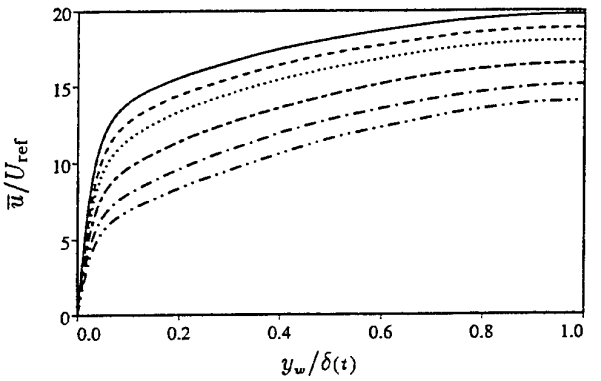


FIGURE 8. Mean velocity for Case II: ——— , $\exp(-A_{11}t) = 1.0$; - - - - , $\exp(-A_{11}t) = 1.05$; ····· , $\exp(-A_{11}t) = 1.1$; — - —, $\exp(-A_{11}t) = 1.2$; —·—, $\exp(-A_{11}t) = 1.3$; —···—, $\exp(-A_{11}t) = 1.4$. Reference velocity $U_{\text{ref}} = 1.02u_\tau(0)$.

by adverse pressure gradients. Webster, DeGraaff & Eaton (1996) have recently made similar observations regarding the dominant influence of the APG over skewing in their exerimental study of the 3D boundary layer over a swept bump. These findings point to the relevance of the subject of the next section, 2D APG wall layers.

RESULTS: 2D APG STRAIN

Our previous computations have shown that much of the behavior seen in the Case I results discussed above is also present when only the strain components created by an adverse pressure gradient are applied to the channel flow: a comparable increase in turbulent kinetic energy and decrease in a_1 is observed when $A_{11} = -A_{22} = -0.51u_\tau(0)/\delta(0)$ (half as large as the corresponding Case I terms) for the Series B runs presented in CKS. Consequently, there is little need to repeat Case I with A_{13} and A_{33} set to zero as a 2D APG run. Instead, we choose parameters that are more representative of the APG experiments of Nagano, Tagawa & Tsuji (1992) and Spalart & Watmuff (1993), in an attempt to come as near as possible to a spatially developing counterpart. Although we do not expect the present temporal and previous spatial flows to ever exactly correspond (if for no other reason than we are using a finite-width channel geometry to approximate the semi-infinite-domain boundary layer), the closer they can be made to agree the easier similarities and differences will be to understand. Another reason the previous and current studies are not identical is the differing variation of the effective mean pressure fields: the pressure coefficient C_p for the Nagano *et al.* experiment increases linearly with downstream distance x, while for the Spalart & Watmuff flow (which involved a parallel experiment and computation), the turbulence is subjected to a continuous pressure distribution varying smoothly from favorable to zero to adverse, such that at the start of the APG region, $dC_p/dx = 0$, and then increases monotonically downstream. For the present study, the effective C_p variation is shown in figure 7, where $(C_p)_{\text{eff}} = 1 - \exp(-2A_{22}t)$, $A_{22}x_{\text{eff}}(t)/\overline{u}_c(0) = 1 - \exp(-A_{22}t)$, and $x_{\text{eff}}(t)$ is the distance traveled in time t when convecting at the mean centerline velocity, such that $dx_{\text{eff}}/dt = \overline{u}_c(0)\exp(A_{11}t)$. Note that the effective pressure field varies quadratically, with the maximum $d(C_p)_{\text{eff}}/dx_{\text{eff}}$ occurring when the strain is first applied. The streamwise C_p variation is thus qualitatively different for each of the three APG cases.

The Case II parameters are shown in table 1. The constant uniform strain rate used is $A_{11} = -A_{22} = -0.3u_\tau(0)/\delta(0)$; this value implies that for Case II, the effective Clauser parameter $\beta_{\text{eff}} \approx 0.9[u_\tau(0)/u_\tau(t)]^2$, indicating a moderate-strength APG strain. Since the skin friction will decrease in time, β_{eff} becomes larger as time passes. For comparison, we note that in the Nagano *et al.* flow, β grows from less than one to 4.66 over a downstream distance of the order of 100 initial δ_{99} boundary layer thicknesses, while for Spalart & Watmuff, β varies from 0 to 2 over a region of about $20\delta_{99}$. When the present computation is stopped, the effective downstream distance traveled is $x_{\text{eff}} \approx 20\delta(0)$, which corresponds to $A_{22}x_{\text{eff}}/\overline{u}_c(0) \approx 0.3$ (cf. figure 7). During this time β_{eff} grows from about 0.9 to the order of 4.

As described above, the reduction in the surface shear associated with this APG straining field (which is held fixed in time), is accomplished by accelerating the walls in the downstream direction (equivalent to imposing a uniform time-dependent adverse pressure gradient in the channel), such that the mean centerline velocity $\overline{u}_c$ decreases in time with respect to the walls at the rate the freestream velocity U_∞ in the analogous spatial flow changes while moving downstream. This amounts to enforcing $\partial\overline{u}_c/\partial t = U_e(\partial U/\partial x)_e \approx \overline{u}_c A_{11}$ (see CKS). The resulting evolution of the Case II mean velocity is presented in figure 8. While the thickening of the layer (due to the distance between the centerline and walls increasing in time under the influence of the wall-normal stretching $A_{22} > 0$) is hidden by the use of the time-dependent channel halfwidth to normalized the wall-normal coordinate, the reduction in time of the mean surface shear (due to the effective bulk deceleration) is apparent. The drop in skin friction can be seen more clearly in figures 9 (showing the effective C_f history) and 10, which illustrates the temporal evolution of the mean shear across the channel.

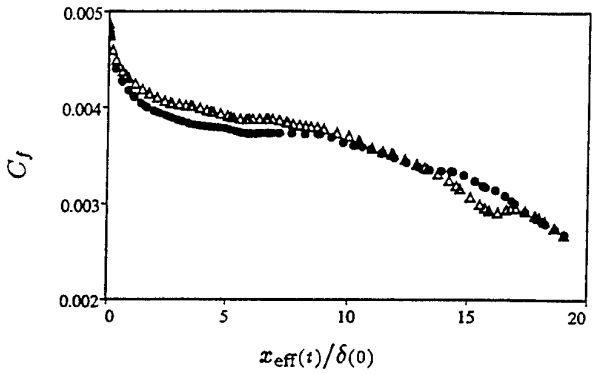


FIGURE 9. Mean skin friction history for Case II: symbols from two independent ensembles. C_f based on current mean centerline velocity $\overline{u}_c(t)$.

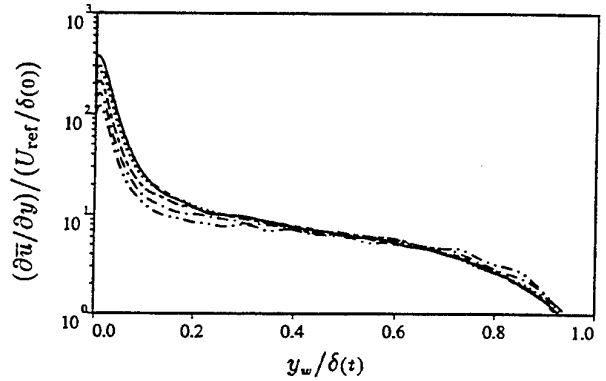


FIGURE 10. Mean shear for Case II: symbols as in figure 8.

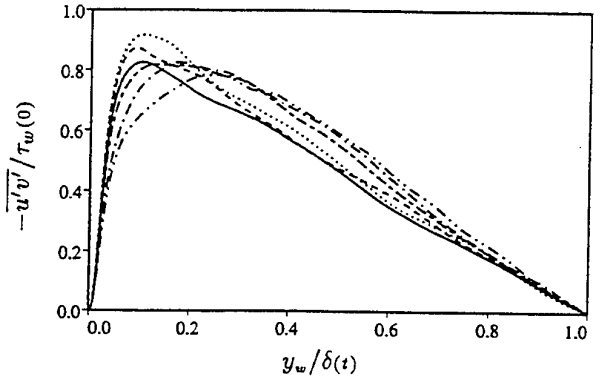


FIGURE 11. Reynolds stress for Case II: symbols as in figure 8. Normalized by initial wall shear stress $\tau_w(0)$

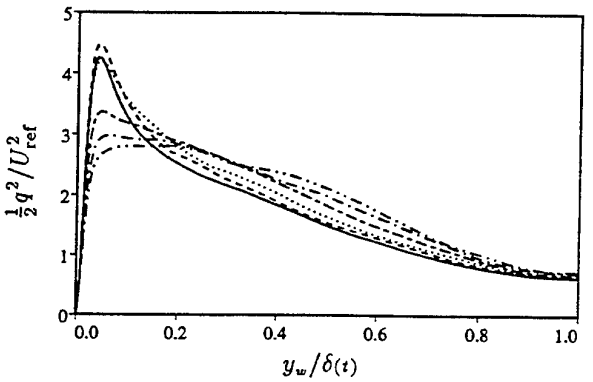


FIGURE 12. Turbulent kinetic energy $q^2/2 = \overline{u_i'u_i'}/2$ for Case II: symbols as in figure 8.

Near the wall $\partial\overline{u}/\partial y$ decreases rapidly, while in the outer layer the mean shear (i.e. spanwise vorticity) at a given y_w/δ remains nearly constant. Since this is the proper behavior of a 2D flow that experiences no spanwise straining (i.e. vorticity is conserved), figures 9 and 10 imply that the strategy of imposing both the mean strain and bulk deceleration in the channel successfully produces the mean flow conditions found in both the inner and outer regions of APG boundary layers – and therefore demonstrates the validity of the current approach.

The different dynamics of the inner and outer layers is revealed in figures 11 and 12, which respectively show the variation in time of the turbulent shear stress and turbulent kinetic energy. Near the wall, after a brief increase both quantities drop drastically, as a result of the reduced C_f, while farther out both $-\overline{u'v'}$ and q^2 rise to levels noticeable higher than their initial values. As was found for the earlier APG simulations mentioned above (Series B of CKS), which impose larger strain rates than are used here, the increase in both shear stress and energy is accompanied by an outer-layer decrease of the structure parameter, the ratio of the two. The level to which a_1 has dropped after the same total strain $\exp(-A_{11}t)$ is much less, however, than the value observed at larger strain rates. Apparently the extent of the alteration of the structure of the turbulence depends upon the rate at which it is strained.

The final two figures, 14 and 15, show the inner-layer scaling of the turbulent kinetic energy $k = \overline{u_i'u_i'}/2$ and mean velocity $\overline{u}$, respectively. Both exhibit the same general outer-layer behavior observed in the Nagano *et al.* and Spalart & Watmuff experiments. In particular we note that an outer-layer peak in the k^+ profile develops due to the APG strain, and $\overline{u}^+$ for $y^+ > 100$ becomes larger and larger. Near the wall, however, the present k^+ results show less of a tendency to collapse than they do in the Nagano *et al.* flow. The mean velocities in figure 15 also differ from the Nagano *et al.* and Spalart & Watmuff profiles: here, there is no indication of the downward shift below the standard logarithmic profile found in the earlier APG studies. Instead, $\overline{u}^+$ first rises above then relaxes back toward the initial 2D value. This difference, which is probably related to the slight near-wall increase observed in q^2 and $-\overline{u'v'}$ immediately after the strain is applied (figures 11 and 12) could be due to differences in the strength and history of the APG (recall that for the present flow the effective dC_p/dx is greatest when the strain is applied, and decreases thereafter). It could also be a unique feature of the temporally evolving flow; as mentioned above, because the irrotational strain is applied to the walls, temporally and spatially developing shear layers cannot be expected to exactly correspond. Moreover, the temporal-spatial 'mapping' assumes that the turbulent structures at each y_w convect at the same speed, and thus that the current state of the turbulence depends only on the local value of (not the time to which it has been exposed to) the mean shear. Some of the near-wall behavior seen here might therefore be attributable to turbulence that is 'under-aged' compared to its spatial counterpart. On the other hand, the present results suggest that there might not be just one type of 'APG behavior', but rather that nonequilibrium APG turbulent boundary layers can be sensitive to the details of the strain history. We plan to investigate this issue further as our studies of the present flow continue.

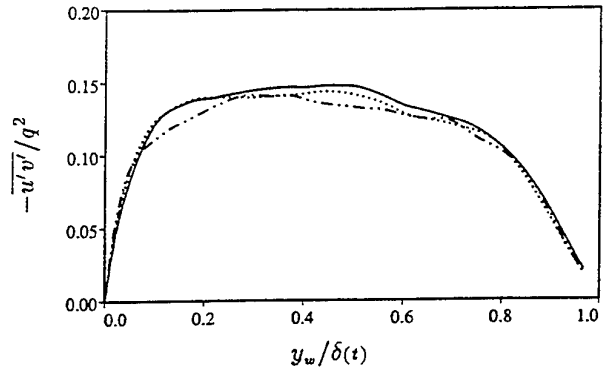


FIGURE 13. Structure parameter $a_1 = -\overline{u'v'}/q^2$ for Case II: symbols as in figure 8.

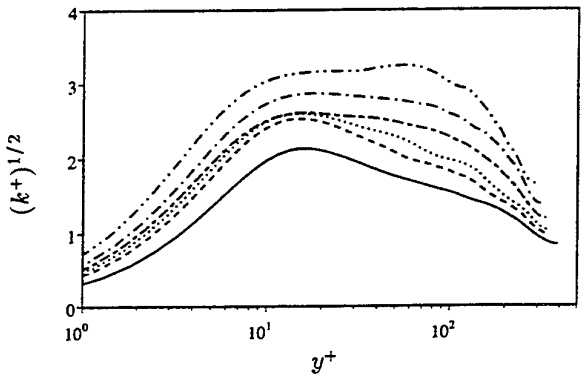


FIGURE 14. Turbulent kinetic energy in wall scaling for Case II (averated over two ensembles): symbols as in figure 8.

SUMMARY AND CONCLUSIONS

DNS of time-developing strained-channel flow has been used to study the physics of pressure-driven boundary layers. Adverse-pressure-gradient effects are found to dominate over those of mean three dimensionality in a flow subjected to the strains present in swept-wing 3D boundary layers. When the APG strain acts alone to emulate the canonical 2D case, the flow is governed by the interaction of the diminished turbulent kinetic energy production associated with the reduced surface-shear stress (caused by the bulk deceleration) and the deformation of the outer layer turbulence. The magnitude of the alteration of the structure of the turbulence in the outer layer depends upon the rate of the applied strain. Under the influence of the APG strain, the maximum turbulent kinetic energy and Reynolds stress shifts to the outer layer, while the wake component of the mean velocity grows. In addition to these findings, which correspond to those of earlier APG boundary layer experiments, we also observe behavior that is unique to the present flow: below the outer region, the mean velocity rises above the standard logarithmic profile, and thus does not follow the trend found in the exeriment of Nagano *et al.* This could be a consequence of the peculiarities of the strained channel approach, or perhaps an indication of the non-universal nature of APG boundary layers.

ACKNOWLEDGEMENTS

This work is sponsored by the Office of Naval Research (Grant No. N00014-94-1-0016), Dr. L. P. Purtell program officer. Computer resources have been supplied by the NAS program at NASA-Ames Research Center and by the San Diego Supercomputer Center.

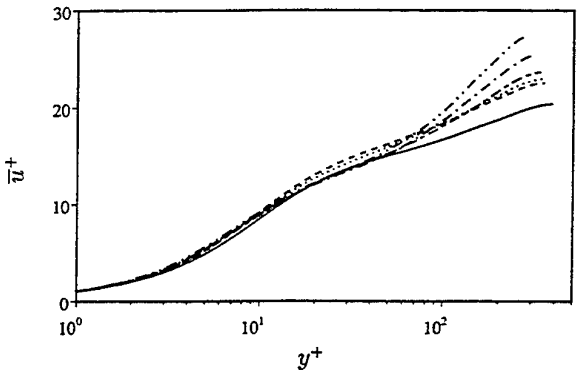


FIGURE 15. Mean velocity in wall scaling for Case II (averaged over two ensembles): symbols as in figure 8.

REFERENCES

Bradshaw, P. 1987 Turbulent secondary flows. *Ann. Rev. Fluid Mech.* **19**, 53–74.

Bradshaw, P., 1988 Effects of extra rates of strain – review. *Summary Lecture, Zoran Zaric Memorial Sem., Dubrovnik.* Hemisphere.

Bradshaw, P. & Pontikos, N. S., 1985 Measurements in the turbulent boundary layer on an 'infinite' swept wing. *J. Fluid Mech.* **159**, 105–130.

Coleman, G. N., Kim, J. & Spalart, P. R., 1996 Direct numerical simulation of strained three-dimensional wall-bounded flows. *Exp. Thermal Fluid Science* (special issue to honor Peter Bradshaw), **13**, 239–251 (referred to herein as CKS).

Eaton, J. K. 1995 Effects of mean flow three dimensionality on turbulent boundary-layer structure. *AIAA J.* **33**, 2020–2025.

Johnston, J. P. & Flack, K. A. 1996 Review – advances in three-dimensional turbulent boundary layers with emphasis on the wall-layer regions. *J. Fluids Engr.* **118**, 219–232.

Kim, J., Moin, P. & Moser, R., 1987 Turbulence statistics in fully developed channel flow at low Reynolds number. *J. Fluid Mech.* **177**, 133–166.

Moin, P., Shih, T.-H., Driver, D. M. & Mansour, N. N. 1990 Direct numerical simulation of a three-dimensional turbulent boundary layer. *Phys. Fluids* **2**, 1846–1853.

Nagano, Y., Tagawa, M. & Tsuji, T. 1992 Effects of adverse pressure gradients on mean flows and turbulence statistics in a boundary layer. *Eighth Symp. on Turbulent Shear Flows, Sept. 9-11, 1991, Münich.* Springer.

Rogallo, R. S., 1981 Numerical Experiments in Homogeneous Turbulence. NASA Tech. Memo. 81315.

Schwarz, W. R. & Bradshaw 1994 Structural changes for a three-dimensional turbulent boundary layer in a 30° bend. *J. Fluid Mech.* **272**, 183–209.

Smits, A. J. & Wood, D. H. 1985 The response of turbulent boundary layers to sudden perturbations. *Ann. Rev. Fluid Mech.* **17**, 321–358.

Spalart, P. R. & Watmuff, J. H. 1993 Experimental and numerical study of a turbulent boundary layer with pressure gradients. *J. Fluid Mech.*, **249**, 337–371.

van den Berg, B., Elsenaar, A., Lindhout, J. P. F. & Wesseling, P. 1975 Measurements in an incompressible three-dimensional turbulent boundary layer, under infinite swept-wing conditions, and comparison with theory. *J. Fluid Mech.* **70**, 127–148.

Webster, D. R., DeGraaff, D. B. & Eaton, J. K. 1996 Turbulence characteristics of a boundary layer over a swept bump. *J. Fluid Mech.* **323**, 1–22.

STRUCTURE OF TURBULENT BOUNDARY LAYER SUBJECTED TO ADVERSE PRESSURE GRADIENT

Y. Nagano, T. Tsuji and T. Houra

Department of Mechanical Engineering,
Nagoya Institute of Technology,
Gokiso-cho, Showa-ku, Nagoya 466, Japan

ABSTRACT

A turbulent boundary layer subjected to a sustained adverse pressure gradient is experimentally investigated. Waveforms of fluctuating velocity components in the boundary layer are remarkably elongated in time in comparison with those in zero-pressure-gradient flows, and thus time scales increase with increasing pressure gradient parameter P^+. It is found that the Taylor time scale is most appropriate to describe the essential characteristics of the non-equilibrium adverse pressure gradient flows. Even the near wall-limiting behavior of streamwise velocity fluctuations for different P^+ is well correlated in the coordinates based on the Taylor time scale. Also, in the boundary layer with an adverse pressure gradient, the contribution of sweep motions becomes equivalent to that of ejections and interactions increase near the wall, which evidently indicates a change in coherent structures.

NOMENCLATURE

C_p	wall static pressure coefficient, $= (\overline{P} - \overline{P}_0)/(\rho \overline{U}_0^2/2)$
f	frequency
$\overline{P}$	mean pressure
P^+	dimensionless pressure gradient parameter, $= \nu(d\overline{P}/dx)/\rho u_\tau^3$
$\overline{P}_0$	reference inlet pressure
R_θ	Reynolds number based on momentum thickness, $= \overline{U}_e\theta/\nu$
$R_u(t)$	auto-correlation coefficient of u
T_E	Eulerian integral time scale, $= \int_0^\infty R_u(t)dt$
t	time
$\overline{U}$	mean velocity in x direction
$\overline{U}_e$	free stream velocity
$\overline{U}_0$	reference inlet velocity
u_τ	friction velocity, $= \sqrt{\tau_w/\rho}$
u,v,w	fluctuating velocity components in x, y and z directions
x,y,z	streamwise, wall-normal and spanwise coordinates
y^+	dimensionless distance from wall, $= u_\tau y/\nu$
β	Clauser pressure gradient parameter, $= (\delta^*/\tau_w)d\overline{P}/dx$
δ_{99}	boundary layer thickness
δ^*, θ	displacement and momentum thicknesses
ν	kinematic viscosity
ρ	density
τ_E	Eulerian dissipation time scale or Taylor time scale, $= \sqrt{2\overline{u^2}/\overline{(\partial u/\partial t)^2}}$
τ_m	time scale corresponding to mean shear rate, $= 1/(\partial\overline{U}/\partial y)$
τ_w	wall shear stress

INTRODUCTION

In theory as well as in practice, it is of fundamental importance to investigate the effects of pressure gradients on the structure of turbulent boundary layers. From our previous experiment on an adverse-pressure-gradient(APG) turbulent boundary layer (Nagano et al. 1992), we have obtained the following results: (1) the standard log-law velocity profile for a zero-pressure-gradient (ZPG) boundary layer does not hold in APG turbulent boundary layers; (2) near-wall distributions of r.m.s. velocity fluctuations cannot scale with the wall parameters, u_τ and ν; and (3) the response time of turbulence to the imposed APG, which relates closely to the redistribution process of turbulent kinetic energy, is different among streamwise, wall-normal and spanwise velocity components.

Although the viscous wall unit is a standard parameter for scaling the equilibrium turbulent boundary layers (Skåre and Krogstad 1994), the above fact implies that another characteristic time scale or length scale must be introduced in order to scale the non-equilibrium APG flows. Thus, the main objectives of the present study are: (i) to reveal the in-depth turbulent structure inherent in the APG flows; (ii) to find an appropriate time scale which provides universal scaling of the near-wall turbulent statistics; (iii) to understand the physical meanings and roles of the time scale in characterizing the APG flows; and (iv) to find structures which cannot be described in terms of the time scale, if any.

Table 1 Flow parameters ($\overline{U}_0$=10.8m/s)

x mm	$\overline{U}_e$ m/s	δ_{99} mm	u_τ m/s	R_θ	P^+	β
525	10.8	13.3	0.481	1070	0	0
925	10.8	19.9	0.465	1620	0	0
523	9.08	16.2	0.390	1290	9.12×10^{-3}	0.77
723	8.18	24.6	0.307	1880	1.93×10^{-2}	2.19
925	7.54	34.2	0.251	2660	2.56×10^{-2}	3.95
1121	6.68	46.1	0.197	3350	2.87×10^{-2}	5.32

EXPERIMENTAL APPARATUS

We used the same experimental apparatus as in Nagano et al. (1992). The important flow parameters are listed in Table 1. Two velocity components in the x and y directions, u and v, were measured with an X-wire (diameter: 3.1 μm; length: 0.6 mm; wire spacing: 0.3 mm.) To convert the hot-wire outputs into the velocity components, we adopted the look-up-table method (Lupetow et al. 1988). The measurement accuracy was checked with the DNS data of the ZPG flow (Spalart, 1988).

In the present APG flow, the pressure gradient dC_p/dx keeps a nearly constant value of 0.6 over 65 mm $\leq x \leq$ 700 mm and then decreases slowly. On the other hand, the pressure gradient parameter normalized by inner variables P^+ and the Clauser parameter β increase monotonously, thus giving moderate to strong adverse pressure gradients.

STATISTICAL CHARACTERISTICS

Mean Velocity and Turbulent Intensities

Figure 1 shows the mean velocity profiles normalized by the friction velocity u_τ. As clearly seen from this figure, the velocity profiles in APG flows lie below the 'standard' log-law profile for ZPG flows. This important nature of the APG flows conforms to our previous result (Nagano et al., 1992), and is also confirmed by the direct numerical simulation (DNS) of Spalart and Watmuff (1993) and by the recent measurement of Debisschop and Nieuwstadt (1996).

The intensity profiles of fluctuating velocity components u, v and w normalized by the free-stream velocity $\overline{U}_0$ at the inlet to the test section are presented in Fig. 2. The abscissa is the distance from the wall normalized with the

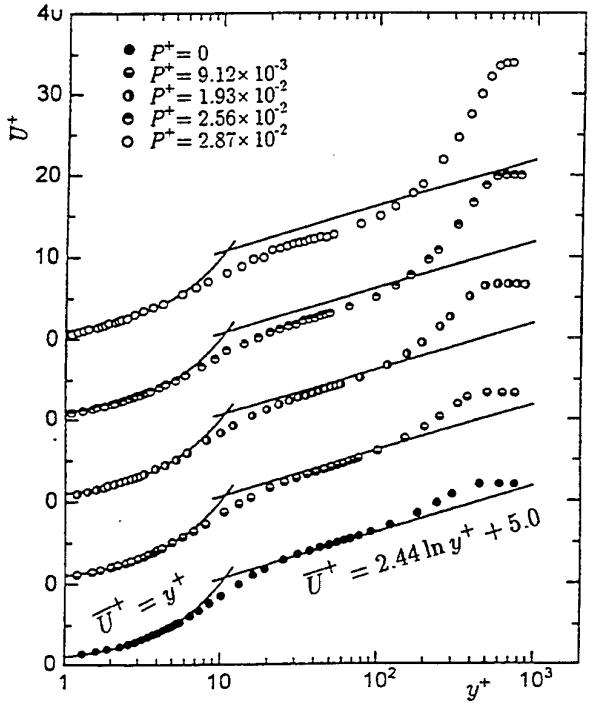


Fig. 1 Mean velocity profiles in wall coordinates in adverse-pressure-gradient flows

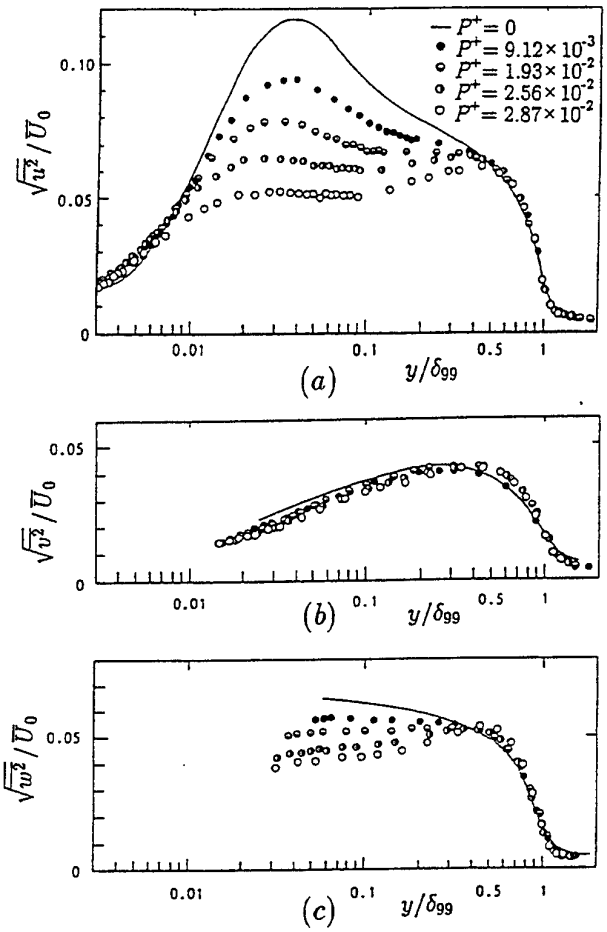


Fig. 2 Turbulence intensities of fluctuating velocity components: (a) streamwise; (b) wall-normal; (c) spanwise

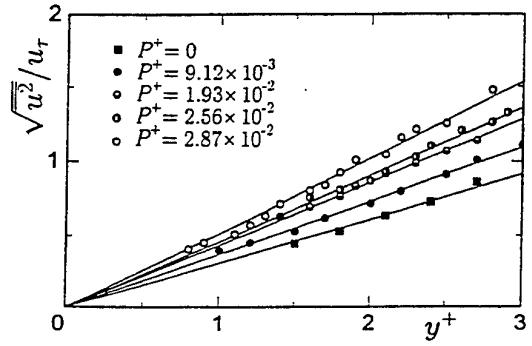


Fig. 3 Wall-limiting behavior of $\sqrt{\overline{u^2}}/u_\tau$

boundary layer thickness δ_{99}. With increasing the APG effect, the reduction of turbulence intensities can be seen in the wall region ($y/\delta_{99} < 0.4$), whereas all the profiles in the outer layer are kept unchanged, i.e., turbulence intensities are unchanged along streamlines of the mean flow lying outside the wall region. The APG changes the intensities of velocity fluctuations near the wall in the order, streamwise (u), spanwise (w), and wall-normal (v) components. These profiles cannot be correlated in wall coordinates even in the near-wall region. As shown in Fig. 3, the distributions of $\sqrt{\overline{u^2}}/u_\tau$ near the wall follow each P^+-dependent straight line which coincides with the origin. The same tendency is also confirmed from the recent DNS (Spalart and Watmuff 1993). This means that the viscous wall unit cannot be used to describe the unique features of the present and DNS's APG flows in non-equilibrium.

To know the basic mechanism of the above feature of APG flows, we have investigated the characteristics of instantaneous signal traces of the fluctuating velocity components u and v together with the Reynolds shear stress uv. The results in the near-wall region and those at the outer edge of the log-law region are shown in Figs. 4(a) and 4(b), respectively, in comparison with the ZPG flow. A circumflex denotes the normalization by the respective r.m.s. value. It is quite clear from Fig. 4(a) that, despite nearly the same R_θ value, the time scales of velocity fluctuations in the wall region of the APG flow are extremely elongated and become different from those in the ZPG flow; that is, turbulent motions of the APG flow become gentle and less active, which may correspond to the observed low production of turbulence energy (Nagano et al. 1992). In the outer region, on the other hand, there is only a little difference in the instantaneous signal traces between the ZPG and APG flows.

Spectra

Power spectra of u and v fluctuations in the log region ($y^+ \simeq 50$) are presented in Figs. 5(a) and 5(b), respectively, against the dimensionless frequency $f' = f\nu/\overline{U_0}^2$. As expected from the waveforms in Fig. 4, the frequencies of energy-containing eddies in both spectra gradually shift toward the lower frequency with increasing P^+. To clarify the APG effect on velocity fluctuations at high frequencies,

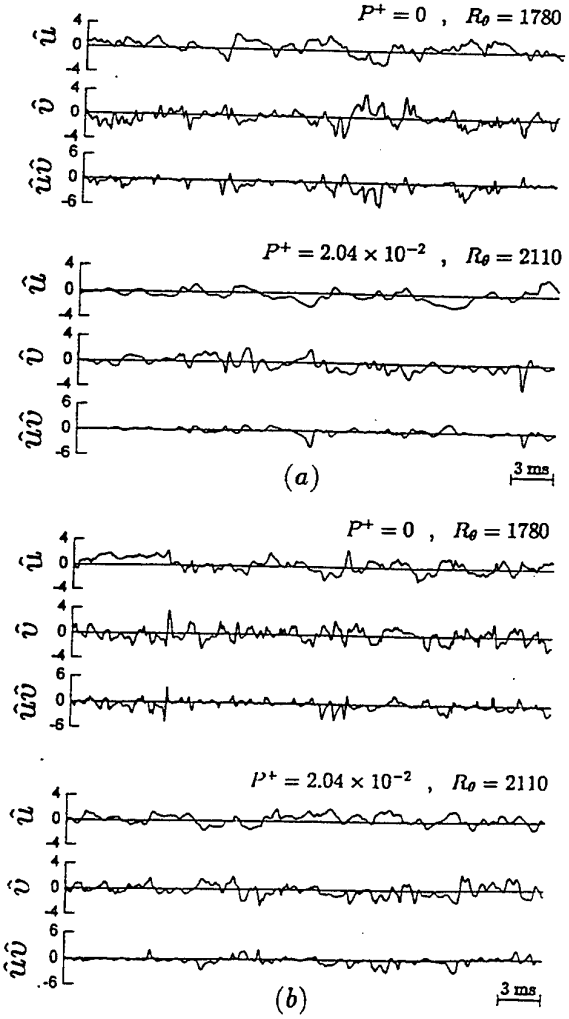


Fig. 4 Signal traces of $\hat{u}$, $\hat{v}$, and $\hat{u}\hat{v}$: (a) inner layer ($y^+ \simeq 23$, $y/\delta_{99} \simeq 0.04$); (b) outer layer($y^+ \simeq 260$, $y/\delta_{99} \simeq 0.5$)

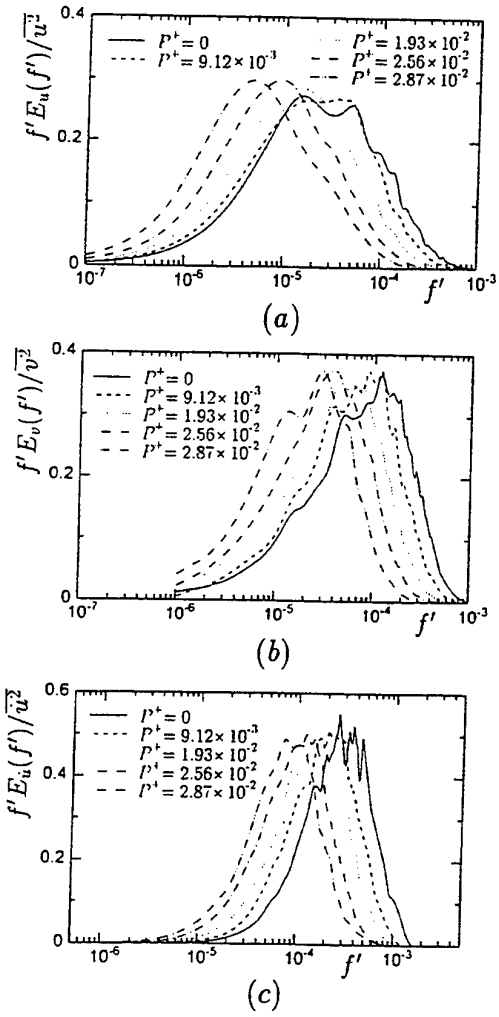


Fig. 5 Power spectra of velocity fluctuation in the log region: (a) streamwise fluctuation u; (b) wall-normal fluctuation v. (c) Spectra of dissipation $\overline{(\partial u/\partial t)^2}$

we have examined dissipation spectra $\overline{(\partial u/\partial t)^2}$ and present them in Fig. 5(c). The dissipation spectra also shift toward the lower frequency as P^+ increases. Such changes in power and dissipation spectra are observed both in the near-wall and outer regions.

Scaling Law

The above facts indicate that an adverse pressure gradient has a strong influence on turbulence statistics selectively in the near-wall region and that it is the time scale that represents the essential characteristics of APG turbulent boundary layers. Thus, we then investigate the flow structures from the viewpoint of temporal behavior of the turbulence quantities, so as to obtain an appropriate time scale which provides a universal scaling law for the near-wall turbulence statistics of APG flows.

In the present study, we have examined the turbulence structures of the APG flow using the following six different characteristic time scales (see Nomenclature for definition):

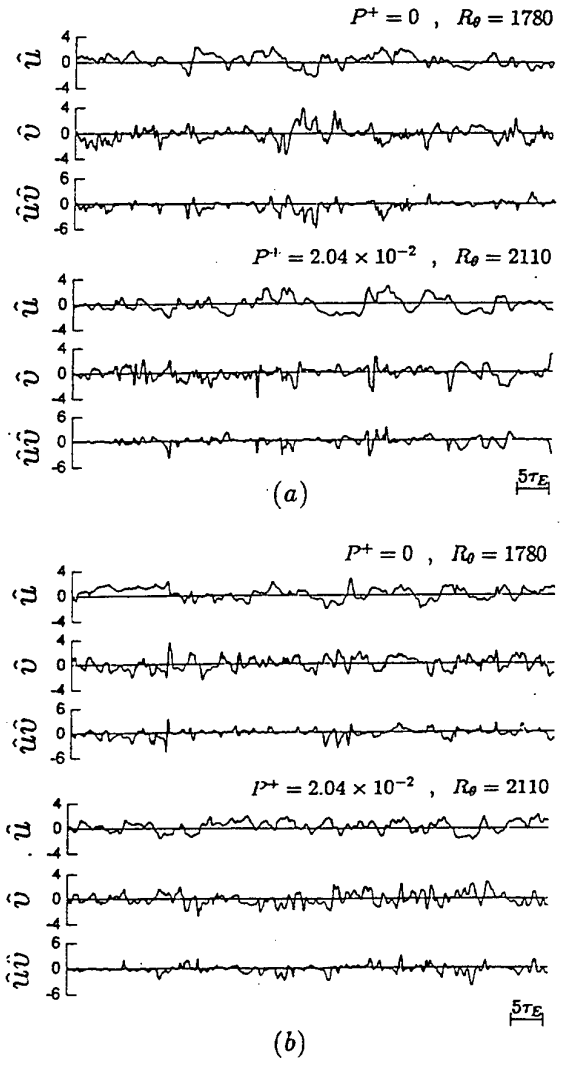


Fig. 6 Signal traces of $\hat{u}$, $\hat{v}$, and $\hat{u}\hat{v}$ normalized by Taylor time scale τ_E: (a) inner layer ($y^+ \simeq 23$, $y/\delta_{99} \simeq 0.04$); (b) outer layer($y^+ \simeq 260$, $y/\delta_{99} \simeq 0.5$)

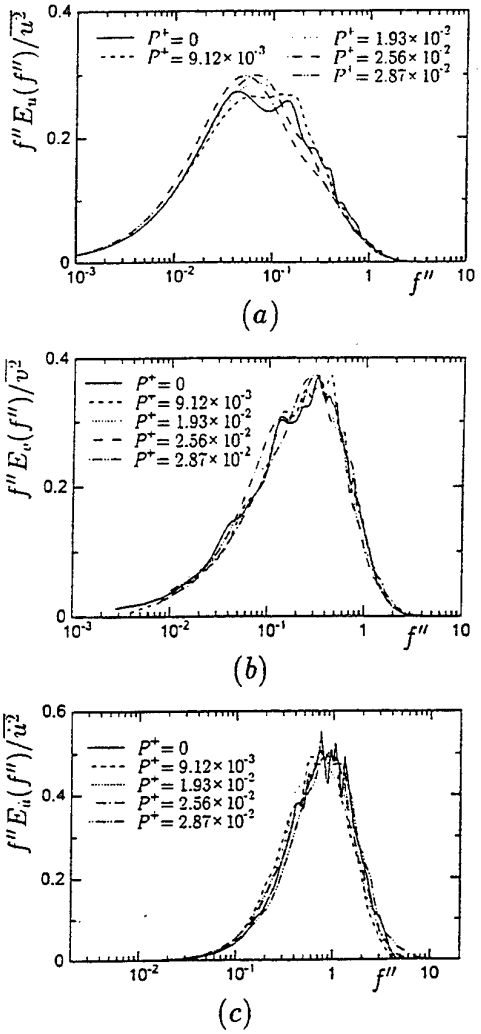


Fig. 7 Power spectra of velocity fluctuation arranged with dimensionless frequency f'' in the log region: (a) streamwise fluctuation u; (b) wall-normal fluctuation v. (c) Spectra of dissipation $\overline{(\partial u/\partial t)^2}$

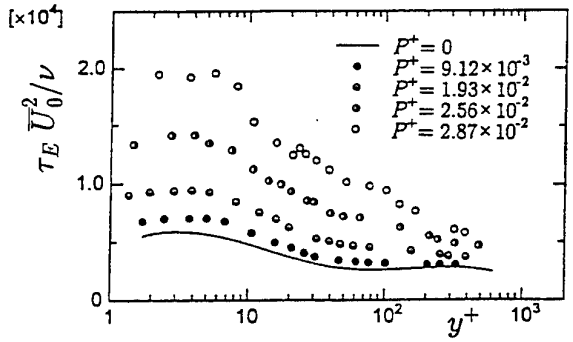


Fig. 8 Distribution of Taylor time scale τ_E

- viscous time scale: ν/u_τ^2
- Kolmogorov time scale: $\sqrt{\nu/\varepsilon}$
- Taylor time scale: τ_E
- time scale for energy-containing eddies: k/ε
- integral time scale: T_E
- time scale corresponding to mean shear rate: τ_m

where k and ε are the turbulent kinematic energy and its dissipation rate, respectively. Note that the viscous time scale ν/u_τ^2 is uniquely determined at a given x location, while the other parameters vary locally in the y direction.

By using the above six time scales, we have analyzed the temporal turbulent structures of the APG flows. As a result, the Taylor time scale τ_E is found to be most appropriate for representing the temporal behavior of turbulence quantities and for universally scaling the turbulence statistics. Generally, in high-Reynolds number flows, the Taylor time scale τ_E and the viscous dissipation ε are related to each other through the expression $\varepsilon = 30\nu\overline{u^2}/(\overline{U}^2\tau_E{}^2)$.

The sample results of scaling raw waveforms in Fig. 4 with τ_E are presented in Fig. 6. The corresponding various power spectra in the log region ($y^+ \simeq 50$) arranged with a new dimensionless frequency, $f'' = f\tau_E$, are presented in Fig. 7. As obviously seen from these figures, we conclude that the Taylor time scale is best scaling parameter for both ZPG and APG flows.

The distributions of the measured Taylor time scale τ_E in the y direction are shown in Fig. 8. One may find that τ_E

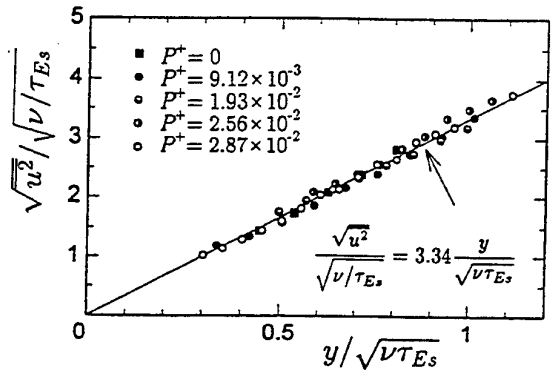


Fig. 9 Scaling of wall-limiting behavior of streamwise intensity $\sqrt{u^2}$ with Taylor time scale τ_{Es}

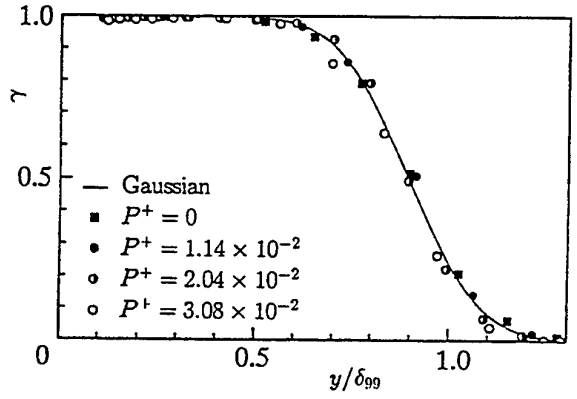


Fig. 10 Intermittency factors γ in APG flow

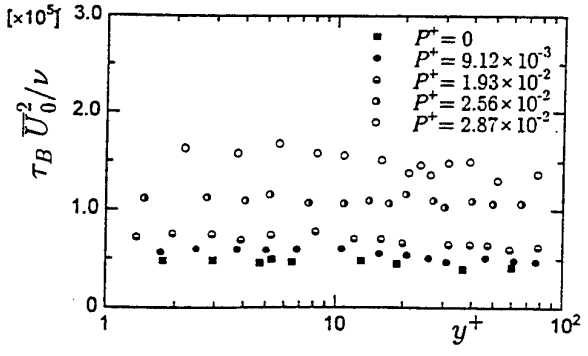


Fig. 11 Mean period of intermittent bursts

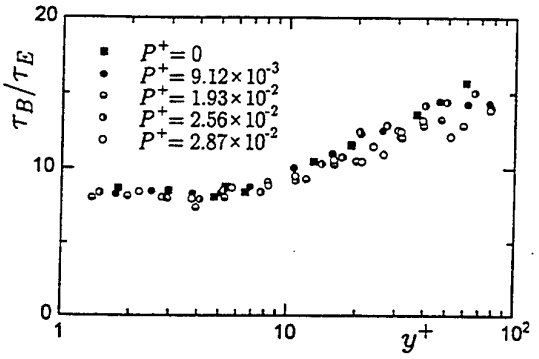
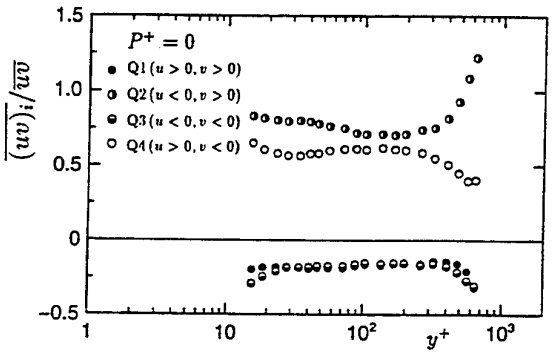


Fig. 12 Mean period of intermittent bursts normalized by τ_E



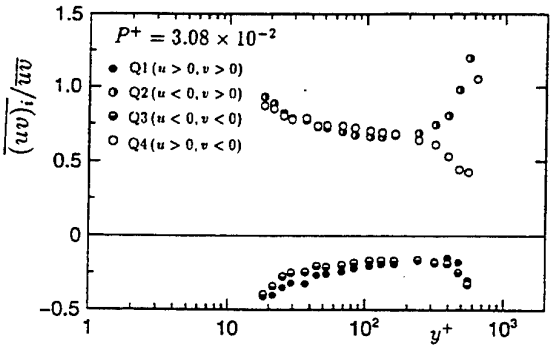


Fig. 13 Fractional contribution to Reynolds shear stress

increases with increasing pressure gradient parameters P^+. In the proximity to the wall, however, τ_E becomes almost constant for a given P^+. In what follows, we apply the characteristic time scale τ_E to scaling various turbulence statistics.

First, we present the scaling of the wall-limiting behavior of streamwise turbulence intensity $\sqrt{\overline{u^2}}$ in Fig. 9. Here, τ_{E_s} defined by a value of τ_E at the outer edge of the viscous sublayer, i.e., $y^+ = 3$, is adopted and the fluctuation intensity and the coordinate y are normalized with the velocity scale $\sqrt{\nu/\tau_{E_s}}$ and the length scale $\sqrt{\nu\tau_{E_s}}$, respectively. If the viscous wall unit is used as a length scale, there appear remarkable differences in the wall-limiting behavior between the ZPG and APG flows with a systematic deviation from the ZPG case as depicted in Fig. 3. On the other hand, the use of the time scale τ_{E_s} makes all the profiles collapse irrespective of the values of P^+ as shown in Fig. 9.

Next, from the waveforms stretched in accordance with the Taylor time scale τ_E in APG flows, we have obtained intermittency factors γ by using the method of Hedley and Keffer(1974). As shown in Fig. 10, the distributions of intermittency factors in APG flows become identical to those in the ZPG flow.

These results suggest that if we make a proper choice of a scaling parameter based on the knowledge of turbulence structures, we may describe the features of adverse pressure gradient flows uniquely even in the non-equilibrium conditions.

DYNAMICAL CHARACTERISTICS

To identify any scale-irrelevant structures hidden in a flow, we investigate dynamical features of APG flows in the following. We first investigate the relation between τ_E and the characteristic time scale pertaining to the bursting phenomena, τ_B, obtained from the short-time averaged auto-correlation function method (Kim et al. 1971, Hishida and Nagano 1979). It becomes obvious from Fig. 11 that the mean burst period τ_B changes strikingly with P^+. However, as shown in Fig. 12, the normalized period τ_B/τ_E tends to collapse for any pressure gradient level. This means that τ_E closely relates to the dynamical coherent structure.

The coherent structure of turbulence may affect statistical values, especially higher order moments (Nagano and Tagawa 1988). Thus, we have examined the fractional contributions to Reynolds shear stress $-\overline{uv}$. Figure 13 shows the results obtained for ZPG and APG flows. In the log region of the ZPG flow, the most contributive motion is the ejection (Q2) and the sweep motion (Q4) follows it. The contributions of interactions (Q1, Q3) are fairly small in comparison with those of the active motions (Q2, Q4). Such behavior is also observed in a pipe flow (Nagano and Tagawa 1988) and is considered to be a nature of the canonical wall flow.

On the other hand, in the APG flow, the situation is remarkably different from that in the ZPG flow. The contributions of ejection and sweep motions (Q2, Q4) become equivalent and increase toward the wall. Correspondingly, the negative contributions of interactions (Q1, Q3) increase near the wall. This fact indicates that in APG flows energy transfer through the turbulent diffusion toward the wall becomes dominant and a relative increase of inactive motions (Q1, Q3) results (Bradshaw 1967).

CONCLUSIONS

Experimental investigation has been made on non-equilibrium turbulent boundary layers subjected to adverse pressure gradients. The results can be summarized as follows:

(1) In the APG flow, the characteristic time scale of the flow is exceedingly elongated in the near-wall region, in comparison with the ZPG flow at nearly the same R_θ. This difference should be related closely to the progressive decrease of the turbulence intensities in the near-wall region and can be ascribed to the retardation of turbulence production.

(2) In the outer region, there is a slight difference in the instantaneous velocity signals and in the distributions of turbulence intensities between the ZPG and APG flows.

(3) The Taylor time scale τ_E is most appropriate to describe the essential characteristics of the near-wall structure of non-equilibrium APG flows.

(4) The conventional scaling law using the viscous time scale ν/u_τ^2 cannot be applied to the scaling of the near-wall statistics of the non-equilibrium APG flows. Instead of ν/u_τ^2, the Taylor scale τ_E in the near-wall region may provide the good scaling law.

(5) In APG flows, the contribution of sweep motions becomes equivalent to that of ejections and interactions increase near the wall, which evidently indicates a change in coherent structures.

REFERENCES

Bradshaw, P., 1967, "The Turbulence Structure of Equilibrium Boundary Layers," *J. Fluid Mech.*, Vol. 29, Part 4, pp. 625–645.

Debisschop, J. R., and Nieuwstadt, F. T. M., 1996, "Turbulent Boundary Layer in an Adverse Pressure Gradient: Effectiveness of Riblets," *AIAA J.*, Vol. 34, pp. 932–937.

Hedley, T. B., and Keffer, J. F., 1974, "Turbulent/Non-Turbulent Decisions in an Intermittent Flow," *J. Fluid Mech.*, Vol. 64, Part 4, pp. 625–644.

Hishida, M., and Nagano, Y., 1979, "Structure of Turbulent Velocity and Temperature Fluctuations in Fully Developed Pipe Flow," *Trans. ASME, J. Heat Transfer*, Vol. 101, pp. 15–22.

Kim, H. T., Kline, S. J., and Reynolds, W. C., 1971, "The Production of Turbulence near a Smooth Wall in a Turbulent Boundary Layer," *J. Fluid Mech.*, Vol. 50, Part 1, pp. 133–160.

Lupetow, R. M., Breuer, K. S., and Haritonidis, J. H., 1988, "Computer-Aided Calibration of X-Probes Using a Look-Up Table," *Exp. Fluids*, Vol. 6, pp. 115–118.

Nagano, Y., and Tagawa, M., 1988, "Statistical Characteristics of Wall Turbulence with a Passive Scalar," *J. Fluid Mech.*, Vol. 196, pp. 157–185.

Nagano, Y., Tagawa, M., and Tsuji, T., 1992, "Effects of Adverse Pressure Gradients on Mean Flows and Turbulence Statistics in a Boundary Layer," *Turbulent Shear Flows 8* (F. Durst et al., eds.), Springer-Verlag, pp. 7–21.

Skåre, P. E., and Krogstad, P.-Å., 1994, "A Turbulent Equilibrium Boundary Layer near Separation," *J. Fluid Mech.*, Vol. 272, pp. 319–348.

Spalart, P. R., 1988, "Direct Simulation of a Turbulent Boundary Layer up to R_θ=1410," *J. Fluid Mech.*, Vol. 187, pp. 61–98.

Spalart, P. R., and Watmuff, J. H., 1993, "Experimental and Numerical Study of a Turbulent Boundary Layer with Pressure Gradients," *J. Fluid Mech.*, Vol. 249, pp. 337–371.

APPLICATION OF TURBULENCE MODELS TO EQUILIBRIUM BOUNDARY LAYERS UNDER ADVERSE PRESSURE GRADIENT

R.A.W.M. Henkes
Faculty of Aerospace Engineering, Delft University of Technology
Kluyverweg 1, 2629 HS Delft, The Netherlands
Present address: Shell Research and Technology Centre Amsterdam
P.O. Box 3003, 1003 AA Amsterdam, The Netherlands

M. Skote and D.S. Henningson[1]
Department of Mechanics, Royal Institute of Technology (KTH)
S-100 44 Stockholm, Sweden
[1] Also: Aeronautical Research Institute of Sweden (FFA), Box 11021, S-161 11 Bromma, Sweden

ABSTRACT

Four classes of turbulence models (algebraic, $k-\epsilon$, $k-\omega$ and a differential Reynolds-stress model) are applied to boundary layers under adverse pressure gradient with a constant equilibrium parameter $\beta = \frac{\delta^*}{\tau_w}\frac{dp}{dx}$. Numerical solutions up to $Re_\theta = 10^6$ give the classical scalings in the inner and outer layer for all models. Comparison is made with experiments of Clauser at $\beta \approx 2$ and 8 and with recent experiments by Skåre and Krogstad at $\beta = 20$. We have also performed new direct numerical simulations at $\beta \approx 0.25$ and 0.65 up to $Re_\theta = 700$. The differential Reynolds-stress model shows the best agreement with the experiments and the DNS.

INTRODUCTION

The present study considers the scalings according to four commonly used turbulence models for equilibrium boundary layers under an adverse pressure gradient. According to Clauser (1954), the boundary layer is in equilibrium if the parameter $\beta = \frac{\delta^*}{\tau_w}\frac{dp}{dx}$ is independent of the streamwise position. The scalings are derived from the turbulence models without making any additional a priori assumptions, which means that the scalings follow from the straightforward numerical solution of the boundary-layer equations. Computations are made up to the very large Reynolds number of $Re_\theta \approx 10^8$, which is sufficient for the similarity scalings to appear. A strong grid refinement was applied close to the wall. By doubling the number of grid points, the solutions were verified to be numerically accurate.

The classical theory, which is mainly due to Clauser (1954) and Coles (1956), finds that the boundary layer can be split up in an inner layer (wall function), with length scale ν/u_τ and velocity scale u_τ, and an outer layer (defect layer), with the velocity scale u_τ and the length scale $\Delta = \delta^* U/u_\tau$ (where U denotes the local free-stream velocity).

The results for the turbulence models are compared with experiments at moderate Reynolds numbers ($Re_\theta = 10^4$ to 10^5) for $\beta \approx 2$ and 8, obtained by Clauser (1954), and with more recent experiments at $\beta = 20$, being close to separation, due to Skåre (1994) and Skåre and Krogstad (1994). Furthermore, the results with the turbulence models are also compared with new direct numerical simulations for $\beta \approx 0.25$ and 0.65 up to $Re_\theta \approx 700$, which we performed with a spectral code.

SCALING ANALYSIS

To derive the scalings of the boundary layer under an adverse pressure gradient one can start from the turbulent boundary-layer equations for an incompressible flow, which read

$$\frac{\partial u}{\partial x} + \frac{\partial v}{\partial y} = 0, \tag{1}$$

$$u\frac{\partial u}{\partial x} + v\frac{\partial u}{\partial y} = -\frac{1}{\rho}\frac{dp}{dx} + \nu\frac{\partial^2 u}{\partial y^2} - \frac{\partial}{\partial y}\overline{u'v'}. \tag{2}$$

Here x and y are the coordinates along and normal to the wall, respectively; u and v are the corresponding velocity components; p is the pressure; ρ is the density; ν is the kinematic viscosity; and $-\overline{u'v'}$ is the Reynolds shear stress.

According to the classical theory, the velocity scale in both the inner and outer layer is the same, namely u_τ, which is the wall-shear stress velocity $(\tau_w/\rho)^{1/2}$, with τ_w being the wall-shear stress $\mu(\partial u/\partial y)_w$. The length scale differs, and is ν/u_τ for the inner layer and $\Delta = \delta^* U/u_\tau$ for the outer layer; δ^* is the displacement thickness, and U is the local outer-edge velocity. Tennekes & Lumley (1972) and Wilcox (1993) have derived a so-called defect-layer equation, which is the equation that describes the similarity solution in the outer layer. There is, however, a striking difference between the derivations of Tennekes & Lumley and Wilcox. We have reconsidered the analysis (for more details see Henkes, 1997a) and find agreement with the results by Tennekes & Lumley.

When it is assumed that molecular diffusion can be neglected in the outer layer, the boundary-layer equations (1)-(2) can be transformed into

$$(\beta-2\omega)f+\gamma f^2+(\alpha-2\beta-2\omega)\eta f'-\chi f'\int_0^\eta f\,d\eta = r', \tag{3}$$

with

$$\alpha = \left(\frac{U}{u_\tau}\right)^2 \frac{d\delta^*}{dx}, \quad \beta = \frac{\delta^*}{\tau_w}\frac{dp}{dx}, \tag{4}$$

$$\omega = \frac{1}{2}\frac{\delta^*}{u_\tau}\left(\frac{U}{u_\tau}\right)^2 \frac{du_\tau}{dx},$$

$$\gamma = \frac{U}{u_\tau}\frac{\delta^*}{u_\tau}\frac{du_\tau}{dx}, \quad \chi = \frac{U}{u_\tau}\frac{d\delta^*}{dx} + \frac{\delta^*}{u_\tau}\frac{dU}{dx}.$$

Here $\eta = y/\Delta$, $f(\eta) = \dfrac{U-u}{u_\tau}$, and $r(\eta) = -\dfrac{\overline{u'v'}}{u_\tau^2}$. A prime denotes differentiation to η.

The coefficients can be developed in a series with respect to the small quantity u_τ/U (see Henkes, 1997a), which gives

$$\alpha = 1 + 3\beta + (1+\beta)C^*\frac{u_\tau}{U} + ..., \tag{5}$$

$$\omega = -\frac{1}{2}\beta - \frac{1}{2\kappa}(1+2\beta)\frac{u_\tau}{U} + ...,$$

$$\gamma = -\beta\frac{u_\tau}{U} - \frac{1}{\kappa}(1+2\beta)\left(\frac{u_\tau}{U}\right)^2 + ...,$$

$$\chi = (1+2\beta)\frac{u_\tau}{U} + ...,$$

with $C^* = \int_0^\infty f^2 d\eta$, and κ is the Von Kármán constant. To leading order eq. (5) gives

$$\alpha = 1 + 3\beta, \quad \omega = -\frac{1}{2}\beta, \quad \gamma = \chi = 0. \tag{6}$$

Therefore, for increasing Re_θ (giving $u_\tau/U \to 0$) equation (3) converges to the following defect-layer equation for the outer layer

$$2\beta f + (1+2\beta)\eta f' = r', \tag{7}$$

with boundary conditions

$$f \to -\frac{1}{\kappa}\ln\eta + C' \quad \text{for} \quad \eta \to 0, \tag{8}$$

$$f \to 0 \quad \text{for} \quad \eta \to \infty,$$

and the integral restriction

$$\int_0^\infty f d\eta = 1. \tag{9}$$

The boundary condition for $\eta \to 0$ follows from matching with the logarithmic wall function, and the integral restriction follows from the conservation of momentum. Equation (7) was also obtained by Tennekes & Lumley, but Wilcox took $\omega = 0$ (instead of $\omega = -\frac{1}{2}\beta$) and thus arrived at a different equation.

TURBULENCE MODELS

To solve the boundary-layer equations (1) and (2) or the defect-layer equation (7), a turbulence model is needed to represent the Reynolds shear stress. The following models are considered:

- Algebraic model of Cebeci & Smith (1974)
- Two-equation low-Reynolds-number $k-\epsilon$ model of Launder & Sharma (1974)
- Two-equation low-Reynolds-number $k-\omega$ model of Wilcox (1993)
- Differential Reynolds-Stress Model (DRSM) of Hanjalić, Jakirlić, and Hadžić (1995)

The algebraic model uses an algebraic relation to approximate the turbulent viscosity which appears in $-\overline{u'v'} = \nu_t\dfrac{\partial u}{\partial y}$. The $k-\epsilon$ model solves differential equations for the turbulent kinetic energy and the turbulent dissipation rate ϵ to model the turbulent viscosity, whereas the $k-\omega$ model solves a differential equation for ω instead of ϵ (where ω is proportional to ϵ/k). The DRSM is the most complete model, as it solves differential equations for all Reynolds shear and normal stresses, as well as for ϵ. More details of the models are given in the cited references, and in Henkes (1997b).

The boundary-layer equations are solved with a marching numerical procedure, after discretization with a second-order finite-difference scheme. A Cartesian grid is used with a very strong grid refinement in the lower part of the inner layer. To account for the growth of the boundary layer in streamwise direction, at several x positions the outer edge was increased and the y grid points were redistributed. All results presented in this paper are guaranteed to be grid independent. This was checked by doubling the number of points in x and y direction. A typical y grid consists of 200 or 400 points.

The defect-layer equation (7) only depends on the single coordinate η. This ordinary differential equation was numerically discretized with a second-order difference scheme, applying 200 or 400 points. An iteration process was used to satisfy the boundary conditions and the integral restriction.

DIRECT NUMERICAL SIMULATIONS

DNS were carried out for the pressure gradients $\beta \approx 0.25$ and $\beta \approx 0.65$ with a code developed at KTH and FFA by Lundbladh *et al.* (1992, 1994). The spectral method applies Fourier modes in the horizontal directions and Chebyshev modes in the wall-normal direction. Since the boundary layer is developing in the downstream direction, the physical boundary conditions in that direction are non-periodic. To capture these with periodic Fourier modes, a fringe region is added downstream of the physical domain, where the flow is forced from the outflow of the physical domain to the inflow. In this way the physical domain and the fringe region together satisfy periodic boundary conditions. The fringe region is implemented by the addition of a volume force having a form designed to minimize the upstream influence. Time integration is performed using a third-order Runge-Kutta method for the advective and forcing terms and Crank-Nicolson for the viscous terms.

The simulations start with a laminar boundary layer at the inflow which is tripped by a random volume force near the wall. All the quantities are nondimensionalized by the free-stream velocity and the displacement thickness at the starting position of the simulation ($x = 0$) where the flow is laminar. At that position $Re_{\delta^*} = 400$. The length (including the fringe), height and width of the computational domain were $450 \times 24 \times 24$ δ^* units.

The number of modes was $480 \times 161 \times 96$, which gives a resolution in plus units of $\Delta x^+ = 16$ and $\Delta z^+ = 4.3$. The useful region was confined to $x^* = x/\delta^* = 150 - 350$ which corresponds to Re_{δ^*} from 550 to 1200 or Re_θ from 330 to 700. The simulations were run for a total of 4500 time units (δ^*/U), and the sampling for the turbulent statistics was performed during the 2000 last time units. The good accuracy of the DNS and its statistics was verified by repeating the computation on a coarser resolution ($320 \times 101 \times 64$ modes), and with a shorter averaging time (1000 time units).

LARGE-RE BEHAVIOUR

The boundary-layer equations were solved for the four turbulence models with different β values. The calculations

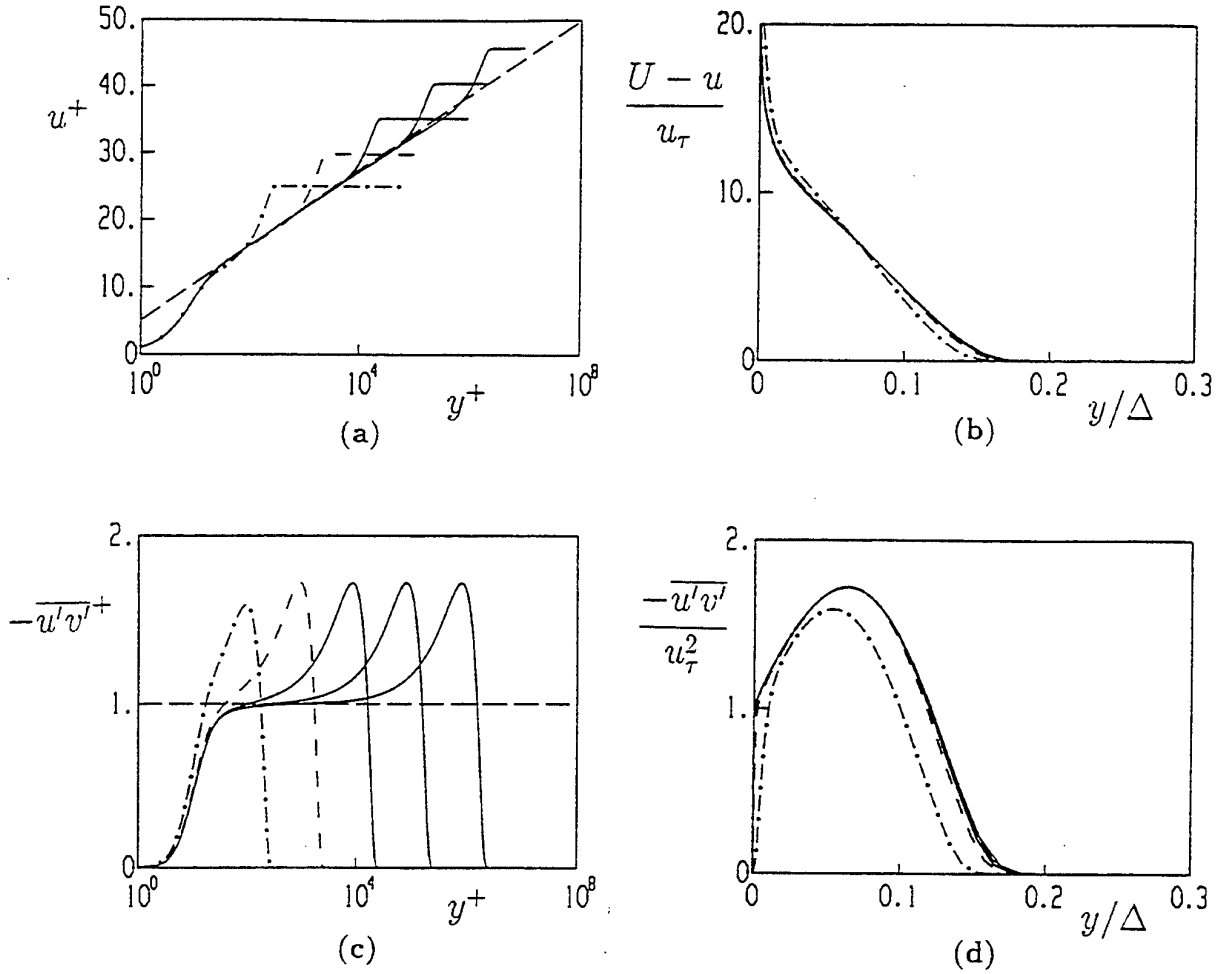


Figure 1: Appearance of the law-of-the-wall and the defect law for increasing Reynolds number according to the DRSM with $\beta = 1$; $Re_\theta = 10^3$ ($- \cdot -$), 10^4 ($- -$), 10^5, 10^6, and 10^7 (solid lines);
Velocity in (a) the inner layer and (b) the outer layer; Reynolds shear stress in (c) the inner layer and (d) the outer layer.
(long dash in (a) denotes the experimental wall function for the velocity, and in (c) the theoretical wall function for the Reynolds shear stress).

were started at $Re_\theta = 300$, where the results from DNS by Spalart (1988) for a zero-pressure gradient were used as starting profiles. At each downstream position the outer-edge velocity was iteratively updated until the chosen β was obtained. The calculations were extended up to about $Re_\theta = 10^8$.

For all considered models the classical scalings turn out to appear for increasing Reynolds number. An example is given in Fig. 1, which shows the velocity and Reynolds-shear stress in the inner and outer layer, as obtained with the DRSM for $\beta = 1$. In the inertial sublayer, being the outer part of the inner layer, the velocity (Fig. 1a) converges to the logarithmic law-of-the-wall; the generally accepted best fit to experiments (having $\kappa = 0.41$ and $C = 5$) is shown as a long-dashed line. The velocity in the outer layer (Fig. 1b), when scaled with u_τ and Δ, converges to a single similarity profile, the so-called defect law. Only the solution for $Re_\theta = 10^3$ shows some deviation from the similarity state, but up to at least graphical accuracy no changes are found from $Re_\theta = 10^4$ on. The Reynolds shear stress in the outer part of the inner layer (Fig. 1c) approaches the wall function $-\overline{u'v'}^+ = 1$. The Reynolds shear stress in the outer layer (Fig. 1d) converges to a similarity shape, which shows a local maximum. The appearance of a maximum for the Reynolds shear stress in the outer layer (with $-\overline{u'v'}/u_\tau^2 > 1$), and also for the turbulent kinetic energy, is characteristic for adverse pressure gradient boundary layers ($\beta > 0$); such a maximum is not found for the zero pressure gradient boundary layer ($\beta = 0$). We checked that the similarity profiles for the different quantities in the inner layer are independent of β, which is in agreement with the classical theory, showing that the same wall function holds independent of the pressure gradient.

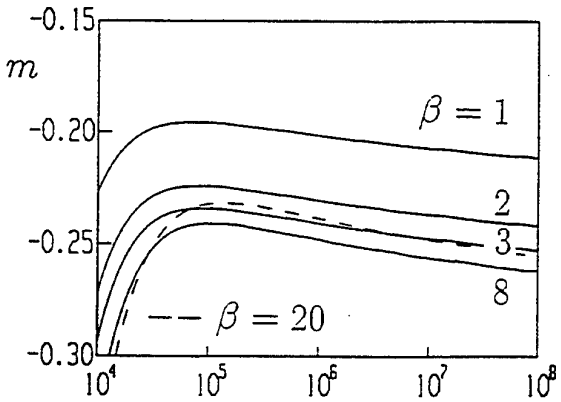
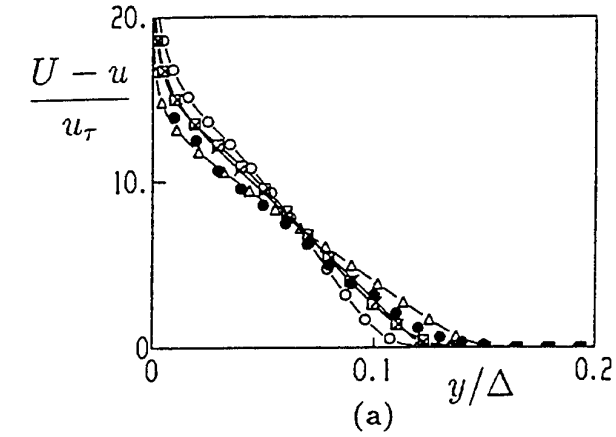
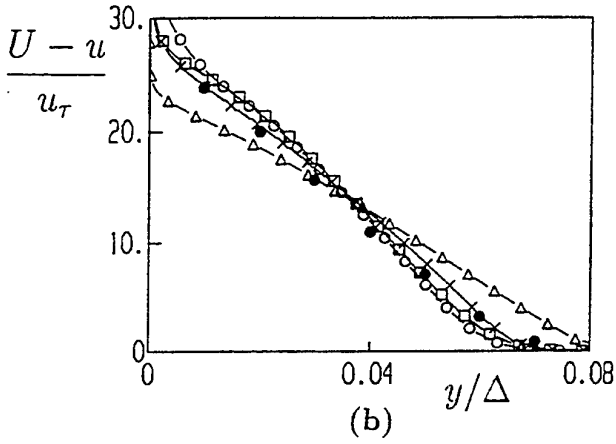


Figure 2: Reynolds-number dependence of the m power in the outer-edge velocity according to the DRSM.





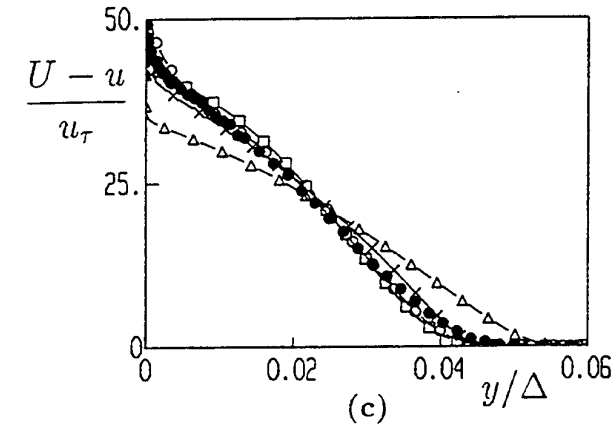
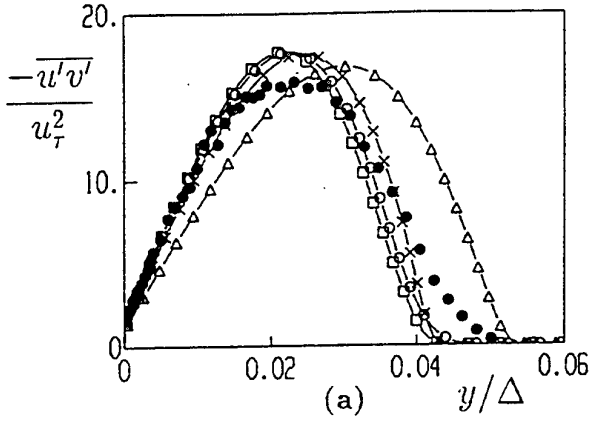
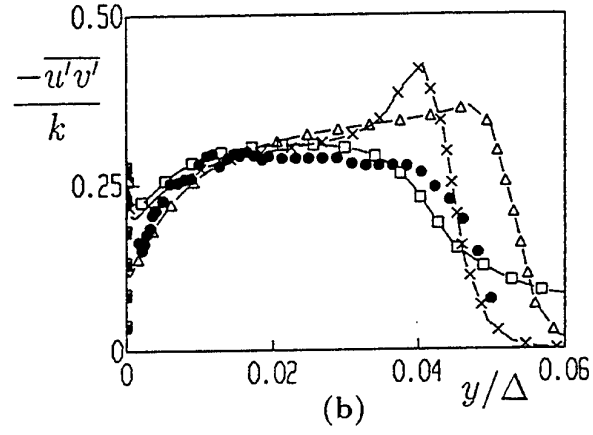


Figure 3: Comparison between turbulence models and experiments for the streamwise velocity under different equilibrium conditions:
(a) $\beta = 2$ (• experiments by Clauser),
(b) $\beta = 8$ (• experiments by Clauser),
(c) $\beta = 20$ (• experiments by Skåre and Krogstad),
models: O–O algebraic; △–△ $k-\epsilon$; ×–× $k-\omega$; □–□ DRSM





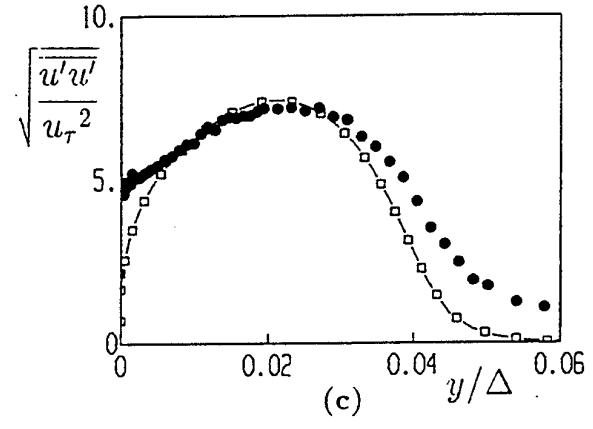


Figure 4: Comparison between turbulence models and experiments for the turbulence in an equilibrium boundary layer with $\beta = 20$:
(a) Reynolds shear stress, (b) structure parameter, (c) Reynolds normal stress along the wall.
models: O–O algebraic: △–△ $k-\epsilon$; ×–× $k-\omega$; □–□ DRSM

We verified that the boundary-layer solution in the outer layer converges to the similarity solution described by the defect-layer equation (7). However, the convergence rate for increasing Re_θ towards the similarity state becomes slower for increasing β. For example, for all β values the shape factor converges to $H = 1$ at $Re_\theta \to \infty$, but the shape factor at $Re_\theta = 10^8$ for $\beta = 0$, 8 and 20 still is 14%, 47%, and 71%, respectively, above its asymptotic value.

An interesting practical question is how the outer-edge velocity should be chosen to realize an equilibrium turbulent boundary layer, as represented by a certain constant β value. Bradshaw (1967) has suggested that a practically constant β results if the outer-edge velocity is chosen as $U \propto (x - x_o)^m$ (where x_0 is a virtual origin, and m is a constant power). To verify this we prescribed m and computed β for increasing Re_θ, but β turns out to be very sensitive to m when m comes closer to -0.25 (that is where turbulent separation is about to occur). This problem was overcome by prescribing β instead of m. Fig. 2 shows the results for the DRSM. Here the local m value is defined as $\frac{x}{U}\frac{dU}{dx}$. The turbulence model does not give a Reynolds-number independent m power for equilibrium layers; instead the power becomes slightly more negative for increasing Reynolds number.

Some authors, including Clauser (1954) (who measured $\beta \approx 2$ and 8), have reported difficulties to establish a stable flow in the windtunnel when the adverse pressure gradient becomes stronger. On the grounds of this experience, Clauser has suggested that the same outer-edge velocity (represented by the same m value) can correspond with two equilibrium boundary layers (i.e. two β values). This means that an established experimental equilibrium boundary layer can suddenly lose stability and jump to the other flow type. This is indeed what is found with the DRSM in Fig. 2. For a given Re_θ (above 10^6) the m-power decreases for β values up to about 8, above which the power increases again. For example, the m value for $\beta = 3$ is almost the same as for $\beta = 20$ (for which experiments were performed by Skåre & Krogstad, 1994). A similar nonuniqueness is found with the other turbulence models.

COMPARISON WITH EXPERIMENTS

The solution in the outer layer, as computed from the boundary-layer equations with different turbulence models, is compared with experiments in Fig. 3 for the streamwise velocity and in Fig. 4 for different turbulence quantities. The computational curves correspond to $Re_\theta = 10^6$ for $\beta = 2$ and 8, and to $Re_\theta = 5 \times 10^4$ for $\beta = 20$. All models, except for the $k-\epsilon$ model, closely predict the experimental streamwise velocity (Fig. 3); the $k - \epsilon$ model overpredicts the experimental wall-shear stress coefficient for $\beta = 20$ at $Re_\theta = 5 \times 10^4$ by 145%. The DRSM is superior, as it gives a value which is only 7% too large, whereas the algebraic model and the $k - \omega$ model give a slightly larger deviation of -15% and $+17\%$, respectively.

All models also closely reproduce the experimental Reynolds-shear stress (Fig. 4a), but the $k - \epsilon$ model somewhat overpredicts the boundary-layer thickness. The DRSM predicts the structure parameter ($= -\overline{u'v'}/k$) best (Fig. 4b), and is in fact very close to the experiments for $\beta = 20$. The DRSM also gives a quite good prediction of the Reynolds normal stresses (Fig. 4c).

With respect to the structure parameter, the experiments in Fig. 4b show that its value is almost constant, and equal to about 0.3, across most of the outer-layer thickness. This implies that the Reynolds shear stress is proportional to the turbulent kinetic energy, as was also discussed by Bradshaw (1967) on the grounds of his own experiments for a weaker adverse pressure gradient. Most turbulence models (including the $k - \epsilon$ model, the $k - \omega$ model, and the DRSM) have chosen the model constants such that the proportionality with the structure parameter 0.3 is reproduced for flows in which the production of turbulence energy P_k ($= -\overline{u'v'}\partial u/\partial y$) equals the turbulent dissipation rate ϵ. For example the $k - \epsilon$ model has $-\overline{u'v'} = \nu_t \partial u/\partial y$, with $\nu_t = c_\mu k^2/\epsilon$. As the constant c_μ is set to 0.09 this gives $-\overline{u'v'}/k = 0.3$ when $P_k = \epsilon$.

COMPARISON WITH DNS

The DNS were performed for the outer edge velocity $U \propto (x - x_0)^m$, with $m = -0.077$ and $m = -0.15$. At the relatively low Re_θ up to which the DNS were feasible, the corresponding equilibrium parameter β is found to be about 0.25 and 0.65, and the shape factor H is about 1.60 and 1.63, respectively.

The calculations with the DRSM at low Reynolds numbers are compared with the new DNS. Profiles for the velocity and turbulence obtained from the DNS at $x^* = 150$ were used as initial data for the model calculations. We varied the initial turbulence and dissipation rate in the model computations, and found that the initial transients already had decayed at $x^* = 335$, where the comparison with the DNS was made. Thus the comparison is meaningful since the difference between the model predictions at low and high Reynolds number (see Fig. 5) are due to the dependence on the Reynolds number and not to the influence of the initial conditions.

Figs 5a,b show close agreement for the velocity profile in inner-layer and outer-layer scalings at $Re_\theta = 670$ and $\beta \approx 0.65$, as computed with the DNS and DRSM. The figure also shows the large-Re similarity state for the DRSM. In fact $Re_\theta = 670$ is still so low that only a small logarithmic part in the inner layer is found. The streamwise Reynolds normal stress for $\beta \approx 0.65$ is compared in Figs 5c,d. The results are shown in both inner and outer layer scalings, and the similarity solution for the DRSM is included as well. Differences between the solution at $Re_\theta = 670$ and the similarity solution are significant. The results with the DRSM closely agree with the DNS at $Re_\theta = 670$, showing that the DRSM reproduces the physics of adverse pressure-gradient boundary layers at relatively low Reynolds numbers. The peak in the Reynolds normal stress in the DNS and DRSM at $Re_\theta = 670$ is part of the inner layer, but there already is a tendency to develop a second peak in the outer layer, which indeed has been established in the similarity solution with the DRSM. New DNS at larger β, which will show an even stronger peak in the outer layer for the turbulent kinetic energy, are underway.

CONCLUSIONS

The numerical solution of the boundary-layer equations up to $Re_\theta = 10^8$ shows that four classes of turbulence models converge to the same classical scalings in the inner and outer layer for turbulent equilibrium boundary layers under an adverse pressure gradient. The solution in the outer layer converges to the defect law described by the defect-layer equation of Tennekes & Lumley, and not to the defect-layer equation of Wilcox (only for $\beta = 0$, both formulations are equal). Convergence to the similarity solution becomes slower for increasing β value. There is a nonunique relation between the m power in the outer-edge velocity and the equilibrium parameter β for all four turbulence models, which is in agreement with the experimental findings of Clauser.

Comparison with experiments, particularly the recent experiments by Skåre and Krogstad at $\beta = 20$, shows that among the tested turbulence models, the Differential Reynolds Stress Model is superior. But also the algebraic model and the $k - \omega$ model are reasonably accurate. The $k - \epsilon$ model gives rather large deviations for strong ad-

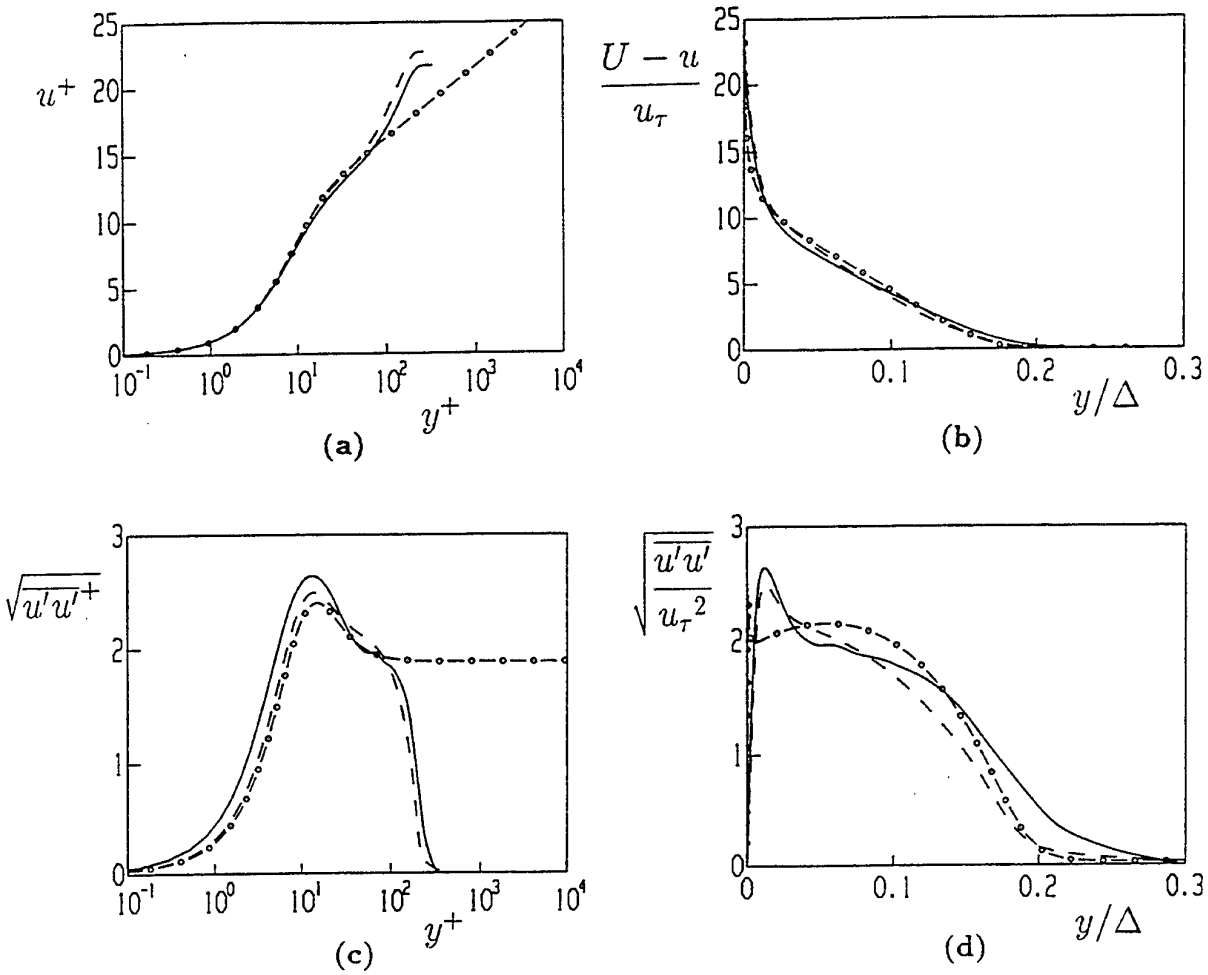


Figure 5: Comparison for $\beta \approx 0.65$; — DNS at $Re_\theta = 670$; - - DRSM at $Re_\theta = 670$; -o- similarity solution for the DRSM. Streamwise velocity in (a) inner-layer scalings, and (b) outer-layer scalings. Streamwise normal stress in (c) inner-layer scalings and (d) outer-layer scalings.

verse pressure gradients, where it considerably overpredicts the wall-shear stress. The DRSM was also compared with our new DNS for $\beta \approx 0.25$ and 0.65 at the relatively low Reynolds number $Re_\theta = 670$. It turns out that the DRSM correctly predicts the low-Reynolds-number effects for the evolution of the boundary layer to its high-Re similarity solution.

REFERENCES

Bradshaw, P., 1967, "The turbulent structure of equilibrium boundary layers," *J. Fluid Mech.*, Vol. 29, pp. 625–645.

Cebeci, T. and Smith, A.M.O., 1974, *Analysis of Turbulent Boundary Layers*, Academic Press, New York.

Clauser, F.H., 1954, "Turbulent boundary layers in adverse pressure gradients," *J. Aero. Sci.*, Vol. 21, 1954, pp. 91–108.

Coles, D., 1956, "The law of the wake in the turbulent boundary layer," *J. Fluid Mech.*, Vol. 1, pp. 191–226.

Hanjalić, K., Jakirlić, S., and Hadžić, I., 1995, "Computation of oscillating turbulent flows at transitional Re-numbers." In *Turbulent Shear Flows* 9, F. Durst et al. (eds), pp. 323-342. Springer-Verlag.

Henkes, R.A.W.M., 1997a, "Scalings of equilibrium boundary layers under adverse pressure gradient according to different turbulence models," Submitted to *AIAA J.*.

Henkes, R.A.W.M., 1997b, "Comparison of turbulence models for attached boundary layers relevant to aeronautics," To appear in *Appl. Sci. Res.*.

Launder, B.E. and Sharma, B.I., 1974, "Application of the energy-dissipation model of turbulence to the calculation of flow near a spinning disk," *Let. Heat Mass Transfer*, Vol. 1, pp. 131–138.

Lundbladh, A., Henningson, D.S. and Johansson, A.V., 1992, "An efficient spectral integration method for the solution of the Navier-Stokes equations," FFA-TN 1992-28, Aeronautical Research Institute of Sweden, Bromma.

Lundbladh, A., Schmid, P.J., Berlin, S. and Henningson, D.S., 1994, "Simulation of bypass transition in spatially evolving flows", Proceedings of the AGARD Symposium on Application of Direct and Large Eddy Simulation to Transition and Turbulence, AGARD-CP-551, 1994.

Skåre, P.E., 1994, "Experimental investigation of an equilibrium boundary layer in strong adverse pressure gradient," University of Trondheim, PhD Thesis, Report NTH 1994:179 (D).

Skåre, P.E. & Krogstad, P.-Å, 1994 "A turbulent equilibrium boundary layer near separation," *J. Fluid. Mech.*, Vol. 187, pp. 61–98.

Spalart, P.R., 1988, "Direct numerical simulations of a turbulent boundary layer up to $Re_\theta = 1410$," *J. Fluid Mech.*, Vol. 187, pp. 61–98.

Tennekes, H. & Lumley, J.L., 1972, *A First Course in Turbulence*, The MIT Press.

Wilcox, D.C., 1993, *Turbulence Modelling*, DCW Industries Inc.

ON THE TURBULENCE STRUCTURE IN SOLID AND PERMEABLE PIPES

C. Wagner and R. Friedrich
Lehrstuhl für Fluidmechanik
TU München
85747 Garching
Germany

INTRODUCTION

The wall blocking effect limits the maximum turbulence kinetic energy production in the wall layer of fully developed channel or pipe flow to levels much lower than those in free shear layers with comparable main shear. This is concluded from sudden pipe expansion flow [5]. In order to analyse the mechanisms of wall blocking in more detail, we performed direct numerical simulations of fully developed flow in a perfectly permeable pipe with no-slip boundary conditions and compared the flow with that in a smooth solid pipe for a Reynolds number of 360 based on diameter D and friction velocity u_τ. Since the Reynolds shear stress vanishes at the wall in both cases, u_τ and thus the mean axial pressure gradient have the same values in both flows. The DNS results show that a wall which is permeable to the wall-normal velocity fluctuations generates higher Reynolds shear stress, but smaller mean shear rate and thus has a considerably reduced mass flux. The increase in pressure fluctuations everywhere in the flow field has an impact on pressure-strain and pressure-velocity correlations. Besides this the intermittent behaviour of the wall normal velocity fluctuations close to the wall is eliminated, leading to low values in the flatness. Instead, the flatness of the other two components is markedly increased. The dramatic change in turbulence structure in the wall layer is evident from contour lines of instantaneous flow quantities.

MEAN MOMENTUM TRANSPORT

The axial momentum transport of statistically steady, fully developed, non-swirling and incompressible flow in a straight circular pipe is governed by the following equation:

$$-\frac{r}{2}\frac{1}{\rho}\frac{\partial\langle p\rangle}{\partial z}+\nu\frac{d\langle u_z\rangle}{dr}-\langle u_z'' u_r''\rangle=0 \qquad (1)$$

It describes the balance between the mean pressure gradient, the viscous and the Reynolds shear stress. The angular brackets indicate statistical averages. Only the mean pressure depends on the axial and radial coordinates z, r. The axial pressure gradient, however, is independent of r. This is a consequence of the mean momentum balance in radial direction. Equation (1) is valid for impermeable as well as permeable walls.

Motivated by the investigations of [3], we define a **perfectly permeable wall** by the following boundary conditions:

$$u_z=u_\varphi=0. \qquad \frac{\partial}{\partial r}(ru_r)=0 \quad \text{at} \quad r=R. \qquad (2)$$

R is the pipe radius. Obviously such a boundary allows the fluctuating flow to move unimpeded through the wall, but inhibits any tangential motion. Thus, there is no wall blocking effect. In contrast to (2) the **solid wall** satifies the boundary conditions:

$$u_z=u_\varphi=u_r=0, \quad \text{at} \quad r=R. \qquad (3)$$

In both cases, the Reynolds shear stress vanishes at the wall, i.e.

$$\langle u_z'' u_r''\rangle=0, \quad \text{at} \quad r=R. \qquad (4)$$

If the same mean pressure gradient

$$\frac{\partial\langle p\rangle}{\partial z}=-\frac{2}{R}\tau_w=-\frac{2}{R}\rho u_\tau^2 \qquad (5)$$

is applied to drive the flow through the solid pipe (Case A) and the permeable pipe (Case B), the Reynolds numbers Re_τ, based on pipe diameter D and friction velocity u_τ of both cases coincide. This is the situation studied in this paper for a low Reynolds number of $Re_\tau=360$. Equation (1) already reflects the linearity of the total shear stress. It can be cast in the following non-dimensional form:

$$\frac{1}{Re_\tau}\frac{d(\langle u_z\rangle/u_\tau)}{d(y/D)}+\frac{\langle u_z'' u_r''\rangle}{u_\tau^2}=1-2\frac{y}{D}. \qquad (6)$$

The y-coordinate is defined by $y=R-r$. Again, eq. (6) holds for cases A and B and allows to derive the universal linear law

$$\frac{\langle u_z\rangle}{u_\tau}=\frac{yu_\tau}{\nu}. \qquad (7)$$

for the viscous sublayer, where the Reynolds shear stress and $2y/D$ are both small. As $\langle u_z'' u_r''\rangle$ grows with the distance from the wall, the differences between both flow cases

arise. Since $\langle u_z'' u_r'' \rangle$ is larger in case B (permeable pipe), the viscous stress must be smaller than in case A, leading to a strongly reduced mass flux through the pipe.

DIRECT NUMERICAL SIMULATION

The incompressible Navier-Stokes equations written in cylindrical (z, φ, r)-coordinates are integrated using second order central differences in space and a semi-implicit time integration scheme. Only convective and diffusive terms involving derivatives in the circumferential direction are treated implicitly in order to avoid unnecessary time step restrictions near the centerline. The second-order accurate leap-frog scheme is used to advance the other convection terms in time, while the Euler-backward scheme is applied to the remaining diffusion terms. The pressure gradient is split into a constant mean value and a fluctuating part. The use of a projection approach leads to a Poisson equation for the fluctuating pressure. FFT in z- and in φ-directions reduces the Poisson problem to a set of 1D Helmholtz problems, each of which is treated with a standard tridiagonal matrix algorithm.

The computational domain, a pipe section of length $5D$, is resolved by 256×128 equidistant grid points in z, φ-directions and 70 points on the radius which are clustered close to the wall. The viscous sublayer (case A) contains 6 points. In terms of wall units the grid spacing is:

$$\begin{aligned} \Delta z^+ = 7.031, \quad \Delta r^+ &= 0.468, ..., 3.963, \\ (r\Delta\varphi)^+ &= 8.813, ..., 0.0972. \end{aligned} \tag{8}$$

The Reynolds number based on u_τ is $Re_\tau = 360$ in both cases. Based on bulk velocity u_b it is $Re_b = 5300$ for the solid pipe and $Re_b = 1931$ for the permeable pipe. This value is considerably lower than the classical critical Reynolds number for pipe flow, namely 2300. Obviously, the removal of the wall blocking effect makes the flow more unstable. In the computation the flow was observed over more than 40 problem times, with the results that the bulk velocity remained stable.

The computation were started in both cases from instantaneous flow fields computed by F. Unger in [3] using linear interpolation.

RESULTS

Statistics

Figures 1 and 2 show the mean velocity normalized with u_τ as a function of r/D and y^+. The strong influence of wall permeability which extracts energy from the mean flow and converts it into turbulent kinetic energy and dissipation rate, is apparent. The computed mean velocities in the solid pipe coincide with LDA measurements of Westerweel et al. [6] and with those presented in [2] (not shown). Recently, Akselvoll and Moin [1] have confirmed the results in [2], performing a DNS with second-order central discretizations in space and decomposing the computational domain into two regions in which different semi-implicit time-integration schemes are used allowing for significant savings in CPU time. Figures 3-6 contain profiles of the three rms-velocity fluctuations and the turbulent kinetic energy. The axial velocity fluctuations in the solid pipe again agree with LDA data. The radial gradients of rms-velocity fluctuations in axial and circumferential directions are steepened close to the permeable wall, and the turbulent kinetic energy is non-zero at this wall due to the finite level of radial fluctuations. The profile of $u_{r,rms}$ in the near wall region suggests that energy is transferred out of $\langle u_r''^2 \rangle$. The contents of equations (1) or (6) is illustrated in figure 7. It shows the linearity of the total shear stress in both cases and higher Reynolds stress for the flow through

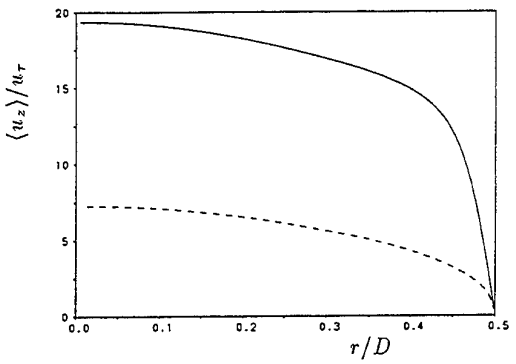


Figure 1: Mean velocity profiles $\frac{\langle u_z \rangle}{u_\tau}$ for solid (——) and permeable pipe (– –).

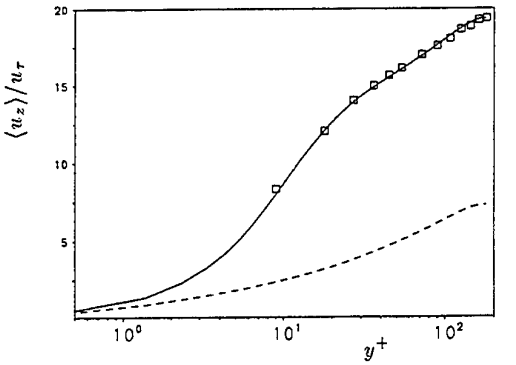


Figure 2: Mean velocity profiles in wall units for solid (——) and permeable wall (– –). The symbol □ denotes LDA measurements of [6].

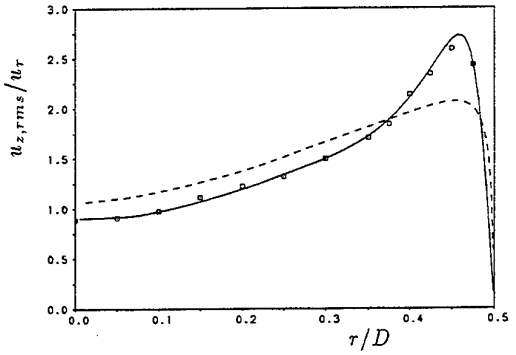


Figure 3: Rms-velocity fluctuations in axial direction: —— solid, – – permeable wall. □ LDA measurements of [6].

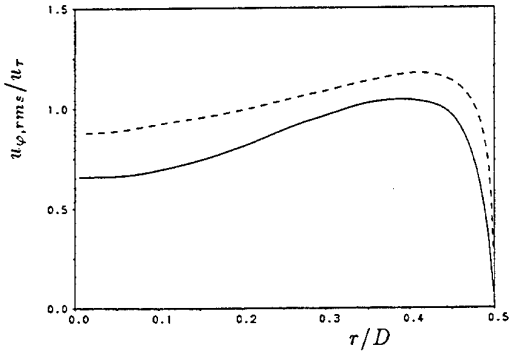


Figure 4: Rms-velocity fluctuations in circumferential direction: —— solid, – – permeable wall.

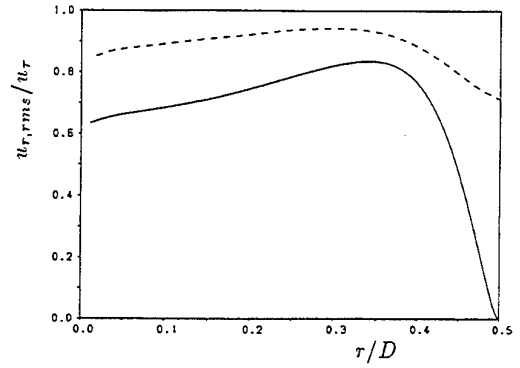


Figure 5: Rms-velocity fluctuations in radial direction: —— solid, – – permeable wall.

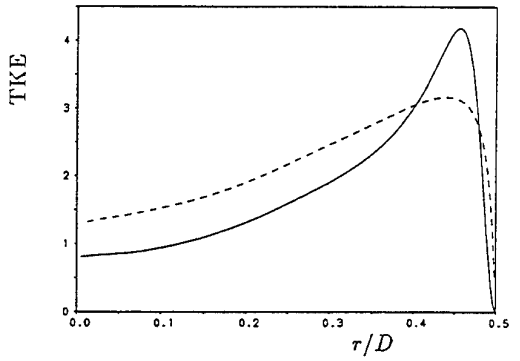


Figure 6: Profiles of turbulent kinetic energy: —— solid, – – permeable wall.

a permeable pipe. The increase in Reynolds stress entrains a decrease in viscous stress and thus in mean velocity.

A remarkable change in the rms-pressure fluctuations is observed, when the wall is made permeable, see figure 8. In the whole cross section p_{rms} increases. The most important differences between cases A and B are observed in the wall layer, where the high level of radial velocity fluctuations in case B leads to a permanent increase in p_{rms} as $r \mapsto R$. The modification in flow structure due to the lack of wall-blocking is also apparent from the rms-vorticity fluctuations in figure 9. The values are normalized by u_τ^2/ν. While in the solid wall case, the rms fluctuations of $\omega_\varphi'', \omega_z'', \omega_r''$ attain values of 0.36, 0.15 and 0.0 at the wall, the rms values of ω_φ'' and ω_z'' are strongly enhanced in the wall layer and their profiles have very similiar shapes (in contrast to the classical case). On the other hand $\omega_{r,rms}$ keeps its constant value till very close to the wall. It is zero at the wall in both cases, but has higher values very close to the permeable wall. From figure 10 we conclude that a perfectly permeable wall brings the flatness of u_r'' down to the level of a random process everywhere, namely 3. Close to a solid wall it reaches values of 18 and more, due to intermittency effects. This role seems now to be occupied by the u_φ''-component. The flatness of u_z'' near the permeable wall also exceeds the value close to the solid wall. These findings indicate remarkable changes in the near wall turbulence structure due to the removal of the wall blocking effect. Fig. 11 contains contour plots of two-point autocorrelation functions in the porous pipe for $p'', u_r'', u_\varphi'', u_z''$ of the type:

$$R_{pp} = \langle p''(z, \varphi, y^+ = 4) p''(z+\Delta z, \varphi+\Delta\varphi, y^+ = 4) \rangle. \quad (9)$$

A comparison with corresponding results for the impermeable pipe (not presented here) shows the increase in

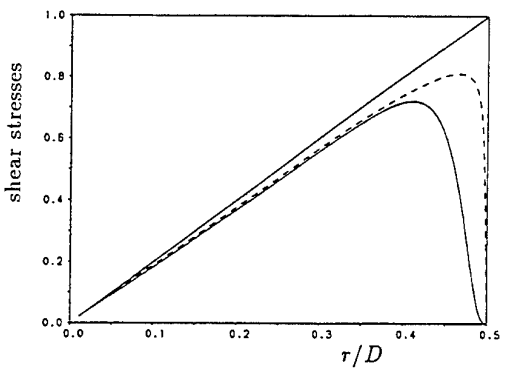


Figure 7: Total shear stress and Reynolds shear stress: —— solid, – – permeable wall.

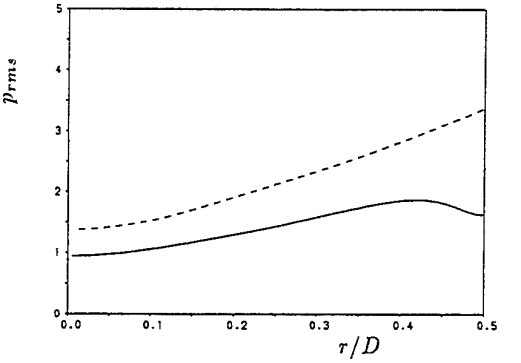


Figure 8: Rms-pressure fluctuations: —— solid, – – permeable wall.

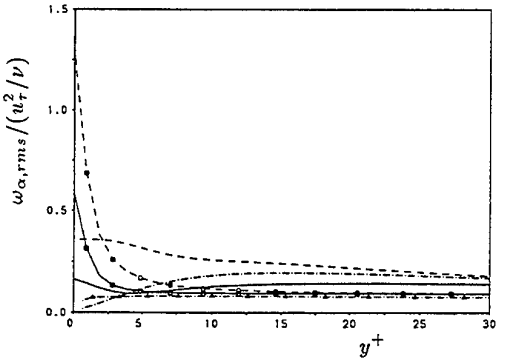


Figure 9: Rms-vorticity fluctuations. (——): $\omega_{z,rms}$, (– –): $\omega_{\varphi,rms}$, (– · –): $\omega_{r,rms}$. Curves with symbols represent the permeable case.

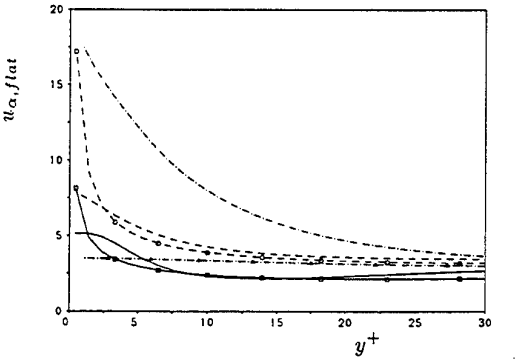


Figure 10: Flatness of velocity fluctuations. (——): $u_{z,flat}$, (– –): $u_{\varphi,flat}$, (– · –): $u_{r,flat}$. Curves with symbols represent the permeable case.

streak spacing in the wall layer of the permeable pipe. Generally speaking, all integral length scales based on these correlation functions increase.

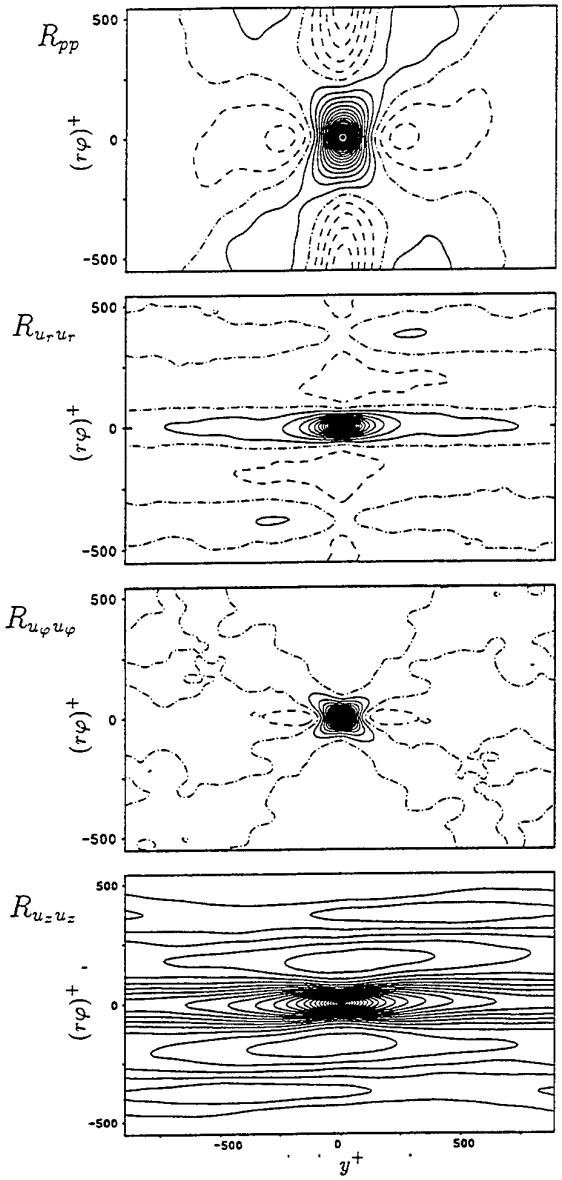


Figure 11: Contour plots of two-point correlation functions at $y^+ = 4$ in the permeable pipe for p'', u_r'', u_φ'', u_z'' (from top to bottom).

Snapshots of the flow field

Solid wall.

Figures 12-13 contain contour lines of axial and radial velocity fluctuations in a cross section perpendicular to the pipe axis. Sweeps ($u_z'' > 0, u_r'' > 0$) and ejections ($u_z'' < 0, u_r'' < 0$) can easily be identified. In a sweep, fluid approaches the wall and carries axial momentum which is higher than the mean. Such an event occurs e.g. near $\varphi = -\pi/3$. Close to the wall, part of the fluid is diverted to the right side, part to the left, enhancing an ejection event around $\varphi = -\pi/2$. The downward motion ($\varphi = -\pi/3$) and the upward motion ($\varphi = -\pi/2$) give rise to thin shear layers in between in which the local dissipation rate is maximum. Streaky structures are made visible via contour lines of u_z'' in a (z, φ) surface at $y^+ = 4$, see figure 14.

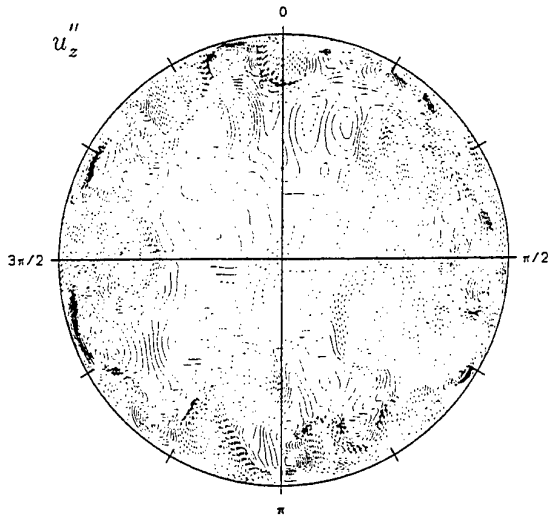


Figure 12: Contour lines of axial velocity fluctuations in an impermeable pipe. (—— , $u_z'' > 0$; - - , $u_z'' < 0$).

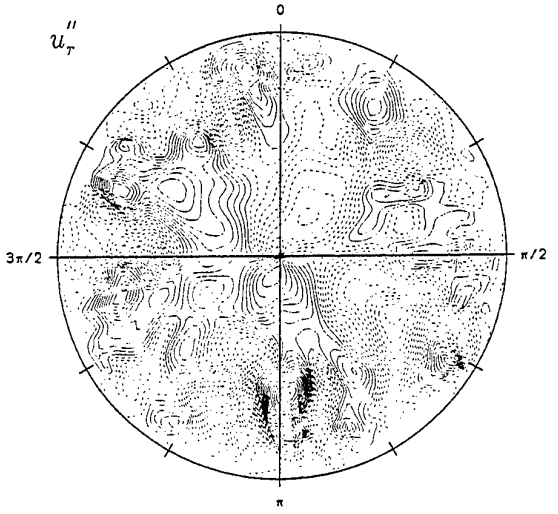


Figure 13: Contour lines of radial velocity fluctuations in an impermeable pipe. (—— , $u_r'' > 0$; - - , $u_r'' < 0$).

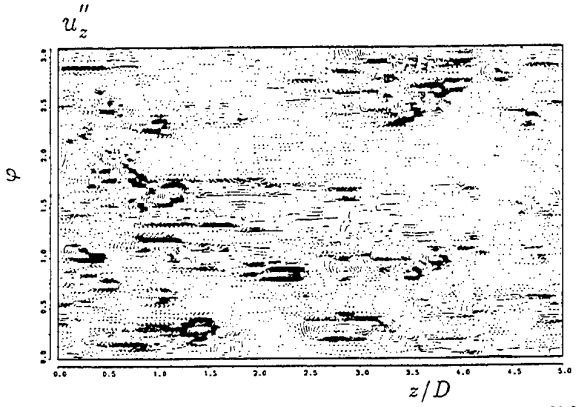


Figure 14: Axial velocity fluctuations near the solid wall ($y^+ = 4$).

Permeable wall.

The examination of contour lines of u_z'', u_r'', u_φ'' in a cross section $z = const$ in figures 15 to 17 immediately reveals the higher degree of freedom this flow experiences, which is two-fold because: 1) the impermeability constraint is relaxed and 2) the local mean shear rate is reduced while the level of velocity fluctuations is in general increased. Pressure fluctuations are presented in figure 18. A comparison of figures 14 with 19 which contain contours of velocity fluctuations in a (z, φ)-surface at $y^+ = 4$ is of great interest since it underlines the differences in turbulence structure of both flows. 'Streaky structures' meander around and broaden due to the reduced shear rates. The pressure fluctuations in figure 20 seem to reflect an increase in circumferential correlation length compared to the solid wall situation. The whole flow bears some similarity with that in the reattachment region of sudden pipe expansion flow where the mean shear is also considerably reduced and contours of two-point pressure correlations shows a characteristic elongation in circumferential direction [4].

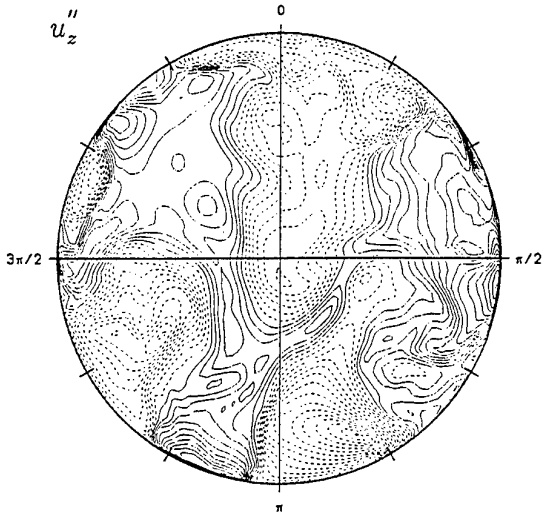


Figure 15: Contour lines of axial velocity fluctuations in the perfectly permeable pipe. (—— , $u_z'' > 0$; – – , $u_z'' < 0$).

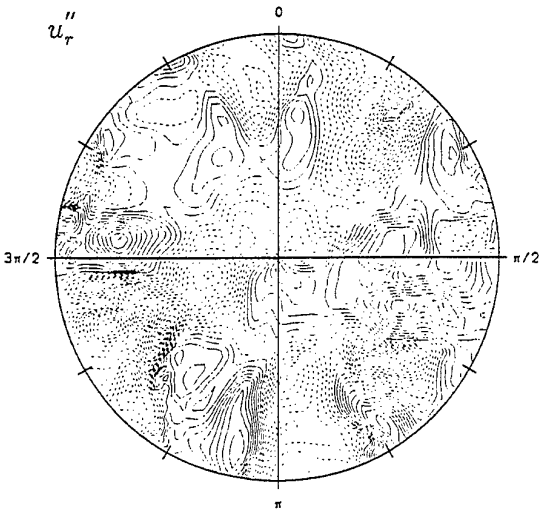


Figure 16: Contour lines of radial velocity fluctuations in the perfectly permeable pipe. (—— , $u_r'' > 0$; – – , $u_r'' < 0$).

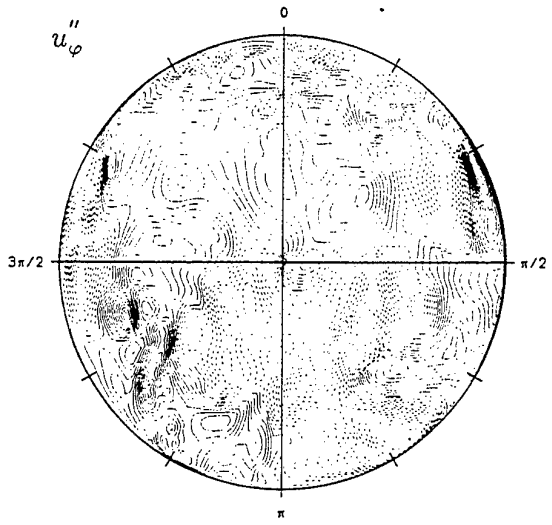


Figure 17: Contour lines of circumferential velocity fluctuations in the perfectly permeable pipe. (—— , clockwise, – – , counterclockwise).

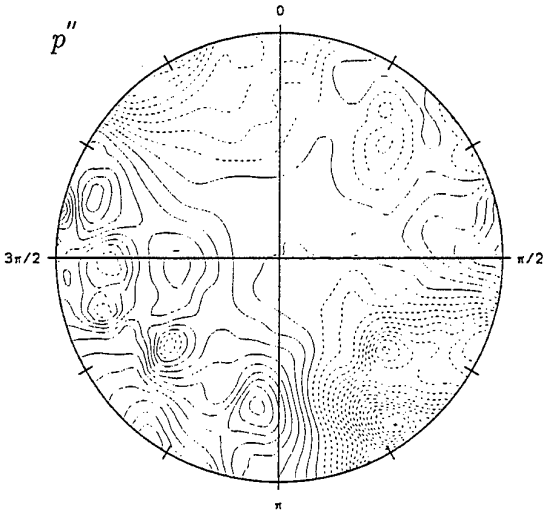


Figure 18: Contour lines of pressure fluctuations in the perfectly permeable pipe. (—— , $p'' > 0$; – – , $p'' < 0$).

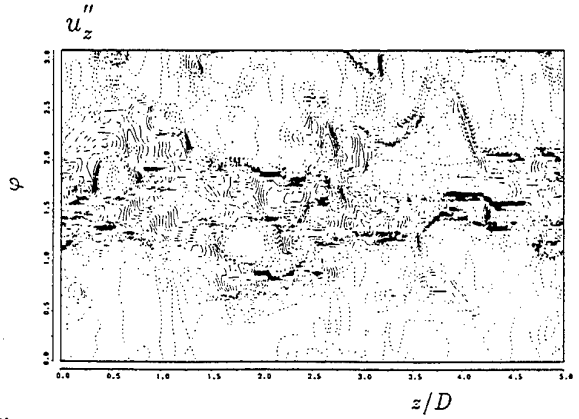


Figure 19: Axial velocity fluctuations near the perfectly permeable wall ($y^+ = 4$).

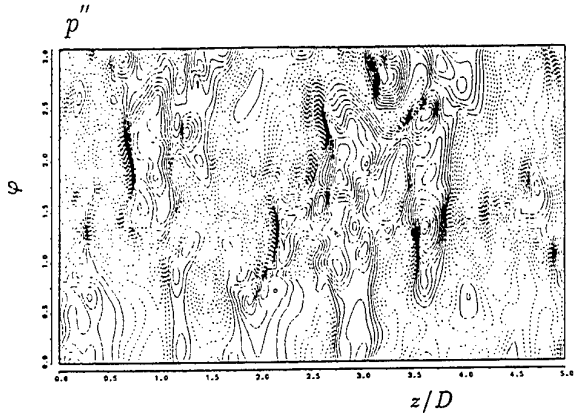


Figure 20: Pressure fluctuations near the perfectly permeable wall ($y^+ = 4$).

REYNOLDS STRESS TRANSPORT

An increase in Reynolds shear stress results in higher maximum production rates of the turbulent kinetic energy and of the variance of axial velocity fluctuations in the near wall region. The balance of $\langle u_z''^2 \rangle$ has the form:

$$0 = -2\langle u_r'' u_z'' \rangle \frac{d\langle u_z \rangle}{dr} + 2\langle \frac{p''}{\rho} \frac{\partial u_z''}{\partial z} \rangle \qquad (10)$$
$$-\frac{1}{r}\frac{d(r\langle u_r'' u_z''^2 \rangle)}{dr} + \nu \left[\frac{1}{r}\frac{d}{dr}(r\frac{d\langle u_z''^2 \rangle}{dr}) \right]$$
$$-2\nu \left[\langle (\frac{\partial u_z''}{\partial r})^2 \rangle + \langle \frac{1}{r^2}(\frac{\partial u_z''}{\partial \varphi})^2 \rangle + \langle (\frac{\partial u_z''}{\partial z})^2 \rangle \right].$$

The production term P_p (the index p denotes the porous case) can be obtained by multiplication of eq. 1 with $a\langle u_z'' u_r'' \rangle$:

$$P_p = a\frac{2}{\nu}\langle u_z'' u_r'' \rangle_s (\frac{r}{R}u_\tau^2 - a\langle u_z'' u_r'' \rangle_s). \qquad (11)$$

where we introduced the ratio $a = \langle u_z'' u_r'' \rangle_p / \langle u_z'' u_r'' \rangle_s$ of Reynolds stresses in the case A and B (the index s denotes the solid case). For $a = 1$ the production term for the solid pipe flow is retained. Evaluating the maximum production rate by varying eq.12 with respect to $\langle u_z'' u_r'' \rangle_s$ leads to:

$$P_{p,max} = \frac{1}{2\nu}(\frac{r}{R}u_\tau^2)^2 \quad \text{for} \quad \langle u_z'' u_r'' \rangle_s = \frac{r}{2aR}u_\tau^2. \qquad (12)$$

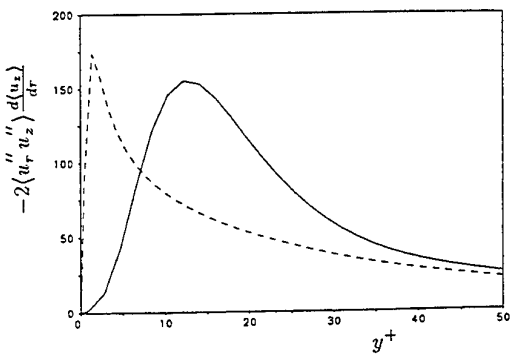


Figure 21: Production rates of axial velocity fluctuations: (——) solid, (– –) permeable wall.

In solid pipe flow ($a = 1$) the balance between Reynolds shear stress and viscous stress (right expression of eq. 12) determines the position of maximum production. Increasing the Reynolds shear stress ($a > 1$), as in case B, leads to a maximum production which is located closer to the wall, where, according to eq. 12, an increased production rate is obtained. This is confirmed in figure 21 comparing profiles of production rates evaluated from DNS data of solid and perfectly permeable pipe flow. Close to the permeable wall the maximum production of axial velocity fluctuations exceeds the maximum value further away from solid wall by $\approx 12\%$.

CONCLUDING REMARKS

Turbulent flow through pipe with permeable and with solid wall driven by the same pressure gradient is studied in this paper by means of direct numerical simulation, in order to improve the understanding of the wall blocking effect. A perfectly permeable wall which satisfies no-slip conditions is a hypothetical case which cannot strictly be realized experimentally. Nevertheless it gives very useful insight into its physical properties and forms a test case for the evaluation of statistical turbulence models and of subgrid scale models.

Some of the key observations are:

- The wall permeability increases the Reynolds shear stress and the maximum TKE production and in turn reduces the mass flux through the pipe.
- The position of the maximum TKE production is much closer to the wall than in the solid wall case, increasing the gradients of turbulence quantities normal to the wall.
- Considerable changes in the turbulence structure occur in the wall layer which are reflected in the rms-vorticity fluctuations and the flatness factors of the velocity fluctuations.

A DNS at a higher Reynolds number is envisaged in order to investigate Reynolds number effects. A DNS of turbulent flow through a partly permeable pipe is under way, a flow case which is more likely to be realized in a physical experiment.

REFERENCES

[1] Akselvoll, K. and Moin, P., 1996, "An efficient method for temporal integration of the Navier-Stokes equations in confined axisymmetric geometries," *J. Comp. Phys.*, Vol. 125, pp. 454-463.

[2] Eggels, J.G.M., Unger, F., Weiss, M.H., Westerweel, J., Adrian, R.J., Friedrich, R. and Nieuwstadt, F.T.M., 1994, "Fully developed turbulent pipe flow: a comparison between direct numerical simulation and experiment," *J. Fluid Mech.*, Vol. 268, pp. 175-209.

[3] Perot, B. and Moin, P., 1995, "Shear free turbulent boundary layers. Part 1. Physical insights into near-wall turbulence," *J. Fluid Mech.*, Vol. 295, pp. 199-227.

[4] Wagner, C., 1996, "Direkte numerische Simulation turbulenter Strömungen in einer Rohrerweiterung," Dissertation, Munich University of Technology, VDI-Verlag, Fortschrittsberichte Reihe 7, Nr. 283.

[5] Wagner, C. and Friedrich, R., 1996, "Reynolds stress budgets of low Reynolds number pipe expansion flow," *Advances in Turbulence 6*, S. Gavrilakis et al. (Eds.), Kluwer Academic Publishers, Dordrecht, pp. 51-54.

[6] Westerweel, J., Adrian, R.J., Eggels, J.G.M. and Nieuwstadt, F.T.M., 1992, "Measurements with particle image velocimetry on fully developed turbulent pipe flow at low Reynolds number," *Proc. of the 6th Int. Symp. on Applications of Laser Technique to Fluid Mechanics*, Lisbon, Portugal, July 20-23.

ON THE LARGE SCALE ORGANIZATION OF A TURBULENT BOUNDARY LAYER DISTURBED BY A CIRCULAR CYLINDER

F. de Souza[1][2], J. Delville[1], J. Lewalle[3], J.P. Bonnet[1]

[1] LEA/CEAT
43 Route de l'Aérodrome
86036 Poitiers Cédex
France

[2] Present address: Institute for Aerospace Research
National Research Council Canada
Ottawa, Ontario, K1A 0R6
Canada

[3] Dept. of Mech., Aerosp. and Manuf. Engg., Syracuse University
151 Link Hall
Syracuse, New York, 13244
U.S.A.

INTRODUCTION

Several studies have been devoted to outer boundary layer manipulators (see Coustols and Savill, 1992, Hamdouni and Bonnet, 1993, Lemay *et al.*, 1995). The effects of various types of manipulators, such as thin ribbons, airfoils and cylinders, have been quantified. It has been shown that the considerable reduction in local skin friction (of the order of 10%) that can be obtained by using such devices is at best equivalent to the form drag of the manipulator itself, leading to no net reduction in drag. However, since in most cases these outer layer manipulators have been shown to reduce the wall heat transfer as well, there is continued interest in their thermal applications. Further, although various hypotheses have been put forward by a number of researchers, there is as yet no consensus on the exact mechanisms of skin friction and heat transfer modification.

The present study deals with a particular configuration of outer layer manipulation in which significant skin friction reduction (more than 30% locally) is accompanied by an increase in heat transfer, in apparent violation of the Reynolds analogy. This flow has been quantified previously by Marumo *et al.* (1978, 1985) and Suzuki *et al.* (1989). Single-point statistics have been obtained by Kawaguchi *et al.* (1984), Suzuki *et al.* (1988) and de Souza *et al.* (1997), with the goal of elucidating the physical processes responsible for this apparent dissimilarity between heat and momentum transfer. However, in addition to knowledge of mean flow characteristics, a full explanation necessitates an investigation of the instantaneous, large scale organization. This is accomplished by applying a number of coherent structure identification techniques to multi-point measurements obtained in the near wake of the circular cylinder manipulator. Three techniques are described and assessed: conditional averaging based on WAG (Window Average Gradient) detection, and two filtering techniques, based respectively on the spectral and on the time-frequency (using wavelets analysis) decomposition of the instantaneous velocity signals. Information on the flow structure and dynamics gleaned from the application of these techniques is analyzed and related to the observed dissimilarity between heat and momentum transfer. In addition, the present study sheds some light on the role of outer layer manipulators whilst providing insight into the interaction between two fundamental and well documented flows: the cylinder wake and the turbulent boundary layer.

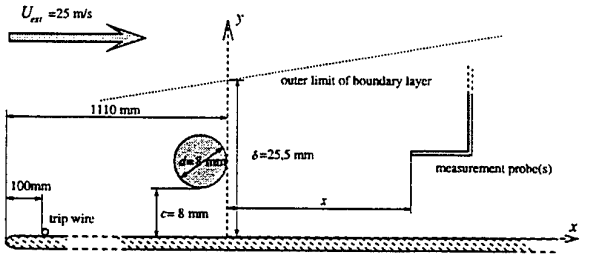


Figure 1: Schematic description of the experimental configuration.

EXPERIMENTAL DETAILS

Experimental Configuration

Experiments were performed in a closed circuit, subsonic wind tunnel with a square test section of cross-sectional dimensions 300 mm × 300 mm and length 2 m. The boundary layer developed on a flat plate placed horizontally at about 100 mm above the test section floor. A circular cylinder of diameter $d = 8$ mm was placed within the fully turbulent, zero-pressure gradient boundary layer of thickness $\delta = 25.5$ mm and Reynolds number (based on momentum thickness) $Re_\theta = 4500$. The cylinder was oriented normal to the free stream direction and parallel to the wall, such that the gap between the cylinder and the wall was $c = 8$ mm (figure 1). The free stream velocity was set at $U_{ext} = 25$ m/s, and the corresponding turbulence intensity was less than 0.25%.

Flow qualification measurements

Flow qualification involved skin friction measurements using the Preston tube technique and velocity measurements using pitot tubes, single and x-type hot-wire probes.

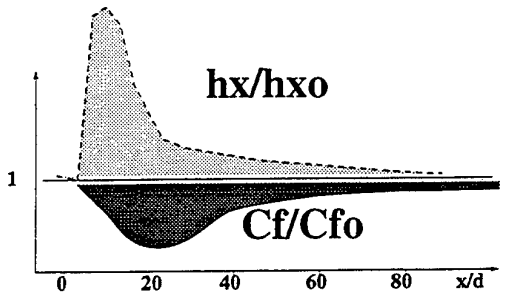


Figure 2: Schematic distribution of the modification of local skin friction (C_f/C_{f_o}) and heat transfer (h_x/h_{x_o}) coefficients due to the cylindrical manipulator.

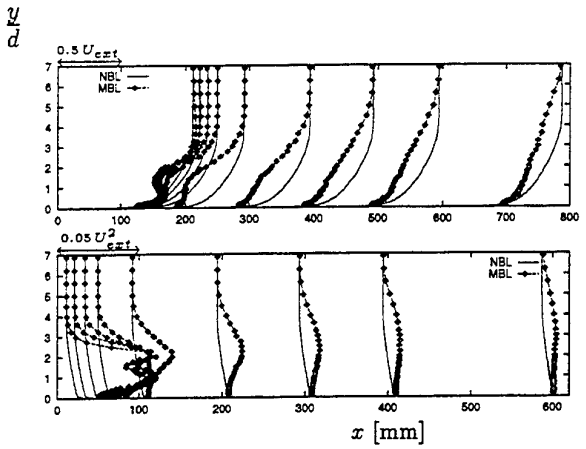


Figure 3: Profiles of mean velocity, $\overline{U}$ (top), and mean-squared fluctuations, $\overline{u'^2}$ (bottom), measured in the manipulated (MBL) and natural (NBL) boundary layer.

These measurements were consistent with those reported in the literature (Marumo *et al.*, 1978, 1985, Suzuki *et al.* 1989). Some of the important features of the flow are described briefly here.

Figure 2 provides a schematic description, obtained from the compilation of our experimental results (de Souza, 1996) and those obtained by Suzuki *et al.* (1989), of the streamwise evolution of the local skin friction and heat transfer coefficients, represented respectively in the forms C_f/C_{f_o} and h_x/h_{x_o} (where the index $_o$ corresponds to unmanipulated flow conditions). The maximum reduction in C_f is of the order of 30% and is located at $x \sim 20$ diameters from cylinder, whereas the maximum heat transfer increase is of the order of 60% and occurs very close to the manipulator ($x \sim 5d$). The downstream evolution of the mean and fluctuating velocity profiles (figure 3) indicate the significance of the disturbance produced in the boundary layer by the cylinder. In particular, the considerable mean velocity deficit has not yet disappeared at over 70 diameters downstream of the cylinder, and the two maxima, typical of profiles of fluctuating velocity in a wake, are only evident in the very near wake ($x/d < 5$).

Multi-point measurements

Multi-point measurements were obtained via hot-wire anemometry, using a rake of 12 x-wires oriented vertically in the (x, y) plane. The vertical spacing between the probes was 4 mm, and the rake was positioned in the manipulated boundary layer so that the probe closest to the wall was at a distance of $y = 1$ mm (corresponding to y^+ values roughly between 50 and 60). For comparison, rake measurements were repeated in the isolated cylinder wake configuration.

The hot-wire probes, fabricated in our laboratory, have platinum-coated tungsten wires of length 0.5 mm and diameter 2.5 μm, and gold-plated Cu-Be prongs. 24 T.S.I. model 1750 constant temperature anemometers were used. All 24 hot-wire signals were acquired simultaneously at a sampling rate of 20 kHz. Further details are provided by de Souza (1996).

EXTRACTION OF LARGE SCALE STRUCTURES

Energy spectra and space-time correlations deduced from the rake measurements reveal that flow in the very near wake ($x/d = 4.25$) is highly organized and periodic. These characteristics gradually disappear with downstream development (de Souza, 1996). In order to "visualize" the instantaneous flow structure, plots of sectional streamlines were constructed from the hot-wire rake measurements using the procedure outlined by Bisset *et al.* (1990). This procedure requires the application of Taylor's hypothesis in order to transform temporal information into spatial information (in the streamwise direction) using a global convection velocity U_c[1]. The sectional streamlines, exactly tangent to the local velocity vectors, are obtained by interpolation. By this procedure, large scale vortical structures are indicated by spiralling streamlines.

The sectional streamline plots generally seemed to indicate that the large scale, spanwise vortices shed from above the cylinder are larger than the lower vortices (figure 6a), and remain coherent at up to greater downstream distances. The coherent structure identification techniques described below permit closer examination of the characteristics of the dominant structures. Three techniques are described here: one leading to an average description of the large scale organization, and two filtering techniques which permit the extraction of instantaneous flow structures.

Conditional Averages Based on the WAG Method

The simplest of the three techniques is the construction of conditional averages based on the WAG (Window Average Gradient) detection method described by Bisset *et al.* (1990). This method is based on the principle that the structures of interest are associated with sudden variations in the transverse instantaneous velocity signal v'. Such is the case for the large scale spanwise vortices typical of a cylinder wake.

Briefly, the WAG function is defined as the difference between the mean values of two successive short lengths of signal within a "window" of a given number of samples. The window is moved point by point through the digitized signal of a single probe which is selected for detection purposes. A detection begins when the WAG function exceeds a predefined threshold, and ends when the function changes sign. The size of the window is not critical, but is adjusted to correspond to approximately half the period of the structures of interest. The threshold is typically set at half the rms value of v', such that the average detection frequency is approximately equal to the average structure frequency (Strouhal frequency). The coherent field is then calculated (using the signals obtained from all probes) as the ensemble average of all detection regions, centered about the point where the WAG function is a maximum.

The WAG method appears to extract successfully the "coherent" large scale structures from the "random", background turbulence (figure 6a,b, where "D" indicates the location of the detection probe). Using this method, the average structure size, position, relative strength and con-

[1]The convection velocity is estimated to be $U_c \simeq 0,8 \times U_{ext}$ (de Souza, 1996).

vection velocity were estimated. However, information pertaining to the dynamics of individual structures is inaccessible, as this would require decomposition of the *instantaneous* velocity field into coherent and random components. Furthermore, the location and type of detected structures may be influenced by the choice of the detection probe (although the results were fairly insensitive to this criteria) as well as by the very nature of the WAG detection function.

These issues were resolved through the use of the two instantaneous filtering techniques described below, which can be considered to be more objective than the WAG method. These filtering methods can permit verification of the conditional averages, and in particular, of the influence of the local detection criteria associated with the WAG method.

Spectral Filtering Method

The spectral filtering method requires no prior knowledge of the position or type of structures to be detected, although it assumes that the dominant structures are considerably localized in the spectral domain. It permits the instantaneous velocity fluctuations u' and v' to be decomposed each into coherent (u_c and v_c) and random (u_r and v_r) components.

The spectral filtering method is based on the assumption that the well-defined, narrow bandwidth peaks in the energy spectral density of the studied flow (figure 4) are associated with the coherent structures of interest. We further assume that most of the energy of the coherent flow field is contained within these peaks. By eliminating these peaks from the energy spectra, therefore, we hope to obtain a reasonable approximation of the energy spectral density of the incoherent flow field, and by extension, the contribution of the coherent flow field. It should be noted that the elimination process does not involve complete rejection of the bandwidth occupied by the peaks. Both coherent and incoherent flow energy can thus coexist at a given frequency.

The above filter is similar to one proposed by Brereton and Kodal (1992, 1994), which also permits decomposition of the turbulent field into organized and random components. However, these authors employ an adaptive filter, which is not the case in the present study.

Procedure.

The following procedure is used to decompose the flow field into coherent and incoherent components (where it is important to note that each component of each probe is treated individually):

1. The energy spectral densities E_u and E_v are calculated for each probe of the rake.
2. The peaks (principal and harmonics) associated with the passage of coherent structures are removed from the spectra of the complete flow field. In order to do this we must:

   - identify the positions f_{max} of local maxima of the energy spectral density;

   - define a frequency band Δf, centered around each maximum: ($\Delta f \sim 300$ Hz);

   - interpolate the spectral density within this defined band using the values of the smoothed spectral density of the complete flow field;

   We thus obtain monotonic spectra without "coherent" peaks, E_{u_r} and E_{v_r}, which we associate with the energy of the incoherent flow field (figure 4).
3. The incoherent energy transfer functions can then be calculated for the u and v components individually

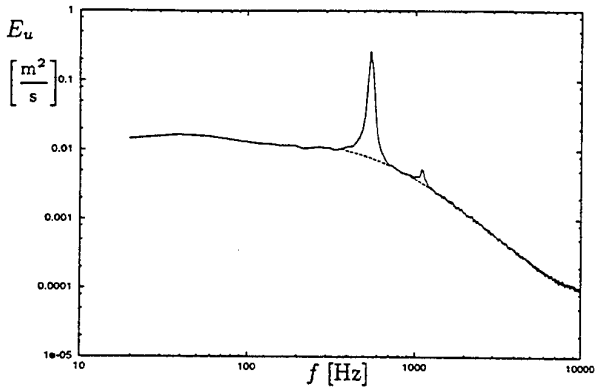


Figure 4: Example of smoothing the energy spectra of the complete flow field E_u (solid line) to obtain the energy spectra of the incoherent field E_{u_r} (dashed line), for the probe located at $y = 5$ mm and $x/d = 4.25$.

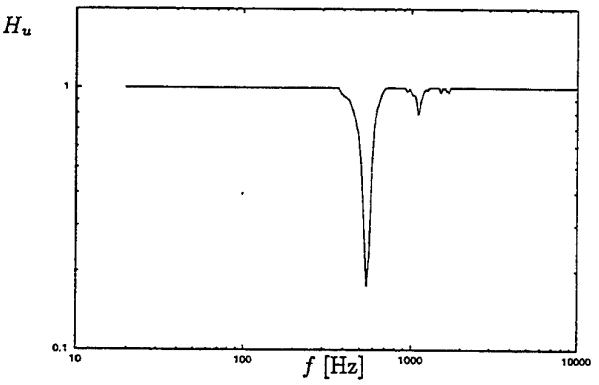


Figure 5: Example of the transfer function H_u obtained for the signal measured at $y = 5$ mm and $x/d = 4.25$.

for each probe of the rake (cf figure 5):

$$H_u(f) = \sqrt{\frac{E_{u_r}(f)}{E_u(f)}} \quad H_v(f) = \sqrt{\frac{E_{v_r}(f)}{E_v(f)}}$$

It should be remarked that although the data is filtered locally, in that each velocity component of each probe is dealt with individually (without taking into account the neighboring probes), this method is nonetheless global in that the information obtained from each probe is treated in the same manner (without preference for any given probe).

To apply the spectral filter to a given instantaneous data sample $u(t), v(t)$, it is required thus to:

- Calculate the Fourier transforms $\hat{u}(f)$ and $\hat{v}(f)$ of the velocity signals by the Fast Fourier Transform (FFT) method;
- Apply the transfer functions $H_u(f)$ and $H_v(f)$ to the Fourier transforms of the respective velocity signals;
- Calculate the inverse Fourier tranforms to obtain the incoherent velocity components;
- Obtain the coherent velocity components by subtraction as follows:

$$u_c(t) = u(t) - \overline{u(t)} - u_r(t)$$

$$v_c(t) = v(t) - \overline{v(t)} - v_r(t)$$

By definition, the incoherent and coherent velocity fields should be uncorrelated. However, this requirement is satisfied automatically only if the incoherent field is obtained by rejecting an entire frequency band; that is, if a given

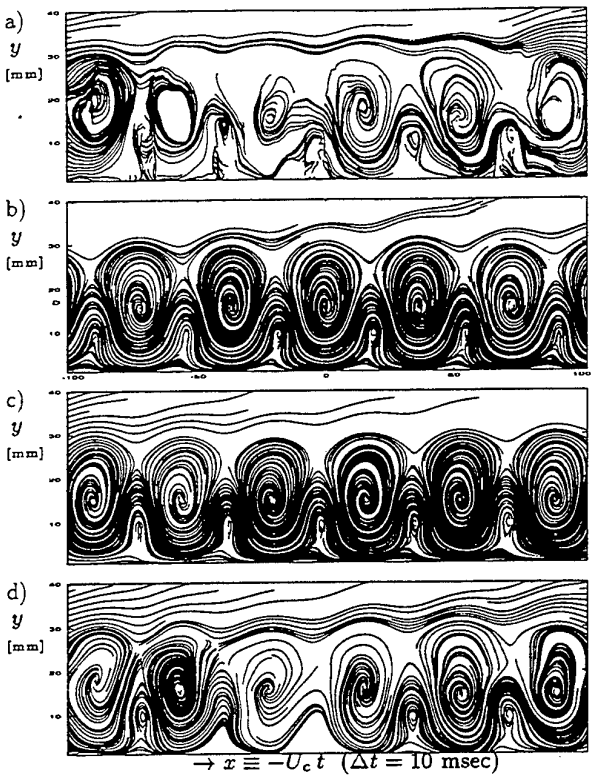


Figure 6: Sectional streamlines of the velocity field measured at $x/d = 4.25$. a) Original field. b) Conditionally-averaged field obtained via the WAG method. c) Spectral-filtered coherent field. d) Wavelet-filtered coherent field.

frequency band cannot simultaneously represent the contributions of both the coherent and incoherent fields. Since this is not the case of the present method, we must ensure that the obtained coherent and random velocity fields are uncorrelated by applying the complementary orthogonalization procedure described below:

$$u_{r_i} = u_{r_i} - u_{c_i} \times \frac{\sum u_{c_i} u_{r_i}}{\sum u_{c_i} u_{c_i}}$$

$$u_{c_i} = u_{c_i} + u_{c_i} \times \frac{\sum u_{c_i} u_{r_i}}{\sum u_{c_i} u_{c_i}}$$

Comments.

The effectiveness of the spectral filtering method is indicated by the results obtained in the manipulated boundary layer (figure 6), and in the isolated cylinder wake (figure 7). The regularity of the corresponding coherent velocity fields is striking. In fact, the instantaneous coherent field of the data measured in the manipulated boundary layer is comparable to the conditionally averaged field (figure 6b), which was obtained from a very large number of events. It appears therefore that the large scale coherent structures can be isolated successfully by using the spectral filter. Furthermore, it can be concluded that the detection criteria associated with the WAG method have relatively little influence on the conditional averages thus obtained.

Wavelets-based Time-Frequency Filter

The second instantaneous filter is based on the time-frequency decomposition of the velocity signals using wavelet analysis. This "intermittent" filtering technique is based solely on the principle that the coherent structures are those which account for most of the turbulent energy in the spatial region of interest, and requires no prior knowledge of the exact location of these structures in the physical or spectral domains. This technique, developed by J. Lewalle (see Lewalle *et al.*, 1996, Bonnet *et al.*, 1996), can thus be considered to be the most objective of the three techniques employed.

The wavelet analysis is performed using one-dimensional, continuous wavelets. The "Mexican Hat" wavelet, represented analytically by the second derivative of the Gaussian function, was chosen arbitrarily for this purpose. This particular wavelet is particularly useful for temporal localization of the local extrema of the signal to be analyzed.

Procedure.

We begin by specifying that for the given flow configuration, the vertical velocity component (normal to the wall) is that which is the most indicative of the passage of large scale structures produced by the cylinder (de Souza, 1996). With this in mind, the filtering procedure is outlined as follows:

- 1. Calculate the wavelet transform of the vertical velocity component for each probe of the rake.
- 2. Calculate for each probe the energy distribution in the time-frequency domain (calculated as the square of the wavelet transform) associated with this velocity component.
- 3. Construct the "average energy map" (which is a spatial average in the y direction of the energy distribution of each of the probes considered "energetically significant" (9 of the 12 probes in the present case).
- 4. Determine an "energy threshold" which is surpassed by a given proportion of the surface (in the time-frequency domain) of the "average energy map"
- 5. Retain the regions of the time-frequency domain where this threshold is exceeded. This defines a mask in the time frequency domain which is subsequently applied in the same manner to each velocity component of each probe.
- 6. Calculate the inverse wavelet transform of the "masked" velocity signals.
- 7. Orthogonalize the coherent and non-coherent pairs of velocity traces (with fixed sum at each instant), so that their respective energies are additive.

Comparison of the 3 methods.

As opposed to classical conditional methods (*i.e.* ensemble averages based on a detection method such as WAG) the time-frequency approach, like the spectral filter, presents the advantage of revealing the *instantaneous contribution* of the coherent part of the signal, and thus provides a tool to analyze particular coherent events. Figure 6d indicates that the time-frequency filter is particularly successful in this respect, as it appears to extract the instantaneous coherent field while permitting a greater distinction to be made between individual structures than does the spectral filtering technique. The irregularity of these structures most likely indicates the presence of coherent events not necessarily associated with the vortices shed from the cylinder, such as wall coherence. It is clear that such events cannot be detected by the two previously described structure identification techniques.

Finally, although the WAG method may be the least objective of the three methods, it has proven to be valuable due to its ability, with relative ease of implementation, to lead to fairly accurate estimations of average structure characteristics such as size, position, convection velocity and relative strength.

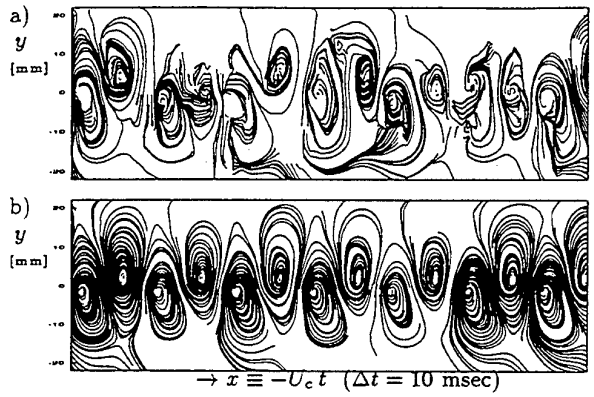


Figure 7: Sectional streamlines of the velocity field measured in the isolated wake at $x/d = 4.25$. a) Original field. b) Spectrally filtered coherent field.

ANALYSIS OF THE FLOW DYNAMICS

Figures 6 and 8 portray examples of particular events which are characteristic of the flow phenomena that intervene in the dissimilarity process.

Consider specifically the near wake of the cylinder ($x/d \sim 4$), where in the manipulated boundary layer configuration, the turbulent intensity profiles have two maxima and the local heat transfer attains its maximum value. A significant difference in flow behaviour can be noted between the manipulated boundary layer (figure 6) and the isolated wake (figure 7) configurations. For each of these configurations the flow organization is very distinct. In the isolated wake, two rows of alternating, spanwise vortices of opposite sign vorticity, typical of a von Karman vortex street, are distributed symmetrically about the cylinder/wake axis. The two rows are visible in the manipulated boundary layer as well. However, the vortex street is highly asymmetrical. The clockwise (negative vorticity) vortices shed from above the cylinder are very large and occupy almost the entire width of the boundary layer, while the vortices shed from below the cylinder are much smaller and remain below the cylinder/wake axis. Measurements obtained further downstream and filtered using the wavelets technique reveal that in the region of maximum skin friction reduction ($x/d \sim 24$) and beyond, only the large, clockwise vortices persist (figure 8).

The identified flow behaviour reveals that the asymmetry of the vortex street produced by the cylindrical manipulator results in preferential movements corresponding to backwards sweeps of fluid towards the wall (caused by the large, spanwise vortices of negative vorticity). These sweeps contribute to reducing the average wall shear stress, while due to their considerable size, they entrain fluid from the outer region towards the wall, contributing simultaneously to an increase in heat transfer (figure 9). The apparent importance of these backward sweeps is consistent with the quadrant analyses performed by Kawaguchi *et al.* (1984) and Suzuki *et al.* (1988), which revealed that turbulent fluid motion corresponding to the third quadrant of the (u', v') plane ($u' < 0$, $v' < 0$) contributes most significantly to the dissimilarity between heat and momentum transfer at the wall.

It could be further suggested that the backwards sweeps induced by the clockwise vortices **complement** the skin friction reduction which is due to the effects of disconnection and decorrelation of the inner and outer regions of the boundary layer by the wake turbulence. This latter mechanism has been associated with thin ribbon and airfoil-type outer layer manipulators (Lemay, 1989), and may well be active in the case of the circular cylinder also. Some support for this hypothesis has been provided by an analysis of

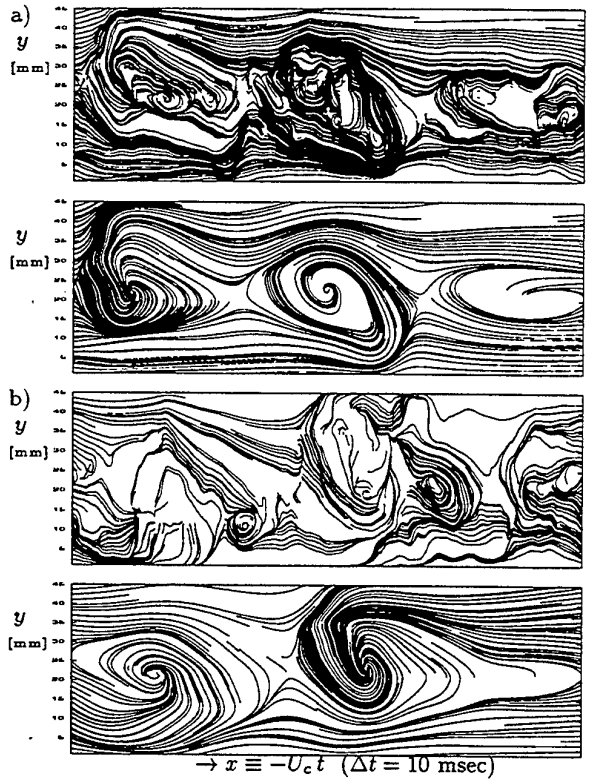


Figure 8: Example of the downstream evolution of the coherent structures in the turbulent boundary layer disturbed by a cylinder. a) $x/d = 24.25$. b) $x/d = 49.25$. The wavelet-filtered field appears below the original field.

the kinetic energy budget by de Souza *et al.* (1997). This would imply then that the large scale vortical structure of the cylinder wake enhances, without modifying, the fundamental mechanism by which outer layer manipulators in general reduce boundary layer skin friction.

CONCLUDING REMARKS

The three conditional analysis techniques, applied to multi-point measurements obtained with a rake of x-wires, have provided valuable insight into the large scale organization of the turbulent boundary layer disturbed by a cylinder. The WAG approach is the most easily implemented, although the least objective, of the three techniques. Nevertheless, it led to fairly accurate estimations of average structure characteristics. Information on the instantaneous dynamics of the organized flow was made available by the

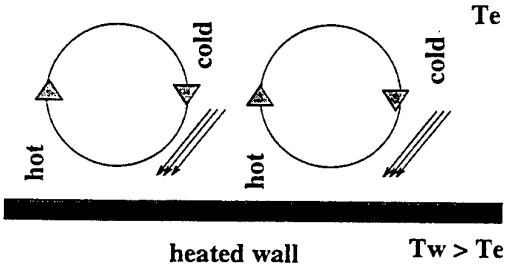


Figure 9: Schematic representation of the mechanism of dissimilarity between heat and momentum transfer in the manipulated boundary layer (large, spanwise vortices of negative vorticity).

two filtering techniques (spectral and wavelets techniques). In particular, the time-frequency filter based on wavelets analysis permitted to extract and analyze particular coherent events most objectively.

We conclude from these analyses that the domination of the upper vortices shed from the cylinder is the key to the observed dissimilarity between momentum and heat transfer in the disturbed boundary layer. The present results are compatible with those obtained from the balance of the turbulent kinetic energy and Reynolds stress budgets (de Souza *et al.*, 1997), and have been supported, to a certain extent, by a potential vortex model of the flow structure (de Souza, 1996). The use of the studied geometry opens new roads towards the differential control of skin friction and heat transfer in turbulent boundary layers.

Acknowledgements : Special thanks are due to H. Garem for his help with the experimental arrangement.

REFERENCES

Bisset, D.K., Antonia, R.A. and Brown, L.W.B., 1990, "Spatial Organization of large structures in the turbulent far wake of a cylinder", *Journal of Fluid Mechanics*, Vol. 218, pp. 439–461.

Bonnet, J.P., Lewalle, J. and Glauser, M.N., 1996, "Coherent structures: past, present and future", in *Advances in Turbulence VI* (S. Gavrilakis, L. Machiels and P.A. Monkewitz, Eds.), Kluwer Ac. Pub.

Brereton, G.J. and Kodal, A., 1992, "A frequency-domain filtering technique for triple decomposition of unsteady turbulent flow", *J. Fluids Engineering*, Vol. 114, pp. 45–51.

Brereton, G.J. and Kodal, A., 1994, "An adaptive filter for decomposition of organized turbulent flows", *Physics of Fluids*, Vol. 6, no. 5, pp. 1775–1786.

Coustols, E. and Savill, A.M., 1992, "Turbulent skin friction drag reduction by active and passive means", AGARD FDP/VKI Special Course on Skin Friction Drag Reduction, March 2-6, Von Karman Institute, Brussels, Belgium.

de Souza, F., 1996, "Experimental study of the wake/wall interaction in a turbulent boundary layer manipulated by a circular cylinder", Ph. D. Thesis, Université de Poitiers, France (in French).

de Souza, F., Delville, J. and Bonnet, J.P., 1997, "Kinetic energy balance in a turbulent boundary layer disturbed by a circular cylinder: classical and conditional approach", *Eleventh Symposium on Turbulent Shear Flows*, Grenoble, France.

Hamdouni, A. and Bonnet, J.P., 1993, "Effect of external manipulators on the heat transfer on a flat plate turbulent boundary layer", *Applied Scientific Research*, Vol. 50, pp. 369–385.

Kawaguchi, Y., Matsumori, Y. and Suzuki, K., 1984, "Structural study of momentum and heat transport in the near wall region of a disturbed turbulent boundary layer", *Proc. 9th Biennial Symp. on Turbulence*, pp. 28.1–28.10.

Lemay, J., 1989, "Etude expérimentale du comportement de la turbulence dans une couche limite incompressible en présence d'un manipulateur externe", Ph.D. Thesis, Laval University, Quebec.

Lemay, J., Bonnet, J.P. and Delville, J., 1995, "Experimental Testing of Diffusion Models in a Manipulated Turbulent Boundary Layer", *AIAA J.*, Vol. 33, no. 9, pp. 1597–1603.

Lewalle, J., Bonnet, J.P. and Delville, J., 1996, "Eduction of coherent structures in a turbulent mixing layer", *49th meeting of the Division of Fluid Dynamics of the American Physical Society*, Syracuse, New York, November 24-26.

Marumo, E., Suzuki, K. and Sato, T., 1978, "A turbulent boundary layer disturbed by a cylinder", *J. Fluid Mech.*, Vol. 87, pp. 121–141.

Marumo, E., Suzuki, K. and Sato, T., 1985, "Turbulent heat transfer in a flat plate boundary layer disturbed by a cylinder", *Int. J. Heat & Fluid Flow*, Vol. 6, no. 4, pp. 241–248.

Suzuki, K., Suzuki, H., Kikkawa, Y. and Kigawa, H., 1989, "Study on a turbulent boundary layer disturbed by a cylinder – effect of cylinder size and position", *Seventh Symposium on Turbulent Shear Flows*, Stanford University, pp. 8.5.1 – 8.5.6.

Suzuki,. H., Suzuki, K. and Sato, T., 1988, "Dissimilarity between heat and momentum transfer in a turbulent boundary layer disturbed by a cylinder", *Int. J. Heat Mass Transfer*, Vol. 31, no. 2, pp. 259–265.

SESSION 34 - ROTATION AND CURVATURE II

PERFORMANCE OF THE SUBGRID-SCALE ALGEBRAIC STRESS MODEL FOR TURBULENT FLOWS IN A ROTATING FRAME

Y. Shimomura
Department of Physics, Keio University
Hiyoshi, Kohoku-ku, Yokohama 223
Japan

ABSTRACT

The subgrid-scale algebraic stress model (SGSASM) of turbulence is tested in large eddy simulation with a few grid points in comparison with the Smagorinsky model (SMGM) and with the direct numerical simulation (DNS). Two types of the SGSASM are investigated in the present paper: zero-equation type (SGSAMS0) and one-equation type (SGSASM1). We try to simulate two kinds of turbulent flows in a rotating frame: one is homogeneous decaying turbulence (Flow A), and the other is periodic turbulent shear flow (Flow B). By referring to the DNS data, we conclude that both the SGSASM0 and the SGSASM1 reproduces Flow A, but the SMGM gets poor under a large system rotation. In Flow B, the crucial differences between three models are detected, and the SGSASM1 of one-equation type agrees best with the DNS.

INTRODUCTION

Large eddy simulation (LES) is still a useful method to numerically reproduce turbulent flows at high Reynolds number in the real world, since the direct numerical simulation (DNS) requires huge memory and much CPU time even in the the recent 'supercomputers'. In LES, we use spatial filters to decompose the flow fields into two parts, or, the grid-scale (GS) and subgrid-scale (SGS) ones:

$$u_i = \overline{u}_i + u_i'', \quad p = \overline{p} + p''. \tag{1}$$

In (1), the overline — means the filtering operation. Therefore, $\overline{u}_i$ and $\overline{p}$ are called the GS parts of the velocity and pressure field, respectively, while u_i'' and p'' are the SGS ones.

In LES, we need the SGS models of the Leonard term L_{ij}, cross terms C_{ij}, and the SGS Reynolds stress R_{ij}, which are defined as

$$L_{ij} = -\left(\overline{\overline{u}_i\overline{u}_j} - \overline{u}_i\overline{u}_j\right), \tag{2}$$

$$C_{ij} = -\left(\overline{\overline{u}_i u_j'' + \overline{u}_j u_i''}\right), \tag{3}$$

$$R_{ij} = -\overline{u_i'' u_j''}. \tag{4}$$

The standard SGS model, which is called the Smagorinsky model (SMGM) (see Smagorinsky, 1963) has the following form:

$$L_{ij} + C_{ij} = 0, \tag{5}$$

$$R_{ij} = -2/3k\delta_{ij} + 2\nu_S\overline{S}_{ij}, \tag{6}$$

where δ_{ij} is the Kronecker delta symbol, and the SGS turbulent energy k and the GS rate of strain tensor $\overline{S}_{ij}$ are respectively defined as

$$k = \frac{1}{2}\overline{u_a'' u_a''}, \tag{7}$$

$$\overline{S}_{ij} = \frac{1}{2}\left(\frac{\partial\overline{u}_i}{\partial x_j} + \frac{\partial\overline{u}_j}{\partial x_i}\right). \tag{8}$$

In (7) and hereafter, the repeated subscripts are summed from 1 to 3. The term ν_S seen in (6) is the SGS eddy viscosity, and it is modeled by using the representative filtering scale Δ as

$$\nu_S = (C_S\Delta)^2\sqrt{2\overline{S}_{ab}\overline{S}_{ab}}. \tag{9}$$

In (9), C_S is called the Smagorinsky constant, which was expected to be universal in various turbulent flows.

However, it is confirmed in recent years that we should choose different values for C_S depending on the turbulent flows simulated. For example, $C_S \cong 0.20$ are optimized (see Antonopoulos-Domis, 1981) in homogeneous isotropic decaying turbulence, $C_S \cong 0.16$ in mixing layers (see Mansour *et al.*, 1978), and $C_S \cong 0.10$ in channel flows (see Piomelli *et al.*, 1988). As the shear rate increases, the C_S seems to be smaller.

In order to overcome this deficiency of SMGM, such models as the dynamic SGS model (see Germano *et al.*, 1991) and filtered-Bardina model (see Horiuti, 1994) are proposed. Both methods are based on the assumption that the SGS turbulences have the property of scale similarity. They work better than the SMGM in the simulation with many grid points. However, if the number of grid points are small, they will not always reproduce turbulence since the concept of scale similarity does not hold well.

The author proposed a new SGS model named the SGS algebraic stress model (SGSASM) (see Shimomura, 1994), which may also overcome the deficiency of the SMGM

mentioned above. The SGSASM is constructed based on the scale separarion concept as in the ensembly averaged model. So, it can simulate turbulences with corse mesh of calculation. Furthermore, the representation of the SGS Reynolds stress in the SGSASM is nonlinear so that it shows the anisotropy of SGS turbulent energy, and we can easily incorporate into the model such various effect of external forces as the Coriolis force in a rotating frame or the buoyant force in thermally-driven flows.

In the real LES of homogeneous decaying turbulence in a rotating frame, the SGSASM of zero-equation type (SGSASM0) well reproduces the flow while the Smagorinsky model gets fatally poor under a large system rotation (see Shimomura, 1995).

In the present paper, we propose the SGSASM of one-equation type (SGSASM1) and investigate the performance of the SGSASM0 and SGSASM1 in comparison with the DNS and the SMGM for periodic turbulent shear flows in a rotating frame.

FORMULATION OF SGSASM1

The SGSASM1 is the SGSASM1 of one-equation type, and is constructed on the analogy of usual algebraic stress model (ASM) (see Rodi, 1975) in the model of ensemble average type by replacing the ensemble average in the ASM with the filter average. Accordingly the sum of the Leonard term L_{ij} and cross term C_{ij} is neglected as in the SMGM. However, there is a different point between the ASM and the SGSASM1 that the transport equation of the energy dissipation rate ϵ is not used in the SGSASM1. Instead, we make one more assumptions in the SGSASM1; ϵ is scaled by the turbulent kinetic energy k and Δ. In constituting the SGSASM1, the modeling of the pressure-strain tensor Π_{ij} is essential. Here, we choose the LRR model (see Launder *et al.*, 1975) as the simplest. In the LRR model, Π_{ij} defined as

$$\Pi_{ij} = \overline{p''\left(\frac{\partial u_i''}{\partial x_j} + \frac{\partial u_j''}{\partial x_i}\right)} + \overline{(L_{ia} + C_{ia} + R_{ia})\frac{\partial u_j''}{\partial x_a}} + \overline{(L_{ja} + C_{ja} + R_{ja})\frac{\partial u_i''}{\partial x_a}}, \quad (10)$$

is given by

$$\Pi_{ij} = -C_1\epsilon b_{ij} + C_2 k\overline{S}_{ij} + C_3 k\times \left(b_{ia}\overline{S}_{ja} + b_{ja}\overline{S}_{ia} - 2/3 b_{ab}\overline{S}_{ab}\delta_{ij}\right) + C_4 k\times \left(b_{ia}\overline{W}_{ja} + b_{ja}\overline{W}_{ia}\right) - C_4 k\left(b_{ia}\epsilon_{jab} + b_{ja}\epsilon_{iab}\right)\Omega_b. \quad (11)$$

Here, we should note that (11) is the expression in a frame rotating at a constant angular velocity Ω_i. In (11), the SGS anisotropoic tensor b_{ij} and the GS vorticity tensor $\overline{W}_{ij}$ are respectively defined as

$$b_{ij} = -\frac{R_{ij}}{2k} - \frac{1}{3}\delta_{ij}, \quad (12)$$

$$\overline{W}_{ij} = \frac{1}{2}\left(\frac{\partial \overline{u}_i}{\partial x_j} - \frac{\partial \overline{u}_j}{\partial x_i}\right), \quad (13)$$

and $\epsilon_{ijk}$is the alternating tensor. The model constants C_1,C_2,C_3, and C_4 are optimized as follows:

$$C_1 = 3.6,\ C_2 = 0.80, C_3 = 1.2,\ C_4 = 1.2, \quad (14)$$

For obtaining the SGSASM1, we assume that the SGS anisotropic tensor b_{ij} is steady in time. If we use the model (11), we construct the SGSASM1 coupled with the transport equation of the SGS turbulent kinetic energy k, in the following form:

$$A_{ijab}b_{ab} = -G_1\tau\overline{S}_{ij}, \quad (15)$$

$$A_{ijkl} = \left[C_1 + 2\left(\frac{P}{\epsilon} - 1\right)\right]\delta_{ik}\delta_{jl} + \tau\Big[G_2\left(\overline{S}_{ik}\delta_{jl} + \overline{S}_{jk}\delta_{il} - 2/3\overline{S}_{kl}\delta_{ij}\right) + G_3\times \left(\overline{W}_{ik}\delta_{jl} + \overline{W}_{jk}\delta_{il}\right) - G_4\Omega_m\left(\epsilon_{ikm}\delta_{jl} + \epsilon_{jkm}\delta_{il}\right)\Big], \quad (16)$$

$$\left(\frac{\partial}{\partial t} + \overline{u}_a\frac{\partial}{\partial x^a}\right)k = P - \epsilon + \frac{\partial}{\partial x^a}\left[\left(C_{kk}\Delta k^{1/2} + \nu\right)\frac{\partial k}{\partial x^a}\right], \quad (17)$$

$$P = -2kb_{ab}\overline{S}_{ab}, \quad (18)$$

$$\epsilon = C_\epsilon\frac{k^{3/2}}{\Delta}, \quad (19)$$

$$\tau = \frac{k}{\epsilon} = \frac{\Delta}{C_\epsilon}k^{-1/2}, \quad (20)$$

$$G_1 = (4/3 - C_2) = 0.53,\quad G_2 = (2 - C_3) = 1.2,\quad G_3 = (2 - C_4) = 1.2,\quad G_4 = (4 - C_4) = 2.8. \quad (21)$$

In the SGSASM1, we numerically solve at each grid poin the coupled linear equations (15) and (17) with (16), (18)-(21) to get the SGS Reynolds stress R_{ij} with the aid of (12). The model constants C_ϵ and C_{kk} are chosen (see Yoshizawa and Horiuti, 1985) in the present paper as

$$C_\epsilon = 1.53,\ C_{kk} = 0.1. \quad (22)$$

The SGSASM of zero-equation type (SGSASM0) previously proposed by Shimomura (1994) is obtained by assuming the balance between the production and the dissipation of k ($P = \epsilon$), and adopt into τ the time scale of the Smagorinsky type

$$\tau = \left(2G_1\overline{S}_{ab}\overline{S}_{ab}\right)^{-1/2}, \quad (23)$$

instead of solving (17) and of using (20). In the SGSASM0, k is determined by

$$k = \left(G_5\Delta/\tau\right)^2, \quad (24)$$

where the model constant G_5 is chosen in the present study as

$$G_5 = 0.65. \quad (25)$$

We easily notice that the SMGM is a trivial case of the SGSASM0. If we set $G_2 = G_3 = 0.0$, or $C_3 = C_4 = 2.0$ in (21), and define G_5 as $G_5 = C_S G_1^{-3/4}$, we find that the SGSASM0 (15), (23), (24) is reduced to the SMGM (6) and (9) for $\Omega_i = 0$. In case of a general rotating frame ($\Omega_i \neq 0$), however, even the above model constants $G_2 = G_3 = 0.0$ do not derive the SMGM because of the presence of terms with G_4. In other words, the effect of frame rotation can be incorporated into the SGSASM0 and SGSASM1, while it can not be in the SMGM.

PERFORMANCE OF MODELS

In this section, we compare the performances of SGSASM0, SMGASM1, SMGM, and DNS. The target flows are homogeneous decaying turbulences (Flow A), and periodic turbulent shear flows (Flow B), both in a rotating frame. These two kinds of flows are studied and the performances of SGSASM, SMGM, and DNS in them are reported in the following subsections, respectively.

The numerical scheme used both in the DNS and in the LES with the SGSASM or the SMGM is the pseudo-spectral method, but the DNS is de-aliased by using 2/3 rule. The forth-order Runge-Kutta method is used in all simulations as the time-marching sheme. The calculated

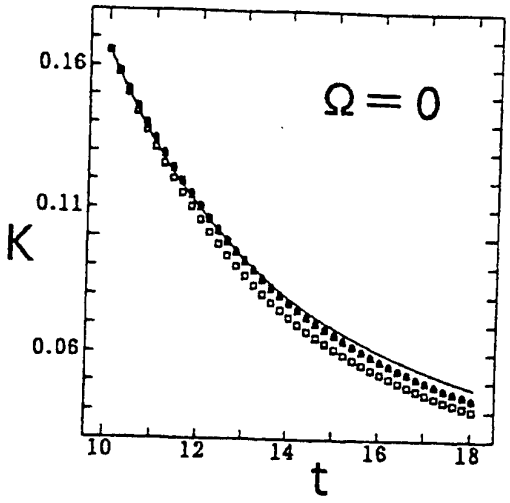


Figure 1: The GS turbulent energy $2k$ versus time for $\Omega = 0$. DNS — ; Smagorinsky model •; SGSASM0 ○; SGSASM1 □.

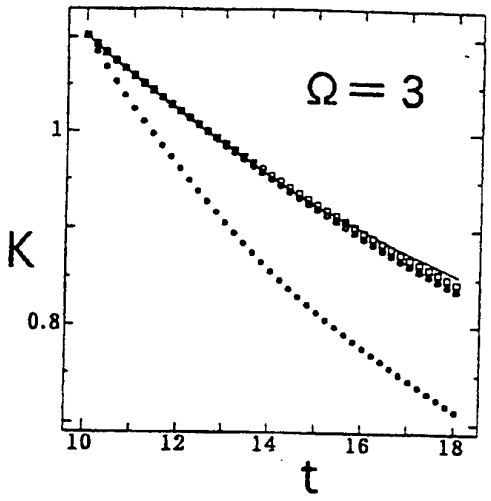


Figure 2: The GS turbulent energy $2k$ versus time for $\Omega = 3$. DNS — ; Smagorinsky model •; SGSASM0 ○; SGSASM1 □.

flow region is the cube of $(2\pi)^3$ dimensionless size in all cases. The numerical caluculations of LES are done with 16^3 or 8^3 grid points, while those of DNS with 64^3 or 128^3. The resluts of DNS shown in this section are obtained from the 16^3 or 8^3 data which are sharp-cut-filtered from the original $[64 \times 2/3]^3 = 42^3$ or $[128 \times 2/3]^3 = 84^3$ data. The initial conditions of LES are also given by the reduced 16^3 or 8^3 data of DNS, processed by this way.

Flow A

In this subsection, we simulate homogeneous decaying turbulences in a rotating frame of a constant angular velocity Ω. We test two cases of different Reynolds Re_λ and Rossby numbers Ro_λ based on the Taylor's micro-scale λ. These dimensionless numbers are defined in the DNS as

$$Re_\lambda = \sqrt{\frac{20}{3}} \frac{K}{\nu\sqrt{Q}}, \tag{26}$$

$$Ro_\lambda = \sqrt{\frac{2}{30}} \frac{\sqrt{Q}}{\Omega}, \tag{27}$$

where ν is the kinematic viscosity, K the turbulent energy, and Q the turbulent enstrophy. The Reynolds numbers Re_λ and the Rossby numbers Ro_λ used at time $t = 10.02$ in two cases are as follows.

$$\Omega = 0, Re_\lambda = 22.9, Ro_\lambda = \infty, \tag{28}$$

$$\Omega = 3, Re_\lambda = 122.7, Ro_\lambda = 0.204. \tag{29}$$

The flows in both cases reach its fully developed states in a rotating frame before $t = 10.02$.

Figures 1 and 2 show the decay of GS turbulent energy $2k$ for $\Omega = 0$ and 3, respectively. In them, the symbol ○ plots the results of SGSASM0, □ does that of SGSASM1, • shows that of SMGM, and the solid line — depicts that of DNS. In an inertial frame, we can find from figure 1 no major difference between the SGSASM0, SMGASM1 and the SMGM, and all agree well with the DNS. However, figure 2 tells that the agreement of SGSASM0 and the SGSASM1 with the DNS is much better than the SMGM in a rotating frame.

Flow B

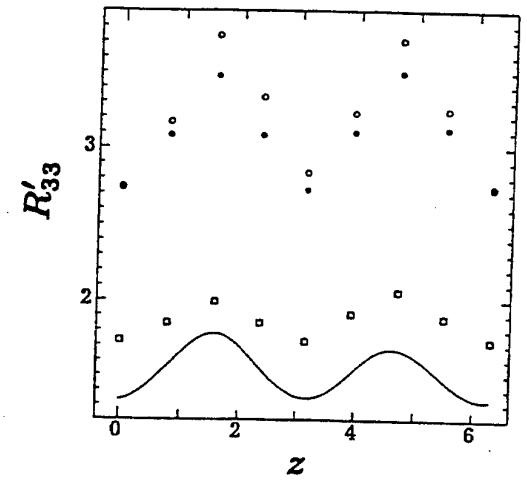


Figure 3: The Reynolds stress R'_{33} versus z for $\Omega = 0$. DNS — ; Smagorinsky model •; SGSASM0 ○; SGSASM1 □.

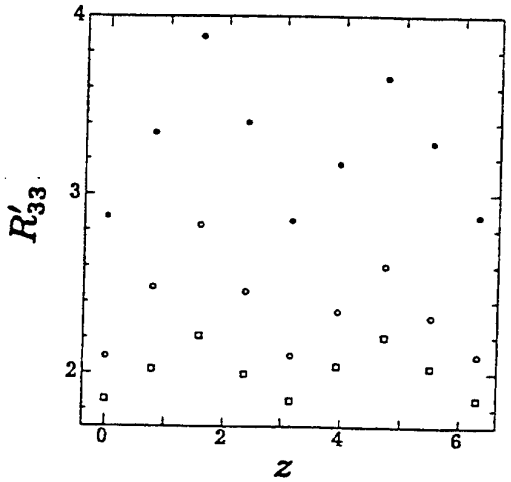


Figure 4: The Reynolds stress R'_{33} versus z for $\Omega = 0.1$. Smagorinsky model •; SGSASM0 ○; SGSASM1 □.

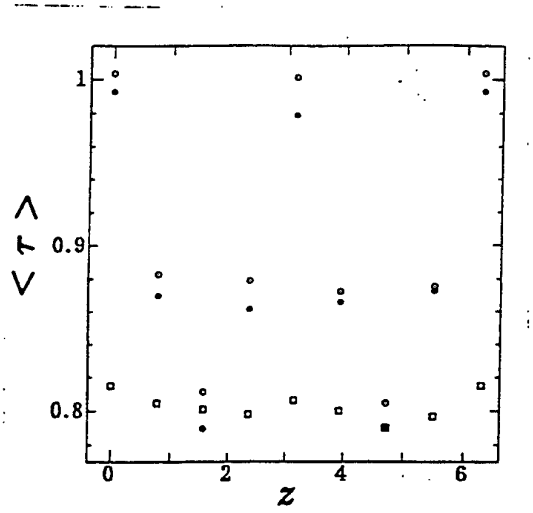


Figure 5: The mean time scale $< \tau >$ versus z for $\Omega = 0$. Smagorinsky model •; SGSASM0 ○; SGSASM1 □.

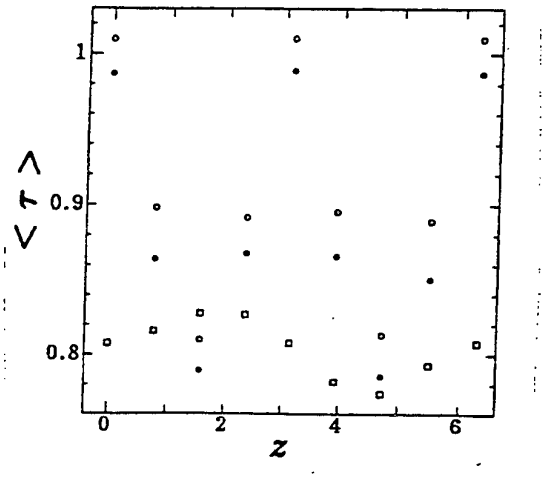


Figure 6: The mean time scale $< \tau >$ versus z for $\Omega = 0.1$. Smagorinsky model •; SGSASM0 ○; SGSASM1 □.

Here, we simulate periodic turbulent shear flows in a rotating frame, whose motions are governed by the Navier-Stokes equation with the inhomogeneous forcing

$$f_i = -(\cos z)\,\delta_{i1}. \tag{30}$$

This flow has a statistically stationary state, and in the following the parenthesis $< \ >$ means the average on the homogeneous $x-y$ plane during the time period $T = 500$, except the DNS. In this flow, the Reynolds number is the only dimensionless parameter given in the DNS by

$$Re = \frac{\langle u_{max} \rangle (2\pi)}{\nu} \sim \frac{2.5 \times (2\pi)}{1.0 \times 10^{-2}} \sim 1571. \tag{31}$$

Now, let us compare the results of SGSASM0, SMGASM1, SMGM, and DNS. In the all subsequent figures 3-6, the symbol ○ shows the results of SGSASM0, □ means those of SGSASM1, • plots those of SMGM, and the solid line draws those of DNS, as in figures 1 and 2.

Figure 3 and 4 describe a Reynolds stress R'_{33} in an inertial frame ($\Omega = 0$) and in an rotating frame ($\Omega = 0.1$), respectively. Here, R'_{ij} is defined as

$$R'_{ij} = \left\langle u'_i u'_j \right\rangle, \tag{32}$$

where

$$u'_i = \overline{u}_i - \langle \overline{u}_i \rangle. \tag{33}$$

In figure 3, we find that the SGSASM1 well agrees with the DNS, while the SMGS and SGSASM0 produces much larger value of R'_{33}. In the case of $\Omega = 0.1$, the DNS has not yet been calculated. However, we notice the big difference between the SGSASM1 and the SMGM, and the SGSASM0 shows the tendency supporting the SGSASM1.

Figure 5 and 6 shows the mean time scale $< \tau >$ for $\Omega = 0$ and $\Omega = 0.1$, respectively. From figure 5 we find that the mean time scale gets small at the large mean shear rate, and it is estimated smaller in the SGSASM1 compared with the SGSASM0 and SMGM. In figure 6 with the system rotation, the mean timescale of SGSASM1 shows the qualitatively different profile from the other two models: it is large at the region where the background vorticity has the same sign as the shear vorticity, and vice versa.

CONCLUSIONS

From the results shown in the previous section, we get the following conclusions.

1. For homogeneous turbulences in a rotating frame, the SGSASM0 and the SGSASM1 even with reatively few grid points (16^3) agree well with the DNS, and they show much better performances than the SMGM since they can incorporate the effect of frame rotation into the model.

2. For periodic turbulent shear flows in an inertial frame, the SGSASM1 agrees best with the DNS among three models.

3. For periodic turbulent shear flows in a rotating frame, three models predicts different results. By executing the DNS, we will determine which is the best model.

Acknowledgements : This work was partially supported by Grant-in-Aid for Scientific Research No. 05240219 from the Ministry of Education, Science and Culture.

REFERENCES

Antonopoulos-Domis, M., 1981, *J. Fluid Mech.*, Vol. 104, pp. 55-.

Germano, M., Piomelli, U., Moin, P. and Cabot, W. H., 1991, *Phys. Fluids*, Vol. A3, pp. 1760-.

Horiuti, K., 1994, in *Proceedings of 94' Workshop on Mathematical Modeling of Turbulent Flows*, 9-1.

Launder, B. E., Reece, G. and Rodi, W., 1975, *J. Fluid Mech.*, Vol. 68, pp. 537-.

Mansour, N. N., Ferziger, J. H. and Reynolds, W. C., 1978, *Report No. TF-11 Stanford University.*

Piomelli, U., Moin, P. and Ferziger, J. H., 1988 *Phys. Fluids*, Vol. 31, pp. 1884-.

Rodi, W., 1976, *Z. Angew. Math. Mech.*, Vol. 56, T219.

Shimomura, Y., 1995, in Proceedings of the International Symposium on mathematical modelling of turbulent flows, Tokyo 1995, H. Daiguji and Y. Miyake, eds., JSCFD, pp. 321–327.

Shimomura, Y., 1994, *J. Phys. Soc. Jpn*, Vol. 63, pp. 5-.

Smagorinsky, J., 1963, *Mon. Weather Rev.* , Vol. 91, pp. 99-.

Yoshizawa, A., and Horiuti, K., 1985, it J. Phys. Soc. Jpn, Vol. 8, pp.2834-2839.

STATISTICS OF RAPIDLY ROTATING TURBULENT PLANE COUETTE FLOW

Helge I. Andersson & Knut H. Bech
Division of Applied Mechanics
Norwegian University of Science and Technology
N-7034 Trondheim, Norway

ABSTRACT

Turbulence statistics, including complete budget data for the individual components of the Reynolds stress tensor, have been compiled from direct numerical simulations of plane Couette flow subjected to strong system rotation. The anticyclonic rotation rate is sufficiently high for the flow to be beyond the regime in which rotational-induced counter-rotating streamwise roll-cells are present. The flow exhibited a number of anomalous characteristics, including a reversal of the conventional Reynolds stress and dissipation rate anisotropies.The one-componentality and the one-dimensionality of the flow field makes it particularly attractive as a physically challenging reference case for the assessment of turbulence closure models.

INTRODUCTION

Rotating channel flows are of obvious engineering relevance, notably within the turbomachinery industry. Pressure-driven turbulent flows in rotating plane channels have been studied experimentally by Johnston, Halleen & Lezius (1972) and more recently by Nakabayashi & Kitoh (1996). The laboratory investigations have been supplemented with large-eddy simulations (LES) by Kim (1983), Miyake & Kajishima (1986), Tafti & Vanka (1991) and Piomelli & Liu (1995) and with direct numerical simulations (DNS) by Kristoffersen & Andersson (1993) and Lamballais, Lesieur & Metais (1996a,b). Due to the presence of a local maximum in the mean velocity distribution, rotating plane Poiseuille flow exhibits at the same time a cyclonic (suction) side and an anticyclonic (pressure) side. System rotation was found to significantly affect the mean flow field which exhibited an appreciable region with mean flow vorticity practically counterbalancing the imposed background vorticity. Moreover, irrespective of the sense of rotation, an imbalance between the Coriolis force and the pressure gradient in the wall-normal direction was responsible for the occurrence of pairs of Taylor-Görtler-like counter-rotating streamwise vortices or roll-cells. It is finally noteworthy that the system rotation did not only change the mean flow pattern but the presence of a Coriolis force tended to damp the turbulence level near the cyclonic side and enhance the turbulent agitation along the anticyclonic side, at least at relatively low rotation rates.

Like the pressure-driven plane Poiseuille flow, the shear-driven plane Couette flow is also among the prototype flows in classical fluid mechanics. However, turbulent plane Couette flow responds differently to system rotation since the mean velocity increases monotonically from one wall to the other. Thus, the mean shear vorticity attains the same sign throughout the flow and, depending on the sense of rotation, the entire Couette channel is exposed either to cyclonic or anticyclonic rotation. This attractive feature of the Couette flow facilitates the further exploration of the intricate and fascinating effects of the Coriolis force, which arises from the imposed system rotation.

Reliable experimental data for plane Couette flow are scarce even in the non-rotating case and rotating plane Couette flow has so far only been studied by Tillmark & Alfredsson (1996). Turbulent flow in an infinitely long Couette channel in spanwise (orthogonal-mode) rotation is on the other hand particularly amenable to explorations by means of direct numerical simulations. To this end a series of DNSs has been performed by Bech & Andersson (1996a, 1996b, 1997) over a wide range of rotation rates. The focus of the present paper is on turbulence statistics which are believed to be useful in the development and validation of second-moment turbulence closure models for rapidly rotating shear flows. Since the Couette flow laminarizes when subjected to even moderate cyclonic rotation, cf. Bech & Andersson (1996a), Komminaho, Lundbladh & Johansson (1996) and Tillmark & Alfredsson (1996), only the influence of substantial anticyclonic rotation will be of any relevance.

PROBLEM FORMULATION AND GOVERNING EQUATIONS

Let us consider the shear-driven turbulent motion of an incompressible fluid between two infinite parallel planes separated a distance 2h, as shown schematically in Figure 1. The constant-pressure flow is induced solely by the constant velocity difference $2U_w$ between the two planes. The Couette channel rotates with constant angular velocity Ω about the spanwise z-axis of a Cartesian coordinate system and the flow is fully developed in the streamwise x-direction. This flow problem is characterized by two independent dimensionless parameters, namely the Reynolds number $Re = U_w h/\nu$ and the rotation number $Ro = 2\Omega h/U_w$. Notice that Ro is inversely proportional to the Rossby number used in geophysical contexts.

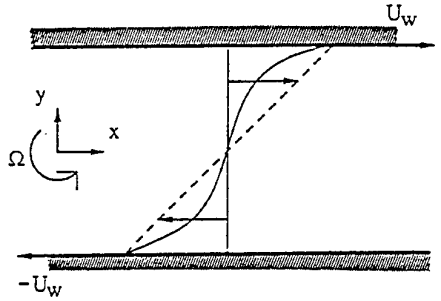


FIGURE 1. Schematic of rotating plane Couette flow. The broken and solid lines identify laminar and turbulent mean velocity profiles, respectively.

Although the instantaneous velocity u'_i is truly varying with time, only results for statistically steady flow situations will be reported in this paper. The non-rotating Couette flow, which is assumed to be homogeneous in xz-planes, is one-componental in x. Moreover, the single mean velocity component U varies only in the y-direction, i.e. the mean flow is 1C-1D according to the Reynolds-Kassinos classification sheme. Notice that the notion of componentality, as suggested by Reynolds & Kassinos (1995), corresponds to the definition of directionality adopted by Gerhart, Gross & Hochstein (1992). Anyhow, when system rotation is imposed, persistent counter-rotating roll cells develop due to the Coriolis instability mechanism, which is present even in laminar plane Couette flow. The mean flow is thereby rendered three-componental and two-dimensional (3C-2D) since the flow pattern now varies over the cross-section, i.e. in the y- and z-directions. The obvious consequence is that the originally one-dimensional turbulence statistics also become two-dimensional. However, at the high rotation number Ro = 0.5, Bech & Andersson (1997) reported that the flow restabilized in the sense that the persistent roll cell pattern observed at low (Ro = 0.01) and moderate (Ro = 0.10 and 0.20) rotation vanished and the mean flow reverted to a practically 1C-1D state.

The presence of roll cells complicates the analysis of the statistics of the true turbulence since i) any statistical moment will vary over the cross-sectional yz-plane, and ii) otherwise vanishing terms in the second-moment equations must be retained. In this paper we therefore consider only the case Ro = 0.5 in which the roll-cell restabilization has set in and only reminiscences are left of the persistent counter-rotating streamwise vortices.

Now, with the assumption of one-componental and one-dimensional mean flow, the instantaneous flow variables (u'_i, p') are decomposed into mean (U_i, P) and turbulent (u_i, p) parts, and the Reynolds-averaged Navier-Stokes equation reduces to an ordinary differential equation in y. The streamwise balance of mean momentum is integrated once to give the constancy of the total (i.e. viscous and turbulent) shear stress τ

$$\mu\, dU/dy - \rho\overline{uv} = \tau_w \qquad (1)$$

where the wall shear stress τ_w is an a priori unknown constant. The overbar denotes averages over an xz-plane and in time. It is noteworthy that the angular velocity Ω does not appear explicitly in equation (1).

The transport equation for the individual components of the Reynolds stress tensor $-\rho\overline{u_iu_j}$ can be expressed in Cartesian tensor notation as:

$$\frac{D\overline{u_iu_j}}{Dt} = P_{ij}+G_{ij}+D_{ij}^{\nu}+D_{ij}^{T}+D_{ij}^{P}+\Phi_{ij}-\epsilon_{ij} \qquad (2)$$

in a rotating frame-of-reference. Here,

$$P_{ij} = -\left(\overline{u_iu_k}\frac{\partial U_j}{\partial x_k} + \overline{u_ju_k}\frac{\partial U_i}{\partial x_k}\right) \qquad (3)$$

$$G_{ij} = -2\Omega\delta_{3k}\left(\overline{u_ju_m}\epsilon_{ikm} + \overline{u_iu_m}\epsilon_{jkm}\right) \qquad (4)$$

$$D_{ij}^{\nu} = \nu\left(\frac{\partial^2\overline{u_iu_j}}{\partial x_k\partial x_k}\right) \qquad (5)$$

$$D_{ij}^{T} = -\frac{\partial}{\partial x_k}\left(\overline{u_iu_ju_k}\right) \qquad (6)$$

$$D_{ij}^{P} = -\frac{1}{\rho}\frac{\partial}{\partial x_k}\left(\overline{pu_i}\delta_{jk} + \overline{pu_j}\delta_{ik}\right) \qquad (7)$$

$$\Phi_{ij} = \overline{\frac{p}{\rho}\left(\frac{\partial u_i}{\partial x_j} + \frac{\partial u_j}{\partial x_i}\right)} \qquad (8)$$

$$\epsilon_{ij} = 2\nu\left(\overline{\frac{\partial u_i}{\partial x_k}\frac{\partial u_j}{\partial x_k}}\right) \qquad (9)$$

The different mechanisms tending to change $\overline{u_iu_j}$ are production due to mean shear (P_{ij}) and rotation (G_{ij}), viscous diffusion (D_{ij}^{ν}) and turbulent diffusion associated with velocity (D_{ij}^{T}) and pressure (D_{ij}^{P}) fluctuations, pressure-strain processes (Φ_{ij}), and viscous dissipation (ϵ_{ij}).

The present assumption of 1C-1D mean flow and the corresponding one-dimensionality of the turbulence statistics makes equation (2) for the second-moments reduce to a coupled set of 4 ordinary differential equations for the unknowns $\overline{u^2}$, $\overline{v^2}$, $\overline{w^2}$ and $\overline{uv}$. In cases where roll cells are present, however, even the secondary shear stresses $\overline{uw}$ and $\overline{vw}$ are non-zero and eq. (2) becomes a set of 6 PDEs in y and z.

NUMERICALLY GENERATED ROTATING COUETTE FLOW

The complete time-dependent three-dimensional Navier-Stokes equations were integrated numerically in time and space on a discrete 256 × 70 × 256 grid system sufficiently fine to resolve all essential scales of the turbulence motion. The computational domain was $10\pi h \times 2h \times 4\pi h$, i.e. the cross-sectional aspect ratio 2π leaved room for 3 pairs of counter-rotating roll cells.

The computer program used for this purpose was an adapted version of the finite-difference code ECCLES developed by Gavrilakis et al. (1986) with second-order central-difference approximations in space and a second-order explicit Adams-Bashforth scheme in time. System rotation was accounted for by implementation of extra body force (Coriolis) terms in the momentum equations. The applicability of the code to DNS of rotating Poiseuille flow was demonstrated by Kristoffersen and Andersson (1993) and Andersson & Kristoffersen (1995). The physical realism of a numerically simulated Couette flow (without rotation) was assessed by comparisons with new experimental data, cf. Bech et al. (1995).

The only rotation number considered here is Ro = 0.5, while the Reynolds number Re was kept constant and equal to 1300 (as for the other rotation numbers). The various statistical

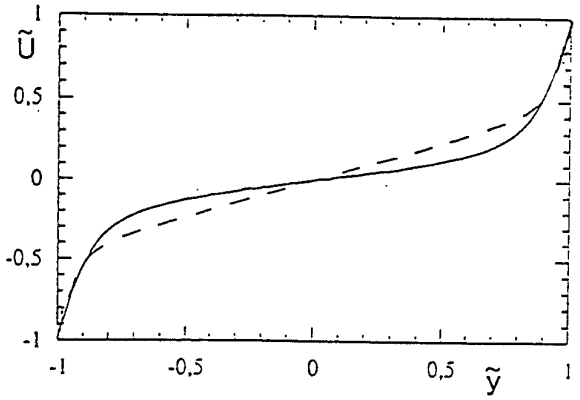


FIGURE 2. Mean velocity profiles for Ro = 0 (solid line) and Ro = 0.50 (broken line).

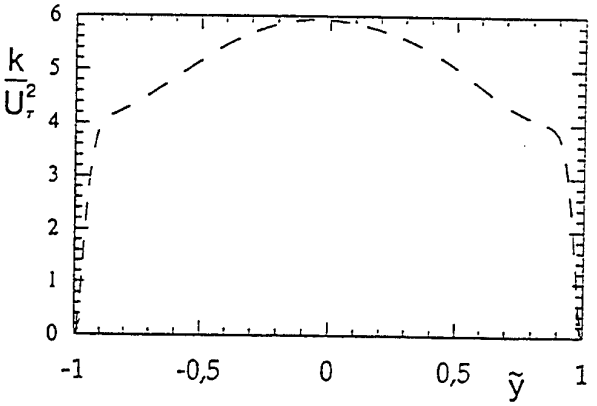


FIGURE 3. Distribution of mean turbulent kinetic energy k for Ro = 0.50 (scaled by U_τ^2 for Ro = 0).

correlations to be presented were obtained by averaging over xz-planes and sampling in time. The sampling period over which statistics were computed was $6.6h/U_\tau$, as compared to $16.4h/U_\tau$ for Ro = 0, where U_τ denotes the friction velocity $(\tau_w/\rho)^{1/2}$. The presence of unusually long streamwise structures in the non-rotating Couette flow made the relatively long sampling period necessary, see Bech et al. (1995). This compares, for instance, with $6h/U_\tau$ over which Moser & Moin (1987) sampled statistics in their curved channel simulation.

RESULTS AND DISCUSSION

Numerically generated results for plane Couette flow subjected to weak (Ro = 0.01) and moderate (Ro = 0.10 and 0.20) anticyclonic system rotation have been published elsewhere; Bech & Andersson (1996a, 1996b, 1997). Here we focus on the high rotation number Ro = 0.50 at which the flow field is again practically free of persistent roll cell structures, i.e. one-componental and one-dimensional. This fairly high Ro is unfortunately far beyond the rotation number which can be reached in the Couette flow apparatus of Tillmark & Alfredsson (1996) at Re = 1300.

It is first of all noteworthy that the variation of $Re_\tau = U_\tau h/\nu$ with Ro reflects the variation of the wall friction velocity U_τ with rotation. The monotonous increase of Re_τ from 82.2 in the non-rotating case up to $Re_\tau = 107.2$ for Ro = 0.20 was ascribed to the presence of gradually more energetic roll cells, cf. Bech & Andersson (1996b). It could therefore be anticipated that Re_τ would decrease when the rotation number was further increased and the roll-cell breakdown set in. The result $Re_\tau = 91.0$ for Ro = 0.50 is indeed lower than at Ro = 0.20, but nevertheless exceeds Re_τ in the non-rotating case by 10 per cent. Notice that the local skin-friction coefficient

TABLE 1. Centreline characteristics and $Re_\tau \equiv U_\tau h/\nu$.

	Ro = 0	Ro = 0.5
Re_τ	82.2	91.0
$d\tilde{U}/d\tilde{y}$	0.22	0.47
S	-	-1.07
$\tilde{P}$ from (13)	$0.842 \cdot 10^{-3}$	$2.133 \cdot 10^{-3}$
$\tilde{P}$ from budgets	$0.849 \cdot 10^{-3}$	$2.122 \cdot 10^{-3}$
$\tilde{\varepsilon}$	$0.995 \cdot 10^{-3}$	$2.328 \cdot 10^{-3}$
$\overline{u^2}/\overline{v^2}$	1.574	0.205

$$C_f \equiv \frac{\tau_w}{\frac{1}{2}\rho U_w^2} = 2\left(\frac{U_\tau}{U_w}\right)^2 = 2\left(\frac{Re_\tau}{Re}\right)^2 \qquad (10)$$

also depends on the system rotation since Re_τ varies with Ro.

Away from the walls, the mean velocity profile U(y) in Figure 2 exhibits a substantial linear region which extends over 80 per cent of the Couette channel. The constancy of dU/dy for Ro = 0.50 is at variance with the observation by Bech & Andersson (1996c) who found that dU/dy varied in accordance with the inverse cosine law deduced by von Kármán (1937) in the non-rotating case. The slope of the linear portion of the mean-velocity distribution was $d\tilde{U}/d\tilde{y} = 0.47$, i.e. significantly steeper than the centreline value 0.22 reported by Bech & Andersson (1996c) for Ro = 0. Here, the dimensionless variables $\tilde{U} = U/U_w$ and $\tilde{y} = y/h$ have been introduced. Although the cross-sectional average of dU/dy (i.e. U_w/h) is unaffected, it is remarkable that the local slope of the mean velocity profile is greater at Ro = 0.5 than for Ro = 0 both at the walls and in the central core region.

In the present one-componental flow, the mean shear rate dU/dy equals the magnitude of the mean flow vorticity - dU/dy in the rotating frame of reference. The local vorticity ratio

$$S = \frac{2\Omega}{-dU/dy} \qquad (11)$$

i.e. the ratio of the imposed background vorticity 2Ω to the mean flow vorticity, has turned out to be an essential parameter in the analysis of the local influence of system rotation. Notice that the dimensionless mean shear rate now can be expressed as

$$\frac{d\tilde{U}}{d\tilde{y}} = -\frac{Ro}{S} \qquad (12)$$

For Ro = 0.50 it was observed that the variation of S across the channel exhibited a plateau with $S \approx -1$ in the central part of the flow, i.e. the mean vorticity 2Ω - dU/dy in an inertial frame is practically driven to zero, the centreline value at y = 0 being S = - 1.07. The observed tendency of the rapidly rotating Couette flow to develop an appreciable region with $S \approx -1$ (or $dU/dy \approx 2\Omega$) is also shared by pressure-driven Poiseuille flow subjected to system rotation.

The distribution of the mean turbulent kinetic energy k, scaled by U_τ^2 for the non-rotating case, in Figure 3 shows that turbulence peaks in the middle of the channel rather than near the walls. The actual maximum level close to 6.0 (for Ro = 0.50) is also substantially higher than that of the conventional near-wall peaks (about 4.2) in the non-rotating case. Since the stress generation due to rotation has no direct influence on k, i.e. $G_{ii} = 0$, the total production of turbulence energy is associated with mean shear. The energy production $P = P_{ii}/2 = P_{11}/2 = -\overline{uv}dU/dy$, scaled

by U_w^3/h, can be expressed as

$$\bar{P} = \left[\left(\frac{Re_\tau}{Re}\right)^2 - Re^{-1}\frac{d\tilde{U}}{d\tilde{y}}\right]\frac{d\tilde{U}}{d\tilde{y}} \qquad (13)$$

where equation (1) has been used to eliminate $\overline{uv}$. From (13) the uniform production $\bar{P}$ in the linear core region for Ro = 0.50 is found to exceed the centreline production in the non-rotating case by a factor 2.5; see Table 1.

The significant energy production in the central part of the rotating Couette flow is likely to explain the unusually high energy level observed. In rotating Poiseuille flow, on the other hand, the turbulence energy k in the core region never exceeded the near-wall peak level of the non-rotating flow, cf. Andersson & Kristoffersen (1995) and Lamballais et al. (1996a). In the latter flow, however, the energy production P inevitably goes to zero at the point of maximum mean velocity. The findings of Andersson & Kristoffersen (1995) moreover revealed localized regions with negative energy production.

It is interesting to recall that the relatively high energy production in the central part of the non-rotating Couette flow is more than outweighed by the viscous energy dissipation $\epsilon = \epsilon_{ii}/2$ and the energy balance is achived by some turbulent diffusion from the near-wall peaks to the centre (Andersson et al. 1992). These findings have been confirmed by more refined simulations by Andersson & Bech (1995) and Komminaho et al. (1996), the latter at Re = 750. The data for the dissipation rate ϵ, scaled by U_w^3/h, reported in Table 1 show that the dissipation also increases with Ro so that a state in which

$$0 \approx P - \epsilon \qquad (14)$$

is nearly retained in the centre. In fact, $P/\epsilon = 0.91$ for Ro = 0.5 as compared to 0.85 in the non-rotating Couette channel.

It is now timely to examine the complete budgets for the four non-zero components of the second-moment tensor $\overline{u_iu_j}$ in Figures 4 and 5 for rotation numbers 0 and 0.5, respectively. The rate-of-change $D\overline{u_iu_j}/Dt$ becomes identically zero in the present flow, and the molecular (D_{ij}^{ν}) and turbulent (D_{ij}^{T}, D_{ij}^{P}) diffusion become significantly smaller near y = 0 than the leading terms in each of the budgets. Thus, the complete equation (2) can be simplified in the central core region to

$$0 \approx P_{ij} + G_{ij} + \Phi_{ij} - \epsilon_{ij} \qquad (15)$$

Furthermore, since the traces of G_{ij} and Φ_{ij} are identically zero, the local equilibrium condition (14) is recovered upon contraction of the indices in equation (15).

At first sigth we were inclined to associate the excess energy level in the centre with the high mean shear rate dU/dy for Ro = 0.5. However, the mean shear production P contributes only to streamwise velocity fluctuations (since $P_{22} = P_{33} = 0$) and the total production of u is

$$P_{11} + G_{11} = (1+S)P_{11} \qquad (16)$$

Since S tends to -1 in the central region of the rapidly rotating Couette flow, the rotational stress generation $G_{11} = 4\Omega\overline{uv}$ outweighs the mean shear production $P_{11} = -2\overline{uv}dU/dy$, cf. Figure 5a, and the reason for the high level of k must therefore be sought elsewhere.

Inspection of the individual terms in the transport equation for $\overline{v^2}$, i.e. Figure 5b, shows that the rotational production $G_{22} = -4\overline{uv}\Omega$ plays an essential role since $P_{22} = 0$. It should be noticed that $G_{22} = -G_{11} \approx P_{11} = 2P$ since $S \approx -1$. The amplification of the turbulence level in the rapidly rotating Couette flow is therefore caused by interactions between the fluctuating Coriolis force $-2\rho\Omega u$ in the wall-normal direction and velocity fluctuations v in that direction. This is indeed confirmed by the observation that the conventional stress anisotropy $\overline{u^2} > \overline{v^2}$ has been reversed for Ro = 0.5; see Table 1. In fact, $\overline{v^2}$ exceeds $\overline{u^2}$ by a factor close to 5. While energy is normally fed from $\overline{u^2}$ into $\overline{v^2}$ (and $\overline{w^2}$) by pressure-strain interactions, as for Ro = 0 in Figure 4b, the role of the pressure-strain interactions has been reversed for Ro = 0.5 since turbulence energy is now being transferred from $\overline{v^2}$ to $\overline{u^2}$ ($\Phi_{11} > 0$ and $\Phi_{22} < 0$ in Figure 5). Since $P_{11} + G_{11} \approx 0$ in the budget for the streamwise velocity fluctuations, we are left with the balance $0 \approx \Phi_{11} - \epsilon_{11}$. Thus, while the essential production mechanism has been changed from that of mean shear (at Ro = 0) to background rotation (at Ro = 0.50), the roles of the streamwise and wall-normal velocity fluctuations have been interchanged.

TABLE 2. Centreline values of the Reynolds stress anisotropies a_{ij} and the dissipation rate anisotropies e_{ij}. The data for the non-rotating case are from Andersson & Bech (1995).

	Ro = 0	Ro = 0.5
a_{11}	0.087	-0.221
a_{22}	-0.066	0.217
a_{33}	-0.022	0.003
$-a_{12}$	0.074	0.087
e_{11}	0.129	-0.085
e_{22}	-0.098	0.038
e_{33}	-0.031	0.047
$-e_{12}$	0.072	0.161

The only off-diagonal component $-\overline{uv}$ of the Reynolds stress tensor was examined in some detail for Ro = 0 by Bech and Andersson (1996c). In plane Couette flow $-P_{12} = \overline{v^2}dU/dy$ remains positive throughout the flow, whereas P_{12} inevitably changes its sign at the position of vanishing mean shear in plane Poiseuille flow. In the slowly rotating counterparts where the conventional anisotropy $\overline{u^2} > \overline{v^2}$ is retained, the Coriolis production $-G_{12} = 2\Omega(\overline{u^2} - \overline{v^2})$ remains positive for both flows when $\Omega > 0$. Thus G_{12} is adding to P_{12} all over the Couette channel, while G_{12} only supports P_{12} on the anticyclonic (pressure) side of the rotating Poiseuille flow and opposes the mean shear production on the cyclonic (suction) side.

In the rapidly rotating Couette flow $-P_{12}$ is substantially increased not only because of the increased mean shear rate dU/dy but also due to the enhancement of $\overline{v^2}$, see Figure 5d. However, the reversal of the normal stress anisotropy makes the rotational generation term change sign and $-G_{12}$ is now becoming a sink term which prevents $-\overline{uv}$ to raise below the upper bound U_τ^2 imposed by equation (1). It is interesting to observe that the total production of $-\overline{uv}$ can be expressed as

$$-P_{12} - G_{12} = 2\Omega\left[\overline{u^2} - \overline{v^2}\left(\frac{S+1}{S}\right)\right] \qquad (17)$$

where the impact of the wall-normal fluctuations becomes vanishingly small in the core region where $S \approx -1$ and the right hand side of (17) reduces to $2\Omega\overline{u^2}$. Thus the total production in equation (17) amounts to a fraction $-S\overline{u^2}/\overline{v^2}$ (or about 0.2) of the mean shear production $-P_{12}$ alone.

So far we have focussed on the relative magnitude of $\overline{u^2}$ and $\overline{v^2}$, which turned out to have a crucial effect on the role played by the various production terms in equation (2). Let us now consider the non-dimensional Reynolds stress anisotropy tensor

$$a_{ij} = \frac{\overline{u_iu_j}}{2k} - \frac{1}{3}\delta_{ij} \qquad (18)$$

and the analogously defined dissipation rate anisotropy tensor:

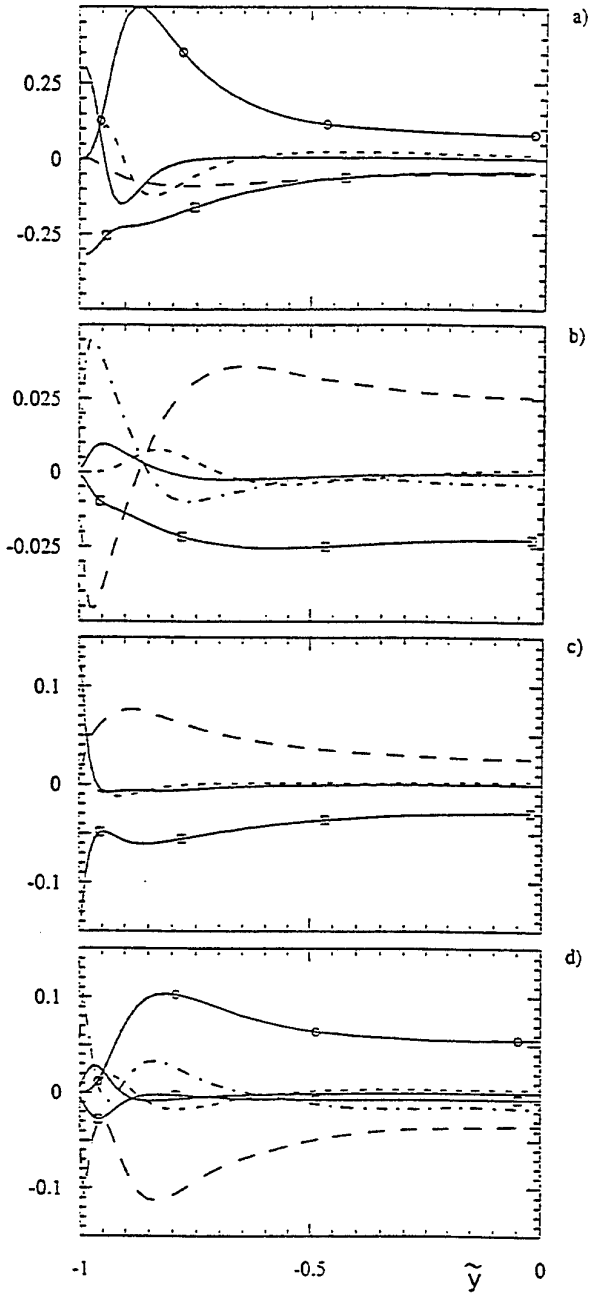


FIGURE 4. Reynolds stress budget data for Ro = 0 scaled by $U_\tau^4/\nu = Re_\tau \cdot U_\tau^3/h$. From Andersson & Bech (1995).

a) $\overline{u^2}$; b) $\overline{v^2}$; c) $\overline{w^2}$; d) $-\overline{uv}$.

—○— Production P_{ij}
——— Viscous diffusion D_{ij}^{ν}
- - - - - - Turbulent diffusion D_{ij}^{τ}
—•— Turbulent diffusion D_{ij}^{p}
– – – – – Pressure-strain Φ_{ij}
—□— Dissipation $-\epsilon_{ij}$

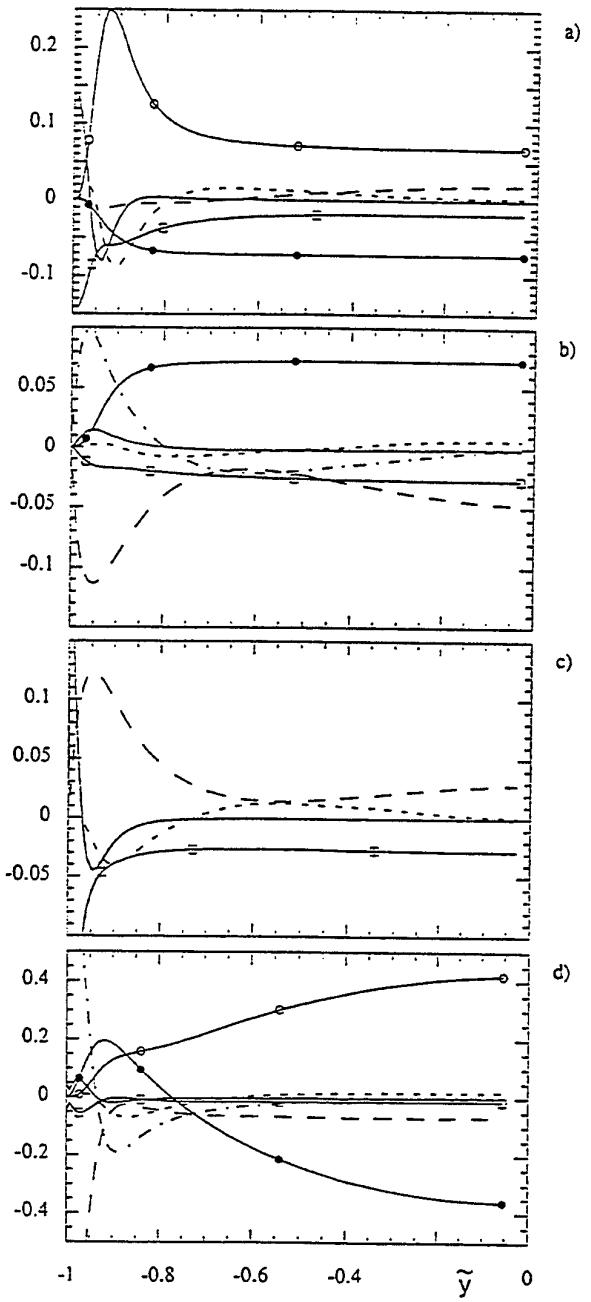


FIGURE 5. Reynolds stress budget data for Ro = 0.50 scaled by $U_\tau^4/\nu = Re_\tau \cdot U_\tau^3/h$. a) $\overline{u^2}/2$; b) $\overline{v^2}/2$; c) $\overline{w^2}/2$; d) $-\overline{uv}$.

Legend as in Fig. 4, except: —●— Rotational production G_{ij}.

$$e_{ij} = \frac{\epsilon_{ij}}{2\epsilon} - \frac{1}{3}\delta_{ij} \qquad (19)$$

The centreline values of a_{ij} and e_{ij} are reported in Table 2. As far as the normal components are concerned, the anisotropies are completely reversed when Ro is raised from 0 to 0.5, whereas the magnitude of the off-diagonal components is increased. Moreover, e_{ij} responds broadly in the same way as a_{ij} to the strong rotation. An anisotropy invariant map (AIM) for a_{ij} showed that the near-wall turbulence, which is fairly close to the one-component limit for Ro = 0, approaches an axisymmetric state in which $u^2 \approx w^2$ for Ro = 0.50. The corresponding AIM for e_{ij} revealed that the dissipation rate tensor was almost isotropic over a greater part of the cross-section than in the non-rotating case.

CONCLUDING REMARKS

The anomalies of turbulence characteristics, like the Reynolds stress and dissipation rate anisotropies, make the rapidly rotating Couette flow a physically challenging test for turbulence closure models aimed at shear flows in noninertial frames-of-reference. The homogeneity of the flow in planes parallel with the moving plates makes any set of differential model equations reduce to a set of ODEs. This particularly attractive feature of the rapidly rotating Couette flow is not shared by its weakly and moderately rotating counterparts.

ACKNOWLEDGEMENTS

The computer simulations were supported by the Research Council of Norway (Programme for Supercomputing) through a grant of computing time. Discussions with Dr. B.A. Pettersson are gratefully acknowledged. Ms T. Rakbjørg and Ms I. Wiggen prepared the camera-ready manuscript with appreciated care.

REFERENCES

Andersson, H.I., and Bech, K.H., 1995, "On Nearly Homogeneous Turbulent Shear Flow," *Proceedings, 10th Symposium on Turbulent Shear Flows*, University Park, PA, pp. 17.7-17.12.

Andersson, H.I., Bech, K.H., and Kristoffersen, R., 1992, "On Diffusion of Turbulent Energy in Plane Couette Flow," *Proceedings of the Royal Society of London*, Series A, Vol. 438, pp. 477-484.

Andersson, H.I., and Kristoffersen, R., 1995, "Turbulence Statistics of Rotating Channel Flow," *Turbulent Shear Flows 9*, F. Durst et al., eds., Springer Verlag, pp. 53-70.

Bech, K.H., and Andersson, H.I., 1996a, "Secondary Flow in Weakly Rotating Turbulent Plane Couette Flow," *Journal of Fluid Mechanics*, Vol. 317, pp. 195-214.

Bech, K.H., and Andersson, H.I., 1996b, "Growth and Decay of Longitudinal Roll Cells in Rotating Turbulent Plane Couette Flow," *Advances in Turbulence VI*, S. Gavrilakis et al., eds., Kluwer, pp. 91-94.

Bech, K.H., and Andersson, H.I., 1996c, "Structure of Reynolds Shear Stress in the Central Region of Plane Couette Flow," *Fluid Dynamics Research*, Vol. 18, pp. 65-79.

Bech, K.H., and Andersson, H.I., 1997, "Turbulent Plane Couette Flow Subject to Strong System Rotation," *Journal of Fluid Mechanics* (submitted).

Bech, K.H., Tillmark, N., Alfredsson, P.H., and Andersson, H.I., 1995, "An Investigation of Turbulent Plane Couette Flow at Low Reynolds Numbers," *Journal of Fluid Mechanics*, Vol. 286, pp. 291-325.

Gavrilakis, S., Tsai, H.M., Voke, P.R., and Leslie, D.C., 1986, "Large-Eddy Simulation of Low Reynolds Number Channel Flow by Spectral and Finite Difference Methods," *Notes on Numerical Fluid Mechanics*, U. Schumann & R. Friedrich, eds., Vieweg, Vol. 15, pp. 105-118.

Gerhart, P.M., Gross, R.J., and Hochstein, J.I., 1992, *"Fundamentals of Fluid Mechanics"*, 2nd ed., Addison-Wesley, Reading, Ma.

Johnston, J.P., Halleen, R.M., and Lezius, D.K., 1972, "Effects of Spanwise Rotation on the Structure of Two-Dimensional Fully Developed Turbulent Channel Flow," *Journal of Fluid Mechanics*, Vol. 56, pp. 533-557.

Kármán, T. von, 1937, "The Fundamentals of the Statistical Theory of Turbulence," *Journal of the Aeronautical Sciences*, Vol. 4, pp. 131-138.

Kim, J., 1983, "The effect of rotation on turbulence structure," *Proceedings, 4th Symposium on Turbulent Shear Flows*, Karlsruhe, pp. 6.14-6.19.

Komminaho, J., Lundbladh, A., and Johansson, A.V., 1996, "Very Large Structures in Plane Turbulent Couette Flow," *Journal of Fluid Mechanics*, Vol. 320, pp. 259-285.

Kristoffersen, R., and Andersson, H.I., 1993, "Direct Simulations of Low-Reynolds-Number Turbulent Flow in a Rotating Channel," *Journal of Fluid Mechanics*, Vol. 256, pp. 163-197.

Lamballais, E., Lesieur, M., and Métais, O., 1996a, "Influence d'une rotation d'entraînment sur les tourbillons cohérents dans un canal," *Comptes Rendus De L'Académie Des Sciences Paris*, Vol. 323, Ser. IIb, pp. 95-101.

Lamballais, E., Lesieur, M., and Métais, O., 1996b, "Effects of Spanwise Rotation on the Vorticity Stretching in Transitional and Turbulent Channel Flow," *International Journal of Heat and Fluid Flow*, Vol. 17, pp. 324-332.

Miyake, Y., and Kajishima, T., 1986, "Numerical Simulation of the Effects of Coriolis Force on the Structure of Turbulence," *Bulletin JSME*, Vol. 29, 3341-3351.

Nakabayashi, K., and Kitoh, O., 1996, "Low Reynolds Number Fully Developed Two-Dimensional Turbulent Channel Flow with Spanwise Rotation," *Journal of Fluid Mechanics*, Vol. 315, pp. 1-29.

Piomelli, U., and Liu, J., 1995, "Large-Eddy Simulation of Rotating Channel Flows using a Localized Dynamic Model," *Physics of Fluids*, Vol. 7, pp. 839-848.

Reynolds, W.C., and Kassinos, S.C., 1995, "One-Point Modelling of Rapidly Deformed Homogeneous Turbulence," *Proceedings of the Royal Society of London*, Series A, Vol. 451, pp. 87-104.

Tafti, D.K., and Vanka, S.P., 1991, "A Numerical Study of the Effects of Spanwise Rotation on Turbulent Channel Flow," *Physics of Fluids A*, Vol. 3, 642-656.

Tillmark, N., and Alfredsson, P.H., 1996, "Experiments on Rotating Plane Couette Flow," *Advances in Turbulence VI*, S. Gavrilakis et al., eds., Kluwer, pp. 391-394.

MODELLING NEAR-WALL EFFECTS IN AXIALLY ROTATING PIPE FLOW BY ELLIPTIC RELAXATION

B. Anders Pettersson[1], Helge I. Andersson, Andreas S. Brunvoll
Division of Applied Mechanics
Norwegian University of Science and Technology
N-7034 Trondheim
Norway

ABSTRACT

The ability to faithfully reproduce the effect of axial rotation on fully developed pipe flow is investigated using a second moment closure model. In particular, the impact of the pressure-strain model is scrutinized by adopting both linear and nonlinear models. Near-wall effects are accounted for by elliptic relaxation and model predictions are verified against direct numerical simulations and experimental results. The results suggest that pressure-strain models cubic in the Reynolds-stress tensor seem unsuitable for this case whereas best overall performance is obtained with a model which retain terms quadratic in the Reynolds stresses. The importance of the stress anisotropy in the logarithmic region is also addressed.

INTRODUCTION

Turbulent flows affected by centrifugal and Coriolis forces are frequently encountered in engineering applications as well as in nature. These body forces are known to considerably alter the mean flow field and the intensity and structure of the turbulence. Since the engineering approach to fluid flow calculations is based on the Reynolds-averaged Navier-Stokes equations (RANS), the success of any CFD analysis relies heavily upon the turbulence model embodied in the actual computer code. It is therefore unfortunate that the widely used $k-\varepsilon$ model, like any other turbulence model which utilizes Boussinesq's linear stress-strain relationship, is unable to naturally account for these effects. The effects of centrifugal and Coriolis forces are, on the other hand, automatically accounted for within the framework of second-moment closure (SMC) modelling which is based on the exact transport equations governing the individual Reynolds-stress components.

Turbulent flow inside an axially rotating pipe is not only of theoretical interest but has also some direct practical applications; e.g. the internal cooling in turbomachinery. Kikuyama *et al.* (1983a) studied experimentally the flow in the entry region of a rotating pipe and Yoo *et al.* (1991) predicted this flow with a number of different closure models, including two near-wall SMC models. Yoo *et al.* (1991) concluded that closures which take into account the anisotropy of the turbulence are required in order to faithfully predict this particular flow and, moreover, that the turbulence near the wall is not in equilibrium. The latter observation consequently imply that the commonly used wall-function approach should be abandoned. In spite of the simple geometry the developing flow is three dimensional and rather complex and thus provides a severe test for any turbulence closure.

Murakami & Kikuyama (1980), Kikuyama *et al.* (1983b), Reich & Beer (1989) and Imao *et al.* (1996) studied experimentally the effect of axial rotation on fully developed turbulent pipe flow. Hirai *et al.* (1988) employed three different turbulence models; two based on the eddy-viscosity hypothesis and one full SMC model. Although their numerical computations used the wall-function approach, they reached the same conclusion as Yoo *et al.* (1991), namley that an anisotropic closure model is required.

An outstanding feature of the fully developed case as compared to the entry flow is that the mean flow field can be considered as one-dimensional and two-componential. The set of governing equations thus reduce to a set of ODEs which can be solved numerically to practically any degree of accuracy and the true performance of the closure model is revealed. The centrifugal force caused by the superimposed circumferential velocity acts stabilising on the turbulence across the entire pipe and the turbulent momentum transfer is strongly suppressed. The present study focuses on the assessment of a near-wall SMC model developed by Durbin (1993). The performance of this state-of-the-art model is explored in fully developed turbulent pipe flow subjected to constant axial rotation.

Substantial advances in SMC modelling have been made in recent years, notably the evolution of closure models free of wall distances and wall normals. This particular feature makes these models applicable to flows with geometrically complex

[1] Present address: Kongsberg Aerospace, P.O.Box 1003, N-3601 Kongsberg, Norway.

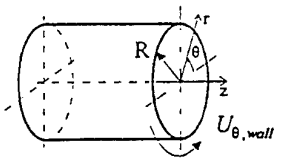


FIGURE 1. Schematic of flow configuration.

boundaries. The very important pressure-strain interaction term is in the focus of much of the research efforts at this closure level, especially its mean-strain contribution. The objective of the present study is to investigate whether non-linear pressure-strain models, used in conjunction with the relaxation approach (Durbin 1993) to model near-wall effects, can improve the predictions as compared to a pressure-strain model which is linear in the Reynolds stresses. Model predictions will be verified against recent experimental results reported by Imao *et al.* (1996) and Direct Numerical Simulation (DNS) data (Eggels *et al.* 1994, Nieuwstadt *et al.* 1996).

MATHEMATICAL MODEL

Consider fully developed turbulent pipe flow subjected to axial rotation, see Figure 1. The mean flow field is assumed to be one-dimensional and two-componential so that the two non-zero mean velocity components $\vec{U}=\{0,U_\theta(r),U_z(r)\}$ are homogeneous in the axial (z) and circumferential (θ) directions. The equations governing the mean momentum can be written as

$$0=\mu\left(\frac{d^2U_z}{dr^2}+\frac{1}{r}\frac{dU_z}{dr}\right)-\frac{1}{r}\frac{d}{dr}\left(r\rho\overline{u_ru_z}\right) \tag{1}$$

$$0=\mu\left(\frac{d^2U_\theta}{dr^2}+\frac{1}{r}\frac{dU_\theta}{dr}-\frac{U_\theta}{r^2}\right)-\frac{1}{r^2}\frac{d}{dr}\left(r^2\rho\overline{u_\theta u_r}\right) \tag{2}$$

for a constant property fluid in a cylindrical coordinate system.

The *a priori* unknown Reynolds shear stresses, $-\rho\overline{u_ru_z}$ and $-\rho\overline{u_\theta u_r}$, can be obtained from the transport equation governing the kinematic Reynolds-stress tensor $-\overline{u_iu_j}$ which can be written as

$$\overbrace{U_k\frac{\partial\overline{u_iu_j}}{\partial x_k}}^{C_{ij}}=\overbrace{-\left(\overline{u_ku_i}\frac{\partial U_j}{\partial x_k}+\overline{u_ku_j}\frac{\partial U_i}{\partial x_k}\right)}^{P_{ij}}+\overbrace{\mu\frac{\partial^2\overline{u_iu_j}}{\partial x_k\partial x_k}}^{d_{ij}^{\nu}}$$
$$\underbrace{-\frac{\partial}{\partial x_k}\left(\overline{u_iu_ju_k}+\frac{\overline{pu_i}}{\rho}\delta_{jk}+\frac{\overline{pu_j}}{\rho}\delta_{ik}\right)}_{d_{ij}^{t}+d_{ij}^{p}}+\wp_{ij}-\frac{\overline{u_iu_j}}{k}\varepsilon \tag{3}$$

where

$$\wp_{ij}=\underbrace{\overline{\frac{p}{\rho}\left(\frac{\partial u_i}{\partial x_j}+\frac{\partial u_j}{\partial x_i}\right)}}_{\phi_{ij}}-\varepsilon_{ij}+\frac{\overline{u_iu_j}}{k}\varepsilon \tag{4}$$

are the convective transport of second moments (C_{ij}), production due to mean shear (P_{ij}), viscous, turbulent and pressure diffusion ($d_{ij}^{\nu},d_{ij}^{t},d_{ij}^{p}$) and, finally, the 'relaxed' pressure-strain tensor ($\wp_{ij}$). The more conventional pressure-strain interactions are denoted ϕ_{ij}.

Turbulent diffusion is modelled by gradient diffusion as

$$d_{ij}^{t}=\frac{\partial}{\partial x_p}\left(C_K\overline{u_pu_l}T\frac{\partial\overline{u_iu_j}}{\partial x_l}\right) \tag{5}$$

whereas the pressure diffusion term is modelled as (Fu 1993)

$$d_{ij}^{p}=-C_K^{*}\frac{\partial}{\partial x_m}\left(\left(\overline{u_iu_n}\delta_{jm}+\overline{u_ju_n}\delta_{im}\right)T\frac{\partial k}{\partial x_n}\right). \tag{6}$$

In order to allow for counter-gradient diffusion only outside the near-wall layer the coefficient $C_K^{*}=0.4AC_K$ is made a function of the stress anisotropy parameter $A=1-\frac{9}{8}(A_2-A_3)$. The objective for adopting Eq.(6) is to decrease the turbulent time scale k/ε in order to reduce the turbulent energy level in the pipe core which otherwise is substantially overpredicted by most models. The time scale is taken as $T=\max\left(k/\varepsilon,\,6\sqrt{\nu/\varepsilon}\right)$. The dissipation-rate tensor (ε_{ij}) is assumed to be isotropic, i.e. $\varepsilon_{ij}=\frac{2}{3}\varepsilon\delta_{ij}$, in the limit of homogeneous turbulence where the relaxed pressure-strain tensor takes its homogeneous form $\wp_{ij}^{h}=\phi_{ij}+\varepsilon a_{ij}$. The Reynolds-stress anisotropy tensor is $a_{ij}=\overline{u_iu_j}/k-\frac{2}{3}\delta_{ij}$. Non-local effects on $\wp_{ij}$, associated with the proximity of a solid boundary, are modelled by elliptic relaxation (Durbin 1993)

$$L^2\nabla^2f_{ij}-f_{ij}=-\wp_{ij}^{h}/k \tag{7}$$

where $f_{ij}=\wp_{ij}/k$. The present study adopts a somewhat modified form of the lenght scale $L=\tilde{C}_L\max\left(k^{3/2}/\varepsilon,\,\tilde{C}_\eta(\nu^3/\hat{\varepsilon})^{1/4}\right)$, cf. Pettersson & Andersson (1997), where the coefficients $\tilde{C}_L=C_LA_2^{1/2}$ and $\tilde{C}_\eta=C_\eta A_2^{-1/2}\exp\left[-\left((1+A_3)/(0.1+A_2)\right)^2\right]$ have been made functions of the second and third Reynolds-stress invariants $A_2=a_{ij}a_{ji}$ and $A_3=a_{ik}a_{kj}a_{ji}$, respectively. The dissipation-rate (ε) in Kolmogorov's length scale was replaced by $\hat{\varepsilon}=\left(\varepsilon^2+\Phi^2\right)^{1/2}$, where $\Phi=2\nu S_{ij}S_{ij}$ is the mean viscous dissipation function, in order to prevent excessive values of L if the flow is relaminarized close to a solid boundary (cf. Pettersson & Andersson 1997). The mean rate-of-strain tensor $S_{ij}=\frac{1}{2}\left(\partial U_i/\partial x_j+\partial U_j/\partial x_i\right)$.

The present study adopts four different pressure-strain models (ϕ_{ij}): (i) the linear 'Isotropization-of-Production' model in which the convective transport (C_{ij}) is included in order to attain a frame indifferent formulation (see e.g. Pettersson *et al.* 1996); (ii) the model by Speziale *et al.* (1991) which is quadratic in the Reynolds-stress tensor and, finally, the two cubic models by (iii) Ristorcelli *et al.* (1995) and (iv) Fu *et al.* (1989). These are hereafter denoted IP, SSG, RLA and FLT, respectively. The RLA model has the same tensorial basis as the FLT model but employ variable coefficients which are functions of the Reynolds-stress invariants. A particularly interesting feature of the RLA model is that it is consistent with the principle of material frame indifference in the limit of two dimensional turbulence and thus represents a more general class of pressure-strain models. The SSG model has proven to outperform the linear IP model for a varity of flows and

TABLE 1. Model constants.

	$C_{\varepsilon 1}$	$C_{\varepsilon 2}$	C_ε	C_K	C_L	C_η
IP	1.44	1.90	0.14	0.19	0.20	80.0
SSG	1.40	1.83	0.19	0.21	0.21	424
RLA	1.45	1.85	0.14	0.19	0.18	647
FLT	1.44	1.85	0.19	0.21	0.33	700

performs equivalently to the RLA model, at least for simple planar flows (Ristorcelli *et al.* 1995).

The dissipation-rate (ε) of turbulent kinetic energy is obtained from its own modelled transport equation

$$\frac{D\varepsilon}{Dt} = \frac{1}{T}\left[C_{\varepsilon 1}\left(1+0.1\frac{P_{ii}}{2\varepsilon}\right)\frac{P_{mm}}{2} - C_{\varepsilon 2}\varepsilon\right] + \frac{d_{ii}^{\nu}}{2} + \frac{C_\varepsilon}{2C_K}d_{ii}^{t} \qquad (8)$$

which is solved coupled with the model equation governing the turbulent kinetic energy

$$\frac{Dk}{Dt} = \frac{P_{ii}}{2} - \varepsilon + \frac{1}{2}\left(d_{ii}^{\nu} + d_{ii}^{t} + d_{ii}^{p}\right). \qquad (9)$$

It should be noted that pressure diffusion is not accounted for in the dissipation-rate model equation (8). Model constants are listed in Table 1.

NUMERICAL APPROACH

A particularly interesting feature of this model problem is that, within the framework of transport modelling, the set of governing model equations reduce to a set of ODEs which can be solved numerically to practically any degree of accuracy. The governing set of equations consists of two equations for the mean flow, five equations for the Reynolds stresses ($\overline{u_r^2}$, $\overline{u_z^2}$, $\overline{u_r u_z}$, $\overline{u_r u_0}$, $\overline{u_0 u_z}$) together with the corresponding relaxation equations and the turbulent kinetic energy and dissipation rate equations. The circumferential stress component is subsequently derived from the relation $\overline{u_0^2} = 2k - \overline{u_r^2} - \overline{u_z^2}$. The resulting difference equations are solved semi-implicitely as coupled k-ε and $\overline{u_i u_j} - f_{ij}$ systems by a pseudo-time-marching scheme until a steady state solution is reached. Spatial derivatives are replaced by second-order accurate central-difference approximations. No-slip boundary conditions were used at the solid walls together with $k = dk/dy = 0$ for the k-ε system and $f_{ij} = -20\nu^2\overline{u_i u_j}/\left(\varepsilon_{wall} y_1^4\right)$ if i and/or j is in the wall-normal direction, $f_{ij} = 0$ else. y_1 is the wall-distance for the wall-adjacent computational node. The boundary conditions for f_{ij} are derived from the local solution of the model equation governing the wall-normal stress component ($\overline{u_r^2}$) at the wall, see Durbin (1993) for further details. Typically 100 grid points were non-uniformly distributed from the wall to the axis of the pipe such that the first computational node was situated at $y^+ \approx 0.5$. The solution was assumed to have reached a steady state when the sum of absolute normalized residuals across the channel normalized with the time step, fell below 10^{-5}.

RESULTS

Model predictions are compared with DNS data (Eggels *et al.* 1994 and Nieuwstadt *et al.* 1996) at $\mathrm{Re}_\tau \equiv u_\tau D/\nu = 360$, which corresponds to $\mathrm{Re} \equiv U_b D/\nu \approx 5300$, and rotation numbers $N \equiv U_{0,wall}/U_b = 0$, 0.32 and 0.61. Here, U_b and u_τ denote the mean bulk velocity and wall friction velocity, respectively. In order to examine the effect of the Reynolds number, comparisons are also made with the experimental results recently reported by Imao *et al.* (1996) at $Re = 20000$ and $N = 0$ and 0.5.

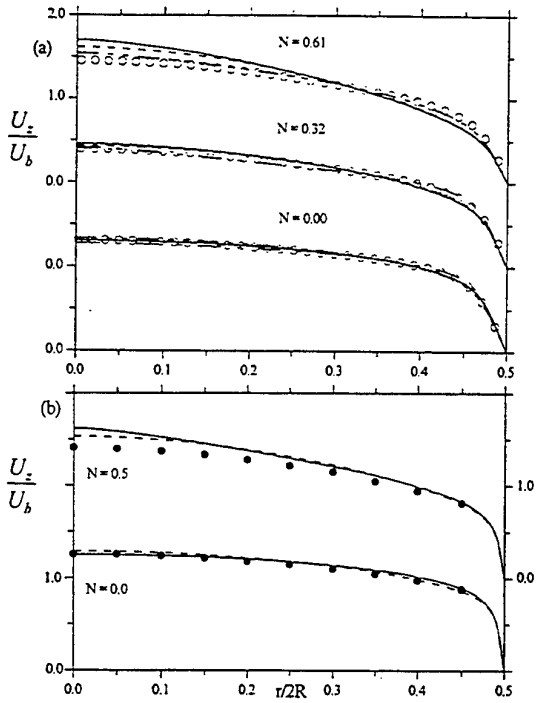


FIGURE 2. Mean axial velocity. Symbols: O: DNS; ●: EXP; Lines: ———: IP; -------: SSG; — - - —: FLT; — - —: RLA.

Mean Flow Quantities

The predicted mean-velocity distributions are compared against DNS data and experimental results in Figures 2 and 3, respectively. The mean axial velocity (U_z) profile is deformed to become more 'laminar-like' due to the axial rotation. The centerline velocity $U_z(r=0)$ in Figure 2 increases with rotation number whereas a reduction can be observed near the wall. Figure 3 displays the mean circumferential velocity and both the DNS data and experimental results indicate a nearly parabolic distribution, i.e. $U_0 \propto r^n$ where $n \approx 2$, except close to the wall where the DNS results indicate an almost linear variation ($n \approx 1$). The best overall performance is achieved by the SSG model, especially concerning the U_0 -component. It is noteworthy that both cubic models (RLA and FLT) fail severely at the highest Re and the former even at the lowest Re. The worst results are therefore not presented in the figures. This surprising failure can be illustrated by the RLA-results in Figure 3a at N = 0.32 where the predicted U_0 -distribution displays the *opposite* trend as compared to the DNS data. Although the FLT model produces the best predictions of the axial mean velocity component, the circumferential component exhibits a nearly linear distribution similar to that obtained with the simple IP model. It should be recalled that a linear U_0 -profile corresponds to solid body rotation, i.e. the laminar solution and the solution obtained with closure models based on Boussinesq's linear stress-strain relationship (see e.g. Hirai *et al.* 1988).

TABLE 2. Friction factor ratio $\lambda/\lambda_{N=0}$.

N	DNS	EXP	IP	SSG	FLT	RLA
0.32	1.11	----	1.16	1.18	1.04	1.05
0.61	1.22	----	1.58	1.64	1.20	----
0.50	----	1.20	1.30	1.33	----	----

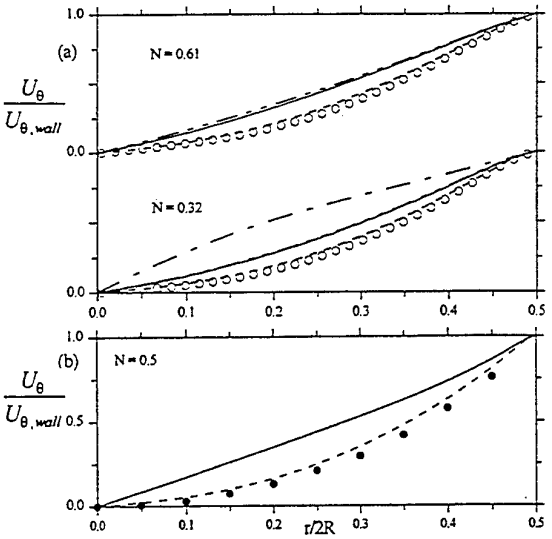


FIGURE 3. Mean circumferential velocity. Legends as in fig. 2.

The centrifugal force caused by the imposed rotation of the pipe acts stabilising on the turbulence. Since the friction velocity is kept constant in the computations at $Re_\tau = 360$, it is expected that the mean bulk velocity should change with the rate of rotation. At Re = 20000, however, the mean bulk velocity is held constant in the computations and this implies that the friction velocity is expected to vary. The stabilising effect of axial rotation on fully developed turbulent pipe flow is summarized in Table 2 where the friction factor $\lambda = 8(u_\tau/U_b)^2$ (cf. Imao *et al.* 1996) is presented for the different rotation numbers. All models, except RLA, are able to capture the reduction of the friction factor with increasing pipe rotation. Both the IP and SSG models, however, overpredict this stabilising effect. Attempts were made to compute the case Re = 20000 and N = 1.0, which was also considered by Imao *et al.* (1996). In the predictions, however, the stabilising influence of the rotation completely quenched the turbulence and the laminar solution was returned. The cubic FLT model seems to be capable of faithfully reproducing the reduced friction factor only at low Re flow and moderate rotation numbers.

Turbulence Quantities

In the present study all components of the Reynolds-stress tensor are nonzero due to the imposed pipe rotation, whereas the $\overline{u_r u_\theta}$ and $\overline{u_\theta u_z}$ components are zero in a fixed pipe. The mean flow field is strongly coupled with the shear-stress components $\overline{u_r u_\theta}$ and $\overline{u_r u_z}$, cf. eqs. (1-2). The predicted shear-stress components are compared with the DNS data in Figure 4 and the results are fully consistent with the accompanying results presented in Figure 2. The $\overline{u_r u_\theta}$-component is best predicted by the SSG model in Figure 4a whereas the IP and FLT models underpredict the peak close to the wall and consequently also the gradient in the pipe core. It should be

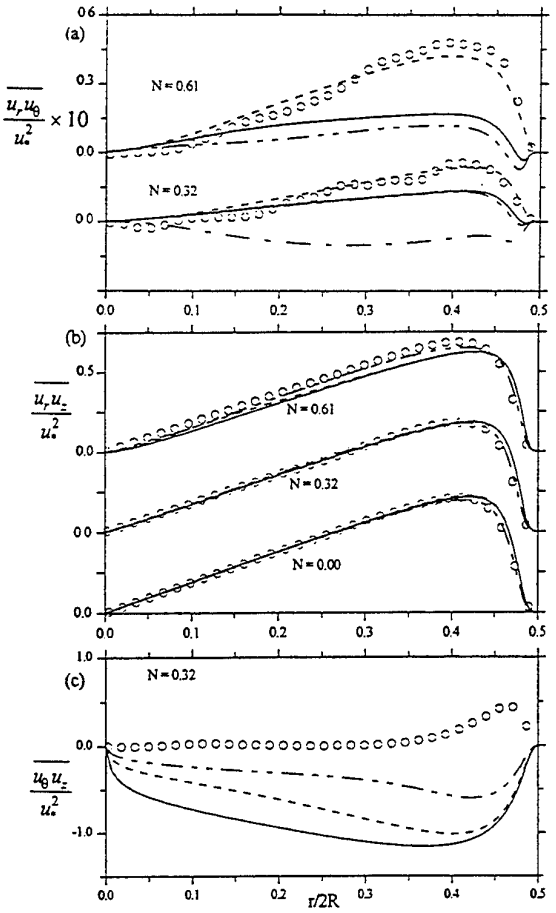


FIGURE 4. Turbulent shear-stresses. Legends as in fig. 2.

noted that the level of $\overline{u_r u_\theta}$ is roughly a decade below that of the two other shear stress components, but $\overline{u_r u_\theta}$ is nevertheless essential in the determination of U_θ. The anomalous prediction of U_θ obtained with the RLA model can be understood by the results in Figure 4a at N = 0.32. Since the model returns a *negative* $\overline{u_r u_\theta}$-component, the opposite effect of the turbulence on the circumferential mean-velocity component is to be expected, i.e. the turbulence tends to *increase* the mean velocity as compared to the laminar solution instead of reducing it. It should be noted that $-d(\rho\overline{u_\theta u_r})/dr$ is the dominating turbulent contribution in equation (2). A possible explanation of this erronous behaviour will be given later. The same line of arguments can be used to explain the almost linear distribution of U_θ in the near-wall region (see Figure 3a) obtained by the models (apart from RLA). The turbulence in the near-wall region tends to increase U_θ since the gradient of $\overline{u_r u_\theta}$ takes a large negative value close to the wall, i.e. the dominating term $-d(\rho\overline{u_\theta u_r})/dr$ in (2) then becomes a source.

In consistence with the predicted U_z-profiles (Figure 2a) is the predicted distribution of $\overline{u_r u_z}$ obtained by the FLT model (Figure 4b) in closest correspondence with the DNS data. The presence of the term $2\overline{u_\theta u_z}U_\theta/r$ in the $\overline{u_r u_z}$ transport equation causes a reduction of the $\overline{u_r u_z}$-component since all models predict $\overline{u_\theta u_z} < 0$ and consequently a subsequent

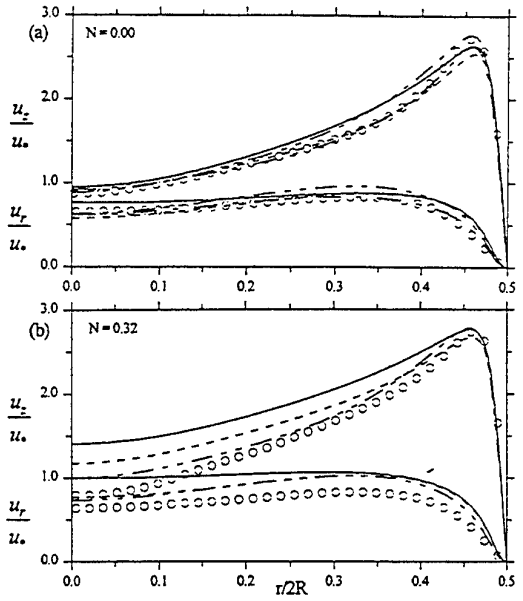


FIGURE 5. Axial and radial rms-distribution. Legends as in figure 2.

'laminarization' of the mean axial velocity profile. However, since the FLT model returns the lowest level of the $\overline{u_\theta u_z}$ - component, less reduction of the $\overline{u_r u_z}$ stress can be expected. A similar trend is also observed at the highest rotation number (not shown here). It is noteworthy that all models predict a negative $\overline{u_\theta u_z}$ stress, in correspondence with experimental results reported by Imao *et al.* (1996) , whereas the DNS data indicate a positive value. It is, however, not possible to draw any firm conclusion about these contradictory findings at present.

The rms-distributions of the axial and radial normal stress-components are shown in Figure 5. The model predictions compare reasonably well with the DNS data in the non-rotating case, whereas the turbulent energy level is significantly overpredicted at N = 0.32. This tendency is even more pronounced at higher rotation rates. Figure 6 display the turbulent kinetic energy distribution at Re = 20000 and N = 0 and 0.5. In contrast to the experimental results, both the SSG and IP model predict an enhanced turbulence level with increased rotation.

DISCUSSION AND CONCLUDING REMARKS

It is noteworthy that both cubic models (RLA and FLT) in combination with Durbin's elliptic relaxation approach fail completely in the present study at the high Re and, furthermore, that the RLA model is unable to predict rotating pipe flow even at low Re. This suggests that the reason for this failure should be sought in the pressure-strain models. Figures 7a-b display the main contributions to the budget of the important $\overline{u_r u_\theta}$ - component at N = 0.32 for the SSG and FLT model, respectively. The magnitude of the relaxed pressure-strain tensor ($\varphi_{r\theta}$) is significantly overpredicted by FLT in the logarithmic layer whereas good agreement is obtained with the SSG model. Closer examination of the individual contributions in the FLT model reveals that the major negative contribution

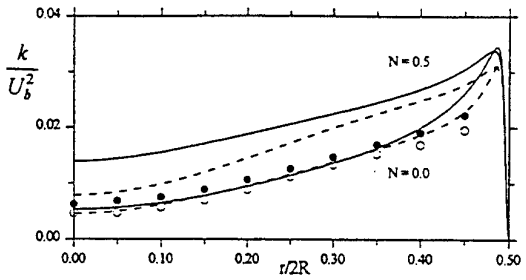


FIGURE 6. Turbulent kinetic energy at Re = 20000. Symbols: EXP; O: N = 0.0, ●: N = 0.5; lines: ——: IP; -------: SSG.

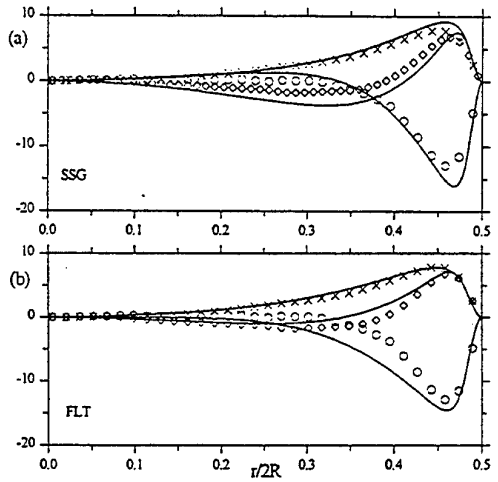


FIGURE 7. Leading terms in the $\overline{u_r u_\theta}$ budget at Re$_\tau$ = 360. (a) SSG, (b) FLT. ×: $-C_{r\theta}$; ◊: $P_{r\theta}$; O: $\varphi_{r\theta}$, scaled by $u_\tau^3/2R$. Symbols: DNS; lines: model predictions.

comes from the quadratic term $(a_{ip}^2 S_{pj} + a_{jp}^2 S_{pi} - \frac{2}{3} < a^2 S > \delta_{ij})$ which has no counterpart in the SSG model. The cubic term, on the other hand, makes a positive contribution. This suggests that the coefficient associated with this term could be altered to make the model applicable to higher rotation numbers. The importance of the cubic term for flows affected by centrifugal or Coriolis forces has been pointed out by Fu *et al.* (1987).

It seems, however, somewhat puzzling that the RLA model completely fails whereas the FLT model produces resonable results in the low-Re case although both models have the same tensorial basis. The only difference between the rapid pressure-strain models is that the RLA model employ variable coefficients whereas the FLT model uses constants. It is, however, very difficult to analyse the direct effect of this difference due to the complexity of the models. Consider instead the equilibrium solution of the $\overline{u_r u_\theta}$ transport equation which can be written as

$$\frac{\overline{u_r u_\theta}}{k} = -\frac{\overline{u_r^2}}{\varepsilon}\frac{dU_\theta}{dr}\frac{1-C_2}{C_1}\left[1-\frac{2\alpha-1}{n}\right] \qquad (10)$$

where the IP model is used for simplicity. It is furthermore assumed that $\overline{u_\theta^2}/\overline{u_r^2} \approx \alpha$ and $U_\theta \propto r^n$ $(\alpha, n > 0)$. The model constants in (10) take their standard values $C_1 = 1.22$ and $C_2 = 0.6$. Since both DNS data and experimental results indicate

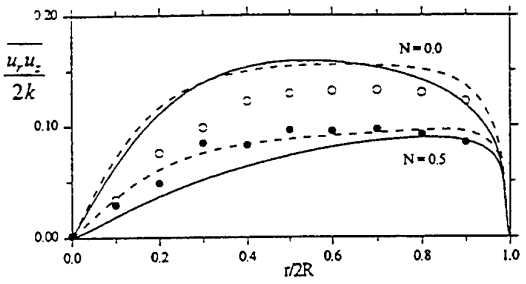


FIGURE 8. Structural parameter at $Re = 20000$. Legends as in figure 6.

that $n \approx 2$, $\overline{u_r u_0} > 0$ only if $\alpha > 3/2$. Hence, the separation between the tangential and radial normal stress components seems crucial in order to reproduce the observed U_0-distribution since it depends directly on the sign of $\overline{u_r u_0}$. It is now interesting to note that the predicted separation between $\overline{u_0^2}$ and $\overline{u_r^2}$ with the FLT model in the non-rotating case is significantly larger than with the RLA model. This is an indirect consequence of the variable coefficients in the RLA model and provides a possible explanation of why the FLT model performs better than the RLA model in the present study. It should, however, be noted that the results obtained with the RLA model in the non-rotating case are in better agreement with the DNS data than the predictions of any other model used in this study.

The substantial reduction of the structural parameter $\overline{u_r u_z}/2k$ in Figure 7 with increased rotation is well captured, especially by the SSG model. These results confirm the findings of Yoo *et al.* (1991), namley the existence of non-equilibrium turbulence in the logarithmic region. This indicates that the commonly used wall-function approach should not be adopted in calculations of axially rotating pipe flow.

The present study has shown that the relaxation model (Durbin 1993 and Pettersson & Andersson 1997) used in conjunction with both linear and non-linear pressure-strain models seems capable of capturing the influence on the turbulence by the proximity of a solid boundary. The quadratic SSG model significantly improved the predictions as compared to the other models. It is also revealed that pressure-strain models which include cubic terms in the Reynolds-stress tensor seem unsuitable for the case considered in this study. However, this failure can most likely be ascribed to the *combination* of the pressure-strain model and the model for the dissipation-rate tensor rather than to the pressure-strain model itself. It is finally noteworthy that the particular gradient-diffusion model adopted in the closure model seems to have only minor influence on the results.

ACKNOWLEDGEMENT

The authors are grateful to Professor F. T. M. Nieuwstadt and Dr J. G. M. Eggels for kindly providing us with the (unpublished) DNS results of the axially rotating pipe flow.

REFERENCES

Durbin, P. A., 1993, 'A Reynolds stress model for near-wall turbulence', *J. Fluid Mech.*, Vol. 249, pp. 465-498.

Eggels, J. G. M., Unger, F., Weiss. M. H., Westerweel, J., Adrian, R. J., Friedrich, R. & Nieuwstadt, F. T. M., 1994, 'Fully developed turbulent pipe flow: a comparison between direct numerical simulation and experiment', *J. Fluid Mech.*, Vol. 268, pp. 175-209.

Fu, S., Launder, B. E. & Tselepidakis, D. P., 1987, 'Accommodating the effects of high strain rate in modelling the pressure strain correlation', UMIST Mech. Engng Dept. report TFD/87/5.

Fu, S., 1993, 'Modelling of the pressure-velocity correlation in turbulence diffusion', *Computers Fluids*, 22, 199-205.

Hirai, S., Takagi, T. & Matsumoto, M., 1988, 'Predictions of the laminarization phenomenon in an axially rotating pipe flow', *ASME J. Fluids Engng*, Vol. 110, pp. 424-430.

Imao, S., Itoh, M. & Harada, T., 1996, 'Turbulent characteristics of the flow in an axially rotating pipe', *Int. J. Heat Fluid Flow*, Vol. 17, pp. 444-451.

Kikuyama, K., Murakami, M. & Nishibori, K., 1983a, 'Development of three-dimensional turbulent boundary layer in an axially rotating pipe', ASME *J. Fluids Engng*, Vol. 105, pp. 154-160.

Kikuyama, K., Murakami, M., Nishibori, K. & Maeda, K., 1983b, 'Flow in a rotating pipe (A calculation of flow in the saturated region)', *Bull. JSME*, Vol. 26, pp. 506-513.

Murakami, M. & Kikuyama, K., 1980, 'Turbulent flow in axially rotating pipes', ASME *J. Fluids Engng*, Vol. 102, pp. 97-103.

Nieuwstadt, F. T. M., Eggels, J. G. M. & Boersma, B. J., 1996, Private communication.

Pettersson, B. A., Andersson, H. I. & Hjelm-Larsen, Ø., 1996, ' Analysis of near-wall second-moment closures applied to flows affected by streamline curvature', in: Engng Turbulence Modelling and Measurements 3, pp. 49-58.

Pettersson, B. A. & Andersson, H. I., 1997, 'Near-wall Reynolds-stress modelling in noninertial frames of reference', *Fluid Dyn. Res.*, Vol. 19, pp. 251-276.

Reich, G. & Beer, H., 1989, 'Fluid flow and heat transfer in an axially rotating pipe-I. Effect of rotation on turbulent pipe flow', *Int. J. Heat Mass Transfer*, Vol. 32, pp. 551-561.

Ristorcelli, J. R., Lumley, J. L. & Abid, R., 1995, 'A rapid-pressure covariance representation consistent with the Taylor-Proudman theorem materially frame indifferent in the two-dimensional limit', *J. Fluid Mech.*, Vol. 292, pp. 111-152.

Speziale, C. G., Sarkar, S. & Gatski, T. B., 1991, ' Modeling the pressure-strain correlation of turbulence: an invariant dynamical system approach', *J. Fluid Mech.*, Vol. 227, pp. 245-272.

Yoo, G. J., So, R. M. C. & Hwang, B. C., 1991, 'Calculation of developing turbulent flows in a rotating pipe', *ASME J. Turbomachinery*, Vol. 113, pp. 34-41.

IMPORTANCE OF A LOCAL ROSSBY NUMBER FOR TURBULENCE IN A WAKE SUBMITTED TO ROTATION

Laurent Tarbouriech, Dominique Renouard
Laboratoire des Ecoulements Géophysiques et Industriels
UJF - INPG - CNRS
BP 53X
F-38041 Grenoble cedex 9
France

ABSTRACT

A PIV system was especially developed for the large LEGI-Coriolis rotating tank and used for experimental studies of a turbulent wake in a rotating reference frame. The wake was generated by moving a vertical cylinder and has Reynolds number $Re=10^4$ or 5.10^5. To gauge the effects of rotation we use a local Rossby number Ro_l computed with the time-averaged local vertical vorticity over two times the background rotation of the turntable. The measurements show that two mechanisms seem to act in the destabilization of an anticyclonic shear layer: one is associated with turbulent enhancement and the other with presence of strong vertical movements. Characteristics of the transverse structure of the mean longitudinal velocity, the mean vertical vorticity, and the horizontal turbulent energy imply that the shear layer is destabilized when $Ro_l<-0.5$ and most strongly destabilized at $Ro_l\simeq-1$. We observe for the first time in an experimental wake, as predicted in previous works, that the profiles of longitudinal velocity tend to be linear when Ro_l is close to -1, and the vorticity of the shear is transversally constant and opposed to the vorticity induced by the background rotation.

INTRODUCTION

The 13 m diameter rotating platform is devoted to the study of geophysical fluid dynamics. It allows for (i) high Reynolds numbers with low velocities and (ii) a very large range of Rossby numbers with low rotation rate, thus avoiding centrifugal effects. The phenomena studied on the platform often have a characteristic size of O(1 m). In this context some authors showed that the rotation acts via the Coriolis force on the tridimensional stability of the flow.

An asymmetric effect on counter-rotating shear layers is observed experimentally when rotation is applied to channel flows (Johnston et al., 1972) and to wakes (Witt and Joubert, 1985). This phenomenon was first explained by the "displaced particle" mechanism (Johnston et al, 1972; Tritton and Davies, 1981) that associates a destabilized (stabilized) shear layer with an increased (decreased) turbulence activity (Bidokhti and Tritton, 1992; Tritton, 1992). This phenomenological mechanism is in good agreement with the Bradshaw criterion (Bradshaw, 1969) which is based on an analogy between curvature and buoyancy effects and with the "Simplified Reynolds Stress Equations" scheme proposed by Johnston et al. (1972). The anticyclonic shear layer (which produces vorticity of the opposite sign of the background rotation) is destabilized when it is submitted to weak rotation but it is restabilized when the rotation becomes strong, i. e. the turbulent activity decreases so as to reach level of the cyclonic ones. This behaviour is also shown by the numerical computations of Métais et al. (1992), Andersson and Kristoffersen (1993) and Lamballais (1996).

The measurements of Watmuff et al. (1985) and some numerical simulations (Kim, 1983; Yang and Kim, 1990; Kristoffersen and Andersson, 1993) highlighted that the destabilization is accompanied by longitudinal structures which could become stronger than the eddies of the main Kelvin-Helmholtz instability (Métais et al., 1995). Lesieur et al. (1991) propose a non linear "mechanism of weak-absolute vorticity stretching" to explain the presence of these strong longitudinal vortices. Their numerical simulations shown that these structures destroy the two-dimensional anticyclonic Kelvin-Helmholtz eddies, which is confirmed by the experimental visualisations of Boyer et al. (1984), Tritton (1985) and Chabert d'Hières et al. (1989). For strong rotation, the longitudinal vortices disappear and the two-dimensional eddies are restabilized as illustrated by these numerical simulations. This phenomenon is confirmed experimentally by the visualizations of Bidokhti and Tritton (1992) and Tarbouriech (1996).

It is clear that a bulk Rossby number based on the background rotation, the initial width of the wake (e. g. the diameter of the cylinder) and the mean flow velocity can not be an efficient parameter for the effects of the rotation on the turbulent shear layers. In the quoted literature, authors used

the maximum local mean shear compared with the background rotation. Our measurements show some variations in the behaviour with the transversal direction of the wake which are not taken account by this number. After a description of the experimental set-up and the PIV (Particle Image Velocimetry) method of measurement we used, we highlight some behaviour and why a local Rossby number computed with the time averaged vertical vorticity over the Coriolis parameter (i. e. two time the background rotation) seems to be a good parameter to describe the effects of rotation on plane turbulent shear layer.

EXPERIMENTAL SET UP

The wake is generated by moving a vertical cylinder in the fluid at rest in the tank, as shown by the sketches of figure 1. The 13 m diameter, 1.2 m high tank is placed on the LEGI-Coriolis rotating platform and it is filled with H=90 cm high fresh, homogeneous water. The rotation rate of the tank is parametrised with the normalized Coriolis parameter $f=2\Omega.d/U$ (Ω is the angular velocity of the tank and d and U are defined below), which is called also the number of rotation. The 10 cm diameter (d), 1 m high cylinder is pulled at a constant speed U=5 cm/s or U=10 cm/s on a circular trajectory, thus the distance between the cylinder and the vertical wall of the tank remains constant. Consequently the experiments are performed for two Reynolds numbers $Re=Ud/\nu=5.10^3$ and 10^4; $\nu=10^{-6}m^2s^{-1}$ being the kinematic viscosity of the fresh water.

In practice all measurements take place along a half circle, starting well after the cylinder begins to move and ending well before it makes a complete circle. A 360° laser sheet lights particles which are seeded in the volume of water. The plane which is illuminated is chosen at mid-depth in order to avoid possible bottom and free surface effects. A camera is fixed at 4 m above the free surface, centred on the axis of the wake with a 1 cm precision. We measure a 1.8 m by 2.8 m area at a fixed distance from the cylinder. In order to avoid optical defects at the crossing of the free surface over the measuring area, we place a 17 mm thick, 2 m by 3 m glass sheet over it. The glass panel at the free surface, the laser sheet, and the bottom of the tank are set parallel to ±3 mm over 3 m. The camera, the glass sheet at the surface, the laser sheet generator and the vertical cylinder are linked together so that the distance L between the cylinder and the center of the measuring area remain constant during the acquisition of a time-series of pictures. This distance can be set between L=20 d and 140 d.

PIV SYSTEM

The measuring system we develop was especially adapted for the case of our large area devise of experiments as explained in detail in several publications (Tarbouriech and Didelle, 1995; Tarbouriech, 1996; Tarbouriech et al., 1997). However we will develop here the basic technique to facilitate an understanding of the following results and discussion.

The fluid is seeded at all depths with quasi-neutrally buoyant, 150 µm mean-diameter particles. A horizontal light sheet is produced at mid-depth by the scan of a continuous 4 W Argon laser beam and illuminates them (side view of figure 1). Through synchronization with a photodetector, 250 sequential photographs, each being recorded with the camera, are acquired at a rate of 4 Hz. The time-series acquisition corresponds to 12 (6) wake wavelengths in the case of $Re=10^4$ (5.10^3), and requires 10 m of film that is developed at 3200 ASA sensitivity. An 8-bit scanner digitizes the 24 mm by 36 mm images to 1282 by 1944 pixels, achieving about 1.5 mm per pixel resolution thanks to the film technique. Crosses marked permanently on the glass panel positioned at the water surface are used to precisely calibrate the position of the images relative to each other after film development and digitization. By both translating and rotating each image, the centroids of the digitized images of the crosses are aligned with subpixel accuracy.

By means of the standard cross-correlation between consecutive pairs of digitized photographs, a velocity vector field is calculated. Each vector is two-components on the plane of the laser sheet: u and v are measured in the longitudinal (x) and the transversal (y) directions of the wake, respectively. With a 250 sequential photographs it is possible to obtain 249 fields defined by 432 (1995) vectors in the case $Re=10^4$ ($Re=5.10^3$), so as to reach a spatial definition of the order of 1 d (0.5 d). We verify that the accuracy of this PIV system applied to the case of the turbulent wake is within 7 % and 15 % of the mean velocity when the $Re=5.10^3$ and 10^4 respectively.

From these time-series of velocity fields it is possible to compute fields of time averaged velocity, vertical vorticity and turbulent intensities. To enhance the convergence of these measurements the 7 (14) central, transversal profiles were averaged together so as to produce mean profile with 1750 (3500) "time"-series elements when $Re=10^4$ ($Re=5.10^3$). The following results will present transversal evolutions of the time average of each data computed as explained above.

RESULTS

Figure 2 shows the mean velocity profiles at L=40 d behind the cylinder when $Re=10^4$. On the cyclonic side (C, y<0) we see an increase of the gradient when the rotation number f increases. The profiles of the mean vertical vorticity ($\langle\omega_z\rangle=\langle\partial u/\partial y-\partial v/\partial x\rangle$), figure 3, demonstrate this trend by the growth of the maximum of $\langle\omega_z\rangle$ and show a narrowing of the cyclonic region when f increases. This behaviour is associated with the stabilization, i. e. the blocking of the energy cascade, by rotation. On the anticyclonic side (AC, y>0), for weak rotation, f=0.02, 0.03 and 0.05, the velocity profiles are wider than without rotation. This is also observable with the vorticity. This can be related to the destabilization generated by the subsequent turbulence enhancement. When rotation is strong, f=0.13 and 0.16, the velocity profiles become closer to the nonrotating case, at least for y<5.3 d and 3.4 d respectively, and this could be interpreted as restabilization. But the two profiles show a minimum for y>3.4 d and 5.3 d which are artefacts. They are due to excessive vertical velocities, as was shown by the horizontal divergence and direct vertical velocity measurements with an acoustic Doppler profiler. These strong vertical movements take the particles out the laser sheet between photographs so as to produce bad measurements.

These different behaviours evolving in the transversal direction show that a parameter based on the maximum shear of the layer related to the background rotation is not sufficient to parametrise the effects of rotation. As suggested by Lesieur et al. (1991) we use a truly local Rossby number

$Ro_l=<\omega_z>/2\Omega$ of which the transversal profiles are represented figure 4. For weak rotation we observe $Ro_l<-1$ on the anticyclonic side of the wake, and for strong rotation the trend is $-1<Ro_l<-0.5$; weak and strong rotations corresponding to the two behaviours exposed in the previous paragraph. This implies that two distinct mechanisms act in the destabilization process. The first, associated with $Ro_l<-1$, manifests itself by the enhancement of the turbulent activity, so that the profiles become wider. The second produces strong vertical movements when $-1<Ro_l<-0.5$ and it could be induced by the presence of strong longitudinal vortices generated by the "mechanism of weak absolute vorticity stretching".

Moreover, figure 5 shows that the anticyclonic velocity profiles are linear when the vorticity of the mean shear is such that $<\omega_z>\simeq -f$ and this corresponds to zones where Ro_l is close to -1. This conclusion was found by Johnston et al. (1972), Metais et al. (1995), and Lamballais (1996) but, to our knowledge, this is the first time that it has been observed experimentally in a rotating wake.

The cases with $Re=5.10^3$ reaches greater values of $|Ro_l|$. Figure 6 shows this at L=20 d behind the cylinder, and the minima outside the wake where y<-3 d are artefacts due to bad lighting of the particles. The profiles of the wake show the same behaviour as the cases $Re=10^4$: the cyclonic side is narrowed and the anticyclonic is widened when the number of rotation increases until f=0.17; this displaces the center of the wake towards the cyclonic side. When rotation becomes very strong (f=0.55) the profile is again symmetric and centered on the profile of the nonrotating case. The profiles of the local Rossby number corresponding to these case (figure 7) show that for f=0.09 and 0.17 Ro_l is close to -1 on the anticyclonic sides, so they are destabilized and they are linear with a slope such that $<\omega_z>\simeq -f$. On the other hand Ro_l is always greater than -0.5 when f=0.55 and there is a total restabilization of the Karman street. In this latter case there is not a linear profile of mean velocity. At this low Reynolds number the vertical velocities remain everytime small and thus the particles stay in the laser sheet between the images so that the measurements do not show artefacts and there are of better quality.

The relevance of Ro_l to estimate the turbulence level is further illuminated by figure 8 which shows the variations of the horizontal turbulent energy $E=<u'^2+v'^2>$ for $Re=5.10^3$ and 10^4; u' and v' are the velocity fluctuations. The E values are computed at the same locations as the Ro_l values and we plot all the Ro_l-E pairs. The nonrotating cases which correspond to $Ro_l=\infty$ have their profiles reconstituted in a separate graph. First we note that the trends are the same for the two Reynolds numbers, the high Reynolds number case is only two times more energetic than the low Re case. Second we see that the maximum of destabilization which occurs for $Ro_l\simeq -1$ corresponds to a maximum of E, and the maximum of stabilization to a minimum of E, when Ro_l tends to zero (very strong rotation or anti-rotation). The transition between destabilization and restabilization is apparently at $Ro_l\simeq -0.5$ which could appear as the neutral value of rotation. When rotation decreases E tends to the value corresponding to that of the no-rotation profile center. The evolution of $<u'^2>$, $<v'^2>$ and the standard deviation of both the vertical vorticity and the horizontal divergence are exactly similar to the E-evolution.

CONCLUSION

These measurements show that there are at least two mechanisms destabilizing a free shear layer submitted to rotation. The first manifests itself by the widening of the shear and it is identified as the result of the mixing produced by the turbulence enhancement. It is thus in good agreement with the so-called "displaced particle theory". An other mechanism is accompanied with strong vertical movements that could be the sign of the presence of longitudinal vortices and occurs when $-1<Ro_l<-0.5$. Both mechanisms act to create destabilization when $Ro_l<-0.5$, with a maximum of intensity (i. e. maximum of turbulent energy) at $Ro_l\simeq -1$. In relation to previous works our local Rossby number Ro_l takes into account the evolutions of the effects in both the longitudinal and the transversal directions, because it is computed with the mean, vertical, local vorticity over two times the background rotation. So this number seems to be better able to describe the effect of rotation on turbulent shear layers than a number computed with the maximum mean vorticity produced at the inflexional point of the shear. Moreover these experiments show clearly that when $Ro_l\simeq -1$ the profiles tend to become linear so that the mean vertical vorticity is constant in the transversal direction and has sign opposite to the rotation number. It is the first work to our knowledge showing this trend in an experimental wake.

REFERENCES

Andersson, H., Kristoffersen, R., 1993, "Reynolds-stress budgets in rotating channel flow", *Proceedings, 9th symposium on turbulent shear flows*, pp. 29.4.1-29.4.6.

Bidokhti, A., Tritton, D., 1992, " The structure of a turbulent free shear layer in a rotating fluid", *J. Fluid Mech.* 241, pp. 469-502.

Boyer, D. L., Kmetz, M., Smathers, L., 1984, "Rotating open channel flow past right circular cylinders", *Geophys. Astrophys. Fluid Dynamics*, vol. 30, pp. 271-304.

Bradshaw, P., 1969, "The analogie entre streamline curvature and buoyancy in turbulent shear flow", *J. Fluid Mech.*, vol. 36, part. 1. pp. 177-191.

Chabert d'Hières, G., Davies, P. A., Didelle, H., 1989, "Laboratory studies of pseudo-periodic forcing due to vortex shedding from an isolated solid obstacle in a homogeneous rotating fluid", *Mesoscale/synoptique coherent structures in geophysical turbulence*, éd. Nihoul J. et Jamart B., Elsevier Science Publishers, Amsterdam, pp. 639-653.

Johnston, J. P., Halleen, R. M., Lezius, D. K., 1972, "Effects of spanwise rotation on the structure of two-dimensional fully developed turbulent channel flow", *J. Fluid Mech.* 56, part. 3, pp. 533-557.

Kim, J., 1983, "The effect of rotation on turbulence structure", *Proceedings, 4th symposium on turbulent shear flows*, Karlsruhe. pp. 6.14-6.19.

Kristoffersen, R., Andersson, H., 1993, "Direct simulation of low-Reynolds-number turbulent flow in a rotating channel", *J. Fluid Mech.* 256, pp. 167-197.

Lamballais, E., 1996, "Simulations numériques de la turbulence dans un canal plan tournant", Ph.D. Thesis, Institut National Polytechnique de Grenoble.

Lesieur, M., Yanase, S., Métais, O., 1991, "Stabilizing and destabilizing effects of a solid-body rotation on quasi-two-dimensional shear layers", *Phys. Fluids* A3 (3), p. 403-407.

Métais, O., Flores, C., Yanase, S., Riley, J. J., Lesieur, M., 1995, "Rotating free-shear flows. Part 2. Numerical similations", *J. Fluid Mech.* 293, pp. 47-80.

Métais, O., Yanase, S., Flores, C., Bartello, P., 1992, "Reorganization of coherent vortices in shear layers under the action of solid-body rotation", *Proceedings, Turbulent shear flow 8.*

Tabouriech, L, 1996, "Développement d'une méthode de vélocimétrie par images de particules pour les grandes dimensions — Application à l'étude expérimentale d'un sillage turbulent soumis à la rotation", Ph.D. Thesis, Institut National Polytechnique de Grenoble.

Tarbouriech, L., Didelle, H., 1996, "PIV appliquée à des domaines de grandes dimensions sur un sillage lointain soumis à une rotation solide", *Proceedings, 6ème Colloque de visualisation et de traitement d'image*, selected article, St-Etienne 1995.

Tarbouriech, L., Didelle, H., Renouard, D., 1997, "Time-series PIV measurements in a very large rotating tank", *submitted in Experiments in fluids.*

Tritton, D., 1992, "Stabilization and destabilization of turbulent shear flow in a rotating fluid", *J. Fluid Mech.* 241, pp. 503-523.

Tritton, D. J., 1985, "Experiments on turbulence in geophysical fluid dynamics. I- Turbulence in rotating fluids", *Turbulence and predictability in geophysical fluid dynamics and climate dynamics*, pp. 172-193.

Tritton, D., Davies, P., 1981, "Hydrodynamic instabilities and the transition to turbulence", *Topics in applied physics*, Swinney and Gollb ed., Springer-Verlag, pp. 229-270.

Witt, H. T., Joubert, P. N., 1985," Effect of rotation on a turbulent wake ",*Proceedings, 5th symposium on turbulent shear flows*, pp. 21.25-21.30.

Yang, K., Kim, J., 1991, "Numerical investigation of instability and transition in rotating plane Poiseuille flow", *Phys. Fluids* A3, vol. 4. pp. 633-641.

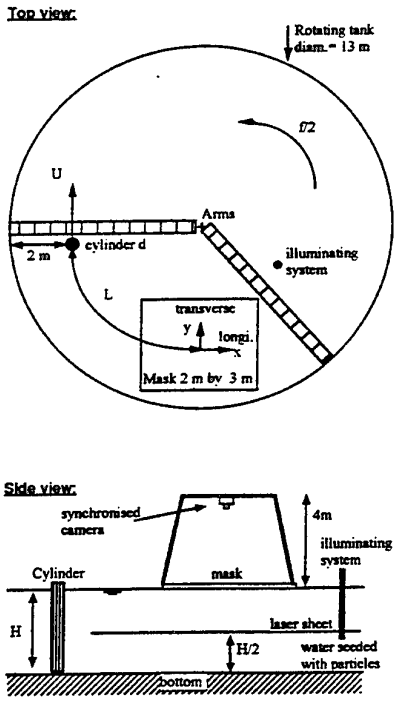


Figure 1 : Sketch of the experimental arrangements. H=1 m and L=40 d and 20 d.

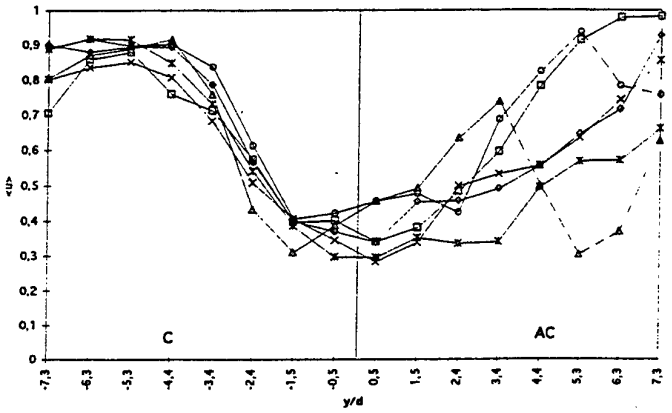


Figure 2 : Transverse profiles of the mean longitudinal velocity. Re=10^4 and L=40 d. □: f=0; ×: f=0.02; *: f=0.03; ◊: f=0.05; O: f=0.13; Δ: f=0.16.

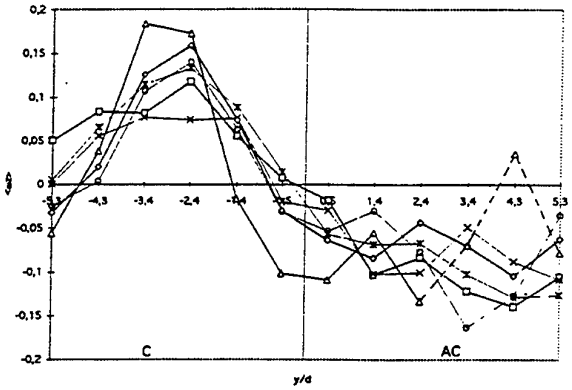


Figure 3 : Transverse profiles of the mean vertical vorticity $<\omega_z>$. Re=10^4 and L=40 d. □: f=0; ×: f=0.02; *: f=0.03; ◊: f=0.05; O: f=0.13; Δ: f=0.16.

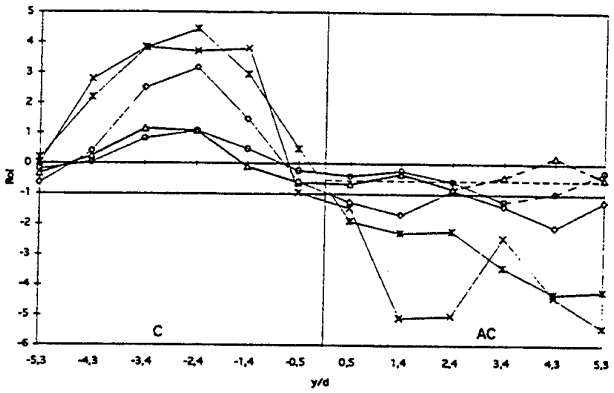


Figure 4 : Profiles of Ro_l, the dashed line represents the level Ro_l=-0.5. Re=10^4 and L=40 d. ×: f=0.02; *: f=0.03; ◊: f=0.05; O: f=0.13; Δ: f=0.16.

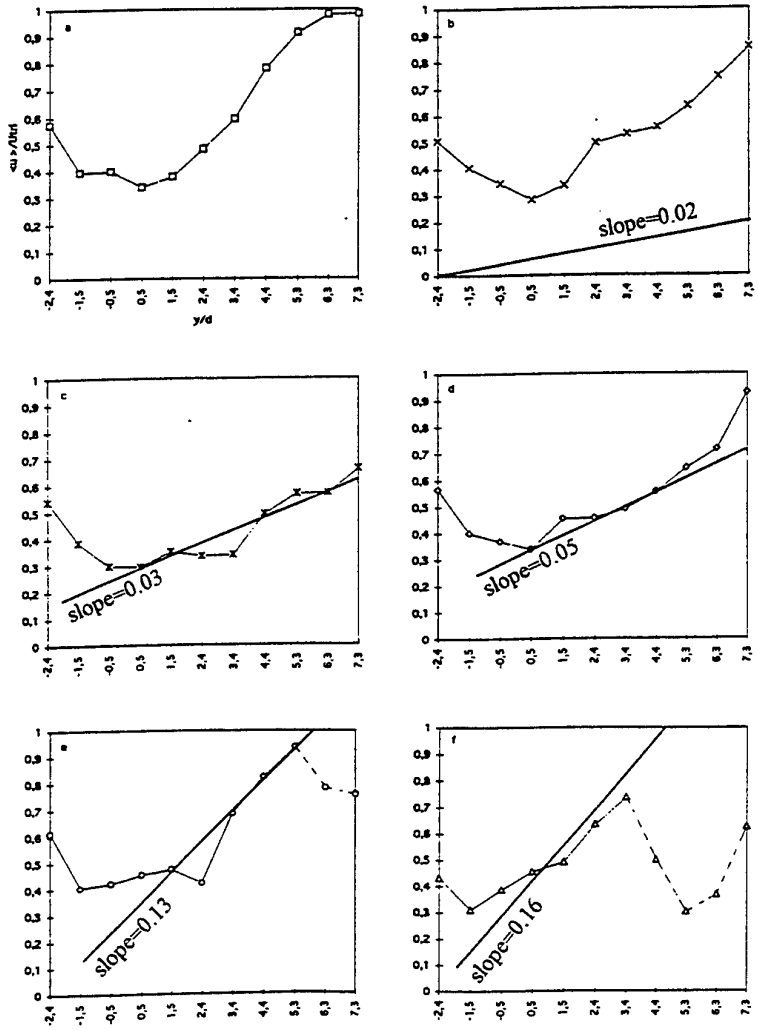


Figure 5 : Profiles of the mean longitudinal velocity on the anticyclonic side of the wake, Re=10^4 and L=40 d. The slopes -f are drawn on the profiles when the latter is linear ($Ro_l \approx -1$). a) f=0; b) f=0.02; c) f=0.03; d) f=0.05; e) f=0.13; f) f=0.16.

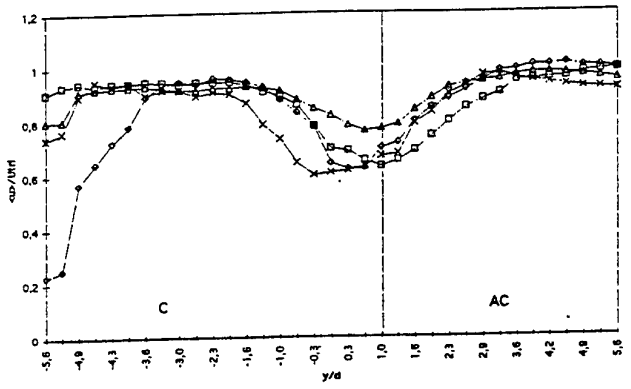


Figure 6 : Transverse profiles of the mean longitudinal velocity. Re=5.10^3 and L=20 d. □: f=0; ◊: f=0.09; ×: f=0.17; Δ: f=0.55.

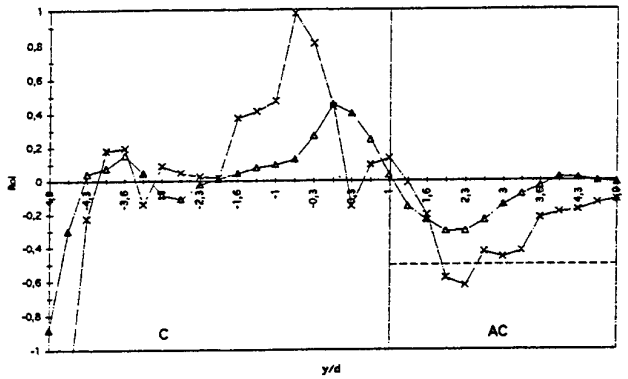


Figure 7 : Profiles of Ro$_f$, the dashed line represents the level Ro$_f$=-0.5. Re=5.10^3 and L=20 d. □: f=0; ◊: f=0.09; ×: f=0.17; Δ: f=0.55.

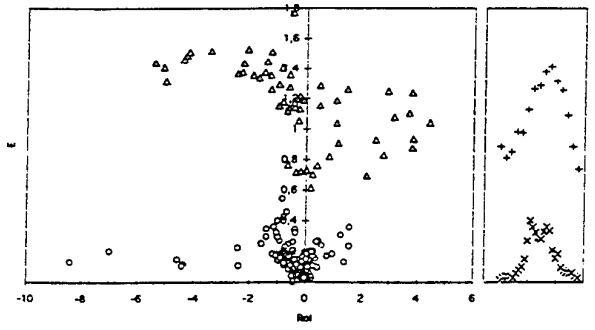


Figure 8 : Evolution of the horizontal turbulent energy E with Ro$_f$ for Re=5.10^3 (O and ×) and Re=10^4 (Δ and +). The no-rotating cases are in the separate graph.

TRANSITION TO 3-D VORTEX BREAKDOWN IN A CLOSED CYLINDER WITH A ROTATING ENDWALL

Fotis Sotiropoulos and Yiannis Ventikos
School of Civil and Environmental Engineering
Georgia Institute of Technology
Atlanta, GA 30332-0355
USA

ABSTRACT

The unsteady three-dimensional incompressible Navier-Stokes equations are solved numerically to simulate vortex breakdown in a closed cylinder with a rotating endwall. The governing equations are integrated in time using a second-order accurate finite-volume numerical method. Calculations are carried out to study the transition to three-dimensional flow occurring when the Reynolds number is increased impulsively from Re=2200, where the flow is steady and axisymmetric with two distinct breakdown bubbles, to Re=3750. The computed results show that the transition process is characterized by the growth of spiral vortices inside the outer-wall boundary layer and the initial formation of a single breakdown bubble along the cylinder axis. Subsequently, three-dimensional disturbances de-stabilize this bubble leading to its collapse and the formation of a non-axisymmetric ring of reversed instantaneous flow centered around a columnar vortex core. The results of this study are in general qualitative agreement with available laboratory observations.

INTRODUCTION

The term vortex-breakdown or vortex bursting denotes the rapid disorganization of a slender longitudinal vortex occurring when a characteristic ratio of azimuthal to axial velocity components is varied (Leibovich (1978), Esqudier (1988), Delery (1994). It was first observed to occur over delta wings and has been subsequently identified in other areas of practical interest, including atmospheric flows (tornadoes), furnaces and gas-turbine combustion chambers, and hydraulic turbine draft-tubes (Liebovich, 1978). Despite an impressive amount of experimental, theoretical, and numerical work, however, there is still neither a general theory of vortex breakdown nor general consensus as to its fundamental nature (Esqudier, 1988).

Sarpkaya (1971) was the first to establish a classification of various types of breakdown occurring when the swirl parameter--generally defined as the ratio of azimuthal to axial characteristic velocity scales--is varied. His experiments, for swirling flow through a circular diffuser, revealed three distinct types of breakdown, namely the double helix, spiral, and bubble type, each appearing with increasing swirl intensity. A more detailed classification was reported by Faler and Leibovich (1977) who identified a total of seven distinct breakdown types for a similar diffuser geometry. Esqudier (1984) carried out a detailed experimental study of flow in a closed cylindrical container with a rotating endwall over a range of rotation speeds and cylinder aspect ratios. In this idealized geometry, Esqudier was able to produce and sustain highly axisymmetric flows containing one or more, depending on the rotational speed and cylinder aspect ratio, breakdown bubbles. In a more recent study, Sorensen (1992) conducted visualization studies for a similar geometry, over a broader range of rotational speeds, and reported that above a critical rotational speed the flow became three-dimensional. The transition process he identified was characterized by the disappearance of the axisymmetric breakdown bubbles and the formation of a slender spiral vortex core rotating around the cylinder axis (Sorensen, 1992).

There have been numerous computational studies of flows with vortex breakdown using the steady and unsteady axisymmetric Navier-Stokes equations (Lopez (1990), Beran and Culick (1992), Sorensen and Christensen (1995), etc.). Three-dimensional numerical simulations have been reported, among others, by Menne (1988), Breuer and Hanel (1990), Spall et al. (1990), and Tromp and Beran (1997). Most of these studies have primarily focused on time-asymptotic breakdown structures and have successfully reproduced both bubble and spiral modes. Tromp and Beran (1997) were the first to investigate the transition from axisymmetric bubble breakdown to the spiral mode for flow through a straight pipe with an axisymmetric throat. Their work demonstrated that vortex strengths which result in non-unique solutions of the axisymmetric Navier-Stokes equations (Beran and Culick (1992)) are also associated with loss of stability to three-dimensional disturbances, a process which eventually leads to transition from bubble to spiral breakdown.

The objective of the present work is to investigate computationally the transition to three-dimensional flow in a closed cylinder driven by a rotating endwall (Escudier (1988), Sorensen (1992)). This geometry is computationally

very convenient since, unlike pipe configurations, it eliminates numerical uncertainties due to inflow and outflow boundary conditions. Yet, as discussed above, previous experiments (Esqudier (1984), Sorensen (1992)) have shown that by appropriately varying the Reynolds number ($=\Omega R^2/\nu$ where Ω is the endwall angular velocity, R is the cylinder radius, and ν is the kinematic viscosity), the flow inside the cylinder can exhibit most of the fundamental physics associated with the various regimes of vortex breakdown. A cylinder aspect ratio of H/R=2 (H is the cylinder length) is selected herein which corresponds to the geometry studied experimentally by both Esqudier (1984) and Sorensen (1992). The numerical approach is based on the finite-volume artificial compressibility method of Sotiropoulos and Ventikos (1997) which solves the unsteady, three-dimensional Navier-Stokes equations in generalized curvilinear coordinates.

THE NUMERICAL METHOD

The present method solves the unsteady, three-dimensional, incompressible Navier-Stokes equations using a dual time-stepping artificial compressibility approach (Sotiropoulos and Ventikos, 1997). The governing equations are formulated in generalized, non-orthogonal, curvilinear coordinates and discretized on a non-staggered mesh via a conservative finite-volume scheme. The convective and viscous terms are approximated using three-point, second-order accurate central-differencing. Fourth-difference, third-order matrix-valued artificial dissipation (Lin and Sotiropoulos (1997a)) terms are explicitly introduced into the discrete governing equation for stability. The spatial resolution of the matrix valued dissipation scheme has been analyzed in detail by Lin and Sotiropoulos (1997a, b) on both uniform and highly-stretched, large aspect ratio meshes.

The physical time derivative in the momentum equations is discretized using a backward second-order accurate formula. A pseudo-temporal derivative is introduced in the unsteady Navier-Stokes equations in order to facilitate the satisfaction of the continuity equation. At every physical time step, this dual-time derivative is driven to a prescribed small tolerance, via a pointwise implicit, Runge-Kutta algorithm enhanced with local (dual) time-stepping, implicit residual smoothing and multigrid acceleration. For further details the reader is referred to Lin and Sotiropoulos (1997a, b) and Sotiropoulos and Ventikos (1997).

FLOW CASE AND COMPUTATIONAL DETAILS

The test case studied herein is flow inside a closed cylindrical container, of aspect ratio H/R=2, driven by a rotating endwall (see Fig. 1). The visualization experiments of Esqudier (1984) and Sorensen (1992) have shown that the flow remains steady and axisymmetric with one ($1500<Re<1800$), two ($1800<Re<2400$), and again one ($2400<Re<2600$) breakdown bubbles for Reynolds numbers less than 2600. At higher Reynolds numbers ($2600<Re<3000$) the flow becomes unsteady with a single axisymmetric breakdown bubble oscillating periodically along the cylinder axis. Further increase of the Reynolds number ($Re>3000$) causes the flow to undergo a dramatic transition resulting to the collapse of the oscillating bubble structure and the formation of a slender vortex core subject to moving wave trains (Sorensen, 1992). At even higher Re ($\cong 3500$), Sorensen (1992) reported that this vortex starts precessing around the axis in a spiral fashion.

The present study seeks to investigate the transition from bubble breakdown to a columnar vortex state. Calculations are first carried out for Re=2200 and the computed steady-state solution is used to initialize the calculation at Re=3750. The computed results discussed below focus exclusively on elucidating the early stages of the transition process. The time asymptotic solution at Re=3750 will be the subject of a future investigation.

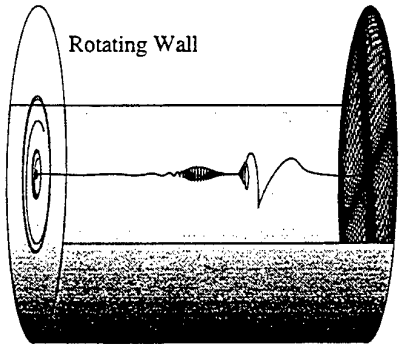


Figure 1. The Esqudier (1984) cylinder.

The computational mesh consists of 100x53x53 nodes in the x-, y-, and z-directions respectively (see Fig. 1). The mesh nodes are spaced uniformly in the axial direction while a stretched mesh is used in the transverse plane (the grid nodes are clustered near the solid walls and the cylinder axis using hyperbolic tangent stretching). It is important to point out that the non-axisymmetric topology of the computational mesh ensures that numerically induced three-dimensional disturbances are always present during the computation. A physical time step of $\Delta t=0.02$ is employed to integrate the flowfield in time. That is, approximately 314 time steps are required for the moving endwall to complete one revolution (2π non-dimensional time units are required for one revolution). For each physical time-step the pseudo-time iterative procedure is declared converged when the residuals for all primitive variables have been reduced below 10^{-8}. This convergence level is typically achieved within 2 to 20 multigrid cycles.

In all subsequently presented figures, time is measured from the moment when the Reynolds number is increased impulsively to 3,750.

RESULTS AND DISCUSSION

The collapse of the axisymmetric breakdown bubbles and the growth of three-dimensional disturbances are depicted in Fig. 2, which shows a sequence of instantaneous views of the computed flowfield in terms of: i) velocity vectors on the y=0 plane; and ii) the u=0 iso-surface (where u is the axial velocity component). The vector plots also include the u=0 contour which in conjunction with the corresponding iso-surface serves to clarify the three-dimensional structure of the reversed flow region. For clarity, however, the piece of the u=0 iso-surface that demarcates the interface between the outer-wall flow, directed from the rotating to the stationary wall, and the core has been omitted from the three-dimensional plots.

In agreement with the experimental observations (Esqudier (1984)) the flow at Re=2200 was found to be steady with two distinct axisymmetric breakdown bubbles forming along the axis of the cylinder (t=0 in Fig. 2). During the early stages of the impulsive acceleration to Re=3750, the core flow remains axisymmetric but the rear bubble grows significantly in size and collides with the front bubble to

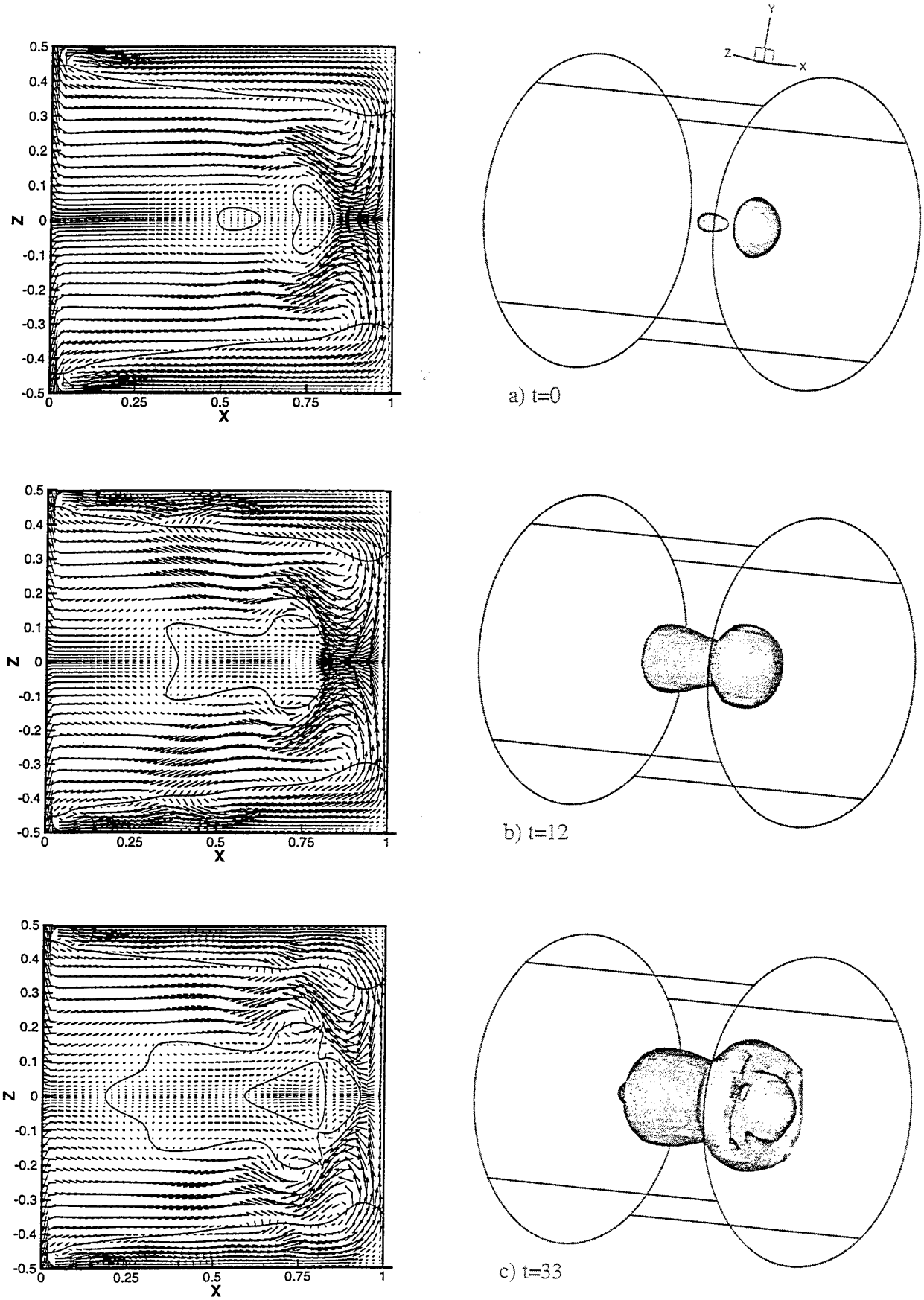
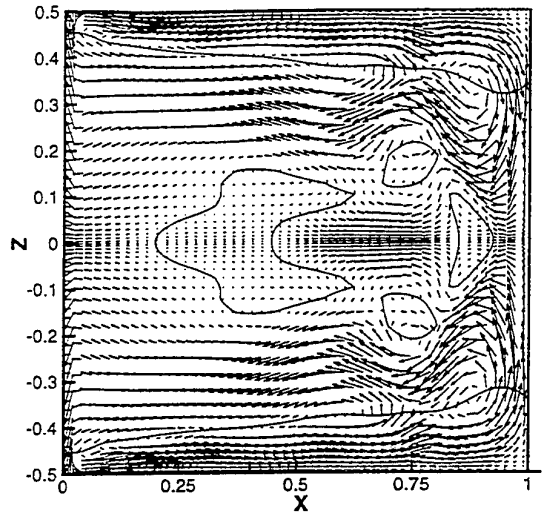
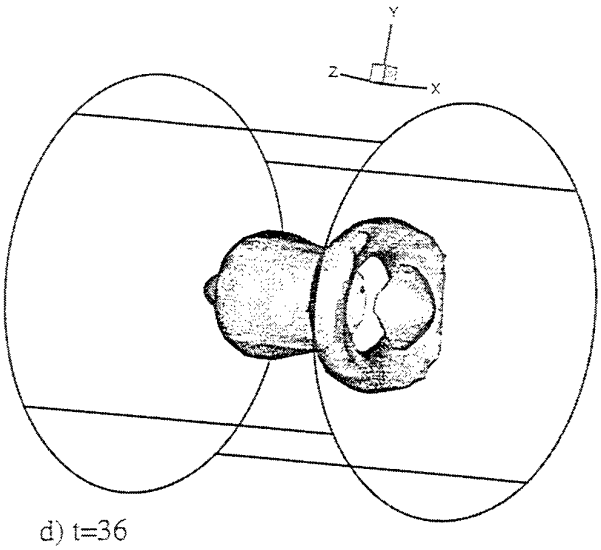
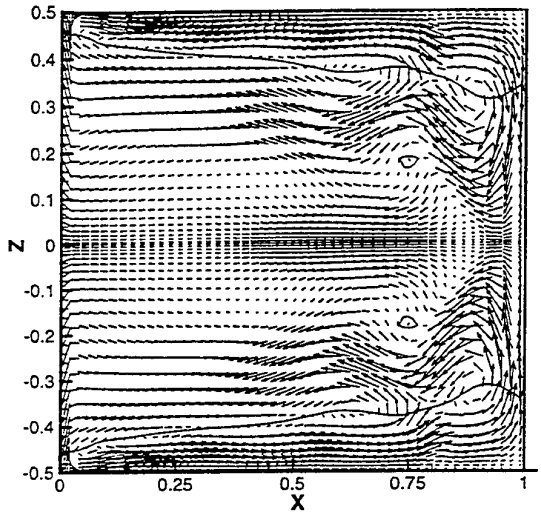


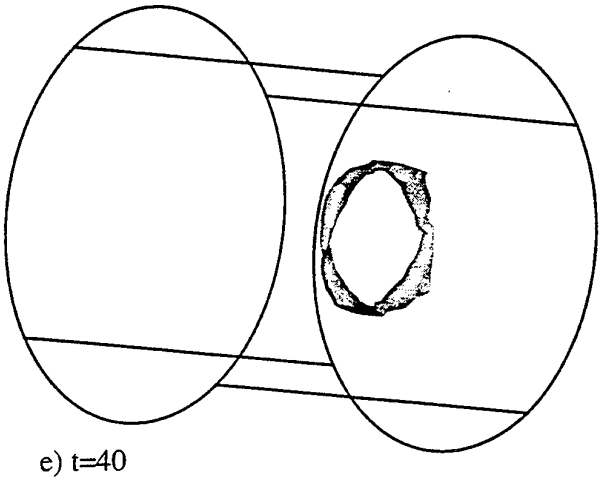
Figure 2. Velocity vectors and u=0 contour on the y=0 plane (left) and u=0 iso-surface (right)



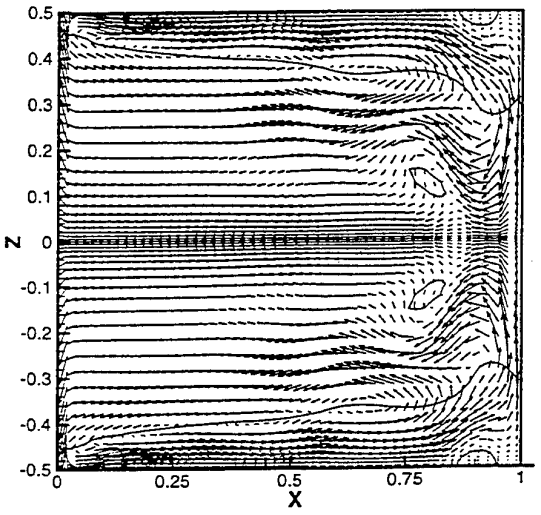


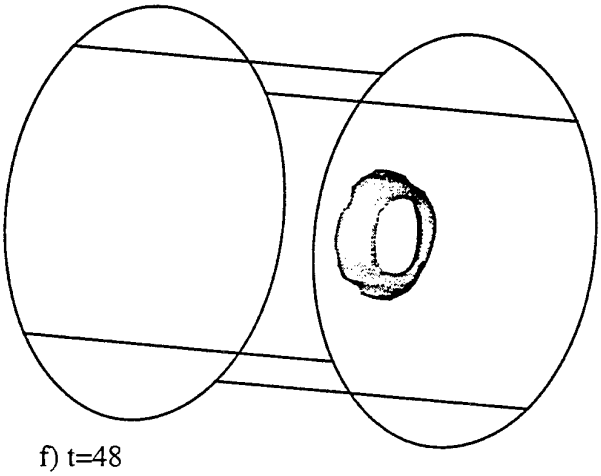
d) t=36





e) t=40





f) t=48

Figure 2. For caption see previous page

form a single structure of reversed instantaneous flow (t=12 in Fig. 2). A remarkable feature in the vector plot of Fig. 2b is the appearance of very intense vortical cells at the interface between the outer flow and the core. Three-dimensional visualizations of the flow field clearly show that these cells are actually the footprints, on the y=0 plane, of spiral vortical structures that develop inside the cylindrical wall boundary layer. This is shown in Fig. 3 which depicts an instantaneous iso-surface of constant radial velocity component (u_r=-0.004) at t=40. Note that this later time, which corresponds to Fig. 2e discussed below, is selected because these vortical structures originate as ring-like vortices and evolve into well defined spirals after several revolutions of the rotating wall (the evolution of these structures will be presented and discussed in detail in a future publication currently in preparation). Similar cells have been observed in the spin-down experiments of Weidman (1976) and the more recent vortex-tube experiment of Escudier et al. (1982). Both studies attributed the origin of such spiral vortices to centrifugal instability of the boundary layer at the outer wall.

At approximately t=20, non-axisymmetric disturbances begin to distort the front (as viewed from the stationary wall) part of the u=0 iso-surface. These disturbances grow rapidly with time and, as seen in Fig. 2c (t=33), render the flow in the vicinity of the stationary wall three-dimensional (as suggested by the shape of the velocity iso-surface, the flow is still axisymmetric in the rear part of the reversed flow region). There are several important features that are clearly evident in Fig. 2c. Although the distorted shape of the iso-surface indicates three-dimensional flow, the vector plot reveals that the flow is symmetric with respect to the axis on θ=constant planes (where θ is the azimuthal angle). This feature, which is observed throughout the present simulation, suggests that the initially axisymmetric flow was de-stabilized by disturbances of even azimuthal wave numbers. The mechanism that triggers the growth of such disturbances is not entirely clear at the moment. Detailed examination of the computed solutions, however, appears to suggest that their emergence is closely linked to the formation of the spiral vortices in the outer wall boundary layer. Furthermore, the breakdown bubble undergoes impressive structural changes, as a region of negative axial velocity develops within its interior, its length grows to approximately 70 percent of the cylinder height, and moves closer to the stationary wall. Yet another significant change of the flow structure, is the reduction of the axial velocity component observed near the axis just upstream of the breakdown bubble. As shown in Figs. 2a and 2b, the axial flow in this region initially exhibits a very pronounced jet-like profile. This shape can be readily explained by continuity arguments and the very strong radial convergence of the stationary-wall Ekman layer toward the center. Fig. 2c, however, suggests a more uniform axial flow profile

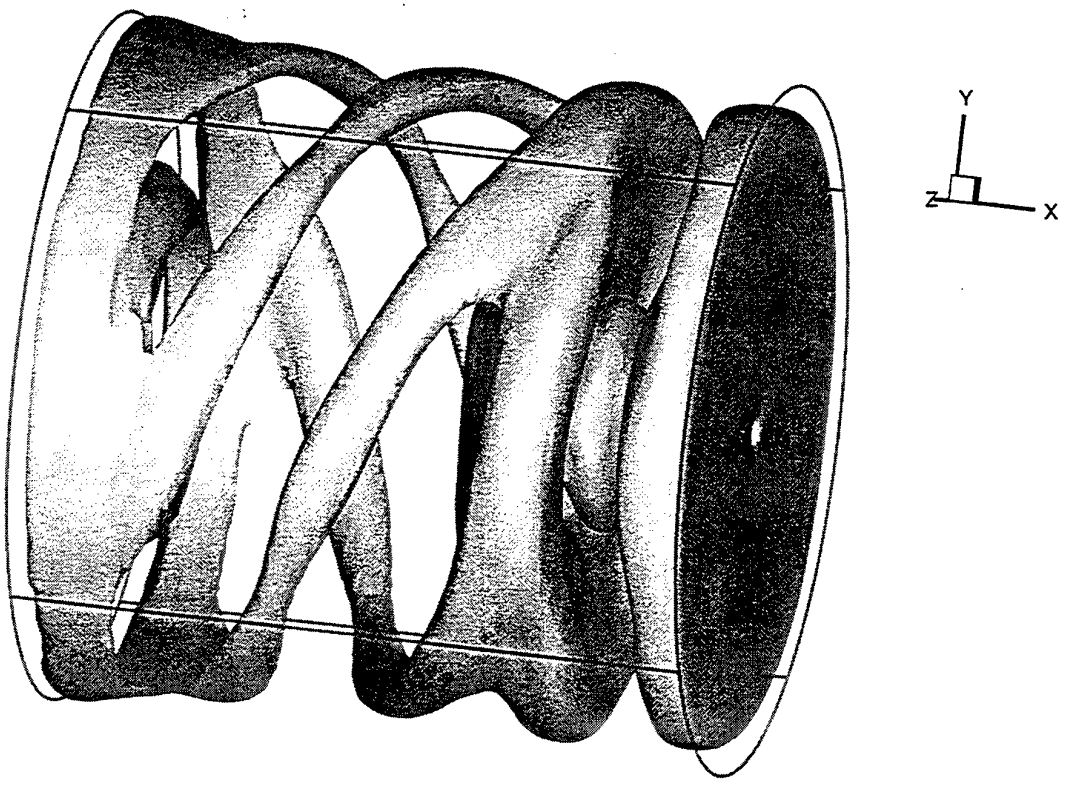


Figure 3. Surface of constant radial velocity (u_r=-0.004) at t=40.

which could be attributed to enhanced radial mixing at the interface with the outer flow induced by the spiral vortices.

The reversed flow bubble breaks down very rapidly in three pieces, two bubble-like structures and a ring, as shown in Fig. 2d which depicts the calculated flowfield at t=36. Shortly thereafter, the two bubbles disappear and only the ring of recirculating flow remains (see Fig. 2e). No stagnation point is present along the cylinder axis where the flow exhibits a columnar vortex structure. Note that most of the axial flow is deflected radially away from the axis but, unlike earlier times (see Figs. 2a to d), this deflection is not sufficiently strong to cause a stagnation point to form on the axis. In fact, the deflected flow starts converging sharply toward the axis almost immediately downstream.

As suggested by Fig. 2f, t=48, the size of the reversed flow ring is oscillating in time but the general quantitative flow features remain the same. Of particular interest is the waviness of the flow around the axis which suggests the propagation of wave-trains along the vortex core.

The present computations are in general agreement with the experimental observations of Sorensen (1992) who also reported a similar collapse of the breakdown bubble and the formation of a slender vortex core subject to moving wave trains. One apparent qualitative discrepancy between the calculations and Sorensen's work is with regard to the Reynolds number at which these phenomena emerge. As already discussed above, Sorensen reported that the columnar vortex structure forms at approximately Re≅3,000 followed by the formation of a spiral core at Re≅3,500. The present calculations were carried out at Re=3,750 and no tendency toward a spiral formation was detected. Since the temporal integration of the flowfield has not been carried out long enough to reach a time asymptotic state, however, no definite conclusions can be drawn at this point. This will be the subject of a future more comprehensive investigation.

CONCLUSIONS

The rotating flow of incompressible fluid inside a circular cylinder with a moving endwall was studied numerically by solving the unsteady, three-dimensional Navier-Stokes equations. Calculations were carried out at a Reynolds number for which previous experiments suggest the emergence of three-dimensional flow. The computed results reveal a number of complex flow phenomena and interactions which dominate the transition process. These include, among others,: i) the formation of spiral vortices inside the cylindrical wall boundary layer, presumably driven by centrifugal instability; ii) the growth of three-dimensional disturbances of even azimuthal wave numbers which result in symmetric, about the axis, flow at θ=const. planes; and iii) the rapid growth and subsequent collapse of a very large breakdown bubble leading to the formation of a columnar vortex subject to moving wave-trains.

The present study revealed a number of previously unexplored phenomena but also raised several questions that require further investigation. Future work will focus on: i) establishing time asymptotic solutions; ii) clarifying the origin and structure of the helical outer flow vortices and their role in the emergence of three-dimensional flow; and iii) elucidating the mechanisms that lead to the evolution of the columnar vortex flow into of a precessing spiral as suggested by the experiments.

ACKNOWLEDGMENTS

This work was supported by Voith Hydro. Inc. and the U.S. Department of Energy under the Advanced Hydroturbine Project. All calculations were carried out on the Cray C-90 supercomputer at the San Diego Supercomputer Center.

REFERENCES

Beran, P. S. and Culick F. E. (1992), "The Role of Non-Uniqueness in the Development of Vortex Breakdown in Tubes," *Journal of Fluid Mechanics* 242, pp. 491-527.

Breuer, M. and Hanel, D. (1990), "Solution of the 3-D Incompressible Navier-Stokes Equations for the Simulation of Vortex Breakdown," *8th GAMM-Conference on Numerical Methods in Fluid Mechanics*, 29, pp. 42-51.

Brucker, C. (1993), "Study of Vortex Breakdown by Particle Tracking Velocimetry (PTV). Part 2: Spiral-type Vortex Breakdown," *Experiments in Fluids* 15, pp. 133-139.

Delery, J. M. (1994), "Aspects of Vortex Breakdown," *Progress in. Aerospace Science* 30, pp. 1-59.

Esqudier, M. P., Bornstein J. and Maxworthy T. (1982), "The Dynamics of Confined Vortices," *Proc. of the Royal Society of London* A 382 , pp. 335-360.

Esqudier, M. P. (1984), "Observations of the Flow Produced in a Cylindrical Container by a Rotating Endwall," *Experiments in Fluids* 2(4), pp. 189-196.

Esqudier, M. P. (1988), "Vortex Breakdown: Observations and Explanations," *Prog. Aerospace Science* 25, pp. 189-229.

Faler, J. H., and Leibovich, S. (1977), "Disrupted States of Vortex Flow and Vortex Breakdown," *Physics of. Fluids* 20(9), pp. 1385-1400.

Leibovich, S. (1978), "The Structure of Vortex Breakdown," *Ann. Rev. of Fluid Mechanics* 10, pp. 221-246.

Lin, F., and Sotiropoulos, F. (1997a), "Assessment of Artificial Dissipation Models for Three-Dimensional, Incompressible Flow Solutions," to appear in the *ASME Journal of Fluids Engineering*.

Lin, F., and Sotiropoulos, F. (1997b), "Strongly-Coupled Multigrid method for 3-D Incompressible Flows Using Near-Wall Turbulence Closures," to appear in the *ASME Journal of Fluids Engineering*.

Lopez, J. M. (1990), "Axisymmetric Vortex Breakdown Part 1. Confined Swirling Flow," *Journal of Fluid Mechanics* 221, pp. 533-552.

Menne, S. (1988), "Simulation of Vortex Breakdown in Tubes," AIAA Paper 88-3573.

Sarpkaya, T. (1971), "On Stationary and Traveling Vortex Breakdowns," *Journal of Fluid Mechanics* 45 (3), pp. 545-559.

Sorensen, J. N. (1992), "Visualization of Rotating Fluid Flow in a Closed Cylinder," Report No. AFM 92-06, Department of Fluid Mechanics, Technical University of Denmark.

Sorensen, J. N., and Christensen, E. A. (1995), "Direct Numerical Simulation of Rotating Fluid Flow in a Closed Cylinder," *Physics of. Fluids* 7 (4), pp. 764-778.

Sotiropoulos, F., and Ventikos, Y. (1997), " A Three-Dimensional Numerical Method for Simulating Unsteady Vortex Breakdown in Confined Swirling Flows," *1997 ASME Fluids Engineering Division Summer Meeting*, Paper FEDSM97-3671, Vancouver, Canada.

Spall, R. E., Gatski, T. B., and Ash, R. L. (1990), "The Structure and Dynamics of Bubble-Type Vortex Breakdown," *Proceedings of Royal Society of London A* 429, pp. 613-637.

Tromp, J. C.. and Beran P. S. (1997), "The Role of Non-Unique Axisymmetric Solutions in 3-D Vortex breakdown," *Physics of. Fluids* 9(5), pp. 992-1002.

Weidman, P. D. (1976), "On the Spin-Up and Spin-Down of a Rotating Fluid. Part 2. Measurements and Stability," *Journal of Fluid Mechanics* 77(4), pp. 709-735.

POSTER SESSION - 3

BLOWING WITH GAS OR WATER

J. BELLETTRE, F. BATAILLE, A. LALLEMAND

Centre de Thermique de Lyon, UPRES A CNRS 5008
INSA de Lyon
20 av. Albert Einstein,
69621 Villeurbanne Cedex,
FRANCE

ABSTRACT

The heat and mass transfer in turbulent boundary layer submitted to injection is studied in order to protect walls subject to high thermal stresses. The main flow is gas (air) and the coolant fluid can be either air or water vapor. The equations of the problem are modeled using a RNG k-ε model and the blowing through a porous plate seen as a micro-injection, the porous plate considered seen as a succession of walls and pores. Results on the velocity and temperature profiles, friction factors and Stanton numbers for different injection rates are obtained for air and vapor injection. Furthermore, they are compared with the literature results showing a good agreement.

I - INTRODUCTION

The effect of injection in a turbulent boundary layer has a lot of applications, nevertheless, the most important is the cooling of porous solid materials which are exposed to high temperature such as nozzle surfaces of rocket motor and need to be protected.

Many authors studied the problem of boundary layer linked with incoming coolant flow. To take into account the blowing, different ways were used as modified law of wall of Stevenson (1968) or Simpson (1970), modified mixing length models (Kays 1972, Landis and Mills 1972) or modified low Reynolds models of So and Yoo (1987), Campolina Franca et al. (1995). Our approach is different and consists to directly model the injection (by considering the porous plate like a succession of walls and pores) and to use a classical model of turbulence for the main flow (for more details, see Bellettre et al. 1997a). This method has the advantage of not using different mathematical modifications due to the blowing (which have to be adapted to each case) but of treating directly the problem.

In this paper, we first present the case of injection with air (the coolant fluid is the same than the main flow); secondly, we focus on injection with water vapor. In both cases, we are interested in the behavior of the fluid dynamic (velocity profile, friction factor) and in the thermal aspect (wall temperature, temperature profile, Stanton number). The objective is to adapt our approach of injection to a different specie and to compare the results with other studies (Romanenko and Kharchenko (1963) or Landis et Mills (1972))

II - PRESENTATION OF THE STUDY

This paper is concerned with the study of a turbulent boundary layer submitted to injection through a porous plate. The configuration of the problem is illustrated in figure 1. Air flows within a 0.2 meter high channel at a steady state. The floor is first constituted of an impermeable wall (1.30 m), then of a porous plate (30 cm) where the cold air is injected. The main flow has a longitudinal velocity, U_1, equal to 10 m/s and the longitudinal turbulent intensity, I_u, is 1 %. The Reynolds number is high enough so that the boundary layer is turbulent before the porous plate. Furthermore, the boundary layer of the developing turbulent flow is two-dimensional. We note x_1 the longitudinal coordinate and x_2 the vertical one (the origin being in the bottom left corner of the channel). This configuration corresponds to the test channel of our laboratory. Consequently, for air injection, the numerical results, for the dynamic and the thermal aspects, can be compared and validated by experimental measurements (Rodet et al., 1997).

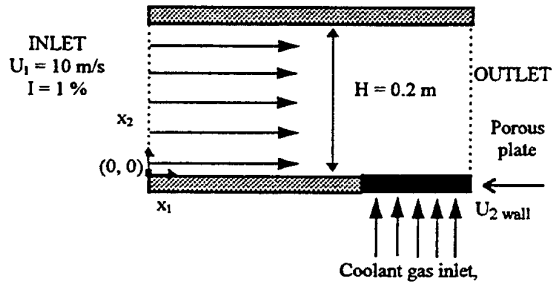


figure 1. Configuration of the problem.

The equations are the continuity, momentum and energy ones where the Reynolds decomposition is applied (equations (1)-(3)). Furthermore, when the case of injection with different species (air-water vapor) is treated, vapor mass budget (4) and diffusion law (5) are added.

$$\frac{\partial \rho U_j}{\partial x_j} = 0 \tag{1}$$

$$\frac{\partial}{\partial x_j}\left(\rho U_i U_j\right) = -\frac{\partial P}{\partial x_i} + \frac{\partial}{\partial x_j}\left(\mu\left[\frac{\partial U_i}{\partial x_j} + \frac{\partial U_j}{\partial x_i}\right] - \frac{2}{3}\mu\frac{\partial U_i}{\partial x_i} - \rho\overline{u_i' u_j'}\right) \tag{2}$$

$$\frac{\partial}{\partial x_j}\left(\rho U_j H\right) = \frac{\partial}{\partial x_j}\left(k_c \frac{\partial T}{\partial x_j}\right) - \frac{\partial}{\partial x_j}\left(\rho\overline{u'_j h'}\right) + U_j \frac{\partial P}{\partial x_j} - \frac{\partial}{\partial x_j}\left(H_v J\right) \tag{3}$$

$$\frac{\partial}{\partial x_j}\left(\rho U_j C\right) = -\frac{\partial}{\partial x_j}(J) \tag{4}$$

$$J = -(\rho D + \frac{\rho \nu_t}{\sigma_m})\frac{\partial C}{\partial x_i} \tag{5}$$

where U, H and P are the mean values of velocity, enthalpy and pressure, u' and h' the velocity and enthalpy fluctuations, ρ the fluid density, μ the dynamic viscosity, k_c the thermal conductivity for the mixture. For the vapor specie, J is the diffusion flux, H_v is the mean value of enthalpy, C the local mass fraction, D the diffusive coefficient in air and σ_m the turbulent Schmidt number (σ_m = 1). In these equations ρ, μ and k_c are temperature and concentration dependent and D is temperature dependent according to tabulated values.

The turbulent Reynolds stresses (equations (6) and (7)) are modeled using a RNG k-ε model (Yakhot and Orszag, 1986).

$$\overline{u'_i u'_j} = -\nu_t\left(\frac{\partial U_i}{\partial x_j} + \frac{\partial U_j}{\partial x_i}\right) + \frac{2}{3}\nu_t \frac{\partial U_i}{\partial x_i}\delta_{ij} + \frac{2}{3}k\,\delta_{ij} \tag{6}$$

$$\overline{u'_j h'} = -\frac{\nu_t}{\sigma_h}\frac{\partial c_p T}{\partial x_j} \tag{7}$$

with σ_h = 0.7 (turbulent Prandtl number) and c_p the mixture specific heat. ν_t is determined by k, the turbulent kinetic energy and ε, the dissipation rate of k, according the relation (8).

$$\nu_t = \nu_{mol}\left\{\left(1 + \sqrt{\frac{C_\mu}{\nu_{mol}}}\frac{k}{\sqrt{\varepsilon}}\right)^2 - 1\right\} \tag{8}$$

where ν_{mol} is the molecular kinetic viscosity and C_μ = 0.0845.

Furthermore, k and ε are obtained from the solution of their respective model transport equations (9) and (10).

$$U_j\frac{\partial k}{\partial x_j} = \frac{\partial}{\partial x_j}\left[\alpha\nu_t\frac{\partial k}{\partial x_j}\right] + \nu_t\left(\frac{\partial U_i}{\partial x_j} + \frac{\partial U_j}{\partial x_i}\right)\frac{\partial U_i}{\partial x_j} - \varepsilon \tag{9}$$

$$U_j\frac{\partial \varepsilon}{\partial x_j} = \frac{\partial}{\partial x_j}\left(\alpha\nu_t\frac{\partial \varepsilon}{\partial x_j}\right) + C_{\varepsilon 1}\frac{\varepsilon}{k}\nu_t\left(\frac{\partial U_i}{\partial x_j} + \frac{\partial U_j}{\partial x_i}\right)\frac{\partial U_i}{\partial x_j} - C_{\varepsilon 2}\frac{\varepsilon^2}{k} - R \tag{10}$$

with, α = 1.39, $C_{\varepsilon 1}$ = 1.42, $C_{\varepsilon 2}$ = 1.68 and $R = \nu_{mol}\left(\frac{\partial U_i}{\partial x_j} + \frac{\partial U_j}{\partial x_i}\right)\left(\frac{\partial u'_i}{\partial x_j}\frac{\partial u'_i}{\partial x_i}\right)$ (calculated according to an algebraic relation).

The near wall effects are taken into account by the Launder and Spalding (1974) logarithmic-law of the wall (11), used under condition of equilibrium. This law is used only for the grid point the nearest from the wall.

$$\frac{U}{U^*} = \frac{1}{\kappa}\ln(Ey^+) \tag{11}$$

for $11 < y^+ < 100$ and where $U^* = \sqrt{\tau_w/\rho} = C_\mu^{1/4} k_p^{1/2}$.

τ_w is the wall shear stress, κ is the von-Karman's constant, E is an empirical constant set equal to 9.8 (smooth wall) and $y^+ = \frac{\rho C_\mu^{1/4} k_p^{1/2} x_2}{\mu} = \frac{\rho U^* x_2}{\mu}$. k_p, the near wall value of k, is determinate by solving the complete transport equation for k with a zero normal gradient assumed at the wall. The boundary condition for ε (ε_p) is given by the equilibrium assumption implying (12).

$$\varepsilon_p = \frac{C_\mu^{3/4} k_p}{\kappa x_{2p}} \tag{12}$$

(x_{2p} being the nearest wall point in vertical coordinate).

For the thermal boundary conditions on the wall, the Launder and Spalding (1974) logarithmic-law of the wall (13) is used for the nearest grid point.

$$\frac{k_c(\Delta T/x_2)}{q} = \frac{1}{\kappa y^+}\frac{\sigma_h}{Pr}\ln\left(Ey^+\right) + \frac{1}{y^+}\left(\frac{\sigma_h}{Pr}\right)^{5/4}\frac{\pi/4}{\sin(\pi/4)}\left(\frac{A}{\kappa}\right)^{1/2}\left(\frac{Pr}{\sigma_h} - 1\right) \tag{13}$$

where q is heat transfer at the wall, $\Delta T = T_w - T_p$ (T_w is the wall temperature and T_p is the near wall temperature), Pr the

fluid Prandtl number, σ_h the turbulent Prandtl number (1.2 near the wall) and A the van Driest constant (A = 26). T_w can be either fixed or calculated according external heat transfer boundary conditions.

These equations permit to solve the motion and the heat transfer of the turbulent boundary layer (numerical method can be seen in Bellettre et al., 1997a). In other hand, we model the blowing by seeing the porous plate as a succession of walls and pores. Consequently, the injection is modeled as a succession of shear stress and fluid source (where the coming fluid is laminar) and the boundary layer is submitted to these two phenomena (Bellettre et al., 1997a).

III - RESULTS WITH AIR

In a first time, we considered injection with air, that is to say that the main flow and the injected flow are same species.

In figure 2, we plotted the longitudinal velocity profile with and without injection. These results correspond to different injection rate ($F = (\rho U_2)_{wall} / (\rho U_1)_{main\ flow}$) varying from 0 to 2%. We can observe that the flow is affected by the injection and leads to an important increase of the boundary layer when the injection rate increases.

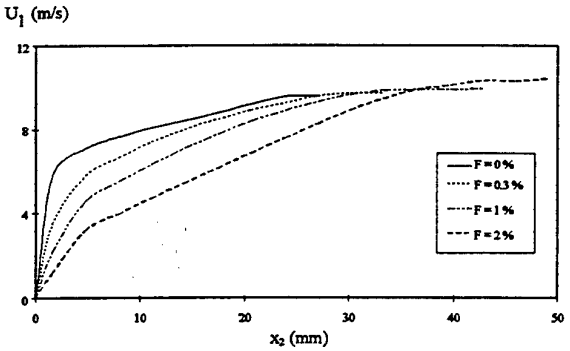


figure 2. Velocity profiles for $0 \le F \le 2$ %.

In figure 3, we plotted the temperature profile for different injection rates in the case where the main flow temperature is 200°C and the temperature of the injected fluid is 100°C. We can see that the temperature closed to the wall decreases a lot, particularly at high injection rate. Consequently, with injection, the heat transfer is reduced and the plate is, then, protected.

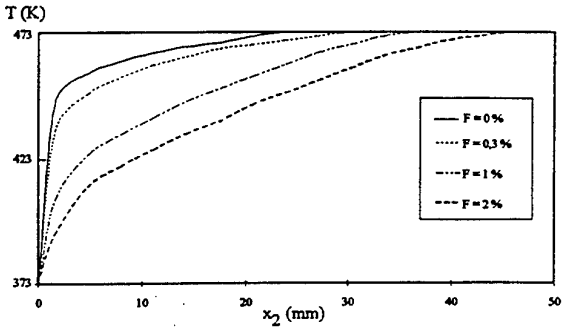


figure 3. Temperature profiles for $0 \le F \le 2$ %.

It has to be noticed that these results, on the velocity and on the temperature, using our model of the porous plate submitted to injection, has been validated with experimental works in Bellettre et al. (1997a).

In this study, we are although interested in the friction factor when blowing occurs. The friction factor (defined by the equation 14), is calculated according to Simpson et al. (1969) correlation (15) where the friction factor without blowing, C_{f0}, is determined by Andersen et al. (1975) relation (16).

$$\frac{C_f}{2} = \frac{\tau_w}{(\rho\ U^2)_{main\,flow}} \tag{14}$$

$$\left.\frac{C_f}{C_{f0}}\right|_{Re_\theta} = \left[\frac{\ln(1+B_f)}{B_f}\right]^{0.7} \tag{15}$$

$$\frac{C_{f0}}{2} = 0.012 Re_\theta^{-0.25} \tag{16}$$

where $B_f = 2\ F\ /\ C_f$, $0.2 < 1 + B_f < 65$ and $\theta = \int_0^\infty \frac{\rho U_1}{(\rho\ U_1)_{main\,flow}}\left(1 - \frac{U_1}{U_{1main\,flow}}\right) dx_2$ (calculated by numerical data integration).

The Stanton number (defined by relation (17)) permits to calculate the heat transfers coefficient, h, between main flow and the wall.

$$St = \frac{h}{(\rho c_p U_1)_{main\,flow}} \tag{17}$$

By the following, we although calculated the Stanton number for different injection rate using the correlation of Whitten et al. (1970) (equation 18).

$$\left.\frac{S_t}{S_{t0}}\right|_{Re_\Delta} = \left[\frac{\ln(1+B)}{B}\right]^{1.25} (1+B)^{0.25} \tag{18}$$

with $S_{t0} = 0.0128 Re_\Delta^{-0.25} Pr^{-0.5}$, $B = F\ /\ S_t$ and $\Delta = \int_0^\infty \frac{\rho U_1}{(\rho U_1)_{main\,flow}} \frac{T - T_{main\,flow}}{T_w - T_{main\,flow}} dx_2$ (calculated by numerical data integration).

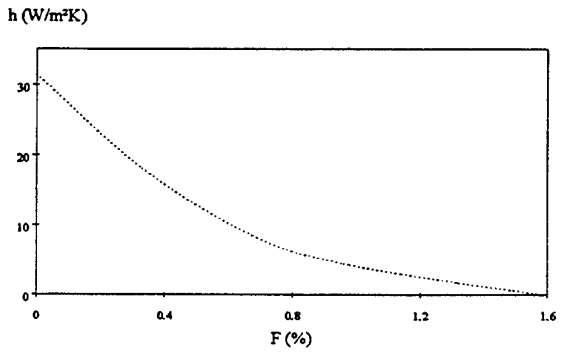


figure 4. Heat transfer coefficient ($0 \le F \le 1.6$ %).

The results for friction factors and Stanton numbers without and with injection of gas has been showed in Bellettre et al.

(1997b) : a classical decrease of friction factor or Stanton number is find. An example of heat transfert reduction is showed on the figure 4.

IV - RESULTS WITH WATER VAPOR

In this part, the main flow is air and the injected fluid is water vapor. The temperature of the air (main flow) is 200°C and the injected fluid temperature is 100°C. In figure 5, the velocity profile is plotted for an injection of air and for an injection of water vapor (the injection rate being equal to 0.5%). We can see that there is not notable difference and that the two profiles collapse.

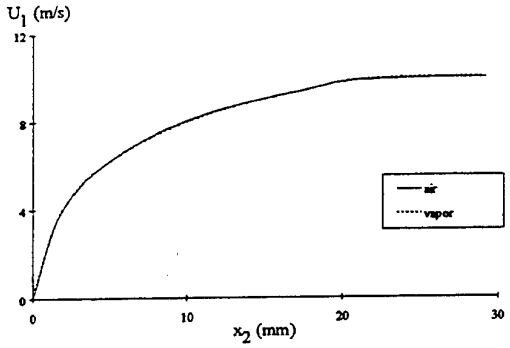


figure 5. Velocity profiles for air or vapor injection.

In the same conditions, the temperature profile is plotted in figure 6. We can observe that the temperature is lower in the case of water injection but the difference is relatively weak. Consequently, the injection of gas or water has little influence on the velocity and temperature profile.

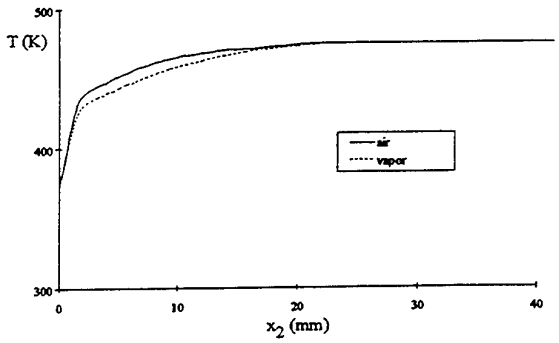


figure 6. Temperature profiles for air or vapor injection.

By the following, we calculated the friction factor and Stanton number for injections of gas and water at different injection rate. The results are compared of numerical work of Landis and Mills (1972) in figures 7 and 8. Landis and Mills (1972) studies have been validated with experimental work of Romanenko and Kharchenko (1963). For both cases, we used the correlations given in paragraph III (equations (15) and (18)).

In figure 7, the ratio of Stanton number for water vapor on Stanton number for air is plotted. We can see that the Stanton number with water injection is lower than the Stanton number with air injection, particularly when the injection rate increases. Furthermore, we can observe that the present results are in good agreement with Landis and Mills (1972) values. This result permit to validate the using of Whitten et al. (1970) correlation which was, initially, established only with air. Nevertheless, as, between 100 °C and 200 °C, the thermal conductivity of water is almost about equal to the air one, we could suppose that this correlation stays valid for air and water vapor.

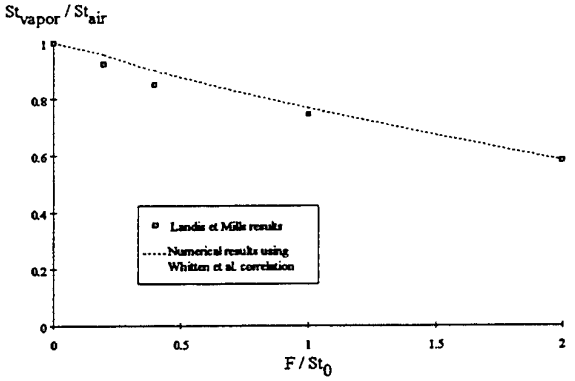


figure 7. Ratio of Stanton number.

In figure 8, the ratio of the friction factor for water vapor on the friction factor for air is plotted. We can see that the results using Simpson and al. (1969) correlation are not satisfactory when comparing with Landis and Mills (1972) values. It seems that, in the case of water vapor, it is not possible to use the Simpson et al. (1969) correlation established, although, for air. An explanation could be that difference of dynamic viscosity (the dynamic viscosity of water is about half the air one (at 100°C)) is not taking into account in the correlation, leading to an overestimation of the friction factor.

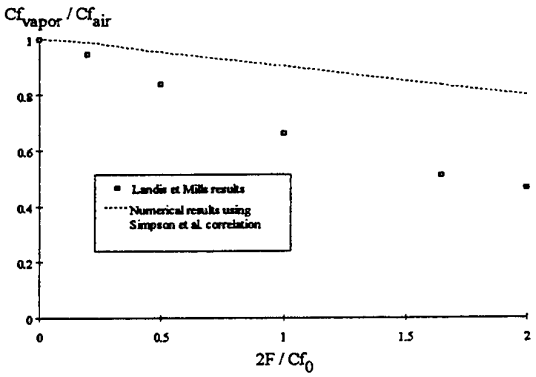


figure 8. Ratio of friction factor coefficients.

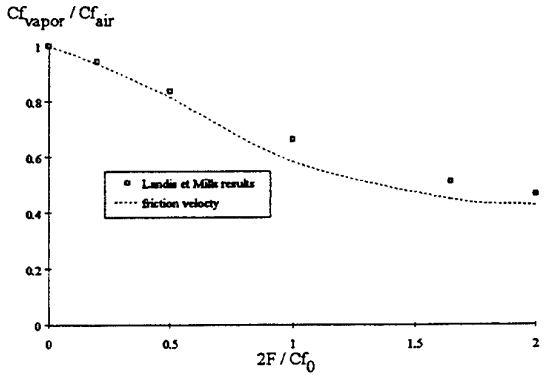


figure 9. Ratio of friction factor coefficients.

Nevertheless, to check our numerical results, we calculated the friction factor using the friction velocity, U*, of the law of the wall (11), which is calculated on each solid element of the porous plate. We again compared with Landis and Mills (1972) data. In figure 9, we can see that a rather good agreement is obtained and that the friction factor of the water vapor is lower than for the air.

V - CONCLUSION

In this paper, we investigated the dynamic and thermal aspect of a turbulent boundary layer submitted to injection of air or water vapor for different injection rates. Only weak discrepancies between air and water profiles have been observed. Nevertheless, the friction factors and Stanton numbers are modified when the injected fluid is not of the same specie and are lower in the case of water injection, specially when the injection rate increases. Using numerical results of our blowing model, it is possible to calculate these dimensionless numbers using a correlation or law of the wall. By the following, a more complete study with water injection including phase change in the porous media would permit to precisely evaluate the interest of using water instead of air.

VI - REFERENCES

Andersen, P. S., Kays, W. M., Moffat, R. J., 1975, "Experimental results for the transpired turbulent boundary layer in an adverse pressure gradient," *J. Fluid Mech.*, Vol. 69, pp. 353-375.

Bellettre, J, Bataille, F., Lallemand, A., 1997a, "Study of a turbulent boundary layer with injection," *ASME Fluids Engineering Division Summer Meeting, Symposium on separated and complex flows*, Vancouver, Canada.

Bellettre, J, Bataille, F., Lallemand, A., 1997b, "Modélisation de l'effusion en présence d'un écoulement pariétal turbulent. Application à la protection thermique des parois," *Journée d'études SFT, section "convection*, Paris, France.

Campolina França, G. A., Tedeschi, G., Lallemand, A., 1995, "Turbulent incompressible flow within a channel with transpiration : solution of the coupled problem porous wall - main flow," *13th Brasilian Congress and 2nd Iberian American Congress of Mechanical Engineering*, Belo Horizonte, Brasil.

Kays, W. M., 1972, "Heat transfer to the transpirated turbulent boundary layer," *Int. J. Heat Mass Transfer*, Vol. 15, pp. 1023-1044.

Landis, R. B., Mills, F., 1972, "The calculation of turbulent boundary layers with foreign gas injection," *Int. J. Heat Mass Transfer*, Vol. 15, pp. 1905-1932.

Launder, B. E., Spalding, D. B., 1974, "The numerical computation of turbulent flow," *Computer Methods Appl. Mech. Eng.*, Vol. 3, pp. 269-288.

Rodet, J. C., Pagnier, P., Morel, R., Lallemand, A., 1997, "Evaluation d'une soufflerie thermique pour des études de refroidissement de matériaux poreux par effusion de gaz ou par transpiration de liquide," *Congrès SFT*, Toulouse, France.

Romanenko, P. N., Kharchenko, V. N., 1963, "The effect of transverse mass flow on heat transfer and friction drag in a turbulent flow of compressible gas along an arbitrarily shaped surface," *Int. J. Heat Mass Transfer*, Vol. 6, pp. 727-738.

Simpson, R. L., Moffat, R. J., Kays, W.M., 1969, "The turbulent boundary layer on a porous plate : experimental skin friction with variable injection and suction," *Int. J. Heat Mass Transfer*, Vol. 12, pp. 771-789.

Simpson, R. L., 1970, "Characteristics of turbulent boundary layers at low Reynolds Numbers with and without transpiration," *J. Fluid Mech.*, Vol.42, pp. 769-802.

So, R. M. C., Yoo, G., 1987, "Low Reynolds Number Modeling of Turbulent Flows With and Without Wall Transpiration," *AIAA Journal*, Vol. 25, pp. 1556-1564.

Stevenson, T. N., 1968, "Inner Region of Transpired Turbulent Boundary Layers," *AIAA Journal*, Vol. 6, pp. 553-554.

Whitten, D. G., Moffat, R. J., Kays, W. M., 1970, "Heat transfer to a turbulent boundary layer with non-uniform blowing and surface temperature," *Proceeding of the Fourth International Heat Transfer Conference*, Versailles, France, paper FC 8.8.

Yakhot, V., Orszag, S. A., 1986, "Renormalization Group Analysis of Turbulence, I. Basic Theory," *J. of Sci. Comput.*, Vol 1, pp. 1-51.

NUMERICAL STUDY OF BUBBLE AND PARTICLE MOTION IN WALL TURBULENCE

I.A. JOIA, T. USHIJIMA, R.J. PERKINS
Laboratoire de Mécanique des Fluides et d'Acoustique,
Ecole Centrale de Lyon
36 av Guy de Collongue,
69131 Ecully, FRANCE

ABSTRACT

A numerical study of bubble and particle motion in the near-wall region of a turbulent boundary layer has been performed using Proper Orthogonal Decomposition. It has been noted that bubbles and particles tend to preferentially concentrate in different regions of the flow. For the conditions which have been investigated, the lift and pressure gradient forces play an important role in bubble motion but not in particle motion.

INTRODUCTION

The understanding and prediction of particle and bubble motion in turbulent flows is of utmost importance in many engineering applications. It has been observed both experimentally and computationally that particles and bubbles tend to accumulate preferentially in certain regions of turbulent flows (see Eaton & Fessler 1994 for a recent review), such regions of high particle concentrations may strongly affect the flow itself and the efficiency of various processes. It has been noted (see eg. Pan & Banerjee 1996) that particles tend to accumulate in low speed streaks of the boundary layer, the accumulation of particles in this region will act to increase heat and mass transfer rates in precisely the regions where these rates would otherwise be low, such particles will distribute themselves 'preferentially' so as to enhance the transfer rates between the wall and the fluid. It has also been noted (eg. Moursali *et al* 1995) that in bubbly flows one may have void fraction peaking close to the wall, such a void fraction distribution may adversely affect transfer rates between the fluid and the wall. In unbounded turbulent flows, coherent structures are also present and their influence on bubble and particle motion may play an important role, for example, one may have reduced combustion efficiency in fuel rich zones which have resulted from preferential fuel droplet accumulation in certain turbulent structures.

In order to be able to enhance any benifitial effects of the presence of a second phase and reduce possible undesirable effects, it is necessary to further our understanding of the interaction between the dispersed phase and turbulent structures.

PROPER ORTHOGONAL DECOMPOSITION

We have simulated the turbulent structure (and its evolution) in the near-wall region of a boundary layer using Proper Orthogonal Decomposition (POD) (see Joia *et al* 1997a, Aubry *et al* 1988, Sanghi & Aubry 1993). POD is a low-dimensional model (for this reason it is computationally cheaper to run than LES) which not only accurately reproduces the coherent structures in the boundary layer but also their temporal evolution. Reproduction of the correct dynamical behaviour of the coherent structures is essential for the study of particle interaction with these structures.

The velocity field is defined in a coordinate system in which the mean flow is in the x–direction, the wall-normal is the y–direction and z denotes the spanwise direction. The wall is located at $y = 0$. The computational domain has dimensions of $Lx^+ = 666$, $Lz^+ = 333$ and $0 \leq y^+ \leq 40$. Periodic boundary conditions are used in the two homogeneous directions (x & z).

A dynamical POD is in essence a spectral simulation, in which the velocity field is given by the sum over a limited number of modes, each weighted by an appropriate, time-varying, coefficient:

$$\mathbf{u}(\mathbf{x}, t) = \sum_{p=1}^{N} a_p(t)\phi_p(\mathbf{x}). \qquad (1)$$

In order to obtain the time dependence of the coefficients $a_p(t)$, the standard Galerkin projection of the Navier-Stokes equations onto the space spanned by the modes is performed. This results in a set of ODE's which determine the time evolution of the coefficients $a_n(t)$, see Joia *et al* (1997a).

The advantages of using POD in dynamical simulations lie in the special properties of the orthogonnal modes, $\phi_p(\mathbf{x})$, which are used in the simulation. These modes are chosen so as to be optimal at capturing the energy in the turbulent velocity fluctuation. The consequence is that, fewer modes are required to represent the velocity field to a given 'accuracy'. The modes are therefore specific to the particular flow being investigated. In order to determine

$\phi_p(\mathbf{x})$, data (in the form of the two-point velocity correlation tensor) concerning the turbulent structures present in the flow is required. We have used modes which were determined from the experiments of Herzog (1986).

BUBBLE AND PARTICLE MOTION

The equation of motion which is used to determine bubble and particle motion through the fluctuating velocity field is:

$$\frac{d\mathbf{v}}{dt} = \frac{\gamma-1}{\gamma+C_M}\mathbf{g} + \frac{1}{\gamma+C_M}\frac{3C_D}{4\phi}|\mathbf{u}-\mathbf{v}|(\mathbf{u}-\mathbf{v}) + \frac{1+C_M}{\gamma+C_M}\frac{D\mathbf{u}}{Dt} + \frac{C_L}{\gamma+C_M}(\mathbf{u}-\mathbf{v})\times\boldsymbol{\omega}, \quad (2)$$

where $\mathbf{v}$ is the particle velocity $\mathbf{u}$ is the fluid velocity at the particle location and in its absence, γ is the relative density of the particle to the carrier fluid, ϕ is the particle diameter, $\mathbf{g}$ is the gravitational vector and C_D, C_M and C_L are respectively the drag, added-mass and the lift coefficients. A value of $1/2$ is used for both the lift and the added-mass coefficients, the value of C_D depends on the particle Reynolds number, $Re_p = \phi|\mathbf{u}-\mathbf{v}|/\nu$:

$$C_D = \frac{24}{Re_p}\left(1.0 + 0.15Re^{0.687}\right). \quad (3)$$

Equation 2 is appropriate for particles on whose surface the no-slip boundary condition is satisfied. The appropriate boundary condition for bubbles in pure water is a shear-free boundary condition, however, small quantities of impurities (surfactants) in the water will impose the no-slip boundary conditions, which is the reason for which eq. 2 is used for bubbles as well as for particles.

We have studied the effects of the different terms in the equation of motion on the motion of both bubbles and on heavy particles. As expected, for heavy particles the dominant forces are the gravitational and drag forces. For the light bubbles, the other terms in the equation also play an important role, it is found that non-linear interactions between the lift and the pressure gradient forces play an important role in bubble motion. In addition, it is seen that light bubbles and heavy particles accumulate in different flow structures.

RESULTS

A representation of the instantaneous flow field produced by POD is shown in fig 2d. Fig 1 shows the mean and rms velocity profiles predicted by POD, they are in reasonable agreement with experimental values.

Bubbles and particles are released randomly in the computational domain and tracked during several Lagrangian timescales of the flow. Figure 2 shows the positions of bubbles and particles (in a zero gravity environment) once they have been allowed the time needed to adjust to the local flow field. Figures 2a-c show bubbles positions, in b the lift force is omitted whereas in c the pressure gradient force is omitted. From these figures we see that neither the lift nor the pressure gradient force are solely responsible for the bubble distribution observed in 2a, rather, it is a non-linear (we cannot simply superpose the two results) interaction between these two forces which gives rise to the observed bubble distribution. Figures 2 e and f show the positions of heavy particles, it is noted that the drag force by itself faithfully reproduces the particle distribution. There is a striking contrast between the bubble positions and the particle positions, since the light bubbles accumulate in different flow structures to the heavy particles. Figure 2d shows a vector plot of the velocity field, one notes from this plot that bubbles tend to accumulate in eddying regions of the flow whereas the heavy particles

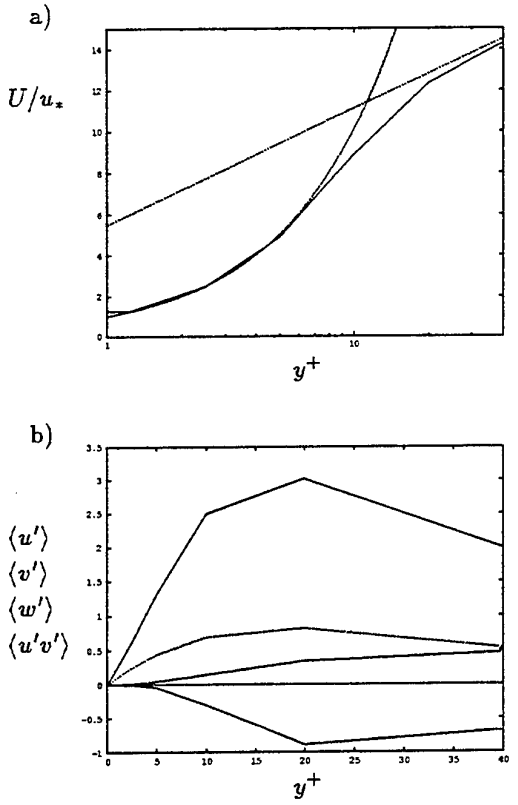


Figure 1: a) The mean velocity profile, U/u_*, on a log-linear graph, included is the linear velocity profile valid for $y^+ < 5$ and the logarithmic profile valid for $y^+ > 30$. b) Turbulence intensities in the boundary layer, from top downwards, $\langle u'/u_* \rangle$, $\langle w'/u_* \rangle$, $\langle v'/u_* \rangle$, $\langle u'v'/u_*^2 \rangle$.

tend to be flung out of these regions. These results are further commented on by Joia *et al* (1997a).

Bubble motion in an upwards flowing boundary layer (gravity acts in the $-x$ direction) has also been studied. In this configuration, bubbles are drawn towards the wall by the lift force resulting from the mean relative velocity between the bubble and the surrounding fluid and the mean velocity gradient in the boundary layer. Bubbles accumulate in a thin layer close to the wall (they are prevented from approaching the wall any closer due to their finite radius). It is noted that this 'mean' attraction of the bubbles towards the wall has the effect of diminishing bubble segregation due to the instantaneous turbulent structure. From the results obtained (see fig 3e and fig 2d) one notes, that under certain conditions, bubbles may be 'ripped' off the wall. The results for bubbles of various terminal velocities V_T^+ and sizes are shown in fig 3. These results are further commented on by Joia *et al* (1997a).

ONGOING DEVELOPMENTS

One of the main limitations of the above described research is that the computational domain is limited to $y^+ = 40$. A POD using the proper orthogonal modes determined from a DNS of channel flow (Kim *et al* 1987) has been developed (Joia *et al* 1997b), as this flow is bounded by two walls, the problem of bubbles and particles escaping from the simulation domain which were previously encountered does not present itself. At the conference, results concerning the single phase properties of this flow and those of bubble and particle motion in a POD simulation of tur-

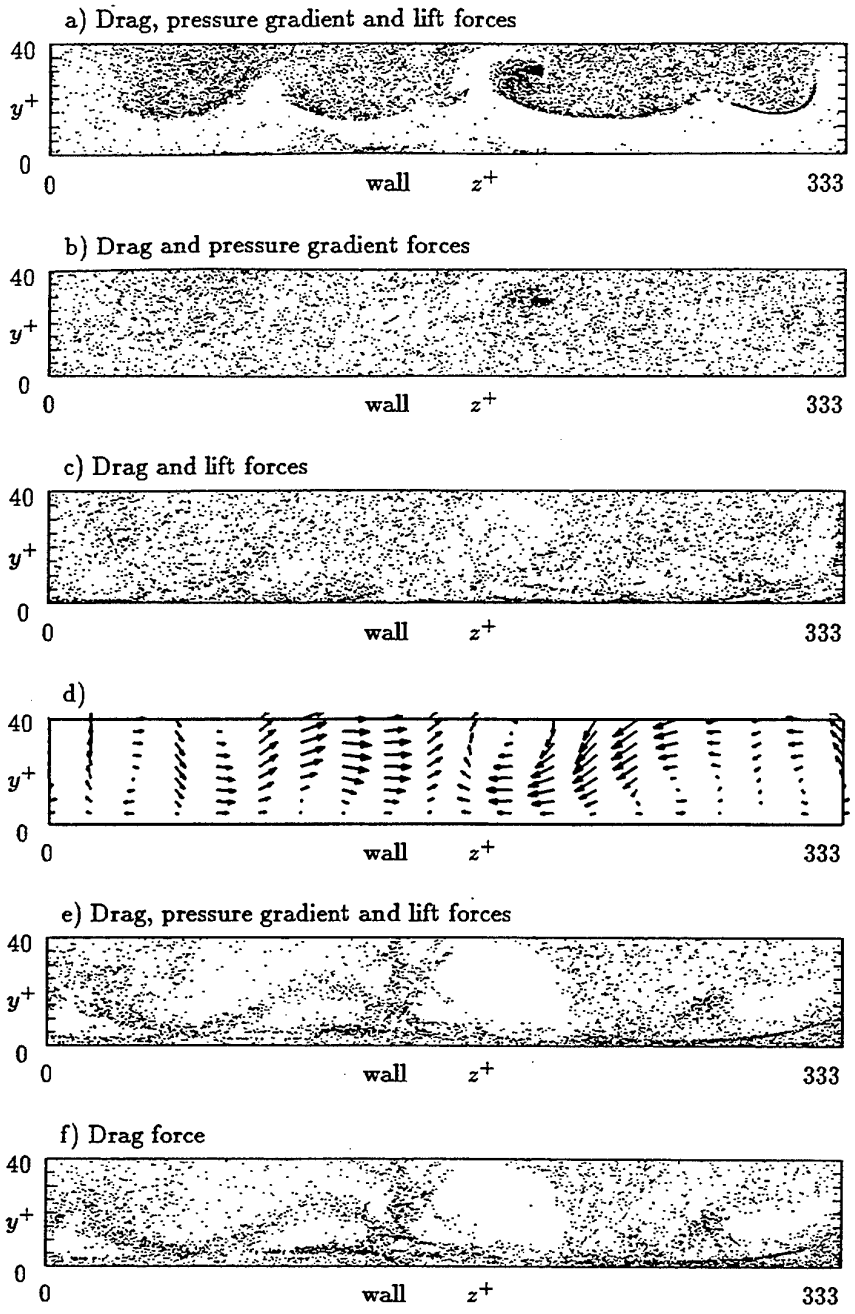


Figure 2: Particle positions and velocity vectors. (a) $\gamma = 0.001$, $\phi^+ = 7.6$, all terms in equation of motion. (b) $\gamma = 0.001$, $\phi^+ = 7.6$, neglecting lift force. (c) $\gamma = 0.001$, $\phi^+ = 7.6$, neglecting pressure gradient force. (d) Velocity vectors (mean flow direction into page). (e) $\gamma = 2000$, $\phi^+ = 0.38$, all terms in equation of motion. (f) $\gamma = 2000$, $\phi^+ = 0.38$, neglecting lift and pressure gradient forces.

bulent channel flow will be presented.

REFERENCES

Aubry, N., Holmes, P., Lumley, J.L. & Stone, E. (1988) The dynamics of coherent structures in the wall region of a turbulent boundary layer. *J. Fluid Mech.*, **192**, pp 115–173.

Eaton, J.K. & Fessler, J.R. (1994) Preferential concentration of particles by turbulence. *Int. J. Multiphase Flow*, **20 SS**, pp 169–209.

Herzog, S. (1986) The large scale structure in the near-wall region of turbulent pipe flow. *Ph.D. thesis, Cornell University.*

Joia I.A., Ushijima T. & Perkins (1997a) Numerical study of bubble and particle motion in a turbulent boundary layer using proper orthogonal decomposition. *accepted to Applied Scientific Research.*

Joia I.A., Ushijima T. & Perkins R.J. (1997b) Characteristic Eddy Dynamical Simulation of Turbulence in a Channel. *in preparation.*

Kim J., Moin P. & Moser R. (1987) Turbulence statistics

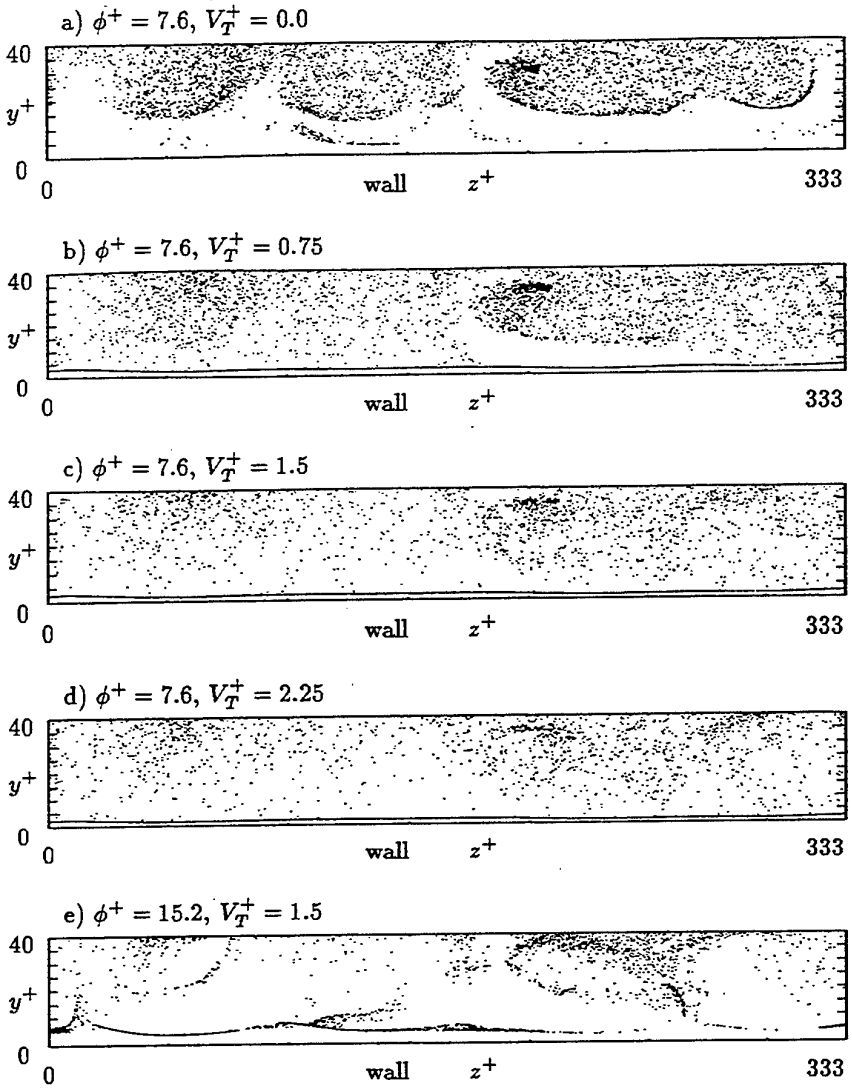


Figure 3: Bubble positions (varying gravity to change the bubble terminal velocity). (a) $\gamma = 0.001$, $\phi^+ = 7.6$, $V_T^+ = 0.0$. (b) $\gamma = 0.001$, $\phi^+ = 7.6$, $V_T^+ = 0.75$. (c) $\gamma = 0.001$, $\phi^+ = 7.6$, $V_T^+ = 1.5$. (d) $\gamma = 0.001$, $\phi^+ = 7.6$, $V_T^+ = 2.25$. (e) $\gamma = 0.001$, $\phi^+ = 15.2$, $V_T^+ = 1.5$.

in fully developed channel flow at low Reynolds number. *J. Fluid Mech* **177**, 133-166.

Moursali, E., Marié, J-L. & Bataille J. (1995) An upward turbulent bubbly boundary layer along a vertical flat plate. *Int. J. Multiphase Flow*, **21, No.1**, pp 107–117.

Pan, Y., Banerjee, S. (1996) Numerical simulation of particle interactions with wall turbulence. *Phys. of Fluids*, **8, No.10**, pp 2733–2755.

Sanghi, S. & Aubry, N. (1993) Mode interaction models for near-wall turbulence. *J. Fluid Mech.*, **247**, pp 455–488.

TURBULENCE MODELING

AND FIRST NUMERICAL SIMULATIONS

IN TURBULENT TWO-PHASE FLOWS

Christophe Morel

CEA Grenoble
DRN / DTP / SMTH
Laboratoire de Modélisation Thermohydraulique
et Développement de Logiciels
17, avenue des Martyrs
38054 GRENOBLE CEDEX 9 FRANCE

ABSTRACT

The subject of this paper is to present a new modeling for the numerical simulation of the three dimensional evolution of dispersed bubbly flows in vertical ducts. We use the time-averaged two-fluid model completed by a two-phase K-ε model to characterise the statistical effects of the turbulence in the liquid phase, and an additional transport equation to calculate the interfacial area density. The complete model has been implemented in the three dimensional module of the CATHARE code. The capabilities of this model will be tested by comparison of the numerical results with experimental data.

1.INTRODUCTION

The subject of two-phase or multiphase flows has become increasingly important during the last thirty years, in a wide variety of engineering systems and practical applications. For example, we can quote boiling water and pressurised water reactors in nuclear industry, direct contact heat exchangers in heat transfer systems, chemical reactors, air lift pumps and so on...

The CATHARE code has been developed at the Commissariat à l'Energie Atomique (France) in order to simulate the thermohydraulic aspects in nuclear power plants in normal and accidental situations. This code is based on a two-fluid six-equation model. Recently, a three dimensional module has been developed in order to simulate three dimensional components like the vessel or the containment.

In the three dimensional approach of two-phase flows, the main difficulties are to model the *statistical effects of the turbulence* (there appears one Reynolds stress tensor for each phase) and the *interfacial transfer terms of mass, momentum and energy.*

We have adopted an eddy viscosity model and a K-ε model to calculate the turbulent diffusion in the continuous liquid phase of dispersed bubbly flows. The turbulence of the dispersed gaseous phase is neglected.

The interfacial interaction terms of mass, momentum and energy are generally related to the *interfacial area density*, namely the contact area between phases per unit volume of mixture. One can write (Ishii, 1990 ; Delhaye & Bricard, 1994) :

interfacial transfers ≈ interfacial area density × driving force

and so the interfacial area density is a very important quantity in two-phase flow studies. In our approach, we use a transport equation to calculate the interfacial area density. This equation is based on a statistical formulation.

In what follows, we will restrict ourselves to the case of *isothermal dispersed bubbly flows without phase change.* The flows studied are assumed to be dispersed but not dilute. We recall that a dilute bubbly flow is a particular case of a dispersed bubbly flow with a very low void fraction.

2.MATHEMATICAL MODEL

The time-averaged equations of the two-fluid model (Ishii, 1975 ; Delhaye & Achard, 1976, 1977) are recalled. As one deals with isothermal flows without phase change, only the mass and momentum equations are presented :

$$\frac{\partial \alpha_k \overline{\rho_k}^k}{\partial t} + \mathrm{div}\left(\alpha_k \overline{\rho_k}^k \overline{\underline{v}_k}^{k=k}\right) = 0 \qquad (1)$$

$$\frac{\partial \alpha_k \overline{\rho_k}^k \underline{\underline{v_k}}^k}{\partial t} + \underline{div}(\alpha_k \overline{\rho_k}^k \underline{\underline{v_k}}^k \underline{\underline{v_k}}^k) = -\underline{\nabla}\left(\alpha_k \overline{p_k}^k\right) + \\ + \underline{div}\left[\alpha_k\left(\overline{\underline{\underline{\tau}}}^k + \underline{\underline{\tau}}_k^T\right)\right] + \alpha_k \overline{\rho_k}^k \underline{g} + \underline{M}_k \qquad (2)$$

In what follows, the closure relations used to express the Reynolds stress tensor in the liquid phase $\underline{\underline{\tau}}_L^T$ and the interfacial transfer of momentum $\underline{M}_k$ are presented.

2.1. Interfacial transfer of momentum

It is assumed here that the interfacial transfer of momentum is the sum of four forces :

$$\underline{M}_k = \underline{M}_k^D + \underline{M}_k^{ma} + \underline{M}_k^l + \underline{M}_k^{DT} \qquad (3)$$

where the four terms in the right hand side of Eq. (3) designate the drag force, the added mass force, the lift force and the turbulent dispersion force respectively. The drag force is given by (Grossetête, 1995 ; Lopez de Bertodano et al., 1994):

$$\underline{M}_G^D = -\underline{M}_L^D = -\frac{3}{4}\alpha \overline{\rho_L}^L \frac{C_D}{d}\left|\underline{\underline{v_G}}^G - \underline{\underline{v_L}}^L\right|\left(\underline{\underline{v_G}}^G - \underline{\underline{v_L}}^L\right) \qquad (4)$$

where C_D is the drag coefficient for which some correlations exist in the litterature (Ishii, 1977 ; Ishii & Zuber, 1979) and d is the mean diameter of the bubbles. For nearly *monodispersed spherical bubbles*, it is related to the void fraction α and the interfacial area density a_i by the definition of the Sauter mean diameter (Delhaye & Bricard, 1994) :

$$d = 6\alpha / a_i \qquad (5)$$

The added mass force is given by (Voinov, 1973 ; Auton et al., 1988 ; Magnaudet et al., 1995) :

$$\underline{M}_G^{ma} = -\underline{M}_L^{ma} = -C_{ma} E(\alpha) \alpha \overline{\rho_L}^L \left[\left(\frac{\partial \underline{\underline{v_G}}^G}{\partial t} + \underline{\underline{v_G}}^G \cdot \underline{\underline{\nabla}} \underline{\underline{v_G}}^G\right) - \left(\frac{\partial \underline{\underline{v_L}}^L}{\partial t} + \underline{\underline{v_L}}^L \cdot \underline{\underline{\nabla}} \underline{\underline{v_L}}^L\right)\right] \qquad (6)$$

$$E(\alpha) = \frac{1+2\alpha}{1-\alpha}$$

where C_{ma} is the added mass coefficient and the coefficient $E(\alpha)$ is a correction factor in order to take into account the presence of the other bubbles (Zuber, 1964, Lamb, 1932).

The lift force is given by (Auton, 1987 ; Auton et al., 1988) :

$$\underline{M}_G^l = -\underline{M}_L^l = -C_l \alpha \overline{\rho_L}^L \left(\underline{\underline{v_G}}^G - \underline{\underline{v_L}}^L\right) \wedge \underline{\nabla} \wedge \underline{\underline{v_L}}^L \qquad (7)$$

where C_l is the lift coefficient.

The last force, namely the turbulent dispersion force, results from the statistical effects of fluctuations when averaging the three other forces. We use here a simple form for the turbulent dispersion force (Anglart et al., 1993 ; Lance & Lopez de Bertodano, 1992 ; Lahey, 1991 ; Lahey & Lopez de Bertodano, 1991) :

$$\underline{M}_G^{DT} = -\underline{M}_G^{DT} = -C_{DT} \overline{\rho_L}^L K_L \frac{\nabla \alpha}{\alpha} \qquad (8)$$

where C_{DT} is the turbulent dispersion coefficient and K_L is the turbulent kinetic energy of the liquid phase.

2.2. Interfacial area density transport equation

The knowledge of the interfacial area density is very important in order to correctly predict the interfacial transfers (see for example Eqs 4 & 5) and to characterise locally the structure of the flow. A transport equation is derived, it is based on a statistical formulation for this quantity (Kalkach-Navarro et al., 1994 ; Navarro-Valenti et al., 1990, Guido-Lavalle et al., 1994, Kocamustafaogullari & Ishii, 1995).

For our applications on bubbly flows in vertical ducts with a possible transition between bubbly and slug flows, we use the following equation for the interfacial area density :

$$\frac{\partial a_i}{\partial t} + \underline{div}\left(a_i \underline{\underline{v_G}}^G\right) = -\frac{2}{3}\frac{a_i}{p}\left(\frac{\partial p}{\partial t} + \underline{\underline{v_G}}^G \cdot \underline{\nabla} p\right) \\ -\frac{c_0}{3}\frac{\alpha}{1-\alpha} a_i \left(1 - \frac{l_G}{l_G^S}\right) H\left(l_G^S - l_G\right) \qquad (9)$$

where it is assumed that the interfacial area density is convected by the mean gas velocity because bubbly flow regimes are considered. The first term in the rhs of Eq. (9) is a source term by gas expansion associated with the pressure gradient (p designates the mean pressure in the flow), and the second term is a sink term by coalescence of the bubbles. This second term is modeled according to Guido-Lavalle et al. (1994), c_0 is a coalescence parameter, H is the Heaviside step function and l_G and l_G^S are the Taylor bubble length and the stable Taylor bubble length respectively. According to Taitel et al. (1980), the stable Taylor bubble length is attained when the length of the liquid slugs between the Taylor bubbles is approximately equal to eight times the diameter of the tube, thus:

$$l_G^S = 8D\frac{\alpha}{1-\alpha} \qquad (10)$$

where D is the tube internal diameter.

2.3. Turbulence modeling

In order to express the Reynolds stress tensor in the liquid phase, we have adopted an eddy viscosity model and a K-ε model, thus the Reynolds stress tensor in the liquid phase is given by :

$$\underline{\underline{\tau}}_L^T = \overline{\rho_L}^L \nu_L^T \left(\underline{\underline{\nabla}} \underline{\underline{v_L}}^L + \underline{\underline{\nabla}}^T \underline{\underline{v_L}}^L\right) - \frac{2}{3}\rho_L\left(K_L + \nu_L^T \underline{div} \underline{\underline{v_L}}^L\right)\underline{\underline{1}} \qquad (11)$$

and the eddy viscosity is given by :

$$\nu_L^T = C_\mu \frac{K_L^2}{\varepsilon_L} \qquad (12)$$

where C_μ is an empirical constant equal to 0.09.

It must be noted that the relations (11) and (12) are single-phase relations and that their validity in the case of two-phase flows should be carefully examined (Kataoka & Serizawa, 1989).

The turbulent kinetic energy K_L and its dissipation rate ε_L are calculated by their balance equations. The equations of the two-phase K-ε model have been derived by many authors (Kataoka & Serizawa, 1988, 1989 ; Simonin, 1991 ; Lance et al., 1984). These equations are very complicated, they contain many interfacial interaction terms and are not usable for practical calculations. Thus we have performed an order of magnitude analysis of the two-phase K-ε model in order to simplify the original equations. This analysis was inspired by that one of Lumley done for the case of single-phase flows (Tennekes & Lumley, 1987 ; Schiestel, 1993) and is presented in another paper (Morel, 1996). We simply here give the K and ε equations used in this work.

$$\begin{aligned}&\frac{\partial(1-\alpha)\overline{\rho_L}^L K_L}{\partial t} + \mathrm{div}\left[(1-\alpha)\overline{\rho_L}^L K_L \underline{\underline{v}}_L^L\right] = \\ &= \mathrm{div}\left[(1-\alpha)\overline{\rho_L}^L \frac{\nu_L^T}{\sigma_K}\underline{\nabla} K_L\right] - (1-\alpha)\underline{\underline{\tau}}_L^T : \underline{\underline{\nabla}}\underline{\underline{v}}_L^L \\ &-(1-\alpha)\overline{\rho_L}^L \varepsilon_L + P_K^i\end{aligned} \qquad (13)$$

where σ_K is a Schmidt number taken equal to 1.

$$\begin{aligned}&\frac{\partial(1-\alpha)\overline{\rho_L}^L \varepsilon_L}{\partial t} + \mathrm{div}\left[(1-\alpha)\overline{\rho_L}^L \varepsilon_L \underline{\underline{v}}_L^L\right] = \\ &= \mathrm{div}\left[(1-\alpha)\overline{\rho_L}^L \frac{\nu_L^T}{\sigma_\varepsilon}\underline{\nabla}\varepsilon_L\right] - C_{\varepsilon 1}\frac{\varepsilon_L}{K_L}(1-\alpha)\underline{\underline{\tau}}_L^T : \underline{\underline{\nabla}}\underline{\underline{v}}_L^L \\ &-C_{\varepsilon 2}(1-\alpha)\overline{\rho_L}^L \frac{\varepsilon_L^2}{K_L} - \frac{2}{3}(1-\alpha)\overline{\rho_L}^L \varepsilon_L \mathrm{div}\underline{\underline{v}}_L^L + P_\varepsilon^i\end{aligned} \qquad (14)$$

where σ_ε is a Schmidt number taken equal to 1.3. $C_{\varepsilon 1}$ and $C_{\varepsilon 2}$ are the single-phase constants equal to 1.44 and 1.92 respectively.

The two terms P_K^i and P_ε^i in Eqs (13) and (14) represent the interfacial source terms of turbulent kinetic energy and dissipation rate. For bubbly flow regimes, it is assumed that the wakes of bubbles add some turbulent kinetic energy to the liquid and the first term is expressed according to Lance et al. (1984) as :

$$P_K^i = -\left(\underline{M}_G^D + \underline{M}_G^{ma}\right)\cdot\left(\underline{\underline{v}}_G^G - \underline{\underline{v}}_L^L\right) \qquad (15)$$

where the drag force and the added mass force have been given in Eqs (4) and (6).

The second term is modeled according to Elgobashi and Abou-Arab (1983) :

$$P_\varepsilon^i = C_{\varepsilon 3}\frac{P_K^i}{\tau} \qquad (16)$$

where $C_{\varepsilon 3}$ is a numerical coefficient of order 1.

Elgobashi and Abou-Arab (1983) expressed the characteristic time τ as the decaying time of the single-phase turbulence :

$$\tau = K_L / \varepsilon_L \qquad (17)$$

As the wake turbulence is created at the characteristic length scale of the bubbles, the decaying time of the wake turbulence was built with the mean diameter of the bubbles d instead of the total turbulent kinetic energy K_L. Dimensional analysis gives :

$$\tau = \left(d^2/\varepsilon_L\right)^{1/3} \qquad (18)$$

3.NUMERICAL RESULTS

The complete model described in the preceding paragraph has been implemented in the three dimensional module of the CATHARE code. In order to illustrate its capacities, the numerical results are compared with experimental data found in the litterature.

The results of two simulations of one bubbly flow studied experimentally by Liu & Bankoff (1990) are first presented. The test section is a vertical duct with an internal diameter equal to 38.1mm. The superficial liquid and gas velocities of the flow simulated are equal to 1.087m/s and 0.067m/s respectively. These conditions correspond to a bubbly flow with a nearly constant bubble diameter equal to 2.5mm. Thus, for these two simulations, the interfacial area density transport equation (9) was not used, and the bubble diameter was imposed equal to 2.5mm. The two simulations were conducted with the same values of the force's coefficients, given by :

$$C_{ma} = C_l = 0.5 \quad C_{DT} = 0.065$$

In the first simulation, the characteristic time (17) originally proposed by Elgobashi & Abou-Arab (1983) was used in the model (16), with a value of the parameter $C_{\varepsilon 3}$ equal to 1.5. The second simulation was conducted with the characteristic time (18) and with a value of the parameter $C_{\varepsilon 3}$ equal to 1.

The comparisons of the two simulations and the experimental profiles in the measuring section (situated at a distance from the inlet equal to 36D) are presented on figure 1.

The compared profiles are those of the void fraction, the mean liquid and gas velocities, and of two component of the Reynolds stress tensor $u' = \overline{\overline{u_L'^2}}^{L\,1/2}$ and $u'v' = \overline{\overline{u_L' v_L'}}^L$ where u and v denote the components of the velocity in the axial and the radial direction respectively.

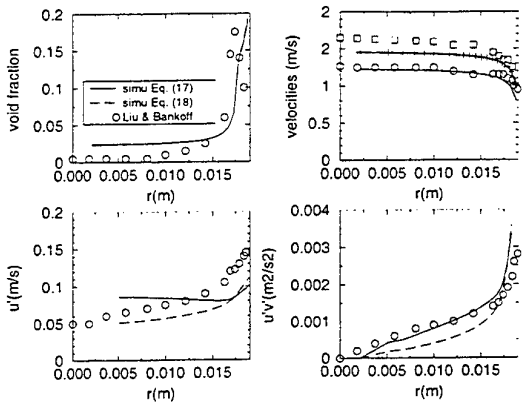


FIG.1 : COMPARISON TO LIU & BANKOFF (1990)

The second experimental study we have simulated is the DEDALE experiment (Grossetête, 1995). The author studied experimentally the evolution of two-phase bubbly flows in a vertical duct, with a possible transition between bubbly flow and slug flow. The tube is 6m long and 38.1 of I.D. There are three measuring sections situated at 8 diameters, 55 diameters and 155 diameters respectively. The author measured the profiles of the void fraction, the interfacial area density, the liquid and gas mean velocities, the bubble frequency, the mean bubble equivalent diameter, and the axial turbulent intensity.

As the measurements at the first measuring section (Z/D=8) are used to determine the entrance conditions at the inlet of the calculation domain, our numerical results are compared only at the two other measuring sections (Z/D=55 and 155).

The results for *four different flows* are presented, corresponding to one value of the liquid superficial velocity and four different values of the gas superficial velocity :

DEDALE 1101 J_L=0.877m/s J_G=0.0588m/s
DEDALE 1103 J_L=0.877m/s J_G=0.1851m/s
DEDALE 1104 J_L=0.877m/s J_G=0.322m/s
DEDALE 1105 J_L=0.877m/s J_G=0.436m/s

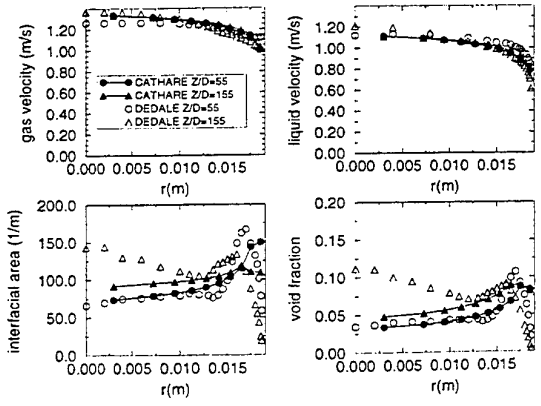


FIG.2A : DEDALE 1101

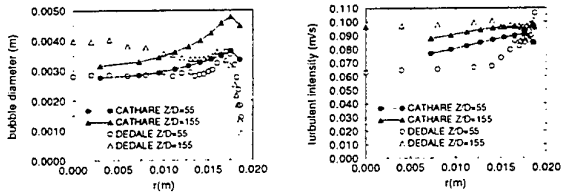


FIG. 2B : DEDALE 1101

The parameters for the simulation of DEDALE 1101 are :

$$C_{ma} = C_l = 0.5 \quad C_{DT} = 0.15 \quad C_{\varepsilon 3} = 1 \quad \tau = \left(d^2/\varepsilon\right)^{1/3} \quad c_0 = 2.5$$

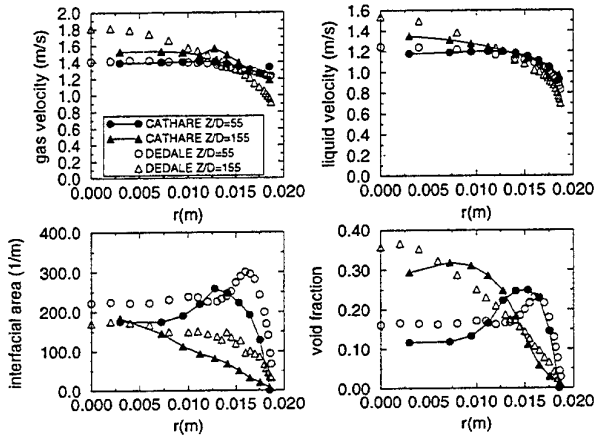


FIG. 3A : DEDALE 1103

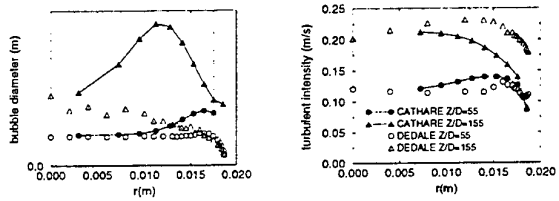


FIG. 3B : DEDALE 1103

The parameters for the simulation of DEDALE 1103 are :

$$C_{ma} = C_l = 0.5 \quad C_{DT} = 0.01 \quad C_{\varepsilon 3} = 1 \quad \tau = \left(d^2/\varepsilon\right)^{1/3} \quad c_0 = 4$$

and the lift coefficient was set to zero when the mean bubble diameter calculated by the code was greater than 5mm. This last modification was inspired by a paper of Zun and Moze (1990), which observed that the bubbles having a diameter greater than approximately 5mm don't go towards the wall.

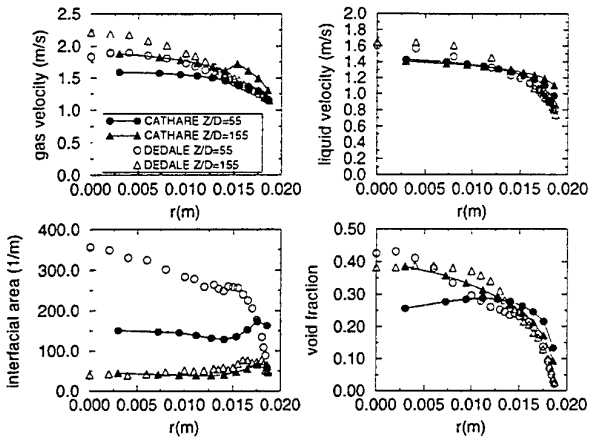


FIG. 4A : DEDALE 1104

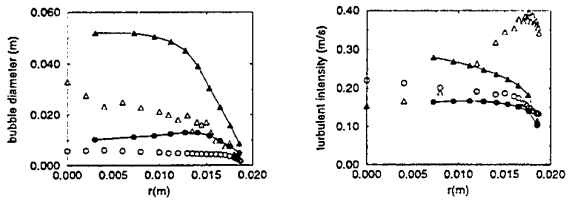


FIG. 4B : DEDALE 1104

The parameters for the simulation of DEDALE 1104 are :

$$C_{ma} = C_l = 0.5 \quad C_{DT} = 0.1 \quad C_{\varepsilon 3} = 1.5 \quad \tau = \left(d^2/\varepsilon\right)^{1/3} \quad c_0 = 5$$

with the modification on the lift coefficient inspired by Zun & Moze (1990).

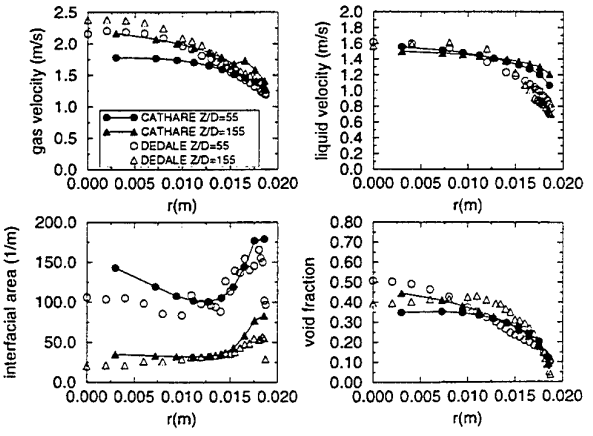


FIG. 5A : DEDALE 1105

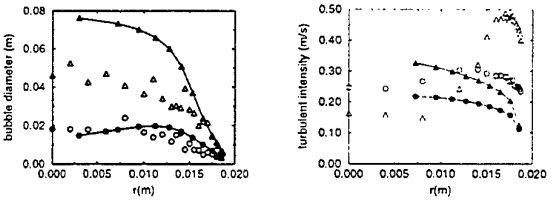


FIG. 5B : DEDALE 1105

The parameters for the simulation of DEDALE 1105 are :

$$C_{ma} = C_l = 0.5 \quad C_{DT} = 0.1 \quad C_{\varepsilon 3} = 1.5 \quad \tau = \left(d^2/\varepsilon\right)^{1/3} \quad c_0 = 5$$

with the modification on the lift coefficient inspired by Zun & Moze (1990).

4.COMMENTS AND CONCLUSIONS

The simulations of the flow studied experimentally by Liu and Bankoff (1990) allowed to test the modification of the Elgobashi and Abou-Arab's model (Eqs. (16) to (18)). The use of the model originally proposed by Elgobashi and Abou-Arab (Eq. (16) and (17)) with a value of the parameter $C_{\varepsilon 3}$ equal to 1.5 gives a better agreement for the quantity u'v' (fig. 1), but the use of the modified model (Eq. (16) and (18)) with a value of the parameter $C_{\varepsilon 3}$ equal to 1 gives a better agreement for the quantity u' (we can see that the aspect of the u' curve is better in this last case).

The simulations of the different flows DEDALE 1101 to 1105 (Grossetête, 1995) show that the present model is able to *qualitatively* reproduce the transition between bubbly to slug flow. Upward bubbly flows are characterised by a void peaking near the wall, and slug flows are characterised by a void coring. We can see that our model reproduces qualitatively the void peaking phenomenon for bubbly flows (1101 and 1103 at Z=55D), and the void coring phenomenon for slug flows (1103 at Z=155D, 1104 and 1105).

The predictions of the interfacial area density in the cases of bubbly flows (1101) and slug flows (1104 at Z=155D and 1105) are qualitatetively good. These predictions show that the coalescence model proposed by Guido-Lavalle et al. (1994) for one dimensional simulations can be successfully applied to multidimensional simulations. The modification of the lift force inspired by Zun and Moze (1990) is also very important.

The comparisons of the Sauter mean diameter of the bubbles, calculated by (5), with the mean equivalent bubble diameter measured by the author in the different cases clearly show the limitation of the relation (5) to bubbly flow regimes.

Acknowledgements : The author is fully indebted to Prof. Jean Marc Delhaye and to Dr. Dominique Bestion for the fruitful discussions they had together and for their encouragement to this work.

REFERENCES

Anglart H., Anderson S., Podowski M.Z., Kurul N., 1993, An analysis of multidimensional void distribution in two-phase flows, *Proceeding of the 6th International Topical Meeting on Nuclear Reactor Thermal Hydraulics (NURETH 6)*, Eds. Courtaud M., Delhaye J.M., October 5-8, Grenoble France, Vol. 1, pp. 139-153.

Auton T.R., 1987, The lift force on a spherical body in a rotational flow. *J. Fluid Mech.*, Vol. 183, pp. 199-218.

Auton T.R., Hunt J.C.R., Prud'homme M., 1988, The force exerted on a body in inviscid unsteady non-uniform rotational flow. *J. Fluid Mech.*, Vol. 197, pp. 241-257.

Delhaye J.M., Bricard P., 1994, Interfacial area in bubbly flow : experimental data and correlations. *Nuc. Eng. & Design* 151, pp. 65-77.

Delhaye J.M., Achard J.L., 1977, On the use of averaging operators in two-phase flow modeling, in *Thermal and Hydraulic aspects of Nuclear Reactor Safety*, Vol. 1 : *Light Water Reactors*, Eds. Jones O.C. and Bankoff S.G., pp. 289-332, ASME, New-York.

Delhaye J.M., Achard J.L., 1976, On the averaging operators introduced in two-phase flow modeling, in *Transient Two-Phase Flow, Proc. CSNI Specialist's meeting*, Toronto, 3,4 august 1976, Eds. Banerjee S., Weaver K.R., Vol. 1, pp. 5-84, AECL, 1978.

Elgobashi S.E., Abou-Arab T.W., 1983, A two-equation turbulence model for two-phase flows, *Phys. Fluids* 26 (4), pp. 931-938.

Grossetête C., 1995, Caractérisation expérimentale et simulations de l'évolution d'un écoulement diphasique à bulles ascendant dans une conduite verticale. Thèse de Doctorat. Ecole Centrale Paris.

Guido-Lavalle G., Carrica P., Clausse A., Qazi M.K., 1994, A bubble number density constitutive equation, *Nuc. Eng. & Design* 152, pp. 213-224.

Ishii M., 1975, *Thermo-fluid dynamic theory of two-phase flow*, Eds Eyrolles Paris

Ishii M., 1977, One-dimensional drift flux model and constitutive equations for relative motion between phases in various two-phase flow regimes. ANL Report No. 77-47.

Ishii M., Zuber N., 1979, Drag coefficient and relative velocity in bubbly, droplet or particulate flows. *AIChE Journal* Vol. 25, No. 5, pp. 843-855.

Ishii M., 1990, Two-fluid model for two-phase flow. *Multiphase Science and Technology*, Eds. Hewitt G.F., Delhaye J.M., Zuber N., Vol. 5, pp. 1-58.

Kalkach-Navarro S., Lahey R.T., Drew D.A., 1994, Analysis of the bubbly slug flow regime transition, *Nuc. Eng. & Design* 151, pp. 15-39.

Kataoka I., Serizawa A., 1988, Interfacial area concentration and its roles in local instant formulation of two-phase flow, *Transient phenomena in multiphase flow*, Afgan N.H. Ed., New-York, NY (USA), Hemisphere Publishing.

Kataoka I., Serizawa A., 1989, Basic equations of turbulence in gas-liquid two-phase flow, *Int. J. Multiphase Flow* Vol. 15, No. 5, pp. 843-855.

Kocamustafaogullari G., Ishii M., 1995, Foundation of the interfacial area density transport equation and its closure relations, *Int. J. Heat Mass Transfer*, Vol. 38, No. 3, pp. 481-193.

Lahey R.T., 1992, Prediction of phase distribution and phase separation phenomena using two-fluid models. *Boiling Heat Transfer*. Lahey R.T.Jr. Ed., pp. 85-122.

Lahey R.T.Jr., Lopez de Bertodano M., 1991, The prediction of phase distribution using two-fluid models. *ASME/JSME Thermal Engineering Proceedings*, Vol. 2, pp. 193-200.

Lamb H., 1932, *Hydrodynamics*. 6th Edition. New-York, Dover Publications.

Lance M., Marié J.L., Bataille J., 1984, Modélisation de la turbulence de la phase liquide dans un écoulement à bulles, *La Houille Blanche*, No. ¾.

Lance M., Lopez de Bertodano M., 1992, Phase distribution phenomena and wall effect in bubbly two-phase flows. *3rd International Workshop on Two-Phase Flow Fundamentals*, June 15-19, Imperial College London.

Liu T.J., Bankoff S.G., 1990, Structure of air/water bubbly flow in a vertical pipe, Int. Symposium on gas-liquid two-phase flows, ASME Winter Annual Meeting, Kim J.H., Rohatgi U.S., Hashemi A. Eds., Nov. 25-30, Dallas, Texas, pp. 9-26.

Lopez de Bertodano M., Lahey R.T., Jones O.C., 1994, Phase distribution in bubbly two-phase flow in vertical ducts, *Int. J. Multiphase Flow* Vol. 20, N° 5, pp 805-818.

Magnaudet J., Rivero M., Fabre J., 1995, Accelerated flows past a rigid sphere or a spherical bubble. Part 1 : Steady straining flow. *J. Fluid Mech.*, Vol. 284, pp. 97-135.

Morel C., 1996, An order of magnitude analysis of the two-phase K-ε model, *31st European two-phase flow group meeting*, Grenoble, June 3-5.

Navarro-Valenti S., Clausse A., Drew D.A., Lahey R.T., 1991, A contribution to the mathematical modeling of bubbly/slug flow regime transition, Chem. Eng. Comm. 102, pp. 69-85.

Schiestel R., 1993, *Modélisation et simulation des écoulements turbulents*, Eds Hermès

Simonin O., 1991, *Modélisation numérique des écoulements turbulents diphasiques à inclusions dispersés*, Ecole de Printemps de Mécanique des Fluides Numérique, Aussois 1991.

Taitel Y., Bornea D., Dukler A.E., 1980, Modeling flow pattern transitions for steady upward gas-liquid flow in vertical turbes, *AIChE J.*, Vol. 26, No. 3, pp. 345-354.

Tennekes H., Lumley J.L., 1987, *A first course in turbulence*, MIT Press.

Voinov O.V., 1973, On the force acting on a sphere in a non-uniform stream of perfect incompressible fluid. *J. Appl. Mech. Tech. Physics* 14, pp. 592-594.

Zuber N., 1964, On the dispersed two-phase flow in the laminar flow regime, Chem. Eng. Sc. 19, p.897.

Zun I., Moze S., 1990, Void fraction profile evolution in bubbly flow, 25th European Two-Phase Flow Group Meeting, paper B2, Varese.

STATISTICAL DESCRIPTION OF THE BUBBLE MOTION IN A TURBULENT BOUNDARY LAYER

S. Tran-Cong, J.L. Marié & R.J. Perkins
Laboratoire de Mécanique des Fluides et d'Acoustique
Ecole Centrale de Lyon/Université Claude Bernard - Lyon I
UMR CNRS 5509
B.P. 163, 69 131 Ecully CEDEX - France
Email:trancong@mecaflu.ec-lyon.fr marie@mecaflu.ec-lyon.fr perkins@mecaflu.ec-lyon.fr

ABSTRACT

The dispersion of air bubbles in a turbulent boundary layer along a flat plate, is investigated experimentally. Bubble trajectories are obtained from films taken with a high speed video camera, and are then analysed using image processing techniques. It is shown that bubble motion depends on the mean equivalent diameter. Bubbles migrate towards the plate (come in contact with the rigid surface and are trapped) or escape into the free-stream. In all cases, the motion has a non-deterministic character, suggesting that the turbulence plays an important role.

INTRODUCTION

The void fraction distribution close to the wall in a turbulent boundary layer is important in many physical processes, including drag and heat transfer, but its prediction remains a challenging problem for many engineering applications. It requires a deep understanding of the physical phenomena which govern bubble motion in a flow.
Several experimental studies of vertical upward flow in pipes (Serizawa *et al*, 1975; Liu, 1993; Zun *et al*, 1992) have shown that the void fraction profile can peak either at the wall or at the centre, depending on the bubble size. This was confirmed recently in the case of a turbulent boundary layer developing along a flat plate (Moursali *et al*, 1995a). By taking high speed video films close to the surface, these authors provided direct evidence that it is mainly the small bubbles ($d_b \sim 3mm$) which migrate towards the plate, are captured there, and generate the wall-peaking, whereas the large ones concentrate in the free-stream, leading to a void-coring distribution. Moreover, they found that these migrations are random and characterized by a short time scale. The latter characteristics together with a suitable scaling analysis (Moursali *et al*, 1995b) suggest that the motion of migrating bubbles might be the result of their interaction with coherent structures in the boundary layer. The objective of the present work is to complete the previous investigation by providing a more detailed experimental description of these phenomena and a better understanding of the underlying mechanisms.

EXPERIMENTAL FACILITY AND INSTRUMENTATION

A detailed description of the facility is given in previous publications (Lance & Bataille, 199; Moursali *et al*, 1995a). The sketch of the experiment is shown in figure 1. The flat plate is located at the center of the test section of a vertical water tunnel. The latter is operated in the upward direction at atmospheric pressure, ambient temperature and at liquid velocities which do not exceed $1.5m/s$. The water was filtered and decalcified, but no other precaution was taken to remove impurities, in view of the dimensions of the facility. Under such conditions, the water is probably contaminated. The plate, which is $15mm$ thick, $400mm$ wide (z-direction), and $2m$ long (x-direction) is made of plexiglass. The leading edge is ogive-shaped, and is located $0.5m$ downstream of the entrance. Boundary layer transition is triggered by a rough abrasive ribbon, $3cm$ wide, stuck on the surface immediately downstream of the leading edge. L.D.A. measurements made in the absence of bubbles showed that the turbulent boundary layer had a standard structure (Schlichting, 1968). Most of the measurements described in this paper were made at a distance of $1m$ downstream of the leading edge, and a liquid free-stream velocity of $1m.s^{-1}$. So, the thickness of the boundary layer (δ) is approximately $22mm$, and the associated Reynolds number is of the order of 22000.
Bubbles are injected at a constant gas flow rate, through one needle located in the test section. This produced a line of bubbles, with the same equivalent diameter, and a regular injection frequency. The range of the equivalent bubble diameters studied lies between $1mm$ and $6mm$. The injection was performed at two different positions in the X-direction ($X = 0.3m$ and $X = 0.8m$), and at different distances Y from the wall, between 0 and $30mm$. Three types of measurements have been performed :

1. To investigate bubble dispersion in the flow, bubbles were released at the lower position (injection at $X = 0.3m$), outside of the boundary layer. The bubble trajectories were filmed using a high-speed video camera shown in figure 2, and were processed automatically, using image analysis techniques (Perkins & Hunt, 1989; Lunde & Perkins, 1995) to yield a statistical analysis

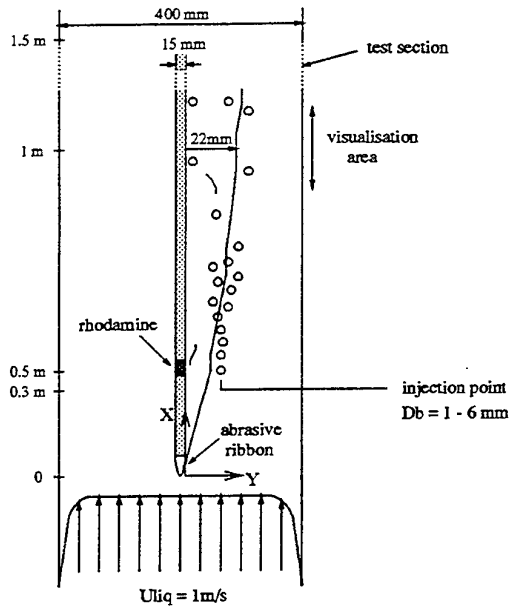


Figure 1: Sketch of the experiment.

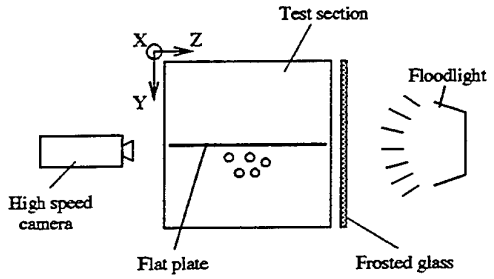


Figure 2: View of the camera and light set-up.

of the trajectories in the wall region, and to study the interface deformations.

2. To quantify the number of bubbles which migrate as a function of the injection distance Y from the wall, the bubbles were released at different positions in the boundary layer ($0 \leq Y \leq 22mm$), at the downstream position ($X = 0.8m$) to reduce the dispersion. At the section $X = 1m$, the bubble frequency at the wall was measured using a laser beam and a photomultiplier to detect the presence of the bubble at the wall (see figure 3). This value has been divided by the total number of bubbles injected into the flow during the same time, measured with an optical probe, to obtain the deflection rate R presented here. The deflection rate has been measured for different bubble diameters.
3. With the same arrangement, the time interval between two bubbles at the wall (two consecutive laser detections) has been measured.

RESULTS

Representative trajectories of bubbles with different diameters are shown in figure 4. The number of frames processed varies between 50 and 70 ; this corresponds to an average acquisition time of the order of $0.1s$. The trends which have been previously identified (Moursali *et al*, 1995a), and summarized in the introduction, are reproduced here. We see that small and large bubbles behave in opposite ways, and the transition between the two

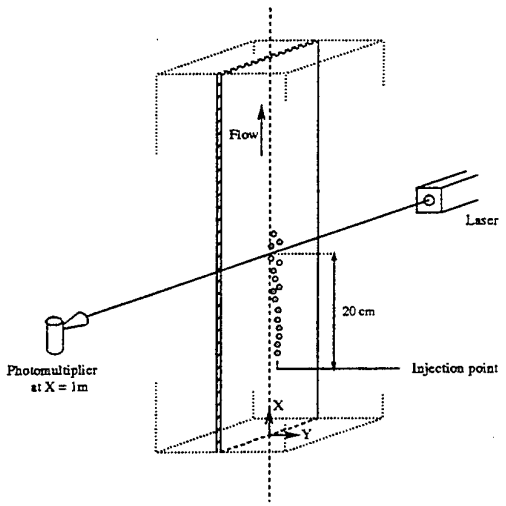
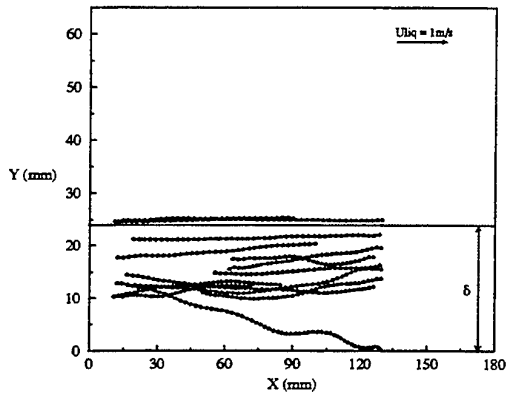


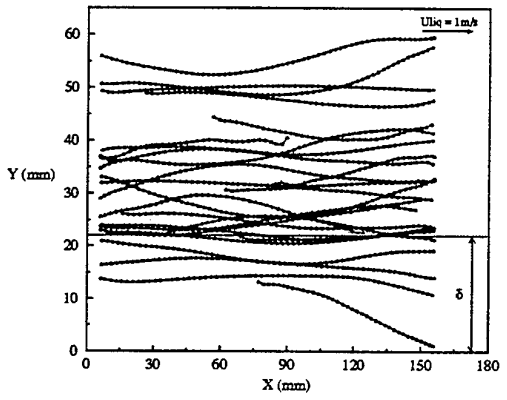
Figure 3: Method for counting the bubble deflection rate at the wall.

behaviours occurs at a diameter of about $4mm$. Below this value (figures 4-a & 4-b), many bubbles are deflected towards the wall and come into contact with the surface where they remain captured. These so called "migrations" are rapid relative to the time scale of the flow, take place only when bubbles rise inside the boundary layer and are far too random to be systematic. In this sense, it is not a deterministic process. Even if they do not migrate, the trajectories of the bubbles in this layer are strongly affected (broad oscillations), compared with those in the free-stream. For bubble diameters greater than $4mm$ (figures 4-c & 4-d), there are still a few bubbles which approach close to the plate. However, none of these is captured at the wall. In order to quantify these trends, a large number of realizations were performed. For each diameter investigated, all the trajectories of the bubbles which migrated to the plate were superposed on the same plot, shifting the impingement points to the same origin, $X = 0$. In this form (figure 5), the motion of the bubbles can be analysed using statistical methods. An analysis of these trajectories is in progress, so a detailed discussion is not yet possible. However, a number of results concerning the average behaviour can be already inferred from the figures. Bubbles of all sizes are deflected towards the plate, and the smaller bubbles are then trapped at the surface (figures 5-a, 5-b & 5-c). However larger bubbles are not trapped, and return to the free stream (figure 5-d).

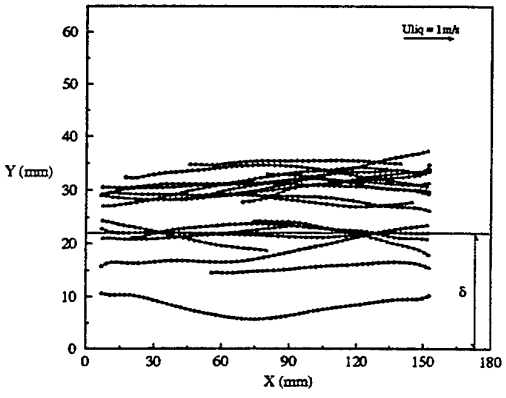
The distances from the surface where the deflections start, are presented figure 6. It varies between half the boundary layer thickness ($\delta/2$) for the $1mm$ and $6mm$ diameter bubbles and δ for the intermediate range $2 - 4mm$. In the boundary layer, significant differences in the trajectories according to the bubble size are visible. For the smallest bubbles ($1mm$ - figure 5-a), we note that fluctuations in direction exist and are quite sudden, similar to the behaviour of light particles. As the diameter increases, the fluctuations persist, but their time scale increases (figures 5-b & 5-c) suggesting that the "apparent inertia" associated with the added mass effect becomes important. This idea is reinforced by the fact that the deflections, which are quite direct for $2mm$ diameter bubbles (figure 5-b) are much less sudden for $3.5mm$ (figure 5-c). These different behaviours in the wall-region can be seen from the measurements of the angle between the wall and the bubble trajectories as the bubbles approach the wall (see figure 7). Close to the wall, the big bubbles approach the surface more slowly, compared with the $2mm$ case (see figures 7-d & 7-b). This



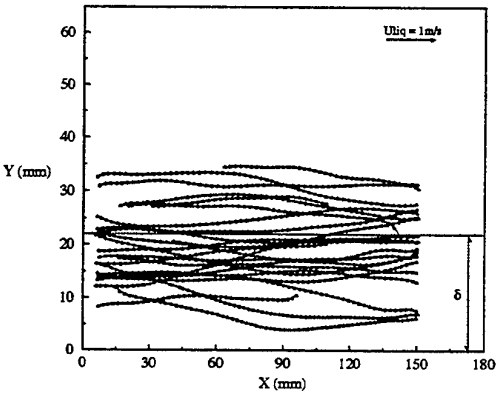
4-a : 1mm diameter bubbles. 61 images processed.



4-b : 3.5mm diameter bubbles. 59 images processed.

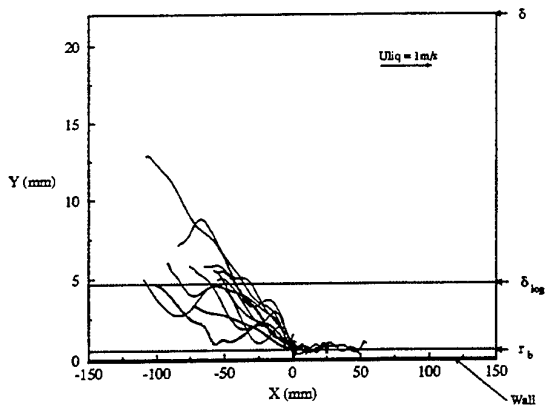


4-c : 4mm diameter bubbles. 60 images processed.

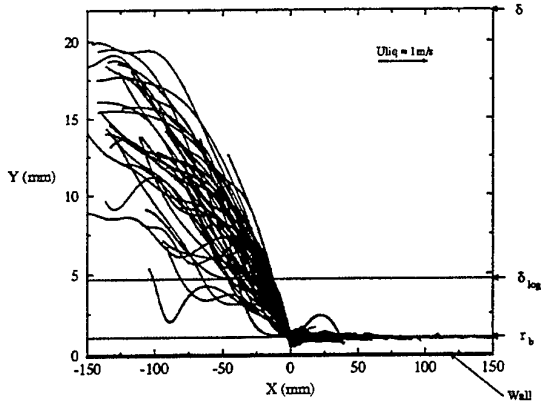


4-d : 6mm diameter bubbles. 70 images processed.

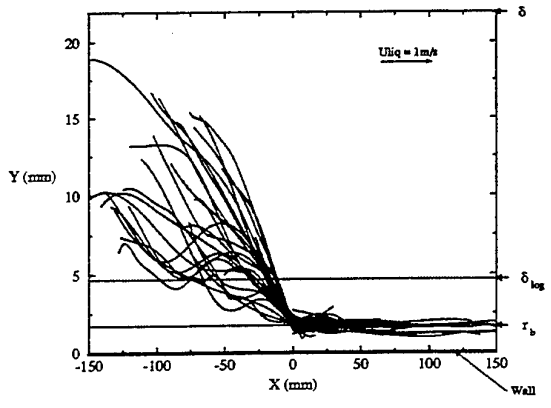
Figure 4: Typical trajectories for different bubble diameters.



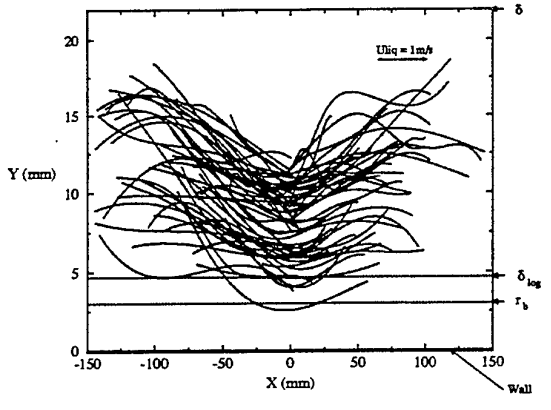
5-a : 1mm diameter bubbles.



5-b : 2mm diameter bubbles.

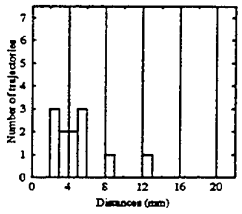


5-c : 3.5mm diameter bubbles.

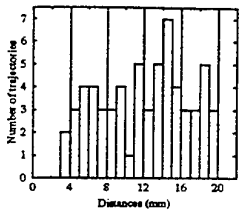


5-d : 6mm diameter bubbles.

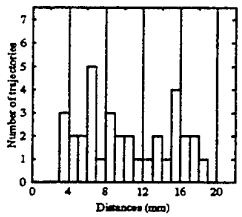
Figure 5: Migrations for different bubble diameters. The impingement points are shifted to the same origin $\mathbf{X = 0}$.



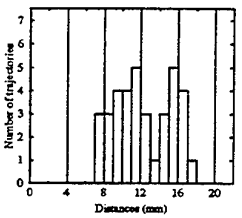
6-a : 1mm diameter bubbles.



6-b : 2mm diameter bubbles.

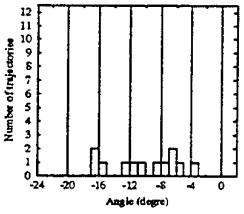


6-c : 3.5mm diameter bubbles.

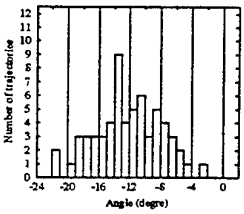


6-d : 6mm diameter bubbles.

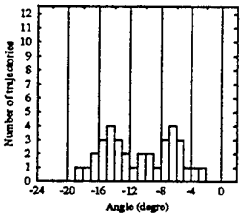
Figure 6: Distances of incipient deflections towards the wall.



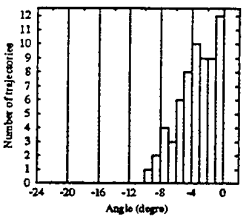
7-a : 1mm diameter bubbles.



7-b : 2mm diameter bubbles.



7-c : 3.5mm diameter bubbles.



7-d : 6mm diameter bubbles.

Figure 7: Impact angles between the bubble trajectories and the wall.

is certainly du to the "inertia" effects.
The rate of bubble deflection at the wall, normalized by the rate of bubble injection, (R), is plotted in figure 8, as a function of the distance Y of the injector from the surface for different bubble diameters. For each diameter, we see that the deflection starts for distances which are in agreement with those deduced from the trajectories. Moreover, R is small for $1mm$ and $6mm$, while it increases for $2mm$ and reaches a maximum for $3.5mm$. This remarkable result is consistent with the findings of others (Zun, 1980). Also, the behaviour exhibited in the limit as $Y = r_b$ (the mean bubble radius) is worth pointing out. Indeed, since in this case the bubbles are released at the surface, the phenomenon which is investigated is purely the capture ability of the plate. Up to $3.5mm$ diameter, the deflection rate is equal to unity, which means that all the bubbles released remain at the wall in a stable motion. Above $4mm$, R decreases indicating that the large bubbles escape from the plate and progressively return to the free-stream. We deduce that $d_b = 4mm$ is a critical value for the capture process. At moment, it is still difficult to scale this in terms of a critical non-dimensional number. According to numerical work on laminar shear flow (Ervin & Tryggvason, 1994), the change of behaviour for large bubbles would be caused by the interface deformation and could therefore be scaled in the form of a critical capillary number. This has yet be confirmed here. It turns out that in our case $4mm$ is also the thickness of the logarithmic layer.
Finally, typical histograms of the time interval between two consecutive laser detections are shown in figure 9. These results are for bubbles with a diameter of $3.5mm$, and two injection distances $Y \sim r_b$ and $Y \sim \delta$. Close to the wall, the distribution is strougly peaked, with a highest probable time of the order of the inverse bubble injection rate. Much further away, the distribution has a very long tail, with a peak at short times ($0.01s$) characteristic of the injection frequency, and a tail corresponding to detection intervals of $1.5 - 2s$. This suggests that the bubbles are deflected and deposed on the plate in small groups, the interval between these groups being related to the time scale of the mechanism which causes the migration. A more detailed analysis of this question is planned.

CONCLUSIONS AND FUTURE WORK

It is shown that the bubbles, with diameters between $1mm$ and $6mm$, are deflected towards the wall in a non-deterministic process. The deflections are rare for $1mm$ and $6mm$ bubbles, but they increase significantly for the intermediate size range $2 - 4mm$. Bubble deformation almost certainly plays an important role in this ; the $1mm$ bubbles are roughly spherical and undeformable ; bubbles in the range $2 - 4mm$ are ellipsoidal and the $6mm$ bubbles experience strong deformations. Moreover, below 4mm the bubbles which impinge on the plate remain captured at the

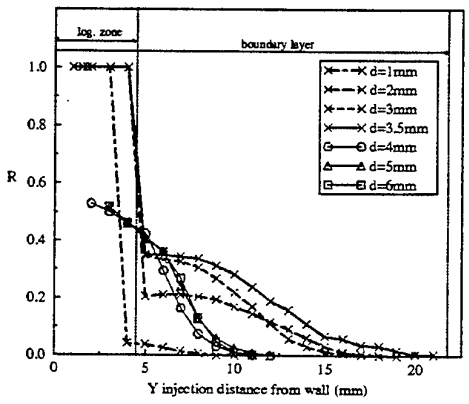


Figure 8: Bubble deposition rate at the wall, for different diameters. Estimation over 120 seconds.

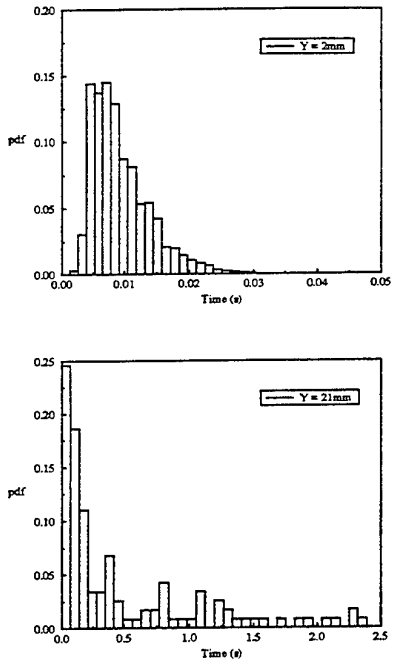


Figure 9: Histogram of time interval between two consecutive bubble laser detections. $\mathbf{d_b = 3.5mm}$.

surface, while the bubbles with a size above this value escape and return to the free-stream.

In the future, this work will continue in two main directions. Since the migrations towards the plate have a non-deterministic character, we may reasonably expect that they are due to the interaction between the bubbles and the turbulence. A possible way to examine this question is to try to visualize both the bubbles and the large scale turbulent structures in the boundary layer. This work is in progress. A preliminary experiment of this type has already been performed, in which rhodamine dye was injected directly into the boundary layer, through a hole in the plate. Photographic recordings appeared to show a correlation between the instantaneous unsteady structure of the boundary layer and the motion of bubbles towards the wall, but the photographic quality was no sufficient to permit a more detailed analysis. We are currently improving the techniques needed for this approach. In parallel, we also intend to calculate the bubble trajectories placed in a Bürgers vortex near a flat plate (simulated using a vortex and its image). This work will be completed with an investigation of the role of interface deformation in the deflection and subsequent capture or escape of the bubble.

REFERENCES

Ervin, E.A. & Tryggvason, G. ,1994, "The rise of bubbles in a vertical shear flow", in *Proceedings of the ASME Winter Annuel Meeting*. Chicago, USA.

Lance, M. & Bataille, J., 1991, "Turbulence in the liquid phase of a uniform bubbly air-water flow", *J. Fluid Mech.*, Vol. 222, pp. 95-118.

Liu, T.J., 1993, "Bubble size and entrance length effects on void development in a vertical channel", *Int. J. Multiphase Flow*, Vol.19, pp. 99-113.

Lunde, K. & Perkins, R.J., 1995, "A method for the detailed study of bubble motion and deformation", in *Advances in Multiphase Flow 1995*, eds., Serizawa, A., Fukano, T. & Bataille, J., pp. 395-405, Elsevier.

Moursali, E., Marié, J.L. & Bataille, J., 1995, "An upward turbulent bubbly boundary layer along a vertical flat plate", *Int. J. Multiphase Flow*, Vol. 21, No. 1, pp. 107-117.

Moursali, E., Marié, J.L. & Bataille, J., 1995, "Law of the wall and turbulent intensity profiles in a bubbly boundary layer at low void fraction", in *Proceedings of 2nd International Conference on Multiphase Flow*, pp. I17-I21, Kyoto, Japan.

Perkins, R.J. & Hunt, J.C.R., 1989, "Particle tracking in turbulent flows". in *Advances in Turbulence 2*, eds., Fernholz, H.H. & Fielder, H.E., pp. 286-291, Springer-Verlag.

Schlichting, H., 1968, "Boundary Layer Theory". *McGraw-Hill, sixth edition*, New-York.

Serizawa, A., Kataoka, I. & Michiyoshi, I., 1975, "Turbulence structure of air-water bubbly flows". Part I, II & III. *Int. J. Multiphase Flow*, Vol. 2, pp. 221-259.

Tomiyama, A., Sou, A., Zun, I., Kanami, N. & Sakagushi, I., 1995, "Effects of Eötvős number and dimensionless volumetric flux on lateral motion of a bubble in a laminar flow". in *2nd International Conference on Multiphase Flow*, Vol. 1, pp. PD11-PD18.

Zun, I., 1980, "The tranverse migration of bubbles influenced by walls in vertical bubbly flow". *Int. J. Multiphase Flow*, Vol. 6, pp. 583-588.

Zun, I., Kljenak, I. & Serizawa, A., 1992, "Bubble coalescence and transition from wall void peaking to core void peaking in turbulent bubbly flow". in *Dynamics of Two-Phase Flows*, eds., Jones, O.C. & Michiyoshi, I., pp. 233-249, Boca Raton, FL.

LARGE EDDY SIMULATION AND MODELLING OF INTER-PARTICLE COLLISION INFLUENCE IN GAS-SOLID TURBULENT SHEAR FLOWS

E. Deutsch, J. Lavieville, M. Sakiz, O. Simonin

IMFT / INPT
Allée du Professeur Camille Soula
31400 Toulouse
France

See late papers

THE EFFECT OF TURBULENCE MODELING ON TURBULENCE MODIFICATION IN TWO-PHASE FLOWS USING THE EULER-LAGRANGE APPROACH

Gangolf Kohnen and Martin Sommerfeld
Institut für Mechanische Verfahrenstechnik und Umweltschutztechnik
Martin-Luther-Universität Halle-Wittenberg, D-06099 Halle (Saale)
Germany

ABSTRACT

The mechanism of turbulence modification induced by the motion of solid particles within a flow are examined and analyzed by performing calculations with the Euler/Lagrange method. In this study the experimental investigations of Kulick et al. (1994) were taken as a basis in order to validate the applied models. There, a channel flow with a length of $L = 5m$ and a half width of $h = 20mm$ was investigated, where air was flowing vertically downward. Based on the channel half width a Reynolds number of $Re_h = 13800$ was obtained. Copper and glass particles of different mean diameters - $d_p = 70\mu m$ for the copper particles and $d_p = 50\mu m$ and $d_p = 90\mu m$ for the glass particles respectively - were added to the flow. The mass loading varied between $2 - 40\%$.

INTRODUCTION

For gas - solid two-phase flows as well as for gas - liquid systems the influence of the dispersed phase on the continuous phase is very important with respect to the objective of the whole process under consideration. The mechanism of turbulence modification induced by the motion of solid, liquid or gaseous particles within a flow are not very well understood in most situations. Due to the variety of parameters involved with this issue it is very difficult to extract a reasonable amount of information from a single experiment. Moreover, the quality (or the accuracy) of the results obtained by experimental investigations has a tremendous impact on the expected success of any model used to predict turbulence modification in such two-phase flow systems.

Basically, there are two classes of reviews available in the literature, where an attempt was made to classify turbulent two - phase flows. One of them is due to Gore & Crowe (1989), where the most relevant experimental investigations are analysed according to the change in turbulence intensity depending on a length scale ratio D_p/L_E, where D_p represents the particle diameter and L_E the integral length scale of the flow, respectively. This analysis resulted in a criterion for D_p/L_E in order to decide, if the particles attenuate the single phase turbulence (values below $D_p/L_E \approx 0.1$) or augment it (values above $D_p/L_E \approx 0.1$). Hetsroni (1989) in his review argued, that such a criterion for determining turbulence attenuation/augmentation could be found solely in the particle Reynolds number Re_p in such a way, that for $Re_p > 400$ wake effects become predominant leading to an enhanced turbulence production and hence to turbulence augmentation. Besides, different results are obtained for wall - bounded turbulent shear flows and free shear flows. Nevertheless, the number of parameters, which can be identified to be relevant for the influence on the change of turbulence intensities in a qualitative manner due to the presence of a dispersed phase, are similar to those of Gore & Crowe (1991):

- Stokes number $St = \tau_p/\tau_f$
- local volume fraction
- flow Reynolds number Re
- particle Reynolds number Re_p
- Length scale ratio D_p/L_E
- relative turbulence intensity $\sqrt{\overline{u'^2}}/\mid U_f - U_p \mid$

In the intermediate time both the criterion due to Gore and Crowe (1989) as well the one due to Hetsroni (1989) are regarded as doubtful. Recent Direct Numerical Simulations (DNS) performed by Squires & Eaton (1990) and Elghobashi & Truesdell (1993) showed the whole complexity of the problem leading to the conclusion, that a rather simple model will merely be able to describe the physics behind such turbulent two - phase flows. Moreover, the results emenating from those DNS are restricted to length scale ratios $D_p/\eta \leq 1$, where η is the Kolmogorov time scale in order to satisfy the applicability of the particle equation of motion. Since turbulence augmentation was observed even in this case under certain conditions, the general applicability of the criteria mentioned above are proved not to be realistic. Those Direct Numerical Simulations revealed the importance of viewing the changes in the transfer function due to particle presence. The close connection of those Direct Numerical Simulations and the experimental investigations performed by Kulick et al. (1994) served as a motivation to study the applicability of current turbulence

models for both phases and to look for improvements of such turbulence models.

NUMERICAL METHOD

The numerical calculations of particle dispersion in a turbulent flow were based on the Eulerian/Lagrangian approach for the continuous and dispersed phase, respectively. The continuous phase was computed by solving the time-averaged Navier-Stokes equations in connection with three different turbulence models. First, the standard $k-\varepsilon$ turbulence model (Launder & Spalding (1974)) served as a reference turbulence model. Moreover, a Reynolds stress turbulence model and a two-time scale model was used. The general form of the elliptic differential equations using a cartesian coordinate system is given for each conserved quantity by:

$$\frac{\partial}{\partial x}(\rho U\phi)+\frac{\partial}{\partial y}(\rho V\phi)-\frac{\partial}{\partial x}(\Gamma\frac{\partial\phi}{\partial x})-\frac{\partial}{\partial y}(\Gamma\frac{\partial\phi}{\partial y})=S_\phi+S_{\phi p}(1)$$

Here, S_ϕ represents the source terms of the continuous phase, $S_{\phi p}$ those of the dispersed phase, and Γ the effective viscosity. The resulting set of equations are solved by using a finite volume discretization scheme and applying an iterative solution procedure based on the SIMPLE algorithm. The convective terms are discretized by using a deferred correction scheme. The diffusive terms are generally discretized by using the central differencing scheme. In order to solve the system of equations a procedure according to Stone (1968) was applied, which is based on an incomplete LU - decomposition technique.

Turbulence modelling of the gaseous phase

In order to estimate the importance of the turbulence model used to represent the turbulent character of the continuous phase within the turbulent two - phase flow, different turbulence models were applied and compared among each other. The standard $k-\varepsilon$ turbulence model served as a reference model. Based on the general form of the conservation equation outlined in eq. 1 this model is characterized by the source terms and effective viscosities as well. Since this is a classical formulation, the reader is referred to Kohnen et al. (1994) for details.

The k-ε model as a representative of the two - equation eddy - viscosity model is widely used due to its easy handling. For a number of flow problems the application of this model leads to satisfactory agreement when compared with experimental results. Nevertheless, for complex flow situations this situation changes. Two major drawbacks can be identified at least in connection with the calculation of turbulent two - phase flow systems:

- The prescription of the linear stress - strain relationship results in a reduced range of use. Shortcomings are apparent for flows which deviate from spectral equilibrium.
- A more pronounced insensitiveness to the orientation of turbulence structures, i.e. to the anisotropy of the normal stresses is realized. The presence of a dispersed phase is basically designated by a change of the anisotropy of the normal stresses.

As a consequence of this the closure adopted herein is a high Reynolds - stress variant of Gibson & Launder (1978). In terms of Cartesian tensor notation this model may be written for plane flows as follows:

$$\frac{\partial[\varrho_f(U_k\overline{u_iu_j})]}{\partial x_k}=D_{ij}+P_{ij}-\varepsilon_{ij}+\Phi_{ij}+S_{\phi p}\qquad(2)$$

D_{ij} is the tensor of turbulent diffusion, P_{ij} the production tensor, Φ_{ij} the tensor to characterize the redistribution process, ε_{ij} the dissipation rate tensor, and $S_{\phi p}$ the particle

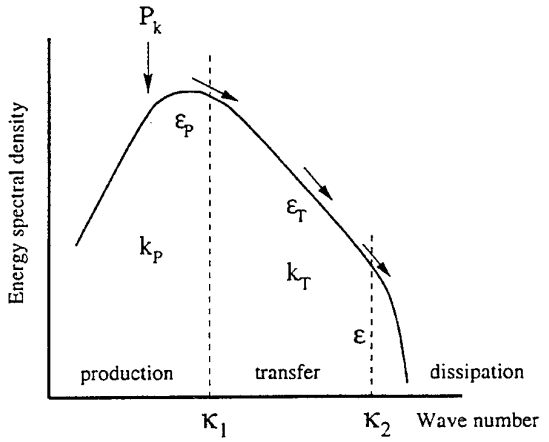


Figure 1: Schematic of the multiscale turbulence model

source term. The equation for the dissipation rate ε is characterized by the following equation:

$$\frac{\partial[\varrho_f(U_l\varepsilon)]}{\partial x_l} = c_{\varepsilon1}\frac{\varepsilon}{k}P_k+\varrho_f c_{\varepsilon2}\frac{\varepsilon^2}{k} + \frac{\partial}{\partial x_l}(\varrho_f c_\varepsilon\frac{k}{\varepsilon}\overline{u_lu_k}\frac{\partial\varepsilon}{\partial x_k})+S_{\phi p}\qquad(3)$$

A special treatment concerning the stability of this system of differential equations is similar to the work of Lien & Leschziner (1991).

In order to assess the relevance of the departure from the equilibrium stage a two - time - scale model was taken as well. For this type of turbulence model the energy spectrum is split up into three regions as shown in Fig. 1. This classification induces two different characteristic wave numbers. Energy assigned to the large turbulent eddies is produced by the mean shear gradient. This region is designated by the production range and covers wave numbers lower than the characteristic wave number κ_1, i.e. $\kappa\leq\kappa_1$. Beyond this wave number energy is transferred due to the energy cascading process to even higher wave numbers until the smallest turbulent eddies, where dissipation occurs (wave numbers $\kappa>\kappa_2$). This part of the wave number spectrum is called dissipation range. The intermediate range designated by $\kappa_2\leq\kappa<\kappa_1$ is called transfer range. Similar to the $k-\varepsilon$ - turbulence model differential equations for the production and the transfer range will be solved each for a turbulent kinetic energy and a corresponding dissipation rate. Hence, the two - time scale turbulence model is characterized by four equations. Within the present study the two - time scale turbulence model of Kim et al. (1987) was taken. With respect to eq. 1 this model is characterized by the source terms and effective viscosities summarized in Table 1. The corresponding set of empirical constants can be found in Kim et al. (1987).

Treatment of the dispersed phase

The dispersed phase was treated by the Lagrangian approach, where a large number of parcels, representing a number of real particles with the same properties, were traced through the flow field. The representation of the particles by parcels was used in order to allow the consideration of the partilce size distribution. The parcels were traced through the flow field by solving a set of ordinary differential equations for the particle location and velocity. For the formulation of the particle equation of motion it was assumed that the Basset history force and the added mass force are neglegible since a large density ratio ϱ_p/ϱ was considered (see Hjelmfelt & Mockros (1966)). The instantaneous fluid velocity itself was determined by using

ϕ	Γ	S_ϕ	$S_{\phi p}$
k_p	μ^*	$P_k - \rho\varepsilon_p$	$S_{k_p p}$
k_t	μ^*	$\rho(\varepsilon_p - \varepsilon_t)$	$S_{k_t p}$
ε_p	μ^*	$C_{p1}\frac{P_k^2}{\varrho_f k_p} + C_{p2}\frac{P_k\,\varepsilon_p}{k_p} - C_{p3}\frac{\varrho_f\,\varepsilon_p^2}{k_p}$	$S_{\varepsilon_t p}$
ε_t	μ^*	$C_{t1}\frac{\varrho_f\,\varepsilon_p^2}{k_t} + C_{t2}\frac{\varrho_f\,\varepsilon_p\,\varepsilon_t}{k_t} - C_{t3}\frac{\varrho_f\,\varepsilon_t^2}{k_t}$	$S_{\varepsilon_t p}$

$$P_k = \mu_t \left\{ 2 \cdot \left[\left(\frac{\partial U}{\partial x}\right)^2 + \left(\frac{\partial V}{\partial y}\right)^2 \right] + \left(\frac{\partial U}{\partial y} + \frac{\partial V}{\partial x}\right)^2 \right\}$$

$$\mu_t = C_\mu \rho \frac{k^2}{\varepsilon_p}; \quad \mu^* = \mu + \mu_t/\sigma_\phi; \quad k = k_p + k_t$$

Table 1: Source terms and effective viscosities within the two - time scale - model

the Markov - sequenz model including a drift correction for the transverse direction as it is described by Sommerfeld et al. (1993). This results in the following equations to determine new particle locations and velocities in a Cartesian coordinate system:

$$\frac{dx_p}{dt} = \tilde{U}_p \qquad \frac{dy_p}{dt} = \tilde{V}_p \qquad \frac{dz_p}{dt} = \tilde{W}_p \quad (4)$$

$$\frac{d\tilde{U}_p}{dt} = \frac{3\rho c_{D_p}\left(\tilde{U} - \tilde{U}_p\right) \mid \vec{U} - \vec{U}_p \mid}{4\rho_p D_p} + g_x$$

$$\frac{d\tilde{V}_p}{dt} = \frac{3\rho c_{D_p}\left(\tilde{V} - \tilde{V}_p\right) \mid \vec{U} - \vec{U}_p \mid}{4\rho_p D_p} \quad (5)$$

$$\frac{d\tilde{W}_p}{dt} = \frac{3\rho c_{D_p}\left(\tilde{W} - \tilde{W}_p\right) \mid \vec{U} - \vec{U}_p \mid}{4\rho_p D_p}$$

The drag coefficient was determined from the correlations:

$$c_{D_p} = \frac{24.0}{Re_p}[1.0 + \frac{1}{6}Re_p^{0.66}] \qquad Re_p < 1000 \quad (6)$$

$$c_{D_p} = 0.44 \qquad Re_p \geq 1000$$

with:

$$Re_p = \frac{D_p \mid \vec{U} - \vec{U}_p \mid}{\nu}$$

Interphase coupling

The particle source terms were calculated using a modified version of the Particle Source in Cell - approximation of Crowe et al. (1977). This model assumes, that the dispersed phase represents a source of mass and momentum in the equations for the continuous phase. The same strategy is taken for all turbulence quantities inherent for the problem. For two - phase flow systems without phase changes, the source term in the continuity equation is zero. For the three components of the momentum equation the so called particle source term is calculated for each time step Δt as follows:

$$S_{up} = -\frac{1}{V_{i,j}} \sum_k \dot{m}_k \cdot N_k \left[\left(U_{P_k}^{t+\Delta t} - U_{p_k}^t\right) - g_x \cdot \Delta t \right]$$

$$S_{vp} = -\frac{1}{V_{i,j}} \sum_k \dot{m}_k \cdot N_k \left[\left(V_{p_k}^{t+\Delta t} - V_{p_k}^t\right) - g_y \cdot \Delta t \right] \quad (7)$$

$$S_{wp} = -\frac{1}{V_{i,j}} \sum_k \dot{m}_k \cdot N_k \left[\left(W_{p_k}^{t+\Delta t} - W_{p_k}^t\right) - g_z \cdot \Delta t \right]$$

Here $\dot{m}_k$ and N_k represent the mass flow rate and the real number of particles within one computational parcel, respectively. $V_{i,j}$ is the volume of the computational cell. In the case, that one particle is crossing a cell face of one control volume in order to enter a neighbouring control volume, the particle source term has to be distributed by interpolation.

Two additional source terms for the turbulent kinetic energy and its dissipation rate have to be formulated in the case of the $k - \varepsilon$ turbulence model. They are:

$$S_{kp} \approx \overline{\tilde{U}_i \tilde{S}_{u_i p}} - U_i S_{u_i p} \quad (8)$$

for the turbulent kinetic energy and

$$S_{\varepsilon p} = 2\mu \overline{\frac{\partial u_i}{\partial x_l} \frac{\partial s_{pu_i}}{\partial x_l}} \sim C_{\varepsilon 3} \frac{\varepsilon}{k} S_{kp} \quad (9)$$

for the dissipation rate. The values designated by a tilde are instantaneous values, the small letters are fluctuating values, and the capital letters are averaged values. The additional constant $C_{\varepsilon 3}$ took a value of $C_{\varepsilon 3} = 1.1$. It should be noted, that for the control volumes adjacent to the wall the source terms of the turbulence quantities for the $k - \varepsilon$ turbulence model as well as for the other turbulence models were set to zero, since no model is available for this region, which is clearly not designated by local isotropic turbulence.

In the case of the reynolds - stress model the following particle source terms for the individual stresses are calculated:

$$\begin{aligned} S_{uup} &= 2 \cdot (\overline{\tilde{U}\tilde{S}_{up}} - US_{up}) \\ S_{vvp} &= 2 \cdot (\overline{\tilde{V}\tilde{S}_{vp}} - VS_{vp}) \\ S_{wwp} &= 2 \cdot (\overline{\tilde{W}\tilde{S}_{wp}} - WS_{wp}) \\ S_{uvp} &= \overline{\tilde{V}\tilde{S}_{up}} + \overline{\tilde{U}\tilde{S}_{vp}} - (VS_{up} + US_{vp}) \end{aligned} \quad (10)$$

The corresponding equation to eq. 9 for the dissipation equation reads as follows:

$$S_{\varepsilon p} = 0.5 \cdot C_{\varepsilon 3} \frac{\varepsilon}{k}(S_{uup} + S_{vvp} + S_{wwp}) \quad (11)$$

using $C_{\varepsilon 3} = 1.1$ in analogy to the $k - \varepsilon$ turbulence model. The particle source terms for the two - time scale turbulence model were formulated in two different ways. First, a proposal of Sato (1996) was used, where the total amount of turbulent kinetic energy emenating from the dispersed phase is distributed to the production and transfer range in the following way:

$$\begin{aligned} S_{k_p p}^1 &= \overline{\tilde{U}_i \tilde{S}_{u_i p}} - U_i S_{u_i p} - 2 \cdot k_t \cdot \sum_i \Delta t_i \cdot \frac{\dot{m}_{k,i}}{\tau_{p,i}} \\ S_{k_t t}^1 &= 2 \cdot k_t \cdot \sum_i \Delta t_i \cdot \frac{\dot{m}_{k,i}}{\tau_{p,i}} \\ S_{\varepsilon_p p}^1 &= C_{\varepsilon p 3} \frac{\varepsilon}{k} S_{k_p p} \\ S_{\varepsilon_t p}^1 &= C_{\varepsilon t 3} \frac{\varepsilon}{k} S_{k_t t} \end{aligned} \quad (12)$$

Due to the fact, that the calculations performed by Sato (1996) were done for two - phase flow systems with larger particles, where one can expect, that the particles do have an influence with the larger turbulent eddies of the production range, an alternative formulation was developed taking into account the fact, that the interaction between the smaller particles will take place more likely with the turbulent eddies represented by the transfer range. Consequently, this approach takes the form:

$$\begin{aligned} S^2_{k_p p} &= 0 \\ S^2_{k_t t} &= \overline{\tilde{U}_i \tilde{S}_{u_i p}} - U_i S_{u_i p} \\ S^2_{\varepsilon_p p} &= 0 \\ S^2_{\varepsilon_t p} &= C_{\varepsilon t 3} \frac{\varepsilon}{k} S_{k_t t} \end{aligned} \quad (13)$$

$C_{\varepsilon p 3}$ and $C_{\varepsilon t 3}$ are constants and took on the values defined by Sato (1996) leading to $C_{\varepsilon p 3} = C_{\varepsilon t 3} = 1.2$. Further details of the two - way coupling procedure can be found in Kohnen et al. (1994).

CONSIDERED FLOW CONFIGURATION

The numerical calculations were based on experiments of Kulick et al. (1994) in a channel flow configuration. In their study a channel with a length of $L = 5m$ and a half width of $h = 20mm$, where air was flowing vertically downward, was taken as test case. Based on the channel half width a Reynolds number of $Re_h = 13800$ was obtained. Copper and glass particles of different mean diameters - $d_p = 70\mu m$ for the copper particles and $d_p = 50\mu m$ and $d_p = 90\mu m$ for the glass particles respectively - were added to the flow. The mass loading varied between $2 - 40\%$.

RESULTS

The calculations for this turbulent two - phase channel flow were performed on a grid with 15000 control volumes distributed over two blocks. At the end of the channel a fully developed single phase flow was assumed. This was taken into account for the calculations of the single phase solution by forwarding the outlet information back to the inlet as long as a fully developed flow was recognized. The inlet conditions of the dispersed phase with respect to the mean and fluctuating velocities could be shown to have a negligible effect on the results at the end of the channel. Since initial conditions had to be specified, the corresponding free fall velocity of each particle was taken depending on the given size distribution and the distance from the particle feeder to the channel entrance. For each coupling iteration a total number of 25000 particles were tracked through the flow field. Using an underrelaxation factor of $\gamma = 0.3$ for smoothing the particle source terms 15 coupling iteration have been performed. The comparison between the experimental and numerical results refer to the velocity information provided at the end of the channel, where a fully developed turbulent two - phase flow was expected.

First of all it should be mentioned, that the influence of the particle mass loading Z within the considered test runs is negligible on the mean velocity profile for all three particle charges under investigation. Hence, there is no change in the gradient of the mean velocity in downward direction due to particle presence. This implies, that the production term can only be altered by the presence of the particles due to changes in the Reynolds stresses. Fig. 2 shows the axial rms - velocity of the fluid induced by glass particles with a mean diameter of $D_p = 50\mu m$ (a) and $D_p = 90\mu m$ (b). In both cases a reduction in turbulence intensity can be observed with increasing mass loading. The agreement is extremely well in the case of the $50\mu m$ particles in the whole cross section except close to the wall, whereas the sharp decrease in turbulence intensity cannot be reproduced by the numerical calculations for the higher mass loadings in the case of the $90\mu m$ particles. Only close to the channel centre a satisfactory agreement can be found. From Fig. 3 it becomes evident, that the effect of particles on the tangential rms - velocity is similar compared to the corresponding axial rms - velocities in Fig. 2. There, the agreement is satisfactory over the whole cross section. However, due to the missing experimental data for the higher mass loading for the $90\mu m$ particles it is difficult to argue, if the particles contribute to an isotropization of turbulence in the intermediate range between the wall and the centreline.

In Fig. 4 the profiles of the axial velocity fluctuations of the continuous phase are outlined depending on the three tested turbulence models. It is obvious, that the Reynolds - stress model reflects the experimental observations best, as it was already observed for the glass particles. Even the different source term formulations for the two - time scale model, inidcated as $QT1$ for eq. 12 and $QT2$ for eq. 13 cannot compensate the drawbacks of this model. Nevertheless, the reduction due to an increased mass loading is heavily underpredicted by all turbulence models. The reason for this may be found by focussing on the possible reasons responsible for changes in the turbulence quantities due to the presence of the particles. First, the particle source terms in the equations for the turbulence quantities, which are called the direct effect of particle motion on turbulence modification, may be one issue. Moreover, there is an indirect effect of particles on turbulence modification, which is associated with structural changes in the underlying turbulent flow field and cannot be covered by the particle source terms. It will be shown, that this indirect effect is responsible for the main reduction at least in the channel center. A major improvement could be achieved by using a model for the constant $C_{\varepsilon 2}$ in the $k - \varepsilon$ model and the Reynolds - stress model, where this constant is assumed to depend on the mass loading and the particle Stokes number, as this was found during the Direct Numerical Simulations of Squires & Eaton (1994) for a grid turbulence. The reason for this dependence was found to be a departure from the balance between the production mechanism due to vortex stretching and the viscous destruction depending on mass loading and particle Stokes number. This modified expression for $C_{\varepsilon 2} = f(\frac{\tau_p}{\tau_f}, \Phi_p)$ can be expressed as follows:

$$\frac{C_{\varepsilon 2}}{C_{\varepsilon 2_o}} = 1 + 20.462 \cdot [4.15 - 1.7 \cdot \frac{\tau_p}{\tau_f}] \cdot (0.75 - \frac{\tau_p}{\tau_f}) \cdot \Phi_p \cdot \frac{k}{\varepsilon} \quad (14)$$

Here, $C_{\varepsilon 2_o}$ is the original constant of the $k - \epsilon$ model and the Reynolds stress model in a single phase flow. It should be stressed here, that this modelled form is only valid in flow regions, which are similar to grid turbulence. For a channel flow, this is most likely at the channel centerline. In Fig. 5 and 6 this indirect effect is taken into account for the axial and tangential velocity fluctuations. Especially at the channel centreline an improved agreement can be found for the $k - \epsilon$ and Reynolds stress model. Concerning the tangential velocity fluctuation, which is depicted for the Reynolds stress model in Fig. 6, this improved reduction is overestimated indicating, that the influence of the particles on the surrounding fluid flow seems to depend on the spatial direction of the individual components of the velocity fluctuation. Moreover, the improvement is restricted to regions close to the channel centre. In order to get improved results for the wall near region, a corresponding relationship for the constant $C_{\varepsilon 1}$ should be determined by Direct Numerical Simulations as well.

CONCLUSIONS

It could be observed, that for the investigated two - phase flow system the importance of the anisotropy, covered by

the choice of using the Reynolds stress model, was predominant compared to the departure of equilibrium represented by the two-time scale model. Moreover, the direct and indirect influence could be identified. In order to quantify the indirect influence a model was developed, which resulted in a correction of the constant $C_{\varepsilon 2}$ depending on the loading and the particle Stokes number. With this model it was possible to get reasonably good results for the prediction of the turbulence attenuation in the centre of the channel. A universal for of this model would require further studies using Direct Numerical simulations in connection with a broader spectrum of the individual parameters.

REFERENCES

Crowe, C.T., Sharma, M.P. and Stock, D.E., 1977, "The particle-source-in-cell (PSI-cell) method for gas-droplet flows", *J. of Fluids Engng.*, Vol. 99, pp. 325 - 332.

Elghobashi, S. and Truesdell, G.C., 1993, "On the two-way interaction between homogeneous turbulence and dispersed solid particles. I: Turbulence modification", *Phys. Fluids A*, Vol. 5(7), pp. 1790 - 1801.

Gibson, M.M. and Launder, B. E., 1978, "Ground effects of pressure fluctuations in atmospheric boundary layers", *JFM*, Vol. 86, pp. 491 - 511.

Gore, R.A. and Crowe, C.T., 1989, "Effect of particle size on modulating turbulent intensity", *Int. J. Multiphase Flow*, Vol. 15, No. 2, pp. 279 - 285.

Gore, R.A. and Crowe, C.T., 1991, "Modulation of turbulence by a dispersed phase", *J. Fluids Engng.*, Vol. 113, pp. 304–307.

Hjelmfelt Jr., A.T. and Mockros, L.F., 1966, "Motion of discrete particles in a turbulent fluid", *Appl. Sci. Res.*, Vol. 16, pp. 149 - 161.

Hetsroni, G., 1989, "Particles-Turbulence Interaction", *Int. J. Multiphase Flow*, Vol. 15, No. 5, pp. 735 - 746.

Kim, S.-W. and Chen, C.-P., 1987, "A Multiple-Time-Scale Turbulence Model based on Variable Partitioning of Turbulent Kinetic Energy Spectrum", *NASA Contractor Report*, NASA CR-179222.

Kohnen, G., Rűger, M. & Sommerfeld, M., 1994, "Convergence behaviour for numerical calculations by the Euler/Lagrange method for strongly coupled phases", *Num. Meth. for Multiphase Flows*, FED Vol. 185, Editors: (Crowe et al.), p. 191-202.

Kulick, J.D., Fessler, J.R. and Eaton, J.K. 1994, "Particle response and turbulence modification in fully developed channel flow", *J. Fluid Mech.*, Vol. 277, pp. 109-134.

Launder, B. E., Spalding, D. B., 1974, "The numerical computation of turbulent flows", *J. Comput. Meth. Appl. Mech. Eng.*, Vol. 3, pp. 269 - 289.

Lien, F. S., Leschziner, M. A., 1991, "Second - moment modelling of recirculating flow with a non - orthogonal collocated finite - volume algorithm", *Proc. 8th Symp. Turbulent Shear Flows*, Paper 20-5, Munich.

Sato, Y., 1996, *Turbulence Structure and Modeling of Dispersed Two-Phase Flows*, Ph.D. - thesis, Dept. Mech. Eng., Keio University.

Sommerfeld, M., Kohnen, G., and Rűger, M., 1993, "Some open questions and inconsistencies of Lagrangian particle dispersion models", *Proc. Ninth Symp. on Turbulent Shear Flows*, Kyoto, Japan, Paper 5.1.

Squires, K.D. and Eaton, J.K., 1990, "Particle response and turbulence modification in isotropic turbulence", *Phys. Fluids A*, Vol. 2(7), pp. 1191 - 1203.

Squires, K.D. and Eaton, J.K., 1994, "Effect of Selective Modification of Turbulence on Two-Equation Models for Particle-Laden Turbulent Flows", *Trans. ASME J. Fluids Engng.*, Vol. 116, pp. 778-784.

Stone, H.L., 1968, "Iterative solution of implicit approximations of multi-dimensional partial differential equations", *SIAM J. num. Anal.*, Vol. 5, pp. 530 - 558.

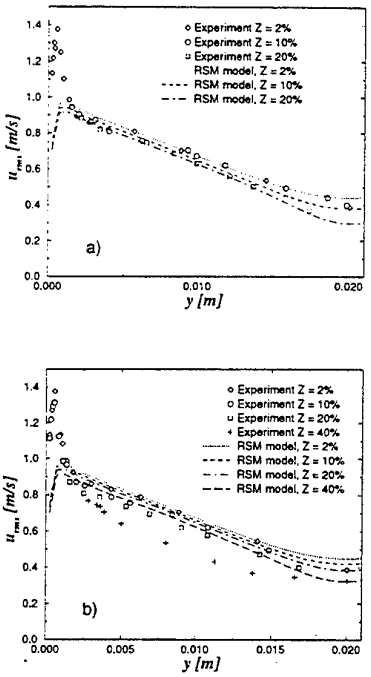


Figure 2: Fluid axial rms - velocity induced by glass particles with different mean diameters depending on the loading Z (RSM): a) $D_p = 50\mu m$; b) $D_p = 90\mu m$

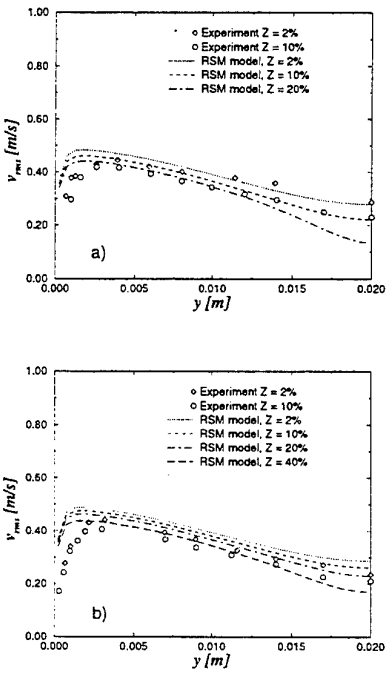


Figure 3: Fluid tangential rms - velocity induced by glass particles with different mean diameters depending on the loading Z (RSM): a) $D_p = 50\mu m$; b) $D_p = 90\mu m$

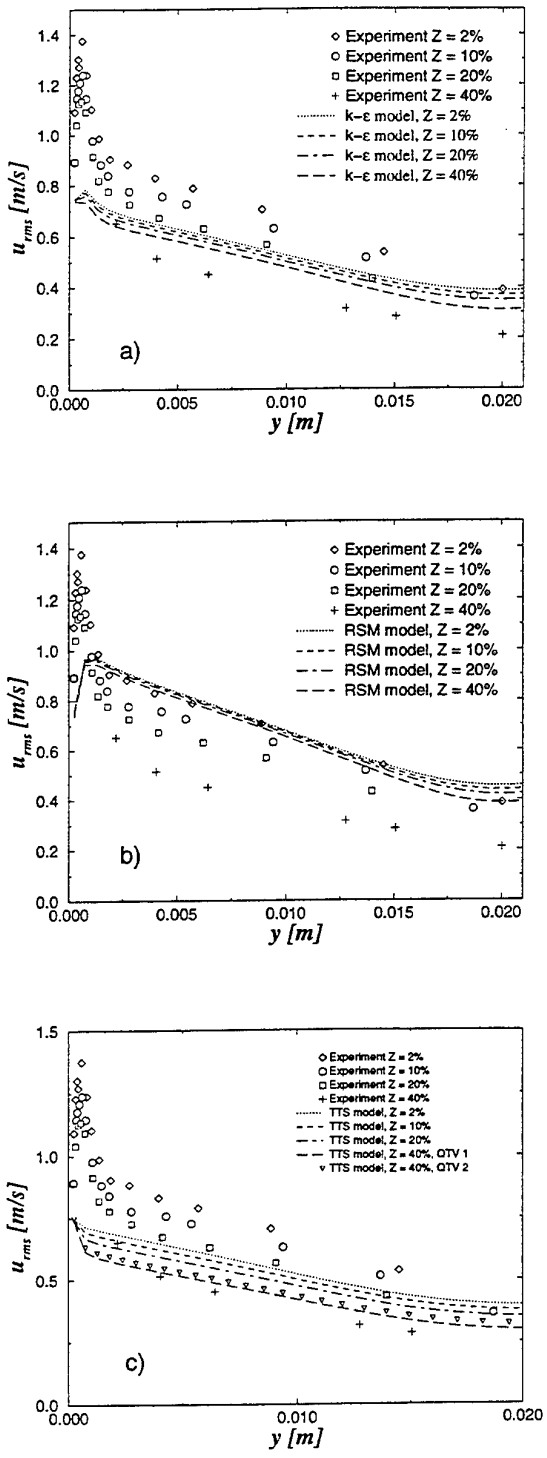


Figure 4: Axial rms - velocity (fluid) induced by the copper particles depending on the loading Z and the turbulence model (without indirect effect): a) $k-\epsilon$ turbulence model; b) Reynolds stress model; c) Two - time - scale model

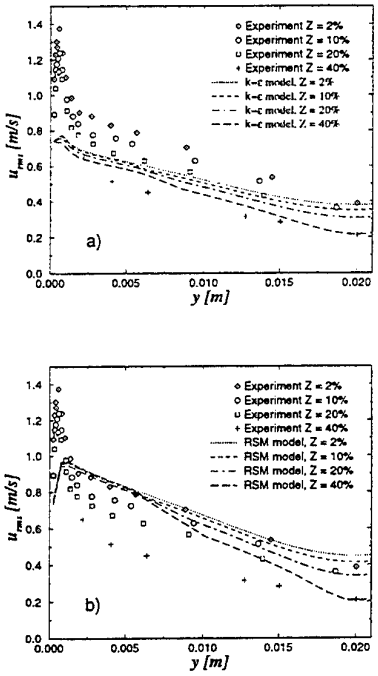


Figure 5: Fluid axial rms - velocity induced by the copper particles depending on the loading Z and the turbulence model (considering modelled indirect effect): a) $k-\epsilon$ model; b) Reynolds stress model

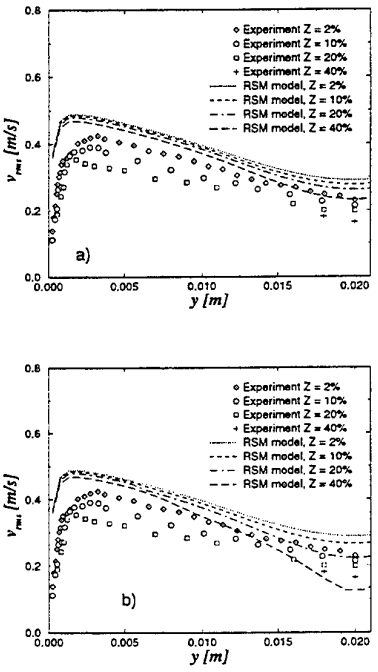


Figure 6: Fluid tangential rms-velocity induced by copper particles depending on the loading Z (Reynolds stress model): a) without; b) with indirect effect

EXTENDED ALGEBRAIC STRESS MODELS FOR PREDICTION OF THREE- DIMENSIONAL AND SEPARATING TURBULENT FLOW

R.J.A.Howard, N.D.Sandham
Engineering Dept
Queen Mary and Westfield College
London, E1 4NS
U.K.

ABSTRACT

The algebraic Reynolds stress model of Gatski and Speziale is extended by allowing the constants within the model to be functions of the invariants of the anisotropy. Although this makes the model non-linear in anisotropic flows our experience is that convergence is rapid. Advantages of this type of modelling are that all components of the Reynolds stress tensor are predicted and thus the invariants can be easily monitored for realisibility. This paper carries out the first stage of analysis of this type of modelling as part of any two equation model. Direct numerical simulation (DNS) results for the standard 2D turbulent channel flow are used in automatic optimisation procedures to find the constants within the ARSM relation. The results are then applied to 3D turbulent shear flows and a 2D turbulent separation bubble flow.

INTRODUCTION

The aim of algebraic Reynolds stress modelling (ARSM) is to extend the physics involved within a turbulence model calculation without significant increase in computational cost beyond that of a standard two-equation model. The algebraic Reynolds stress form of turbulence modelling arises by modelling the convective and diffusive parts of the Reynolds stress transport equation in such a way that the equation becomes algebraic in the Reynolds stress tensor. This means the model still contains much of the physics within the full Reynolds stress transport equations without the cost of solving extra transport equations. Although the algebraic Reynolds stress form of modelling includes much more physics than the standard two equation form it still has not been demonstrated to model accurately all the components of the stress tensor particularly in the near wall region. It is this aspect of ARSM modelling that is addressed in this paper.

It has been suggested that the ARSM form of modelling does not model transport terms in the Reynolds stress equation (Girimaji, 1996) because the transport terms are neglected. As explained later, this is not strictly true in the ARSM model formulation. The formulation is correct in isotropic flows and models the transport terms in anisotropic flows. If improvements to the model formulation are made based on the anisotropy of the flow, then their effect will not interfere with the behaviour of the model in isotropic flows.

The ARSM relation of Gatski and Speziale is used as the basic model since it is widely known and contains the main features of most ARSM models. The pressure strain is represented as a linear function of the anisotropy tensor and the algebraic equation for the anisotropy tensor is made an explicit non-linear function of the strain rate using Pope's (1975), methodology. Regularisation is used to improve the robustness of the final algorithm.

Modifications are carried out based on DNS values for channel flow. The DNS was carried out using a spectral (Fourier - Chebyshev) method details of which are given in Sandham & Howard (1997), Canuto *et al.* (1988) and Kleiser & Schumann (1980). Time discretisation is carried out using a compact 3rd order Runge-Kutta method for the convective terms and the Crank-Nicolson method for the viscous and pressure terms. The code has been written for use on massively parallel machines as discussed in Sandham & Howard (1997). Use of the invariants of the anisotropy in the evaluation of the constants makes the ARSM equation implicit. The DNS profiles for velocity, turbulence kinetic energy and dissipation are used in the right hand side of the ARSM equation to test whether it can produce the correct stress profiles given the exact velocity and dissipation fields.

Having obtained a solution for channel flow the model equation is then applied to a 3-D equilibrium flow field and a turbulent separation and reattachment flow field.

The paper is divided into four main parts. Firstly, formulation of the extended algebraic Reynolds stress turbulence model, secondly, analysis of three dimensional flows, thirdly, analysis of 2D separation and reattachment problem and finally, discussion, conclusions and further work.

EXTENDED ALGEBRAIC REYNOLDS STRESS MODELLING

The algebraic stress model is formed by first assuming that the rate of change of the anisotropy tensor,

$$b_{ij} = \overline{u_i' u_j'}/2K - \delta_{ij}/3,$$

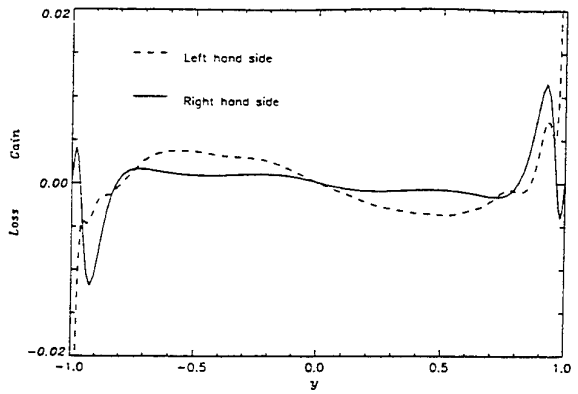


Figure 1: The left hand side is $\partial T_{ijk}/\partial x_k$ and the right hand side is $\tau_{ij}/K(\partial T_k/\partial x_k)$ for the $i = 1, j = 2$ component of the flow.

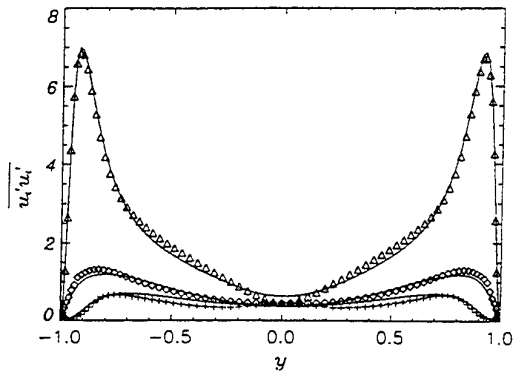


Figure 2: ARSM relation values for the normal stresses $\overline{u_1'u_1'}$ (triangles), $\overline{u_2'u_2'}$ (crosses) and $\overline{u_3'u_3'}$ (diamonds). The lines show the DNS values.

with time is zero

$$\frac{Db_{ij}}{Dt} = 0,$$

which can be written as

$$\frac{D\tau_{ij}}{Dt} = \frac{\tau_{ij}}{K}\frac{DK}{Dt}.$$

The second major assumption is that the transport terms in the τ_{ij} and K transport equations can be decoupled from the production, dissipation and pressure strain terms. This leads to;

$$P_{ij} + \Pi_{ij} - \epsilon_{ij} = \frac{\tau_{ij}}{K}(P - \epsilon), \qquad (1)$$

where P_{ij} is production, Π_{ij} pressure strain and ϵ_{ij} 'dissipation' tensor in the Reynolds stress transport equation and P is production and ϵ is dissipation in the kinetic energy transport equation and

$$\frac{\partial T_{ijk}}{\partial x_k} = \frac{\tau_{ij}}{K}\frac{\partial T_{mmk}}{\partial x_k}, \qquad (2)$$

where

$$T_{ijk} = \nu\frac{\partial \tau_{ij}}{\partial x_k} - (\overline{u_i'u_j'u_k'} + \overline{p'u_i'}\delta_{jk} + \overline{p'u_j'}\delta_{ik}),$$

corresponding to the viscous, turbulent and pressure diffusion respectively in the Reynolds stress transport equation. The decoupling is exact in flows in which the transport terms are zero. For other flows, decoupling the equations in this manner is a model assumption. However, it is a very different assumption than what is commonly stated for ARSM models, which is that this type of modelling assumes no transport. Rather, the ARSM models assume that *the stress transport balances the kinetic energy transport.* Figure 1 shows the left and right hand side of the diffusion balance equation (2) for the 1, 2 component in 2-D channel flow. This shows how the model is in error very close to the wall.

The Gastki & Speziale (1993), relation has the final form

$$\tau_{ij} = \frac{2}{3}K\delta_{ij} - \frac{6(1+\eta^2)\alpha_1 K}{3 + \eta^2 + 6\zeta^2\eta^2 + 6\zeta^2}$$

$$\left[S_{ij}^* + (S_{ik}^*\Omega_{kj}^* + S_{jk}^*\Omega_{ki}^*) - 2(S_{ik}^*S_{kj}^* - \frac{1}{3}S_{kl}^*S_{kl}^*\delta_{ij})\right]$$

$$S_{ij}^* = \frac{1}{2}g\frac{K}{\epsilon}(2 - C_3)S_{ij},\ \Omega_{ij}^* = \frac{1}{2}g\frac{K}{\epsilon}(2 - C_4)\omega_{ij}$$

$$\eta = (S_{ij}^*S_{ij}^*)^{\frac{1}{2}},\ \zeta = (\Omega_{ij}^*\Omega_{ij}^*)^{\frac{1}{2}}$$

$$\alpha_1 = (C_2 - \frac{4}{3})/(C_3 - 2)$$

$$g = (\frac{1}{2}C_1 + \frac{P}{\epsilon} - 1)^{-1}$$

We make use of the suggestion that the constants within the model can be made functions of the invariants of the anisotropy tensor. This allows us to tune the constants to give better solutions for the stress tensor as compared with DNS. Automatic optimisation procedures are used to do this. The ultimate aim for this study is to solve this equation in conjunction with the relevant two equation model transport equations for K and ϵ and the momentum equation, optimising the constants on the full closed modelled problem. However, this represents a highly complex optimisation problem. As a first step towards achieving this goal, the DNS values for velocity, turbulence kinetic energy (K) and dissipation (ϵ) are used in the ARSM shear stress relation. The P/ϵ term is removed from the g equation bearing in mind the point made by Girimaji (1996) about the cost and accuracy implications of iterating the ARSM relation on the P/ϵ ratio. The constants C_1, C_2, C_3, C_4 are made functions of the anisotropy invariants $II_b = b_{ij}b_{ji}$ and $III_b = b_{ij}b_{jk}b_{ki}$ in an expression of the form

$$C_1 = C_{11} + C_{12}II_b^{\frac{1}{2}} + C_{13}III_b^{\frac{1}{3}}.$$

The resulting set of equations are optimised with reference to 2D channel flow DNS. The convergence rate for this non-linear expression was found to rapid so we do not perceive it to be a problem with regard to computational cost. This, in effect, means that, assuming the rest of the model can produce the correct velocity, turbulence kinetic energy and dissipation profiles, it will produce the stress values as shown in figures 2 and 3. The direct stresses (Figure 2) are modelled quite well by this equation; with small errors near the centre of the channel where the models predicts isotropic turbulence due to the absence of strain rates. However there are some problems in the modelling of the shear stress (Figure 3). The main discrepancies occur just above the wall and towards the peak in the shear stress. Improvements in the optimisation method and more localised weighting with reference to the DNS could correct some of these problems. Another possibility for improvement is inclusion of other non-dimensional parameters. For the purpose of the present study we now investigate the applicability of the model to more complex near-wall turbulence.

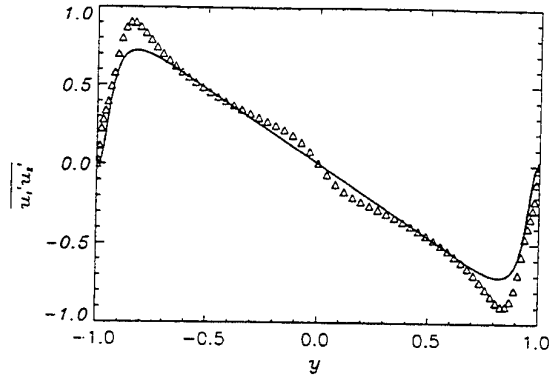


Figure 3: ARSM relation values for the shear stress $\overline{u_1'u_2'}$ (triangles). The line shows the DNS value.

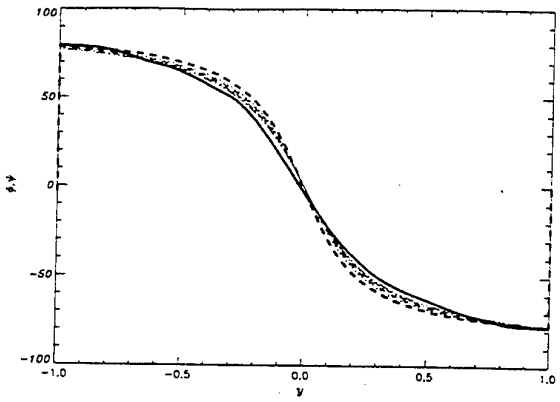


Figure 4: The 3D equilibrium flow shear stress and strain rate angles, ϕ and ψ (degrees). Direct numerical simulation and two equation modelling comparison. The solid line is the DNS result for strain angle and the dashed line stress angle. The other lines represent the two-equation model results.

THREE DIMENSIONAL SKEW FLOWS

Simulation and modelling of time dependent, non-equilibrium three dimensional skew flows were investigated by Howard & Sandham (1996). In these flows the obvious failing of the standard two-equation model comes in the eddy viscosity relation $\overline{(u_i'u_j')} = \nu_t \partial \overline{u_i}/\partial x_j$. In the non-equilibrium skew flows investigated it was found that the angle through which the shear stress was skewed was different from the angle through which the strain rate was skewed. As shown by the eddy viscosity relation the models are not able to capture this effect. A solution to this is to include a non-equilibrium flow modification to the eddy viscosity relation after Speziale (1987): $\overline{(u_i'u_j')} = \nu_t \partial \overline{u_i}/\partial x_j + f(\dot{S}_{ij})$, where a function of the Oldroyd derivative,

$$\dot{S}_{ij} = \frac{DS_{ij}}{Dt} - \frac{\partial \overline{u}_i}{\partial x_k} S_{kj} - \frac{\partial \overline{u}_j}{\partial x_k} S_{ki},$$

is added to the eddy viscosity. The form of this additional function is the subject of further work but it is clear that it will be zero in steady equilibrium flow.

Not surprisingly, a more appropriate test for equilibrium models is that of an equilibrium 3D flow. The 3D equilibrium flow investigated is obtained by setting one wall of a channel moving at a constant speed in the spanwise direction with a mean driving pressure gradient maintained in the streamwise direction. When this flow is allowed to settle to a steady state it produces a 3D equilibrium flowfield made up of a Poisseuille flow in the streamwise direction and a Couette flow in the spanwise direction. Figure 4 shows the shear stress angle $\phi = \arctan(\overline{u_1'u_2'}/\overline{u_3'u_2'})$ and strain rate angle $\psi = \arctan(\partial \overline{u}_1/\partial x_2/\partial \overline{u}_3/\partial x_2)$ angles for this flow. From this figure it can be seen that the angles through which the shear stress and strain rate have been skewed are almost the same across the whole flowfield. This would tend to support the suggestion that the difference in the two angles is an indication of how close the flow is to an equilibrium state. Differences between the angles are due to the fact that the DNS was not run for sufficient time for the flows to settle down fully to the equilibrium state. Also shown in figure 4 are the two-equation model results of the models discussed in Sandham & Howard (1996) for this flow. They show that the models give a good representation of the flow angles.

Figures 5 and 6 show the $\overline{u_1'u_2'}$ and $\overline{u_3'u_2'}$ stresses as produced by the DNS compared to both the two equation models and the new ARSM relation. The results show that

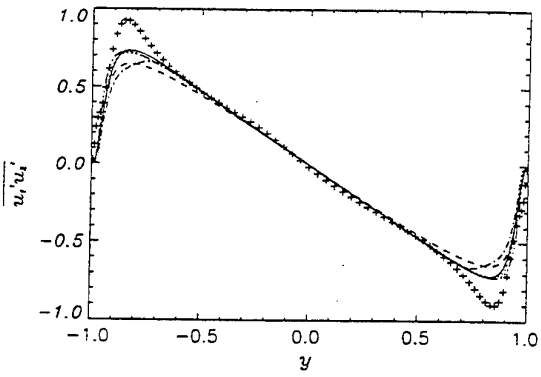


Figure 5: The 3D equilibrium flow shear stress component $\overline{u_1'u_2'}$. The model profiles are Launder & Sharma (1975) (dotted), Chien (1982) (dashed), Kawamura & Kawashima (1995) (dash dotted) and $k-g$ (Kalitzin, Gould & Benton, 1996) (dash treble dotted). The DNS values are the lines. The crosses are the extended ARSM results.

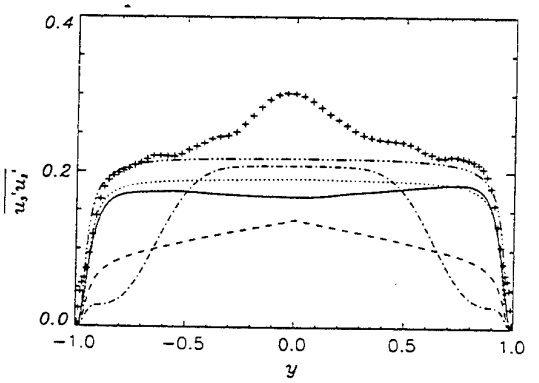


Figure 6: The 3D equilibrium flow shear stress component $\overline{u_3'u_2'}$. The model profiles are Launder & Sharma (1975) (dotted), Chien (1982) (dashed), Kawamura & Kawashima (1995) (dash dotted) and $k-g$ (Kalitzin, Gould & Benton, 1996) (dash treble dotted). The DNS values are the lines. The crosses are the extended ARSM results.

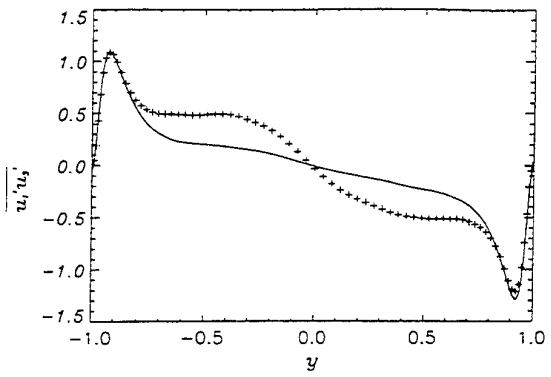


Figure 7: The equilibrium skew flow. ARSM relation values for the shear stress component $\overline{u_1' u_3'}$ (crosses). The line shows the DNS values.

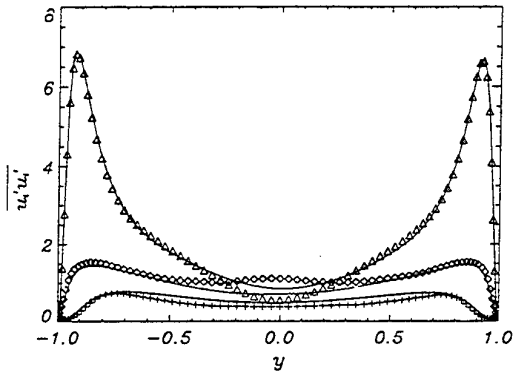


Figure 8: The equilibrium skew flow. ARSM relation values for the normal stresses $\overline{u_1' u_1'}$ (triangles), $\overline{u_2' u_2'}$ (crosses) and $\overline{u_3' u_3'}$ (diamonds). The lines show the DNS values.

the two-equation models all model the $\overline{u_1' u_2'}$ component well. However, the models of Chien (1982) and Kawamura & Kawashima (1995) both have problems in modelling the $\overline{u_3' u_2'}$ component. Figure 7 shows the $\overline{u_3' u_1'}$ component. Since there is no $\partial \overline{u}_1/\partial x_3$ or $\partial \overline{u}_3/\partial x_1$ straining in this flow the two-equation models are unable to show a $\overline{u_3' u_1'}$ component to the shear stress so the DNS result is compared with the ARSM relation. Similarly the direct stresses of the DNS and ARSM only are shown in figure 8. These results show that the ARSM gives the right character to each of the individual stress components but still has some problems modelling important features such as the peak and the near wall behaviour of the $\overline{u_1' u_2'}$ component, with additional problems in the centre of the channel for almost all the components. However, each of the two-equation models required some near wall damping function to fix their near wall behaviour whereas the ARSM relation has no such correction added.

In order for turbulence models to be applied for general engineering flows such as those over swept wings it is necessary for the models to be able to model non-equilibrium flows also. As discussed earlier, modifications to the models can be made for non-equilibrium flow and one of the benefits put forward about ARSM models is the possibilty of their being able to calculate non-equilibrium flows. The next set of results show the performance of the models in a time dependent skew flow. In this flow both of the

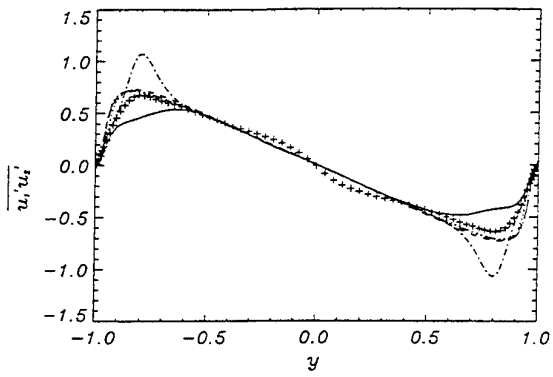


Figure 9: The 3D non-equilibrium flow shear stress component $\overline{u_1' u_2'}$. The model profiles are Launder & Sharma (1975) (dotted), Chien (1982) (dashed), Kawamura & Kawashima (1995) (dash dotted) and $k-g$ (Kalitzin, Gould & Benton, 1996) (dash treble dotted). The DNS values are the lines. The crosses are the extended ARSM results.

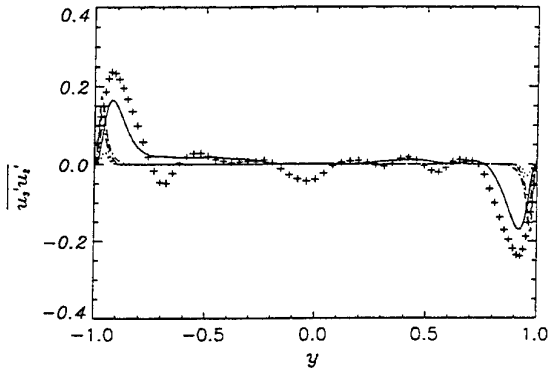


Figure 10: The 3D non-equilibrium flow shear stress component $\overline{u_3' u_2'}$. The model profiles are Launder & Sharma (1975) (dotted), Chien (1982) (dashed), Kawamura & Kawashima (1995) (dash dotted) and $k-g$ (Kalitzin, Gould & Benton, 1996) (dash treble dotted). The DNS values are the lines. The crosses are the extended ARSM results.

walls of the channel have been impulsively started in the spanwise direction and the flowfield produced after the initial disturbance is studied (see Howard & Sandham, 1996). Figures 9 to 12 show the shear stress components for the non-equilibrium flow. The ARSM model is able to capture quite well the changes in the magnitude of the normal stresses, (for example the reduction of $\overline{u_1' u_1'}$ from 7.0 to 4.1) but it does not quite manage to get the correct magnitude for the peaks in the shear stresses $\overline{u_3' u_3'}$, $\overline{u_2' u_3'}$, $\overline{u_1' u_3'}$ and $\overline{u_1' u_2'}$.

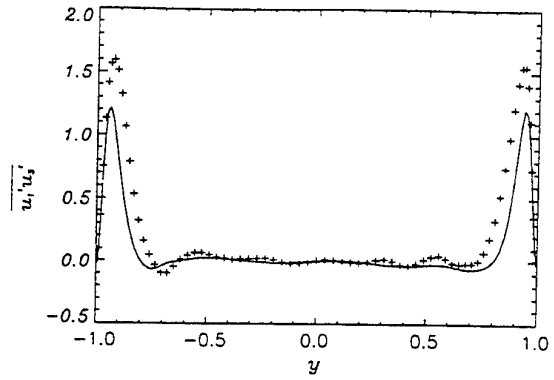


Figure 11: The non-equilibrium skew flow. ARSM relation values for the shear stress component $\overline{u_1'u_3'}$ (crosses). The line shows the DNS values.

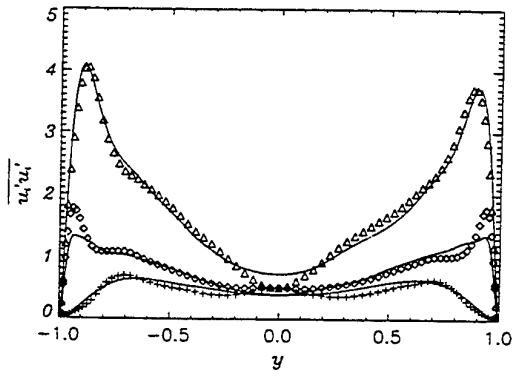


Figure 12: The non-equilibrium skew flow. ARSM relation values for the normal stresses $\overline{u_1'u_1'}$ (triangles), $\overline{u_2'u_2'}$ (crosses) and $\overline{u_3'u_3'}$ (diamonds). The lines show the DNS values.

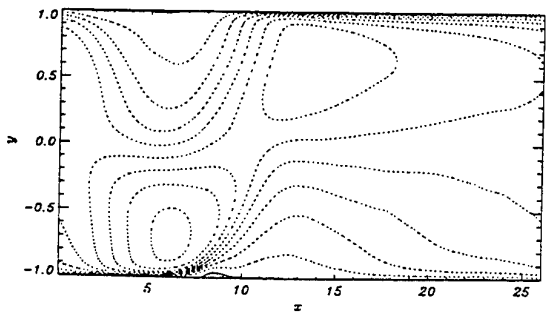


Figure 13: Streamwise velocity field in the turbulent separation and reattachment DNS. Lines show zero or negative velocity contours, dashed lines show positive velocity contours. The flow is from left to right.

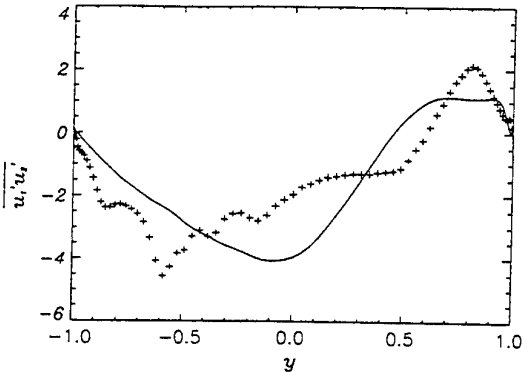


Figure 14: The separation and reattachment flow. A wall-normal profile at $x = 20.5$. The lower wall is at $y = -1$. ARSM relation values for the shear stress component $\overline{u_1'u_2'}$ (crosses). The line shows the DNS values.

TURBULENT SEPARATION AND REATTACHMENT

Turbulent separation bubbles can occur in flows such as those over wings as they approach the stall and high Reynolds number flows over uneven surfaces. They are accompanied by increased levels of drag and turbulent fluctuations.

The separation bubble simulated in this study is generated by applying a distributed body force within the domain of a turbulent channel flow and allowing the flow to readjust to the new conditions. The flow conditions created to produce the turbulent separation bubble here are thus broadly analogous to those that cause a turbulent separation bubble to occur in the flow over a wing with separation in regions of large adverse pressure gradient.

The distributed body force per unit area ($d\overline{p}/dx$) applied varies between $\pm 40u_\tau^2\rho/d$ sinusoidally in the streamwise direction over half the streamwise length of the channel. The forcing over the upper surface of the channel is the reverse of the forcing over the lower surface in order to satisfy continuity. The direct numerical simulation code used is a spectral channel code and thus the flow is required to be periodic in the streamwise and spanwise directions. Since the forcing is applied to half the streamwise length of the channel, the flow is allowed to relax in the remaining half of the channel. So the inflow to the forced region is approximately the steady channel flow already simulated. This has the added benefit that no fringe region is required so the turbulence is not distorted. Such simple boundary conditions also make the flow suitable as a test of turbulence models The velocity field of the DNS is shown in figure 13. Separation can be observed at $x = 8.0$ and reattachment at $x = 10$ on the lower surface. There is also a region of low velocity/separated flow on the upper surface between $x = 2.0$ and $x = 7.0$.

This flow obviously contains many features which are important but very difficult for turbulence models to capture, such as separation and reattachment. In order to test the effectiveness of the extended algebraic stress model in this flowfield the DNS velocity, turbulence kinetic energy and dissipation profiles at different streamwise locations are put into the optimised ARSM relation and the resulting turbulence stresses produced are compared with the DNS stresses. Figures 14 and 15 show example profiles at $x = 13.8$ for the $\overline{u_1'u_2'}$ and $\overline{u_1'u_1'}$ shear stress components. The wall normal direction is on the x-axis on these plots and -1 represents the lower wall. From these plots it can be seen that the ARSM relation gets the general flow fea-

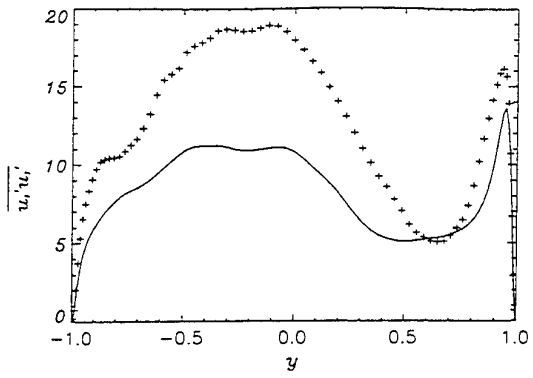


Figure 15: The separation and reattachment flow. A wall-normal profile at $x = 13.8$. ARSM relation values for the shear stress component $\overline{u_1'u_1'}$ (crosses). The line shows the DNS values.

tures but misses the peak values both near the wall and towards the channel centreline. Calculation of this flow has not been carried out by a two-equation model at this stage. However, the separation point and the separated region will be difficult for a model to calculate since the turbulent transport in that region is significant.

CONCLUSIONS

The ARSM relation of Gatski & Speziale (1993), has been modified and optimised using the invariants of the anisotropy to get a good representation of the Reynolds stress tensor for 2-D channel flow. The optimised ARSM expression (OARSM) was tested by inserting DNS velocity, turbulence kinetic energy and dissipation profiles and allowing the expression to converge. The converged values for the shear stress tensor were compared to the DNS values. There were some problems in the modelling of the flow near the channel centreline for the direct stresses, since isotropic flow results when no strain rate is present. Also the wall value and near wall peak for the shear stress were not perfect. Further work will include improvements in the optimising methods and addition of other parameters to correct these deficiencies.

The OARSM was tested in equilibrium and non-equilibrium 3-D flows. This involved inserting the DNS velocity and dissipation profiles into the OARSM expression and evaluating the stress tensor. The results were also compared with four two-equation models. Plots of the off diagonal shear components $\overline{u_1'u_2'}$ and $\overline{u_3'u_2'}$ unsurprisingly showed the OARSM had similar errors to 2-D flow calculations with no improvement in the shear stress over standard two-equation models. There are however two important points involved in the OARSM approach; firstly, there are no wall damping corrections, and secondly the modelling of the remaining stress tensor components is on the whole quite good compared with the two-equation models which cannot model these components at all. Some encouragement may be gained from the fact that the model, though only tuned to 2D channel flow, was able to compute key features of the 3D skewed flow case without further tuning.

The OARSM was tested in a flow involving a turbulent separation bubble. The OARSM expression again managed to model the correct features of the stress tensor using only velocity, turbulence kinetic energy and dissipation profiles. In this flow the OARSM showed a larger discrepancy in the normal stresses than for the other flows examined. This can be attributed to the non-equilibrium nature of this flow and the importance of correct modelling the transport terms in the OARSM formulation.

Acknowledgements : This research is funded by British Aerospace (operations) Ltd. (Sowerby Research Centre). Time on the Cray T3D is provided by EPSRC under grants GR/K 43902 and GR/K 43957.

REFERENCES

Canuto, C., Hussaini, M.Y., Quarteroni, A. and Zang, T., 1988, *Spectral Methods in Fluid Dynamics*, Springer.

Chien, K.-Y., 1982, "Predictions of channel and boundary layer flows with a low Reynolds-number turbulence model", *AIAA J.* **20**, No.1, 33-38.

Gatski, T.B. and Speziale C.G., 1993, "On explicit algebraic stress models for complex turbulent flows", *J. Fluid Mech.*, Vol. **254**, pp. 59–78.

Girimaji, S.S., 1996, "Fully explicit and self-consistent algebraic reynolds stress model", *Theoretical and Computational Fluid Dynamics*, Springer-Verlag, 8,pp.387–402

Howard, R.J.A. and Sandham, N.D., 1996, "Simulation and modelling of the skew response of turbulent channel flow to spanwise flow deformation",*Proc. Second ERCOFTAC Workshop for Direct and Large Eddy simulation*, Grenoble, France, 16-19th Sept.

Kalitzin, G., Gould, A.R.B. and Benton, J., 1996, "Application of two-equation turbulence models to aircraft design", *34th Aerospace Sciences Meeting, AIAA-96-0327*, Reno, Jan 15-18.

Kawamura, H. and Kawashima, N., 1995, "A proposal of k–$\tilde{\epsilon}$ model with relevance to the near wall-turbulence", *Int. Symp. on Turbulence, Heat and Mass Transfer*, Lisbon.

Kleiser, L. and Schumann, U., 1980, "Treatment of incompressibility and boundary conditions in 3-D numerical spectral solutions of plane channel flows", In *Proc. 3rd GAMM Conf. on Numerical Methods in Fluid Mechanics*, (Ed. E.H. Hirschel), 165-173, Vieweg.

Launder, B.E. and Sharma, B.I., 1975, "Application of the energy-dissipation model of turbulence to the calculation of flow near a spinning disc", *Letters in Heat and Mass transfer*, **1**, 131-138.

Pope, S.B., 1975, "A more general effective viscosity hypothesis", *J. Fluid Mech.*, Vol. **72**, pp. 331–340.

Sandham, N.D. and Howard, R.J.A., 1997, "Direct simulation of turbulence using massively parallel computers.",*Proc. Parallel CFD*, Manchester, May 19-21.

Speziale, C.G., 1987, "On nonlinear $K-l$ and $K-\epsilon$ models of turbulence", *J. Fluid Mech.*, Vol. **178**, pp. 459–475.

COMPUTATION OF UNSTEADY FLOWS BY USING A SEMI-DETERMINISTIC APPROACH WITH NONLINEAR TURBULENCE MODEL

A. Kourta
IMFT
Av. du Prof. Camille Soula
F–31400 Toulouse
France

and
CERFACS
42, avenue Gustave Coriolis
F–31057 Toulouse
France

ABSTRACT

Periodic vortex shedding produced by shear layers in turbulent flows is not correctly predicted by using classical turbulence models. A semi-deterministic approach is developed in order to correctly compute unsteady flows and analyze the effects of turbulence on this mechanism. The unsteady organized structures are computed and turbulent motion is taken into account by a first order model based on a nonlinear relationship between Reynolds stresses and phase average velocity gradients. Model coefficients are explicit functions of the phase average of both strain and rotation. This model first applied to the well known case of a backward-facing step flow and results are compared to experimental data. Then it is extended to the computation of a simplified configuration of a rocket booster. In this last case, the natural unsteadiness of the flow is captured. The interaction between the vortex shedding and the acoustic is described and the turbulence effects are characterized.

INTRODUCTION

Shear layers developing behind sharp solid discontinuities produce instabilities and vortex shedding able to interfer with acoustic waves in confined chamber. Such a situation can be found in solid propellant rocket motors. Indeed, the observed periodic vortex shedding in rocket motors (Flandro and Jacobs (1973), Flandro (1986), Brown *et al.* (1981)) is the result of a strong coupling between the instability of mean shear flow and organ-pipe acoustic modes in the chamber. The feedback from the acoustic waves provides the control signal for the aerodynamic instability. A first attempt to predict this phenomenon was presented in previous papers by Kourta (1995, 1996a, 1996b) by solving the unsteady compressible Navier-Stokes equations without introducing turbulence models. Interesting results have been found for the aeroacoustic coupling, but in view of full scale computations, turbulence has to be addressed if one wants realistic predictions of the instability frequencies and of the resulting levels of pressure and thrust oscillations.

A semi-deterministic approach is developed in order to correctly compute unsteady flows and analyze the effects of turbulence on this mechanism. This approach has been developed by Reynolds and Hussain (1972) and by Haminh and Kourta (1993) for turbulent flows with organized structures. It is based on splitting the instantaneous motion into an unsteady ensemble average motion and an incoherent and random motion. The unsteady organized structures are computed and turbulent motion is taken into account by a first order model based on a nonlinear relationship between the phase average of Reynolds stresses and velocity gradients. Model coefficients are explicit functions of the phase average of both strain and rotation.

The use of ensemble averaging leads to a set of equations looking identical to the one obtained with time averaging so called Reynolds averaging, except that the Reynolds shear stress is replaced by the ensemble-averaged shear stress, which can be interpreted as "organized Reynolds stresses". Unknown turbulent correlations are related to the phase averaged flow field by using a first order model. The standard first order models present two limits. The first one is that the model coefficients are constant and are determined under equilibrium or isotropic turbulence conditions. Thus they are not universal. The second point is that these models use Boussinesq's isotropic eddy-viscosity concept which assumes that the unknown correlations are proportional to the mean deformation tensor. The concept fails for flows where the normal stresses play an important role. This suggests the need for a more general model for complex flows overcoming both limitations listed before. For this reason, in steady state, more general closure relations have been derived by Shih *et al.* (1993) (see also Zhu and Shih (1994)). They contain both linear and nonlinear terms of the average velocity gradient. The same approach is extended to a semi-deterministic approach to develop unsteady calculation. The use of phase averaging allows to compute deterministic coherent structures, while the effects of incoherent structures are modelled. The unknown correlations are expressed in term of the phase average velocity gradients of the higher order. In the present study the quadratic form is used. An important behaviour of the present model is that the coefficients are not constant but functions of the flow mechanisms.

The first case computed is the backward facing step flow. The calculated results have been compared in detail with

experimental data and with those obtained using classical $k-\epsilon$ model. The improvements with this new approach are clearly shown. This approach is then used to compute the flow and the aeroacoustic interactions in a simplified configuration of the booster. In this configuration vortex shedding exists and is coupled to the second acoustic mode of the chamber. The interaction between the aerodynamic instability and the acoustic is analyzed and the impact of the tubulence on this mechanism is characterized.

GOVERNING EQUATIONS

Decomposition

The starting point of the present approach is the decomposition of any instantaneous physical variable (ϕ) into coherent organized ($\widehat{\phi}$) and incoherent random (ϕ_r) parts:

$$\phi(x_k,t) = \widehat{\phi}(x_k,t) + \phi_r(x_k,t) \qquad (1)$$

This decomposition can be obtained by phase averaging, which is averaging over a large ensemble of points having the same phase. In particular this decomposition will be fully satisfied if a pseudo-periodic component exists in the flow and it will the case in this work.

It should be noticed that due to the nature of both parts in the decomposition, the cross correlation between coherent and incoherent motion ($\widehat{\phi.\phi_r}$) must be zero. This feature was used by Brereton and Kodal (1994) to define a filtering procedure for performing such a decomposition. Under these assumptions, the resulting phase-averaged Navier-Stokes equations look identical to the Reynolds averaged Navier-Stokes equations, except the Reynolds shear stress is replaced by the phase-averaged shear stress.

In the following the generally admitted mass-weighted averaging procedure is retained for all transportable variables in compressible flows: $\tilde{\phi} = \frac{\widehat{\rho\phi}}{\widehat{\rho}}$, the mass-weighted phase average $\tilde{\phi}$ is time-dependent.

Turbulence model

The use of ensemble averaging leads to an open set of equations. The time-dependent approach gives identical equations with the same number of unknown correlations to be modelled as for the classical stationnary approach. The closure law of turbulent stresses ($\widehat{u_i u_j}$) used is similar to the one obtained by Shih *et al.* (1993) (see also Zhu and Shih (1994)) and used by these authors to compute steady flows. Using the same derivation (invariance theory and realizability conditions), the closure model can be obtained as follows (see Kourta and Haminh (1995), for details):

$$\widehat{\rho u_i u_j} = 2.\mu_t S_{ij} + T_{ij} - \frac{2}{3}\widehat{\rho}\tilde{k}\delta_{ij} \qquad (2)$$

with

$$\mu_t = C_\mu \frac{\widehat{\rho}\tilde{k}^2}{\tilde{\epsilon}}$$

and by taken only a quadratic form of T_{ij} we finally obtain:

$$T_{ij} = -\frac{\widehat{\rho}\tilde{k}^3}{\tilde{\epsilon}^2} f(\eta,\xi)[C_{\tau 1}(\frac{\partial \tilde{U}_i}{\partial x_k}\frac{\partial \tilde{U}_k}{\partial x_j} + \frac{\partial \tilde{U}_j}{\partial x_k}\frac{\partial \tilde{U}_k}{\partial x_i} - \frac{2}{3}\Pi\delta_{ij}) +$$

$$C_{\tau 2}(\frac{\partial \tilde{U}_i}{\partial x_k}\frac{\partial \tilde{U}_j}{\partial x_k} - \frac{1}{3}\Pi'\delta_{ij}) + C_{\tau 3}(\frac{\partial \tilde{U}_k}{\partial x_i}\frac{\partial \tilde{U}_k}{\partial x_j} - \frac{1}{3}\Pi'\delta_{ij})] \qquad (3)$$

f and C_μ are dependent on the time scale ratio of the turbulence to the phase average strain rate η and on the time scale ratio of the turbulence to the phase average rotation ξ:

$$f(\eta,\xi) = \frac{1}{A_2 + \eta^3 + \gamma_2\xi^3}$$

$$C_\mu(\eta,\xi) = \frac{2/3}{A_1 + \eta + \gamma_1\xi} \qquad (4)$$

with:

$$\Pi = \frac{\partial \tilde{U}_k}{\partial x_l}\frac{\partial \tilde{U}_l}{\partial x_k} \qquad \Pi' = \frac{\partial \tilde{U}_k}{\partial x_l}\frac{\partial \tilde{U}_k}{\partial x_l}$$

$$\eta = \frac{\tilde{k}S}{\tilde{\epsilon}} \qquad \xi = \frac{\tilde{k}\Omega}{\tilde{\epsilon}}$$

$$S = (2S_{ij}S_{ij})^{1/2} \qquad S_{ij} = \frac{1}{2}\left[\frac{\partial \tilde{U}_i}{\partial x_j} + \frac{\partial \tilde{U}_j}{\partial x_i}\right]$$

$$\Omega = (2\Omega_{ij}\Omega_{ij})^{1/2} \qquad \Omega_{ij} = \frac{1}{2}\left[\frac{\partial \tilde{U}_i}{\partial x_j} - \frac{\partial \tilde{U}_j}{\partial x_i}\right]$$

It is worthwhile noticing that both the linear part coefficient C_μ and the nonlinear part coefficient f depend on η and ξ. In previous work using the same kind of model, for practical reason the time scale ratio of the turbulence to the rotation ξ is not introduced in both coefficients C_μ and f. In this approach, the unsteady motion of coherent structures involve the rotation effect on all coefficients, thus all terms in formula (4) are maintained in the computation and the model is in fact more complete than the ones usually retained for stationary mean flow computations.

To acheive the closure process the phase-averaged turbulent kinetic energy of the turblent motion and its phase-averaged dissipation ($\tilde{k}$, $\tilde{\epsilon}$) have to be determined by using two transport equations (Kourta and HaMinh (1995)). To account of near wall flow, low turbulent Reynolds number model having the same form as Jones-Launder near wall model (Jones and launder (1972), Kourta and HaMinh (1995)) is used.

The model coefficients are given on table (1).

It can be noticed that if we only conserve the linear part of the model ($C_{\tau 1}$, $C_{\tau 2}$ and $C_{\tau 3}$ equal to zero) and C_μ equal to 0.09 we obtain the standard Jones-Launder model.

The most outstanding difference with a model used to compute steady state developped by Shih *et al.* (1993) is the use of low Reynolds number modelling in contrast with the use of wall function.

$C_{\epsilon 1}$	$C_{\epsilon 2}$	σ_k	σ_ϵ
1.44	1.92	1.0	1.3

$C_{\tau 1}$	$C_{\tau 2}$	$C_{\tau 3}$	A_1	A_2	γ_1	γ_2
-4	13	-2	1.25	1000	0.9	1

Table 1: Model coefficients

To sum up we can say that the use of this approach for the unsteady flows with organized structures is motived by the fact that this model is more general than classical first order models and is not limited to Boussinesq's isotropic eddy viscosity concept. This feature make it more adequate for predicting the unsteadiness.

METHODOLOGY

The numerical method used is a version of the explicit Mac Cormack scheme (MacCormack (1985), Kourta (1996a)). It consists of a predictor-corrector approach. For each time step, forward or backward approximations for the inviscid part is used and central differences for the viscous terms.

The computational domain of the backward-facing step is between 0.0m and 0.7m in the horizontal direction and between 0.0m and 0.2m in the vertical one. The step of

height H=0.06m is positioned at 0.1m from the origin of this domain. The mesh used contains 90× 50 grid points (HaMinh and Kourta (1993)).

The computational configuration of a rocket booster is presented on Fig. 1. The grid (318× 30) is the same as the one used by Lupoglazoff and Vuillot (1992). The length of the chamber was chosen in such a way that the first mode frequency was close to the critical frequency of the shear layer (f_{cr} = 1320 Hz) (Luppoglazoff and Vuillot (1992), Kourta (1996a). The length of this plane motor is 0.47 m with 0.2 m length grain.

In both cases, the mesh is refined in the shear layer in order to capture vortex shedding mechanism.

For the backward-facing step, the upper boundary is treated as a plane of symmetry. The lower boundary fitted to the step wall, is considered as a no-slip boundary. The total pressure and the total temperature, the inlet flow angle and the outlet static pressure are given.

The boundary conditions imposed to the rocket booster are given in table (2). No slip condition are imposed to inert wall where the velocity and normal pressure gradient are equal to zero. In injecting wall, the mass flow rate, the temperature and zero tangential velocity are specified. For the outflow boundary, the supersonic classical first order extrapolations are used.

Concerning turbulent quantities, $\tilde{k}$ and $\tilde{\epsilon}$ are set to zero at the wall.

For initial conditions, computations are started from rest.

Head end	no slip
Aft end	supersonic outflow
Internal side	symmetry
External side	A1:injecting wall A2:no slip condition

A1 and A2 are given on Fig. 1.

Table 2: Boundary conditions (rocket booster)

For the backward-facing step the free stream Mach number of the flow is approximately 0.27 and the step-height Reynolds number is about 10^6.

Table (3) presents the physical values used for the rocket booster. Where ρ_p is the propellant density, V_c the propellant burning rate, $\dot{m}$ the injection mass flow rate $(\rho v)_{inj}$, T_f the flame temperature, a the speed of sound, R the perfect gas constant, μ_{lam} the dynamic viscosity, γ the ratio of specific heats and Pr the Prandtl number.

The time step used is equal to $dt = 1.623 \times 10^{-7}$ seconds. 350000 iterations have been performed. The computation was done on a Convex C220 computer and for one time step 1.1 CPU seconds are needed.

ρ_p	V_c	$\dot{m}$	T_f	a
1633	13 10^{-3}	21.201	3387	1075.43
	R	μ	γ	Pr
	299.53	36 10^{-5}	1.14	1.

Table 3: Physical values (rocket booster) (S.I. units)

COMPUTATIONAL RESULTS

Backward-facing step flow

Experimental investigations have shown that the backward-facing step flow exhibits a low-frequency unsteadiness (Eaton and Johnston (1980), Driver and Seegmiller (1985), Driver *et al.* (1985), Pronchick and Kline (1983), Nezu and Nakagawa (1987), Celenligil and Mellor (1985), Kim *et al.* (1978), Armaly *et al.* (1983),...). In the reattachment zone, the flow near the wall is seen to be intermittently changing dierctions over ±1 step height from the mean reattachment point. When the semi deteministic model is used the mean value of this length is approximately equal to 7.97H which is in good agreement with experimental results of Eaton and Jonhston (1980).

In order to obtain the time-averaged values, the numerical simulation results are averaged over an integral number of cycles. Mean velocity profiles normalized by the free stream velocity at the inlet section are shown on Fig. 2, at two different streamwise positions in the reattachment zone. On the same figures, are presented experimental data, from Eaton and Johnston (1980) as well as computed results obtained with Jones-Launder $k - \epsilon$ low Reynolds number model. The comparison with experimental data clearly shows the improvement with the present approach.

The spectra analysis of velocity and pressure signals attests the existence of the organized motion. The energy spectra of the pressure (Fig. 3) present two distinct peaks, the dominant one at frequency $f_1 = 181Hz$, and another one less important corresponding to the frequency $f_2 = 54Hz$. In the shear layer (X=2.H; Y=0.5H), the energy spectra present one distinct peak corresponding to the frequency f_1: it corresponds to the vortex structures in the mixing layer; The second peak is observed in this zone but with very low intensity: as pointed out by Driver *et al.* (1985) , this low frequency is due to the flapping motion of the shear layer.

Strouhal	f_1	f_2	
S_{t1}	0.11	0.036	this study
	0.07		Eaton and Johnston
	0.04-0.07		Nezu and Nakagawa
	0.10		Celenligil and Mellor
S_{t2}	0.199	0.059	this study
	0.200	0.060	Driver *et al.*

Table 4: Strouhal numbers (backward-facing step)

The nondimensional frequencies are presented in table (4). The results of the present study are compared with the literature. Strouhal numbers are based either on the free stream velocity and the step height: $S_{t1} = fH/U_0$; or on the shear layer velocity ($U_{sh} = 0.5 \times U_0$) and the shear layer width (b=DU/(du/dy)$_{max}$): $S_{t2} = fb/U_{sh}$.The results obtained by this numerical simulation are quite consistant with experimental data.

Vortex shedding in the simplified rocket motor

The model validated in the previous geometry is applied to analyse turbulence effects on the interaction between the aerodynamic instability and the acoustic inside simplified rocket motor configuration. The goal of this part is to capture the vortex shedding and the interaction with the acoustic. Special attention is given to evaluate effects of turbulence on this interaction.

The time evolution of the thrust and corresponding spectrum are presented on Fig. 4. Signal is not regular compared to the viscous non turbulent case where the time evolutions were monochromatic (Kourta (1996a)). Turbulence produces a superimposition of another organized motion to the vortex shedding one. The spectrum does not present a single peak as it was observed in the viscous non turbulent case (Kourta (1996a). The peak at the frequency close to

the second longitudinal mode is also detected in the present turbulent case. The difference with the non turbulent case is the appearance of another frequency (1910Hz).

Figures (5) presents the spectra of the longitudinal velocity component at two points located downstream of the shear layer origin. One point is in the shear layer (top) and the other one (bottom) is in the near solid wall. The spectra show peaks at 1910 Hz and 2600 Hz both in the near wall region and in the shear layer. In the near wall region, the peak at 1910 Hz is more intense than in the shear layer and can be higher than the other frequency peaks (Fig. 5, bottom). In the shear layer region the second longitudinal mode is the predominant frequency.

The time evolution of the iso-vorticity contours (Fig. 6) during one period corresponding to the second longitudinal acoustic mode confirms that this acoustic mode controls the flow and the vortex shedding. However, the structures are less marked than in the case without turbulence and the intensity of the concentrated vorticity is smaller. The observed values of the turbulent viscosity was of order of one hundred molecular viscosity in the shear layer. The same results are also obtained with LES by Silvestrini (1996). The time evolution of the coherent part of the turbulent kinetic energy during one period (Fig. 7) shows that the turbulent quantity evolutions are also controlled by this longitudinal acoustic mode. So the longitudinal evolution inside the chamber is globally controlled by the second longitudinal acoustic mode.

The other source of instability observed in the chamber is characterized by a frequency of 1910 Hz. This can be interpreted as a secondary instability which affects mainly the near wall flow. It appears as a bulk oscillation in this region which affects the whole chamber. Origin of this instability can be associated to separation of the boundary layer upstream of the nozzle as found by Silvestriniet *al.* (1995) and Silvestrini (1996) using L.E.S. approach. It is produced by compression effects in the nozzle and probably enhanced by the presence of the turbulence yielding a thicker boundary layer along the nozzle wall. For this reason this instability was not detected in a previous simulation performed in the non turbulent case (Kourta (1996a)).

CONCLUSIONS

The present study is devoted to the simulation of the vortex shedding in turbulent shear flows. The use of phase averaging allows to compute deterministic coherent structures, while the effects of incoherent structures are modelled. The unknown correlations are expressed in term of the phase average velocity gradients of the higher order. In the present study the quadratic form is used. An important behaviour of the present model is that the coefficients are not constant but functions of the flow mechanisms. They depend on the time scale ratio η and ξ. In the near wall region damping functions compatible with the model are used.

This model is first applied to a backward-facing step for data validation. The results are in agreement with experimental data. Compared to classical models improvements are obtained. The reattachment length, the time-averaged quantities and the related Strouhal numbers are well predicted.

The validated model is then applied to analyse the flow inside a simplified configuration of rocket motor where vortex shedding has been observed. The vortex shedding is correctly predicted. Comparatively to a non-turbulent viscous simulation the monochromatic state does not exist in the turbulent case. Two frequencies are detected: 1910 Hz and 2700Hz, the last one corresponds to a second longitudinal acoustic mode. Apparently, the flow and the vortex shedding is controled by the second longitudinal acoustic mode as it was the case in non-turbulent simulations. The 1910 Hz frequency is more intense in the near wall region and associated to compression effects in the nozzle.

Acknowlegments

This work has been supported by CNES/ONERA contract no 93/3040. Part of computations has been done with the help of IDRIS (CNRS) computer. I express special thanks to Dr H.C. Boisson and Pr. H. HaMinh for valuable comments.

REFERENCES

Flandro, G., and Jacobs,H., 1973, "Vortex generated sound in cavities", *AIAA paper 73-1014.*

Flandro, G., 1986, "Vortex driving mechanism in oscillatory rocket Flows", *Journal of Propulsion and Power*, Vol. 3, No. 3, pp. 206–214.

Brown, R., Dunlap, R., S. Young, and Waugh, R., 1981, "Vortex shedding as a source of acoustic energy in segmented solid rocket", *Journal of Spacecraft*, Vol. 8, pp. 312–319.

Kourta, A., 1996a, "Acoustic-mean flow interaction and vortex shedding in solid rocket motors", *Int. Journal for Numerical Methods in Fluids*, Vol. 22, pp. 449–465.

Kourta, A., 1995, "Vortex shedding in solid rocket Motors", *AIAA paper 95-0727.*

Kourta, A., 1996b, "Vortex shedding in segmented solid rocket Motors", *Journal of Propulsion and Power*, Vol. 2, No. 2, pp. 371–376.

Reynolds, W.C., and Hussain, A.K.M.F., 1972, "The mechanics of an organized wave in turbulent shear flow. Part3. Theoretical models and comparisons with experiments", *J. Fluid Mech.*, vol. 54, part 2, pp. 263–288.

Haminh, H., and Kourta, A., 1993, "Semi-determinisic turbulence modelling for flows dominated by strong organized structures", *Ninth Symopsium on Turbulent Shear Flows* , pp. 10-5(1–6).

Zhu, J., and Shih, T.-H., 1994, "Computation of confined coflow jets with three turbulence models", *Int. J. for Numerical Methods in Fluids*, vol. 19, pp. 939–956.

Shih, T.-H., Zhu, J., and Lumley, J.L., 1993, "A realizable Reynolds stress algebraic equation model", *NASA Technical Memorandum 105993*, ICOMP-92-27; CMOTT-92-14.

Brereton, G.J. and Kodal,A., 1994, "An adaptive turbulence filter for decomposition of organized turbulent flows", *Phs. Fluids* 6(5), pp. 1775-1786.

Kourta, A., and Haminh, H., 1995, "Turbulence et aéroacoustique dans les moteurs de fusée", *Conference on Propulsive Flows in Space Transportation Systems*, Bordeaux, France, pp. 464–477.

Jones, W.P. and Launder, B.E., 1972, "The prediction of laminarization with a two-equation model of turbulence", *Int. J. of Heat and Mass Transfer*, Vol. 15, pp. 301–314.

MacCormack, R., 1995, "Current status of numerical solutions of the Navier-Stokes equations", *AIAA paper 85-0032.*

Luppoglazoff, N., and Vuillot, F., 1992, "Numerical simulation of vortex shedding Phenomenon in 2D Test Case Solid Rocket Motors", *AIAA paper 92-0776.*

Eaton, J.K., and Johnston, J.P., 1980, "Turbulent flow reattachment: an experimental study of the flow and structures behind a backward-facing step", *Report MD-39*, Stanford University.

Driver, D.M., and Seegmiller, H.L., 1984, "Features of a reattaching turbulent shear layer in divergent channel flow", *AIAA Journal*, vol.23, n. 2, pp. 163–171.

Driver, D.M., Seegmiller,H.L., and Marvin, J.G., 1986, "Time dependent behavior of a reattaching shear layer", *AIAA Journal*, vol.25, n. 7, pp. 914–919.

Pronchick, S.W., and Kline, S.J., 1983, "An experimental investigation of the structure of a turbulent reattaching flow behind a backward-facing step", *Report MD-42*, Stanford University.

Nezu, I., and Nakagawa, H., 1987, "Turbulent structures of backward-facing step flow and coherent vortex shedding from reattachment in open channel flows",' *Turbulent Shear Flow Conference*.

Celenligil, M.C., and Mellor, G.L., 1985, "Numerical solution of two dimensional turbulent separated flows using a Reynolds stress closure model", *Journal of Fluid Engineering*, vol. 107, pp. 467–476.

Kim, J., Kline, S.J., and Johnston, J.P., 1978, "Investigation of saparation and reattachment of a turbulent shear layer: flow over a backward-facing step", *Report MD-37*, Stanford University.

Armaly, B.F., Durst, F., Pereira, J.C.F., and Schönung, 1983, "Experimental and theoretical investigation of backward-facing step flow", *J. Fluid Mech.*, vol.127, pp. 473–496.

Silvestrini, J.H., Comte, P., and Lesieur, M., 1995, "Simulation de grandes échelles: Application aux moteurs à propergol solide segmentés", *Conference on Propulsive Flows in Space Transportation Systems*, Bordeaux, France, pp. 205–220.

Silvestrini, J.H., 1996, "Simulation de grandes échelles des zones de mélange: application à la propulsion solide des lanceurs spatiaux", *Thèse de Doctorat de l'Institut National Polytechnique de Grenoble*, France.

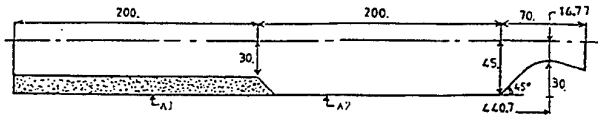


Figure 1: Computational domain of a rocket booster

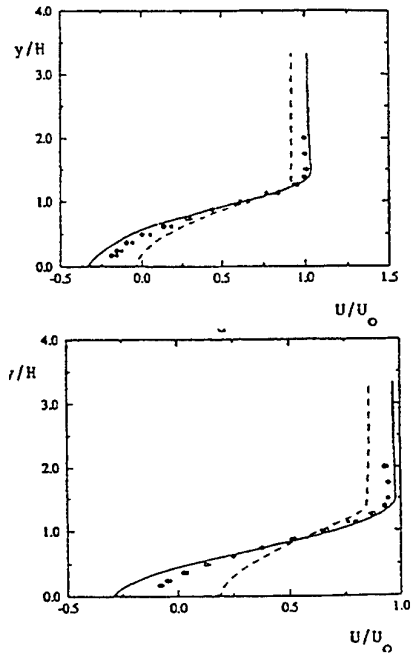


Figure 2: Backward-facing step: mean velocity profiles, symbols: experiments, dashed line: Jones-Launder $k-\epsilon$ model, solid line: semi-deterministic model (top: x/H=4 ; bottom: x/H=6)

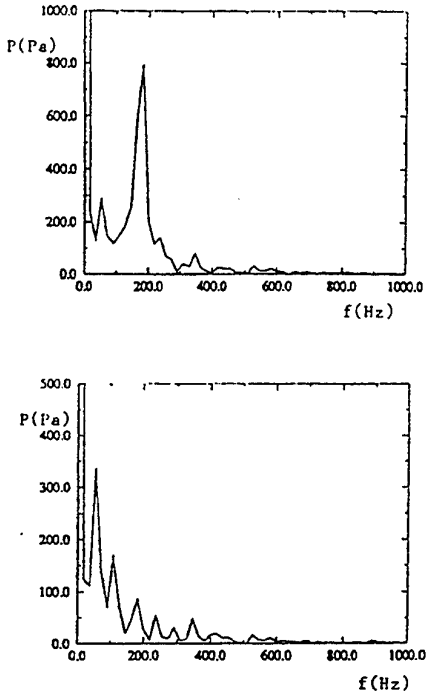


Figure 3: Backward-facing step: spectra of the pressure (top: x/H=6 , y/H=0.5; bottom: x/H=8 , y/H=0.5)

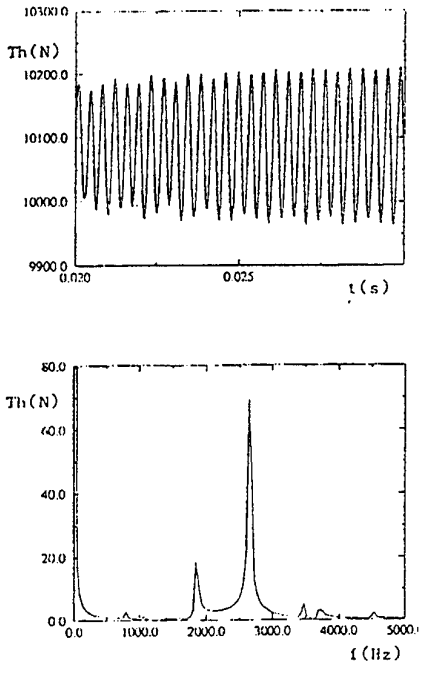
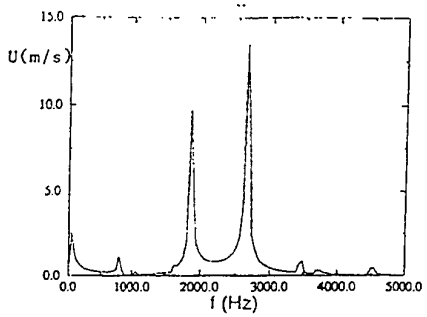


Figure 4: Rocket booster: Time history and spectrum of the thrust



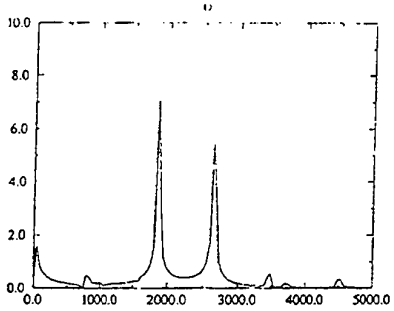


Figure 5: Rocket booster: Spectra of the U velocity component (top: x/L=0.78 , y/L=0.0824; bottom: x/L=0.73 , y/L=0.0075)

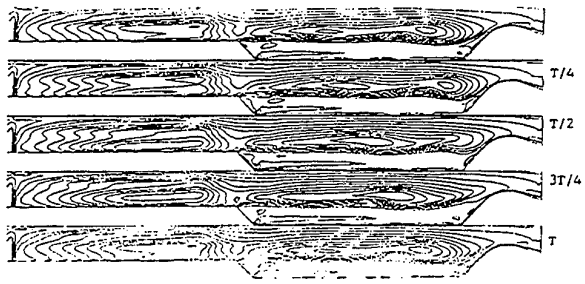


Figure 6: Rocket booster: Iso-vorticity during one period

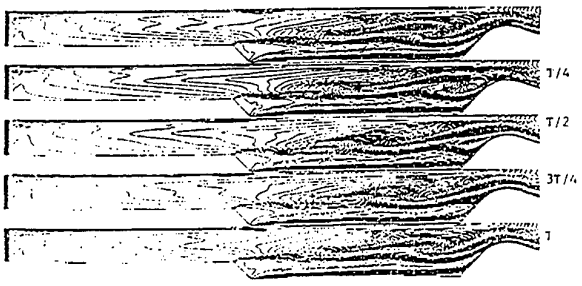


Figure 7: Rocket booster: Iso-turbulent kinetic energy during one period

SWIRL FLOW SIMULATION BY MEANS OF REYNOLDS STRESS TURBULENT MODELLING

Miroslav A. Sijerčić and Stevan Đ. Nemoda
Laboratory for Thermal Engineering and Energetics
Institute of Nuclear Sciences - Vinča,
PO Box 522,
11001 Belgrade
Yugoslavia

ABSTRACT

Prescribed are a model description and some results of mathematical modelling and computer simulation of swirling flow in conical diffuser based on the Reynnolds stresses closure. The flow is described by a system of time averaged conservation equations for the mean momentum in axial, radial and tangential direction. The equation set contains also transport equations for the Reynolds stresses themselves. The control volume approach is adapted for casting elliptic partial equations in to finite difference form. The difference equations are solved by an iterative line-by-line technique. Under-relaxation is used to achieve numerical stability. A conical diffuser with 20 degree included angle is described with small steps at the wall boundary. The intensity of the swirl is not enough to causes the recirculation zone. The paper presents detailed plots of profiles of velocity components, turbulent characteristics and comparisons of the predicted results with hot-wire measurements available in literature.

INTRODUCTION

In the research of turbulent swirling flows the accent is placed mainly at the analysis of recirculatiing swirling flows due to the wider area of application for this type of rotating flows. However, swirling flow also has important applications in conical diffusers without recirculation. In nonswirling flow in the diffuser there is often flow separation near the wall, usually having adverse effects. Centrifugal force of the rotating flow makes it possible to avoid this affect and for flow to acquire characteristics of parabolic flows. At the same time the flow acquires specific form, different from the swirling flows with strong recirculation, usual in combustors or swirling free jets. There are indications that models of turbulent viscousity do not encompass adequately all effects of swirling flows, caused mainly by centrifugal and Coriolis effects. Therefore, in this article, we have chosen the stress model of turbulence.

MATHEMATICAL MODEL

Closure of the system of Reynolds equations of momentum and continuity for stationary turbulent flow of incompressible fluid:

$$\frac{\partial}{\partial x_j}\left(\rho U_i U_j\right) = \rho f_i - \frac{\partial P}{\partial x_i} + \frac{\partial}{\partial x_j}\left[\mu\frac{\partial U_i}{\partial x_j} - \rho\overline{u'_i u'_j}\right] \quad , \quad \frac{\partial(\rho U)}{\partial x_i} = 0.$$

has been carried out based on the solution of equations for turbulent stress, having the exact form:

$$U_k\frac{\overline{\partial u_i u_j}}{\partial x_k} = -\left[\overline{u_j u_k}\frac{\partial U_i}{\partial x_k} + \overline{u_i u_k}\frac{\partial U_j}{\partial x_k}\right] + \frac{\partial}{\partial x_k}\left(\nu\overline{\frac{\partial u_i u_j}{\partial x_k}}\right) - \left[2\nu\overline{\frac{\partial u_i}{\partial x_k}\frac{\partial u_j}{\partial x_k}}\right] +$$
$$+\left[\overline{\frac{p}{\rho}\left(\frac{\partial u_i}{\partial x_j} + \frac{\partial u_j}{\partial x_i}\right)}\right] - \frac{\partial}{\partial x_k}\left[\overline{u_i u_j u_k} + \overline{\frac{p}{\rho}\left(\delta_{jk}u_i + \delta_{ik}u_j\right)}\right]$$

or: $$C_{ij} = G_{ij} + T_{ij} + E_{ij} + \Phi_{ij} + \mathcal{D}_{\varepsilon}$$

Convective transport (C_{ij}), production due to main flow deformations (G_{ij}), and viscous diffusion (T_{ij}), may be used in their exact form. For modeling of the other terms, approximations based on the model described in (Launder at al. 1975) have been chosen. Redistribution between components of stress (interactions of pressure and flow deformations) is given as:

$$\Phi_{ij} = -c_1\frac{\varepsilon}{k}\left(\overline{u_i u_j} - \frac{2}{3}\delta_{ij}k\right) - \alpha\left(G_{ij} - \frac{2}{3}\delta_{ij}G\right)$$
$$-\beta\left(D_{ij} - \frac{2}{3}\delta_{ij}G\right) - \gamma k\left(\frac{\partial U_i}{\partial U_j} + \frac{\partial U_j}{\partial U_j}\right) + \Phi_{ij,w}$$

where are:

$k = \overline{u_k u_k}/2$ and $G = G_{kk}/2$

kinetic energy of turbulence, and the production of turbulent kinetic energy respectively and δ_{ij} is Kronecker delta, while:

$$D_{ij} = -\left(\overline{u_i u_k}\frac{\partial U_k}{\partial x_i} + \overline{u_j u_k}\frac{\partial U_k}{\partial x_i}\right) \text{ and}$$

$$G_{ij} = -\left(\overline{u_i u_k}\frac{\partial U_i}{\partial x_k} + \overline{u_j u_k}\frac{\partial U_j}{\partial x_k}\right)$$

Modeling of the influence of the wall on the redistribution of stress components is given by the expression:

$$\Phi_{ij,w} = \left[0{,}125\frac{\varepsilon}{k}\left(\overline{u_i u_j} - \frac{2}{3}\delta_{ij}k\right) + 0{,}015\left(G_{ij} - D_{ij}\right)\frac{k^{1,5}}{\varepsilon x_2}\right],$$

where x_2 is the distance from the wall, encompassing distances from all influential walls at the cross section. Coefficients α, β and γ are mutually dependent and are determined by coefficient c_2: $\alpha = (8 + c_2)/11$, $\beta = (8c_2 - 2)/11$, $\gamma = (30c_2 - 2)/55$. Viscous destruction is described by the dissipation of turbulent kinetic energy ε, ($E_{ij} = -2/3\varepsilon$), for which the transport equation is solved:

$$U_j\frac{\partial \varepsilon}{\partial x_j} = \frac{\partial}{\partial x_i}\left[(\nu + c_\varepsilon\frac{k}{\varepsilon}\overline{u_i u_j})\frac{\partial \varepsilon}{\partial x_j}\right] + c_{\varepsilon 1}G\frac{\varepsilon}{k} - c_{\varepsilon 2}\frac{\varepsilon^2}{k}$$

Diffusion transport of turbulent stress components is modeled by the expression:

$$\mathcal{D}_{ij} = c_s\frac{\partial}{\partial x_k}\left(\frac{k}{\varepsilon}\overline{u_k u_t}\frac{\partial \overline{u_i u_j}}{\partial x_t}\right)$$

Model has six constants, whose values have been proposed based on the experimental data and numerical optimization, and are given as:

c_1	c_2	c_s	$c_{\varepsilon 1}$	$c_{\varepsilon 2}$	c_ε
1,5	0,4	0,22	1,45	1,9	0,15

Model equations have been developed in cylindrical coordinate system. Modelled transport equations of flow turbulent quantities can be expressed as follows:

$\overline{u^2}$ - Reynolds stress:

$$\frac{\partial}{\partial x}(U\overline{u^2}) + \frac{1}{r}\frac{\partial}{\partial r}(rV\overline{u^2}) = \frac{1}{r}\frac{\partial}{\partial r}\left[r\nu\frac{\partial \overline{u^2}}{\partial r}\right] + \frac{\partial}{\partial x}\left(\nu\frac{\overline{u^2}}{\partial x}\right) -$$
$$-2\left(1 - \alpha + 0.015\frac{k^{1.5}}{\varepsilon y_w}\right)\cdot\left(\overline{uv}\frac{\partial U}{\partial r} + \overline{u^2}\frac{\partial U}{\partial x}\right) -$$
$$-\left(c_1 - 0.125\frac{k^{1.5}}{\varepsilon y_w}\right)\frac{\varepsilon}{k}\left(\overline{u^2} - \frac{2}{3}k\right) + \frac{2}{3}(\alpha + \beta)G - \frac{2}{3}\varepsilon +$$
$$+c_s\frac{1}{r}\frac{\partial}{\partial r}\left[r\frac{k}{\varepsilon}\left(\overline{v^2}\frac{\partial \overline{u^2}}{\partial r} + \overline{uv}\frac{\partial \overline{u^2}}{\partial x}\right)\right] + c_s\frac{\partial}{\partial x}\left[\frac{k}{\varepsilon}\left(\overline{u^2}\frac{\partial \overline{u^2}}{\partial x} + \overline{uv}\frac{\partial \overline{u^2}}{\partial r}\right)\right] +$$
$$+2\left(\beta + 0.015\frac{k^{1.5}}{\varepsilon y_w}\right)\cdot\left(\overline{u^2}\frac{\partial U}{\partial x} + \overline{uv}\frac{\partial V}{\partial x} + \overline{uw}\frac{\partial W}{\partial x}\right) + 2\gamma k\frac{\partial U}{\partial x}$$

$\overline{v^2}$ - Reynolds stress:

$$\frac{\partial}{\partial x}(U\overline{v^2}) + \frac{1}{r}\frac{\partial}{\partial r}(rV\overline{v^2}) - 2\frac{W}{r}\overline{vw} = \nu\left[\frac{1}{r}\frac{\partial}{\partial r}\left(r\frac{\partial \overline{v^2}}{\partial r}\right) + \frac{\partial}{\partial x}\left(\frac{\partial \overline{v^2}}{\partial x}\right) -\right.$$
$$\left. -\frac{2}{r^2}(\overline{v^2} - \overline{w^2})\right] - 2\left(1 - \alpha + 0.015\frac{k^{1.5}}{\varepsilon y_w}\right)\cdot\left(\overline{v^2}\frac{\partial V}{\partial r} - \overline{vw}\frac{W}{r} + \overline{uv}\frac{\partial V}{\partial x}\right) -$$
$$-\frac{2}{3}\varepsilon - \left(c_1 - 0.125\frac{k^{1.5}}{\varepsilon y_w}\right)\frac{\varepsilon}{k}\left(\overline{v^2} - \frac{2}{3}k\right) + 2\left(\beta + 0.015\frac{k^{1.5}}{\varepsilon y_w}\right)\cdot$$
$$\cdot\left(\overline{uv}\frac{\partial U}{\partial r} + \overline{vw}\frac{\partial W}{\partial r} + \overline{v^2}\frac{\partial V}{\partial r}\right) + \frac{2}{3}(\alpha + \beta)G +$$
$$+c_s\frac{\partial}{\partial x}\left[\frac{k}{\varepsilon}\left(\overline{u^2}\frac{\partial \overline{v^2}}{\partial x} + \overline{uv}\frac{\partial \overline{v^2}}{\partial r} - 2\frac{\overline{uw}}{r}\overline{vw}\right)\right] +$$
$$+c_s\frac{1}{r}\frac{\partial}{\partial r}\left[r\frac{k}{\varepsilon}\left(\overline{uv}\frac{\partial \overline{v^2}}{\partial x} + \overline{v^2}\frac{\partial \overline{v^2}}{\partial r} - 2\frac{\overline{(vw)^2}}{r}\right)\right] -$$
$$-2\frac{c_s}{r}\frac{k}{\varepsilon}\left[\overline{uw}\frac{\partial \overline{vw}}{\partial x} + \overline{vw}\frac{\partial \overline{vw}}{\partial r} + \frac{\overline{w^2}}{r}(\overline{v^2} - \overline{w^2})\right] + 2\gamma k\frac{\partial V}{\partial r}$$

$\overline{w^2}$ - Reynolds stress:

$$\frac{\partial}{\partial x}(U\overline{w^2}) + \frac{1}{r}\frac{\partial}{\partial r}(rV\overline{w^2}) + 2\frac{W}{r}\overline{vw} =$$
$$\nu\left[\frac{1}{r}\frac{\partial}{\partial r}\left(r\frac{\partial \overline{w^2}}{\partial r}\right) + \frac{\partial}{\partial x}\left(\frac{\partial \overline{w^2}}{\partial x}\right) + \frac{2}{r^2}(\overline{v^2} - \overline{w^2})\right] -$$
$$-2\left(1 - \alpha + 0.015\frac{k^{1.5}}{\varepsilon y_w}\right)\left(\overline{uw}\frac{\partial W}{\partial x} + \overline{vw}\frac{\partial W}{\partial r} + \overline{w^2}\frac{V}{r}\right) -$$
$$-\frac{2}{3}\varepsilon - \left(c_1 - 0.125\frac{k^{1.5}}{\varepsilon y_w}\right)\frac{\varepsilon}{k}\left(\overline{w^2} - \frac{2}{3}k\right) +$$
$$+\frac{2}{3}(\alpha + \beta)G - 2\left(\beta + 0.015\frac{k^{1.5}}{\varepsilon y_w}\right)\left(\overline{w^2}\frac{V}{r} - \overline{vw}\frac{W}{r}\right) +$$
$$+c_s\frac{\partial}{\partial x}\left[\frac{k}{\varepsilon}\left(\overline{u^2}\frac{\partial \overline{w^2}}{\partial x} + \overline{uv}\frac{\partial \overline{w^2}}{\partial r} + 2\frac{\overline{uw}}{r}\overline{vw}\right)\right] +$$
$$+c_s\frac{1}{r}\frac{\partial}{\partial r}\left[r\frac{k}{\varepsilon}\left(\overline{uv}\frac{\partial \overline{w^2}}{\partial x} + \overline{v^2}\frac{\partial \overline{w^2}}{\partial r} + 2\frac{\overline{(vw)^2}}{r}\right)\right] +$$
$$+2\frac{c_s}{r}\frac{k}{\varepsilon}\left[\overline{uw}\frac{\partial \overline{vw}}{\partial x} + \overline{vw}\frac{\partial \overline{vw}}{\partial r} + \frac{\overline{w^2}}{r}(\overline{v^2} - \overline{w^2})\right] + 2\gamma k\frac{V}{r}$$

$\overline{uv}$ - Reynolds stress:

$$\frac{\partial}{\partial x}(U\overline{uv}) + \frac{1}{r}\frac{\partial}{\partial r}(rV\overline{uv}) - \frac{\overline{uw}}{r}W =$$
$$\nu\left[\frac{1}{r}\frac{\partial}{\partial r}\left(r\frac{\partial \overline{uv}}{\partial r}\right) + \frac{\partial}{\partial x}\left(\frac{\partial \overline{uv}}{\partial x}\right) - \frac{\overline{uv}}{r^2}\right] -$$
$$-\left(1 - \alpha + 0.015\frac{k^{1.5}}{\varepsilon y_w}\right)\left(\overline{uv}\frac{\partial U}{\partial x} + \overline{v^2}\frac{\partial U}{\partial r} + \overline{u^2}\frac{\partial V}{\partial x} + \overline{uv}\frac{\partial V}{\partial r} - \overline{uw}\frac{W}{r}\right) -$$
$$-\left(c_1 - 0.125\frac{k^{1.5}}{\varepsilon y_w}\right)\varepsilon\frac{\overline{uv}}{k} + \left(\beta + 0.015\frac{k^{1.5}}{\varepsilon y_w}\right)\cdot$$
$$\cdot\left(\overline{u^2}\frac{\partial U}{\partial r} + \overline{uv}\frac{\partial V}{\partial r} + \overline{uw}\frac{\partial W}{\partial r} + \overline{uv}\frac{\partial U}{\partial x} + \overline{v^2}\frac{\partial V}{\partial x} + \overline{vw}\frac{\partial W}{\partial x}\right) +$$
$$+c_s\frac{\partial}{\partial x}\left[\frac{k}{\varepsilon}\left(\overline{u^2}\frac{\partial \overline{uv}}{\partial x} + \overline{uv}\frac{\partial \overline{uv}}{\partial r} + \frac{(\overline{uw})^2}{r}\right)\right] +$$
$$+\frac{c_s}{r}\frac{\partial}{\partial r}\left[r\frac{k}{\varepsilon}\left(\overline{uv}\frac{\partial \overline{uv}}{\partial x} + \overline{v^2}\frac{\partial \overline{uv}}{\partial r} + \overline{uw}\frac{\overline{vw}}{r}\right)\right] -$$
$$-c_s\frac{k}{\varepsilon}\left[\overline{uw}\frac{\partial \overline{uv}}{\partial x} + \overline{vw}\frac{\partial \overline{uv}}{\partial r} + \overline{w^2}\,\overline{uw}\right] + \gamma k\left(\frac{\partial U}{\partial x} + \frac{\partial V}{\partial x}\right)$$

$\overline{vw}$ - Reynolds stress:

$$\frac{\partial}{\partial x}(U\overline{vw})+\frac{1}{r}\frac{\partial}{\partial r}(rV\overline{vw})+(\overline{v^2}-\overline{w^2})\frac{W}{r}=$$
$$\nu\left[\frac{\partial^2}{\partial x^2}(\overline{vw})+\frac{1}{r}\frac{\partial}{\partial r}\left(r\frac{\partial}{\partial r}(\overline{vw})\right)-\frac{4}{r^2}\overline{vw}\right]-\left(1-\alpha+0.015\frac{k^{1.5}}{\varepsilon y_w}\right)\cdot$$
$$\left(\overline{v^2}\frac{\partial W}{\partial r}+\overline{vw}\frac{V}{r}+\overline{uv}\frac{\partial W}{\partial x}-\overline{w^2}\frac{W}{r}+\overline{uw}\frac{\partial V}{\partial x}+\overline{vw}\frac{\partial V}{\partial r}\right)-$$
$$-\left(c_1-0.125\frac{k^{1.5}}{\varepsilon y_w}\right)\varepsilon\frac{\overline{vw}}{k}+\left(\beta+0.015\frac{k^{1.5}}{\varepsilon y_w}\right)\cdot$$
$$\left(\overline{uw}\frac{\partial U}{\partial r}+\overline{vw}\frac{\partial V}{\partial r}+\overline{w^2}\frac{\partial W}{\partial r}-\overline{v^2}\frac{W}{r}+\overline{vw}\frac{V}{r}\right)+$$
$$+c_s\frac{\partial}{\partial x}\left[\frac{k}{\varepsilon}\left(\overline{u^2}\frac{\partial\overline{vw}}{\partial x}+\overline{uv}\frac{\partial\overline{vw}}{\partial r}+\frac{\overline{uw}}{r}(\overline{v^2}-\overline{w^2})\right)\right]+$$
$$+\frac{c_s}{r}\frac{\partial}{\partial r}\left[r\frac{k}{\varepsilon}\left(\overline{uv}\frac{\partial\overline{vw}}{\partial x}+\overline{v^2}\frac{\partial\overline{vw}}{\partial r}+\frac{\overline{vw}}{r}(\overline{v^2}-\overline{w^2})\right)\right]+$$
$$+c_s\frac{k}{\varepsilon}\left[\frac{\overline{vw}}{r}\frac{\partial}{\partial r}(\overline{v^2}-\overline{w^2})+\frac{\overline{uw}}{r}\frac{\partial}{\partial x}(\overline{v^2}-\overline{w^2})-4\frac{\overline{w^2}}{r^2}vw\right]+$$
$$+\gamma k\left(\frac{\partial W}{\partial r}-\frac{W}{r}\right)$$

$\overline{uw}$ - Reynolds stress:

$$\frac{\partial}{\partial x}(U\overline{uw})+\frac{1}{r}\frac{\partial}{\partial r}(rV\overline{uw})+\overline{uv}\frac{W}{r}=$$
$$\nu\left[\frac{\partial^2}{\partial x^2}(\overline{uw})+\frac{1}{r}\frac{\partial}{\partial r}\left(r\frac{\partial}{\partial r}(\overline{uw})\right)-\frac{\overline{uw}}{r^2}\right]-\left(1-\alpha+0.015\frac{k^{1.5}}{\varepsilon y_w}\right)\cdot$$
$$\left(\overline{uv}\frac{\partial W}{\partial r}+\overline{uw}\frac{V}{r}+\overline{u^2}\frac{\partial W}{\partial x}+\overline{vw}\frac{\partial U}{\partial r}+\overline{uw}\frac{\partial U}{\partial x}\right)-$$
$$-\left(c_1-0.125\frac{k^{1.5}}{\varepsilon y_w}\right)\varepsilon\frac{\overline{uw}}{k}+\left(\beta+0.015\frac{k^{1.5}}{\varepsilon y_w}\right)\cdot$$
$$\left(\overline{uw}\frac{\partial U}{\partial x}+\overline{vw}\frac{\partial V}{\partial x}+\overline{w^2}\frac{\partial W}{\partial x}-\overline{uv}\frac{W}{r}+\overline{uw}\frac{V}{r}\right)+$$
$$+c_s\frac{\partial}{\partial x}\left[\frac{k}{\varepsilon}\left(\overline{u^2}\frac{\partial\overline{uw}}{\partial x}+\overline{uv}\frac{\partial\overline{uw}}{\partial r}+\frac{\overline{uw}}{r}\overline{uv}\right)\right]+$$
$$+\frac{c_s}{r}\frac{\partial}{\partial r}\left[r\frac{k}{\varepsilon}\left(\overline{uv}\frac{\partial\overline{uw}}{\partial x}+\overline{v^2}\frac{\partial\overline{uw}}{\partial r}+\frac{\overline{vw}}{r}\overline{uv}\right)\right]+$$
$$+c_s\frac{k}{\varepsilon}\left[\frac{\overline{vw}}{r}\frac{\partial\overline{uv}}{\partial r}+\frac{\overline{uw}}{r}\frac{\partial\overline{uv}}{\partial x}-\frac{\overline{w^2}}{r^2}\overline{uw}\right]+\gamma k\frac{\partial W}{\partial x}$$

The dissipation equation used with the Reynolds stresses model is the same as that of mean closure model, with the exception that the transport term is modelled in terms of the stresses as:

$$\frac{\partial}{\partial x}(U\varepsilon)+\frac{1}{r}\frac{\partial}{\partial r}(rV\varepsilon)=\frac{\partial}{\partial x}\left(\nu\frac{\partial\varepsilon}{\partial x}\right)+\frac{1}{r}\frac{\partial}{\partial r}\left(r\nu\frac{\partial\varepsilon}{\partial r}\right)+c_{\varepsilon 1}\frac{\varepsilon}{k}G-$$
$$-c_{\varepsilon 2}\frac{\varepsilon^2}{k}+c_\varepsilon\frac{\partial}{\partial x}\left[\frac{k}{\varepsilon}\left(\overline{u^2}\frac{\partial\varepsilon}{\partial x}+\overline{u}\right)\right]+c_\varepsilon\frac{1}{r}\frac{\partial}{\partial r}\left[r\frac{k}{\varepsilon}\left(\overline{uv}\frac{\partial\varepsilon}{\partial x}+\overline{v^2}\frac{\partial\varepsilon}{\partial r}\right)\right]$$

Production of turbulent kinetic energy $k=0{,}5\left(\overline{u^2}+\overline{v^2}+\overline{w^2}\right)$ is defined as:

$$P=\overline{uv}\frac{\partial U}{\partial r}+\overline{u^2}\frac{\partial U}{\partial x}+\overline{v^2}\frac{\partial V}{\partial r}-\overline{vw}\frac{W}{r}+\overline{uv}\frac{\partial V}{\partial x}+\overline{vw}\frac{\partial W}{\partial r}+\overline{w^2}\frac{V}{r}+$$
$$+\overline{uw}\frac{\partial W}{\partial x}$$

To define boundary conditions, the concept of so called "two - layer wall functions" has been used.

BOUNDARY CONDITIONS AND NUMERICAL SCHEME

The computational inflow boundary is set at downstream from the diffuser entrance, which is shown in Figure 1. Diffuser (Clausen at al. 1993) has been set up at the exit of the channel with rotating swirl generator (260mm in diameter). The length of the diffuser with the spreading angle of 20° and the surface ratio of 2.84 has been 510mm. Reynolds number, based on the mean air velocity at the entrance U_0=11.6m/s has been $Re=DU_0/\nu$=177000, and swirling number based on the ratio of

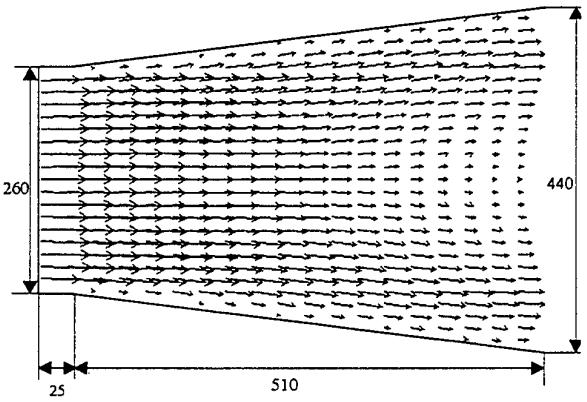


FIG. 1. SCHEMATIC DIAGRAM OF SWIRL DIFFUSER WITH CALCULATED VELOCITY VECTORS.

the maximum of circumferential and mean axial velocity W_{max}/U_0=0.59. Swirl at the entrance, of type "solid body rotation", has been sufficient to prevent flow separation near the wall, but at the same time insufficient to cause recirculation in the central part of the diffuser.

Numerical solution of the given system of equations has been obtained using the control volume method with iterative procedure of convergence to the solution. Non-uniform numeric grid has been used in calculations, with 47 control nodes in axial and 77 nodes in radial direction, while the conical geometry of diffuser has been simulated with gradually widening of the calculation domain, increasing the number of active control volumes along the radius.

CALCULATION RESULTS

The aim of this work is to analyse feasibility of the prediction of swirling flow in conical diffuser, based on the comparison of the experimental results with the results obtained using mathematical model (Armfield at al. 1990). Radial profiles of axial velocities (Figure 2), obtained based on the experiments and using numerical simulation, have characteristic shape: due to constant volume flow when cross section increases the total level of axial velocity gradually decreases along the diffuser, and due to the effects of centrifugal force velocity maximum appear near the wall. Besides the fact that profiles obtained using the model have the expected characteristic shape with maximal near the wall, they also follow the movement of these maximal towards the axis. Due to the flow spreading and the influence of the walls, tangential velocity decreases (Figure 3), but the shape of type "rotation of solid body" is mostly preserved along the greater part of the channel. Profile spreads and maximum moves along the radius at downstream locations. Model illustrates this development of tangential velocity.

Large gradients of the main flow velocity cause the increase of kinetic energy along the diffuser (Figure 4), while in cross sections close to the exit from the diffuser level of turbulent kinetic velocity decreases according to the decrease in axial velocity and rotation decay. Calculation yields qualitative picture of turbulent kinetic energy development and relatively good quantitative agreement of profiles with experimental data. Certain disagreements of calculated profiles from the experimental data can be seen in the descending part of radial profiles. Using the model somewhat lower gradient of the decrease in the turbulent kinetic energy is obtained along the diffuser axis than that obtained experimentally.

Similar conclusions can also be drawn based on the analysis of radial profile diagrams of turbulent stress components $\overline{u^2}$, $\overline{v^2}$, $\overline{w^2}$, $\overline{uv}$ and $\overline{vw}$ shown on Figures 5 through 9 respectively. Values of stress increase sharply near the wall and then decrease up to an order of magnitude at the distance from the wall not greater than quarter of the diameter. Besides those maximum of radial profiles increase gradually along the diffuser, and then near the diffuser exit acquire somewhat lower values. Profiles of turbulent stress components obtained using the proposed model describe adequately turbulent characteristics near the wall, although the of decrease along the radius is somewhat lower than in profiles obtained experimentally.

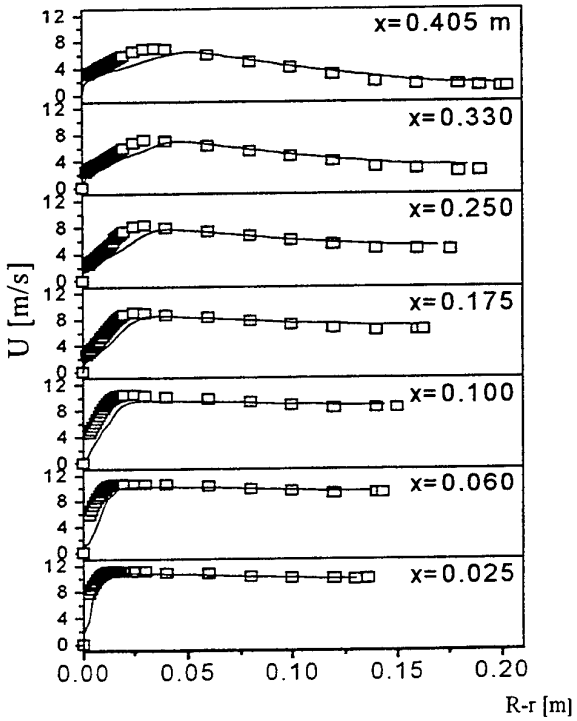


FIG. 2. AXIAL VELOCITY PROFILES
(□ EXPERIMENT, — MODEL)

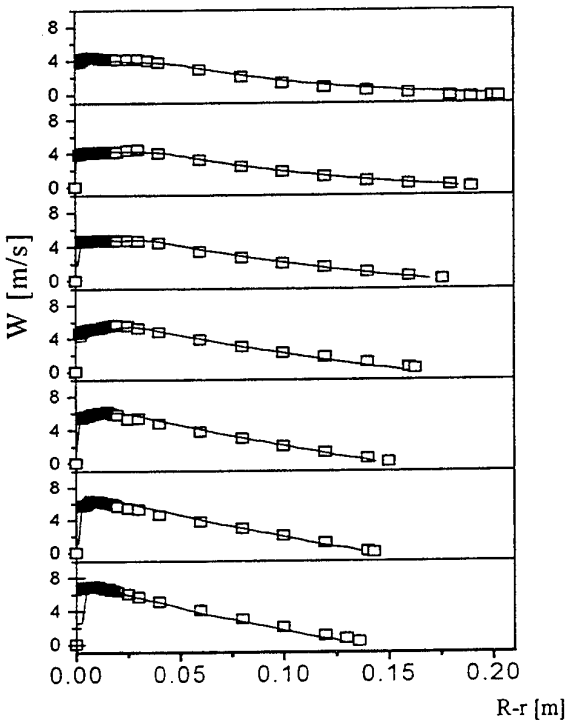


FIG. 3. RADIAL PROFILES OF SWIRL VELOCITY

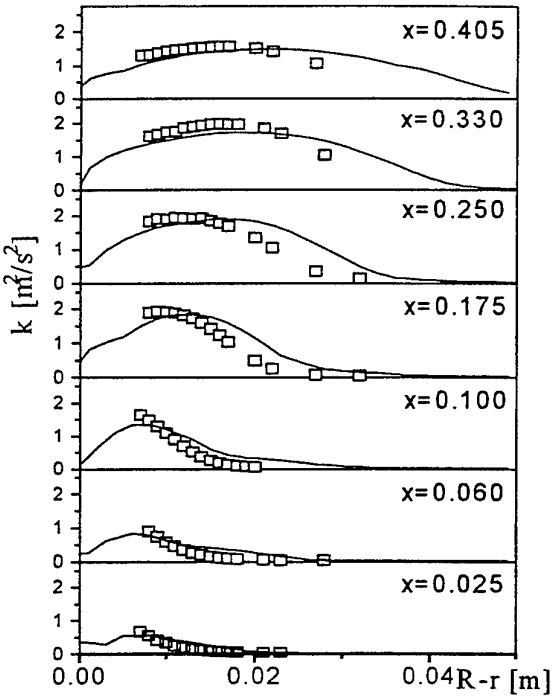


FIG. 4. RADIAL PROFILES OF TURBULENT KINETIC ENERGY.

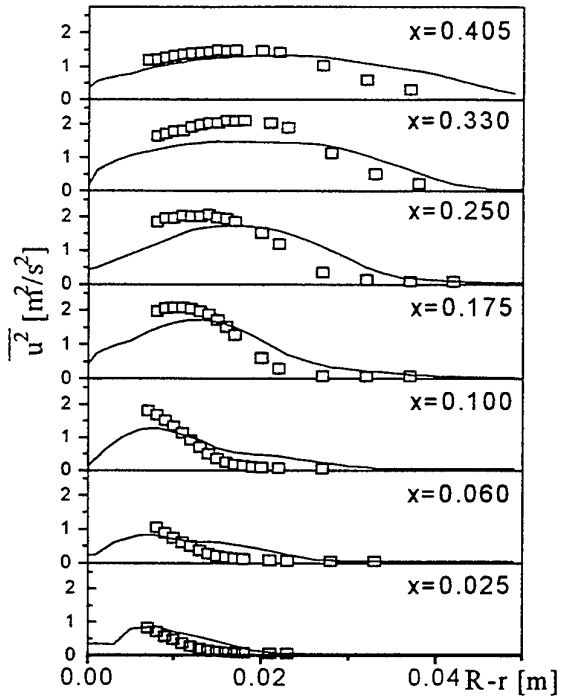


FIG. 5. RADIAL PROFILES OF REYNOLDS STRESS $\overline{u^2}$.

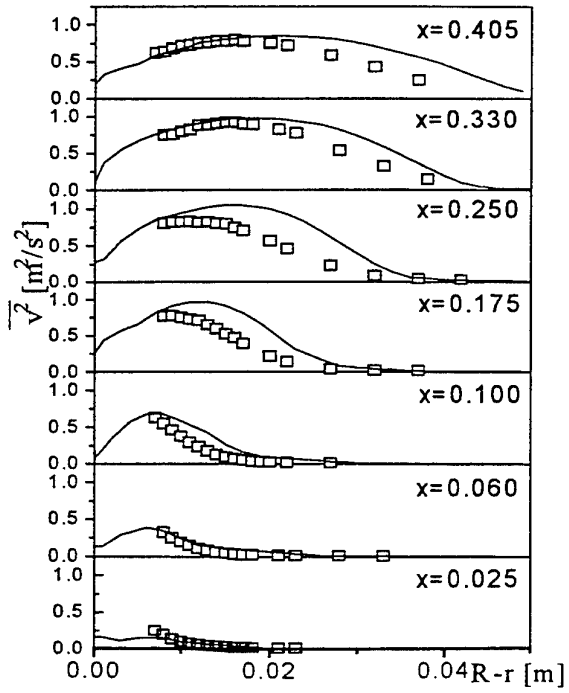


FIG. 6. RADIAL PROFILES OF REYNOLDS STRESS $\overline{v^2}$.

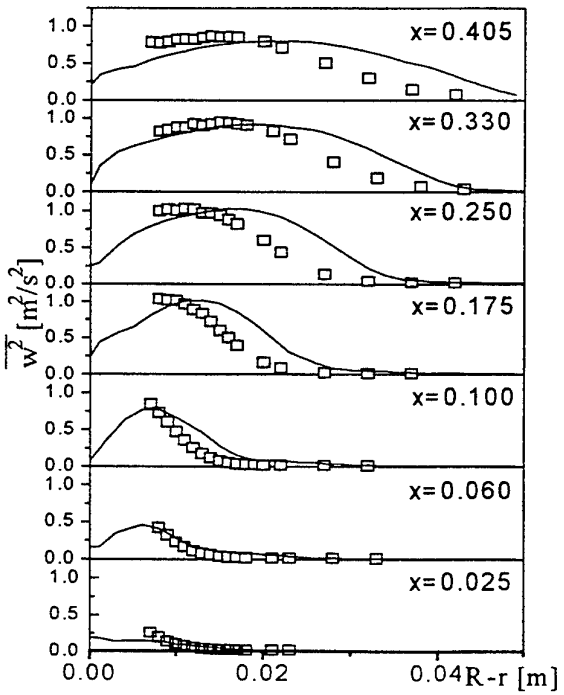


FIG. 7. RADIAL PROFILES OF REYNOLDS STRESS $\overline{w^2}$.

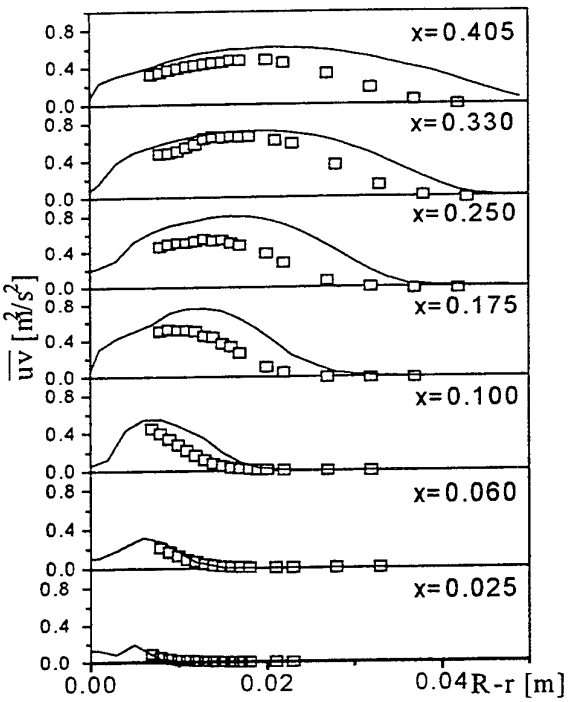


FIG. 8. RADIAL PROFILES OF REYNOLDS STRESS $\overline{uv}$.

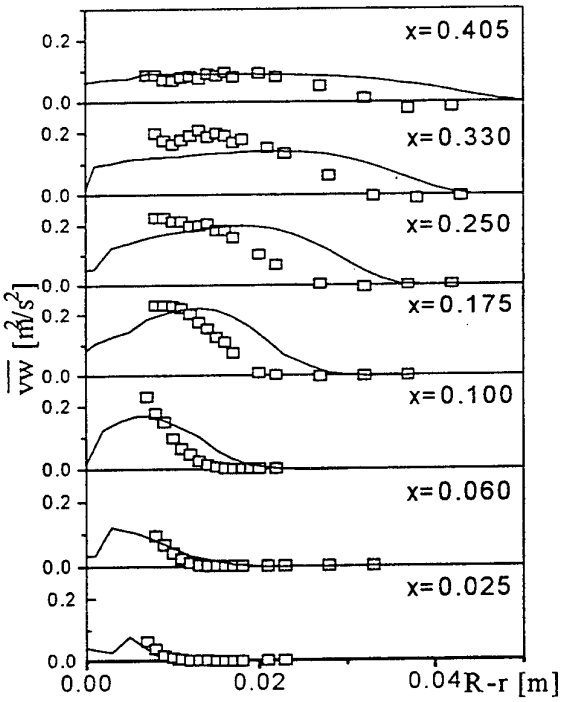


FIG. 9. RADIAL PROFILES OF REYNOLDS STRESS $\overline{vw}$.

CONCLUSION

In this paper, mathematical model of turbulent flow based on the stress model of turbulence has been shown. Model verification against experimental results has been carried out for the case of swirling flow in conical diffuser. Radial profiles of mean axial tangential velocities have been analysed, as well as the development of turbulent stress values along the radius in peripheral area of the diffuser. General agreement between profiles obtained from the model and experimental data is acceptable. Certain differences may be noted in the position of maximum at downstream profiles of axial velocities and in the levels of decrease gradients of turbulent stress radial profiles. These may be alleviated by further optimization of the model.

REFERENCES

Armfield, S. W, Cho, N. H and Fletcher, C .A .J, 1990, "Prediction of Turbulence Quantities for Flow in Conical Diffusers" ,AIAA *Journal*, Vol. 28, No. 3, pp. 453-460.

Clausen, P. D., Koh, S. G. and Wood, D. H., 1993, "Measurments of a Swirling Turbulent Boundary Layer Developing in a Conical Diffuser," *Exp. Thermal and Fluid Science*, Vol. 6, No. 39.

Launder, B. E., Reece, G. J and Rodi, W., 1975, "Progress in the Development of a Reynolds-Stress Turbulence Closure", *J. Fluid Mech.*, Vol. 68, part 3, pp. 537-566.

MODELING TURBULENT FLOW IN A CURVED DUCT OF SQUARE CROSS SECTION

Y. D. Choi, J. K. Shin, and K. H. Chun
Department of Mechanical Engineering, Korea University
Sungpukku, Seoul 136-701, Korea.

J. A. C. Humphrey
Department of Aerospace and Mechanical Engineering,
Tucson, Arizona 85721, USA.

ABSTRACT

Fine grid calculations are reported for the developing turbulent flow in a curved duct of square cross section with a radius of curvature to hydraulic diameter ratio $\delta = R_c/D_H = 3.357$ and a bend angle of 720 deg. A sequence of modeling refinements is introduced; the replacement of wall function by a fine mesh across the sublayer and a low Reynolds number algebraic second moment closure up to the near wall sublayer in which the non-linear return to isotropy model and the cubic-quasi-isotropy model for the pressure strain are adopted; and the introduction of a multiple source model for the exact dissipation rate equation. Each refinement is shown to lead to an appreciable improvement in the agreement between measurement and computation.

INTRODUCTION

Over the last twenty years, turbulent flows in a curved duct of square cross section with a bend angle of 180 deg have been a matter of primary concern as benchmark test flows, because they provide a three dimensional flow field with strong secondary motions in a simple flow passage. The mean cross-stream flow in the curved duct configuration is driven by a centrifugal force-radial pressure gradient force imbalance. The pair of counter-rotating vortices so engendered, appearing as a pair of recirculating cells in the cross-stream plane, break down into a complex multi-cellular pattern as the flow progresses along the curved duct.

Chang et al.(1983) and Choi et al.(1990) have provided detailed experimental data on the development of a turbulent flow around a square sectioned 180 deg bend with a bend radius equal to 3.357 times the hydraulic diameter of the duct. The Reynolds number of the flow was 56,690 based on bulk average velocity W_B and the fluid kinematic viscosity ν. Chang et al.(1983) and Johnson(1984) attempted to predict the flowfield by employing the standard k-ε eddy-viscosity model (EVM) of turbulence, but the model did not capture well the effect of streamline curvature on the Reynolds stresses. However, Choi et al.(1989) obtained the marked improvements in the agreement with the measured velocity profiles and the computed one, by employing a fine mesh in place of wall function to resolve the buffer and viscous sublayer, and by replacing the usual k-ε eddy viscosity model with an algebraic second-moment closure.

Main purpose of the present study is to examine the velocity development of the statistically stationary flow in a passage through the bend with a square cross section and a bend angle of 720 deg. We can improve the prediction of the streamwise velocity profiles by a sequence of refinements in turbulence modeling; the introduction of a low Reynolds number algebraic second moment closure up to viscous sublayer in which the non-linear return to isotropy model and cubic-quasi-isotropy model for the pressure strain are adopted; and the introduction of a multiple source model developed for the exact dissipation rate equation.

MEAN FLOW EQUATION

Fig.1 is the configuration of interest and defines the coordinates and symbols used. The duct is coiled with a negligible pitch angle which is neglected in the calculations. The equation of mean motion to the turbulent flow around a square-sectioned bend are conveniently expressed in cylindrical coordinates. X and Y map the cross-sectional plane, which progress around the bend, is expressed through angle the θ, and thus

Continuity

$$\frac{1}{r_c}\left\{\frac{\partial}{\partial X}(\rho r_c U)+\frac{\partial}{\partial Y}(\rho r_c V)+\frac{\partial}{\partial \theta}(\rho W)\right\}=0 \qquad (1)$$

Mean Momentum

$$\rho C(\Psi)+S_C(\Psi) = D(\Psi)+S_D(\Psi) - \rho R(\Psi)+\rho S_R(\Psi)+S_P(\Psi) \qquad (2)$$

where Ψ refers to the velocity component and operators $C(\Psi)$, $D(\Psi)$, and $R(\Psi)$ have the following significance:

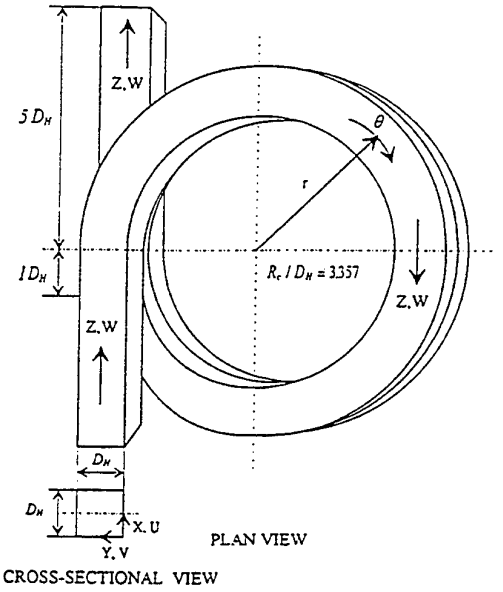


Fig. 1. Schematic showing the 720° curved duct and tangents.

$$C(\Psi)=\frac{1}{r_c}\left\{\frac{\partial}{\partial X}(r_c U\Psi)+\frac{\partial}{\partial Y}(r_c V\Psi)+\frac{\partial}{\partial\theta}(W\Psi)\right\}$$

$$D(\Psi)=\frac{1}{r_c}\left\{\frac{\partial}{\partial X}\left(r_c\mu\frac{\partial\Psi}{\partial X}\right)+\frac{\partial}{\partial Y}\left(r_c\mu\frac{\partial\Psi}{\partial Y}\right)+\frac{1}{r_c}\frac{\partial}{\partial\theta}\left(\mu\frac{\partial\Psi}{\partial\theta}\right)\right\}$$

$$R(\Psi)=\frac{1}{r_c}\left\{\frac{\partial}{\partial X}(r_c\overline{u\psi})+\frac{\partial}{\partial Y}(r_c\overline{v\psi})+\frac{\partial}{\partial\theta}(\overline{w\psi})\right\}$$

The term $R(\Psi)$ expresses the action of the turbulent stresses, ψ denoting the fluctuation component of velocity in equation and overbar the usual Reynolds averaging. $S_P(\Psi)$, $S_C(\Psi)$, $S_D(\Psi)$, and $S_R(\Psi)$ are the source terms as indicated in Table 1.

Table 1 $S_P(\Psi)$, $S_C(\Psi)$, $S_R(\Psi)$, $S_D(\Psi)$

Ψ	$S_P(\Psi)$	$S_C(\Psi)$	$S_R(\Psi)$
U	$-\frac{\partial P}{\partial X}$	0	0
V	$-\frac{\partial P}{\partial Y}$	$\frac{W^2}{r_c}$	$\frac{\overline{w^2}}{r_c}$
W	$-\frac{1}{r_c}\frac{\partial P}{\partial\theta}$	$-\frac{VW}{r_c}$	$-\frac{\overline{vw}}{r_c}$

Ψ	$S_D(\Psi)$
U	$\frac{\partial}{\partial X}\left(\mu\frac{\partial U}{\partial X}\right)+\frac{1}{r_c}\frac{\partial}{\partial Y}\left(r_c\mu\frac{\partial V}{\partial X}\right)+\frac{1}{r_c}\frac{\partial}{\partial\theta}\left(\mu\frac{\partial W}{\partial X}\right)$
V	$\frac{\partial}{\partial X}\left(\mu\frac{\partial U}{\partial Y}\right)+\frac{1}{r_c}\frac{\partial}{\partial Y}\left(r_c\mu\frac{\partial V}{\partial Y}\right)+\frac{\partial}{\partial\theta}\left(\mu\frac{\partial}{\partial Y}\left(\frac{W}{r_c}\right)\right)+2\mu\left((V-\frac{\partial W}{\partial\theta})/r_c^2\right)$
W	$\frac{1}{r_c}\frac{\partial}{\partial X}\left(2\mu\frac{\partial U}{\partial\theta}\right)+\frac{1}{r_c}\frac{\partial}{\partial Y}\left(\mu\left(\frac{\partial V}{\partial\theta}+W\right)\right)+\frac{1}{r_c^2}\frac{\partial}{\partial\theta}\left(\mu\left(\frac{\partial W}{\partial\theta}-2V\right)\right)-\mu\frac{\partial}{\partial Y}\left(\frac{W}{r_c}\right)-\frac{\mu}{r_c^2}\frac{\partial V}{\partial\theta}$

TURBULENCE MODEL

Reynolds stresses $\overline{u_iu_j}$ in mean momentum equations are obtained from the following tensor form of algebraic second moment(ASM) closure :

$$\frac{\overline{u_iu_j}}{k}(P-\varepsilon)=P_{ij}-\varepsilon_{ij}+\phi_{ij} \tag{3}$$

$$P_{ij}=-\left(\overline{u_iu_k}\frac{\partial U_j}{\partial x_k}+\overline{u_ju_k}\frac{\partial U_i}{\partial x_k}\right) \tag{4}$$

$$\phi_{ij}=\overline{\frac{p}{\rho}\left(\frac{\partial u_i}{\partial x_j}+\frac{\partial u_j}{\partial x_i}\right)} \tag{5}$$

$$\varepsilon_{ij}=2\nu\overline{\frac{\partial u_i}{\partial x_k}\frac{\partial u_j}{\partial x_k}} \tag{6}$$

Models for φ_{ij} adopted here are basically the developed by Shin(1995) for plane channel flows. The slow part of pressure strain is given as :

$$\phi_{ij1}=-C_1\left\{a_{ij}+C_1'\left(a_{ik}a_{kj}-\frac{1}{3}\delta_{ij}A_2\right)\right\}\varepsilon \tag{7}$$

where $a_{ij}(\equiv\overline{u_iu_j}/k-2/3\,\delta_{ij})$ is the anisotropy tensor of $\overline{u_iu_j}$ and $A_2(\equiv a_{ij}a_{ji})$ is the second invariant of a_{ij}. For the rapid part of pressure strain, cubic-quasi-isotropic model proposed by Launder and Tselepidakis(1991) is modified by using model coefficient C_2 :

$$\begin{aligned}\phi_{ij2}=&-C_2\left\{\left(P_{ij}-\frac{1}{3}\delta_{ij}P_{kk}\right)-\frac{1}{2}\varepsilon a_{ij}\left(\frac{P_{kk}}{\varepsilon}\right)\right.\\&+\frac{1}{3}\left[\frac{\overline{u_ku_j}\;\overline{u_lu_i}}{k}\left(\frac{\partial U_k}{\partial x_l}+\frac{\partial U_l}{\partial x_k}\right)\right.\\&\left.\left.-\frac{\overline{u_lu_k}}{k}\left(\overline{u_iu_k}\frac{\partial U_j}{\partial x_l}+\overline{u_ju_k}\frac{\partial U_i}{\partial x_l}\right)\right]\right.\\&+\frac{r}{0.6}[A_2(P_{ij}-D_{ij})\\&\left.+3a_{li}a_{kj}(P_{lk}-D_{lk})]\right\}\end{aligned} \tag{8}$$

$$D_{ij}=-\left(\overline{u_iu_k}\frac{\partial U_k}{\partial x_j}+\overline{u_ju_k}\frac{\partial U_k}{\partial x_i}\right)$$

Model forms for the coefficients C_1, C_1', C_2 and r are selected carefully for the Reynolds stresses and the pressure strains in plane channel flows to be matched with DNS data[Mansour et al.(1987)]. The forms adopted are :

$$C_1=2.5A^{1/4}\{1-\exp(-0.1R_t^{5/8})\}$$
$$C_1'=0.8$$
$$C_2=0.95(AA_2)^{0.25}[1-\exp\{-(0.0055R_t)^4\}]$$
$$r=\min(0.6,\ A^{0.5})$$

Contribution of wall reflection to the pressure strain is usually handled by a way of wall corrections for both φ_{ij1} and φ_{ij2}. For present proposes, we adopted the version of Gibson and Launder(1978) :

$$\phi_{ij1}^w=C_1^w\frac{\varepsilon}{k}\left(\overline{u_ku_m}n_kn_m\delta_{ij}-\frac{3}{2}\overline{u_ku_i}n_kn_j-\frac{3}{2}\overline{u_ku_j}n_kn_i\right)\cdot f(l/x_n) \tag{9}$$

$$\phi_{ij2}^w=C_2^w\left(\phi_{km2}n_kn_m\delta_{ij}-\frac{3}{2}\phi_{ki2}n_kn_j-\frac{3}{2}\phi_{kj2}n_kn_i\right)f(l/x_n) \tag{10}$$

$$f(l/x_n) = \frac{k^{1.5}}{2c_l\varepsilon x_n}\left(1+\sqrt{1+\frac{47.4}{R_t}}\right)$$

where n_k and x_n represent a normal vector and a distance from the wall respectively and the model coefficients C_1^w and C_2^w are taken as :

$$C_1^w = 4.5\{1-0.95\exp(-0.954R_t^{0.25})\}\exp(-14A) + 0.6A^{0.25}$$
$$C_2^w = 0.3A^{0.25}$$

In the near wall flow ε_{ij} departs form isotropy. Launder and Tselepidakis(1991) proposed the following near wall model for the dissipation rate of Reynolds stresses :

$$\varepsilon_{ij}^* = \frac{\varepsilon}{k}(\overline{u_iu_j}+\overline{u_iu_k}n_jn_k+\overline{u_ju_k}n_in_k + \overline{u_ku_l}n_kn_ln_in_j)/(1+3/2\,\overline{u_pu_q}n_pn_q/k) \quad (11)$$

We suppose that the highly non-isotropic limiting dissipation rates expressed by equation(11) gradually return way to an isotropic behavior as the Reynolds stress field becomes more-isotropic :

$$\varepsilon_{ij} = f_\varepsilon\varepsilon_{ij}^* + (1-f_\varepsilon)\varepsilon_{ij}^{iso} \quad (12)$$

The transition function f_ε that produces the change over between a ε_{ij}^* and ε_{ij}^{iso} may plausibly be modelled in terms of turbulence Reynolds number. We take a form of $f_\varepsilon=1-\exp[-(R_t/150)^2]$. A nonlinear relationship between eij($=\varepsilon_{ij}/\varepsilon-2\delta_{ij}/3$) and a_{ij} was recently proposed by Hallbäck , Groth and Johansson(1990) based on an expression of $e_{ij}=a_{ij}[1+3/4(1/2A_2-2/3)-3/4(a_{ij}a_{ji}-1/3A_2\delta_{ij})]$. We can improve the agreement between the computed ε_{ij} profiles and DNS data [Kim, Moin and Morser(1987)] by taking the model form of ε_{ij}^{iso} from Hallbäck et al.'s expression.

$$\varepsilon_{ij}^{iso} = \varepsilon\left[\left\{1+\frac{3}{4}\left(\frac{1}{2}A_2-\frac{2}{3}\right)\right\}a_{ij} - \frac{3}{4}\left(a_{ik}a_{kj}-\frac{1}{3}A_2\delta_{ij}\right)\right]+\frac{2}{3}\delta_{ij}\varepsilon \quad (13)$$

Turbulence energy and its dissipation rate in the above second moment closure are obtained from the following transport equations.

Turbulence Energy

$$C(k) = D(k) + S_D(k) + \Pi(k) + P_k - \rho\varepsilon \quad (14)$$

where

$$C(k) = \frac{1}{r_c}\left\{\frac{\partial}{\partial X}(r_cUk)+\frac{\partial}{\partial Y}(r_cVk)+\frac{\partial}{\partial\theta}(Wk)\right\}$$

$$D(k) = \frac{1}{r_c}\left\{\frac{\partial}{\partial X}\left[r_c(\mu+\rho C_k\frac{k}{\varepsilon}\overline{u^2})\frac{\partial k}{\partial X}\right] + \frac{\partial}{\partial Y}\left[r_c(\mu+\rho C_k\frac{k}{\varepsilon}\overline{v^2})\frac{\partial k}{\partial Y}\right] + \frac{\partial}{r_c\partial\theta}\left[(\mu+\rho C_k\frac{k}{\varepsilon}\overline{w^2})\frac{\partial k}{\partial\theta}\right]\right\}$$

$$S(k) = \frac{\rho C_k}{r_c}\left\{\frac{\partial}{\partial X}\left[r_c\frac{k}{\varepsilon}(\overline{uv}\frac{\partial k}{\partial Y}+\frac{\overline{uw}}{r_c}\frac{\partial k}{\partial\theta})\right] + \frac{\partial}{\partial Y}\left[r_c\frac{k}{\varepsilon}(\overline{uv}\frac{\partial k}{\partial X}+\frac{\overline{vw}}{r_c}\frac{\partial k}{\partial\theta})\right] + \frac{\partial}{r_c\partial\theta}\left[\frac{k}{\varepsilon}(\overline{uw}\frac{\partial k}{\partial X}+\overline{vw}\frac{\partial k}{\partial Y})\right]\right\}$$

$$P_k = -\rho\left[\overline{u^2}\frac{\partial U}{\partial X}+\overline{uv}\left(\frac{\partial V}{\partial X}+\frac{\partial U}{\partial Y}\right) + \overline{uw}\left(\frac{\partial W}{\partial X}+\frac{\partial U}{r_c\partial\theta}\right)+\overline{v^2}\frac{\partial V}{\partial Y} + \overline{vw}\left(\frac{\partial W}{\partial Y}+\frac{\partial V}{r_c\partial\theta}-\frac{W}{r_c}\right)+\overline{w^2}\left(\frac{\partial W}{r_c\partial\theta}+\frac{V}{r_c}\right)\right]$$

Turbulence Energy Dissipation Rate

$$C(\varepsilon) = D(\varepsilon) + S_D(\varepsilon) + \Pi(\varepsilon) + P_\varepsilon^1 + P_\varepsilon^2 + P_\varepsilon^3 + P_\varepsilon^4 - \Gamma \quad (15)$$

where operator $C(\varepsilon)$,$D(\varepsilon)$,$S_D(\varepsilon)$ are defined for the turbulence energy equation but, with C_k replaced by C_ε, P_ε^i(i=1,2,3,4) denotes the various production rates and Γ the dissipation rate of ε. A multiple source model for the exact dissipation rate equation was introduced to simulate the complex behaviors of the dissipation rate in the near wall sublayer. In this modeling, each source term in the exact dissipation rate equation is modelled individually to satisfy the wall limiting condition as approaching to the wall.

The mixed production rate P_ε^1 is derived theoretically by substituting the equation(11) and the assumption of $\varepsilon_{ij}^{iso}=2/3\,\delta_{ij}\varepsilon$ into equation(12).

$$P_\varepsilon^1 = -\varepsilon_{ij}S_{ij} = f_\varepsilon\frac{\varepsilon}{k}(P_k-2\,\overline{u_2u_j}S_{2j})/(1+3/2\,\overline{u_2^2}/k) \quad (16)$$

The transition function $f_\varepsilon=1-\exp[-(R_t/87)^2]$ is adopted and subscript 2 denotes a normal direction from the wall. The production rate by mean velocity P_ε^2 can be closely related by $P_k\varepsilon/k$. We modify the standard model form for P_ε^2 by multiplying a damping function f_{d2} to satisfy the wall limiting condition and an amplification function f_{A2} to consider the amplifying effect of turbulence anisotropy on the P_ε^2. The taken form is

$$P_\varepsilon^2 = C_{\varepsilon 2}f_{d2}f_{A2}\frac{P_k\varepsilon}{k} \quad (17)$$
$$f_{d2}=1-\exp(y_\varepsilon^+/2.75);\quad f_{A2}=\exp(A_3^3/2)$$
$$C_{\varepsilon 2}=1.0;\quad A_3 = a_{ij}\,a_{jk}\,a_{ki}\,.$$

Wall damping functions for the source terms can be formulated by using a parameter, y^*, the dimensionless distance from the wall. However, the use of y^* as a parameter of damping functions is restricted only to simple channel flows due to the difficulty in obtaining of y^* in complex flow passages. We have investigated alternative dimensionless distances which can replace y^* in the complex geometries. Abe et al.(1994) used $y^*(=y(\nu\varepsilon)^{1/4}/\nu)$ instead of y^*, because it can be easily obtained in any flow passage. Since y^* is, however, not proportional to y^+ above $y^+=30$, we introduce a new parameter y_ε^+ as a parabolic function of y^*.

$$y_\varepsilon^+ = y^*(1+0.0248y^*)/(\varepsilon_w^+)^{1/4} \quad (18)$$

where $\varepsilon_w^+=0.226$ are adopted. y_ε^+ has nearly the same value as y^+ up to $y^+=200$.

Wall limiting condition for the gradient production rate P_ε^3 is fulfilled by multiplying a damping function f_{d3} to the Rodi and Mansour's model(1993).

$$P_\varepsilon^3 = f_{\varepsilon 3}\left(C_{\varepsilon 3}^1 \nu \frac{k}{\varepsilon}\overline{v^2}(U_{,yy})^2\right) + C_{\varepsilon 3}^2 \nu \frac{k}{\varepsilon} k_{,y} U_{,y} U_{,yy} \quad (19)$$

$$f_{\varepsilon 3} = 1/(1-\exp(-y_\varepsilon^+/4.0)); \quad C_{\varepsilon 3}^1 = 0.4; \quad C_{\varepsilon 3}^2 = 0.045.$$

Turbulence production rate P_ε^1 can well be matched to DNS data by multiplying a damping function $f_\varepsilon = 1-\exp[-(y_\varepsilon^*/C_{d4})^2]$ to the standard model form ε^2/k. The form is taken as :

$$P_\varepsilon^4 = C_{\varepsilon 4} f_{\varepsilon 4} \frac{\varepsilon^2}{k}, \quad (20)$$

$$f_{\varepsilon 4} = (1-\exp(-y_\varepsilon^+/5.5))^3, \quad C_{\varepsilon 4} = 3.3.$$

Damping functions $f_{\varepsilon t}$ and f_{d5} and an amplification function f_{A5} are multiplied to the standard model form ε^2/k.

$$\Gamma = C_{\varepsilon 5} f_{\varepsilon t} f_{A5} f_{d5} \frac{\varepsilon^2}{k} \quad (21)$$

$$f_{\varepsilon t} = 1-0.3\exp(-(R_t/6)^2); \quad f_{d5} = \tanh^2(y_\varepsilon^+/7.5);$$

$$f_{A5} = \exp(3.3(E_3 A_3)^3); \quad C_{\varepsilon 5} = 4.78.$$

Damping function $f_{\varepsilon t}$ considers the increasing effect of turbulence energy decaying rate on Γ as the turbulence Reynolds number R_t decreases. A hyperbolic tangent function f_{d5} is used to meet the wall limiting condition. Amplification function f_{A5} is multiplied to Γ term with the effect of small and large scale turbulent anisotropies on P_ε^1 and P_ε^2. Since P_ε^1 and P_ε^2 are both affected by small and large scale turbulence anisotropies, a parameter E_3A_3 is selected to formulate the amplification function of Γ, where $E_3 = (= e_{ij}e_{jk}e_{ki})$ is the third invariant of dissipation rate anisotropy tensor e_{ij}.

The effects of pressure transport of k and ε equations in the viscous sublayer are included by taking the following Nagano and Shimada's(1993) model.

$$\Pi(k) = -\frac{\partial}{\partial x_k}\left(\frac{1}{2}\nu f_{wk}\frac{k}{\varepsilon}\frac{\partial \varepsilon}{\partial x_k}\right) \quad (22)$$

$$\Pi(\varepsilon) = \frac{1}{2}\nu\frac{\partial}{\partial x_k}\left\{(1-f_{wk})f_{wk}\frac{\varepsilon}{k}\frac{\partial k}{\partial x_k}\right\} \quad (23)$$

$$f_{wk} = \exp[-(y_\varepsilon^+/9.0)^2]$$

NUMERICAL ASPECTS

These computations were based on a semi-elliptic discretization of the Reynolds equations in which the streamwise diffusion was dropped but the full three-dimensional effects were included in the pressure field. The grid employed to cover the half cross-section of the duct between the symmetry planes and on each wall the mesh size was 52 × 80 in the normal and radial directions, respectively, and 380 nodes were imposed in the streamwise direction. The inlet plane to the calculation domain was set one hydraulic diameter upstream of the physical inlet plane to the curved duct located at zero degree. At this location fits to the velocity and turbulent kinetic energy measurements for fully developed flow in a straight duct, obtained by Melling and Whitelaw(1978) are prescribed. The exit plane of the calculation domain was set five hydraulic diameters downstream of the physical exit plane of the curved duct located at 720 deg. 10 and 15 nodes were imposed for the inlet and outlet tangents, respectively. The nondiffusive QUICK approximation is used for discretizing the convective transport in the cross-sectional plane of the duct.

DISCUSSION OF COMPUTATIONS

Fig.2 shows a comparison between the streamwise profiles measured by Chang et al.(1983) and present computations. In this figure, IP denotes the Isotropisization of Production Model, IPC, the IP model + cubic term, and CQI, the Cubic Quasi-Isotropic Model. A key factor in obtaining the correct streamwise velocity flow profiles is the prediction of the strong secondary motion. Adding a cubic term to the IP model induces stronger secondary motion by reducing the Reynolds stresses in the near wall region. This leads to deeper troughs in the streamwise velocity profiles than those obtained with the IP model.

Fig.3 shows that changing the constant C_1' in the return to isotropy model affects the accuracy of prediction of the streamwise velocity. For all the cases, CQI model was adopted for the rapid part of the pressure strain term. Launder and Tselepidakis(1991) proposed C_1=0.7, but Sarkar and Speziale(1990) argued that C_1' must be -2/3 for the model to satisfy realizability. However, we have proved from fifth order analysis that C_1' must vary from the limiting value of -2/3 in the high Reynolds number region of the flow to high positive values in approaching the wall [Shin(1995)]. Present predictions show that a value of C_1'=0.8 yields the best overall agreement with the streamwise velocity profiles of Chang et al.(1983).

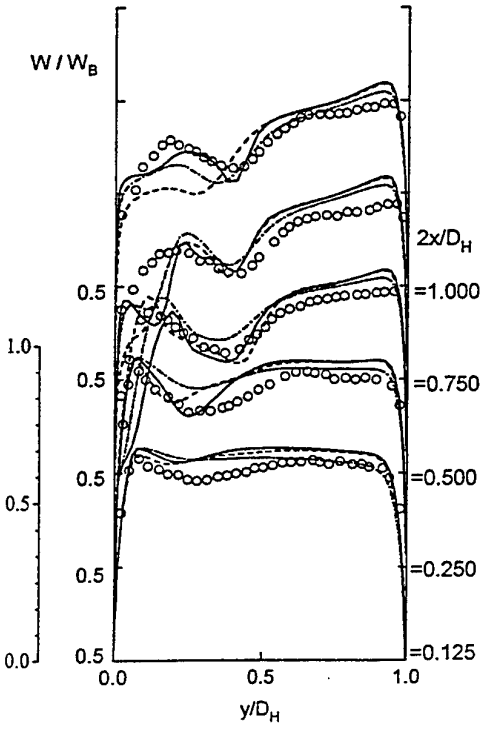


Fig. 2. Comparison between predicted and measured normalized W velocity profile at 135 deg. ○ ; Measurements, Chang et al.(1983) : ····· ; IP model(C_1'=0.0) : ·—· : CQI model (C_1'=0.8) : —— ; IPC model(C_1'=0.8).

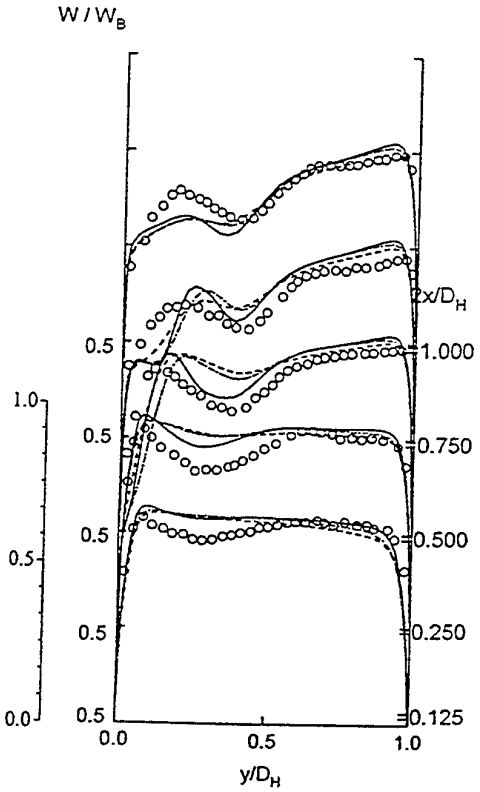


Fig. 3. Comparison between predicted and measured normalized W velocity profile at 135 deg. ○ ; Measurements, Chang et al.(1983) : ····· ; C_1'=-2/3 : ·—· ; C_1'=0.0 : —— ; C_1'=0.8.

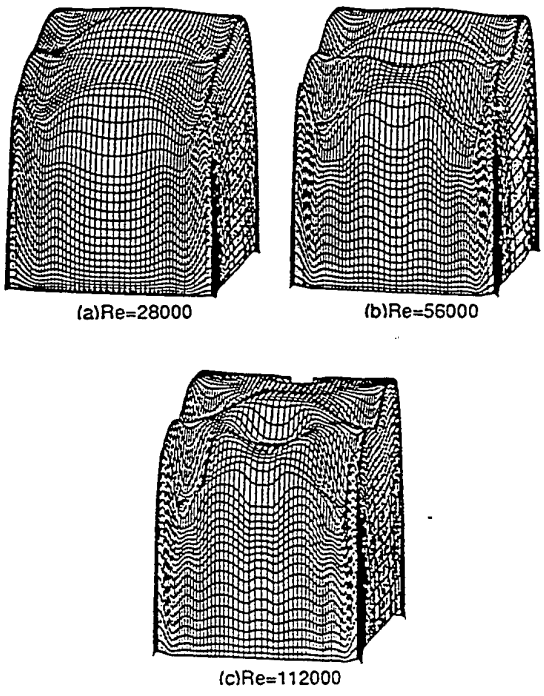


Fig. 4. Comparison of normalized axial velocity W/ W_B distribution for different three Reynolds numbers at θ =225 deg..

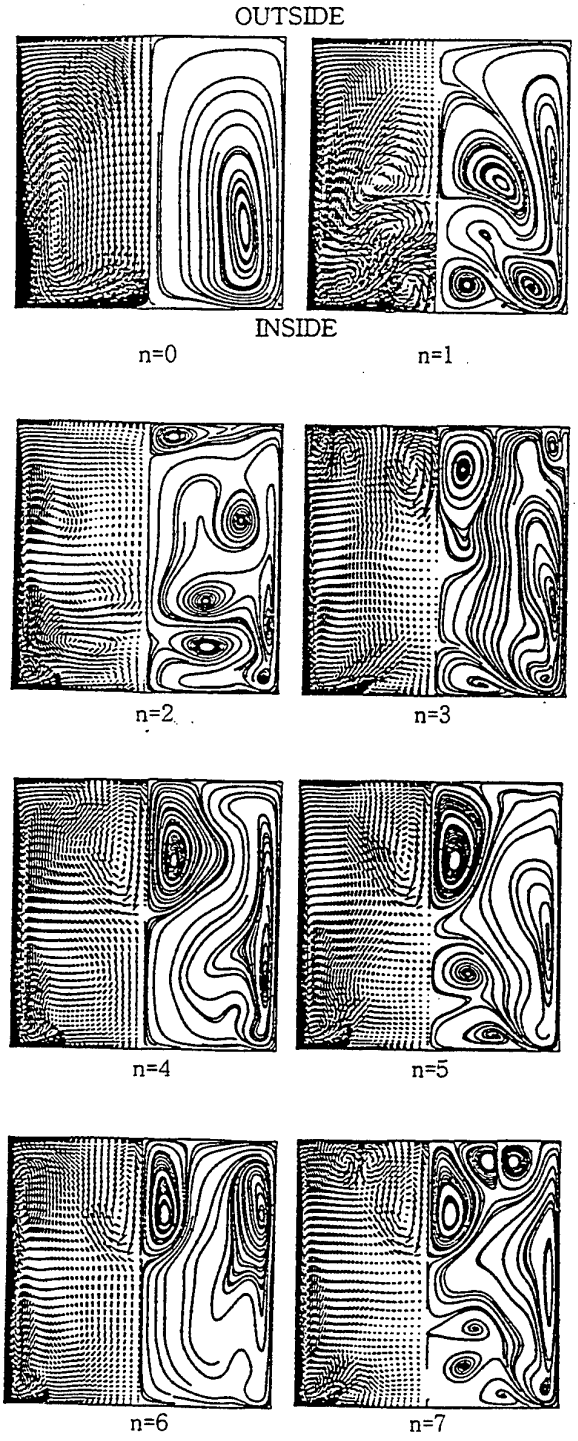


Fig. 5. Secondary flow represented by vectors and streamlines at the $(2n+1)\,\pi/4$ stations.

The vector and streamline plots in Fig.4 show the variation of the secondary flow with position in the bend every 90 deg. The strong counter-rotating secondary motions developed in the entrance region break up into multi-cell vortices after the 90 deg location. The multi-cell vortices become increasingly complex but eventually decay in the passage through the bend. Beyond 225 deg location we observe the collapse of the multi-cell vortices

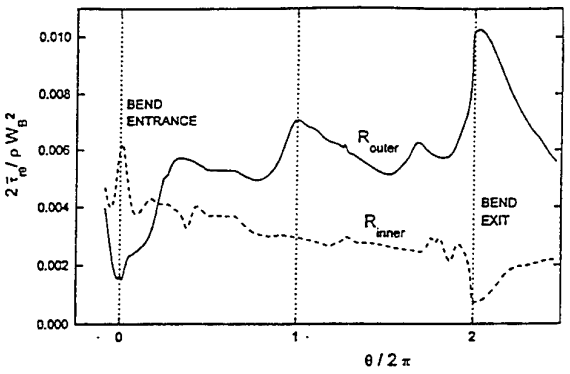


Fig. 6. Average shear stresses of the outer and inner walls normalized by$(1/2)/\rho W_B^2$.

from which form a larger new pattern of vortices in the outer radius wall region. These resemble Görtler vortices, which are known to appear along the outer wall of curved channels and ducts. Several minor vortices arise and cease alternatively in the outer wall region but the pattern does not grow to a fully developed form.

Orthographic projections of the streamwise velocity profiles at the plane of 225 deg for different Reynolds numbers are compared in Fig.5. As the Reynolds number increases, multi-cell vortices make the ripples of streamwise velocity profile more complex and formate deeper troughs. At Re=112,000, Görtler type vortices developed only in the outer wall region make a deep valley in the streamwise velocity profiles.

Averaged shear stresses $\overline{\tau}_{r\theta}$ for the outer and inner walls are normalized by $1/2\,\rho\,W_B^2$ and compared in Fig.6. In the bend entrance region, $\overline{\tau}_{r\theta}$ of the inner wall is higher than that of the outer wall, due to the acceleration of the streamwise velocity on the inner wall side and the deceleration on the opposite side. Beyond 180 deg, however, the magnitude of the shear stresses are reversed. Through the bend, $\overline{\tau}_{r\theta}$ of the outer wall increases with large variations up to the exit. On the other hand, $\overline{\tau}_{r\theta}$ of the inner wall decreases rather monotonically. This large variation of the shear stress at the outer wall may be caused by continuous deformations of the Görtler type vortices in that region. Approaching to the bend exit $\overline{\tau}_{r\theta}$ of the out wall jumps abruptly, but $\overline{\tau}_{r\theta}$ of the inner wall drops on the contrary.

CONCLUSIONS

Present paper reported the calculation of the developing turbulent flow in a curved duct of square cross section with a radius of curvature to hydraulic diameter ratio 3.357 and a bend angle of 720 deg. The following conclusions may be drawn;

1. Improvements of the prediction of the streamwise velocity profiles can be obtained by replacing the standard algebraic second moment (ASM) closure by a low Reynolds number ASM and the introduction of multiple source model for the exact dissipation rate equation.

2. Refined values for the model coefficients C_1 and C_1' in the non-linear model for the slow part of the pressure strain term have improved the prediction of the troughs in the streamwise flow profiles which are now in better agreement with the experiment.

3. Further improvement of the prediction of the streamwise velocity profiles is obtained by modifying Launder and Tselepidakis's cubic-quasi-isotropy model for the rapid part of the pressure strain term.

4. The strong counter-rotating secondary motions developed in the entrance region break up into multi-cell vortices after 90 deg, but the multi-cell vortices eventually decay and form a Görtler type vortices in the outer radius wall region.

REFERENCES

Abe, K., Kondoh, T. and Nagano, Y., 1994, "A New Turbulence Model for Predicting Fluid Flow and Heat Transfer in Separating and Reattaching Flow-I. Flow Field Calculation," International Journal Heat and Mass Transfer, Vol. 37, No. 1, pp. 139-151.

Chang, S.M., Humphrey, J.A.C. and Modavi, A., 1983, "Turbulent Flow in a Strongly Curved U-bend and Downstream Tangent of Square Cross Sections," PCH Physics Chemical Hydrodynamics, Vol. 4, pp. 243-269.

Choi, Y.D., Moon, C. and Yang, S.H., 1990, "Measurement of Turbulent Flow Characteristics of Square Duct with a 180° Bend by Hot Wire Anemometer," Proc. of International Symposium of Engineering Turbulent Modeling and Measurement, pp. 429-438.

Gibson, M.M., and Launder, B.E., 1978, "Ground Effects on Pressure Fluctuations in the Atmospheric Boundary Layer," Journal of Fluid Mechanics, Vol. 86, pp. 491-511.

Hallbäck, M., Groth, J. and Johansson, A.V., 1990, "An Algebraic Model for Nonisotropic Turbulent Dissipation Rate in Reynolds Stress Closure.", Phys. Fluids A(2), Vol. 10, pp. 1854-1866.

Johnson, R.W., 1984, "Turbulent convecting Flow in a Square Duct with a 180° Bend ; an Experimental and Numerical Sturdy," Ph.D.Thesis, Faculty of Technology, University of Manchester.

Nagano, Y. and Shimada., M., 1993, "Modelling The Dissipation Rate Equation for Two-Equation Turbulence Model," Proc. of 9th Symposium on Turbulence Shear Flow, Kyoto, Japan, August, 23-2.

Launder, B.E. and Tselepidakis, D.P., 1991, "Directions in Second-Moment Modeling of Near-Wall Turbulence," AIAA paper 91-219, 29th, Aerospace Science Meeting, Reno, Nevada.

Mansour, N.N., Kim, J. and Moin, D., 1988, "Reynolds Stress and Dissipation Rate Budgets in a Turbulent Channel flows," Journal of Fluid Mechanics, Vol. 194, pp. 15-44.

Melling, A. and Whitelaw, J.H., 1976, "Turbulent Flow in a Rectangular Duct," Journal of Fluid Mechanics, Vol. 78, pp. 289

Rodi, W. and Mansour, N.N., 1993, "Low Reynolds Number k- ε Modeling with the Aid of Direct Simulation Data," Journal of Fluid Mechanics, Vol. 250, pp. 509-529.

Sarkar, S. and Spezile, C.G., 1990, "A Simple Nonlinear Model for the Return to Isotropy in Turbulence," The Phys. Fluids A, Vol. 2. pp. 84-93.

Shin, J.K, 1995, "A Study on the Development and Application of Low Reynolds Number Second Moment Turbulence Closure," Ph.D, Thesis, Korea University.

COHERENCE OF VORTICES IN A ROTATING FLUID

Stéphane Leblanc and Fabien S. Godeferd

Laboratoire de Mécanique des Fluides et d'Acoustique
UMR 5509 CNRS
Ecole Centrale de Lyon
BP 163, 69131 Ecully Cedex
France

INTRODUCTION

In a rotating fluid, the Coriolis force strongly affects coherence and stability of quasi two-dimensional vortices aligned with the rotation axis. Experimental evidence of such structures is extensive (see the review by Hopfinger and van Heijst 1993). In a rotating tank, a diffusive turbulence produced by an oscillating grid leads, above a certain distance from the grid, to the formation of "long-lived" coherent vortices, which do not emerge in the non-rotating case (Hopfinger, Browand and Gagne 1982). Other laboratory experiments have shown the existence of two-dimensional vortices with various complex topologies such as monopolar, dipolar, tripolar and triangular vortices, sometimes observed in direct numerical simulations of two-dimensional turbulence (Kloosterziel 1990; Kloosterziel and van Heijst 1991).

Emergence of columnar vortices from isotropic turbulence is outside the scope of the present paper because it involves complex mechanisms that cannot be explained by the Taylor–Proudman theorem, which only concerns a linear and steady regime. Thus, in rotating homogeneous turbulence, Cambon, Mansour and Godeferd (1996) have shown that the linear regime which consists of inertial waves cannot explain the transition from three-dimensional to two-dimensional turbulence, which is ultimately triggered by non-linear interactions. However, the long persistence of these structures suggest that they are insensitive (or stable) to perturbations with rapid growth rate.

Are linear mechanisms able to explain the *"presence of intense cyclonic vortices and (much) weaker anticyclonic vortices"* as observed experimentally by Hopfinger *et al.* (1982) and others in rotating fluids (Kloosterziel 1990; Bidokhti and Tritton 1992), and by numerical simulations (Smyth and Peltier 1994; Bartello, Métais and Lesieur 1994; Cambon *et al.* 1994; Carnevale *et al.* 1997; Lollini and Cambon 1997)?

Of course the present study does not contain the answer to this question, but reviews and adds some elements on this complex topic, with a particular attention to the role of stagnation points, by investigation of the effects of the Coriolis force on the two-dimensional Taylor–Green flow, which exhibits both cyclones and anticyclones.

LINEAR MECHANISMS

Tilting vorticity

In a rotating frame, the relative motion of an incompressible fluid is governed by the Navier–Stokes and continuity equations, which may be written, in dimensionless form (Leblanc and Cambon 1997*a*):

$$\partial_t \boldsymbol{u} + \boldsymbol{S}\boldsymbol{u} + \tfrac{1}{2}\boldsymbol{\omega}_t \times \boldsymbol{u} = -\boldsymbol{\nabla}\pi + \nu\nabla^2\boldsymbol{u},\ \boldsymbol{\nabla}\cdot\boldsymbol{u} = 0,$$

where $\boldsymbol{S}$ is the symmetric rate-of-strain tensor $S_{ij} = \frac{1}{2}(u_{i,j} + u_{j,i})$ and

$$\boldsymbol{\omega}_t = \boldsymbol{\omega} + 4\boldsymbol{\Omega}$$

is the "tilting vorticity" (Cambon *et al.* 1994), and π the modified pressure including the contribution of the centrifugal force.

The relative velocity field $\boldsymbol{u}(\boldsymbol{x},t)$ has been non-dimensionalized by a characteristic velocity scale U, the position vector $\boldsymbol{x}$ by a characteristic length-scale L. Time t and angular velocity $\boldsymbol{\Omega}$ have been non-dimensionalized by L/U, such that $|\boldsymbol{\Omega}|$ may be seen as the inverse of a *global* Rossby number. Finally, ν is the inverse of the Reynolds number.

Linear problem

In a Cartesian coordinate frame $(\boldsymbol{e}_x, \boldsymbol{e}_y, \boldsymbol{e}_z)$ rotating with angular velocity vector $\boldsymbol{\Omega} = \Omega\boldsymbol{e}_z$, let $\boldsymbol{U}(x,y,t)$ and $\Pi(x,y,t)$ describe a *two-dimensional* basic flow, perturbed by a *three-dimensional* infinitesimal disturbance $\boldsymbol{u}(\boldsymbol{x},t)$ and $\pi(\boldsymbol{x},t)$. The linearized Navier–Stokes equations read

$$D_t\boldsymbol{u} + \boldsymbol{S}\boldsymbol{u} + \tfrac{1}{2}\boldsymbol{W}_t \times \boldsymbol{u} = -\boldsymbol{\nabla}\pi + \nu\nabla^2\boldsymbol{u},\ \boldsymbol{\nabla}\cdot\boldsymbol{u} = 0,$$

where $D_t = \partial_t + \boldsymbol{U}\cdot\boldsymbol{\nabla}$ and now $\boldsymbol{S} = \frac{1}{2}(\boldsymbol{\nabla}\boldsymbol{U} + \boldsymbol{\nabla}\boldsymbol{U}^T)$. $\boldsymbol{W}_t = (W + 4\Omega)\boldsymbol{e}_z$ is the tilting vorticity of the basic flow. No coefficient of the linear problem involves a z-dependence, therefore it is possible to seek perturbations of the following form:

$$(\boldsymbol{u},\pi)(\boldsymbol{x},t) \to \mathrm{e}^{\mathrm{i}kz}(\boldsymbol{u},\pi)(x,y,t),$$

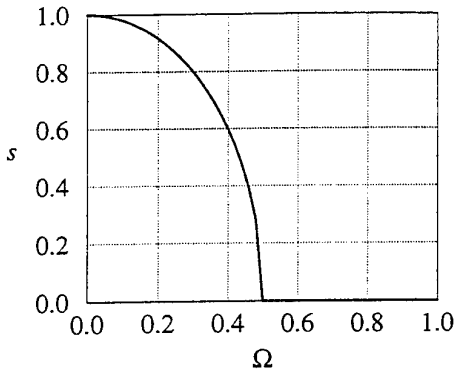


Figure 1: Growth rate s of short-wave pressureless instabilities for the hyperbolic (solid lines) and elliptical (dashed lines) stagnation points in function of the dimensionless rotation rate Ω. Square cells ($\rho = 1$): the streamlines are circular in the vortex cores.

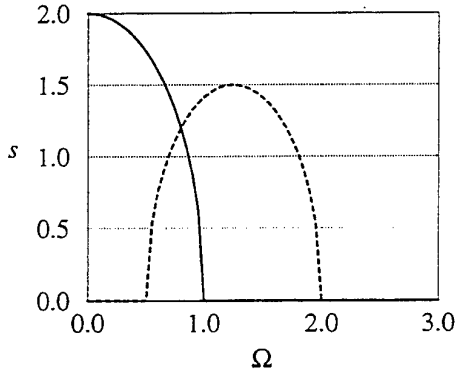


Figure 2: See previous caption. Rectangular cells ($\rho = 2$): the streamlines are elliptical in the vortex cores and the two kinds of instabilities (elliptical and hyperbolic) may compete.

where the spanwise wave number k is real to ensure homogeneity. The linear problem reads:

$$D_t \boldsymbol{v} + \boldsymbol{M}\boldsymbol{v} = -\boldsymbol{\nabla}\pi + \nu(\nabla^2 - k^2)\boldsymbol{v},$$
$$D_t w = -ik\pi + \nu(\nabla^2 - k^2)w,$$
$$\boldsymbol{\nabla}\cdot\boldsymbol{v} + ikw = 0.$$

$\boldsymbol{v}(x,y,t)$ is the projection of $\boldsymbol{u}(x,y,t)$ on the (x,y)-plane, whereas $w(x,y,t)$ is its spanwise component. $\boldsymbol{\nabla}(\,)$, $\boldsymbol{\nabla}\cdot(\,)$ and $\nabla^2(\,)$ are operators in the (x,y)-plane. The 2×2 "inertial tensor" $\boldsymbol{M}$ is defined by:

$$\boldsymbol{M} = \boldsymbol{\nabla U} + \boldsymbol{C} \quad \text{with} \quad \boldsymbol{C} = \begin{pmatrix} 0 & -2\Omega \\ 2\Omega & 0 \end{pmatrix}.$$

$\boldsymbol{C}$ is the "Coriolis tensor", and in a curvilinear plane coordinate frame, $\boldsymbol{M}$ involves an additional antisymmetric "curvature tensor" (Leblanc and Cambon 1997*a*, 1997*b*). The two eigenvalues of $\boldsymbol{M}$ are solutions of the characteristic equation

$$\lambda^2 + \Phi = 0 \quad \text{with} \quad \Phi = -\tfrac{1}{2}\boldsymbol{M}:\boldsymbol{M} = -\tfrac{1}{2}\mathrm{tr}(\boldsymbol{M}\,\boldsymbol{M}^T).$$

Φ is the second invariant of the inertial tensor $\boldsymbol{M}$, and may be expressed as:

$$\Phi = -\tfrac{1}{2}\boldsymbol{S}:\boldsymbol{S} + \tfrac{1}{4}\boldsymbol{W_t}\cdot\boldsymbol{W_t}. \qquad (1)$$

Inviscid instabilities

For *inviscid* and *steady* basic flows, Leblanc and Cambon (1997*a*) pointed out that the Pedley–Bradshaw criterion (Pedley 1969), the generalized Rayleigh criterion (Kloosterziel 1990; Kloosterziel and van Heijst 1991) and the stability condition for unbounded quadratic flows (Craik 1989; Cambon *et al.* 1994) may be reduced to the following: a *sufficient* condition for instability is that

$$\Phi < 0$$

somewhere in the flow domain. In accordance with Bayly (1988), they showed that the short-wave behavior ($k \gg 1$) of the inviscid instabilities ($\nu = 0$) is given at first order by a "pressureless" analysis, governed by the simplified problem:

$$D_t \boldsymbol{v} + \boldsymbol{M}\boldsymbol{v} = 0.$$

Stagnation points

Using the "geometrical optics" stability theory developed recently by Lifschitz and coworkers (Lifschitz and Hameiri 1991; Lifschitz 1991, 1994; Bayly, Holm and Lifschitz 1996; Lebovitz and Lifschitz 1996), it is possible to show that the pressureless problem makes sense and that the inviscid basic flow is unstable to short-wave instabilities if

$$\Phi(\boldsymbol{x}_0) < 0 \qquad (2)$$

on a stagnation point $\boldsymbol{U}(\boldsymbol{x}_0) = 0$ (if any), located at $\boldsymbol{x}_0 = (x_0, y_0)$ (Leblanc 1997). $\Phi(\boldsymbol{x}_0)$ is given by (1). This is a *sufficient* condition for instability. For complex vortical flows such as Stuart vortices or Taylor–Green cells, instabilities from hyperbolic and/or elliptical stagnation points are deduced easily (Leblanc and Cambon 1997*b*).

Without any Coriolis force ($\Omega = 0$), the above condition says simply that instability occurs if the basic flow exhibits a hyperbolic stagnation point, in accordance with Lagnado, Phan-Thien and Leal (1984) and with Friedlander and Vishik (1991). This condition is then weaker than Lifschitz and Hameiri's result (1991) stating that any steady flow with a stagnation point (elliptical, hyperbolic or pure-shear like) is unstable. However, in a rotating frame, the conclusion is not as straightforward.

For example, it is well-known that the Coriolis force may kill three-dimensional instabilities so that, at *zero absolute vorticity*

$$\boldsymbol{W}(\boldsymbol{x}_0) + 2\boldsymbol{\Omega} = 0, \qquad (3)$$

any vortex core with elliptical or circular streamlines located at $\boldsymbol{x}_0$ is stabilized by rotation (Craik 1989; Cambon *et al.* 1994; Bayly *et al.* 1996; Lebovitz and Lifschitz 1996; Leblanc 1997).

On the other hand, and in accordance with the rapid distortion analysis (RDT) for homogeneous turbulence (Cambon 1982; Cambon, Teissèdre and Jeandel 1984; Cambon *et al.* 1994), any stagnation point is unstable at *zero tilting vorticity*

$$\boldsymbol{W}(\boldsymbol{x}_0) + 4\boldsymbol{\Omega} = 0. \qquad (4)$$

NON-LINEAR AND VISCOUS EFFECTS

Taylor–Green cells

The aim of the present work is to study the effects of viscosity and non-linearity on short-wave three-dimensional perturbations, and to evaluate the validity of the stability

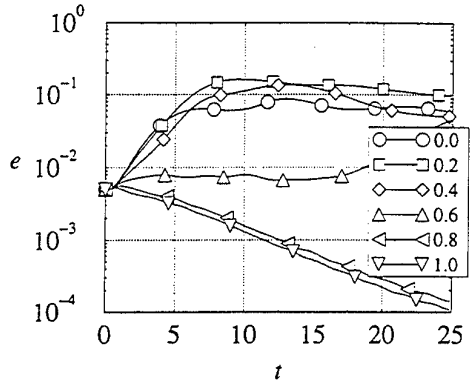


Figure 3: Energy perturbation $e(t)$ for various rotation rates Ω. Square cells ($\rho = 1$): the initial energy ratio is 2.0%.

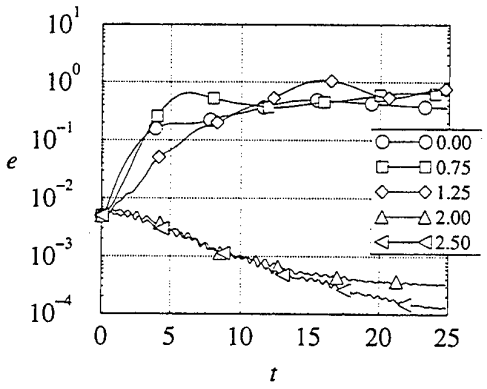


Figure 4: See previous caption. Rectangular cells ($\rho = 2$): the initial energy ratio is 0.8%.

condition (2) on "realistic" flows. Direct numerical simulations have been performed using a pseudo-spectral code. The initial conditions are three-dimensional perturbations superimposed to an initially two-dimensional basic flow: the Taylor–Green cells (in dimensionless form)

$$\Psi(x, y, t) = f(t) \sin(x) \sin(\rho y)$$

where $f(t) = \exp(-\nu(1 + \rho^2)t)$ represents the slow viscous decay of the basic flow and $\rho \geq 1$ the shape factor: if $\rho = 1$, the cells are square and the vortex cores exhibit locally circular streamlines, otherwise, the cells are rectangular and the vortex cores locally elliptical. The basic flow always exhibits hyperbolic stagnation points. In the inviscid case, the basic flow is steady.

Note that without Coriolis force, the three-dimensional instabilities of Taylor–Green rectangular cells have been computed numerically by Bayly (1989) and by Lundgren and Mansour (1996). However, their boundary conditions did not allow the hyperbolic instability to develop.

The results reported here correspond to square ($\rho = 1$) and rectangular ($\rho = 2$) cells.

Owing to the symmetries of the Taylor–Green cells, it is sufficient to consider $\Omega \geq 0$. Then a cell with positive vorticity will be called *cyclonic*, and *anticyclonic* otherwise.

Theoretical predictions

Bandwidths of inviscid instabilities ($\nu = 0$) may be deduced easily when considering the stagnation points. Thus, it may be verified that at hyperbolic stagnation points, $\Phi(\boldsymbol{x}_0) = 4\Omega^2 - \rho^2$, so that exponential instability to short-wave perturbations occurs when

$$0 < 2\Omega < \rho.$$

In the anticyclonic vortex cores, the circular or elliptical stagnation points are such that $\Phi(\boldsymbol{x}_0) = (\rho^2 + 2\Omega)(1 + 2\Omega)$, so that instability occurs when

$$1 < 2\Omega < \rho^2.$$

If $\rho = 1$ (square cells), the cores are circular and stable. If $\rho > 1$ (rectangular cells), elliptical anticyclones are destabilized by a weak rotation. Cyclones with elliptical cores are stable to such instabilities.

These unstable bandwidths are plotted on Figs. 1–2: $s = \sqrt{-\Phi}$ is the Lagrangian growth rate of the pressureless modes (Leblanc 1997). It is clear from these figures that, for some rotation rates, the instabilities may compete, as previously observed for the Stuart vortices (Leblanc and Cambon 1997*b*). It also clearly shows that the Coriolis force acts like a "tuner" for the different kinds of instabilities: owing to the magnitude of the rotation rate Ω, hyperbolic and/or elliptical instabilities are promoted.

Recall that these theoretical predictions only concern the pressureless modes (with pure spanwise and constant wave vector), and the general case of time-dependent wave vectors is much more complex and generally needs a computational approach (Pierrehumbert 1986; Bayly 1986; Craik 1989; Cambon *et al.* 1994; Bayly *et al.* 1996; Lebovitz and Lifschitz 1996).

According to the geometrical optics stability theory, these inviscid results may be extended to the viscous case (Lifschitz 1991). Indeed, on any fixed time interval, the viscous basic flow considered here converges uniformly to the inviscid flow ($\nu = 0$, $f(t) \equiv 1$) uniformly when $\nu \to 0$. So that, according to Lifschitz (1991), at sufficiently small viscosity (high Reynolds number), it is possible to construct an initial perturbation so that instability will occur according to the inviscid mechanisms. At a given Reynolds number ($1/\nu$), viscosity acts as a cut-off at high wave numbers.

The short-wave perturbation added to the basic flow at the initial time for the direct numerical simulations has a small but finite amplitude. However it may be verified that by construction, pressureless perturbations have a constant wave vector (Leblanc 1997), so that instabilities of stagnation points according to (2) will not be killed by non-linear effects (Lifschitz 1991). This will be reported in a further work.

DIRECT NUMERICAL SIMULATIONS

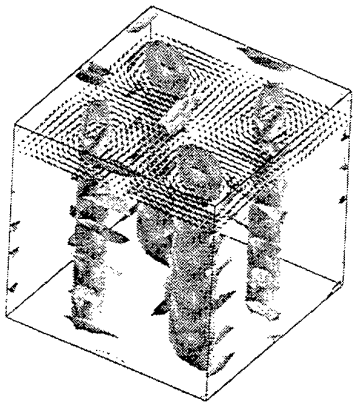
Pseudo-spectral code

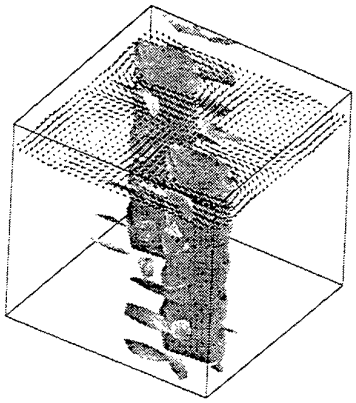
The computations have been performed with a pseudo-spectral code written and developed initially by C. Staquet (ENS Lyon, France) for stably stratified turbulence (Staquet and Godeferd 1997). The time scheme is third order accurate and viscous terms are treated implicitly. The semi-conservative formulation allows to introduce the rotation of the frame as an additional term to the vorticity advection one.

Direct numerical simulations with Reynolds 400 ($\nu = 1/400$) and moderate resolution 64^3 are reported here. Higher resolution calculations with higher Reynolds numbers will be performed later on.

Results

Instability is evaluated by the instantaneous kinetic en-





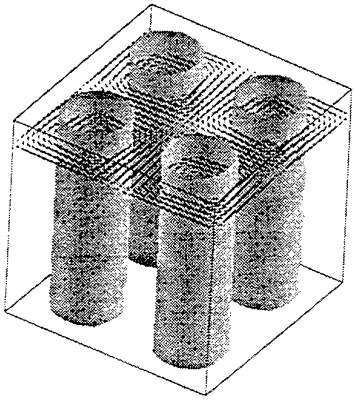
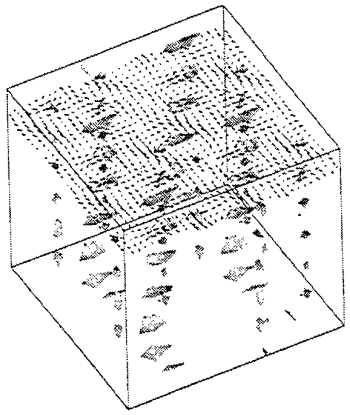
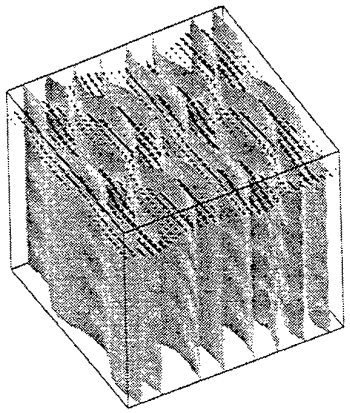


Figure 5: Square cells ($\rho = 1$). Top: $\Omega = 0.0$. Middle: $\Omega = 0.2$. Bottom: $\Omega = 1.0$.





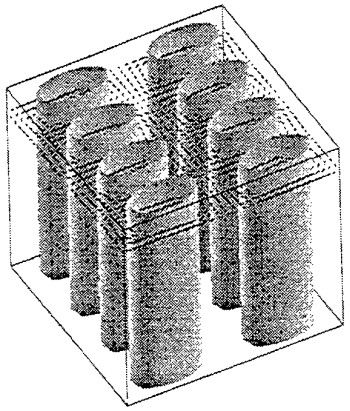


Figure 6: Rectangular cells ($\rho = 2$). Top: $\Omega = 0.00$. Middle: $\Omega = 1.25$. Bottom: $\Omega = 2.50$.

ergy of the perturbation:

$$e(t) = \frac{1}{2}\int_{\mathcal{D}} |\boldsymbol{u}'(\boldsymbol{x},t) - \boldsymbol{U}(\boldsymbol{x},t)|^2 d\boldsymbol{x}$$

where $\boldsymbol{u}'$ is the perturbed flow and $\boldsymbol{U}$ is the analytical velocity field of the Taylor–Green cells. The flow is stable if $e(t)/e(0) \to 0$ when $t \to \infty$ and unstable otherwise (Joseph 1976). The initial amplitude of the perturbation is evaluated with the energy ratio $e(0)/E(0)$, $E(t)$ being the overall kinetic energy of the unperturbed basic flow.

Energy perturbation is plotted on Figs. 3–4 for various rotation rates Ω. For square cells (Fig. 3), the results are in good agreement with the theoretical predictions plotted on Fig. 1, except for $\Omega = 0.6$: the energy of the perturbation keeps a constant level and grows ultimately to destabilize the basic flow. This is maybe a consequence of the fact that the initial ratio is relatively high (2%). For destabilizing rotation rates, the initial growth is close to exponential (note the log-scale for e on Figs. 3–4), and instabilities saturate non-linearly.

A better agreement is found for rectangular cells (Fig. 4): instability occurs according to the stability conditions plotted on Fig. 1. However, when instability occurs, it is difficult to say whether it grows on elliptical or hyperbolic stagnation points (see the case $\Omega = 0.75$ for which both should happen). The case $\Omega = 2.5$ corresponds at the initial time to a zero absolute vorticity (3) in the anticyclonic elliptical vortex cores $W(\boldsymbol{x}_0, 0) + 2\Omega = 0$: it leads to stability, according to theoretical results.

Comments

Concerning the rectangular case ($\rho = 1$), it is known that the stability of elliptical vortex cores under the effect of rotation may be characterized by three different regimes, well described by Bayly *et al.* (1996) and by Lebovitz and Lifschitz (1996). The first one corresponds to instability with respect to perturbations with pure spanwise (and constant wave vectors): they correspond to the pressureless modes which are unstable according to (2), and the unstable bandwidth is centered around the zero tilting vorticity (4). The second regime is thin stable region centered around the zero absolute vorticity (3). And the third and last regime corresponds to instability with respect to oblique (and time-dependent) wave vectors, needing a Floquet analysis, as in the non-rotating case (Pierrehumbert 1986; Bayly 1986; Craik 1989; Cambon *et al.* 1994; Bayly *et al.* 1996; Lebovitz and Lifschitz 1996). Concerning the hyperbolic points, the stability with respect to general wave vectors remains an open question.

According to the present results, it seems that the choice of our initial perturbation does not excite these oblique unstable modes: for example, in the rectangular case for $\Omega = 2.5$ (Fig. 4), it is clear that anticyclones are stable because it corresponds to the zero absolute vorticity case. However, simultaneously, cyclones could be unstable to oblique wave vectors by their elliptical cores, since they do not belong to the stable regime. Then, it seems that oblique modes are not excited non-linearly, in spite of the finite (but small) amplitude of the initial perturbation.

Visualizations

Three-dimensional visualizations of the perturbed fields at the dimensionless time $t = 25$ are plotted on Figs. 5–6 for various rotation rates. Iso-surfaces of the vorticity magnitude and velocity fields in (x, y)-planes (perpendicular to Ω) are plotted.

For square cells (Fig. 5), the non-rotating case (top) shows that the hyperbolic instability after non-linear saturation does not destroy completely the initial Taylor–Green cells, which, even if perturbed, conserve their columnar shape. The manifestation of the hyperbolic instability may be observed by the formation of "digitations" (vertical superposition of vorticity ribs aligned with the x- or the y-axis) located between the cells, according to the vortex line stretching mechanism along the principal axis of extensional rate well-known in RDT analysis, and also described by Lagnado *et al.* (1984). For moderate rotation (middle), the destabilizing Coriolis force, which acts initially on hyperbolic stagnation points, finally contaminates the whole flow to break down the anticyclones and reinforce the cyclones simultaneously, as soon observed by large eddy simulations (Cambon *et al.* 1994). A larger rotation (bottom) kills the short-wave perturbation and restores the unperturbed Taylor–Green cells.

This picture is modified for rectangular cells (Fig. 6) because of the presence of both hyperbolic and elliptical instabilities. The non-rotating case (top) shows the three-dimensional breakdown of the plane basic flow. Contrary to the square case, it seems that elliptical instability has been excited non-linearly by the hyperbolic instability, leading to a complex three-dimensional flow. For a moderate rotation (middle), elliptical anticyclones are destabilized whereas cyclones and hyperbolic stagnation points are linearly stable (see Fig. 1 for $\Omega = 1.25$). A dramatic change in the flow topology occurs: under the effect of rotation, the flow is reorganized in counter-currents with weak variability in the vertical z-direction. For a larger rotation rate (bottom) the elliptical instability is killed in anticyclones (zero absolute vorticity), and the whole flow is stable.

CONCLUSION

Direct numerical simulations of two-dimensional viscous Taylor–Green cells perturbed three-dimensionally and subjected to background rotation have been performed using a pseudo-spectral code. Comparisons with theoretical predictions from the geometrical optics stability theory for short-wave perturbations have been done, with a good agreement. The role of stagnation points (elliptical and/or hyperbolic), which may compete under the tuning effect of the Coriolis force, has been clearly shown through the computations, even at moderate Reynolds number.

The geometrical optics stability theory appears to be a very powerful tool to study the coherence of vortices in a rotating frame. Instead of "coherence" one should better say "linear stability" of vortices, because, as mentioned in Introduction, reorganization of the flow in columnar structures and transition towards two-dimensionality under the effect of rotation involve non-linear complex mechanisms, which may probably not be characterized by simple criteria based on the flow topology.

Acknowledgements: The authors are grateful to Dr. Chantal Staquet who made available her pseudo-spectral code and to Dr. Claude Cambon for fruitful discussions and friendly encouragements. Computations were carried out on Cray C98 of IDRIS (Institut du Développement et des Ressources en Informatique Scientifique, France). S.L. was supported by the MENESR.

REFERENCES

Bartello, P., Métais, O. and Lesieur, M., 1994, "Coherent structures in rotating three-dimensional turbulence," *J. Fluid Mech.*, Vol. 273, pp. 1–29.

Bayly, B.J., 1986, "Three-dimensional instability of elliptical flow," *Phys. Rev. Lett.*, Vol. 57, pp. 2160–2163.

Bayly, B.J., 1988, "Three-dimensional centrifugal-type instabilities in inviscid two-dimensional flows," *Phys. Fluids*, Vol. 31, pp. 56–64.

Bayly, B.J., 1989, "Computations of broad band instabilities in a class of quasi-two-dimensional flows," in *Math-*

ematical aspects of vortex dynamics (ed. R.W. Miksad *et al.*), American Society of Mechanical Engineers, pp. 71–77.

Bayly, B.J., Holm, D.D. and Lifschitz, A., 1996, "Three-dimensional stability of elliptical vortex columns in external strain flows," *Phil. Trans. R. Soc. Lond.* A, Vol. 354, 895–926.

Bidokhti, A.A. and Tritton, D.J., 1992, "The structure of a turbulent free shear layer in a rotating fluid," *J. Fluid Mech.*, Vol. 241, pp. 469–502.

Cambon, C., 1982, "Etude spectrale d'un champ turbulent incompressible soumis à des effets couplés de déformation et de rotation imposés extérieurement," PhD thesis, University of Lyon I, France.

Cambon, C., Benoît, J.-P., Shao, L. and Jacquin, L., 1994, "Stability analysis and large eddy simulation of rotating turbulence with organized eddies," *J. Fluid Mech.*, Vol. 278, pp. 175–200.

Cambon, C., Mansour, N.N. and Godeferd, F.S., 1997, "Energy transfer in rotating turbulence," *J. Fluid Mech.*, Vol. 337, pp. 303–332.

Cambon, C., Teissèdre, C. and Jeandel, D., 1985, "Etude d'effets couplés de déformation et de rotation sur une turbulence homogène," *J. Méc. Théo. Appl.*, Vol. 4, pp. 629–657.

Carnevale, G.F., Briscolini, M., Kloosterziel, R.C. and Vallis, G.K., 1997, "Three-dimensionally perturbed vortex tubes in a rotating flow," *J. Fluid Mech.*, in press.

Craik, A.D.D., 1989, "The stability of unbounded two- and three-dimensional flows subject to body forces: some exact solutions," *J. Fluid Mech.*, Vol. 198, pp. 275–292.

Friedlander, S. and Vishik, M., 1991, "Instability criteria for the flow of an inviscid incompressible fluid," *Phys. Rev. Lett.*, Vol. 66, pp. 2204–2206.

Hopfinger, E.J., Browand, F.K. and Gagne, Y., 1982, "Turbulence and waves in a rotating tank," *J. Fluid Mech.*, Vol. 125, pp. 505–534.

Hopfinger, E.J. and Heijst, G.J.F. van, 1993, "Vortices in rotating fluids," *Ann. Rev. Fluid Mech.*, Vol. 25, pp. 241–289.

Joseph, D.D., 1976, *Stability of Fluid Motions I* (2 Vols.), Springer.

Kloosterziel, R.C., 1990, "Barotropic vortices in a rotating fluid," PhD thesis, University of Utrecht, The Netherlands.

Kloosterziel, R.C. and Heijst, G.J.F. van, 1991, "An experimental study of unstable barotropic vortices in a rotating fluid," *J. Fluid Mech.*, Vol. 223, pp. 1–24.

Lagnado, R.R., Phan-Thien, N. and Leal, L.G., 1984, "The stability of two-dimensional linear flows," *Phys. Fluids*, Vol. 27 (5), pp. 1094–1101.

Leblanc, S., 1997, "Stability of stagnation points in rotating flows," *Phys. Fluids*, submitted.

Leblanc, S. and Cambon, C., 1996, "Stability of the Stuart vortices in a rotating frame," in *Advances in Turbulence VI* (ed. S. Gavrilakis, L. Machiels and P.A. Monkewitz), Kluwer, pp. 351–354.

Leblanc, S. and Cambon, C., 1997*a*, "On the three-dimensional instabilities of plane flows subjected to Coriolis force," *Phys. Fluids*, Vol. 9 (5), pp. 1307–1316.

Leblanc, S. and Cambon, C., 1997*b*, "Effects of the Coriolis force on the stability of Stuart's vortices," *J. Fluid Mech.*, submitted.

Lebovitz, N.R. and Lifschitz, A., 1996, "Short-wavelength instabilities of Riemann ellipsoids," *Phil. Trans. R. Soc. Lond.* A, Vol. 354, 927–950.

Lifschitz, A., 1991, "Short wavelength instabilities of incompressible three-dimensional flows and generation of vorticity," *Phys. Lett.* A, Vol. 157, pp. 481–487.

Lifschitz, A., 1994, "On the stability of certain motions of an ideal incompressible fluid," *Adv. Appl. Math.*, Vol. 15, pp. 404–436.

Lifschitz, A. and Hameiri, E., 1991, "Local stability conditions in fluid dynamics," *Phys. Fluids* A, Vol. 3, pp. 2644–2651.

Lollini, L. and Cambon, C., 1997, "Numerical simulations of inhomogeneous turbulence generated by an oscillating grid and subjected to solid-body rotation," in *Computation and visualization of three-dimensional vortical and turbulent flows*, in press.

Lundgren, T.S. and Mansour, N.N., 1996, "Transition to turbulence in an elliptic vortex," *J. Fluid Mech.*, Vol. 307, pp. 43–62.

Pedley, T.J., 1969, "On the stability of viscous flow in a rapidly rotating pipe," *J. Fluid Mech.*, Vol. 35, pp. 97–115.

Pierrehumbert, R.T., 1986, "Universal short-wave instability of two-dimensional eddies in an inviscid fluid," *Phys. Rev. Lett.*, Vol. 57, pp. 2157–2159.

Smyth, W.D. and Peltier, W.R., 1994, "Three-dimensionalization of barotropic vortices on the f-plane," *J. Fluid Mech.*, Vol. 265, pp. 25–64.

Staquet, S. and Godeferd, F.S., 1997, "Statistical modelling and direct numerical simulations of decaying stably stratified turbulence: Part. 1. Flow energetics," *J. Fluid Mech.*, submitted.

Computations of Strongly Swirling Flows with Quadratic Pressure-Strain Model

J. C. Chen and C. A. Lin
Department of Power Mechanical Engineering
National Tsing Hua University
Hsinchu, TAIWAN 30043

Abstract

The present study concerns with simulating turbulent strongly swirling flows by eddy viscosity model and Reynolds stress transport model variants with linear and quadratic form of the pressure-strain models. Flows with different inlet swirl numbers, 2.25 and 0.85, were investigated. Detailed comparisons of the predicted results and measurements were presented to assess the merits of model variants. For the swirl number 2.25 case, due to the inherent capability of the Reynolds stress models to capture the strong swirl and turbulence interaction, both the linear and quadratic form of the pressure-strain models predict the flow adequately. In strong contrast, the $k-\epsilon$ model predicts an excessive diffusive flow fields. For the swirl number 0.85 case, both the $k-\epsilon$ and Reynolds stress model with linear pressure-strain process, show an excessive diffusive transport of the flow fields. The quadratic pressure strain model, on the other hand, mimics the correct flow development with recirculating region being correctly predicted.

Introduction

Swirling motion is often employed as a mechanism to further promote or control mixing between the fuel spray jet and the adjacent air, and, in some occasions, to stabilise the combustion zone due to the presence of the swirl-induced central recirculation region. Since the decay of swirl induced central recirculation zone has profound effects on flame stabilisation and mixing in combustion systems, a prior knowledge of the flow characteristics is beneficial during the design process.

From a theoretical point of view, a two-dimensional swirling flow is considerably more complicated than two-dimensional plane flows, for additional strains arise due to the azimuthal motion, requiring the solution for azimuthal momentum. Indeed, the strain field may be said to be virtually as complex as any three-dimensional flow. Swirl introduces intense azimuthal streamline curvature and hence curvature-turbulence interaction affect all six independent stress components.

Due to its importance, numerous numerical studies have been made by various researchers to study the effects of swirl in a variety of combustor geometries[1]-[6]. The studies demonstrate that the superiority of stress closures over the $k-\epsilon$ model in the prediction of swirling flows, though the merits of various stress model variants differ at different swirl levels and swirler type. For strongly swirling flows, for example, the superiority of the stress models[4] is reflected primarily by the lower level of shear stresses due to the proper representation of the interaction between swirl-induced curvature and stresses. Among the stress models, due to the nature of the convection and diffusion transport of stresses is modelled, it was addressed[3] that ASM scheme is not to be used in axi-symmetric swirling flows where significant stress transport processes in the overall Reynolds stress budget prevails. Instead, a Reynolds stress transport model should be adopted.

While cubic and quadratic pressure strain models had been applied to further explore the effects of non-linear pressure-strain models on predicting free swirling flows, the majority of the confined swirling flow predictions, however, are still limited to the linear models. The present research aims at investigating the capability of variants of Reynolds stress turbulence models, linear and quadratic pressure-strain models, on strongly swirling flows. Flows with swirl numbers, 2.25 and 0.85, form the basis of the investigations.

Turbulence Models

In the present application, turbulence is described either by the high-Reynolds-number $k-\epsilon$ eddy-viscosity model[7] or by high-Reynolds-number Reynolds-stress closures. The focal point of Reynolds stress model is the pressure-strain term ϕ_{ij} which identifies pressure/strain interaction and consists of three model components, representing, respectively, "return to isotropy", "isotropisation of mean-strain and turbulence correlation" and "redistributive effects arising from wall reflection of pressure fluctuations". Variants of the pressure-strain variants were investigated.

The first stress model closure variant (IPCM)

adopted here is that of Fu et al.[2], which may be written as:

$$\phi_{ij1} = -1.8\rho\frac{\epsilon}{k}[\overline{u_iu_j} - \frac{\delta_{ij}}{3}\overline{u_ku_k}] \quad (1)$$

$$\phi_{ij2} = -0.6[P_{ij} - C_{ij} - \frac{\delta_{ij}}{3}(P_{kk} - C_{kk})] \quad (2)$$

$$\phi_{ijw} = 0.5\rho\frac{\epsilon}{k}[\overline{u_ku_m}n_kn_m\delta_{ij} - \frac{3}{2}\overline{u_ku_i}n_kn_j - \frac{3}{2}\overline{u_ku_j}n_kn_i]f + 0.3[\phi_{km2}n_kn_m\delta_{ij} - \frac{3}{2}\phi_{ik2}n_kn_j - \frac{3}{2}\phi_{jk2}n_kn_i]f \quad (3)$$

where

$$P_{ij} = -\rho\overline{u_iu_k}\frac{\partial U_j}{\partial x_k} - \rho\overline{u_ju_k}\frac{\partial U_i}{\partial x_k}$$

$$C_{ij} = \partial\rho U_k\overline{u_iu_j}/\partial x_k$$

n_i is the wall-normal unit vector in the direction i and $f = C_\mu^{0.75}k^{1.5}/(\epsilon\kappa y)$ with y being the distance to the closest wall, taken along the co-ordinate line normal to the wall.

Instead of the linear pressure-strain model, a second variant (SSG) proposed by Speziale et al.[8], employs quadratic form,

$$\phi_{ij1} = -(3.4\epsilon + 1.8P_k)b_{ij} + 4.2\epsilon(b_{ik}b_{kj} - \frac{1}{3}b_{kl}b_{kl}\delta_{ij}) \quad (4)$$

$$\phi_{ij2} = (0.8 - 1.3\sqrt{b_{kl}b_{kl}})kS_{ij} + 1.25k(b_{ik}S_{jk} + b_{jk}S_{ik} - \frac{2}{3}b_{kl}S_{kl}\delta_{ij}) + 0.4k(b_{ik}W_{jk} + b_{jk}W_{ik}) \quad (5)$$

where

$$S_{ij} = \frac{1}{2}(\frac{\partial U_i}{\partial x_j} + \frac{\partial U_j}{\partial x_i}),\ W_{ij} = \frac{1}{2}(\frac{\partial U_i}{\partial x_j} - \frac{\partial U_j}{\partial x_i}),$$

$$b_{ij} = \frac{\overline{u_iu_j}}{\overline{u_ku_k}} - \frac{1}{3}\delta_{ij},\ P_k = -\rho\overline{u_iu_j}\frac{\partial U_i}{\partial x_j}.$$

It should be pointed out the SSG model does not contain wall reflection term.

Numerical algorithm

This scheme solves discretised versions of all equations on a staggered finite-volume arrangement. A staggered storage is adopted not only for the velocity components but also for the shear stresses - an arrangement which aids stability by ensuring a strong numerical coupling between stresses and primary strains. The principle of mass-flux continuity is imposed indirectly via the solution of pressure-correction equations according to the SIMPLE[9] algorithm. The flow-property values at the volume faces contained in the convective fluxes which arise from the finite-volume integration process are approximated by the quadratic upstream-weighted interpolation scheme QUICK[10]. The numerical meshes, of sizes 90x60 and 120x90, are non-uniform both in the x and y directions. Initial tests on the influences of the convection schemes revealed that the differences between the second order QUICK and the first order hybrid scheme were negligible small. It was also found that the two grids generate exactly the same results. Therefore, the mesh employed will be deemed to be satisfactory and further refinements of the mesh will not be beneficial.

Though the present case is a steady state solution, it was found that using a time marching process will enhance stability, especially when stress models are employed. The solution process consists of a sequential algorithm in which each of the eleven sets of equations, in linearised form, is solved separately by application of an alternate-direction tri- or penta-diagonal line-implicit solver. Convergence was judged by monitoring the magnitude of the absolute residual sources of mass and momentum, normalised by the respective inlet fluxes. The solution was taken as having converged when all above residuals fell below 0.01%.

Boundary Conditions

At the wall, the tangential velocity component U was assumed to vary logarithmically between the semi-viscous sublayer, at $y_v^+ = 11.2$, and the first computational node lying in the region $30 < y^+ < 100$. This treatment yielded boundary conditions for the shear stresses and also permitted the volume-averaged near-wall generation rates of the tangential normal stresses to be computed over the associated near-wall finite volumes (The generation of the wall-normal intensity was assumed negligibly small). The linear variation of the turbulent length scale, $L = \kappa y/C_\mu^{3/4}$, in the log-law region, together with $\epsilon = k^{3/2}/L$, and the invariant value $\epsilon = 2\mu_l k_v/(\rho y_v^2)$ in the viscous sublayer, allowed the volume-averaged dissipation rate to be determined. This same L-variation was also used to prescribe explicitly the dissipation rate at the near-wall computational node, serving as the boundary condition for inner-field cells.

Results and Discussions

Sudden-expanding pipe flow

Before proceeding to the discussion of swirling flows, it is instructive to focus first on the performances of variants of turbulence models on sudden expanding pipe flows free from swirling inlet. The pipe expansion ratio is 1.5. The inlet velocity is known to be 19.2 m/s, corresponding to a Reynolds number of $1.25\text{x}10^5$ based on the inlet pipe diameter, while its mean and turbulence quantities were taken from the

experiment of Ahmed and Nejad[11]. Experimental data are available from 0.38 step heights downstream the sudden expansion at which point the numerical simulation starts.

The capability of different models can be observed by reference to Figure 1, showing comparisons between predicted and measured axial velocity along the centreline, which indicates the SSG model returned the best axial velocity development, though the difference among the stress models at regions $X/H < 10$ is marginal. The $k-\epsilon$ model predicted a more rapid development of axial velocity indicating a more diffusive flowfield simulated and this can be further affirmed by reference to Figure 2, which shows the predicted mean and turbulence quantities at $X/H = 2$. Regarding the turbulence quantities, the SSG model also exhibited better results, a reflection of the better predicted mean flow results, than the rest of the models.

So et al.'s strongly swirling flow S=2.25

This case is designed to examine the interaction between swirl-induced curvature and turbulence. Experimental data had been obtained by So et al.[12]. This consists of a pipe into which an annular swirling stream is introduced together with a non-swirling central jet. The latter is introduced to inhibit extensive reverse flow (vortex breakdown) along the centre-line. The swirl number, S,

$$S = \frac{\int_0^{r_o} UWr^2 dr}{r_o \int_0^{r_o} U^2 r dr} \tag{6}$$

for this case is 2.25, where r_o is the radius of the pipe. According to the rule of thumb proposed by Squire, a sub-critical state is reached when the maximum swirl velocity to the averaged streamwise velocity exceeds unity. It was found by Escudier and Keller that sub-critical state flow is highly sensitive to the perturbation far downstream. In the present case, the velocity ratio is well above unity and the flow is thus sub-critical. Therefore, in the present computations the exit axial velocity is prescribed from measurements to avoid the predictive uncertainties.

A sub-critical state appears to reflect a strong decay in turbulent mixing, and a corresponding dominance of convective features, making the governing equations nearly hyperbolic in nature. This is confirmed from the measured axial and tangential velocity, shown in Figures 3 and 4. Stress model predictions and experimental data show the shape of the mean flow profiles to remain similar over the whole length of domain, and this implies that the mixing is weak. The $k-\epsilon$ predictions show, on the contrary, an excessive radial diffusive transport, with a faster decay of the centreline axial velocity and early return of solid body rotation of the swirling motion.

The superiority of the stress models is rooted in their ability to return the depression of the shear stress levels in response to the swirl-related strain. Although the stress model predictions indicate a lower level of shear stresses, no measured shear stresses are available to support the simulations. Both the measurements and predictions show an nearly isotropic normal stresses. Among the predictions, the stress models return a lower level of normal stresses and agree with the measurements, shown in Figures 5 and 6. It should be noted that in the present case the difference between the linear and quadratic pressure-strain model is not significant. However, SSG model does predict a slightly lower level of normal stresses and hence shear stresses. This issue will be addressed in the section to follow.

Kitoh's strongly swirling flow S=0.85

The present case considers swirling flow in a straight circular pipe with a free-vortex type swirling inlet[13]. The swirl intensity, Ω,

$$\Omega = \frac{2\pi \int_0^{r_o} UWr^2 dr}{\pi r_o^3 U_m^2} \tag{7}$$

of the present case is 0.97, where U, W and U_m are the axial, tangential and bulk velocity, respectively, r and r_o are the radial position and pipe radius. This swirl intensity corresponds to a swirl number of 0.85. Due to the presence of the high swirl intensity at the inlet and the absence of the central jet as observed in the previous case, extensive reverse flow is present in most of the flow domain. Experimental data are available from 5.7 pipe diameter downstream the test section at which point the numerical simulation starts. It should be pointed out that the inlet plane straddles across the recirculation zone.

The most dramatic effect of the model's performance can be referred to the centreline axial velocity distributions, shown in Figure 7, and the axial and tangential velocity profiles, shown in Figures 8 and 9. It can be clearly seen that both the $k-\epsilon$ and IPCM model predict an over excessive diffusive profiles. In strong contrast, both the measurements and SSG model indicate an extended region of recirculation zone. The excessive nature of $k-\epsilon$ model in strongly swirling flow is consistent to what was observed previously. However, the IPCM model's performance needs to be further investigated.

The cause of this behaviour can be traced back to the formulation of the modelled form of pressure-strain process. The pressure-strain term of $\overline{uv}$ of SSG model can be expressed in terms of that of IPCM and is as,

$$(\phi_{\overline{uv}})_{SSG} = (\phi_{\overline{uv}})_{IPCM}$$

$$\underbrace{+\epsilon(0.2 - 1.8\frac{P_k}{\epsilon})b_{12}}_{A} \underbrace{+ 4.2\epsilon[(b_{11}+b_{22})b_{12} + b_{13}b_{23}]}_{B}$$

$$\underbrace{- 0.65\sqrt{b_{kl}b_{kl}}k\frac{\partial U}{\partial r}}_{C} \underbrace{+ k(0.425b_{11} - 0.375b_{22})\frac{\partial U}{\partial r}}_{D}$$

$$\underbrace{+kb_{13}(0.425\frac{\partial W}{\partial r}+1.575\frac{W}{r})}_{E} \quad (8)$$

where the wall reflection terms of IPCM have been neglected. It should be noted that terms B, C and the production related part of term A do not exist in the linear pressure strain models.

The reduced level of the shear stress predicted by the SSG model, shown in Figure 10 at $X/H = 12.3$, can be traced back to the formulations of the pressure-strain process. It is clear that the major terms A, D, E act as extra sink terms, relative to IPCM model, for predicted $\overline{uv}$ adopting SSG model. Across the non-equilibrium shear layer where the production term P_k is much higher than the turbulence dissipation rate ϵ, this makes the effect of term A even more pronounced. This reduced level of shear stresses predicted by SSG, shown in Figures 10 to 12, is consistent to what was observed earlier of the mean velocity profiles.

Conclusion

Computations of strongly swirling flows were performed by $k-\epsilon$ model and variants of Reynolds stress transport model with linear, IPCM, and quadratic, SSG, form of the pressure-strain models. Comparisons of the predictions with measurements indicated that For the S=2.25 case, due to the inherent capability of the Reynolds stress models to capture the strong swirl and turbulence interaction, both the linear and quadratic form of the pressure-strain models predict the flow adequately. In strong contrast, the $k-\epsilon$ model predicts an excessive diffusive flow fields. For the Kitoh's case, S=0.85, the correct axial flow recovery predicted by SSG was attributed to the lower level of $\overline{uv}$ predicted by the models, and this could be traced back to the modelled form of the pressure-strain term, after examining the formulations of the pressure-strain models. Overall, the SSG model is found to produce lower level of turbulence in regions of high shear and this agrees with what the measurements show.

Acknowledgements

This research work was supported by the National Science Council of Taiwan under grant NSC-85-2212-E-007-023 and the computational facilities were provided by the National Centre for High-Performance Computing of Taiwan which the authors gratefully acknowledge.

References

[1] Gibson, M.M. and Younis, B.A., 1986, "Calculation of Swirling Jet with a Reynolds stress Closure," Physics of Fluids, Vol 29, No. 1, pp. 38-48. pp. 1435-1443.

[2] Fu, S., Launder, B. E. and Leschziner, M. A., 1987, "Modelling Strongly Swirling Recirculating Jet with Reynolds-Stress Transport Closure," Proceedings 6th Symp. on Turbulent Shear Flows, Toulouse, pp.17.6.1-17.6.6

[3] Fu, S., Huang, P. G., Launder, B. E. and Leschziner, M. A., 1988, "A Comparison of Algebraic and Differential Second-Moment Closure for Axisymmetric Turbulent Shear Flows with and without Swirl," Journal of Fluids Engineering, Transaction of ASME, Vol. 110, June, pp. 216-221.

[4] Hogg, S. and Leschziner, M.A., 1989, "Computation of Highly Swirling Confined Flow with a Reynolds Stress Turbulence Model," AIAA J., Vol 27, pp. 57-63.

[5] Wennerberg, D and Obi, S., 1993, "Predictions of Strongly Swirling Flows in Quarl Expansions with a Non-Orthogonal Finite-Volume Method and a Second Moment Turbulence Closure," Proceedings of the Second International Symposium on Engineering Turbulence Modelling and Measurements, Florence, Italy, 31st May-2nd June, pp.197-206.

[6] Lin, C. H., Lin, C. A. and Chen, J. C., "Modelling Influences of Inlet Swirl Profiles on Dump Combustor Flows," AIAA Journal, December 1996, pp. 2630-2632.

[7] Jones, W.P. and Launder, B.E., 1972, "The Prediction of Laminarisation with a Two-Equation Model of Turbulence," Int. J. Heat Mass Transfer, Vol. 15, pp. 301-314.

[8] Speziale, C. G., Sarkar, S., and Gatski, T. B., 1991, "Modelling the Pressure-Strain Correlation of Turbulence: An Invariant Dynamical Approach," Journal of Fluid Mechanics, Vol. 227, pp. 245-272.

[9] Patankar, S.V., 1980, "Numerical Heat Transfer and Fluid Flow," Hemispher Publishing Corporation.

[10] Leonard, B.P., 1979, "A Stable and Accurate Convective Modelling procedure Based on Quadratic Upstream Interpolation," Comp. Meth. Appl. Mech. Eng., Vol. 19, pp. 59-98.

[11] Ahmed, S.A. and Nejad, A. S., 1992, "Swirl Effects on Confined Flows in Axisymmetric Geometries," J. of Propulsion and Power, Vol 8, No. 2, pp. 339-345.

[12] So, R. M. C., Ahmed, S. A. and Mongia, H. C., 1984, "An Experimental Investigation of Gas Jets in Confined Swirling Air Flow," NASA CR-3832.

[13] Kitoh, O., 1991, "Experimental study of turbulent swirling flow in a straight pipe," Journal of Fluid Mechanics, Vol. 225, pp. 445-479.

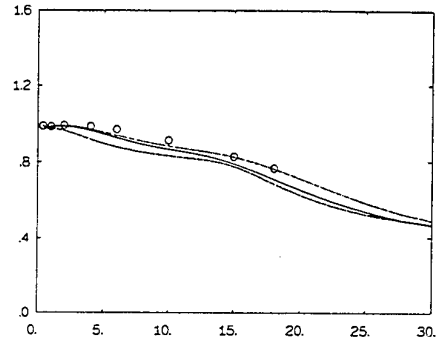


Figure 1: Centreline axial velocity-sudden expanding pipe

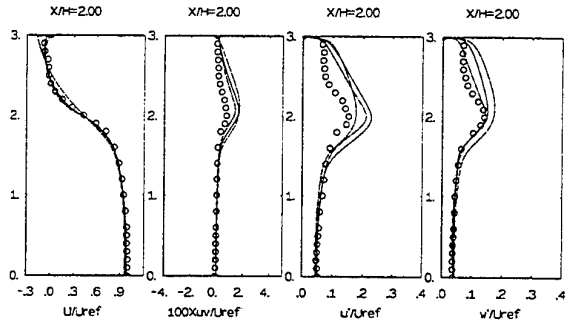


Figure 2: Comparisons of predictions and measurements at $X/H = 2$-sudden expanding pipe

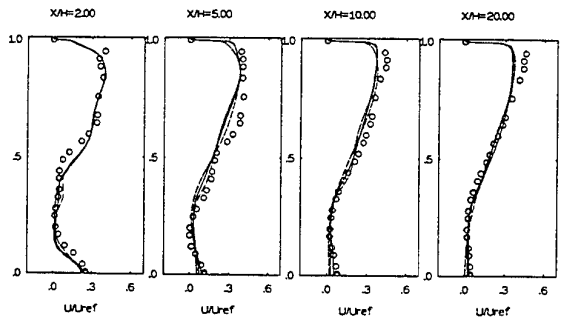
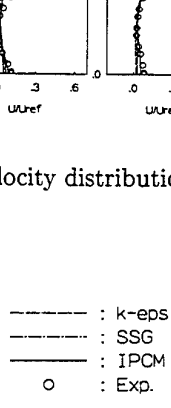


Figure 3: Axial velocity distributions-So et al.'s case



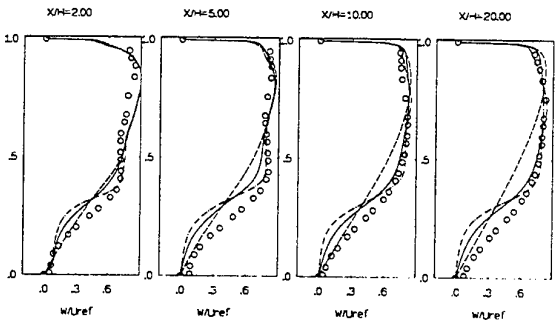


Figure 4: Tangential velocity distributions-So et al.'s case

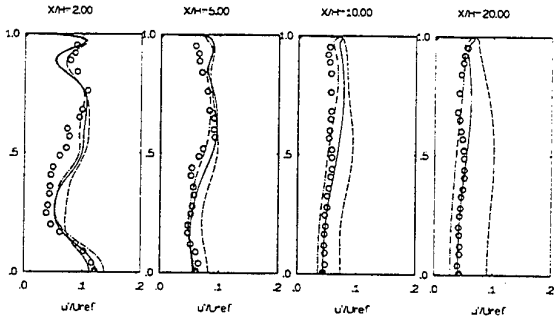


Figure 5: $\overline{uu}$ distributions-So et al.'s case

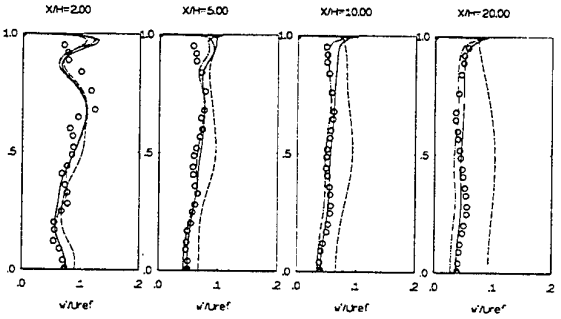


Figure 6: $\overline{ww}$ distributions-So et al.'s case

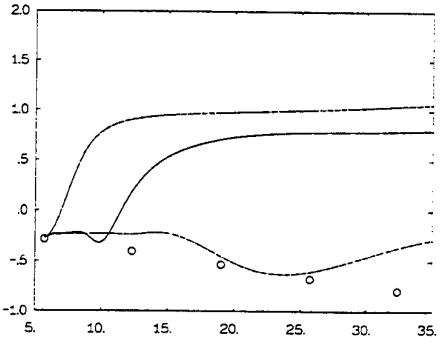


Figure 7: Centreline axial velocity distributions-Kitoh's case

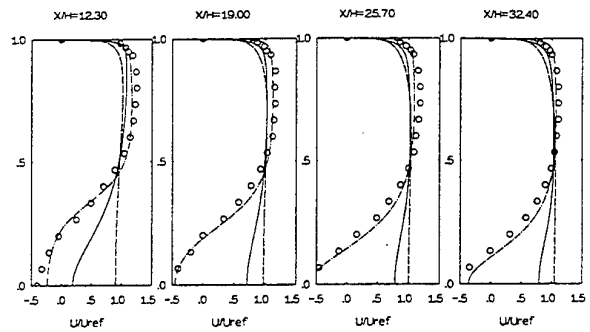


Figure 8: Axial velocity distributions-Kitoh's case

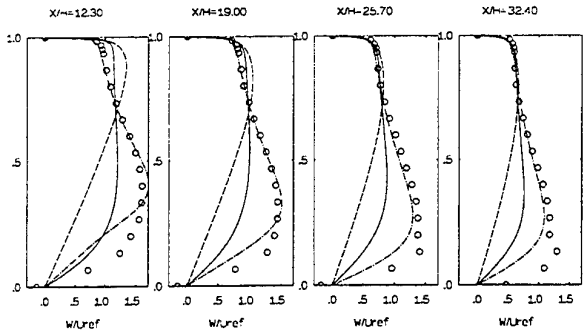


Figure 9: Tangential velocity distributions-Kitoh's case

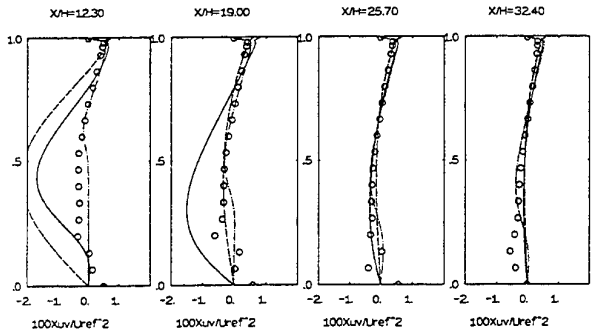


Figure 10: $\overline{uv}$ distributions-Kitoh's case

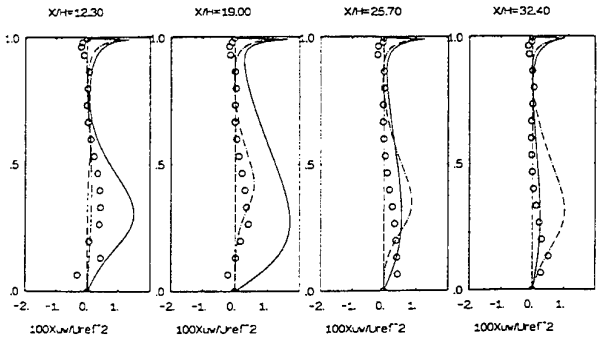


Figure 11: $\overline{uw}$ distributions-Kitoh's case

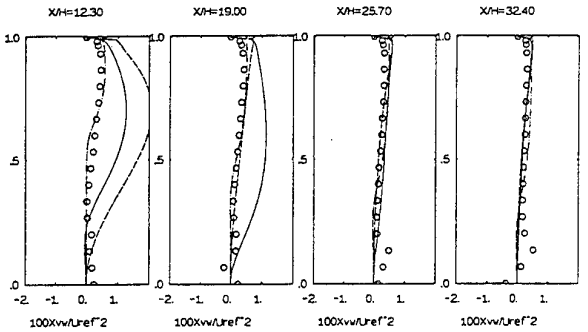


Figure 12: $\overline{vw}$ distributions-Kitoh's case

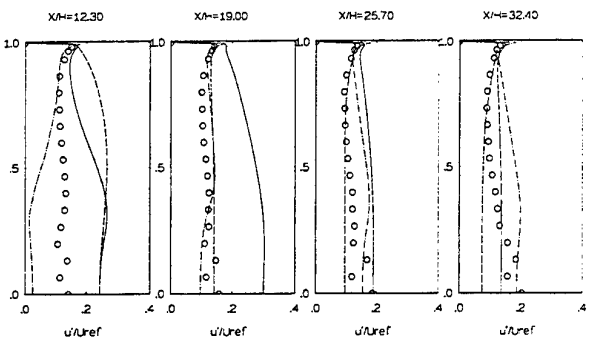


Figure 13: $\overline{uu}$ distributions-Kitoh's case

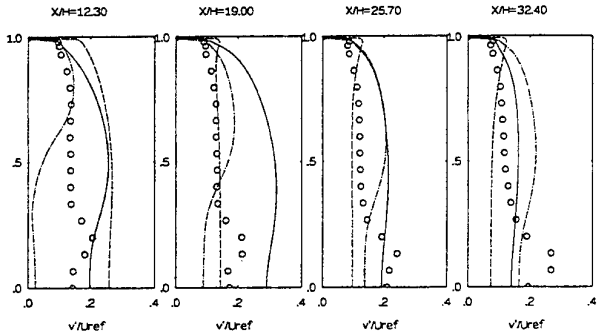


Figure 14: $\overline{vv}$ distributions-Kitoh's case

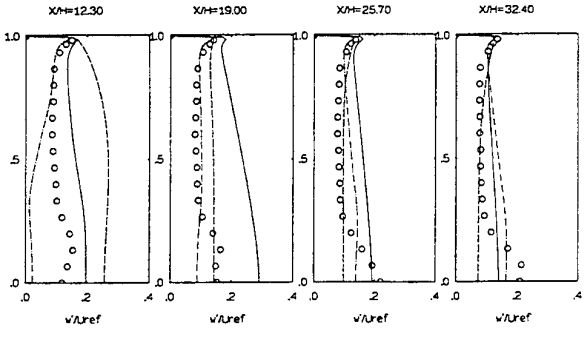


Figure 15: $\overline{ww}$ distributions-Kitoh's case

REPARTITION OF THE ENERGY IN COMPRESSIBLE TURBULENCE

F. BATAILLE[1], Y. ZHOU[2,3], J.P. BERTOGLIO[4]

[1] INSA, Centre de Thermique de Lyon, UPRES A CNRS 5008
20 av. A. Einstein, 69620 Villeurbanne, France

[2] Institute for Computer Applications in Science and Engineering
NASA Langley Research Center, Hampton, VA 23681, USA

[3] IBM Research Division, T.J. Watson Research Center,
P.O. Box 218, Yorktown Heights, NY 10598, USA.

[4] Laboratoire de Mecanique des Fluides et d'Acoustique, UMR CNRS 5509
ECL, 36, av. Guy de Collongue, 69130 Ecully, France

INTRODUCTION

In this paper, we study the energy transfer process in the compressible turbulence. A better understanding of how the energy is been transfered between the solenoidal and compressible modes is needed for developing practical engineering models. Despite the publications of many papers (see review by Lele (1995)), it is fair to say that the nature of the energy transfer process in the compressible turbulence is not clear yet.

We will borrow the basic methodology developed originally for incompressible turbulence. We also need to introduce the appropriate compressible energy transfer terms. Furthermore, we note that these type of studies require a substantial spectral scale range of interactions. Direct numerical simulations (DNS) of compressible turbulence is restricted to very small Reynolds numbers. As a result, it is very hard to utilize the DNS databases since these simulations are limited to very low Reynolds numbers and have only very limited spectral ranges. A way to generate high Reynolds number databases is by using two-point closure models. The Eddy-Damped-Quasi-Normal-Markovian (EDQNM) models (Orszag (1970); Lesieur (1990)) is widely used. Although EDQNM has included closure assumptions (Lesieur (1990)), we note that for incompressible turbulence, it has been found that EDQNM provides essentially same energy transfer and triadic transfer function as that of DNS (Domaradzki and Rogallo (1990), Ohkitani and Kida (1992)).

In this paper, we perform a detailed analysis of the nonlinear transfer terms including the most fundamental building block of the energy transfer process, the triadic interactions.

COMPRESSIBLE EDQNM MODEL

The EDQNM governing equations of weakly compressible isotropic turbulence are the following (Bataille and Bertoglio (1993a); Bataille (1994); Bertoglio et al. (1996)):

- an equation for the spectrum (E^{SS}) of the solenoidal part of the velocity field:

$$\frac{\partial}{\partial t}E^{SS}(K,t) = -2\nu K^2 E^{SS}(K,t) + T^{SS}(K,t) \qquad (1)$$

- an equation for the spectrum (E^{CC}) of the "purely compressible" part of the velocity field:

$$\frac{\partial}{\partial t}E^{CC}(K,t) = -2\nu' K^2 E^{CC}(K,t)$$

$$+T^{CC}(K,t) - 2c_0 K E^{CP}(K,t) \qquad (2)$$

- an equation for the spectrum of the potential energy (E^{PP}) associated with the pressure:

$$\frac{\partial}{\partial t}E^{PP}(K,t) = 2c_0 K E^{CP}(K,t); \qquad (3)$$

- an equation for the spectrum of the pressure-velocity correlation (E^{CP}):

$$\frac{\partial}{\partial t}E^{CP}(K,t) = -\nu' K^2 E^{CP}(K,t) + T^{CP}(K,t)$$

$$+c_0 K(E^{CC}(K,t) - E^{PP}(K,t)) \qquad (4)$$

In the case of a Stokes fluid:

$$\nu' = \frac{\lambda + 2\mu}{<\rho>} = \frac{4}{3}\nu \qquad (5)$$

μ and λ, two dynamic viscosities, are assumed to be uniform. The different contributions of the solenoidal and compressible transfer (T^{SS} and T^{CC}) are given in Appendix.

We note that $T^{SS} = T_S^{SS} + T_C^{SS}$ where T_S^{SS} is identical to that of the incompressible turbulence and T_C^{SS} is generated by interacting with compressible modes (see Appendix). We found that T^{SS} has the usual shape observed in incompressible turbulence studies (Fig. 1). Specifically, T^{SS} is negative in the large scales and positive for small scales. Physically this corresponds to the energy transfer from the large scales to the smaller ones. Therefore, the contribution, in front of T_S^{SS}, from T_C^{SS} is negligible (Bataille et al. (1995)). In all the figures, the transfer terms T(K) are given in $m^3 s^{-2}$ and K is in m^{-1}.

For a low turbulent Mach number, the compressible transfer is positive for all spectral space. Hence, $T^{CC}(K)$ is responsible for the production of compressible energy

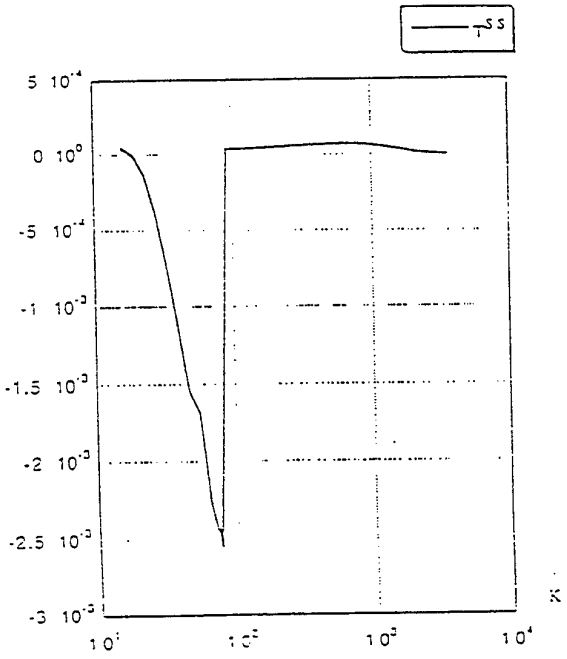


figure 1. Solenoidal transfer term

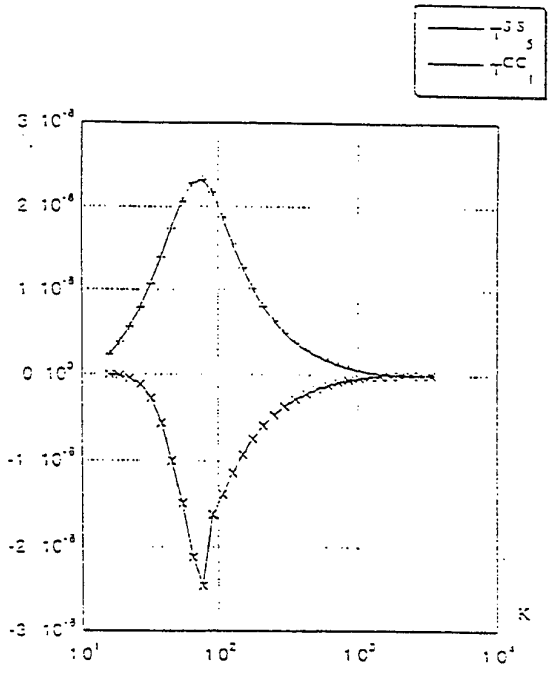


Figure 3 : T^{SS}_{5} and T^{CC}_{1}

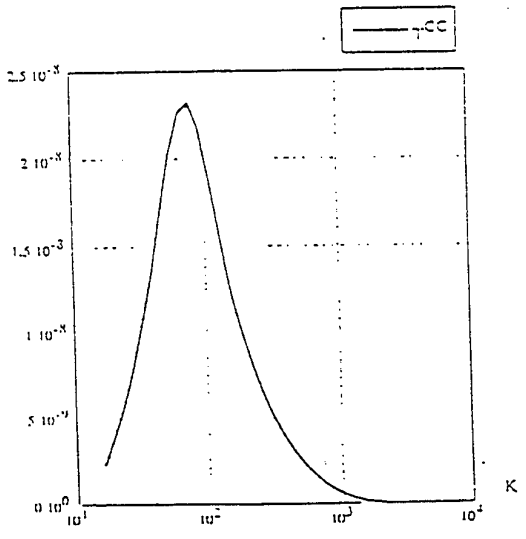


Figure 2 : Compressible transfer term

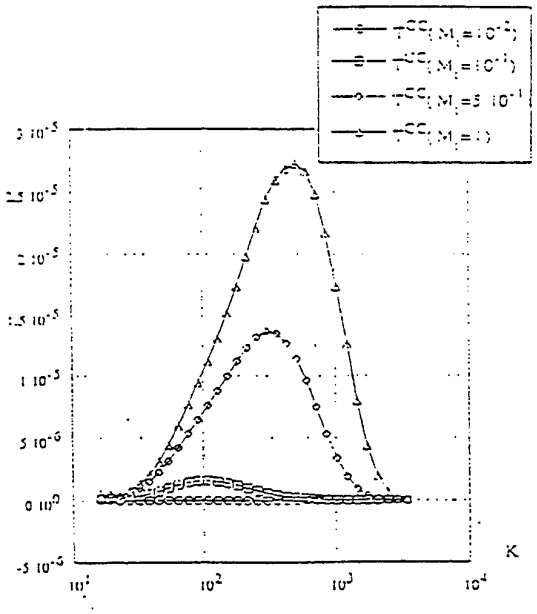


Figure 4 : Compressible transfer term at different M_t

(Figure 2). Using the individual contributions of each terms composing the solenoidal and compressible transfers (Bataille and Bertoglio (1995)), we can find that one term, in T_C^{SS}, is dominant, noted T_5^{SS} and that, after taking into account cancellations, one term is dominant in T^{CC}, noted T_1^{CC}.

When we plot these two terms (T_5^{SS} and T_1^{CC}), we find that they have similar magnitude but with an opposite sign (Figure 3). They are essentially responsible of the energy exchanges between the solenoidal and compressible parts. Specifically, $T_1^{CC}(K)$ is the "input" energy term on the compressible mode whereas $T_5^{SS}(K)$ is the "output" term in the equation of the solenoidal mode. For a careful study of each individual contributions in the energy transfer function, see Bataille and Bertoglio (1993b). Based on these results obtained in spectral space, we can think that there is a local transfer of energy from the solenoidal mode to the compressible mode.

The total solenoidal transfer term is not influenced by the compressibility (not shown) because the most important contributions are the incompressible ones but the total compressible transfer term $T^{CC}(K)$ is dependent on the compressibility (e.g., turbulent Mach number). Figure 4 demonstrates that as the turbulent Mach number increases, a shift of the peak spectrum of $T^{CC}(K)$ towards the large K appears. A complete analysis of each contributions of $T^{CC}(K)$ would shown (Bataille and Bertoglio (1993b)) that the most important contribution (T_1^{CC}) is not responsible of this peak shift. Two others terms (noted T_3^{CC} and T_6^{CC}), involving interactions among the compressible mode, become important contributions at high turbulent Mach numbers and lead to a cascade type of compressible energy transfer. This cascade mechanism will be investigated in the next section.

TRIADIC INTERACTIONS

The most fundamental building blocks of the energy transfer process are the triadic interactions. Specifically, we would like to study the triadic energy transfer $T(K,P,Q)$ for a given mode K due to its interactions with all the pairs of modes P and Q = K - P that form a triangle. For this reason, we introduce the triadic energy transfer function, $T(K,P,Q)$, according to

$$T^{SS}(K) = \sum_{P,Q=|\mathbf{K}-\mathbf{P}|} T^{SS}(K,P,Q) \qquad (6)$$

$$T^{CC}(K) = \sum_{P,Q=|\mathbf{K}-\mathbf{P}|} T^{CC}(K,P,Q). \qquad (7)$$

The average procedure is performed over spherical shell since the turbulence is isotropic.

An examination of the purely incompressible contributors reproduces the results of incompressible turbulence (Domaradzki and Rogallo (1990), Yeung et al. (1991, 1995), Ohkitani and Kida (1992), Zhou (1993a-b) and Zhou et al. (1996)) and again indicates that the purely solenoidal triadic energy transfer is not affected by compressible effects (not shown).

We have found from the previous section that particular attention should be paid to the T_5^{SS} term since it is the term that is responsible for 'output' energy from solenoidal to compressible mode. Since this term represents an energy output at a localized spectral region, we refer to it as the radiative (emission) triadic energy transfer. Figure 5 illustrates this type of interaction from various Q values at the given value of P ($P = 512$) for $M_t = 10^{-2}$. It is clear that the triadic interaction of this term is quite different from those of purely incompressible terms. As the Mach number increases, the magnitude of the 'output' energy increases but the basic structure remains.

We now turn our attention to the triadic interactions in compressible energy transfer, $T^{CC}(K,P,Q)$. In Figure 6, we present $T^{CC}(K,P,Q)$ for various Q values when P is in the inertial range ($P = 512$). For this low Mach number ($M_t = 10^{-2}$), we observe that the structures of $T^{CC}(K,P,Q)$ are rather similar for differing Q values. All of them show the *radiative* (absorption) type of energy transfer.

Figure 7 shows the triadic $T_1^{CC}(K,P,Q)$ contribution for various Q (P being equal to 512) at $M_t = 10^{-2}$. Comparing figures 5 and 7, we find that the absorption type of triadic energy transfer functions have the same magnitude but opposite sign as those of the emission type ($T_5^{SS}(K,P,Q)$). We can see in Figure 8 that $T_1^{CC}(K,P,Q)$ increases when the turbulent Mach number increases but, as for $T_5^{SS}(K,P,Q)$, its structure stays the same. In fact, we can observe (not shown) that the triadic interactions $T_1^{CC}(K,P,Q) \approx -T_5^{SS}(K,P,Q)$ for all turbulent Mach numbers. Consequently, we conclude that all compressible energy has been transferred locally (in spectral space) from the solenoidal component.

As the Mach number increases, some small terms (T_3^{CC} and T_6^{CC}) in the compressible energy transfer increase rapidly (Bataille et al., 1997). In fact, at high Mach number, these terms are responsible for the cascade of compressible turbulence. To demonstrate this point, we plot the total compressible energy transfer term, $T^{CC}(K,P,Q)$, at different high Mach numbers (Figure 9). It is clear that $T^{CC}(K,P,Q)$ changes its characteristic features from radiative to cascade as the turbulent Mach number increases. Furthermore, if we plot $T_3^{CC}(K,P,Q) + T_6^{CC}(K,P,Q)$, for different turbulent Mach numbers, we can observe the compressible energy cascade (Figure 10). From this analysis, we conclude that, at high turbulent Mach numbers, the cascade of compressible turbulence is a direct result of the fact $T_3^{CC}(K,P,Q) + T_6^{CC}(K,P,Q) > T_1^{CC}(K,P,Q)$ in the inertial range of the spectrum.

CONCLUSION

We have investigated the energy transfer process of compressible turbulence using EDQNM closure and the triadic energy transfer functions. We found that compressible energy is transferred locally from the solenoidal part to the compressible part. Furthermore, we observed that there is an energy cascade of the compressible energy transfer when the turbulent Mach number increases. In another paper presented at the conference, a modified version of the EDQNM model for compressible turbulence is proposed (Fauchet et al. (1997)). The application of the present type of detailled analysis to the new model is planned to confirm the observed mechanismes.

Acknowledgments

The authors would like to thank Marcel Lesieur for providing a computational code used in the present study. This research was supported by the National Aeronautics and Space Administration under NASA Contract No. NAS1-19480 while the first and second authors were in residence at the Institute for Computer Applications in Science and Engineering (ICASE), NASA Langley Research Center, Hampton, VA 23681-0001. The first author was also partially supported by the Foreign Ministry of the French government.

REFERENCES

BATAILLE, F., BERTOGLIO, J.P., 1993a. "Short and long time behavior of weakly compressible turbulence",

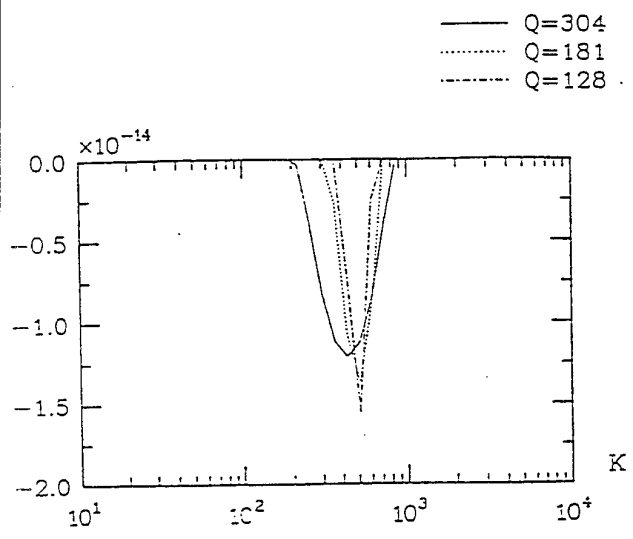


figure 5 : Triadic $T^{SS}{}_5$ for different Q

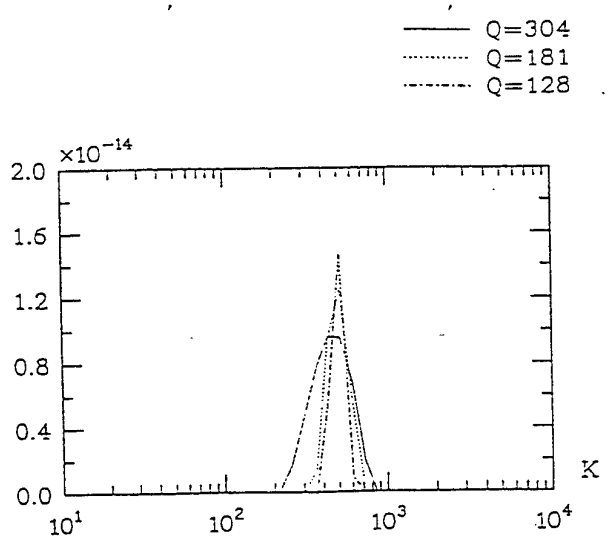


Figure 7 : Triadic $T^{CC}{}_1$ for different Q

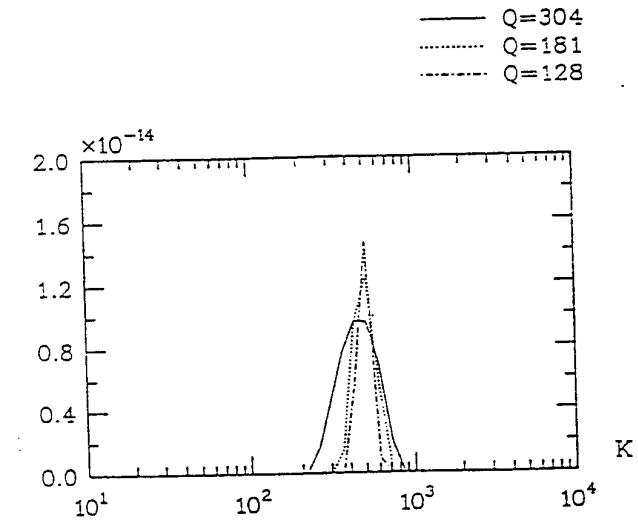


Figure 6 : Triadic compressible transfer term for different Q

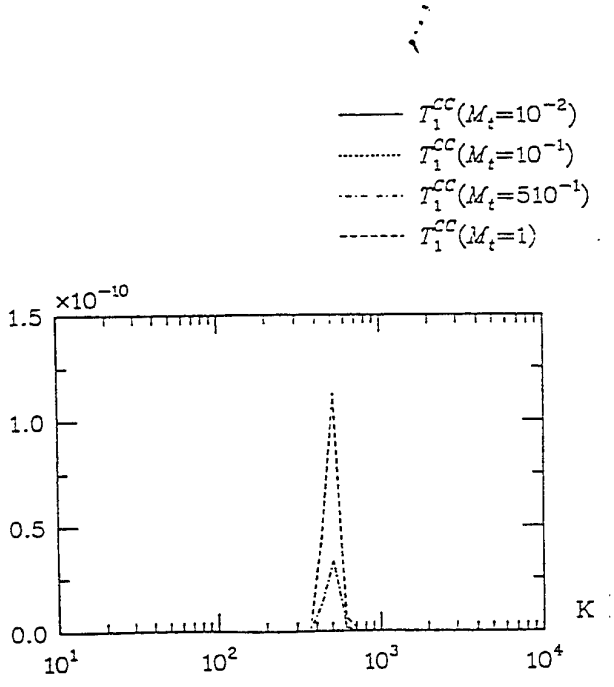


Figure 8 : Triadic $T^{CC}{}_1$ at different M_t

ASME Fluids Engineering Conference, Washington.

BATAILLE, F., BERTOGLIO, J.P., 1993a. "Study of spectral transfers for weakly compressible turbulence", 5th International Symposium on Refined Flow Modelling and Turbulence Measurements, Paris, Presse des Ponts et Chaussees, pp. 107-116.

BATAILLE, F., 1994. "Etude d'une turbulence faiblement compressible dans le cadre d'une modelisation Quasi-Normale avec Amortissement Tourbillonnaire", These Ecole Centrale de Lyon.

BATAILLE, F., BERTOGLIO, J.P., and ZHOU, Y., 1995. "Energy transfer in compressible turbulence," *NASA Contractor Report 198216; ICASE Report 95-65*

BATAILLE, F., BERTOGLIO, J.P., and ZHOU, Y., 1997, "Energy transfer and triadic interactions in compressible turbulence," *ICASE Report* (in press)

BERTOGLIO, J.P., BATAILLE, F., MARION, J.D., 1996. "Two-point closures for weakly compressible turbulence", submitted to Physics of Fluids.

DOMARADZKI, J.A., ROGALLO, R.S., 1990. "Local energy transfer and nonlocal interactions in homogeneous, isotropic turbulence", Phys. Fluids A, vol. 2, p. 413.

FAUCHET, G., SHAO, L., WUNENBURGER, R., BERTOGLIO, J.P., 1997. "An improved two-point closure for weakly compressible turbulence and comparisons with large eddy simulations", 11th Symp. on Turb. Shear Flows, Grenoble.

LELE, S.K., 1995. "Compressibility effects on turbulence", Ann. Rev. Fluid Mech., vol. 26, p. 211.

LESIEUR, M., 1990. "Turbulence in Fluids", Kulwer, Dordrecht.

OHKITANI, K., KIDA, S., 1992. "Triad interactions in a forced turbulence", Phys. Fluids A, vol. 4, p. 794.

ORSZAG, S.A., 1970. "Analytical theories of turbulence", Journal of Fluid Mechanics, vol. 41, part 2, pp. 363-386.

YEUNG, P.K., BRASSEUR, J.G., 1991. "The response of isotropic turbulence to isotropic and anisotropic forcing at large scales", Phys. Fluids A, vol. 3, p. 884.

YEUNG, P.K., BRASSEUR, J.G., WANG, Q., 1995. "Dynamics of direct large-small scale coupling in coherently forced turbulence: Concurrent physical- and Fourier-space views", Journal of Fluid Mech., vol. 283, p. 43.

ZHOU, Y., 1993a. "Degrees of locality of energy transfer in the inertial range", Phys. Fluids A, vol. 5, p. 1092.

ZHOU, Y., 1993b. "Interacting scales and energy transfer in isotropic turbulence," Phys. Fluids A, vol. 5, p. 2511.

ZHOU, Y., YEUNG, P.K., BRASSEUR, J.G., 1996. "Scale disparity and spectral transfer in anisotropic numerical turbulence", Phys. Rev. E, vol. 53, p. 1261.

Appendix

In equations (1)-(4), T^{SS}, T^{CC}, T^{CP} are the transfer terms. As we are interested in the solenoidal and compressible transfer terms, only the different contributions of these two transfer terms are given by the following. The different contributions of T^{CP} can be found in Bertoglio et al. (1996).

The solenoidal and compressible transfer terms are composed of different contributions:

$$T^{SS} = T_S^{SS} + T_C^{SS} \tag{8}$$

$$T_S^{SS} = T_1^{SS} + T_3^{SS} \tag{9}$$

$$T_C^{SS} = T_2^{SS} + T_4^{SS} + T_5^{SS} \tag{10}$$

$$T^{CC} = T_1^{CC} + T_2^{CC} + T_3^{CC} + T_4^{CC} + T_5^{CC} + T_6^{CC} \tag{11}$$

$$T^{CP} = T_1^{CP} + T_2^{CP} + T_3^{CP} + T_4^{CP} + T_5^{CP} + T_6^{CP} \tag{12}$$

Different contributions appearing in the transfer term acting on the solenoidal field are:

$$T_1^{SS} = \int_\Delta \frac{K^3}{PQ} \frac{1 - xyz - 2y^2z^2}{2} \theta_{KPQ}^{SS-SS-SS} \tag{13}$$

$E^{SS}(P,t)E^{SS}(Q,t)dPdQ$

$$T_2^{SS} = \int_\Delta \frac{K^3}{PQ} \frac{(1-y^2)(x^2+y^2)}{1-x^2} \theta_{KPQ}^{SS-SS-CC} \tag{14}$$

$E^{SS}(P,t)E^{CC}(Q,t)dPdQ$

$$T_3^{SS} = -\int_\Delta \frac{P^2}{Q} (xy + z^3) \theta_{KPQ}^{SS-SS-SS} \tag{15}$$

$E^{SS}(K,t)E^{SS}(Q,t)dPdQ$

$$T_4^{SS} = \int_\Delta \frac{P^2}{Q} (2xy) \theta_{KPQ}^{SS-SS-CC} \tag{16}$$

$E^{SS}(K,t)E^{CC}(Q,t)dPdQ$

$$T_5^{SS} = -\int_\Delta \frac{P^2}{Q} (z(1-z^2)) \theta_{KPQ}^{SS-CC-SS} \tag{17}$$

$E^{SS}(K,t)E^{SS}(Q,t)dPdQ$

Different contributions to the transfer term in the E^{CC} equation are:

$$T_1^{CC}(K,t) = \int_\Delta \frac{K^3}{PQ} ((x+yz)^2) \theta_{KPQ}^{CC-SS-SS} \tag{18}$$

$E^{SS}(P,t)E^{SS}(Q,t)dPdQ$

$$T_2^{CC}(K,t) = \int_\Delta \frac{K^3}{PQ} \frac{(x^2-y^2)^2}{(1-x^2)} \theta_{KPQ}^{CC-SS-CC} \tag{19}$$

$E^{SS}(P,t)E^{CC}(Q,t)dPdQ$

$$T_3^{CC}(K,t) = \int_\Delta \frac{K^3}{PQ} (x^2) \theta_{KPQ}^{CC-CC-CC} \tag{20}$$

$E^{CC}(P,t)E^{CC}(Q,t)dPdQ$

$$T_4^{CC}(K,t) = -\int_\Delta \frac{P^2}{Q} 2z(1-z^2) \theta_{KPQ}^{CC-SS-SS} \tag{21}$$

$E^{CC}(K,t)E^{SS}(Q,t)dPdQ$

$$T_5^{CC}(K,t) = -\int_\Delta \frac{P^2}{Q} (2z^3 - z + xy) \theta_{KPQ}^{CC-CC-SS} \tag{22}$$

$E^{SS}(Q,t)E^{CC}(K,t)dPdQ$

$$T_6^{CC}(K,t) = \int_\Delta \frac{P^2}{Q} (2xy) \theta_{KPQ}^{CC-CC-CC} \tag{23}$$

$E^{CC}(K,t)E^{CC}(Q,t)dPdQ$

The integration in the P, Q plane extends over a domain such that **K**, **P** and **Q** form a triangle.

In the left hand sides of the above equations, the polynomial expressions in x, y, z are coefficients associated with the geometry of the triad. x, y, and z are the cosines of the angles respectively opposite to **K**, **P**, **Q** in the triad **K**, **P** and **Q**.

In above equations, functions θ are the decorrelation times involved in the model. They are calculated by integration over time of a product of three response function from the DIA equations. Their expressions can be found in Bertoglio et al. (1996).

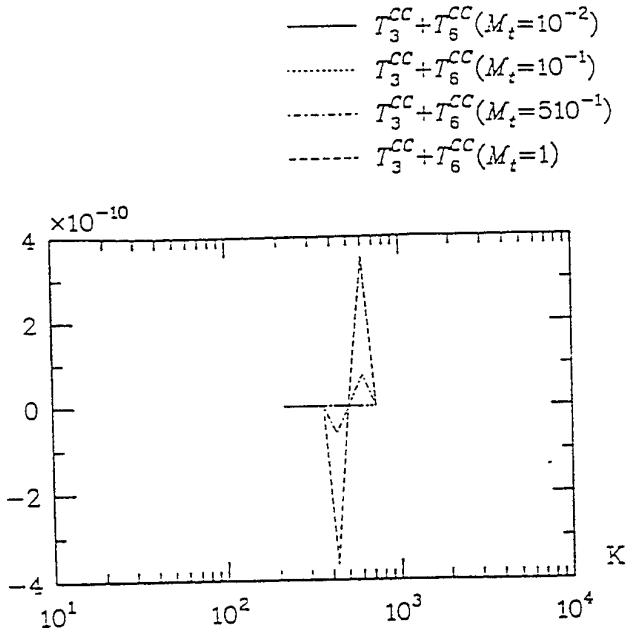


figure 9 : Triadic T^{CC} at different high M_t

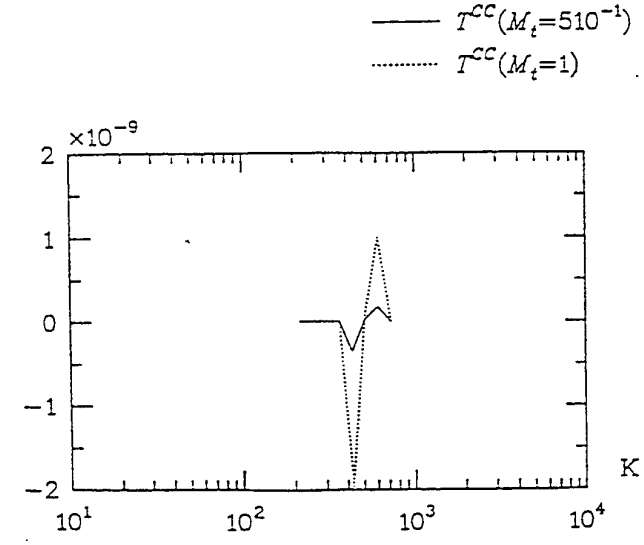


Figure 10 : Triadic $T^{CC}{}_3 + T^{CC}{}_6$ at different M_t

MODELLING OF EXTRA-COMPRESSIBILITY TERMS IN HIGH SPEED TURBULENT FLOWS

Christine Lejeune and Azzedine Kourta

Institut de Mecanique des Fluides de Toulouse
UMR CNRS/INP-UPS 5502
Avenue du Prof. Camille Soula
31400 Toulouse
FRANCE

ABSTRACT

This paper deals with the development of turbulence models for high speed turbulent flows. Special attention is devoted to the pressure-dilatation correlation Π_d that represents an important contribution of dilatational effects on the turbulent kinetic energy budget. The modelling of this term is based on linear acoustics. A simple order-of-magnitude analysis, including isentropic hypothesis for the thermodynamic properties of the fluid permits to deduce an algebraic expression for Π_d. A modified turbulence model including extra-compressibility terms is finally tested on a supersonic mixing layer with a convective Mach number varying from *0.2* to *1.0*. Our numerical results are in good agreement with the experimental data from other authors.

I. INTRODUCTION

The renewed interest in high speed flows highly correlated with hypersonic aircraft projects has recently provided the motivation for exploring compressibility effects. In this context extensive direct numerical simulations and experiments have been conducted during the last few years. The concrete evidence of intrinsic compressibility effects on turbulence is given by a crude reduction in the turbulent kinetic energy growth rate (Blaisdell *et al.*, 1993). Furthermore, recent studies concerning supersonic mixing layers have shown a significant decrease in all three Reynolds normal stresses (Elliott *et al.*, 1990). The first interpretations of Zeman (1990,1991) and Sarkar *et al.* (1991,1992) in order to explain those effects were centered on additional energy losses associated with dilatational terms. These terms are the pressure-dilatation correlation $\Pi_d = \overline{p' \partial u_i' / \partial x_i}$ and the compressible part of the turbulent dissipation rate $\overline{\rho}\varepsilon_d = 4/3\nu\overline{\left(\partial u_i' / \partial x_i\right)^2}$ appearing in the turbulent kinetic energy equation. With approaches based on very different considerations previous authors have proposed to represent Π_d but also $\overline{\rho}\varepsilon_d$ as functions of the turbulent Mach number. More recently, the reduced turbulent production related to the anisotropy of the Reynolds stress tensor have been recognized to be an other important stabilizing effect of compressibility (Sarkar, 1995). A model for the integrated pressure-strain correlation has been developed in 1996 by Vreman *et al.* and connected to the mixing layer growth rate.

In this paper we present the development of a new closure scheme for the pressure-dilatation term. We have used not only the turbulent Mach number but also the density variance as possible compressibility parameters. In order to isolate intrinsic compressibility effects, the flow in consideration is supposed to be nearly isentropic and $\rho' \approx \left(\partial\rho/\partial p\right)_s p'$. The new closure for Π_d, developed under above asumptions, introduces a new unknown term in the averaged Navier-Stockes equations. This term is the density variance and will be described through a convection-diffusion equation.

II. THE TURBULENT KINETIC ENERGY

Let first consider the turbulent kinetic energy equation for a compressible flow. Using the mass-weighted average we have:

$$\frac{D\overline{\rho}\tilde{k}}{Dt} = P_k - Diff_k - \overline{\rho}\tilde{\varepsilon} + \Pi_d - \overline{u_i''}\frac{\partial\overline{P}}{\partial x_i} + \overline{u_i''}\frac{\partial\overline{\tau}_{ij}}{\partial x_j}$$

In the above equation $P_k = \overline{\rho u_i'' u_j''} \partial \tilde{u}_i / \partial x_j$ is the kinetic energy production.

$Diff_k = \partial / \partial x_i (\overline{\rho k u_j''} - \overline{p' u_j''} - \overline{\tau_{ij} u_j''})$ denotes diffusion terms resulting from the turbulent motion, the velocity-pressure interaction and the molecular mechanisms respectively.

$\overline{\rho} \varepsilon = \mu (\overline{\tau_{ij}'' \partial u_i'' / \partial x_j})$ is the turbulent dissipation rate per unit volume.

The last three terms are extra-compressibility correlations. $\Pi_d = \overline{p' \partial u_i'' / \partial x_i}$ represents the work of the pressure fluctuations acting during the volume changes of the fluid particles. Refering to linear acoustics, Π_d permits readjustments of energy in order to ensure the condition $F \approx 1$. The partition factor F, defined by $\overline{p_c'^2} / (\overline{\rho}^2 \tilde{a}^2 \overline{u_i''^2})$, represents the ratio of the kinetic energy k_c to the potential energy $\overline{p_c'^2} / 2\gamma\overline{p}$ of the acoustic waves. In D.N.S. of compressible homogeneous shear flows (Blaisdell *et al.*, 1993) Π_d is observed to be predominantly negative and to represent a non negligible fraction of the turbulent kinetic energy production ($\Pi_d \approx 10\% P_k$). In consequence, Π_d requires a careful modelling in the $(k-\varepsilon)$ turbulence model.

The last two terms of the turbulent kinetic energy equation are associated with transfer mechanisms between the mean and the turbulent kinetic energies (Huang *et al.* 1995). The former $\overline{u_i''} \partial \overline{P} / \partial x_i$ is a term of interaction between the mass flux $\overline{u_i''} = -\overline{\rho' u_i'} / \overline{\rho}$ and the spatial variation of the static pressure. It may be important in configurations involving high pressure gradients (i.e. shock turbulence interaction). The last term of the right hand side is generally neglected in the modelling procedure. The simulations of Huang *et al.* (1995) have shown that both $\overline{u_i''}$ and $\overline{\tau_{i2}}$ are significant in the near wall viscous region where they represent the major compressibility contribution. In free shear flows this term seems to be negligible and our calculation gives $(\overline{u_i'' \partial \tilde{\tau}_{ij} / \partial x_j}) / (\overline{p' \partial u_i' / \partial x_i}) \approx 0$.

III. A MODELLING FOR THE PRESSURE-DILATATION TERM

Using the equations of linear acoustics, and more particularly the linearized mass equation, it is possible to write the normalized rate of change of the density fluctuation as a function of the fluctuating dilatation:

$$\frac{\partial u_i'}{\partial x_i} = -\frac{1}{\rho} \frac{\partial \rho'}{\partial t} \qquad (1)$$

Such approximatition is acceptable if we consider the problem on the fast scale τ_a that represents the time requires for an acoustic disturbance to cross an energy containing eddy. Hence τ_a is the ratio of the lenght of a large eddy l by the sound speed $a = (\partial p / \partial \rho)_s$. On the acoustic time scale, the turbulent diffusion but also the molecular processes can be ignored. An order-of-magnitude of the right hand side of equation (1) gives the approximative form for the fluctuating divergence of velocity:

$$\frac{\partial u_i'}{\partial x_i} = O\left(\frac{1}{\rho_o} \frac{\rho_o'}{\tau_a} \right)$$

where ρ_o and ρ_o' denote an order of magnitude for the mean and fluctuating density respectively.
Using the main variables of our problem and replacing τ_a by $M_t \tilde{k} / \varepsilon$ we propose to model the density-dilatation correlation as:

$$\overline{\rho' \frac{\partial u_i'}{\partial x_i}} = \alpha \frac{\overline{\rho'^2}}{\overline{\rho}} \frac{\varepsilon}{\tilde{k}} \frac{1}{M_t} \qquad (2)$$

Owing to the isentropic hypothesis, we finally obtain the following scheme for the pressure-dilatation term:

$$\overline{p' \frac{\partial u_i''}{\partial xi}} = \alpha \frac{\overline{\rho'^2}}{\overline{\rho}^2} \frac{\gamma \overline{p}}{M_t} \frac{\varepsilon}{\tilde{k}} \qquad (3)$$

The previous expression involves two compressibility parameters: $\overline{\rho'^2} / \overline{\rho}^2$ and M_t. The mean static pressure $\overline{p}$ and the turbulent time scale $\tau_t \approx \tilde{k} / \varepsilon$ are also encountered in the closure scheme.

When the flow becomes an incompressible constant density one, expression (3) has to tend to zero. We know that the incompressible part of the fluctuating pressure p_i' generally scales as $O(\rho_o u^2)$ while the compressible component is $p_c' = O(\rho' a^2)$. Here u denotes an order-of-magnitude for the fluctuating velocity. Hence these flows are characterized by a ratio $\overline{p_c'^2} / \overline{p_i'^2} \approx \rho'^2 / \rho_o^2 M_t^4$ tending to zero. Since the turbulent Mach number also tends to zero and since the acoustic time scale $\tau_a = \tilde{k} M_t / \varepsilon$ and the mean static pressure $\overline{p}$ have finite limits, Π_d tends to zero when the density becomes constant.

In high speed flows the adjustable model coefficient α is predominantly negative according to numerical and physical considerations of Sarkar et *al.* (1992). Futhermore, under the Boussinesq hypothesis ($\overline{\phi u_i''} \propto -\nu_t \, \partial\overline{\phi} / \partial x_i$) the propagation speed of acoustic disturbances is $\bar{a}\sqrt{1+\gamma/3M_t^2}$. Using the latter relationship, the general form of α is $\beta\sqrt{1+\gamma/3M_t^2}$ where β is a constant. The calibration of β will be discussed in §V.

The turbulent kinetic energy evolution is coupled with the mean calorific energy one since:

$$\frac{D\bar{\rho}\tilde{T}}{Dt} = \frac{1}{C_v}\left[-\frac{\partial}{\partial x_i}(\overline{\rho\theta u_i''}) - \frac{\partial \overline{q_i}}{\partial x_i} - \Pi_d - \bar{p}\frac{\partial \tilde{u}_\beta}{\partial x_\beta} + \bar{\rho}\varepsilon\right]$$

The energy losses of $\bar{\rho}\tilde{k}$ through the pressure-dilatation are proportional to the relative variance amount $\overline{\rho'^2}/\bar{\rho}^2$. In order to obtain a good representativity of the various processes involving changes in the density variation we have used a complete transport equtation to describe this quantity. The open equation for $\overline{\rho'^2}$ as given by Taulbee et *al.* (1991) is:

$$\frac{D\overline{\rho'^2}}{Dt} = \underbrace{-\frac{\partial(\overline{\rho'^2 u_i''})}{\partial x_i}}_{(I)} \underbrace{-2\overline{\rho' u_i''}\frac{\partial \bar{\rho}}{\partial x_i}}_{(II)} \underbrace{-\overline{\rho'^2}\frac{\partial \tilde{u}_\beta}{\partial x_\beta}}_{(III)}$$
$$\underbrace{-2\bar{\rho}\overline{\rho' \frac{\partial u_\beta''}{\partial x_\beta}}}_{(IV)} \underbrace{-\overline{\rho' \rho' \frac{\partial u_\beta''}{\partial x_\beta}}}_{(V)}$$

The rate of change of the density variance is equal to the sum of the turbulent transport (I), the production due to the mean density gradient (II) and the mean compression (III), the density-dilatation correlations (IV+V). The first term on the right hand side can be modelled using a gradient hypothesis (Taulbee et *al.* 1991):

$$\overline{\rho'^2 u_i''} = \overline{\rho'^2}\,\overline{u_i''} + \overline{\rho'^2 u_i'} \propto -\mu_t \frac{\partial \overline{\rho'^2}/\bar{\rho}}{\partial x_i}$$

Since the present work focuses on intrinsic compressibility effects let us consider a nearly constant mean density flow. In this particular case, contributions of terms (I) and (II) are expected to be negligible. As a first approximation we have adopted for the density-velocity correlation :

$$\overline{\rho' u_i''} = -\frac{\nu_t}{\sigma_\rho}\frac{\partial \bar{\rho}}{\partial x_i}$$

Density fluctuations are then amplified owing to the non-linear terms (IV) and (V). For small $\rho'/\bar{\rho}$, it is possible to neglect (V) behind (IV) which is represented by (2).

IV. THE NUMERICAL METHOD

The governing equations described in the previous section can be written into a vector form as follows: $\partial W/\partial t + \partial F/\partial x + \partial G/\partial y = H$. W is the unknown vector:

$$W = \left[\bar{\rho}, \bar{\rho}\tilde{u}, \bar{\rho}\tilde{v}, \bar{\rho}\tilde{E}, \bar{\rho}\tilde{k}, \bar{\rho}\varepsilon, \overline{\rho'^2}\right]$$

The equation of state for perfect gases $\bar{p} = \bar{\rho} r \tilde{T}$ is used to achieve the closure.

The numerical method is a finite volume version of the explicit Mac Cormack scheme (Kourta, 1996). It consists in a predictor-corrector approach. At each time step, for advancing the numerical solution a forward or a backward approximation is used for the inviscid part of the flux vector. The viscous terms are approximated by central differences.

Since the modified governing equations contain additional source terms, the Courant-Friedricks-Lewy (CFL) is set to *0.5*.

A supersonic shear layer is computed using a multiblock technique. The computational domain consits of two blocks of equal dimension 0.024×0.500 *m* with a 100×100 uniform grid.

The boundary conditions are the following: at the inflow, the profiles are specified for the velocity, the density, the temperature, the turbulent kinetic energy, the dissipation rate and the density variance. At the outflow classical first order extrapolations suitable for supersonic outflow are used. Finally, at the lower and upper boundaries farfield conditions are specified.

For initial conditions, the inflow profiles are used throughout the computational domain.

V. RESULTS

The mixing layer develops between two parallel supersonic airstreams as sketched in **Fig. 1.** Temperature, density and primary bottom stream values are deduced from the operating conditions of the experiment led by Goebel *et al.* (1990). When the specific heat ratio γ has the same value for both streams, the convective Mach number is given by: $M_c = (U_2 - U_1)/(a_2 + a_1)$.

However, in our calculation, the higher secondary freestream velocity was changed in order to obtain a

convective Mach number varying from *0.2* to *1.0*. The total temperature of the bottom stream was 295 K and the pressure distribution through the layer was almost uniform.

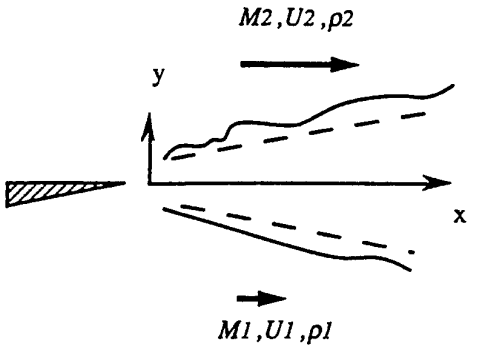


Fig. 1 Schematic of the flow field

The main mixing layer operating conditions for the reference case are given in **table 1.**

Table 1:

PHYSICAL VALUES (S.I. units)

$U_{1,2}$	$M_{1,2}$	$T_{1,2}$	$\rho_{1,2}$
409.00	1.40	211.00	0.809
519.00	2.04	160.00	1.066

Let us denote U^* the normalized velocity: $(U-U_1)/(U_2-U_1)$. According to self-similarity conditions, the nondimensional mixing layer thickness is defined as $\eta=(y-y_o)/\delta$ where y_o is the location of $U^*=1/2$. The shear layer thickness δ is equal to y_2-y_1 where y_1 (respectively y_2) is a ten percent thickness: $U^*=0.1$ (respectively $U^*=0.9$).

In **Fig. 2** the computed values of $\delta'=d\delta/dx$ are nondimensionalized with the growth rates of incompressible mixing layers δ'_o considered at the same velocity ratio r and density ratio s. The incompressible parameter δ'_o is given by the empirical formula (Goebel *et al.*, 1990)

$$\delta'_o=\frac{1}{\sigma_o}\frac{(1-r)(1+\sqrt{s})}{(1+r\sqrt{s})},\quad \sigma_o=11 \qquad (4)$$

It is shown that the effect of β is to reduce the normalized growth rate down to 87% from $|\beta|=5\times10^{-2}$ to $|\beta|=1$. The comparison with the experimental data of the ratio δ'/δ'_o for a highly compressible mixing layer with $M_c=0.8$ (Gruber *et al.*, 1993) suggests a value of $|\beta|=10^{-1}$.

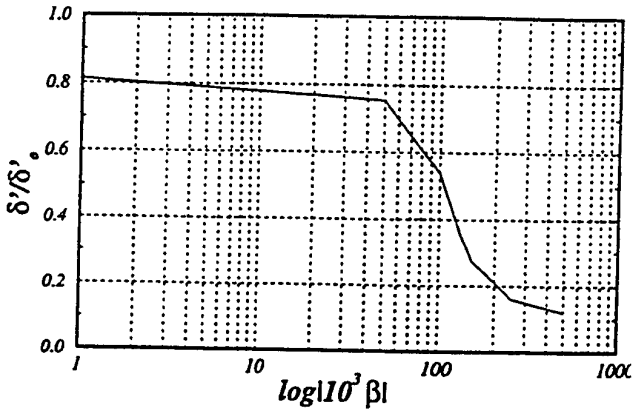


Fig. 2 Dependance of the normalized spreading rate on the model constant

The compressibility effects on the spreading rate, as a function of the convective Mach number is given in **Fig. 3.** Papamoschou et *al.* (1988) propose an empirical expression of the form:

$$\delta' = \delta'_o \times \Phi(M_c)$$

where Φ is a function of the convective Mach number.

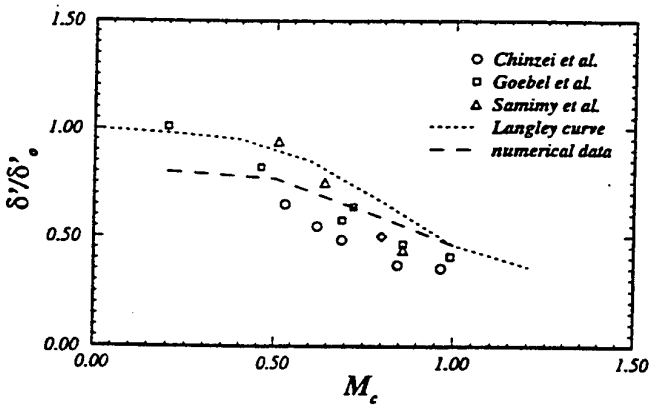


Fig. 3 Shear layer growth rate variation

The calculated growth rates of the present study are compared with experimental data. The dashed curve is the so-called "Langley curve" proposed by Birch et *al.* in 1972. Significant scatter due to experimental uncertainties, influence of the dual-stream tunnel geometry, lack of accuracy in the location of the edge of the layer and of the self-preserving region of the flow can be observed and the

experimental accuracy on δ' is probably no better than 10% (Smith et al.). The numerical results agree very well with those from other researchers for $M_c \geq 0.5$. When computing an incompressible mixing layer with $M_c = 0.2$, the ratio δ' / δ'_o is approximatively 20% lower than the one given by the Langley consensus. A possible explanation is that the relation giving δ'_o from (4) has been established for subsonic incompressible shear layers while in our calculation both streams are supersonic.

The maximum value of the turbulent shear stress as a function of M_c is given in **Fig. 4**. The computed variations of $\sigma_{uv} = -\overline{\rho u'' v''} / \left(\bar{\rho}(U_2 - U_1)^2\right)$ are compared to recent measurements from various authors. The dashed line represents the shear stress deduced from the "Langley curve" (Barre et *al.*, 1994). At low Mach numbers some abnormally high values are observed probably due to blockage effects in the experiment of Goebel et *al.* (1990). Discarding these points, it is clear from **Fig. 4** that computations with the compressible model (3) are in fairly good agreement with the observed trends of decrease of the Reynolds shear stress.

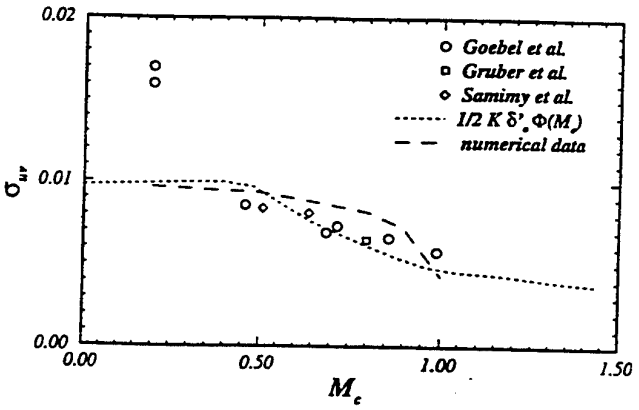


Fig. 4 Maximum value of the Reynolds shear stress

VI. CONCLUSION

In this paper a first order closure model for compressible high speed shear flows has been presented. The pressure-dilatation correlation is derived from a parametric expression developed on the basis of linear acoustics. This extra-compressibility term is expressed as a function of the turbulent Mach number and the density variance. A transport equation for this latter quantity is used in addition to those of k and ε. The predictions of the new model are tested on a supersonic shear layer. Some important parameters of the flow have been compared with physical experiments for $M_c \leq 1.0$. The results indicate that the model is able to quantitatively predict the reduction of the normalized mixing layer growth rate for high Mach numbers. However, as a $(k-\varepsilon)$ model can not correctly estimate the increasing anisotropic structure resulting from compressibility effects, the supersonic mixing layer studied suffers a small uncertainty on its Reynolds shear stress.

REFERENCES

Barre S., Quine C. and Dussage J.P., 1994, "Compressibility Effects on the Structure of Supersonic Mixing Layers: experimental results," *Journal of Fluid Mechanics*, Vol. 259, pp. 47-78

Birch S.F. and Eggers J.M., 1972, "A Critical Review of the Experimental Data for Developped Free Turbulent Shear Layers," *Free Turbulent Shear Flows, NASA Rep. SP-321*, pp. 11-40

Blaisdell G.A., Mansour N.N et Reynolds W.C, 1993, "Compressible Effects on the Growth and Structure of Homogeneous Turbulent Shear Flows," *Journal of Fluid Mechanics*. Vol. 256, pp. 443-485

Goebel S.G., Dutton J.C., Krier H. and Rence J.P., 1990, "Mean and Turbulent Velocity Measurements of Supersonic Mixing Layers," *Experiments in Fluids (8)*, pp. 263-272

Elliott G.S. and Samimy M., 1990, "Compressible Effects in Free Shear Layers," Phys. Fluids A 2,, pp. 1231

Gruber M.R. and Dutton J.C., 1993,"Three Dimensional Velocity Field in a Compressible Mixing Layer," AIAA Journal, Vol. 31 (11), pp. 2061-2067

Huang P.G, Coleman G.N. and Bradshaw P., 1995, "Compressible Turbulent Channel Flows," *Journal of Fluid Mechanics*, Vol. 305, pp. 185-218

Kourta A., 1996, "Acoustic-mean Flow Interaction and Vortex Shedding in Solid Rocket Motors," *International Journal for Numerical Methods in Fluids*, Vol. 22, pp. 449-465

Papamoschou D. and Roshko A., 1988,"The Compressible Turbulent Shear Layers," *Journal of Fluid Mechanics*, Vol 197, pp. 453-477

Sarkar S., Erlebacher G., Hussaini M.Y. and Kreiss H.O., 1991, "The Analysis and Modelling of Dilatational Terms in Compressible Turbulence," *Journal of Fluid Mechanics*, Vol. 227, pp. 473-493

Sarkar S., 1992, "The Pressure-Dilatation Correlation in Compressible Flows," *Physics of Fluids* A 4 (12), pp. 2674-2682

Sarkar S., 1995, "The Stabilizing Effect of Compressibility in Turbulent Shear Flows," *Journal of Fluid Mechanics* , Vol. 282, pp. 163-186

Smith A.J., Dussauge J.P., "Turbulent Shear Layer in Supersonic Flow," *American Institute of Physics* , Woodbury, New-York, pp. 139-159

Taulbee D. and VanOsdol J., 1991, "Modeling Turbulent Compressible Flows: the mass fluctuating velocity and squared density," *AIAA Paper 91-0524*

Vreman A.W., Sandham N.D. and Luo K.H., 1996, "Compressible Mixing Layer Growth Rate and Turbulence

Characteristics", *Journal of Fluid Mechanics* , Vol 320, pp. 265-258

Zeman O., 1990, "Dilatation Dissipation: the concept and application in modelling compressible mixing layers," *Physics of Fluids A 2 (2)*, pp. 178-188

Zeman O., 1991, "On the decay of Compressible Isotropic Turbulence," *Physics of Fluids* A 3 (5), pp. 951-955

ASSESSMENT OF AN IMPLICIT, PARALLEL, MULTIGRID DRIVEN ALGORITHM FOR LARGE EDDY SIMULATION

Eran Arad[1] and Luigi Martinelli
Department of Mechanical and Aerospace Engineering
Princeton University
Princeton, New Jersey 08544
USA
[1]Present Address: RAFAEL
P.O.Box. 2250, Haifa 31021
Israel

ABSTRACT

An implicit time marching method, using multigrid technique, is used for large eddy simulation. The program is implemented on parallel computers using message-passing. The efficiency and validity of this approach, originally developed for Reynolds Averaged Navier-Stokes equations, are evaluated. The formulation is initially based on a Smagorinsky model, but it is general enough to allow for more advanced SGS models. An effort is directed towards the solution of spatially developing flow, as a first step towards performing large eddy simulations on a realistic geometry.

INTRODUCTION

Turbulent flows possess a wide range of space and time scales. Numerical simulation of turbulence requires that all the relevant scales (or frequencies) are properly represented in the numerical model. Consequently, spectral methods are the most common approach for both direct and large eddy simulation (cf. Kim *et al.* 1987, Cabot *et al.* 1993). It has been shown that these methods are able to produce accurate results on rather coarse mesh (Kim *et al.* 1987). The use of spectral methods is, however, convenient only for flows in simple domains and simple boundary conditions. The objective of simulating complex flow fields introduced a relatively new trend, of using more flexible numerical representations, such as finite differences, finite volumes and spectral elements schemes (cf. Rai and Moin 1989, Lund and Moin 1995). Although these approaches are much more suitable for dealing with irregular geometries, they bring with them larger truncation and aliasing errors, and usually some kind of artificial dissipation. These errors have a significant effect on the accuracy and the required resolution for LES (Lund *et al.* 1995b). However, with simulation of realistic flows in mind, it is important to verify the ability and limitations of these methods. The present work is within this context of LES technology development for complex flows. A highly efficient and well validated finite volume, multigrid driven method (Tatsumi *et al.* 1995), is used for the solution of the LES time dependent equations. The scheme is applied on distributed memory parallel computers, using domains decomposition technique.

As part of the validation phase of the method, a spatially developing boundary layer on a flat plate is solved. The DNS data of Spalart (1988) is used as a benchmark. Initial results were presented by Arad and Martinelli (1996). The efficiency of this scheme on a parallel, distributed memory environment, is further evaluated.

MATHEMATICAL FORMULATION

The present formulation for large eddy simulation is obtained by applying a filter on the compressible, time dependent Navier-Stokes equations. As Favre filter is not used, the formulation is compressible in the resolved scales, but is incompressible in the subgrid-scales. Such a method is suitable only for moderate Mach numbers. For the sake of simplicity, at this preliminary stage, the Leonard and the cross terms are included in the residual stress tensor τ_{ij}. Shaanan *et al.* (1975) have showed that L_{ij} is of the same order and magnitude as the truncation error of a second order finite difference scheme. Ferziger (1993) observed that the benefit/cost ratio of separate treatment of these terms, may not be large enough to justify this practice. Pursuing the concept of simple modeling, the SGS (subgrid-scale) stress tensor is modeled using Smagorinsky model, with damping on the wall:

$$\tau_{ij} = -2\overline{\rho}\nu_t\left(\overline{S_{ij}} - \tfrac{1}{3}\overline{S_{kk}}\delta_{ij}\right) \;\; ; \;\; q_j = -\frac{\nu_t}{Pr_t}\overline{\rho}\frac{\partial \overline{E}}{\partial x_j}$$
$$\nu_t = (C_s D\Delta)^2\left(\overline{S_{ij}}\;\overline{S_{ij}}\right)^{1/2} \qquad (1)$$

where Pr_t is the so-called turbulent Prandtl number, Δ is the filter size, C_s is the model coefficient ($C_s = 0.2$ is used), S_{ij} is the strain rate tensor, $\overline{E}$ is the total energy of the filtered variables and D is a wall-induced damping function (described below).

When a uniform mesh is used, the definition of the filter size is clear-cut: The most common choice (Ferziger 1993) is:

$$\Delta = (\Delta_x \Delta_y \Delta_z)^{1/3} \qquad (2)$$

For engineering applications at high Reynolds number, especially for external aerodynamics, a non-uniform mesh

is mandatory to resolve the thin near wall (or wing) layers while at the same time to cover a large flow domain. Therefore, the filter size Δ varies with the local mesh spacing. Jones and Wille (1995) and Miet *et al.* (1995) showed, that for smoothly varying mesh, the error induced by the commutation of filtering with local filter size, is of the same order as the discretization error of the numerical scheme applied. On a strongly stretched mesh, the use of formulation(2) will cause large values of the SGS eddy viscosity far away from the wall (where Δ_y is large). Consequently, small fluctuations in the velocity field will be artificially amplified. A more robust formulation for the filter size can be obtained by replacing Δ_y by $\hat{\Delta}_y$, which is the harmonic mean of Δ_y and the average value of Δ_y in the wall vicinity (designated by $\overline{\Delta_y}$):

$$\Delta = \left(\Delta_x \hat{\Delta}_y \Delta_z\right)^{1/3}$$
$$\hat{\Delta}_y = \left[\frac{1}{\left(\frac{1}{\Delta_y}\right)^{\omega} + \left(\frac{1}{\overline{\Delta_y}}\right)^{\omega}}\right]^{1/\omega} \tag{3}$$

That way, $\hat{\Delta}_y = \Delta_y$ near the wall, and is equal to $\overline{\Delta_y}$ far away from the wall (resulting bounded values of the eddy viscosity), with smooth transition between the two values. In this study ω was taken as 3, to allow for a small transition region. The distribution of $\hat{\Delta}_y$ in a boundary layer mesh is given in figure 2.
To account for the damping influence of the wall proximity, an exponential function is used, in (1):

$$D = \left[1 - \exp\left(-\frac{y_+}{A_+}\right)\right]^{\beta} \; ; \; A_+ = 25 \tag{4}$$

The well known Van-Driest function is recovered for $\beta = 1$. Yet, it was found that higher values of β where required in order to have proper representation of the viscous sublayer.

NUMERICAL METHOD

The governing equations are discretized using a finite volume, cell-centered formulation, yielding a set of ordinary differential equations which can be written as follows:

$$\frac{d}{dt}\left(\mathbf{w}_{ijk} V_{ijk}\right) + \mathbf{R}\left(\mathbf{w}_{ijk}\right) = 0 \tag{5}$$

where $\mathbf{w}$ is a vector of the flow variables: $\mathbf{w} = \left\{\bar{\rho}, \bar{\rho}\tilde{u}, \bar{\rho}\tilde{v}, \bar{\rho}\tilde{w}, \bar{\rho}\tilde{E}\right\}^T$. V_{ijk} is the cell volume. The residual $\mathbf{R}\left(\mathbf{w}_{ijk}\right)$ is obtained by evaluating the sum of integral fluxes of the governing equations, to the second order of accuracy. In order to obtain a fully-implicit algorithm, all the terms in the above equation should be evaluated at $n+1$ level*[1]. Jameson (1991) suggested to approximate the $\frac{d}{dt}$ operator by an implicit backwards difference formula of the kth order of accuracy (in time):

$$\frac{d}{dt} = \frac{1}{\Delta t} \sum_{q=1}^{k} \frac{1}{q} \left[\Delta^-\right]^q \tag{6}$$

where $\Delta^- = \mathbf{w}^{n+1} - \mathbf{w}^n$. A low dispersion scheme is obtained by using a third order accurate approximation, recasting equation (5) into the following form:

$$\frac{11}{2\Delta t} V\mathbf{w}^{n+1} - \frac{9}{\Delta t} V\mathbf{w}^{n} + \frac{9}{2\Delta t} V\mathbf{w}^{n-1} - \\ - \frac{1}{\Delta t} V\mathbf{w}^{n-2} + \mathbf{R}\left(\mathbf{w}^{n+1}\right) = 0 \tag{7}$$

Second order time discretization of this kind are A-stable when applied to a test linear differential equation, while the third order approximation is stiffly stable (Alonso *et al.* 1995). Fourth order approximation was found to be unstable, in this application.
A modified residual, $\mathbf{R}^*(\mathbf{w})$ is defined, as follows:

$$\mathbf{R}^*\left(\mathbf{w}^{n+1}\right) = a_0 V\mathbf{w}^{n+1} + a_1 V\mathbf{w}^{n} + \\ + a_2 V\mathbf{w}^{n-1} + a_3 V\mathbf{w}^{n-2} + \mathbf{R}\left(\mathbf{w}^{n+1}\right) \tag{8}$$

where the a_k coefficients are defined in equation (7). Now, iterations to a steady-state in pseudo-time, t^*

$$\frac{d\left(V\mathbf{w}\right)}{dt^*} + \mathbf{R}^*(\mathbf{w}) = 0 \tag{9}$$

can be carried out. This is done using an explicit (in pseudo-time) multistage time stepping scheme (Jameson 1991). Since the details of the pseudo-transient evolution are immaterial, the parameters of the schemes are optimized for faster convergence. Further more, application of various convergence acceleration techniques, like multigrid, local time step and residual averaging (Martinelli and Jameson 1988) becomes possible.
Following the suggestion of Melson *et al.* (1993), the first term on the right hand of equation (8) is treated implicitly, within the multi-stage scheme.

$$U^0 = W^n$$
$$\left(1 + \alpha_k \lambda\right) U^k = U^0 - \frac{\alpha_k \Delta t^*}{V} R^*\left(U^{k-1}\right) + \\ + \alpha_k \lambda U^{k-1} \qquad k = 1, 2, ..K \tag{10}$$
$$W^{n+1} = U^K$$

where U^k is the vector of variables at stage k of the K stages scheme (5 stages were used) and α_k are the scheme coefficients. $\lambda = a_0 \Delta t^* / \Delta t$. This approach is equivalent to rescaling the pseudo-time step for every cell in the domain. Though it does not lead to a noticeable improvement in convergence, it increases considerably the robustness of the method.

BOUNDARY AND INITIAL CONDITIONS

The boundary conditions which are described in this section apply for a flat plate boundary layer case. No-slip conditions are imposed on the solid boundary, and a zero pressure gradient normal to the surface is specified. With the objective of establishing a technique for realistic flows, the more costly concept of spatially developing boundary layer (Guo *et al.* 1996) is adopted here, specifying inflow and outflow conditions. Periodic conditions are used only in the spanwise directions. Inflow and external far-field conditions (in the direction normal to the wall) are set using approximate non-reflecting boundary conditions, based on the linearized characteristic approach (Baker and Jameson 1984). The two surfaces are located at a large distance from the plate, so that an inviscid formulation is a reasonable approximation. A slip surface is set in-front of the plate. On the outflow boundary, the pressure and entropy are extrapolated downstream. A buffer region, with cells that grow gradually in size, was added at the end of the solution domain. This highly dissipative region is used since specification of non-reflecting boundary conditions for viscous flow is not simple.
The numerical solution of the laminar equations is used as initial conditions. A disturbance is applied in the first time step, in order to perturb the flow. Assuming that the flow is parallel to the wall, the most general form of 3D disturbance is of a traveling wave whose amplitude varies with y, and which moves along the wall at an angle $\theta = \tan^{-1}\beta/\alpha$ with respect to the x axis:

$$u = \bar{u} + u' \; ; \; u' = \hat{u}(y) e^{i(\alpha x + \beta z - \omega t)} \tag{11}$$

Using the linear stability theory, Sandham and Reynolds (1991) established that the free-flow Mach number has a

[1]* where n is the time counter, e.g. $t = t_0 + n\Delta t$

significant effect on which wave is the most unstable. For $M < 0.6$ it appears that the 2D wave ($\theta = 0$) is the most unstable, while for higher Mach number an oblique wave is the most unstable. Based on that concept, the following flow field was used as initial conditions:

$$u_i(x,y,z) = (U_i)_L + \hat{u}_i(y)e^{i(\alpha x - \omega t)}$$
$$\hat{u}_i(y) = A_i r e^{-\gamma y^2} \qquad (12)$$

where A_i is the amplitude, $(U_i)_L$ is the laminar solution and r is a random number uniformly distributed between -0.5 and 0.5, different for each spatial location and for each computational variable. The exponential term guarantees that the disturbances decay in the free stream.
As discussed by Arad and Martinelli (1996), the rate of growth of the oscillations appears to be very slow. This is the case, since unlike periodic domains (in the mean-flow direction), where there is a constant feeding of disturbances from the outflow to the inflow boundary, only initial perturbation of the flow was applied. In order to accelerate the appearance of turbulent flow, two additional mechanisms are now employed: Low amplitude disturbances, similar to formulation 12, are introduced both in the inflow boundary and on a "transition" strip, located a short distance behind the plate leading edge. Though these perturbations affect the transitional characteristics of the flow, they are not supposed to influence the fully turbulent regions.

PARALLEL IMPLEMENTATION

The computer code is parallelized for a distributed memory platform using a domain decomposition approach, a SPMD (Single Program Multiple Data) strategy and the MPI (Message Passing Interface Standard) library for message passing (MPI 1995). The computational domain is decomposed into sub-domains, each attached to a processor node responsible for all arithmetic in it. Only border data need to be transmitted between sub-domains. Thus, the communication cost is low, as the ratio of communication to arithmetics is proportional to the surface to volume ratio. In order to obtain a good load balance, uniform decomposition among the processors is employed. While an ideal sub-domain would have equal number of points in each direction, the partition size is also affected by availability of computational resources. Another constraint is imposed by the multigrid algorithm: At least 16^3 mesh points per domain are required, if four level multigrid and the related speedup are to be preserved.
The convergence acceleration techniques, in particular the multigrid and the residual smoothing, are global in nature, since they both increase the rate of information transfer throughout the computational domain. This feature implies a larger communication volume, which might hinder parallel performance. In order to address this problem, the two techniques were applied locally in each sub-domain, and not globally. That way the inter-domain data transfer is not increased. As a result, the parallel performance is not reduced. This approach is suitable for the coarse-grain decomposition that is used in this study. Applied for a massivly parallel paradigm, it would eliminate the effect of the acceleration techniques. These subjects are further discussed in the next section.

APPLICATIONS

Test Case Description

A flat plate boundary layer is solved to validate the the present method, by comparison with results of Direct Numerical Simulation (Spalart 1988). The DNS results are for momentum thickness Reynolds number at the range of 300 to 1410. This case was selected because such a detailed data base allows much more extensive comparisons than experimental results. Though the present formulation is compressible, Tatsumi *et al.* (1995) have shown that the stability and accuracy of the algorithm is preserved down to low Mach numbers, well within the incompressible regime. Hence, the computations were done for Mach number of 0.15.
A long flat plat (about 200 δ_*, where δ_* is the displacement thickness) is solved. The inflow boundary is located about 300 δ_* in front of the plate leading edge. In the lateral direction, the solution domain is about 65 δ_*. The far field boundary is set at the distance of 500 δ_* away from the plate. A $192 \times 128 \times 48$ mesh is used, with nearly uniform distribution of the mesh in x (stream-wise direction) and z (spanwise) direction. $\Delta x_+ \approx \Delta z_+ = 35$. In the vertical direction (y), the following transformation is used:

$$y = \frac{c(x)\eta}{1 + c(x) - \eta} \qquad \eta = \frac{j-1}{NY-1}, ...j = 1, NY \qquad (13)$$

where NY is the number of points in the y direction. $c(x)$ changes with x as an hyperbolic tangent, allowing slow expansion of the mesh. The mesh stretching in the vertical direction allows for $\Delta y_+ \leq O(1)$.
In figure 1 the domains boundaries, of a 32 domains configuration are plotted (in a 2D cut). For clarity, the correct aspect ratio between the axes is not preserved in the figure.

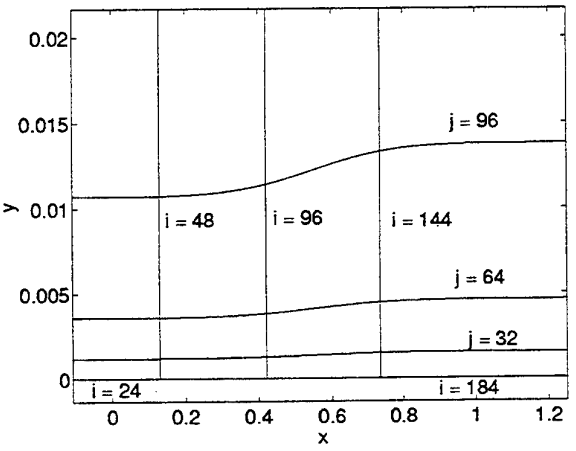


Figure 1: Domain boundaries near the plate, in a 192x128x48 mesh. Plate at $i \in (24, 184)$; 32 domains.

The smooth and gradual growth of y can be seen in figure 2, where Δy is plotted ($\hat{\Delta}$y is defined in equation 3).

Verification of Efficiency

The efficiency of the scheme relies mainly on two components: Implicit time stepping algorithm and parallel computation. As described above , the two techniques are not separated, and require special implementation in order to gain the desirable efficiency.

Implicit Time Stepping for LES .

The first subject that we consider here is the time-accuracy of the scheme. Jameson (1991) used a second order time dependent algorithm, while other authors (Alonso *et al.* 1995) found it necessary to use a third order scheme, like the one given in(7). Using the present computer code for the solution of Stokes flow (oscillating plate), the analytical solution was recovered using both order of accuracy. Different result are obtained for the turbulent flow simulation. The time histories of the friction coefficient on the wall are plotted in figure 3. The second order scheme appears to introduce excessive damping on the oscillating flow field.

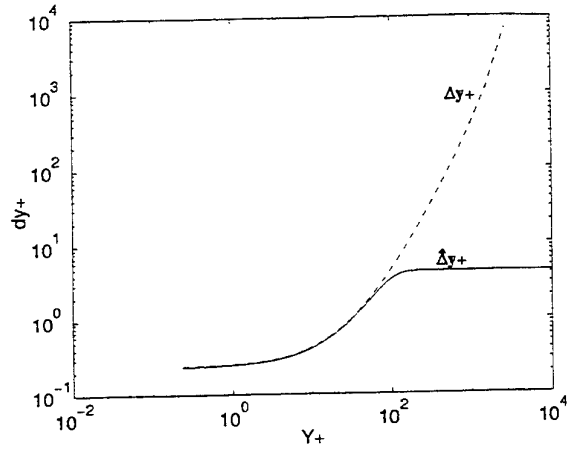


Figure 2: Distribution of filter size ($\hat{\Delta}_y$) in the direction normal to the wall, in a 192x128x48 boundary layer mesh.

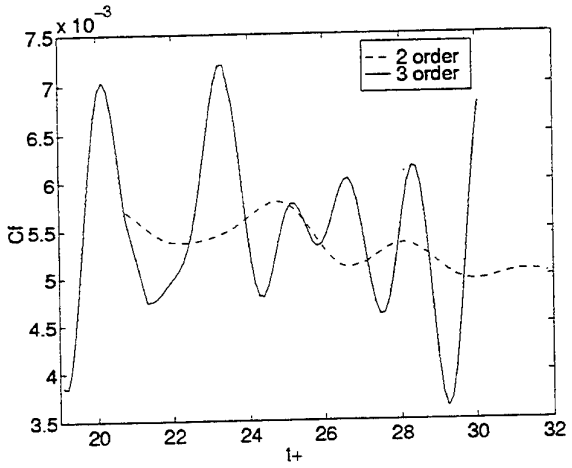


Figure 3: Effect of the accuracy of the time dependent algorithm. Friction coefficient at at $Re_x = 9.8 \times 10^4$.

Implicit schemes alleviate the restrictions on time step size, related to numerical stability. However, for large eddy simulation, their usefulness might be limited by two major factors: First, the computational time step cannot exceed the characteristic time scales of the physical phenomenon, while the smallest time scales of turbulent flow are very small. Then, the work required in each time step may become excessively large, compared with the much simpler explicit methods. Thus, the implicit approach may pay off for problems where there is very large variation in the mesh size. The use of explicit scheme would result in a very severe restriction on the time step, based on the smallest cells of mesh. This is very much the case in the present problem and in most of the problems involving external flow. The size of the computational cells changes by four orders of magnitude across the solution domain (see figure 2).
Choi and Moin (1994) pointed out, that while the viscous time scale in the sub-layer is $O(1)$ (in wall unit), much smaller computational time step is required for explicit or semi-implicit scheme. Thus, Kim *et al.* (1987) used $\Delta t_+ = 0.0676$ for channel simulation using a semi-implicit algorithm. Arad and Martinelli (1996) found out that using a time step that is larger than 0.2 affects the frequency and amplitude of the oscillations. The effect of the computational time step on the accuracy is illustrated in figure 4. This is actually consistent with the results of Choi and

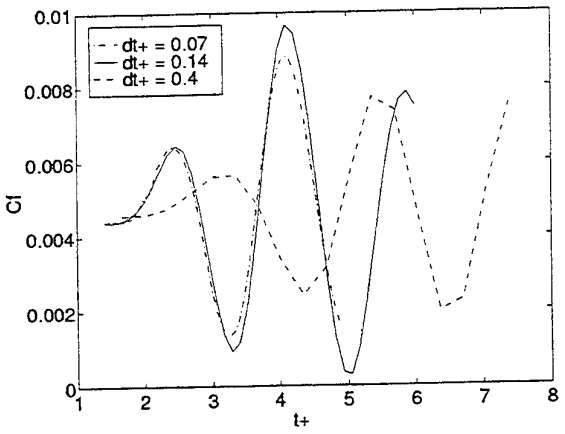


Figure 4: Effect of computational time step. Data taken at $Re_x = 9.8 \times 10^4$.

Moin (1994): They presented a similar effect of the time step on the time histories of wall-shear rate (for a different flow field and scheme). The last authors, though, selected to use a large time step ($\Delta t_+ = 0.4$), as they showed that the averaged turbulent intensities are much less sensitive to the integration step. As this is an initial assessment of the present scheme for LES, we took a very conservative approach, and used $\Delta t_+ = 0.165$.
The implicit formulation is obtained using internal iterations for each time steps (described above). The attenuation of the residual at one time step is plotted in figure 5, for a 1.2 million points mesh which is described in the test case definition. Four levels of multigrid were used, together with residual smoothing and local time step. As a result, the norms of the residues are attenuated by more then three orders of magnitude within 20 cycles. Application

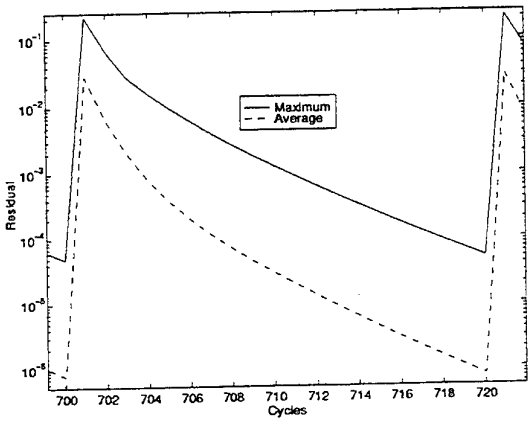


Figure 5: Reduction of the residual within one time steps.

of the scheme with these parameters accomplishes a four time speedup compared with explicit algorithm. Yet, each multigrid cycle requires more operations than an explicit solution. Hence, the true speedup should be obtained from *CPU* time comparison. It appears that a single multigrid cycle requires 1.5 the time of an explicit step. Hence, using a very conservative estimate for the permissible time step,

the present implicit scheme, applied in large eddy simulation, produces a 2.5-3 speedup. This improvement is not as significant as the one that is obtained for low Reynolds number flow (Alonso 1995), and is not enough to allow for solving more complicated realistic geometries. Further refinement of the scheme. including the use of preconditioners, may improve the balance.

Parallel Speedup .

The major parameter that affects the parallel efficiency (other than hardware characteristics) is the ratio between the inter-node information transfer and floating-point computation per-processor (This ratio is often called task granularity). The task granularity is directly related to the numerical techniques that are used, as discussed above. It is also affected by two more basic characteristics of the task itself: The number of floating-point operations per grid point and the size of the grid in each domain (processor). The number of operations per grid point in large eddy simulation is larger than that of laminar Navier-Stokes solution (due to the sub-grid scale computation). Both of them require much more operations per point than the inviscid equations solution. Furthermore, LES requires a fine resolution, that is at least an order of magnitude higher than sufficient resolution for the solution of the Euler equations. Accordingly, the parallel speedup for large eddy simulation can be higher than laminar Navier-Stokes solutions and simulation of inviscid flow. The fine resolution contributes to increase the optimal number of processors in the computation. In a way, these characteristics compensate for the tendency of the convergence acceleration techniques (mainly multigrid and residual smoothing) to increase the granularity of the task. That tendency is more dominant in inviscid simulation.

The speedup that was obtain by parallel computation is presented in figure 6. The laminar computation was performed on a $96 \times 32 \times 48$ mesh (150000 points). The LES data is taken using the 1.2 million point mesh which is described above. The computations were done on an IBM SP2 machine. The speedup efficiency, defined here as the ratio between the actual and the ideal speedup, is also written on the figure. It can be seen that while only 77% speedup is obtained using 16 processors with the coarse mesh, the fine mesh calculations are at 91% speedup, and 32 nodes calculation on the fine mesh is performed with 85% speedup.

The cache size of the processors also plays a role in the code efficiency. Extending beyond the cache size, slows down the computation. This effect was felt when the fine mesh was divided into less the four sub-domains. In order to correct for this effect, the base calculation time for the ideal speedup was defined as four time larger than that of four nodes net.

Results

Accurate evaluation of averaged quantities and higher moments, require time integration over a very large period. Due to the size of the problem, which is dictated by Reynolds number and the fact that this is a spatially developing flow field, the fulfillment of this requirement is only partial. Nevertheless, the results which are given below already approach the DNS data, and have a certain indicative value in assessing the quality of this approach.

The contours of the main velocity component, on an horizontal plane at $y_+ = 20$ is plotted in figure 7. The lines that cross the flow domain are sub-domain boundaries, in a six domain configuration. Re_x reaches the value of 2.5×10^5 at the end of the plate.

The mean velocity is compared with the DNS data, at $Re_x = 2. \times 10^5$ in figure 8. The averaging was done for $t_+ \in (215, 640)$. Although this is definitely too short integration period, it can be seen that the logarithmic region is well developed. The solution is in very good agreement with the DNS (Spalart 1988) data.

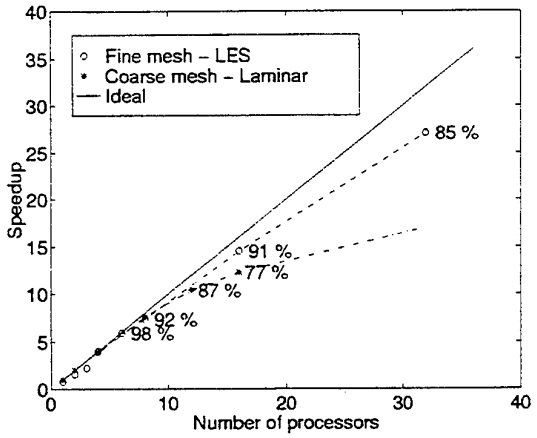


Figure 6: Computation speedup versus number of nodes in MPI network.

The intensity of the oscillations in the main flow direction is presented in figure 9. Reasonable agreement with the oscillations of the DNS calculation was achieved. The subgrid eddy viscosity is plotted in figure 10. The present results are compared to the eddy viscosity which is calculated according to its definition, out of the DNS data. The good agreement that is is displayed, was obtained only when the wall-proximity damping power, β (see equation 4) was greater then one.

CONCLUDING REMARKS

This paper describes initial assessment of a parallel, multigrid driven, finite volume scheme for large eddy simulation. The study is conducted to identify the advantages and limitations, of this scheme for LES.

The application of the multigrid parallel computation was found to be very efficient, while using coarse grain domain-decomposition. On the other hand, the implicit time stepping scheme, which was very effective in other cases, appears to produce only moderate speedup, compared with semi-implicit or explicit schemes. However, the evaluation of the permissible time step applied here is very conservative. Further refinement of the scheme and gaining some more experience in the performance of this method for LES, may improve the efficiency.

Though the quality of validation is limited, due to too short time integration, the averaged values that were calculated from these results appear to develop in agreement with DNS data.

REFERENCES

Alonso J. J., Martinelli L. and Jameson A., "Multigrid Unsteady Navier-Stokes Calculations with Aeroelastic Applications", AIAA 95-0048, 1995.

Arad E. and Martinelli L., "Large Eddy Simulation of Compressible Flow Using a Parallel, Multigrid Driven Algorithm", AIAA-96-2065, 27th AIAA Fluid Dynamics Conference. New Orleans, 1996.

Baker T.J. and Jameson A. , "Multigrid Solution of The Euler Equations for Aircraft Configuration", AIAA-84-0093, 1984.

Cabot W. and Moin P., "Large Eddy Simulation of Scalar Transport with The Dynamic Subgrid Model", in Galperin B. and Orszag S. A. (Eds.), "Large Eddy Simulation of Complex Engineering and Geophysical Flows", Cambridge Univ. Press, 1993.

Choi H. and Moin P., "Effects of The Computational Time Step on The Numerical Solutions of Turbulent Flow", J. of Computational Physics, Vol. 113, 1-4, 1994.

Ferziger J. H., "Subgrid Scale Modeling", in Galperin B. and Orszag S. A. (Eds.), "Large Eddy Simulation of Complex Engineering and Geophysical Flows", Cambridge Univ. Press, 1993.

Guo Y., Kleiser L. and Adams N A., "Comparison of Temporal and Spatial Numerical Simulation of Compressible Boundary Layer Transition", AIAA J., Vol. 34, No. 4, p. 683, April 1996.

Jameson A., "Time Dependent Calculations Using Multigrid, With Applications to Unsteady Flows Past Airfoils and Wings", AIAA 91-1596, 1991.

Jones W. P. and Wille M., "Large Eddy Simulation of A Jet in A Cross Flow", 10th Symp. of Turbulent Shear Flow, 1995.

Kim J. Moin P. and Moser R., "Turbulence Statistics in Fully Developed Channel Flow at Low Reynolds Number", J. Fluid Mech., Vol. 177, pp 133-166, 1987.

Lund T. S. and Moin P., "Large Eddy Simulation of A Boundary Layer on A Concave Surface", 10th Symp. of Turbulent Shear Flow, 1995.

Lund T., Kaltenbach H. J. and Akselvoll K., "The Behavior of Centered Finite Difference Schemes for Large Eddy Simulation", in 6 Int. Symp. on Comp. Fluid Dyn., Lake Tahoe, 1995b.

Martinelli L. and Jameson A., "Validation of A Multigrid Method for The Reynolds Averaged Equations", AIAA 88-0414, 1988.

Melson N. D., Santric M. D., Atkins H. L., "Time accurate Navier-Stokes Calculation with Multigrid Acceleration", 6th Copper Mt. Conf. on MG, 1993.

Miet P., Laurence D. and Nitrosso B., "Large Eddy Simulation with Unstructured Grids and Finite Elements", 10th Symp. of Turbulent Shear Flow, 1995.

"MPI: A Message Passing Interface Standard", University of Tennessee, 1995.

Rai M. M. and Moin P., AIAA 89-0369, Reno 1989.

Shaanan S., Ferziger J. H. and Reynolds W. C., " Numerical Simulation of Sheared Turbulent Flow", Thermosciences Division, Dept. of Mech. Engg., Stanford Univ., Rept. No. TF-6, 1975.

Sandham N. D. and Reynolds W. C. "Three Dimensional Simulation of Large Eddies in The Compressible Mixing Layer", J. of Fluid Mech., Vol. 224, pt. 133, 1991.

Spalart P., "Direct Numerical Simulation of Turbulent Boundary Layer up to $Re_\theta = 1410$", J. Fluid Mech., Vol. 187, pp 61-98,1988.

Tatsumi S., Martinelli L. and Jameson A., "A New High Resolution Scheme for Compressible Flows with Shocks", AIAA 95-0466, Reno 1995.

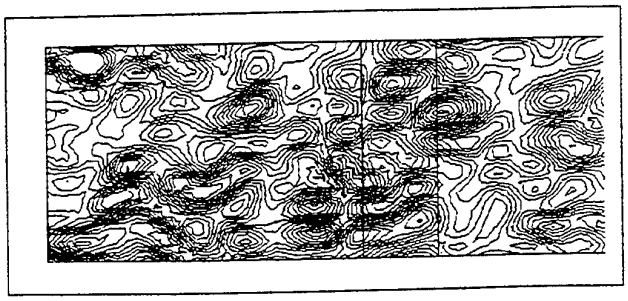


Figure 7: Contours of the instantaneous u velocity component, on an horizontal plane, at $y_+ = 20$

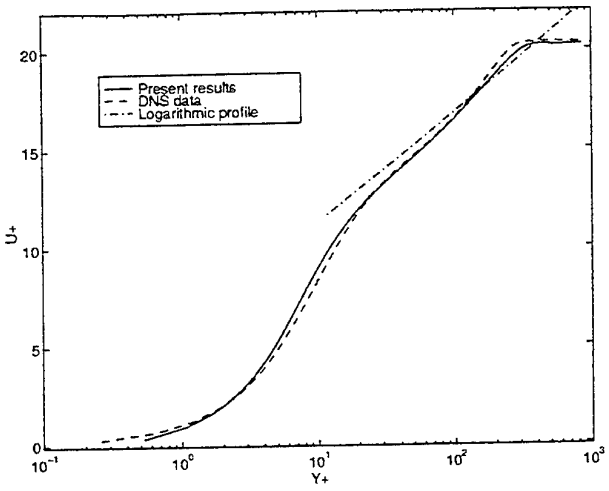


Figure 8: Mean velocity at $Re_x = 2. \times 10^5$.

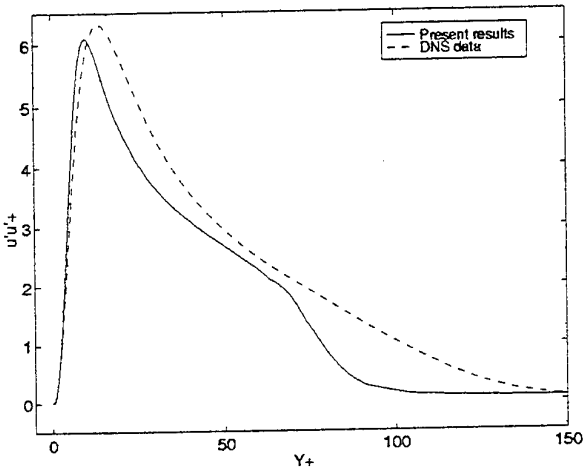


Figure 9: Reynolds stress $\overline{u'u'}_+$ at $Re_x = 2. \times 10^5$.

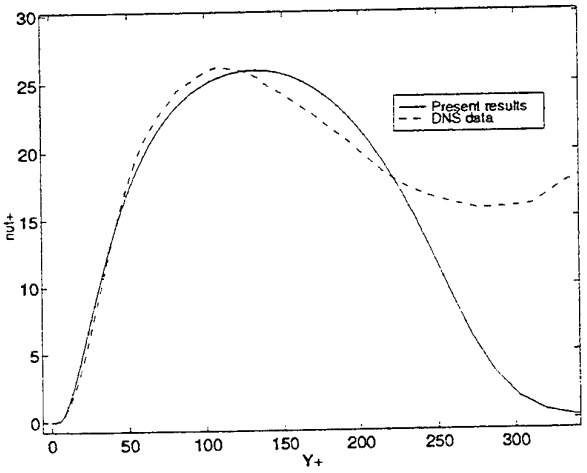


Figure 10: Subgrid-Scale Eddy Viscosity at $Re_x = 2. \times 10^5$.

NUMERICAL METHODS FOR DIRECT NUMERICAL SIMULATION OF FLOW PAST A SQUARE CYLINDER

R.W.C.P. Verstappen and A.E.P. Veldman
Department of Mathematics, University of Groningen
P.O.Box 800, 9700 AV Groningen, The Netherlands

ABSTRACT

This contribution deals with algorithm development for direct numerical simulation (DNS) of incompressible turbulent flow. Significant improvements of numerical algorithms (keywords: high-order discretization and efficient time-integration), together with the improvements in computer performance, have opened the possibility of performing DNS at Reynolds numbers in the range $10^4 - 10^5$. As an example, we consider a DNS of a turbulent flow past a long, square cylinder at $Re = 22,000$. The computed bulk quantities (among others the mean Strouhal number and the drag coefficient) of the flow past the cylinder as well as mean velocity profiles at various locations in this flow agree well with the available experimental data.

INTRODUCTION

Direct Numerical Simulation (DNS) is the most accurate, but also the most expensive, way of computing turbulent flow. All dynamically significant scales of motion are to be resolved from the unsteady, incompressible Navier-Stokes equations. In view of the computational complexity of DNS, our first concern is to push the algorithmic efficiency as far as we can get. In this way we are preparing ourselves for the arrival of the coming generations of powerful computers on which DNS at higher Reynolds numbers will become feasible.

In this paper, we will focus on a turbulent flow which lies just within the present reach of DNS: a three-dimensional, unsteady flow past a long, square cylinder at $Re = 22,000$ (at zero angle of attack). This flow has served as a test case for two workshops. A summary of the (RANS and LES) results presented at these workshops can be found in Rodi *et. al* (1997) and Voke (1997). Experimental data is also available for comparison (see Lyn *et al.* (1994, 1995), McLean *et al.* (1992) and Lee (1975)). The experimentalists reported both bulk quantities (among others the mean Strouhal number and drag coefficient) and a number of profiles at various locations in the flow. Lyn *et al.* (1995) measured a turbulence level of 2% at four and a half diameters upstream from the cylinder. Since that is all that is known about the inflow condition, we will locate the inflow far upstream and assume that the flow is laminar there. Transition will take place in the shear layers near the sides of the square cylinder, and is not triggered explicitly. Results of the simulation can be found in the second part of this paper.

The first part describes the numerical methods employed to simulate the flow past the cylinder. We discuss both the time advancement scheme and the spatial discretization technique.

To start, we consider a family of explicit second-order one-leg time-integration methods, and look for the member of this family with the best linear stability properties. We compare the numerical efficiency of this member with that of the frequently applied second-order method of Adams and Bashforth. This comparison demonstrates that Adams-Bashforth is not best choice for convection dominated flows. For such flows, there are one-leg methods with better stability properties: tuned one-leg methods allow for a step size that is roughly twice as large as the largest step for which Adams-Bashforth is stable. The amount of computational work per time step of these one-leg methods is approximately equal to that of Adams-Bashforth. Thus, a cost reduction by a factor of about two can be achieved with regard to Adams-Bashforth, whereas the accuracy is just as good. It may be noted that the computational effort of such tuned one-leg methods is of about the same level as that of a three-stage Runge-Kutta method where the Poisson equation for the pressure is solved only (!) at the final stage (like in Le and Moin (1991)), an approach which may lead to instabilities.

Next, we discuss a fourth-order finite volume method. Any grid that is used for DNS need to be so fine that the smallest length scales in the flow can be resolved accurately. The number of grid points that is needed per smallest length scale depends upon the discretization method that is applied. This number determines the efficiency of the simulation method to a high degree. A reduction by a factor of two, for example, yields a saving of about one order of magnitude in the use of computing time as well as memory (in three spatial dimensions). For this reason higher-order accurate DNS methods have been developed.

There are several ways of making higher-order methods. We construct a fourth-order method as the Richardson ex-

trapolate of a classical second-order finite volume method. The results of this fourth-order finite volume method and the underlying second-order method are compared for a direct numerical simulation of turbulent flow in a cubical lid-driven cavity at $Re = 10,000$ and also with experimental data. The fourth-order results are clearly superior to the second-order results, even if the number of grid points per spatial dimension is half that of the second-order simulation. Hence, the fourth-order finite volume method yields a saving of about one order of magnitude in both computing time and memory.

TIME ADVANCEMENT

The time step of explicit time integration methods for DNS is not limited by accuracy requirements, but by those of convective stability (see Verstappen and Veldman (1993)). Thus, there is room for improvement. This holds in particular for the second-order accurate method of Adams and Bashforth, which is often applied to integrate (the convective terms of) the Navier-Stokes equations in time.

We consider a family of second-order, explicit, one-leg time-integration methods and look for the method with the best linear stability properties. Here it may be remarked that, as a further improvement, a multi-time stepping strategy can be added to the most stable one-leg method. In a multi-time stepping approach, each cluster of grid points uses its own local time step, whereas the simulation as a whole remains time accurate. More details on multi-time stepping can be found in Van der Ven *et al.* (1995, 1996), *e.g.*

The 'one' in one-leg refers to the fact that these methods evaluate the right-hand side of the differential equation

$$u' = f(u) \tag{1}$$

at one point only. Here, the prime denotes a differentiation with respect to the time t.

In this section, we focus on the model problem (1), where the right-hand side f contains both the diffusive and convective terms of the Navier-Stokes equations; u denotes the velocity. The pressure and the incompressibility constraint are not considered here, since they are treated implicitly in time and consequently do not yield a stability restriction.

We construct a family - parameterized by α - of second-order one-leg methods for solving Equation (1) numerically. Our aim is to determine α such that the corresponding method allows for the largest possible time step for convection dominated flows. That is, possesses the largest region of convective stability.

We denote the velocity at time $t = n\delta t$ by u^n. At time $t = (n + \alpha - \frac{1}{2})\delta t$, we apply the midpoint rule to integrate the differential equation (1) over one time step δt:

$$u^{n+\alpha+1/2} - u^{n+\alpha-1/2} = \delta t f(u^{n+\alpha}). \tag{2}$$

The time-discrete velocity is defined at integer levels only. We assume that the velocity has been computed up to and including an integer level n. Then, the velocity u^{n+1} at the next integer time level can be solved from Equation (2) if the velocities at non-integer time levels are approximated in terms of velocities at integer levels. We approximate the off-step velocity $u^{n+\alpha}$ by a linear extrapolation of u^n and u^{n-1}:

$$u^{n+\alpha} = (1 + \alpha)u^n - \alpha u^{n-1}.$$

The off-step velocity $u^{n+\alpha\pm1/2}$ is approximated by a linear interpolation between $u^{n\pm1}$ and u^n. Substituting these off-step approximations in Equation (2) gives the following family of one-leg schemes

$$(\alpha + \tfrac{1}{2})u^{n+1} - 2\alpha u^n + (\alpha - \tfrac{1}{2})u^{n-1} = \delta t f(u^{n+\alpha}) \tag{3}$$

This family is second-order accurate for all $\alpha \neq -1/3$, and is third-order accurate for $\alpha = -1/3$. Its error constant is given by $C_3 = (1 + 3\alpha)/6$.

Taking $\alpha = 1/2$, we have a one-leg method which is the twin of Adams-Bashforth. According to Adams-Bashforth we ought to take $\frac{3}{2}f(u^n) - \frac{1}{2}f(u^{n-1})$ instead of $f(u^{n+1/2})$. One- and two-leg methods are identical if f is linear, and thus have the same region of linear stability. They differ when the right-hand side f is nonlinear. For instance, for $f(u) = \lambda(t)u$ with $\lambda(t) < 0$ and $u^n > 0$ the solution u^{n+1} of Equation (3) is smaller than u^n (for any time step) as it should be, while the solution obtained with the associated multi-step method does not satisfy the inequality $u^{n+1} < u^n$ unconditionally. In addition, it is emphasized by Nevanlinna and Liniger (1978) that (some) one-leg methods are more reliable than their corresponding multi-step methods when used with variable time steps.

For $\alpha = 0$ the leapfrog method is obtained. This method cannot be used to integrate a diffusive flux in time, since it is not stable: the linear stability region of leapfrog consists of all purely imaginary numbers with modulus smaller than or equal to one.

We search for the one-leg method with the best convective stability properties. Figure 1 shows the linear stability domain of the one-leg method for $\alpha = 0.05$ and $\alpha = 0.5$ (Adams-Bashforth). The stability domain is pressed against the imaginary axis when α goes to zero. In the limit $\alpha = 0$, the stability domain becomes equal to that of the leapfrog method.

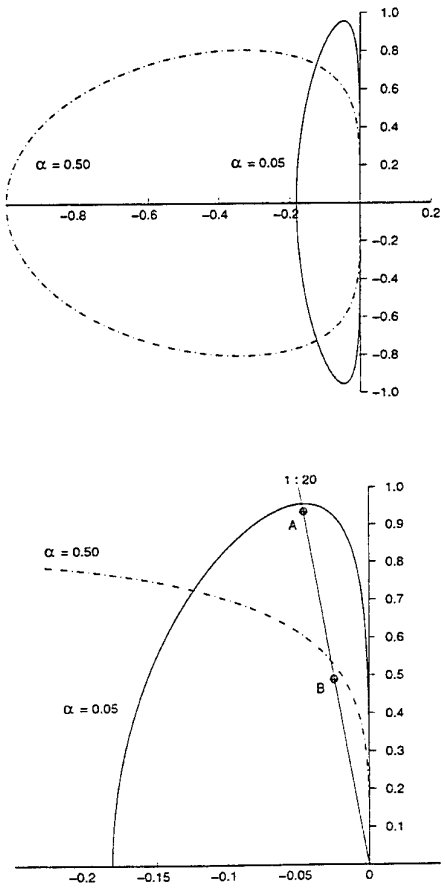


Figure 1: The upper picture shows the stability domain of the one-leg method (3) for $\alpha = 0.05$ and $\alpha = 0.5$. The lower picture shows a blow up of the stability domains near the positive imaginary axis.

Since convective stability puts the most severe restriction on the time step, we look for stability domains which include eigenvalues $\lambda = x + iy$, where the real part x is negative and the absolute value of the imaginary part y is much larger than the absolute value of the real part. Here, 'much' can range from one to two orders of magnitude. For a DNS of a flow past a square cylinder at $Re = 22,000$ with a smallest grid size of $\delta x = 5\ 10^{-3}$ and a maximum velocity $U_{\max} = 1$, for example, $|x| : |y|$ is of the order of $Re\delta x^2 : \delta x/U_{\max} \approx 1 : 100$.

Under these conditions, the one-leg method with $\alpha = 0.05$ outperforms Adams-Bashforth. The lower picture in Figure 1 shows a blow up of the stability domains of both methods near the positive imaginary axis. The points denoted by A and B lie on the line $|x| : |y| = 1 : 20$. The point A lies close to the boundary of the stability domain for $\alpha = 0.05$; B lies near to the boundary of the stability domain for $\alpha = 0.5$. A lies approximately two times as far from the origin as B. Thus, the time step of the one-leg method with $\alpha = 0.05$ can be enlarged by a factor of two compared to Adams-Bashforth. For $|x| : |y| = 1 : 10$ this factor is about 1.5; for $|x| : |y| = 1 : 100$ it is approximately 2.5. We have carried out a number of numerical test calculations. The results demonstrate that the one-leg method with $\alpha = 0.05$ requires indeed about two times less computational effort than the second-order method of Adams and Bashforth, whereas its accuracy is just as good.

To implement the one-leg scheme (3) using minimal storage, we write Equation (3) in terms of $\delta u^{n+1/2} = u^{n+1} - u^n$ and u^n. In this form, we need to store just two quantities, namely $a = \delta u^{n-1/2}$ and $b = u^n$. Indeed, the computation of one step can be implemented as follows: $(\alpha + \frac{1}{2})a := (\alpha - \frac{1}{2})a + \delta t f\,(b + \alpha a)$ and $b := a + b$.

SPATIAL DISCRETIZATION

The flow domain is covered by an orthogonal, weakly stretched, grid. The velocity and pressure are defined on the grid as proposed by Harlow and Welsh (1965). The time-discrete momentum equations are applied to control volumes. All spatial integrations (over the control volumes as well as over their surfaces) are approximated by means of the midpoint rule, with linear interpolations for the convective flux and central differences for the diffusive flux.

The leading term of the truncation error of the approximation consists of second-order terms. The terms next in size are of order four. Hence, elimination of the leading term results in a fourth-order method.

To eliminate the leading term of the truncation error of the second-order method, the momentum equations are also integrated over control volumes that are three times larger. Figure 2 illustrates the definition of such a larger control volume for the horizontal component of the momentum equation. The definition of a control volume for the vertical component is obtained by a rotation of Figure 2 one quarter of a turn.

The large control volume that is depicted in Figure 2 is chosen in such a way that its corners coincide with positions of the vertical velocity. Three times larger volumes are the smallest ones possible with corners at these positions. The coinciding of corners with vertical velocities implies that one discretization method can be used for the spatial integration of the momentum equations over both the original control volumes and the larger volumes. Two times larger control volumes, for instance, have corners that do not coincide with positions of the vertical velocity, and thus, do require additional high-order interpolations (*e.g.* for the cross terms in the convective flux).

The discrete conservation law for the original control volume is expressed in terms of nearby velocities: for the horizontal component in terms of five nearby horizontal velocities and four nearby vertical velocities; see Figure 2. The

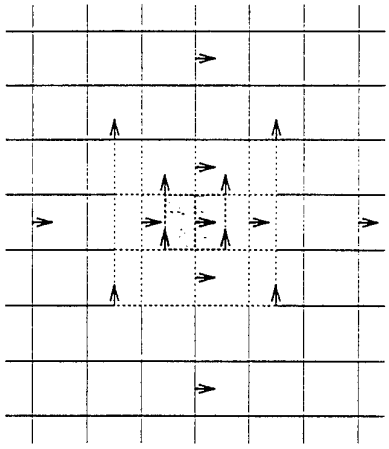


Figure 2: An original (*i.e.*, the darkest) and a three-times larger control volume for the horizontal component of the momentum equation.

same interpolation, differentiation and integration rules are applied to the three times larger control volume. Hence, the truncation error in the integration of the momentum equations over the three times larger control volume is of the same form as the truncation error in the integration over the original control volume.

On a uniform grid, the leading term of the truncation error in the approximation of the conservation law to a three times larger volume is precisely nine times as large as the leading term of the approximation to a corresponding original volume. Thus, subtracting 1/8 times the result of the integration of the conservation law over the large control volume from 9/8 times the result of the second-order integration we may eliminate the second-order terms of the truncation error and obtain a fourth-order accurate finite-volume method for the Navier-Stokes equations.

For a conservative discretization the flux through a surface has to be computed independent of the control volume in which it is considered. Two adjacent control volumes see one flux through their common surface; one sees it as an ingoing flux, the other sees it as an outgoing flux. This fundamental property is lost if the weights in the Richardson extrapolation depend on control volumes. Therefore, we use the weights 9/8 and -1/8 also for weakly stretched grids. Finally, it may be noted that, for constant weights, the matrix that represents the discretization of a second-order derivative is symmetric; the discretization of a first-order derivative is anti-symmetric. The favorable influence of this property of the coefficient matrix on the global discretization error has been stressed already by Veldman and Rinzema (1992).

In the vicinity of boundaries, some three times larger control volumes do not fit into the flow domain. A misfit is treated separately: here, the leading term in the truncation error of the numerical integration of fluxes through some parts of the boundary of a control volume is not eliminated, *i.e.* the second-order finite-volume discretization is used for misfitting parts.

We update the velocity by integrating the momentum equations over one time step whereafter the result is corrected by adding a conservative vector field (the gradient of the pressure correction) in such a way that the mass is conserved in control volumes centred on the pressures. Obviously, we can also apply the balance of mass to three times larger control volumes and use these control volumes to eliminate the leading term in the truncation error. Thus, a fourth-order-accurate spatial discretization of the conti-

nuity equation can be derived.

We have compared the outcomes of the fourth-order finite-volume method and the underlying second-order finite-volume method for a direct numerical simulation of the flow in a cubical lid-driven cavity at $Re = 10,000$. Experimental results are available for comparison (see Prasad and Koseff (1989)). The experimental data consists of mean velocities and turbulence intensities along two centerlines in the plane of symmetry. The velocity measurements have been performed with an optical laser-Doppler anemometer system. The Reynolds number is based on the speed at which the upper-lid of the cavity is driven and the height of the cavity. The overall error in an instantaneously measured velocity is about 0.6%.

The Richardson extrapolation improves the results significantly. For example, on a stretched 50^3 grid (the grid spacing is geometrically stretched away from the wall; the largest mesh width is approximately seven times wider than the smallest), the agreement between the mean velocities and turbulence intensities obtained with the fourth-order method and the experiments is better than the agreement between the results of the second-order method on a 100^3 grid and the experiments. To illustrate this, mean velocities as obtained from the second-order DNS, the fourth-order DNS and from the experiment are compared in Figure 3.

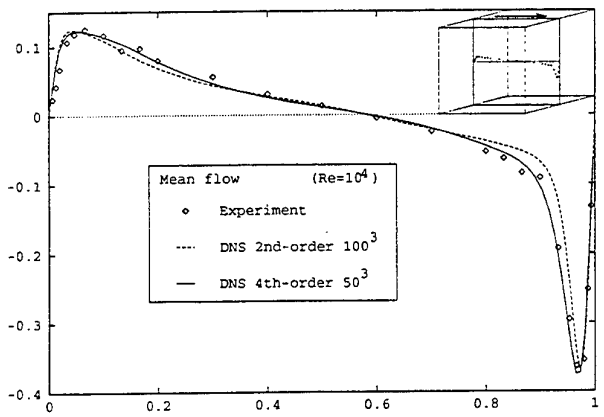


Figure 3: Second- and fourth-order DNS *vs.* experiment in a 3D driven cavity at Re =10,000. Shown is the vertical mean velocity on the horizontal centerline in the symmetry plane of the cavity.

In this example, the fourth-order results are clearly superior to the second-order results, whereas the computational effort is about twenty times less. Indeed, the CPU-time per grid point and time step of both methods is comparable, a 50^3 grid has 8 times less grid points than a 100^3 grid, it allows for a twice as large a time step (note that the time step is restricted by the CFL-condition), and the number of iterations needed to solve the pressure correction from the Poisson equation is somewhat less for a 50^3 grid than for a 100^3 grid: $8 \times 2 \times 1.25 = 20$.

Also for the flow past a square cylinder at $Re = 22,000$, the fourth-order method performs better than the second-order method. On a $280 \times 210 \times 64$ grid all our second-order simulations crashed (due to insufficient spatial resolution), while the fourth-order simulation method performed well. Results can be found in the next section.

Near the surface of the cylinder the mesh spacing should be small, in all spatial directions, to resolve the near-wall physics. Away from the surface, the grid is stretched in the direction normal to the surface to save grid points. This one-directional stretching, however, does not save one grid point in the directions perpendicular to that of the stretching. As a result, a large number of grid points is placed far away from the cylinder, that is there where they are not needed. In addition, we have to limit the stretching, since otherwise the control volumes become too flat far away from the cylinder. To avoid all this, and thus to reduce the required computing time and memory, we can combine the fourth-order finite-volume method with a zonal embedded grid technique. For that purpose, we have developed an accurate, conservative discretization method at zonal boundaries of staggered grids. The grid size at the coarse side of a zonal boundary is always three times the grid size at the fine side. Thus, a control volume at a coarse side meets three smaller cells at a zonal interface. For a large control volume, the flux through the interface can be computed, as if there is no interface at all. The middle of the three smaller cells gets precisely one third of this flux. The remaining two-third is divided among the remaining two smaller cells, where the amount that each one gets depends on the magnitude of the fluxes through neighboring large cells. The leading term of the truncation error is eliminated using a Richardson extrapolation (both for interfacial cells and internal cells). Presently, this approach is tested for a flow past a square cylinder and is compared to a single-zone approach.

FLOW PAST A SQUARE CYLINDER

The flow past a square cylinder at $Re = 22,000$ (at zero angle of attack) has served as a test case for two RANS/LES workshops. A summary of the results presented at these workshops can be found in Rodi *et. al* (1997) and Voke (1997). Experimental data is available for comparison. An overview of the experimentally determined bulk quantities is given in Table 1. It may be noted the mean lift coefficient has not been measured; it should be zero.

The coordinate system that we have used for the computation has its origin at the centre of the cylinder. All quantities are normalized by the cylinder width and the inflow velocity. The stream-wise direction is denoted by x, the lateral direction by y and the spanwise direction by z. The components of the velocity in these directions are given by u, v and w, respectively.

The flow is assumed to be periodical in the spanwise direction. The spanwise boundaries are taken four diameters apart, that is the period in z equals four diameters.

The inflow boundary is located at $x = -7$, *i.e.* six and a half diameters upstream of the cylinder. We prescribe the following laminar inflow condition at $x = -7$: $u = 1, v = 0, w = 0$. Experiments that have been performed by Lyn *et al.* (1995) indicate a turbulence level of about 2% at four and a half diameters upstream from the cylinder. Since no more information was reported, we take the flow to be laminar at six and a half diameters upstream. The lateral boundaries are located at $y = \pm 7$. At these boundaries we have imposed $u_{yy} = w_{yy} = p_y = 0$, where p denotes the pressure.

The outflow boundary is positioned at $x = 20$. At the outflow, we impose the same conditions as at the lateral boundaries, albeit that the pressure gradient need not to vanish at the outflow. The outflow conditions read $v_{xx} = w_{xx} = 0$ and $p_x =$ constant, where the constant is determined such that the mass inflow equals the mass outflow at each time step. As expected, the constant pressure gradient at the outflow turns out to be approximately zero. Yet, allowing it to differ from zero reduces the number of iterations needed to satisfy the incompressibility contraint substantially.

In addition, in a buffer zone ($x = 15 - 20$) the Reynolds number is decreased from 22,000 to 1,000 to suppress (non-

Table 1: Experimental results of the flow past a long, square cylinder by Lyn *et al.* (1995), McLean *et al.* (1992) and Lee (1975), respectively.

	Lyn *et al.* (1995)
Mean Strouhal number	0.133 ± 0.003
Mean drag coefficient Cd	2.1
Mean lift coefficient Cl	-
Rms fluctuation of Cd	-
Rms fluctuation of Cl	-

	McLean *et al.* (1992)
Mean Strouhal number	-
Mean drag coefficient Cd	1.9 - 2.1
Mean lift coefficient Cl	-
Rms fluctuation of Cd	0.1 - 0.2
Rms fluctuation of Cl	0.7 - 1.4

	Lee (1975)
Mean Strouhal number	-
Mean drag coefficient Cd	2.05
Mean lift coefficient Cl	-
Rms fluctuation of Cd	0.16 - 0.23
Rms fluctuation of Cl	-

physical) waves which are reflected by the artificial outflow boundary. It may be emphasized that the grid spacing in the buffer zone is taken so large that the time step is not restricted by a viscous stability condition in the buffer region.

No-slip boundaries are imposed at the cylinder surface.

We have used a $280 \times 210 \times 64$ staggered grid to cover the computational domain. The grid is stretched in x and y, and uniform in the spanwise direction. The first grid point is spaced 0.005 from the cylinder surface. The grid is stretched out away from the cylinder surface by means of a sinh function; the ratio of the largest to smallest grid size is approximately 200 (in x) and 100 (in y). It may be emphasized that we have not adapted the weights in the Richardson extrapolation to the stretching of the grid. As explained in the previous section, we always use the constant weights 9/8 and -1/8, since these weights result in a conservative discretization.

The discrete Poisson equation for the pressure is solved with a combination of a Fast Fourier Transform method in the spanwise direction and a Modified Incomplete Choleski Conjugate Gradient (MICCG) method in the resulting spectral space. After the Fourier transform (which can be computed in parallel over the x and y directions), the discrete Poisson equation falls apart into a set of mutually independent 2D Klein-Gordon-Fokker equations. This set of mutually independent equations is distributed over 16 vector-processors of a CRAY J90, and each equation is solved using MICCG.

The Incomplete Choleski preconditioner is modified according to Gustafson (1978). The MICCG code is fully vectorized by an explicit reordering of the unknowns along diagonals of grid planes perpendicular to the spanwise direction. The implementation of the preconditioned iterative method is optimized as proposed by Eisenstat (1981). The initial guess for the MICCG-iteration is obtained by an extrapolation of the pressure correction from three previous time levels. Thus, a fully parallel/vector implementation is achieved.

The equations for the high frequencies in the spanwise direction have a stronger diagonal than those for the low frequencies (due to the FFT). Consequently, the MICCG iterations converge faster for the high frequencies than for the low ones. This unbalance in work load is almost completely undone by the fact that the initial guesses for the low frequencies are much better than those for the high frequencies. The net differences in work load per processor are too small to bother about.

The start-up of the flow plus three shedding cycles have been computed. Averages are computed over three shedding cycles and the spanwise direction. Velocities are also averaged over the top and bottom halves. Table 2 shows the mean Strouhal number, the mean drag coefficient Cd, the mean lift coefficient Cl and the root-mean-square fluctuations of Cd and Cl.

Table 2: Bulk quantities as obtained by means of DNS

	DNS
Mean Strouhal number	0.133
Mean drag coefficient Cd	2.09
Mean lift coefficient Cl	0.005
Rms fluctuation of Cd	0.178
Rms fluctuation of Cl	1.45

So far, we have only computed three full shedding cycles. Results of longer computations will be available at the conference. Yet, the averages over as little as three shedding cycles of all computed bulk quantities fall already within the range set by the experiments, except for the root-mean-square of the fluctuations of the lift coefficient Cl. The rms fluctuation of Cl seems to be slightly overestimated by the DNS.

Figure 4 displays a visualisation of a snapshot of the simulation of the flow near a square cylinder. This visualisation has been made using the spot noise technique. For details on the spot noise technique the reader is referred to the Ph.D. Thesis of De Leeuw (1997). Figure 4 illustrates the complexity of the flow above, below, and in particular, past the square cylinder.

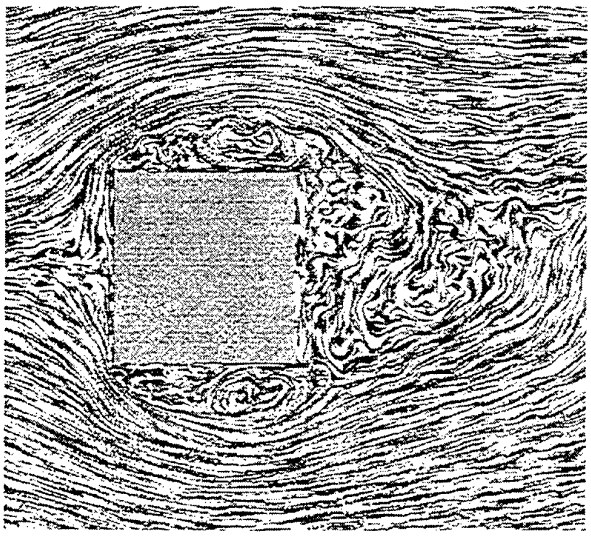


Figure 4: Spot noise visualisation of a snapshot of a flow near a square cylinder at Re=22,000.

Figure 5 shows a comparison of mean stream-wise velocities of DNS with experimental data at four locations

past the cylinder. The agreement between the experimental data and the numerical data is good.

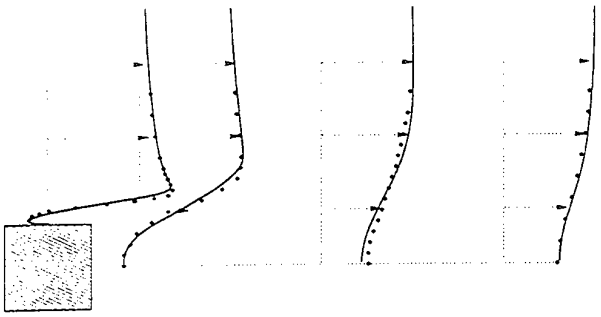


Figure 5: A comparison of mean velocities of the DNS with experimental results. The experimental data is taken from ERCOFTAC Database Case 43; see also Lyn *et al.* (1995). Shown is the mean stream-wise velocity. The continuous lines correspond to the DNS; the experimental data is depicted by the dots.

An instantaneous value of the skin friction on the four walls of the square cylinder is depicted in Figure 6. The skin friction is visualized using spot noise, too.

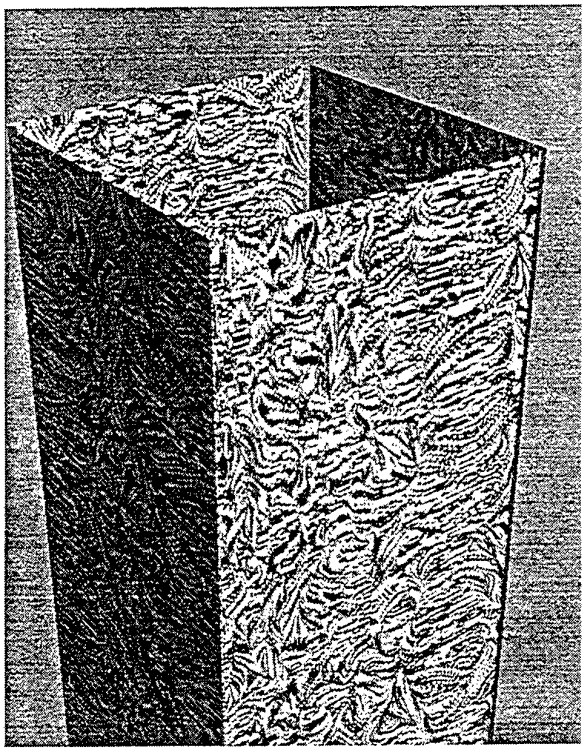


Figure 6: Spot noise visualisation of the skin friction at the cylinder.

CONCLUSION

It has been demonstrated that the algorithmic improvements (in particular space discretization and time-integration), together with the improvements in computer performance, have opened the possibility of performing a DNS of a three-dimensional turbulent flow past a long, square cylinder at $Re = 22,000$.

Acknowledgements: The Stichting Nationale Computerfaciliteiten (National Computing Facilities Foundation, NCF) with financial support from the Nederlandse Organisatie voor Wetenschappelijk Onderzoek (Netherlands Organization for Scientific Research, NWO) is gratefully acknowledged for the use of supercomputer facilities.

Wim de Leeuw (CWI) is gratefully acknowledged for making the visualizations with the spot noise technique.

REFERENCES

Eisenstat, S.C., 1981, "Efficient implementation of a class of preconditioned Conjugate Gradient methods," *SIAM J. on Sci. and Stats. Comp.*, Vol. 2, pp. 1–4.

Gustavson, I., 1978, "A class of first order factorization methods," *BIT*, Vol. 18, pp. 142–156.

Harlow, F.H., and Welsh, J.E., 1965, "Numerical calculation of time-dependent viscous incompressible flow of fluid with free surface," *Phys. Fluids*, Vol. 8, pp. 2182–2189.

Le, H., and Moin, P., 1991, "An improvement of fractional step methods for the incompressible Navier-Stokes equations," *J. Comp. Phys.*, Vol. 92, pp. 367–379.

Lee, B.E., 1975, "The effect of turbulence on the surface pressure field of square prisms," *J. of Fluid Mech.*, Vol. 69, pp. 263–282.

Leeuw, W. de, 1997, "Presentation and exploration of flow data," Ph.D. Thesis, Technical University of Delft, Delft, The Netherlands.

Lyn, D.A., and Rodi, W., 1994, "The flapping shear layer formed by flow separation from the forward corner of a square cylinder," *J. of Fluid Mech.* Vol. 267, pp. 353–376.

Lyn, D.A., Einav, S., Rodi, W., and Park, J.H., 1995, "A laser-Doppler-velocimetry study of ensemble-averaged characteristics of the turbulent near wake of a square cylinder," *J. of Fluid Mech.* Vol. 304, pp. 285–316.

McLean, I., and Gartshore, I., 1992, "Spanwise correlations of pressure on a rigid square section cylinder," *J. of Wind Eng.*, Vol. 779, pp. 41–44.

Nevanlinna, O., and Liniger, W., 1978, "Contractive methods for stiff differential equations; Part I," *BIT*, Vol. 18, pp. 457–474.

Prasad, A.K., and Koseff, J.R., 1989, "Reynolds number and end-wall effects on a lid-driven cavity flow," *Physics of Fluids A*, Vol. 1, pp. 208–218.

Rodi, W., Ferziger, J.H., Breuer, M., and Pourquié, M., 1997, "Status of Large Eddy Simulation: Results of a workshop," to appear in *ASME J. of Fluids Eng.*

Ven, H., van der, Maurits, N.M., and Veldman, A.E.P., 1995, "Explicit multi time stepping algorithm for convection dominated flow problems," NLR Report TP 95502 L, National Aerospace Laboratory NLR, The Netherlands.

Ven, H., van der, Niemann-Tuitman, B.E., and Veldman, A.E.P., 1996, "An explicit multi time stepping algorithm for aerodynamic flows,", to appear in *J. Comp. Appl. Math.*

Veldman, A.E.P., and Rinzema, K., 1992, "Playing with nonuniform grids," *J. of Eng. Math.*, Vol. 26, pp. 119-130.

Verstappen, R.W.C.P., Wissink, J.G., and Veldman, A.E.P., 1993, "Direct numerical simulation of driven cavity flows," *Appl. Sci. Res.*, Vol. 51, pp. 377–381.

Verstappen, R.W.C.P., and Veldman, A.E.P., 1997, "A comparison of low-order DNS, High-order DNS and LES," to appear in: *Direct and Large Eddy Simulation II*, J.P. Chollet *et al.*, eds., Kluwer Academic Publishers, Dordrecht, The Netherlands.

Voke, P.R., 1997, "Flow past a square cylinder: test case LES2," to appear in: *Direct and Large Eddy Simulation II*, J.P. Chollet *et al.*, eds., Kluwer Academic Publishers, Dordrecht, The Netherlands .

GENERATION OF INITIAL AND BOUNDARY CONDITIONS FOR LARGE-EDDY SIMULATIONS OF WALL-BOUNDED FLOWS

David C. Weatherly and James M. McDonough
Mechanical Engineering Department
University of Kentucky
Lexington, Kentucky 40506-0108
United States of America

ABSTRACT

As a step toward the practical development of a new class of large-eddy simulation (LES) schemes, we demonstrate that the gross structures of turbulent boundary layers can be established in a computed solution by applying seed perturbations typical of the near-wall streak/vortex interaction. The test problem is a zero pressure gradient supersonic boundary layer (Mach = 2.85) at high Reynolds number ($Re_\theta = 8 \times 10^4$). An immediate application for the procedure is the preparation of initial conditions and time-dependent upstream boundary conditions for conventional LES of turbulent wall-bounded flows when it is impractical to simulate the entire upstream transition and turbulence development regions. The computed flowfields reported here are affected by systematic error; future improvements are suggested to reduce this error. However, the procedure is easy and even as currently formulated it may prove useful in some circumstances.

INTRODUCTION

The motivation of this work comes from our efforts to construct a new family of large-eddy simulation (LES) schemes. These new schemes are based on a formulation known as Additive Turbulent Decomposition (ATD) (McDonough et al., 1984(a,b); Hylin & McDonough, 1994). The novelty of the ATD turbulence modeling schemes is in the mechanism by which the effects of unresolved turbulence are brought to bear on the resolved part of the solution. To illustrate, we can compare the derivations of the conventional LES formulation and the new ATD formulation.

The derivation of the conventional LES formulation proceeds in three steps. The governing equations are first written in terms of solution variables that have been formally decomposed into resolved and unresolved parts. Then the operator that defines the resolved part of the solution is applied to each term in the governing equations. Finally, the terms that cannot be constructed solely from the computed resolved quantities are grouped separately. In general these latter terms are the filtered products of resolved and unresolved quantities, and they must be modeled to the extent possible. Our ability to model these terms with any degree of universality has been impaired by the lack of adequate theory to relate the modeled quantities to the resolved solution.

The derivation of the ATD formulation is similar to the LES formulation, with two exceptions. The parts of the decomposed solution are referred to as the large- and small-scale parts, to distinguish the set of large-scale length scales from those resolved in computation. In addition the final step in the LES derivation, the separation of computable terms from those that must be modeled, is not carried out. The resulting equations govern the evolution of the large-scale part of the solution, and their terms depend formally on both the large- and small-scale solutions. The requirement for modeling arises from the fact that the small-scale part of the solution cannot be described in detail in a practical calculation. In this case the turbulence model is required to generate a representation of the small-scale solution itself, rather than the more abstract quantities derived from that solution in the LES formulation. The challenge of modeling is to represent the most dynamically relevant aspects of the small-scale solution in a computational basis that may include length scales only slightly smaller than those that describe the large-scale part of the solution.

Direct modeling of the dynamically active component of the small-scale solution is consistent with our current understanding of turbulence physics. Theories of energy transfer among turbulence length scales suggest that the large-scale solution is most strongly affected by the octave of small-scale features with sizes just below those of the large-scale solution. There is no scale separation between these length scales and those of the large-scale solution, so it is inappropriate to attempt to represent their effect by homogenization. (We note that recent refinements of the ATD formulation use a three-range decomposition, and the effect of the smallest range of scales on the large-scale solution could legitimately be taken into account by homogenization.) Rogallo & Moin (1984) distinguished between local and nonlocal transfer among features of differing length scales in their discussion of conventional turbulence models for LES: "The interaction between scales of similar size retains the full complexity of the original turbulence problem, so there is little hope of modeling the

local effects well." A similar sentiment was expressed by Piomelli, Yu, & Adrian (1996), who described the spatial distribution of energy transfer to larger and smaller scales associated with typical coherent structures found in turbulent boundary layer flows; they were skeptical that conventional turbulence models could be made to account for the distributions they found. On the other hand, direct representation of coherent structures in the modeled small-scale solution could induce the proper energy transfer in a natural way.

As the above implies, the new approach also has the advantage that the quantities to be modeled have immediate physical relevance. The most important aspect of the interaction between large- and small-scale solutions is the transfer of turbulent energy. The instantaneous mechanisms of this transfer have received increasing attention in the last ten years, and direct numerical simulations have helped to confirm some of the proposed explanations for the transfer. It is an overall goal of our ongoing work to apply the results of those studies to the construction of ATD turbulence models.

Our working conception of the interscale energy transfer mechanisms in wall-bounded turbulent flow is drawn from several sources, and it is described briefly as follows. Robinson's analysis (1991) of a direct numerical simulation (DNS) of a low Reynolds number incompressible boundary layer suggested that low-speed streaks and quasi-streamwise vortices mutually regenerate each other in the buffer layer (see also: Jimenez & Moin 1991; Zhou, Adrian, & Balachandar 1996; Trefethen et al. 1993; Brooke & Hanratty 1993), and he observed that in this cycle, spanwise vortices are by-products that migrate out from the wall, spreading and merging to form the large δ-scale structures of the outer region. Indications are that this behavior is generic for incompressible boundary layers at higher Reynolds numbers, and for compressible layers also (Spina, Smits, & Robinson, 1993). At higher Reynolds numbers, it is speculated that the merging of spanwise vortices of similar orientation produces single larger structures from pairs of smaller ones, and at the same time the winding of one vortex around the core of another concentrates its vorticity into thinner and thinner sheets, until local perturbations cause portions of the sheets to rapidly roll up into the long thin vortex filaments observed in direct numerical simulations of isotropic and homogeneous turbulence (Overman & Zabuskey, 1982; Lundgren, 1982; Gilbert, 1988; Vincent & Meneguzzi, 1991; Hunt & Vassilicos, 1991; Porter, Pouquet, & Woodward, 1994; Moffatt, Kida, & Ohkitani, 1994).

In the first-described chain of events the near-wall streaks and vortices, which are among the smallest features in the flow, act as seeds that grow into the largest features in the flow; this represents energy flow from small- to large-scale flow features. The roll-up of thin sheets of vorticity generated in the vortex merger process transfers energy from larger features to the smallest scales. Here we concentrate on the first aspect of the presumed process, energy transfer to larger scales, because it is responsible for initiation and maintenance of the gross turbulent features that can be resolved in a computation of the large-scale flow. This is a first-order effect in such a computation in comparison with the energy drain to smaller scales associated with the roll-up of vorticity sheets.

In a simulation of a wall-bounded turbulent flow by an ATD scheme as described above, the task of the modeled small-scale solution is ideally to reproduce the smallest resolvable features in the physical sequence of events that feeds energy to ever-larger structures, so that all the succeeding events in the cycle can occur naturally in the large-scale solution as it evolves. However, it should be noted that from a strictly numerical point of view these smallest resolvable features, which might be referred to as the initiating features of the large-scale turbulence, need not appear in the computed solution at their proper physical scales. For example, Moin & Kim (1982) reported that the streaky structures in the viscous sublayer of their plane channel flow LES appeared at about twice their physical size. In fact, it may be useful to incorporate into our computations some of the physical turbulence mechanisms that occur at unresolvable scales by inducing them to occur at much larger resolvable scales. Recall that the modeled small-scale features must be dynamically active; it might be easier to achieve this activity in models of the smaller features rather than of the larger ones. In the work reported here, the mutual regeneration of streaks and vortices in the near-wall layer is stimulated to occur at resolvable scales. The theory of the function of this mechanism (Trefethen et al., 1993) indicates that it should be possible to initiate it even with quite crude representations of the coherent structures involved, so it is a natural place to begin our studies. We seek to learn whether this mechanism can be used to establish large-scale turbulence structures of the proper type in our computed solutions.

Besides furthering our understanding of energy transfer mechanisms in the context of ATD turbulence modeling schemes, the induction of large-scale turbulent motion in simulations of wall-bounded flows has immediate application to preparation of initial and boundary conditions for conventional LES computations. In many such computations, the location and geometry of the physical domain makes it impractical to simulate the entire upstream transition and turbulence development regions. Yet it is necessary to provide an initial field with appropriate turbulence structure and a time-dependent inflow boundary condition that likewise reflects appropriate turbulence structure. In the following sections we demonstrate the use of the streak/vortex interaction mechanism in a procedure that establishes such large-scale structure.

PROCEDURE

Here we consider preparation of initial and boundary conditions for a turbulent supersonic boundary layer (M = 2.85, Re_θ = 80,000) over a flat plate (Settles, Vas, & Bogdonoff, 1976). The domain of interest is well downstream of the windtunnel inlet, and at this location the layer is about 2.1 cm (0.83 in.) thick. This thickness is equivalent to 10,000 wall units, so that the buffer layer thickness is only about 0.3% of the overall layer thickness. For economic reasons, the grid is to have a uniform spacing of 0.127 cm (0.05 in.); this places the first cell center from the wall at y^+ = 300, well into the log region, and at most perhaps three or four cells will be located in the log layer. In this case, the initiating features should properly be the spanwise vortices characteristic of the log layer. This requires an efficient wall model, for example as in Balaras, Benocci, & Piomelli (1996). However, instead we attempt a cruder but conceptually simpler approach. We augment the domain of interest with a short upstream region to allow for fast spatial transition and development of turbulent structure from the initially laminar flow conditions. At the upstream boundary we introduce perturbations designed to directly stimulate the streak/vortex interaction mechanism, characteristic of the buffer layer, to occur at gross scales in the computed solution. Although the ATD formulation is not used here (nor is any turbulence model), these perturbations in the boundary condition represent a first step toward the modeled small-scale solution in that formulation above. This strategy should induce the establishment of developed turbulent structure over a relatively short downstream region, since it bypasses the lengthy stages observed in transitions forced by classical linear instability modes.

The working fluid is air, assumed an ideal gas. The Navier-Stokes equations for compressible flow are integrated with the finite-volume GASP (Generalized Aero-

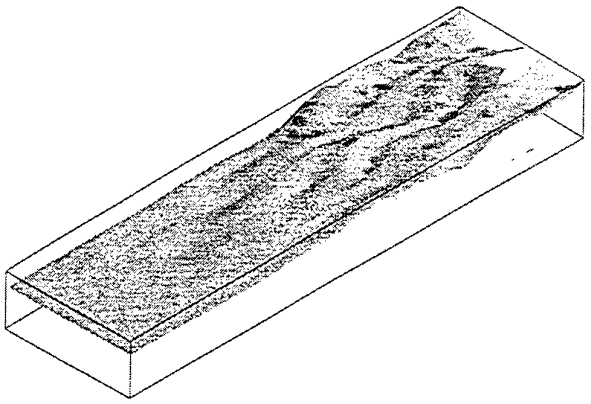


Figure 1: Boundary layer edge. Vorticity magnitude isosurface; level = 2% maximum vorticity magnitude.

dynamic Simulation Program) flow solver of Walters and his students at Virginia Polytechnic Institute. In this case, third order upwind interpolation without limiting and Roe's flux difference scheme are used to compute the inviscid fluxes at the cell faces, and a second order centered difference scheme approximates the viscous fluxes at those locations. Time integration is by the implicit Euler method. At each step, the solve is carried out directly using an alternating direction implicit operator splitting. No turbulence model is used. The domain is 9.0×1.0×2.5 inches in the streamwise, wall-normal, and spanwise directions, respectively. The grid carries 180×20×50 cells, spaced uniformly in the corresponding coordinate directions. The time step is set to 1.0 μsec so that the corresponding CFL number is approximately 1.0 over most of the grid. No-slip adiabatic conditions are specified at the plate surface. Tangent flow is maintained at the side walls, and outflow conditions (extrapolated from domain interior) are enforced at the downstream boundary and at the domain face opposite the plate. The initial velocity and temperature profiles are the Chapman & Rubesin (1949) laminar profiles for an adiabatic plate. These profiles are also imposed as fixed boundary conditions at the upstream boundary.

At the upstream boundary, the fixed laminar velocity and pressure fields are modified by time-dependent perturbations applied to several circular regions arranged spanwise across the plate surface. The perturbations are intended to approximate sections through streamwise vortices. Their form is derived from an analysis of flow with purely circular streamlines. The purely azimuthal perturbation velocity is assigned a parabolic dependence on radial position r, with a maximum at the mid-radius of the vortex section. For a perturbation of maximum radius R,

$$|v_\theta| \propto 1 - (\frac{2r}{R} - 1)^2 \tag{1}$$

The radial dependence of the corresponding pressure perturbation is determined by the radial momentum equation in circular polar coordinates

$$\frac{\partial p}{\partial r} = -\rho \frac{v_\theta}{r} \tag{2}$$

under the simplifying assumption of constant density and neglecting radial and axial velocity components. Perturbation pressure is taken to be zero at the outer diameter of the perturbation; it decreases and reaches a minimum at the center of the swirl. The diameter of the perturbations remains constant throughout the calculations, but their amplitude is time dependent. The amplitude varies sinusoidally during active periods of fixed length.

The swirl perturbation parameters are the maximum azimuthal velocity A relative to the average local sound speed a_0 of the base flow, and the active time period t_p. The temporal and spatial variation of the perturbation velocity and

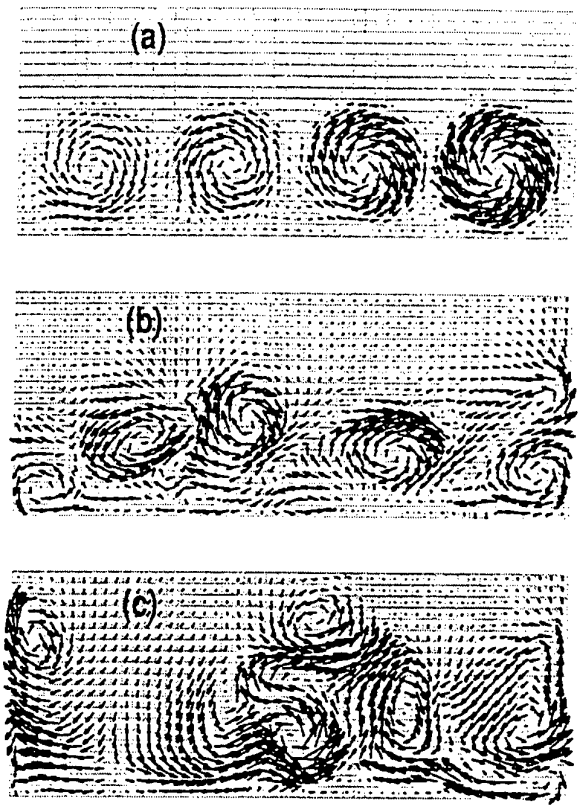


Figure 2: Cross-stream velocity fields. Streamwise stations: (a), 0%; (b), 50%; (c), 100%.

pressure for a grid cell within the swirl radius R are specified in terms of the current swirl time t and the cell center coordinates (y_c, z_c) relative to the swirl center. The cell center is a distance r from the swirl center, $0 \le r \le R$, and this is recast for convenience:

$$s = \frac{2r}{R} - 1 \tag{3}$$

where $-1 \le s \le 1$. Then the perturbations are given by the expressions

$$\Delta v = \pm A\, a_0 \sin(\pi \frac{t}{t_p})(1 - s^2)(\frac{z_c}{R}) \tag{4}$$

$$\Delta w = \mp A\, a_0 \sin(\pi \frac{t}{t_p})(1 - s^2)(\frac{y_c}{R}) \tag{5}$$

$$\Delta p = -\rho_0 (A\, a_0 \sin(\pi \frac{t}{t_p}))^2 \cdot(\frac{2}{3} - (s - \frac{1}{3}s^3 + \frac{1}{4}(1 - s^2)^2)), \tag{6}$$

where ρ_0 is the average local density of the base flow. The sense of rotation for individual swirls is constant during the active time period t_0. At the end of each active period, the sense of rotation is reset randomly, and an inactive period of a random percentage of $0.75\, t_p$ is specified.

The size, strength, and duration of the perturbations necessary to trigger formation of turbulent structure is likely a function of the flow conditions, the grid spacing, and the solution scheme. We speculate that two conditions on the size must be satisfied for these perturbations to induce formation of large-scale turbulence structure. First, for a given kinematic viscosity, the product of the perturbation diameter and the velocity difference across this distance in the background shear flow must be larger than a minimum value. Trefethen et al. (1993) construct a

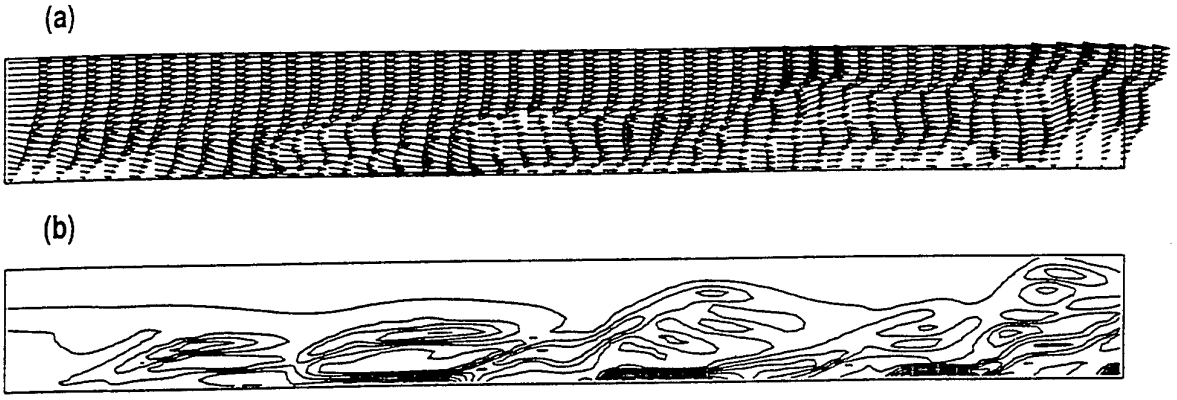


Figure 3: Streamwise plane at 50% spanwise station; (a), velocity field; (b), spanwise vorticity contours.

Reynolds number with these three quantities. The typical sizes of features in the viscous and buffer layers in a turbulent wall-bounded flow indicate that the minimum value of this Reynolds number for self-regenerating turbulent motion is about 1000 universally. Second, for a given discretization scheme, the perturbation diameter must be large enough relative to the grid spacing that features of that size can move through the domain with minimal diffusive and dispersive error. For the standard second- and third-order finite volume schemes we have used, this appears to dictate a minimum diameter of about 12-14 cells; we hope and expect that somewhat smaller perturbation diameters would suffice for schemes with better resolution.

For the calculations reported here, four circular perturbation regions are applied. Each of these regions has a diameter of 1.52 cm (0.6 in.), or 12 grid cells; this is about 75% of the boundary layer thickness, a large perturbation indeed. The maximum tangential velocity is specified to be 40% of the local speed of sound; this is about 20% of the freestream velocity (1875 ft/sec). The fixed-length active periods last 50 time steps (50.0 μsec), and the inactive periods vary randomly over the range of 0-37 time steps. The calculations have been run for 2000 time steps, or a total of 2.0 *msec* of elapsed time. In this period, about 50 features with the scale of the boundary layer thickness pass a given point.

RESULTS

We observe formation of large-scale structure in the computed solution. Representative visualizations of the solution at step 1000 (1.0 *msec*) are included as Figures 1-4. The structure begins to develop at the upstream end of the domain. Large bulges appear in the interface between rotational and irrotational fluid (boundary layer edge) only one-third of the domain length downstream. These can be seen in Figure 1, which shows an isosurface of vorticity magnitude at the level of 2% of the solution maximum. Figure 2 shows cross-stream velocity vectors in the layer. The varying strength of the vortical perturbations can be seen at the upstream station. At successive downstream stations, the fields become much less orderly; typical cross-stream velocity magnitudes remain about the same as at the inlet. Figure 3 shows the streamwise velocity field and the corresponding spanwise vorticity field for a wall-normal streamwise plane centered in the domain. The interface bulges and their typical sloping backs with sharp gradients are observed in these images. In Figure 4, isosurfaces of low pressure and of low velocity are combined to show the locations of strong quasi-streamwise vortices and streaks, respectively. These are of the typical form observed by Robinson and others in direct numerical simulations of boundary layer flows at low Reynolds numbers. Cross-stream velocity vectors plotted on a section through one such vortex verify the circulation there.

An average of the streamwise velocity profiles over 36 locations in the downstream 2/3 of the domain and over time steps 1000-2000 is shown in Figure 5. The velocity values have been normalized by the friction velocity derived from the computed velocity gradient and the molecular viscosity at the wall. The profile has been transformed according to the procedure of Van Driest and plotted in semi-log format against height in wall-units for comparison with standard correlations for incompressible boundary layers. Also plotted in the figure is the line along which the logarithmic part of the experimentally-measured profiles fall when presented in the same way.

Overall, the computed profile has the same qualitative features as the experimental profile. However, the friction exerted on the wall by the computed flow is perhaps 20% of that exerted by the physical flow. This affects the normalization of both velocity and height directly, and the slope of the logarithmic region indirectly; all these quantities differ from the corresponding experimental values by approximately the same factor of about 5. The plot does not reveal that even if this is taken into account, the computed profile has a much stronger wake component than the experimental profile, with a noticeably larger difference between the velocities at the inner and outer edges of the wake part of the computed profile.

CONCLUSIONS

One of the goals of this work has been to demonstrate that stimulation of the seed mechanism that presumably establishes the gross turbulence structure of physical boundary layers can also establish such structure in the computational model of the layer. We conclude from these observations that large-scale turbulent structure can indeed be induced by time-dependent vortical perturbations applied at the upstream boundary. The results imply that the streak/vortex interaction mechanism might well be used in the construction of ATD turbulence models. However, our experiments indicate that the perturbations must be large, say 12-14 grid cells in diameter, to act effectively in the manner intended in the ATD formulation. At present, practical computations are limited to domains that are not many multiples of this size. As a result the small-scale component of the computational basis in an ATD calculation using the current discretization scheme would occupy a significant part of that basis. It would be preferable if the modeled small-scale features were compu-

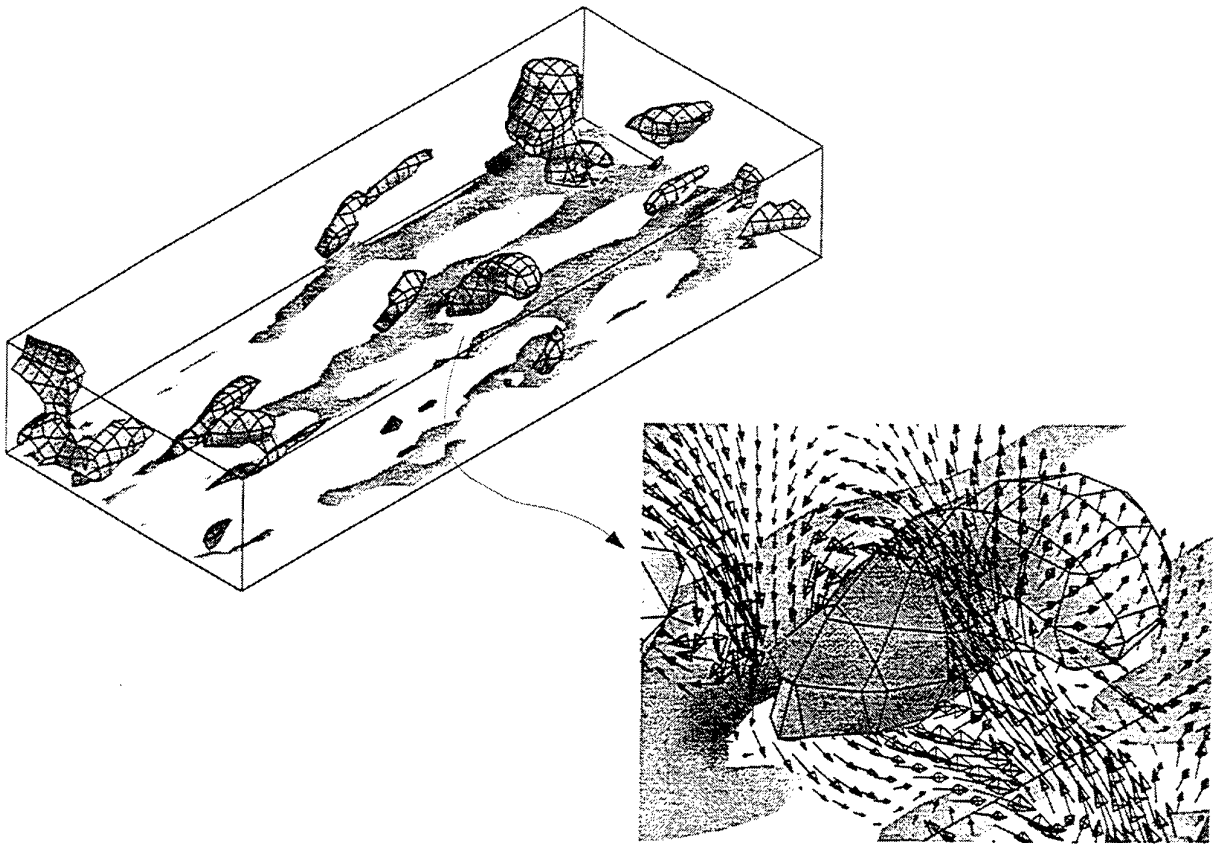


Figure 4: Streak/vortex structure, downstream 2/3 of domain. Inset: circulation around vortex in cross-stream plane.

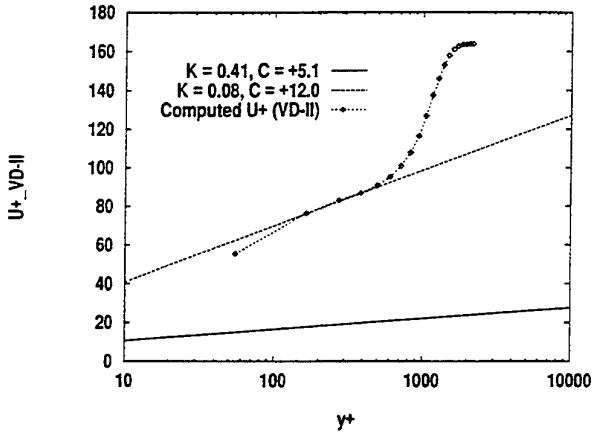


Figure 5: Velocity profile comparison.

tationally active at sizes of only 3-5 grid cells; this would allow a much larger percentage of the computational basis to be devoted to description of the large-scale solution. The improvement might be achieved with high-resolution schemes designed to minimize dissipative and dispersive error at high wavenumbers.

The streak/vortex interaction mechanism is observed to operate in the computed solution at a scale grossly larger than its correct physical scale. This is consistent with our intention to evoke the physics of the near-wall region in the computed solution, rather than to achieve a result that is quantitatively comparable to the experimental results. For example, significant turbulent shear stress is present in the physical boundary layer even at the grid cell center adjacent to the wall; however, we have not accounted for this stress, but instead included only the molecular diffusive stress that dominates in the viscous sublayer and buffer regions of the boundary layer. This affects the computed velocity profile in a systematic way, yielding computed wall friction well below that of the physical case.

However, it is natural to extend the uniform grid procedure used here to grids clustered in the wall-normal direction. In such case we anticipate that upstream perturbations constructed similarly in square (in computational space) arrays of grid cells would induce streak/vortex interactions at more physical scales, at least in the wall-normal direction. This in turn should lead to more correct values of computed skin friction and probably improved velocity profiles. On stretched grids the perturbations would be more or less elliptical in physical space, and the distributions of azimuthal velocity and pressure must be derived with this geometry in mind. This extension will be pursued in the future.

The turbulent structure of the computed layer is established within a short distance of the upstream boundary. Thus only a minimal region need be provided upstream of the physical domain of interest to develop the proper conditions, and a relatively brief preliminary computation suffices to establish the initial turbulent condition for the entire domain. For supersonic flow, the solution in the upstream development region may then be integrated alone to accumulate a time-dependent turbulent upstream boundary condition for the main region of interest.

Finally, having noted some positive aspects of the results, we must admit that from the standpoint of absolute accuracy, the current computed solution might seem

to be of negligible value. However, the mere fact that large-scale coherent structures are present in the solution may be useful. This could be the case in circumstances in which the turbulence structure at the largest scales is decisive to the phenomenon of interest. An example of such a phenomenon may be the interaction of a shock with a turbulent boundary layer over a compression ramp.

REFERENCES

E. Balaras, C. Benocci, and U. Piomelli. "Two-layer approximate boundary conditions for large-eddy simulations." *AIAA Journal*, 34(6):1111–9, June 1996.

J. W. Brooke and T. J. Hanratty. "Origin of turbulence-producing eddies in a channel flow." *Physics of Fluids A*, 5:1011–22, 1993.

D. R. Chapman and M. W. Rubesin. "Temperature and velocity profiles in the compressible laminar boundary layer with arbitrary distribution of surface temperature." *Journal of the Aeronautical Sciences*, 16:547–565, September 1949.

A. D. Gilbert. "Spiral structures and spectra in two-dimensional turbulence." *Journal of Fluid Mechanics*, 193:475–97, 1988.

J. C. R. Hunt and J. C. Vassilicos. "Kolmogorov's contributions to the physical and geometrical understanding of small-scale turbulence and recent developments." *Proceedings of the Royal Society of London A*, 434:183–210, 1991.

E. C. Hylin and J. M. McDonough. "Chaotic map models for the small-scale quantities in an additive decomposition of the Navier-Stokes equations. Part 1. Theory." Mechanical Engineering Department Report CFD-01-94, University of Kentucky, Lexington, KY 40506-0108, 1994.

J. Jimenez and P. Moin. "The minimal flow unit in near-wall turbulence." *Journal of Fluid Mechanics*, 225:213–40, 1991.

T. S. Lundgren. "Strained spiral vortex model for turbulent fine structure." *Physics of Fluids*, 25(12):2193–2203, December 1982.

J. M. McDonough, J. C. Buell, and R. J. Bywater. "A comparison of routes to a strange attractor in one-dimensional local models of turbulent free and forced convection." ASME Paper 84-WA/HT-16, American Society of Mechanical Engineers, 345 E. 47 St., New York, NY 10017, 1984.

J. M. McDonough, R. J. Bywater, and J. C. Buell. "An investigation of strange attractor theory and small-scale turbulence." AIAA Paper AIAA-84-1674, American Institute of Aeronautics and Astronautics, 1633 Broadway, New York, NY 10019, 1984.

H. K. Moffatt, S. Kida, and K. Ohkitani. "Stretched vortices - the sinews of turbulence; large-Reynolds-number asymptotics." *Journal of Fluid Mechanics*, 259:241–64, 1994.

P. Moin and J. Kim. "Numerical investigation of turbulent channel flow." *Journal of Fluid Mechanics*, 118:341–77, 1982.

E. A. Overman II and N. J. Zabuskey. "Evolution and merger of isolated vortex structures." *Physics of Fluids*, 25(8):1297–1305, August 1982.

U. Piomelli, Y. Yu, and R. J. Adrian. "Subgrid-scale energy transfer and near-wall turbulence structure." *Physics of Fluids*, 8(1):215–24, 1996.

D. H. Porter, A. Pouquet, and P. R. Woodward. "Kolmogorov-like spectra in decaying three-dimensional supersonic flows." *Physics of Fluids*, 6(6):2133–42, 1994.

S. K. Robinson. "Coherent motions in the turbulent boundary layer." *Annual Review of Fluid Mechanics*, 23:601–639, 1991.

R. S. Rogallo and P. Moin. "Numerical simulation of turbulent flows." *Annual Reviews of Fluid Mechanics*, 16:99–137, 1984.

G. S. Settles, I. E. Vas, and S. M. Bogdonoff. "Details of a shock-separated turbulent boundary layer at a compression corner." *AIAA Journal*, 14(12):1709–1715, December 1976.

E. F. Spina, A. J. Smits, and S. K. Robinson. "The physics of supersonic turbulent boundary layers." *Annual Review of Fluid Mechanics*, 26:287–319, 1994.

L. N. Trefethen, A. E. Trefethen, S. C. Reddy, and T. A. Driscoll. "Hydrodynamic stability without eigenvalues." *Science*, 261:578–584, July 1993.

A. Vincent and M. Meneguzzi. "The spatial structure and statistical properties of homogeneous turbulence." *Journal of Fluid Mechanics*, 225:1–20, 1991.

J. Zhou, R. J. Adrian, and S. Balachandar. "Autogeneration of near-wall vortical structures in channel flow." *Physics of Fluids*, 8(1):288–90, 1996.

ON OPTIMUM FILTER SIZE AND EFFICIENT NUMERICAL VISCOSITY FOR LARGE-EDDY SIMULATION OF COMPLEX FLOWS AROUND A SQUARE CYLINDER

K. Nozawa[(1)], T. Tamura[(2)]

[(1)] Izumi Research Inst.
Shimizu Corp.
2-2-2, Uchisawai-cho, Chiyoda-ku, Tokyo 100
Japan

[(2)] Department of Environmental Physics and Eng.
Tokyo Inst. of Tech.
4259, Nagatsuta Midori-ku, Yokohama 226
Japan

ABSTRACT

The methodology to reduce the influence of numerical viscosity of necessary evil higher-order upwind scheme in large eddy simulation for complex flows around bluff bodies is proposed and its effectiveness is discussed. Both techniques of extended filter, which is two and four times as large as grid size, for LES and decreasing numerical viscosity of upwind scheme with embedded mesh are applied to the flow around a square cylinder at $Re = 22,000$, and the calculated results are compared with experimental data. The effectiveness of the methodology is recognized in the improvement of the overestimating drag coefficient and of the underestimating stochastic component of fluctuating transverse velocity in the shear layer.

INTRODUCTION

In the flow around a bluff cylinder, there is a large area with high shear rate which requires high resolution for a turbulence simulation. It is impossible or very expensive to cover all these area with sufficiently fine mesh. Without using any stabilizing technique or adding an artificial diffusion, we can hardly avoid both numerical instability and numerical oscillation. The use of a higher-order upwind scheme is a way to avoid these numerical errors and to reduce the computational cost. The influence of numerical viscosity, however, tends to become too large for the turbulent flow where eddy viscosity of LES works without any carefulness to the use of a upwind scheme.

It is preferable that numerical viscosity works to avoid numerical instability at non-turbulent area where strong shear exist but eddy viscosity generated by the dynamic procedure is restraint, and furthermore, that eddy viscosity works effectively with a minimum influence of numerical viscosity at turbulent area. In order to realize this, we employ methods to reduce the influence of the numerical viscosity of upwind scheme at the area where eddy viscosity of LES must work. The decrease of the coefficient of numerical diffusion terms of a 3rd-order upwind scheme and the extension of LES filter are the methods to suppress the influence of numerical viscosity. By applying these methods to the complex turbulent flow, the effect of eddy viscosity exceeds that of numerical viscosity, on the other hand it is possible to avoid numerical instability.

Nozawa *et al.* (1996) apply LES using the 3rd-order upwind scheme to turbulent channel flows at $Re_\tau = 180$, where subgrid-scale eddy viscosity is generated by the dynamic procedure. In this simulation, filter width ($\bar{\Delta}$) of LES was set to be $2h$ and $4h$ (h is grid size) instead of $1h$ and the coefficient of numerical diffusion terms of 3rd-order upwind scheme was decreased (the coefficient of numerical diffusion terms was decrease one-third of that of Kawamura and Kuwahara (1984)). The mean velocity profiles agreed well with DNS data and the turbulent intensities were also improved to match the DNS data. From the result it is possible to suppress the numerical effect due to the choice of the filter width and decreasing the coefficient of numerical diffusion terms.

In this paper, the methodology is applied to the complicated flow past a square cylinder at $Re = 22,000$. Mean and fluctuating velocities are compared with those of experiment. In this calculation, the technique of embedded meshes is also employed for the computation of turbulent flows with various scales to fine the resolution in the vicinity of the body. This study aims to check the validity of reducing the effect of numerical dissipation in LES, and to clear the reason of restriction of improvement on this way.

NUMERICAL METHOD

The numerical procedures are based on the MAC method. For the time marching, we use the first order Euler's explicit scheme. On spatial discretization the second-order central differencing is employed except the convective terms. Third-order upwind scheme is employed for the convective terms.

$$\left[c\frac{\partial u}{\partial x}\right]_i = c_i \frac{-u_{i+2} + 8u_{i+1} - 8u_{i-1} + u_{i-2}}{12h} + \alpha\,|c_i|\,\frac{u_{i+2} - 4u_{i+1} + 6u_i - 4u_{i-1} + u_{i-2}}{12h} \quad (1)$$

The second term of the right hand side of eq.(1) is a numerical diffusion term, and the coefficient, α, is the parameter to decrease the numerical viscosity in this study. The

Table 1: Case specification

	$\alpha = 3$	$\alpha = 1$	$\alpha = 0.5$
$\bar{\Delta}/h = 1$	K1	U1	—
$\bar{\Delta}/h = 2$	K2	U2	H2
$\bar{\Delta}/h = 4$	K4	U4	H4
no LES	K0		

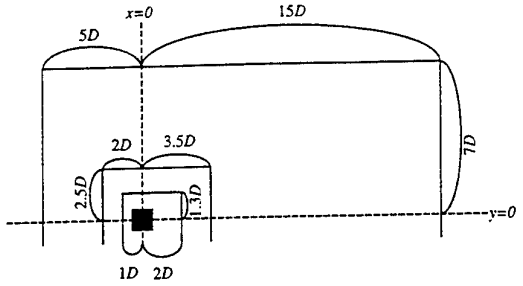


Figure 1: Computational domain.

pressure field is obtained by solving Poisson equation using SOR (successive over-relaxation method).

Periodic boundary condition is employed at the spanwise and transverse directions. Velocity data at the periodic boundary are exchanged every time step, and pressure data are exchanged every iteration step. The convective type outflow boundary condition is employed at outflow boundary and the convective velocity is set to be uniform inflow velocity. The pressure gradient at outflow boundary is set to be zero. At the surface of the cylinder, non-slip boundary condition is employed, and no wall function is employed.

Here, we apply the dynamic subgrid-scale model based on the Smagorinsky model by Germano *et al.* (1991). The model coefficient C is evaluated using the least square approach by Lilly (1992). The dynamic model based on the Smagorinsky model used to overestimate the backward-scatter and it will cause numerical instability without using any stabilizing technique (see Ghosal *et al.* (1995)). In this study, in order to stabilize, the total viscosity is bounded to be non-negative, although the coefficient C is not averaged over spanwise direction.

Table 1 shows the calculation cases in this study. The variable α in the table correspond with the coefficient, α, of the second term of right hand side of eq.(1). $\bar{\Delta}$ is the width of grid-filter, and h is the size of a grid. In the cases of $\bar{\Delta}/h = 4$, the filter width in the spanwise direction and all the directions in the most outer mesh is $2h$. In the dynamic procedure, test-filter is introduced to calculate the model coefficient, C, and the ratio of test-filter width and grid-filter width is fixed to be 2.0 at all calculation cases.

COMPUTATIONAL CONDITIONS

The computational domain dimension is $20D$ for the streamwise direction, where D is the section dimension, $14D$ for the transverse direction and $4D$ for the spanwise direction (Figure 1). The blockage ratio was about 7%. The approaching flow is assumed to be uniform (U_0) on the inflow surface boundary and the Reynolds number based on the inflow velocity, U_0, and the breadth of the square cylinder, D, is 22,000.

Table 2: Number of nodes

N_{1x}, N_{1y}, N_{1z}	121	114	42
N_{2x}, N_{2y}, N_{2z}	89	81	50
N_{3x}, N_{3y}, N_{3z}	111	109	66

In this study, the technique of embedded meshes is employed. The whole Computational domain is covered with three Cartesian non-staggered grids. The size and the location of each mesh could be seen in Figure 1 and the origin is taken at the center of the square cylinder. The number of nodes of each mesh is also shown in Table 2, where N_{mi} denotes the number of grid points in i direction of mth mesh from outside. For the most inner mesh, which covers the cylinder, unequal discretization is used to concentrate the grids in the near-wall region and the region where the shear layer separated from the forward corner of the cylinder locates. The size of the finest grid near windward face is $D/200$, $D/100$ at the face parallel to the flow, $D/50$ at the leeward face. The thickness of laminar boundary layer formed in the windward face, is about $D/40$ at the corner of the square cylinder. From this, there are at least a few grids in the boundary layer of the surface of the cylinder. The most outer mesh is also stretched to save the grid points. In order to capture the three-dimensional behavior of the separated shear flow, which will have influence on the character of flow, the resolution of the spanwise direction is set to be $D/16$ at the most inner mesh.

In this study, totally nine simulations are performed with same computational conditions except the size of numerical viscosity and the size of grid-filter. Non-dimensional time step size of this calculation is 0.0008 (tU_0/D) and it costs about 19 hours per one shedding cycle on one processor of FUJITSU VX.

RESULTS AND DISCUSSION

For evaluation of statistics, data are taken every 0.1 non-dimensional time (tU_0/D), and all the averaging are computed over at least ten shedding cycles and the homogeneous direction. No blockage correction are applied to the data. In this study, some of the data is taken phase averaging procedure, and phase-averaged v (transverse) velocity profile is traced as the trigger for matching the first phase (see Rodi *et al.* (1995)).

Mean and fluctuating forces

The mean drag coefficients, C_D, are illustrated in Figure 2. In this study, C_D are overestimated compared with those of experiments, in which C_D are in the range from 2.0 to 2.25. If the blockage effect is in account, C_D will reduce by 10 percent, but it is still overestimating. We can see the relation between drag coefficient and the two parameter, α and $\bar{\Delta}$, that the combination of extended grid-filter and small coefficient of numerical diffusion terms reduce an overestimating C_D in this study. The most overestimating value of C_D is 2.72 at case K1 ($\alpha = 3.0$, $\bar{\Delta} = 1h$), and it will be improved to 2.44 at case H4 ($\alpha = 0.5$, $\bar{\Delta} = 4h$).

The simulated values of root mean square of drag coefficient, $rmsC_D$, and root mean square of the lift coefficient, $rmsC_L$, are plotted at the higher edge of the experimental data, although the experimental data are scattered (Figure 3, 4) . The simulated $rmsC_L$ seems to be converged to 1.6-1.7, according as the size of grid-filter.

Figure 5 shows the mean wind pressure coefficient of case H4 on the surface of the cylinder, compared with experimental data by Lee (1975) and by Otsuki *et al.* (1978). The other simulated cases are not shown here because of the similar distribution feature of pressure. In the windward face, the simulated pressure distribution correspond

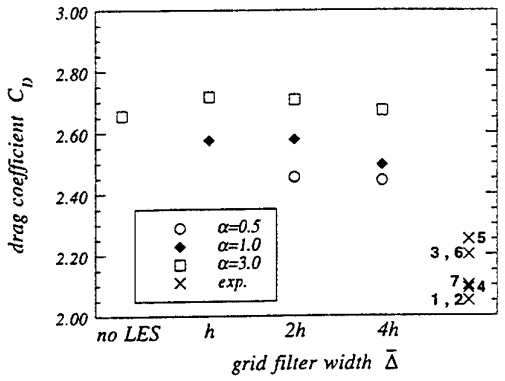


Figure 2: Comparison of mean drag coefficient with experiment: ×, experiments (1, Vickery (1966); 2, Lee (1975); 3, Laneville *et al.* (1975); 4, Otsuki *et al.* (1978); 5, Mizota and Okajima (1981); 6, Bearman and Obasaju (1982); 7, McLean and Gartshore (1992)).

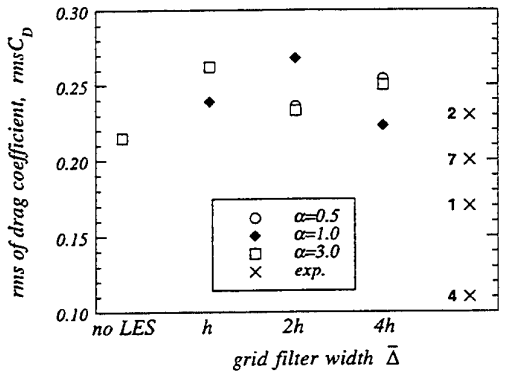


Figure 3: Comparison of rms drag coefficient with experiment.: ×, experiments (For symbol key, see caption to Figure 2).

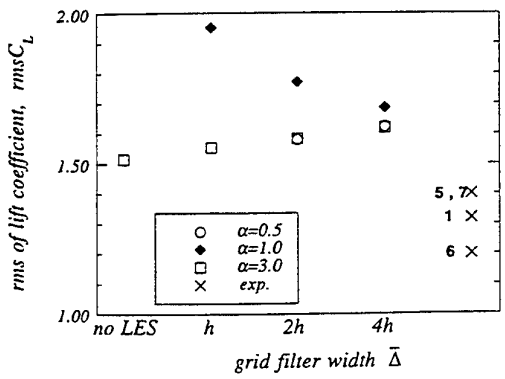
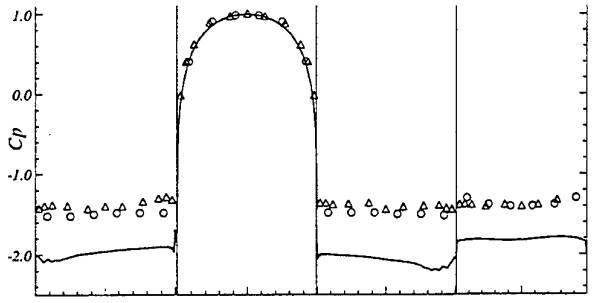
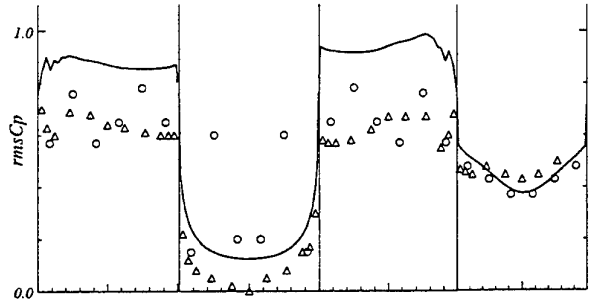


Figure 4: Comparison of rms lift coefficient with experiment.: ×, experiments (For symbol key, see caption to Figure 2).



(a) mean pressure coefficient



(b) rms pressure coefficient

Figure 5: Mean and fluctuating pressure coefficient on the surface of the cylinder compared with experiment: ——, case H4; ○, Lee (1975); △, Otsuki *et al.* (1978).

well with the experiments. Except the windward face, the wind pressure coefficient $-C_p$ is overestimated at all faces compared with experiment. In the leeward face, base pressure coefficient is about 1.8, while it is about 1.4 in experiment data, and this causes excessive drag in this study. Anyway, it is interesting that these features are improved by the combination of extended grid-filter and small numerical viscosity accord with decrease of the coefficient of numerical diffusion terms. The pressure distribution, however, doesn't improved enough to reduce C_D to be 2.0-2.1 as many experimental results show.

Mean velocity distribution in the wake

Figure 6 shows mean streamwise velocity profiles in case H2 and case K1 at center axis of wake. Most remarkable difference between experiment and simulation is that the recircluation zone located behind the cylinder is very small. The recirculation lengths, l_R, which is measured from the origin in this study, are all in the range 0.97–1.21, and are very short compared with experimental result ($l_R = 1.38$ by Lyn (1992) and $l_R = 1.50$ by Mizota and Okajima). The maximum negative streamwise velocity is also small in this recirculation region.

Periodic and stochastic velocity components

The instantaneous velocity, $u(t)$ can be decomposed into ensemble-averaged (average over space and time) component, U, and fluctuating component, $u'(t)$ ($u'(t) = u(t) - U$). In the flow where periodic vortex shedding exist, fluctuating velocity, $u'(t)$, can be also decomposed into periodic component, $\tilde{u}(t)$, and stochastic component, $u''(t)$ ($u''(t) = u'(t) - \tilde{u}$).

Figure 7 shows the intensity of periodic transverse velocity, $\langle\tilde{v}\tilde{v}\rangle$, of case K1 and H2, at center axis of wake. $\langle\ \rangle$ indicates a ensemble-averaged quantity. In case H2,

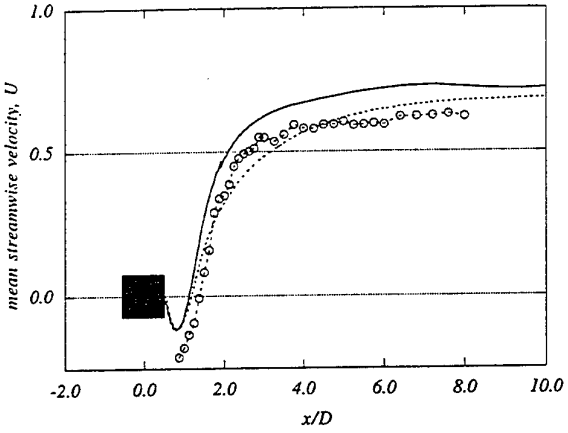


Figure 6: Mean streamwise velocity profiles compared with experiment at $y = 0$: ——, case H2; ----, case K1; -o-, Lyn (1992).

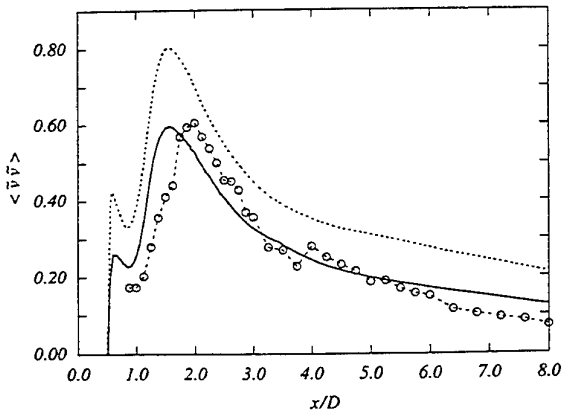


Figure 7: Periodic velocity component, $\langle \tilde{v}\tilde{v} \rangle$, compared with experiment at $y = 0$: ——, case H2; ----, case K1; -o-, Lyn (1992).

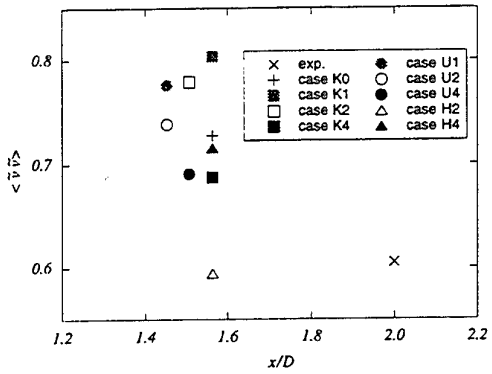


Figure 8: Maximum value of periodic velocity component, $\langle \tilde{v}\tilde{v} \rangle$, at $y = 0$: ×, Lyn(1992).

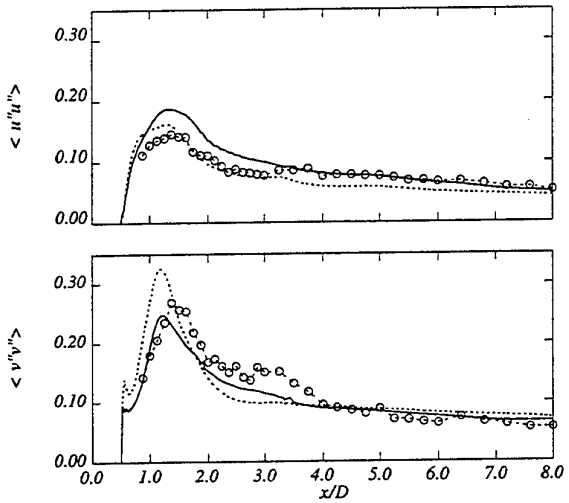


Figure 9: Stochastic velocity component, $\langle u''u'' \rangle$, $\langle v''v'' \rangle$, compared with experiment: ——, case H2; ----, case K1; -o-, Lyn (1992).

the profiles agree well with experiment compared with case K1, but the location of maximum value shift toward the cylinder. The shift of the location of the maximum value toward the cylinder can also be seen in all the other cases. The maximum values on each cases at center axis of wake are plotted on Figure 8. Except the case H2, all the cases overestimate maximum value from 13% to 33%, but extension of grid-filter improve the overestimating maximum value. Wake region is fully turbulent so that it is more effectual to use wider grid-filter to avoid the influence of numerical viscosity. The stochastic component of fluctuating velocity intensity is not small in this flow (Figure 9). In both direction, $\langle u''u'' \rangle$ and $\langle v''v'' \rangle$ are in good agreement with experiment at $x \approx 4.0$ and its downstream. The location of maximum value shift upstream, and this correspond to that of periodic component. The maximum value of $\langle v''v'' \rangle$ of this study is in the range 0.17–0.33, and there is no relation between the maximum value and the change of the grid-filter size or the coefficient of numerical diffusion terms.

The shear layer region

The flow separated from the forward corner of the cylinder, formed strong shear layer in the side, and this feature of this determined the whole character of the flow. The mean streamwise velocity, U, profile of case K1 and H4 at $x = 0.0$ is shown in Figure 10. The shear layer in this

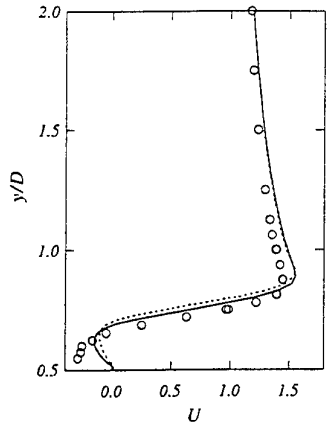


Figure 10: Mean streamwise velocity profiles compared with experiment at $x = 0$: ——, case H2; ----, case K1; -o-, Lyn (1992).

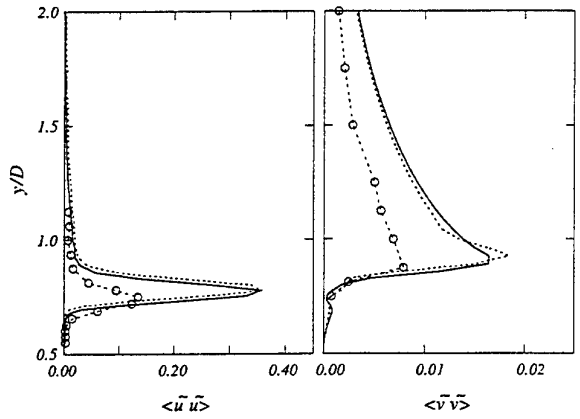


Figure 11: Periodic component of fluctuating velocity compared with experiment at $x = 0$: ——, case H2; ----, case K1; -o-, Lyn (1992).

study is formed a little further from the sidewall of the cylinder compared with experiment. This feature can be seen in all the other calculated cases.

A periodic component of fluctuating velocity in the side is caused by flapping of the shear layer due to the shedding of Kàrmàn vortices. Figure 11 shows streamwise and transverse intensities of periodic velocity component, $\langle\tilde{u}\tilde{u}\rangle$, $\langle\tilde{v}\tilde{v}\rangle$, of case K1 and H2 at $x = 0.0$. In all the numerical cases $\langle\tilde{u}\tilde{u}\rangle$ and $\langle\tilde{v}\tilde{v}\rangle$ are overestimated at the shear layer region compared with experiment. Most of the cases has twice as large as periodic component than experimental one. The methodology suggested in this study doesn't improve these overestimated quantities.

In this numerical study, the difference of stochastic component, $\langle v''v''\rangle$, from those of experiment is quite remarkable (Figure 12). The underestimating of $\langle v''v''\rangle$ can be improved with decreasing the numerical viscosity from numerical diffusion terms. The maximum value of $\langle v''v''\rangle$ is still 25% of that of experiment by Lyn (1992). The stochastic component of fluctuating transverse velocity in a shear layer has something to do with the transition to turbulence. The lack of transverse stochastic component, therefore, might be a fatal feature to simulate a flow around a square cylinder correctly.

Figure 13 shows the spanwise correlation of fluctuating pressure difference across the center line. High correlation in spanwise direction might come from the weak fluctuating

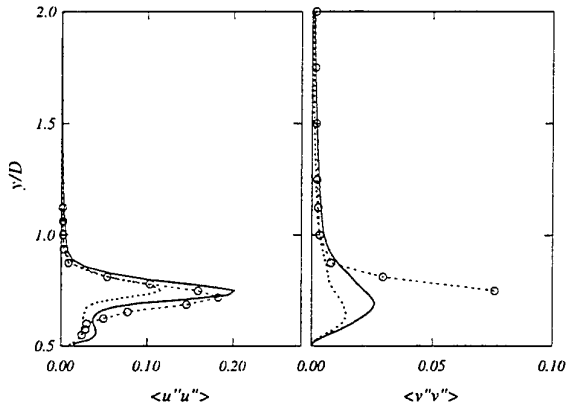


Figure 12: Stochastic component of fluctuating velocity compared with experiment: ——, case H2; ----, case K1; -o-, Lyn (1992).

Table 3: Maximum value of stochastic component of fluctuating velocity intensity, $\langle v''v''\rangle$, at $x = 0$

	$\alpha = 3$	$\alpha = 1$	$\alpha = 0.5$
$\bar{\Delta}/h = 1$	0.0140	0.0227	—
$\bar{\Delta}/h = 2$	0.0185	0.0216	0.0257
$\bar{\Delta}/h = 4$	0.0172	0.0211	0.0261
no LES	0.0224		

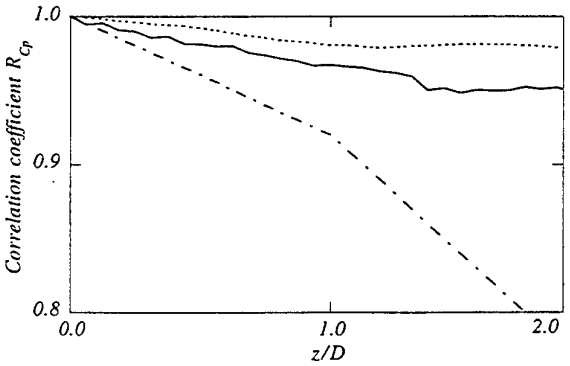


Figure 13: Spanwise correlation of the fluctuating pressure difference across the center line ($x = 0$):——, case H2; ----, case K1; — - —, Vickery (1966).

of shear layer in the spanwise direction, and this causes strong force to the side of the cylinder. The small aspect ratio ($H/D = 4$) might be a reason of the strong two-dimensional flow. The lack of the stochastic component of fluctuating transverse velocity is also a factor of the high correlation.

CONCLUSION

We suggest the method to avoid the influence of numerical viscosity caused by using necessary evil upwind scheme in large eddy simulation for the complex turbulent flow around a bluff body. The methodology to reduce the influence of numerical viscosity is to use extended grid-filter to the LES and to decrease the coefficient of numerical diffusion terms of 3rd order upwind scheme. We apply this methodology to the flow around a square cylinder, and check the validity of this methodology.

The extended grid-filter combined with the small α reduce the overestimating drag coefficient from 2.72 to 2.44. These changes don't work at excessive $rmsC_D$ and $rmsC_L$. The recirculation region behind the cylinder is small at all the calculated cases, and the maximum negative streamwise velocity is also underestimated compared with experiment. The periodic component of fluctuating velocity is improved with the methodology suggested in this study. One of the characteristic feature in this numerical study is the lack of the stochastic component of fluctuating transverse velocity at $x = 0.0$, where the shear layer is formed. The use of small α will recover the stochastic component, but it is not enough, yet, compared with experiment.

In a case of a square cylinder, a characteristic feature of a shear layer separated from a forward corner has strong influence to a whole flow. In this study, the shear layer is not fully turbulent with the laminar inflow, and the effect of SGS stress is not strong. From this aspect the decrease of numerical viscosity is more effective than using extended grid-filter. In the case that a characteristic feature of a fully turbulent flow has strong influence to a whole flow, however, the use of extended grid-filter has more effectiveness.

REFERENCES

Bearman, P. W. and Obasaju, E. D., 1982, "An experimental study of pressure fluctuations on fixed and oscillating square cylinders", *J. Fluid Mech.*, Vol. 119, pp. 297–312.

Germano, M., Piomelli, U., Moin, P. and Cabot, W. H., 1991, "A dynamic subgrid-scale eddy viscosity model", *Phys. Fluids* A 3(7), pp. 1760–1765.

Kawamura, K. and Kuwahara, K., 1984, "Computation of high Reynolds number flow around a circular cylinder with surface roughness", *AIAA-84-0340.*

Laneville, A., Gartshore, I. S. and Parkinson, G. V., 1975, "An explanation of some effects of turbulence on bluff bodies", *Proc. 4th Int. Conf. Wind Effects on Buildings and Structures*(London), Cambridge Univ. Press.

Lee, B. E., 1975, "The effect of turbulence on the surface pressure field of a square prism", *J. Fluid Mech.*, Vol. 69, pp. 263–282.

Lilly, D. K., 1992, "A proposed modification of the Germano subgrid-scale closure method", *Phys. Fluids* A 4(3), pp. 633–635.

Lyn, D. A., 1992, *ERCOFTAC Database*, Case 43.

Lyn, D. A. and Rodi, W., 1994, "The flapping shear layer formed by flow separation from the forward corner of a square cylinder", *J. Fluid Mech.*, Vol. 267, pp. 353–376.

McLean, I. and Gartshore, I., 1992, "Spanwise correlations of pressure on a rigid square section cylinder", *J. Wind Eng. Ind. Aero.*, 41–44, pp. 797–808.

Mizota, T. and Okajima, A., 1981, "Experimental studies of time mean flows around rectangular prisms", *J. Civil Eng., Trans. of JSCE*, 327, pp. 49–58 (in Japanese).

Nozawa, K., Tamura, T. and Takakuwa, A., 1996 "Large eddy simulation using 3rd-order upwind scheme – testing with turbulent channel flows", *Proc. 28th Symposium on Turbulence*, pp.257-258 (in Japanese).

Otsuki, Y., Fujii, K., Washizu, K. and Ohya, A., 1978. "Wind Tunnel experiments on aerodynamic forces and pressure distributions of rectangular cylinders in a uniform flow", *Proc. of the 5th Symposium on Wind effect on Structures*, pp. 169–175 (in Japanese).

Rodi, W., Ferziger, J. H., Beruer, M. and Pourquie, M., 1995, *Workshop on Large Eddy Simulation of Flows past Bluff Bodies.*

Vickery, B. J., 1966, "Fluctuating lift and drag on a long cylinder of square cross-section in a smooth and in a turbulent stream". *J. Fluid Mech.*, Vol. 25, pp. 481–494.

WAVELET VELOCITY CORRELATION ANALYSIS IN A PLANE TURBULENT JET

Hui LI
Department of Mechanical Engineering
Kagoshima University
1-21-40, Korimoto
Kagoshima City 890
JAPAN

ABSTRACT

In present study, the definition of the wavelet spatial statistics using wavelets are first proposed, in order to study the characteristics of statistics in both frequency and physical space. Then, the wavelet spatial statistics are used to analyzing the coherent structure of large scale eddy motions and the structure of the energy transfer over a two-dimensional frequency-physics plane in a plane jet. It is found that in the shear layer of the near field the behavior of wavelet Reynolds stress reversals are clearly observed at several frequencies and developed at x/b_0=2, 6 and 10. This phenomenon indicates that fluctuation energy is reversed back into the mean flow, and the interaction between positive and negative production at different frequencies dominates the eddy formation and the merging process in the developing region.

INTRODUCTION

The plane jet is a commonly used model for study of the two-dimensional turbulent flow or eddy structure. Since Crow and Champagne (1971) first studied the coherent structure of a turbulent jet, the physics of a plane turbulent jet has been widely investigated for several decade years. It has become well-known fact that the large-scale eddy motion of the plane turbulent jet exhibits an symmetric, periodic and apparent flapping motion in similarity region, and the evolution and interaction of large-scale organized structures play an important role in a turbulent jet spreading and momentum transfer. Until now the conventional statistical methods, such as, space-time correlation functions, spectra, coherent functions, conditional sampling methods and visualization techniques are well established usual techniques for gaining information regarding the nature of turbulent structure or eddy motion. However, turbulence or eddy motion is characterized by the existence of multiple spatial scales, some important spatial information are lost owing to the non-local nature of the Fourier analysis. For example, conventional statistical methods can not reveal the behavior of Reynolds stress reversals in scale space. The visualization of organized motions in shear layers also showed that the conditional sampling measurement had been hiding very important features of turbulence, as pointed by Laufer (1975).

In recent 15 years, there has been growing interest in the wavelet analysis of signals, which can combine time-space and frequency-space analyses to produce a potentially more revealing picture of time-frequency localization of signals. As a tool for analysis of multiscale signals, the wavelet transform was originated in geophysics in early 1980's for the analysis of seismic signal. Now, wavelet analysis has been formalized into a rigorous mathematical framework and have been applied to numerous diverse areas such as mathematics, physics, turbulence, signal processing, image processing, numerical analysis, nonlinear dynamics, fractal, and multifractal analysis, and others.

However, the wavelet analysis is relatively new to the field of turbulence, having mostly been developed in the present decade, and have not yet been applied to their full potential in this area of fluid mechanics. Recent reviews on wavelets and related multiscale techniques in turbulence were presented by Farge et al. (1996). Until now the wavelet analysis has been widely used to reveal various turbulent or eddy structure, such as, fully developed turbulence, jet, boundary layer, mixing layer, wake flow, surface wave field, multiphase flow and others. In this paper we only describe the application of the wavelet analysis to the experimental study of jet.

In the limited open literature available, Everson et al. (1990) analyzed two-dimensional dye concentration data from a turbulent jet using the wavelet transform, and revealed the nature and self-similarity of the inner structure of the jet. Lewalle et al. (1994) applied the wavelet transform to velocity signals in the inner mixing layer of a coaxial jet and analyzed the dominance of non-periodic vortices at a given time scale. Li and Nozaki (1995a) displayed very different scale eddies, the breakdown of a large eddy and the successive branching of a large eddy structure in a plane turbulent jet by analyzing the

velocity signals at various positions with the wavelet transform. A wavelet decomposition of fluctuating velocities in a planar jet was used to the Reynolds stress in scale space by Gordeyev and Thomas (1995). Walker et al. (1995) investigated the multiple acoustic modes and the shear layer instability waves of the jet by wavelet transform. Using wavelet decomposition the unsteady aspects of the transition of a jet shear layer are studied by Gordeyev et al. (1995). In order to reveal the self-similarity of the structure of eddy motion in a plane turbulent jet in both scale and time delay, Li and Nozaki (1995b, 1996, 1997) and Li (1997) proposed a wavelet auto-correlation and wavelet cross-correlation analysis based on the wavelet transform. Besides these application studies, several new tools and diagnostics based on the wavelet transform, such as, wavelet intermittency, wavelet Reynolds number, local wavelet spectrum and wavelet correlation functions were developed, and they offer the potentials extracting new information from various flow fields. However, the distribution of Reynolds stress reversals in frequency space and physical space have not been clear yet. In order to extract new information of turbulent flows that can not be obtained by conventional statistical methods, it is necessary to develop new analytical techniques.

The major objective of this work is to develop a few new definitions of wavelet statistical quantities using wavelet transform, such as, wavelet Reynolds stress, wavelet triple velocity correlation, wavelet skewness and flatness factors, and characterizes the distribution of these wavelet statistical quantities in both frequency-space and physical-space.

Then, these wavelet statistical quantities are applied to the near field flow structure analysis of a plane turbulent jet, and reveal the turbulence and eddy structure in both frequency-space and physical-space.

CONTINUOUS WAVELET TRANSFORM

For completeness, a brief review of the continuous wavelet transform is described. The wavelet transform of a real square integrable signal $s(t)$ with finite energy is defined as the integral transform with a family of functions $\psi_{f,t}(b) = f\psi^*(f(b-t))$ called wavelets and given as

$$\begin{aligned} WT(t,f) &= \int_{-\infty}^{\infty} s(b)\psi_{f,t}(b)db \\ &= f\int_{-\infty}^{\infty} s(b)\psi^*(f(b-t))db \end{aligned}, \qquad (1)$$

where $WT(t,f)$ is called the *wavelet coefficients* of $s(t)$ with respect to the analyzing wavelet $\psi(t)$, f and t are a dilatation parameter and analyzing position (here * stands for complex conjugate), respectively.

$\psi(t)$ is a function of $L^2(\Re)$ called an *analyzing wavelet* or *mother wavelet*, the choice of $\psi(t)$ is neither unique nor arbitrary. The function $\psi(t)$ is a function with unit energy chosen so that it has: (1) compact support, or sufficiently fast decay, to obtain localization in space; (2) has zero mean, i.e., $\int_{-\infty}^{\infty}\psi(t)dt = 0$. The requirement of zero mean is called the *admissibility condition.*

It is well known that several wavelet functions, such as Mexican hat, Morlet and Gabor function, are commonly used as an analyzing wavelet. The choice of the appropriate wavelet function depends on the kind of information what we want to extract from the signal. In this study we choose to use the following complex-valued, modulated Gaussian analyzing wavelet known as the Morlet wavelet.

$$\psi(t) = e^{-i\omega_0 t} - e^{-\omega_0^2/2} e^{-\frac{t^2}{2}}, \qquad \omega_0 \geq 5. \qquad (2)$$

Since for $\omega_0 \geq 5$, the second term in (2) can be negligible, which is usually approximated as

$$\psi(t) = e^{-i\omega_0 t} e^{-\frac{t^2}{2}}. \qquad (3a)$$

The Morlet wavelet is complex-valued, enabling one to extract information about the amplitude and phase of signal being analyzed. Its Fourier transform can be written as

$$\hat{\psi}(\omega) = \sqrt{2\pi} e^{-\frac{(\omega-\omega_0)^2}{2}}. \qquad (3b)$$

It is apparent that Morlet wavelet $\psi(t)$ is localized around $t=0$, and $\hat{\psi}(\omega)$ is localized around the central frequency $\omega_c = \omega_0$. Same as previous paper (Li, 1997), the central frequency is defined as $\omega_c = \omega_0 = 2\pi$, so that the wavelet dilatation parameter f represents a frequency. Then $f\psi^*(f(b-t))$ is localized around the position t and around the central frequency f. From Eq.(1) the wavelet coefficient using Morlet wavelet may describe a signal as localized strength of the signal over a time-frequency plane.

If the analyzing wavelet $\psi(t)$ satisfies the admissibility condition, the signal $s(t)$ can be retrieved from the wavelet coefficient by

$$s(t) = \frac{1}{C_\psi}\int_0^{\infty}\int_{-\infty}^{\infty} WT(f,b)\psi(f(t-b))df db, \qquad (4)$$

where $C_\psi = \int_{-\infty}^{\infty}\frac{|\hat{\psi}(\omega)|^2}{|\omega|}d\omega$. Equation is called the inverse wavelet transform formula. The wavelet transform is also an energy preserving transformation, i.e., an isometry,

$$\int_{-\infty}^{\infty} s(t)s^*(t)dt = \frac{1}{C_\psi}\int_0^{\infty}\int_{-\infty}^{\infty} WT(f,b)WT^*(f,b)df db, \qquad (5)$$

which is a generalization of Parseval's theorem. This expression shows that the wavelet coefficient $WT(t,f)$ is the energy of $s(t)$ for the frequency f at the position (or time) b, and $WT(f,b)WT^*(f,b)$ is called a *scalogram.*

In general, for two function *s(t)* and *g(t)* we have

$$\int_{-\infty}^{\infty} s(t)g^*(t)dt = \frac{1}{C_\psi}\int_0^{\infty}\int_{-\infty}^{\infty} WT_s(f,b)WT_g^*(f,b)df db, \qquad (6)$$

where the product $WT_s(f,b)WT_g^*(f,b)$ can be called a *cross scalogram.*

WAVELET SPATIAL STATISTICS

The purpose of this section is to develop a few new tools for characterizing the local statistics at every scale in turbulent flows based on the wavelet transform. In usual statistics analysis, the power spectral density or correlation functions provide a measure of the relevance of each scale of motion, however, important spatial information is lost owing to the non-local nature of the Fourier modes. In order to overcome limitations of the usual statistics, we define the wavelet velocity correlation functions, including wavelet Reynolds stress function and wavelet triple velocity correlation function, and use them to reveal more detailed information about the turbulence in more complete statistical terms in this paper.

Wavelet Reynolds Stress Function

It is well known that the Fourier analysis can not describe the distribution of Reynolds stress reversals in frequency space due to its the non-local nature. However, The information about Reynolds stress reversals is very important for analyzing the structure of the energy transfer in the turbulence. In this section we develop the wavelet Reynolds stress function using the continuous wavelet coefficients of the fluctuating velocity, which can describe the Reynolds stress distribution in frequency space.

In general, the conventional Reynolds stress component $-\overline{u_i u_j}$ can be written as the following form

$$-\overline{u_i u_j} = -\frac{1}{T}\int_{-\infty}^{\infty} u_i(t)u_j(t)dt = -\frac{1}{T}\int_{-\infty}^{\infty}\int_{-\infty}^{\infty} \hat{u}_i(\omega_1)\hat{u}_j(\omega_2)d\omega_1 d\omega_2 \quad (7)$$

where T is an average time.

As mention above, the wavelet coefficients can describe a signal as strength of the signal at a given frequency and time, which is a zero-mean random process. In the present study, we use wavelet coefficients $Wu_i(t,f)$ and $Wu_j(t,f)$ of fluctuating velocity components u_i and u_j to define a new Reynolds stress function, which is called a *wavelet Reynolds stress function* $-\overline{Wu_i Wu_j}(f)$, by the formula

$$-\overline{Wu_i Wu_j}(f) = -\frac{1}{T}\int_{-\infty}^{\infty} Wu_i(f,t)Wu_j(f,t)dt, \quad (8)$$

where $-\overline{Wu_i Wu_j}(f)$ is called *wavelet shear stress* for $i \neq j$, and is called *wavelet normal stress* or *wavelet fluctuation intensity* for $i = j$. From Eq.(6), the relation between From $-\overline{u_i u_j}$ and $-\overline{Wu_i Wu_j}(f)$ can be written as

$$\begin{aligned} -\overline{u_i u_j} &= -\frac{1}{T}\int_{-\infty}^{\infty} u_i(t)u_j(t)dt \\ &= -\frac{1}{TC_\psi}\int_0^{\infty}\int_{-\infty}^{\infty} Wu_i(f,b)Wu_j^*(f,b)dfdb \\ &= -\frac{1}{C_\psi}\int_0^{\infty}\overline{Wu_i Wu_j}(f)df \end{aligned} \quad (9)$$

From above equation it is clear that the wavelet Reynolds stress represents the distribution of the Reynolds stress in frequency space and is a real-valued function. Corresponding to Eq.(7), in Fourier space, Eq.(8) can be rewritten as

$$-\overline{Wu_i Wu_j}(f) = -\frac{1}{T}\int_{-\infty}^{\infty}\int_{-\infty}^{\infty} \hat{u}_i(\omega_1)\hat{u}_j(\omega_2)\bar{\psi}\left(\frac{\omega_1}{f}\right)\bar{\psi}\left(\frac{\omega_2}{f}\right)d\omega_1 d\omega_2 \quad (10)$$

The wavelet Reynolds stress permits the identification of the contributions of the different frequencies to Reynolds stress, which is a quantity directly related to the structures of the flow.

Wavelet Triple Velocity Correlation Function

Analogizing with the wavelet Reynolds stress function, we define the *wavelet triple velocity correlation function* as

$$-\overline{Wu_i Wu_j Wu_k}(f) = -\frac{1}{T}\int_{-\infty}^{\infty} Wu_i(f,t)Wu_j(f,t)Wu_k(f,t)dt. \quad (11)$$

From above equations it is clear that the wavelet triple velocity correlation can also represent the distribution of the velocity correlation in frequency space.

Wavelet Skewness and Flatness Factors

We perform some statistical calculations before averaging in physical space, which will extract more detailed information from the fluctuating velocity. Meneveau (1991) proposed the definition of the flatness factor based on the discrete wavelet transform. For investigating deviations from Gaussian behavior in frequency space, we define the wavelet skewness and flatness factors using continuous wavelet coefficients of the fluctuating velocity as

$$WS(f) = \frac{\overline{Wu^3(f)}}{\left[\overline{Wu^2(f)}\right]^{\frac{3}{2}}}, \quad (12)$$

$$WF(f) = \frac{\overline{Wu^4(f)}}{\left[\overline{Wu^2(f)}\right]^{2}}, \quad (13)$$

respectively. Here the averaging is performed over t at a given frequency. It is believe that such statistical quantities may give useful insight about the spatial properties of turbulence in frequency space.

EXPERIMENTAL APPARATUS AND PROCEDURE

A definition sketch of a plane jet is shown in Fig.1, where x is the streamwise coordinate and y is the lateral coordinate. The jet is generated by a blower-type wind tunnel having flow-straightening elements, screens, and settling length, a 24:1 contraction leading to a 300x20 *mm* nozzle (the nozzle width $2b_0$ is 20*mm*). For all measurements, the jet is operated at a constant Reynolds number *Re*=5000 (exit velocity is 4.8m/s)

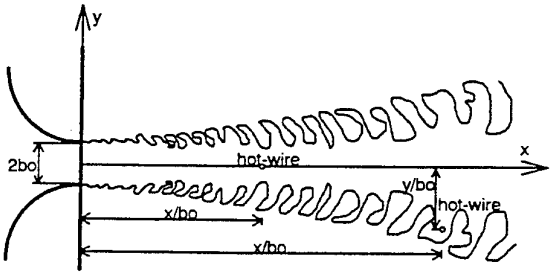


FIGURE 1 Experimental apparatus

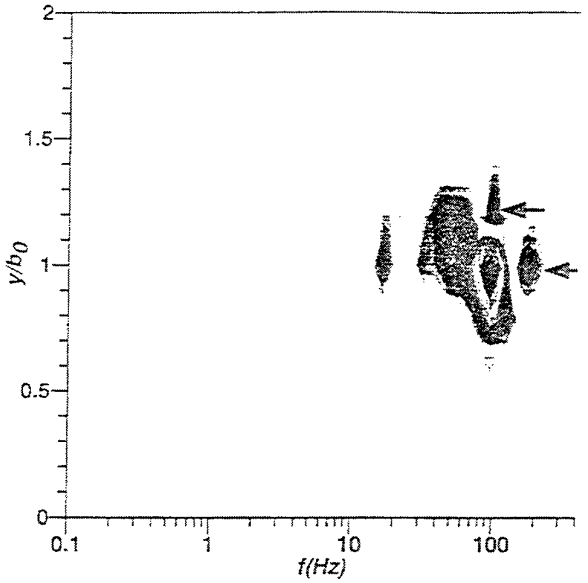


FIGURE 2(a) Variation of $\overline{WuWv}(f)/U_0^2$ cross the jet at x/b_0=2

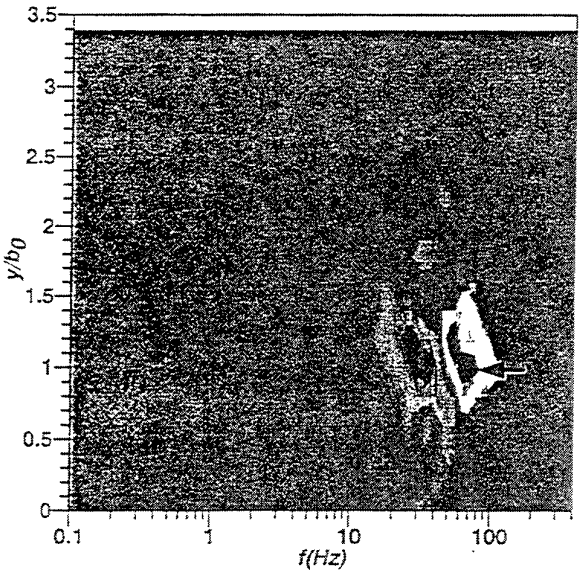


FIGURE 2(b) Variation of $\overline{WuWv}(f)/U_0^2$ cross the jet at x/b_0=6

based upon nozzle width $2b_0$. The velocity components of u, v are measured simultaneously using a X type hot wire probe located in the (x, y)-plane. The recording frequency is 10kHz and the record length is 6 seconds.

RESULTS AND DISCUSSION

Wavelet Shear Stress

It is well known that positive turbulent shear stress $\overline{uv}$ induces positive production, while negative turbulent shear stress exhibit negative production, due to the existence of the negative mean velocity gradient in a jet shear layer region. Until now, this phenomenon of negative production existed in physical space has only been detected in shear layer of excited jet (Hsiao et al, 1994), but distribution of negative production in both frequency space and physical space have not been clear yet

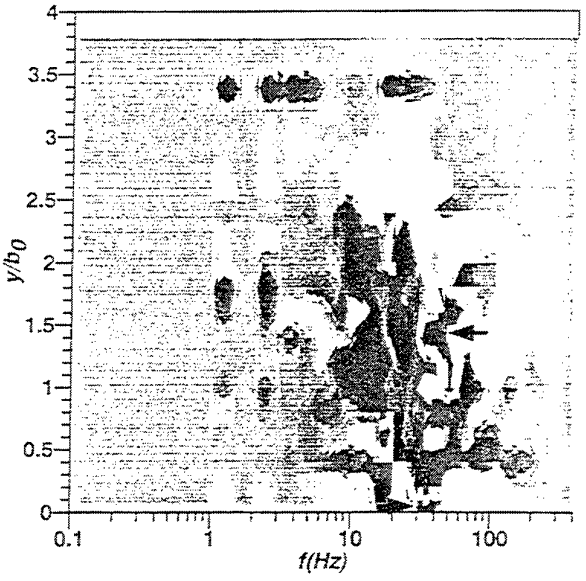


FIGURE 2(c) Variation of $\overline{WuWv}(f)/U_0^2$ cross the jet at x/b_0=10

in a plane jet.

In this paper, the near field characteristics of a plane jet is studied by the wavelet Reynolds stress. Figure 2 shows the distribution of the wavelet Reynolds stress along y-direction at x/b_0=2, 6 and 10. The values of the wavelet Reynolds stress are normalized with respect to the exit velocity U_0^2, while the distance y is normalized by the nozzle half width b_0.

At x/b_0=2, as shown in Figure 2(a), it is apparent that a positive-value region of $\overline{WuWv}(f)/U_0^2$ exits at f=100Hz in the shear layer (y/b_0=1.0), which indicates the maximum turbulent energy. In the neighborhood of this area two negative peaks of $\overline{WuWv}(f)/U_0^2$ (which are pointed by arrows) are observed at f=100Hz and 110Hz around y/b_0=1.2 and 1.0, respectively. It is called *wavelet Reynolds stress reversals*. Physically, this behavior signifies that fluctuation energy is reversed back into the mean flow at two frequencies in the shear layer, and results in a decrease of turbulent energy.

At x/b_0=6 the distribution of $\overline{WuWv}(f)/U_0^2$ along y-direction is shown in Figure 2(b). The frequency of the positive peak in $\overline{WuWv}(f)/U_0^2$ at y=1.0b_0 decreases. This exhibits the growth of eddies in the shear layer. Comparing to x/b_0=4, two evident negative region of $\overline{WuWv}(f)/U_0^2$ become a peak around f=60Hz in the shear layer (y/b_0=1.0), and the frequency of wavelet Reynolds stress reversals decrease.

The variation of $\overline{WuWv}(f)/U_0^2$ at the downstream location x/b_0=10 is presented in Figure 2(c). The negative regions of $\overline{WuWv}(f)/U_0^2$ appear at f=35Hz near central line and at f=40Hz in the shear layer (y/b_0=1.5), and a positive peak of appears at f=1.5Hz around y/b_0=1.5. At this location the potential core fades, and the region of the wavelet Reynolds stress reversals moves toward spreading direction and central line.

The interaction between positive and negative production at different frequency leads to the eddy formation and the merging process in the shear layer, and dominates the jet spreading in the developing region.

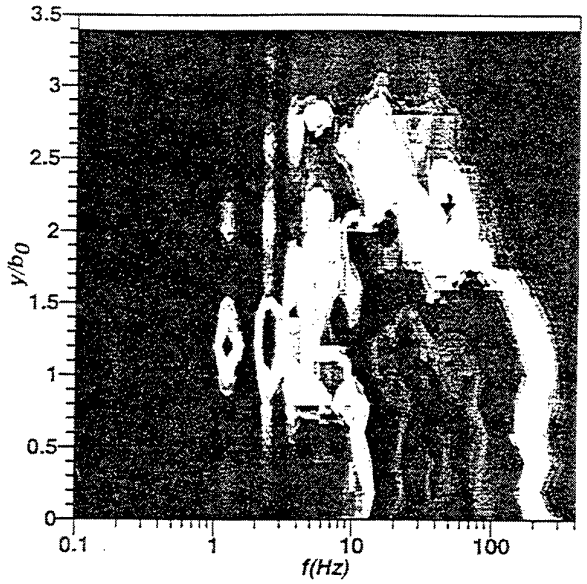


FIGURE 3(a) Variation of $\sqrt{\overline{Wu^2}(f)}/U_0$ cross the jet at x/b_0=6

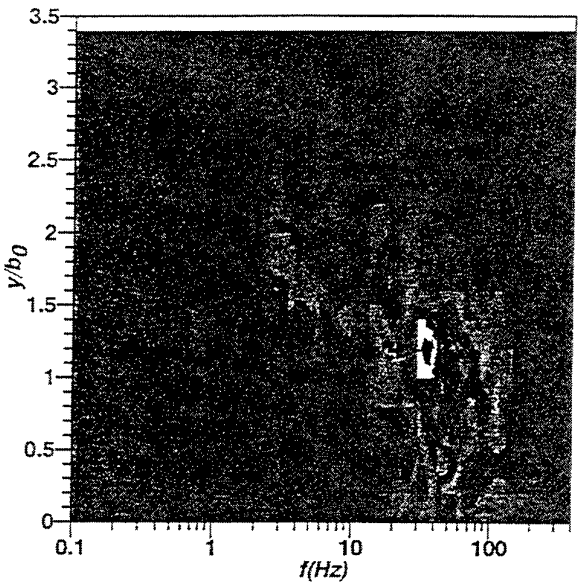


FIGURE 4(a) Variation of $\overline{Wu^2Wv}(f)/U_0^3$ cross the jet at x/b_0=6

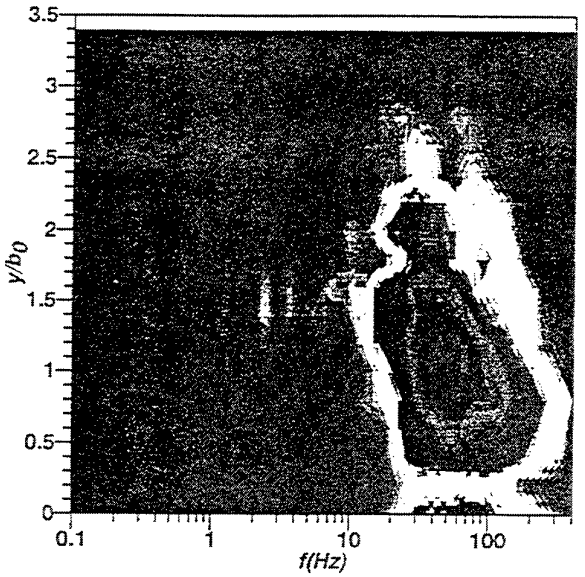


FIGURE 3(b) Variation of $\sqrt{\overline{Wv^2}(f)}/U_0$ cross the jet at x/b_0=6

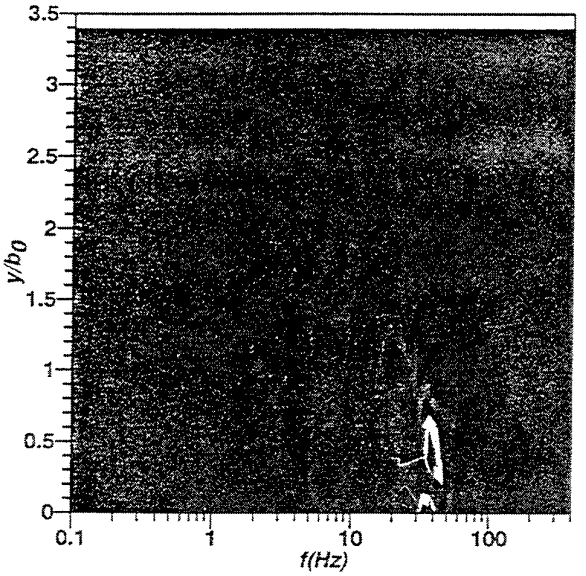


FIGURE 4(b) Variation of $\overline{Wu^3}(f)/U_0^3$ cross the jet at x/b_0=6

Wavelet Fluctuation Intensity

The transverse direction variation in the wavelet fluctuation intensity of $\sqrt{\overline{Wu^2}(f)}$ and $\sqrt{\overline{Wv^2}(f)}$ at x/b_0=6, which is normalized with respect to the exit velocity U_0, are shown in Figure 3. The wavelet fluctuation intensity represents the distribution of the turbulent energy in the frequency space, the energy at various frequencies is transferred from the mean motion directly to $\sqrt{\overline{Wu^2}(f)}$. The interchange of energy between $\sqrt{\overline{Wu^2}(f)}$ and $\sqrt{\overline{Wv^2}(f)}$ is associated with the eddy interaction mechanism, i.e. eddy formation and the merging process. From Figure 3(a), it is evident that local maxima region in $\sqrt{\overline{Wu^2}(f)}/U_0$ is observed from y/b_0=0 to 1.0 around f=30Hz. This signifies that fluctuation intensity at this frequency is much more intense ranging from the centerline to the shear layer, and visualizes that the energy is transferred from the mean motion to $\sqrt{\overline{Wu^2}(f)}$ with this frequency.

The distribution of $\sqrt{\overline{Wv^2}(f)}/U_0$ at x/b_0=6 is shown in Figure 3(b). It is found that the position of local maxima region of fluctuation intensity appears at f=50Hz around y/b_0=1.0. This indicates that the interchange of energy between $\sqrt{\overline{Wu^2}(f)}$ and $\sqrt{\overline{Wv^2}(f)}$ happens at this frequency in the shear layer.

Wavelet Triple Velocity Correlation

The variation of wavelet triple velocity correlation ($\overline{Wu^2Wv}(f)/U_0^3$ and $\overline{Wu^3}(f)/U_0^3$) across the jet are shown in Figure 4. From Figure 4(a) it is found that $\overline{Wu^2Wv}(f)/U_0^3$ attains a maximum around f=50Hz at y/b_0=1.0. The negative peak of $\overline{Wu^2Wv}(f)/U_0^3$ appears in shear layer (y/b_0=1.2) around f=35Hz, which results from the fact that $\overline{Wu^2}(f)/U_0^3$ peaks at positive y and some diffusion of $(Wv(t,f))^2$ with f=35Hz towards the center of the jet occurs.

Figure 4(b) shows the distribution of $\overline{Wu^3}(f)/U_0^3$ across the jet. Two negative peaks with f=35Hz and 40Hz are observed around y/b_0=0 and 0.5, respectively.

Wavelet Flatness Factors

The lateral distribution of $WF(f)$ of u-velocity component in both frequency and physical space at x/b_0=6 is shown in Figure 5. A large region of $WF(f)$ that is larger than Gaussian value 3 is observed around f=30Hz ranging from y/b_0=0 to 1.0.

CONCLUSIONS

In present study, in order to study the characteristics of statistics in both frequency and physical space, the definition of the wavelet spatial statistics using wavelets are developed. Then, the wavelet spatial statistics are used to analyzing the structure of the energy transfer over a two-dimensional frequency-physics plane in a plane jet. It is found that in shear layer of the near field the behavior of wavelet Reynolds stress reversals are clearly observed at several frequencies and developed. The frequency of wavelet Reynolds stress reversals decreases toward downstream. This phenomenon indicates that fluctuation energy is reversed back into the mean flow, and the interaction between positive and negative production at different frequencies dominates the eddy formation and the merging process in the developing region.

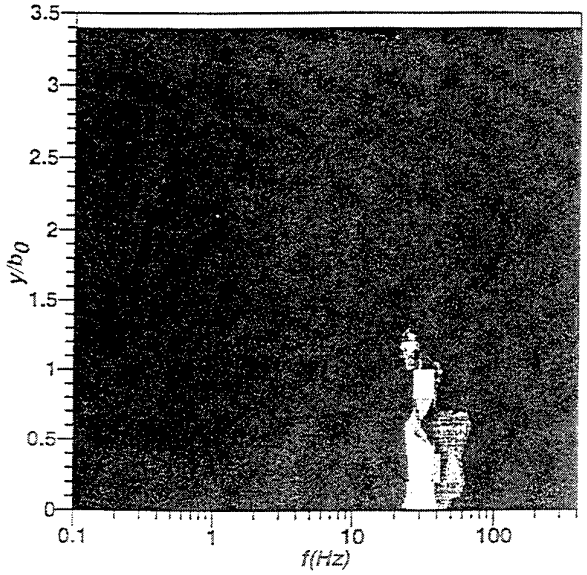


FIGURE 5 Variation of $WF(f)$ cross the jet at x/b_0=6

REFERENCES

Crow, S. C., and Champagne, F. H., 1971, "Orderly Structure in Jet Turbulence", J. Fluid Mech., Vol.48, pp.547-591.

Everson, R. and Sirovich, L., 1990, "Wavelet Analysis of the Turbulent Jet", Phys. Lett., Vol.145, No.6, pp.314-322.

Farge, M., Kevlahan, N., Perrier, V. and Goirand, E., 1996, "Wavelets and Turbulence", Proc. IEEE, Vol.84, No.4, pp.639-669.

Gordeyev, S. V. and Thomas F. O., 1995, "Measurement of Reynolds Stress Reversal in a Planar Jet by Means of a Wavelet Decomposition", Turbulent Flows ASME, FED-Vol.208, pp.49-54.

Gordeyev, S. V., Thomas F. O., and Chu, H. C., 1995, "Experimental Investigation of Unsteady Jet Shear Layer Dynamics Using a Wavelet Decomposition", Unsteady Flows ASME, FED-Vol.216, pp.167-172

Hsiao, F. B. and Huang, J. M., 1994, "On the Dynamics of Flow Structure Development in an Excited Plane Jet", ASME Journal of Fluids Engineering, Vol.116, No.4, pp.714-720.

Laufer, J., 1975, "New Trends in Experimental Turbulence Research", Ann. Rev. Fluid Mech., Vol.7, pp.307-320.

Lewalle, J., Petagna P. and Buresti G., 1994, "Wavelet Statistics of the Near-Field Structure of a Coaxial Jet", AIAA Paper 94-2323.

Li, H., 1997, Wavelet Auto-correlation Analysis and Its Application to Experimental Studies", to be published in ASME, Journal of Fluids Engineering.

Li, H. and Nozaki, T., 1995a, "Wavelet Analysis for the Plane Turbulent Jet (Analysis of Large Eddy Structure)", JSME International Journal, Fluids and Thermal Engineering, Vol.38, No.4, pp.525-531.

Li, H. and Nozaki, T., 1995b, "Wavelet Auto-correlation Analysis of a Plane Turbulent Jet", Flow Visualization Ⅶ, Begell House, Inc, pp.365-370.

Li, H., and Nozaki, T., 1996, "Wavelet Cross-Correlation Analysis and Its Application to Two-Dimensional Vortex Flow", Vortex Flows and Vortex Methods ASME, FED-Vol.238, pp.97-104.

Li, H., and Nozaki, T., 1997, "Application of Wavelet Cross-Correlation Analysis to a Plane Jet", JSME International Journal, Fluids and Thermal Engineering, Vol.40, No.1, pp.58-66.

Meneveau, C., 1991, "Analysis of Turbulence in the Orthonormal Wavelet Representation", J. Fluid Mech., Vol.232, pp.469-520.

Walker, S. H., Gordeyev, S. V., and Thomas F. O., 1995, "A Wavelet Transform Analysis Applied to Unsteady Jet Screech Resonance", High Speed Jet Flows ASME, FED-Vol.214, pp.103-108.

TURBULENCE CHARACTERISTICS OF A THREE-DIMENSIONAL TURBULENT BOUNDARY LAYER ON A ROTATING DISK WITH AN IMPINGING JET

H. S. Kang, J. Y. Yoo, H. Choi
Department of Mechanical Engineering
Seoul National University
Seoul 151-742
Korea

ABSTRACT

An experimental study has been performed on a shear-driven three-dimensional turbulent boundary layer over a rotating disk with an impinging jet located at the center of the disk, in order to investigate the turbulence characteristics of the three-dimensional turbulent boundary layer developed in this flow. A relatively strong spanwise flow (radial outflow) generated from the impinging jet is added to the spanwise flow induced from the rotating disk, and thus the mean flow direction is significantly changed. Six components of the Reynolds stresses are measured by aligning the miniature X-wire probe to the mean velocity direction. The ratio of the wall-parallel shear stress magnitude to the turbulent kinetic energy in the near-wall region is significantly decreased by the impinging jet. In the case of the free rotating disk flow the shear stress vector lags behind the mean velocity gradient vector in the whole boundary layer, while the lag is reduced or the lead occurs as the impinging jet speed increases.

INTRODUCTION

Reynolds stress data for a three-dimensional turbulent boundary layer (3D TBL) of a flow recovering on a flat plate behind a 45° swept wing were first reported by Bradshaw and Terrell (1969). The three-dimensionality was weak with a maximum angle of 9° between the tunnel axis and the surface streamline. When the flow is turned by an obstacle, the adverse pressure gradient is often stronger and the turning is more rapid than for swept wings. Anderson and Eaton (1989) investigated a 3D TBL around a wedge that was attached to the wall and pointed against the upstream direction. Values of the structure parameter a_1 were as low as 0.03 and the ratio of the spanwise to streamwise eddy viscosity was as low as 0.2. A significant drop in a_1 and a low eddy viscosity ratio were also found by Dechow and Felsch (1977). The Ekman layer, the prototype of planetary boundary layers, was simulated by Coleman et al. (1990). In the free stream, the pressure gradient is perpendicular to the flow direction and is balanced by the Coriolis force. The structural parameter profile varied greatly and was mostly below 0.15. The difference between the direction of the Reynolds shear stress and the mean velocity gradient was small. Littell and Eaton (1994) performed an experiment for a shear-driven 3D TBL on a rotating disk. Profiles of the Reynolds stresses, normalized with the friction velocity, collapsed well when plotted against the distance from the wall, normalized with the momentum thickness for different values of the rotation speed. Conditional averaged two-point correlation was also performed.

Consistent findings observed in most 3D TBLs are the following:

(1) The Townsend's structural parameter is lower than that of two-dimensional turbulent boundary layers.

(2) The direction of the wall-parallel shear stress vector does not coincide with the direction of the mean velocity gradient vector. That is, the eddy viscosity concept is not valid.

The objective of the present study is to investigate the turbulence characteristics of the shear-driven three-dimensional turbulent boundary layer. The main differences of the present experiment from previously studied 3D TBL experiments are that (1) the present 3D TBL is a quasi-equilibrium 3D TBL in which the three-dimensionality is applied continuously from the origin in contrast with other pressure-driven 3D TBLs where an initial 2D TBL is developed to a 3D TBL by an abrupt spanwise pressure gradient; (2) the rotation adds the Coriolis effect to the basic equation and changes turbulence structures; (3) a relatively strong spanwise flow (radial outflow) generated from the impinging jet is added to the spanwise flow induced by the rotating disk and also changes turbulence structures. In the present study, the mean velocity, six components of the Reynolds shear stresses are measured using the hot-wire anemometry.

METHOD

A schematic of the experimental setup is shown in Fig. 1,

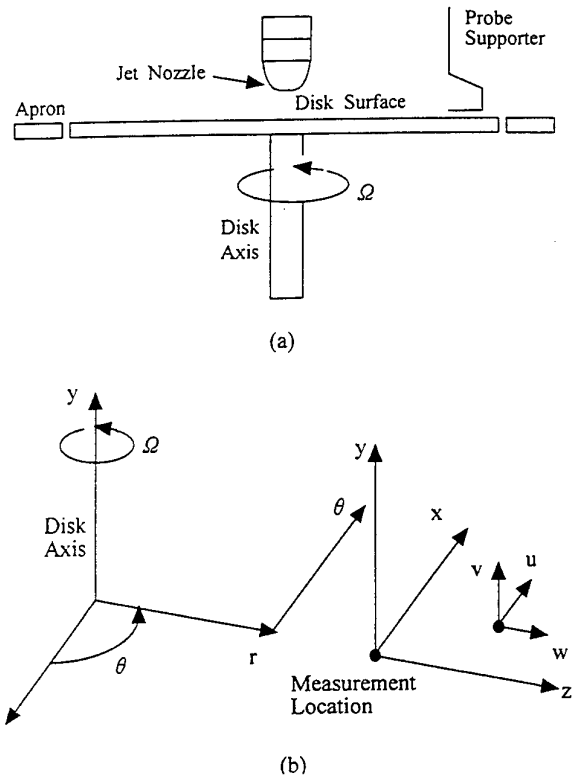


Fig. 1 (a) Schematic of the experimental setup; (b) coordinate system used in the present study.

together with the coordinate system used in this study. The disk diameter used in this experiment was 1 m and the disk surface was polished so that its flatness was less than 10 μm. The vertical fluctuation of the disk surface at r = 490 mm was $\pm$ 18 μm and the horizontal run-out at the disk periphery was $\pm$ 50 μm. The height between the disk surface and the jet exit was fixed at 31 mm, the diameter of the jet exit (D) was 30 mm, and the measurement location was r = 0.421 m. The jet speed (U_{jet}) were 0 m/s, 17.7 m/s, 35.3 m/s, and 52.8 m/s ($Re_j = U_{jet}D/\nu$ = 0, 3.5 x 10^4, 7.0 x 10^4, 1.05 x 10^5) at each disk rotation speed of 407 rpm and 814 rpm ($Re_r = \Omega r^2/\nu$ = 5.0 x 10^5, 1.0 x 10^6).

A single hot-wire probe (Dantec 55P11) with 5 μm diameter was used to determine the velocity magnitude and flow angle by yawing it. The uncertainty in measuring flow angles was within $\pm 1.5^\circ$. Turbulence data were measured using a custom-made X-wire probe. A 2.5 μm platinum-coated tungsten wire which had been copper-plated was soldered on the X-probe prong and subsequently etched for an active length to diameter ratio of 200. The wire spacing was 0.34 mm and the measurement volumes of the X-wire probe in the wall unit were nearly l^+ = 18 and 34 for the free rotating disk speeds of Re_r = 0.5 x 10^6 and 1.0 x 10^6 respectively. Six components of the Reynolds stresses are measured by rolling the miniature X-wire probe to be placed at four different roll angles with the probe stem aligned in the mean velocity direction. The uncertainty of the turbulence statistics measured with the X hot-wire near the wall was the same as the uncertainty estimated with an X hot-wire of Dantec according to Anderson and Eaton (1989), i.e. $\overline{u'^2}$, $\overline{v'^2}$, $\overline{w'^2}$ had 5% uncertainty, $\overline{u'v'}$, $\overline{u'w'}$ 10%, and $\overline{v'w'}$ 15%. However, as the probe moved away from the wall, the uncertainty is supposed to rise because the local

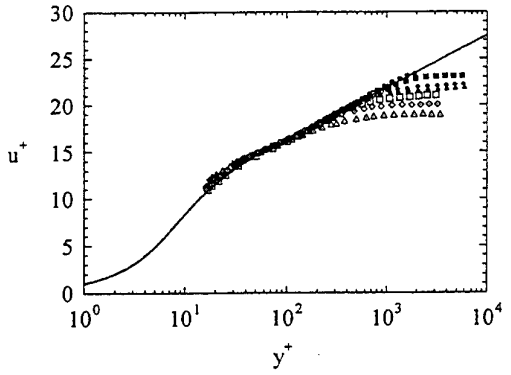


Fig. 2 Streamwise velocity profiles in wall unit (○ Re_r = 5.0x10^5, Re_j = 0; □ Re_r = 5.0x10^5, Re_j = 3.5x10^4; ◇ Re_r = 5.0x10^5, Re_j = 7.0x10^4; △ Re_r = 5.0x10^5, Re_j = 1.05x10^5; ● Re_r = 1.0x10^6, Re_j = 0; ■ Re_r = 1.0x10^6, Re_j = 3.5x10^4; ◆ Re_r = 1.0x10^6, Re_j = 7.0x10^4; ▲ Re_r = 1.0x10^6, Re_j = 1.05x10^5)

mean velocity became smaller and the turbulence intensity increased.

The r, θ, y components in the cylindrical coordinate are transformed to z, x, y components in the cartesian coordinate, respectively. The velocity components, u_r (radial), u_θ (tangential), u_y (wall-normal), in the cylindrical coordinate correspond to the w (spanwise), $u + r\Omega$ (streamwise), and v (wall-normal) velocity components, respectively, where $u = u_\theta - r\Omega \leq 0$.

RESULT

MEAN VELOCITY

Figure 2 shows the streamwise velocity distribution in wall units. In this figure the solid line represents the law of the wall in 2D TBL, where the van Driest model is applied to the buffer region. Here $u^+ = -\overline{u}/u_\tau$, $y^+ = yu_\tau/\nu$ and u_τ is the friction velocity defined by $u_\tau = U\sqrt{c_f/2}$. The present data is fitted to the log law to find the friction velocity. In the present study, the wake region appeared in a 2D TBL under the adverse pressure gradient is absent. The absence of the wake region appears in a favorable pressure gradient boundary layer. This result agrees to that of Littell and Eaton's free rotating disk flow (1994). Therefore, the flow in the present study may be regarded as a favorable pressure gradient type flow. However, the reason that the wake region is absent remains unclear, because the flow over the rotating disk cannot support any streamwise pressure gradient owing to the symmetry. Figure 2 shows that as the jet Reynolds number increases, the data is deviated from the law of the wall. It is not clear whether the law of the wall is valid in the present flow. Therefore, the method of finding u_τ based on the law of the wall must be verified by directly measuring the wall-shear stress.

Figure 3 shows the nondimensionalized streamwise and spanwise velocity profiles. As the ratio of the jet Reynolds number to the rotation Reynolds number ($\beta = Re_j/Re_r$) increases, the streamwise velocity profile becomes a little fuller shape, and the nondimensionalized maximum spanwise velocity $(\overline{w}/U)_{max}$ and the y-directional height at the maximum velocity $(y/\delta_2)_{max}$ also increase. As shown in Fig. 3(b), at low jet Reynolds numbers, the spanwise flow is mainly generated by the centrifugal force induced from the rotating disk, while a relatively strong spanwise flow generated from

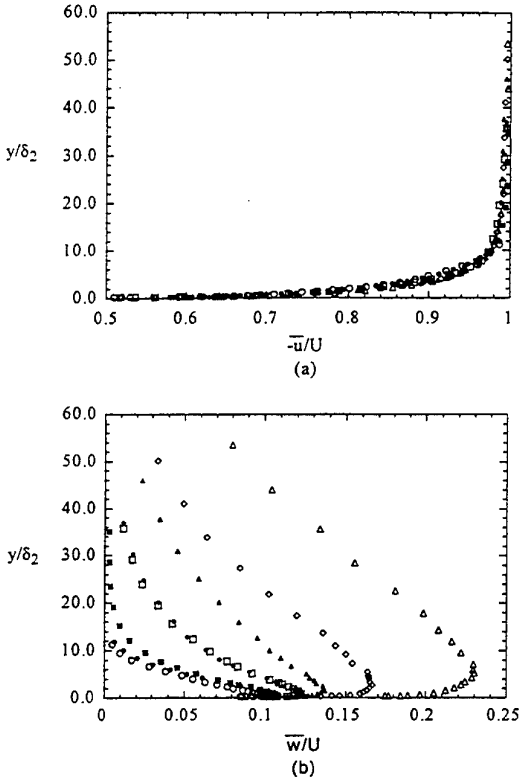


Fig. 3 Mean velocity profiles in the rotating coordinate system: (a) streamwise velocity; (b) spanwise velocity. Legends are the same as in Fig. 2.

the impinging jet is added at high jet Reynolds numbers.

Figure 4 shows the hodograph of the wall parallel mean velocity components, $-\overline{u}$ and $\overline{w}$. This hodograph was used by Johnston (1960) to develop his own triangular model on 3D TBL. In Fig. 4, $\overline{w}/U$ shows a typical behavior of 3D TBL flow; w starts to fall after passing the peak as the probe approaches the wall. As β increases, the peak is formed at higher value of $-\overline{u}/U$ and the spanwise velocity decreases rapidly in the outer region of the boundary layer. When a profile drops linearly to the zero point near the wall, this flow is a collateral flow which has no twisting of the velocity vector. However, when the second derivative of a profile is not zero, then the flow is a three-dimensional flow over the whole range of the boundary layer. Recently Degani et. al. (1992) showed by using an asymptotic analysis that flow became collateral near the wall for the three-dimensional turbulent boundary confined to large Reynolds number near a plane of symmetry. Unfortunately it cannot be clarified here owing to the absence of the experimental data near the wall. For a small turning angle ($\sin\gamma \approx \gamma$ i.e. $\gamma < 15°$), the following SWH model (Squire and Winter (1951), and Hawthorne (1951)) can be used to evaluate the spanwise velocity magnitude in the outer region of the boundary layer:

$$\frac{\overline{w}}{U} = -2\gamma\left(1 - \frac{-\overline{u}}{U}\right) \qquad (1)$$

The solid lines in Fig. 4 represent the SWH model. The SWH model overestimates the spanwise velocity as shown in Fig. 4.

REYNOLDS STRESSES

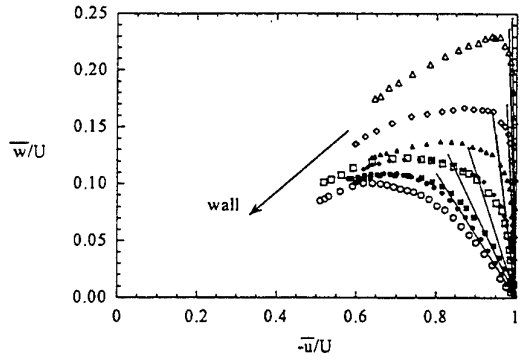


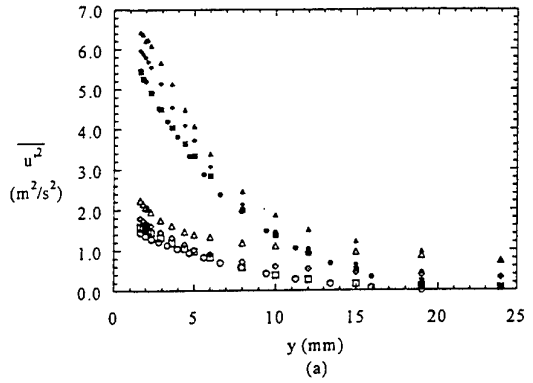
Fig. 4 Hodograph of wall parallel velocities. Legends are the same as in Fig. 2.

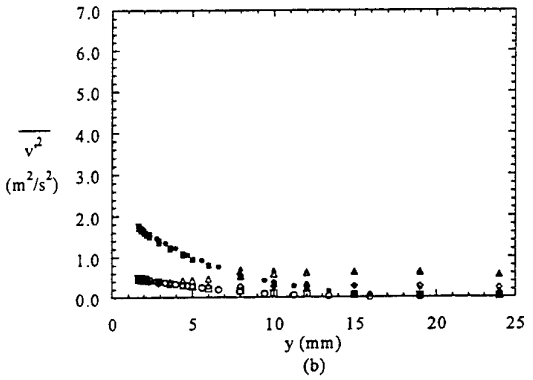
Figure 5 shows the streamwise, spanwise, and wall-normal Reynolds normal stresses in the outer layer. Unlike the free-rotating disk flow by Littell and Eaton (1994), the friction velocity and momentum thickness are not proper parameters for the normalization of the present flow. Therefore, all the data are shown in real scales. Because the error of the hot-wire measurement is large at the edge of the boundary layer, the experimental data are shown within y = 25 mm. As β increases, $\overline{u'^2}$ and $\overline{w'^2}$ increase, while $\overline{v'^2}$ shows little variation near the wall but large increase away from the wall.

Figure 6 shows the Reynolds shear stresses. As the jet Reynolds number increases, $\overline{u'v'}$ is suppressed near the wall, while it increases away from the wall. Below $y \cong 10$ mm, $\overline{v'w'}$ is smaller than $\overline{u'v'}$, but at large β and $y > 10$ mm $\overline{v'w'}$ is larger than $\overline{u'v'}$, which is due to the existence of the spanwise mean velocity gradient in this range. $\overline{v'w'}$ is negative near the wall, because the sign of the spanwise mean velocity gradient changes from a negative value to a positive value near the wall. The height where $\overline{v'w'} = 0$ should be the height where $\partial\overline{w}/\partial y = 0$ in order that the eddy viscosity model assumption should be satisfied. However, in this study $y_{\overline{v'w'}=0}$ is slightly less than $y_{\partial\overline{w}/\partial y=0}$. The profile of $\overline{v'w'}$ has a distinct peak and the peak moves away from the wall as the jet Reynolds number increases. This is related to the fact that the height where the spanwise velocity gradient is equal to zero moves away from the wall as the jet Reynolds number increases (Fig. 3(b)). Figure 6(c) shows the profile of $\overline{u'w'}$. As β increases, $\overline{u'w'}$ is smaller near the wall, while $\overline{u'w'}$ is larger at $y > 15$ mm.

STRUCTURAL PARAMETERS

The ratio of the wall-parallel normal stress magnitude $\overline{u'^2} + \overline{w'^2}$ to the wall-normal stress $\overline{v'^2}$ is shown in Fig. 7. The rise of this stress ratio implies the reduction of the eddy coherence (Schwarz and Bradshaw (1994)). In the free rotating disk flow the stress ratio monotonically increases as y increases, which agrees with the result of Littell and Eaton (1994). When the jet speed increases, a peak is formed and moves to the wall. The decrease of the stress ratio after the peak may be related to the increase of the eddy coherence due to the formation of the relatively strong and thick spanwise flow. Considering that, as the wall-normal distance increases, the ratio of stresses monotonically decreases in 2D TBL (Klebanoff (1955)) and most of other 3D TBLs (Anderson and Eaton (1989), Bradshaw and Pontikos (1985)), the turbulence structure of the present flow is basically different from other flows.





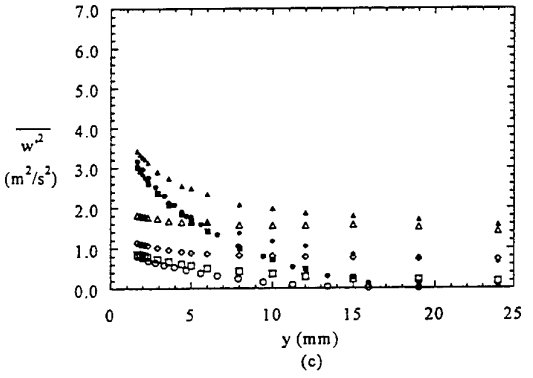
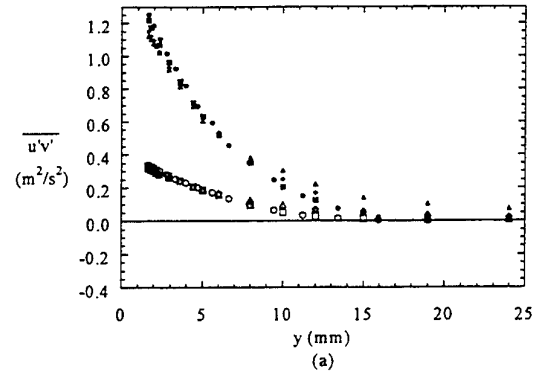
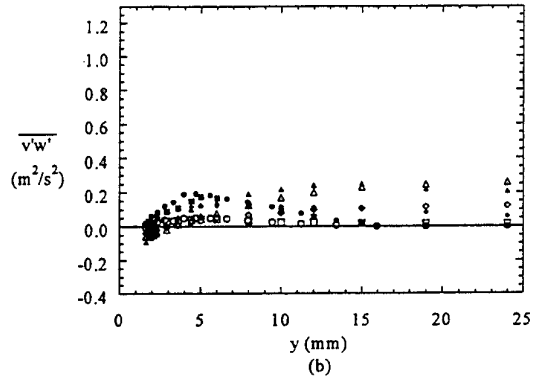


Fig. 5 Reynolds normal stresses: (a) $\overline{u'^2}$; (b) $\overline{v'^2}$; (c) $\overline{w'^2}$. Legends are the same as in Fig. 2





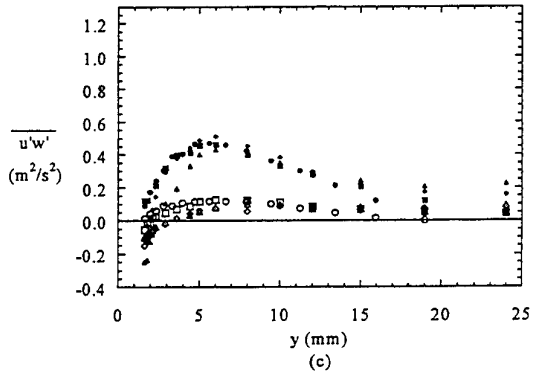


Fig. 6 Reynolds shear stresses: (a) $\overline{u'v'}$; (b) $\overline{v'w'}$; (c) $\overline{u'w'}$. Legends are the same as in Fig. 2

A parameter representing the characteristics of turbulence structures is the Townsend's structural parameter a_1. This is defined as the ratio of the wall parallel turbulent shear stress vector magnitude to twice the turbulent kinetic energy and is invariant to the rotation about the wall-normal axis:

$$a_1 = \frac{\sqrt{(\overline{u'v'})^2 + (\overline{v'w'})^2}}{q^2} \qquad (2)$$

This parameter represents the efficiency of eddies which produce the turbulence shear stress at a given turbulent kinetic energy. In case of 2D TBL, the structural parameter has a nearly constant value of 0.15. However, the value of a_1 generally decreases in the presence of the mean spanwise flow. Figure 8 shows the structural parameter a_1 of the present study. In case that the spanwise flow increases or β increases, a_1 decreases near the wall. It is attributed to the large increase of the turbulent kinetic energy compared to the increase of the wall parallel Reynolds shear stresses $\sqrt{(\overline{u'v'})^2 + (\overline{v'w'})^2}$ as shown in Figs. 5 and 6. Therefore, the presence of the spanwise flow reduces the efficiency of the eddies which produce the turbulent shear stress. In the case of the free rotating disk flow, monotonic drop in a_1 is observed over the boundary layer as y increases, However, in the case of large β 's, a_1 increases after monotonic fall due to the increase of the shear stress $\overline{v'w'}$ as shown in Fig. 6(b). In Spalart and Watmuff (1993), the reduction of a_1 is observed in the 2D TBL with an adverse pressure gradient. However, in the present study the reduction of a_1 is caused by the increasing spanwise flow near the wall rather than by an inactive motion in adverse pressure gradient

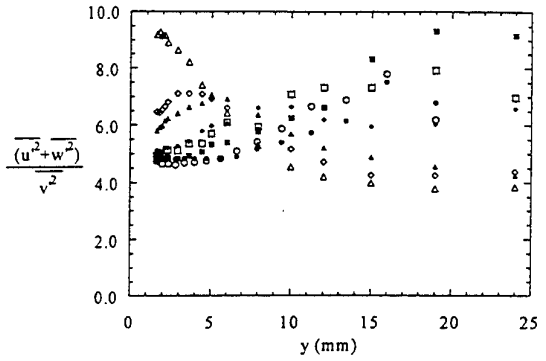


Fig. 7 Normal stress ratio. Legends are the same as in Fig. 2.

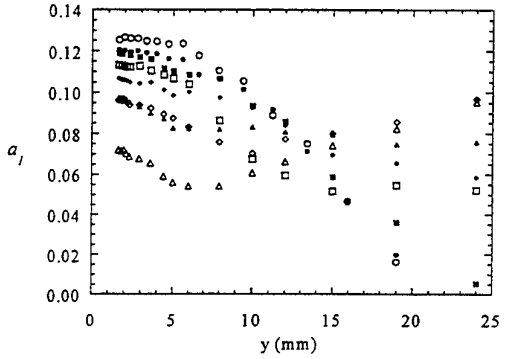


Fig. 8 Townsend's structural parameter a_1. Legends are the same as in Fig. 2.

(Littell and Eaton (1994)).

The deviation from the isotropic eddy-viscosity model can be shown by using the eddy-viscosity ratio N_e, which is defined as the ratio of the spanwise viscosity coefficient to the streamwise viscosity coefficient:

$$N_e \equiv \frac{\nu_{T_w}}{\nu_{T_x}} = \frac{-\overline{v'w'}/(\partial \overline{w}/\partial y)}{-\overline{u'v'}/(\partial \overline{u}/\partial y)} \qquad (3)$$

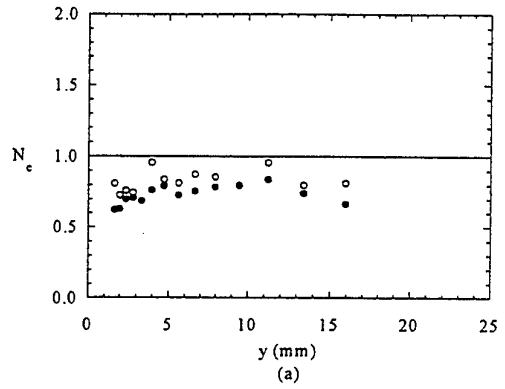
When N_e = 1, the isotropic eddy-viscosity model is satisfied, while N_e < 1 means that the direction of the shear stress vector lags behind the direction of the mean velocity gradient vector.

Figures 9(a) and (b) show the eddy-viscosity ratios in the free rotating disk flow and rotating disk flow with an impinging jet, respectively. While the shear stress vector lags behind the mean velocity gradient vector over the entire boundary layer in the free rotating disk flow, the lag of the shear stress vector is reduced as the spanwise flow increases. In the case of Re_r = 5.0 x 10^5 and Re_j = 1.05 x 10^5 in which the most strong spanwise flow is formed, the shear stress vector leads over the boundary layer except the near-wall region.

The Prandtl's mixing length in 2D TBL can be extended to 3D TBL as follows (Cebeci and Smith(1974)):

$$l^2 = \frac{[(\overline{u'v'})^2 + (\overline{v'w'})^2]^{1/2}}{[(\partial \overline{u}/\partial y)^2 + (\partial \overline{w}/\partial y)^2]} \qquad (4)$$

This mixing length is invariant with respect to the rotation about the wall-normal axis. Figure 10 shows the mixing length of



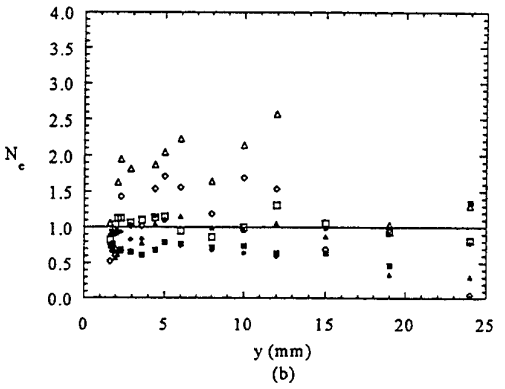


Fig. 9 Eddy-viscosity ratio: (a) free rotating disk flow; (b) rotating disk flow with an impinging jet. Legends are the same as in Fig. 2.

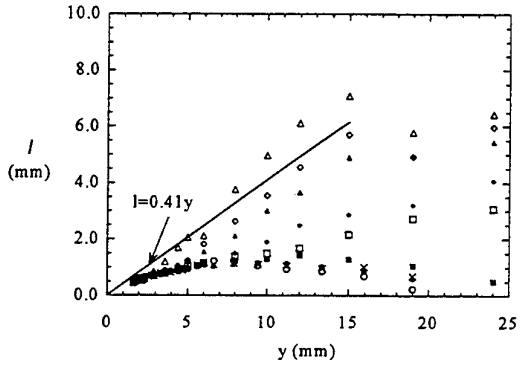


Fig. 10 Prandtl's mixing length. Legends are the same as in Fig. 2.

the flow together with a solid line which represents the mixing length in 2D TBL. A mixing length smaller than $l = 0.41y$ indicates suppression of the wall-parallel shear stress magnitude. In free rotating disk flow, the mixing length is shorter and the region of a constant mixing length is thinner than in 2D TBL. A similar trend is also seen in pressure-driven 3D TBL. As β increases, the mixing length also increases due to the increase of the wall-parallel shear stress magnitude.

CONCLUSION

An experimental study has been performed on a shear-driven

three-dimensional turbulent boundary layer over a rotating disk with an impinging jet located at the center of the disk, in order to investigate the turbulence characteristics of the three-dimensional turbulent boundary layer developed in this flow. The following conclusions are obtained from the present study:

(1) Two wall-parallel Reynolds shear stresses, $\overline{u'v'}$ and $\overline{v'w'}$ are largely affected by the jet impingement. The primary Reynolds shear stress $\overline{u'v'}$ is suppressed near the wall as the jet speed increases. The maximum position of the secondary shear stress $\overline{v'w'}$ moves away from the wall as the jet speed increases.

(2) When the jet speed increases, the Townsend's structural parameter a_1 decreases near the wall, where the strong spanwise flow reduces the efficiency of the eddies which produce the shear stress.

(3) In the free rotating disk flow the shear stress vector lags behind the mean velocity gradient vector over the whole boundary layer, while the lag of shear stress vector is reduced or the lead occurs as the jet speed increases.

ACKNOWLEDGEMENT

The present work was supported by Turbo and Power Machinery Research Center (TPMRC). The authors thank Daewoo Heavy Industrial Ltd. for the help in making the rotating rig and also thank Prof. Kyunghwan Yoon for the help with the experimental setup.

REFERENCES

Anderson, S. D. and Eaton, J. K., 1989, "Reynolds Stress Development in Pressure-Driven Three-Dimensional Turbulent Boundary Layers," *J. Fluid Mech.*, Vol. 202, pp. 263-294.

Bradshaw, P. and Pontikos, N. S., 1985, "Measurements in the Turbulent Boundary Layer on an 'Infinite' Swept Wing," *J. Fluid Mech.*, Vol. 159, pp. 105-130.

Bradshaw, P. and Terrell, M. C., 1969, "The Response of a Turbulent Boundary Layer on an 'Infinite' Swept Wing to the Sudden Removal of Pressure Gradient," *NPL Aero Report*, No. 1305.

Cebeci, T. and Smith, A. M. O., 1974, "*Analysis of Turbulent Boundary Layers*," Academic Press.

Coleman, G. N., Ferziger, J. H., and Spalart, P. R., 1990, "A Numerical Study of the Turbulent Ekman Layer," *J. Fluid Mech.*, Vol. 213, pp. 313-348.

Dechow, R. and Felsch, K. O., 1977, "Measurements of the Mean Velocity and of the Reynolds Stress Tensor in a Three-Dimensional Turbulent Boundary Layer Induced by a Cylinder Standing on a Flat Wall," *Proc. 1st Turbulent Shear Flows Symposium*, University Park, Pennsylvania, pp. 18-20.

Degani, A. T., Smith, F. T. and Walker, J. D. A., 1992, "The Three-Dimensional Turbulent Boundary Layer near a Plane of Symmetry," *J. Fluid Mech.*, Vol. 234, pp. 329-360.

Hawthorne, W. R., 1951, "Secondary Circulation in Fluid Flow," *Proc. of the Royal Society London Series* A, Vol. 206, pp. 374-387.

Johnston, J. P., 1960, "On the Three-Dimensional Turbulent Boundary Layer Generated by Secondary Flows," *ASME J. Basic Eng.*, Vol. 82, pp. 233-248.

Klebanoff, P. S., 1954, "Characteristics of Turbulence in a Boundary Layer With Zero Pressure Gradient," *NACA* TN 3178 Rep. 1247.

Littell, H. S. and Eaton, J. K., 1994, "Turbulence Characteristics of the Boundary Layer on a Rotating Disk," *J. Fluid Mech.*, Vol. 266, pp. 175-207.

Schwarz, W. R. and Bradshaw, P., 1994, "Turbulence Structural Change for a Three-Dimensional Turbulent Boundary Layer in a 30° Bend," *J. Fluid Mech.*, Vol. 272, pp. 183-209.

Spalart, P. R., 1989, "Theoretical and Numerical Study of a Three-Dimensional Turbulent Boundary Layer," *J. Fluid Mech.*, Vol. 205, pp. 319-340.

Spalart, P. R. and Watmuff, J. H., 1993, "Experimental and Numerical Study of a Turbulent Boundary Layer with Pressure Gradient," *J. Fluid Mech.*, Vol. 249, pp. 337-372.

Squire, H. B. and Winter, K. G., 1951, "The Secondary Flow in a Cascade of Airfoils in a Nonuniform Stream," *J. Aero Sci.*, Vol. 18, pp. 271-277.

AN AXISYMETRIC WALL JET WITH ITS AXIS REMOVED FROM THE WALL AND THE EFFECT OF THE WALL ON THE EVOLUTION OF COHERENT STRUCTURES

A. Benaissa, D. Ewing and A. Pollard
Department of Mechanical Engineering,
Queen's University at Kingston
Ontario, K7L 3N6
CANADA

ABSTRACT

The influence of the proximity of a wall on the development of an axi-symmetric jet and the consequences of this on the evolution and dynamics of coherent structures is the subject of this paper. Mean velocity hot wire data and flow visualisation are used to infer some basic characteristics of the effects of wall-to-jet distance. The anisotropic spread rates are found to depend on the distance above the wall, the wall parallel spread rate being greater than the wall normal. Coherent structure detection techniques have been applied; the results from this component of the study will be presented at the meeting.

INTRODUCTION

Three dimensional wall jets have been widely investigated, Launder and Rodi (1983), Pollard and Schwab (1986), Matsuda et al. (1990), Sullivan and Pollard (1996). In all these cases, the jets were flush-mounted with the wall (non-elevated) and the nozzles were flush with a back plane to stop entrainment from behind the nozzle exit plane. Matsuda *et al*, who used a round nozzle, and Sullivan and Pollard, who used a 10:1 aspect ratio rectangular jet, found near field coherent structures, which are formed in the jet, became distorted and stretched though interaction with the wall.

The evolution of a round jet situated above a plane wall has received some attention, Davis and Winarto (1980), who investigated the effect of elevating an axisymetric jet from the wall; however, their nozzle did not appear to be attached to a back plane. These authors concentrated on the distribution of the mean and some turbulence stresses in the far field of the jet (X/D ~ 48). They suggest that, in the far field, the large lateral spread rate, which far wall exceeds the spread in the plane perpendicular to the wall, is due to large scale motion in which components of velocity directed towards or away from the surface are associated with outflow or inflow along the surface.

The round jet is a canonical-type flow, and the distribution and evolution of coherent structures in it continue to attract close scrutiny, from experiments, Citriniti (1995), and from the simulation community, see, for example, Lasheras and Meiburg (1991). These investigations reveal that these jets consist of ring-type vortices that undergo a variety of instability mechanisms (see Fiedler 1996) to produce a corrugated structure. Citriniti's data suggest in the round jet there are features consistent with the corrugations, or lobes, that link one vortex to its predecessor that exhibit features of longitudinal vorticity. It is suggested here the entrainment and the subsequent evolution of these structures is impaired by the wall in the near-field and leads to the effects in the far field noted by Davis and Winato (1980).

The aim of this work is to investigate how the presence and proximity of the wall affects the near field development of a jet and how the jet transitions from a free jet into a wall jet. While the wall can be expected to alter the jet structure in the near field, the identification of this(ese) structure(s) after the jet has merged with the wall needs investigation.

EXPERIMENTAL DETAILS

A low speed air jet is fed from a settling chamber through a 25:1 area contraction to a 7.1 cm diameter nozzle. The nozzle is attached to a back plane that allows the whole nozzle and

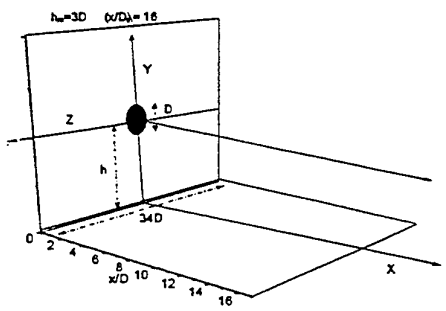


Figure 1: Schematic of the wall-jet facility. X, Y and Z are axial, wall-normal and span-wise (transverse) coordinates

settling chamber assembly to be moved vertically relative to a fixed wall. A schematic of the facility is given in figure 1.

The jet to wall distances considered here are h/D=1, 2 and 3. The interrogation volume spans 16, 2.5 and +/- 3 diameters in the axial, wall normal and jet span (parallel to the wall) direction, respectively. It is important to recognize that results are presented using a Cartesian system as oppose to either a cylindrical-polar coordinate system or one that uses the local jet coordinates. The origin of the coordinate system is on the wall below the jet centerline.

The jet exit velocity was 20 m/s, which corresponds to a Reynolds number of Re=9.0 x 10^4. Velocity data were acquired using rakes of hot wire probes, which consisted of a single X-probe and five single hot wires, arranged in a line either perpendicular or parallel to the wall. The nominal separation between the probes is 4 mm, and this corresponds to about 0.1 integral length scales when the wires are located 4 diameters downstream of the jet exit. The minimum wall-to-wire distance is about 0.18D, thus the very near-wall details of the wall flow can not be resolved.

The spectra of u and v were measured for wall to jet centre-line displacement h/D=1. The vortex shedding frequency is 100 Hz, which gives a Strouhal number, St = fD/U = 0.355. This places the jet well inside the preferred mode of excitation for round jet, 0.2< St <0.6, Fiedler (1996) and is in accord with Matsuda et al. (1990).

PRESENTATION AND DISCUSSION OF RESULTS

The evolution of the axial mean velocity profiles on the central plane of the jet for jet heights h/D=1, 2 & 3 are shown in figures 2a, b, c. A comparison of these three cases indicates that the effect of the wall on jet development is more pronounced for the h/D=1 case, as expected.

The contours of mean velocities at four Y-Z planes are displayed in figure 3, for h/D=1 and in figure 4 for h/D=2. All velocities are normalised using the maximum axial mean velocity on the given plane, U_m. The distance from the wall to the position of the local maximum axial mean velocity, y_{max}, decreases with axial distance, as indicated by the contour plot of axial mean velocity in the X-Y wall-normal plane, figure 5, for h/D=1. At both jet heights, the spread in the wall normal and wall parallel directions is symmetric up to X/D=3; thereafter, the wall influence is evident, particularly in the lateral spread of the h/D=1 case at farther downstream locations. The magnitudes of the wall normal mean velocity, V, display expected bi-planar symmetry. At h/D=1, these velocities indicate a positive (away from the wall) peak value in the centre, surrounded by a field of negative V. This indicates the positive peak in V above the jet centreline, noted at h/D=2, has grown. This is consistent with the decrease in y_{max} and that at h/D=2, the jet contacts the wall at greater X/D than in the h/D=1 case. The spanwise mean velocity contours indicate trends similar to those observed for the V velocity. The W-contours, for h/D=1, indicate that early in the jet development the wall influence alters both the magnitude and the gradients in the wall parallel velocity. The increase in lateral spread noted from the axial mean velocity contours can be related to the negative lateral (away-from-the-centreline wall parallel) velocity, combined with negative (towards-the-wall) off-axis wall normal velocities.

The near field behaviour of this jet, for the h/D=0 case, has been more extensively investigated (e.g., Ewing et al.,1997). The flow visualisation from this study indicate the jet evolves into a shape reminiscent of a pie in cross-section similar to that shown in figure 2 of Davis and Winarto (1980). A photograph, taken in the Y-Z plane at X/D=6 is given in figure 6. The picture illustrates the instantaneous realisation of the flow, and highlights the vericose entrainment surface, the ejection of fluid in the wall parallel direction. While this picture represents the flow for the limiting case of h/D=0, it remains to be determined if the present situation where the jet is elevated above the wall produces similar behaviour. Pictures for the present case of h/D>0 are not available at the time the paper was written; a video will be presented at the conference.

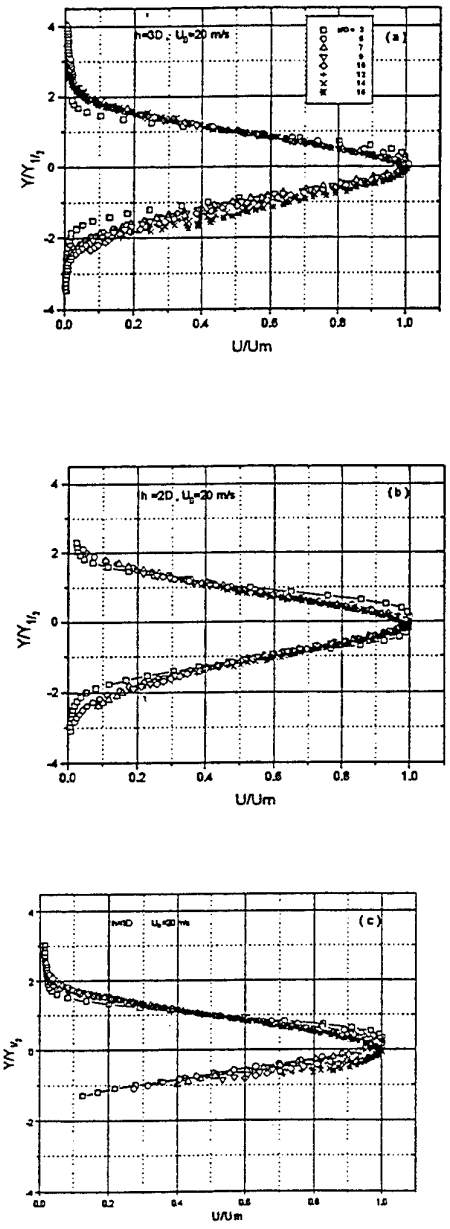


Figure-2a, b, c

Figure-2 : Profiles of mean velocity (X-Y plane) at different distance from the jet exit and for the three heights of the jet : a) h=3D, b) h=2D, c) h=1D.

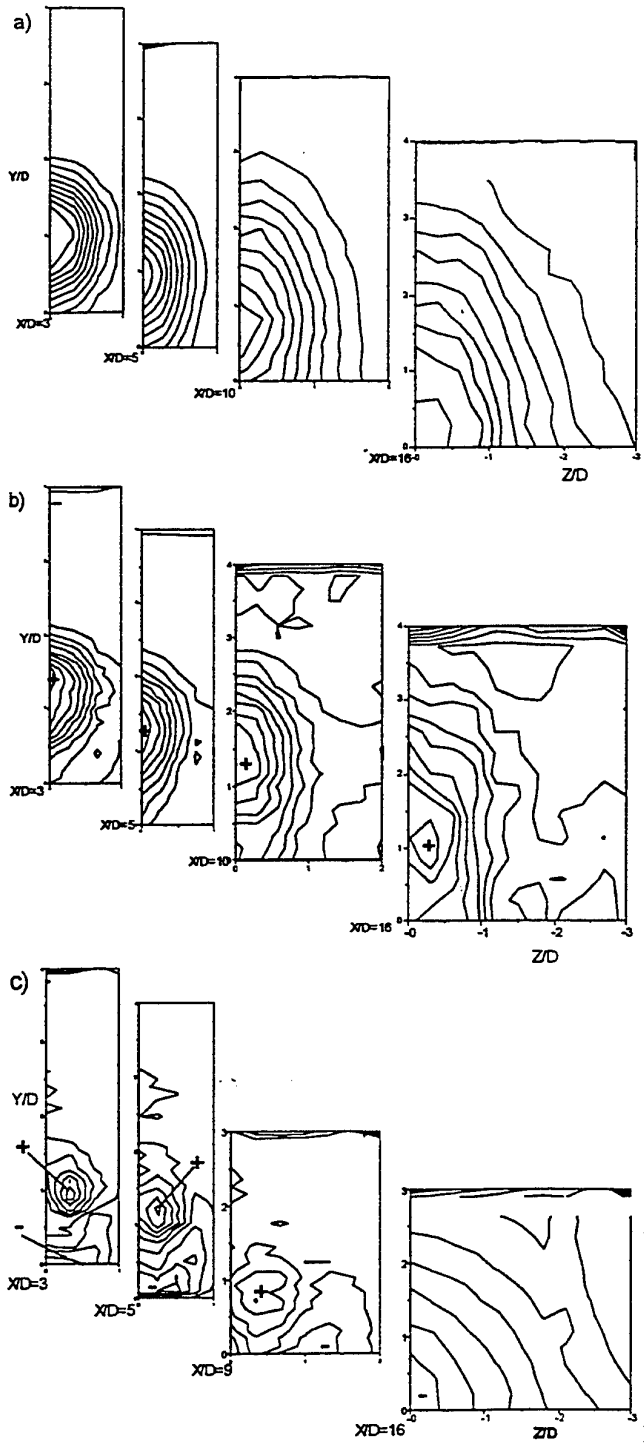


Figure 3: Contours of mean velocities, h/D=1. (a) U/U_m; (b) V/U_m; (c) W/U_m. The +/- signs indicate: V positive: away-from-the-wall V; W negative: away-from-the-centreline W. Centreline is left and wall is bottom.

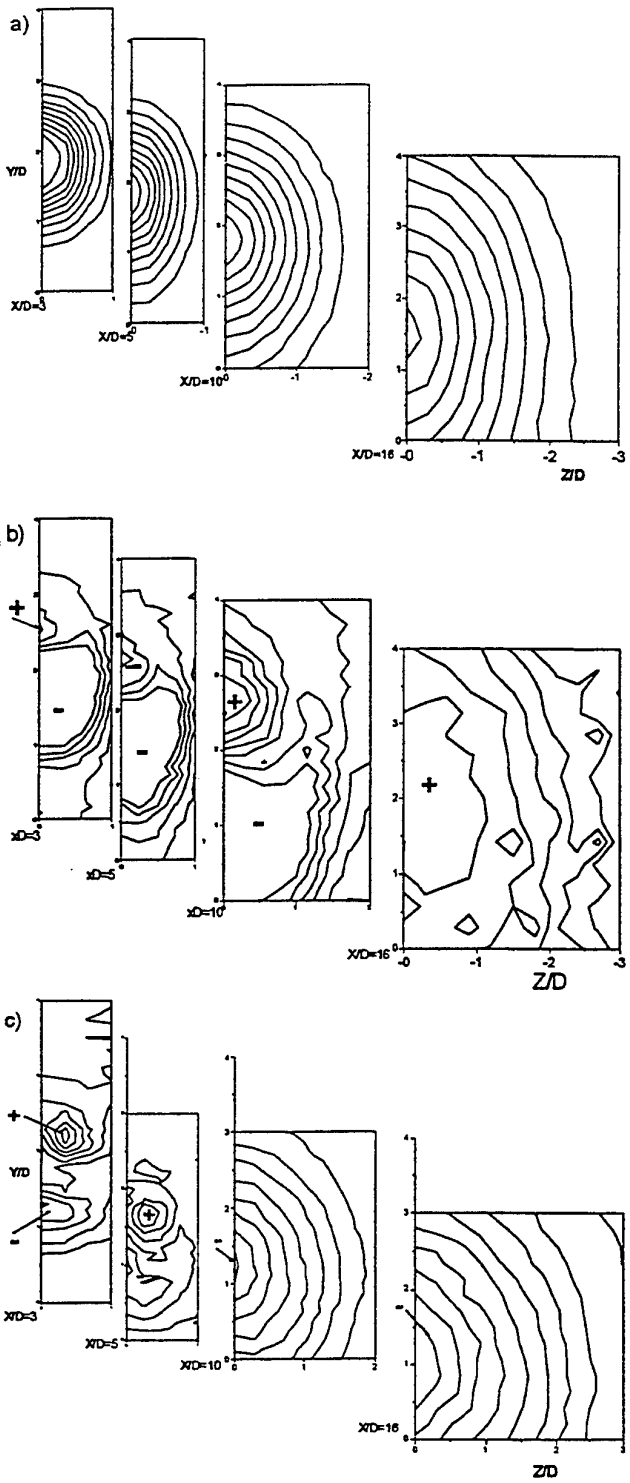


Figure 4: Contours of mean velocities, h/D=2. (a) U/U_m; (b) V/U_m; (c) W/U_m. The +/- signs indicate: V positive: away-from-the-wall V; W negative: away-from-the-centreline W. Centreline is left and wall is bottom.

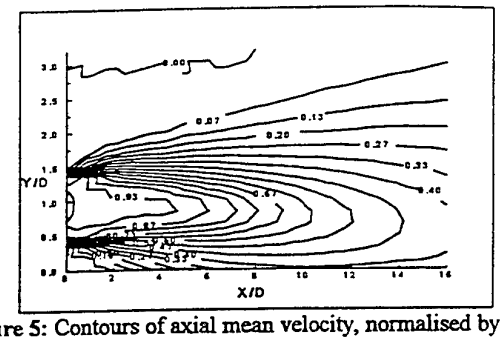


Figure 5: Contours of axial mean velocity, normalised by mean exit velocity, h/D=1.

It is hypothesised though that a similar interaction may play an important role in creating the anisotropic spread rate in the elevated wall jet. To investigate this aspect, conditional averaged measurements have been done, using the WAG method of Antonia et al. (1987). The findings from this component of the study will be presented at the meeting.

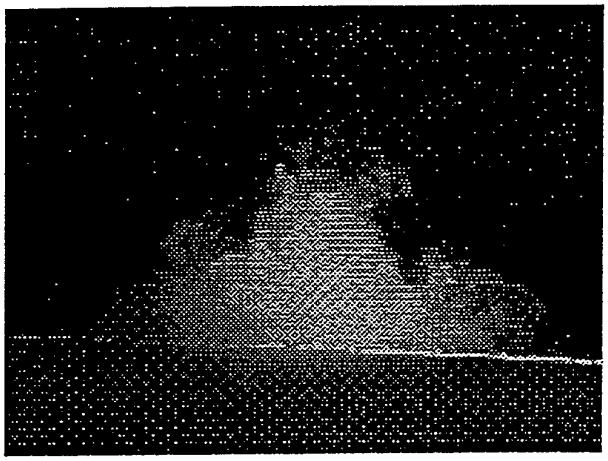


Figure 6: Flow visualisation of CO_2 vapour at about X/D=6, for h/D=0, from Ewing et al. (1997). Flow is out of page, view is about 45 degrees above and to one side of the main flow axis. Note the ejection of vapour in the spanwise direction, parallel to wall; the wall is highlighted by bright streak of laser light.

CONCLUSION

Experimental results describing the effect of the proximity of a wall on the evolution of an axi-symmetric jet have been presented. The mean velocity measurements show that the spread in the span wise direction is increased with proximity of the jet to the wall. The flow visualization experiment reveals the existence of a large scales features resulting from the interaction of rink vortex and the wall. These events await the application of a detection scheme, which will be reported at the meeting.

Acknowledgments

This work is supported by grants and fellowships from the Natural Sciences and Engineering Research Council of Canada.

References

Antonia, R.A., Browne, L.W.B, and Bisset, D.K. (1987): Symmetric and antisymmetric modes in the turbulent far wake, Proceedings, 6th Symposium Turbulent Shear Flows, Toulouse.

Davis, M.R., and Winarto, H. (1980): jet diffusion from a circular nozzle above a solid plane. J Fluid Mech., vol 101, part 1, pp. 201-221, 1980.

Ewing, D., Benaissa, A., Pollard, A., Citriniti, J., Abrahamsson, H. and Lofdahl, L. (1997): Contribution of large structures to the anisotropic spread rate in a wall jet issuing from a round nozzle, submitted for presentation, 10th Int'l. Symp. Transport Phenomena, Kyoto, Japan, November.

Fiedler, H.E. (1996): Free turbulent shear flows- basics and principles of their control, Proceedings Shortcourse in Flow control Fundamentals and Practices, Cargese, Corsica.

Lasheras, J.C. and Meiburg, E. (1991): On the three dimensional dynamics of coherent vortical structures forming in free shear flows, Turbulence and Coherent Structures, Metais and Lesieur (eds.), selected papers from Turbulence 89: Organised Structures and Turbulence in Fluid Mechanics, Kluwer Academic Publishers.

Launder, B.E. and Rodi, W. (1983): The turbulent wall jet-measurements and modeling, Annual Reviews Fluid Mechanics. no. 15, pp. 429-459.

Matsuda, H., Iida S., and Hayakawa, M. (1990): Coherent structures in a three-dimensional wall jet, Transaction of the ASME, Vol. 112, pp. 462-465.

Newman, B., Patel, R., Savage, S. and Tjio, H. (1972): Three dimensional wall jet originating from a circular orifice, Aero. Quart., Vol 23, pp. 188-200.

Pollard, A. and Schwab, R.R. (1988): The near-field behavior of rectangular free jets: an experimental and numerical study, Proceedings First World Conference on experimental Heat Transfer, Fluid Mechanics and Thermodynamics, pp. 1510-1517, Dubrovnik, Yugoslavia.

Sullivan, P. (1995): Coherent structure identification in the near field of a three-dimensional wall jet. PhD thesis, Queen's University.

Sullivan, P. and Pollard, A. (1996): Coherent structure identification from the analysis of hot-wire data Measurement Science and Technology, Vol. 7, pp. 1498-1516.

VELOCITY STRUCTURE FUNCTIONS IN A TURBULENT PLANE JET

B. R. Pearson and R. A. Antonia
Department of Mechanical Engineering
University of Newcastle, N.S.W. 2308, Australia

Abstract

Measurements have been made of moments, up to order eight, of the longitudinal velocity increment δu on the centreline of a turbulent plane jet in the self-preserving region of the flow. The Taylor microscale Reynolds number R_λ is in the range 600–1200. The magnitude of ζ_u, the scaling exponent for $\langle(\delta u)^n\rangle$ in the inertial range (IR), has been obtained from either the conventional method (by plotting $\langle(\delta u)^n\rangle$ vs r) or the extended self-similarity (ESS) technique, where $\langle|\delta u|^n\rangle$ is plotted against $\langle|\delta u|^3\rangle$. The former estimates increase slightly with R_λ while the latter do not depend on R_λ; this discrepancy appears to reflect the slight difference between $\langle(\delta u)^3\rangle$ and $\langle|\delta u|^3\rangle$ in the inertial range. Measurements of both δu and δv (where v is the lateral velocity fluctuation) were made at $R_\lambda = 600$. The IR scaling exponents of δv are significantly smaller than those of δu. The likely dependence on R_λ of ζ_v is discussed. The departure from isotropy in the inertial range is also discussed.

1 Introduction

Significant attention has been given to the phenomenology of small scale turbulence since the observation of Batchelor and Townsend (1949) that the turbulent energy dissipation rate, ϵ, is intermittent. The R_λ dependence of small scale turbulence has received particular attention. Recently, a series of experiments in the same apparatus with low temperature helium as the working fluid, over a large R_λ range, was completed (Tabeling et al. 1996; Willaime et al. 1996). They observe an increase in $-S_{\dot{u}}$, the skewness of the velocity derivative, and $F_{\dot{u}}$, the flatness factor of the velocity derivative, with R_λ only up to, ≈ 700. For larger R_λ, their data suggest that $-S_{\dot{u}}$ and $F_{\dot{u}}$ may in fact decrease. They consider $R_\lambda \approx 700$ to be a transitional Reynolds number, above which the turbulence becomes less intermittent in the dissipative range, possibly as a result of the weakening or breakdown of strong vortex filaments which are more coherent for $R_\lambda < 700$. This R_λ trend contrasts that reported earlier by Van Atta and Antonia (1980) and recently reassessed and confirmed by Sreenivasan and Antonia (1997).

Another extensively studied aspect of small scale turbulence — not unrelated to the first — is the behaviour of $\langle(\delta u)^n\rangle \equiv \langle[u(x+r) - u(x)]^n\rangle$ in the inertial range. This quantity exhibits a power-law behaviour in the IR, viz.

$$\langle(\delta u)^n\rangle \sim r^{\zeta_u(n)} \quad .$$

The magnitude of the exponent $\zeta_u(n)$ increasingly departing from the Kolmogorov (1941) or K41 prediction $\zeta_u(n) = n/3$ as n increases. This anomalous scaling (e.g. Anselmet et al 1984; Vincent and Meneguzzi 1991) may be thought to be the signature of small-scale intermittency (e.g. Sreenivasan and Antonia 1997). There is a significant body of evidence to suggest that ζ_u does not depend on R_λ. Arneodo et al. (1996) obtained estimates of ζ_u^a, the exponent associated with

$$\langle|\delta u|^n\rangle \sim \langle|\delta u|^3\rangle^{\zeta_u^a(n)} \quad ,$$

using the extended self-similarity (ESS) method of Benzi et al. (1993), for different flows and Reynolds numbers ($30 < R_\lambda < 5000$). The magnitudes of ζ_u and ζ_u^a were nearly equal, making it unnecessary to distinguish between ζ_u and ζ_u^a. The results pointed to a universal distribution of $\zeta_u(n)$. As noted by Ciliberto et al. (1996), this universality is unlikely to apply in non-homogenous and non-isotropic situations, e.g. the near-wall region. The present authors (Antonia and Pearson 1997) have observed that the magnitudes of $\zeta_v(n)$ and $\zeta_w(n)$, the exponents associated with the transverse velocity components v and w respectively, are significantly smaller than those of $\zeta_u(n)$ at least for the particular flow (cylinder wake, $R_\lambda \simeq 230$) which they investigated. It seems unlikely that ζ_v, ζ_w (or ζ_θ where θ is the temperature fluctuation) do not depend on R_λ — at least for laboratory turbulent shear flows. Another issue of relevance is how to interpret the anomalous scaling of different velocity increments in the context of a departure from isotropy of IR scales.

In this paper, we reexamine the issue of the R_λ dependence through measurements of the longitudinal structure function ($n \leq 8$) in the same flow (a plane jet). The focus on the same flow — as for the Tabeling et al. experiment — avoids the effect of possibly different large-scale anisotropies, associated with different flows, on small-scale structure statistics. Although the R_λ range considered is not large (600–1200) it is ad-

equate in the sense that it straddles the transitional zone observed by Tabeling et al. (1996).

We assess the R_λ dependence of both ζ_u and ζ_u^* since a small difference in IR behaviour has been observed (e.g. Herweijer 1995) between $\langle(\delta u)^3\rangle$ and $\langle|\delta u|^3\rangle$ and, whereas Kolmogorov's (1941) equation predicts $\langle(\delta u)^3\rangle \sim r$ in the IR, there is as yet no theoretical justification for $\langle|\delta u|^3\rangle \sim r$.

2 Experimental Details

Two different wind tunnels and nozzle geometries were used for generating the plane jets. Both tunnels were supplied by variable frequency controlled centrifugal-type blowers. The more extensive measurements were made with a single hot wire, downstream of a two-dimensional nozzle (two-dimensional contraction ratio of 10, width $h = 165$ mm). X-wire measurements were made in a jet exiting from a two-dimensional contraction (ratio = 14) with $h = 42$ mm.

For $h = 165$ mm, u was measured at $x = 50h$ from the nozzle exit plane. The jet exit velocity, U_j, could be varied in the range 5 m/s to 30 m/s. The turbulence Reynolds number, R_λ ($\equiv u'\lambda/\nu$), at the measurement station, ranged from 800 to 1400; λ is the longitudinal Taylor microscale, u' is the rms longitudinal velocity and ν is the kinematic viscosity of air. The Kolmogorov length scale, η ($\equiv \nu^{3/4}/\langle\epsilon\rangle^{1/4}$), ranged from 0.08 mm to 0.4 mm. The value of $\langle\epsilon\rangle$ was estimated from $\langle(\partial u/\partial t)^2\rangle$ via the isotropic relation $\langle\epsilon\rangle = 15\nu\langle(\partial u/\partial x)^2\rangle$ and Taylor's hypothesis $\partial/\partial x = -\langle U\rangle^{-1}(\partial/\partial t)$; partial experimental support for this hypothesis in the context of correlation functions was presented, for this flow, in Antonia et al. (1984). The 1.27 μm diameter Wollaston (Pt-10% Rh) wire (etched length, $l = 0.25$ mm; $1.3 \leq l/\eta \leq 3.2$) is operated with a constant temperature anemometer and an overheat ratio of 0.5. The anemometer signal is first amplified and low-pass filtered at a cut-off frequency f_c approximately equal to the Kolmogorov frequency (0.8 kHz $\leq f_\kappa \leq$ 8 kHz). It is then digitized at twice this frequency. The record length range is 1.5×10^6 to 1.0×10^7 samples. The record durations were sufficiently long enough to ensure statistical convergence of the moments up to $n = 8$, in the inertial range (e.g. at $r = \lambda$, $\langle(\delta u)^6\rangle$ is in error by 3% according to the method of Camussi et al. 1996).

Simultaneous u and v measurements (Antonia et al., 1997) were made on the centreline at $53h$ from the exit plane of the 42 mm nozzle. The X-probe (2.5 μm diameter wire of 0.5 mm length) was operated in constant-temperature mode at an overheat of 0.5. U_j was 25 m/s and R_λ was 600 at the measurement station. The signals were low-pass filtered at $f_c \simeq f_K$ (f_K = Kolmogorov frequency) of 12.5 kHz. The record duration (50 s $\equiv 1.25 \times 10^6$ samples per channel) is sufficient for convergence of moments, up to order six, in the inertial range. Using the procedure of Camussi et al. (1996), the error for the sixth-order moment is estimated to be 4%.

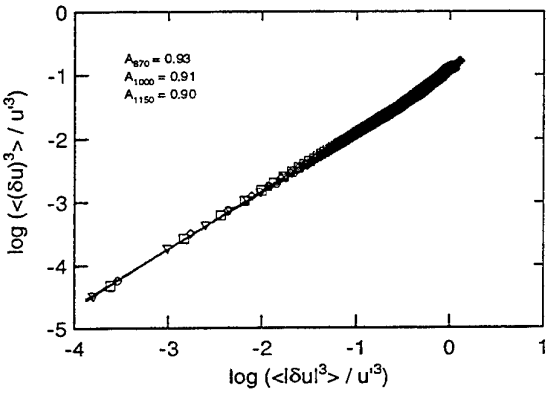


Figure 1: Cross-plot of $(\delta u)^3$ against $|\delta u|^3$, $R_\lambda = 600-1150$. $\Diamond$, $R_\lambda = 870$; $\square$, 1000; ∇, 1150; —, extent of curve fit.

3 Results

Table 1 shows the estimated exponents for the moments of the longitudinal velocity structure function, δu. Both the general case, $\zeta_u(n)$, and absolute case, $\zeta_u^a(n)$, exponents are tabulated. For the general case, the n^{th} moment of (δu) was plotted against r on a log-log scale. A least-squares linear regression analysis was applied to data in the range $40 \leq r^* \leq 300$; the asterisk denotes normalization by Kolmogorov scales. This range was estimated from an approximate plateau region observed when $(\delta u^*)^3$ was plotted against r^* (for $R_\lambda = 600$, the range was $40 < r^* < 250$). In nearly all cases, the square of the correlation, ρ, was ≈ 1.0. This value did deteriorate with an increase in both n and R_λ but to no worse than $\rho \simeq 0.98$. For the absolute case, the ESS method of Benzi et al. was adapted to the same r^* ranges for the general structure function case. This consisted of cross-plotting the n^{th} moment of $|\delta u|$ against $\langle|\delta u|^3\rangle$. A cross-plot on a log-log scale and linear regression was used to estimate these exponents.

Figure 1 shows the ratio of $\langle(\delta u)^3\rangle$ to $\langle|\delta u|^3\rangle$ is not 1. Benzi et al. assume $|\langle(\delta u)^3\rangle| \cong \langle|\delta u|^3\rangle^A$, with $A = 1$. If this is true, then the cross-plot of these terms should give an exponent, e.g. A, of 1. We do not find this for the current experiment. In fact, we find a slight R_λ dependence for A (Figure 1). Clearly, A decreases with R_λ increasing in the IR. This is in accord with the findings of Herweijer (1995) although we find a greater difference in A. The values of $\zeta_u^a(n)$ are in good agreement with published data (e.g. Noullez et al. 1996; Arneodo et al. 1996).

TABLE 1 u STRUCTURE FUNCTION EXPONENTS

R_λ		n						
		2	3[§]	4	5	6	7	8
600	ζ_u^a	0.70	—	1.27	1.52	1.76	1.99	2.21
	ζ_u	0.76	0.98	1.38	1.49	1.79	1.89	2.21
800	ζ_u^a	0.70	—	1.27	1.52	1.74	1.91	2.04
	ζ_u	0.71	0.95	1.29	1.46	1.73	1.84	1.87
870	ζ_u^a	0.70	—	1.27	1.50	1.71	1.88	2.04
	ζ_u	0.70	0.94	1.26	1.52	1.71	2.06	2.02
1000	ζ_u^a	0.70	—	1.27	1.50	1.71	1.88	2.03
	ζ_u	0.71	0.92	1.29	1.44	1.74	1.83	2.06
1150	ζ_u^a	0.70	—	1.27	1.52	1.74	1.93	2.10
	ζ_u	0.72	0.93	1.31	1.54	1.78	—	2.13

[†]plotted against $\langle|\delta u|^3\rangle$; [‡]plotted against r^*; [§]$\zeta_u^a(3)$ is not shown since it is trivially equal to 1.

TABLE 2 v STRUCTURE FUNCTION EXPONENTS — COMPARISON WITH WAKE

R_λ		n						
		2	3	4	5	6	7	8
600	ζ_v^a	0.61	0.86	1.08	1.29	1.46	1.63	1.78
	ζ_v	0.65	—	1.16	—	1.56	—	1.92
230[§]	ζ_v^a	0.57	—	1.10	1.20	1.38	1.51	1.62

[†]plotted against $\langle|\delta u|^3\rangle$; [‡]plotted against r^*; [§]cylinder wake.

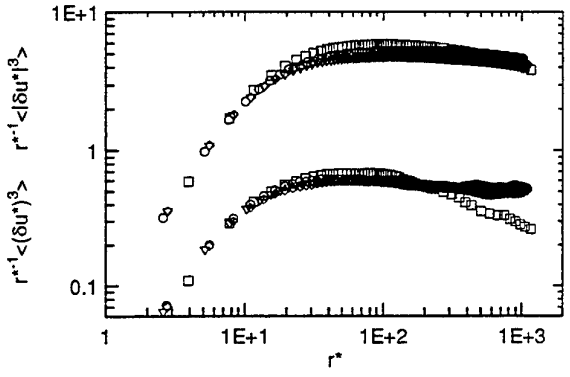


Figure 2: Weighted third-order moments of δu^* and $|\delta u^*|$, $R_\lambda = 600 - 1150$. $r^{*-1}\langle(\delta u^*)^3\rangle$: □, $R_\lambda = 600$; ◇, 870; ▽, 1000; ○, 1150. $r^{*-1}\langle|\delta u^*|^3\rangle$: □, $R_\lambda = 600$; ◇, 870; ▽, 1000; ○, 1150.

From the exponents shown in Table 1, two conclusions can be drawn. First, there is no discernible trend for exponents of the n^{th} moment with R_λ; if any trend did exist, it was slight and masked by experimental error. Secondly, there is a difference between the general, $\zeta_u(n)$, and absolute, $\zeta_u^a(n)$, exponents. The general exponents are higher compared to the absolute ones. This correlates the findings shown in Figure 1.

Figure 2 shows the weighted plots $r^{*-1}\langle(\delta u^*)^3\rangle$ and $r^{*-1}\langle|\delta u^*|^3\rangle$. The higher magnitude of $\langle|\delta u^*|^3\rangle$ is due to $|\delta u|$ not being mean-subtracted. Despite this, the shape of $\langle|\delta u|^3\rangle$ agrees well with $\langle(\delta u)^3\rangle$ in the dissipative range (DR) and IR. The shape of $\langle|\delta u|^3\rangle$ seems very similar to $\langle(\delta u)^3\rangle$ except for an extended plateau region. We are still unclear as to how to interpret this. From this figure we have chosen the region for exponent estimation. For all R_λ investigated, the range $40 < r^* < 300$ appears to correspond, in shape, for both $\langle(\delta u)^3\rangle$ and $\langle|\delta u|^3\rangle$. A clear observation for this flow type is the disagreement with K41. The value of the constant ($\simeq 0.695$) falls well short of the K41 value of 4/5 and this may be related to the anomalous scaling and a lack of local isotropy. The result $\zeta_u(3) < 1$ does follow the trend of $\zeta_u(n)$ (Table 1). The interpretation of $\zeta_u(3) \neq 1$ can either be taken as evidence of departure from local isotropy or reflect the effect of intermittency. The question of what this observation means with respect to the anomalous scaling remains to be answered.

Figure 3 shows ESS-type cross-plots of $\langle|\delta u|^n\rangle$ against $\langle|\delta u|^3\rangle$ (n = 2, 4 and 8) for R_λ = 600 and 1000. The third-order moments of $|\delta u|$ are normalized with the velocity fluctuation rms for convenience only, since the normalization used is trivial when only power exponents are required. The figure shows, for all n, no R_λ dependence of each gradient which, on log-log scales, is equivalent to the exponent $\zeta_u^a(n)$. The only R_λ effect is to locate the plot to lower values of the abscissa and ordinate.

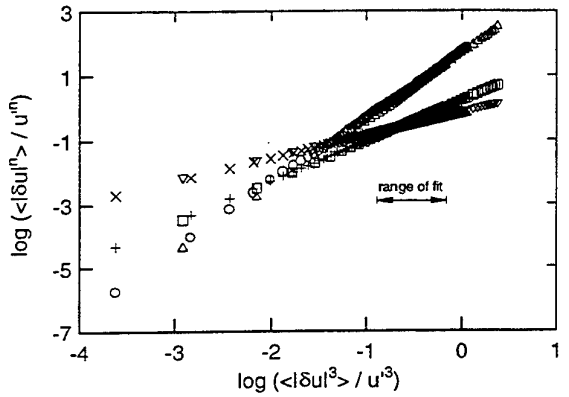


Figure 3: Cross-plot of the n^{th} moment of $|\delta u|$ against $\langle|\delta u|^3\rangle$. $n = 8$: $\triangle$, $R_\lambda = 600$; $\circ$, 1000. $n = 4$: $\square$, $R_\lambda = 600$; $+$, 1000. $n = 2$: ∇, $R_\lambda = 600$; $\times$, 1000.

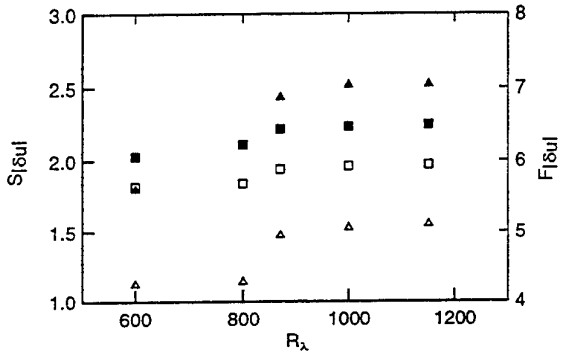


Figure 4: R_λ dependence of $S_{|\delta u|}$ and $F_{|\delta u|}$, $R_\lambda = 600-1150$. $\triangle, \blacktriangle$, $F_{|\delta u|}$; $\square, \blacksquare$, $S_{|\delta u|}$; filled symbols, $r^* = 15$; unfilled symbols, $r^* = \lambda/\eta$.

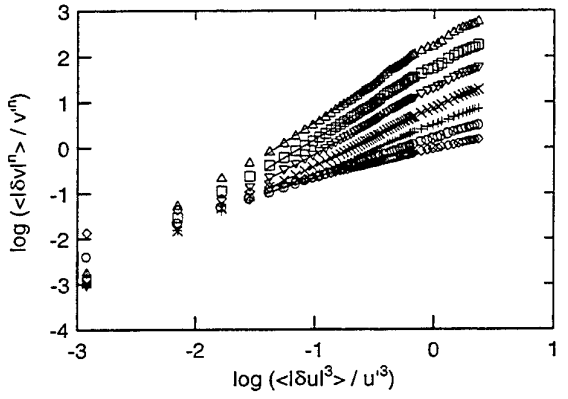


Figure 5: Cross-plot of the n^{th} moment of $|\delta v|$ against $\langle|\delta u|^3\rangle$, $R_\lambda = 600$. $\Diamond$, $\langle|\delta v|^2\rangle$; $\circ$, $\langle|\delta v|^3\rangle$; $+$, $\langle|\delta v|^4\rangle$; $\times$, $\langle|\delta v|^5\rangle$; ∇, $\langle|\delta v|^6\rangle$; $\square$, $\langle|\delta v|^7\rangle$; $\triangle$, $\langle|\delta v|^8\rangle$; —, range of fit.

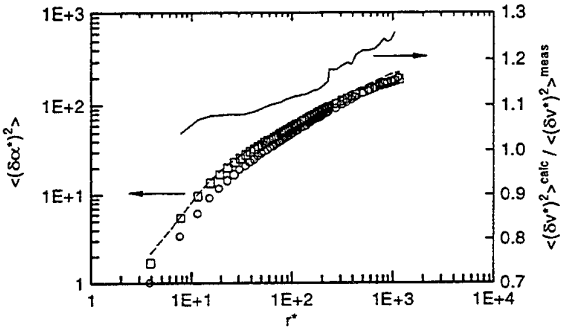


Figure 6: Isotropic calculation of $\langle(\delta v^*)^n\rangle$., $R_\lambda = 600$. $\circ$, $\langle(\delta u^*)^2\rangle^{meas}$; $\bullet$, $\langle(\delta v^*)^2\rangle^{meas}$; $- -$, $\langle(\delta v^*)^2\rangle^{calc}$; —, $\langle(\delta v^*)^2\rangle^{calc}/\langle(\delta v^*)^2\rangle^{meas}$.

Figure 4 shows the values for the skewness, $S_{|\delta u|}$, and the flatness, $F_{|\delta u|}$ ($\equiv F_{\delta u}$), of $|\delta u|$. A value of $r = \lambda$ is used for each R_λ. These values fall within the IR. The general trend is for both $S_{|\delta u|}$ and $F_{\delta u}$ to increase with R_λ. The severe increase from $R_\lambda = 800$ to 870 is due to a higher sampling frequency to Kolmogorov frequency ratio, f_s/f_K. In fact, the trend is repeatable for all r^* where confidence in the measurement is high, for example $r^* > 10$. We can conclude, even for the DR, that both $S_{|\delta u|}$ and $F_{\delta u}$ increase as R_λ increases.

For $R_\lambda = 600$, the values of ζ_u^a and ζ_v^a were estimated from least squares linear regressions to cross-plots of $\log\langle|\delta u|^n\rangle$ and $\log\langle|\delta v|^n\rangle$ vs $\log\langle|\delta u|^3\rangle$. The square of the correlation, ρ, indicates that the fit is of good quality for both u and v and at all n. The magnitude of ζ_v^a (Figure 5) is, allowing for the experimental uncertainty, discernibly smaller than that of ζ_u^a (see Table 2). The difference becomes proportionately larger as n increases; it increases from 13% for $n = 2$ to 22% for $n = 8$. Note that the inequality $\zeta_v^a(n) < \zeta_u^a(n)$ is consistent with the observation (Sreenivasan 1996) that the IR slope of the v-spectrum remains smaller than that of the u-spectrum in a wider range of flows and for $R_\lambda \lesssim 3000$. While the present values of ζ_u and ζ_v are (as noted earlier) larger than those of ζ_u^a and ζ_v^a, there is little question about ζ_v being smaller than ζ_u (Table 2). Although X-wire measurements were made at only $R_\lambda = 600$, a likely increase of ζ_v^a with R_λ can be inferred from the comparative data shown in Table 2. The values of ζ_v^a in the jet ($R_\lambda = 600$) are greater than those in the wake ($R_\lambda = 230$), especially at the largest n. Taking into account Sreenivasan's variation of the spectral slope for transverse velocity components and the near-constancy of ζ_u^a with R_λ (Tables 1 and 2), one may cautiously surmise that the difference between ζ_v^a and ζ_u^a may asymptotically disappear at sufficiently large R_λ (of order several thousands). This trend is worth verifying experimentally.

Local isotropy is assumed in K41 and the Kolmogorov equation. It is also implicit in most cascade-type models that have been proposed to account for small-scale intermittency. It is obviously of interest to assess the degree to which a departure from local isotropy can affect the difference between ζ_v and ζ_u.

For $n = 2$, local isotropy requires that

$$\langle(\delta v)^2\rangle = \left(1 + \frac{r}{2}\frac{\partial}{\partial r}\right)\langle(\delta u)^2\rangle \quad . \qquad (1)$$

The experimental values of $\langle(\delta u)^2\rangle$, $\langle(\delta v)^2\rangle$ are shown in Figure 6 (the normalization is on Kolmogorov scales); also included are the values of $\langle(\delta v)^2\rangle$ calculated using Eq. (1) and the ratio $\langle(\delta v)^2\rangle^{calc}/\langle(\delta v)^2\rangle^{meas}$. As expected, agreement with isotropy is approached as r^* decreases. The ratio increases as r^* increases; this is consistent with $\zeta_v(2)$ being smaller than $\zeta_u(2)$. The relative behaviour of $\langle(\delta v)^4\rangle$ and $\langle(\delta u)^4\rangle$ was examined by Antonia et al. (1997) in the context of local isotropy. It was noted that, in the IR, $\langle(\delta v)^4\rangle^{meas}$ also falls below the value calculated using isotropy, the deviation being somewhat greater than for $n = 2$. It would be reasonable to expect that the deviation would increase with n. It would also seem reasonable that the departure from local isotropy (which, in general, also depends on the mean shear) will decrease as R_λ increases and hence the inequality $\zeta_v < \zeta_u$ could vanish at sufficiently large R_λ (the asymptotic limit may depend on n).

4 Conclusions

Moments, up to order eight, of the longitudinal velocity increment in the self-preserving region of a plane jet indicate that the IR scaling exponent, as determined by the ESS method, is essentially independent of R_λ. A slight increase with R_λ is observed when the exponent is determined by the conventional manner. The relative magnitudes of the exponents associated with δu and δv suggest that the scaling for v is more anomalous, with reference to K41, than that for u. It is argued that the difference between these two scalings reflects to a large extent the anisotropy in the inertial range and should disappear as R_λ becomes large. The skewness and flatness factors of $|\delta u|$ for both inertial and dissipative range separations, increase with R_λ contrary to the recent observations of Tabeling et al.

Acknowledgement

The support of the Australian Research Council is gratefully acknowledged.

References

Anselmet, F., Gagne Y., Hopfinger, E. J. and Antonia, R. A. 1984. *J. Fluid Mech.*, **140**, 63-89.

Antonia, R. A., Browne, L. W. B., Britz, D. and Chambers, A. J., 1984. *Phys. Fluids,* **27**, 87-93.

Antonia, R. A., Ould-Rouis, M., Zhu, Y. and Anselmet, F. 1997. *Europhys. Lett.*, **37**, 85-90.

Antonia, R. A. and Pearson, B. R. 1997. (submitted)

Arneodo, A. et al. 1996. *Europhys. Lett.*, **34**, 411-416.

Batchelor, G. K. and Townsend, A. A. 1949. *Proc. Roy. Phys. Soc.*, **A199**, 238-255.

Benzi, R., Ciliberto, S., Tripiccione, R., Baudet, C., Massaioli, F. and Succi, S. 1993. *Phys. Rev. E*, **48**, R29.

Camussi, R., Baudet, C., Benzi, R. and Ciliberto, S. 1996. *Phys. Rev. E.* (in press)

Ciliberto, S., Benzi, R., Biferale, L. and Struglia, M. V. 1996. In S. Gavrilakis, L. Machiels and P. A. Monkewitz (eds.) *Advances in Turbulence VI*, 191-196.

Herweijer, J. 1995. Ph.D. Thesis, Technische Universiteit Eindhoven.

Kolmogorov, A. N. 1941. *CR Akad. Sci. USSR*, **30**, 301-305.

Kolmogorov, A. N. 1962. *J. Fluid Mech.*, **13**, 82-85.

Sreenivasan, K. R. 1996. *Phys. Fluids*, **8**, 189-196.

Sreenivasan, K. R. and Antonia, R. A. 1997. *Ann. Rev. Fluid Mech.*, **29**, 435-472.

Tabeling, P., Zocchi, G., Belin, F., Maurer, J. and Willaime, H. 1996. *Phys. Rev. E*, **52**, 1613-1621.

Van Atta, C. W., Antonia, R. A. 1980. *Phys. Fluids*, **23**, 252-257.

Vincent, A. and Meneguzzi, M. 1991. *J. Fluid Mech.*, **225**, 1-20.

Willaime, H., Belin, F., Maurer, J. and Tabeling, P. 1996. In S. Gavrilakis, L. Machiels and P. A. Monkewitz (eds.) *Advances in Turbulence VI*, 271-274.

Numerical Study of the Detached Flow Aerodynamical Sound

S Huang* and C Béguier**

* Gas Turbine Establishment of China 6, Xinjun street, Xindu, 610500 Sichuan, CHINA

** Institut de Recherche des Phénomènes Hors Equilibre -UMR n°6295 du CNRS12, Av. du Général Leclerc,13003, Marseille

Abstract :

A numerical study, based on the macro-simulation method, is carried out to determine the aerodynamical sound of a turbulent separated flow. The macro-simulation method uses a Large Eddy Simulation (LES) code to obtain the large structures of the flow, the small structures being modelled by a sub-grid scale eddy viscosity. The radiated aerodynamical sound is obtained in the far field, from the Lighthill-Curle formalism. The method permits to dissociate the different sources of the aerodynamical sound: the wall noise, due to the wall-pressure fluctuations, the shear noise, due to the large scale quadrupole sources, and the turbulence self noise, generated by the small scale quadrupole sources.The case of the normal backward facing step is presented and the different emitted noises are analysed and compared one to each other. Some theoretical hypotheses are tested.

1.Introduction

The aerodynamical sound theory [Lighthill. 1952 and 1962] was founded on the analogy between the sources of quadrupole type and the Reynolds stresses, of the equation system of the radiated far acoustic field. The Lighthill's theory is remarkably simple and the basic equation is rigorously exact, although it does not give explanations about the physical aspects of the sound generation itself.

Further, it has been proposed [Ribner. 1962] to describe the aerodynamical sound sources from the local pressure fluctuations. The eddy stretching phenomenon was identified as the fundamental mechanism of the sound generation [Powell. 1964]. The calculation of the intensity of the radiated far field sound generated by the homogenous isotropic turbulence has been obtained with a certain number of hypotheses [Proudman.1952]. However all these theories do not change the basic theory of Lighthill and the applications are coming up against the definition of the quadrupole sources appearing in the free flows.

An extension of the Lighthill's theory to the case of flows over a rigid wall was obtained [Curle. 1955] showing that the wall is equivalent to a surface dipole repartition ; the source intensity being proportional to the space derivative of the wall pressure fluctuations.

The analysis of the phenomena brings out the importance of the wall pressure field as excitator in the fluid-structure coupling. Also we can distinguish two aspects of the aerodynamical sound: firstly the radiated sound produced by the vibrations of the structure and secondly the sound generated by the eddies of the flow.

From the Lighthill-Curle's theory, the study of this pressure field is a first stage of a more complete process able to determine the sound generated by the velocity fluctuations and defining the quadrupole sources.

To solve the numerical problem of the aerodynamical determination, we chose the macro-simulation method[Béchara et al.1994]with, in a first step, the resolution of the big structures of the aerodynamical field by a simulation of "LES" type and a small structure modelling from a sub-grid scale eddy viscosity [Silveira et al.1993] Then, the acoustic field is solved by applying the Lighthill-Curle's integration in the control volume. The total radiated noise in the far field will be dissociated in three parts : first, the wall noise, due to the fluctuating wall pressure ; secondly, the shear noise, due to the large scale quadrupole sources and thirdly, the turbulence self noise, due to the modelled small scale quadrupole sources. This method can be applied to all type of flows, free or wall-flow, with detachment as the flow over a normal backward-facing step which is further studied in details.

2.Numerical Method

2.1. The Lighthill-Curle Formalism

For an homogeneous compressible viscous fluid, the Navier-Stokes equation system can be written with a_0 and ρ_0, being the sound velocity and the mean volumic mass as :

$$\begin{cases} \dfrac{\partial(\rho-\rho_0)}{\partial t}+\dfrac{\partial(\rho u_i)}{\partial x_i}=0 \\ \dfrac{\partial(\rho u_i)}{\partial t}+a_0{}^2\dfrac{\partial(\rho-\rho_0)}{\partial x_i}=-\dfrac{\partial T_{ij}}{\partial x_j} \\ \dfrac{\partial^2(\rho-\rho_0)}{\partial t^2}-a_0{}^2\dfrac{\partial^2(\rho-\rho_0)}{\partial x_i{}^2}=\dfrac{\partial^2 T_{ij}}{\partial x_i \partial x_j} \end{cases} \qquad (1)$$

successively for the continuity equation, the three equations of motion and the divergency equation. The homogeneity is relative to the mean quantities written with a zero index. Such equation system is equivalent to that for the sound propagation with the source terms on the right side, expressed from the Lighthill's tensor :

$$T_{ij}=\rho(u_iu_j)+\left[(p-p_0)-a_0^2(\rho-\rho_0)\right]\delta_{ij}+\tau_{ij} \qquad (2)$$

At high Reynolds number, τ_{ij}, the viscous stresses can be neglected before the turbulent stresses $(\rho u_i u_j)$; except in the viscous sublayer near the wall, but this region is sufficiently small to consider its influence on the radiated noises as negligeable. And, without heat sources, the pressure fluctuations will be considered as isentropic. consequently, the term in brackets is closed to zero. On the other hand. the differences between $\rho(u_iu_j)$ and $\rho_0(u_iu_j)$ are proportional to the Mach number and for subsonic flows, the Lighthill's tensor can be reduced to:

$$T_{ij} \equiv \rho_0(u_iu_j) \qquad (3)$$

From this simplification, it can be shown that an integral solution of the propagation system (1) can be obtained in the following form :

$$(\rho(\vec{x},t)-\rho_0)=\frac{1}{4\pi a_0^2}\left[\frac{\partial^2}{\partial x_i\partial x_j}\left(\frac{1}{a_0^2}\iiint_{(V)}\frac{\rho(u_iu_j)(\vec{y},t-\tau)}{r}d^3\vec{y}\right)-\frac{\partial}{\partial x_i}\iint_{(S)}\frac{p_i(\vec{y},t-\tau)}{r}d^2\vec{y}\right] \qquad (4)$$

according to the Lighthill-Curle formalism.

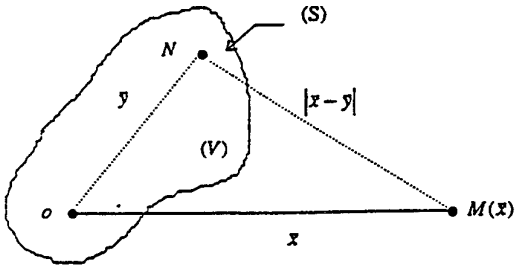


Fig. 1: Integration scheme.

As shown in Fig. 1, (V) is the control volume of the studied flow of (S) surface. ;. $r=\|\vec{x}-\vec{y}\|$ expresses the distance between the listening point M$(\vec{x})$ in the far field and the running point N$(\vec{y})$ of the control volume, for the first integral and, of the surface, for the second integral. Such a solution can be obtained by introducing the Green function with the Sommerfeld's boundary conditions. In the expression (4) $(\rho(\vec{x},t)-\rho_0)$ expresses the volumic mass fluctuations in the far field. By squaring these fluctuations. the radiated noise can be obtained. The volumic distribution of the quadrupole sources are given by $\dfrac{\partial^2}{\partial x_i\partial xj}\rho_0(u_iu_j)$ and the surfacial distribution of the dipole sources by $\dfrac{\partial}{\partial xi}p_i$ with

$p_i=\sigma_{ij}.n_j$ and $\tau=r/a_0$, .being a time delay.

If $|\vec{x}|\geq\lambda_0$, where λ_0 is the fundamental sound wave length and if $\lambda_0 >> L$, where L is a characteristic length of the volume (V). then it can be shown that (4) can be simplifyied in the far field as :

$$(\rho(\vec{x},t)-\rho_0)\equiv\frac{1}{4\pi a_0^2}\left[\frac{x_ix_j}{r^3}\frac{\partial^2}{\partial t^2}\left(\iiint_{(V)}\rho(u_iu_j)(\vec{y},t-\tau)d^3\vec{y}\right)-\frac{x_i}{|\vec{x}|^2}\frac{\partial}{\partial t}\left(\iint_{(S)}p_i(\vec{y},t-\tau)d^2\vec{y}\right)\right] \qquad (5)$$

The effects of refraction and convection, by the flow itself on the sound propagation. are not considered here, as in certain recent works [.Lilley.1971 and Béchara.1992] In the present method. the interaction between the different sources of noise. as wall and shear noises. can be determined but not the interactions with the flow itself.

2.2-The "LES" Simulation Method

For flows at high Reynolds number, as the detached boundary layer over a backward-facing step $(R_e=6\times10^5)$ the separation between big and small structures can be realized. And an inertial zone can be defined between the dissipation and the production regions in the spectral domain. A filtering operation is then defined from a convolution product in the wave number space Ω. To realize such a separation and then, for an instantaneous variable Φ with a filtering function F and a frequency bandwidth ΔF ,we can write:

$$\overline{\Phi}=\int_\Omega F(\vec{x}-\vec{x}',\Delta F)\Phi(\vec{x}',t)dx'$$

giving the decomposition: $\Phi=\overline{\Phi}+\Phi'$

where Φ' is the residual field of small scale, if $\overline{\Phi}$ expresses the large scale contributions. If this filtering operation is applyied to the Navier-Stokes incompressible equation system, we obtain in this case:

$$\begin{cases} \dfrac{\partial\overline{u}_i}{\partial x_i}=0 \\ \dfrac{\partial\overline{u}_i}{\partial t}+\overline{u}_j\dfrac{\partial\overline{u}_i}{\partial x_j}=-\dfrac{1}{\rho}\dfrac{\partial\overline{p}}{\partial x_i}+\nu\dfrac{\partial^2\overline{u}_i}{\partial x_i\partial x_j}-\dfrac{\partial\tau_{ij}}{\partial x_j} \\ \tau_{ij}=L_{ij}+C_{ij}+R_{ij} \end{cases} \qquad (6)$$

where L_{ij} is the Leonard's tensor, C_{ij} is a crossed tensor and $R_{ij} = < u_i' u_j' >$ is the sub-grid tensor relative to the small structures.

To close the system, we shall consider that R_{ij} is given by : $R_{ij} = -2\nu_t \bar{S}_{ij} + \frac{1}{3}\delta_{ij}\tau_{kk}$

with $\bar{S}_{ij} = \frac{1}{2}\left(\frac{\partial \bar{u}_i}{\partial x_j} + \frac{\partial \bar{u}_j}{\partial x_i}\right)$ and, (7)

$\nu_t = 0.067\, C_K^{-3/2} \Delta \sqrt{\bar{F}_2(\bar{x}, \Delta, t)}$

where F_2 is a structural function of 2nd order[Métais and Lesieur.1992] with $\bar{F}_2 = < \|\bar{u}(\bar{x} + \bar{r}, t) - \bar{u}(\bar{x}, t)\|^2 >_{r=\Delta}$ and C_K , the constant of Kolmogorov, equal to 1.4. ; $\Delta = (\Delta V)^{1/3}$ is the computational mesh size and $\bar{F}_2$ is the turbulence energy square for the cut-off frequency.

In fact, the local equations (6) are integrated in small elementary volumes of discretization : $\Delta V = \Delta x \Delta y \Delta z$

At the iteration (n), a resolution of the equation system (6) is obtained by using a semi-implicite method.The pressure equation of Poisson's type, is linear as $Ap = s$, for which the symmetrical matrix (A) only depends on the geometry of the control volume.

The pressure gradients are evaluated by a scheme of 2nd order. The inversion of the matrix (A) is obtained from the conjugated gradient iterative method with a $(SSOR)$ conditioner[Lascaux and Théodor.1994]. The convective fluxes are determined from a .3rd order Quick-Sharp scheme[Leonard.1988 and Gaskell and Lau.1988]. The time interpolation is realized from a 3rd order Runge-Kutta scheme.

From this resolution we obtain the expression of $\bar{u}_i^{(n)}$ as a function of the pressure at the time (n) and of the convective fluxes at the time (n-1) :

$$\bar{u}_{ijk}^{(n)} = SM_{xijk}^{(n-1)} \frac{\Delta t}{\Delta x_j}\left(\bar{p}_{ijk}^{(n)} - \bar{p}_{i-1jk}^{(n)}\right) \quad (9)$$

2.3-The Acoustic code :

To solve (5) at each iteration time it is possible to pass through the Fourier's space, from which , and for a given function $s(x) \in L_1\left(R^n\right)$, a pair of Fourier's transforms can be defined as:

$$\begin{cases} \bar{s}(k) = \int_{-\infty}^{+\infty} s(x) \exp(-2\pi j k x) dx \\ s(x) = [\bar{s}(k)]^{-1} \end{cases}$$

$$\begin{cases} \dfrac{\partial s(x)}{\partial x} = 2\pi j [k \bar{s}(k)]^{-1} \\ \dfrac{\partial^2 s(x)}{\partial x^2} = -4\pi^2 [(k^2 \bar{s}(k)]^{-1} \end{cases} \quad (10)$$

By applying these transformations to $p_s(t)$ and to $\rho_0(\bar{u}_i\bar{u}_j + < u_i' u_j' >)$, it is possible to calculate their first and second time derivatives. and then. their integration in the control volume. The fluctuating specific mass in the far field is then obtained and. the radiated sound intensity is deduced.

3.- Separated Flow over a Backward-Facing Step

3.1-Discretization :

The control volume is a parallelepipedic box with a length of 20H in the downstream direction in order to contain all the perturbations of detachment and reattachment. The step presents a lateral expansion of 10H to minimize the 3D perturbations in the mean plane. A supplementary width of 2H is moreover considered to can apply the slip conditions on the east and on the west sides of the control volume.

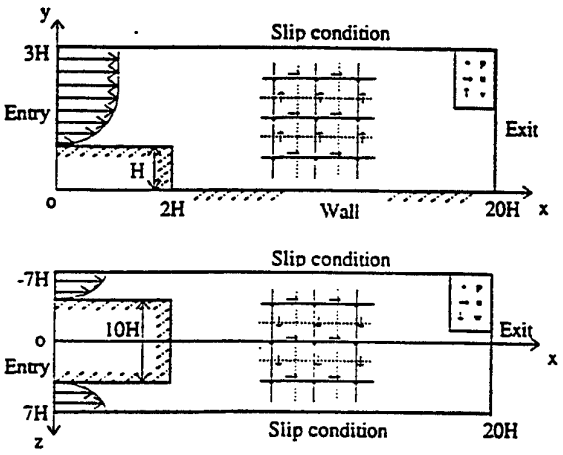


Fig.2 Scheme of the control volume

At the entry section. situated at 2H above the step we consider a fully developed boundary layer, expanding normally up to 0.3H.These conditions were chosen in similitude with the experimental case of the swept backward-facing step[E.Le Huu-Nho.1994]., for which the Reynolds number relative to the step was equal to 37000.

The discretization of the control volume was realized in such a way that the number of elementary volumes was approximately taken equal to (150000) , with $(69 \times 51 \times 46)$ successively, for the segmentation in the $\vec{ox}$, $\vec{oy}$ and $\vec{oz}$ directions : .

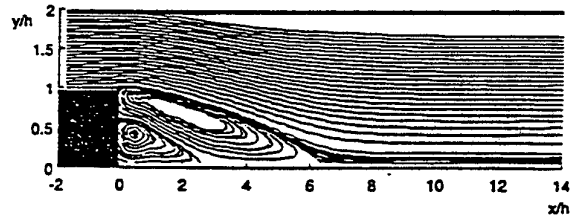
Free boundary conditions with $(\partial \bar{u}/\partial y = 0)$ are considered on the north, east and west sides and wall conditions $(\bar{u} = \bar{v} = \bar{w} = 0)$, on the south side. Turbulent boundary layer velocity profiles $\bar{u}(y,z)$ are defined at the entry section with a white noise of 2% for the initial turbulence intensity. At the exit section, a convection condition of type: $\partial \bar{u}/\partial t + U_S\, \partial \bar{u}/\partial x = 0$, is considered with U_S being the mean velocity in the section.

The inversion of the matrix A, the storage and the averaging operations for the different variables of the aerodynamically field needs the use of computer as *IBM/SP2* machine for which, after 1500 iterations to stabilize the beginning of the calculation and, with a *CFL* criteria of 0.2, the

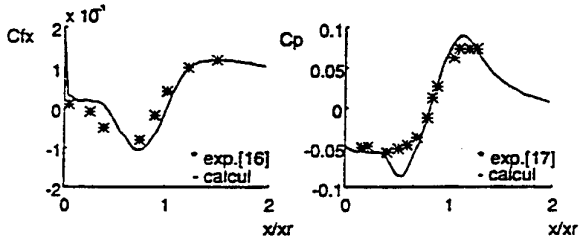
totality of a passage, including (7000) iterations, needs (2^h) of *CPU* time.

3.2-Mean Dynamic Fields and Large Scales Structures

Fig. 3 shows the general characteristics of the detached flow over the normal backward-facing step in the symmetry plane. The recirculating region is expanding up to the section x/h=6, where the reattachment is happening. An additional counter-rotating corner eddy appears which is also found from experimental studies. The wall friction and pressure coefficient evolutions fit rather well the experimental data [Sinha et al.1981 ; Jovic and Driver.1995] as it can be seen in Fig. 3b) and Fig. 3c).



a) mean velocity calculated



b) skin friction coefficient c) wall pressure coefficient

Fig.3 Mean Flow

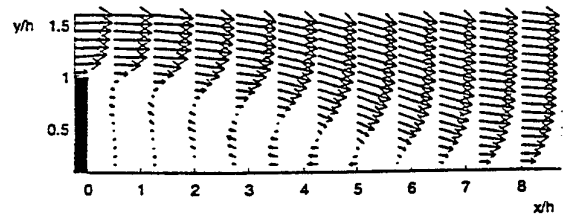


Fig. 4 Mean Velocity Profiles

The mean velocity profiles in the (o, x, y) mean plane are drawn on Fig. 4 at different downstream sections. Undoubtedly, they show that the reattachment is close to the section x/h=6 where the stream near the wall is separating in the upstream and downstream directions On Fig. 5 we have plotted the iso-rotational curves at a given time: $t^* = 300$ $(with\ t^* = t.U_{e/H})$. and its evolution at five successive steps further $(\Delta t^* = 5)$. In such a configuration the large vortex structures are appearing, as their time evolution, the eddies being generated from the Kelvin-Helmholtz (K-H) instability. This vortex structure interacts with the lower plate at the reattachment section. The vortex layer is submitted to the vortex-pairing phenomenon and some eddies, which are not destroyed by the wall interaction, remain during a certain time in the boundary layer after reattachment. As it can be seen on Fig. 6 for the corresponding instantaneous streamlines, there are also small eddies which are produced in the recirculating region.

To each detaching vortex, starting from the step corner, a pressure doublet is produced in the (o, x, y) plane as shown in Fig. 7. The pressure field induces wall fluctuations in relation

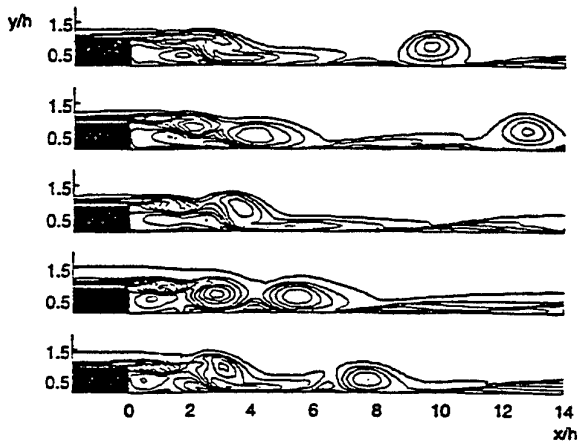


Fig. 5 Instantaneous Vorticity Field .

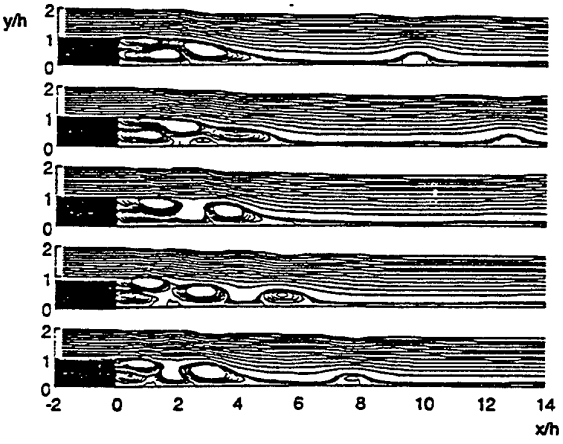


Fig. 6 Instantaneous Streamlines Field..

with the intensity of the doublet sources according to the Curle's theory.

The variations of the sub-grid eddy viscosity, drawn on Fig. 8, are important in the vortex layer, with peaks happening in the stretching regions between two vortices. This fact induces a relatively complicated configuration of the isoviscosity curves.

From a comparison between calculations and experimental data [Driver and Seegmiller.1985] of the turbulence intensity square profile : $(\langle u'^2\rangle + \langle v'^2\rangle)/(2U_e^2)$ at different sections downstream of the step. Here and there, some differences appear which can be explained from geometrical differences between the two cases, but, the levels are approximately the same and it can be considered sufficient for the validity of our "LES" determination.

The variation of the Strouhal number along the vortex layer can be studied from both, the velocity and the pressure spectra. Just behind the step at X/H = 0.1, the Strouhal number($S = f_0.H/U_e$) is equal to 0.23 and after reattachment this value is divided by two, which is a consequence of the vortex pairing, stimulated here by the presence of the reattachment.

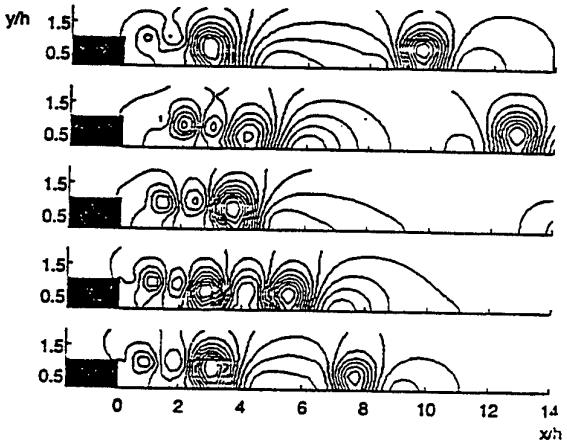


Fig.7 Instantaneous Pressure Field.

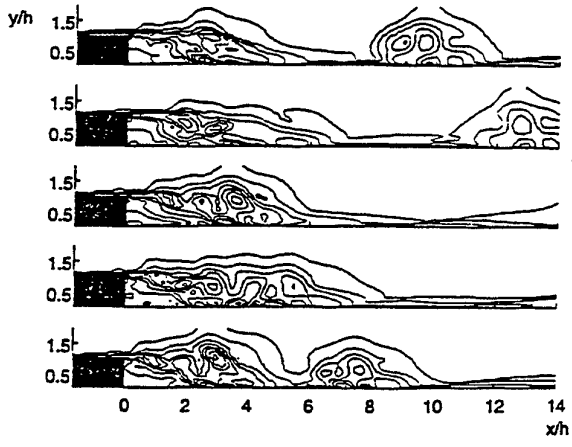


Fig. 8 Instantaneous Iso-Viscosity Curves.

The wall-vortex interaction provides a deceleration of the vortices and can eventually produce the capture of the following vortex. The new formed vortex is sufficiently of high intensity to pass through the reattachment point and to continue in the boundary layer where it is developing relatively independently to the other vortices.

3.3-The Radiated Acoustic Fields

The aerodynamical field determination from the "LES" code permits to calculate the intensity of the quadrupole and of the dipole sources by means of the Lighthill-Curle formalism. The large structures are expressively determined from the L.E.S. code, while the small structures are modelled by a sub-grid eddy viscosity. So it is possible to distinguish three kinds of sound sources. one, coming from the large eddy structures, associated with the shear noise, another, coming from the small scale eddy structures, associated with the turbulence self noise and thirdly, ;the wall pressure fluctuations giving the wall noise.

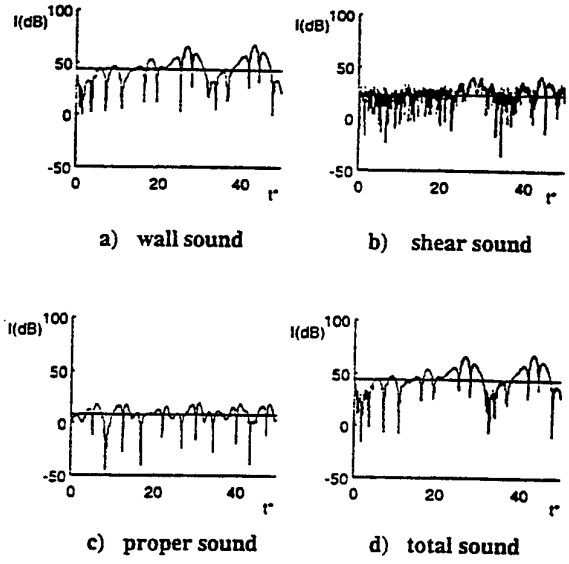


Fig. 9 Radiated Noise Time Evolution.

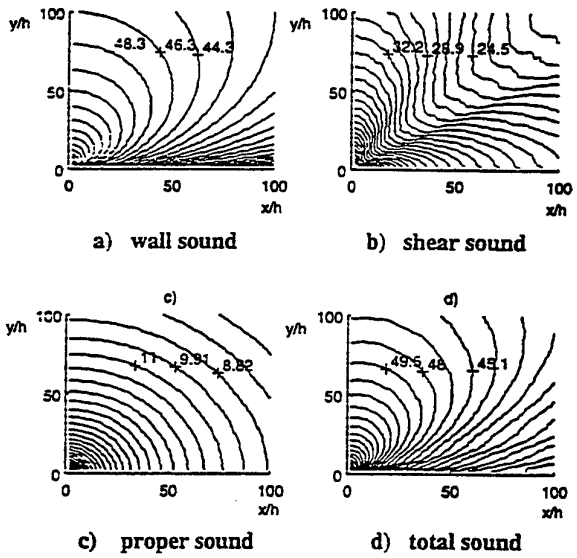


Fig. 10 Aerodynamical Noise Intensities

The acoustic field was calculated in the symmetry plane of the backward-facing step and the radiated noises were determined in the far field of the first plane quarter.

From the previous decomposition we have drawn on Fig. 9, the evolution in time of these three different noises, obtained at a listening point (x/h=100; θ=45°) in the far field.

The noise intensity is given in decibels with respect to the reference level of $10^{-12} W/m^2$, [Proudman.1952].We can note that the wall noise is $20dB$ higher than the shear noise which, itself, is $15dB$ higher than the turbulence self noise. The total noise intensity is close to the wall noise as predicted by Curle for wall flows.

The calculations show that the shear and the turbulence self noises are much smaller in intensity than the wall noise.

The directions of propagation are also different, as it can be seen in Fig. 10. For the wall noise the maximum intensity is obtained normally to the wall; while, for the shear noise, there are two maximums in the directions normal to the wall and along the downstream axis, with a minimum at 45°. Only the turbulence self noise appears as quasi isotropic. The shear noise presents contributions in the high frequency range, while the wall noise contributions are in the low frequency range. The turbulence self noise appears in the low frequency range, certainly due to the turbulence modelling.

The total radiated noise seems relatively identical to the wall noise ; however it presents certain modulations induced by the shear noise when the signal is lower than a certain level.

4.Conclusions

This numerical determination, from the macro-simulation method, permits to calculate the instantaneous variations of the different sources of sound generated by the aerodynamics, specifically induced by the detaching eddies.

The method uses simultaneously a "LES" simulation for the aerodynamical field and an acoustic code obtained from the Lighthill-Curle formalism. The sound intensities are determined in the far field, for the wall noise, generated by the wall-pressure fluctuations, for the shear noise, generated by the large scale quadrupole sources and for the turbulence self noise,or sub-grid noise, induced by the small scale quadrupole sources, modelled from a sub-grid eddy viscosity.

The method seems general and can be applyied to all type of turbulent flows, with or without detachment, or which are developing on a rigid wall. The case of the detaching flow over a backward-facing step is studied in details. The results give a validation of the Curle's hypothesis according to the quadrupole sources can be neglected before the wall dipole sources for wall flows .This calculation gives also the levels of the different aerodynamical radiated sounds and their principal directions of propagation.

At a listening point, in the far field of the backward-facing step flow, the shear noise is $20dB$ lower than the wall noise and $15dB$ higher than the turbulence self noise. The shear noise presents frequency contributions higher than the wall noise with a weakness in the 45° direction, while the turbulence self noise is quasi isotropic.

It should be interesting to compare these numerical results with experimental data, but the difficulties of measuring and separating the different aerodynamical radiated noises give back difficult this confrontation.and still show the importance of the numerical prediction.

References

Béchara, W., "Modélisation du bruit d'écoulements turbulents libres," thèse de doctorat Ecole Centre de Paris, 1992.

Béchara, W., Bailly, C., Lafon, P. and Candel, S. M., "Stochastic approach to noise modelling for free turbulent flows," *AIAA Journal*, vol. 32, n°3, 1994, pp. 455-463.

Curle, N., "The influence of solid boundaries upon aerodynamic sound," Proc. Roy. Soc. of London, series A, vol. 231, 1955, pp. 505-513.

Driver, D. and Seegmiller, H. L., "Features of a reattaching turbulent shear layer in divergent channel flow," *AIAA Journal*, vol. 32, n°2, 1985, pp. 163-171.

Gaskell, P. H. and Lau, A. K. C., "Curvature-compensated convective transport: smart, a new boundedness-preserving transport algorithm," *International Journal for Numerical Methods in Fluids*, vol. 8, 1988, pp. 617-641

Jovic, S. and Driver, D., "Reynolds number effect on the skin friction in separated flows behind a backward-facing step," *Experiments In Fluids*, vol. 18, n°6, 1995, pp. 464-467.

Lascaux, P. and Théodor, P., "Analyse numérique matricielle appliquéeàl'artl'ingénieur,"*Masson,ParisMilanBarcelone*,1994.

Le Huu-Nho, E., "Etude expérimentale de l'écoulement autour d'une marche descendante en dérapage," thèse de doctorat université d'Aix Marseille II , 1994.

Léonard, B. P., Simple high-accuracy resolution program for convective modelling of discontinuities," *International Journal for Numerical Methods in Fluids*, vol. 8, 1988, pp.1291-1318.

Lighthill, M. J., "On sound generated aerodynamically," Proc. Roy. Soc. of London, series A, vol. 211, 1952, pp. 564-587.

Lighthill, M. J., " Sound generated aerodynamically," Proc. Roy. Soc. of London, series A, vol. 267, 1962, pp.147-182.

Lilley, G. M., "The generation and radiation of supersonic jet noise," AFAPL-TR-72-53, 1971.

Métais, O. and Lesieur, M., " Spectral large-eddy simulation of isotropic and stable stratified turbulence," *Journal of Fluid Mechanics*, n°239, 1992, pp. 157-194.

Powell, A., "Theory of vortex sound," J.A.S.A., vol. 36, n°1, 1964, pp. 177-195.

Proudman, I., "The generation of noise by isotropic turbulence," Proc. Roy. Soc. of London, series A, vol. 214, 1952, pp. 119-132.

Ribner, H. S., "Aerodynamic sound form by fluid dilatation's." UTIA report, n°86, ceniv. Toronto, 1962.

Silveira, N. A., Grand, D., Métais, O. and Lesieur, M., "A numerical investigation of the coherent vortices in turbulence behind a backward-facing step," *Journal of Fluid Mechanics*, vol. 256, 1993, pp. 1-25.

Sinha, S. N., Gupta, A. K. and Oberai, M. M., "Laminar separating flow over backsteps and cavities," *AIAA Journal*, vol. 19, n°12, 1981, pp. 1527-1530.